

000015

## Fully Automated LGE Thresholding using Weighted Total Variation Denoising and Persistent Homology

C. Sheagren \* (1); T. Escartin, (1); P. Krahn, (1); G. Wright, (1)

(1) Medical biophysics, Sunnybrook Health Sciences Centre, Toronto, Canada

### Abstract

#### Background

Late Gadolinium Enhancement (LGE) MRI is a powerful tool for cardiac disease risk stratification [1]. Regions of hyperintensity in LGE images correlate well with cardiac fibrosis, and regions of heterogeneous infarct are associated with all-cause cardiac mortality [2]. The clinical standard method for delineating fibrotic and healthy tissue regions is Full-width Half-maximum (FWHM) thresholding, which has been shown to be more repeatable than N-standard deviation-based thresholding methods [3] but still requires substantial operator input, particularly with high-resolution volumetric LGE. Manual intervention adds inter-operator variance, which can lead to differing interpretations of scar morphology and heterogeneity. This motivates the need for robust, fully-automated thresholding to repeatably locate and quantify fibrotic structures. Our approach uses edge-preserving denoising and topologically informed signal intensity selection to automate FWHM thresholding.

#### Methods

The 3D LGE image volumes examined in this study were acquired at 3 Tesla in a pre-clinical porcine model of MI (N=5). MI was created by 100-minute LAD occlusions distal to the first diagonal branch before allowing the animals to recover for 5 weeks. 3D LGE volumes were acquired 15 minutes post-Gadolinium injection. Manual epicardial and endocardial contours of the LV were drawn and used for both automated and ground truth manual FWHM thresholding. Weighted Total Variation (wTV) denoising was used to flatten statistical noise while preserving image edges, notably between blood, myocardium, and infarct. The approach from [4] was implemented in pytorch and extended to 3D. Persistent Homology (PH) was used to calculate a 2D representation of the images' topological features, stratified by signal intensity (SI) [5]. Finally, k-means clustering was used to automatically identify representative remote myocardium and dense scar SIs, which are used for the FWHM calculation. See Fig. 1 for a pictorial description of the workflow, and see Fig. 2 for sample segmentations. Topological FWHM thresholding (topo-FWHM) was compared against manual FWHM tissue segmentations. Volumetric alignment was evaluated using Dice and Jaccard similarity coefficients; scar and gray zone mass were calculated and analyzed with linear regression and Bland-Altman analysis; and an external observer also scored the segmentation quality for both manual FWHM and topo-FWHM segmentation methods.

#### Results

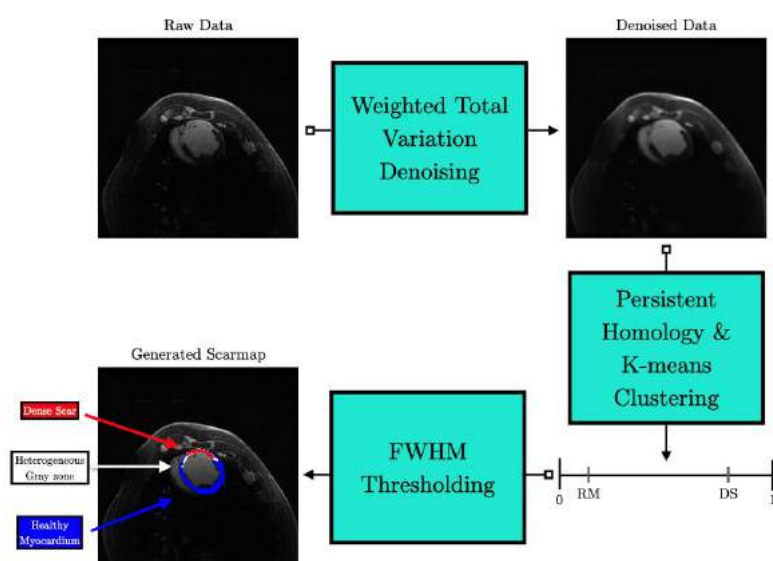
topo-FWHM segmentations have similar quality to the ground truth manual threshold maps and demonstrate good overall alignment with average Dice coefficients of [0.95, 0.27, 0.57] for [myocardium, gray zone, scar], respectively. High Pearson correlation coefficients were

observed, with low Bland-Altman bias, but topo-FWHM underestimates scar volume as compared to manual FWHM. Observer scores for manual and topo-FWHM segmentations were similar, but the small number of images limits potential statistical conclusions.

## Conclusions

In conclusion, our fully-automated method provides robust segmentation of LGE images, which is critical for identifying cardiac fibrosis.

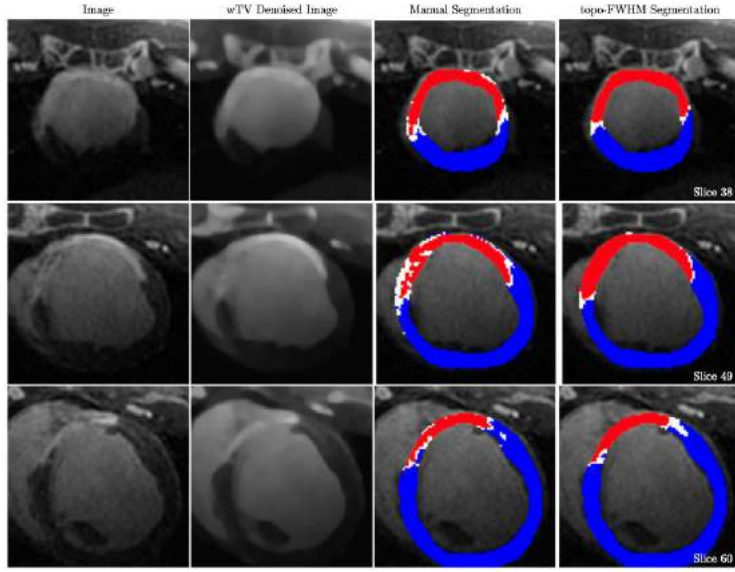
**Figure/Table 1**



**Caption 1**

Figure 1: Raw data is first denoised using wTV denoising, then PH is calculated and a persistence diagram generated. K-means clustering is performed with 5 cluster centers, and the extremal cluster centers are used as representative remote myocardium (RM) and dense scar (DS) SI. Standard FWHM thresholding was then performed.

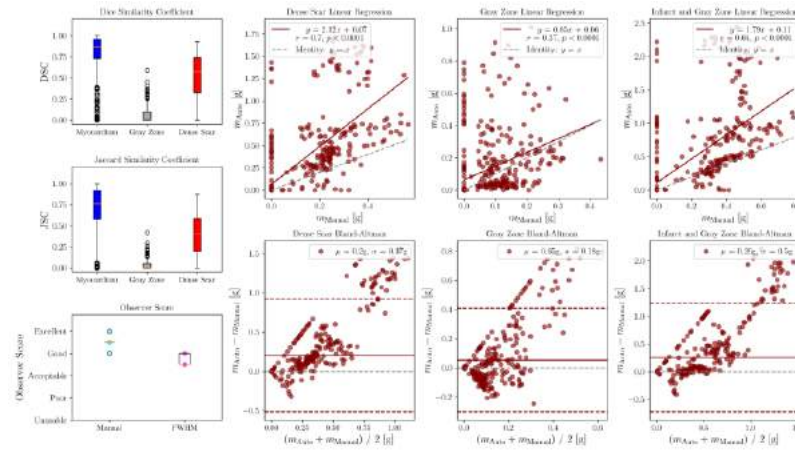
**Figure/Table 2**



**Caption 2**

Figure 2: Original and thresholded LGE images from multiple slices of a single animal. wTV denoising preserves large edges corresponding to tissue borders while smoothing statistical noise. topo-FWHM borders are visually similar to manual FWHM segmentation borders, with more pronounced edges between scar and peri-infarct gray zone.

**Figure 3**



**Caption 3**

Figure 3: Thresholding metrics. Good overlap was observed between manual FWHM and topo-FWHM segmentations as assessed by Dice and Jaccard similarity coefficients. High

Pearson correlation coefficients were observed in linear regression, and low bias was observed with Bland-Altman analysis.

### **Bibliographic References**

[5] Shizuo Kaji, Takeki Sudo, and Kazushi Ahara. Cubical Ripser: Software for computing persistent homology of image and volume data, 2020., [4] Prashant Athavale, Robert Xu, Perry Radau, Adrian Nachman, and Graham A. Wright. Multiscale properties of weighted total variation flow with applications to denoising and registration. *Medical Image Analysis*, 23(1):28–42, 2015., [3] Andrew S. Flett, Jonathan Hasleton, Christopher Cook, Derek Hausenloy, Giovanni Quarta, Cono Ariti, Vivek Muthurangu, and James C. Moon. Evaluation of Techniques for the Quantification of Myocardial Scar of Differing Etiology Using Cardiac Magnetic Resonance. *JACC: Cardiovascular Imaging*, 4(2):150–156, 2011., [2] André Schmidt, Clerio F. Azevedo, Alan Cheng, Sandeep N. Gupta, David A. Bluemke, Thomas K. Foo, Gary Gerstenblith, Robert G. Weiss, Eduardo Marbán, Gordon F. Tomaselli, João A.C. Lima, and Katherine C. Wu. Infarct Tissue Heterogeneity by Magnetic Resonance Imaging Identifies Enhanced Cardiac Arrhythmia Susceptibility in Patients With Left Ventricular Dysfunction. *Circulation*, 115(15):2006–2014, 2007., [1] Andrew T. Yan, Adolphe J. Shayne, Kenneth A. Brown, Sandeep N. Gupta, Carmen W. Chan, Tuan M. Luu, Marcelo F. Di Carli, H. Glenn Reynolds, William G. Stevenson, and Raymond Y. Kwong. Characterization of the Peri-Infarct Zone by Contrast-Enhanced Cardiac Magnetic Resonance Imaging Is a Powerful Predictor of Post-Myocardial Infarction Mortality. *Circulation*, 114(1):32–39, 2006.

Speaker: C. Sheagren

Category: Arrhythmia, Late Gadolinium Enhancement, Automated Processing



000021

## **Additional value of T1 and T2 mapping techniques for the detection of myocardial involvement in systemic sclerosis**

A. Pepe \* (1); L. Gargani (2); C. Bruni (3); C. Cavallaro (4); M. Gobbo (5); A. D'agostino (6); G. D'Angelo (2); N. Martini (7); F. Grigioni (4); G. Sinagra (5); R. De Caterina (6); S. Mavrogeni (8); M. Matucci-Cerinic (3); A. Meloni (7)

(1) U.o.c. imaging multimodale cardiovascolare e neuroradiologico, Fondazione G. Monasterio CNR-Regione Toscana, Padua, Italy; (2) Institute of clinical physiology, National Research Council, Pisa, Italy; (3) Department of experimental and clinical medicine, division of rheumatology, University of Florence, Firenze, Italy; (4) Cardiovascular department, University Campus Bio-Medico, Roma, Italy; (5) Cardiovascular department, University of Trieste, Trieste, Italy; (6) Cardiovascular division, University of Pisa, Pisa, Italy; (7) U.o.c. imaging multimodale cardiovascolare e neuroradiologico, Fondazione G. Monasterio CNR-Regione Toscana, Pisa, Italy; (8) Department of cardiology, Onassis Cardiac Surgery Center, Athens, Greece

### **Abstract**

**Background.** The pathogenesis of myocardial involvement in systemic sclerosis (SSc) is mainly related to recurrent myocardial inflammation and microvascular ischemia, ending in irreversible myocardial fibrosis. Lake Louise Criteria (LLC) have been extensively used for the CMR-based diagnosis of myocardial inflammation and have been recently revised with the implementation of T1 and T2 mapping techniques.

This study aimed to evaluate the prevalence of cardiac involvement by native T1 and T2 mapping and to assess the diagnostic performance of mapping in conjunction with the conventional LLC in SSc patients.

**Methods:** Fifty-two consecutive SSc patients ( $52.63 \pm 13.44$  years, 80.8% females) underwent CMR.

According to original LLC, a positive diagnosis of inflammation was established with the presence of at least two out of 3 of the following CMR features: edema by T2-weighted sequences, hyperemia, and necrosis/fibrosis by late gadolinium enhancement (LGE). According to the updated LLC, the diagnosis of myocarditis required the combined presence of a T1 criterion (presence of LGE or increased T1 value or increased extracellular volume-ECV value) and a T2 criterion (hyperintensity in T2 weighted-STIR or increased T2 value). Cut-off values previously determined at our MR center were applied for the definition of increased T1, T2 and ECV values.

**Results.** Twenty-two (42.3%) patients had an increased native global heart T1 value. Thirty-one (59.6%) patients had an elevated global myocardial T2 value. Non-ischemic focal

myocardial fibrosis by LGE was detected in 25 (48.1%) patients and edema by STIR T2-weighted images in 7 (13.5%) patients.

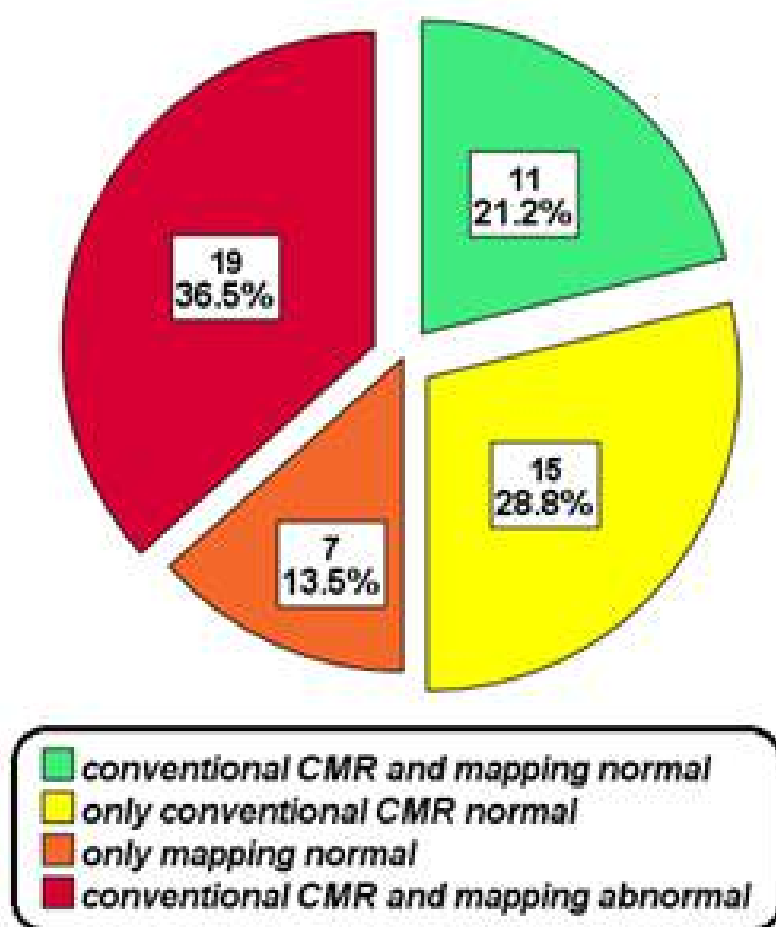
Only 21.2% of patients had normal conventional CMR (no LGE and no edema by STIR T2-weighted) and normal native mapping indices. An increase in native T1 and/or T2 was present in the 57.7% of the patients (15 out of 26) with normal conventional CMR (Figure).

The original LLC was fulfilled in 7 (13.5%) patients and all of them had also a positive updated LLC. The updated LLC was fulfilled in 31 patients (59.6%). The Cohen's Kappa was 0.19 (95%CI 0.05-0.33). The overall agreement between the two criteria was 53.85%, the positive agreement 36.84% and the negative agreement 63.64%.

The McNemar's test revealed a significant difference between the two criteria (absolute difference in proportion 46.15%; Chi-square 22.04;  $P < 0.0001$ ).

**Conclusion.** Our findings suggest that in SSc the mapping techniques can have an additional value in comparison with the conventional CMR in the detection of myocardial involvement. Further studies are recommended to explore the prognostic value of the mapping techniques.

**Figure/Table 1**



## **Caption 1**

Figure 1

Speaker: A. Pepe

Category: Parametric Mapping, Systemic Sclerosis , Inflammation

000022

## Increased myocardial extracellular volume is associated with myocardial iron overload in thalassemia major

A. Meloni \* (1); L. Pistoia (1); N. Martini (1); V. Positano (1); A. De Luca (2); G. Guerrini (3); P. Giovangrossi (4); M. Murgia (5); G. Sinagra (2); A. Pepe (6)

(1) U.o.c. imaging multimodale cardiovascolare e neuroradiologico, Fondazione G. Monasterio CNR-Regione Toscana, Pisa, Italy; (2) Cardiovascular department, University of Trieste, Trieste, Italy; (3) U.o. pediatria e neonatologia, Ospedale Della Misericordia Grosseto, Grosseto, Italy; (4) Servizio di immunoematologia e medicina trasfusionale, Santa Maria Goretti Hospital, Latina, Italy; (5) Centro provinciale per le microcitemie, Ospedale San Martino di Oristano, Oristano, Italy; (6) U.o.c. imaging multimodale cardiovascolare e neuroradiologico, Fondazione G. Monasterio CNR-Regione Toscana, Padua, Italy

### Abstract

**Background.** T2\* cardiovascular magnetic resonance (CMR) has been used for two decades as a non-invasive tool for quantifying myocardial iron overload (MIO). More recently, the myocardial extracellular volume (ECV) by CMR has been introduced as a surrogate marker of interstitial fibrosis. This is the first study relating ECV and T2\* values by a segmental approach including the entire left ventricular (LV) wall in thalassemia major (TM) patients. Moreover, the correlation of ECV with cardiac function and replacement fibrosis was investigated.

**Methods.** Eighty-six TM patients (51 females,  $40.6 \pm 8.0$  years) consecutively enrolled in the Extension-Myocardial Iron Overload in Thalassemia Network underwent CMR at 1.5T. The imaging protocol included: native and post-contrast T1 mapping, T2\* for MIO quantification, cine images for cardiac function quantification, and late gadolinium enhancement (LGE) technique for the detection of replacement myocardial fibrosis. T1 and T2 values were assessed in all 16 myocardial segments. Segmental ECV values were calculated with input of native and post-contrast myocardial segmental and blood pool T1 values and same-day hematocrit. Global value was the mean of all segmental values.

**Results.** Global ECV values were significantly higher in females than in males ( $34.0 \pm 7.3\%$  vs  $30.8 \pm 7.1\%$ ;  $P=0.037$ ), but were not correlated with age.

Significant MIO (global heart  $T2^* < 20$  ms) was found in 8 (9.3%) patients. Global ECV values were significantly higher in patients with significant MIO than in patients without significant MIO ( $42.7 \pm 9.7\%$  vs  $31.7 \pm 5.8\%$ ;  $P < 0.0001$ ) (Figure 1A). The ECV value was not available for 55 segments, due to the presence of significant artifacts in native and/or post contrast T1 images. Out of the considered 1321 segments, 186 (14.15) had a  $T2^* < 20$

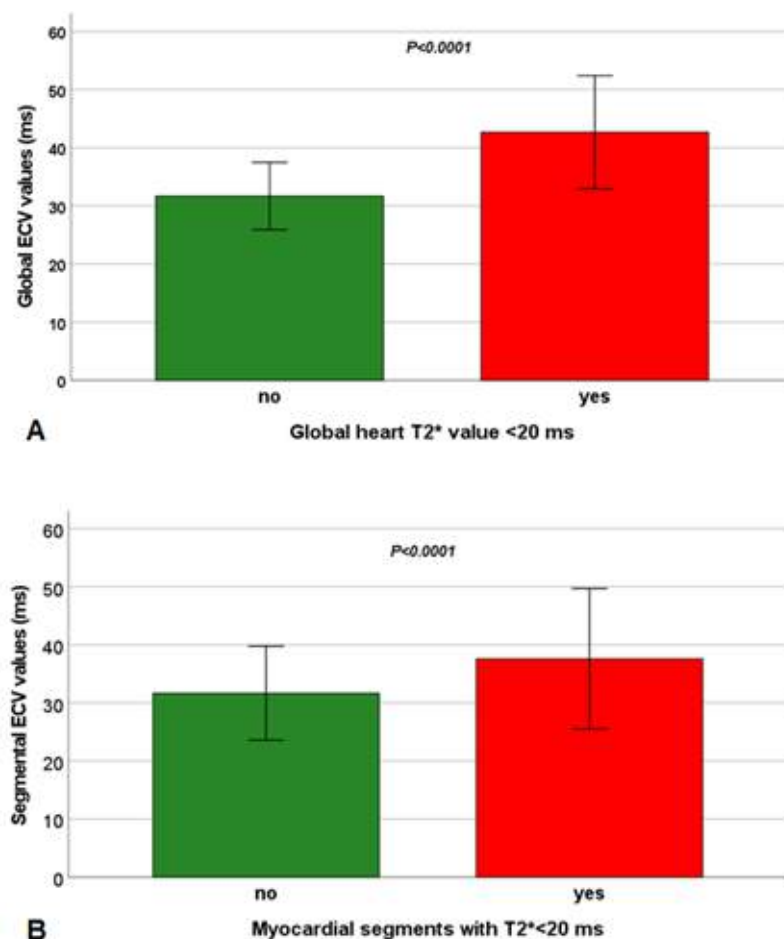
ms. Segments with pathological T2\* had significantly higher ECV values than segments with normal T2\* ( $37.6 \pm 12.1\%$  vs  $31.7 \pm 8.1\%$ ;  $P < 0.0001$ ) (Figure 1B).

No correlation was detected between global ECV and biventricular volume indexes or ejection fraction and left ventricular mass index.

Replacement myocardial fibrosis was detected in 36 patients (42.4%). The 81.1% of patients had two or more foci of fibrosis. Global ECV was comparable between patients with and without macroscopic myocardial fibrosis ( $33.8 \pm 8.0\%$  vs  $31.9 \pm 6.1\%$ ;  $P = 0.244$ ). Segments with LGE (N=106) had comparable ECV values than LGE-negative segments ( $32.2 \pm 10.2\%$  vs  $32.4 \pm 8.9\%$ ;  $P = 0.440$ ).

**Conclusion.** Myocardial ECV is significantly increased in TM patients with MIO, suggesting that the ECV quantification may provide additional insight into the pathophysiology of iron-mediated heart failure. The absence of a correlation between ECV values and LGE seems to indicate that these parameters may reflect different findings (diffuse or focal fibrosis) underlying peculiar pathological processes.

**Figure/Table 1**



Speaker: A. Meloni

Category: Parametric Mapping, Thalassemia, Extracellular Volume Fraction

000023

## Identification of Hemodynamic Biomarkers for Bicuspid Aortic Valve induced Aortic Dilation using Machine Learning

P. Franco \* (1); J. Sotelo, (2); A. Guala (3); L. Dux-Santoy, (3); A. Ruiz-Muñoz (3); A. Evangelista (3); J. F. Rodriguez Palomares (3); D. Mery, (4); R. Salas, (5); S. Uribe, (6)

(1) Biomedical imaging center, millennium nucleus for cardiovascular magnetic resonance, Pontificia Universidad Católica de Chile, Santiago, Chile; (2) School of biomedical engineering, millennium nucleus for cardiovascular magnetic resonance, Universidad de Valparaíso, Valparaíso, Chile; (3) Department of cardiology, Hospital Universitari Vall d'Hebron, Barcelona, Spain; (4) Department of computer science, Pontificia Universidad Católica de Chile, Santiago, Chile; (5) School of biomedical engineering, Universidad de Valparaíso, Valparaíso, Chile; (6) Biomedical imaging center, millennium nucleus for cardiovascular magnetic resonance, Pontificia Universidad Católica de Chile, Santiago, Chile

### Abstract

**Background:** Several studies have demonstrated the existence of altered hemodynamics in bicuspid aortic valve (BAV) patients [1,2]. The objective of this study was to identify which hemodynamic parameters allow an accurate classification between BAV patients with dilated and non-dilated ascending aorta using machine learning (ML) algorithms.

**Methods:** 4D flow CMR data of 48 healthy volunteers and 67 BAV patients were acquired in a 1.5T GE-MR Signa Scanner using the VIPR sequence [3]. Table 1 shows the clinical and demographic data. *In-vivo* image processing and quantification by a finite element method, fully described elsewhere [4-5]. At peak systole, different hemodynamic parameters were calculated in the ascending aorta (AAo) and aortic arch (AArch). Furthermore, a machine learning model was designed to select hemodynamic parameters that adequately separate healthy volunteers (HV) and BAV patients (non- and dilated ascending aorta) using sequential forward selection (SFS) and principal component analysis (PCA). The used classifiers were minimum distance, linear discriminant analysis (LDA), k-nearest neighbors (KNN), quadratic discriminant analysis, Mahalanobis distance, support vector machine (SVM), neural network, and random forest. The performance of the classification was evaluated using stratified 10-fold cross-validation. A confusion matrix was constructed based on prediction results in each training and validation sample. The sensitivity, specificity, precision, and accuracy of the search strategies were calculated. Additionally, the Pearson correlation method was used to calculate the correlation matrix between all the hemodynamic parameters. Hierarchical clustering was then applied to classify its rows/columns into different groups.

**Results:** The number of selected features was defined by eliminating highly correlated or constant features that maximized the accuracy of each classification experiment. The five top-performing features selected by SFS were velocity angle, forward velocity, vorticity, and backward velocity in AAo; helicity density in AArch, and PCA were forward velocity, velocity, and velocity angle in AAo; and velocity and energy loss in AArch. Using features selected by SFS, common classifiers as KNN resulted in an accuracy of over 86% and 91.34% accuracy with SVM-Linear. Using features selected by PCA, almost all classifiers were close to 90% accuracy. The best result was obtained by combining five features selected by SFS in

LDA, getting a  $96.31 \pm 1.76$  % accuracy, followed by SFS followed by random forest, which resulted in  $96.00 \pm 0.83$  % accuracy, as shown in Table 2. Analysis of the hierarchical clustering (Figure 1) shows that the parameters selected by SFS corresponded to three different clusters. Instead, parameters selected by PCA corresponded to mainly one cluster, which may explain the lower accuracy of the classifiers when using PCA for feature selection.

**Conclusions:** Five hemodynamic features (velocity angle, forward velocity, vorticity, and backward velocity in AAo and helicity density in AArch) can characterize BAV patients with aortic dilation. Also, we validate how relevant are these features in a classification problem. One of the strengths of our study is that it provides a comprehensive overview of the relative performance of different ML algorithms for disease prediction. Hence, non-linear interactions can be associated with the selected features that better identify HV and BAV patients. This important information of relative performance can be used to aid researchers in the selection of an appropriate ML algorithm for their studies.

**Figure/Table 1**

				BAV Dilation Group		
	HV	BAV	p-value	NON-DIL	DIL	p-value
N	48	67		18	49	
Age (year)	48.71 $\pm$ 12.57	47.74 $\pm$ 15.06	0.998	46.68 $\pm$ 14.35	48.28 $\pm$ 15.44	0.698
Men (%)	52.08	58.21	0.514	72.22	51.02	0.121
Weight (kg)	70.81 $\pm$ 10.53	72.18 $\pm$ 13.25	0.587	74.72 $\pm$ 13.05	72.42 $\pm$ 13.59	0.534
Height (cm)	171.23 $\pm$ 7.82	169.45 $\pm$ 10.85	0.364	172.33 $\pm$ 8.60	168.69 $\pm$ 11.33	0.221
BSA (m <sup>2</sup> )	1.83 $\pm$ 0.16	1.83 $\pm$ 0.21	0.995	1.88 $\pm$ 0.20	1.82 $\pm$ 0.22	0.349
SBP (mmHg)	130.15 $\pm$ 18.85	134.88 $\pm$ 17.55	0.114	133.78 $\pm$ 18.12	135.17 $\pm$ 17.05	0.773
DBP (mmHg)	73.41 $\pm$ 10.09	76.43 $\pm$ 8.73	0.128	77.39 $\pm$ 6.99	77.33 $\pm$ 9.03	0.981
Diameter SoV (mm)	30.32 $\pm$ 3.92	35.91 $\pm$ 4.69	< 0.001*	33.28 $\pm$ 3.74	36.08 $\pm$ 4.41	0.019*
Diameter AAo (mm)	27.89 $\pm$ 3.71	39.37 $\pm$ 6.74	< 0.001*	32.72 $\pm$ 4.17	42.82 $\pm$ 5.19	< 0.001*
Z score SoV	-0.25 $\pm$ 1.18	1.30 $\pm$ 1.30	< 0.001*	0.27 $\pm$ 0.82	1.33 $\pm$ 1.05	< 0.001*
Z score AAo	-0.14 $\pm$ 0.91	2.89 $\pm$ 1.52	< 0.001*	0.98 $\pm$ 1.07	3.71 $\pm$ 0.98	< 0.001*

**Caption 1**

**Table 1.** Demographical and clinical data for the healthy volunteers (HV) and BAV patients. Quantitative data are expressed as the mean  $\pm$  SD. BSA, body surface area; DBP, diastolic blood pressure; SBP, systolic blood pressure and SoV, sinus of Valsalva.

**Figure/Table 2**



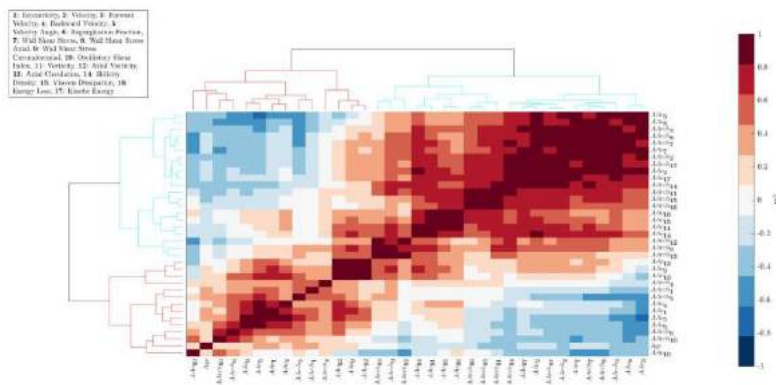
		LDA			Random Forest		
		All features	SFS	PCA	All features	SFS	PCA
HV class	Precision (%)	100.00 ± 0.00	100.00 ± 0.00	100.00 ± 0.00	98.01 ± 1.19	99.49 ± 1.12	99.09 ± 1.30
	Specificity (%)	100.00 ± 0.00	100.00 ± 0.00	100.00 ± 0.00	99.05 ± 0.81	99.45 ± 0.84	100.00 ± 0.93
	Sensitivity (%)	94.17 ± 12.01	97.49 ± 6.51	97.48 ± 7.44	95.39 ± 1.51	94.22 ± 1.30	97.13 ± 1.62
NON-DIL BAV class	Precision	69.38 ± 48.42	88.42 ± 32.40	63.49 ± 4.80	67.44 ± 9.45	78.02 ± 4.16	79.83 ± 9.80
	Specificity (%)	96.49 ± 5.51	98.41 ± 4.15	95.33 ± 7.51	94.32 ± 1.53	96.39 ± 0.65	96.43 ± 1.70
	Sensitivity (%)	80.36 ± 37.39	86.03 ± 22.05	78.42 ± 4.29	80.39 ± 6.41	99.40 ± 2.71	95.02 ± 9.57
DIL BAV class	Precision	92.48 ± 17.02	93.01 ± 11.38	94.01 ± 1.00	95.50 ± 3.22	100.00 ± 0.75	99.03 ± 2.84
	Specificity (%)	95.32 ± 9.80	96.44 ± 7.12	96.43 ± 7.71	97.09 ± 2.19	100.00 ± 0.55	99.44 ± 2.09
	Sensitivity (%)	98.05 ± 6.33	99.59 ± 2.60	93.29 ± 1.10	93.44 ± 2.70	97.04 ± 1.32	95.32 ± 2.70
Accuracy (%)		93.86 ± 2.24	96.31 ± 1.76	91.05 ± 2.29	92.00 ± 1.80	96.00 ± 0.83	96.00 ± 2.70

**Caption 2**

**Table 2.** Accuracy, precision, specificity, and sensitivity of different combinations of classifiers and all features, and five features selected by SFS and PCA. Each experiment was done using 10 group cross-validation and repeated 10 times with confidence interval 95%.

		LDA			Random Forest		
		All features	SFS	PCA	All features	SFS	PCA
HV class	Precision (%)	100.00 ± 0.00	100.00 ± 0.00	100.00 ± 0.00	98.01 ± 1.19	99.49 ± 1.12	99.09 ± 1.30
	Specificity (%)	100.00 ± 0.00	100.00 ± 0.00	100.00 ± 0.00	99.05 ± 0.81	99.45 ± 0.84	100.00 ± 0.93
	Sensitivity (%)	94.17 ± 12.01	97.49 ± 6.51	97.48 ± 7.44	95.39 ± 1.51	94.22 ± 1.30	97.13 ± 1.62
NON-DIL BAV class	Precision	69.38 ± 48.42	88.42 ± 32.40	63.49 ± 4.80	67.44 ± 9.45	78.02 ± 4.16	79.83 ± 9.80
	Specificity (%)	96.49 ± 5.51	98.41 ± 4.15	95.33 ± 7.51	94.32 ± 1.53	96.39 ± 0.65	96.43 ± 1.70
	Sensitivity (%)	80.36 ± 37.39	86.03 ± 22.05	78.42 ± 4.29	80.39 ± 6.41	99.40 ± 2.71	95.02 ± 9.57
DIL BAV class	Precision	92.48 ± 17.02	93.01 ± 11.38	94.01 ± 1.00	95.50 ± 3.22	100.00 ± 0.75	99.03 ± 2.84
	Specificity (%)	95.32 ± 9.80	96.44 ± 7.12	96.43 ± 7.71	97.09 ± 2.19	100.00 ± 0.55	99.44 ± 2.09
	Sensitivity (%)	98.05 ± 6.33	99.59 ± 2.60	93.29 ± 1.10	93.44 ± 2.70	97.04 ± 1.32	95.32 ± 2.70
Accuracy (%)		93.86 ± 2.24	96.31 ± 1.76	91.05 ± 2.29	92.00 ± 1.80	96.00 ± 0.83	96.00 ± 2.70

**Figure 3**



**Caption 3**

**Figure 1.** Dendrogram and hierarchical clustering result based on average linkage method, for all hemodynamic parameters of HV and BAV patients, in AAO and AArch regions.

### Bibliographic References

- 1.- Allen BD, van Ooij P, Barker AJ, et al. Thoracic aorta 3D hemodynamics in pediatric and young adult patients with bicuspid aortic valve. *J Magn Reson Imaging*. 2015; 42(4): 954-63.
- 2.- Guala A., Rodriguez-Palomares J., Galian-Gay L., et al. Partial Aortic Valve Leaflet Fusion Is Related to Deleterious Alteration of Proximal Aorta Hemodynamics. *Circulation* 2019;139(23):2707–9. Doi: 10.1161/CIRCULATIONAHA.119.039693.
- 3.- Gu T, Korosec FR, Block WF, et al. PC VIPR: a high-speed 3D phase-contrast method for flow quantification and high-resolution angiography. *AJNR Am J Neuroradiol*. 2005;26(4):743-9.
- 4.- Sotelo J, Dux-Santoy L, Guala A, et al. 3D axial and circumferential wall shear stress from 4D flow MRI data using a finite element method and a laplacian approach. *Magn Reson Med* 2018 May;79(5):2816-2823. 10.1002/mrm.26927
- 5.- Sotelo J, Valverde I, Martins D, Bonnet D, Boddaert N, Pushparajan K, Uribe S, Raimondi F. Impact of aortic arch curvature in flow haemodynamics in patients with transposition of the great arteries after arterial switch operation. *Eur Heart J Cardiovasc Imaging*. 2021 Jan 31;jeaa416. doi: 10.1093/ehjci/jeaa416. Epub ahead of print. PMID: 33517430.

Speaker: P. Franco

Category: 4D Flow, Bicuspid Aortic Valve, Accuracy and Effectiveness

000025

## DEep learning-based rapid Spiral Image REconstruction (DESIRE) for Free-breathing High-resolution Spiral Real-time Cardiac Cine Imaging at 1.5 T

J. Wang \* (1); R. Zhou (2); X. Wang (1); M. Awad (1); M. Salerno (3)

(1) Biomedical Engineering, University of Virginia, Charlottesville, United States of America; (2) School of Artificial Intelligence , Beijing University of Posts and Telecommunications, Beijing, China; (3) Cardiology, radiology, and medical imaging, University of Virginia, Charlottesville, United States of America

### Abstract

**Background** Cardiac magnetic resonance (CMR) real-time cine imaging, is clinically useful for patients with impaired breath-hold capacity and/or arrhythmias[1]. Currently, clinically available real-time imaging using parallel imaging and/or compressed-sensing require long reconstruction times[1]. We sought to develop real-time cardiac cine imaging including both GRE and bSSFP using fast spiral acquisitions and deep learning-based rapid imaging reconstructions, to make high-quality and rapid reconstruction for free-breathing high-resolution spiral real-time cardiac cine imaging feasible (Figure 1-A).

**Methods** Figure 1-B illustrates the proposed 3D U-Net[2] based reconstruction network. The inputs to the network are concatenated complex-valued cine image series from a single slice location following coil-selection[3], and adaptive phase combination[4] of the NUFFT-gridded[5] multi-coil images. The outputs are concatenated complex-valued image series. Networks for GRE and bSSFP images were trained separately.

Cine image data with 1.5 mm spatial resolution, 40 ms temporal resolution and whole-heart coverage were acquired from 18 patients and healthy volunteers undergoing clinical studies at 1.5 T SIEMENS Aera scanner[3] (Figure 1-C). The reference image was spiral L1-SENSE:

$$\underset{x}{\operatorname{argmin}} ||F_u Sx - y||_2^2 + \lambda ||\Psi x||_1$$

where  $x$  is the dynamic image series to be reconstructed,  $S$  is the coil sensitivity maps[4],  $F_u$  is the inverse Fourier gridding operator[5],  $y$  is the acquired data,  $\psi$  is the finite time difference sparsifying operator,  $I$  is the identity matrix.  $\lambda=0.06$  was chosen as a tradeoff between image quality and temporal fidelity.

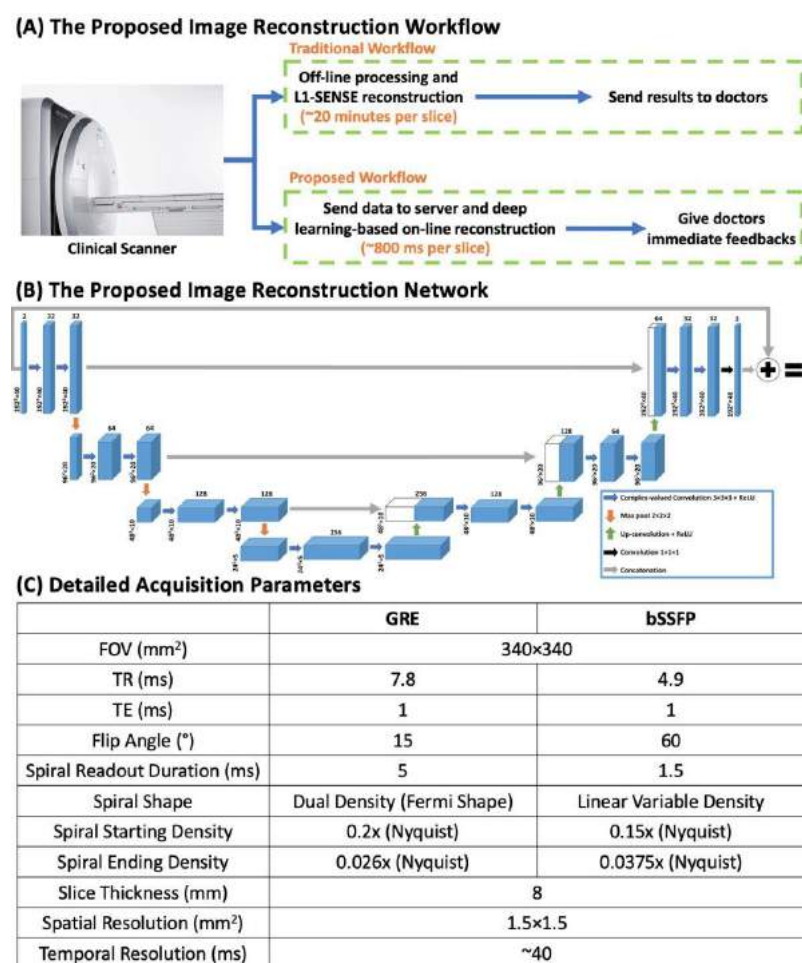
120 slices from 13 subjects were used for training, and another 14 slices from 5 subjects were used for testing. During training, images were cropped into 192×192×40 (Frames) to save GPU memory. This corresponds to 1.5 seconds of cine data capturing a single beat for heart rate above 40 BPM. The training and testing was conducted using PyTorch on four NVIDIA Tesla P100 GPUs with 150 epochs using an L1 loss. Both structural SSIM and RMSE were assessed. Images were also graded by an experienced cardiologist (5 excellent, 1 poor).

**Results** Figure 2 and Figure 3 show examples from the test data for the GRE and bSSFP imaging, respectively. For GRE, the mean SSIM and RMSE in test data were 0.908±0.035

and  $0.016 \pm 0.005$ , respectively. For bSSFP, the mean SSIM and RMSE in test data were  $0.953 \pm 0.029$  and  $0.011 \pm 0.005$ , respectively. For GRE, image quality scores were  $4.5 \pm 0.5$  and  $4.6 \pm 0.5$  for L1-SENSE and DESIRE, respectively. While for bSSFP, image quality scores were  $4.4 \pm 0.4$ , and  $3.9 \pm 0.4$  for L1-SENSE and DESIRE, respectively. The reconstruction time was  $\sim 800$  ms per slice, while the reconstruction time of L1-SENSE was  $\sim 20$  minutes.

**Conclusion** The proposed image reconstruction technique (DESIRE) enabled fast and high-quality image reconstruction for both GRE and bSSFP free-breathing high-resolution spiral real-time cardiac cine imaging.

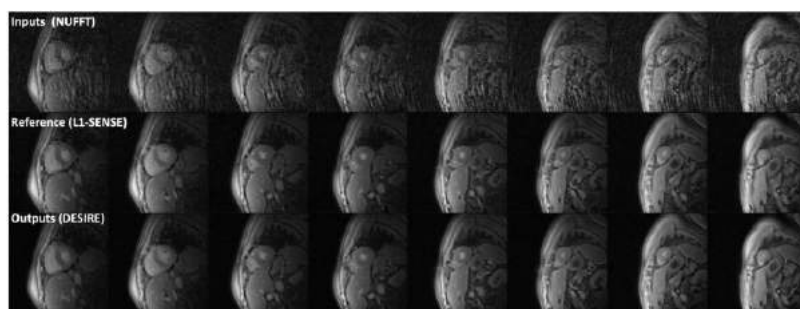
**Figure/Table 1**



**Caption 1**

Figure 1. The proposed deep learning-based image reconstruction workflow and the proposed 3D U-Net based reconstruction network (DESIRE). In (B), the numbers above each layer denote the number of kernels at each layer, and the corresponding image shape at each layer is also labelled. (C) shows detailed acquisition parameters for GRE and bSSFP cine imaging which have the similar temporal and spatial resolution.

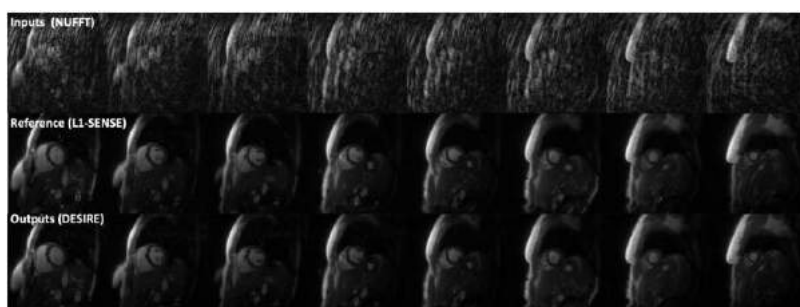
**Figure/Table 2**



**Caption 2**

Figure 2. GRE real-time cine images from a patient with 8 slices reconstructed using L1-SENSE and the proposed DESIRE image reconstruction network. Good image quality was demonstrated using the proposed image reconstruction network. This case reconstructed using DESIRE has an SSIM of  $0.892 \pm 0.026$ , a RMSE of  $0.019 \pm 0.004$  and an image quality score of 4 (5, excellent; 1, poor). The image quality score for L1-SENSE was 4 as well.

**Figure 3**



**Caption 3**

Figure 3. bSSFP real-time cine images from a patient with 8 slices reconstructed using L1-SENSE and the proposed DESIRE image reconstruction network. Good image quality was demonstrated using the proposed image reconstruction network. This case reconstructed using DESIRE has an SSIM of  $0.919 \pm 0.030$ , a RMSE of  $0.020 \pm 0.004$  and an image quality score of 3.5 (5, excellent; 1, poor) while the image quality score for L1-SENSE was 4.5.

## **Bibliographic References**

1. Feng L, Srichai MB, Lim RP, et al. Highly accelerated real-time cardiac cine MRI using k-t

SPARSE-SENSE. Magnetic Resonance in Medicine 2013;70:64–74., 2. Ronneberger O, Fischer P, Brox T. U-Net: Convolutional Networks for Biomedical Image Segmentation. arXiv:1505.04597 [cs] 2015., 3. Zhou R, Yang Y, Mathew RC, et al. Free-breathing cine imaging with motion-corrected reconstruction at 3T using SPiral Acquisition with Respiratory correction and Cardiac Self-gating (SPARCS). Magnetic Resonance in Medicine 2019;82:706–720., 4. Walsh DO, Gmitro AF, Marcellin MW. Adaptive reconstruction of phased array MR imagery. Magnetic Resonance in Medicine 2000;43:682–690., 5. Fessler JA, Sutton BP. Nonuniform fast Fourier transforms using min-max interpolation. IEEE Transactions on Signal Processing 2003;51:560–574.

Speaker: J. Wang

Category: Real Time, Cine Imaging, Spiral

000026

## Changes in CMR parameters and prediction of cardiac complications in thalassemia major: fibrosis tells us more than iron

A. Pepe \* (1); L. Pistoia (2); P. Giuliano (3); N. Giunta (3); G. Restaino (4); M. Zerbini (5); E. Grassedonio (6); V. Spadola (7); L. Rigoli (8); P. P. Bitti (9); V. Positano (2); A. Meloni (2)

(1) U.o.c. imaging multimodale cardiovascolare e neuroradiologico, Fondazione G. Monasterio CNR-Regione Toscana, Padua, Italy; (2) U.o.c. imaging multimodale cardiovascolare e neuroradiologico, Fondazione G. Monasterio CNR-Regione Toscana, Pisa, Italy; (3) Cardiologia con utic, A.R.N.A.S. Ospedali Civico Di Cristina Benfratelli, Palermo, Italy; (4) Dipartimento di immagini, Fondazione di Ricerca e Cura "Giovanni Paolo II", Campobasso, Italy; (5) Diagnostica per immagini e radiologia interventistica, Ospedale del Delta, Lagosanto, Italy; (6) Sezione di scienze radiologiche - dipartimento di biopatologia e biotecnologie mediche, University Hospital Policlinico Paolo Giaccone, Palermo, Italy; (7) Unità operativa semplice di microcitemia, Azienda Ospedaliera Civile - O.M.P.A. Ragusa, Ragusa, Italy; (8) Unità operativa complessa di pediatria d'urgenza, A.O.U. Policlinico "Gaetano Martino", Messina, Italy; (9) Servizio immunoematologia e medicina trasfusionale, The Hospital San Francesco, Venosa, Italy

### Abstract

**Background.** Cardiovascular magnetic Resonance (CMR) has dramatically changed the clinical practice and improved the prognosis in thalassemia major (TM).

This is the first study evaluating the predictive value of changes in CMR parameters (myocardial iron, function, and fibrosis) for cardiac complications in TM.

**Methods:** We followed prospectively 709 TM patients (374 females;  $29.77 \pm 8.53$  years) consecutively enrolled in the Myocardial Iron Overload in Thalassemia (MIOT) Network who performed a baseline and a 1st follow up CMR scan after 18 months. Myocardial iron overload (MIO) was measured by multislice multiecho T2\* technique and atrial dimensions and biventricular function by cine images. Macroscopic myocardial fibrosis was detected by late gadolinium enhancement technique.

Risk classes were defined based on the 4 patterns of MIO from worst to normal. For patients with baseline MIO (at least one segmental T2\* < 20 ms), improvement was defined as a transition to a better risk class, stabilization as no change in risk class, and worsening as a transition to a worse risk class. For patients without baseline MIO, the worsening was the transition to a worse risk class.

The percentage change was used for continuous variables. For biventricular ejection fractions, improvement was a % change > 10%, stabilization a % change between -10% and 10%, and worsening a % change < -10%. For biventricular volumes, LV mass index, and atrial areas, improvement was a % change < -10%, stabilization a % change between -10% and 10%, and worsening a % change > 10%.

Myocardial fibrosis was considered absent if not detected in any of the two CMRs and present if detected in at least one examination.

**Results:** During a mean follow-up of  $89.4 \pm 33.3$  months, cardiac events were recorded in 50 (7.1%) patients: 24 (48%) episodes of heart failure, 24 (48%) arrhythmias (23 supraventricular and 1 hypokinetic), and 2 (4.0%) pulmonary hypertension. Mean time from the 1st follow up CMR to the development of a cardiac complication was  $75.31 \pm 35.35$  months.

In the univariate Cox regression analysis, cardiac iron clearance and myocardial fibrosis were identified as univariate prognosticators (Table 1). In the multivariate analysis only myocardial fibrosis remained an independent predictor factor.

**Conclusion.** The presence of myocardial fibrosis at the baseline CMR or developed within 18 months emerges as the strongest long-term predictor for cardiac complications in TM. Our data demonstrate the importance in using the contrast medium for CMR scans in thalassemia patients.

**Figure/Table 1**

	<b>Univariate analysis</b>	
	<b>HR (95%CI)</b>	<b>P</b>
<i><b>Pattern of MIO</b></i>		
<b>improvement</b>	Reference	
<b>stabilization</b>	2.07 (0.95-4.48)	0.067
<b>worsening</b>	3.09 (1.22-7.86)	0.018
<i><b>LV EDVI</b></i>		
<b>improvement</b>	Reference	
<b>stabilization</b>	1.87 (0.80-4.33)	0.147
<b>worsening</b>	2.30 (0.91-5.85)	0.080
<i><b>LV mass index</b></i>		
<b>improvement</b>	Reference	
<b>stabilization</b>	0.63 (0.29-1.35)	0.235
<b>worsening</b>	1.05 (0.51-2.17)	0.890



***LV EF***

<b>improvement</b>	Reference	
<b>stabilization</b>	0.99 (0.46-2.17)	0.992
<b>worsening</b>	0.72 (0.22-2.38)	0.586
<b><i>RV EDVI</i></b>		
<b>improvement</b>	Reference	
<b>stabilization</b>	0.97 (0.48-1.98)	0.931
<b>worsening</b>	1.43 (0.65-3.15)	0.373
<b><i>RV EF</i></b>		
<b>improvement</b>	Reference	
<b>stabilization</b>	1.64 (0.76-3.57)	0.210
<b>worsening</b>	0.64 (0.17-2.40)	0.506
<b><i>Left atrial area index</i></b>		
<b>improvement</b>	Reference	
<b>stabilization</b>	1.22 (0.53-2.79)	0.640
<b>worsening</b>	1.13 (0.44-2.95)	0.800
<b><i>Right atrial area index</i></b>		
<b>improvement</b>	Reference	
<b>stabilization</b>	1.36 (0.57-3.29)	0.490
<b>worsening</b>	1.69 (0.61-4.69)	0.312
<b><i>Myocardial fibrosis</i></b>		
<b>present</b>	Reference	
<b>absent</b>	1.89 (1.09-3.49)	0.041

**Caption 1**

**Table 1.** Results of univariate Cox regression analysis.

Speaker: A. Pepe

Category: T2\*, Prognosis, Thalassemia

000028

## **Examining the Effects of Cardiac 4D Flow Protocol Standardization on Scan Time Efficiency across Multiple MRI Systems**

M. Pradella \* (1); M. Collins (1); S. Chu (1); M. Kramer (2); M. Zimmermann (3); R. Davids (4); M. Scott (5); A. Korutz (6); B. Allen (1); R. Avery (6); J. Carr (1); M. Markl (1)

(1) Radiology, Northwestern University Feinberg School of Medicine, Chicago, United States of America; (2) Global product management, Siemens Healthineers, Erlangen, Germany; (3) Digital health, Siemens Healthineers, Salt Lake City, United States of America; (4) Cardiovascular imaging, Siemens Medical Solutions USA, Inc., Chicago, United States of America; (5) Digital health, Siemens Healthineers, Harrison, United States of America; (6) Radiology, Northwestern Memorial Hospital, Chicago, United States of America

### **Abstract**

#### **Background**

4D flow MRI often involves cumbersome scan setup that can be heterogeneous across scanners and patients, leading to lengthy and unpredictable 4D flow sequence and cardiac MRI (CMR) exam durations. In August 2020, we implemented a new, easy-to-use, standardized 4D flow protocol at our large tertiary center. The purpose of this study was to utilize a novel radiology analytics platform to examine the real-world effects of these protocol changes regarding 4D flow sequence duration and overall CMR exam efficiency.

#### **Methods**

All CMR exams that included 4D flow from 10/2019–03/2021 across four 1.5T MRI systems (2x Avanto, Sola, Aera, Siemens Healthineers, Germany) were retrospectively included. The standardized 4D flow protocol utilized a simplified planning workflow which only required positioning a 3D data volume over the heart and whole chest vasculature in coronal orientation. Data acquisition used retrospective ECG-gating during free breathing (no respiratory navigation, spatial resolution: 2.6x2.6x2.5-3.1mm, temporal resolution: 40ms, parallel imaging with GRAPPA R=2). On one of the 1.5 T systems (Sola), compressed sensing (CS) was applied with an acceleration factor of R=10. A cloud-based analytics platform (teamplay, Siemens Healthineers, Germany) linked directly with the vendor neutral archive (VNA), was used to gather exam information (incl. sequence and CMR exam durations) via DICOM headers (Figure 1).

#### **Results**

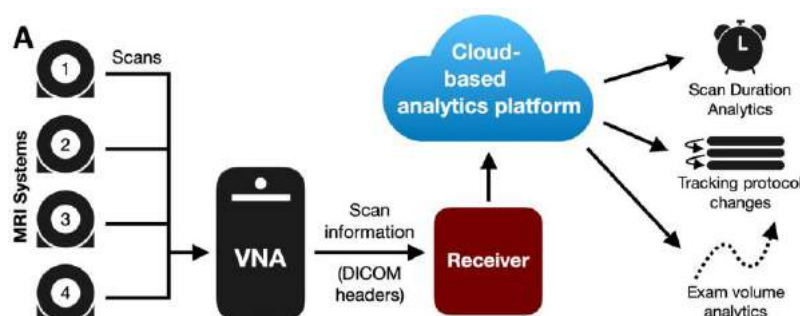
One-thousand-seventy CMR exams including a 4D flow series (old protocols: 376, standardized protocol: 694) in 1023 patients (mean age: 54.5±15.5 years) were identified by the analytics platform. The mean number of exams including a non-standardized 4D flow sequence was 28.5 exams/month before August 2020. After implementation of the standardized protocol between 08-10/2020, the average increased by more than 2-fold to 91.6 exams/month (Figure 2A).

The median sequence duration of the standardized 4D flow protocol was longer compared to the non-standardized sequences (12:00 vs. 11:04min,  $p=0.002$ ; Figure 3A). However, we observed a substantially reduced 4D flow scan time variability for the standardized protocol (interquartile range (IQR) 3:03 vs. non-standardized: 11:03min). Furthermore, the overall exam duration was significantly shorter for exams with the standardized protocol (57:03 vs. 65:47min, IQR=22:37 vs. 25:13min,  $p<0.001$ ; Figure 3B). This effect was also observed in bimonthly evaluation: after implementation of the standardized protocol, scan durations were more consistent and constantly below one hour (Figure 2B).

## Conclusions

A standardized 4D flow MRI protocol decreased the median overall exam duration significantly by over nine minutes. The 4D flow series acquisition was slightly longer for the standardized protocol, however, we expect that minimization of planning time lead to the reduction in overall exam duration. Application of advanced reconstruction methods like compressed sensing could further reduce scan times. The analytics platform demonstrated its utility in the analysis of scan efficiencies and the real-world impact of protocol implementations on MRI exam workflow.

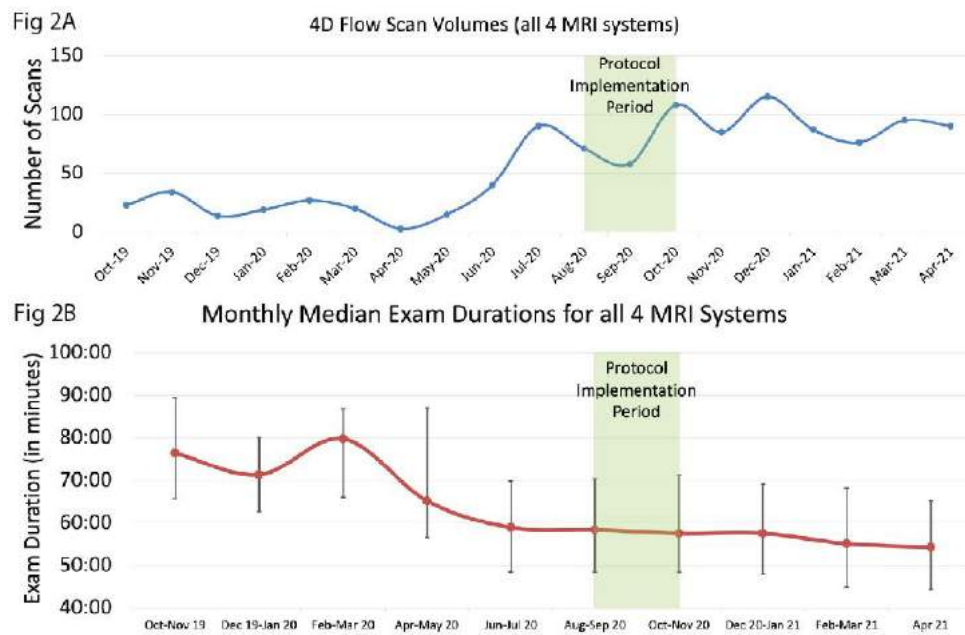
**Figure/Table 1**



**Caption 1**

Fig 1: Schematic illustration of data flow in the cloud-based analytics platform (teamplay, Siemens Healthineers). All four imaging modalities send data to a vendor neutral archive (VNA) which is queried to extract information on exams (scan durations and scan volumes).

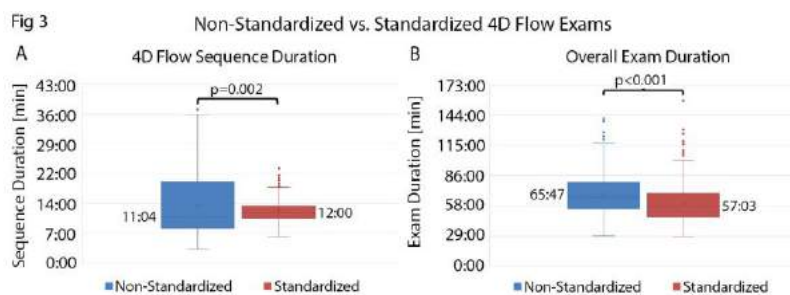
**Figure/Table 2**



## Caption 2

Fig 2: A) Total number of MRI scans including 4D flow protocols between 10/2019–04/2021. The standardized 4D flow MRI protocol was implemented between 08-10/2020. B) Median bimonthly exam durations incl. 95% confidence interval for all four scanners.

## Figure 3



## Caption 3

Fig 3: A) Box plot comparing median 4D flow protocol durations between non-standardized and standardized protocols. B) Comparison of exam duration shows significantly shorter exam duration after implementation of the standardized protocol.

Speaker: M. Pradella

Category: 4D Flow, Quantification, Accuracy and Effectiveness

## A Review and Comparison of Unwrapping Methods in Dual Velocity-Encoding MRI

P. Franco \* (1); L. Ma (2); S. Schnell (3); M. Markl (4); C. Bertoglio, (5); S. Uribe, (1)

(1) Biomedical imaging center, millennium nucleus for cardiovascular magnetic resonance, Pontificia Universidad Católica de Chile, Santiago, Chile; (2) Department of radiology and neurosurgery, Northwestern University, Evanston, United States of America; (3) Institut für physik, Universität Institut für Physik, Greifswald, Germany; (4) Department of radiology, Northwestern University Feinberg School of Medicine, East Superior Street, Chicago, IL, USA, Chicago, United States of America; (5) Bernoulli institute, University of Groningen, Groningen, Netherlands

### Abstract

**Background:** 4D flow MRI can measure time-resolved blood flow velocity in a large 3D volume as the whole heart. However, when low and high velocities are present in the FOV, the accuracy of the 4D flow data may be inadequate. If the VENC is set low to have higher velocity-to-noise ratio (VNR) in the low velocities, it may result in velocity aliasing in areas of high velocity. Unwrapping methods have been proposed to solve aliasing artifacts, increase VNR, provide more reliable measurements, and allow more flexibility in the selection of VENC. For this reason, unwrapping methods have been developed as Standard Dual-VENC (SDV) [1], Optimal Dual-VENC (ODV) [2], and triple-VENC (TV) [3] (Figure 1a). This work aims to compare Dual-VENC methods using *in-vitro* and *in-vivo* datasets.

**Methods:** Multi-VENC 4D flow MRI data were acquired in a constant rotation and pulsative flow phantoms using a 1.5T MAGNETOM Aera System Siemens. Additionally, 2D PC-MRI data were acquired in eight healthy volunteers using a clinical 1.5T MR Scanner Philips. The raw data was obtained, and the reconstruction of each bipolar gradient was performed offline using MATLAB. Data from the multiple coils were combined using the proposed method [4]. We used VENCs of 50, 75, and 150 cm/s for the *in-vitro* and *in-vivo* datasets. We implemented and compared the SDV, ODV, and TV methods. Furthermore, we developed a correction method based in the information provided by the ODV. For every pixel of the image, we found 8-connected pixels, calculating the mean velocity of the neighborhood. If this has the same sign as a central pixel. Then, we found a local minimum (positive or negative, according to the case). And finally, replace the velocity value. We also present an analytical noise analysis of the velocity estimates of the different methods.

**Results:** Regarding the noise analysis, we analytically computed the velocity estimate variance ( $\text{Var}(u)$ ), as shown in Figure 1b. The SDV and TV methods leads to  $\text{Var}(u_{\text{SDV}}) = \text{Var}(u_{\text{TV}}) = \text{Var}(u_2)$  when the unwrapping is successful. Nonetheless, in the classical ODV method – when both VENC images share the background phase – only if  $\beta \geq 0.8376$  then  $\text{Var}(u^*) \leq \text{Var}(u_2)$ . Therefore, we suggest a modified version of the ODV, which allows for faster computations and with  $\text{Var}(u^*) = \text{Var}(u_2)$  as for the other methods.

The unwrapping results for the constant rotative and pulsative flow phantoms are presented in Figure 2. The ODV and TV algorithms successfully unwrapped all voxels without any residual velocity aliasing. Figures 3 shows the velocity profiles on the ascending and descending aorta in two volunteers, using the same VENC combinations and reconstruction

methods. The SDV cannot handle the aliasing when both VENC values are lower than the true velocity (i.e., 75,50). In contrast, ODV and TV can successfully reconstruct unaliased images from two aliased ones. Nevertheless, TV triconditional outperformed the results compared to the TV biconditional method. Furthermore, the ODV corrected unwrapping algorithm successfully unwrapped all voxels without any residual velocity aliasing.

Regarding the computational time, ODV is slower than TV and SDV (i.e., Times: ODV:  $\approx 96.0$  s, TV-biconditional:  $\approx 1.8$  s, TV-triconditional:  $\approx 3.6$  s, and SDV:  $\approx 0.4$  s).

**Conclusions:** The ODV and TV unwrapping methods lead to the same results in both phantom and volunteers. Nevertheless, the ODV showed a larger computational time, but with the potential of correcting wrong unwrapping results at isolated voxels.

## Figure/Table 1

(a) 1- Standard Dual-VENC (SDV) (Lee *et al.*, Magn Reson Med, 1995)

$$k = N.I. \left( \frac{u_{high} - u_{low}}{2VENC_{low}} \right) \quad u_{SDV} = u_{low} + 2VENC_{low}k$$

2- Optimal Dual-VENC (ODV) (Carillo *et al.*, IEEE Transactions on Medical Imaging, 2018)

$$J_{dual}(u) = 2 - \cos\left(\frac{\pi}{VENC_{high}}(u_{high} - u)\right) - \cos\left(\frac{\pi}{VENC_{low}}(u_{low} - u)\right) \quad u^* = \operatorname{argmin}(J(u)), \quad u \in [-u_{max}, u_{max}]$$

3- Bi-conditional unwrapping (Ma *et al.*, Magn Reson Med, 2019)

$$u_{TV \text{ biconditional}} = \begin{cases} VENC_2 < u_2 - u_i < 3VENC_2: u_2 + 2VENC_2 \\ -3VENC_2 < u_2 - u_i < -VENC_2: u_2 - 2VENC_2 \\ 3VENC_2 < u_2 - u_i < 5VENC_2: u_2 + 4VENC_2 \\ -5VENC_2 < u_2 - u_i < -3VENC_2: u_2 - 4VENC_2 \\ \text{Or} \\ VENC_1 < u_1 - u_i < 3VENC_1: u_2 + 2VENC_2 \\ -3VENC_1 < u_1 - u_i < -VENC_1: u_2 - 2VENC_2 \\ 3VENC_1 < u_1 - u_i < 5VENC_1: u_2 + 4VENC_2 \\ -5VENC_1 < u_1 - u_i < -3VENC_1: u_2 - 4VENC_2 \end{cases}$$

4- Tri-conditional unwrapping (Ma *et al.*, Magn Reson Med, 2019)

$$u_{TV \text{ triconditional}} = \begin{cases} VENC_2 < u_2 - u_i < 3VENC_2: u_2 + 2VENC_2 \\ -3VENC_2 < u_2 - u_i < -VENC_2: u_2 - 2VENC_2 \\ 3VENC_2 < u_2 - u_i < 5VENC_2: u_2 + 4VENC_2 \\ -5VENC_2 < u_2 - u_i < -3VENC_2: u_2 - 4VENC_2 \\ \text{Or} \\ VENC_1 < u_1 - u_i < 3VENC_1: u_2 + 2VENC_2 \\ -3VENC_1 < u_1 - u_i < -VENC_1: u_2 - 2VENC_2 \\ 3VENC_1 < u_1 - u_i < 5VENC_1: u_2 + 4VENC_2 \\ -5VENC_1 < u_1 - u_i < -3VENC_1: u_2 - 4VENC_2 \\ \& \\ VENC_i < u_1 - u_2 < VENC_i: u_2 + 2VENC_2 \\ -3VENC_i < u_1 - u_2 < -VENC_i: u_2 - 2VENC_2 \\ 3VENC_i < u_1 - u_2 < 5VENC_i: u_2 + 4VENC_2 \\ -5VENC_i < u_1 - u_2 < -3VENC_i: u_2 - 4VENC_2 \end{cases}$$

$$u_i = \frac{\varphi_2 - \varphi_1}{\pi} VENC_i$$

$$VENC_i = \frac{VENC_1 VENC_2}{VENC_1 - VENC_2}$$

Note: Subscripts *high* (1 or i) and *low* (1 or 2), it depends on the combination: i+1, i+2, and 1+2.

## (b) 1- SDV and TV bi- and tri-conditional Noise Analysis

$$\operatorname{Var}(u_{SDV}) = \operatorname{Var}(u_{TV \text{ biconditional}}) = \operatorname{Var}(u_{TV \text{ triconditional}}) = \operatorname{Var}(u_2)$$

### 2- ODV Noise Analysis

$$J_{dual}(u) = 2 - \cos\left(\frac{\pi}{VENC_1}(u_1 - u)\right) - \cos\left(\frac{\pi}{VENC_2}(u_2 - u)\right)$$

In the optimal dual encoding method, the unwrapped motion corresponds to the global minimum with smallest magnitude, which we will denote  $u_*$ . Due to the fact that the global minimum is also a local minimum.

$$\begin{aligned} J'_{dual}(u_*) &= -\frac{\pi}{VENC_1} \sin\left(\frac{\pi}{VENC_1}(u_1 - u_*)\right) - \frac{\pi}{VENC_2} \sin\left(\frac{\pi}{VENC_2}(u_2 - u_*)\right) \\ &= -\frac{\pi}{VENC_1} \sin\left(\frac{\pi}{VENC_1}(u_1 - u_* + 2k_1 VENC_1)\right) - \frac{\pi}{VENC_2} \sin\left(\frac{\pi}{VENC_2}(u_2 - u_* + 2k_2 VENC_2)\right) = 0 \end{aligned}$$

Hence, we can approximate the sin-terms by its arguments leading to:

$$\begin{aligned} \operatorname{Var}(u_*) &= (VENC_1^{-2} + VENC_2^{-2})^{-2} (\operatorname{Var}(u_1) VENC_1^{-4} + \operatorname{Var}(u_2) VENC_2^{-4} + 2VENC_1^{-2} VENC_2^{-2} \operatorname{Cov}(u_1, u_2)) \\ &= (VENC_1^{-2} + VENC_2^{-2})^{-2} (2\sigma_u^2 VENC_1^{-2} + 2\sigma_u^2 VENC_2^{-2} + 2VENC_1^{-2} VENC_2^{-2} \operatorname{Cov}(u_1, u_2)) \\ &= \frac{\operatorname{Var}(u_2)}{1 + \beta^2} \left(1 + \frac{1}{(1 + \beta^2)\beta}\right) \end{aligned}$$

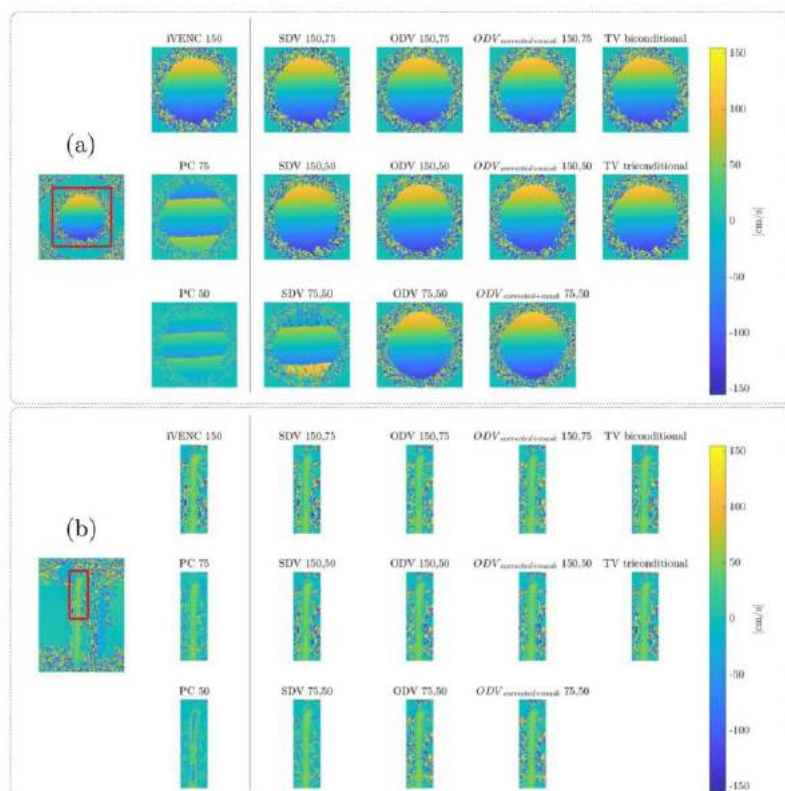
$$\beta = \frac{VENC_2}{VENC_1}$$



## Caption 1

**Figure 1:** (a) Standard Dual-VENC, Optimal Dual-VENC, and Bi- and Tri-conditional unwrapping methods. (b) Noise Analysis for Dual-VENC unwrapping methods.

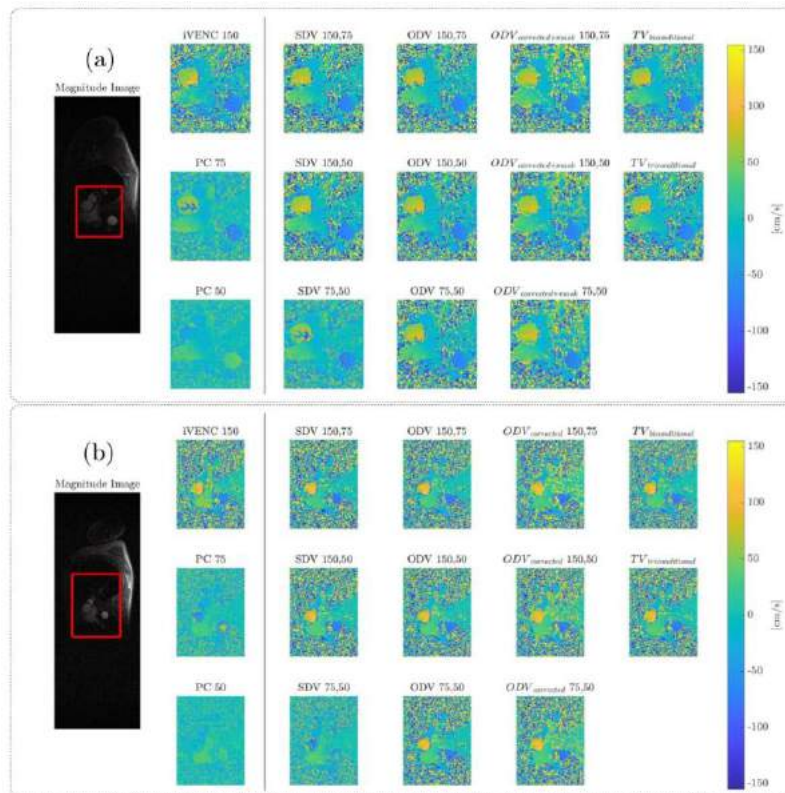
## Figure/Table 2



## Caption 2

**Figure 2:** (a) Rotation and (b) Pulsatile Phantom. First row: x-direction phase image at peak systole, second row: triple-VENC images, third row: SDV images, fourth row: ODV images, fifth row: ODV corrected with masking ROI images, and sixth row: TV bi- and tri-conditional images. PC: single-VENC PC-MRI; SDV: Standard Dual-VENC Method; ODV: Optimal Dual-VENC Method; TV: Triple-VENC Method.

## Figure 3



**Caption 3**

**Figure 3:** (a) Volunteer 1, (b) Volunteer 2. First row: x-direction phase image at peak systole, second row: triple-VENC images, third row: SDV images, fourth row: ODV images, fifth row: ODV corrected with masking ROI images, and sixth row: TV bi- and tri-conditional images. PC: single-VENC PC-MRI; SDV: Standard Dual-VENC Method; ODV: Optimal Dual-VENC Method; TV: Triple-VENC Method.

### Bibliographic References

- 1.- Lee AT, Pike B and Pelc NJ, Three-Point Phase-Contrast Velocity Measurements with Increased Velocity-to-Noise Ratio, Magn Reson Med. 1995; 33(1):122-6., 2.- Carrillo H, Osses A, Uribe S and Bertoglio C. Optimal Dual-VENC (ODV) Unwrapping in Phase-Contrast MRI. IEE Trans Med Imaging. 2019; 38(5):1263-1270. , 3. – Ma Le, Markl M, Chow K, Vali A, Wu C, Schnell S. Efficient triple-VENC phase-contrast MRI for improved velocity dynamic range. Magn Reson Med. , 4.- Bernstein MA, Grgic Mladen, Brosnan TJ, Pelc NJ. Reconstructions of Phase Contrast, Phased Array Multicoil Data. Magn Reson Med. 1994; 32(3):330-4.

Speaker: P. Franco

Category: 4D Flow, Flow, Phase Contrast

000034

## The prognostic value of quantitative myocardial perfusion in patients with prior surgical revascularization

A. Seraphim \* (1); B. Dowsing, (1); K. Rathod, (2); S. Hunain, (1); K. Patel, (1); K. Knott, (1); S. Zaman, (3); I. Johns (3); Y. Razvi, (4); R. Patel, (4); H. Xue (5); D. Jones, (2); M. Fontana, (4); G. Cole (3); R. Uppal, (6); R. Davies, (1); J. Moon (1); P. Kellman (5); C. Manisty (1)

(1) Cardiac imaging, St Bartholomew's Hospital, London, United Kingdom; (2) Interventional cardiology, St Bartholomew's Hospital, London, United Kingdom; (3) Cardiac imaging, Imperial College, Healthcare NHS Trust, London, United Kingdom; (4) Cardiac imaging, Royal Free London NHS Foundation Trust, London, United Kingdom; (5) National heart lung, and blood institute, National Institutes of Health, Bethesda, United States of America; (6) Department of cardiac surgery, St Bartholomew's Hospital, London, United Kingdom

### Abstract

**Background:** Patients with prior coronary artery bypass graft (CABG) surgery typically have complex coronary disease and remain at high risk of adverse events. Quantitative myocardial perfusion indices predict outcomes in native vessel disease, but their prognostic performance in patients with prior CABG is unknown.

**Objectives:** To evaluate whether stress myocardial blood flow (MBF) and perfusion reserve (MPR) derived from perfusion mapping cardiac magnetic resonance (CMR) can independently predict adverse outcomes in patients with prior CABG.

**Methods:** Retrospective analysis of consecutive patients referred for adenosine stress perfusion CMR with prior CABG. Perfusion mapping was performed in-line with automated quantification of myocardial blood flow. Primary outcome was a composite of all-cause mortality and major adverse cardiovascular events defined as non-fatal myocardial infarction and late revascularization. Associations were evaluated using Cox proportional hazards models after adjusting for comorbidities and CMR parameters.

**Results:** 341 patients (median age 67 years, 86% male) were included. Stress MBF was independently associated with age ( $B=-0.25$ ,  $p<0.001$ ), sex (female,  $B=0.10$ ,  $p=0.045$ ) and the amount of global late gadolinium enhancement (LGE) ( $B=-0.19$ ,  $p=0.003$ ), whilst MPR was associated with age ( $B=-0.019$ ,  $p<0.001$ ) and the presence of diabetes mellitus ( $B=-0.241$ ,  $p<0.001$ ). Over a median follow up of 638 days (IQR 367, 976), 81 (24%) patients reached the primary outcome. Both stress MBF and MPR independently predicted outcome after adjusting for known prognostic factors, including the presence of ischemia on visual assessment, cardiac function and the extent of myocardial scar. The adjusted hazard ratio

(HR) for 1ml/g/min decrease in stress MBF was 2.56 (95%CI, 1.45-4.35) and for 1unit decrease in MPR the adjusted HR was 1.61 (95%CI, 1.08-2.38). Stress MBF remained predictive of outcome even when cases undergoing revascularization within 12-months of the CMR study were excluded from the analysis.

## Conclusions

In patients with prior surgical revascularization, global stress myocardial blood flow and perfusion reserve independently predict adverse outcomes. This is independent of known predictors (age, diabetes, prior PCI, infarction, cardiac function and measured regional ischaemia). Understanding the impact of myocardial perfusion on outcomes can transform how we measure the success of revascularization, improve patient risk stratification and help re-evaluate our therapeutic targets.

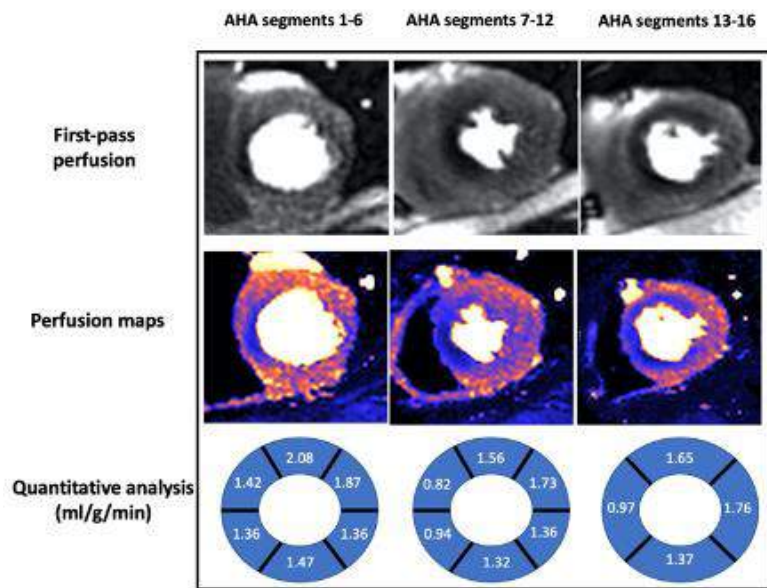
**Figure/Table 1**

Predictors	Death or MACE
<b>Stress myocardial blood flow (MBF)</b>	
<b>Unadjusted</b>	
Hazard ratio (95% CI) per 1x SD decrease	1.49 (1.18-1.92)
<i>P</i> value	<0.001
<b>Adjusted*</b>	
Hazard ratio (95% CI) per 1x SD decrease	1.59 (1.20-2.08)
<i>P</i> value	<0.001
Model <i>Chi-square</i> value	26.25
<b>Myocardial Perfusion Reserve (MPR)</b>	
<b>Unadjusted</b>	
Hazard ratio (95% CI) per 1x SD decrease	1.33 (1.04-1.69)
<i>P</i> value	0.021
<b>Adjusted</b>	
Hazard ratio (95% CI) per 1x SD decrease	1.35 (1.05-1.75)
<i>P</i> value	0.020
Model <i>Chi-square</i> value	20.9
MACE (myocardial infarction and coronary revascularization). Model for was adjusted for age, sex, left ventricular ejection fraction (LVEF), diabetes, history of previous PCI and global LGE (5x SD method used in this model).	

**Caption 1**

**Table 1. Cox Proportional Hazard Models for stress MBF and MPR as predictors of death or MACE**

**Figure/Table 2**

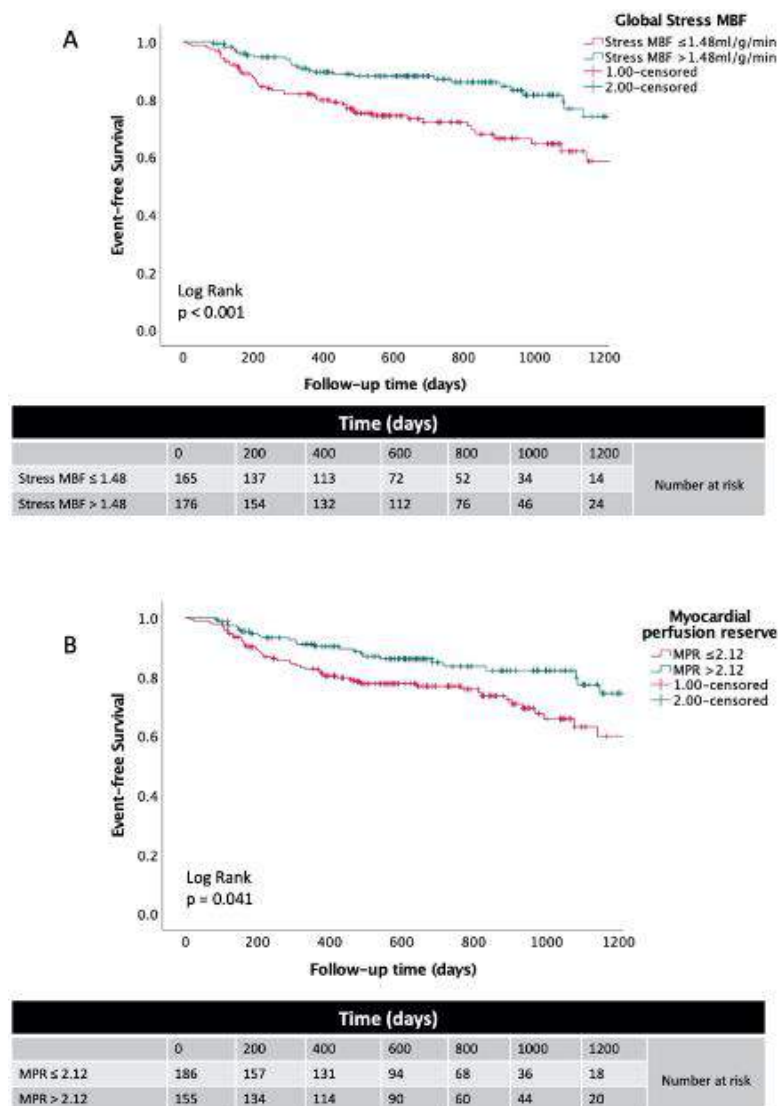


**Caption 2**

**Figure 2. Analysis of stress myocardial blood flow (MBF).**

Top row: First pass perfusion imaging of basal, mid and apical short axis slices. Middle row: Quantitative perfusion mapping generated in-line, with both global and segmental MBF estimated without user input (Bottom row).

**Figure 3**



### Caption 3

**Figure 3. Kaplan-Meier event-free survival curves for stress myocardial blood flow (MBF) and myocardial perfusion reserve (MPR)**

Event-free survival curves for death and major adverse cardiovascular events (non-fatal myocardial infarction and unplanned revascularization) according to (A) stress MBF (1.48ml/g/min) and (B) MPR (2.12).

Speaker: A. Seraphim

Category: CABG, Perfusion, Prognosis

000035

## Rosette Cardiac MRF for Simultaneous Myocardial T1, T2, and Fat Fraction Mapping

Y. Liu \* (1); J. Hamilton (1); N. Seiberlich (1)

(1) Radiology, University of Michigan, Ann Arbor, United States of America

### Abstract

**Background:** Cardiac MR Fingerprinting (cMRF) is an efficient method for measuring myocardial T1 and T2 from a single scan<sup>1</sup>. Previously, water-fat separation has been incorporated in the cMRF framework<sup>2</sup>, including our previous work using rosette trajectories to provide water-fat separated T1/T2 maps and proton density weighted images<sup>3</sup>. While water-fat separation helps remove quantitative errors caused by water-fat partial volume effects, quantitative fat fraction mapping may provide additional value in diagnosing diseases like intramyocardial fat infiltration<sup>4</sup>. In this work, rosette cardiac MRF is extended to enable simultaneous myocardial T1, T2, and fat fraction mapping from a single scan.

**Methods:** A rosette trajectory with eight lobes and a readout duration of 7.7ms was designed to suppress fat signals at -220Hz for 1.5T. The previously reported 15-heartbeat ECG-triggered 2D cMRF sequence structure was used in this study<sup>3</sup>. Spatial resolution of 1.6x1.6mm<sup>2</sup> and a slice thickness of 8mm were employed in all experiments. After water-fat separation and B0 correction, water and fat T1 and T2 maps were generated by matching undersampled images (one image per TR) to a dictionary that models the patient's cardiac rhythm, as described in our previous work<sup>3</sup>. To generate quantitative proton density fat fraction (PDFF) maps, the 8-lobe trajectory was divided into 9 segments (Figure 1a). Data from each segment were projected onto a low-dimensional subspace derived from the SVD of the dictionary. Subspace images corresponding to the first singular value were retained; images from each of the 9 rosette segments served as multi-echo images and were used to generate a PDFF map using Hierarchical IDEAL<sup>5</sup>.

All experiments were performed on a 1.5T scanner (Siemens Sola, Erlangen, Germany). The proposed rosette cMRF method was applied on an in-house built fat fraction phantom and the fat fraction results were compared with 3-point Dixon GRE measurements with optimal echo times at 1.5T (1.9/3.4/4.9ms). T1 and T2 measurements in the T2 layer of the ISMRM/NIST MRI system phantom were compared with gold standard values measured using inversion-recovery and single-echo spin-echo methods. Twelve healthy subjects were scanned after written informed consent in this IRB-approved study. Mid-ventricular level short axis slices in the heart were acquired using the proposed rosette cMRF sequence and the original spiral cMRF sequence. Conventional T1 and T2 mapping scans (MOLLI and T2-prepared bSSFP) were also performed on eight of the subjects. Significant difference between different methods was considered with  $P < 0.05$  in a student's t-test.

**Results:** Fat fraction (Figure 1b), and T1 and T2 (Figure 1c-d) measurements using rosette cMRF all agree well with reference values. In the heart, the averaged T1 and T2 values of all subjects measured using rosette cMRF, spiral cMRF, and conventional methods are summarized in Table 1. Compared with MOLLI, spiral cMRF yielded similar T1 values while rosette cMRF generated significantly higher T1 values, possibly due to reduced fat contamination. Both spiral and rosette cMRF yielded lower T2 values compared with the



conventional method, which is consistent with previous findings<sup>3</sup>. Averaged PDFF in the septum was -0.8%. Representative maps from one subject are shown in Figure 2.

**Conclusions:** This study shows that rosette cMRF enables efficient cardiac tissue characterization by quantifying myocardial T1, T2, and fat fraction simultaneously. Patient cohorts with abnormal fat deposition will be investigated in the future.

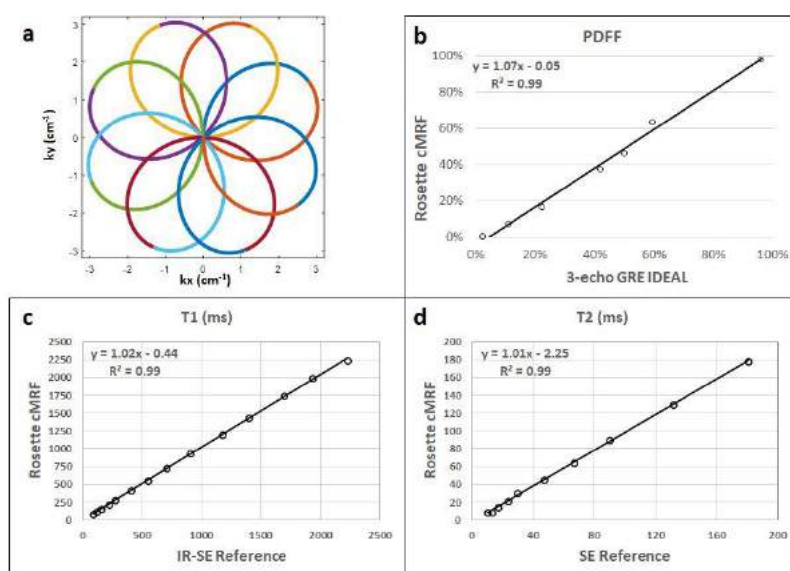
**Figure/Table 1**

	T1 (ms)	T2 (ms)
<b>Rosette cMRF</b>	1081.8 ± 33	40.1 ± 1.3
<b>Spiral cMRF</b>	997.4 ± 53.6	36.9 ± 2.9
<b>Conventional</b>	991.5 ± 19.6	45.7 ± 2.6

**Caption 1**

**Table 1.** Averaged T1 and T2 values in the entire mid-ventricular slice of 12 healthy subjects acquired using rosette cMRF compared with spiral cMRF and conventional methods (MOLLI for T1 and T2-prep bSSFP for T2).

**Figure/Table 2**

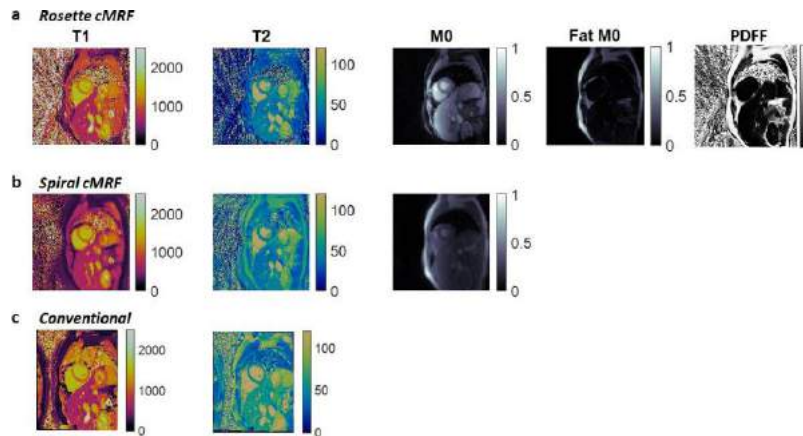


**Caption 2**

**Figure 1.** (a) The proposed rosette trajectory, where each segment used to generate multi-echo images is indicated by different colors. PDFF measurements in the fat fraction phantom

(b) and T1 and T2 measurements in the ISMRM/NIST phantom (c-d) compared with reference values.

**Figure 3**



**Caption 3**

**Figure 2.** Representative T1, T2, and FF maps in a healthy subject acquired using rosette cMRF compared with T1 and T2 maps measured by spiral cMRF and conventional methods.

### Bibliographic References

5. Tsao, J. & Jiang, Y. Hierarchical IDEAL: Fast, robust, and multiresolution separation of multiple chemical species from multiple echo times. *Magn. Reson. Med.* 70, 155–159 (2013)., 1. Hamilton, J. I. et al. MR fingerprinting for rapid quantification of myocardial T1, T2, and proton spin density. *Magn. Reson. Med.* 77, 1446–1458 (2017)., 2. Jaubert, O. et al. Water–fat Dixon cardiac magnetic resonance fingerprinting. *Magn. Reson. Med.* 00, 1–17 (2019)., 3. Liu, Y., Hamilton, J., Eck, B., Griswold, M. & Seiberlich, N. Myocardial T1 and T2 quantification and water–fat separation using cardiac MR fingerprinting with rosette trajectories at 3T and 1.5T. *Magn. Reson. Med.* (2021). doi:10.1002/mrm.28404, 4. Kellman, P. et al. Multiecho dixon fat and water separation method for detecting fibrofatty infiltration in the myocardium. *Magn. Reson. Med.* 61, 215–221 (2008).

Speaker: Y. Liu

Category: Fat, Parametric Mapping, Non-Cartesian

000036

## Real-time Free-breathing Cine Cardiovascular Magnetic Resonance with Tiny-golden Angle Radial K-space Trajectory

Y. C. I. Chan \* (1); L. Braunstorfer, (1); W. Y. R. Fok, (1); L. Browne (2); M. H. Moghari, (2)

(1) Department of computer science, Technical University of Munich, Garching, Germany;

(2) Department of radiology, Children's Hospital Colorado and School of Medicine, University of Colorado, Aurora, CO, United States of America

### Abstract

**Background:** Accurate assessment of ventricular volumes and ejection fractions is a central part of a cardiovascular magnetic resonance (CMR) examination [1]. This evaluation is typically performed using a retrospective electrocardiogram (ECG)-gated segmented k-space cine balanced steady-state free precession (bSSFP) acquisition during breath-hold (BH). In patients who cannot BH and when there is a severe arrhythmia, multiple signal averages during free-breathing (FB) is commonly used that results in inconsistent image quality due to cardiac and respiratory motion [2]. Accordingly, we developed a new real-time FB 2D cine bSSFP imaging technique that uses a conventional respiratory navigator to trigger the image acquisition at the transition of respiratory end-inspiration to expiration, and 1) minimizes respiratory and cardiac motion artifacts, and 2) images the entire cardiac cycle. The proposed technique was then validated in patients and compared with the conventional BH acquisition in terms of ventricular volume measurements.

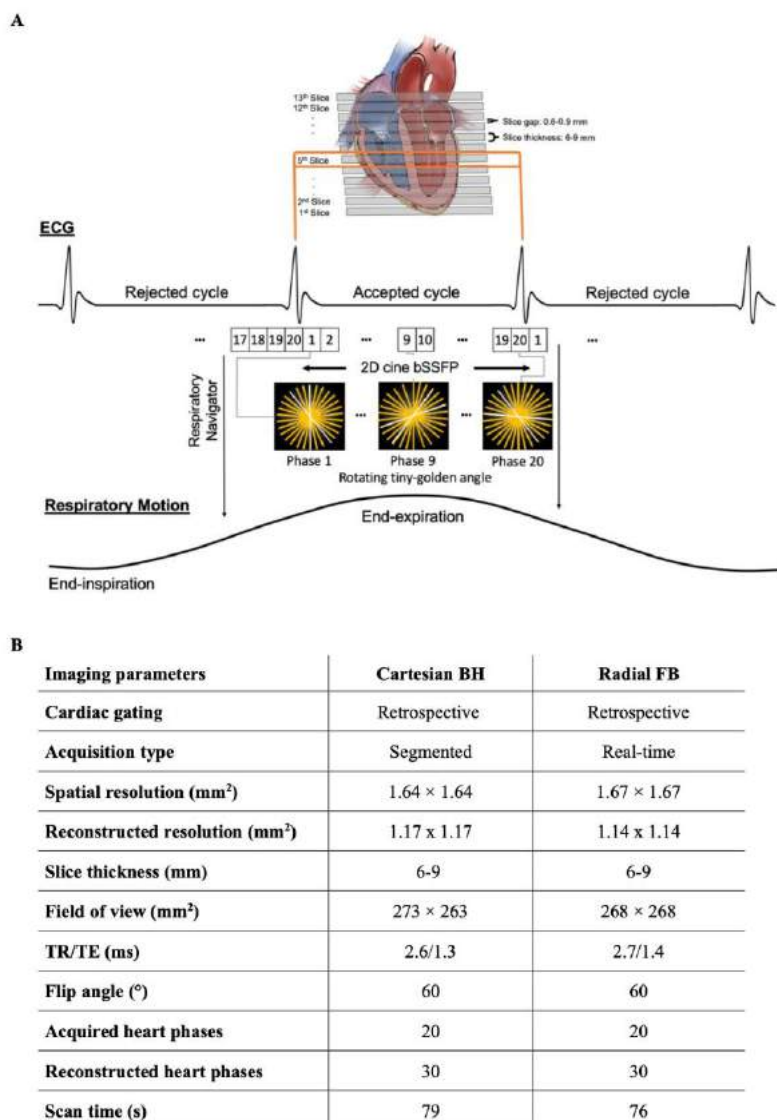
**Methods:** A schematic diagram of the real-time FB 2D cine bSSFP acquisition technique is shown in Figure 1A. A stack of multiple 2D slices is prescribed to cover the heart from base to apex in the short-axis view. A retrospective ECG-gated bSSFP sequence with Cartesian k-space trajectory was modified to a tiny-golden angle radial k-space trajectory [3]. A respiratory navigator is placed at the dome of the right hemi-diaphragm to continuously track the respiratory motion and trigger the real-time cine acquisition when a transition from respiratory end-inspiration to expiration is detected. Real-time cine data is accepted only from cardiac cycles occurring entirely during the transition from respiratory end-inspiration to expiration. Offline, the radial k-space data is binned into 20 cardiac phases based on the recorded ECG signal. Coil sensitivity maps are calculated, and the radial data is reconstructed using iGRASP reconstruction algorithm [4]. The 2D cine radial and Cartesian images were then compared in terms of left and right ventricular volumes. A two-tailed paired Student's t-test was used for statistical analysis and a p-value  $\leq 0.05$  was considered statistically significant.

**Results:** Prospective validation was performed in 9 patients (5 females, median age 17 (6-31) years-old) by obtaining in each 2 complete ventricular image stacks in a short-axis view using 2 different acquisition schemes: 1) standard segmented BH and 2) real-time FB on a 1.5T Philips Ingenia scanner (Figure 1B). Midventricular short-axis images with two sequences from 2 patients are shown in Figure 2. As shown in Table 1, there were no significant differences between real-time FB and BH for the end-diastolic volume, end-systolic volume, stroke volume, and ejection fraction (all p-values  $\geq 0.133$ ). Acquisition time of real-time FB was comparable to BH acquisition ( $76.0 \pm 4.9$  seconds vs.  $79.2 \pm 14.6$  seconds, p-value=0.543). The reconstruction time of real-time FB was  $\approx 3.6$  hours.

**Conclusions:** We developed a novel real-time FB 2D cine bSSFP imaging technique with tiny-golden angle radial k-space trajectory. This technique yielded comparable ventricular measurements to the traditional segmented BH acquisition and might be a useful approach for very young or ill patients who cannot hold their breath or have severe arrhythmia.

**Acknowledgement:** We would like to thank Janet Mcgee and Kathleen Jensen for countering the cine images and measuring the ventricular volumes.

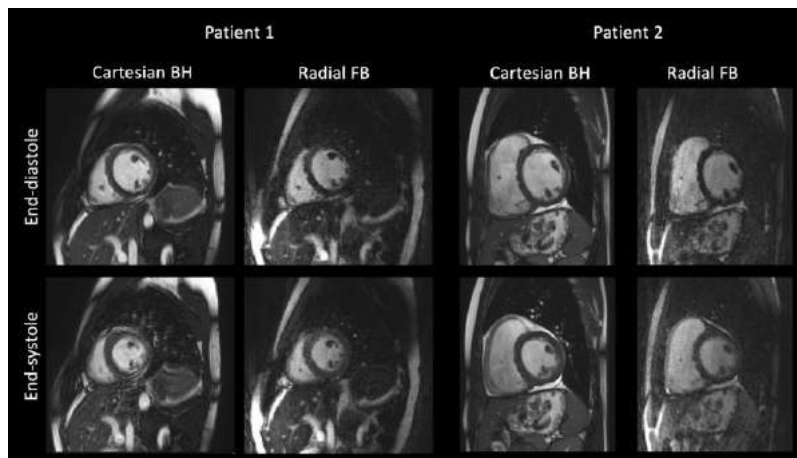
**Figure/Table 1**



**Caption 1**

**Figure 1:** (A) A schematic diagram of the proposed real-time free-breathing 2D cine balanced steady-state free precession (bSSFP) acquisition technique. (B) Imaging parameters of the conventional Cartesian breath-hold (BH) and proposed radial free-breathing (FB) cine bSSFP sequences used in the patient study.

**Figure/Table 2**



**Caption 2**

**Figure 2:** Midventricular short-axis images in end-systole and end-diastole acquired with segmented Cartesian breath-hold (BH) and real-time radial free-breathing (FB) cine balanced steady-state free precession sequences from a 17-years-old male patient with left ventricle dysfunction (Patient 1) and a 16-years-old male patient with dilated idiopathic cardiomyopathy (Patient 2).

**Figure 3**

N = 9	Left ventricle				Right ventricle			
	EDV (ml)	ESV (ml)	SV (ml)	EF (%)	EDV (ml)	ESV (ml)	SV (ml)	EF (%)
Cartesian BH	141.2±59.5	75.8±41.2	65.4±23.1	48.7±8.8	155.7±90.3	86.2±64.6	69.6±29.6	47.2±8.3
Radial FB	132.9±52.8	72.9±41.8	60.0±20.2	48.2±12.9	144.4±89.2	84.1±62.0	60.3±30.6	43.7±7.1
Mean % difference	4.9±14.4	6.0±23.5	7.7±20.1	2.8±13.2	6.7±29.2	0.28±32.8	13.5±33.0	7.3±17.6
P-value	0.368	0.645	0.358	0.839	0.321	0.801	0.133	0.271

**Caption 3**

**Table 1.** Ventricular measurements for segmented Cartesian breath-hold (BH) and real-time radial free-breathing (FB) cine balanced steady-state free precession acquisitions (n=9). Values are mean ± standard deviation. EDV, end-diastolic volume; ESV, end-systolic volume; EF, ejection fraction; and SV, stroke volume. P-value is calculated using a two-tailed paired Student's t-test.

### **Bibliographic References**

2. Moghari MH, Komarlu R, Annese D, Geva T, Powell AJ. Free-breathing steady-state free precession cine cardiac magnetic resonance with respiratory navigator gating. *Magn Reson Med* 2015;73(4):1555-1561., 3. Wundrak S, Paul J, Ulrici J, Hell E, Rasche V. A Small Surrogate for the Golden Angle in Time-Resolved Radial MRI Based on Generalized Fibonacci Sequences. *IEEE Trans Med Imaging* 2015;34(6):1262-1269., 4. Feng L, Grimm R, Block KT, Chandarana H, Kim S, Xu J, Axel L, Sodickson DK, Otazo R. Golden-angle radial sparse parallel MRI: combination of compressed sensing, parallel imaging, and golden-angle radial sampling for fast and flexible dynamic volumetric MRI. *Magn Reson Med*. 2014 Sep;72(3):707-17. doi: 10.1002/mrm.24980. Epub 2013 Oct 18. PubMed PMID: 24142845; PubMed Central PMCID: PMC3991777., 1. Kramer, C.M., et al., Standardized cardiovascular magnetic resonance (CMR) protocols 2013 update. *J Cardiovasc Magn Reson*, 2013. 15(1): p. 91. 2.

Speaker: Y. C. I. Chan

Category: Free Breathing, Real Time, Radial Imaging

000037

## Time course of left atrial (LA) structural and functional response to extensive anterior ST-elevation acute myocardial infarction (STEMI): the LAST-PASS MRI sub-study

Y. Kato \* (1); W. H. Lee (1); T. Pezel (2); M. Natsumeda (3); Y. Ohyama (4); C. Noda (1); B. Ambale-Venkatesh (5); K. Takagi (6); J. Lima (1); Y. Ikari (3)

(1) Cardiology, Johns Hopkins University, Baltimore, United States of America; (2) , , Massy; (3) Cardiology, Tokai University, Tokyo, Japan; (4) Cardiology, Gunma University, Maebashi, Japan; (5) Radiology, Johns Hopkins University, Baltimore, United States of America; (6) Cardiology, National Cerebral and Cardiovascular Center, Suita, Japan

### Abstract

**Background:** Abrupt deterioration of the left ventricular (LV) function in ST-elevation acute myocardial infarction (STEMI) requires compensation/adaptation in other cardiac chambers including the left atrium (LA). The prognostic value of LA parameters, e.g. LA reservoir strain, is inconsistent among studies in post-STEMI, suggestively the granularity of LA parameters in this cohort [1–3]. We investigated the acute and chronic phase LA indices and its change (delta-LA) in relation with myocardial scar assessed by late gadolinium enhancement (LGE) to understand its time course response in patients with anterior STEMI.

**Methods:** LAST-PASS study is an on-going multi-center prospective study in Japan (NCT03950310) recruiting patients with a first-episode STEMI with a culprit of proximal LAD, onset <6 hrs, initial TIMI flow of 0-1, and received a primary percutaneous coronary intervention. Exclusion criteria are: history of coronary artery bypass graft surgery or any cardiac device. Participants without atrial fibrillation received two CMR exams on 1.5T scanner at acute (5 to 9 days post index STEMI) and chronic (6 months) phases. The CMR protocol included CINE (temporal resolution of  $\approx 30$  ms) and LGE (at 17 min post 0.15 mmol/kg of Gadovist, Bayer Schering Pharma, Berlin-Wedding, Germany). Multimodality tissue tracking software (MTT; version 6.0, Toshiba, Japan) was used for the LA analysis. LV function and LGE were quantified using QMass (version 7.6, Medis Medical Imaging Systems, Leiden, the Netherlands). The cross-sectional association between the LA indices and LGE at acute and chronic phases and the association between the delta-LA indices and acute phase LGE were investigated with and without adjustment for age, sex, body-mass index, and mitral regurgitation (MR). The associations stratified by MR were also investigated.

**Results:** **Table 1** shows the participant demographics, LA indices, and other MRI indices with and without MR. All the LA indices presented larger volume or worse function in cases with MR at the acute and chronic phases. The LA volumetric and ejection fraction (EF) indices were associated with the LGE after adjustment in the acute phase. At the chronic phase, all the LA indices were associated or presented a trend of association with the extent of LGE (**Table 2**). In the stratified analysis by MR (**Figure 1**), at the acute phase, LAEFtotal, LAEFbooster, LAVmin, and booster strain rate presented an association or its trend with LGE scar in cases without MR while no association in cases with MR. In the chronic phase, all the LA indices were associated with LGE scar extent in cases with MR while in cases without MR, only the LAEFtotal, LAEFbooster, and booster strain rate presented a trend of association with LGE, which associations were already observed at the

acute phase. Delta-LA indices were not associated with the acute phase LGE scar extent in all cases or in the stratified analysis by MR.

**Conclusions:** The insufficient adaptation of LA to acute and sub-acute post-STEMI hemodynamics is reflected in the poor association of acute phase, or, delta- LA indices with the extent of LGE scar. At the chronic phase with stabilized hemodynamics, the associations are more significant particularly in cases with MR, which is an important factor to accelerate the LA remodeling. The diastolic dysfunction progression in proportion to the scar size is suggested from the developed association in booster strain and strain rate in cases with and without MR (**Table 2, Figure 1**). Time post index STEMI should be taken into consideration when interpreting LA indices in patients post-STEMI.

**Figure/Table 1**

	Acute phase All cases	Chronic phase All cases	All cases comparison P value	Acute phase with MR	Acute phase without MR	Acute phase comparison by MR P value	Chronic phase with MR	Chronic phase without MR	Chronic phase comparison by MR P value
<b>Participant demographics</b>									
N	66	57	N/A	20	46	N/A	12	45	N/A
Days between index STEMI and MRI	6.7±1.3	189.3±18.1	<0.01**	6.9±1.6	6.7±1.2	0.51	188±23	189.6±16.9	0.49
Age (y/o)	62.9±11.8	64.0±11.7	<0.01**	64.9±9.6	62.0±12.7	0.27	65.0±9.1	63.8±12.4	0.67
Male, N (%)	58 (87.9)	49 (86.0)	0.75	15 (75.0)	43 (93.5)	0.03*	9 (75.0)	40 (88.9)	0.22
Body mass index (kg/m2)	23.3±2.9	23.2±3.2	0.069	23.3±2.9	23.3±2.8	0.88	23.5±4.5	23.1±2.8	0.95
Mitral regurgitation, N (%)	20 (30.3)	12 (21.1)	0.24	20 (100)	0 (0)	<0.01**	12 (100)	0 (0)	<0.01**
<b>LA indices</b>									
Indexed LAVmax (ml/m2)	31.3 (25.7 – 36.4)	32.5 (25.6 – 40.6)	0.96	34.5 (27.6 – 43.5)	29.4 (25.3 – 36.3)	0.034*	48.3 (39.1 – 52.1)	30.3 (21.0 – 36.5)	<0.01**
Indexed LAVmin (ml/m2)	13.9 (11.0 – 21.4)	13.3 (10.1 – 20.7)	0.24	19.8 (12.0 – 24.5)	13.5 (10.6 – 18.2)	0.029*	23.7 (20.9 – 34.0)	12.0 (8.8 – 17.0)	<0.01**
LAEFtotal (%)	53.5 (46.6 – 58.3)	55.3 (47.9 – 62.3)	0.016*	48.7 (42.6 – 56.4)	53.8 (48.4 – 59.6)	0.12	46.1 (37.0 – 51.3)	57.9 (50.3 – 62.7)	<0.01**
LAEFbooster (%)	38.6 (34.6 – 44.6)	42.7 (34.9 – 49.1)	0.041*	36.2 (27.7 – 43.1)	39.9 (36.4 – 44.9)	0.046*	33.7 (27.1 – 37.4)	44.7 (36.6 – 44.7)	<0.01**
Strain_reservoir (%)	25.4 (21.2 – 31.3)	29.5 (22.5 – 35.5)	<0.01**	24.2 (18.0 – 31.6)	26.5 (22.6 – 30.7)	0.27	26.9 (13.6 – 30.3)	31.0 (24.1 – 38.1)	0.046*
Strain_booster (%)	14.8 (9.8 – 18.1)	15.8 (13.9 – 18.3)	0.04*	13.0 (9.3 – 16.0)	15.3 (11.3 – 18.4)	0.23	14.8 (6.0 – 16.6)	16.0 (14.0 – 19.9)	0.12
Strain_rate_reservoir (sec <sup>-1</sup> )	1.2 (0.98 – 1.5)	1.2 (0.97 – 1.4)	0.36	1.0 (0.8 – 1.5)	1.2 (1.0 – 1.4)	0.23	1.1 (0.7 – 1.3)	1.2 (1.0 – 1.5)	0.072
Strain_rate_booster (sec <sup>-1</sup> )	-1.4 (-1.8 – -1.1)	-1.4 (-1.8 – -1.2)	0.34	-1.2 (-1.3 – -1.1)	-1.5 (-1.8 – -1.2)	0.19	-1.2 (-1.4 – -0.7)	-1.5 (-1.8 – -1.2)	0.075
<b>Other MRI LV indices</b>									
LVEF (%)	39.1 (32.8 – 44.4)	46.8 (37.9 – 50.1)	<0.01**	38.7 (29.7 – 42.4)	40.0 (35.4 – 45.6)	0.16	43.1 (30.6 – 48.6)	47.6 (41.2 – 51.8)	0.16
Global_Scar (%) by LGE	19.1 (12.0 – 30.7)	13.6 (8.9 – 21.6)	<0.01**	25.5 (18.2 – 36.0)	17.5 (9.4 – 27.8)	0.010*	12.9 (10.6 – 36.7)	14.0 (7.7 – 20.4)	0.21

**Caption 1**

**Table 1.** Participants demographics, LA indices, and MRI LV indices at the acute and chronic phases in all cases and cases by mitral regurgitation (MR). The values at the acute and chronic phases or by MR were compared with Wilcoxon signed-rank test or chi-square test. \*\* P<0.01; \* P<0.05.

**Figure/Table 2**



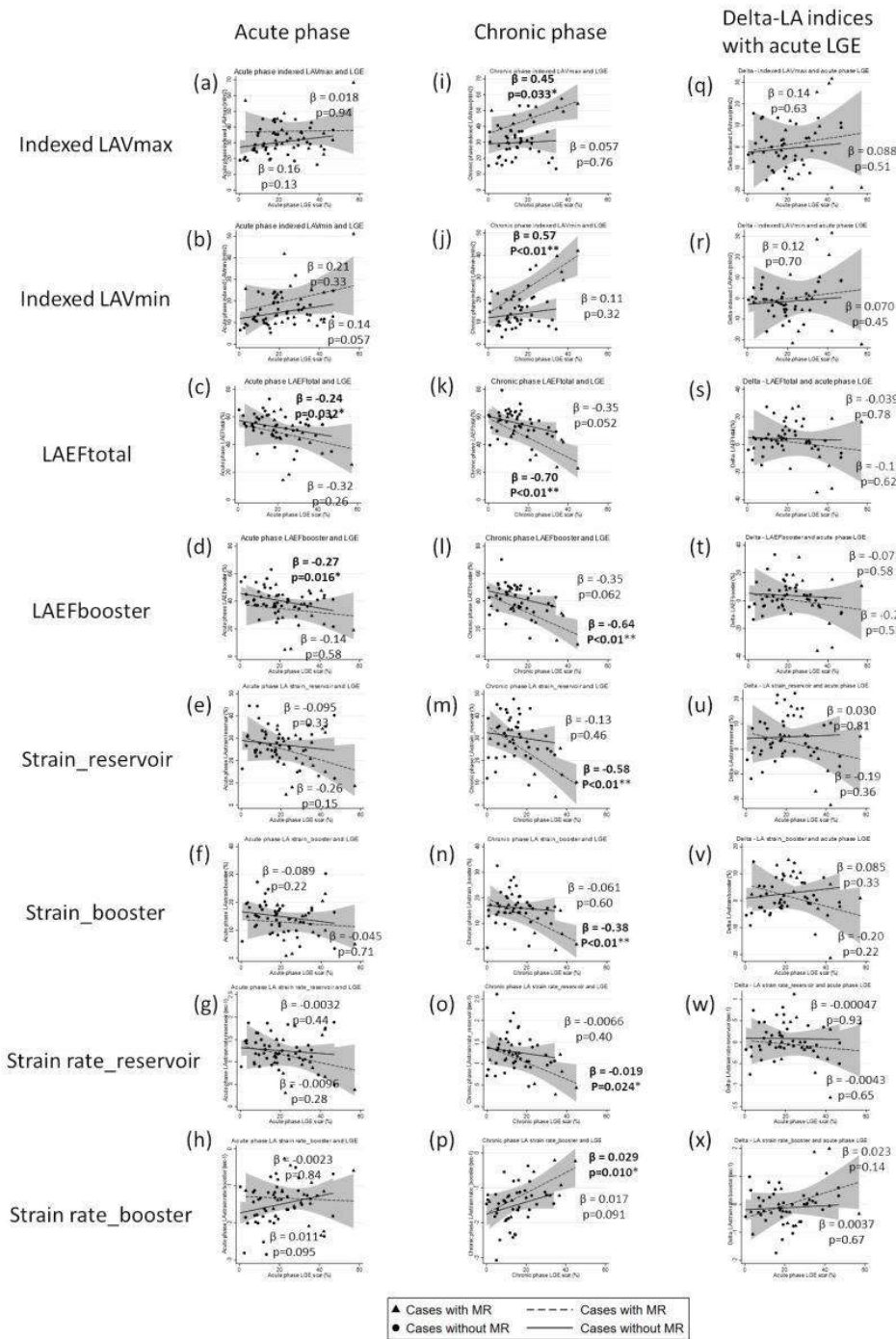
(a)	Acute phase cross-sectional association of LA indices with LGE scar(%)	Simple linear regression		Adjusted with age, sex, BMI, and mitral regurgitation	
		$\beta$	p	$\beta$	p
	Indexed LAVmax (ml/m2)	0.18	0.057	0.12	0.21
	Indexed LAVmin (ml/m2)	<b>0.22</b>	<b>&lt;0.01**</b>	<b>0.19</b>	<b>0.022*</b>
	LAEFtotal (%)	<b>-0.31</b>	<b>&lt;0.01**</b>	<b>-0.32</b>	<b>&lt;0.01**</b>
	LAEFbooster (%)	<b>-0.29</b>	<b>&lt;0.01**</b>	<b>-0.26</b>	<b>0.020*</b>
	Strain_reservoir (%)	<b>-0.18</b>	<b>0.033*</b>	-0.17	0.066
	Strain_booster (%)	-0.095	0.108	-0.068	0.27
	Strain_rate_reservoir (sec <sup>-1</sup> )	-0.0064	0.082	-0.0068	0.086
	Strain_rate_booster (sec <sup>-1</sup> )	0.0084	0.13	0.0069	0.24

(b)	Chronic phase cross-sectional association of LA indices with LGE scar(%)	Simple linear regression		Adjusted with age, sex, BMI, and mitral regurgitation	
		$\beta$	p	$\beta$	p
	Indexed LAVmax (ml/m2)	<b>0.38</b>	<b>0.016*</b>	<b>0.20</b>	<b>0.16*</b>
	Indexed LAVmin (ml/m2)	<b>0.42</b>	<b>&lt;0.01**</b>	<b>0.30</b>	<b>&lt;0.01**</b>
	LAEFtotal (%)	<b>-0.59</b>	<b>&lt;0.01**</b>	<b>-0.53</b>	<b>&lt;0.01**</b>
	LAEFbooster (%)	<b>-0.56</b>	<b>&lt;0.01**</b>	<b>-0.46</b>	<b>&lt;0.01**</b>
	Strain_reservoir (%)	<b>-0.38</b>	<b>&lt;0.01**</b>	<b>-0.34</b>	<b>0.018*</b>
	Strain_booster (%)	<b>-0.23</b>	<b>0.010*</b>	-0.17	0.062
	Strain_rate_reservoir (sec <sup>-1</sup> )	<b>-0.014</b>	<b>0.015*</b>	-0.012	0.059
	Strain_rate_booster (sec <sup>-1</sup> )	<b>0.025</b>	<b>&lt;0.01**</b>	<b>0.020</b>	<b>0.011*</b>

## Caption 2

**Table 2.** The simple linear regression between the LA indices with LGE scar (%) and with adjustment at the acute phase (a) and at the chronic phase (b). The association of the booster strain rate with LGE scar revealed significant at chronic phase, suggesting the LA adjustment/compensation. \*  $p < 0.05$ ; \*\*  $p < 0.01$ .

## Figure 3



**Caption 3**

**Figure 1.** The association between the LA indices with LGE scar (%) by mitral regurgitation (MR) at acute phase (a to h), chronic phase (i to p), and delta-LA indices with LGE scar (%) (q to x). The correlation coefficient ( $\beta$ ) and p-value are presented on each panel. \*  $p < 0.05$ ; \*\*  $p < 0.01$ .

### **Bibliographic References**

3. Ersbøll M, Andersen MJ, Valeur N, Mogensen UM, Waziri H, Møller JE, et al. The prognostic value of left atrial peak reservoir strain in acute myocardial infarction is dependent on left ventricular longitudinal function and left atrial size. *Circ Cardiovasc Imaging* [Internet]. 2013;6:26–33. Available from: <http://www.ncbi.nlm.nih.gov/pubmed/23192848>, 2. Antoni ML, ten Brinke EA, Atary JZ, Marsan NA, Holman ER, Schalij MJ, et al. Left atrial strain is related to adverse events in patients after acute myocardial infarction treated with primary percutaneous coronary intervention. *Heart* [Internet]. 2011;97:1332–7. Available from: <http://www.ncbi.nlm.nih.gov/pubmed/21613636>, 1. Schuster A, Backhaus SJ, Stiermaier T, Navarra J, Uhlig J, Rommel K-P, et al. Left Atrial Function with MRI Enables Prediction of Cardiovascular Events after Myocardial Infarction: Insights from the AIDA STEMI and TATORT NSTEMI Trials. *Radiology* [Internet]. 2019;293:292–302. Available from: <http://www.ncbi.nlm.nih.gov/pubmed/31526253>

Speaker: Y. Kato

Category: Left Atrium, Acute Myocardial Infarction, Late Gadolinium Enhancement

000039

**Prognostic value and optimal thresholds of valve and chamber quantification in surgery for aortic and mitral regurgitation: a prospective cardiac magnetic resonance imaging study**

T. K. M. Wang \* (1); Z. Popovic, (2); L. Rodriguez, (2); M. Bolen, (2); L. A. Moennich, (2); K. Rutkowski, (2); B. Griffin, (2); R. Grimm, (2); S. Flamm (2); D. Kwon, (2)

(1) Section of cardiovascular imaging, Cleveland Clinic Main Campus, Euclid Avenue, Cleveland, United States of America; (2) Section of cardiovascular imaging, Cleveland Clinic Main Campus, Cleveland, United States of America

**Abstract**

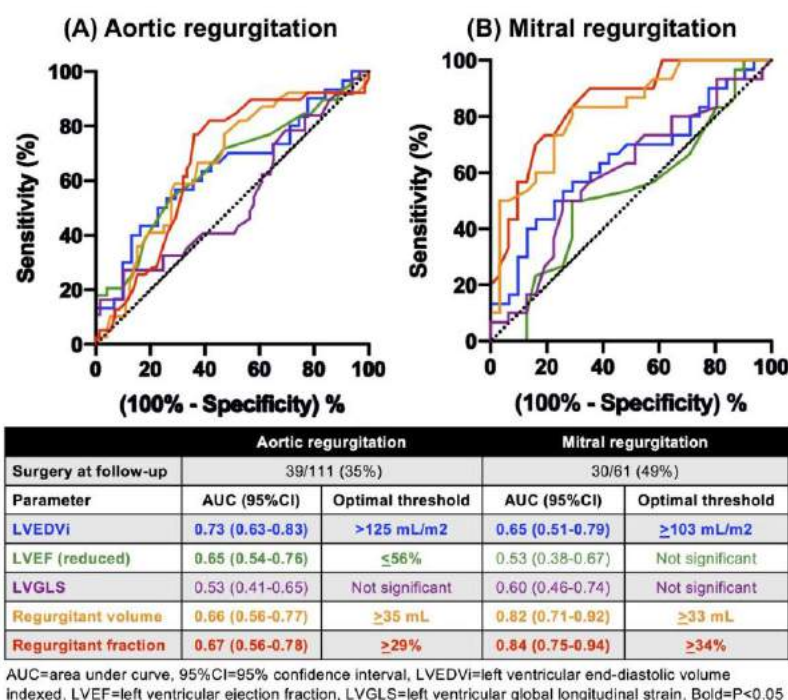
**Background:** Magnetic resonance imaging (MRI) has shown prognostic value on top of transthoracic echocardiography for valvular heart diseases, however its discriminative ability and optimal thresholds for undertaking valve surgery remain not well established. We evaluate the predictive value and optimal thresholds of quantitative parameters by cardiac MRI to identify aortic (AR) and mitral (MR) regurgitation patients having valve surgery during follow-up.

**Methods:** Patients with moderate-to-severe AR (n=111) and MR (n=61) by echocardiography undergoing MRI were prospectively studied. Area under the receiver-operative characteristics curve (AUC) and multivariable Cox regression analyses were performed to assess if symptoms and MRI parameters were associated with undergoing valve surgery during follow-up and their thresholds.

**Results:** Mean regurgitant volumes (RV) and fractions (RF) were 50 mL and 46% in AR patients (37% symptomatic) and 53 mL and 51% in MR patients (51% symptomatic). Valve surgery was performed in 39 (35%) AR and 30 (49%) MR patients during mean follow-up  $1.0 \pm 0.6$  years, with no deaths. AUC analyses and optimal thresholds of MRI parameters to identify valve surgery during follow-up are shown in Table 1. Optimal MRI-based thresholds for surgery were AR-RV  $\geq 35$  mL, AR-RF  $\geq 29\%$ , MR-RV  $\geq 33$  mL and MR-RF  $\geq 34\%$ . Multivariable analyses results are listed in Figure 2. Left ventricular end-diastolic volume indexed was independently associated with undergoing surgery in AR patients, while higher RV or RF and symptoms were independently associated with undergoing surgery in MR patients.

**Conclusion:** Optimal MRI-valve quantification thresholds to undergo surgery were significantly lower than contemporary echocardiography guidelines, emphasizing the need for separate MRI-based thresholds for severe regurgitation. Chamber remodeling were more prognostic for proceeding to valve surgery in AR patients, and RV or RF more prognostic in MR patients.

Figure/Table 1



Caption 1

Figure 1: Receiver-operate characteristics analyses and optimal thresholds for MRI parameters to identify valve surgery during follow-up in (a) aortic regurgitation and (b) mitral regurgitation patients.

Figure/Table 2

	Aortic regurgitation	Mitral regurgitation
Covariates	Hazards ratio (95%CI)	Hazards ratio (95%CI)
<b>Model 1</b>		
Symptoms	1.67 (0.86-3.25)	<b>2.63 (1.20-5.77)</b>
LVEDVi (10 mL/m <sup>2</sup> increase)	<b>1.17 (1.08-1.27)</b>	1.08 (0.85-1.38)
LVEF (10% decrease)	1.46 (0.93-2.30)	
Regurgitant volume (10 mL increase)	1.14 (0.98-1.33)	<b>1.34 (1.12-1.63)</b>
<b>Model 2</b>		
Symptoms	1.53 (0.79-2.98)	<b>2.75 (1.26-6.03)</b>
LVEDVi (10 mL/m <sup>2</sup> increase)	<b>1.13 (1.03-1.23)</b>	1.10 (0.89-1.38)
LVEF (10% decrease)	1.34 (0.89-2.00)	
Regurgitant fraction (10% increase)	1.24 (0.98-1.58)	<b>2.26 (1.5103.36)</b>

95%CI=95% confidence interval, LVEDVi=left ventricular end-diastolic volume indexed, LVEF=left ventricular ejection fraction. Model 1 uses regurgitant volume, model 2 uses regurgitant fraction. Bold=P<0.05

## **Caption 2**

Figure 2: Multivariable Cox proportional hazards regression of symptoms and MRI parameters to be independently associated with valve surgery during follow-up in aortic and mitral regurgitation patients

Speaker: T. K. M. Wang

Category: Mitral Regurgitation, Aortic Regurgitation, Cardiac Surgery

**000041**

**Native T1 mapping for myocardial tissue characterization in patients with different forms of dilated cardiomyopathy, a comparative study with late gadolinium enhancement**

H. elsafty \* (1); R. M. Mary (2); M. D. Tamer (1); H. Ibraheem (2); E. Reda (1); E. Mohammed (1)

(1) radiology, Tanta University, Tanta, Egypt; (2) Radiology, National Heart Institute (Imbaba), Cairo, Egypt

**Abstract**

**Background:**

Dilated cardiomyopathy is a heart muscle disorder defined by the presence of a dilated volumes and poorly functioning left or both ventricles. It can be primary (genetic, mixed or predominantly familial non genetic, or secondary (inflammatory, autoimmune, endocrine as thyrotoxicosis and ischemic). Native T1-mapping is an advanced technique that provides quantitative information for assessment of diffuse myocardial fibrosis, edema and inflammation in number of disease states. Moreover native T1 mapping offers a future method for quantifying myocardial fibrosis in patients with advanced chronic kidney disease and patient with end stage renal disease on dialysis without need for gadolinium based contrast agents. The main goal of this work was to assess the potential value of segmental quantification of myocardial fibrosis using native T1 mapping in dilated cardiomyopathy in comparison to late contrast enhancement imaging.

**Methods:**

All CMR examinations were performed using 1.5 T CMR scanner with a phase array cardiac coil. Besides the conventional CMR viability protocol, all patients underwent myocardial tissue mapping using look-locker inversion recovery (LLI) technique. The LL single-slice T1 determinations were performed at six time points before gadolinium administration using an inversion recovery True FISP LL sequence. Short-axis T1 maps images were manually assessed using dedicated software. A ROI >12 pixels was drawn manually on the pre-contrast images in each segment of the basal, mid-ventricular and apical cuts excluding the apex giving a total of 16 segments in each patient (three slice protocol).

**Results:**

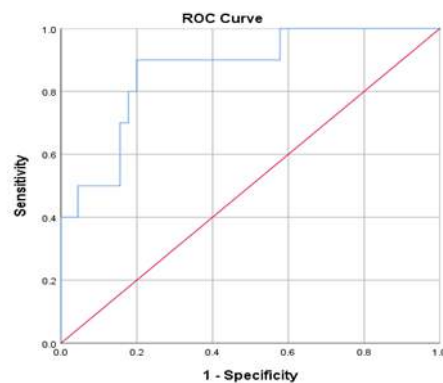
The native T1 values of a total 720 segments (16 segments in 45 patients (46.33±14.85 years) with DCM (ischemic 73%, post myocarditis 22%, Duchene 1.3% and idiopathic 3.7% of total cases). These were compared with 160 segments of 10 healthy volunteers (55 ± 13 years). Native T1 values were significantly higher in most of myocardial segments with LGE than in those without including the control group especially in mid LV septal segments (1130.85 ± 79.79 ms vs 1047.74 ± 42.74 ms;  $P = 0.001$ ). Also the current study showed T1 values were significantly higher than normal even in segments unaffected by LGE, ( $P < 0.01$ ) in DCM

group. A receiver operating characteristic (ROC) analysis revealed the appropriate cutoff value of 1072 ms for identifying myocardial fibrosis with a sensitivity of 90% and specificity of 80 %.

#### Conclusions:

Non-contrast T1-mapping is a novel method for objectively detecting myocardial fibrosis with a high diagnostic performance especially in patients who cannot afford gadolinium contrast agents as patients with end stage renal disease. In the present study, the T1 threshold value of 1072 ms provided high specificity and sensitivity for evaluating LGE in patients with DCM.

**Figure/Table 1**

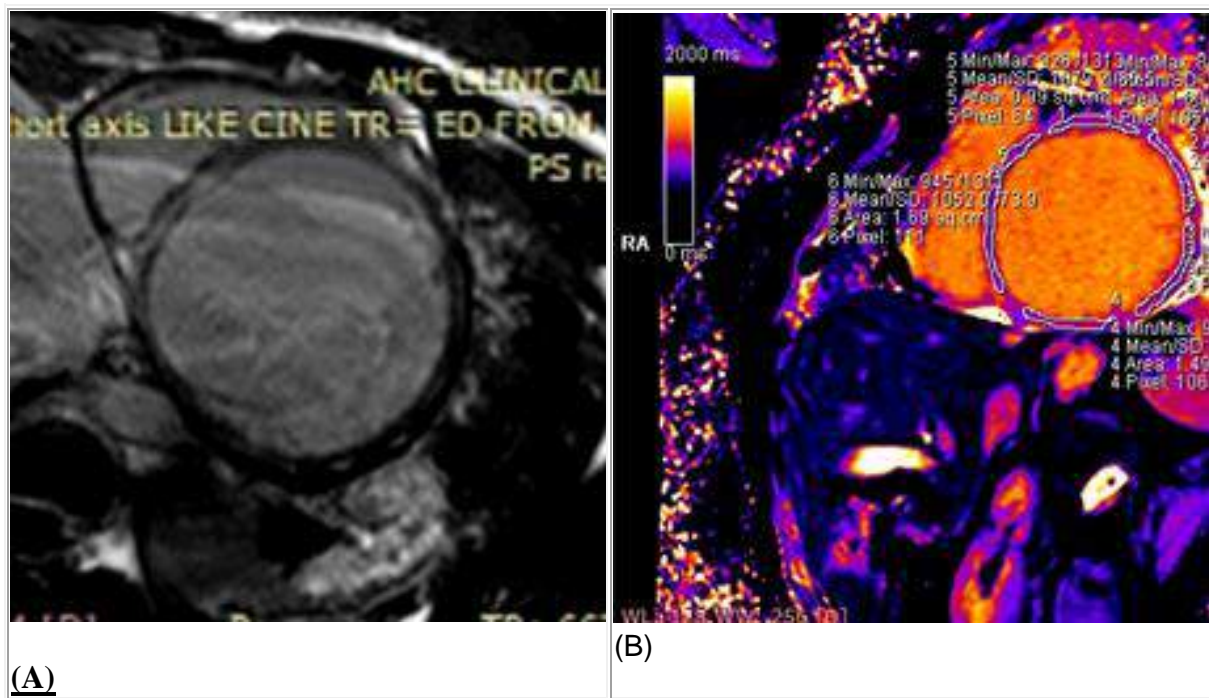


Receiver operator characteristic curve for identifying septal late gadolinium enhancement (LGE) based on native T1 values acquired by non-contrast-enhanced T1 mapping

**Figure/Table 2**

(a)





**37Y male presented by shortness of the breath ,ECG shows complete bundle branch block, ECHO findings compatible with DCM**

(A)short axis LGE (late gadolinium enhancement )shows mid wall septal enhancement (B) Non-contrast-enhanced T1 mapping shows that the native T1 value of the corresponding regions including LGE (enclosed by a arrow) is 1105ms which is more than 1072

**Bibliographic References**

Puntmann VO, Voigt T, Chen Z, et al: Native T1 mapping in differentiation of normal myocardium from diffuse disease in hypertrophic and dilated cardiomyopathy. J Am Coll Cardiol Img 6:475–484, 2013., Sibley CT, Noureldin RA, Gai N, et al. (: T1 mapping in cardiomyopathy at cardiac MR: comparison with endomyocardial biopsy. Radiology 265:365,2012., Suttie JJ, Piechnik SK, Ferreira VM, et al): Myocardial tissue characterization using magnetic resonance non contrast t1 mapping in hypertrophic and dilated cardiomyopathy Circ Cardiovasc Imaging;5:726–733,2012

Speaker: H. elsafty

Category: Dilated Cardiomyopathy, Mapping Techniques, Fibrosis

000042

## **Acute myocarditis mimicking HCM in a patient with Marfan's syndrome and morphologically abnormal mitral valve**

N. Sharrack \* (1); A.-M. Poenar, (1); A. Simms, (2); J. Greenwood (1); S. Plein (1)

(1) Licamm, Leeds institute of Cardiovascular and Metabolic Medicine, Leeds District, UK, United Kingdom; (2) Cardiology, Leeds General Infirmary, Leeds, United Kingdom

### **Abstract**

A 40-year-old man with a past medical history of Marfan's Syndrome and mild aortic root dilatation presented to the emergency department with chest pain and troponin elevation.

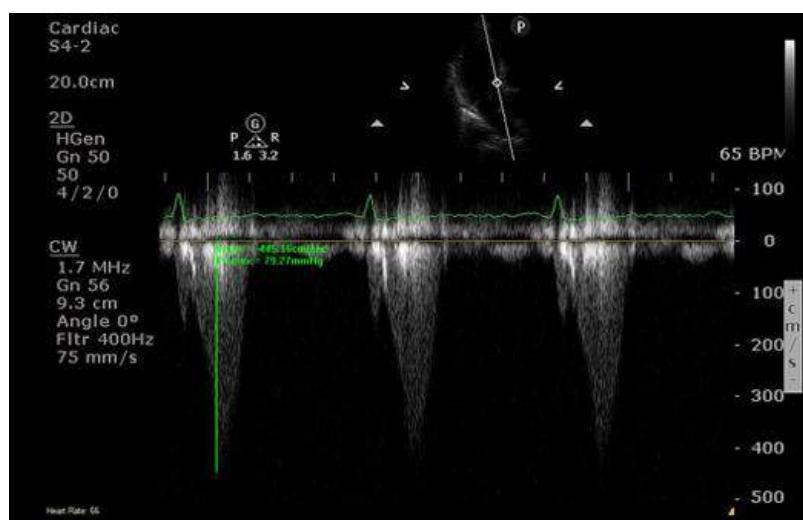
Admission ECG showed LVH and subtle ST elevation and T wave inversion in V1. CT aortogram promptly excluded an acute aortic syndrome. Bedside echocardiography showed a non-dilated LV with LVH and angulation of the septum with chordal systolic anterior motion (SAM) resulting in significant LVOT obstruction and moderate mitral regurgitation. There was akinesia of the mid anterior, anterolateral, anteroseptal and all apical segments, with preservation of function basally and overall severe global LV impairment (LVEF 30-35%). Coronary angiography revealed non-obstructive coronary arteries. Subsequent echocardiography 6 days post-admission confirmed the presence of asymmetric septal LVH (17mm), significant LVOT obstruction (79mmHg on Valsalva, figure 1) with resolution of the regional wall motion abnormalities and systolic dysfunction LVEF 75%. Findings were reported to be in keeping with HCM.

The initial differential diagnosis included all causes of acute coronary syndrome (ACS). After exclusion of a coronary event and aortic dissection, differentials included the causes of myocardial infarction with non-obstructive coronary arteries (MINOCA), specifically: Takotsubo cardiomyopathy, myocarditis and HCM. Giving the atypical clinical and echocardiographic presentation, a CMR scan was undertaken on day 7. CMR revealed a non-dilated LV with good systolic function (LVEF 58%), asymmetric LVH (septum 17mm versus lateral wall 7mm) with chordal SAM resulting in a non-significant LVOT obstruction. Native T1 and T2 mapping showed increased values. Late gadolinium enhancement (LGE) images revealed focal, linear mid-wall fibrosis in the basal-to-mid septum which excluded a Takotsubo cardiomyopathy (figure 2).

A CMR 26 months before the current admission showed a normal septal wall thickness of 11 mm. There was a similar appearance of the mitral valve with thickening of the tips, chordal SAM and flow acceleration in the LVOT. CMR findings raised the suspicion of acute myocarditis. The asymmetric septal hypertrophy was assumed to be caused by acute oedema rather than HCM. Interval CMR imaging undertaken 4 months after discharge, showed significant reduction in the septal hypertrophy from 17mm to 11mm similar to measurements from 2018 consistent with resolution of the myocardial oedema (figure 3). There was normalisation of native T1 and T2 values, but persistent septal mid-wall fibrosis.

This is a rare and interesting case that required several different imaging tests, over a period of months, to confirm the diagnosis. The unusual presentation of septal oedema in myocarditis had resulted in LVOT obstruction. The presence of a morphologically abnormal mitral valve, often seen in patients with Marfan's syndrome, exacerbated the LVOT obstruction. Repeat CMR imaging showed complete resolution of the septal hypertrophy and oedema with normalisation of the T1 and T2 relaxation times, allowing a confident diagnosis of myocarditis and differentiation from HCM.

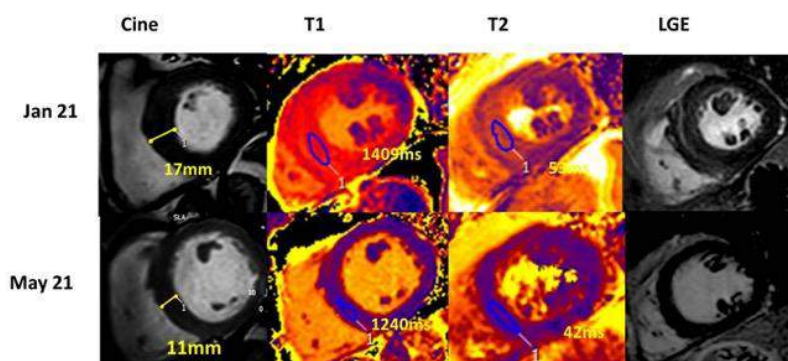
**Figure/Table 1**



**Caption 1**

Figure 1: TTE on admission showing Continuous Wave doppler through the LVOT showing a maximum velocity of 4.5m/s and peak gradient of 79mmHg.

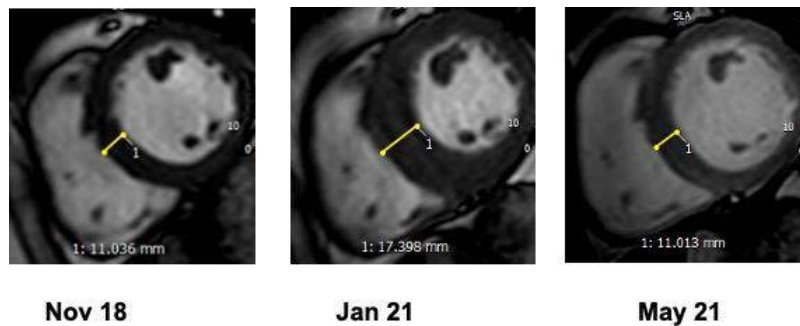
**Figure/Table 2**



**Caption 2**

Panel showing septal hypertrophy and oedema in January (17mm): T1 in septum raised at 1409ms ( 1190+/- 50ms 3T Philips ingenia), T2 mGRaSE raised at 53ms in the mid septum (reference range 44-51ms 3T Philips) with resolution of septal hypertrophy (12mm) and oedema in May 2021: T1 in septum 1240ms (1190+/- 50ms 3T Philips), T2 mGRaSE (42ms mid LV (reference range 44-51ms). LGE in January shows mid wall enhancement in the septum which has almost resolved in May 2021

**Figure 3**



**Caption 3**

Figure 3: Slices from CMR showing LV septal wall thickness dimensions in November 2018 at 11mm, increasing to 17mm in January 21, back to 11mm in May 2021.

Speaker: N. Sharrack

Category: Myocarditis, Hypertrophic Cardiomyopathy, Marfan

000043

**The prognostic value of cardiac magnetic resonance imaging in patients with a working diagnosis of myocardial infarction and unobstructed coronary arteries (MINOCA) — An outcome study with up to 10 years of follow-up**

R. Konst \* (1); M. Parker, (2); Y. Kaolawanich, (3); S. Elias-Smale, (1); R. Nijveldt, (1); R. Kim, (2)

(1) Cardiology, Radboud University Medical Center, Nijmegen, Netherlands; (2) Medicine, Duke University, Durham, United States of America; (3) Medicine, Faculty of Medicine Siriraj Hospital, Mahidol University, Bangkok, Thailand

**Abstract**

**Background:** Patients with a working diagnosis of myocardial infarction with unobstructed coronary arteries (MINOCA) represent a heterogeneous cohort. Prognosis could vary substantially depending on the underlying etiology. Although Cardiac Magnetic Resonance imaging (CMR) is considered a key diagnostic tool in these patients, there is limited data linking the CMR diagnosis with outcome.

**Methods:** This study is a prospective, longitudinal outcomes registry of 252 consecutive patients (57% female, mean age 54±16 years) with a working diagnosis of MINOCA, clinically referred for CMR. We determined the relationships between the prespecified CMR diagnoses of acute myocardial infarction (AMI), myocarditis, nonischemic cardiomyopathy (NICM), normal CMR study, and major adverse cardiovascular events (MACE).

**Results:** The CMR diagnosis was AMI in 63 patients (25%), myocarditis in 33 (13%), NICM in 111 (44%), normal CMR in 37 (15%) and Other in 8 (3%) (**Figure 1**). A specific nonischemic cause was diagnosed allowing MINOCA to be ruled-out in 57% of the cohort (**Figure 1**). During up to 10 years of follow-up (1595 patient-years), MACE occurred in 84 patients (33%), which included 64 deaths (25%). The unadjusted cumulative 10-year rate of MACE was 47% in AMI, 24% in myocarditis, 50% in NICM, and 4% in patients with a normal CMR (log-rank  $p < 0.001$ ). The CMR diagnosis provided incremental prognostic value over clinical factors including age, gender, CAD risk factors, presentation with ST elevation, and peak troponin (incremental  $\chi^2$  17.9,  $p < 0.001$ ); and patients with diagnoses of AMI, myocarditis, and NICM had worse MACE-free survival than patients with a normal CMR (**Figure 2**).

**Conclusions:** In patients with a working diagnosis of MINOCA, CMR allows ruling-out true MINOCA in 57% of patients. CMR diagnoses of AMI, myocarditis, and NICM are associated with worse MACE-free survival, whereas a normal CMR study portends a benign prognosis. These findings underline the importance of performing CMR for both diagnostic and prognostic purposes in patients with the working diagnosis of MINOCA.

**Figure/Table 1**

**Caption 1**

Study flowchart

## **Figure/Table 2**

### **Caption 2**

Age-adjusted cumulative incidence of MACE according to CMR diagnosis

Speaker: R. Konst

Category: Acute Myocardial Infarction, Myocarditis, Nonischemic Cardiomyopathy

000044

## Fontan Surgical Planning on Children with Single-ventricle Heart Disease and Glenn Physiology using Computational Fluid Dynamics

E. Javadi \* (1); S. Jamali (1); A. J. Powell (2); M. Di Miaria (3); M. Stone (4); V. Kheyfets (5); L. Browne (6); M. Moghari (6)

(1) Mechanical and industrial engineering, Northeastern University, Boston, United States of America; (2) Department of cardiology, Boston Children's Hospital, Boston, United States of America; (3) Department of cardiology, Children's Hospital Colorado, Aurora, United States of America; (4) Department of surgery, Children's Hospital Colorado, Aurora, United States of America; (5) Department of bioengineering, University of Colorado, Aurora, United States of America; (6) Department of radiology, Children's Hospital Colorado, Aurora, United States of America

### Abstract

**Background:** The final stage of single-ventricle (SV) surgical palliation is the Fontan procedure where an extracardiac conduit is commonly used to redirect inferior vena cava (IVC) blood to the right and left pulmonary arteries (RPA and LPA), bypassing the heart, and resulting in a total cavopulmonary connection (TCPC). Although this surgery can be lifesaving, SV patients suffer from decreased exercise capabilities due to elevated blood flow power loss (PL) [1] and pulmonary arteriovenous malformations because of asymmetric hepatic flow distribution (HFD) to the left and right lungs [2]. Therefore, it is important to optimally design the TCPC connection to have minimize PL and balance HFD to the lungs. In this study, we used computational fluid dynamics (CFD) to design optimal conduits for SV patients following bi-directional Glenn to determine the optimal strategy for Fontan completion.

**Methods:** We retrospectively identified 10 patients in Glenn stage (median age 3.2 (1.3-5.3) yrs, 9 male) who underwent cardiovascular magnetic resonance (CMR) and cardiac catheterization exams for the assessment of Glenn pathway and measurement of blood flow and pressure in the RPA, LPA, and superior vena cava (SVC). To generate a 3-dimensional (3D) patient-specific mesh model for each patient, the axial images from the 3D whole-heart CMR angiogram were manually segmented. Assuming the blood flow at SVC and pressures at RPA and LPA as inputs to our model, CFD simulation was performed to compute the blood flow in the RPA and LPA. The results were then compared with the net blood flow in the RPA and LPA measured by CMR to validate the accuracy of the developed CFD model. The schematic of the CFD model is shown in Figure 1, representing the inputs and outputs for the simulations. After validating the CFD model, two types of TCPC conduits, T-junction and Y-graft, were constructed for each patient. The cross section of IVC coming out of the liver was segmented and then a tube was generated to connect the IVC to the branch pulmonary arteries using SpaceClaim software [3]. Based on the pulmonary resistances calculated from catheterization, post-Fontan blood flow in the SVC and IVC for each TCPC configuration was estimated and the developed CFD model was used to estimate the PL and HFD to the left and right lungs. The anastomosis location of TCPC conduit was modified until the minimum PL and balanced HFD were achieved. The PL and HFD of the two types of TCPC conduits were then compared.



**Results:** For SV patients at Glenn physiology, there was good agreement between the net blood flow distributions within the RPA and LPA computed by CFD and CMR measurements (ICC= 0.98, P-value  $\geq 0.21$ ) with an error of less than 10% (Table 1). Figure 2 shows the generated T-junction and Y-graft TCPC conduits for the 10 SV patients with the CFD results showing the blood flow circulation from the IVC and SVC (or LSVC and RSVC when both were present) to the RPA and LPA. The mean PL for Y-graft was 24% lower than T-junction ( $5.37 \pm 3.77$  mW vs.  $7.07 \pm 4.36$  mW; P-value  $\leq 0.001$ ). The absolute difference between the HFD to the right and left lungs was significantly lower in the Y-graft compared to the T-junction ( $4.92 \pm 2.74\%$  vs.  $18.51 \pm 12.40\%$ ; P-value=0.004).

**Conclusions:** Compared to the T-junction TCPC connection, a Y-graft conduit had a lower PL and yielded a more evenly balanced HFD. The findings of this study support a potential role for CFD in determining the optimal TCPC conduits for patients with SV physiology to minimize PL and balance HFD with the hope of improving long-term outcomes.

**Figure/Table 1**

Patients	Inlet (SVC or RSVC+LSVC)	Outlet (RPA)			Outlet (LPA)		
	2D flow measured by CMR (l/min)	Measured by CMR (l/min)	Simulated by CFD (l/min)	Error (%)	Measured by CMR (l/min)	Simulated by CFD (l/min)	Error (%)
1	1.44	0.58	0.60	3.45	0.86	0.85	1.16
2	1.84	0.97	0.88	9.28	0.87	0.80	8.04
3	1.62	0.55	0.57	3.64	1.07	1.05	1.87
4	1.28	0.71	0.70	1.41	0.57	0.55	3.51
5	1.49	0.98	0.92	6.12	0.51	0.50	1.96
6	1.04	0.54	0.55	1.85	0.50	0.51	6.00
7	1.34	0.79	0.81	2.53	0.55	0.59	7.27
8	1.46	0.73	0.77	5.48	0.73	0.69	5.48
9	2.07	1.55	1.46	6.41	0.51	0.55	7.84
10	1.69	1.03	0.95	7.77	0.86	0.80	9.09
Mean $\pm$ SD	1.53 $\pm$ 0.29	0.84 $\pm$ 0.31	0.82 $\pm$ 0.27	4.79 $\pm$ 2.63	0.68 $\pm$ 0.19	0.67 $\pm$ 0.18	3.22 $\pm$ 2.90

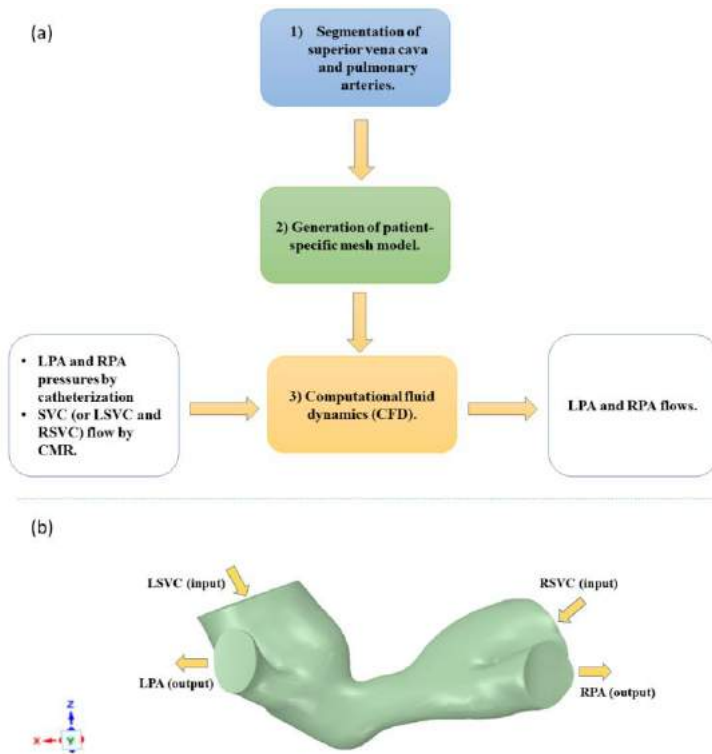
Data are presented as mean  $\pm$  standard deviation. CFD, computational fluid dynamics; CMR, cardiovascular magnetic resonance; LPA, left pulmonary artery; LSVC, left superior vena cava; RPA, right pulmonary artery;

RSVC, right superior vena cava; SVC, superior vena cava. Error (%) =  $\frac{|CMR_{flow} - CFD_{flow}|}{CMR_{flow}} \times 100$ .

**Caption 1**

Comparing CFD-simulated flow and CMR-measured flow at RPA and LPA from 10 single-ventricle patients with Glenn physiology.

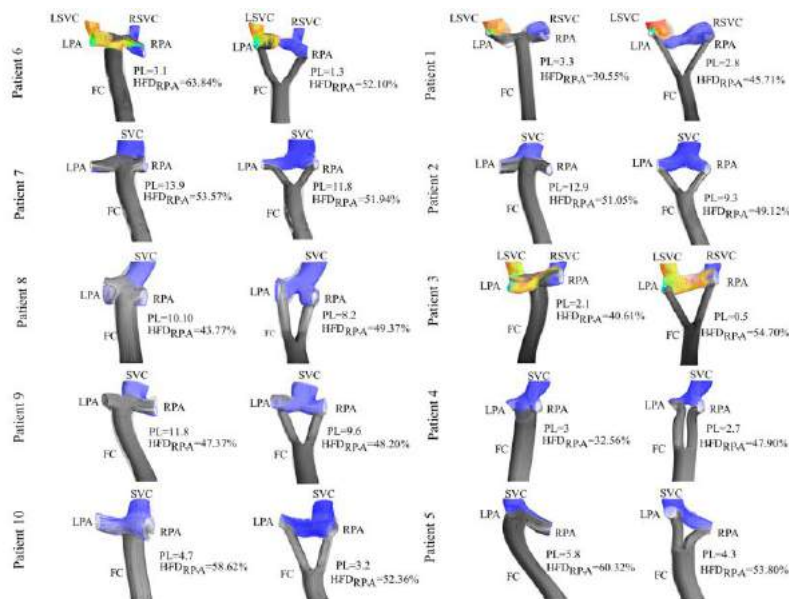
**Figure/Table 2**



## Caption 2

CFD Model for estimation of hemodynamic parameters in Glenn pathways. (a) CFD simulation workflow. (b) Generated 3D model and boundary conditions for one Glenn patient. Inputs to the model are SVC (or LSVC and RSVC) blood flow measured by CMR, and pressure values in RPA and LPA measured by catheterization. Outputs from the model are blood flow in RPA and LPA.

## Figure 3



**Caption 3**

Streamlines of simulated blood flow in constructed T-junction and Y-graft for 10 patients. The colors indicate estimated blood flow distributions from SVC (or LSVC and RSVC) and IVC to RPA and LPA. FC, Fontan conduit; HFD\_RPA, hepatic flow distribution to the RPA; and PL, power loss.

### Bibliographic References

Funding sources: This work is supported by NIH-NHLBI (1R01HL149807-01). , [3]SpaceClaim, A., ANSYS. Inc.: Canonsburg, PA, USA, 2019., [2]Duncan, B.W. and S. Desai, Pulmonary arteriovenous malformations after cavopulmonary anastomosis. *Ann Thorac Surg*, 2003. 76(5): p. 1759-66., [1] Khiabani, R.H., et al., Exercise capacity in single-ventricle patients after Fontan correlates with haemodynamic energy loss in TCPC. *Heart*, 2015. 101(2): p. 139-43.

Speaker: E. Javadi

Category: Single Ventricle, Computational Fluid Dynamics, Fontan

000045

## Visualization and quantification of fetal cardiac function with doppler ultrasound-gated cine imaging and 4D flow MRI

E. K. Englund \* (1); L. Browne (1); T. Fujiwara (1); R. Friesen (2); M. H. Moghari (1); A. Barker (1)

(1) Radiology, Children's Hospital Colorado, University of Colorado Anschutz Medical Campus, Aurora, United States of America; (2) Pediatric cardiology, Children's Hospital Colorado, University of Colorado Anschutz Medical Campus, Aurora, United States of America

### Abstract

**Background:** The fetal cardiovascular system has several distinctive features, including the umbilical vein, ductus venosus, ductus arteriosus, and foramen ovale. Isolating cardiac motion to visualize the fetal circulatory patterns can be difficult due to high fetal heart rates ( $>130$ bpm). Overall, these features present challenges to obtaining a comprehensive evaluation of fetal cardiac function and flow by MRI. The use of doppler ultrasound-gating for cine and 4D flow [1] MRI hold promise for overcoming these challenges. The purpose of this abstract is to demonstrate our experience using doppler ultrasound-gated cine MRI to capture fetal cardiac motion and preliminary utility of 4D flow MRI to visualize and quantify the fetal circulation.

**Methods:** In this IRB-approved study with ongoing recruitment, 10 healthy pregnant volunteers (gestational age =  $34.6 \pm 1.4$  weeks) were scanned at 1.5T (n=6) or 3T (n=4) (Philips Ingenia MRI). Images were obtained using a torso coil with the volunteers lying supine/decubitus according to comfort. Scout images were acquired to determine the location of the fetal heart. Once verified, a doppler ultrasound gating device (Northh Medical) [2,3] was positioned superficially over the fetal heart and secured tightly with an elastic band. Localizers were repeated to ensure proper placement of the doppler probe and to plan fetal cardiac acquisitions. Cine balanced steady-state free precession (bSSFP) images of the fetal heart were acquired in the axial plane. If possible (dictated by amount of fetal motion) a combination of standard cardiac planes were also acquired. When achievable, anatomical images were acquired during maternal breath-hold. Following cine acquisitions, and provided that a consistent fetal cardiac gating signal persisted, 4D flow data were acquired. Pulse sequence parameters are summarized in Table 1. Flow in the umbilical vein, ascending aorta, and main pulmonary artery were quantified using EnSight (Ansys, Inc.).

**Results:** Fetal cardiac gating was not achieved in one volunteer due to motion. In an additional 3 participants, fetal motion and/or time prevented the ability to acquire 4D flow data. Therefore, cine bSSFP images of the fetal heart were obtained in 9 volunteers, with 4D flow data in 6. Two of the 4D flow datasets were not of sufficient quality for quantitative analysis (due to fetal motion or insufficient gating).

Across all 9 healthy volunteers, the average fetal heart rate was  $139 \pm 7$  bpm. Example short-axis views acquired at 1.5T and 3T are shown in Figure 1. Figure 2 shows 4D flow pathline visualization of the fetal circulation. Distinctive features of the fetal circulation including blood flow in the umbilical vein and ductus venosus, shunting through the foramen ovale

from the right to left atrium, and flow through the ductus arteriosus are visualized. Across the four subjects, average flow in the ascending aorta was  $1.5 \pm 0.7$  mL/beat, main pulmonary artery was  $2.3 \pm 0.7$  mL/beat, and umbilical vein was  $1.5 \pm 1.0$  mL/beat.

**Discussion & Conclusion:** Preliminary results demonstrate the utility of 4D flow MRI for visualization and quantification of blood flow in the fetal circulation. If we assume fetal mass of 1.5-2 kg, these results are in reasonable agreement with prior reports of typical fetal values [4, 5]. Use of doppler ultrasound-gating allowed acquisition of both cine images of the fetal heart as well as 4D flow MR data with the success rates increasing in later volunteers due to experience. We found experience, doppler probe placement, and training of staff to be critical for success. Continued development of fast and motion-robust acquisitions will enhance our ability to capture fetal cardiac motion and blood flow.

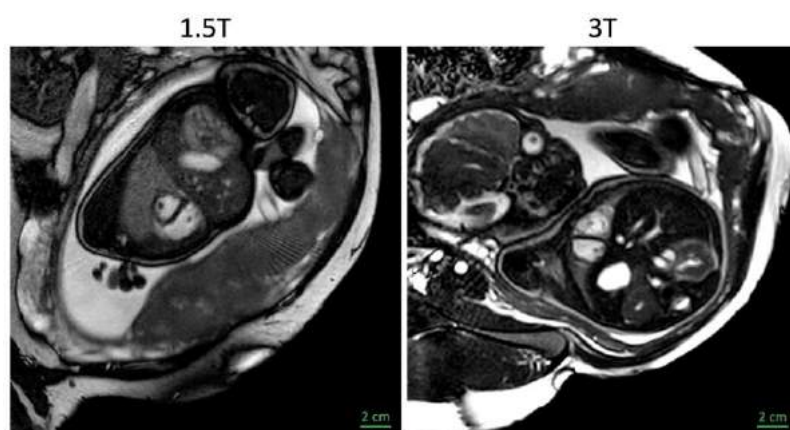
**Figure/Table 1**

	Cine bSSFP	4D Flow
TR (ms)	4.0 [2.4-4.7]	3.2 [3.1-3.4]
TE (ms)	2.0 [1.2-2.3]	2.0 [1.9-2.1]
Flip angle (degrees)	71 [60-75]	6
Duration (s)	44 [8-185]	173 [131-218]
Averages	1.4 [1-4]	1
Acquisition Matrix	205×220 [112×107-260×308]	117×116 [80×78-144×144]
Reconstruction diameter (mm)	273 [180-366]	293 [200-360]
Slice thickness (mm)	6 [3-10]	2.5
Temporal resolution (ms)	30 [13-44]	47 [41-50]
SENSE factor	1.4×1 [1×1-3×1]	2×1.5

**Caption 1**

Table 1. Summary of pulse sequence parameters for cine bSSFP and 4D flow acquisitions. Data are shown as mean [range] unless only one parameter value was used for all scans.

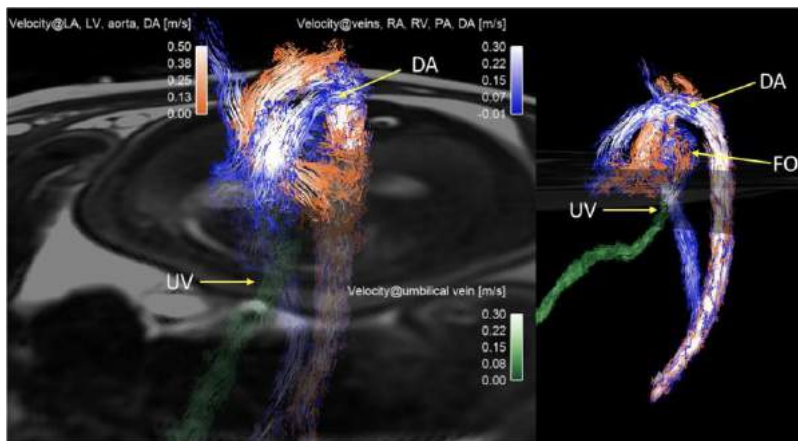
**Figure/Table 2**



## Caption 2

Figure 1. Short axis views in two healthy volunteers acquired at 1.5T (gestational age, GA=32 weeks) and 3T (GA=35 weeks) during maternal breath-hold. The right and left ventricles are well visualized throughout the fetal cardiac cycle.

## Figure 3



## Caption 3

Figure 2. 4D flow pathline visualization in a volunteer (GA=35 weeks) in coronal and sagittal views, showing flow in the umbilical vein/ductus venosus (UV, green), venous/right heart (blue) and arterial/left heart (orange). Right and left heart pathlines mix in the atria through the foramen ovale (FO) and in the descending aorta post ductus arteriosus (DA).

## Bibliographic References

1. Dyverfeldt P, Bissell M, Barker AJ, Bolger AF, Carlhall CJ, Ebbers T, Francios CJ, Frydrychowicz A, Geiger J, Giese D, Hope MD, Kilner PJ, Kozerke S, Myerson S, Neubauer S, Wieben O, Markl M. 4D flow cardiovascular magnetic resonance consensus statement. *J Cardiovasc Magn Reson*. 2015;17:72., 2. Kording F, Yamamura J, de Sousa MT, Ruprecht C, Hedström E, Aletras AH, Ellen Grant P, Powell AJ, Fehrs K, Adam G, Kooijman H, Schoennagel BP. Dynamic fetal cardiovascular magnetic resonance imaging using Doppler ultrasound gating. *J Cardiovasc Magn Reson*. 2018; 20:17., 3. Kording F, Schoennagel BP, de Sousa MT, Fehrs K, Adam G, Yamamura J, Ruprecht C. Evaluation of a Portable Doppler Ultrasound Gating Device for Fetal Cardiac MR Imaging: Initial Results at 1.5T and 3T. *Magn Reson Med Sci*. 2018;17:308-317., 4. Prsa M, Sun L, van Amerom J, Yoo SJ, Grosse-Wortmann L, Jaeggi E, Macgowan C, Seed M. Reference ranges of blood flow in the major vessels of the normal human fetal circulation at term by phase-contrast magnetic resonance imaging. *Circ Cardiovasc Imaging*. 2014;7:663–70., 5. Schrauben EM, Saini BS, Darby JRT,

Soo JY, Lock MC, Stirrat E, Stortz G, Sled JG, Morrison JL, Seed M, Macgowan CK. Fetal hemodynamics and cardiac streaming assessed by 4D flow cardiovascular magnetic resonance in fetal sheep. *J Cardiovasc Magn Reson*. 2019;21:8.

Speaker: E. K. Englund

Category: Fetal, 4D Flow, Cardiac Function

000046

## Septal Segmental Displacement is Related to Right Ventricular Remodeling and Intracardiac Vorticity in Repaired Tetralogy of Fallot Patients

S. Kollar \* (1); B. Klas (2); F. Capuano (3); O. Toro-Salazar (4); L. Olivieri (1); Y.-H. Loke (1)

(1) Cardiology, Children's National Hospital, Washington, United States of America; (2) Product marketing manager, TomTec Corp, Chicago, United States of America; (3) Department of fluid mechanics, Universidad Politècnica de Catalunya, Barcelona, Spain; (4) Cardiology, Connecticut Children's Medical Center, Hartford, United States of America

### Abstract

**Background:** Repaired Tetralogy of Fallot (rTOF) patients experience right ventricular (RV) remodeling secondary to chronic pulmonary insufficiency (PI). The adaptive mechanisms of the RV in response to chronic PI have not been clarified. Atypical septal wall recruitment towards the RV, otherwise known as septal segmental displacement, can be seen in rTOF patients (**Figure 1**). rTOF patients also have abnormal intracardiac vorticity (the spinning motion of blood) as a result of PI. Thus, we hypothesize that these two phenomena are related, and investigated septal segmental displacement as part of right ventricular remodeling in rTOF patients.

**Methods:** This was a retrospective study consisting of cardiac magnetic resonance (CMR) studies from 36 rTOF patients (all with transannular patch, no subsequent surgical intervention) and 36 control patients. The control group was size-matched against the rTOF cohort by RV end-diastolic volume, consisting of 17 with normal RVs and 19 with other forms of dilated RVs (RVD, such as partial anomalous pulmonary venous return). All datasets included cine and 4D flow imaging. Feature tracking of the RV wall was performed by conventional software (QStrain, Medis). The average magnitude of septal segmental displacement was calculated via custom algorithms, then indexed to RV size (RV-SSDi). Systolic/Diastolic vorticity of both right/left ventricle was quantified with 4D flow research software (ITFlow, Cardio Flow Design). Correlations of RV-SSDi were performed against conventional CMR parameters, strain, and intracardiac vorticity.

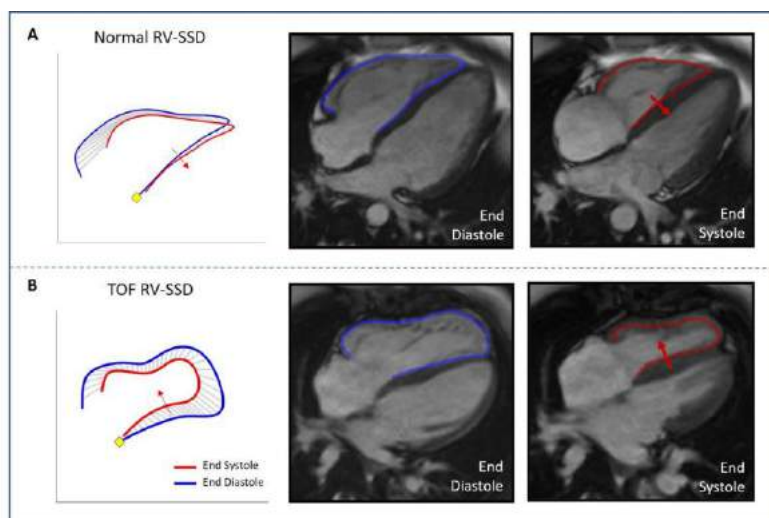
**Results:** There was no significant difference in RV size between rTOF and controls ( $210 \pm 88$  mL vs  $194 \pm 88$  mL,  $p = 0.4345$ ). rTOF patients demonstrated abnormal septal segmental displacement with a mean RV-SSDi of  $0.85 \pm 0.60$ , compared to  $-0.04 \pm 0.86$  in controls ( $p < 0.0001$ ). On subgroup analysis, there was still higher magnitude of RV-SSDi in the rTOF cohort even when compared to the RVD subgroup (**Figure 2**). RV-SSDi correlated with improved RV global longitudinal strain (GLS) and RV ejection fraction (EF) (**Figure 3 A-B**). RV-SSDi also correlated with increased RV systolic vorticity, as well as increased RV and LV diastolic vorticity (**Figure 3 C-D**). RV-SSDi correlated with shorter QRS duration ( $r = -0.4855$ ,  $p = 0.0042$ ).

**Conclusions:** Patients with rTOF have significantly higher RV-SSDi, regardless of RV size. RV-SSDi is related to RV function and intracardiac flow in rTOF patients. RV-SSDi appears to be an adaptive mechanism to preserve function and is related to intracardiac vorticity as a result of PI. Future longitudinal studies should assess RV-SSDi, which may be



a useful parameter in determining optimal timing for pulmonary valve replacement prior to irreversible RV dysfunction.

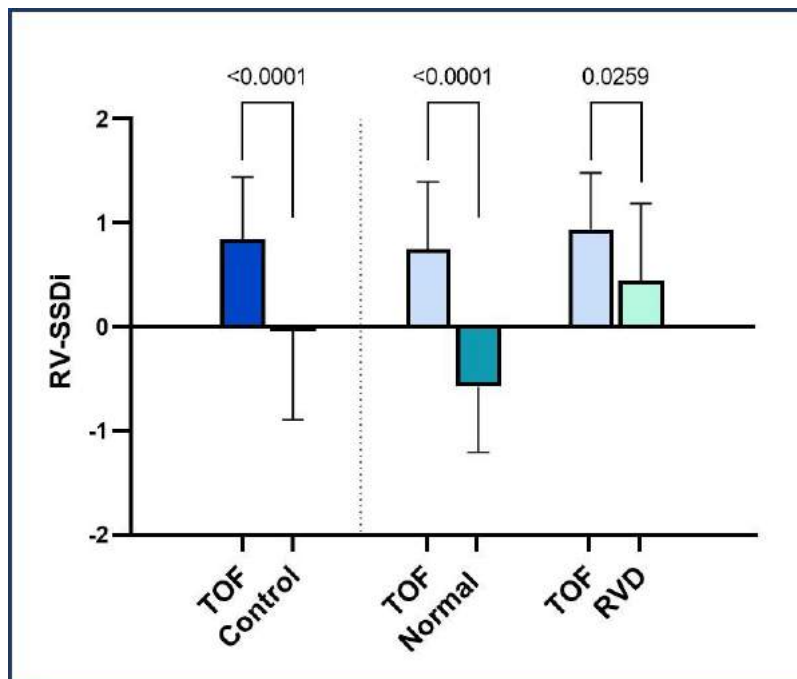
**Figure/Table 1**



**Caption 1**

**Figure 1:** Tissue tracking analysis demonstrating endocardial wall motion in end diastole (blue) and end systole (red). RV-SSD is the magnitude and direction of septal motion from end diastole to end systole. **A)** Normal RV-SSD with septal wall motion towards the LV. **B)** Abnormal RV-SSD in a TOF patient with septal wall motion towards the RV.

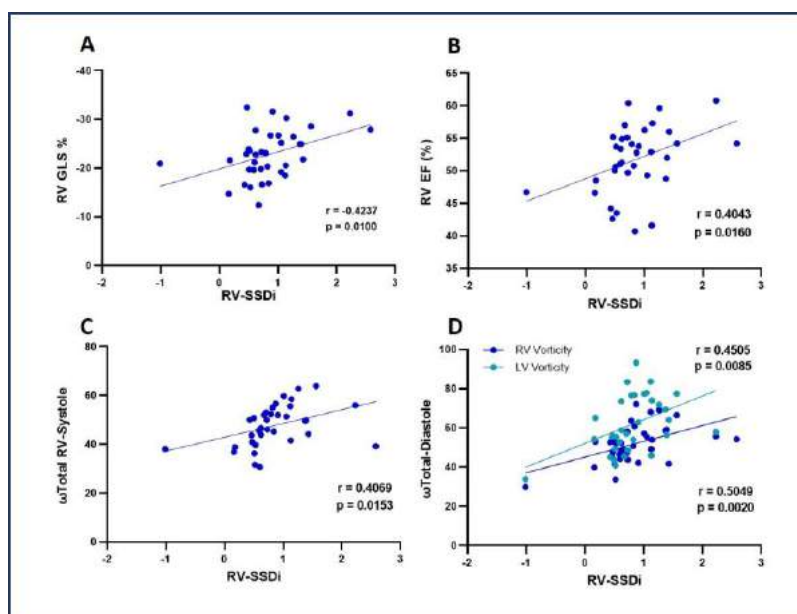
**Figure/Table 2**



**Caption 2**

**Figure 2:** The 36 rTOF patients compared to the 36 Control (Normal + RVD) patients, demonstrated significantly higher RV-SSDi values. There was even greater difference between the rTOF patients compared to the normal subgroup. Less difference, although still statistically significant, noted between rTOF patients and the RVD subgroup.

**Figure 3**



### Caption 3

**Figure 3:** **A)** More positive RV-SSDi correlated with improved RV GLS. **B)** More positive RV-SSDi correlated with improved RV EF. **C)** Increased RV-SSDi correlated with increased RV systolic vorticity. **D)** Increased RV-SSDi correlated with increased RV and LV diastolic vorticity.

### Bibliographic References

Geva, T. (2013). Indications for pulmonary valve replacement in repaired tetralogy of fallot: The quest continues. In *Circulation* (Vol. 128, Issue 17, pp. 1855–1857). Lippincott Williams & Wilkins Hagerstown, MD . <https://doi.org/10.1161/CIRCULATIONAHA.113.005878>, Loke, Y.-H., Capuano, F., Cleveland, V., Mandell, J. G., Balaras, E., & Olivieri, L. J. (2020). Prevalence and clinical significance of cardiovascular magnetic resonance adenosine stress-induced myocardial perfusion defect in hypertrophic cardiomyopathy. <https://doi.org/10.1186/s12968-021-00789-2>

Speaker: S. Kollar

Category: Tetralogy of Fallot, Tissue Tracking, 4D Flow

000048

## Deep Learning-based Reconstruction for Highly Accelerated 4D Flow MRI

H. Berhane \* (1); A. pathrose (2); M. Scott (2); P. McCarthy (3); C. Malaisrie (3); B. Allen (2); R. Avery (4); M. Markl (5)

(1) Biomedical engineering, Northwestern University, Chicago, United States of America; (2) Radiology, Northwestern University Feinberg School of Medicine, Chicago, United States of America; (3) Cardiac surgery, Northwestern University Feinberg School of Medicine, Chicago, United States of America; (4) Radiology, Northwestern Hospital, Chicago, United States of America; (5) Radiology, Northwestern University, Chicago, United States of America

### Abstract

**Purpose:** 4D flow MRI provides comprehensive assessment of cardiovascular hemodynamics. However, its current clinical usage is hindered by long scan times. Recently, sparse k-space sampling and Compressed Sensing (CS) reconstruction have substantially reduced scan times [1,2]. However, iterative CS reconstruction requires lengthy processing times and results in underestimations of hemodynamic measurements compared to conventional 4D flow MRI[1, 2]. Thus, we aimed to develop a 3D Dense U-Net convolutional neural network (CNN) for improved reconstruction of highly subsampled 4D flow MRI to improve hemodynamic quantification and reconstruction times.

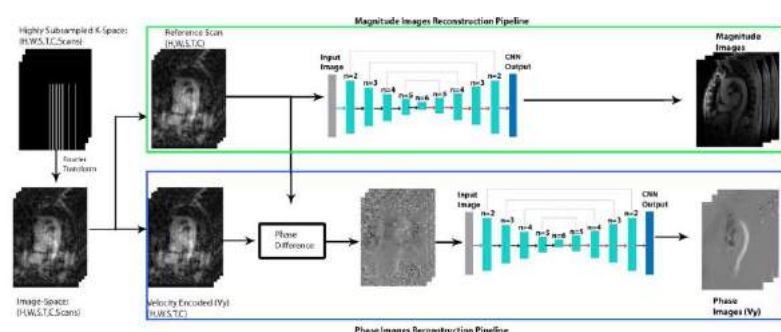
**Methods:** 18 subjects ( $58 \pm 15$  y old; 14 M) with aortic disease were prospectively recruited to undergo four aortic 4D flow MRI scans: (1) conventional 4D flow MRI with GRAPPA ( $R=2$ ) and three CS accelerated scans with (2) CS,  $R=5.7$ , (3) CS,  $R=7.7$ , (4) CS,  $R=10.2$ . All scans used a 1.5T MRI (Area, Siemens) with identical 3D aorta coverage, spatial resolution (2.4-4.2 mm<sup>3</sup>), and velocity encoding. For scans 2-4, data acquisition and inline CS reconstruction used previously described frameworks [3][4]. For CNN reconstruction, a 3D Dense U-Net was employed as previously described[5]. Figure 1 provides an outline for the CNN-based reconstruction. After zero padding and Fourier transform, image-space datasets were used as CNN inputs. Conventional 4D flow MRI (GRAPPA,  $R=2$ ) served as ground truth data for CNN training and testing (10-fold cross validation). For the magnitude images, the reference scan was used as an CNN input, while the phase difference data (subtraction of velocity-encoded and reference scan) were used for flow images. The loss function consisted of a structural similarity index (SSIM) loss function + mean squared error. For assessing image quality of magnitude images, SSIM values (CS/CNN vs. conventional 4D flow MRI) were calculated and reported as median [interquartile range]. 4D flow analysis involved qualitatively comparing the 3D streamlines and peak velocity maximum intensity projections (MIPs) (Figure 2) and quantitatively comparing the peak velocity, net flow, and peak flow at the ascending aorta (AAo), aortic arch, and descending aorta (DAo).

**Results:** CNN reconstruction times were  $135.6 \pm 4.8$  seconds, compared to ~240-360 seconds for CS. CNN reconstruction improved quality of magnitude images, independent of acceleration factor (Median SSIM,  $R=5.7$ , CNN 0.88 [0.86-0.89], CS 0.71 [0.70-74];  $R=7.7$ , CNN 0.87 [0.85-0.87], CS 0.71 [0.69-0.72];  $R=10.2$ , CNN 0.87[0.86-0.87], CS 0.71 [0.68-0.74]. Figure 2 provides examples of velocity MIPs and 3D streamlines for conventional 4D flow compared to CS/CNN-reconstructed data for  $R=5.7$ , 7.7, and 10.2. The CNN retained

similar velocity profiles and flow patterns as conventional 4D flow. These findings are corroborated by results in Table 1 (Bland-Altman comparisons of the CNN/CS-reconstructed data for R=5.7, 7.7, 10.2 vs. conventional 4D flow). CNN-reconstruction resulted in considerably improved flow quantification with less underestimation compared to the CS-reconstructed data (CNN: 5-12.8% vs. while CS 10.4-35.6%) across all acceleration factors.

**Discussion:** The CNN-based reconstruction showed moderate to excellent agreement with conventional 4D flow MRI, alleviating the hemodynamic underestimation and providing faster reconstruction compared to CS. In addition, CNN-derived 4D flow MRI showed better agreement in the magnitude images compare to the CS, however the acceleration factor seems to have very little impact on the agreement.

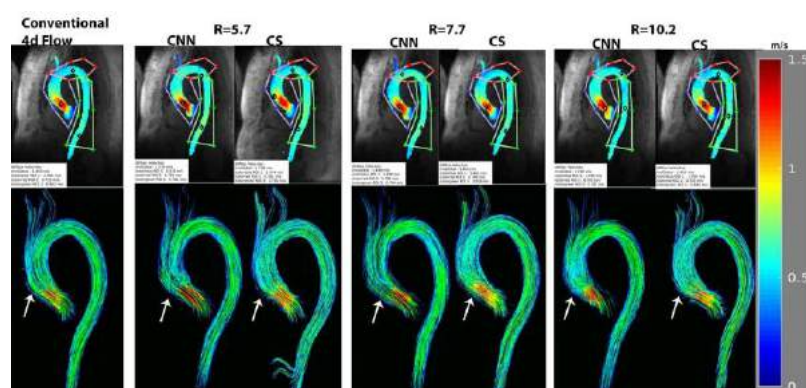
**Figure/Table 1**



**Caption 1**

**Figure 1:** The workflow for the deep learning-base reconstruction of 4D flow MRI. From kspace, the data is Fourier transformed into image space and divided into the reference and velocity encoded scans. The reference scan is used to generate magnitude images, and from the velocity-encoded data, the phase difference images is used to make phase images.

**Figure/Table 2**



**Caption 2**

**Figure 2:** Systolic velocity MIPs and 3D streamlines for conventional 4D flow MRI (GRAPPA, R=2) and CNN/CS-reconstructed 4D flow MRI (R=5.7, 7.7, 10.2). Top row: MIPs and manually drawn ROIs for peak velocities in the AAo, arch, and DAo. Bottom row: white arrow indicates regional vortex flow, which was preserved in the CNN-reconstructed data.

**Figure 3**

Acc factor	Aorta region	Method	Peak Vel	Net Flow	Peak Flow
R = 5.7	AAo	CNN	0.00 (9.3%)	0.57 (10.1%)	0.65 (11.0%)
		CS	0.1 (13.8%)	1.3 (18.5%)	12.0 (19.3%)
	arch	CNN	0.03 (7.3%)	1.5 (11.5%)	1.7 (9.1%)
		CS	-0.02 (20.7%)	-2.3 (12.1%)	-11.0 (12.5%)
	DAo	CNN	0.01 (8.6%)	0.12 (12.1%)	-4.7 (5.0%)
		CS	0.04 (23.0%)	0.53 (13.9%)	8.3 (13.8%)
R = 7.7	AAo	CNN	0.05 (10.9%)	0.91 (10.6%)	-2.5 (8.6%)
		CS	-0.14 (15.5%)	1.7 (28.9%)	1.8 (14.7%)
	arch	CNN	0.03 (10.3%)	0.72 (11.0%)	-5.76 (12.7%)
		CS	-0.01 (10.8%)	2.4 (22.5%)	-10.0 (17.4%)
	DAo	CNN	0.00 (10.4%)	0.34 (10.4%)	-0.85 (8.2%)
		CS	-1.7 (28.9%)	0.63 (22.8%)	-13.0 (13.1%)
R = 10.2	AAo	CNN	0.02 (11.4%)	1.2 (9.0%)	14.0 (9.7%)
		CS	-0.13 (23.3%)	-2.6 (23.1%)	3.2 (20.9%)
	arch	CNN	0.02 (11.0%)	0.97 (12.2%)	-1.4 (13.5%)
		CS	-0.05 (35.6%)	-2.7 (19.8%)	-14.0 (14.6%)
	DAo	CNN	-0.03 (8.5%)	-0.04 (12.8%)	3.7 (10.0%)
		CS	0.01 (15.4%)	-1.3 (21.3%)	-19.0 (19.0%)

**Caption 3**

**Table 1:** Bland-Atman results comparing conventional 4D flow MRI (GRAPPA, R=2) to either the CNN-reconstructed or CS-reconstructed data for all three acceleration factors (R=5.7, 7.7, 10.2). Results are reported as the bias and the percent difference from the reference mean.

## Bibliographic References

- Berhane, H., et al., Fully automated 3D aortic segmentation of 4D flow MRI for hemodynamic analysis using deep learning. *Magn Reson Med*, 2020. 84(4): p. 2204-2218., 5.
- Wetzel, J., et al., High-resolution dynamic CE-MRA of the thorax enabled by iterative TWIST reconstruction. *Magn Reson Med*, 2017. 77(2): p. 833-840., 4.
- Uecker, M., et al., ESPIRiT--an eigenvalue approach to autocalibrating parallel MRI: where SENSE meets GRAPPA. *Magn Reson Med*, 2014. 71(3): p. 990-1001., 3.
- Ma, L.E., et al., Aortic 4D flow MRI in 2 minutes using compressed sensing, respiratory controlled adaptive k-space reordering, and inline reconstruction. *Magn Reson Med*, 2019. 81(6): p. 3675-3690., 2.
- Pathrose, A., et al., Highly accelerated aortic 4D flow MRI using compressed sensing: Performance at different acceleration factors in patients with aortic disease. *Magn Reson Med*, 2021. 85(4): p. 2174-2187., 1.

Speaker: H. Berhane

Category: 4D Flow, Aorta, Velocity

000049

## **High-resolution non-contrast free-breathing CMRA for detection of coronary artery disease: validation against invasive coronary angiography**

M. S. Nazir \* (1); A. Bustin (1); R. Hajhosseiny (2); M. Yazdani (1); M. Ryan (1); V. Vergani (1); R. Neji (3); K. Kunze (3); P. G. Masci (1); D. Perera (4); S. Plein (5); A. Chiribiri (1); R. M. Botnar (1); C. Prieto (1)

(1) Biomedical Engineering and Imaging Sciences, King's College London Waterloo Campus, London, United Kingdom; (2) Biomedical Engineering and Imaging Sciences, King's College London, London, United Kingdom; (3) Siemens healthineers, Siemens - Frimley, Frimley, United Kingdom; (4) Cardiovascular medicine, King's College London Waterloo Campus, London, United Kingdom; (5) Licamm, Leeds institute of Cardiovascular and Metabolic Medicine, Leeds District, UK, United Kingdom

### **Abstract**

#### Background

Coronary artery disease (CAD) is the single most common cause of death worldwide. Recent technological developments with Cardiovascular Magnetic Resonance Angiography (CMRA) allow high-resolution free-breathing imaging of the coronary arteries at submillimeter resolution without the need for contrast in a predictable scan time of ~10 minutes. [1] The objective of this study was to determine the diagnostic accuracy of high-resolution CMRA for CAD detection against the gold standard of invasive coronary angiography (ICA).

#### Methods

Forty-five patients (15 female, mean age  $62 \pm 10$  years) with suspected CAD underwent sub-millimeter-resolution (0.6mm<sup>3</sup>) non-contrast CMRA at 1.5T. Prior to imaging, patients were administered with intravenous beta blockers to optimise heart rate control and sublingual glyceryl trinitrate to promote coronary vasodilation. Obstructive CAD was defined by lesions with  $\geq 50\%$  stenosis by quantitative coronary angiography on ICA.

#### Results

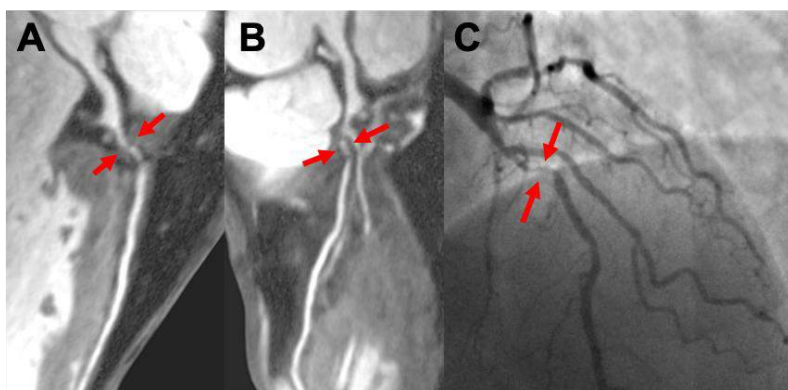
The mean duration of image acquisition was  $10.44 \pm 2.10$  minutes. On a per patient analysis, the sensitivity, specificity, positive predictive value and negative predictive value (95% confidence intervals) were 95% (75–100), 54% (36–71), 60% (42–75) and 93% (70–100), respectively. On a per vessel analysis the sensitivity, specificity, positive predictive value and negative predictive value (95% confidence intervals) were 80% (63–91), 83% (77–88), 49% (36–63) and 95% (90–98), respectively. Typical case examples are shown in figure 1 and figure 2.



## Conclusion

As an important step towards clinical translation, we demonstrated a good diagnostic accuracy for CAD detection using high-resolution CMRA, with high sensitivity and negative predictive value. Future evaluation with combined cardiac MR stress perfusion and late gadolinium enhancement may provide a comprehensive multiparametric assessment of CAD. Future multicenter evaluation is now required to translate this to the clinic.

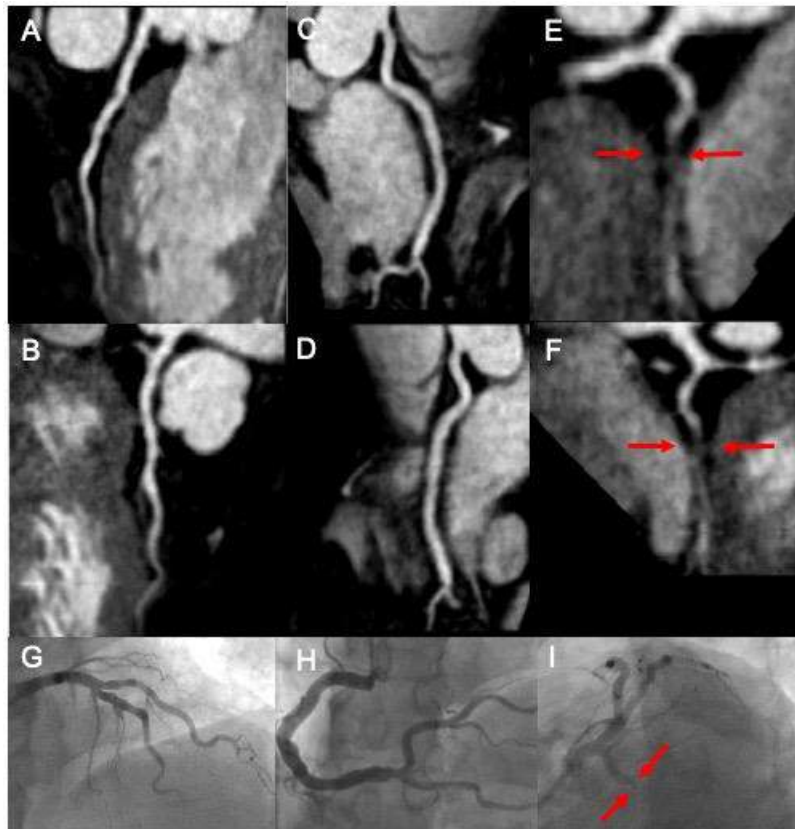
## **Figure/Table 1**



## **Caption 1**

3D curved multi-planar reformat of a Cardiovascular Magnetic Resonance Angiography in a male patient with exertional chest pain with a history of hypertension. There is an obstructive lesion ( $>50\%$ ) in the left anterior descending artery (Panel A and B, red arrows). These findings were confirmed during invasive coronary angiography (Panel C).

## **Figure/Table 2**



## Caption 2

3D curved multi-planar reformats of a CMRA in a patient with chest pain with history of hypertension, hypercholesterolemia and a family history of coronary artery disease. There is no significant disease in the left anterior descending (Panel A and B) or right coronary artery (Panel C and D). However, there is an occluded left circumflex artery, red arrows (Panel E and F). These findings were confirmed during invasive coronary angiography (Panel G-I)

## Bibliographic References

1. Bustin A, Rashid I, Cruz G, Hajhosseiny R, Correia T, Neji R, et al. 3D whole-heart isotropic sub-millimeter resolution coronary magnetic resonance angiography with non-rigid motion-compensated PROST. J Cardiovasc Magn Reson. 2020;22(1):24.

Speaker: M. S. Nazir

Category: Coronary Angiography, Coronary Arteries, coronary Artery Disease

000050

## **Native T1-mapping using CMR detects myocardium at risk during the first week following myocardial infarction in swine: verification against contrast enhanced SSFP**

T. Lav \* (1); D. Nordlund (1); C. Xanthis (1); K. chow (2); A. Aletras (3); R. Jablonowski (1)

(1) Clinical physiology, department of clinical sciences lund, Lund University, Skåne University Hospital, Lund, Sweden; (2) Siemens medical solutions usa, Inc., Chicago, Illinois, United States of America; (3) Laboratory of computing, medical informatics and biomedical-imaging technologies, School of Medicine, Faculty of Health Sciences, Aristotle University of Thessaloniki, Thessaloniki, Greece

### **Abstract**

#### **Background**

In patients with acute ST-elevation myocardial infarction (STEMI), assessment of the salvageable myocardium, i.e. myocardium at risk (MaR), provides valuable clinical information (1). Assessment of MaR can be performed using contrast-enhanced steady state free precession (CE-SSFP) cardiovascular magnetic resonance (CMR) images. This, however, necessitates administration of gadolinium (Gd) contrast to patients (2). This method can be time consuming and contrast administration may not be advisable for patients with severe renal insufficiency. It has been shown that non-contrast native T1 imaging allows quantification of MaR in patients with STEMI (3) and additionally that the extent of MaR is stable over the first week following acute ischemia/reperfusion (4). However, it is not clear if CE-SSFP and native T1-mapping can be used interchangeably for the assessment of MaR. Therefore, the aim was to verify the extent of MaR using native T1 mapping against CE-SSFP as reference.

#### **Materials and methods**

Seven pigs underwent balloon occlusion of the left anterior descending coronary artery (LAD) for 40 minutes followed by reperfusion. CMR was performed at 1.5T (MAGNETOM Aera, Siemens Healthcare, Erlangen, Germany) at 2 hours, 24 hours and seven days after reperfusion. Native T1 maps were acquired with a prototype sequence in both long axis and one short axis slice using both a modified look-locker inversion recovery (MOLLI) and a saturation recovery single-shot acquisition (SASHA). A short-axis stack of CE-SSFP images was acquired after Gd-contrast administration. The same experimental protocol was used for another cohort of four pigs for one CMR scan at four days post reperfusion where native T1 maps, using both MOLLI and SASHA, and CE-SSFP images were acquired in full short-axis stacks. All image analysis was done using the software Segment version 3.0 R7568 (<http://segment.heiberg.se>) (5). Myocardium at risk was delineated by first defining epi- and endocardium followed by manually identifying hyperintense areas. In the group with one slice coverage for native T1, the corresponding CE-SSFP slice was defined. Spearman correlation tests and bias according to Bland-Altman was used to compare methods.

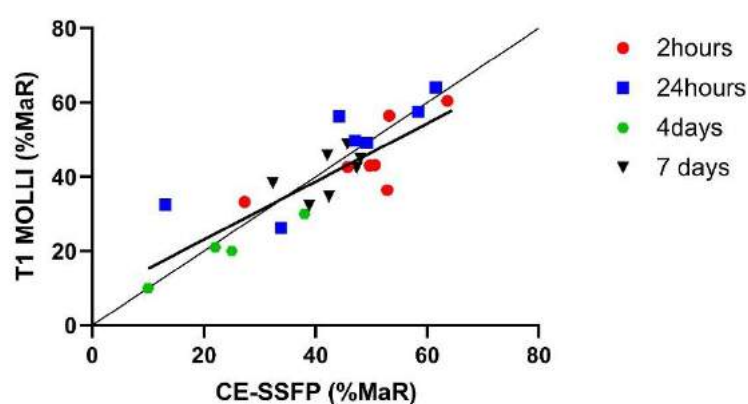
#### **Results**

A total of  $n = 21$  slices were compared between native T1 mapping and CE-SSFP at 2 hours, 24 hours and 7 days. At 4 days a total of  $n = 26$  slices were compared. Native T1 mapping using MOLLI showed a correlation of  $r=0.83$  ( $P < 0.001$ ) with a bias of  $1.0 \pm 7.5\%$  MaR and for SASHA the correlation was  $r= 0.78$  ( $p = 0.001$ ) with a bias of  $1.4 \pm 8.3\%$  MaR.

## Conclusion

There was a strong correlation for assessment of myocardium at risk between native T1 mapping, using both MOLLI and SASHA compared to CE-SSFP. Thus, in situations where gadolinium contrast cannot be administered to patients, native T1 mapping may provide an alternative assessment of MaR.

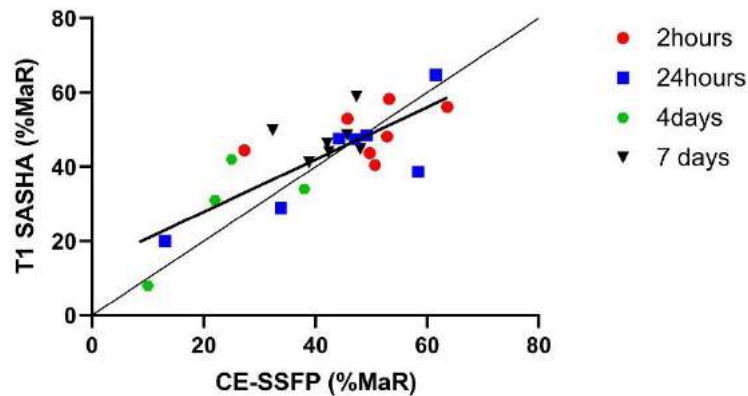
## Figure/Table 1



## Caption 1

**Figure 1.** Correlation between native T1 mapping using MOLLI and contrast-enhanced SSFP (CE-SSFP) demonstrating a correlation with  $r = 0.83$ .

## Figure/Table 2



## Caption 2

**Figure 2.** Correlation between native T1 mapping using SASHA and contrast-enhanced SSFP (CE-SSFP) demonstrating a correlation with  $r = 0.78$ .

## Bibliographic References

5. E. Heiberg, J. Sjögren, M. Ugander, M. Carlsson, H. Engblom, and H. Arheden, Design and Validation of Segment – a Freely Available Software for Cardiovascular Image Analysis, BMC Medical Imaging, 10:1, 2010., 4.
- Alkhalil M, Borlotti A, De Maria GL, et al. Dynamic changes in injured myocardium, very early after acute myocardial infarction, quantified using T1 mapping cardiovascular magnetic resonance. J Cardiovasc Magn Reson. 2018;20:82. , 3.
- Bulluck H, Hammond-Haley M, Fontana M, et al. Quantification of both the area-at-risk and acute myocardial infarct size in ST-segment elevation myocardial infarction using T1-mapping. J Cardiovasc Magn Reson. 2017;19(1):57., 2.
- Sörensson P, Heiberg E, Saleh N, et al. Assessment of myocardium at risk with contrast enhanced steady-state free precession cine cardiovascular magnetic resonance compared to single-photon emission computed tomography. J Cardiovasc Magn Reson. 2010;12:25. , 1.
- Ibanez B, Aletras AH, Arai AE, et al. Cardiac MRI Endpoints in Myocardial Infarction Experimental and Clinical Trials: JACC Scientific Expert Panel. J Am Coll Cardiol. 2019;74:238-256.

Speaker: T. Lav

Category: Acute Myocardial Infarction, Native T1, Area at Risk



000051

## Left Ventricular Apical Aneurysm in Fabry Disease: Implications for Clinical Significance and Risk Stratification

L. Kuo \* (1); H.-C. Chang (2); D.-M. Niu (3); W.-C. Yu, (1)

(1) Internal Medicine, Cardiology, Taipei Veterans General Hospital, Taipei, Taiwan; (2) Cardiology, Taipei Veterans General Hospital Su-Ao Branch, Taipei, Taiwan; (3) Pediatrics, Taipei Veterans General Hospital, Taipei, Taiwan

### Abstract

#### Background

More than 50% of patients with Fabry disease (FD) present with cardiac phenotype, and left ventricular hypertrophy (LVH) is the most frequent manifestation. Among FD patients with LVH, a rare and novel presentation of left ventricular apical aneurysm (LVAA) has been reported. This study aimed to investigate the clinical incidence of LVAA and its impacts on prognosis among FD patients.

#### Methods

We retrospectively analyzed 268 FD patients in a tertiary medical center between January 2003 to September 2020. Two patients with ischemic LVAA were excluded. LVH and LVAA were confirmed either by echocardiography or cardiovascular magnetic resonance imaging (Figure 1). The primary endpoints were a composite of heart failure (HF) hospitalization, sustained ventricular tachycardia (VT), ischemic stroke, and death.

#### Results

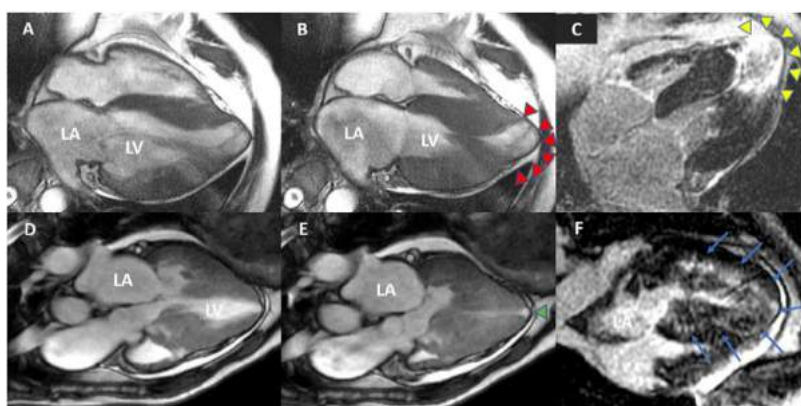
Of 266 FD patients, there were 105 (39.5%) patients had LVH, and 11 (10.3%) of them had LVAA (age  $67.5 \pm 9.5$  years, 8 males [72.7%]). After a mean follow-up of  $49.3 \pm 34.8$  months, 8 patients experienced primary endpoints, including 5 (45.5%) HF hospitalizations, 3 (27.3%) VT, 1 (9.1%) stroke, and 4 (36.4%) deaths (Figure 2). The risk for composite adverse events was significantly higher in patients with LVAA compared with those without (8 [72.7%] vs 17 [18.1%]), leading to significantly lower event-free survival in patients with LVAA (Log-Rank  $P < 0.001$ , Figure 3). The presence of LVAA was independently associated with an increased risk of composite adverse events (hazard ratio: 3.59; confidence interval: 1.30-9.91,  $P = 0.01$ ) after the adjustment with age, gender, advanced HF, renal function, dyslipidemia, atrial fibrillation, left ventricular ejection fraction of  $< 40\%$ , average  $E/e'$ , and LV mass index.



## Conclusions

LVAAs present in around 10% of patients with Fabry cardiomyopathy and is strongly associated with an increased risk of adverse cardiovascular events. The identification of this phenotype would be useful to identify high-risk patients with Fabry cardiomyopathy, among whom more aggressive treatments may be considered.

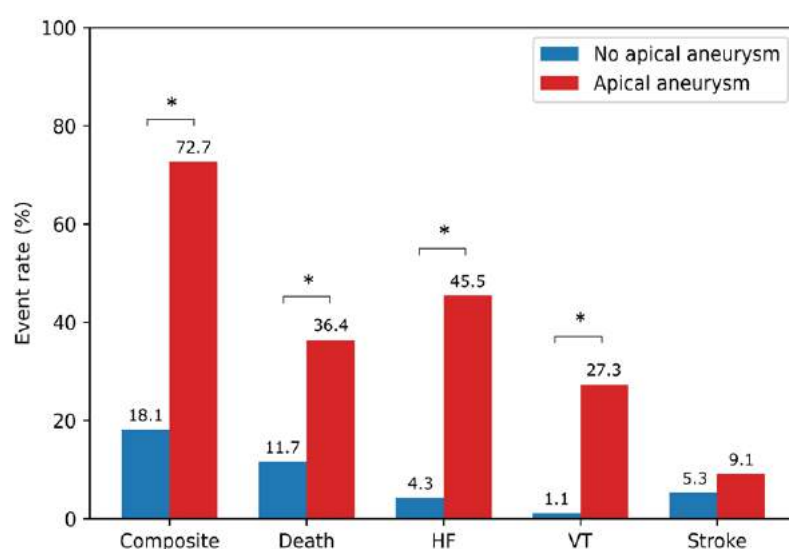
**Figure/Table 1**



**Caption 1**

Figure 1A, 1B, 1D, 1E: left ventricular apical aneurysm is identified on cine images of LV end-diastolic phase and end-systolic phase; 1C, 1F: late gadolinium enhancement of LV on delayed contrast-enhanced images. LA: left atrium, LV: left ventricle.

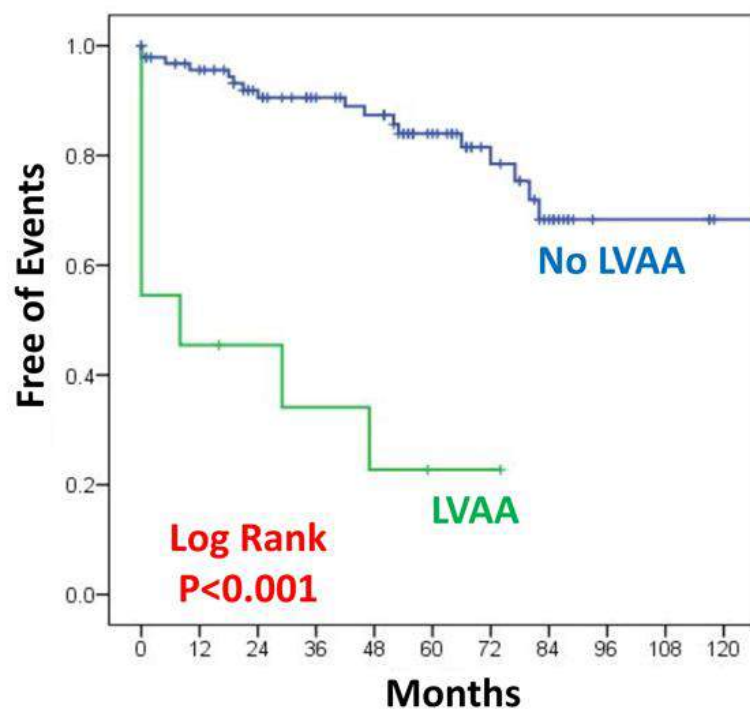
**Figure/Table 2**



## Caption 2

Comparison of clinical cardiovascular outcomes with and without left ventricular apical aneurysm in Fabry cardiomyopathy patients. HF: heart failure, VT: ventricular tachycardia.\* indicates P value <0.05.

## Figure 3



## Caption 3

Kaplan-Meier survival curve showing freedom from composite of adverse cardiovascular events in Fabry cardiomyopathy patients with left ventricular apical aneurysm compared with those without. LVAA: left ventricular apical aneurysm.

## Bibliographic References

Left ventricular apical aneurysm: a novel phenotype of Fabry's disease, Eur Heart J Cardiovasc Imaging . 2014 May;15(5):585. doi: 10.1093/ehjci/jet197.

Speaker: L. Kuo

Category: Fabry Disease, Nonischemic Cardiomyopathy, Heart Failure

000052

## Ultra-short saturation recovery time reduces underestimation of the arterial input function in quantitative cardiac perfusion MRI

L. Fan \* (1); K. Hong, (1); L.-Y. Hsu, (2); B. Allen (1); D. Lee (3); D. Kim (1)

(1) Department of radiology, Northwestern University Feinberg School of Medicine, Chicago, United States of America; (2) Department of radiology and imaging sciences, National Institutes of Health, Bethesda, United States of America; (3) Division of cardiology, internal medicine, Northwestern University Feinberg School of Medicine, Chicago, United States of America

### Abstract

**Introduction:** Quantitative cardiac perfusion MRI is a promising method for diagnosis of multi-vessel obstructive disease and microvascular disease and for conducting longitudinal studies. To avoid underestimation of the arterial input function (AIF) arising from the nonlinear relationship between the gadolinium concentration ([Gd]) and signal, it is recommended to use a short saturation recovery time (TS)[1, 2](23-27 ms) and T2\* correction. To our knowledge, no study has investigated an optimal TS for avoiding underestimation of the AIF. In this study, we obtained first-pass cardiac perfusion MRI data using radial k-space sampling with a minimum TS of 10 ms and retrospectively derived five AIF images with TS ranging from 10 to 21.2 ms (2.8 ms steps) using k-space weighted image contrast (KWIC) filters [3], in order to determine an optimal TS for avoiding underestimation of the AIF.

### Methods:

**Human Subjects & Pulse Sequence:** We prospectively enrolled 20 subjects (mean age =  $59 \pm 14$  years, 8/12 males/females) and performed resting perfusion scans during administration of 0.075 to 0.1 mmol/kg of gadobutrol using a previously described pulse sequence with radial k-space sampling [4]. Relevant imaging parameters included: FOV=384mmx384mm, matrix size =192x192, TE/TR=1.5/2.8 ms, flip angle = 15°, nominal TS = 10 ms, and 38 radial spokes per frame (corresponding to an acceleration factor of 5).

**Image reconstruction and quantitative analysis:** For tissue function (TF) image reconstruction (see Fig. 1a), we reconstructed images by excluding the first 19 radial spokes and applying a KWIC filter to maintain the center of the last radial spoke only to enhance the signal to noise ratio. For the AIF (see Fig. 1b), we reconstructed five different KWIC filtered images using all 38 radial spokes, maintaining the center of k-space from the first to fifth radial spoke only to produce effective TS from 10 to 21.2 ms (2.8 ms steps). We then quantified five myocardial blood flow (MBF) maps (same TF image, five different AIF images) using the following steps: same optical flow based motion correction and segmentation for all sets, signal intensity to [Gd] conversion using the Bloch equation, theoretical T2\* correction to AIF, and pixel-by-pixel MBF quantification using Fermi.

**Results:** Five subjects were excluded from AIF and MBF quantifications due to poor motion correction. As shown in Figure 2, shorter effective TS linearizes the relationship between signal and [Gd], decreases the peak normalized signal, increases peak [Gd] and

correspondingly decreases MBF values. For a statistical summary of results from 15 subjects, see Table 1. Compared to TS = 10 ms, higher TS values produced significantly decreased peak AIF and increased MBF ( $p < 0.05$ ). The resting MBF (0.70 ml/g/min) calculated from AIF with TS of 10ms agrees better with the resting MBF reported by two cardiac PET studies [5]: (a) mean MBF = 0.71 ml/g/min in 363 healthy subjects using  $^{13}\text{N}$ -ammonia and (b) mean MBF = 0.74 ml/g/min in 382 healthy subjects using  $^{82}\text{Rb}$ .

**Conclusion:** This study demonstrates that TS of 10 ms significantly reduces underestimation of the AIF compared with conventionally used TS of 23-27 ms. Limitation of this study is that it lacks ground truths for AIF and MBF. This is a common problem for quantitative cardiac first-pass perfusion studies in patients, unless one is able to conduct a PET-MR study on the same day (equipment + radiotracer challenges).

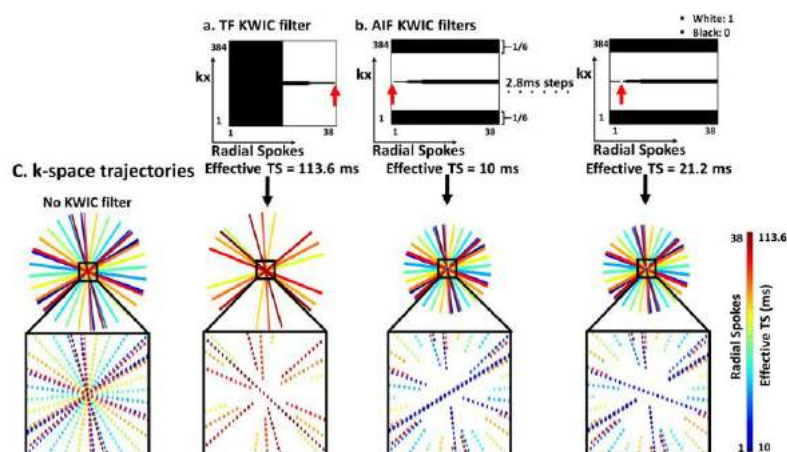
**Figure/Table 1**

TS (ms)	10	12.8	15.6	18.4	21.2
AIF (mM)	12.64 $\pm$ 3.22	10.26 $\pm$ 2.54*	8.72 $\pm$ 2.09*	7.77 $\pm$ 1.88*	7.21 $\pm$ 1.78*
MBF (ml/g/min)	0.70 $\pm$ 0.11	0.86 $\pm$ 0.13*	1.01 $\pm$ 0.15*	1.12 $\pm$ 0.16*	1.23 $\pm$ 0.18*

**Caption 1**

**Table 1.** Statistical summary of the peak AIF and resting MBF values from 15 subjects. Five out of twenty subjects were excluded due to poor motion correction. Reported values represent mean  $\pm$  standard deviation. Both the AIF and MBF values were significantly different across TS values. \*  $p < 0.05$ .

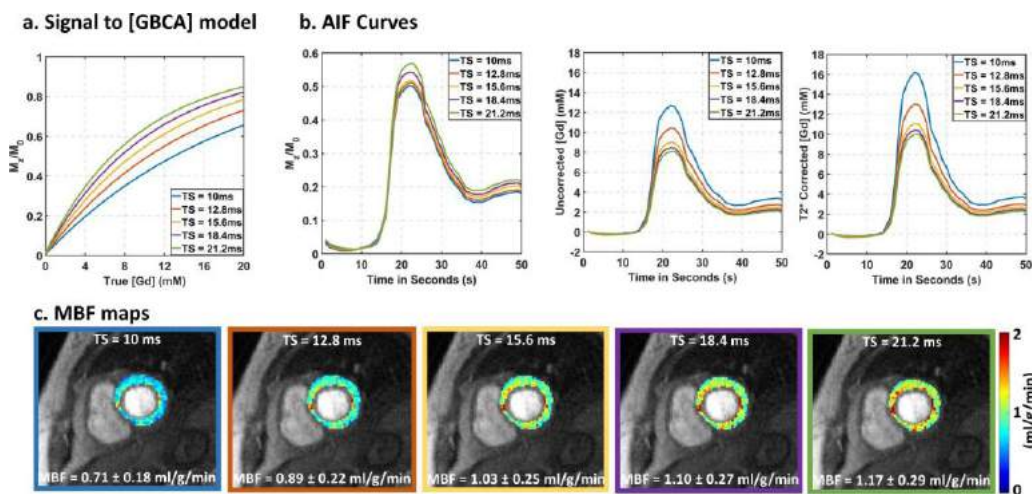
**Figure/Table 2**



## Caption 2

**Figure 1.** Different KWIC filters were applied to the same raw k-space to generate: (a) TF image with TS of 113.6 ( $= 10+2.8*37$ ) ms; (b) Five different AIF images with TS ranging from 10 to 21.2 ms (2.8 ms steps). Red up arrows indicate sampled center of k-space. (c) Original k-space trajectory (column 1) and KWIC filtered trajectories (columns 2-4).

## Figure 3



## Caption 3

**Figure 2.** (a) Plots describing the relationship between the normalized signal and [Gd] for five different TS values; (b) plots of the AIF signal-time curves, and uncorrected and T2\* corrected AIF [Gd]-time curves; (c) the corresponding MBF maps with mean and standard deviation values as shown.

## Bibliographic References

5. Murthy, V.L., et al., Clinical Quantification of Myocardial Blood Flow Using PET: Joint Position Paper of the SNMMI Cardiovascular Council and the ASNC. J Nucl Med, 2018. 59(2): p. 273-293., 4. Naresh, N.K., et al., Accelerated, first-pass cardiac perfusion pulse sequence with radial k-space sampling, compressed sensing, and k-space weighted image contrast reconstruction tailored for visual analysis and quantification of myocardial blood flow. Magn Reson Med, 2019. 81(4): p. 2632-2643., 3. Song, H.K. and L. Dougherty, k-space weighted image contrast (KWIC) for contrast manipulation in projection reconstruction MRI. Magn Reson Med, 2000. 44(6): p. 825-32., 2. Kellman, P., et al., Myocardial perfusion cardiovascular magnetic resonance: optimized dual sequence and reconstruction for quantification. J Cardiovasc Magn Reson, 2017. 19(1): p. 43., 1. Gatehouse, P.D., et al.,

Accurate assessment of the arterial input function during high-dose myocardial perfusion cardiovascular magnetic resonance. J Magn Reson Imaging, 2004. 20(1): p. 39-45.

Speaker: L. Fan

Category: Arterial Input Function, First-Pass Perfusion, Quantification

000053

**Efficacy of increasing adenosine to overcome the effects of caffeine for optimal myocardial perfusion imaging: A volunteer study using coronary sinus flow measurement and T1 mapping of LV myocardium and spleen**

Y. Kurobe \* (1); K. Kitagawa (2); T. Kokawa (1); M. Takafuji (1); M. Ishida (1); H. Sakuma (1)

(1) Department of Radiology, Mie University, Tsu, Japan; (2) Department of Advanced Diagnostic Imaging, University Hospital, Tsu, Japan

**Abstract**

**Background:** Caffeine, a competitive antagonist of adenosine, should be avoided for 12-24 hours prior to myocardial perfusion imaging with adenosine (1). However, it is not uncommon for patients to accidentally ingest caffeine. Whether increasing the dose of adenosine can eliminate the effects of caffeine has not been fully elucidated (2-4). In the present study, we investigated the increase in myocardial blood flow (MBF) induced by adenosine during caffeine ingestion and abstinence by measuring coronary sinus flow (CsF) using phase-contrast cine MRI (PC-MRI). In addition, we measured T1 in myocardium and spleen to investigate its potential as an indicator of stress adequacy in subjects with caffeine ingestion.

**Methods:** Healthy volunteers (n=20, 10 females, age  $30\pm 3$  years) who abstained from caffeine for 24 hours underwent MRI scan twice within 1 month, 1 hour after taking a 166 mg caffeine tablet and 1 hour after taking a placebo, in random order. A blood sample was taken just before the MRI scan to measure the caffeine level in the blood. Quantification of CsF and T1 mapping was performed at rest and during adenosine infusion ( $120\text{ }\mu\text{g/kg/min}$ ). If the heart rate (HR) did not increase by more than 10 beats/min, the dose of adenosine was increased stepwise by  $30\text{ }\mu\text{g/kg/min}$ , with CsF measurement and T1 mapping repeated at each step. All MR images were acquired using Philips 3.0-T scanners. PC-MRI for CsF was performed with TR/TE = 5/3 ms, flip angle 10 deg., acquired temporal resolution of 50 ms reconstructed to 25 phases through the cardiac cycle, and VENC 80 cm/sec. T1 mapping was performed using a 5s(3s)3s MOLLI sequence with TR/TE = 2.6/1.1 ms, flip angle 35 deg. and slice thickness 10 mm. During a 11s breath-hold, 8–13 MOLLI images were acquired. MBF was calculated as  $\text{CsF} \times \text{HR} / \text{left ventricular mass}$  on cine MRI.

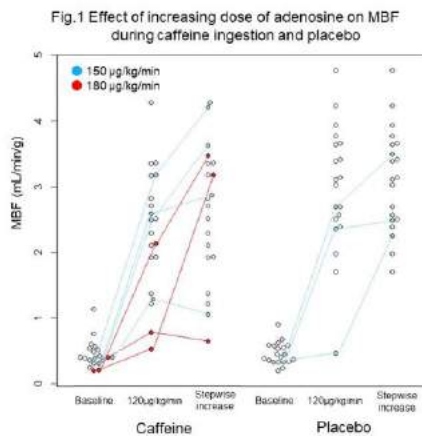
**Results:** Blood caffeine levels ranged from 3.8 to 12 mg/L after 1 hour of caffeine intake, and from 0.00 to 2.2 mg/L after 24 hours of caffeine abstinence with placebo. There was no difference between caffeine and placebo in baseline MBF at rest ( $0.45\pm 0.21$  vs  $0.46\pm 0.17$  mL/min/g,  $p=0.726$ ), baseline myocardial T1 ( $1206\pm 39$  vs  $1218\pm 51$  ms,  $p=0.300$ ) and baseline splenic T1 ( $1336\pm 116$  vs  $1345\pm 130$  ms,  $p=0.324$ ). At adenosine dose of  $120\text{ }\mu\text{g/kg/min}$ , ingestion of caffeine resulted in significantly lower MBF ( $2.30\pm 0.95$  vs  $2.97\pm 0.97$  mL/min/g ( $p<0.001$ ), shorter myocardial T1 ( $1297\pm 68$  vs  $1350\pm 70$  ms,  $p<0.001$ ) and shorter splenic T1 ( $1319\pm 124$  vs  $1361\pm 134$  ms,  $p=0.001$ ). To achieve HR increase of  $>10$  bpm/min, 7 subjects on caffeine and 3 subjects on placebo required a stepwise increase in adenosine, resulting in the MBF increment of  $>1.0$  mL/min/g in 4/7 and 1/3 subject(s), respectively. Overall, the MBF was lower with caffeine compared to placebo ( $2.60\pm 1.02$  vs  $3.11\pm 0.79$  mL/min/g ( $p=0.012$ )(Fig. 1). There was an excellent linear correlation between MBF and myocardial T1 for both caffeine ( $r=0.83$ ,  $p<0.001$ ) and placebo ( $r=0.82$ ,  $p<0.001$ ), while no



correlation was observed for splenic T1 (caffeine:  $r=0.07$ ,  $p=0.677$ ; placebo:  $r=0.21$ ,  $p=0.194$ )(Fig. 2).

**Conclusions:** Although submaximal hyperemia in subjects with caffeine ingestion may be overcome by increasing the dose of adenosine, HR increase of  $>10$  bpm/min is not a reliable criterion to determine the subjects who should receive increased doses of adenosine. Since myocardial T1 correlates well with MBF with or without caffeine intake, it could be a good indicator of stress adequacy.

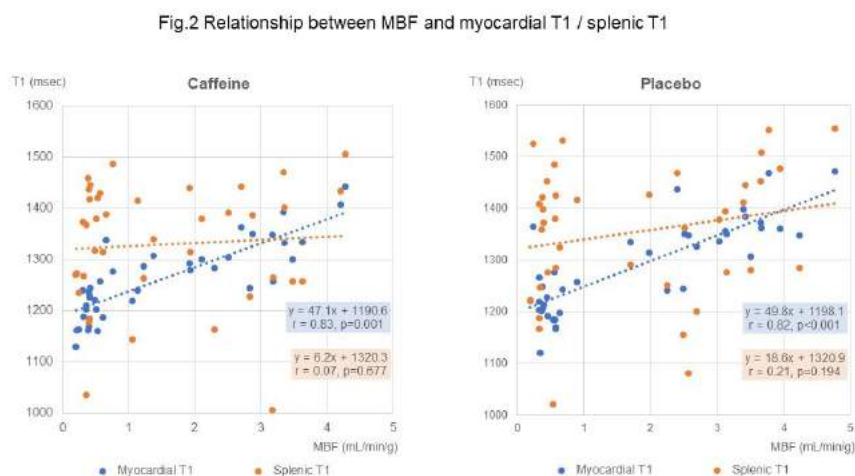
**Figure/Table 1**



**Caption 1**

Red and blue indicate volunteers who required an adenosine load of 180 µg/kg/min or 150 µg/kg/min to obtain a heart rate increase of 10 or more, respectively.

**Figure/Table 2**



## Caption 2

There was an excellent linear correlation between MBF and myocardial T1(blue) for both caffeine ( $r=0.83$ ,  $p<0.001$ ) and placebo ( $r=0.82$ ,  $p<0.001$ ), while no correlation was observed for splenic T1(orange) (caffeine:  $r=0.07$ ,  $p=0.677$ ; placebo:  $r=0.21$ ,  $p=0.194$ ).

## Bibliographic References

1) van Dijk R, Ties D, Kuijpers D, van der Harst P, Oudkerk M. Effects of Caffeine on Myocardial Blood Flow: A Systematic Review. *Nutrients*. 2018;10(8):1083., 2) Karamitsos TD, Ntusi NA, Francis JM, Holloway CJ, Myerson SG, Neubauer S. Feasibility and safety of high-dose adenosine perfusion cardiovascular magnetic resonance. *J Cardiovasc Magn Reson*. 2010;12(1), 3) Kuijpers D, Prakken NH, Vliegenthart R, van Dijkman PR, van der Harst P, Oudkerk M. Caffeine intake inverts the effect of adenosine on myocardial perfusion during stress as measured by T1 mapping. *Int J Cardiovasc Imaging*. 2016;32(10):1545-53., 4) Seitz A, Kaesemann P, Chatzitofi M, Löbig S, Tauscher G, Bekerredjian R, Sechtem U, Mahrholdt H, Greulich S. Impact of caffeine on myocardial perfusion reserve assessed by semiquantitative adenosine stress perfusion cardiovascular magnetic resonance. *J Cardiovasc Magn Reson*. 2019;21(1):33.

Speaker: Y. Kurobe

Category: Adenosine, Native T1, Phase Contrast

000055

## Dual-venic Dual-echo (DVDE) Phase-contrast MRI for Simultaneous Measurement of Arterial and Venous Blood Flow

J. Jang \* (1); Y. Zhao (1); J. Smink (2); A. Powell (3); L. Browne (4); M. Moghari (4)

(1) Clinical science, Philips Healthcare, Boston, United States of America; (2) Clinical science, Philips Healthcare, Best, Netherlands; (3) Department of pediatrics and department of cardiology, Harvard Medical School and Boston Children's Hospital, Boston, United States of America; (4) Department of radiology, Children's Hospital Colorado, Aurora, United States of America

### Abstract

**Background:** Phase-contrast (PC) MRI is a key component of cardiovascular exams for the measurement of blood velocity and flow [1]. To enable PC-MRI with a higher velocity-to-noise ratio (VNR) without velocity aliasing artifact while minimizing the acquisition time, a dual-venic dual-echo (DVDE) PC-MRI has been proposed which acquires both high- and low-venic images within a single repetition time [2, 3]. In this work, we sought to evaluate a DVDE technique for simultaneous evaluation of arterial and venous blood flow.

**Methods:** Seven patients referred for clinical cardiovascular MRI exams (5 female, median age 10 (1-31) years old) were imaged on Philips Ingenia 1.5 T scanner. For each patient, two conventional single-venic flow measurements were acquired using a high-venic (200 cm/s) and a low-venic (70 – 100 cm/s) in an axial imaging plane to quantify arterial blood flow at ascending and descending aorta (AAo and DAo) and venous blood flow at superior vena cava (SVC). The DVDE sequence was then acquired using both high- and low-venics (venic1 = 200 cm/s and venic2 = 70 – 100 cm/s) in the same imaging plane and DVDE single-echo and combined images were reconstructed inline on the scanner [2]. Typical imaging parameters used for the single-venic and DVDE PC-MRI were as follows: spatial resolution=1.5×1.5 mm, slice thickness=6 mm, field-of-view=250×208 mm, flip-angle=12°, acquired heart-phases=20 reconstructed to 30, SENSE=2, and number of signals averages=3.

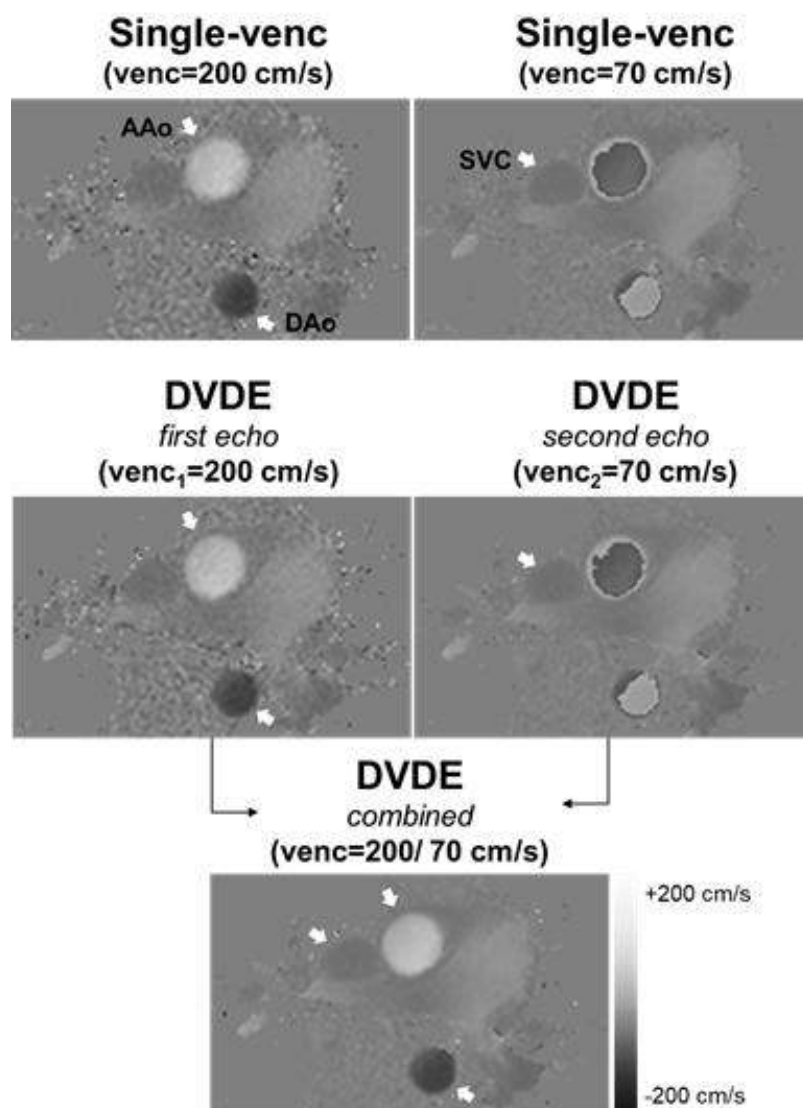
For each vessel of interest, blood velocity and flow were compared in the single-venic vs. the DVDE single-echo and DVDE combined images. VNR was also compared as the mean to the standard deviation of velocities in diastole. The blood flow measurements and VNR were then statistically compared using a Wilcoxon signed-rank test and  $p < 0.05$  was considered statistically significant. The intraclass correlation coefficient (ICC) was calculated to evaluate the agreement between the measurements.

**Results:** Fig. 1 shows DVDE image demonstrating high VNR of low-venic image without velocity aliasing artifacts. In the AAo and DAo, both the DVDE high-venic first echo and DVDE combined images demonstrated similar blood velocity and flow compared to the single high-venic acquisition (Table. 1 and Fig. 2). In the SVC, both the DVDE low-venic second echo and DVDE combined images demonstrated similar blood velocity and flow compared to the single low-venic acquisition (Table. 1 and Fig. 2). In arterial blood flow, the DVDE single echo showed similar VNR, while DVDE combined demonstrated higher VNR compared to the single-venic image (AAo,  $0.08 \pm 0.04$  vs.  $0.08 \pm 0.08$  and  $0.31 \pm 0.17$ ,  $p = 0.5$  and  $0.02$ ; DAo,  $0.32 \pm 0.17$  vs.  $0.35 \pm 0.21$  and  $0.59 \pm 0.38$ ,  $p = 0.61$  and  $0.04$ ). In venous

blood flow, VNR were similar in all measurements (SVC,  $0.92 \pm 0.44$  vs.  $1.21 \pm 0.42$  and  $1.15 \pm 0.41$ ,  $p = 0.63$  and  $0.66$ ). The average imaging time of DVDE acquisition was 20% faster than the combined imaging time of the high- and low-*venc* sequences (single-*venc*,  $1:23 \pm 0:18$  min (high-*venc* =  $0:41 \pm 0:09$  min and low-*venc*  $0:42 \pm 0:09$  min) vs. DVDE,  $1:10 \pm 0:13$  min).

**Conclusions:** DVDE allows simultaneous imaging of arterial and venous blood flow in a single scan with improved VNR and similar blood flow measurements compared to the single-*venc* PC-MRI. Future work will evaluate this technique in a 4D-flow acquisition for the simultaneous measurement of arterial and venous blood flow with three-directional velocity-encoding.

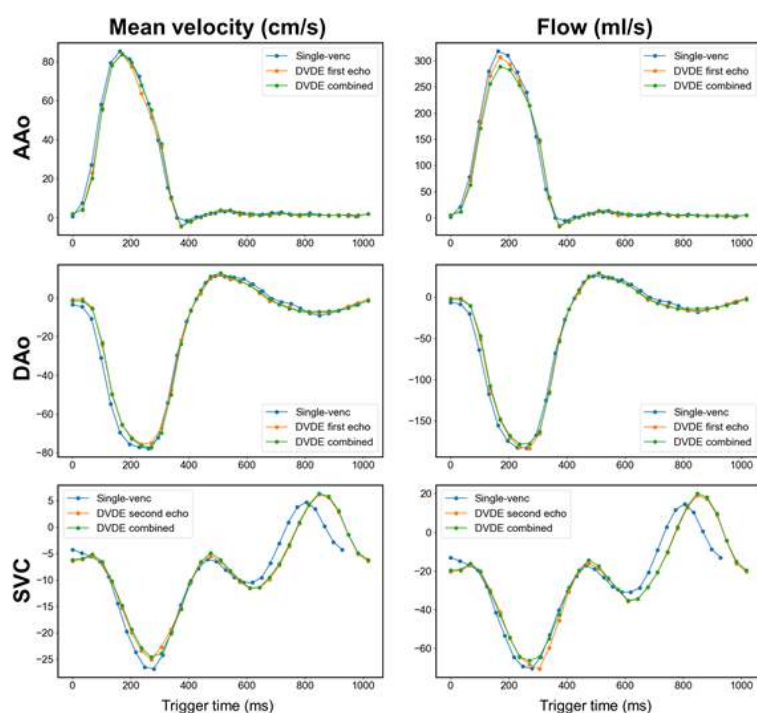
**Figure/Table 1**



**Caption 1**

**Figure 1.** Velocity images from single-venc and DVDE PC-MRI from a 16-year-old male patient with dilated cardiomyopathy. For the single-venc images, two separate measurements were acquired in the same imaging plane with different venc values to measure arterial flow in the ascending and descending aorta (AAo and DAo) and venous flow in the superior vena cava (SVC). DVDE images from each echo show similar velocities to the corresponding single-venc images. The DVDE combined image demonstrates both arterial and venous blood flow with the VNR of the low-venc image without velocity aliasing artifacts.

**Figure/Table 2**



**Caption 2**

**Figure 2.** Mean velocity and flow over the cardiac cycle in AAo, DAo, and SVC in a 16-year-old male patient with dilated cardiomyopathy. Blood velocity and flow measured using DVDE is similar to that of the single-venc in arterial blood flow in AAo and DAo (venc = 200 cm/s) and venous blood flow in SVC (venc = 70 cm/s).

**Figure 3**

	Max. Mean velocity (cm/s)			Mean flow (ml/s)		
	Single-venc	DVDE	DVDE	Single-venc	DVDE	DVDE
AAo	(200 cm/s)	(200 cm/s)	combined	(200 cm/s)	(200 cm/s)	combined

Mean	68.07	68.07	69.4	51.74	51.74	54.35
SD	20.85	21.14	21.36	23.25	20.67	20.63
ICC		1.0	0.99		0.9	0.82
95% CI		[0.97, 1.0]	[0.93, 1.0]		[0.47, 0.99]	[0.18, 0.97]
p-value		0.27	0.31		0.74	0.74
<b>DAo</b>	Single-venc	DVDE	DVDE	Single-venc	DVDE	DVDE
	(200 cm/s)	(200 cm/s)	combined	(200 cm/s)	(200 cm/s)	combined
Mean	82.21	81.11	84.11	31.64	31.2	31.11
SD	10.0	14.13	14.34	16.61	14.97	15.72
ICC		0.98	0.96		0.97	0.96
95% CI		[0.87, 1.0]	[0.77, 0.99]		[0.81, 1.0]	[0.74, 0.99]
p-value		0.24	0.61		0.61	0.31
<b>SVC</b>	Single-venc	DVDE	DVDE	Single-venc	DVDE	DVDE
	(70-100 cm/s)	(70 cm/s)	combined	(70-100 cm/s)	(70 cm/s)	combined
Mean	35.87	34.59	32.59	19.34	18.72	18.79
SD	9.35	8.52	5.85	10.77	9.85	10.1
ICC		0.97	0.92		1.0	0.99
95% CI		[0.79, 1.0]	[0.56, 0.99]		[0.99, 1.0]	[0.94, 1.0]
p-value		0.24	0.06		0.4	0.4

### Caption 3

**Table 1:** Blood velocity and flow measurements in all patients (n=7). Maximum mean velocity and mean flow were similar between single-venc vs. DVDE single-echo and combined in both arterial and venous blood flow at AAO, DAAo, and SVC. SD, standard deviation; ICC, intraclass correlation coefficient; and CI, confidence interval.

### Bibliographic References

1. Pelc NJ, Herfkens RJ, Shimakawa A, Enzmann DR. Phase contrast cine magnetic resonance imaging. Magn Reson Q 1991;7:229–254. , 2. Jang J, Zhao Y, Smink J, Powell JP. Moghari HM. Dual-venc dual-echo cardiovascular phase-contrast MRI. SCMR 2021., 3. Ajala A, Zhang J, Pednekar A, Buko E, Wang L, Cheong BY, Hor PH, Muthupillai R. Mitral valve flow and myocardial motion assessed with dual-echo dual-velocity cardiac MRI.

Radiology: Cardiothoracic Imaging. 2020 Jun 25;2(3):e190126.

Speaker: J. Jang

Category: Phase Contrast , Blood Flow, Velocity

000056

**Ventricular function and tissue characterization by Cardiac MRI is reassuring in children 6-9 months following hospitalization for Multisystemic Inflammatory Syndrome in Children (MIS-C)**

M. P. DiLorenzo \* (1); K. Farooqi (2); A. Shah (1); A. Channing (1); J. K. Harrington (1); T. J. Connors (3); K. Martirosyan (1); U. S. Krishnan (1); A. Ferris (1); R. Weller (1); D. L. Farber (4); J. D. Milner (5); M. Gorelik (5); E. B. Berman-Rosenzweig (1); B. R. Anderson (1)

(1) Department of pediatrics, division of cardiology, Columbia University Irving Medical Center, New York, United States of America; (2) Department of pediatrics, division of cardiology, Columbia University Medical Center, Broadway, New York, United States of America; (3) Department of pediatrics, division of critical care, Columbia University Irving Medical Center, New York, United States of America; (4) Department of microbiology and immunology, Columbia University Irving Medical Center, New York, United States of America; (5) Department of pediatrics, division of pediatric allergy, immunology, and rheumatology, Columbia University Irving Medical Center, New York, United States of America

**Abstract**

**Background:** Multisystem Inflammatory Syndrome in Children (MIS-C) is a severe life threatening manifestation of infection SARS-CoV-2. Acute cardiac dysfunction and resultant cardiogenic shock were common in children diagnosed with MIS-C. While most children recover rapidly from acute illness, the long-term impact on the myocardium and cardiac function is unknown.

**Methods:** In this prospective study, cardiac MRI (CMR) was performed on patients <21 years of age with a history of MIS-C, 6-9 months following hospitalization. Per institutional protocol, patients underwent clinical CMR if they had a history of left ventricular ejection fraction (LVEF) <50% at any time, persistent symptoms, or ECG abnormalities. Research CMR was offered to all other MIS-C patients over 10 years old. A GE 1.5T Explorer magnet scanner was utilized. CMR protocol included conventional short and long axis balanced steady state free precession (bSSFP) cine, basal and mid-ventricular short axis T2-prepared bSSFP (T2 mapping), T2 weighted turbo spin echo imaging, and pre- and post-contrast (~15 min following administration of gadolinium-based contrast) T1 mapping with extracellular volume (ECV) using Modified Look-Locker Inversion recovery sequences (MOLLI). First pass perfusion was performed in a short axis plane to assess for perfusion defects and phase sensitive inversion recovery imaging was performed in long and short axis planes to assess for late gadolinium enhancement (LGE).

**Results:** In total, 13 patients underwent CMR (eight clinical, five research). Median age at CMR was 13.6 years (interquartile range [IQR] 11.9-16.0); median time from hospitalization was 8.2 months (IQR 6.8-9.6). Twelve patients had normal ventricular function with a median LVEF of 58% (IQR 56-59) and median right ventricular (RV) EF of 52% (IQR 51-55). One subject had globally low normal EF (52%). There was normal T2 and pre-contrast T1 times as compared to scanner reference ranges (Table 1). ECV was calculated in 10 subjects and was normal. There was qualitatively no evidence of edema by T2 weighted imaging or perfusion



defects on first pass perfusion imaging. One subject had LGE at the inferior insertion point and mid-ventricular inferolateral region, with normal ventricular function, no evidence of edema or perfusion defects, and normal T1 times. When stratifying by a history of abnormal LVEF (LVEF <55%) on echocardiography during initial hospitalization, LVEF by CMR was slightly lower among subjects with history of an abnormal LVEF (56.3 [IQR 53.4-58.0] vs 58.7 [58.0-60.0],  $p=0.04$ ). There was no difference in indexed LV or RV volumes, RV EF, T1 or T2 times based on a history of decreased LVEF (Table 2).

**Conclusions:** Although many children with MIS-C present acutely with cardiac dysfunction, recovery is overall excellent with minimal to no evidence of residual cardiac dysfunction or myocardial involvement. LVEF by CMR at 6-9 months among children with LV dysfunction at presentation remains lower than among those without, though it reaches normal range. The long-term functional implications of this finding and the cardiac implications of MIS-C more broadly are unclear and may warrant further study.

**Figure/Table 1**

Parameter	Median (IQR)	Range	Reference ranges (Median, Range)
LVEF (%)	58 (56.3-59)	52.0-62.0	
RVEF (%)	52 (51-54.9)	49.1-61.0	
LVEDV (mL)	138 (108.5-172.7)	67.0-221.9	
LVEDVi (mL/m <sup>2</sup> )	81.6 (72.3-93.5)	66.6-110.5	
RVEDV (mL)	145.6 (130-153.2)	52.4-240.2	
RVEDVi (mL/m <sup>2</sup> )	88.2 (74.9-93.0)	67.3-122	
Native T1 (ms)			
Base	1032 (984-1062)	825-1099	1019 (955-1100)
Mid	1000 (984-1035)	820-1055	984 (947-1073)
Global	1010 (991-1051)	836-1089	1032 (952-1076)
T2 mapping (ms)			
Base	49.6 (47.4-51.7)	37.3-55.5	51 (46-54.8)
Mid	49.2 (45.9-51.1)	40.9-53.6	50.2 (40-53.4)
Apex	52.7 (51.0-55.8)	47.1-57.0	54 (48-62.1)
ECV (%)			
Base (n=8)	24 (23-25)	17-26	
Mid (n=10)	24 (21-28)	18-29	
Global (n=8)	22.5 (21.5-26.5)	20-29	

**Caption 1**

CMR values for subjects with MIS-C with scanner reference ranges. LV, left ventricle; RV, right ventricle; EF, ejection fraction; EDV, end-diastolic volume; EDVi, indexed end-diastolic volume; ECV, extracellular volume.

**Figure/Table 2**

Parameter	Low LVEF	Normal LVEF	P value
LVEF (%)	56.3 (53.4-58)	58.7 (58-60)	0.04
RVEF (%)	51.6 (50.3-52.8)	55.4 (51-56)	0.20
LVEDV (mL)	128 (76.4-138)	179 (139-210.2)	0.03
LVEDVi (mL/m <sup>2</sup> )	74.5 (72.1-88.2)	89.4 (80.1-105.1)	0.25
RVEDV (mL)	149.1 (75-147.4)	178.9 (130.1-206.4)	0.09
RVEDVi (mL/m <sup>2</sup> )	88.2 (70.8-91)	86.8 (74.9-105.2)	0.39
Native T1 (ms)			
Base	1032 (975-1036)	1028.5 (993-1090)	0.63
Mid	988 (977-1019)	1020 (996-1043)	0.20
Global	1002 (990-1047)	1022 (993-1083)	0.52
T2 mapping (ms)			
Base	49.6 (46.2-53.7)	49.6 (48.4-51.6)	0.89
Mid	48.1 (45.6-52.5)	49.9 (48.1-51.1)	0.62
Apex	52.7 (51-55.7)	53.7 (51-56.6)	0.75
ECV (%)			
Base (n=8)	25 (20.5-26.0)	23.5 (23-24)	0.37
Mid (n=10)	21 (21-27.4)	26 (22-28)	0.60
Global (n=8)	22.5 (21-26)	23.5 (21.5-26.5)	0.88

**Caption 2**

Comparison of CMR parameters based on history of LV dysfunction on echocardiography during admission. Values presented as median (IQR). LV, left ventricle; RV, right ventricle; EF, ejection fraction; EDV, end-diastolic volume; EDVi, indexed end-diastolic volume; ECV, Extracellular volume.

### Bibliographic References

Sirico D, Basso A, Reffo E, Cavaliere A, Castaldi B, Sabatino J, Meneghel A, Martini G, Da Dalt L, Zulian F, Di Salvo G. Early Echocardiographic and Cardiac MRI Findings in Multisystem Inflammatory Syndrome in Children. J Clin Med. 2021 Jul 29;10(15):3360, Webster G, Patel AB, Carr MR, Rigsby CK, Rychlik K, Rowley AH, Robinson JD. Cardiovascular magnetic resonance imaging in children after recovery from symptomatic

COVID-19 or MIS-C: a prospective study. J Cardiovasc Magn Reson 2021 Jul 1; 23(1):86 , Farooqi KM, Chan A, Weller RJ, Mi J, Jiang P, Abrahams E, Ferris A, Krishnan US, Pasumarti N, Suh S, Shah AM, DiLorenzo MP, Zachariah P, Milner JD, Rosenzweig EB, Gorelik M, Anderson BR. Columbia University Interdisciplinary MIS-C Follow-up Program and the CUIMC Pediatric/Adult Congenital Heart Research Collaborative. Longitudinal Outcomes for Multisystem Inflammatory Syndrome in Children. Pediatrics 2021 Aug; 148(2).

Speaker: M. P. DiLorenzo

Category: Pediatric , MOLLI, Parametric Mapping

000057

### **3-Dimensional Late Gadolinium Enhancement Imaging to Evaluate Left Atrial Dysfunction in a Child with Mitral Stenosis**

K. Jurow \* (1); A. J. Powell (2); A. Prakash (2); R. Margossian, (2); J. Jang (3); D. Castellanos (2)

(1) Department of Cardiology, Longwood Avenue, Boston, MA, USA, Boston children's Hospital, Fairland Street, Boston, United States of America; (2) Department of cardiology and department of pediatrics, Boston Children's Hospital and Harvard Medical School, Boston, United States of America; (3) Clinical science, Philips Healthcare, Boston, United States of America

#### **Abstract**

##### **Description of Clinical Presentation**

A 19-month-old male with high-risk neuroblastoma was treated with chemotherapy, chimeric antibody therapy, stem cell transplant, proton radiation directed at the right adrenal gland, and right adrenalectomy. At age 4 years, he developed mild mitral stenosis, which progressed over several years. He underwent percutaneous balloon mitral valvuloplasty at age 8. One year later, he developed progressive exercise intolerance and a worsening mitral valve stenosis gradient by echocardiography. A catheterization revealed a mean left atrial (LA) pressure of 18 mm Hg and a mitral valve inflow gradient of 6-7 mm Hg at rest. Of note, the LA V-wave was 30 mm Hg in the absence of mitral regurgitation, raising the question of reduced left atrial compliance. The patient was then referred for a cardiac magnetic resonance examination (CMR) with late gadolinium enhancement (LGE) to evaluate for left atrial fibrosis.

##### **Diagnostic Techniques and Their Most Important Findings**

The CMR was performed with a 1.5T Philips scanner. The examination included 3-dimensional (3D) Dixon LGE imaging of the LA using an ECG-gated, respiratory navigated, inversion recovery prepared gradient echo pulse sequence (TE 2.4 ms, TR 5.2 ms, FA 20 degrees). 3D LGE was performed 30 minutes after contrast injection (1,2). The inversion time was chosen to null the ventricular myocardium plus 10 ms, and images were acquired during ventricular mid-diastole. The LGE images were analyzed using the Circle ADAS 3D software module (Circle Cardiovascular Inc., Calgary, AB, Canada). Thresholds for fibrosis and scarring were adopted based on a prior study that also used the ADAS software (3).

The CMR findings were significant for a mildly dilated LA, with LGE along the inferior aspect, leftward wall, atrial septum, and pulmonary vein walls. Atrial LGE was quantified as 8% of the total left atrial surface area. The LA is shown in image 1 and a representative 3D color map is shown in image 2. The left ventricle was mildly dilated with an ejection fraction of 53%. There was no left ventricular LGE.

##### **Learning Points From This Case**

In adults, there is growing recognition of the utility of 3D LGE CMR examination of the LA, including to predict risk of recurrence of atrial fibrillation (AF) prior to an ablation (1) and to assess LA function in patients with AF (4). However, there is little reported use in the

pediatric population. Our case illustrates the successful acquisition of a 3D LGE sequence in a 9 yo patient and quantification of his left atrial scar burden. The 3D LGE examination provided diagnostic utility as the atrial LGE in this patient is likely related to atrial fibrosis and dysfunction, which correlates well with both the patient's clinical presentation and hemodynamic findings in the catheterization lab. In the 4-month interval since the CMR, no cardiac medication or treatment plan changes have been made as the patient's clinical status remains stable. While this case highlights the potential diagnostic utility of a 3D atrial LGE assessment, further investigation into the diagnostic and prognostic utility of such an assessment in the pediatric population is needed. Potential areas of utility include identification of ablation targets and pre-procedural prognostication for atrial arrhythmia ablations in children with congenital heart disease, and assessment of atrial function in patients with congenital heart disease or cardiomyopathy.

### **Figure/Table 1**

#### **Caption 1**

Multi-planar reformatted images from the 3D LGE sequence are shown focusing on the LA (labeled). The top panel is an axial view, and the bottom panels represent oblique views that are separated by 90 degrees. LGE is noted along the atrial septum as well as the superior and inferior walls of the atrium.

### **Figure/Table 2**

#### **Caption 2**

A 3D color-coded map of the LA is shown. The image intensity ratio (IIR) is calculated as the ratio of the signal intensity of each pixel to the mean blood pool intensity. The IIR is then color-coded, with values  $> 1.3$  (threshold for dense atrial fibrosis) displayed in red. LGE is noted predominantly along the atrium septum and inferior aspect of the left atrium.

### **Bibliographic References**

3. Benito EM, Carlosena-Remirez A, Guasch E, Prat-González S, Perea RJ, Figueras R,

Borràs R, Andreu D, Arbelo E, Tolosana JM, Bisbal F, Brugada J, Berruezo A, Mont L. Left atrial fibrosis quantification by late gadolinium-enhanced magnetic resonance: a new method to standardize the thresholds for reproducibility. *Europace*. 2017 Aug 1;19(8):1272-1279. doi: 10.1093/europace/euw219. PMID: 27940935., 2. Chubb, H., Karim, R., Roujol, S. et al. The reproducibility of late gadolinium enhancement cardiovascular magnetic resonance imaging of post-ablation atrial scar: a cross-over study. *J Cardiovasc Magn Reson* 20, 21 (2018). <https://doi.org/10.1186/s12968-018-0438-y>, 1. Marrouche NF, Wilber D, Hindricks G, et al. Association of Atrial Tissue Fibrosis Identified by Delayed Enhancement MRI and Atrial Fibrillation Catheter Ablation: The DECAAF Study. *JAMA*. 2014;311(5):498–506. doi:10.1001/jama.2014.3, 4. Habibi M, Lima JA, Khurram IM, Zimmerman SL, Zipunnikov V, Fukumoto K, Spragg D, Ashikaga H, Rickard J, Marine JE, Calkins H, Nazarian S. Association of left atrial function and left atrial enhancement in patients with atrial fibrillation: cardiac magnetic resonance study. *Circ Cardiovasc Imaging*. 2015 Feb;8(2):e002769. doi: 10.1161/CIRCIMAGING.114.002769

Speaker: K. Jurow

Category: Atrial Fibrosis, Pediatric , Late Gadolinium Enhancement

000062

## Simultaneous lumen and vessel wall imaging for efficient comprehensive assessment of aortic disease

C. Munoz \* (1); A. Fotaki (1); R. Hajhosseiny (1); K. Kunze (2); R. Neji (2); R. M. Botnar (1); C. Prieto (1)

(1) School of Biomedical Engineering and Imaging Sciences, King's College London, London, United Kingdom; (2) Siemens healthineers, Siemens - Frimley, Frimley, United Kingdom

### Abstract

**BACKGROUND:** Bright and black-blood imaging are relevant contrasts for the assessment of aortic disease(1), as they enable the depiction of cardiovascular anatomy and detection of luminal abnormalities, and characterization of plaque burden and detection of thrombus, respectively. In current clinical practice, these contrasts are acquired in separate scans: bright-blood images are typically acquired under free-breathing using 3D sequences and relying on diaphragmatic navigators to minimize the effect of respiratory motion, whereas black-blood images are generally acquired under breath-hold as 2D slices in different orientations(1). Such approach results in prolonged scan times and potential misregistration between images due to both patient motion and the different geometries used for each scan. Here we address these issues by accelerating and extending a previously introduced motion-compensated iT2Prep-BOOST sequence(2). The sequence provides high-quality co-registered 3D bright and black-blood images for the assessment of aortic lumen and vessel wall from a short scan of ~8 minutes.

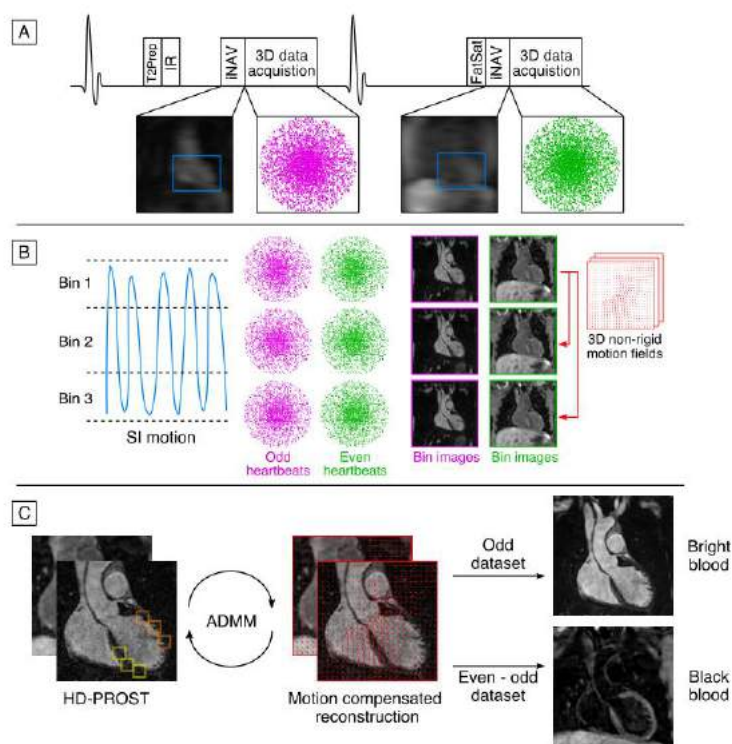
**METHODS:** Acquisition consists of an ECG-triggered interleaved 3D balanced SSFP sequence (Fig 1a), where a T2Prep-IR module is applied before data acquisition in odd heartbeats (bright-blood dataset for lumen visualization) and no preparation is applied in even heartbeats(2). In both even and odd heartbeats 3D data is acquired with an undersampled variable-density Cartesian trajectory with spiral profile order(3,4). 2D image-navigators (iNAVs) acquired at each heartbeat enable 100% respiratory efficiency without data rejection. Beat-to-beat 2D translational and bin-to-bin 3D non-rigid motion are estimated from the iNAVs and the 3D data itself (Fig 1b) and integrated into a non-rigid motion-compensated HD-PROST(5) reconstruction (Fig 1c). Finally, subtraction of the two bright-blood datasets is used to create the black-blood datasets for vessel wall visualization.

Eight patients (7 male,  $27 \pm 6$  yr) were scanned at 1.5T (MAGNETOM Aera, Siemens Healthcare, Germany) using the proposed approach. 3D images were acquired with iT2Prep-BOOST (coronal orientation, resolution=1.3mm<sup>3</sup> isotropic, FOV=300×400×104-156mm<sup>3</sup>, 4× undersampling, T2Prep= 40ms, TI=110ms, TE/TR=1.41/3.24ms, bandwidth=965 Hz/px). For assessment of the thoracic aorta, patients also underwent conventional bright-blood free-breathing diaphragmatic navigator gated 3D MR angiography (T2-prepared bSSFP sequence, sagittal orientation, resolution 1.4/1.5mm<sup>3</sup> isotropic, FOV=240×400×134-168mm<sup>3</sup>, T2Prep=40ms) and 2D breath-held black-blood single shot fast spin echo (HASTE) (axial orientation, 1.56mm in-plane resolution, 8 mm slice thickness, 23-36 slices), with additional orientations acquired depending on each patient. Scan time was recorded for all sequences.

**RESULTS:** Average scan time for the conventional sequences was  $13.3\pm3.7$ min in total, while for the proposed 3D iT2Prep-BOOST approach was significantly shorter ( $7.95\pm1.24$ min,  $P=0.002$ ). Visually improved quality of aortic luminal signal with attenuation of flow related artefacts can be observed with the proposed bright-blood technique (Fig 2), which also requires a shorter acquisition time and offers a complementary black-blood image for assessment of the vessel wall. Furthermore, improved coverage and resolution was observed for the black-blood 3D images compared to conventional 2D black-blood imaging (Fig 3).

**CONCLUSION:** The proposed iT2Prep-BOOST provides excellent depiction of the aortic lumen and wall, with a predictable scan time of around 8 minutes, and holds promise for comprehensive assessment of aortic disease.

**Figure/Table 1**

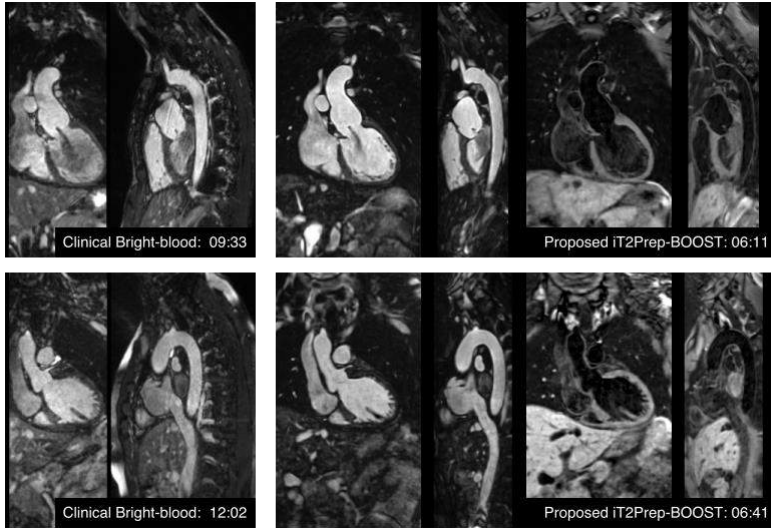


**Caption 1**

Figure 1. (A) 3D data acquisition is performed in an interleaved fashion, with a T2Prep-IR preparation pulse used in odd heartbeats; and fat saturation used in even heartbeats. (B) 3D non-rigid motion is estimated from 3D bin images, and (C) used to reconstruct regularized motion corrected images that are then used to obtain the bright and black-blood datasets.

**Figure/Table 2**

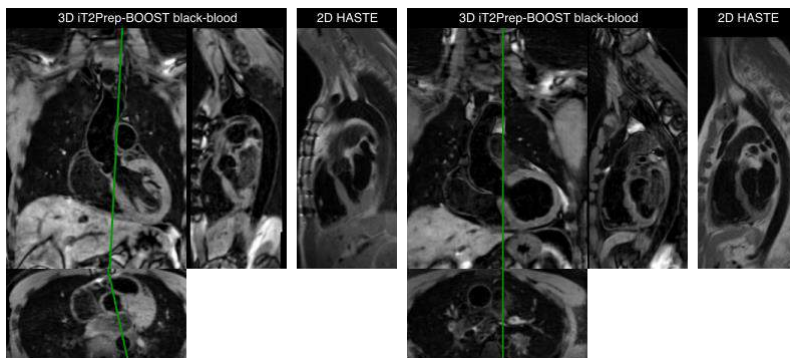




### Caption 2

Figure 2. Visual comparison of clinical bright-blood datasets and the proposed iT2Prep-BOOST sequence for two representative patients. The iT2Prep-BOOST bright-blood images offer excellent depiction of the thoracic aorta, comparable to the clinical standard, while providing a co-registered black-blood image for assessment of the aortic wall from a short efficient scan.

### Figure 3



### Caption 3

Figure 3. Visual comparison of clinical 2D HASTE black-blood datasets and the proposed 3D iT2PrepIR black-blood for two representative patients. A similar depiction of the aortic wall can be observed, while the proposed 3D iT2Prep-BOOST offers full volumetric coverage and higher image resolution.

## **Bibliographic References**

1. Kramer CM, Barkhausen J, Bucciarelli-Ducci C, Flamm SD, Kim RJ, Nagel E. Standardized cardiovascular magnetic resonance imaging (CMR) protocols: 2020 update. *J Cardiovasc Magn Reson* 2020;22:17., 2. Milotta G, Ginami G, Cruz G, Neji R, Prieto C, Botnar RM. Simultaneous 3D whole-heart bright-blood and black-blood imaging for cardiovascular anatomy and wall assessment with interleaved T2prep-IR. *Magn Reson Med* 2019;82:312–25., 3. Prieto C, Doneva M, Usman M, et al. Highly efficient respiratory motion compensated free-breathing coronary MRA using golden-step Cartesian acquisition. *J Magn Reson Imaging* 2015;41:738–46., 4. Bustin A, Ginami G, Cruz G, et al. Five-minute whole-heart coronary MRA with sub-millimeter isotropic resolution, 100% respiratory scan efficiency, and 3D-PROST reconstruction. *Magn Reson Med* 2019;81:102–115., 5. Bustin A, Lima da Cruz G, Jaubert O, Lopez K, Botnar RM, Prieto C. High-dimensionality undersampled patch-based reconstruction (HD-PROST) for accelerated multi-contrast MRI. *Magn Reson Med* 2019;81:3705–3719.

Speaker: C. Munoz

Category: Aorta, Accelerated Imaging, 3D

000065

## Feasibility of obtaining 3D delayed enhancement imaging in patients with tachycardia or arrhythmia: A pilot study

J. Craft \* (1); R. Parikh (1); J. Weber, (1); X. Bi, (2); M. Schmidt (3); K. Kunze (4); R. M. Botnar (5); C. Prieto (5)

(1) Cardiac Imaging, St Francis Hospital, Dematteis Research Center, Greenvale, United States of America; (2) Siemens, Siemens Medical Solutions USA, Inc, Los Angeles, United States of America; (3) Siemens, Siemens Healthineers, Erlangen, Germany; (4) Siemens healthineers, Siemens - Frimley, Frimley, United Kingdom; (5) Biomedical Engineering and Imaging Sciences, King's College London, London, United Kingdom

### Abstract

**Background:** Segmented late gadolinium enhancement (LGE) imaging in patients with tachycardia and arrhythmia can be technically challenging. Motion corrected single-shot (MOCO) 2D LGE has shown robust image quality in patients with arrhythmia[1]; however, 3D LGE is still affected by the limitations of segmented imaging. Therefore, an unmet clinical need remains to obtain high quality 3D LGE datasets in particular clinical scenarios, such as pre-planning for invasive electrophysiology studies. We aim to determine the feasibility of 3D LGE using an image based navigator (iNav) in a pilot study of patients with tachycardia or arrhythmia

**Methods:** A prototype 3D LGE sequence with Dixon water-fat separation, image navigation (iNav), a Cartesian variable-density spiral-like trajectory and in-line non-rigid motion-compensated reconstruction (NR) leading to 100 percent scan efficiency was used as previously described[2,3]. All CMR scans were performed on a 3T MAGNETOM Skyra (Siemens) at a single center. Among patients referred for clinically indicated CMR, 5 patients (2 females) ranging in age from 67 to 77 years were identified for the study. Ten minutes after injection of 0.15 mmol/kg Gadavist, 2D MOCO LGE images were acquired in the short axis orientation. In the long axis orientation, breath-hold inversion recovery GRE was used to minimize the effects of through-plane motion in capable patients; otherwise MOCO 2D LGE was also performed in long axis orientations. After completion of 2D LGE, 3D LGE was performed in the axial orientation with the prototype sequence using the following parameters: FOV 320 X 320 mm, slice thickness 1.3 mm, in-plane spatial resolution 1.25 X 1.25 mm, TE 1.3 ms, bandwidth 850 Hz/Px, data window duration 82-100 ms, segments per shot 17-21. For both sets of images, the acquisition was moved to systole (40% of the nominal RR interval, or zeroing the trigger delay if this was not possible). The following scan conditions were present: Patient 1: cardiac sarcoidosis, normal sinus rhythm with frequent APCs identified on pre-scan EKG; patient 2: ischemic cardiomyopathy, premature ventricular contractions during scan; patient 3: dilated cardiomyopathy, premature ventricular contractions during scan; patient 4: sinus tachycardia, HR 105 BPM on cardiac cines; patient 5: normal sinus rhythm with frequent atrial premature contractions on pre-scan EKG. Two physicians (with 7 years and 1 year experience respectively), blinded and independently analyzed the 2D and 3D LGE datasets for image quality and semi-quantitative LGE using the 17 segment model.

**Results:** Figures 1 A-E demonstrate the EKG, 2D and 3D LGE images acquired in patient 5. In total 85/85 segments of the 3D LGE were interpretable, rated by reader 1 and 83/85 segments were rated as interpretable for reader 2. For 2D LGE, 85/85 segments were rated by both readers as interpretable. There was near perfect intra-observer agreement between 2D LGE and 3D LGE for both readers. Inter-observer agreement for 2D and 3D LGE datasets was moderate-substantial (figure 2).

**Conclusion:** The pilot study suggests 3D LGE imaging using the prototype sequence is feasible in patients with tachycardia and arrhythmia. A predictable scan duration can be traded for a smaller data window duration which results in reduced susceptibility to cardiac motion. A larger study is needed to determine if the robustness of image quality is broadly observed.

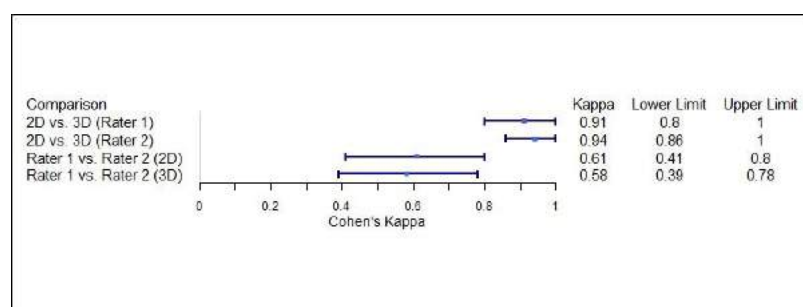
**Figure/Table 1**



**Caption 1**

Figure 1. EKG obtained immediately before MRI scan in patient 5 demonstrating frequent atrial premature contractions (a). 2D LGE images (b, c), and 3D LGE images (d, e) Note the enhancement in the basal inferolateral wall is not represented on the 2D long axis image (\*), and the increased partial volume effect in the basal anteroseptum (dashed arrow).

**Figure/Table 2**



**Caption 2**

Figure 2: Cohen's Kappa statistic of 2D vs. 3D LGE showed near-perfect agreement on a per segment basis with moderate to substantial agreement between rater 1 and rater 2.

### **Bibliographic References**

1) Piehler KM, Wong TC, Punttil KS, et al. Free-breathing, motion-corrected late gadolinium enhancement is robust and extends risk stratification to vulnerable patients. *Circ Cardiovasc Imaging*. 2013;6(3):423-432., 2) Munoz, C., Bustin, A., Neji, R. et al. Motion-corrected 3D whole-heart water-fat high-resolution late gadolinium enhancement cardiovascular magnetic resonance imaging. *J Cardiovasc Magn Reson* 22, 53 (2020)., 3) Cruz, G., Atkinson, D., Henningsson, M. et al. Highly Efficient Nonrigid Motion-Corrected 3D Whole-Heart Coronary Vessel Wall Imaging. *Magn Res Med* 77, 1894-1908 (2017).

Speaker: J. Craft

Category: 3D, Respiratory Self-gating, Late Gadolinium Enhancement

000068

## **Comprehensive flow imaging in neonates using 4D flow magnetic resonance imaging without contrast or general anesthesia**

P. Sjöberg \* (1); E. Hedstrom (2); K. Fricke (3); P. Frieberg (1); C. Weismann (3); P. Liuba, (3); M. Carlsson (4); J. Töger (1)

(1) Clinical physiology, department of clinical sciences lund, Lund University, Skåne University Hospital, Lund, Sweden; (2) Clinical Physiology, Department of Clinical Sciences Lund, Lund University, Skåne University Hospital, Lund, Sweden, Lund, Sweden; (3) Pediatric cardiology, department of clinical sciences lund, lund university, Skåne University Hospital, Lund, Sweden, Lund, Sweden; (4) Laboratory of clinical physiology, nhlbi, National Institutes of Health, Bethesda, United States of America

### **Abstract**

#### **Background**

Neonates with congenital heart disease often require interventions early in life, and accurate blood flow quantification may give important clinical and prognostic information. Three-dimensional time-resolved cardiovascular magnetic resonance (CMR) flow imaging (4D flow) has the potential to provide accurate flow with simplified image planning and reduced scan time, also reducing the need for general anesthesia. It is however unclear how 4D flow compares with reference standard 2D flow in neonates. Therefore, the aims were to 1) assess accuracy and precision of 4D versus 2D flow in neonates; and 2) compare time needed for 4D flow sequence acquisitions compared to the current standard using multiple 2D flows.

#### **Methods**

Neonates (n=17, median age 18 days (range 6-25), BSA  $0.21 \pm 0.02$  m<sup>2</sup>) were included median 5 (range 4–18) days after surgery for aortic coarctation. Cardiovascular MR was performed at 1.5T (MAGNETOM Aera, Siemens Healthcare, Erlangen, Germany) using “feed-and-sleep” supported by chloral hydrate if needed. CMR protocol included a 4D flow prototype sequence covering the whole aorta and 2D flow acquired in the ascending aorta, descending aorta, brachiocephalic trunk, left common carotid artery, and left subclavian artery. Scan planes for 2D flow were placed on a high-resolution 3D T1-weighted black-blood sequence (Figure 1). Images were analyzed in Segment v3.2 R8408 for 2D flow (Medviso AB, Lund, Sweden) and CAAS MR Solutions 5.1.1 for 4D flow (Pie Medical Imaging, Maastricht, the Netherlands). Net flow in vessels from 4D flow were compared to 2D flow as reference. Internal consistency was computed as the difference between ascending aorta flow volume and the sum of flow volumes in neck vessels and descending aorta.

#### **Results**

Acquisition time for 2D flow strategy (T1-weighted black-blood 3D and multiple 2D flow scans) was median 17 minutes (range 11-26), and for 4D flow median 5 minutes (range 4-9),  $p < 0.001$ . Time for planning and sequence preparation was not included. Measurements were acquired with 4D flow from all vessels in all patients, example in Figure 2. 2D flow could not be measured in the brachiocephalic artery in one patient, in the left carotid artery in two

patients and the left subclavian artery in three patients. The 4D flow data correlated with 2D flow, however with a systematic error (Figure 3). Bland Altman analysis shows a bias of  $-0.06 \pm 0.08$  l/min (Figure 3). Internal consistency was  $-0.08 \pm 0.12$  l/min or  $-14 \pm 18$  % for 2D flow and  $-0.03 \pm 0.08$  l/min or  $-5 \pm 13$  % for 4D flow.

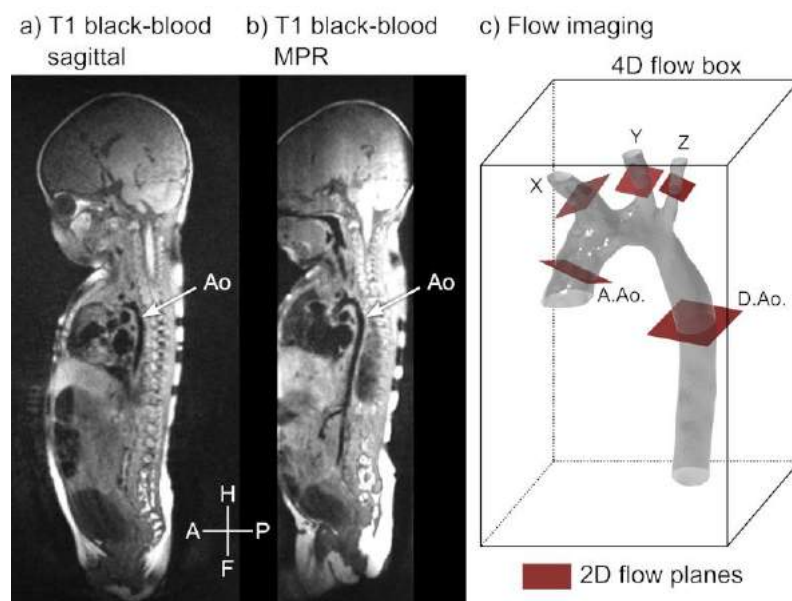
## Conclusion

Four-dimensional flow underestimates flow volumes compared to 2D flow but is time-efficient and can be acquired in neonates without general anesthesia. High internal consistency suggests that 4D flow may be superior to 2D flow in evaluating shunts and collateral flow.

## Acknowledgments

We thank Ning Jin at Siemens Medical Solutions USA Inc., Cleveland, Ohio, USA for providing the prototype 4D flow sequence. We also thank Pie Medical for providing an evaluation version of the software CAAS 4D flow.

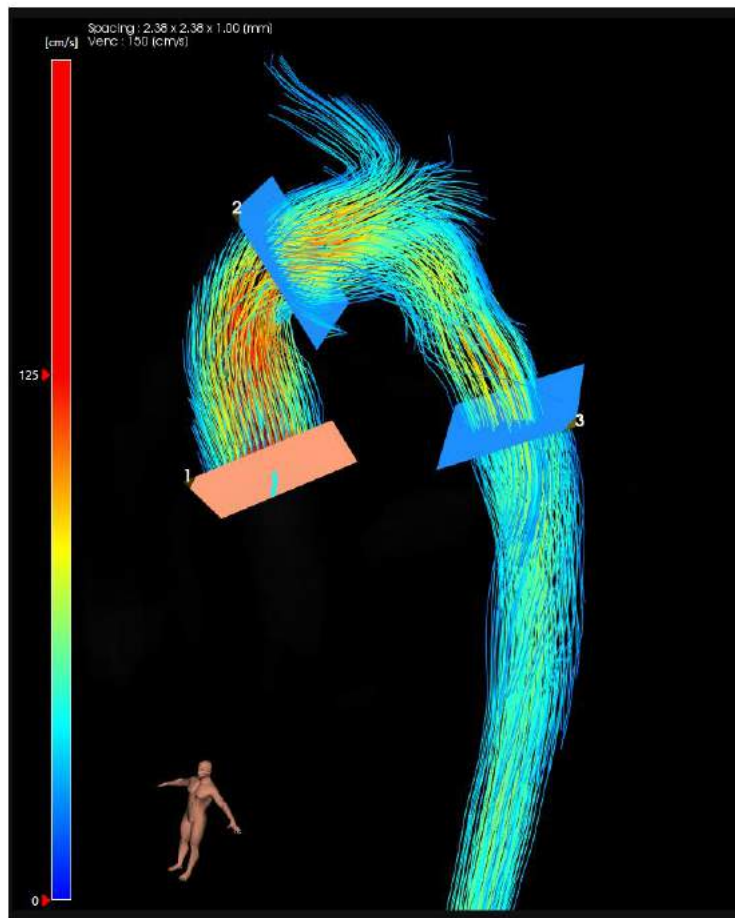
## Figure/Table 1



## Caption 1

Figure 1: Scan planning. a) A 3D T1-weighted black-blood image where aorta is partially visible. b) The same image stack using multi-planar reformatting (MPR) where aorta is more clearly visible. c) Schematic image with a 3D model of aorta in grey, a 4D flow box covering the whole aorta and red square planes showing locations of 2D flow planes.

## Figure/Table 2

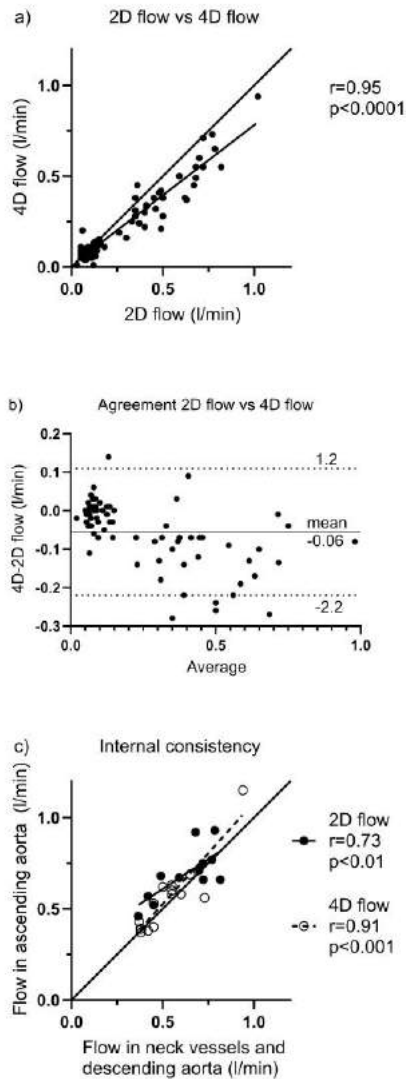


## Caption 2

Figure 2: Streamlines acquired with 4D flow without general anesthesia showing the aortic flow in a neonate early after surgery for aortic coarctation.

## Figure 3





### Caption 3

Figure 3: a) Scatter plot showing correlation between methods and systematic error with underestimation of flow volumes by 4D flow compared to 2D flow. b) Bland-Altman plot showing that 4D flow underestimates flow volumes compared to 2D flow. d) Scatter plot showing internal consistency with higher degree of correlation for 4D flow than for 2D flow.

Speaker: P. Sjöberg

Category: 4D Flow, Coarctation, Congenital Heart Disease

000069

## Classic presentation for a rare cardiomyopathy

A. Khan \* (1); B. M. Cabuay, (2); J. Cavalcante (3); S. Mackey-Bojack, (4)

(1) Cardiology, United Heart & Vascular Clinic - St. Paul, Saint Paul, United States of America; (2) Cardiology, Minneapolis Heart Institute Foundation, Minneapolis, United States of America; (3) Cardiology, Minneapolis Heart Institute® — Abbott Northwestern Hospital (Minneapolis), Minneapolis, United States of America; (4) Pathology, United Hospital, Saint Paul, United States of America

### Abstract

Description of clinical presentation.

76 year old female with a history of rheumatoid arthritis was admitted with shortness of breath and chest heaviness. Clinical presentation was consistent with heart failure. Symptoms improved with diuresis. She had been hospitalized with similar symptoms a month prior and at that time been initiated on guideline recommended medical therapy.

Diagnostic techniques and their most important findings.

Echocardiogram revealed a mildly reduced left ventricular ejection fraction, LVEF 45% with apical hypokinesis. Given wall motion abnormality and elevated troponins in the setting of chest heaviness, she underwent coronary angiography, which revealed normal coronary arteries. Cardiac MRI showed normal LV size, mild concentric increase in wall thickness and mildly decreased LV systolic function with apical hypokinesis. The LVEF was 45%. Global, circumferential mid myocardial delayed enhancement was noted. MRI raised suspicion for an infiltrative process (figure 1 and 2). A technetium PYP scan was negative for TTR amyloid. Primary AL was excluded with negative free LC, serum and urine immunofixation. She subsequently underwent an endomyocardial biopsy. This demonstrated myocyte cytoplasmic vacuolization and absence of inflammatory cells, consistent with hydroxychloroquine (HCQ) toxicity (figure 3).

Learning points from this case.

Hydroxychloroquine has been used for the treatment of malaria and as a disease modifying antirheumatic drug (DMARD) for rheumatoid arthritis, systemic lupus erythematosus and Sjogrens disease. Recently it has also been used for treatment of patients with COVID-19.

HCQ is typically well tolerated. Side effects are mostly non cardiac in nature. Cardiac toxicity includes ventricular arrhythmias and cardiomyopathies. Acute HCQ cardiotoxicity is related to its class I antiarrhythmic effect. HCQ causes QRS and QT prolongation, increasing the risk of ventricular arrhythmias including Torsade de pointes. Chronic usage of HCQ increases risk of conduction disease and cardiomyopathies related to intracellular deposition of metabolites, disruption of autophagy, myofiber necrosis and mitochondrial damage.

Risk factors for HCQ induced cardiomyopathy include female gender, age greater than 60, renal dysfunction, prolonged use, higher doses and concomitant NSAID usage. Once the

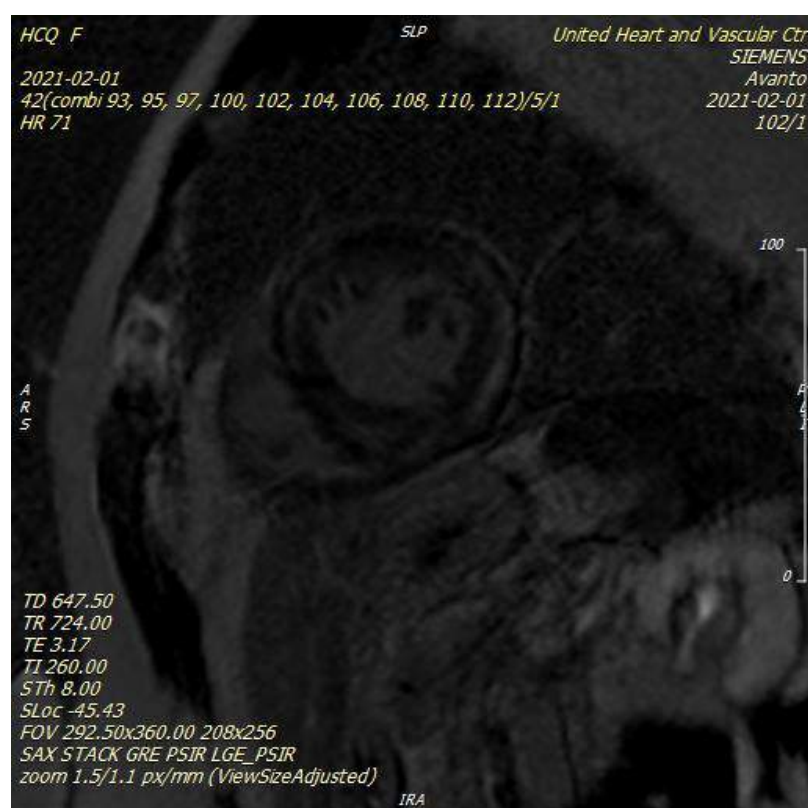
diagnosis of HCQ induced cardiomyopathy is established, HCQ should be immediately discontinued. Partial or complete normalization of LV function is possible.

On imaging, biventricular dilation, left ventricular hypertrophy, LV dysfunction, apical wall motion abnormalities and restrictive filling pattern have been reported. Cardiac MRI data on HCQ toxicity is limited. Several case reports have noted extensive mid myocardial delayed enhancement. One recent case report however showed no delayed enhancement in a biopsy proven case of HCQ cardiomyopathy.

Our patient has now been of HCQ for 3 months. Rheumatoid arthritis has been stable with initiation of Remicade. From a heart failure stand point she has been doing well without need for readmission. Follow up imaging to assess LVEF is planned.

This case highlights awareness for more rare cardiomyopathies and the role of cardiac MRI and endomyocardial biopsies in making the diagnosis.

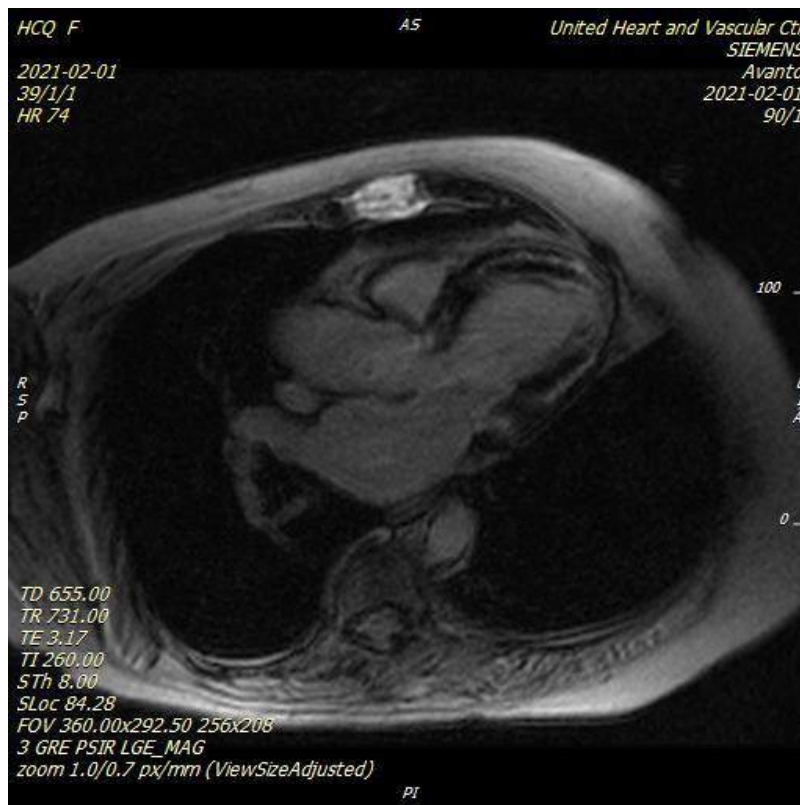
**Figure/Table 1**



**Caption 1**

Mid short axis delayed enhancement image. Global mid myocardial delayed enhancement.

**Figure/Table 2**

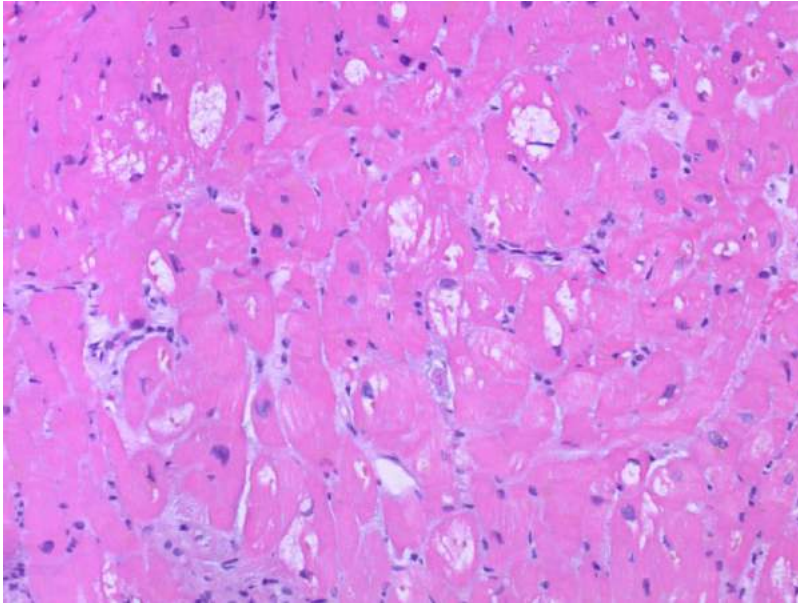


**Caption 2**

3 chamber delayed enhancement image. Prominent mid myocardial delayed enhancement.

**Figure 3**

1.



### **Caption 3**

Hematoxylin and eosin stained section showing vacuolated cardiomyocytes (original magnification 200x)

Speaker: A. Khan

Category: Cardiomyopathy, Cardiotoxicity, Nonischemic Cardiomyopathy

000071

## **CMR guides management in a repaired complex conotruncal defect - the hidden intramural VSD revealed**

P. Sinha \* (1); E. Tham (1); J. Pagano (1); S. Urschel (1)

(1) Pediatric cardiology, Stollery Children's Hospital, Edmonton, Canada

### **Abstract**

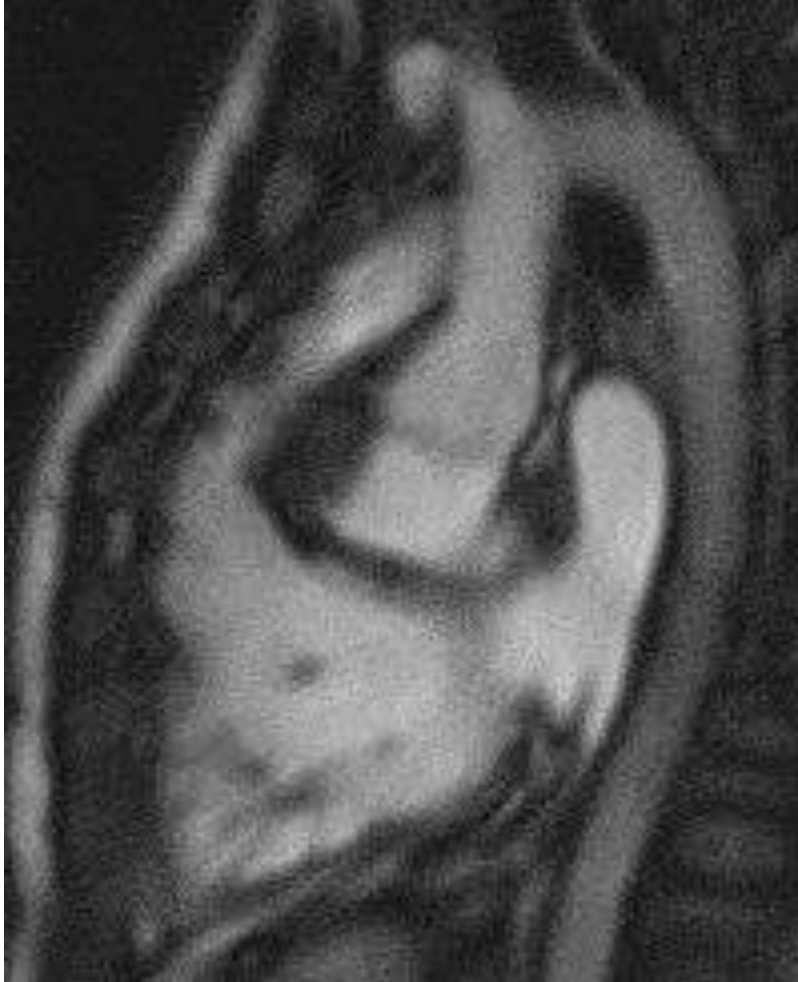
**Description of Clinical Presentation:** An 8-year-old girl underwent a follow-up Cardiac MRI (CMR). She had a history of Transposition of the great arteries with a single right coronary artery, a posteriorly malaligned VSD, and subpulmonary stenosis repaired with a Rastelli procedure and VSD enlargement and a 12 mm Contegra RV to PA conduit. Subsequent procedures included replacement of the RV to PA conduit with a 16 mm Contegra conduit and relief of LVOT obstruction, later followed by Melody valve implantation. She had noticed progressively limited exercise capacity. Examination revealed normal vitals and no respiratory distress. There was a harsh III/VI ejection systolic murmur and a soft early diastolic murmur at the upper right sternal border and no hepatomegaly.

**Diagnostic Techniques and Their Most Important Findings:** ECG showed sinus rhythm with complete RBBB. The exercise stress test showed reduced exercise capacity, but no evidence of ischemia or arrhythmia. Echocardiogram was difficult, with limited sonographic windows, showing a dilated and hypertrophied RV with normal function, an unobstructed LVOT, and normal LV size and function. There was no obvious residual VSD and the conduit and branch pulmonary arteries could not be adequately visualized. CMR showed a narrowed RV-PA conduit (Figure 1) with moderate stenosis and mild regurgitation (RF 13%), unobstructed branch pulmonary arteries, and LV-to-Aorta pathway. The interventricular septum was flattened throughout the cardiac cycle. There was mild right ventricular hypertrophy with RVEF of 45% and LVEF 47%. The known single right coronary was demonstrated with a lengthy LMCA course immediately underneath the mid-to-distal portion of the conduit and anterior to the aortic root (Figure 2A). Cine images (Figure 3) and 3D MRA (Figures 2B-D) showed a residual intramural VSD, with the mouth measuring about 1cm, however, flow quantification revealed no significant shunt with a Qp:Qs of 1.08:1. The VSD seemed largely contained by RV trabeculations and muscle bundles. Given her progressive decline in exercise capacity and that she will soon reach the limit of her 16mm conduit, future intervention would include catheter versus surgical options. With the relief of the RVOT obstruction, the shunting from the residual intramural VSD may become more apparent, therefore coupled with the risk of coronary compression with stent placement, surgical conduit replacement with concomitant intramural VSD closure will be the preferred modality.

**Learning Points from this Case:** Intramural VSDs have been described in 11% of children after repair of conotruncal malformations. They occur when the VSD patch is anchored to RV trabeculations instead of the ventriculofundibular fold, resulting in shunting of blood around the VSD patch into trabeculations within the RV causing a left to right shunt. Because of their anterior location, they are difficult to locate on standard echo and transesophageal echo is required for detection. In this case, we see that widespread RV trabeculations restricted the amount of shunt from this defect that was missed on echocardiograms. Future interventions to relieve conduit stenosis may result in a more significant shunt if the intramural VSD is not concomitantly repaired, accordingly, the shunt will need to be quantified and the VSD gradient visualized intraoperatively. We outline the value that CMR

played in detecting the size and location of an intramural VSD as well as identifying the abnormal coronary artery course. CMR should be utilized for complex TGA repairs when interventional versus surgical management decisions are contemplated.

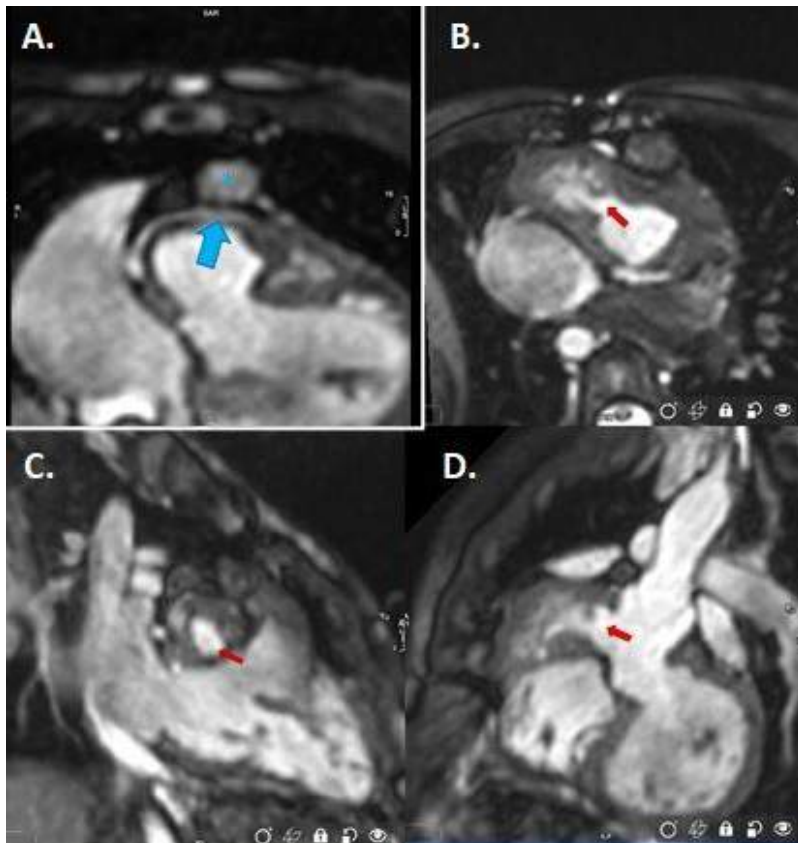
**Figure/Table 1**



**Caption 1**

RVOT view showing a narrowed RV-PA conduit

**Figure/Table 2**



## Caption 2

3D MRA reconstruction showing A: The course of the left main coronary artery (blue arrow) behind the RV-PA conduit (\*) and B-D: 3D multiplanar reformatting profiling the intramural VSD (red arrow) in corresponding planes which appears to be contained by RV muscle bundles and trabeculations as seen in D.

## Figure 3





### Caption 3

Short-axis oblique cine at the base of the heart showing the mouth of the intramural VSD (red arrow) into RV trabeculations

### Bibliographic References

5. Saedi S, Parsaee M. Intramural ventricular septal defect. *International Journal of Cardiovascular Practice*. 2017 Jul 29;2(3):70-2., 4. Patel ND, Kim RW, Pornrattanarungsi S, Wong PC. Morphology of intramural ventricular septal defects: Clinical imaging and autopsy correlation. *Annals of pediatric cardiology*. 2018 Sep;11(3):308., 3. Buratto E, Naimo PS, Konstantinov IE. Intramural ventricular septal defect after repair of conotruncal anomalies: Is there light at the end of the tunnel?. *The Journal of thoracic and cardiovascular surgery*. 2016 Sep 1;152(3):696-7., 2. Patel JK, Glatz AC, Ghosh RM, Jones SM, Natarajan S, Ravishankar C, Mascio CE, Spray TL, Cohen MS. Intramural ventricular septal defect is a distinct clinical entity associated with postoperative morbidity in children after repair of conotruncal anomalies. *Circulation*. 2015 Oct 13;132(15):1387-94., 1. Preminger TJ, Sanders SP, Van Der Velde ME, Castaneda AR, Lock JE. "Intramural" residual interventricular defects after repair of conotruncal malformations. *Circulation*. 1994 Jan;89(1):236-42.

Speaker: P. Sinha

Category: Surgical Planning, Congenital Heart Disease, Image Analysis

000073

### 3D Motion Compensation with Cone Trajectories - in silico Validation Using the MR-XCAT Framework

J. Patel \* (1); C. Sheagren (1); F. Jouybari (2); S. Hassan (1); O. Addy (3); C. Macgowan (2); G. Wright, (1)

(1) Medical biophysics, Sunnybrook Health Sciences Centre, Toronto, Canada; (2) Medical biophysics, The Hospital for Sick Children, Toronto, Canada; (3) Research, HeartVista, Inc., Los Altos, United States of America

#### Abstract

##### Background

Real-time image-navigated cardiac motion estimation is a promising technique for improving catheter alignment during MR-guided catheter interventions in the heart. During interventions, the heart is displaced due to cardiac and respiratory motion, complicating direct tracking methods. As such, fast and accurate image-navigated motion correction is needed to correct for the heart motion present. Image registration encodes 3D motion displacement between images and can be performed to align myocardial surfaces across heartbeat-by-heartbeat image-navigators (iNAVs). Cone trajectories are used to rapidly encode motion and sample the k-space centre, enabling robust volumetric reconstructions in a diastole sampling window [1]. Motion accuracy can be compromised due to high acceleration factors that can lead to poor image quality and aliasing artifacts; motion estimation consistency also can decrease due to variances in the k-space sampling patterns. In this study, we propose an in silico framework to examine the accuracy and consistency of the heartbeat-by-heartbeat respiratory motion estimation with 3DiNAVs for different undersampling patterns.

##### Methods

An in-silico Cardiac-Torso (XCAT) anatomical phantom was used to provide 3D ground-truth respiratory motion [2]. MR acquisition was simulated by encoding the numerical phantom with the non-Cartesian cone sampling pattern and reconstructing data with parallel imaging and compressed sensing [3]. The following acquisition parameters were used: FOV = 28 x 28 x 14cm; TE/TR = 0.5/6ms; acquisition window = 200ms; isotropic spatial resolution ranges from 4.4 to 7 mm; and five respiratory phases were used, with the end-expiratory phase as a reference landmark. To analyze motion consistency across different k-space sampling schemes, we sampled each respiratory phase at multiple resolutions using four sampling patterns: 1. (MD Random) multiple distinct sets of maximum distance (MD) trajectories; 2. (MD Repeating) one distinct set of MD trajectories repeated across cardiac cycles; 3. (GA Random) multiple distinct sets of golden angle (GA) trajectories; and 4. (GA Repeating) one distinct set of GA trajectories repeated across cardiac cycles, see Fig: 1 [4]. Non-rigid image registration was performed with SimpleITK, and myocardial alignment was evaluated across resolution, respiratory phase, and sampling pattern using mean surface distance (SD) and maximum Hausdorff distance (HD). For details on the simulation pipeline, see Fig. 2.

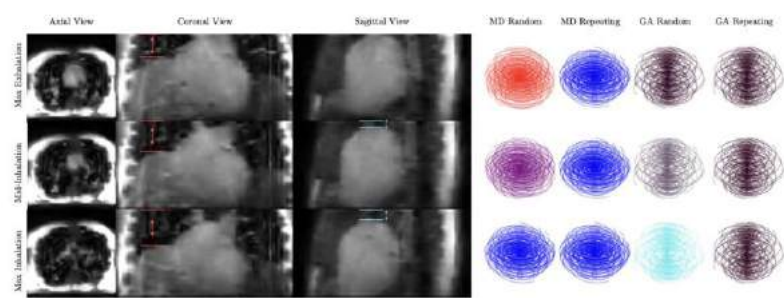
##### Results

The mean SD and maximum HD between myocardial surfaces from MD Random, MD Repeating, GA Random and GA Repeating was compared across spatial resolutions/acceleration factors and respiratory phases. For highly accelerated images, the minimal overall error was observed at a spatial resolution of 5.5mm (R=7.0) (Fig. 3). The goal is to maximize motion accuracy while minimizing the acceleration factor needed to reduce computation time. However, in our simulation results, the mean SD and max HD suffers at higher resolution ( $r<5.1\text{mm}$ ) due to residual undersampling artifacts, and at lower resolution ( $r>5.5\text{mm}$ ), SD increases due to the lower spatial resolution and poor spatial image quality. Note that the MD Random, GA Random and GA Repeating sampling perform similar to each other over the spatial resolutions, and the optimal spatial resolution was found to be 5.5mm, higher than other groups observed likely due to differences in contrast [5].

### Conclusions

Effects of spatial resolution and sampling pattern on motion estimation and motion accuracy were analyzed. The optimum for consistent, accurate heart motion estimation was found to be 5.5mm isotropic resolution, for GA Repeating, GA Random and MD Random.

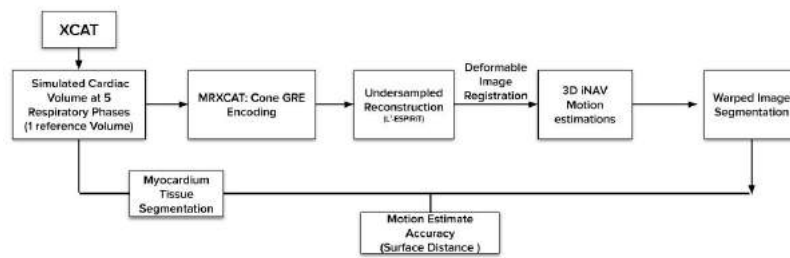
**Figure/Table 1**



**Caption 1**

Examples of 3D navigator images calculated with MRXCAT pipeline in different respiratory states along with the trajectories of the sampling patterns.

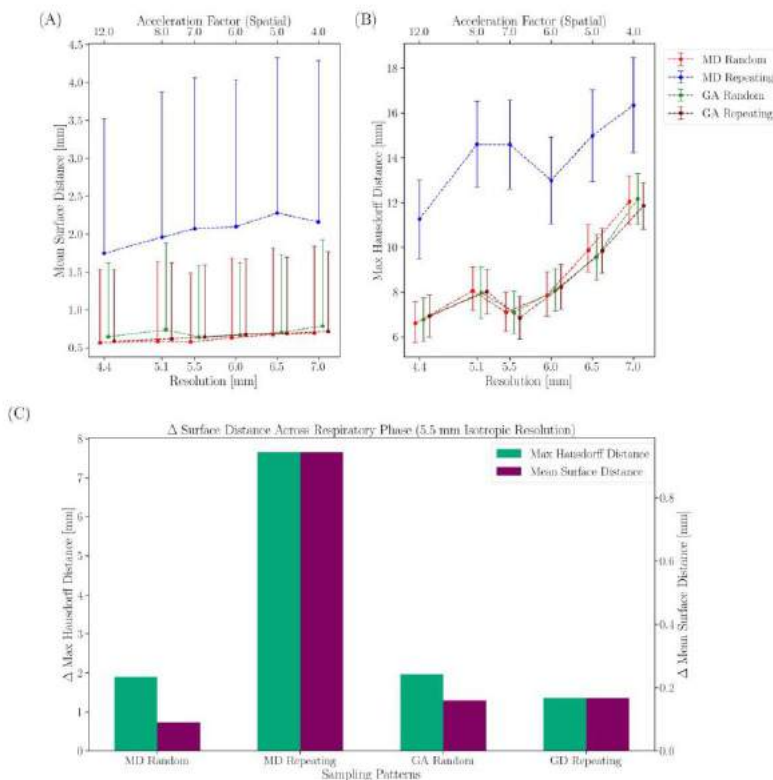
**Figure/Table 2**



**Caption 2**

Visual overview of simulation and registration framework. Simulated volumes are generated with XCAT, and non-Cartesian MR encoding with undersampled reconstruction is used to obtain iNAV images. iNAV volumes are registered, and warped image segmentations are compared to reference tissue segmentations to evaluate motion accuracy.

**Figure 3**



**Caption 3**

A. Mean SD at various spatial resolutions; error bars correspond to standard deviation. B. Max HD at various spatial resolutions and acceleration factors. C. Magnitude difference in mean SD and max HD over four respiratory phases at 5.5mm spatial resolution.

## **Bibliographic References**

[5] Srivathsan P. Koundinyan et al. "Unraveling the Effect of Spatial Resolution and Scan Acceleration on 3D Image-Based Navigators for Respiratory Motion Tracking in Coronary MR Angiography". In: arXiv e-prints, arXiv:1910.12185 (Oct. 2019), arXiv:1910.12185. arXiv:1910.12185 [physics.med-ph]., [4] Nii Okai Addy et al. "High-resolution variable-density 3D cones coronary MRA". In: Magnetic Resonance in Medicine 74.3 (2015), pp. 614–621. doi:<https://doi.org/10.1002/mrm.25803>., [3] Martin Uecker et al. "ESPIRiT - an eigenvalue approach to autocalibrating parallel MRI: Where SENSE meets GRAPPA". In: Magnetic Resonance in Medicine 71.3 (2014), pp. 990–1001. doi:<https://doi.org/10.1002/mrm.24751>., [2] Lukas Wissmann et al. "MRXCAT: Realistic numerical phantoms for cardiovascular magnetic resonance". In: Journal of cardiovascular magnetic resonance: official journal of the Society for Cardiovascular Magnetic Resonance 16 (Aug. 2014), p. 63. doi:[10.1186/PREACCEPT-1164254289127237](https://doi.org/10.1186/PREACCEPT-1164254289127237)., [1] Paul T. Gurney, Brian A. Hargreaves, and Dwight G. Nishimura. "Design and analysis of a practical 3D cones trajectory". In: Magnetic Resonance in Medicine 55.3 (2006), pp. 575–582. doi:<https://doi.org/10.1002/mrm.20796>.

Speaker: J. Patel

Category: Accelerated Imaging, Interventional CMR, Motion Correction

000074

## Rapid Variable Flip-angle T2 Quantification (RavFa-T2) of the Myocardium Using Balanced Steady-state Free Precession

C. Marquet \* (1); A. J. Powell (2); B. Fonseca (3); L. Browne (4); J. Jang (5); M. H. Moghari (6)

(1) Informatics, Technical University Munich, Munich, Germany; (2) Department of cardiology, Boston Children's Hospital, Boston, United States of America; (3) Department of pediatrics, Children's Hospital Colorado, University of Colorado Anschutz Medical Campus, Aurora, United States of America; (4) Department of radiology, Children's Hospital Colorado, Aurora, United States of America; (5) Mr r&d clinical science na, Philips Healthcare, Boston, United States of America; (6) Department of radiology, University of Colorado and Children's Hospital Colorado, Aurora, United States of America

### Abstract

**Background:** Transverse magnetization decay, characterized by the tissue-specific transverse relaxation time (T2), has long been used for tissue characterization in cardiovascular magnetic resonance (CMR). Parametric T2-mapping with CMR imaging can be used to noninvasively quantify changes in myocardial tissue composition [1]. Traditional techniques require relatively long breath holds and long overall scan time which can limit clinical applicability. To avoid such restrictions, we developed and validated a novel method (RavFa-T2) that applies a balanced steady-state free precession (bSSFP) sequence [2] with a variable flip-angle scheme to quantify the myocardial transverse relaxation time with a scan time of less than 4 seconds.

**Methods:** RavFa-T2 acquires four single-shot bSSFP images in 4 consecutive heartbeats at the same cardiac phase during a single breath-hold (Figure 1). Thus, the acquisition time is heartrate dependent and  $\leq 4s$  assuming a heartrate of  $\geq 60bpm$ . The images are acquired with increasing flip angles ( $30^\circ$ ,  $67^\circ$ ,  $103^\circ$ ,  $140^\circ$ ) after ten linear startup pulses. To quantify myocardial T2, the signal intensity of the 4 images is fitted pixelwise with a nonlinear least-squares algorithm to a function dependent on the transient phase of bSSFP [3]. The feasibility of RavFa-T2 approach was investigated in a phantom and a 2-center *in-vivo* study. The phantom study was performed to compare RavFa-T2 to the gold-standard spin-echo (SE) (TR/TE: 10000/32\*10ms, FA:  $90^\circ$ , acquisition time: 82 min.), and T2-Prep [4] (TR/TE: 2.65/1.33ms, FA:  $35^\circ$ , rest period: 2 heartbeats, T2-Prep delay: 0, 25, 50, and 75ms, acquisition time:  $\leq 12s$ ). The experiments were performed on the myocardial vials of the T1MES phantom [5], and RavFa-T2 and T2-Prep acquisitions were repeated at 4 different heartrates (60, 80, 100, 120 bpm). The 2-center *in-vivo* study was performed with the same sequence parameters as for the phantom study at institution 1 (22 patients, 14 female, median age 28.5 (11-60) years old) and institution 2 (14 patients, 6 female, median age 18.5 (6-31) years old). The scans were performed on Philips Achieva and Ingenia 1.5T scanners. The quantification algorithms were implemented in MATLAB (MathWorks Inc., Natick, MA, USA). The method evaluation was based on accuracy (mean error compared to SE) and precision (pixelwise standard deviation within a region-of-interest). A two-tailed paired Student's t-test was used for statistical analysis and a p-value  $\leq 0.05$  was considered statistically significant.

**Results:** Using SE as the gold standard, in the phantom study, the accuracy of RavFa-T2 was better than T2-Prep and in the *in-vivo* study, the precision of RavFa-T2 was better than T2-Prep (Table 1, all p-values <0.001). The acquisition time of RavFa-T2 was consistently shorter than T2-Prep (Table 1, p-value <0.001). Compared to T2-Prep, RavFA-T2 qualitatively demonstrated a better signal-to-noise ratio and allowed easier visual detection of the myocardium (Figure 2).

**Conclusion:** In our 2-center *in-vivo* study we have shown that RavFa-T2 provides higher precision myocardial T2 values as compared to T2-Prep with a shorter acquisition time. This should improve the clinical applicability of T2 mapping especially in children and patients who have difficulty with breath holds.

**Figure/Table 1**

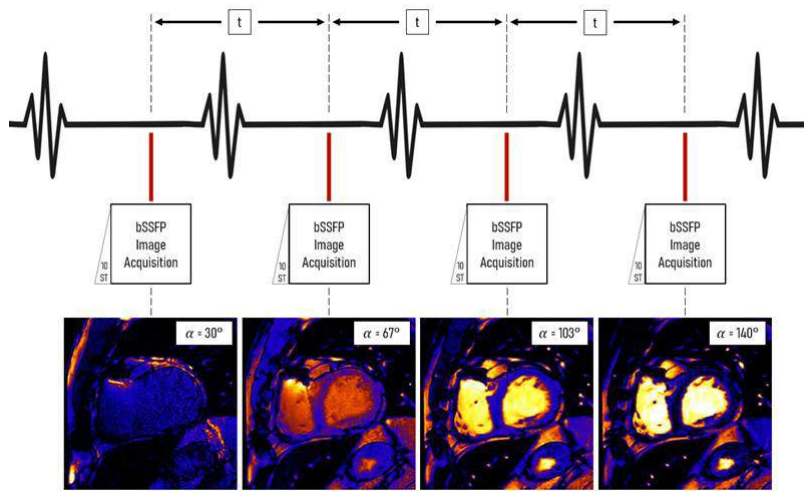
	Myocardial T <sub>2</sub> (ms)	P-value	Scan Time (s)
Phantom Study			
SE (golden standard)	50.33 ± 0.38		4920
RavFA-T <sub>2</sub>	46.13 ± 3.78	<0.001 (compared to SE)	≤4
T <sub>2</sub> -Prep	59.83 ± 1.45	<0.001 (compared to SE)	≤12
In-vivo Study at Institution 1 (n=22)			
RavFA-T <sub>2</sub>	40.75 ± 2.88	<0.001	3.27
T <sub>2</sub> -Prep	52.94 ± 3.18		9.82
In-vivo Study at Institution 2 (n=14)			
RavFA-T <sub>2</sub>	44.81 ± 3.29	<0.001	3.71
T <sub>2</sub> -Prep	54.28 ± 3.83		11.14

**Caption 1**

Comparing T2 quantification of RavFA-T2 with SE and T2-Prep in phantom study. Comparing RavFA-T2 with T2-Prep in 2-center *in-vivo* study. T2 values are mean ± standard deviation. Phantom Study: Accuracy of RavFa-T2 compared to SE was higher than T2-Prep with lower precision. *In-vivo* study: Precision of RavFa-T2 was higher than T2-Prep.

**Figure/Table 2**

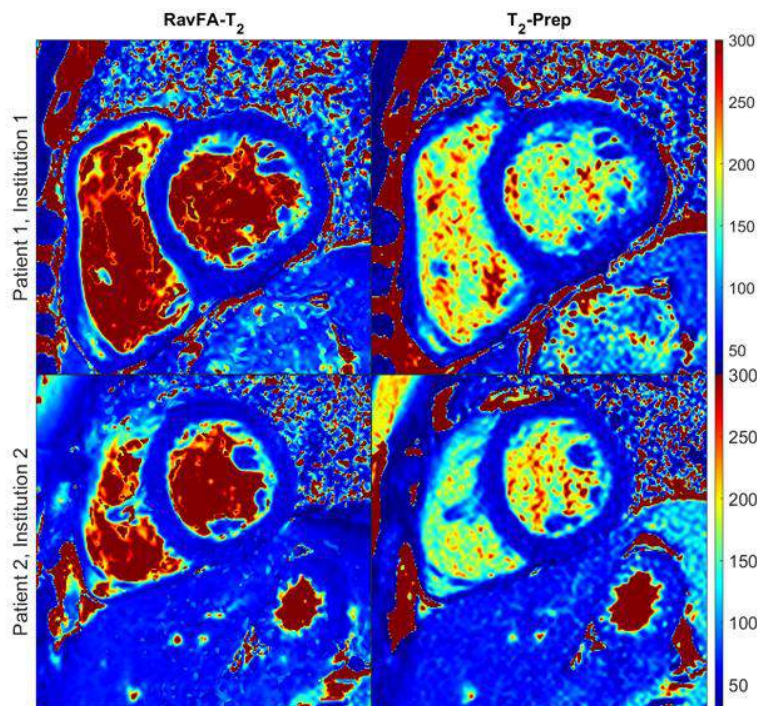




**Caption 2**

RavFA-T2 acquisition scheme. Four images are acquired at the same cardiac phase within 4 consecutive heartbeats ( $t$  time between heartbeats) during breath-hold in  $\leq 4$ s. Each image is acquired with a different flip angle ( $30^\circ$ ,  $67^\circ$ ,  $103^\circ$ ,  $140^\circ$ ) using bSSFP sequence after ten linear startup pulses (ST).

**Figure 3**



### Caption 3

T2-maps of RavFA-T2 and T2-Prep from one patient at institution one (54-year-old male with mild right ventricular dilation and pulmonary stenosis), and from one patient at institution two (13-year-old female with family history of arrhythmogenic right ventricular dysplasia).

### Bibliographic References

[5] Captur G, Gatehouse P, Keenan KE, et al. A medical device-grade T1 and ECV phantom for global T1 mapping quality assurance—the T1 Mapping and ECV Standardization in cardiovascular magnetic resonance (T1MES) program. *J Cardiovasc Magn Reson*. 2016;18(1):58. doi:10.1186/s12968-016-0280-z, [4] Huang T-Y, Liu Y-J, Stemmer A, Poncelet BP. T2 measurement of the human myocardium using a T2-prepared transient-state trueFISP sequence. *Magn Reson Med*. 2007;57(5):960-966. doi:<https://doi.org/10.1002/mrm.21208>, [3] Scheffler K. On the transient phase of balanced SSFP sequences. *Magn Reson Med*. 2003;49(4):781-783. doi:10.1002/mrm.10421, [2] Oppelt A, Graumann R, Barfuss H, Fischer H, Hartl W, Schajor W. FISP, a novel, fast pulse sequence for nuclear magnetic resonance imaging. *Electromedica*. 1986;54(1):15-18., [1] Kim PK, Hong YJ, Im DJ, et al. Myocardial T1 and T2 Mapping: Techniques and Clinical Applications. *Korean J Radiol*. 2017;18(1):113-131. doi:10.3348/kjr.2017.18.1.113

Speaker: C. Marquet

Category: Rapid Imaging, Tissue Characterization, Myocardium

000075

## **Improved Myocardial Scar Visualization with Two-minute Free-breathing Joint Bright- and Black-blood Late Gadolinium Enhancement Imaging**

A. Bustin \* (1); S. Sridi (2); A. Maillot (1); X. Pineau (2); M. Nuñez-Garcia (1); M. Sermesant (1); D. El Hamrani (1); J. Magat (1); J. Naulin (1); S. Clément-Guinaudeau (2); G. Dournes (2); M. Montaudon (2); F. Laurent (2); P. Jaïs (1); M. Stuber (3); H. Cochet (1)

(1) Ihu liry, electrophysiology and heart modeling institute, Université de Bordeaux – INSERM U1045, Bordeaux; (2) Department of cardiovascular imaging, Hôpital Cardiologique du Haut-Lévêque, CHU de Bordeaux, Bordeaux; (3) Department of diagnostic and interventional radiology, Lausanne University Hospital and University of Lausanne, Lausanne, Switzerland

### **Abstract**

#### **Background:**

Black-blood late gadolinium enhancement (LGE) techniques are increasingly being used to uncover myocardial scar patterns that may be otherwise confused with blood signal on conventional bright-blood LGE, especially when involving the subendocardium (1). With signal-attenuated blood and dark muscle representation, these techniques may however be hampered by a lack of anatomical information, making spatial localization of myocardial injuries a challenging task. Here we propose to combine both bright- and black-blood imaging in a single time-efficient free-breathing exam to obtain LGE images with unprecedented scar contrast and localization.

#### **Methods:**

**Acquisition:** This Scar-specific imaging with Preserved myOcardial visualizaTion (SPOT) is a single-shot ECG-triggered 2D bSSFP sequence that acquires bright- and black-blood LGE images in an interleaved fashion (Fig.1). In odd heartbeats, a 180° inversion pulse is followed by a T1p module (2) to generate black-blood contrast (for better scar visualization) whereas in even heartbeats only a T1p module is played out to generate bright-blood contrast (for better scar localization). Imaging parameters were: 10-20 slices, 4 signal averages, 1.4x1.4mm<sup>2</sup> in-plane resolution, 8mm slice thickness, spin-lock frequency/duration=500Hz/27ms, FA=60°, GRAPPA x2, ~160ms acquisition window, TE/TR=1.2/2.8ms, bandwidth=870Hz/pixel, inversion time determined from a prior scout acquisition. **Reconstruction:** A non-rigid in-line motion correction algorithm was implemented on the scanner to register the 8 single-shot images to the same respiratory position, followed by image averaging. Three series of images were displayed on the scanner console: a bright-blood image, a black-blood counterpart, and a coloured fusion of both. **Experiments:** 54 patients (44 males, age 18-82yo) with known ischemic heart disease underwent CMR at 1.5T (Siemens Aera) with the reference breath-held 2D PSIR (3) and the proposed free-breathing SPOT 15min after injection of 0.2mmol/kg gadoteric acid (in random order). An experienced radiologist graded the overall image quality (1:poor, 4:excellent) and categorized LGE findings for each dataset as absent or definite with confidence or inconclusive.

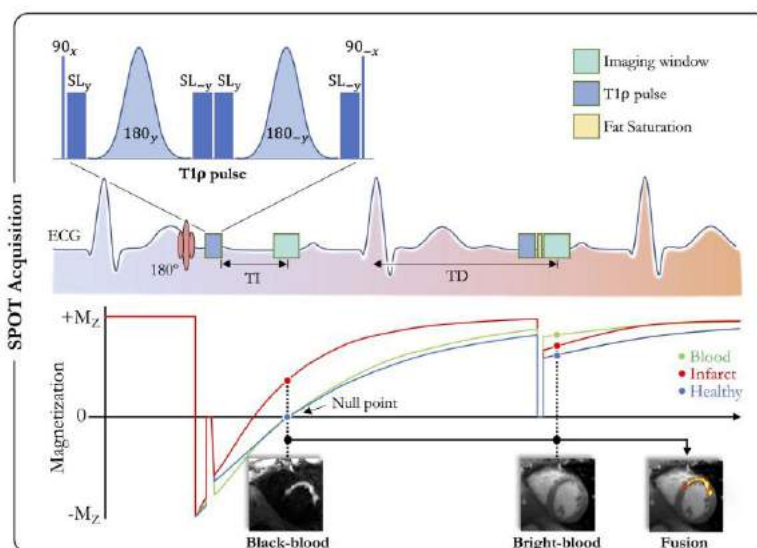
#### **Results:**

SPOT images were acquired with full ventricular coverage during free-breathing in  $1\text{min}56\text{s}\pm30\text{s}$  (PSIR:  $4\text{min}48\text{s}\pm1\text{min}16\text{s}$ ,  $P<.01$ ). The homogenous suppression of blood and healthy myocardium on the black-blood images enabled a better visualization of myocardial scars on the SPOT images with remarkable spatial localization (Figs.2-3). Image quality was consistent among the two techniques (free-breathing SPOT:  $3.7\pm0.5$  vs. breath-held PSIR:  $3.6\pm0.7$ ,  $P=.21$ ). SPOT could identify 17% more hyperenhanced segments than PSIR (323 vs. 277,  $P<.01$ ). Seventeen patients (31%) had inconclusive LGE segments on PSIR. SPOT clearly showed hyperenhanced segments at these locations in 12/17 and could rule out areas of hyperenhancement in 5/17.

## Conclusions:

SPOT can play a critical role in imaging patients with structural heart disease as it delivers images with unprecedented scar contrast embedded in a detailed heart anatomy and, in so doing, may provide opportunities for earlier detection and therapeutic management of structural heart disease.

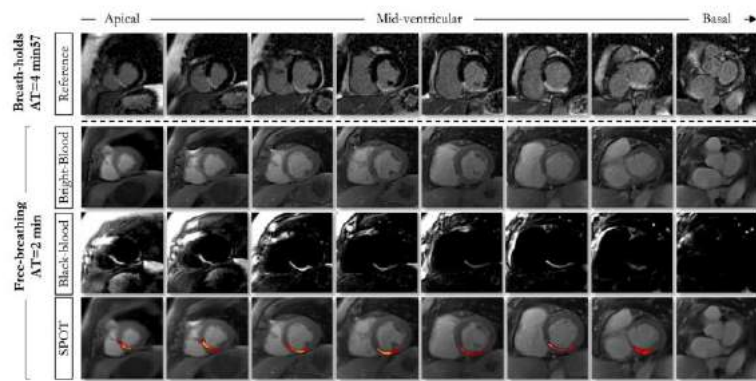
**Figure/Table 1**



**Caption 1**

**Figure 1.** Schematic overview of the proposed free-breathing joint bright- and black-blood SPOT sequence. In the odd heartbeats a  $180^\circ$  inversion pulse is followed by an adiabatic T1 $\rho$  preparation module to generate a black-blood contrast. In the even heartbeats only a T1 $\rho$  module is played out to generate a bright-blood contrast. Abbreviations: ECG, electrocardiogram; TSL, spin lock time; SL, spin lock; IR, inversion recovery; Mz, longitudinal magnetization; TI, inversion time; TD, trigger delay.

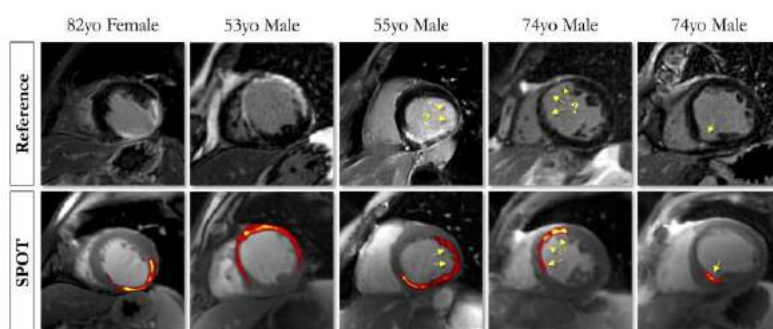
**Figure/Table 2**



**Caption 2**

**Figure 2.** Full ventricular comparison between the reference breath-held PSIR (top) and the proposed free-breathing SPOT (bottom) images in a 58-year-old female patient with infero and inferoseptal myocardial infarction. SPOT clearly identifies the areas of scar with good agreement between the two imaging techniques.

**Figure 3**



**Caption 3**

**Figure 3.** Examples of SPOT (bottom) images obtained in five patients with myocardial infarction. LGE areas are easily seen and localized with SPOT, including on segments where subendocardial scars are hard to detect on the reference PSIR (top, yellow arrowheads).

## Bibliographic References

1. Holtackers RJ, Van De Heyning CM, Chiribiri A, Wildberger JE, Botnar RM, Kooi ME. Dark-blood late gadolinium enhancement cardiovascular magnetic resonance for improved detection of subendocardial scar: a review of current techniques. J. Cardiovasc. Magn.

Reson. 2021;23:1–18 doi: 10.1186/s12968-021-00777-6., 2. Bustin A, Toupin S, Sridi S, et al. Endogenous assessment of myocardial injury with single-shot model-based non-rigid motion-corrected T1 rho mapping. J. Cardiovasc. Magn. Reson. 2021;(In Press)., 3. Kellman P, Arai AE, McVeigh ER, Aletras AH. Phase-sensitive inversion recovery for detecting myocardial infarction using gadolinium-delayed hyperenhancement. Magn. Reson. Med. 2002;47:372–383 doi: 10.1002/mrm.10051.

Speaker: A. Bustin

Category: Pulse Sequences, Black Blood, Late Gadolinium Enhancement

000077

## AI Analysis for low-field CMR: A head-to-head comparison of cine MRI at 0.35T, 1.5T, and 3.0T

X. Zu (1); J. Varghese (2); O. Simonetti (3); Q. Tao \* (1)

(1) Department of imaging physics, Delft University of Technology (TU Delft), Delft, Netherlands; (2) Dorothy m. davis heart & lung research institute, Ohio State University, Columbus, United States of America; (3) Davis heart and lung research institute, The Ohio State University, Columbus, United States of America

### Abstract

**Background :** Low-field cardiovascular magnetic resonance (CMR) is promising for cardiac imaging, offering the potential to significantly reduce costs compared to conventional 1.5T and 3.0T CMR. Despite compromised signal-to-noise ratio (SNR), low-field cine CMR has shown sufficient image quality for visual evaluation and manual quantification [1][2]. This study aims to investigate if the state-of-the-art artificial intelligence (AI) method trained on conventional 1.5T and 3.0T CMR data can perform fully-automated analysis on lower SNR, low-field cine CMR images.

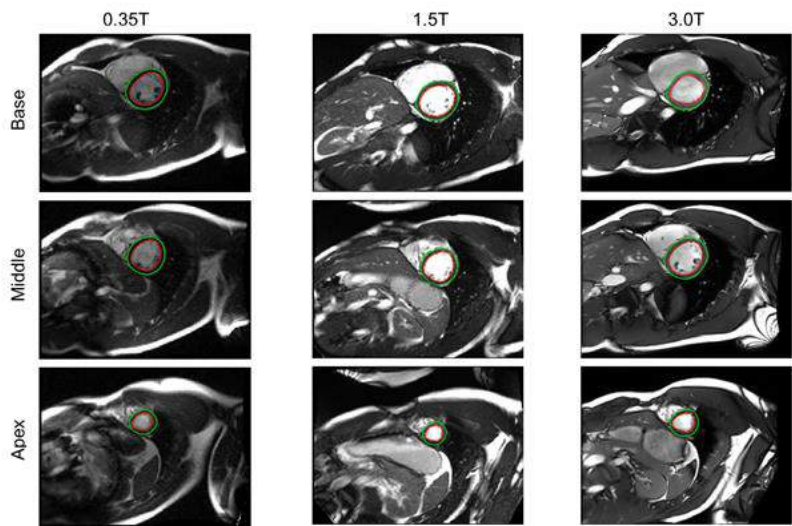
**Methods :** Six volunteers (mean age,  $33.2 \pm 8.2$  years) underwent CMR exams at 0.35T, 1.5T, and 3.0T. A short-axis stack of ECG-triggered, segmented cine steady state free precession (SSFP) images were acquired, each slice with a single breath-hold. The endocardial and epicardial contours of the left ventricle at end-systole (ES) and end-diastole (ED) were generated and manually edited by an expert using SuiteHeart software (Neosoft, Pewaukee, WI). All cine acquisitions were subsequently analysed by an in-house developed AI tool, which was trained and validated on independent 1.5T and 3.0T CMR data [3]; no low-field data was used to train the network. The performance of AI analysis on low-field CMR was evaluated by comparing manual and AI segmentation of blood pool and myocardium, using Dice index and contour-to-contour distances. Estimated left ventricular ejection fraction (LVEF) were compared head-to-head across 3 field strengths.

**Results :** AI analysis yielded highly correlated measurements of LV structural and functional parameters compared with manual analysis. With manual contours as reference, the Dice indices were  $0.90 \pm 0.09$  (blood pool) and  $0.82 \pm 0.12$  (myocardium), for automated AI analysis of 0.35T cine MRI. Compared to low-field CMR, the corresponding Dice indices for blood pool and myocardium were  $0.93 \pm 0.08$  ( $p=0.7$  by unpaired T test) and  $0.87 \pm 0.12$  ( $p=0.3$ ) for 1.5T, and  $0.91 \pm 0.10$  ( $p=0.7$ ) and  $0.88 \pm 0.09$  ( $p=0.3$ ) for 3.0T, respectively. Figure 1 shows the images and fully automated AI analysis from one subject. Figure 2 shows the overall statistics of blood pool and myocardium across all slices. A bias between manual and AI analysis was observed, possibly caused by different convention of manually tracing contours. The bias was however consistent across the field strengths, with the average distance between manual and AI contours  $0.8 \pm 0.4$  pixels at the endocardial side for low-field CMR (vs.  $1.0 \pm 0.5$  pixels for 1.5T and  $1.2 \pm 0.6$  pixels for 3.0T), and  $0.6 \pm 0.4$  pixels at the epicardial side (vs.  $0.6 \pm 0.3$  pixels for 1.5T and  $0.6 \pm 0.3$  pixels for 3.0T). The estimated LVEF was  $66.0 \pm 5.2\%$ ,  $63.9 \pm 6.3\%$ ,  $66.2 \pm 5.6\%$  for 0.35T, 1.5T, and 3.0T, respectively (Figure 3). No statistical significance was found between any two field strengths.



**Conclusions :** The AI algorithm trained on conventional CMR data can automatically analyse low-field cine CMR in an accurate manner, suggesting adequate image contrast and SNR from low-field cine CMR. Left ventricle segmentation by AI achieved sub-pixel accuracy on low-field data compared with manual analysis, and the estimated structural and functional parameters correlated well with those from clinical 1.5T and 3.0T CMR.

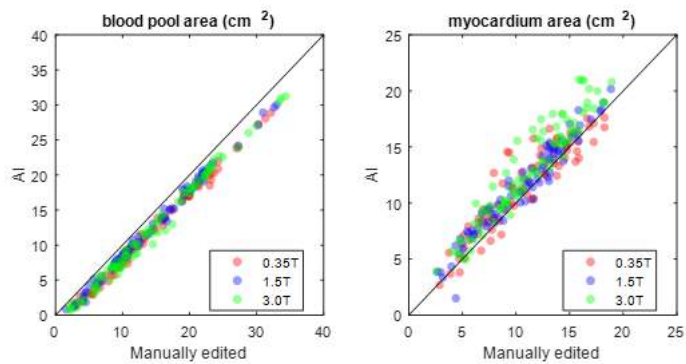
**Figure/Table 1**



**Caption 1**

Figure 1. Examples of cine MRI images of one subject imaged at 0.35T, 1.5T, and 3.0T. Basal, middle, and apical slices are shown at the end-diastolic phase. Endocardial and epicardial contours derived from the fully automatic AI tool are overlaid on the original images.

**Figure/Table 2**

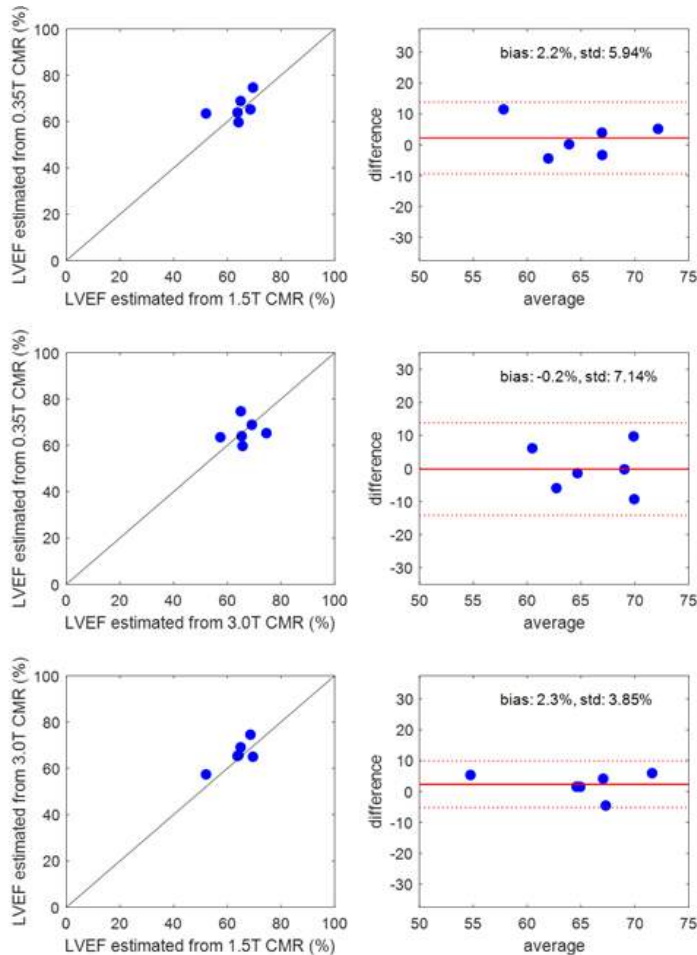


**Caption 2**



Figure 2 . Comparison of the segmented left ventricle blood pool and myocardium area per slice in 18 cine acquisitions (6 subjects \* 3 field strengths) from manually edited contours and AI-generated contours. Different colors denote different field strengths. The overall correlation is 0.99 and 0.95, respectively (both  $p < .0001$ ).

**Figure 3**



**Caption 3**

Figure 3. Bland-Altman analysis of AI Estimated LVEF parameters at different field strengths, 0.35T, 1.5T, and 3.0T, for 6 subjects. The estimated LVEF was  $66.0 \pm 5.2\%$ ,  $63.9 \pm 6.3\%$ ,  $66.2 \pm 5.6\%$  for 0.35T, 1.5T, and 3.0T. No statistical significance was found between any two pairs.

## Bibliographic References

[1] Varghese J, Craft J, Crabtree CD, Liu Y, Jin N, Chow K, Ahmad R, Simonetti OP.

Assessment of cardiac function, blood flow and myocardial tissue relaxation parameters at 0.35 T. NMR Biomed. 2020 Jul;33(7):e4317. , [2] Restivo MC, Ramasawmy R, Bandettini WP, Herzka DA, Campbell-Washburn AE. Efficient spiral in-out and EPI balanced steady-state free precession cine imaging using a high-performance 0.55T MRI. Magn Reson Med. 2020 Nov;84(5):2364-2375., [3] Tao Q, Yan W, Wang Y, Paiman EHM, Shamonin DP, Garg P, Plein S, Huang L, Xia L, Sramko M, Tintera J, de Roos A, Lamb HJ, van der Geest RJ. Deep Learning-based Method for Fully Automatic Quantification of Left Ventricle Function from Cine MR Images: A Multivendor, Multicenter Study. Radiology. 2019 Jan;290(1):81-88.

Speaker: Q. Tao

Category: Cine Imaging, MR Post-Processing, Cardiac Function

000079

## 4D Flow MRI Assessment of Stability of Hemodynamics in patients with Fontan Connection

E. Weiss \* (1); C. Rigsby (2); J. Robinson (3); M. Markl (4)

(1) Department of radiology, Northwestern University Feinberg School of Medicine, Chicago, United States of America; (2) Medical imaging, Ann & Robert H. Lurie Children's Hospital of Chicago, Chicago, United States of America; (3) Pediatric cardiology, Ann & Robert H. Lurie Children's Hospital of Chicago, East Chicago Avenue, Chicago, United States of America; (4) Department of radiology, Northwestern University Feinberg School of Medicine, East Superior Street, Chicago, IL, USA, Chicago, United States of America

### Abstract

**Background:** Single ventricle physiology is a severe, complex congenital heart defect that often requires a 3 step surgical series completed with a total cavo-pulmonary connection (TCPC, Fontan Connection). While these patients have a 20-year survival rate of 76% [1], 70% percent of patients will experience Fontan failure by age 50 [2]. However, individual risk factors for Fontan failure are poorly understood. Previous studies have shown that TCPC hemodynamic measures may be implicated in Fontan failure, but there is a dearth of data to investigate these measures overtime. We aimed to investigate longitudinal changes in hemodynamics in patients with TCPC and their associations with cardiac function.

**Methods:** A total of 9 patients with TCPC who underwent at least two standard-cardiac MRI exams (including 4D flow) were included (table 1) in this retrospective study. The ejection fraction (EF) and end diastolic volume indexed to body surface area (EDVi) at baseline (BL) and follow-up (FU) were collected from the radiologist report. Manual 3D segmentation of the Fontan connection, including the inferior and superior vena cava (IVC and SVC) and the left and right pulmonary arteries (LPA and RPA) was completed for each scan. As shown in Fig 1, parametric flow maps were calculated to quantify voxel-wise kinetic energy (KE), peak velocity, and stasis (% of cardiac cycle velocity  $<0.1\text{m/s}$ , fig1c). An automated centerline was calculated for the RPA, LPA and the caval veins (fig 1a) and used to define 5 3D Fontan segments: IVC, SVC, LPA, RPA and the connection (fig1b). Mean values for KE, peak velocity, and stasis were quantified for each Fontan segment (e.g., peak velocity in fig2) and changes between BL and FU were calculated for each patient.

**Results:** The study cohort (33% female,  $19\pm9$  years old,  $3.7\pm1.8$  year follow up time) is summarized in table 1. Between BL and FU, there was significant increase in KE in the IVC ( $.7\mu\text{J}/\text{year}$ ,  $p=0.02$ ) and LPA ( $1\mu\text{J}/\text{yr}$ ,  $p=0.01$ ), while all other hemodynamic metrics were stable over time ( $p>0.1$ ). Additionally, there were no differences in the yearly change in any flow metric between those with lateral tunnel vs extracardiac Fontan. Four patients had greater than 5% decrease in EF between BL and FU. There was a trend towards increased peak velocity in the IVC between those with  $>5\%$  EF decrease vs stable EF ( $5.3\text{cm/s}$  vs  $1.6\text{cm/s}$ ,  $p=0.06$ , fig2c). Moreover, we found significant increased EDVi correlated with reduced peak velocity in the IVC ( $r=-0.9$ ,  $p<0.001$ ) and connection region ( $r=-0.7$ ,  $p=0.02$ ).

**Conclusions:** We implemented a novel, voxel-wise hemodynamic analysis pipeline for patients with TCPC and found that hemodynamic metrics were remarkably stable in 9 patients

regardless of Fontan type. We found that peak velocity in the IVC may change with worsening cardiac function. This may be related to upstream hepatic changes which are hypothesized to be associated with Fontan failure and other adverse outcomes [3,4]. Future studies would include a larger cohort with a more diverse set of outcomes.

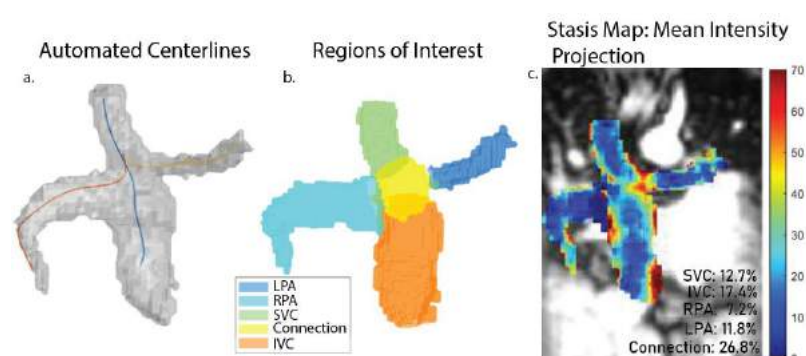
**Figure/Table 1**

<i>Subject</i>	<i>Age (gender)</i>	<i>GA (BL/FU)</i>	<i>F/u time (years)</i>	<i>Fontan type</i>	<i>EF (BL/FU)</i>	<i>EDVi (BL/FU)</i>
1	15 (F)	Y/Y	0.83	Extracardiac	50.5/50	122/116
2	21 (M)	N/N	7.1	Lateral Tunnel	52/50	57/70
3	13 (M)	Y/Y	2.8	Extracardiac	48/60.2	86/85
4	16 (M)	N/N	3.4	Lateral Tunnel	49/49	128/120
5	28 (M)	N/N	2.3	Lateral Tunnel	55/49	115/98
6	35 (F)	N/N	5.1	Lateral Tunnel	38/42	60/60
7	9 (F)	N/N	3.8	Extracardiac	50/52	65/55
8	22 (M)	N/N	3.3	Lateral Tunnel	47/44	138/143
9	9 (M)	Y/N	5.3	Extracardiac	22/20	108/63

**Caption 1**

Table 1. Cohort characteristics. Age is reported in years. Of note, patient 9 was the only patient to have a change in general anesthesia status between baseline (BL) and follow up (FU). Patients 1, 5, 8, and 9, had a percent decrease of at least 5% ( $\Delta EF/EF$  at BL).

**Figure/Table 2**

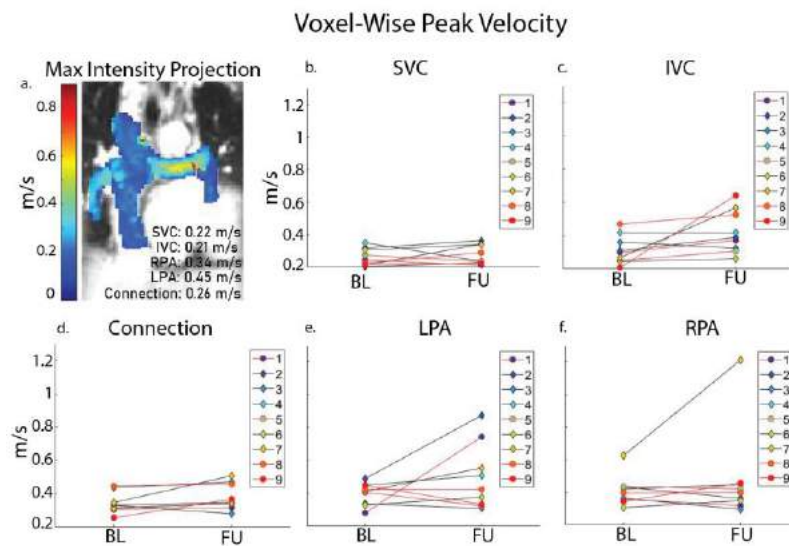


**Caption 2**

Fig 1. The Fontan connection was segmented manually for each scan and had automate centerlines calculated (a) for 1) caval veins, 2) RPA, 3) LPA. Planes were place along the

centerlines to delineate the 5 segments of interest (b). Voxel-wise parameter maps were calculated for the segmentation.

**Figure 3**



**Caption 3**

Fig 2. Peak velocity for each segment. An example map is shown of subject 9 at BL(a) as well as BL and FU data for each segment and subject (b-f). Subjects with redlines and diamond markers had >5% decrease in EF over the follow-up duration. Abbreviations: Baseline (BL), follow up (FU).

### Bibliographic References

Kiesewetter, C. H., Sheron, N., Vettukattill, J. J., Hacking, N., Stedman, B., Millward-Sadler, H., ... & Veldtman, G. R. (2007). Hepatic changes in the failing Fontan circulation. *Heart*, 93(5), 579-584.

Dennis M, Zannino D, Plessis du K, et al. Clinical outcomes in adolescents and adults after the Fontan procedure. *J Am Coll Cardiol* 2018;71:1009–17.

Dabal, R. J., Kirklin, J. K., Kukreja, M., Brown, R. N., Cleveland, D. C., Eddins, M. C., & Lau, Y. (2014). The modern Fontan operation shows no increase in mortality out to 20 years: a new paradigm. *The Journal of thoracic and cardiovascular surgery*, 148(6), 2517-2524.

Speaker: E. Weiss

Category: 4D Flow, Fontan, Single Ventricle

000082

## A Clinical Validation of a Machine Learning-Based Right Ventricular Segmentation Algorithm for Cine Short Axis CMR Images

J. Åkesson \* (1); E. Ostenfeld (1); M. Carlsson (1); H. Arheden (1); E. Heiberg (1)

(1) Clinical physiology, department of clinical sciences lund, Lund University, Skåne University Hospital, Lund, Sweden

### Abstract

#### Background

Right ventricle (RV) volume and ejection fraction are of clinical and prognostic relevance to assess and are typically obtained from manual delineations. The delineation process can be time-consuming and prone to inter-observer variability. Machine learning methods based on Convolutional Neural Networks (CNNs) can be used for automating cardiac delineation [1, 2]. However, data on actual clinical applicability is scarce. Therefore, this study aimed to develop and validate a CNN-based algorithm for RV delineation in end diastole (ED) and end systole (ES) with the goal of making it robust and useful in a clinical environment, and also freely available for research.

#### Methods

Cine short axis images from 1330 patients and normal subjects were collected from a) clinical referrals and b) in-house research projects. The images had manual delineations of the RV that were all quality-controlled before inclusion. The data was split into one set for development (n=1114) and one test set *S1* (n=216). The developed algorithm is a combination of three subsequent CNNs; one that selects slices containing a cross-section of the RV (in concordance with previous research [3]), one that locates the center of the RV (for automated cropping), and one that performs binary segmentation [4].

Validation was carried out on *S1* (n=216) and a separately acquired set of clinical referrals *S2* (n=50). Each subject in *S2* was manually delineated by two expert observers (O1 and O2). The algorithm's delineations were compared to reference delineations and subjectively rated by O1 as a) good enough for clinical use or in need of b) minor or c) major corrections. Delineations on *S2* rated as b) or c) were corrected manually by O1 and O2. The times for both manual corrections and for manual delineations on *S2* were noted.

#### Results

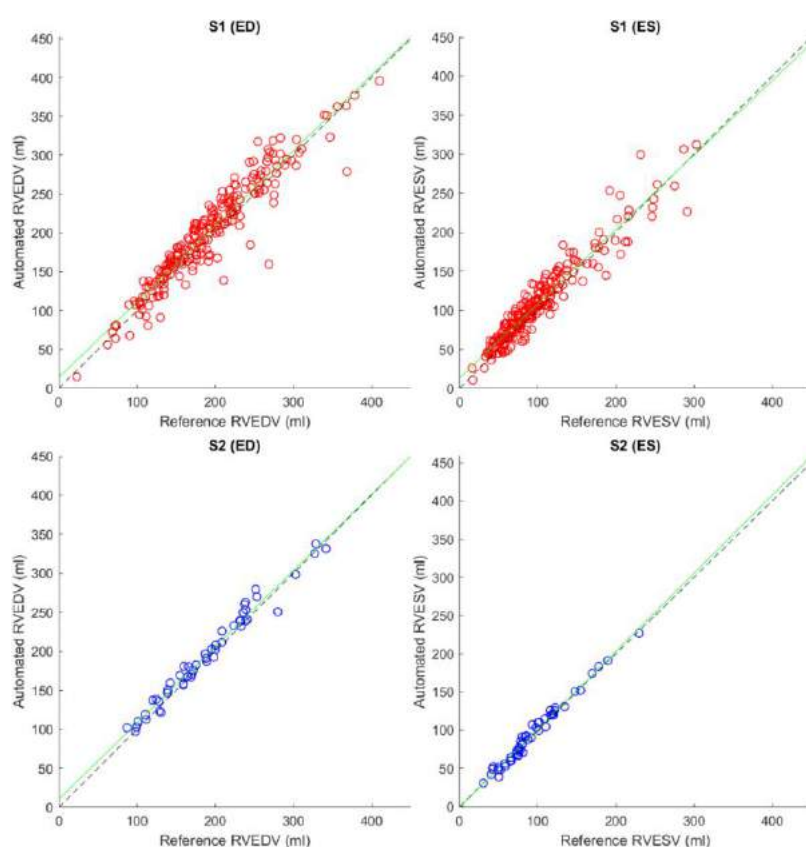
Figure 1 shows scatter plots for *S1* and *S2*. Figure 2 shows inter-method and inter-observer differences for *S2*. For *S1*, 38 % of delineations were rated as good, and 50 % as in need of minor corrections. The mean errors in percentage units of mean reference volumes were  $5 \pm 11$  % (ED) and  $8 \pm 16$  % (ES). For *S2*, 58 % were good enough for clinical use, and remaining delineations (n=21) only needed minor corrections. The mean errors in percentage units of mean observer mean reference volumes were  $4 \pm 7$  % (ED) and  $-4 \pm 8$  % (ES) for O1 and  $2 \pm 6$  % (ED) and  $6 \pm 8$  % (ES) for O2. The mean inter-observer errors were  $-2 \pm 8$  % (ED) and  $11 \pm 11$  % (ES). Figure 3 shows inter-observer volume differences for corrected and

for manual delineations. The mean absolute volume difference for a minor correction was 6 ml (3 %) for ED and 3 ml (3 %) for ES. The mean correction time was approximately 1/3 of the mean time for a manual delineation.

## Conclusions

A CNN-based algorithm for RV delineation in ED and ES was developed and validated. The inter-method error was of similar magnitude as the inter-observer error. Of all delineations, 49 % needed only minor corrections. Corrected delineations lowered inter-observer variability and average delineation time compared to manual delineations. In conclusion, the results indicate robustness and actual clinical applicability of the algorithm, which will be made freely available in the software *Segment* [5].

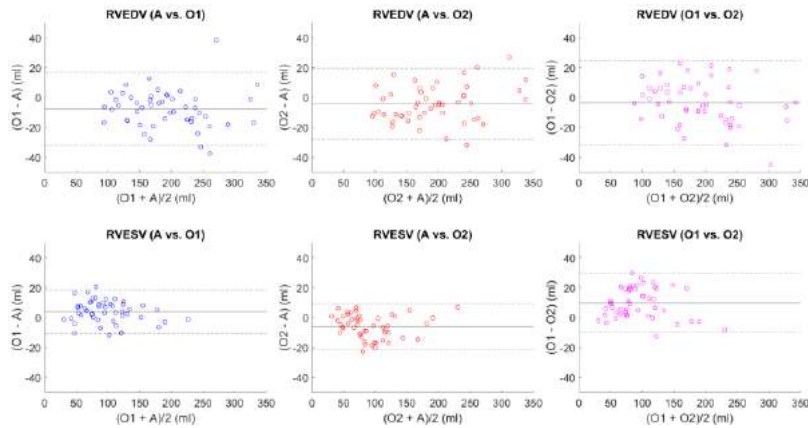
**Figure/Table 1**



**Caption 1**

*Scatter plots showing the algorithm's automated RVEDV (left column) and RVESV (right column) plotted against the corresponding reference volumes. The upper row subfigures show set S1 and the bottom row subfigures show set S2. Each graph contains an identity line (dashed) and a least squares line (green).*

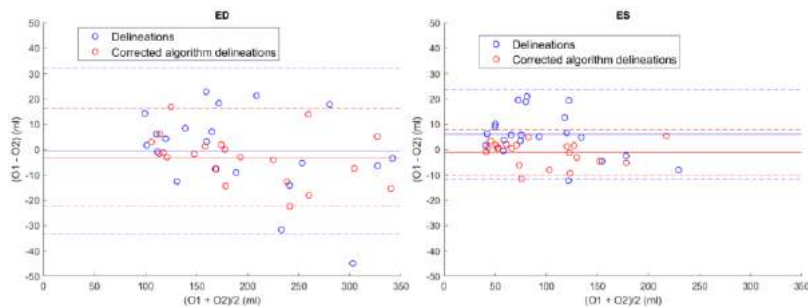
**Figure/Table 2**



**Caption 2**

*Bland-Altman plots showing the inter-method and inter-observer volume differences between the algorithm (A) and Observer 1 (O1) to the left, between A and Observer 2 (O2) in the middle, and between O1 and O2 to the right. The top row shows RVEDV, and the bottom row shows RVESV.*

**Figure 3**



**Caption 3**

*Bland-Altman plots showing the volume differences between observers O1 and O2 in the RVEDV (left) and the RVESV (right) from manual delineations (blue) and manual corrections of algorithm delineations (red) for the 21 delineations from S2 that were rated as in need of manual corrections.*

## Bibliographic References

[1] Bai W, Sinclair M, Tarroni G, Oktay O, Rajchl M, Vaillant G, et al. Automated cardiovascular magnetic resonance image analysis with fully convolutional networks. Journal



of Cardiovascular Magnetic Resonance. 2018 Dec 1;20(1):65. , [2] Isensee F, Jaeger PF, Full PM, Wolf I, Engelhardt S, Maier-Hein KH. Automatic Cardiac Disease Assessment on cine-MRI via Time-Series Segmentation and Domain Specific Features. In: Pop M, Sermesant M, Jodoin P-M, Lalande A, Zhuang X, Yang G, et al., editors. Statistical Atlases and Computational Models of the Heart. ACDC and MMWHS Challenges [Internet]. Cham: Springer International Publishing; 2018 [cited 2021 Sep 22]. p. 120–9. (Lecture Notes in Computer Science; vol. 10663). , [3] Berggren K, Hedstrom E, Ehrenborg KS, Carlsson M, Engblom H, Ostenfeld E, Jogi J, Atar D, Ekelund U, Arheden H, Heiberg E. Multiple Convolutional Neural Networks for Robust Myocardial Segmentation. In: Proceedings of SSBA 2020. , [4] Ronneberger O, Fischer P, Brox T. U-Net: Convolutional Networks for Biomedical Image Segmentation. In: Navab N, Hornegger J, Wells WM, Frangi AF, editors. Medical Image Computing and Computer-Assisted Intervention – MICCAI 2015 [Internet]. Cham: Springer International Publishing; 2015 [cited 2021 Sep 22]. p. 234–41. (Lecture Notes in Computer Science; vol. 9351). , [5] Heiberg E, Sjögren J, Ugander M, Carlsson M, Engblom H, Arheden H. Design and validation of Segment-freely available software for cardiovascular image analysis. BMC medical imaging. 2010 Jan 11;10(1):1-3.

Speaker: J. Åkesson

Category: Right Ventricle, Segmentation, Softwares

000088

## **Left ventricular ejection fraction measured with same day 2D echocardiography and cardiovascular magnetic resonance in patients with suspected cardiotoxicity**

M. S. Nazir \* (1); M. S. Andres, (2); T. Murphy, (2); S. Rosen, (2); R. Khattar (3); A. Chiribiri (4); S. Plein (5); S. Prasad (6); D. Pennell (6); A. J. Baksi, (6); A. Lyon, (2)

(1) Cardio-oncology service, King's College London Waterloo Campus, Stamford Street, London, United Kingdom; (2) Cardio-oncology service, Royal Brompton Hospital, Guy's and St Thomas' NHS Foundation Trust, , London, UK, United Kingdom; (3) Department of echocardiography, Royal Brompton Hospital, Guy's and St Thomas' NHS Foundation Trust, , London, United Kingdom; (4) Biomedical Engineering and Imaging Sciences, King's College London Waterloo Campus, London, United Kingdom; (5) Licamm, Leeds institute of Cardiovascular and Metabolic Medicine, Leeds District, UK, United Kingdom; (6) Cardiovascular magnetic resonance unit, Royal Brompton Hospital, Guy's and St Thomas' NHS Foundation Trust,, London, UK, United Kingdom

### **Abstract**

#### Background

Left ventricular ejection fraction (LVEF) is widely used for the assessment of cardiotoxicity in cancer patients who receive cardiotoxic cancer therapies. Cardiovascular Magnetic Resonance (CMR) is the gold standard for the assessment of LVEF, but 2D echocardiography is the most widely used imaging modality. Several studies have previously reported the comparison of LVEF derived from 2D echocardiography and CMR. (1-3) The objective of this study was to compare LVEF measured by 2D echocardiography to CMR in cancer patients with suspected cardiotoxicity and the potential impact on downstream clinical decision making.

#### Methods

In this prospective single centre observational study, we compared LVEF derived from 2D echocardiography and CMR in 745 patients who underwent imaging with both modalities on the same day. We excluded cases with suboptimal image quality and those in which a 2D Biplane's Simpsons analysis could not be performed. Agreement of LVEF was determined by Bland-Altman analysis, intraclass correlation coefficient (ICC) and clinically relevant thresholds for cardiotoxicity. (4, 5)

#### Results

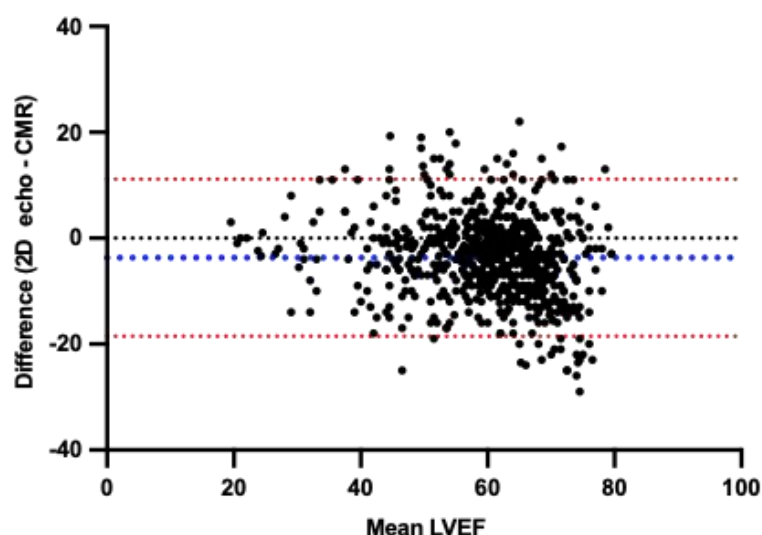
The mean age of patients was  $60 \pm 5$  years, and female:male ratio of 62:38. LVEF (%) measured by 2D echocardiography was significantly lower compared to CMR, (median 60 [interquartile range 54-65]) vs median 63 [interquartile range 56-69],  $p < 0.001$ ). Using Bland-

Altman analysis, there was a mean bias of  $-3.7 \pm 7.6$  (95% limits of agreement  $-18.5$  to  $11.1\%$ ) of 2D echocardiography versus CMR derived LVEF (**Figure 1**). Overall, there was a moderate agreement between the two measurements with ICC of  $0.72$  (95% confidence interval  $0.56 - 0.80$ ,  $p < 0.0001$ ). On subgroup analysis, the agreement was moderate across a range of clinically relevant LVEF thresholds (**Table 1**). Using established thresholds for cardiotoxicity, there was disagreement between the two modalities in 9.3%, 9.9% and 13.3% of patients according to thresholds at 50%, 53% and 55%, respectively (**Figure 2**).

## Conclusions

2D echocardiography and CMR are not interchangeable for the assessment of LVEF. 2D echocardiography has wide variations in measurements of up to  $\pm 15\%$  compared to CMR and this leads to a substantial amount of disagreement according to clinically relevant thresholds for cardiotoxicity. Emerging techniques with 3D echocardiography, myocardial strain and CMR guided approaches to patient management should be considered in future studies.

**Figure/Table 1**



**Caption 1**

**Figure 1.** Bland-Altman plot which demonstrates same day left ventricular ejection fraction (LVEF) with 2D echocardiography and Cardiovascular Magnetic Resonance (CMR),  $n=745$ . Dashed blue line: mean bias. Dashed red lines: 95% upper and lower limits of agreements.

**Figure/Table 2**

Threshold for LVEF	Cohen's Kappa	p value
< 55%	0.64	< 0.001

< 53%	0.69	< 0.001
< 50%	0.63	< 0.001
< 40%	0.64	< 0.001
< 35%	0.69	< 0.001

## Caption 2

**Table 1.** Agreement of left ventricular ejection fraction according to clinically relevant for cardiotoxicity and heart failure. LVEF: Left ventricular ejection fraction.

## Figure 3



## Caption 3

**Figure 2.** Diagram which demonstrates the correctly classified and incorrectly classified patients using 2D echocardiography (n=745), at three relevant thresholds for cardiotoxicity.

## Bibliographic References

1. Bellenger NG, Burgess MI, Ray SG, Lahiri A, Coats AJ, Cleland JG, et al. Comparison of left ventricular ejection fraction and volumes in heart failure by echocardiography, radionuclide ventriculography and cardiovascular magnetic resonance; are they interchangeable? *Eur Heart J.* 2000;21(16):1387-96., 2. Hoffmann R, von Bardeleben S, ten Cate F, Borges AC, Kasprzak J, Firschke C, et al. Assessment of systolic left ventricular function: a multi-centre comparison of cineventriculography, cardiac magnetic resonance imaging, unenhanced and contrast-enhanced echocardiography. *Eur Heart J.* 2005;26(6):607-16., 3. Pellikka PA, She L, Holly TA, Lin G, Varadarajan P, Pai RG, et al. Variability in Ejection Fraction Measured By Echocardiography, Gated Single-Photon Emission Computed Tomography, and Cardiac Magnetic Resonance in Patients With Coronary Artery Disease and Left Ventricular Dysfunction. *JAMA Network Open.* 2018;1(4):e181456-e., 4. Dobson R, Ghosh AK, Ky B, Marwick T, Stout M, Harkness A,

et al. British Society for Echocardiography and British Cardio-Oncology Society guideline for transthoracic echocardiographic assessment of adult cancer patients receiving anthracyclines and/or trastuzumab. *Echo Research and Practice*. 2021;8(1):G1-G18., 5.

Zamorano JL, Lancellotti P, Rodriguez Muñoz D, Aboyans V, Asteggiano R, Galderisi M, et al. 2016 ESC Position Paper on cancer treatments and cardiovascular toxicity developed under the auspices of the ESC Committee for Practice Guidelines: The Task Force for cancer treatments and cardiovascular toxicity of the European Society of Cardiology (ESC). *Eur Heart J*. 2016;37(36):2768-801.

Speaker: M. S. Nazir

Category: Nonischemic Cardiomyopathy, Ejection Fraction, Heart Failure

000089

## Assessment of Microstructural Remodeling in Myocardial Infarction Using Advanced Diffusion Metrics

A. Wilson \* (1); X. Kang (1); T. Cork (1); L. Perotti (2); D. Ennis (1)

(1) Radiology department, Stanford University School of Medicine, Stanford, United States of America; (2) Mechanical and aerospace engineering, University of Central Florida, Orlando, United States of America

### Abstract

**Background:** In response to an infarct, the myocardium undergoes significant microstructural remodeling, which can be measured using diffusion tensor imaging (DTI). Typical DTI metrics include the helix angle (HA), sheetlet angle, fractional anisotropy (FA) and the mean diffusivity (MD). However, reconstruction methods have been developed for brain DTI that can capture additional diffusion metrics, such as the complexity (CX), apparent fiber density (AFD) and the fixel number (FN). Herein, we aim to examine the sensitivity and specificity of these advanced diffusion tensor metrics compared with the established cardiac DTI metrics in a large animal model of myocardial infarction (MI).

**Methods:** Healthy pig hearts ( $n = 15$ ) and infarct pig hearts ( $n = 4$ ) underwent ex vivo MRI (Siemens 3T Prisma) with a 15-channel knee coil. One post-contrast high-resolution T1-weighted anatomical image (T1W) was acquired for each subject using a three-dimensional fast low angle shot (3D-FLASH) sequence and diffusion weighted images (DWIs) were acquired using a multi-shot readout-segmented spin-echo sequence. Scan parameters for all the subjects were: (1) T1W image: TR = 12 ms, TE = 3.15 ms, flip angle =  $25^\circ$ , voxel size  $1 \times 1 \times 1$  mm<sup>3</sup>, 160 axial slices; (2) Five sets of DWIs: TR = 18100 ms, TE = 62 ms, flip angle =  $180^\circ$ , voxel size  $1 \times 1 \times 1$  mm<sup>3</sup>, 128 axial slices,  $b = 1000$  s/mm<sup>2</sup>, 30 directions. DWIs were co-registered and resampled to anatomical image space using FSL, and calculation of MD, FA, FN, CX and AFD was performed using the software package Mrtrix3.

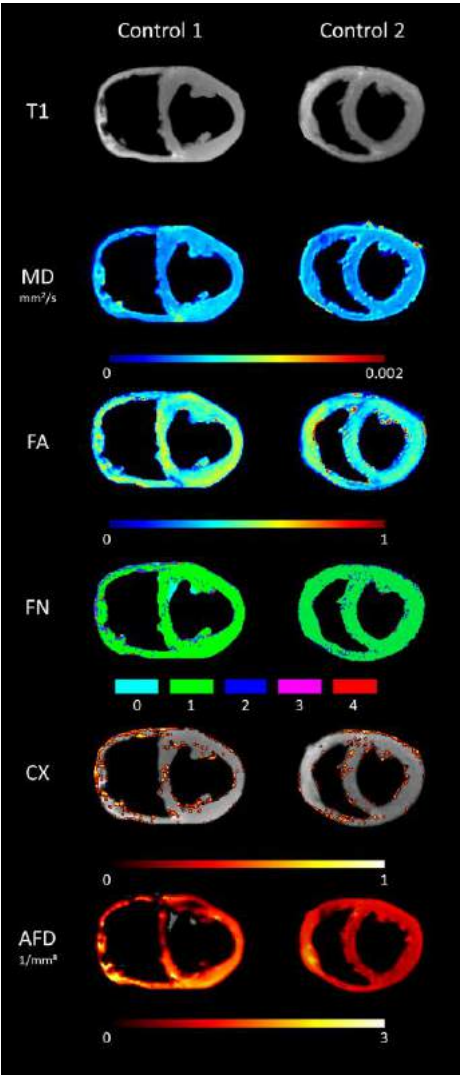
**Results:** T1W images show gadolinium enhancement in the infarct region. Infarct regions showed significantly lower FA ( $0.23 \pm 0.05$ ) than both remote regions ( $0.36 \pm 0.03$ ,  $P < .001$ ), and control hearts ( $0.36 \pm 0.06$ ,  $P < .001$ ). Additionally, infarct regions had significantly greater MD ( $0.29 \pm 0.05$  mm<sup>2</sup>/s) than both remote regions ( $0.20 \pm 0.03$  mm<sup>2</sup>/s,  $P < .05$ ) and control hearts ( $0.21 \pm 0.02$  mm<sup>2</sup>/s,  $P < .001$ ). Infarct regions had similar AFD ( $0.12 \pm 0.11$ ) to both remote regions ( $0.11 \pm 0.01$ ,  $ns$ ) and control hearts ( $0.12 \pm 0.01$ ,  $ns$ ). Infarct regions had greater CX ( $0.218 \pm 0.091$ ) than both remote regions ( $0.15 \pm 0.016$ ,  $ns$ ) and control hearts ( $0.149 \pm 0.032$ ,  $P < .05$ ). Most myocardial voxels had a single predominant population of fibers (FN=0: 7%, FN=1: 69%, FN $\geq$ 2: 25%). Infarct regions had greater average FN ( $1.47 \pm 0.15$ ) than both remote regions ( $1.33 \pm 0.13$ ,  $ns$ ), and control hearts ( $1.27 \pm 0.12$ ,  $P < .05$ ).

**Discussion:** The invariants of the diffusion tensor, FA and MD were able to distinguish areas of microstructural remodeling. The complexity metric indicates the spread of fibers within a single voxel. The complexity is zero when FN = 1: all fibers align along a single direction. For FN  $\geq$  2, fibers are spread over multiple directions, and the complexity increases. The increased complexity in the infarct region likely results from the loss of organization due to

cell death and fibrosis. The remaining myocytes within the infarct may also grow and remodel along new directions due to the altered mechanics.

Conclusion: We conclude that advanced diffusion metrics, such as complexity and fixel number, provide additional microstructural information for analysis of cardiac DTI.

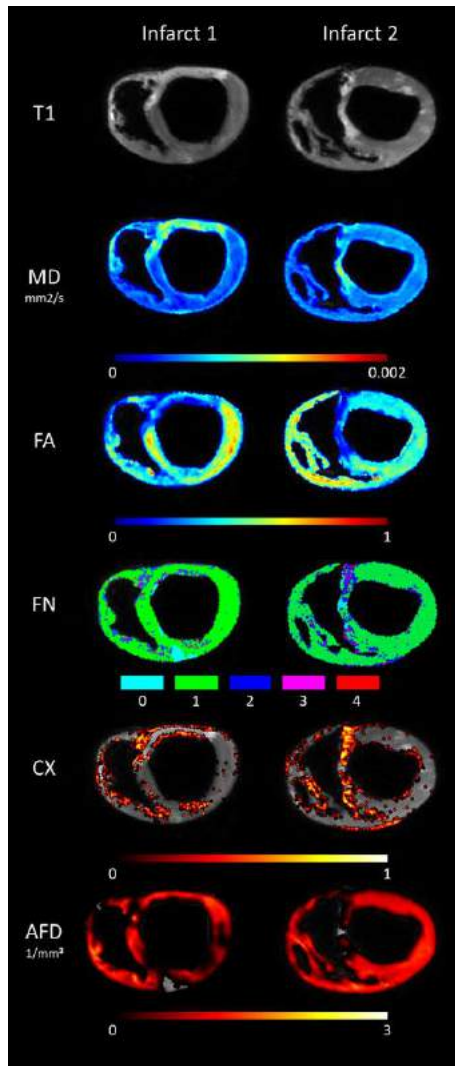
Figure/Table 1



Caption 1

Figure 1: **Control heart diffusion maps.** For two control hearts the short-axis T1 weighted images are shown along with mean diffusivity (MD), fractional anisotropy (FA), fixel number (FN), complexity (CX), and apparent fiber density (AFD) maps.

Figure/Table 2

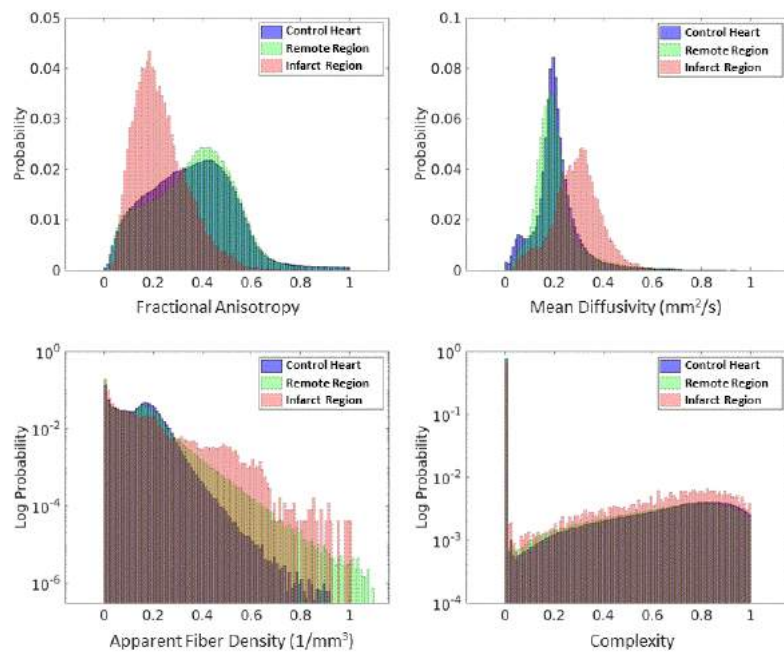


## Caption 2

**Figure 2: Infarct heart diffusion maps.** For two control hearts the short-axis T1 weighted images are shown along with mean diffusivity (MD), fractional anisotropy (FA), fixel number (FN), complexity (CX), and apparent fiber density (AFD) maps.

## Figure 3





### Caption 3

**Figure 3: Diffusion metric probability distributions.** Voxels are divided into control hearts, and infarct and remote regions for the infarcted hearts. The probability distributions of fractional anisotropy (top left), mean diffusivity (top right), apparent fiber density (bottom left) and complexity (bottom right) are shown.

Speaker: A. Wilson

Category: Diffusion Weighted Imaging, Chronic Myocardial Infarction, Acute Myocardial Infarction

000090

# Cardiac magnetic resonance first-pass perfusion study on myocardial microcirculation dysfunction after chemotherapy in gynecological malignant tumors

Z. Zhou \* (1); Y. Guo (2); M. Yang (2)

(1) , West China Clinical Medical College, Sichuan University, Chengdu, China; (2) West china second university hospital, sichuan university, chengdu, china, Department of Radiology, Chengdu, China

## Abstract

**Background:** Thanks to the advancement of tumor treatment methods, the survival rate and survival time of tumor patients have been improved and prolonged. Therefore, the cardiovascular injury associated with tumor treatment is also receiving increasing attention. A variety of drugs in tumor chemotherapy can affect the function of myocardial vascular endothelium, and the function of myocardial microcirculation, as an important factor affecting cardiac blood supply and oxygen metabolism, also plays an important role in cardiovascular risk stratification. Therefore, this study aims to explore the changes of myocardial microcirculation function and risk factors of myocardial microcirculation dysfunction in patients with gynecological malignant tumor after chemotherapy by using the CMR first-pass perfusion sequence.

**Methods:** From September 2018 to December 2020, this study prospectively enrolled 69 chemotherapy patients (34 of whom completed the CMR review) and 38 healthy volunteers, and analyzed the subjects' myocardial perfusion index (PI) through CMR first-pass perfusion images. One-way Anova or Kruskal-Wallis test was used to compare the difference of myocardial PI between two CMR scans and the control group. And multivariate linear regression was used to explore the independent correlation factors of myocardial PI.

**Results:** This study found that the mean value of myocardial PI in chemotherapy patients was slightly lower than that in the control group on the first CMR examination, but there was no statistical difference ( $13.22 \pm 2.44$  vs.  $12.63 \pm 2.70$ ,  $P = 0.719$ ). However the myocardial PI of chemotherapy patients in the second CMR examination was significantly lower than that of the control group ( $13.22 \pm 2.44$  vs.  $11.63 \pm 2.94$ ,  $P = 0.016^*$ ). There was no significant correlation between myocardial PI, Creatine kinase isoenzyme (CK-MB), and myoglobin (MYO) ( $P > 0.05$ ). And there was no significant difference in myocardial PI between the long-term course treatment group and the short group ( $12.13 \pm 2.73\%$  vs.  $13.06 \pm 3.11\%$ ,  $P = 0.104$ ). Correlation analysis showed that chemotherapy was independently related to the decline of myocardial PI ( $\beta = -0.303$ ,  $P < 0.001^*$ ), but there was no significant correlation between the number of chemotherapy and myocardial PI ( $r = -0.142$ ,  $P = 0.106$ ).

**Conclusions:** Chemotherapy for gynecological malignant tumors can cause myocardial microcirculation dysfunction in patients. However, with the increase of the number of chemotherapy, the dysfunction of myocardial microcirculation in patients will not be further aggravated. CMR first-pass perfusion is a good imaging method for evaluating myocardial microcirculation in patients undergoing chemotherapy.

Figure/Table 1

**Table 1 The myocardial PI in patients and normal controls**

	Normal controls	1st CMR patients	2nd CMR patients
Global LV, %	13.22 ± 2.44	12.63 ± 2.70	11.63 ± 2.94*
Basal slice, %	12.62 ± 2.48	12.50 ± 3.10	11.59 ± 3.86
Middle slice, %	13.15 ± 2.96	12.67 ± 2.96	11.54 ± 2.91*
Apical slice, %	14.21 ± 3.65	12.69 ± 2.94	11.68 ± 3.23*

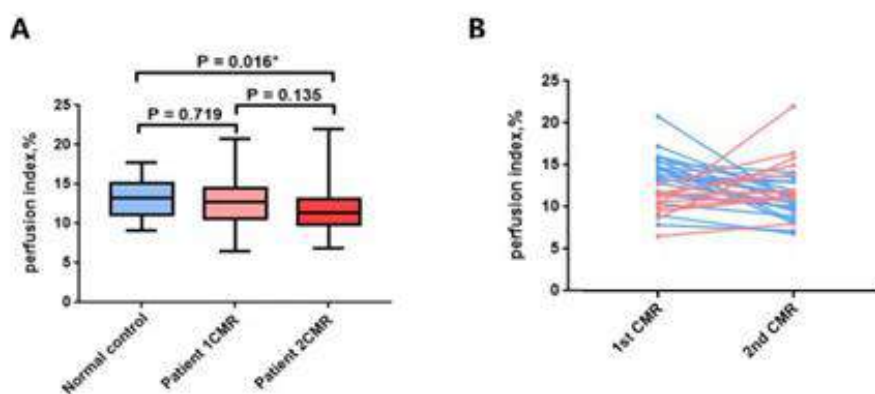
### Caption 1

Abbreviation: LV=Left ventricular; PI= Perfusion index

\*, P < 0.05 vs. Normal controls

&, P < 0.05 vs. 1st CMR examination

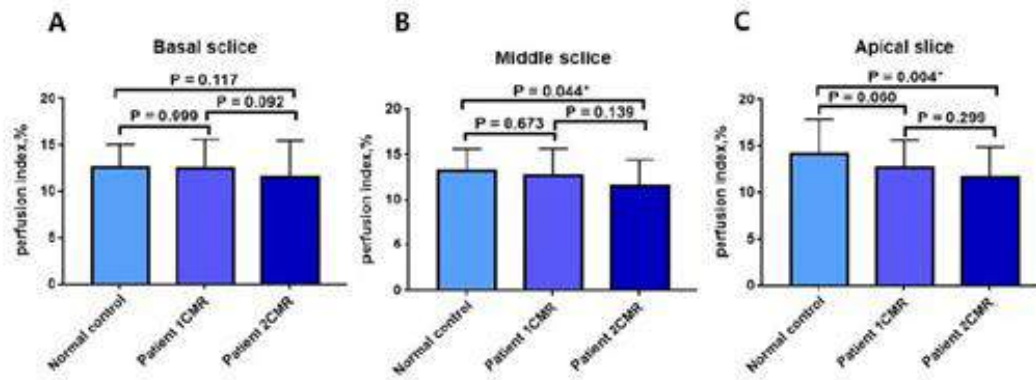
**Figure/Table 2**



### Caption 2

**Figure 1 Comparison of myocardial PI between chemotherapy patients and normal control**

### Figure 3



**Caption 3**

**Figure 2 Comparison of myocardial PI at different slices in subjects**

Speaker: Z. Zhou

Category: Chemotherapy, Cardiac Events, Tumor

000091

## **T1- and T2-parametric mapping at 1.5 Tesla: influence of heart rates in phantom study and healthy volunteers**

M. Fenski \* (1); D. Viezzer (1); V.-A. Nguyen, (2); S. Hufnagel, (3); C. Kolbitsch, (3); J. Schulz-Menger (1)

(1) Working group on cardiovascular magnetic resonance, Charité – Universitätsmedizin Berlin, ECRC, MDC, Helios Klinikum Berlin Buch, DZHK, Berlin, Germany; (2) Working group on cardiovascular magnetic resonance, Charité – Universitätsmedizin Berlin, ECRC, MDC, Helios Klinikum Berlin Buch, DZHK, Berlin, Germany, Germany; (3) Quantitative mri, Physikalisch-Technische Bundesanstalt (PTB), Braunschweig and Berlin, Berlin, Germany

### **Abstract**

**Background:** T1 and T2 parametric mapping sequences are increasingly used in cardiac MRI for tissue characterization in various disease entities. Several technical and biological factors confounding quantification results have been described.

**Aim:** To evaluate the impact of heart rate on T1 and T2 mapping sequences using the T1MES phantom and healthy volunteers.

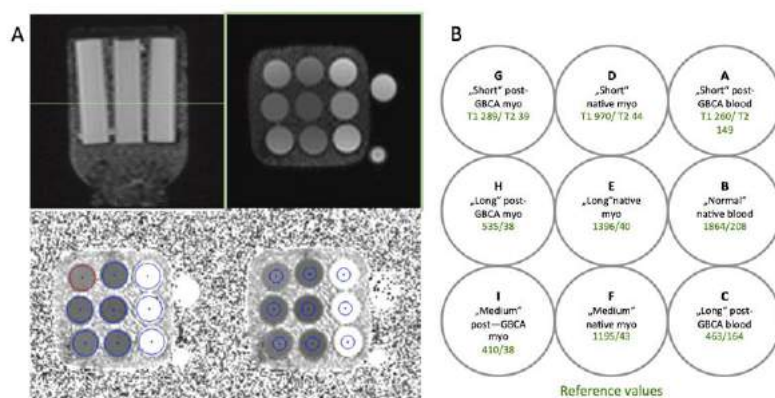
**Methods:** All CMR studies were performed on a 1.5 Tesla scanner (Magnetom AvantoFit, Siemens Healthcare) equipped with a 32-channel cardiac coil. We conducted an in-vitro study using the T1MES Phantom (Fig. 1) and a retrospective analysis of healthy volunteer data, obtained between 2013 and 2021 in our center. For the in vitro study 3 parametric mapping sequences (T1-MOLLI 5(3)3) [IR-preparation, readout: bSSFP, voxel-size: 1.4 x 1.4 mm, TR: 3.9 ms, TE: 1.13 ms; FA: 35°, FOV: 270 x 360 mm], T2prep-bSSFP [T2-preparation 0, 25, 55 ms, voxel-size: 1.6 x 1.6 mm, TR 3.1 ms, TE: 1.15 ms, FA: 70°, FOV: 270 x 360 mm] and T2- spoiled gradient echo readout [sGRE] [T2-preparation 0, 25, 55 ms, voxel-size: 1.6 x 1.6 mm, TR: 5.6 ms, TE 2.97 ms, FA: 15°, FOV: 270 x 360 mm]) were consecutively acquired in sinus rhythm with heart rates of 60 to 130 bpm in steps of 10 bpm. For ECG simulation we used an external commercial device (ES 300, SPI electronics). For healthy volunteers a multiple linear regression model was used to assess the impact of different factors on T1 and T2 times. Following variables were included: age, gender, heart rate and excluded backwards if not significant. Heart rate dependency in in-vitro measurements was tested using linear regression and Spearman's correlation.

**Results:** For tubes representing medium and long myocardial T1 properties measured T1 and T2 values correlated strongly with heart rate (see Figure 2). In these tubes higher heart rates caused a significant decrease in T1 and T2 values. Regarding all tubes, the normalized slope of the (T1 or T2)/ heart rate regression equation did correlate strongly with reference T1 values (T2-bSSFP:  $r = -.99$ ,  $p < .01$ ; T2-sGRE:  $r = -.95$ ,  $p < .01$ ; T1-MOLLI:  $r = -.83$ ,  $p <$

.01), i.e. higher T1-reference values caused an increasingly negative slope. For the in-vivo study we identified 62 healthy volunteer datasets (42 female; median age 35 [19-70]) with basal and midventricular short axis native T1-MOLLI 5(3)3 and T2-bSSFP images. Heart rate [bpm] (median 68 [IQR 62-76]; [Min-Max] 41-107) did not correlate significantly with septal T1 or T2 values when adjusting for gender and age (T1:  $p \geq .14$ ; T2:  $p \geq .26$ ). See Figure 3 for correlation between heart rate and T1 or T2 values.

Conclusion: T1-MOLLI, T2-bSSFP and T2-sGRE sequences did show a significant heart rate dependency in-vitro that is strongly correlated to longitudinal relaxation times of the tissue. Although no heart rate dependency in our in-vivo study could be shown, caution should be applied in patients with high heart rates because subtle T1 or T2 increases may disappear as shown in our in-vitro study. In future studies a stronger correlation might be observed when including a cohort with a wider heart rate range.

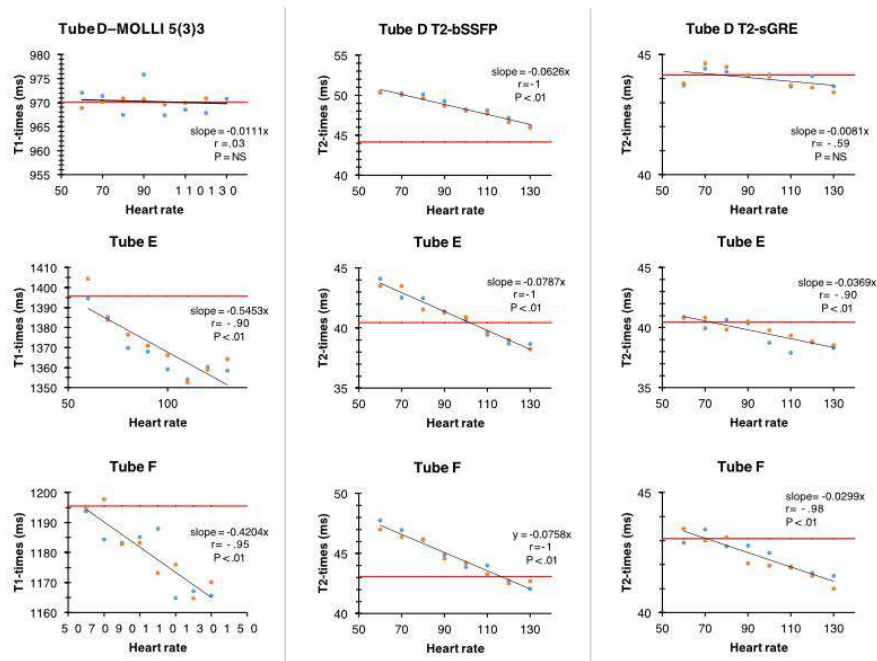
**Figure/Table 1**



**Caption 1**

(A) Nine ROIs were placed in the middle of each tube in the first mapping image. The diameter was halved to occupy the central 50% by area. ROIs were automatically forwarded onto every subsequent image. (B) Reference values for T1/T2 obtained with a slow inversion recovery (IR) spin echo and multi-echo spin echo technique.

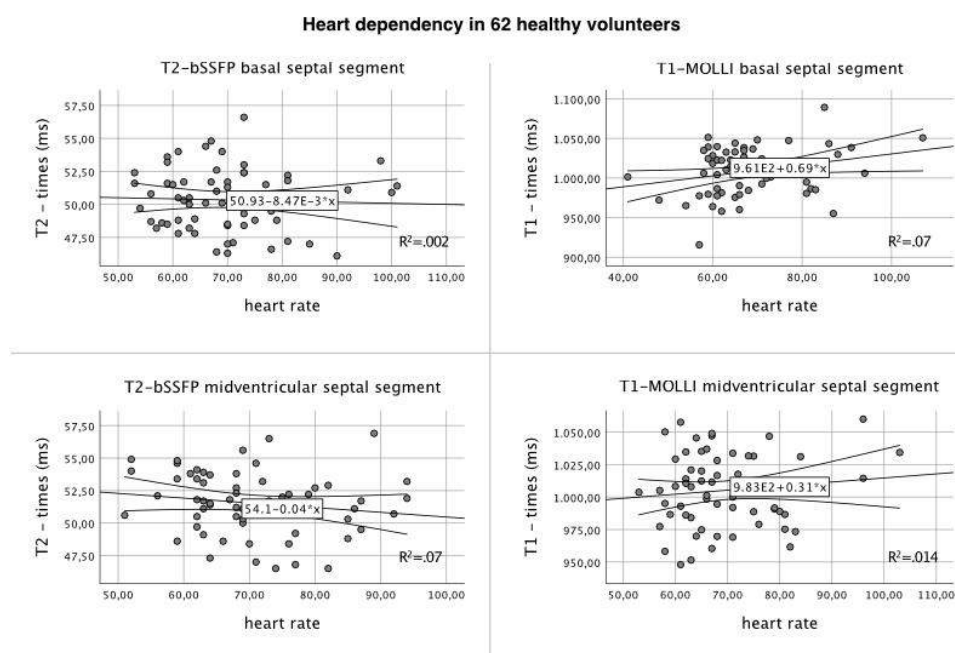
**Figure/Table 2**



**Caption 2**

2 Heart rate dependency for tubes representing short, long and medium (top to bottom) native myocardial T1 values, T1 | T2-times (ms) assessed by T1-MOLLI 5(3)3, T2prep-bSSFP and T2prep-sGRE, blue dots = 1st measurement, orange dots = 2nd measurement, black line: regression line for the mean value, red line: reference T1 or T2

**Figure 3**



### **Caption 3**

Dependency between heart rate and T1 | T2 times per basal and midventricular septal segment, assessed by T1-MOLLI 5(3)3 and T2prep-bSSFP, shown are linear regression line and 95% confidence interval; heart rate did not correlate significantly with septal T1 or T2 values when adjusting for gender and age (T1:  $p \geq .14$ ; T2:  $p \geq .26$ )

### **Bibliographic References**

Captur G, Gatehouse P, Keenan KE, Heslinga FG, Bruehl R, Prothmann M, et al. A medical device-grade T1 and ECV phantom for global T1 mapping quality assurance - the T1 Mapping and ECV Standardization in cardiovascular magnetic resonance (T1MES) program. J Cardiovasc Magn Reson [Internet]. 2016;18(1):1–20. Available from: <http://dx.doi.org/10.1186/s12968-016-0280-z>

Speaker: M. Fenski

Category: Mapping Techniques, Tissue Characterization, Tachycardia



000094

## Hospitalized patients with Covid-19 and bacterial sepsis have similar T1 and T2 abnormalities on CMR

M. Shanmuganathan \* (1); R. Kotronias, (2); M. Burrage, (1); A. Banerjee (3); A. Borlotti (2); M. Emfietzoglou (2); C. Xie (1); F. Marin (2); B. Raman (4); A. Menzter (5); P. Manley (3); A. Fletcher (3); E. Tunnicliffe (1); S. Neubauer (1); S. Piechnik (1); K. Channon (2); V. Ferreira (1)

(1) Division of cardiovascular medicine, Oxford Centre for Magnetic Resonance (OCMR), Headington, United Kingdom; (2) Division of cardiovascular medicine, University of Oxford, Oxford, United Kingdom; (3) Radcliffe department of medicine, University of Oxford, Oxford, United Kingdom; (4) Division of cardiovascular medicine, Oxford Centre for Magnetic Resonance (OCMR), Oxfordshire, United Kingdom; (5) Nuffield department of medicine, Wellcome Centre for Human Genetics, Oxford, United Kingdom

### Abstract

**Background:** High prevalence of cardiac abnormalities on cardiovascular magnetic resonance imaging (CMR) have been reported at 3-6 months after COVID-19 illness (1,2). However, a more recent case-control study found no excess in CMR abnormalities in healthcare workers with mild COVID-19 at 6 months (3). These discrepancies may relate to heterogeneity in the severity of COVID-19, prevalence of past cardiac disease, scan methodologies and lack of control groups. We aimed to assess if these abnormalities were present during the acute illness and if they differ from hospitalized patients with bacterial sepsis.

**Method:** We conducted a prospective study of 50 participants in three cohorts: 1) patients hospitalized for COVID-19 (n=24); 2) patients hospitalized for bacterial sepsis (n=7); and 3) asymptomatic controls with cardiovascular risk factors (n=19). Ethics approval was obtained and all participants gave written informed consent. Exclusion criteria included known cardiac disease, previous COVID-19 illness (verified on antibody testing), COVID-19 vaccination and hemodynamic or respiratory instability. COVID-19 severity was graded on the World Health Organization four-point scale on chest imaging (4). All patients underwent CMR (Siemens 3T) during hospital treatment for their acute illness, including slice-matched cine, native T1-mapping (ShMOLLI), T2-weighted imaging, extracellular volume (ECV) quantification, and late gadolinium enhancement (LGE) imaging.

**Results:** Baseline characteristics showed no significant difference in age, sex, and risk factors among the three groups (Table 1). 66% of COVID-19 patients had  $\geq$  grade 2 severity. In the sepsis cohort, 3 patients had pneumonia, 2 had cellulitis and 2 had urinary tract infections. Elevated Troponin was present in 9 (38%) patients with COVID-19 and 1 (17%) with sepsis. All three groups had similar LVEF, RVEF, ECV fraction and frequency of LGE abnormalities. Two participants each from the COVID-19 (8%), sepsis (28%), and control (11%) cohorts had non-ischemic LGE, whilst one each from the COVID-19 and control groups had myocardial infarction.

Global myocardial T1 and T2 ratio (myocardial vs skeletal muscle signal intensity) were significantly higher in patients with sepsis (1253±50 ms, 1.53±0.33) and COVID-19 (1217±40 ms, 1.45±0.36) compared to controls (1182±22 ms, 1.13±0.09) (all  $p < 0.05$ ), with no significant differences between the COVID-19 and sepsis groups (Figure 1). 11/31 (35%) patients from the combined COVID-19 and sepsis cohorts had an abnormally high global T1 (>2SD normal range); these patients had significantly higher LVEF (68±8% vs 62±5%,  $p=0.04$ ), suggesting a more hyperdynamic state. There were no significant differences in ECV among the three groups.

**Conclusion:** In this prospective study, patients with acute moderate-severe COVID-19 requiring hospitalization had similar acute cardiac findings on CMR compared to patients with other sepsis; both groups showed similar biventricular function and frequency of abnormal LGE, but significantly higher myocardial T1 and T2 when compared to outpatient controls with risk factors. These changes may be due to myocardial edema, inflammation or increased MBV during a septic illness. The clinical significance of imaging findings in patients with acute COVID-19 can depend on imaging techniques and should be interpreted within the clinical context and in reference to appropriate control groups. Larger follow-up studies will provide more insights into the longer-term impact of acute imaging findings in survivors of COVID-19.

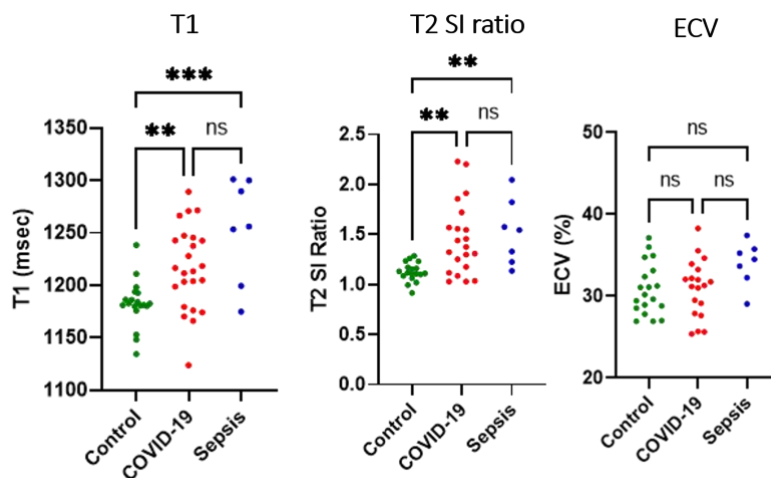
**Figure/Table 1**

	Control (n=19)	COVID-19 (n=24)	Sepsis (n=7)	P
<b>Demographics</b>				
Age (years)	57±12	57±15	56±15	0.987
Gender (Male %)	63	71	57	0.774
Ethnicity (White Caucasian %)	74	71	86	0.907
Past history of cardiac disease	0	0	0	1
Smoker (%)	11	42	14	0.054
Diabetes (%)	0	8.3	14	0.257
Hypertension (%)	16	33	43	0.314
COPD/Asthma (%)	0	21	29	0.042
<b>Vital signs*, blood test results* and hospital treatment (* - most abnormal results for hospitalized participants)</b>				
Temperature	37.13±0.5	37.96±0.71 <sup>a</sup>	38.21±0.69 <sup>a</sup>	<0.001
Oxygen saturation (%)	97.37±1.8	90.29±4.57 <sup>a</sup>	94±2.7	<0.001
Systolic blood pressure (mmHg)	136±16	103±22 <sup>a</sup>	101±21 <sup>a</sup>	<0.001
Heart rate (bpm)	67±7	97±17 <sup>a</sup>	108±12 <sup>a</sup>	<0.001
White blood cell count (10 <sup>9</sup> /L)	5.63±1.9	7.74±4.8 <sup>b</sup>	12.03±4.5 <sup>a</sup>	0.004
Lymphocyte count (10 <sup>9</sup> /L)	1.74±0.69	0.70 (0.49-1.07) <sup>a</sup>	1.35±0.57	0.011
Haematocrit	0.43±0.03	0.40±0.04 <sup>b</sup>	0.38±0.04 <sup>a</sup>	0.012
D-dimer (ng/ml)	227 (167-447)	1690 (778-33323) <sup>a</sup>	1230 (727-2976) <sup>a</sup>	<0.001
Ferritin (pg/ml)	94 (52-407)	522 (353-2071) <sup>a</sup>	393 (283-858)	0.001
C-reactive protein (mg/L)	1 (0.69-4.10)	122 (65-221) <sup>a</sup>	218 (109-318) <sup>a</sup>	<0.001
Troponin-I (ng/ml)	1.99 (1.99-6)	10 (5-384) <sup>a,b</sup>	1.99 (1.99-638)	<0.001
Elevated Troponin (>34ng/ml) (%)	0	38 <sup>a</sup>	14	0.004
NT-pro-BNP (pg/ml) (normal <400)	53 (25-334)	223 (70-1264) <sup>b</sup>	167 (54-421)	0.002
COVID-19 severity score ≥2 on CT	N/A	66	N/A	N/A
Pulmonary embolism diagnosed (%)	N/A	17	0	0.550
Treatment with steroids (%)	N/A	54	0	0.025
Treatment with Remdesivir (%)	N/A	46	0	0.033
Treatment with antibiotics (%)	N/A	71	100	0.161
Non-invasive or invasive ventilation (%)	N/A	21	0	0.562
<b>CMR findings</b>				
Time of CMR scan after admission (days)	N/A	3.5 (1-7)	2 (2-3)	0.502
Heart rate during scan (bpm)	67±7	72±15	76±15	0.245
LV ejection fraction (%)	62±7	65±6	63±7	0.550
RV ejection fraction (%)	60±6	58±6	60±5	0.632
Global T1 (ms)	1182±22	1217±40 <sup>a</sup>	1253±50 <sup>a</sup>	0.001
Elevated T1 (>1244ms, >mean+2SD in healthy subjects in 3T) n (%)	0 (0)	6 (25) <sup>a</sup>	5 (71) <sup>a</sup>	<0.001
T2 Signal intensity ratio (T2SI)	1.13±0.09	1.45±0.36 <sup>a</sup>	1.53±0.33 <sup>a</sup>	0.001
Global Extra cellular volume (ECV) (%)	31±3	31±4	34±3	0.080
Presence of pathological LGE# n (%)	3 (16)	3 (13)	2 (28)	0.621
Presence of Ischaemic LGE n (%)	1 (5)	1 (4)	0 (0)	
Presence of non-ischaemic LGE n (%)	2 (11)	2 (9)	2 (28)	0.678

## Caption 1

Baseline demographics, vital signs and blood test results (\*worst values during hospitalization), treatment administered and CMR findings. One-way ANOVA, Kruskal-Wallis test or Fisher's exact test was performed where appropriate a - statistical comparison with control cohort, b -comparison with COVID-19 cohort,  $p < 0.05$ .

## Figure/Table 2



## Caption 2

T1 values, extracellular volume fraction (ECV%) and T2 signal intensity (T2SI) ratio were obtained from ShMOLLI T1-maps and T2 weighted images offering full heart coverage. Key: \*\*\* =  $p < 0.001$ , \*\* =  $p < 0.01$ , ns = non-significant  $p \text{ value} \geq 0.05$ .

## Bibliographic References

4. World Health Organization. (2020). Use of chest imaging in COVID-19: a rapid advice guide, 11 June 2020. <https://apps.who.int/iris/handle/10665/332336> (accessed 24/5/2021), 3.
- Joy G, Artico J, Kurdi H, et al. Prospective Case-Control Study of Cardiovascular Abnormalities 6 Months Following Mild COVID-19 in Healthcare Workers. JACC Cardiovasc Imaging. 2021 May 5:S1936-878X(21)00356-9., 2.
- Friedrich MG, Cooper LT. What we (don't) know about myocardial injury after COVID-19. Eur Heart J. 2021 May 14;42(19):1879-1882, 1.
- Kim JY, Han K, Suh YJ. Prevalence of abnormal cardiovascular magnetic resonance

findings in recovered patients from COVID-19: a systematic review and meta-analysis.  
Journal of Cardiovascular Magnetic Resonance. 2021 Sep 3;23(1):100

Speaker: M. Shanmuganathan

Category: Native T1, T2, Inflammation

000095

## Mitral Regurgitation Flow Assessment Using 4D flow MRI: Impact of Fluid Dynamics

J. Lee \* (1); A. Gupta (1); L. Ma (1); O. Mason (2); E. Wu (2); J. Thomas (2); M. Markl (1)

(1) Radiology, Northwestern University Feinberg School of Medicine, Chicago, United States of America; (2) Cardiology, Northwestern Memorial Hospital, Chicago, United States of America

### Abstract

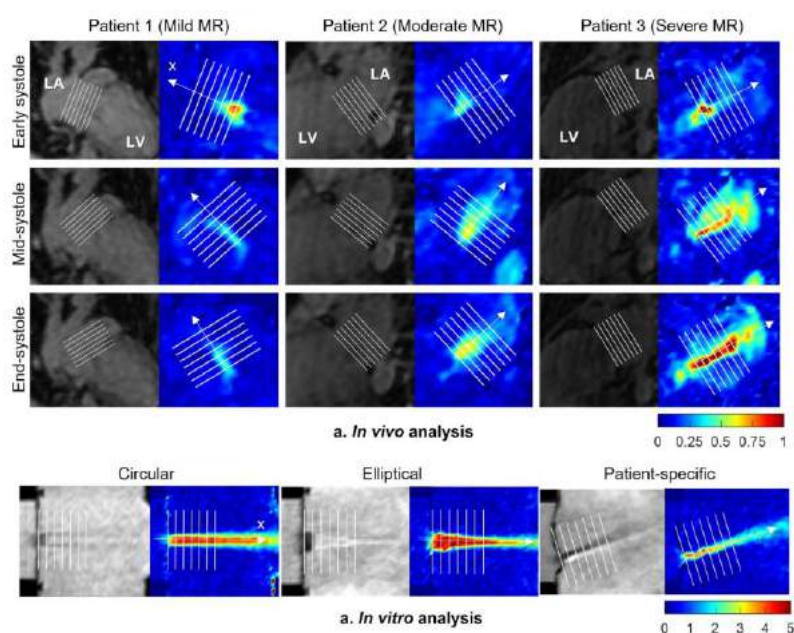
**Background:** Severe mitral regurgitation (MR) is associated with decreased survival but early surgical or minimally invasive repair has been shown to improve prognosis.[1-3] Accurate assessment of MR severity is thus important but is hindered by the dynamic and complex morphology of high-velocity MR flow jets. CMR can quantify MR using an indirect approach by subtracting aortic forward flow volume from the left ventricular stroke volume to quantify regurgitant volume (RVol), a measure of the disease severity.[4] However, its application is limited when multiple valvular regurgitation or cardiac shunts are present. 4D flow MRI, on the other hand, enables the direct measurement of RVol by retrospective tracking of the MR flow jet. However, jet flow volume is known to increase as the jet travels downstream due to flow entrainment effect indicating that directly quantified RVol can be overestimated depending on the measurement location along the jet. In addition, fluid dynamics theory predicts that jet momentum remains constant throughout the jet and is determined by the flow rate  $\times$  velocity at the orifice, providing a metric to characterize MR flow free from the location constraint. The goal of this study was to employ in-vitro and in-vivo 4D flow MRI to systematically investigate 1) the impact of flow entrainment on RVol estimation accuracy and 2) the feasibility of momentum for MR jet flow characterization.

**Methods:** Three patients with mild, moderate and severe MR underwent prospectively ECG gated 4D flow MRI (spatial resolution=2.4–2.5 x 2.4–2.5 x 2.6–3.0 mm<sup>3</sup>, encoding velocity=150 cm/s, TR=4.7 ms, TE=2.4 ms, temporal resolution=37.6 ms, flip angle=7–15°, Siemens Avanto 1.5 T). In-vitro pulsatile MR-mimicking flow jets (RVol = 46–60 ml/beat, 4–6 m/s peak velocity) were generated using a circular, elliptical and patient-specific MR orifices (figure 1b). Retrospectively-gated 4D flow MRI was performed for the in-vitro flow jets (1.5 mm isotropic voxel, velocity encoding=500 cm/s, TR=4.7–5.0 ms TE=1.93–2.16 ms, flip angle=12°, temporal resolution=37.2–39.2 ms, Siemens Sola 1.5T). Cross-sectional flow rate and momentum of MR flow jets were quantified along the jet at various distances from the orifice, ( $x=0$  to 30 mm) (figure 1) and integrated over time to calculate jet flow volume and momentum-time-integral (MTI). For in-vivo flow analysis, the 2D plane orientations were readjusted manually following the jet movement.

**Results:** Jet flow volume in patients with moderate and severe MR linearly increased with the axial distance ( $R^2=0.81–0.86$ ,  $p<0.005$ ) while mild MR remained steady throughout the jet (Figure 2a). In-vitro flow jets also demonstrated a linear increase in flow volume with the axial distance ( $R^2=0.85–0.96$ ,  $p<0.005$ ) (Figure 2b). Flow volumes quantified close to the orifice ( $x\leq 5$  mm) were comparable to RVol, while in-vitro analysis revealed underestimation of RVol at the orifice ( $x=0$ ), likely due to partial volume effects. MTI of moderate and severe MR patients (Figure 3a) and all in-vitro flow jets (Figure 3b) demonstrated no consistent increase with the axial distance but rather a fluctuation around a mean at  $5\leq x\leq 30$  mm.

Conclusion: We demonstrated that downstream from the valve, MR jet flow volume overestimates RVol due to flow entrainment, while underestimation occurs at the orifice due to partial volume effects. RVol prediction accuracy appears to be optimal at 5 mm from the valve. On the other hand, MTI was much less sensitive to the location due to momentum conservation of a jet suggesting that MTI could be a reliable jet flow metric to characterize MR flow using 4D flow MRI.

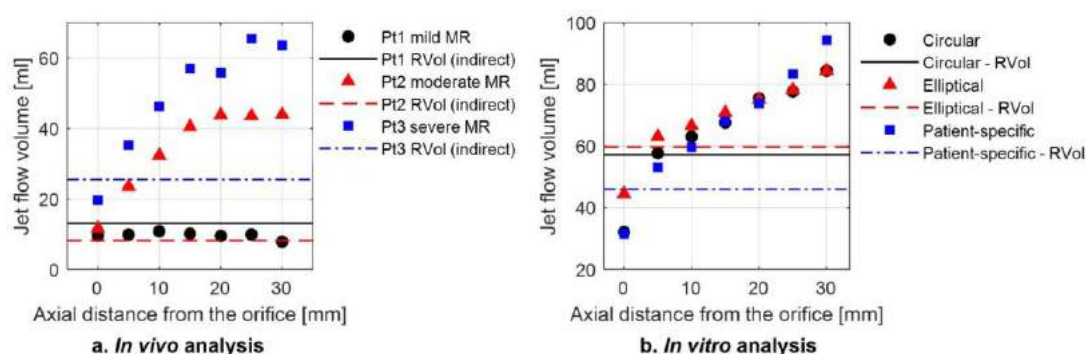
**Figure/Table 1**



**Caption 1**

Figure 1. A schematic illustration of MR flow jet analysis. Signal magnitude (left) and flow velocity images (right) are shown. White lines indicate 2D flow analysis planes along the jet axis, x. (a) In-vivo MR flow jet of three patients at early, mid and end-systole. (b) in-vitro flow jets through a circular, elliptical and patient-specific MR orifice models.

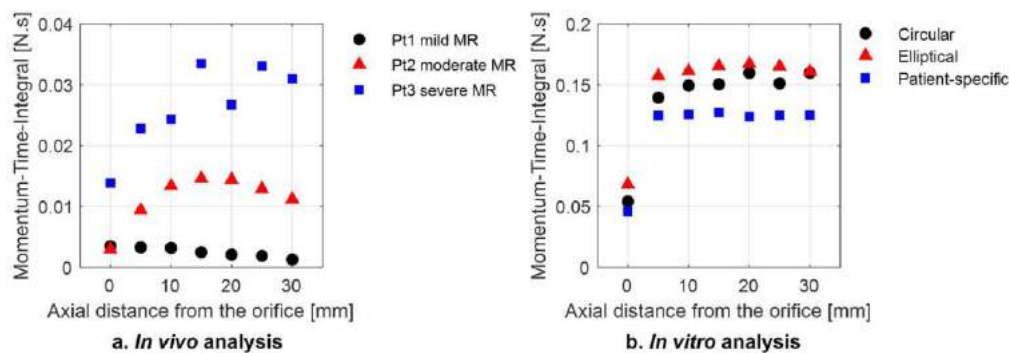
**Figure/Table 2**



## Caption 2

Figure 2. Flow volume as a function of quantification distance from the orifice along the jet axis. (a) in-vivo analysis of patients with mild, moderate, severe MR and comparison with indirectly measured RVol by 2D CMR sequences. (b) In-vitro analysis of a circular, elliptical and patient-specific orifice flow jet, and comparison with a ground-truth RVol.

## Figure 3



## Caption 3

Figure 3. Momentum-time-integral against quantification distance from the orifice along the jet axis. (a) in-vivo analysis of an MR flow jet in patients with mild, moderate, severe MR. (b) In-vitro analysis of circular, elliptical and patient-specific orifice flow jet.

## Bibliographic References

4. Zoghbi WA, Adams D, Bonow RO, Enriquez-Sarano M, Foster E, Grayburn PA, et al. Recommendations for noninvasive evaluation of native valvular regurgitation: a report from the American Society of Echocardiography developed in collaboration with the Society for Cardiovascular Magnetic Resonance. *J Am Soc Echocardiogr.* 2017;30(4):303-371., 3. Rossi A, Dini FL, Faggiano P, Cicoira M, Frattini S, Simioniuc A, et al. Independent prognostic value of functional mitral regurgitation in patients with heart failure. A quantitative analysis of 1256 patients with ischaemic and non-ischaemic dilated cardiomyopathy. *Heart.* 2011;97(20):1675-1680., 2. Enriquez-Sarano M, Avierinos J-F, Messika-Zeitoun D, Detaint D, Capps M, Nkomo V, et al. Quantitative determinants of the outcome of asymptomatic mitral regurgitation. *N Engl J Med.* 2005;352(9):875-883., 1. Otto CM, Nishimura RA, Bonow RO, Carabello BA, Erwin III JP, Gentile F, et al. 2020 ACC/AHA guideline for the management of patients with valvular heart disease: a report of the American College of Cardiology/American Heart Association Joint Committee on Clinical Practice Guidelines. *J Am Coll Cardiol.* 2021;77(4):e25-e197.

Speaker: J. Lee

Category: 4D Flow, Mitral Regurgitation, Valvular Heart Disease



000097

## A Rare Cause of Acute Chest Pain in a Healthy Young Man

M. J. Rafiee \* (1); M. Khaki (2); L. Haririsanati (2); F. Babaki (3); M. Chetrit (4)

(1) Research institute, cardiovascular imaging service, McGill University Health Centre Glen Site (MUHC), Montreal, Canada; (2) Faculty of medicine and health sciences, McGill University, Montreal, Canada; (3) Medicine, University of Montreal, Montréal, Canada; (4) Research institute, cardiovascular imaging service, McGill University Health Centre Glen Site (MUHC), Montréal, Canada

### Abstract

#### Clinical presentation:

An otherwise healthy 37-year-old man presented to the emergency department (ED) with sudden-onset pleuritic chest pain in his right anterior lower chest radiating to the upper abdomen. The symptoms started a day before presentation after a powerlifting training session (graded 6/10). There were no associated signs or symptoms such as fever, cough, palpitation, shortness of breath.

#### Diagnostic Techniques and Findings:

His physical exam and laboratory tests, including ECG, D-dimer, troponin I, and CRP, were unremarkable. A 1.5 T MRI revealed an encapsulated, oval-shaped, and fat-intensity nodule (18x11 mm) with a surrounding thin, low signal rim in the right epipericardial fat (**Fig. 1A,1B**). Subsegmental atelectasis of the right middle lobe (**Fig. 2A**), as well as small pleural effusion with mild focal thickening of the adjacent right cardiophrenic pleura and pericardium (**Fig. 2B**), were evident. After gadolinium injection, linear enhancement of the adjacent inflamed pleura and pericardium were observed (**Fig. 2C,2D**), suggesting inflammation. We diagnosed epipericardial fat necrosis (EPFN) based on the clinical and imaging findings.

#### Discussion and Learning points:

EPFN affects both genders equally, with an average age of 50(1). Its underlying aetiologies remain unclear (1, 2); in this patient, however, hemorrhagic necrosis due to increased intravascular pressure during the Valsalva maneuver may have played a role in the pathogenesis(1, 2). EPFN frequently involves the left side and is characterized by a sudden onset pleuritic chest pain lasting between a few hours to several days and unremarkable ECG, laboratory tests, and physical examination(1, 2). Although CT scan has been suggested as a modality of choice to detect EPFN, it has a high risk of exposure to ionizing radiation as well as a limited ability to characterize minimal focal changes in pericardial fat, leading to underdiagnosis of this pathology (2, 3). Cardiac MRI(CMR) has been approved as a robust and non-invasive imaging modality for the evaluation of acute chest pain. MRI with dedicated techniques is an accurate method to characterize adipose tissue (1, 3); it can distinguish EPFN from other fat-containing tumours in the anterior mediastinum, such as lipomas and liposarcomas (3). Having said that, CMR has remained underused for the assessment of chest pain despite recent technical advancement; only a limited number of reported cases have used MRI to confirm EPFN in adult patients (1, 3-5). Considering the MRI findings of previous EPFN cases, the most common MRI findings for acute EPFN can be 1) high signal intensity

lesion with a thin hypointense rim in T2-weighted images, 2) signal loss in the lesion in fat-suppressed images, and 3) enhancement of peripheral capsule of the lesion in contrast-enhanced images.

Overall, EPFN is an overlooked cause of acute chest pain, so clinicians must be vigilant to identify this condition after ruling out more severe causes. Besides suggestive clinical context, using cardiac MRI as a single-scan assessment may be helpful to differentiate both life-threatening and underdiagnosed self-limited causes of acute chest pain.

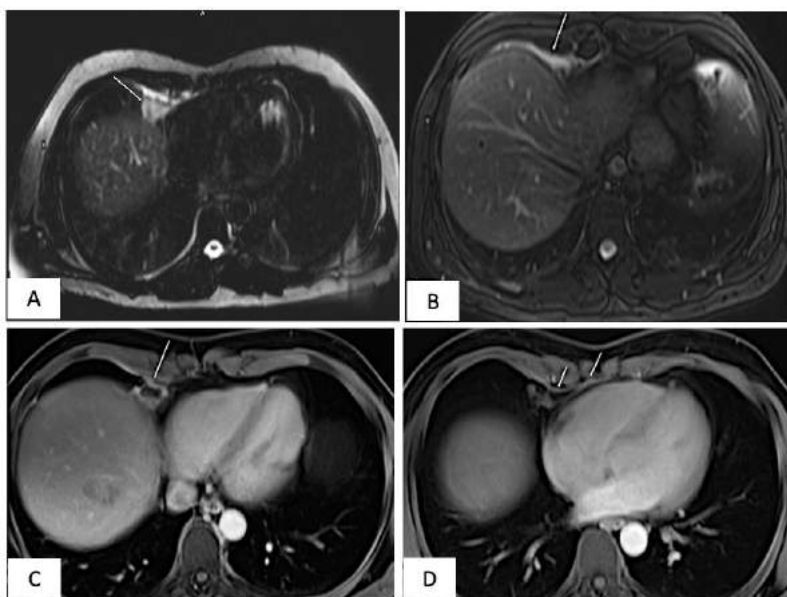
**Figure/Table 1**



**Caption 1**

(A) Coronal T1-weighted image reveals well encapsulated, high signal intensity lesion (18x11mm) with a thin surrounding hypointense rim in the right cardiophrenic space (arrow), (B1,2) Axial T1 weighted in-phase and out-of-phase images show a fat content lesion in the right cardiophrenic space by showing signal intensity loss on the out-of-phase sequence, compared to the in-phase(B2, arrow).

**Figure/Table 2**



## **Caption 2**

(A) Axial T2-weighted fat-suppressed image at the level of the right cardiophrenic space shows subsegmental atelectasis of adjacent right middle lobe, (B) Axial T2-weighted image reveals a minimal right-sided pleural effusion, (C, D) Axial T1-weighted images after Gadolinium injection at the level of the right cardiophrenic space show linear enhancement of lesion capsule and the adjacent inflamed pericardium and pleura, respectively (arrows).

Speaker: M. J. Rafiee

Category: Chest Pain, Pericardial Disease, Fat Suppression

000098

## Utility of Ferumoxytol-Enhanced Cardiac Magnetic Resonance Imaging and 3D Reconstruction in the Evaluation and Management of Complex Ventricular Septal Defects

R. Ghosh \* (1); A. Zuppa (2); C. Mascio (3); J. Chen (4); J. Rome (1); M. O'byrne (1); M. Jolley (2); K. Whitehead (1)

(1) Cardiology, Children's Hospital of Philadelphia, Philadelphia, United States of America; (2) Anesthesiology and critical care medicine, Children's Hospital of Philadelphia, Philadelphia, United States of America; (3) Cardiothoracic surgery, West Virginia University, Morgantown, United States of America; (4) Cardiothoracic surgery, Children's Hospital of Philadelphia, Philadelphia, United States of America

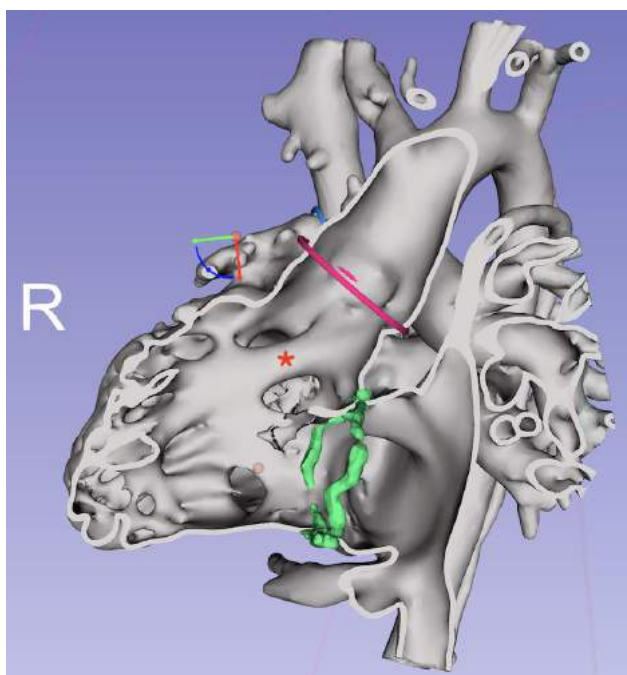
### Abstract

**Introduction:** Surgical repair of complex ventricular septal defects (VSD) can be challenging in the setting of a hypertrophied and heavily trabeculated right ventricle. Traditional imaging modalities are often inadequate to precisely delineate the location of the defect and contextualize the anatomy within the surrounding structures. Ferumoxytol is an iron-based contrast agent with a prolonged blood pool phase and delayed intracellular uptake that allows for high-spatial resolution cardiac magnetic resonance imaging (FE-CMR). We assessed the utility of FE-CMR and FE-CMR derived 3D reconstructions in the evaluation and management of patients with multiple and complex VSDs.

**Methods:** This is a retrospective observational case series of patients who underwent FE-CMR and 3D reconstruction to assess complex VSDs whose anatomy was not clear based on echocardiography, from 4/2018 – 12/2020. CMR was performed on a 1.5 Tesla scanner (*Magnetom Avanto, Siemens*) and ferumoxytol (*Feraheme, AMAG Pharmaceuticals*) was administered at 4mg/kg. Navigated cardiac gated inversion recovery FLASH sequences were gated to both systole and diastole. Segmentation and post-processing of the anatomy was performed using FDA-approved software (*Mimics Innovation Suite, Belgium*) and 3D models were visualized in virtual reality using open-source software ([www.slicer.org](http://www.slicer.org)). Baseline data on anatomic diagnoses, number and location of VSDs, prior procedures and management plan were collected. Primary outcome was a change in anatomic VSD diagnoses after FE-CMR. Secondary outcomes were a change in procedural management plan based on 1) FE-CMR data alone 2) visualization of 3D anatomy.

**Results:** There were 12 patients with a median age of 5.5 months (3, 13.7) who underwent FE-CMR for complex VSDs. Of those, 9 had concomitant congenital heart disease (obstructive left-sided lesions n=3; conotruncal abnormality n=3; other n=3). Four had prior attempts at surgical closure, 3 of whom required post-operative extracorporeal membrane oxygenation (ECMO) support. After FE-CMR, 11 (92%) had a change in anatomic VSD diagnosis. Change in procedural management occurred in 9 patients (75%), 4 based on FE-CMR alone.

**Conclusions:** FE-CMR enables detailed evaluation of multiple VSDs and can reliably elucidate their size, location, and the surrounding anatomic context. The information derived from FE-CMR 3D visualization allows for comprehensive assessment of patient-specific



## Caption 2

STLs of patient-specific anatomy viewed digitally from the right ventricular side of the defect. Star = Muscle bundle within VSD; Pink = Aortic Annulus; Green = Tricuspid Annulus

## Figure 3



## Caption 3

Figure 3a) Intraoperative view of the muscle bundle within the VSD and 3b) after the muscle bundle was excised.

Speaker: R. Ghosh

Category: 3D, Ferumoxylol, Congenital Heart Disease

000099

## Dynamic Pressure-Volume Loop Analysis using Real-Time MRI during Inferior Vena Cava Occlusion

F. Seemann \* (1); J. M. Kahn, (1); R. Ramasawmy, (1); C. G. Bruce, (1); D. Herzka (1); A. Jaimes (1); W. H. Schenke (1); K. O'Brien (1); R. Lederman (1); A. Campbell-Washburn (1)

(1) Cardiovascular branch, National Heart, Lung, and Blood Institute, National Institutes of Health, Bethesda, United States of America

### Abstract

**Background.** Left ventricular (LV) contractility and compliance are valuable parameters to evaluate cardiac function and impact of intervention. Contractility and compliance can be derived from dynamic recordings of LV pressure-volume (PV) loops during inferior vena cava (IVC) occlusion to alter preload. However, the conductance PV loop catheters used in a traditional catheterization lab require extensive calibration and provide unreliable volume measurements (1,2). We propose a method to quantify contractility and compliance from dynamic PV loops using simultaneous measurements of pressure from an LV catheter and volume from real-time MRI during IVC occlusion.

**Methods.** Dynamic preload alteration with abrupt IVC balloon inflation within the MRI scanner was performed in 10 pigs, to derive load independent measures of LV performance. Four pigs were naïve, and six were examined 30 days post transcatheter aortic banding, in an attempt to increase afterload. Real-time long-axis 4-chamber CMR cine images were acquired at breath-hold with a bSSFP sequence ( $TE/TR/\theta = 1.4\text{ms}/77\text{ms}/80^\circ$ ,  $2.3 \times 2.3 \times 6\text{mm}$  reconstructed resolution,  $360 \times 270\text{mm}$  FOV, acceleration rate 3,  $76\text{ms}$  temporal resolution, 326 timeframes) on a high-performance 0.55T MRI system (prototype MAGNETOM Aera, Siemens) (3). Conventional breath-held short-axis cine images were acquired for volume validation. A Physiological Recording in MRI Environment (PRiME) system that filters MRI-induced noise (4) to record six lead ECG, LV and aortic pressures, and MRI gradient waveforms, with  $1\text{kHz}$  sampling frequency. Images and PRiME recordings were acquired simultaneously prior to and during IVC occlusion.

Time-resolved 2D LV segmentation was performed, from which a 3D LV volume was derived using center line rotation. End diastole (ED) and end systole (ES) were automatically detected in each heartbeat. Long-axis 3D volumes in the first recorded heartbeat were validated with a short-axis 3D volumes at ED and ES. Pressure and ECG were temporally aligned with imaging using the recorded MRI gradient waveforms, with ED detected from the ECG R-wave peak and ES from the dicrotic notch in the aortic pressure. PV loops were derived by pairing synchronized pressure and volume curves based on ED and ES detections (Figure 1). Linear ES and ED PV relations (ESPVR, EDPVR) were derived from the first ten PV loops, to avoid autonomic tone impact on inotropy and loading conditions. Contractility was defined as the ESPVR slope, and compliance was as the inverse of the EDPVR slope. Average isovolumic relaxation constant  $\tau$ ,  $dP/dt$  max, and  $dP/dt$  min were reported.

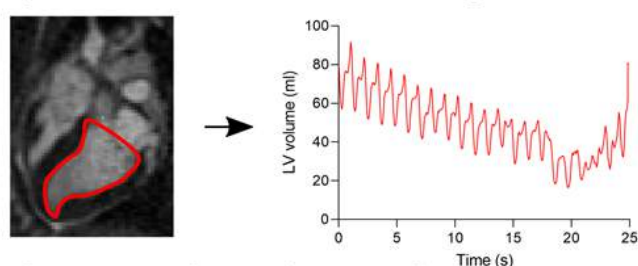
**Results.** Real time invasive LV pressure and 4-chamber volume acquisition during IVC occlusion was feasible in the MRI scanner, and PV loops were derived in all experiments. Example PV loops and corresponding ESPVR and EDPVR are shown in Figure

2. The pressure gradient across the aortic band was  $10 \pm 6$  mmHg, which was considered modest and not clinically significant. Correspondingly, there were no differences between the naïve pigs and banded model in contractility, compliance, tau,  $dP/dt$  max, and  $dP/dt$  min (Figure 3). Difference in long-axis vs short axis volumes were  $9.0 \pm 8.9$  ml at ED, and  $-5.2 \pm 7.4$  ml at ES.

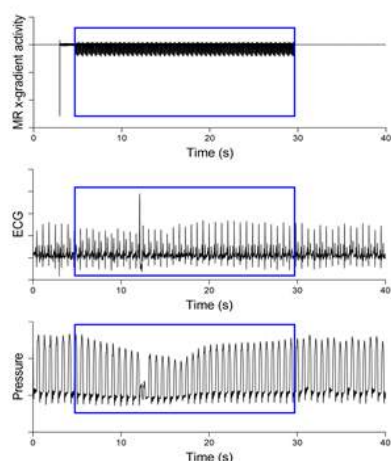
**Conclusion.** Dynamic PV loops during a real-time MRI guided IVC occlusion can be used to derive quantitative metrics of LV contractility and compliance. An animal model with clinically significant alterations in cardiac function is warranted to determine if this technique can detect changes in contractility and compliance.

**Figure/Table 1**

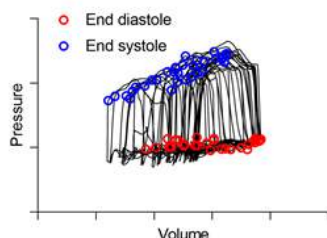
**A) LV volume from 4-chamber MR image**



**B) LV pressure from PRiME recording**



**C) Pair pressure and volume signals**



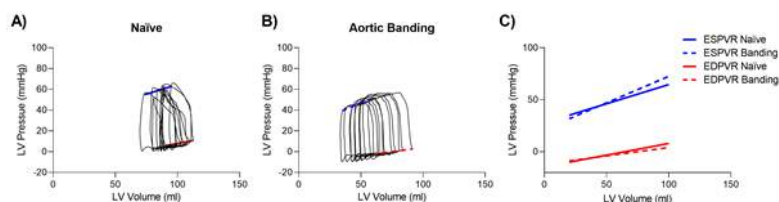
**Caption 1**

Dynamic PV loops were acquired during IVC occlusion. A) 3D LV volume was derived from long-axis segmentations. B) Pressure and ECG recorded simultaneously to imaging were



detected from the MRI gradient activity (blue rectangles). C) PV loops were derived by pairing pressure and volume. ESPVR and EDPVR were derived from ED (red) and ES (blue).

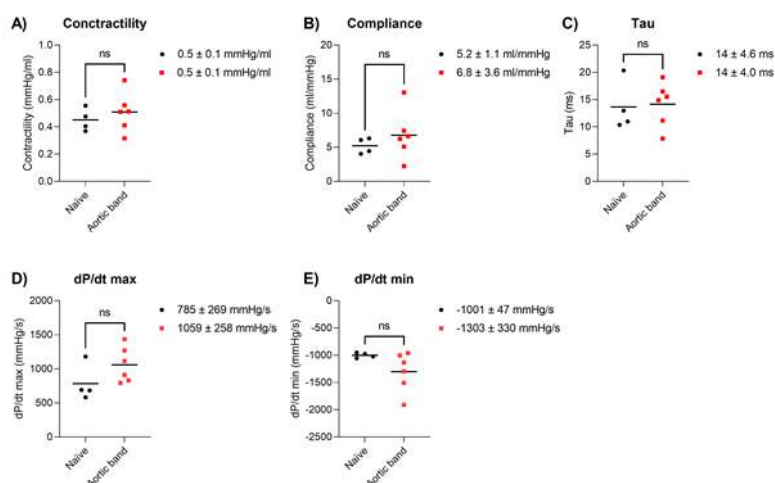
**Figure/Table 2**



**Caption 2**

Examples of ten derived PV loops (black) with corresponding ESPVR (blue) and EDPVR (red) lines in **A)** a naïve pig and **B)** a pig 30 days post aortic banding. **C)** Combined ESPVR and EDPVR from naïve and banded pigs in **A)** and **B)**, which due to the modest pressure gradient over the aortic banding were similar in both cases.

**Figure 3**



**Caption 3**

Comparison of **A)** contractility, **B)** compliance, **C)** tau, **D)** maximum dP/dt, and **E)** minimum dP/dt at baseline and 30 days post aortic banding. Naïve and banded models were unpaired. ns, non-significant.

## **Bibliographic References**

Acknowledgement. We would like to acknowledge the assistance of Siemens Healthcare in the modification of the MRI system for operation at 0.55T under an existing cooperative research agreement (CRADA) between NHLBI and Siemens Healthcare., 1. Burkhoff D. The conductance method of left ventricular volume estimation. Methodologic limitations put into perspective. *Circulation* 1990;81(2):703–6. Doi: 10.1161/01.CIR.81.2.703., 2.

Kuehne T., Yilmaz S., Steendijk P., et al. Magnetic Resonance Imaging Analysis of Right Ventricular Pressure-Volume Loops. *Circulation* 2004;110(14):2010–6. Doi: 10.1161/01.CIR.0000143138.02493.DD., 3. Campbell-Washburn AE., Ramasawmy R., Restivo MC., et al. Opportunities in Interventional and Diagnostic Imaging by Using High-Performance Low-Field-Strength MRI. *Radiology* 2019;293(2):384–93. Doi: 10.1148/radiol.2019190452., 4. Kakareka JW., Faranesh AZ., Pursley RH., et al. Physiological Recording in the MRI Environment (PRiME): MRI-Compatible Hemodynamic Recording System. *IEEE J Transl Eng Heal Med* 2018;6:1–12. Doi: 10.1109/JTEHM.2018.2807813.

Speaker: F. Seemann

Category: Interventional CMR, Real Time, Physiological monitoring

000100

## Regional myocardial contractility for early detection of radiation effect on the heart: a preclinical study

E.-S. Ibrahim \* (1); S.-A. Brown, (2); L. Frank, (1); J. Stojanovska (3); J. Baker, (4); C. Bergom (5)

(1) Department of radiology, Medical College of Wisconsin, Milwaukee, United States of America; (2) Department of medicine, Medical College of Wisconsin, Milwaukee, United States of America; (3) Department of radiology, New York University, New York, United States of America; (4) Department of surgery, Medical College of Wisconsin, Milwaukee, United States of America; (5) Department of radiation oncology, Washington University in St. Louis, St. Louis, United States of America

### Abstract

**Background:** With increased rates of lung cancer survival, cardiovascular toxicity has become a major cause of mortality in lung cancer patients. Radiation therapy (RT) plays an integral role in treating advanced lung cancer, despite high incidence of RT-induced cardiovascular diseases. The current paradigm for cardiac function assessment and management of cardiovascular disease relies primarily upon the assessment of ejection fraction (EF). However, EF alone is limited in both its diagnostic and prognostic ability, as ventricular remodeling could compensate for regional cardiac dysfunction to maintain normal EF. In this study, we investigated the capability of advanced CMR parameters of heart mechanics for early detection of RT-induced cardiotoxicity in a rat model of lung cancer, with end goal to help with risk stratification and treatment management to avoid cardiovascular complications.

**Methods:** Adult salt-sensitive rats, which have been previously shown to be sensitive to cardiovascular injury, received whole-heart radiation to 24 Gy using 3 equally-weighted fields with an X-RAD SmART Irradiator. The rats were imaged on a small-animal 9.4T Bruker MRI scanner using a 4-element surface coil at 8- and 10-weeks post-RT and the results compared to sham irradiated rats (n=18). The optimized CMR exam included cine and tagging images covering the heart. The CMR images were analyzed using cvi42 software to measure EF and using the InTag package to measure regional peak systolic strain, based on which the percentage of normally contracting myocardium (*Contractility-Index*) was determined based on the AHA 17-segment model, where a myocardial segment is considered normally contracting if its peak systolic strain exceeds a threshold value based on measurements from the sham rats. Contractility-Index measurements were compared to EF and peak strain in different rat groups. Statistical analysis was conducted to measure significance of the measurement differences between different rat groups.

**Results:** EF increased post-RT ( $78 \pm 0.7\%$  ( $P=0.014$ ) and  $78 \pm 1.2\%$  ( $P=0.014$ ) at 8wk and 10wk post-RT, respectively) compared to the sham rats ( $69 \pm 2.6\%$ ), which could be attributed to undergoing ventricular remodeling. However, peak systolic strain and Contractility-Index decreased post-RT (**Table 1, Figure 1**). This can be explained by the nonlinear inverse relationship between EF and Contractility-Index, in which Contractility-Index spanned a wide range of measurements between 22% and 79% for rats in different groups despite normal EF ( $\geq 60\%$ ) for all rats. When comparing Contractility-Index to corresponding peak strain values

in different rats, Contractility-Index showed more reduction post-RT than did the strain values (**Figure 1**), i.e. the Contractility-Index parameter is more sensitive than myocardial strain to RT.

**Conclusion:** Contractility-Index is an early marker for detection of RT-induced subclinical cardiac dysfunction before global function is affected, and it is more sensitive than peak systolic strain. The translational value of the results presented in this study is important as early detection of RT-induced cardiotoxicity would help with risk stratification such that cardioprotective therapy could be initiated in patients at risk to avoid clinical cardiac dysfunction and subsequent heart failure with associated morbidity, mortality, and high health care cost.

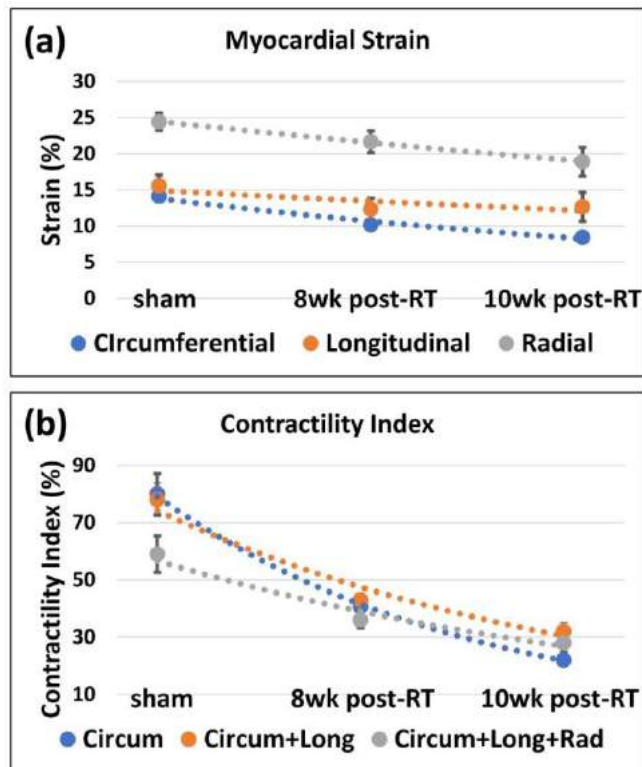
**Figure/Table 1**

	Sham	8 weeks post-RT	<i>P-value</i>	10 weeks post-RT	<i>P-value</i>
<b>EF (%)</b>	69±2.6%	78±0.7%	0.014	78±1.2%	P=0.014
<b>Circumferential strain (%)</b>	-14.7±0.8	-10.2±0.3	0.002	-8.3±0.2	<0.001
<b>Longitudinal Strain (%)</b>	-15.7±0.7	-12.3±0.5	0.003	-12.2±0.9	0.010
<b>Radial Strain (%)</b>	24.4±1.2	21.7±1.5	0.194	18.9±2.0	0.045
<b>Contractility-Index-cc (%)</b>	79±7	41±4	0.002	22±1	<0.001
<b>Contractility-Index-ll (%)</b>	64±7	42±4	0.020	42±7	0.047
<b>Contractility-Index-rr (%)</b>	60±4	47±7	0.148	35±6	0.010

**Caption 1**

**Table-1.** Myocardial peak-strain and Contractility-Index measurements in sham and irradiated rats, showing reduction in myocardial contractility post-RT. cc, ll, rr: circumferential, longitudinal, and radial directions, respectively. Values represented as mean±SEM. *P-values* calculated vs. sham.

**Figure/Table 2**



## Caption 2

**Figure 1. Contractility-Index is a sensitive marker of RT-induced cardiotoxicity.** (a) Peak-systolic strain is reduced post-RT. (b) Contractility-Index is significantly reduced post-RT compared peak-strain reduction in (a), even when combining different strain directions. Error bars represent  $\pm$ SEM.

## Bibliographic References

EH Ibrahim et al. JACC Cardio-Oncology 2021;3:113-30, EH Ibrahim et al. Magn Reson Imaging 2020;73:130-7, RA Schlaak et al. Cancers (Basel) 2020;12(2)

Speaker: E.-S. Ibrahim

Category: Strain, Cardiac Function, Animal Experimentation

000101

## Obese Heart Failure with Preserved Ejection Fraction : A Clinical and CMR Strain Investigation

J. He \* (1); M. Lu (1)

(1) Magnetic resonance imaging, fuwai Hospital, Beijing, China

### Abstract

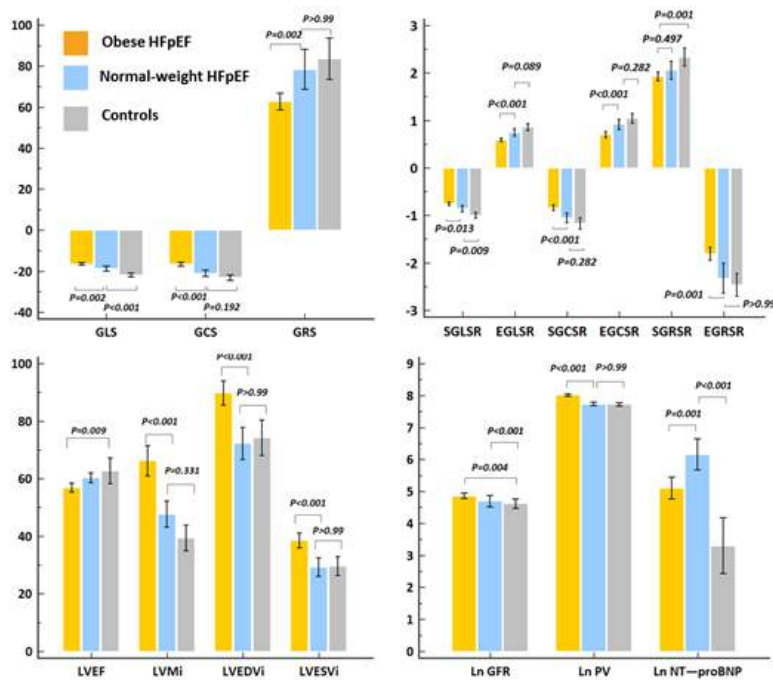
**BACKGROUND:** Obesity related heart failure with preserved ejection fraction (HFpEF) is an independent phenotype, notably common in China. Cardiovascular magnetic resonance imaging-feature tracking (CMR-FT) allows for recognizing subtle and early functional alterations of this phenotype. This study therefore aimed to investigate the clinical features and CMR-FT derived subtle clinical dysfunction in Obese HFpEF phenotype.

**METHODS:** We prospectively included 101 obese HFpEF, 46 normal-weight HFpEF patients and 30 clinically healthy controls with CMR and echocardiography from Aug 2019 to Jul 2021. Clinical features and CMR-FT derived strain parameters were recorded and analyzed.

**RESULTS:** Compared with normal-weight HFpEF, obese HFpEF patients were younger males ( $48\pm15$  vs  $64\pm10$  years,  $P<0.001$ ), used more calcium channel blocker ( $48.5\%$  vs.  $23.9\%$ ,  $P<0.05$ ), and showed higher plasma volume ( $3104\pm651$  vs.  $2324\pm343$  mL,  $P<0.001$ ), hypersensitive C-reactive protein (Hs-CRP, median,  $1.30$  vs.  $0.84$  mg/L,  $P<0.05$ ). Moreover, obese HFpEF patients showed greater left ventricular (LV) mass index, LV end-diastole volume index, LV end-systole volume index and worse CMR-FT derived strain parameters (all  $P\leq0.001$ ) compared to normal-weight HFpEF and clinically healthy controls. After adjusting for age, sex, diastolic blood pressure, calcium channel blocker use, estimated plasma volume, Hs-CRP, and N-terminal pro-brain natriuretic peptide levels, only early-diastolic global longitudinal strain rate (EGLSR,  $0.60\pm0.03$  vs.  $0.74\pm0.05/s$ ,  $P=0.031$ ), early-diastolic global circumferential strain rate (EGCSR,  $0.72\pm0.04/s$  vs.  $0.91\pm0.07/s$ ,  $P=0.033$ ), early-diastolic global radial strain rate ( $-1.90\pm0.11/s$  vs.  $-2.47\pm0.19/s$ ,  $P=0.023$ ) and global circumferential strain (GCS,  $-18.5\pm4.0\%$  vs  $-21.7\pm2.5\%$ ,  $P=0.048$ ) were obviously impaired in obese HFpEF versus normal-weight HFpEF patients. In addition, increased plasma volume and body mass was modestly, inversely associated with GCS, EGLSR, and EGCSR (all  $P<0.01$ ).

**CONCLUSIONS:** In this well-defined obese HFpEF cohort, higher volume overload and inflammatory response, and more impaired EGLSR, EGCSR, and EGRSR are prominent characteristics, comparing with normal-weight HFpEF. Myocardial strain may potentially assist in identification of obese HFpEF phenotype.

Figure/Table 1



## Caption 1

Differences among obese HFPEF (orange), normal-weight HFPEF (blue) and controls (gray). LVEF (%), left ventricular ejection fraction; LVEDVi/LVESVi (mL/m<sup>2</sup>), left ventricular end-diastole/end-systole volume index; LVMi (g/m<sup>2</sup>), left ventricular end-diastole mass index; PV (mL), plasma volume.

Speaker: J. He

Category: Heart Failure Preserved Ejection Fraction, Obesity, Feature Tracking

000102

**Pediatric flows: practical experience, with intrasession repeatability of aortic and pulmonary flows and Qp/Qs ratios**

R. Wage \* (1); S. Moscatelli, (1); P. Gatehouse (1); I. Voges (2); R. H. Mohiaddin (1); S. Krupickova (1); S. Nielles-vallespin (1); D. Pennell (1)

(1) Cardiac mri, Royal Brompton Hospital, London, United Kingdom; (2) Cardiac mri, University Hospital Schleswig-Holstein, Lübeck, Germany

**Abstract**

**Background:** Two-dimensional (2D) through-plane phase-contrast (PC) cines (“flows”) also enable assessments of shunts by the Qp/Qs ratio of RV/LV (by either ml/beat or by cardiac output CO l/min), and also of valve regurgitation, most usefully in pediatrics without ionising radiation. The reliability of pediatric flows was unknown at our centre; further, we needed to know the clinical flow repeatability before trialling faster methods. We therefore assessed the intrasession repeatability of flows.

**Methods:** Flows were repeated in the ascending aorta (STJ) and main pulmonary artery (MPA) at the same acquisition parameters and image planes during routine clinical appointments in 51 pediatric patients with congenital heart disease at 1.5T, Avanto FIT and Aera, VE11C SP1, Siemens Healthineers). The STJ and MPA flow acquisitions (Table 1: definitions and parameters) were planned from cine images of the LV and RV outflow tracts respectively, using two orthogonal outflow tract cines of each to optimise image planning. CFI42 (5.10; Circle CFI) flow analysis (single observer, 25 years’ experience) used background corrections from static tissue (Fig 1). If a repeat flow in ml/beat changed by more than 15ml, the acquisition and analysis of both were scrutinised for human errors. After testing for overall differences by paired t-testing, the repeatability was defined (1) at  $\pm 2SD$  (i.e.  $\approx 19$  in 20 confidence) for LV and RV in ml/beat and CO l/min, also Qp/Qs by ml/beat and l/min.

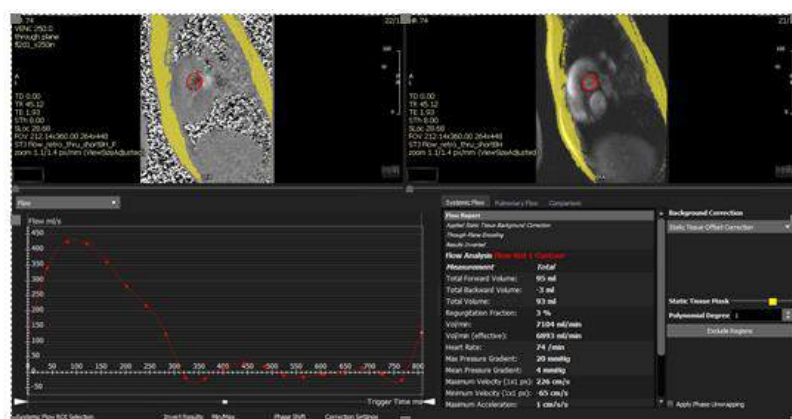
**Results and Discussion:** No significant changes occurred between repeat flows in HR, LV and RV ml/beat and l/min CO ( $p > 0.05$ ,  $n = 50$ , except RVCO  $p = 0.045$ ). The 95% confidence intervals of the LoA (Fig 2) were: LV  $\pm 11$  ml/beat, RV  $\pm 10$  ml/beat, LVCO =  $\pm 1.2$  l/min, RVCO =  $\pm 1.1$  l/min, Qp/Qs by ml/beat =  $\pm 0.22$ , Qp/Qs by l/min =  $\pm 0.26$ . No mistake explaining four of five outliers ( $> 15$  ml/beat repeat difference) was found and they remained uncorrected; two were associated with high RR variability. Repeatability was not degraded by shorter BH scans. The Qp and Qs used for Qp/Qs ratio were usually acquired sequentially to reduce sensitivity to HR changes. Using CO l/min for QP/QS seems marginally detrimental compared to ml/beat. Flows demand compromised resolution (frame time, pixel size) and SNR in certain planes in large patients and especially with poor BH capability, so the observation of no impact on repeatability down to 7HB was unexpected. Only two patients were acquired by FB scans; their apparent enhanced repeatability may arise from the averaging of FB scans, but is inconclusive. Post-scan flow analysis should not degrade repeatability but operator inattention, pitfalls and software flaws add errors. This work was only intrasession repeatability, not intersession reproducibility.



**Conclusion:** Intrasection repeatability of QP/QS is comparable to the  $\pm 0.1$  of note in clinical cardiology. As for any complex test, technical optimisation needs expert CMR radiography and also analysis; however, unexplained outliers including physiological variations seem endemic, and it appears that clinicians will always need to moderate CMR flow and Qp/Qs results based on their other clinical knowledge of each patient.

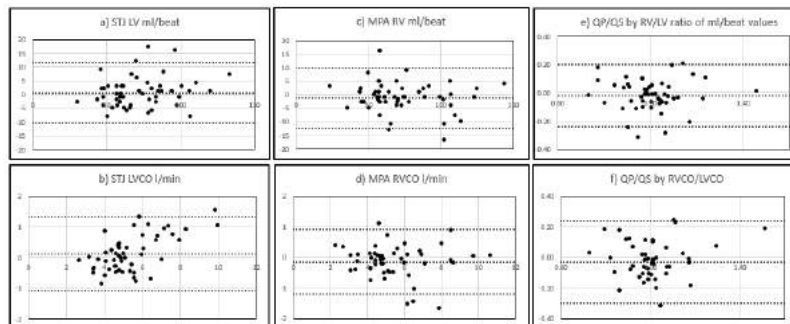
Definitions and Parameters	Long BH	Short BH	Free-breathing
HBs (Heartbeats)	11-15	7-10	35-40
Rawdata lines (per HB)	5	6	7
TR (ms) @ VENC 120 cm/s	4.4	4.0	3.5
Time per acquired cine frame (ms)	44	48	49
TE (ms) @ VENC 120 cm/s	2.3	2.2	1.9
FOV (mm) (PE FOV adapted to plane)	360	360	360
Acqd resIn FE(mm) PE(mm) @ 360mm FOV	1.6 2.0	1.6 2.0	1.6 2.0
PE rawdata zero-filled fraction	12.5%	25%	25%
FA (deg)	20	20	20
SLT (mm)	8	8	8
ADC(Hz/mm) @360mm FOV	297	367	517
Parallel imaging (GRAPPA) Factor	2	2	3
Parallel imaging reference lines	24 (in scan)	24 (prescan)	24 (in scan)
Long-term averaging vs Resp motion	No	No	5

**Definitions and Acquisition Parameters.** FOV was adapted to each plane, PE FOV affecting HBs. VENC was adapted to each vessel, ideally marginally below aliasing of vessel peak velocity.



Example of STJ flow analysis (Circle CMR42 v5.10)

**Figure 3**



**Caption 3**

Bland-Altman plots of the repeat flows, with mean and mean  $\pm$  2SD limits of agreement (horizontal dashed lines): a) LV ml/beat, b) LVCO l/min, c) RV ml/beat, d) RVCO l/min, e) Qp/Qs by ratio of RV/LV ml/beat and f) Qp/Qs by ratio of RV/LV COs l/min.

### Bibliographic References

(1) Bland and Altman, Lancet, 1986;1:307-10.

Speaker: R. Wage

Category: Flow, Pediatric , Reproducibility

**000103**

## **Usefulness of a comprehensive CMR protocol in a patient with pulmonary hypertension**

F. Bosio \* (1); H. Hasaneen (1); P. Marino (1); N. Chung (1); M. Alam (1); A. Villa (1)

(1) Cardiovascular imaging, King's College London Guy's Campus, London, United Kingdom

### **Abstract**

#### **DESCRIPTION OF CLINICAL PRESENTATION**

A 79-year-old woman with a background of lung and skin sarcoid was referred due to increasing shortness of breath on exertion. A transthoracic echocardiogram was performed showing pulmonary hypertension (PH) with right ventricle (RV) dilatation and dysfunction. A cardiovascular magnetic resonance (CMR) scan was requested to investigate possible cardiac involvement from sarcoidosis and pulmonary thromboembolic disease.

#### **DIAGNOSTIC TECHNIQUES AND THEIR MOST IMPORTANT FINDINGS**

Axial survey images of the chest showed bilateral bronchiectasis, patchy ground glass opacities and consolidation, and diffuse fibrotic reticulations (Figure 1) with mediastinal and left lower deep cervical lymph nodes, all sub centimetric in short axis diameter. These findings were not unexpected and consistent with chest computed tomography (CT) findings.

The CMR scan revealed a normal left ventricle (LV) end-diastolic volume with normal global systolic function. However, the RV appeared dilated with mildly impaired function [RV ejection fraction (RVEF) = 42%] (Fig 2), mild RV hypertrophy, paradoxical septal motion and insertional late gadolinium enhancement (LGE), in keeping with the echo finding of PH. The main pulmonary artery (MPA) appeared dilated, as well as the right pulmonary artery (RPA) and the left pulmonary artery (LPA).

T2 weighted images short axis (SA) and long axis were performed showing a normal myocardial signal intensity. The lack of myocardial oedema on T2w images and typical LGE images confirmed the absence of cardiac sarcoidosis. Lung perfusion and 4D angiography confirmed the absence of pulmonary thrombo-embolic disease.

Phase contrast flow mapping comparison of the aorta and MPA showed a calculated Qp:Qs of 1.35. Given the unexpected finding, 4D angiography was reviewed and partial anomalous pulmonary venous drainage (PAPVD) between the right upper pulmonary vein and the superior vena cava (SVC) was detected (Figure 3). Right heart catheterization confirmed these findings.

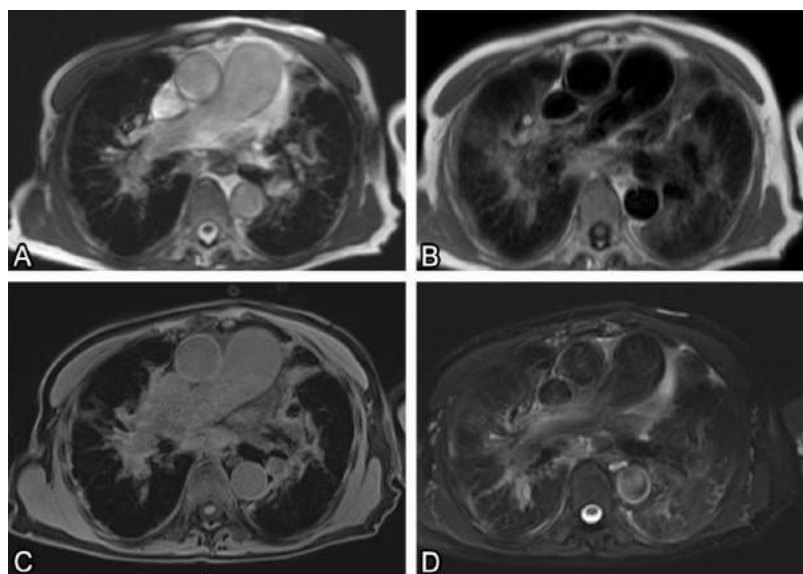
#### **LEARNING POINTS FROM THIS CASE**

CMR was able to exclude myocardial oedema and/or scar due to cardiac sarcoidosis, while confirming indirect signs of pulmonary hypertension, thought to be induced by the underlying lung disease.

Our comprehensive CMR protocol includes volumes and function assessment, myocardial tissue characterization, 4D pulmonary and systemic angiography, lung perfusion and flow assessments, enabling the assessment of multiple signs/disease in one single examination.

In our case, Qp/Qs raised the suspicion of another possible cause of PH, which was subsequently confirmed while reviewing the CMR angiography images.

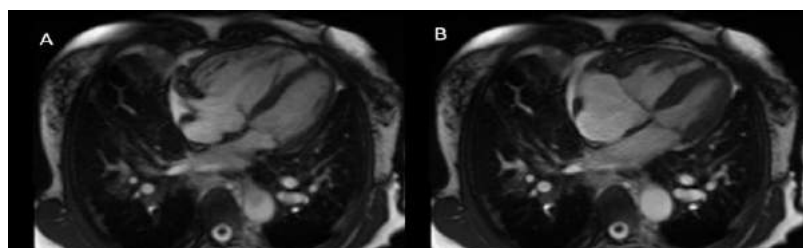
**Figure/Table 1**



**Caption 1**

Figure 1: Axial images of the chest showing sarcoidosis lung involvement. A: T2 High-Resolution localizer, 2D single-shot bSSFP sequence. B: T2 weighted 2D single-shot Turbo Spin Echo (HASTE). C: PD-weighted ultra-short TE (UTE) 3D stack of spirals UTE-VIBE. D: high-resolution 2D T2-weighted BLADE sequence with SPAIR fat suppression.

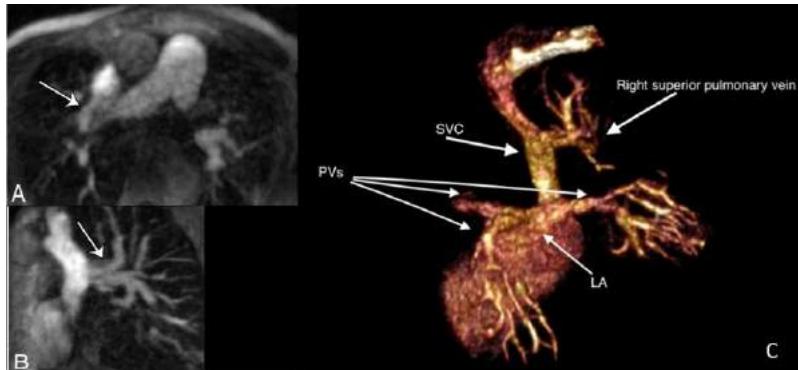
**Figure/Table 2**



**Caption 2**

Figure 2: Cine Steady-State Free Precession 4 Chamber in end diastolic phase (A) and end systolic phase, showing a RV dilatation and impairment (B)

**Figure 3**



**Caption 3**

Figure 3: maximum intensity projection (MIP) reconstruction of 4D angiography images (A-B) and 3D Whole Heart reconstruction (C), showing partial anomalous pulmonary venous drainage (PAPVD) between the right upper pulmonary vein and the superior vena cava (SVC) (arrows). PVs: pulmonary veins.

Speaker: F. Bosio

Category: 4D Flow, Pulmonary Hypertension, Anomalous Venous Return

**000104**

## **The role of CMR in the diagnosis of acute eosinophilic myocarditis**

F. Bosio \* (1); A. Hua (1); T. Ismail (1)

(1) Cardiovascular imaging, King's College London Guy's Campus, London, United Kingdom

### **Abstract**

#### Description of clinical presentation

A 28-year-old man presented with a 4-week history of abdominal pain, bloody diarrhoea, weight loss, fever, and rigors. He also reported chest discomfort particularly after his meals, which responded well to omeprazole. Blood tests revealed an eosinophil count of 28 (normal range  $0-0.4 \times 10^9/l$ ), high-sensitivity troponin T 693 ng/L (normal range 0-13 ng/l) and NT-pro-brain natriuretic peptide (BNP) of 2223ng/l (normal range  $<400ng/l$ ). He was found to be thrombocytopenic with a platelet count of 35 (normal range  $150-400 \times 10^9/l$ ). A 12-lead electrocardiogram (ECG) revealed T wave inversion in the inferior leads. Stool results and a bone marrow aspirate excluded a parasite infection and haematological malignancy respectively as possible causes of eosinophilia. There was no history or clinical signs of asthma, sinusitis, or mononeuritis multiplex. Cardiovascular magnetic resonance (CMR) was requested to assess for possible myocarditis. He was treated with high dose steroids and heart failure medications which he responded well to.

#### Diagnostic Techniques and Their Most Important Findings

CMR normal left ventricle (LV) size with moderate systolic dysfunction (LV Ejection Fraction=43%).

T2 weighted Turbo Spin Echo (TSE) and whole heart T2 mapping sequences [FIG 1] were performed to characterise possible inflammation. The T2 TSE images revealed a diffusely increased signal in the basal to mid-anterior and inferior walls (Fig 1). T2-mapping showed an increased value of T2 times (56-62 ms, normal  $<55$  ms) in the basal-mid anterior and basal-apical inferior and basal to mid inferolateral segments.

Native T1 was significantly elevated in the basal to mid-anterior, septal, inferior and inferolateral walls [Fig 2a], the apical septum and apical inferior walls with a value of 1100-1200 ms, normal 890-1035ms. A focal area of subendocardial low T1 (886ms) was noted in the basal inferior sub-endocardial wall which likely represents intramyocardial haemorrhage.

Early gadolinium enhancement images revealed the presence of microvascular obstruction in the basal-anterior wall, in the basal to mid-inferoseptum, inferior walls and apical septum.

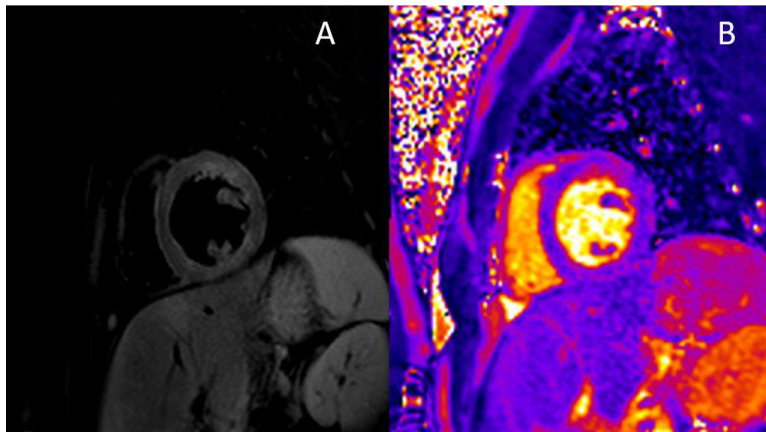
Late gadolinium enhancement (LGE) images revealed extensive diffuse sub-endocardial myocardial enhancement of the basal-mid anterior, inferoseptal, inferior, inferolateral, and apical inferior segments [Fig 2b-3]. There is also mid-wall enhancement of the mid-apical septum [Fig 3] and near transmural enhancement of the apical inferior wall.

### Learning Points from this Case

The CMR findings are in keeping with acute/fulminant eosinophilic myocarditis/endomyocarditis.

CMR is an invaluable tool to perform tissue characterisation and help guide patient's management. A repeat CMR scan was performed after 6 weeks, which revealed resolution of myocardial inflammation and recovery in LV function.

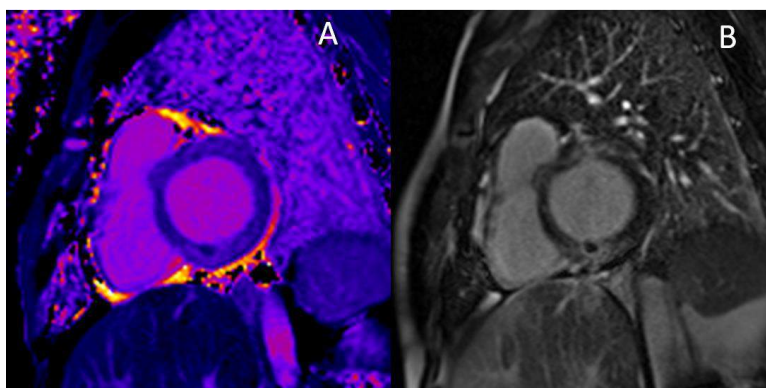
**Figure/Table 1**



**Caption 1**

Figure 1: Short Axis slice in T2 Weighted TSE (A) and Whole Heart T2 Mapping (B) Sequences

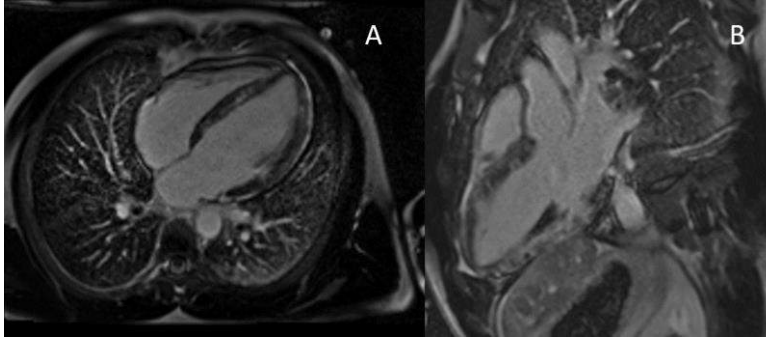
**Figure/Table 2**



**Caption 2**

Figure 2: Short Axis slice in Native T1 MOLLI (A) and LGE (B)

**Figure 3**



**Caption 3**

Figure 3: Four chamber (A) and 3 Chamber (B) White Blood Moco LGE

Speaker: F. Bosio

Category: T2, Mapping Techniques, Eosinophilic Myocarditis



000105

## Fast and robust motion correction of cardiovascular magnetic resonance T1-mapping using data-driven convolutional neural networks for generalisability

R. A. Gonzales \* (1); Q. Zhang (1); B. Papież (2); K. Werys (1); E. Lukaschuk (1); I. A. Popescu (1); M. K. Burrage (1); M. Shanmuganathan (1); V. Ferreira (1); S. Piechnik (1)

(1) Radcliffe department of medicine, University of Oxford, Oxford, United Kingdom; (2) Big data institute, University of Oxford, Oxford, United Kingdom

### Abstract

**Background:** Quantitative cardiovascular magnetic resonance (CMR) T1-mapping has shown promise for advanced tissue characterisation in routine clinical practice [1]. However, T1-mapping is prone to motion artefacts, which affects its robustness and clinical interpretation [2]. Current methods for motion correction on T1-mapping are model-driven with no guarantee on generalisability, limiting its widespread use. Emerging data-driven deep learning approaches have shown good performance in general image registration tasks. It is desirable to develop a deep learning method for T1-mapping motion correction that is also generalisable.

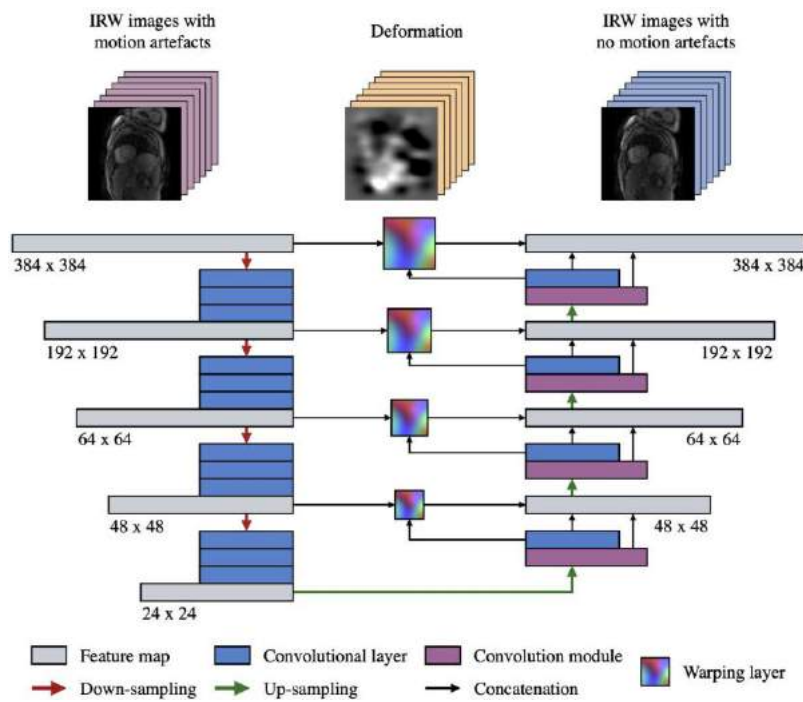
**Methods:** We designed a convolutional neural network (CNN) solution for fast and robust motion artefact correction in T1-maps (ShMOLLI), developed using the UK Biobank imaging dataset. The CNN combines an encoder-decoder architecture [3] for producing deformation fields with warping layers [4] to apply such deformation to the feature maps in a coarse-to-fine manner (Fig. 1). The training set comprised of 1536 mid-ventricular T1-maps with strictly no motion, which were synthetically deformed to simulate motion artefacts. The model was evaluated on 200 samples with severe motion (n=50), moderate motion (n=100) and mild to no motion (n=50). For validation, 3 human experts visually assessed for motion in the T1-map, with motion scores ranging from 0% (strictly no motion) to 100% (very severe motion).

**Results:** The proposed model successfully and rapidly (<1 second per T1-map) suppressed a wide range of motion artefacts. Overall, it significantly reduced motion scores from  $37.1 \pm 21.5$  to  $13.3 \pm 10.5$  ( $p < 0.001$ ). In each assessed category, the motion scores were significantly reduced from  $55.8 \pm 18.7$  to  $18.6 \pm 14.3$  (severe motion), from  $35.5 \pm 18.9$  to  $12.7 \pm 9.2$  (moderate motion), and from  $21.7 \pm 13.8$  to  $9.4 \pm 6.4$  (mild to no motion; all  $p < 0.001$ ). In an exploratory study, the proposed model achieved a better registration than the traditional inline motion correction method [5] (Fig. 3), subject to further investigation.

**Conclusion:** The presented data-driven deep learning CNN model is effective and robust for correction of artefacts from myocardial motion in T1-maps. It can be adapted and generalised

to enhance parametric mapping methods, paving the way towards reliable quantitative medical imaging for immediate clinical interpretation.

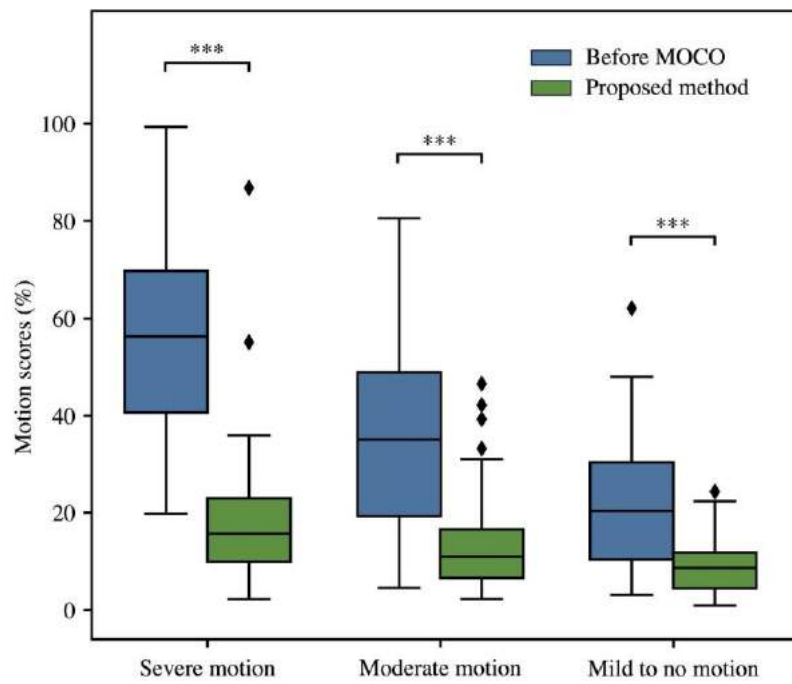
**Figure/Table 1**



**Caption 1**

Structure of the proposed motion correction convolutional neural network. A stack of 7 inversion recovery-weighted (IRW) images from T1-mapping is input into the encoder-decoder structure on a per-channel basis. The warping layers estimate the optical flow from all the channels at each scale. The last warping layer generates the deformation required to correct the motion artefacts.

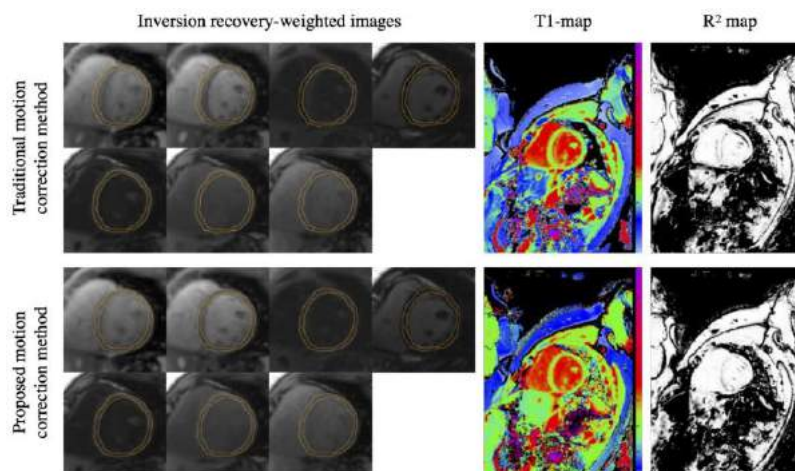
**Figure/Table 2**



**Caption 2**

Performance of the proposed method in motion correction of T1-maps. Box and whisker plot of motion scores in non-parametric terms of three data groups, before (blue) and after motion correction by the proposed method (green). \*\*\*  $p < 0.001$

**Figure 3**



**Caption 3**

Performance of the traditional motion correction method (first row) compared against the proposed data-driven CNN method in motion correction of T1-maps. Each inversion recovery-weighted image is overlaid by identical myocardial contours for identifying motion.

### **Bibliographic References**

[1] Ferreira, V.M. and S.K. Piechnik, CMR Parametric Mapping as a Tool for Myocardial Tissue Characterization. Korean Circulation Journal, 2020. 50(8): p. 658., [2] Messroghli, D.R., et al., Human Myocardium: Single-Breath-hold MR T1 Mapping with High Spatial Resolution—Reproducibility Study. Radiology, 2006. 238(3): p. 1004-1012., [3] Ronneberger, O., P. Fischer, and T. Brox, U-Net: Convolutional Networks for Biomedical Image Segmentation. 2015, Springer International Publishing. p. 234-241., [4] Sun, D., et al. PWC-Net: CNNs for Optical Flow Using Pyramid, Warping, and Cost Volume. 2018. IEEE., [5] Xue, H., et al., Motion correction for myocardial T1 mapping using image registration with synthetic image estimation. Magnetic Resonance in Medicine, 2012. 67(6): p. 1644-1655.

Speaker: R. A. Gonzales

Category: Motion Correction, T1 , Myocardium

000109

## Cardiac Magnetic Resonance Imaging in the United States, 2013-2019

J. W. Goldfarb \* (1); J. J. Cao (1)

(1) Cardiac Imaging, St Francis Hospital and Heart Center, Roslyn, United States of America

### Abstract

#### Background:

Cardiac magnetic resonance (CMR) imaging's ease of use is improving, and indications are expanding. Available noninvasive CMR diagnostic imaging tools include morphologic, functional, blood flow, and oncologic imaging as well as myocardial tissue characterization and stress testing. The recent use of CMR before the COVID-19 pandemic (January 2020) has not been reported. The goal of this study is to provide an update on the recent use of CMR in the US and document and describe CMR practice and practitioners in the US Medicare population from 2013-2019.

#### Methods:

A retrospective cross-sectional analysis of Medicare Part B physician payments (2013-2019) was performed. CMR providers and examinations were identified using the unique Healthcare Common Procedure Coding System (HCPCS) codes. The number of CMR providers, services, and payments were summarized annually and analyzed for trends. Additionally, the medical specialty, gender, and rural/urban location characteristics were compared to similar physicians.

#### Results:

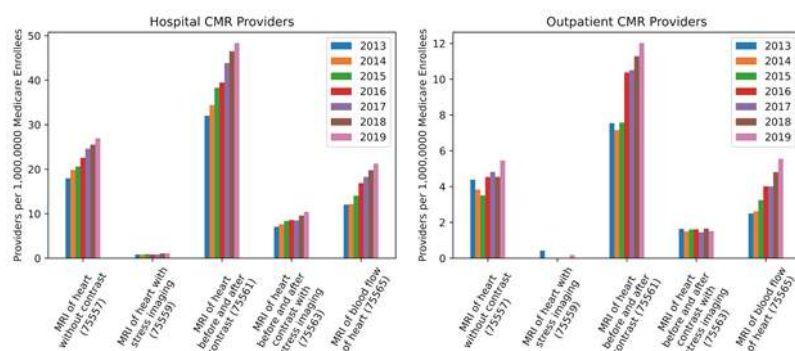
From 2013-2019, there was a steady increase in both the number of CMR practitioners (51%) and exams (116%) (Figures 1 and 2). 85% of CMR exams were performed in the Hospital vs the freestanding outpatient setting. Also, there was a larger exam volume growth in the hospital vs the outpatient setting; 124% vs 81%. Although professional reading fees increased by 2.4 to 6.8%, global fee payments were reduced by -14.0 to -22.6%; Table 1.

CMR providers were mostly men. In 2013, 14.8% of high volume CMR providers were women. This steadily increased to 18.1% in 2017 and then reduced slightly to 17.7% in 2018 and 2019. Radiology providers had a larger market share, 52.7% vs 43.5%. The vast majority (97.7%) of providers were urban focused. 2.1% of providers were located in a large rural city or town. And only 0.2% of providers were located in a small or isolated rural town. The number of providers in a large rural city or town doubled during the time period.

#### Conclusions:

Before the Covid-19 pandemic, CMR realized a yearly increase in providers and use. Reimbursement for CMR exams saw significant reductions. Provider characteristics remained largely unchanged.

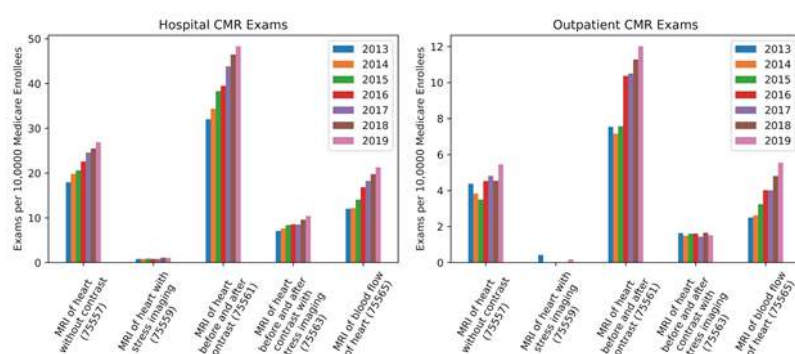
**Figure/Table 1**



**Caption 1**

Figure 1. CMR providers for each type of CMR exam in the hospital and freestanding outpatient settings. CMR exams increased over the time period.

**Figure/Table 2**



**Caption 2**

Figure 2. CMR exams for each type of exam in the hospital and freestanding outpatient facility settings. The majority of CMR exams were performed in the hospital setting.

**Figure 3**

		2013	2014	2015	2016	2017	2018	2019	2018-2019 Change
MRI of heart w/o contrast (75557)	Hospital	\$ 110.42	\$ 115.47	\$ 115.63	\$ 115.07	\$ 116.16	\$ 116.61	\$ 117.90	6.7%
	Outpatient Facility	\$ 250.28	\$ 254.77	\$ 258.74	\$ 260.24	\$ 264.62	\$ 264.87	\$ 228.55	-22.5%
MRI of heart w/ stress imaging (75559)	Hospital	\$ 135.25	\$ 140.01	\$ 138.56	\$ 138.33	\$ 140.67	\$ 138.09	\$ 139.37	2.4%
	Outpatient Facility	\$ 343.94						\$ 270.75	-71.8%
MRI of heart w/ and w/o contrast (75561)	Hospital	\$ 122.00	\$ 127.85	\$ 128.74	\$ 128.02	\$ 128.70	\$ 128.73	\$ 130.48	0.4%
	Outpatient Facility	\$ 403.31	\$ 356.95	\$ 344.32	\$ 317.34	\$ 315.35	\$ 334.24	\$ 327.37	-18.8%
Stress MRI of heart w/ and w/o contrast (75563)	Hospital	\$ 139.07	\$ 144.49	\$ 144.71	\$ 144.18	\$ 143.65	\$ 144.24	\$ 145.81	4.8%
	Outpatient Facility	\$ 381.95	\$ 397.56	\$ 398.83	\$ 475.28	\$ 354.97	\$ 424.50	\$ 407.71	-14%
MRI of blood flow of heart (75565)	Hospital	\$ 11.73	\$ 12.30	\$ 12.24	\$ 12.26	\$ 12.27	\$ 12.31	\$ 12.47	6.3%
	Outpatient Facility	\$ 58.85	\$ 45.33	\$ 44.80	\$ 40.81	\$ 42.12	\$ 43.54	\$ 39.79	-32.4%

### Caption 3

Table 1. Physician payments by exam type. In the hospital setting, the physician payment is the professional fee and in the freestanding outpatient setting, the payment is the global fee (technical +professional).

Speaker: J. W. Goldfarb

Category: Contrast, Stress CMR, Post-Contrast

000110

## Change in ECV mapping with chemotherapy treatment in light-chain amyloidosis correlates with prognosis: Is this the new T2\*?

R. Patel \* (1); A. Martinez-Naharro (1); T. Kotecha (2); N. Karia, (3); L. Chacko (1); Y. Razvi, (1); S. Ravichandran (1); J. Brown (3); S. Law (1); C. Quarta (1); S. Mahmood (1); B. Wisniowski (1); S. Pica (1); H. Lachmann (1); J. Moon (4); D. Knight (2); C. Whelan (1); L. Venneri (1); H. Xue (5); P. Kellman (5); J. Gillmore (1); P. Hawkins (1); A. Wechalekar (1); M. Fontana (1); S. Sachchithanantham (1)

(1) National Amyloidosis Centre, Royal Free London NHS Foundation Trust, London, United Kingdom; (2) Cardiology, Royal Free London NHS Foundation Trust, London, United Kingdom; (3) Cardiovascular sciences, UCL Institute of Cardiovascular Science, London, United Kingdom; (4) Cardiac mri, Barts Health, London, United Kingdom; (5) National institutes for health, NHLBI, Bethesda, United States of America

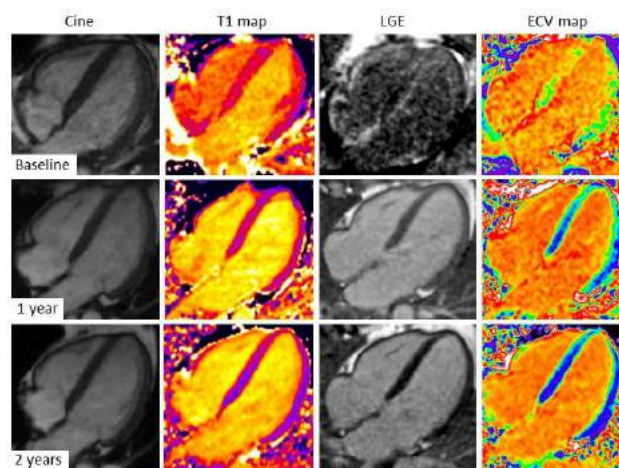
### Abstract

**Background:** Cardiac involvement in light-chain amyloidosis is the major determinant of mortality. Response to chemotherapy is traditionally assessed by reductions in amyloid production (serum free light chains; FLC) or N-terminal pro-B-type natriuretic peptide (NT-proBNP), but neither directly measure the cardiac amyloid burden. Cardiovascular magnetic resonance (CMR) with extra-cellular volume (ECV) mapping can quantify amyloid deposition within the myocardium. Our aims were to determine the capability of CMR with ECV mapping to track response to chemotherapy, assess the correlation between haematological response and changes in cardiac amyloid, and determine the association between changes in cardiac amyloid and survival. **Methods:** In total, 176 patients with cardiac light-chain amyloidosis treated with chemotherapy were assessed with serial measurements of NT-proBNP, FLC and CMR with ECV mapping at baseline (before initiation of chemotherapy), 6 months, 12 months & 24 months after starting chemotherapy. Hematological response was categorized by reductions in FLC as either: complete response (CR), very good partial response (VGPR), partial response (PR) or no response (NR). CMR response was categorized by changes in ECV as either: progression ( $\geq 0.05$  increase), stable ( $< 0.05$  change) or regression ( $\geq 0.05$  decrease). **Results:** After 6 months of chemotherapy, 61% of patients achieved a CR or VGPR and 39% achieved a PR or NR. Amyloid regression on CMR was observed in 3% of patients (all having either CR or VGPR) and amyloid progression was observed in 32% of patients (with 61% having either a PR or NR and 39% having either a CR or VGPR). After 1 year of chemotherapy, 71% of patients achieved a CR or VGPR and 29% achieved a PR or NR. Amyloid regression on CMR was observed in 22% of patients (all having either CR or VGPR) and amyloid progression was observed in 22% of patients (with 63% having either a PR or NR and 37% having either a CR or VGPR). After 2 years of chemotherapy, 80% of patients achieved a CR or VGPR and 20% achieved a PR or NR. Amyloid regression on CMR was observed in 38% of patients (all having either a CR or VGPR) and amyloid progression was observed in 14% of patients (with 80% having either a PR or NR and 20% having either a CR or VGPR). During a mean follow-up period of  $40 \pm 15$  months, 36 (25%) patients died. CMR response at 6 months predicted death (progression HR 3.821; 95% CI 1.950-7.487;  $p < 0.001$ ) and remained independently associated with prognosis after adjusting for both haematological response & NT-proBNP ( $p < 0.01$ ). **Conclusions:** CMR with ECV mapping demonstrates that cardiac amyloid deposits frequently regress following



chemotherapy, but only in patients who achieve a CR or VGPR, emphasising the importance of a deep haematological response following chemotherapy. Changes in amyloid burden seen using ECV mapping are independently associated with prognosis, highlighting the pivotal role of CMR in redefining the response to chemotherapy in patients with cardiac light-chain amyloidosis.

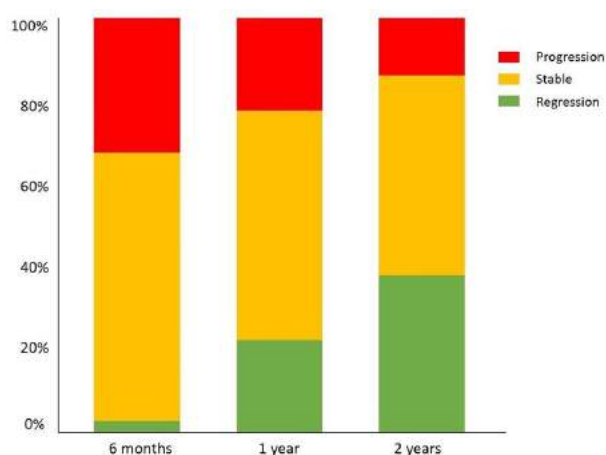
**Figure/Table 1**



**Caption 1**

Figure 1 – Cardiac AL amyloid regression on serial CMR scans at baseline, 1 year and 2 years after treatment with chemotherapy. Reductions in LV wall thickness (cine imaging), native T1 mapping, LGE imaging & ECV mapping within the myocardium are demonstrated progressively over the course of treatment. (LGE: late gadolinium enhancement)

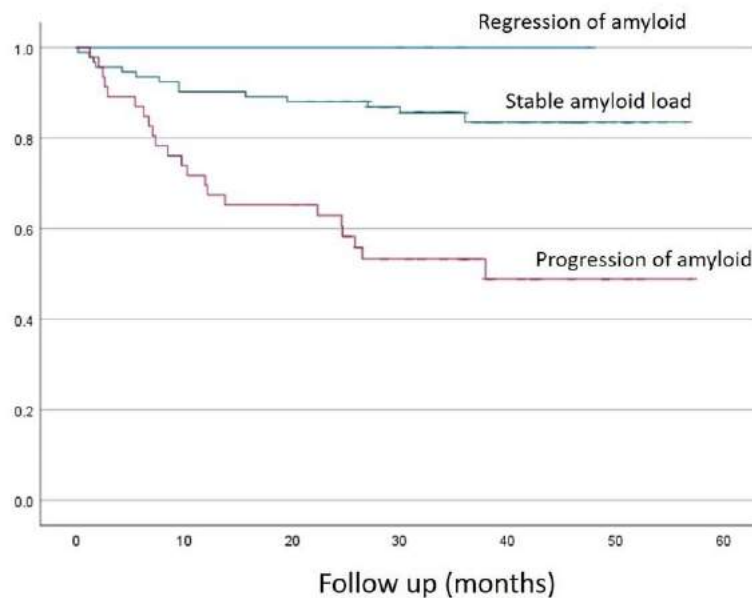
**Figure/Table 2**



**Caption 2**

Figure 2 – Bar chart representing the proportion of patients with each grade of CMR response to chemotherapy at each time points studied. Amyloid progression defined as  $\geq 5\%$  increase in ECV (red bars), stable amyloid load defined as  $< 5\%$  change in ECV (yellow bars) and amyloid regression defined as  $\geq 5\%$  decrease in ECV (green bars).

**Figure 3**



**Caption 3**

Figure 3 – Kaplan-Meier survival curves displaying survival in all patients according to change in amyloid burden (measured by the change in ECV on follow-up CMR) after 6 months of treatment with chemotherapy.

Speaker: R. Patel

Category: Amyloidosis , Chemotherapy, Prognosis

000111

## Fully automatic AI-based extraction of mitral valve motion parameters on long axis CINE images – validation and application on N=2000 patient datasets

S. S. Yoon \* (1); C. Fischer (2); S. Toupin (3); T. Pezel (4); J. Garot (4); J. Wetzl (5); A. Maier (1); D. Giese (5)

(1) Pattern recognition lab, University of Erlangen-Nuremberg, Erlangen, Germany; (2) Department of medical imaging, Technical University of Berlin, Berlin, Germany; (3) ., Siemens Healthcare France, Saint-Denis; (4) Cardiovascular magnetic resonance laboratory, Institut Cardiovasculaire Paris Sud, Massy; (5) Magnetic resonance, Siemens Healthcare GmbH, Erlangen, Germany

### Abstract

#### Background

The overall prevalence of heart failure with preserved ejection fraction is reported to be 1.1-5.5% in the general population and is often related to diastolic dysfunction [1]. Mitral valve (MV) motion parameters, assessable using CMR [2], have been shown to help the diagnosis of cardiac dysfunction. To fully automatically extract MV motion parameters, we propose an AI-based prototype system which tracks MV annulus landmarks on time-resolved two- and four-chamber CMR cine views (2CHV, 4CHV). Parameters such as displacements, velocities, or mitral annular plane systolic excursion (MAPSE) are automatically extracted. The performance of the proposed system is evaluated on a large CMR dataset (N=2000).

#### Methods

The used system is detailed in [3]. Briefly, it consists of two sequential neural networks with a processing step in between (Fig. 1a). Initially, a localization network (2D UNet) is applied to localize both MV annulus insertion points as well as the apex. Based on these points, the image processing step consists in rotating, cropping, and interpolating the images, allowing a standardized image impression for both long axis views. Finally, the tracking network (3D UNet) is applied to the processed series and tracks the MV annulus insertion points over the cardiac cycle. The system was trained on (N=166) multivendor, multi-field strength, ground truth annotated datasets [4].

A total of 2000 datasets, acquired on MAGNETOM Aera 1.5T scanner (Siemens Healthcare, Erlangen, Germany) from January 2016 to September 2017 [5], were used for parameter extraction. 200 of these datasets were additionally annotated semi-automatically and used to evaluate the performance of the system.

Four motion parameters were automatically derived (Fig. 1b): (1) The atrioventricular plane displacement (AVPD) was obtained by computing the distance of the plane spanned by the MV insertion points relative to the first frame, (2) the atrioventricular plane velocity (AVPV) was derived as the discrete temporal derivate of the AVPD, (3) the maximum diameter of the annulus was derived as the maximum distance between the mitral valve annulus points, and (4) the lateral and septal MAPSE, calculated as the maximum AVPD excursion.

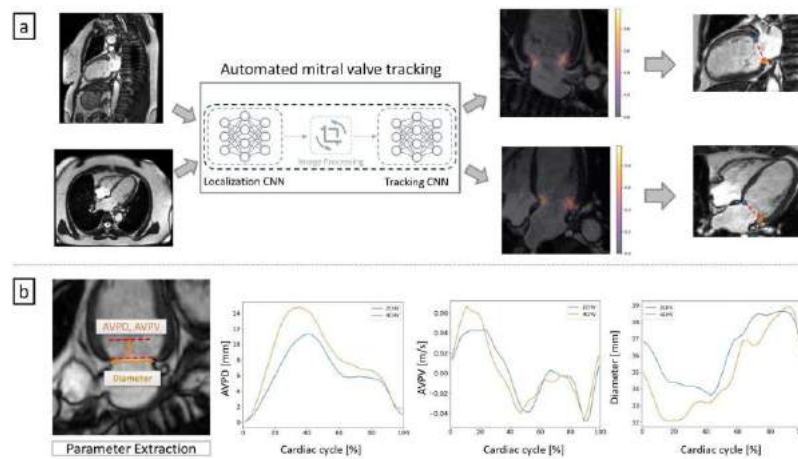
## Results

The accuracy of the system (Fig. 2) resulted in deviations of  $1.1 \pm 0.9$  mm,  $0.01 \pm 0.49$  m/s,  $1.61 \pm 1.06$  mm,  $1.63 \pm 1.15$  mm, for AVPD, AVPV, diameter and MAPSE respectively. Initial statistic on all datasets (Fig. 3) revealed a mean lateral and septal MAPSE of  $11.4 \pm 3.1$  mm and  $10.5 \pm 3.0$  mm for 2CHV and  $11.2 \pm 2.7$  mm and  $9.6 \pm 2.6$  mm for 4CHV respectively.

## Conclusions

The results demonstrate the versatility of the proposed system to automatically extract several MV motion parameters. The proposed system enables the automatic extraction of clinically relevant MV motion parameters and can improve the automation of MV based analyses.

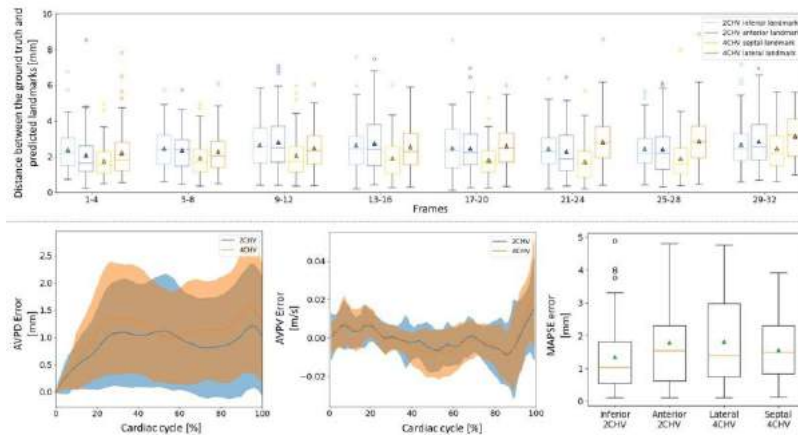
**Figure/Table 1**



**Caption 1**

a) Overview of the proposed system. As an input series, 2CHV/4CHV CINE series are taken. The output of the tracking convolutional neural network (CNN) are heatmaps corresponding to probability distributions of the mitral valve annulus landmarks for each timepoint. b) From left to right, the parameters of interests, AVPD, AVPV, diameter of an exemplary dataset.

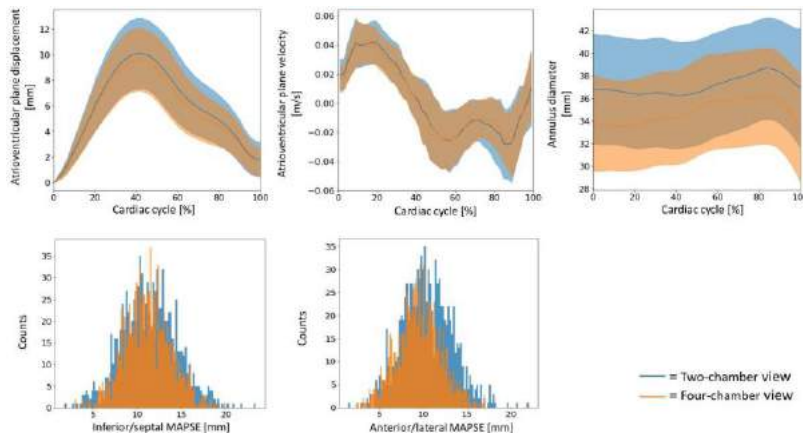
**Figure/Table 2**



**Caption 2**

Performance analysis of the proposed system. A part of the study dataset ( $n=200$ ) was semi-automatically annotated for the 2CHV and 4CHV CINE series. First row: Distance errors between the ground truth and the predicted inferior/septal and anterior/lateral landmarks. Four consecutive frames were averaged and plotted using boxplots. Second row: AVPD, AVPV and MAPSE deviations.

**Figure 3**



**Caption 3**

Mean and standard deviations of AVPD, AVPV and diameters as well as histograms of MAPSE extracted from all 2000 two-chamber (blue) and four-chamber (orange) datasets.

## **Bibliographic References**

[1] Oktay, A. Afşin, Jonathan D. Rich, and Sanjiv J. Shah. "The emerging epidemic of heart failure with preserved ejection fraction." *Current heart failure reports* 10.4 (2013): 401-410., [2] Ramos, João G., et al. "Comprehensive cardiovascular magnetic resonance diastolic dysfunction grading shows very good agreement compared with echocardiography." *JACC: Cardiovascular Imaging* 13.12 (2020): 2530-2542., [3] Monzon, Maria, et al. "Fully automatic extraction of mitral valve annulus motion parameters on long axis CINE CMR using deep learning." *ISMRM 2021* , [4] Fonseca, Carissa G., et al. "The Cardiac Atlas Project—an imaging database for computational modeling and statistical atlases of the heart." *Bioinformatics* 27.16 (2011): 2288-2295., [5] Pezel, Théo, et al. "Vasodilatation stress cardiovascular magnetic resonance imaging: Feasibility, workflow and safety in a large prospective registry of more than 35,000 patients." *Archives of Cardiovascular Diseases* 114.6-7 (2021): 490-503.

Speaker: S. S. Yoon

Category: Automated Processing, Mitral Valve, MR Post-Processing

000112

## Phase contrast MRI measurements in the descending aorta can provide new biomarkers for patients with chronic aortic regurgitation

F. Truedsson \* (1); C. L. Polte, (2); O. Bech-Hanssen, (3); Å. A. Johnsson, (4); S. A. Gao, (3); K. M. Lagerstrand, (5)

(1) Radiation physics, Gothenburg University, Gothenburg, Sweden; (2) Department of cardiology, Institute of Medicine, Gothenburg, Sweden; (3) Department of clinical physiology, Institute of Medicine, Gothenburg, Sweden; (4) Department of radiology, Institute of Clinical Sciences, Gothenburg, Sweden; (5) Department of radiation physics, Institute of Clinical Sciences, Gothenburg, Sweden

### Abstract

**Background:** Aortic regurgitation (AR) severity by cardiovascular MRI can be directly assessed by through-plane phase contrast MRI (PC-MRI) in an image plane orthogonally to the blood flow in the ascending aorta [1]. For patients with dilated ascending aortas, though, the AR severity may be underestimated due to complex flow and through-plane heart motion [2,3]. Holodiastolic flow reversal measured in the middescending thoracic aorta have been suggested to be indicative of severe AR [4]. Accordingly, the aim of this study was to investigate whether PC measurements in the descending aorta can provide new biomarkers for grading AR severity that can be used to separate patients with severe from non-severe AR. (Preliminary findings from an ongoing larger study are presented).

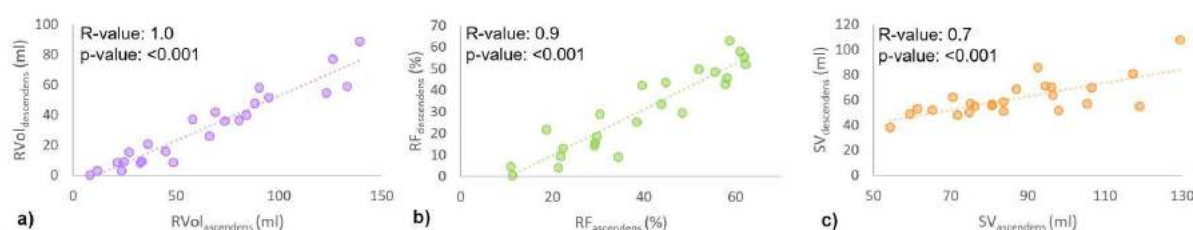
**Methods:** From a group of 43 patients with chronic AR, a subgroup of 24 patients with a non-dilated ascending aorta ( $<40$  mm) was selected (age =  $53 \pm 16$  years; 5 females; moderate [ $n=9$ ], severe [ $n=15$ ], according to echocardiography) to assess AR severity without the influence of complex flow and through-plane heart motion effects. PC measurements were performed in an image plane orthogonal to the flow in the ascending aorta, also covering the descending aorta (slice thickness = 8 mm, voxel size =  $2.5 \times 2.5$  mm<sup>2</sup>, TR/TE = 4.8/2.9 ms, BW = 477.8 Hz/pixel, flip angle =  $12^\circ$ , phases per cardiac cycle = 40, acc factor = 2, TFE factor = 4, TFE shots = 13, NSA = 1). Detailed flow analyses of the PC measurements were performed using the freely available software Segment (<http://segment.heiberg.se>). Flow rate curves in the ascending and descending aorta were generated and from them, several quantitative flow measures were extracted, such as conventional PC measures used in the ascending aorta, echocardiographic measures, as well as novel PC measures. Also, the aortic diameter was extracted in the analysis. Patients were graded according to outcome-based thresholds to have severe or non-severe AR based on RF  $> 33\%$  in the ascending aorta [5]. Conventional PC measures in the ascending and descending aorta were compared using the Pearson correlation coefficient (R). Mann-Whitney U test was used for comparison of flow measures between patients with severe and non-severe AR. Correction for multiple testing was performed using the Bonferroni correction, where the p-value was adjusted to 0.006. Statistical analysis was performed using MATLAB (R2018a, The MathWorks, Inc., Natick, Massachusetts, United States, 2018).

**Results:** A strong association was found between conventional PC measures, i.e. regurgitation volume, regurgitation fraction and stroke volume, in the ascending and descending aorta, where the regurgitation volume and fraction showed the strongest association

(Figure 1). For patients with severe AR, the regurgitation volume, regurgitation fraction, holodiastolic flow reversal and the amount of holodiastolic flow reversal in the descending aorta were significantly higher, and the peak regurgitated velocity and the ratio of mean peak velocity in diastole and systole were significantly lower than for patients with non-severe AR (Table 1).

**Conclusions:** Our findings indicate that PC flow measures in the descending aorta can separate between severe and non-severe AR. This may be an approach to assess AR severity in patients with dilated aortas whose PC measurements in the ascending aorta are affected by complex flow and through-plane heart motion.

**Figure/Table 1**



**Caption 1**

Figure 1. Correlation plots between flow measures, i.e. regurgitation volume (RVol, a), regurgitation fraction (RF, b) and stroke volume (SV, c), in the ascending and descending aorta

**Figure/Table 2**

	Non-severe AR n=10	Severe AR n=14	p-value
Aortic diameter (mm)	27±3	30±4	0.08
<b>PC measures used in the ascending aorta</b>			
Regurgitation volume (ml)	9±6	47±20	<0.001*
Regurgitation fraction (%)	13±9	43±14	<0.001*
Stroke volume (ml)	60±10	62±18	1.0
<b>Echocardiographic measures</b>			
End-diastolic velocity (cm/s)	-19±7	-27±8	0.02
End-diastolic velocity >20 cm/s (no (%))	6 (60)	10 (71)	0.02
<b>Novel PC measures</b>			
Holodiastolic flow reversal (no (%))	0(0)	11(79)	<0.001*
Percentage of holodiastolic flow (%)	36±27	94±22	<0.001*
Peak velocity of the regurgitated flow (cm/s)	-35±9	-53±15	0.004*
The ratio of mean peak velocity in diastole and systole (%)	23±6	12±11	0.001*

Data are presented as the mean ± standard deviation (SD). The significance of the differences between non-severe and severe AR are presented as p-values. Holodiastolic flow reversal = flow reversal with a minimum flow of 10 ml/s that persists through the entirety of diastole [4]; Percentage of holodiastolic flow = the percentage of flow reversal during diastole that is at least 10 ml/s

\*Indicates significant difference

**Caption 2**



Table 1. Cardiovascular magnetic resonance characteristics in the descending aorta in patients with chronic aortic regurgitation and non-dilated aortas (<40 mm), separately for patients with non-severe and severe AR

### **Bibliographic References**

5. Myerson SG, d'Arcy J, Mohiaddin R et al (2012) Aortic regurgitation quantification using cardiovascular magnetic resonance: association with clinical outcome. *Circulation* 126:1452-1460, 4. Bolen MA, Popovic ZB, Rajiah P et al (2011) Cardiac MR assessment of aortic regurgitation: holodiastolic flow reversal in the descending aorta helps stratify severity. *Radiology* 260:98-104, 3. Lagerstrand KM, Truedsson F, Gao SA et al (2021) Importance of through-plane heart motion correction for the assessment of aortic regurgitation severity using phase contrast magnetic resonance imaging. *Magn Reson Imaging* , 2. Truedsson F, Polte CL, Gao SA et al (2021) Importance of complex blood flow in the assessment of aortic regurgitation severity using phase contrast magnetic resonance imaging. *Int J Cardiovasc Imaging* , 1. Myerson SG (2012) Heart valve disease: investigation by cardiovascular magnetic resonance. *J Cardiovasc Magn Reson* 14:7-7

Speaker: F. Truedsson

Category: Aorta, Aortic Regurgitation, Phase Contrast

000113

## Improving automated segmentation of long and short axis cine DENSE data using 2D+time convolutional neural networks

H. Barbaroux \* (1); A. D. Scott (2); A. A. Young (1)

(1) Department of biomedical engineering, King's College London, London, United Kingdom; (2) Cmr unit, The Royal Brompton and Imperial College, Sydney Street, London, United Kingdom

### Abstract

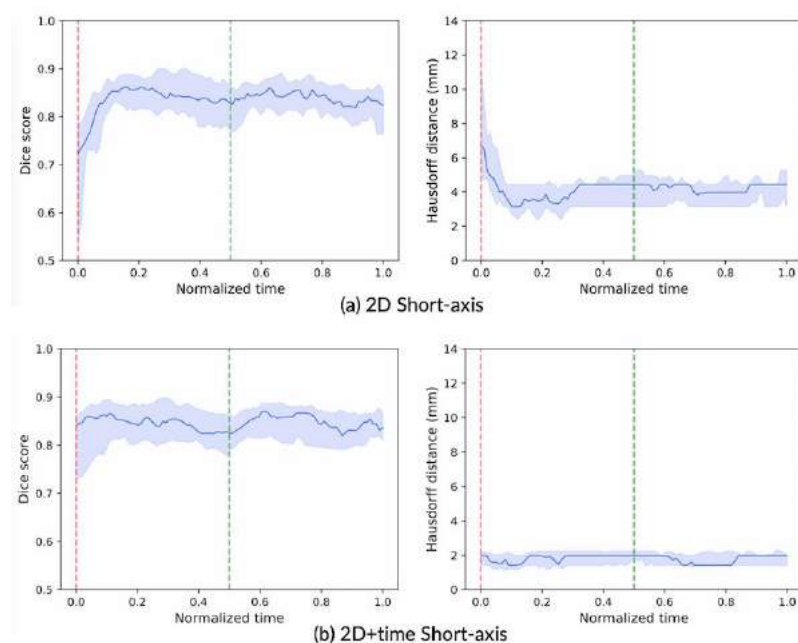
**Background:** Cine Displacement Encoding with Stimulated Echoes (DENSE) is a CMR technique providing precise myocardial strain at a pixel level [1]. Processing DENSE images into meaningful motion and strain information is tedious and user dependent, as it requires manual input. One time-consuming aspect of the processing pipeline is the segmentation of the left ventricular (LV) myocardium. Deep learning methods, and particularly Convolutional Neural Networks (CNNs), have been used increasingly for automated segmentation of medical images over the past 5 years [2, 3], and are explored in the present study for automated LV myocardial segmentation of long and short-axis images from cine DENSE data.

**Methods:** nnU-Net models (self-adapting U-Net framework, [4]) were trained to segment the LV myocardium in short-axis and four-chamber magnitude 2D cine DENSE images. To act as gold-standard labels, all the cases were labelled manually using the DENSEanalysis open-source Matlab software [5]. The dataset consisted of 2 direction encoded breath hold acquisitions (typical spatial resolution of  $3.4 \times 3.4 \times 8 \text{ mm}^3$ ) from 117 short-axis slices (25 healthy subjects, 3 DCM patients, 3 HCM patients and 6 recovered DCM patients with left bundle branch block) and 28 four-chamber slices (9 healthy subjects and 6 recovered DCM patients). The cohort was split 80%/20% to create a training set and an independent test set. Training subjects were split into 4 folds for cross-validation (CV) training. Two different architectures were implemented and compared: a 2D architecture, and a 2D+time variant, for which frames of each dataset were stacked in a third dimension and processed with 3D nnU-Net. Networks were evaluated using DICE score and Hausdorff distance using the manual segmentation as a ground truth. A temporal analysis was conducted on the independent test sets, to evaluate and compare 2D/2D+time results over the cardiac cycle.

**Results:** Both 2D and 2D+t networks were able to automatically segment cine DENSE data in the long and short axis. Mean DICE scores and Hausdorff distances were respectively  $0.82 \pm 0.06 / 0.83 \pm 0.05$  and  $5.0 \pm 2.3 / 4.2 \pm 1.6 \text{ mm}$  for 2D/2D+time networks in the short axis, and  $0.81 \pm 0.02 / 0.84 \pm 0.02$  and  $14.1 \pm 10.2 / 8.6 \pm 4.7 \text{ mm}$  in the long axis. Using 2D architectures, the temporal analysis shows a clear drop in performance for early frames of the cardiac cycle, at end-diastole (Fig. 1a, 2a). This is due to the poor image contrast between blood and myocardium in the early frames, as the blood has not left the imaging slice yet (Fig. 3). In comparison, the 2D+time networks mitigate that behavior (Fig. 1b, 2b), by increasing the DICE score by up to 0.21 and 0.48 in the early frames (respectively for short-axis and long-axis) and reducing the Hausdorff distance by up to 88% and 71%.

**Conclusion:** Segmentation is a key stage in developing automatic DENSE processing, with recent work demonstrating a 2D CNN based automated DENSE analysis pipeline for short axis data [3]. Here we leverage 3D architectures for 2D+time processing, which were shown to improve the models' performance for the low-contrast initial frames over 2D only. Furthermore, we demonstrate the effectiveness of the segmentation for both long and short axis data. Additional strategies, like Recurrent Neural Networks, could be investigated to further exploit temporal correlations in cine DENSE data. Deep learning is showing significant potential for automated processing in medical imaging, and will be key to facilitating the transition of DENSE processing towards online automated solutions at acquisition time.

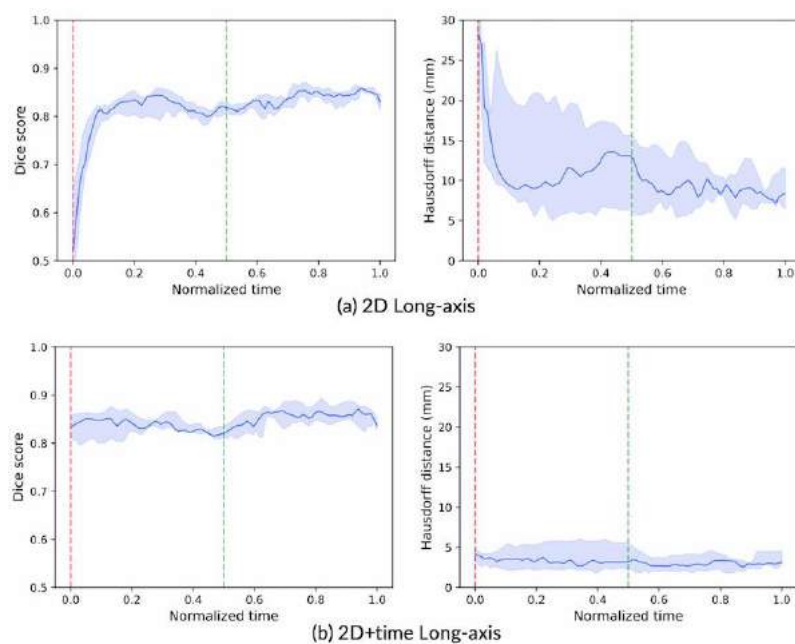
**Figure/Table 1**



**Caption 1**

Figure 1: Short-axis segmentation performance over the cardiac cycle (independent test set with 25 cases). Top row: 2D, Bottom row: 2D+time. Time was normalized so that end-diastole corresponds to  $t=0$  (red line) and end-systole to  $t=0.5$  (green line). Blue curve: median performance. Shaded area: interquartile range.

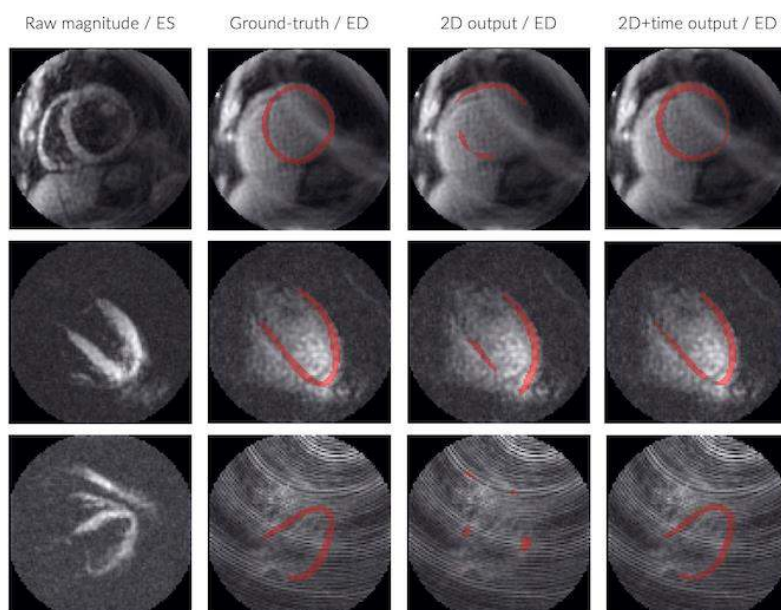
**Figure/Table 2**



**Caption 2**

Figure 2: Long-axis segmentation performance over the cardiac cycle (independent test set with 6 cases). Top row: 2D, Bottom row: 2D+time. Time was normalized so that end-diastole corresponds to  $t=0$  (red line) and end-systole to  $t=0.5$  (green line). Blue curve: median performance. Shaded area: interquartile range.

**Figure 3**



### Caption 3

Figure 3: Inference examples for an early frame. Red area: segmentation mask. Top and middle rows are examples of low contrast due to blood, respectively on short-axis and long-axis studies. The bottom row shows a case with severe reconstruction artefacts in early frames (four-chamber). ES: End-systole, ED: End-diastole.

### Bibliographic References

[5] A. D. Gilliam and J. D. Suever, and contributors, “DENSEanalysis”, 2021. Available: <https://github.com/denseanalysis/denseanalysis>., [4] F. Isensee, P. F. Jaeger, S. A. Kohl, J. Petersen, and K. H. Maier-Hein, “nnU-Net: A self-configuring method for deep learning-based biomedical image segmentation,” *Nature Methods*, vol. 18, no. 2, pp. 203–211, 2021., [3] S. Ghadimi, D. A. Auger, X. Feng, et al., “Fully-automated global and segmental strain analysis of DENSE cardiovascular magnetic resonance using deep learning for segmentation and phase unwrapping,” *Journal of Cardiovascular Magnetic Resonance*, vol. 23, no. 1, p. 20, 2021., [2] O. Ronneberger, P. Fischer, and T. Brox, “U-Net: Convolutional networks for biomedical image segmentation,” 2015. Available: <https://arxiv.org/pdf/1505.04597>., [1] D. Kim, F. H. Epstein, W. D. Gilson, and L. Axel, “Increasing the signal-to-noise ratio in DENSE MRI by combining displacement-encoded echoes,” *Magnetic Resonance in Medicine*, vol. 52, no. 1, pp. 188–192, 2004.

Speaker: H. Barbaroux

Category: Segmentation, DENSE, Image Analysis

000117

## Development of Deep Learning Virtual Native Enhancement for Gadolinium-Free Myocardial Infarction and Viability Assessment

Q. Zhang \* (1); M. K. Burrage (2); M. Shanmuganathan (2); R. A. Gonzales (2); C. Nikolaidou (2); I. A. Popescu (2); E. Lukaschuk (2); S. Neubauer (2); V. Ferreira (2); S. Piechnik (2)

(1) Oxford centre for clinical magnetic resonance research (ocmr), Oxford Centre for Magnetic Resonance (OCMR), Headington, Oxford, United Kingdom; (2) Oxford centre for clinical magnetic resonance research (ocmr), University of Oxford, Oxford, United Kingdom

### Abstract

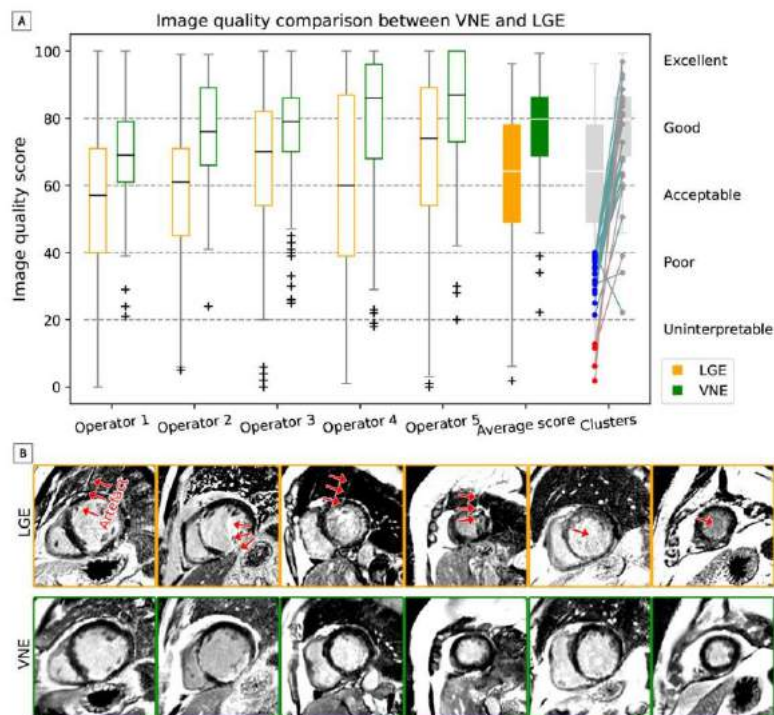
**Background:** Late gadolinium enhancement (LGE) on cardiovascular magnetic resonance (CMR) is the imaging gold standard for assessment of chronic myocardial infarction (MI) and myocardial viability. However, LGE requires intravenous contrast agent administration, which increases the cost and lengthens the CMR procedure. Artificial intelligence-based virtual native enhancement (VNE) [1] has recently emerged as a promising alternative to LGE and is well-validated in patients with hypertrophic cardiomyopathy. We hypothesized that VNE can be further extended to assess chronic MI.

**Methods:** Information on myocardial tissue properties and wall motion is derived from native T1-mapping, inversion recovery-weighted images, and cine images, which are input into a deep learning generator to produce VNE images [1]. We collected 1602 sets of images of chronic MI to train the neural networks, using a modified conditional generative adversarial network approach. The trained VNE imaging module was tested on 145 independent image materials from 43 patients with chronic MI. Five blinded observers independently assessed the image quality of VNE and LGE using a scale from 0-100 guided by 5 categories from “uninterpretable” to “excellent”. Regions of interest of the left ventricle, remote myocardium, and blood pool were segmented semi-automatically for scar quantification. Interobserver variability was calculated as standard deviation (SD) and intra-class correlation (ICC). Correlation between scar quantification by VNE and LGE was assessed using linear regression and ICC.

**Results:** VNE provided significantly better image quality than LGE, as assessed by all 5 operators ( $p < 0.001$ ; Figure 1A). Interobserver variability was  $SD = 9.6 \pm 1.1$  with  $ICC = 0.79 \pm 0.04$ . For “uninterpretable” (Figure 1A, red clusters;  $n = 4$ ) or “poor” (blue;  $n = 19$ ) LGE cases, VNE significantly improved the quality of all but 1 image. Conventional LGE can be affected by breathing artefacts and low signal-to-noise ratio (Figure 1B), while VNE produced better and more consistent image quality with better-defined myocardial borders. VNE detected and located areas of infarction in high visuospatial agreement with LGE (Figure 2). Scar burden quantification by VNE correlated strongly with LGE in 43 test patients (Figure 3;  $R = 0.83$ ,  $p < 0.001$ ,  $ICC = 0.91$ ).

**Conclusions:** Deep learning-based VNE produces “virtual LGE” by effectively serving as a “virtual contrast agent” that enhances native CMR signals, with significantly better image quality, high agreement in visuospatial distribution and quantification of scar burden compared to conventional LGE in chronic MI. VNE has enormous potential to replace LGE in common cardiac pathologies to significantly improve clinical practice, reduce CMR scan time and costs, and expand the reach of CMR in the near future.

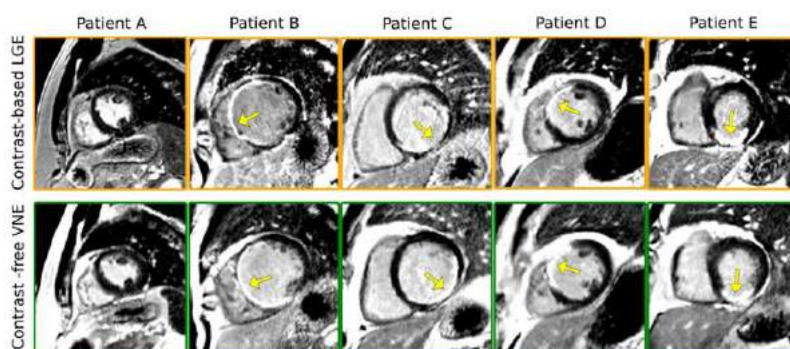
### Figure/Table 1



## Caption 1

Figure 1. LGE and VNE image quality assessment on chronic infarction cases. A: VNE offers significantly better image quality, as assessed by 5 blinded operators and their average scores (all  $p < 0.001$ ). B: Examples of image quality improvement by VNE. Arrows point to artefacts and poor contrast in the LGE images.

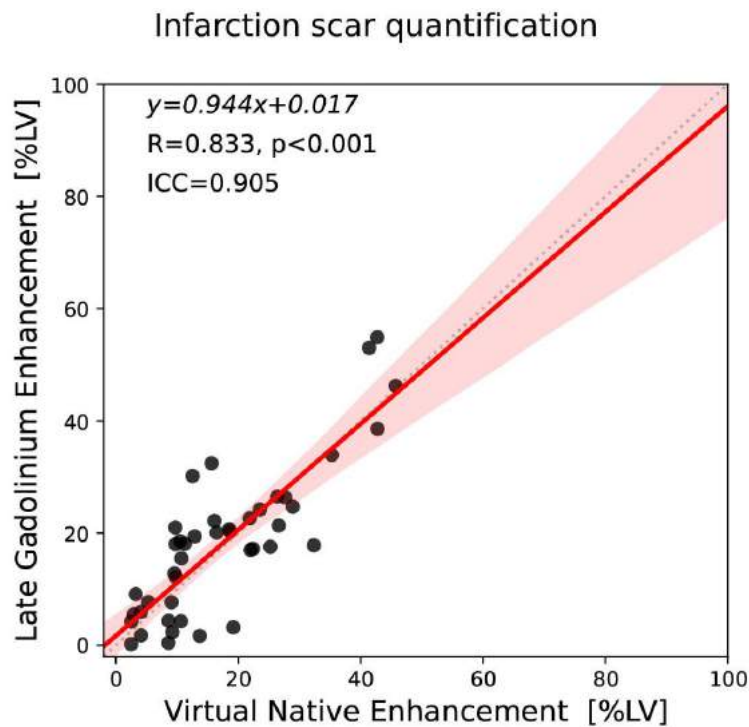
## Figure/Table 2



## Caption 2

Figure 2. Examples to illustrate high visuospatial agreement between virtual native enhancement (VNE) and conventional late gadolinium enhancement (LGE) for the detection of chronic myocardial infarction (arrows).

**Figure 3**



**Caption 3**

Figure 3. VNE correlated strongly with conventional LGE in quantifying myocardial infarction scar burden in 43 test patients.

### Bibliographic References

Zhang, Qiang, et al. "Toward replacing late gadolinium enhancement with artificial intelligence virtual native enhancement for gadolinium-free cardiovascular magnetic resonance tissue characterization in hypertrophic cardiomyopathy." *Circulation* 144.8 (2021): 589-599. <https://doi.org/10.1161/CIRCULATIONAHA.121.054432>

Speaker: Q. Zhang

Category: Chronic Myocardial Infarction, Non-Contrast, Tissue Characterization



000118

## **Pediatric Patients with Post-COVID-19 Vaccination Myocarditis Have Greater Strain Than Those With Non-Vaccine Myocarditis**

D. Vaiyani \* (1); M. D. Elias, (1); D. M. Biko (2); K. K. Whitehead (1); M. A. Harris, (1); S. L. Partington, (1); M. A. Fogel, (1)

(1) Cardiology, Children's Hospital of Philadelphia, Philadelphia, United States of America;  
(2) Radiology, Children's Hospital of Philadelphia, Philadelphia, United States of America

### **Abstract**

#### Background

There have been reports of myocarditis following messenger RNA vaccination against COVID-19. We sought to describe cardiac magnetic resonance (CMR) findings among these patients in a pediatric cohort.

#### Methods

This study was a retrospective chart review at a large academic center of patients who were clinically diagnosed with post-vaccine myocarditis undergoing CMR. Data collected included demographics, clinical course, T1 and T2 parametric mapping, signal intensity on T2-weighted dark blood turbo inversion recovery magnitude (TIRM) imaging, ventricular function, and areas of delayed enhancement. Post processing strain analysis was performed using feature tracking. Strain values, T1 values and ventricular function were compared to age- and gender-matched controls with non-vaccine myocarditis using a Wilcoxon Rank Sum test.

#### Results

Among 12 patients with presumed post-vaccine myocarditis, 11 were male and 11 presented after the second vaccination dose, typically within 4 days (Table 1). All patients presented with chest pain and elevated troponin, and nearly all patients had electrocardiographic changes suggestive of myocarditis, yet typically with normal ventricular function on echocardiography. Patients were treated with nonsteroidal anti-inflammatory medication and discharged within 4 days after presentation. The majority of patients (10/12) met CMR criteria for myocarditis. All patients had delayed enhancement on gadolinium imaging typically seen in the lateral and inferior walls on the left ventricle (Figure 3) but only five had prolonged T1 values. Additionally, 10 patients met criteria for edema based on skeletal muscle to myocardium signal intensity ratio on TIRM imaging, and only 5 patients had prolonged T2 values. Compared to the non-vaccine myocarditis cohort, patients with post-vaccine myocarditis had greater short-axis global circumferential (median -21.3% versus -19.5%,  $p=0.03$ ) and global radial strain (median 40.9% versus 34.4%,  $p=0.02$ ), as well as greater right ventricle function (median 65.7% versus 60%,  $p=0.02$ ) and cardiac output (4.2 versus 3.6 L/min/m<sup>2</sup>,  $p=0.0066$ ). There was no difference in left ventricular function, long axis global longitudinal or radial strains (Table 2). There was also no significant difference in extracellular volume (27.9 versus 29.1,  $p=0.58$ ) nor T1 values.

## Conclusions

Post vaccine myocarditis appears to be a self-limited illness, largely in males after the second dose, with near universal late enhancement typically located in the inferior and/or lateral wall. Patients with post-vaccine myocarditis have greater short-axis global circumferential and radial strains but similar native and contrast enhanced T1 values compared to those with non-vaccine myocarditis.

**Figure/Table 1**

Patient	Age (years)	Gender	Vaccine Given	Vaccine Dose	Symptom Onset	Symptoms	Peak Troponin-I	Peak BNP	EKG Changes
1	12	M	BNT1262b2 (Pfizer)	Second	3 days	Chest Pain	5.87	118 (a)	T-wave inversion in inferior leads
2	16	M	BNT1262b2 (Pfizer)	Second	1 day	Chest Pain, Fever, Myalgias, Malaise	14.6	419 (a)	PR depression, Nonspecific T-wave changes
3	13	M	BNT1262b2 (Pfizer)	Second	1 day	Chest Pain, Fever, Headache, Nausea	18.83	35	ST Elevation in Anterolateral and Inferolateral leads
4	17	M	BNT1262b2 (Pfizer)	Second	2 days	Chest Pain, Nausea	25.75	87	None
5	17	M	BNT1262b2 (Pfizer)	Second	3 days	Chest Pain	8.12	30.1	ST Elevation, PR Depression in Inferolateral Leads
6	15	M	BNT1262b2 (Pfizer)	Second	1 day	Chest Pain, Fever, Nausea	88.38	293.4	ST Elevation in Inferolateral Leads
7	14	M	BNT1262b2 (Pfizer)	Second	3 days	Chest Pain, Malaise, Fever, Nausea, Myalgias	1.95	<10	Nonspecific T-wave Changes

8	16	M	BNT1262b 2 (Pfizer)	Second	22 days	Chest Pain	13.13	31	ST Elevation, T-wave inversion in inferolateral leads
9	17	F	BNT1262b 2 (Pfizer)	Second	2 days	Chest Pain, Malaise, Fever	7.06	20.2	T wave inversion in inferior leads
10	13	M	BNT1262b 2 (Pfizer)	Second	2 days	Chest Pain, Malaise, Fever	15.15	56.6	ST Elevation in Inferolateral Leads, T wave Inversions in Inferior Leads
11	14	M	BNT1262b 2 (Pfizer)	First	3 days	Chest Pain, Malaise, Fever	8.48	31.2	ST elevation in Inferolateral Leads
12	16	M	BNT1262b 2 (Pfizer)	Second	4 days	Chest Pain	22 (b)	not drawn	Sinus rhythm, premature ventricular complex

### Caption 1

a NT-proBNP with listed normal values < 125 pg/mL

b high sensitivity troponin level in ng/L, with normal values listed as < 14 ng/L

Troponin-I measured in ng/mL; BNP = Brain natriuretic peptide, in pg/mL

### Figure/Table 2

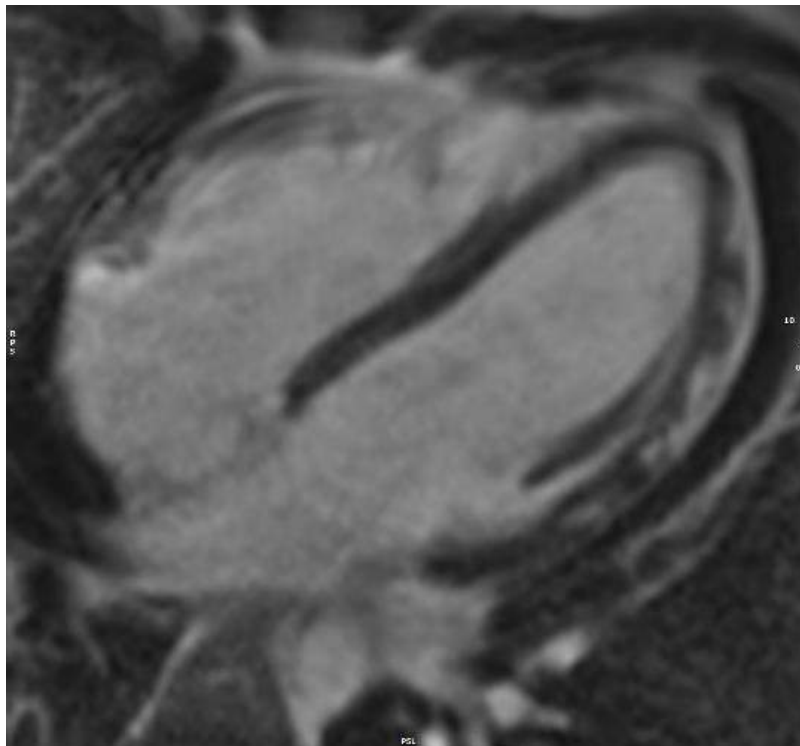
	Study Patients		Age Matched Controls		p value
	Median	IQR	Median	IQR	
<b>LV Ejection Fraction</b>	70.5	63.5, 77.0	66	62.0, 70.5	0.21
<b>RV Ejection Fraction</b>	65.7	58.0, 69.8	60	51.5, 62.5	0.02
<b>Indexed Cardiac Output</b>	4.2	3.9, 4.8	3.6	3.1, 3.7	0.0066

<b>Short Axis Global Circumferential Strain</b>	-21.3	-22.5, -20.5	-19.5	-21.0, -17.1	0.03
<b>Short Axis Global Radial Strain</b>	40.9	37.8, 45.8	34.4	28.6, 39.1	0.02
<b>Long Axis Global Longitudinal Strain</b>	-19.1	-20.7, -17.9	-17.8	-19.9, -15.6	0.34
<b>Long Axis Global Radial Strain</b>	33.8	32.2, 39.0	33.5	25.9, 36.0	0.62
<b>Native T1a</b>	1033	1018, 1094	1028	1020, 1068	0.97
<b>Contrast T1a</b>	447	426, 469	431	381, 446	0.10

## Caption 2

a Patient 4 was excluded from T1 value analysis as their study was done with a 3 Tesla scanner while their age-matched control study was done with a 1.5 Tesla scanner

## Figure 3



## Caption 3

Four chamber bright blood delayed enhancement imaging of patient 8 demonstrating enhancement in the mid and apical anterolateral regions.

**Bibliographic References**

Ferreira VM, Schulz-Menger J, Holmvang G, et al. Cardiovascular Magnetic Resonance in Nonischemic Myocardial Inflammation: Expert Recommendations. *Journal of the American College of Cardiology* 2018; 72(24): 3158-76., Dionne A, Sperotto F, Chamberlain S, et al. Association of Myocarditis With BNT162b2 Messenger RNA COVID-19 Vaccine in a Case Series of Children. *JAMA Cardiol* 2021., Marshall M, Ferguson ID, Lewis P, et al. Symptomatic Acute Myocarditis in Seven Adolescents Following Pfizer-BioNTech COVID-19 Vaccination. *Pediatrics* 2021., Shaw KE, Cavalcante JL, Han BK, Gossel M. Possible Association Between COVID-19 Vaccine and Myocarditis: Clinical and CMR Findings. *JACC Cardiovasc Imaging* 2021.

Speaker: D. Vaiyani

Category: Pediatric , Myocarditis, Cardiac Strain

000125

## Recalcitrant intracardiac masses in a teenager: A case of Hughes-Stovin syndrome

S. Ro \* (1); S. Hashemi, (1); T. Slesnick (1)

(1) Pediatric Cardiology, Children's Healthcare of Atlanta - Egleston Hospital, Atlanta, United States of America

### Abstract

#### Description of Clinical Presentation:

A 16-year-old previously healthy male presents to an emergency room with fevers, chills and a 15-lb weight loss over the past three weeks. Initial work-up revealed elevated inflammatory markers and a positive blood culture for *Cutibacterium acnes* bacteremia. His chest CT demonstrated bilateral septic pulmonary emboli and a CMR showed multiple masses within the right ventricular (RV) cavity concerning for bacterial endocarditis (Figure 1). He was taken to the operating room for surgical debulking with partial removal of the RV mass with an inconclusive tissue biopsy. He was discharged from the hospital on intravenous (IV) vancomycin and ceftriaxone. He returned 6 weeks later with persistent fevers and weight loss. An echocardiogram revealed a new mobile mass in the right atrium (RA) as well as multiple RV masses (Figure 2). He had multiple thrombi in his left iliac vein, right subclavian and right axillary veins. He returned to the operating room for further resection. The tissue biopsy revealed inflammatory infiltrate supportive of bacterial endocarditis and the patient was discharged on IV penicillin G and levofloxacin. Two weeks later, he returned with continued fevers and weight loss. A repeat chest CT revealed two large right pulmonary artery mycotic pseudoaneurysms in the distribution of pulmonary emboli seen on the prior chest CT (Figure 3). The patient began having hemoptysis, and subsequently underwent device closure of the ostia of the right pulmonary artery pseudoaneurysms followed by a right lower lobectomy. Given these symptoms of persistent fevers, a prothrombotic state, and new pulmonary pseudoaneurysms, he was diagnosed with a variant of Behcet's disease called Hughes-Stovin syndrome, characterized by thrombophlebitis and multiple pulmonary aneurysms predominantly in young males. The intracardiac masses were thought to be recurring intracardiac thrombi. He was started on corticosteroids and transitioned to cytotoxin two weeks later and has remained afebrile with improving appetite.

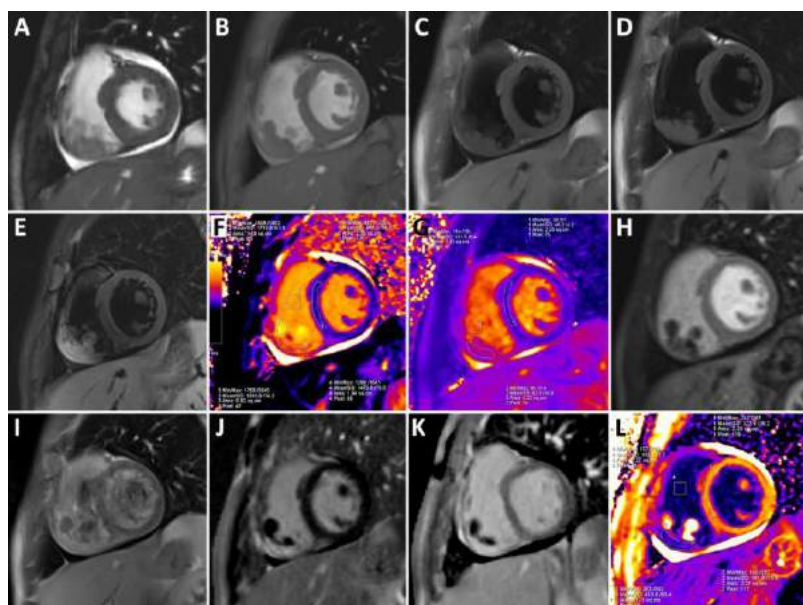
#### Diagnostic Techniques and Their Most Important Findings:

CMR was used to characterize the intracardiac masses. The initial MRI revealed a large, lobulated intracardiac mass along the inferior and anterior basilar and mid RV free wall. It was highly unusual that this suspected endocarditis along the RV free wall did not involve the tricuspid valve. The mass had elevated T1 and T2 values compared to the myocardium and was hyperintense on T2 STIR images. There was nearly absent perfusion within the pedunculated masses and no evidence of late gadolinium enhancement, unlike the base of the mass which showed enhancement. The pedunculated portions appeared to have a high free fluid content, similar to the pericardial effusion (Figure 1). Based on the fluid-filled, hypoperfusing and heterogeneous characteristics of the mass, the differential diagnoses included myxoma, atypical sarcoma, infectious or inflammatory process.

#### Learning Points from this Case:

CMR can help characterize the tissue of an intracardiac mass but in the setting of a systemic inflammatory disorder such as Hughes-Stovin syndrome, a multimodality approach is needed to distinguish thrombi from cardiac tumors or vegetations. This case demonstrates the importance of considering a systemic inflammatory process in the presence of multiple vascular masses that are unresponsive to antibiotics or anticoagulation.

**Figure/Table 1**



**Caption 1**

Initial cardiac MRI showing a heterogenous intracavitary RV mass on SSFP (A), spoiled gradient echo (B), T1-weighted Turbo spin echo (TSE) (C), T2-weighted TSE (D), T2 STIR (E), native T1 map (F), T2 map (G), first pass perfusion (H), post-contrast T1-weighted TSE (I), PSIR (J), PSIR with long inversion time (K) and post-contrast T1 map.

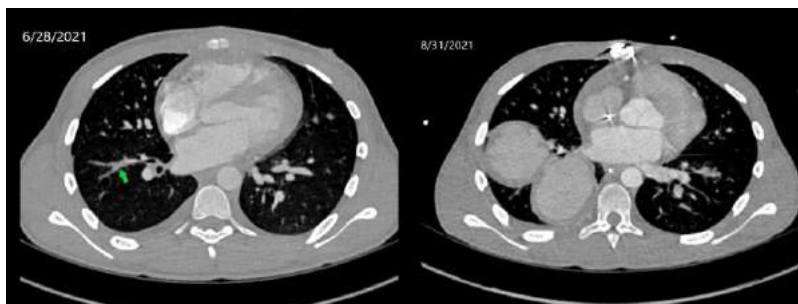
**Figure/Table 2**



### Caption 2

Echocardiogram revealed a highly mobile, pedunculated mass (3.5 x 1.5 cm at greatest width) attached to the wall of the right atrial appendage and multiple large masses along the RV free wall just inferior to the tricuspid valve annulus.

### Figure 3



### Caption 3

A CTA of the chest demonstrates the formation of two right lower lobe masses with central enhancement which are in continuity with the pulmonary artery branches, consistent with pulmonary artery pseudoaneurysms (right image) that was not present two months prior (left image). Green arrow signifies septic emboli seen at that time.

### Bibliographic References

Ng MY, Boutet A, Carette S, de Perrot M, Cusimano RJ, Nguyen ET. Behcet disease presenting with cardiac and pulmonary masses. Canadian Journal of Cardiology 2015,31:1204.e5-1204.e7, Khalid U, Saleem T. Hughes-Stovin syndrome. Orphanet Journal of Rare Diseases 2011,6:15

Speaker: S. Ro

Category: Cardiac Mass, Pediatric , Children



## Improved strain analysis of cine images by deep learning from DENSE

Y. Wang \* (1); C. Sun (2); S. Ghadimi (1); D. Auger (1); P. Croisille (3); M. Viallon (3); J. J. Cao (4); J. Cheng (4); A. Scott (5); P. Ferreira (5); J. Oshinski (6); D. Ennis (7); K. Bilchick (8); F. Epstein (1)

(1) Biomedical Engineering, University of Virginia, Charlottesville, United States of America; (2) Biomedical engineering, University of Virginia, Columbia, United States of America; (3) Creatis cnrs 5220 inserm u1206 research lab, radiology department, INSA Lyon, Villeurbanne; (4) Cardiac imaging, St Francis Hospital and Heart Center, Roslyn, United States of America; (5) Cardiovascular magnetic resonance unit, The Royal Brompton Hospital, London, United Kingdom; (6) Department of radiology and imaging sciences, Emory University School of Medicine, Atlanta, United States of America; (7) Department of radiology, Stanford University, Stanford, United States of America; (8) Cardiovascular division, department of medicine, University of Virginia Health System, Charlottesville, United States of America

### Abstract

**Background:** CMR myocardial strain imaging is used diagnostically and prognostically for many types of heart disease. Feature tracking (FT) is the most widely used and convenient method for strain MRI; however, it is less accurate than strain-dedicated acquisitions like displacement encoding with stimulated echoes (DENSE) (1-4) especially for segmental strain. FT tracks myocardial contours instead of intramyocardial tissue because the myocardium appears very uniform on cine MRI and lacks features to track (5). FT then uses an imperfect model to compute strain, which reflects tissue deformation. In contrast, DENSE directly measures intramyocardial tissue displacement; however, it requires additional acquisitions. As DENSE provides both myocardial contours and accurate intramyocardial tissue displacement information, we investigated the use of DENSE data to train deep networks to predict intramyocardial tissue motion from contour motion. This deep learning (DL) approach, termed DENSE-trained strain analysis (DTSA), may provide the clinical convenience of FT and accuracy similar to DENSE.

**Methods:** A 3D convolutional neural network (CNN) with encoder-decoder structure was trained to predict intramyocardial displacement from contour motion (Fig. 1A). During training, the inputs were a time series of myocardial contours derived from DENSE magnitude images and the ground truth data were DENSE tissue displacement measurements. Because DENSE and cine images at matched slice locations share similar motion patterns, we tested our trained model using contours derived from standard cine images. Data pre-processing: We segmented the DENSE and cine images, binarized the images by filling the myocardium area with 1 and the outside area and blood pool with 0, and cropped the images to a fixed size:  $N_x \times N_y$ . Data augmentation was performed using 90° rotations. Cine images were scaled to match the resolution range of DENSE images. The input size for the network was  $N_x \times N_y \times N_t$ , with  $N_t$  representing the number of temporal frames. The output size was  $2 \times N_x \times N_y \times N_t$ , with the factor of 2 accounting for displacements in two directions. Datasets: DENSE training datasets are described in Fig. 1B, and included a total of 42 patients with various pathologies such as left bundle branch block (LBBB), hypertrophic cardiomyopathy,

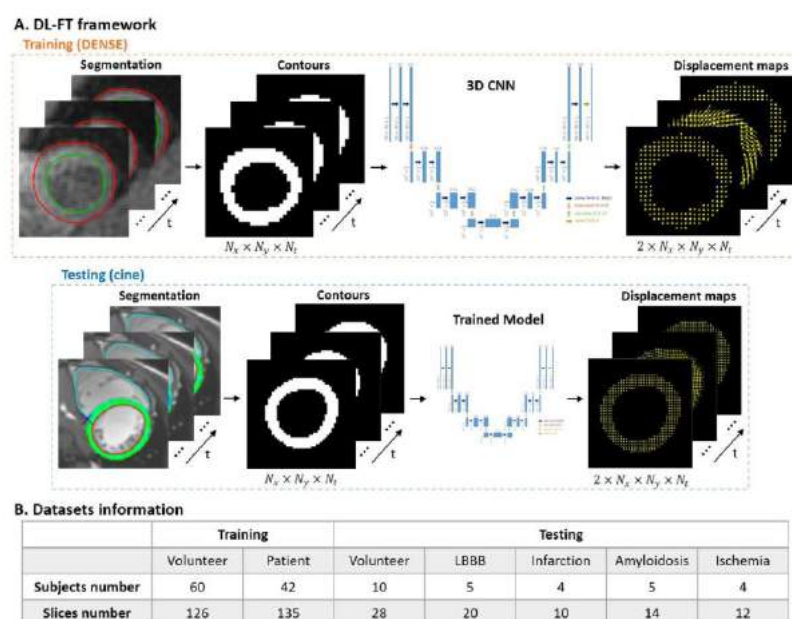
dilated cardiomyopathy, infarction, coronary artery disease and hypertension. The model was tested on cine images of 10 volunteers and 18 patients in 3 short-axis views (base, mid-level and apex) (Fig. 1B).

**Results:** Fig. 2 shows examples comparing DTSA, DENSE, and commercial FT (SuiteHEART, NeoSoft) for a healthy subject and a LBBB patient. End-systolic circumferential strain (Ecc) maps are shown for DTSA and DENSE, and segmental strain curves are shown for all three methods. DTSA shows better agreement with the ground truth (DENSE) than FT with respect to global and segmental circumferential strain-time curves. Correlation plots, Bland-Altman plots (Fig. 3A, B), intraclass correlation (ICC) and coefficient of variation (CoV) (Fig. 3C) all show that DTSA outperformed FT for both global and segmental Ecc.

**Conclusions:** The proposed DTSA network showed the ability to depict detailed intramyocardial motion, which is challenging for optical-flow based FT methods. The proposed network showed improved performance for both global and segmental Ecc compared to commercial FT results.

**Acknowledgements:** NIH R01HL147104, UVA Ivy Biomedical Innovation Fund and AHA 2020AHAPRE0000203801.

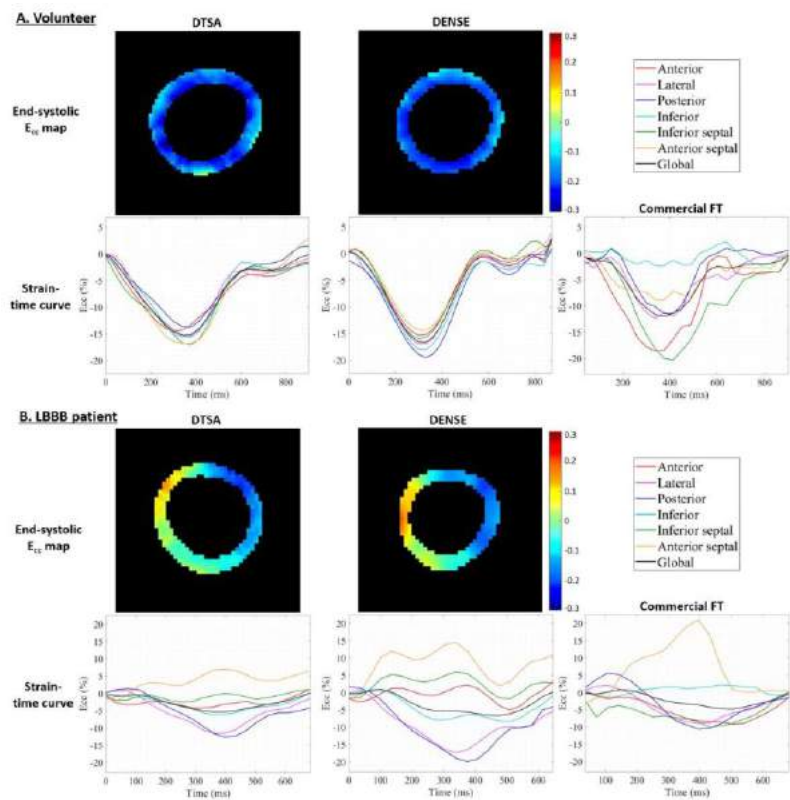
**Figure/Table 1**



**Caption 1**

**Fig 1.** (A) Schematic showing the use of deep learning to predict intramyocardial displacement from contour motion, and (B) description of CMR datasets used for training and testing.

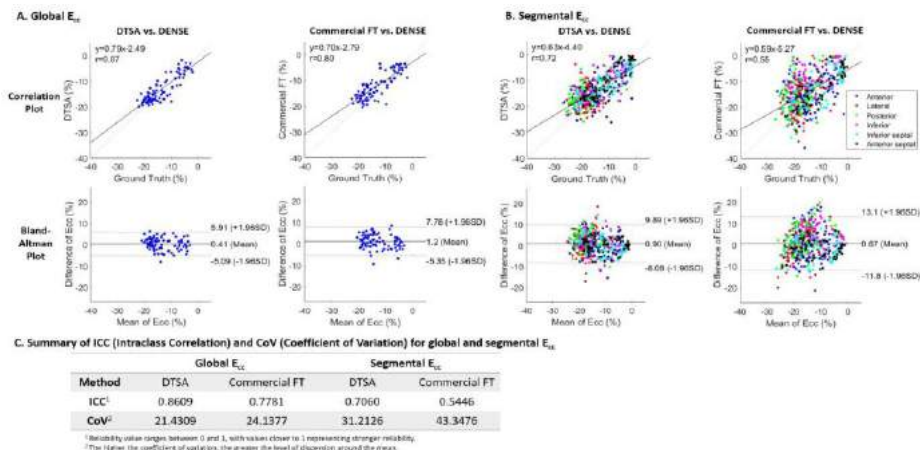
Figure/Table 2



Caption 2

**Fig 2.** Examples comparing DTSA, DENSE, and commercial FT (SuiteHEART, NeoSoft) for a healthy subject (A) and a LBBB patient (B). End-systolic strain maps are shown for DTSA and DENSE (A, B), and segmental strain curves are shown for all three methods (A, B).

Figure 3



### Caption 3

**Fig 3.** Correlation plots, Bland-Altman plots, ICC and CoV comparing DTSA and FT with DENSE ground truth data for the analysis of Ecc. (A) Global Ecc, (B) segmental Ecc, and (C) summary of ICC and CoV for global and segmental Ecc.

### Bibliographic References

[1] Wehner GJ, Jing L, Haggerty CM, Suever JD, Chen J, Hamlet SM, Feindt JA, Mojsejenko WD, Fogel MA, Fornwalt BK. Comparison of left ventricular strains and torsion derived from feature tracking and DENSE CMR. *Journal of Cardiovascular Magnetic Resonance*. 2018 Dec;20(1):1-1., [2] Lin K, Meng L, Collins JD, Chowdhary V, Markl M, Carr JC. Reproducibility of cine displacement encoding with stimulated echoes (DENSE) in human subjects. *Magn Reson Imaging*. 2017;35:148-53., [3] Bilchick KC, Auger DA, Abdishektai M, Mathew R, Sohn MW, Cai X, et al. CMR DENSE and the Seattle Heart Failure Model Inform Survival and Arrhythmia Risk After CRT. *JACC Cardiovasc Imaging*. 2020;13(4):924-36., [4] Mangion K, Loughrey CM, Auger DA, McComb C, Lee MM, Corcoran D, et al. Displacement Encoding With Stimulated Echoes Enables the Identification of Infarct Transmurality Early Postmyocardial Infarction. *J Magn Reson Imaging*. 2020;52(6):1722-31., [5] Schuster A, Hor KN, Kowallick JT, Beerbaum P, Kutty S. Cardiovascular Magnetic Resonance Myocardial Feature Tracking: Concepts and Clinical Applications. *Circ Cardiovasc Imaging*. 2016;9(4):e004077.

Speaker: Y. Wang

Category: Feature Tracking, DENSE, Strain

000127

## Free-breathing self-gated continuous-IR spiral T1 mapping: A comparison of dual flip-angle and Bloch-Siebert B1-corrected techniques

R. Zhou \* (1); Y. Yang (2); J. Wang (3); J. P. Mugler, (4); M. Salerno (5)

(1) School of Artificial Intelligence , Beijing University of Posts and Telecommunications, Beijing, China; (2) Biomedical engineering and imaging institute and department of radiology, Icahn School of Medicine at Mount Sinai, New York, United States of America; (3) Biomedical engineering, University of Virginia, Virginia, United States of America; (4) Radiology & medical imaging, biomedical engineering, University of Virginia, Virginia, United States of America; (5) Cardiology, radiology & medical imaging, biomedical engineering, University of Virginia, Virginia, United States of America

### Abstract

**Background:** Cardiac T1 maps have been increasingly used to assess both focal and diffuse myocardial processes in cardiomyopathy (1,2). For self-gated acquisition using a continuous Look-Locker strategy, both B1 and slice profile effects(3,4) need to be considered to quantify T1. Previously, we proposed a 2FAs (5) technique to obtain T1 and flip-angle-scale maps in a single free-breathing self-gated continuous IR acquisition. To further improve T1 mapping accuracy, here we propose a Bloch-Siebert B1-corrected single flip angle acquisition under free-breathing and cardiac self-gating, and demonstrate it in phantom and in-vivo experiments.

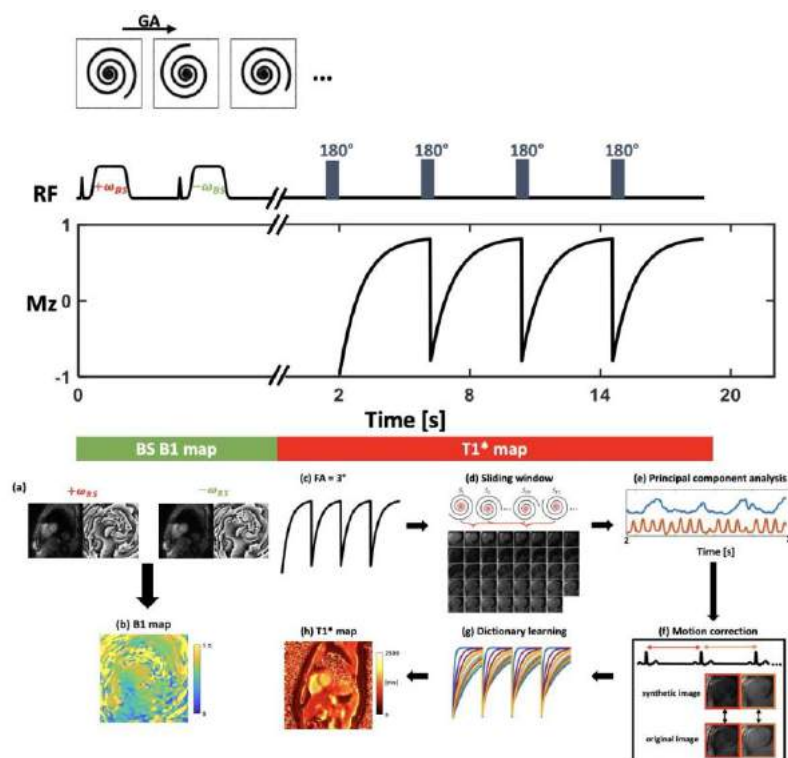
**Methods:** Experiments were performed at 3T (Prisma/Skyra, Siemens) in a T1MES phantom(6) and 18 human subjects (3 healthy volunteers and 15 patients undergoing clinically ordered cardiac magnetic resonance imaging). Healthy volunteers only underwent pre-contrast scans, while patients received a gadolinium-based contrast agent during the scan to perform both pre- and post-contrast acquisitions. Data were continuously acquired using a dual density spiral-out trajectory, rotated by the golden angle ( $137.5^\circ$ ) in time. During the first 2 seconds, off-resonance Fermi RF pulses were applied to generate a Bloch-Siebert (BS) shift B1 map(7), and the subsequent data were acquired with an IR RF pulse applied every 4 seconds (Figure 1). Self-gating cardiac triggers were extracted from a sliding-window heart image navigator. Respiratory motion correction was performed by rigidly registering the original image with its corresponding synthetic image that is generated from PCA, as they shared similar image contrast. Then, the T1\* map was obtained by fitting the 3-parameter model using dictionary-learning (8) reconstructed images. The final T1 map was generated from the B1 and the T1\* maps by using a look-up table that accounted for slice profile and B1 effects, yielding more accurate T1 values. T1 values were compared to those from IR spin echo (phantom only), MOLLI(9), SASHA(10) and 2FAs(5) results. For BS B1 mapping, parameters included: Fermi pulse duration = 8 ms, off-resonance shift =  $\pm 4$  kHz, KBS = 79.73 rad/G<sup>2</sup>, B1,peak = 0.0544 G; FOV = 340 × 340 mm<sup>2</sup>, spatial resolution = 10 × 10 × 8 mm<sup>3</sup>, TR/TE = 40.2/9.14 ms, flip angle = 15°. For T1\* mapping, parameters included: TR/TE = 8.35/1.45 ms, RF pulse TBW = 5.4, FOV = 340 × 340 mm<sup>2</sup>, spatial resolution = 1.5 × 1.5 × 8 mm<sup>3</sup>, flip angle = 3°.

**Results:** The proposed technique showed good agreement with the “gold-standard” technique IR spin-echo results in the phantom experiment (Figure 2), with the highest bias for the

longest T1 tube was less than 5%. For in-vivo studies (Figure 3), in terms of the myocardium T1 values, both the proposed technique and the previously proposed dual flip-angle method were more similar to SASHA results than to MOLLI results. MOLLI is known to underestimate T1 values, especially in pre-contrast studies. For blood pool T1 values, there is a slightly over-estimate of T1 values for 1FA+B1 results, which is potentially due to inflow effects, which is a known shortcoming for all continuous acquisition strategies.

**Conclusion:** In a single acquisition, a free breathing Bloch-Siebert shift B1 map, and a self-gated B1 and slice profile corrected T1 map were acquired. This technique was compared to our prior dual-flip angle approach and yielded more accurate T1 values in the myocardium.

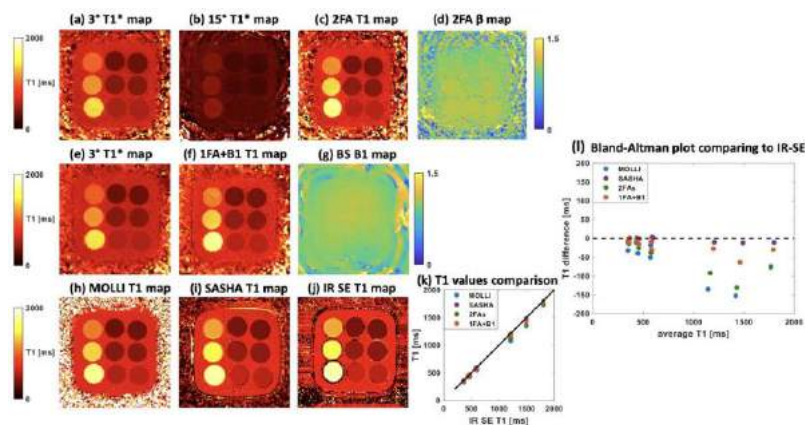
**Figure/Table 1**



**Caption 1**

Figure 1. Image acquisition and processing. All data is acquired using a spiral-out k-space trajectory rotated in time by the golden angle (GA). During the first two seconds, data is acquired in combination with off-resonance Fermi pulses, applied at positive and negative frequency shifts getting phase images (a), and used to reconstruct the Bloch-Siebert (BS) B1 map (b). Remaining data (c) is acquired with inversion pulses applied at 4s intervals, and used to reconstruct the T1\* map. Low-resolution image navigators (d) were generated using a sliding window approach, from which self-gated cardiac triggers (e) were extracted using principal component analysis. Then, respiratory motion was corrected by rigid registration on each heartbeat (f). Next, a dictionary (g) was generated based on the acquisition parameters and a range of T1 and B1+ values, and dictionary learning reconstruction was performed to create the T1\* map (h).

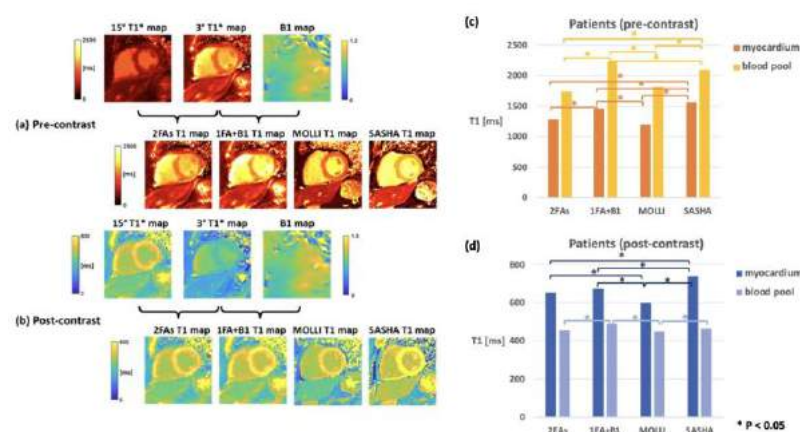
**Figure/Table 2**



**Caption 2**

Figure 2. Phantom results. The 3° (a) and 15° (b) T1\* maps from the 2FAs method were used to generate the T1 map (c) and flip angle scale-factor (β) map (d). The 3° T1\* map (e) and Bloch-Siebert shift B1 map (g) from the 1FA+B1 method were used to generate T1 map (f). The proposed T1 maps from the 2FAs and 1FA+B1 methods were compared to those from MOLLI (h), SASHA(i) and IR-SE (j). The T1 values from ROIs in each of the 9 tubes for the 2FAs, 1FA+B1, MOLLI and SASHA techniques were compared to IR-SE (k). (l) shows a Bland-Altman plot comparing the 2FAs, 1FA+B1, MOLLI and SASHA techniques with IR-SE.

**Figure 3**



**Caption 3**



Figure 3. Patient example. Short-axis basal slices from pre-contrast (a) and post-contrast (b) acquisition for a patient with coronary artery disease are shown. As indicated by the brackets,  $3^\circ$  and  $15^\circ$  T1\* maps are used to generate the 2FAs T1 map, while  $3^\circ$  T1\* and BS B1 maps are used to generate the 1FA+B1 T1 map. MOLLI and SASHA T1 maps are shown for comparison. (c) Pre-contrast T1 quantification comparison among 2FAs technique, 1FA+B1 technique, MOLLI and SASHA for patients. Orange bars show the myocardium T1 values and yellow bars represent the blood pool T1 values. (d) Post-contrast T1 quantification for patients. Dark blue bars show the myocardium T1 values and light blue bars represent the blood pool T1 values.

### Bibliographic References

1. Liu S, Han J, Nacif MS, et al. Diffuse myocardial fibrosis evaluation using cardiac magnetic resonance T1 mapping: sample size considerations for clinical trials. *J. Cardiovasc. Magn. Reson.* 2012;14:90 doi: 10.1186/1532-429X-14-90.
2. Jr ANA, Melo MDT De, Lima CR, et al. Myocardial T1 mapping and extracellular volume quantification in patients with left ventricular non-compaction cardiomyopathy. *Eur. Hear. J. - Cardiovasc. Imaging* 2018:1–8 doi: 10.1093/ehjci/jeu022.
3. Yarnykh VL. Optimal radiofrequency and gradient spoiling for improved accuracy of T1 and B1 measurements using fast steady-state techniques. *Magn. Reson. Med.* 2010;63:1610–1626 doi: 10.1002/mrm.22394.
4. Stikov N, Boudreau M, Levesque IR, Tardif CL, Barral JK, Pike GB. On the accuracy of T1 mapping: Searching for common ground. *Magn. Reson. Med.* 2015;73:514–522 doi: 10.1002/mrm.25135.
5. Zhou R, Weller DS, Yang Y, et al. Dual-excitation flip-angle simultaneous cine and T1 mapping using spiral acquisition with respiratory and cardiac self-gating. *Magn. Reson. Med.* 2021;86:82–96 doi: 10.1002/mrm.28675.
6. Captur G, Gatehouse P, Kellman P, et al. A T1 and ECV phantom for global T1 mapping quality assurance: The T1 mapping and ECV standardisation in CMR (T1MES) program. *J. Cardiovasc. Magn. Reson.* 2016;18:1–4 doi: 10.1186/1532-429x-18-s1-w14.
7. Sacolick LI, Wiesinger F, Hancu I, Vogel MW. B1 mapping by Bloch-Siegert shift. *Magn. Reson. Med.* 2010;63:1315–1322 doi: 10.1002/mrm.22357.
8. Ravishankar S, Bresler Y. MR image reconstruction from highly undersampled k-space data by dictionary learning. *IEEE Trans. Med. Imaging* 2011;30:1028–1041 doi: 10.1109/TMI.2010.2090538.
9. Messroghli DR, Radjenovic A, Kozerke S, Higgins DM, Sivananthan MU, Ridgway JP. Modified look-locker inversion recovery (MOLLI) for high-resolution T1 mapping of the heart. *Magn. Reson. Med.* 2004;52:141–146 doi: 10.1002/mrm.20110.
10. Chow K, Flewitt JA, Green JD, Pagano JJ, Friedrich MG, Thompson RB. Saturation recovery single-shot acquisition (SASHA) for myocardial T1 mapping. *Magn. Reson. Med.* 2014;71:2082–2095 doi: 10.1002/mrm.24878.

Speaker: R. Zhou

Category: T1 , Free Breathing, Self-Gating



000129

## **A Semi-automatic Method to Simultaneously Measure Respiratory Variation in Mitral and Tricuspid Inflow Velocity using Real Time Phase Contrast Cardiac Magnetic Resonance – Normal Values and Clinical Feasibility**

S. Thalén \* (1); P. Sorensson, (2); D. Giese (3); H. Engblom, (4); M. Ugander, (5)

(1) Clinical Physiology, Karolinska Institute, Stockholm, Sweden, Sweden; (2) Medicine, Karolinska Institute, Stockholm, Sweden; (3) ., Siemens Healthcare GmbH, Erlangen, Germany; (4) Clinical physiology, Karolinska Institute, Stockholm, Sweden; (5) Kolling institute, The University of Sydney, Camperdown, Australia

### **Abstract**

**Background:** Echocardiography has shown that patients with constrictive pericarditis or hemodynamically significant pericardial effusion show an increased respiratory variation in early mitral and tricuspid inflow velocities. The methodology for quantification of respiratory variation in early mitral and tricuspid inflow velocities using real time phase contrast (RT-PC) cardiovascular magnetic resonance (CMR) images is currently cumbersome and manual. The aim of this study was to develop a method for simultaneously quantifying the respiratory variation in mitral and tricuspid inflow velocities using semi-automatic analysis of RT-PC CMR images, and determine feasibility and normal values.

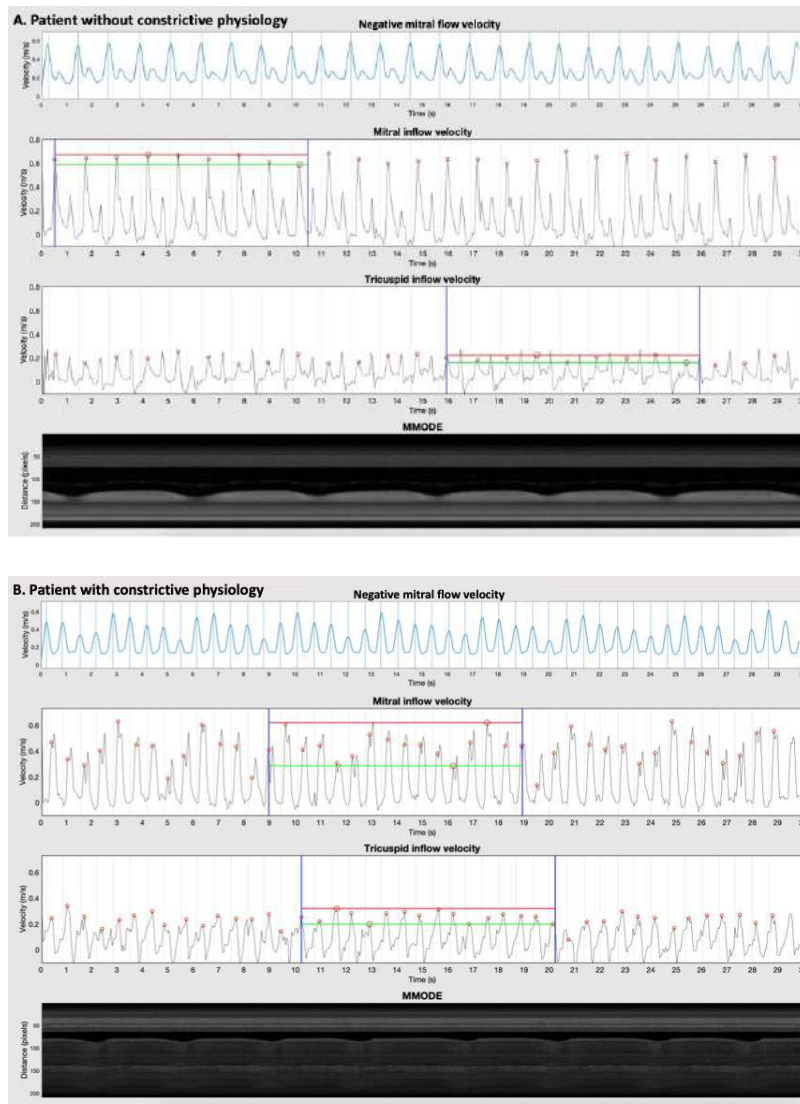
**Methods:** Clinically referred patients (n=38, age 61±19 years, 66% male) with no pericardial effusion or pericardial thickening underwent through-plane RT-PC CMR imaging using a prototype sequence at 1.5T MAGNETOM Aera (n=19) or 3T MAGNETOM Skyra (n=19) in a basal short-axis view over a 30 s acquisition during free breathing. Image acquisition parameters were: echo spacing 3.7 ms, water excitation pulse with flip angle 10°, slice thickness 8 mm, FOV 360x266 mm, matrix 208x135, aliasing velocity 150 cm/s and shared velocity encoding enabled. One patient with constrictive pericarditis was imaged to illustrate clinical feasibility.

Image analysis was performed using an in-house developed plugin to Segment (Medviso AB, Lund, Sweden). The user manually delineated a region of interest encompassing the mitral and tricuspid orifices, respectively. The peak negative mitral flow component, marking the middle of systole, is then used to segment the data into individual cardiac cycles. M-mode signal intensities over the lung-diaphragm interface allow for visualizing breathing. The peak early velocity of each cardiac cycle is identified and the contiguous 10 s period of time with the lowest variation in early mitral and tricuspid inflow velocities is identified.

**Results:** No difference between 1.5T and 3T regarding early inflow velocity variation across the mitral (p=0.13) or tricuspid (p=0.15) valves was found. Thus, data from both field strengths were combined. The normal range of respiratory variation in early inflow velocity across the mitral valve was (mean±SD [95% limits], 22%±8% [6-37%]) and across the tricuspid valve was (43±21% [3-84%]). The patient with constrictive pericarditis had a respiratory variation in inflow velocity across the mitral valve of 116% and across the tricuspid valve of 61%. A comparison to a patient without constrictive physiology is shown in figure 1 and 2.

**Conclusion:** This study has demonstrated feasibility and presented normal values for semi-automatic analysis of the respiratory variation in early mitral and tricuspid inflow velocity using RT-PC CMR available as a plug-in for freely available software.

**Figure/Table 1**



**Caption 1**

**Figure 1-2.** Examples from two patients (A and B) showing negative mitral flow, mitral and tricuspid inflow RT-PC velocity data as analysed by the software plugin. The bottom panel shows M-mode over the diaphragm to visualize breathing.

Speaker: S. Thalén

Category: Real Time, Phase Contrast , Pericardial Disease

000130

### 3D joint T1/T1 $\rho$ mapping and fat imaging for myocardial tissue characterization

M. G. Crabb \* (1); K. P. Kunze (2); C. Velasco (1); A. Fotaki (1); A. Hua (1); R. Neji (2); C. Prieto (1); R. M. Botnar (1)

(1) School of Biomedical Engineering and Imaging Sciences, King's College London, London, United Kingdom; (2) MR Research Collaborations, Siemens Healthcare Limited, Frimley, United Kingdom

#### Abstract

**Background:** In patients with suspected myocardial infarction, Late-Gadolinium Enhancement (LGE) images are often acquired in concert with T1 maps acquired pre and post gadolinium contrast injection to detect focal and diffuse scarring. In patients with renal dysfunction or contrast agent allergy, a non-contrast approach would be of great value. Furthermore, characterization of fibrofatty infiltration of the myocardium has been shown to be clinically relevant. T1 $\rho$  is a sensitive marker for assessment of macromolecular-water interaction and native T1 $\rho$  mapping has shown potential for non-contrast imaging of fibrosis as an alternative to LGE [1]. Additionally, joint mapping sequences may improve accuracy and protocol efficiency, avoid misregistration over sequentially acquired sequences and provide anatomical images for further diagnosis [2]. Here we propose a novel free-breathing, 3D whole-heart joint T1/T1 $\rho$  mapping with Dixon encoding sequence to provide non-contrast 3D T1 and T1 $\rho$  maps with isotropic resolution and co-registered water and fat volumes for comprehensive myocardial tissue characterization in a single scan.

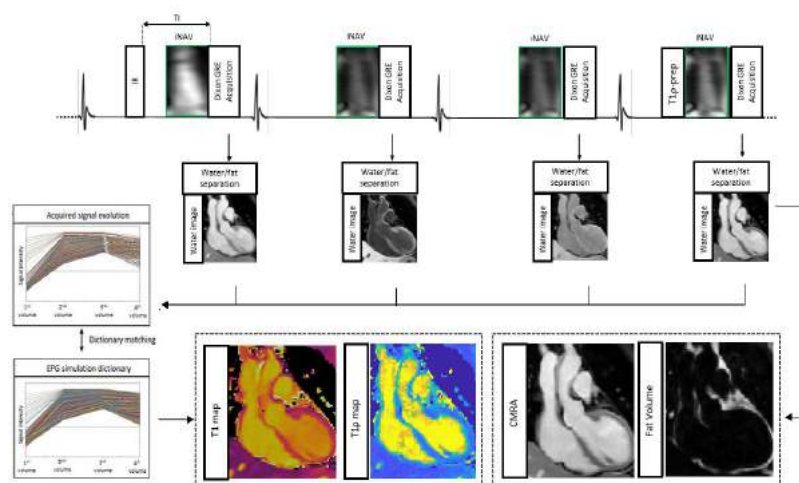
**Methods:** The ECG-triggered 3D joint T1/T1 $\rho$  prototype sequence (Fig. 1) consists of a repeating set of preparation modules over 4 heartbeats (HBs): IR preparation, no preparation, no preparation and T1 $\rho$  preparation. A 2-point Dixon GRE read-out is used (TE1/TE2/TR=2.38/4.76/6.71ms, flip angle=8°, bandwidth=453 Hz/pixel) in every HB. To accelerate the sequence, a variable-density 3D Cartesian trajectory with spiral profile order (VD-CASPR) is used to acquire 3x undersampled data every HB. 2D image navigators (iNAVs) are acquired prior to each spiral and used to perform beat-to-beat translational Right-Left (RL)/Foot-Head (FH) respiratory motion estimation and correction, as well as to bin the 3D data into 4 respiratory bins for estimation of bin-to-bin 3D non-rigid motion. The eight 3D image contrasts (out-of-phase (OP) and in-phase (IP) echoes for each HB) are reconstructed using non-rigid motion corrected HDPROST, with patch-based multi-dimensional (within patch, between patches and across contrasts) low-rank regularisation [3]. Water and fat images are subsequently estimated from the reconstructed IP/OP HB images [4]. An EPG simulation of the sequence was implemented yielding a dictionary with variable T1/T2/T1 $\rho$  parameters, and matching performed by maximising the inner-product of the dictionary and water HB images pixel-by-pixel.

**Results:** Data was acquired on a 1.5T MR scanner (MAGNETOM Aera, Siemens Healthcare, Erlangen, Germany). *Phantoms:* In phantoms, good agreement was observed between estimated T1 and T1 $\rho$  values and those from 2D spin-echo (SE) measurements, 2D MOLLI and 2D T1 $\rho$  [5] over the range of T1 and T1 $\rho$  values typical for myocardium, blood, and scar (Fig. 2). *In-vivo:* Data was acquired in one patient (HR = 63 $\pm$ 4 bpm), with an acquisition window of ~100 ms at mid-diastole. Total scan-time was ~12 mins (3x undersampling, spatial

resolution  $2 \times 2 \times 2 \text{ mm}^3$ ). Fig. 3 illustrates water, fat, T1 and T1 $\rho$  maps estimated from dictionary matching.

**Conclusions:** Preliminary 3D joint T1/T1 $\rho$  mapping and fat imaging results demonstrate good agreement in phantoms, and promising results *in-vivo*. Further work will include acquisition of a larger cohort of subjects for validation as well as patients with suspected myocardial infarction (with LGE as reference) to assess suitability of T1 $\rho$  maps as an alternative to LGE imaging.

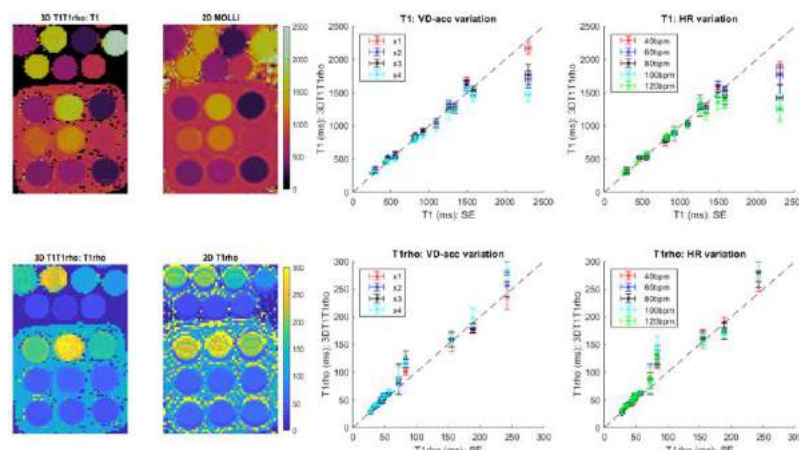
**Figure/Table 1**



**Caption 1**

3D joint T1/T1 $\rho$  mapping and fat imaging sequence schematic diagram. HB1: IR (TI=120 ms), HB2/3: no-preparation, HB4: T1 $\rho$ -prep (spin-lock (SL) duration/frequency = 40 ms/400 Hz). Four separate SL pulses of alternating phases and two adiabatic refocusing pulses with opposite phases are used to make T1 $\rho$ -prep more robust to B0/B1 inhomogeneities [5].

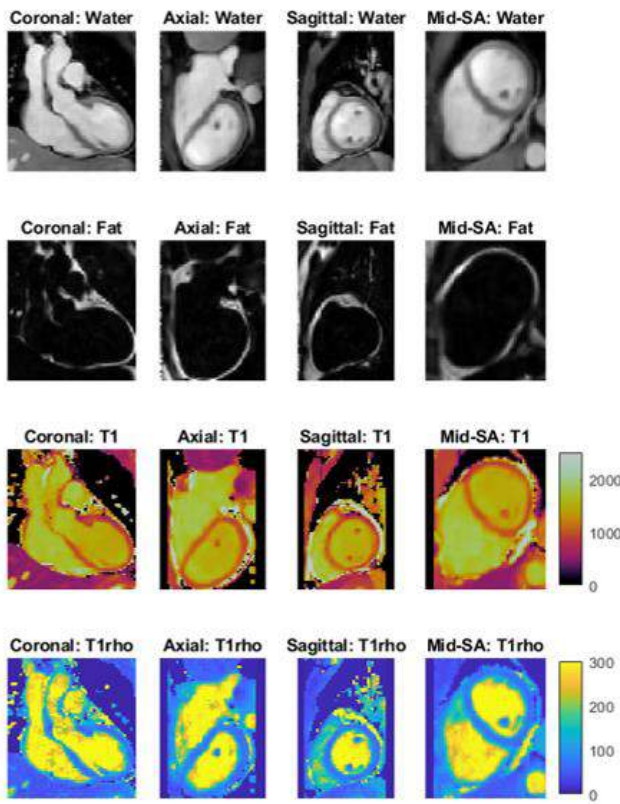
**Figure/Table 2**



## Caption 2

Phantoms. Left: proposed 3D T1/T1 $\rho$ , 2D MOLLI, 2D T1 $\rho$  mapping. Middle/Right: proposed 3D T1/T1 $\rho$  sequence vs 2D T1 and 2D T1 $\rho$  SE values, as function of undersampling (VD-acc) factor and heart-rate (HR). Good agreement is observed for T1 <~2000ms, T1 $\rho$  <~70ms, and poorer agreement outside this range due to the 40ms T1 $\rho$  duration and 4 HBs between IR pulses.

## Figure 3



## Caption 3

Fat, Water, T1 and T1 $\rho$  mappings from proposed 3D joint T1/T1 $\rho$  mapping with Dixon encoding sequence, in Coronal, Axial, Sagittal and mid Short-Axis (SA) views. Non-rigid motion-corrected HD-PROST is used to reconstruct 3D HB images, and T1/T1 $\rho$  maps estimated by dictionary matching through an EPG simulation of the sequence.

### **Bibliographic References**

[5] Qi H. et al. J. Cardiovasc. Magn. Reson. 2020; 22:12, [4] Liu J. et al. Magn. Reson. Med. 2016; 78:1862-1869, [3] Bustin A. et al. Magn. Reson. Med. 2019; 81(6):3705-3719, [2] Milotta G. et al. Magn. Reson. Med. 2020; 84:3009-3026, [1] Witschey W. R. et al. J. Cardiovasc. Magn. Reson. 2012; 14(1):37

Speaker: M. G. Crabb

Category: 3D, Tissue Characterization, Chronic Myocardial Infarction

000131

## Free-breathing whole-heart cine imaging in a minute or less – application of the radial 3D-SWIG method

A. Fyrdahl \* (1); A. Ullvin (2); N. Seiberlich (1); M. Ugander (3); A. Sigfridsson (2)

(1) Radiology, University of Michigan, Ann Arbor, United States of America; (2) Department of clinical physiology, Karolinska University Hospital, and Karolinska Institutet, Stockholm, Sweden; (3) Kolling institute, royal north shore hospital, and northern clinical school, Sydney Medical School, University of Sydney, Sydney, Australia

### Abstract

**Background:** Cardiovascular MRI (CMR) can be time-consuming, as multiple survey scans and image orientations are commonly required to visualize the anatomy and motion of the whole heart. Each acquisition is commonly acquired under a breath-hold, followed by a recovery period for the patient. In this work, we are proposing a novel sampling ordering that is uniquely suited for whole-heart imaging, and demonstrate how this method can enable three-dimensional whole-heart imaging, without breath-holding, and with acquisition times of a minute or less.

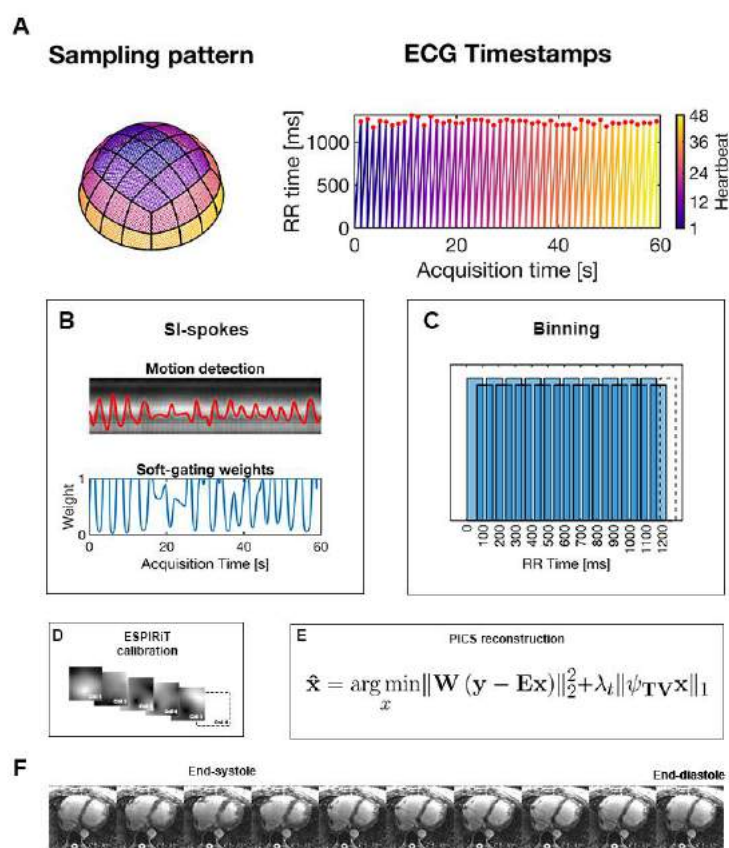
**Methods:** The 3D sector-wise golden-angle (3D-SWIG) sampling ordering (1) is based on the conventional double-golden-angle sampling (2), but k-space lines acquired during each heartbeat are constrained to fall within a wedge of k-space, and the wedges are collected sequentially in a discretized spiral pattern. In this work, the number of wedges was selected to be 48. Every 22nd k-space line was acquired in a superior-inferior orientation and used as a navigator in the reconstruction. In addition to the routine CMR protocol, the proposed 3D-SWIG method was implemented in a prototype bSSFP pulse sequence. Relevant sequence parameters were: FOV = 220 mm<sup>3</sup>, matrix size = 176<sup>3</sup>, TE/TR = 1.79/3.61 ms, flip angle = 115 deg. The 3D-SWIG acquisition was performed under free-breathing. The routine 2D Cartesian bSSFP short-axis cine stack was also used in the analysis, with the following parameters: FOV = 360×270 mm<sup>2</sup>, slice-thickness = 8 mm, matrix size = 256×192, TE/TR = 1.19/2.85 ms, flip angle = 50 deg, segmentation factor = 15, GRAPPA (R=2) with 36 calibration lines, 10–12 slices. Patients (N=16) with referral for CMR were scanned at 1.5 T (MAGNETOM AERA, Siemens Healthcare, Erlangen, Germany). The 2D Cartesian images were reconstructed on the scanner, and the 3D-SWIG images were reconstructed using the BART Toolbox to yield a total of 20 temporally overlapping frames with a temporal footprint of 100 ms. An overview of the acquisition and reconstruction can be seen in Figure 1. All images underwent manual left-ventricular segmentation to yield end-diastolic volume (EDV) and end-systolic volume (ESV), using the freely available software Segment version 3.2 R8757 (3). Stroke volume (SV) and ejection fraction (EF) were calculated. A random subset of patients was re-analyzed by the original observer and a second observer to assess inter- and intra-observer variability.

**Results:** The acquisition time was  $48 \pm 6$  seconds for the 3D-SWIG method and  $239 \pm 14$  seconds for the 2D Cartesian method, including time for breath-hold commands and recovery periods between breath-holds. Representative reconstructed images from both methods can be seen in Figure 2. The manual segmentation showed generally good agreement. Mean bias was found to be -2.8% for EF, -5.4 ml for SV, 5 ml for ESV, and -0.4 ml for EDV. The intra-

observer analysis of EF showed excellent agreement (ICC = 0.98) and the inter-observer analysis showed a good agreement (ICC = 0.89). Bland-Altman plots can be seen in Figure 3.

**Conclusions:** While EDV had a very strong agreement, ESV was generally overestimated, which could have been caused by a low temporal resolution (4). However, a mean difference of -2.8% EF is close to what has been found in previous reproducibility studies (5). In summary, the feasibility of the 3D-SWIG method for efficient free-breathing functional CMR has been demonstrated in a cohort of 16 patients.

**Figure/Table 1**

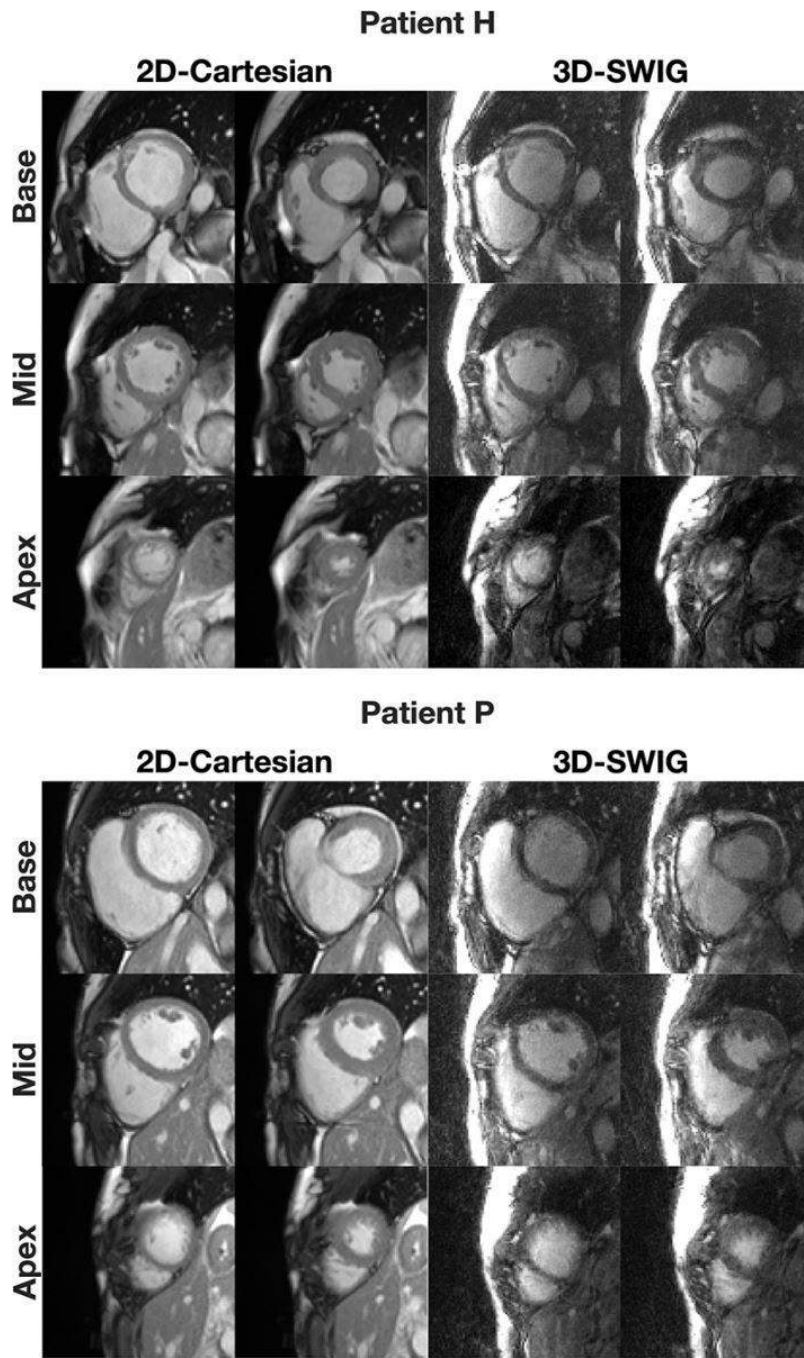


**Caption 1**

**Figure 1.** Image acquisition and reconstruction. A) Sampling pattern and ECG timestamps. B) Superior-inferior spokes are used to calculate soft-gating weights. C) Binning to 20 temporally overlapping frames. D) Coil sensitivity maps using ESPIRiT. E) Reconstruction using parallel imaging and compressed sensing F) Transversal images over the cardiac cycle.

**Figure/Table 2**

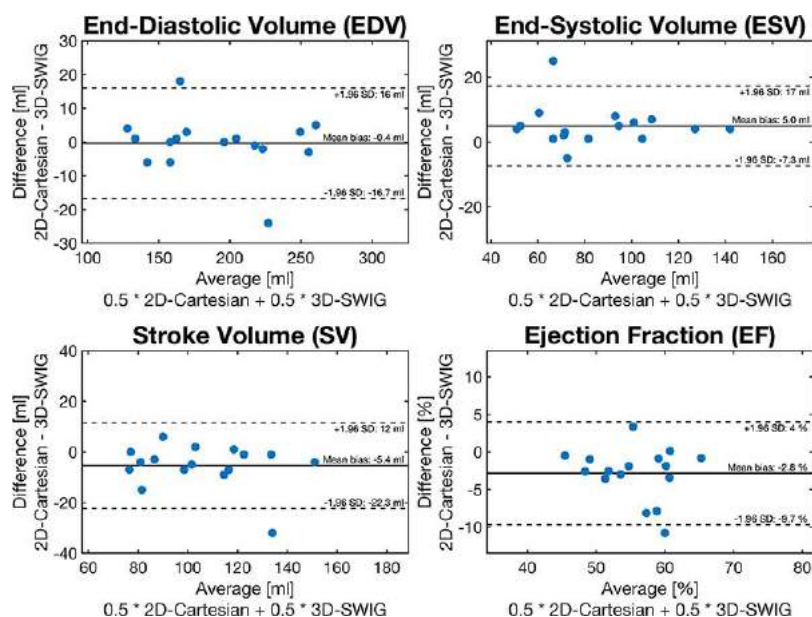




**Caption 2**

**Figure 2.** Representative examples from two of the subjects reformatted to short-axis orientation in diastole and systole. For the 3D-SWIG acquisition, a total of 4 slices (nominal slice thickness 1.7 mm) have been merged to create a reconstructed slice thickness of 6.8 mm to better match the 8 mm slice thickness used in the 2D-Cartesian images.

**Figure 3**



**Caption 3**

**Figure 3.** Bland-Altman plots describing the bias and limits of agreements of manual left-ventricular segmentation performed on the 2D-Cartesian and 3D-SWIG acquisitions, respectively.

### Bibliographic References

1. Fyrdahl A, Ramos JG, Ugander M, Sigfridsson A. 3D sector-wise golden-angle (3D-SWIG) – Improved k-space uniformity after ECG binning compared to golden-angle profile ordering. In: Proc. 28th Annu. Meet. ISMRM. ; 2020. p. 3715., 2. Chan RW, Ramsay EA, Cunningham CH, Plewes DB. Temporal stability of adaptive 3D radial MRI using multidimensional golden means. Magn. Reson. Med. 2009;61:354–363., 3. Heiberg E, Carlsson M, Arheden H, Ugander M, Sjögren J, Engblom H. Design and validation of Segment - freely available software for cardiovascular image analysis. BMC Med. Imaging 2010;10:1–13., 5. Coulden R, Sonnex E. Inter-observer variation in LV analysis in a dedicated CMR unit: the impact of audit and consensus guideline on reproducibility. J. Cardiovasc. Magn. Reson. 2014;16:P372., 4. Inoue Y, Nomura Y, Nakaoka T, Watanabe M, Kiryu S, Okubo T, Ohtomo K. Effect of temporal resolution on the estimation of left ventricular function by cardiac MR imaging.

Speaker: A. Fyrdahl

Category: 3D, Whole Heart , Golden Angle



000132

## Cardiovascular magnetic resonance detects subclinical myocardial injury in patients with acute ischemic stroke: insights from the CORONA-IS pilot study

E. Blaszczyk \* (1); S. Hellwig, (2); H. Saad, (3); R. Ganeshan, (2); H. Stengl, (2); C. Nolte (2); J. Fiebach, (2); M. Endres, (2); J. Kuhnt, (1); J. Gröschel, (1); J. Schulz-Menger (1); J. F. Scheitz, (2)

(1) Dzhk (german centre for cardiovascular research), partner site berlin, berlin, germany, Charité University Medicine Berlin, Working Group on CMR, ECRC, MDC, HELIOS Klinikum Berlin Buch, Berlin, Germany; (2) Klinik für neurologie mit experimenteller neurologie, Charité - Universitätsmedizin Berlin, Campus Benjamin Franklin, Berlin, Germany; (3) Working group on cardiovascular magnetic resonance, Charite Universitätsmedizin Berlin, Campus Buch, Berlin, Germany

### Abstract

**Background** Ischemic stroke (IS) and heart failure are known to be major causes of morbidity and mortality. The term “stroke-heart syndrome” has been established for cardiac dysfunction that occurs during the first few days after an acute ischemic stroke (AIS). In our CORONA-IS (Cardiomyocyte injury following Acute Ischemic Stroke) study, we aimed to prospectively evaluate the burden of (sub)clinical myocardial injury in patients with AIS by applying CMR with in-depth myocardial tissue characterization.

**Methods** Patients with AIS underwent CMR at 3T within 72-120 hours after the index stroke. Patients with persistent atrial fibrillation were excluded. The following parameters were assessed: morphology and function of left/right ventricle (LV, RV) and left/right atrium (LA, RA) applying SSFP cine; for focal fibrosis late gadolinium enhancement (LGE) and for diffuse changes parametric T2- and T1-mapping were performed. To detect myocardial deformation global longitudinal strain (GLS) was measured applying feature tracking (CVI42).

**Results** Overall, 115 patients with AIS were prospectively included. CMR was performed in 101/115 (88%), and 91/101 (90%) patients received contrast media. In addition, 10 healthy volunteers underwent CMR without contrast media application. Focal fibrosis was detected in 30/91 (35%). Twenty (67%) had an ischemic LGE pattern (Figure 1A). An embolic source could be suspected in 10/30 (33%) patients (Figure 1B). Only in 3/30 (9%) patients an antecedent MI was documented. No significant differences were found between patients with and without focal fibrosis in LV/ RV volume and function (LVEDV-I  $p=0.727$ , LVSV-I  $p=0.535$ , LVEF  $p=0.101$ , RVEDV-I  $p=0.501$ , RVSV  $p=0.232$ , RVEF  $p=0.331$ ). 20% of patients without LGE (10/61) presented reduced LVEF  $<50\%$ . GLS was significantly lower in patients with focal myocardial injury (LGE+) -123% vs. LGE(-) -16%  $p=0.028$ ). GLS was significantly reduced (-15.5%) already in patients with LVEF  $>50\%$ . (Table 1 B). In patients with focal myocardial fibrosis, LA was significantly larger (LAEDV-I 37 vs. 51 ml/m<sup>2</sup>  $p=0.021$ ) and the LAEF (53 vs 41%  $p>0.004$ ) was significantly lower. Table 1B. We found significant differences in T1 times between LGE+ and LGE- patients. Patients with focal fibrosis had higher T1 (basal: LGE+) 1235 ms vs. LGE(-) 1198 ms,  $p=0.048$ ; medial: LGE+) 1245ms vs. LGE(-) 1179ms,  $p=0.007$ , apical: LGE+) 1246ms vs. LGE(-) 1158ms,  $p=0.014$  and T2 values (basal: LGE+) 42ms vs. LGE(-) 40ms,  $p=0.001$ ;

medial:LGE(+) 42ms vs. LGE(-) 40ms,  $p=0.002$ , apical:LGE(+) 44ms vs. LG(-) 42ms,  $p=0.045$ ) also in regions without focal findings (Figure 2).

**Conclusions** It is feasible to perform early CMR scans in severely ill AIS patients. More than one third of AIS patients showed focal myocardial fibrosis. Atrial enlargement and a decrease of atrial function were seen in patients without any previously diagnosed supraventricular arrhythmias. These findings suggest a high proportion of subclinical cardiac involvement in patients with AIS indicating a relevant risk of development of heart failure/deterioration of LV function as well as atrial/ventricular arrhythmias.

#### Figure/Table 1

1A

1B

#### Caption 1

**1A.** 82-year-old patient with unknown IHD and ischemic LGE pattern – septal infarct (arrows). Late gadolinium enhancement in 4ch view (1), 3ch view (2) and short axis (3).

**1B.** 70-year-old patient without known heart disease and ischemic LGE-pattern suspected of an embolic cause within the inferior wall (arrows). LGE in short axis (1) and 2 CV (2).

#### Figure/Table 2

#### Caption 2

MR non-contrast imaging techniques showing increased native T1 values in patients with focal changes.

#### Figure 3

### **Caption 3**

1A. Baseline patients' characteristics.

1B. Basic CMR parameters: volume and function.

### **Bibliographic References**

1 Scheitz JF, Nolte CH, Doehner W, Hachinski V, Endres M. Stroke-heart syndrome: clinical presentation and underlying mechanisms. *The Lancet Neurology* 2018;17:1109-1120.

Speaker: E. Blaszczyk

Category: Tissue Characterization, Stroke, Function

000133

## **Comparison of CMR Findings in Symptomatic Patients with Different COVID-Related Syndromes**

R. GARG \* (1); M. Chetrit (2); M. Friedrich (3)

(1) Cardiovascular imaging, McGill University Health Centre Glen Site (MUHC), Montreal, Canada; (2) Research institute, McGill University Health Centre Glen Site (MUHC), Montréal, Canada; (3) Departments of Medicine and Diagnostic Radiology, Division of Experimental Medicine, Centre Universitaire de Santé McGill Site Glen, Montréal, Canada

### **Abstract**

#### **Description of clinical presentation:**

Involvement of the myocardium has been identified in acute COVID-19 infections, post-COVID-19 syndrome and following administration of the mRNA COVID-19 vaccines. Cardiac MRI (CMR) continues to play a central role in assessing these patients non-inversely. Herein, we present the CMR findings in the cases belonging to each of the groups scanned at our center. CMR findings from symptomatic patients presenting with COVID-related myocardial injury were compared, including 1) acute COVID-19, 2) clinically chronic disease (post-COVID syndrome), and 3) new onset diseases after COVID-19 mRNA vaccination (post-COVID-vaccine). All patients were referred for a clinical CMR for suspected myocardial injury, with or without an increase in troponin. An increased troponin level was found in all patients (100%) with acute COVID -19, in 17/25 (68%) with post-COVID syndrome, and in 9/13 (69%) after vaccination. Other clinical criteria used were severity and cardiac type symptoms, temporal relationship of symptom onset with COVID-19 or mRNA COVID-19 vaccine, with exclusion of other possible causes explaining the symptoms.

#### **Diagnostic techniques and their most important findings:**

We enrolled patients who underwent a clinical CMR exam because of symptomatic acute COVID-19 (n=5), post-COVID syndrome (n=25), or previous COVID-19 vaccination (n=13). The average time interval from symptom onset to CMR was 4 (+/-2.3) days in acute COVID-19, 3.7(+/-3.1) months in post-COVID syndrome, and 6.6 (+/-4.5) days in post-COVID-vaccine patients. The patients were scanned on clinical MRI systems (1.5T or 3T) with the following protocol: Cine (short axis stack) for function, T1 maps for myocardial tissue integrity (3 short axis slices), T2 maps for edema (3 short axis slices), and LGE for replacement fibrosis (short axis stack). Images were analyzed according to standard clinical protocols (Figure 2). T1 and T2 maps were evaluated compared with local normal values. Patients with post-COVID syndrome and post-vaccine patients were younger than patients with acute COVID-19 (Table 1). LVEF was mildly reduced in patients with acute COVID-19 and in post-COVID syndrome but not in symptomatic patients after vaccination. A regional wall motion abnormality was typically co-located with the region of myocardial edema and/or scar. In all 3 groups, regional or global myocardial edema was a frequent finding (73 to 80%), with global edema being more common. Irreversible injury (LGE) had a non-ischemic, typically subepicardial distribution, mostly in lateral and inferolateral segments, with the basal slices being most affected in post-vaccine patients. In post-vaccination patients, pericardial thickening and co-located effusion adjacent to the inferior wall was observed in 5/13 (38%) patients (Figure 3).

### Learning points:

Patients with symptoms associated with COVID-related conditions suggestive of cardiac involvement show similarities with respect to the presence and regional distribution of myocardial injury. In contrast to acute COVID-19 or post-COVID syndrome, myocardial T1 was less frequently abnormal and global systolic function was less often impaired in patients after COVID-19 vaccination.

**Figure/Table 1**

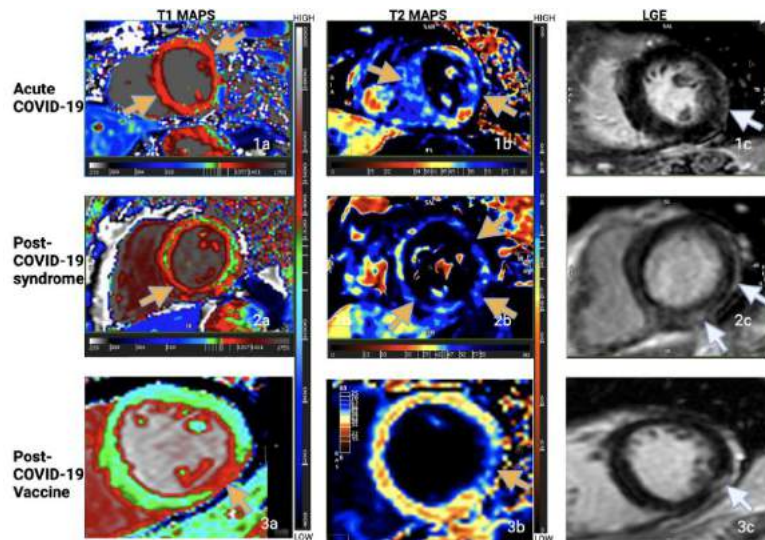
Characteristics	Acute COVID-19n=5	Post-COVID Syndromen=25	Post-COVID vaccinen=13
Mean age (years)	64.8	44	41
Sex (%females)	57%	62.5%	17%
Mean LVEF	48.2%	51%	63%
High T1(%patients)	60%	50%	33%
High T2(%patients)	80%	73%	75%
Most common LGE pattern and location(n, %)	Subepicardial/anterolateral, lateral segments (n=2; 40%)	Subepicardial/lateral and inferolateral segments (n=8; 32%)	Subepicardial/inferolateral segment (n=6; 46%)

**Caption 1**

**Table 1: Table summarizing the significant characteristics in the three groups of patients.**

**Figure/Table 2**





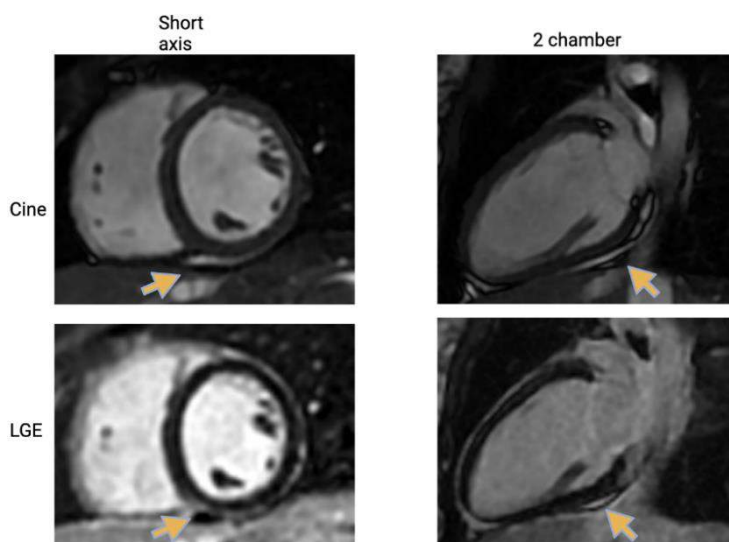
**Caption 2**

**Figure 2: T1 maps, T2 maps, LGE imaging from one patient from each of the groups.**

Increased T1 and T2 times in the maps as shown by the yellow arrows.

Subepicardial lateral or inferolateral scar in the basal or mid slices as shown by the white arrows.

**Figure 3**



**Caption 3**

**Figure 3: Pericarditis in a patient from Group 3.**

Pericardial effusion (yellow arrow) adjacent to the inferior wall, in cine and LGE images of two chamber and short axis view.

Speaker: R. GARG

Category: Edema, Myocarditis, Scar

000134

## Uncommon Etiology of Unrecognized Myocardial Infarction Using Cardiac Magnetic Resonance

M. Nasir \* (1); N. Fonseka (2); C. Gangireddy (2); M. Gannon, (2)

(1) Internal Medicine, Lewis Katz School of Medicine at Temple University Hospital, Philadelphia, United States of America; (2) Cardiology, Lewis Katz School of Medicine at Temple University Hospital, Philadelphia, United States of America

### Abstract

**Clinical Presentation:** A 50 year-old man with a past medical history of gout and coronary artery disease (calcium score of 24 Agatston units in the left anterior descending artery) presented for cardiology evaluation for abnormal preoperative electrocardiogram (EKG) showing frequent premature ventricular contractions (PVCs). He had no cardiopulmonary symptoms and did not complain of palpitations. He lived an active lifestyle and exercised regularly without complaints. An echocardiogram was notable for low to normal left ventricular systolic function, ejection fraction (LVEF) 50-55% with mild inferior septal hypokinesis and possible basal inferior wall hypokinesis. A 24-hour event monitoring showed 29% PVC burden and he was started on Metoprolol succinate 25mg daily. The patient underwent exercise nuclear stress test and was able to perform 13.4 metabolic equivalents (METs) without symptoms or ischemic changes on EKG. He was found to have frequent PVCs at rest that declined with exercise. Ultimately, given his PVC burden and risk for tachycardia-induced cardiomyopathy he was referred to an electrophysiologist for possible PVC ablation. He subsequently underwent cardiac magnetic resonance (CMR) to evaluate for a focus of the monomorphic PVCs. This study demonstrated low normal left ventricular systolic function, LVEF 50% with inferior wall hypokinesis. There was a chronic myocardial infarction (MI) in the right coronary artery distribution with moderate hypokinesis in the corresponding segments. Subsequent invasive coronary angiography showed luminal abnormalities consistent with a healed spontaneous coronary artery dissection (SCAD) of the right coronary artery (RCA) and TIMI 3 flow. He was started on dual antiplatelet therapy.

**Diagnostic Techniques and Most Important Findings:** Rest echocardiography demonstrated LVEF 50-55% with basal inferior severe hypokinesis. Rest CMR steady-state free precession imaging demonstrated moderate hypokinesis of the basal inferior and mid inferior, and mid inferolateral walls with low normal LVEF at 50%. There was an absence of increased signal intensity on T2-weighted imaging. Late gadolinium enhancement (LGE) imaging showed a non-transmural chronic infarction in the entire inferior wall with extension into the basal and mid inferolateral segments. Invasive angiography confirmed a previously healed RCA dissection.

**Learning Points from this case:** Unrecognized myocardial infarction can occur from atherosclerotic plaque as well as non-obstructive epicardial processes. CMR aids in identifying myocardial infarction from epicardial causes without obstructive atherosclerotic plaque such as SCAD. Myocardial infarction without obstructive coronary artery disease (MINOCA) is an underrecognized cause of cardiovascular morbidity which could have

resulted in a tachycardia-induced cardiomyopathy in this case. Our patient's invasive angiography confirmed the presence of a chronic healed, RCA SCAD and identified a cause of ventricular ectopy.

### Figure/Table 1



### Caption 1

Figure 1. Identification of Unrecognized Myocardial Infarction. (A) EKG rhythm strip from 24-hour ambulatory monitoring demonstrates ventricular trigemini with single ventricular focus.

### Caption 2

(B) Short-axis basal phase-sensitive inversion recovery (PSIR) late gadolinium enhancement (LGE) imaging demonstrates myocardial infarction (red arrow) involving the inferoseptum, inferior, and inferolateral segments. (C) 2-chamber PSIR LGE imaging demonstrated basal to partial apical inferior myocardial infarction (red arrow). (D) Invasive angiography demonstrates chronic healed dissection (red arrow) in the right coronary artery.

Speaker: M. Nasir

Category: Arrhythmia, Chronic Myocardial Infarction, Coronary Angiography

000135

## Cardiac Amyloidosis: A Tale of Two Fibrils

D. Davies \* (1); Y. Kathleen (1); C. Ian (1); P. Araoz (2)

(1) Cardiovascular Diseases, Mayo Clinic, Rochester, United States of America; (2) Radiology, Mayo Clinic, Rochester, United States of America

### Abstract

**Description of Clinical Presentation:** A 76-year-old, physically active Italian male was hospitalized for *S. pneumoniae* sepsis and atrial fibrillation with rapid ventricular response. Transthoracic echocardiogram showed left ventricular concentric hypertrophy and reduced systolic function (ejection fraction of 36%). He was treated with cardioversion and antiarrhythmic therapy. In the setting of severe infection, he underwent hematologic workup, which identified abnormal monoclonal IgG lambda protein. A bone marrow biopsy was performed and showed no evidence of multiple myeloma, amyloidosis, or lymphoma, however there were increased lambda-restricted plasma cells (8%). A subsequent cardiac MRI showed normalization of his ejection fraction in addition to atrial and ventricular wall hypertrophy with diffuse, and diffuse patchy late gadolinium enhancement of all chambers. In the absence of AL amyloidosis, no further evaluation for cardiac amyloidosis was pursued.

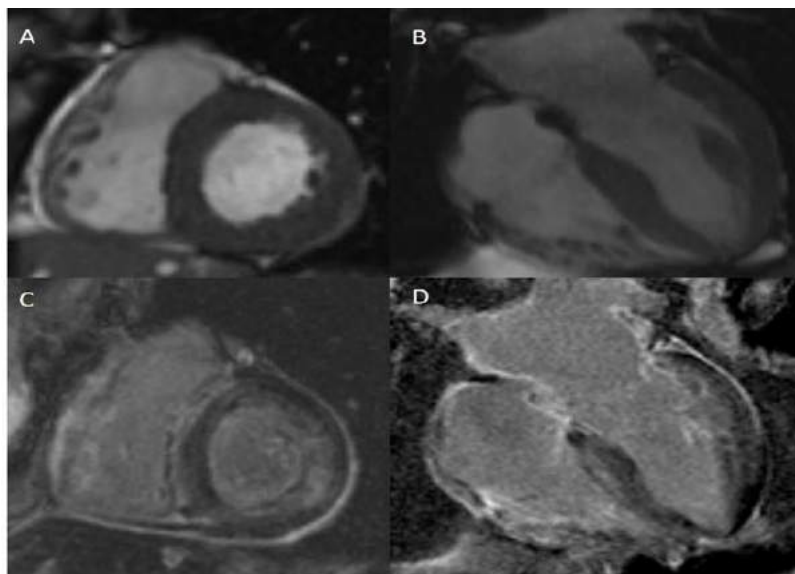
Two years later, he noted persistent exertional fatigue and decreasing cardiac fitness (by estimated VO<sub>2</sub> max) on his wearable device and requested second opinion. Physical examination noted normal vitals, regular rate and rhythm, and a 1/6 early systolic murmur. The exam was otherwise negative for pulmonary rales, jugular venous distention, or lower extremity edema.

**Diagnostic Techniques and Their Most Important Findings:** Laboratory analysis revealed elevated troponin and b-type natriuretic peptide, with a normal blood count and renal function. Serum immunofixation confirmed monoclonal IgG lambda protein. A repeat fat aspirate was performed showing AL amyloid deposition (IgG lambda). His outside cardiac MRI was obtained and re-interpreted, again showing classic features of cardiac amyloidosis including abnormal myocardial nulling, increased right and left ventricular wall thickness (17 mm basal septal thickness) with normal biventricular systolic function, as well as diffuse subendocardial gadolinium enhancement involving all cardiac chambers. A 99m-technetium pyrophosphate scan was performed, revealing visual grade 3 myocardial uptake with a heart/contralateral ratio of 2.0 at 3 hours (abnormal  $\geq 1.3$ ), most suspicious for transthyretin (ATTR) cardiac amyloidosis. An endomyocardial biopsy was then performed showing marked interstitial amyloid deposition with mass spectrometry confirming isolated ATTR deposition.

### Learning Points from this Case:

This rare case demonstrates amyloid deposits of different precursor subtypes can co-exist. It illustrates the classic MRI findings of cardiac amyloidosis, the complementary value of multimodality imaging, and the importance of organ-specific pathologic confirmation in patients with cardiac amyloidosis when clinical information is discordant on the amyloid subtype.

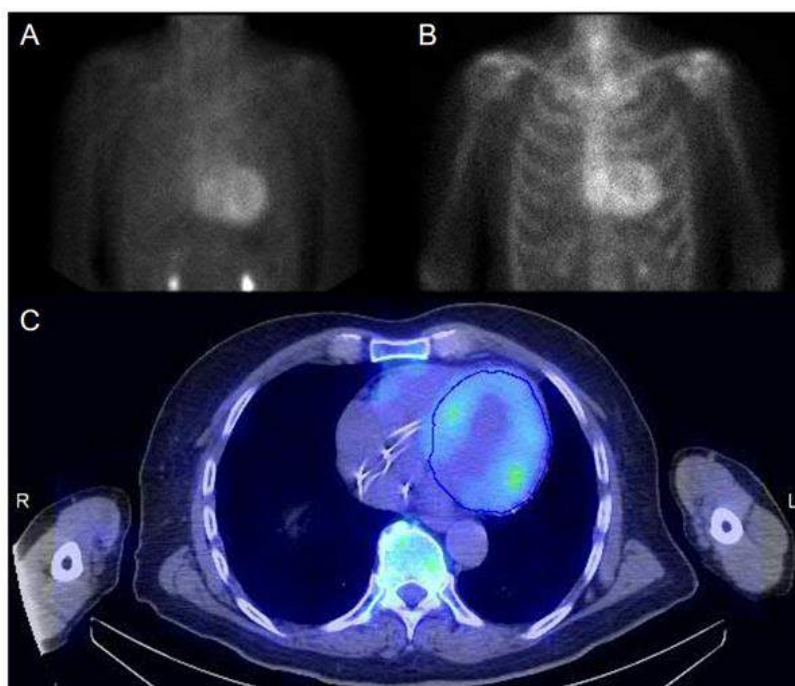
### Figure/Table 1



### Caption 1

**Figure 1:** Diastolic still-frame from the steady state free precession (SSFP) short axis (A) and 4-chamber (B) views demonstrates concentric left ventricular hypertrophy, measuring up to 17 mm. Postcontrast delayed myocardial imaging demonstrated sub-endocardial to partial thickness delayed gadolinium enhancement particularly from the base to mid left-ventricular level (C). There was also diffuse bi-atrial and right ventricular late gadolinium enhancement (D).

### Figure/Table 2



## Caption 2

**Figure 2:** 99m-Technetium pyrophosphate scintigraphy showing increased myocardial uptake at 15 minutes (A) and 3 hours (B) with confirmed myocardial localization on SPECT/CT fusion imaging (C).

Speaker: D. Davies

Category: Amyloidosis , Chronic Heart Failure, Gadolinium

000136

**Non-invasive cardiac magnetic resonance imaging quantification of pressure-volume relation in athletes and controls at rest and moderate exercise**

B. Östenson \* (1); J. Edlund (1); E. Heiberg (1); E. Ostenfeld (1); H. Arheden (1); K. Steding-Ehrenborg (1)

(1) Clinical physiology, department of clinical sciences lund, Lund University, Skåne University Hospital, Lund, Sweden

**Abstract**

**Background:** Endurance athletes have an exceptional capacity to increase cardiac output from rest to exercise (1). The exact mechanisms behind this improved cardiac reserve are not yet fully understood. Using pressure-volume loops, measures of cardiac function such as ventricular efficiency, contractility, and ventricular-arterial coupling can be determined. Ventricular efficiency and contractility are known to increase during exercise (2). Optimal ventricular-arterial coupling at rest is defined as when the mechanical properties of the left ventricle and artery system are about equal (3). However, the effect of exercise is less known. Cardiac magnetic resonance (CMR) short-axis images and brachial pressure can be used to calculate non-invasive pressure volume loops (4). Using this novel method, the aim of this study was to compare ventricular efficiency, contractility and ventricular-arterial coupling in athletes and sedentary controls at rest and during exercise.

**Methods:** Thirteen endurance athletes (median 48 [IQR 34-60] years) and ten age and sex matched sedentary controls (training volume  $\leq 150$  minutes of physical exercise per week) were included. All subjects underwent CMR at rest and during moderate intensity supine exercise defined as 60% of maximal heart rate using a Lode ergometer (Lode BV, Groningen, The Netherlands). When subjects reached target heart rate, pedaling was stopped. Breath-hold cine images were acquired immediately after exercise cessation. To ensure high heart rates during image acquisition, exercise was interleaved with exercise cessation. Typically, one to three short-axis slices were acquired during cessation in the scanner for 8–12 seconds before the next exercise session started. This was repeated until the whole heart was included. Short-axis cine images were manually delineated in all slices and time frames to obtain time-resolved delineations. Brachial pressure was measured at rest and exercise during the image acquisition. Pressure-volume loops were thereafter calculated in the software Segment (4,5) (<http://segment.heiberg.se>).

**Results:** Ventricular efficiency increased in athletes and sedentary controls from rest to exercise (athletes: 70 [66–73] to 78 [75–80] %,  $p < 0.01$ ; controls: 68 [63–72] to 75 [73–78] %,  $p < 0.01$ ). Arterial elastance (EA) decreased (athletes: 0.8 [0.7–0.9] to 0.7 [0.7–0.9] mmHg/ml,  $p < 0.05$ ; controls: 1.0 [0.9–1.2] to 0.9 [0.8–1.0] mmHg/ml,  $p < 0.05$ ) and contractility measured as end-systolic elastance (EES) increased (athletes: 1.0 [0.9–1.1] to 1.1 [0.9–1.2] mmHg/ml,  $p < 0.01$ ; controls: 1.1 [0.9–1.2] to 1.2 [1.0–1.3],  $p < 0.01$  mmHg/ml). Ventricular-arterial coupling (EA/EES) decreased in both groups (athletes: 0.9 [0.8–1.0] to 0.7 [0.6–0.8],  $p < 0.01$ ; controls: 1.0 [0.9–1.1] to 0.7 [0.7–0.8],  $p < 0.01$ ).

**Conclusions:** Both athletes and sedentary controls increased contractility leading to increased efficiency and decreased ventricular-arterial coupling during moderate supine exercise. This



indicates that during exercise increased contractility and reduced arterial elastance are prioritized over optimal ventricular-arterial coupling.

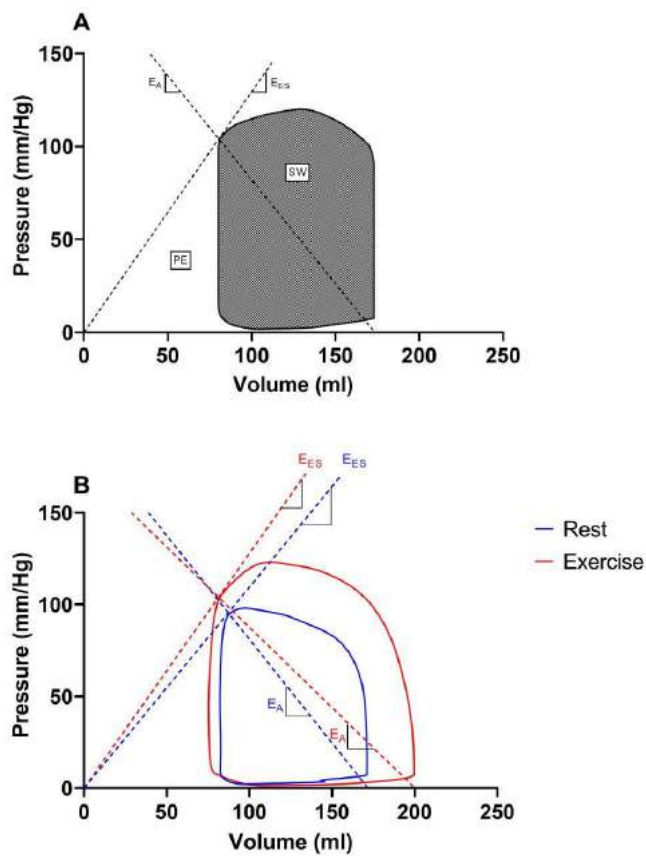
**Figure/Table 1**

	Rest Athletes (n=13)	Controls (n=10)	Exercise Athletes (n=13)	Controls (n=10)	Δ Athletes (n=13)	Controls (n=10)
<b>Heart rate and pressure</b>						
<b>HR (BPM)</b>	52 [48–60]	59 [51–67]	86 [80–94] †	90 [82–94] †	34 (66%)	29 (48%)
<b>SBP (mmHg)</b>	113 [104–122]	114 [109–129]	124 [118–137] †	129 [121–140] †	11 (10%)	16 (14%)
<b>DBP (mmHg)</b>	70 [61–78]	65 [62–77]	74 [66–89] †	71 [67–84]	4 (6%)	6 (10%)
<b>RPP (BPM*mmHg)</b>	6200 [5600–6800]	6200 [5700–8700]	11200 [10000–12200] †	11400 [9900–12800] †	5000 (81%)	5200 (84%)
<b>Cardiac volumes and function</b>						
<b>LVM (g)</b>	99 [89–118] *	71 [70–92]	104 [94–127] *†	77 [72–98] †	5 (5%)	6 (8%)
<b>EDV (ml)</b>	218 [198–244] *	191 [180–207]	233 [211–265] †	203 [197–233]	15 (7%)	12 (6%)
<b>ESV (ml)</b>	98 [84–111]	92 [82–99]	94 [74–101] †	78 [71–89] †	-4 (-4%)	-13 (-15%)
<b>SV (ml)</b>	124 [103–134] *	102 [98–107]	149 [131–164] *†	130 [119–144] †	25 (20%)	28 (24%)
<b>EF (%)</b>	57 [53–59]	54 [50–57]	64 [61–66] †	63 [60–64] †	7.6 (13%)	8.3 (15%)
<b>CO (L/min)</b>	6.3 [5.0–7.5]	6.6 [5.5–6.9]	11.0 [9.4–13.7] †	11.8 [11.1–13.2] †	4.7 (74%)	5.3 (80%)
<b>Cardiovascular hemodynamics</b>						
<b>SW (J)</b>	1.5 [1.1–1.6]	1.3 [1.2–1.3]	1.9 [1.7–2.3] †	1.8 [1.6–1.9] †	0.4 (27%)	0.5 (40%)
<b>PE (J)</b>	0.6 [0.5–0.8]	0.6 [0.5–0.7]	0.6 [0.5–0.8]	0.6 [0.5–0.7]	-0.06 (-9%)	0 (0%)
<b>PVA (J)</b>	2.1 [1.7–2.4]	1.9 [1.7–2.0]	2.4 [2.2–3.1] †	2.4 [2.1–2.6] †	0.3 (18%)	0.5 (25%)
<b>VE (%)</b>	70 [66–73]	68 [63–72]	78 [75–80] †	75 [73–78] †	7 (11%)	7 (11%)
<b>MEP (J/s)</b>	1.3 [0.9–1.5]	1.2 [1.1–1.6]	2.6 [2.0–2.9] †	2.7 [2.2–3.0] †	1.3 (102%)	1.5 (122%)
<b>EEV (J/ml)</b>	0.016 [0.015–0.018]	0.018 [0.016–0.020]	0.017 [0.015–0.018]	0.018 [0.017–0.018]	0.00004 (-0.3%)	-0.00009 (-0.5%)
<b>EES (mmHg/ml)</b>	1.0 [0.9–1.1]	1.1 [0.9–1.2]	1.1 [0.9–1.3] †	1.2 [1.0–1.3] †	0.1 (11%)	0.2 (15%)
<b>EA (mmHg/ml)</b>	0.8 [0.7–0.9] *	1.0 [0.9–1.2]	0.7 [0.7–0.8] *†	0.9 [0.8–1.0] †	-0.1 (-14%)	-0.1 (-14%)
<b>EA/EES</b>	0.9 [0.8–1.0]	1.0 [0.9–1.1]	0.7 [0.6–0.8] †	0.7 [0.7–0.8] †	-0.2 (-19%)	-0.3 (-30%)

## Caption 1

Cardiovascular hemodynamics at rest and exercise. Data expressed as median [IQR]. Delta values ( $\Delta$ ) are absolute differences between median exercise and median rest, with relative change expressed as percentage in parenthesis. \* $p < 0.05$  intergroup comparison at rest vs exercise. † $p < 0.05$  intragroup comparison of rest vs exercise.

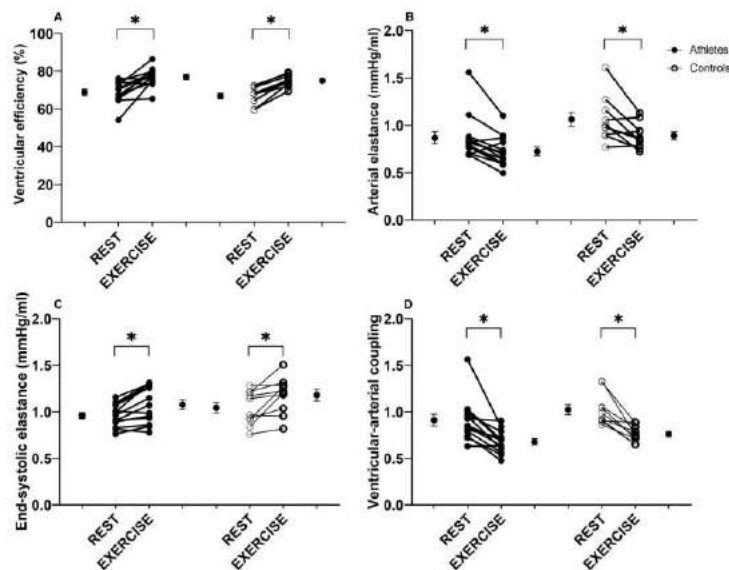
## Figure/Table 2



## Caption 2

Pressure-volume diagrams of the left ventricle. A: schematic figure of a pressure-volume loop with cardiac hemodynamics indicated. Dashed lines indicate the slopes of end-systolic elastance (EES) and arterial elastance (EA). B: pressure-volume loop of one test subject at rest (blue) and during exercise (orange).

## Figure 3



### Caption 3

Cardiac response to exercise. Graphs illustrate change of ventricular efficiency (panel A), arterial elastance (panel B), end-systolic elastance (panel C), and ventricular-arterial coupling (panel D) from rest to exercise. Athletes are represented by closed circles and controls with open circles. Plots are individual values and error bars denote mean  $\pm$  SEM.

### Bibliographic References

1. Scharhag J, Schneider G, Urhausen A, Rochette V, Kramann B, Kindermann W. Athlete's heart: Right and left ventricular mass and function in male endurance athletes and untrained individuals determined by magnetic resonance imaging. *J Am Coll Cardiol*. 2002;40(10):1856–63.
2. Asanoi H, Kameyama T, Ishizaka S, Miyagi K, Sasayama S. Ventriculoarterial coupling during exercise in normal human subjects. *Int J Cardiol*. 1992;36(2):177–86.
3. Chen CH, Nakayama M, Nevo E, Fetters BJ, Lowell Maughan W, Kass DA. Coupled systolic-ventricular and vascular stiffening with age: Implications for pressure regulation and cardiac reserve in the elderly. *J Am Coll Cardiol*. 1998;32(5):1221–7.
4. Seemann F, Arvidsson P, Nordlund D, Kopic S, Carlsson M, Arheden H, et al. Noninvasive Quantification of Pressure-Volume Loops From Brachial Pressure and Cardiovascular Magnetic Resonance. *Circ Cardiovasc Imaging*. 2019;12(1):e008493.
5. Heiberg E, Sjögren J, Ugander M, Carlsson M, Engblom H, Arheden H. Design and validation of Segment - freely available software for cardiovascular image analysis. *BMC Med Imaging*. 2010;10(1):1.

Speaker: B. Östenson

Category: Exercise Stress, Ventricular Function, Athlete

000137

## **Presence of Ebstein Anomaly, Hypertrophic Cardiomyopathy and LV Non Compaction: Coincidence or Shared Genetic Underpinning**

J. Uppal, \* (1); G. Sandhu (1); P. Nijjar (1)

(1) Cardiology, University of Minnesota, Minneapolis, United States of America

### **Abstract**

#### **Description of Clinical Presentation:**

A 60-year-old male with no prior cardiac history was hospitalized for sepsis and acute respiratory failure. Medical history was significant for diabetes, hypertension, and chronic kidney disease. He was diagnosed with a murmur at age 20 but the cause was never established. Prior to this admission, he was well without any cardiac symptoms. During his hospital stay, a transthoracic echocardiogram was performed that was suggestive of an Ebstein anomaly. There was also severe left ventricular (LV) outflow tract obstruction which was presumed to be secondary to hyperdynamic LV function. Cardiac magnetic resonance (CMR) was ordered for further evaluation.

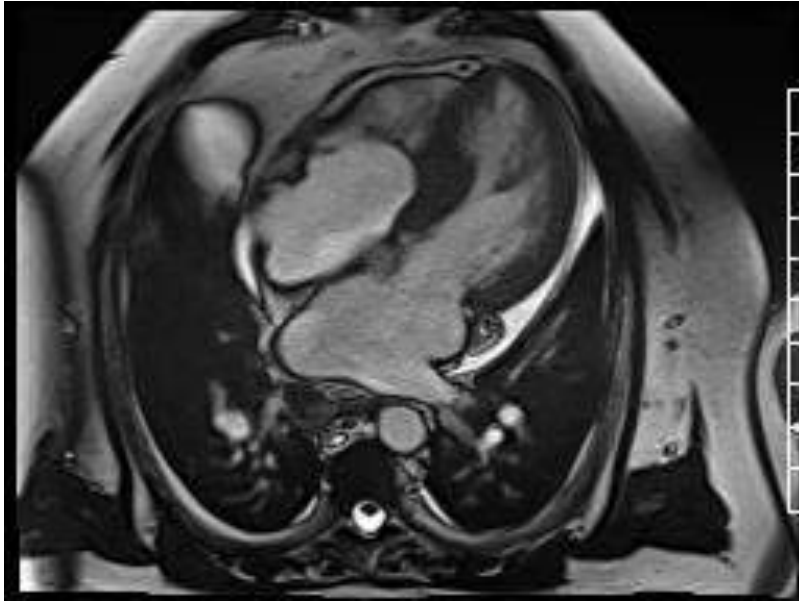
#### **Diagnostic Techniques and Their Most Important Findings:**

CMR cine imaging confirmed Ebstein anomaly, with apical displacement of the tricuspid valve septal leaflet, moderate tricuspid regurgitation and atrialization of the right ventricle. There was moderate asymmetric septal hypertrophy with systolic anterior motion of the mitral valve causing LV outflow tract flow acceleration. These findings were consistent with hypertrophic obstructive cardiomyopathy (HCM). Additionally, there was LV hypertrabeculation compatible with LV non-compaction (LVNC). Genetic testing was advised.

#### **Learning Points from this Case:**

Ebstein anomaly is a rare congenital heart malformation without a clear genetic cause. It can occasionally be associated with other heart defects suggesting a potentially common genetic origin. CMR is an excellent test for comprehensive evaluation of suspected adult congenital heart disease and to diagnose additional heart defects that are not apparent on echocardiography. Mutations in the *MYH7* gene are well known to cause HCM and LVNC. In a cohort study of 141 probands with Ebstein anomaly, *MYH7* mutations were found in 8, and 6 of whom also had LVNC. Seven distinct mutations were found; 2 were known to cause HCM. Presence of additional malformations, specifically HCM and LVNC, with Ebstein anomaly may not be a coincidence and rather point to a shared genetic cause.

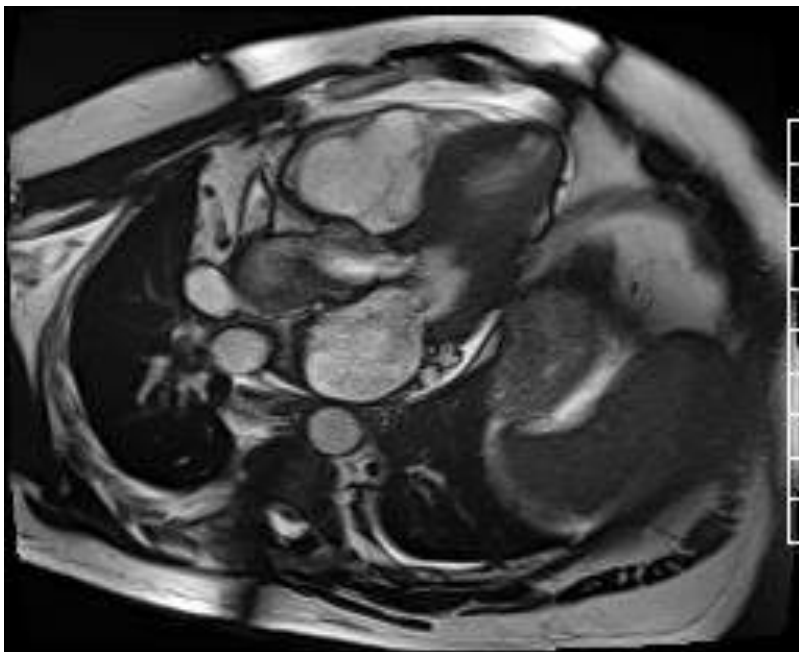
### **Figure/Table 1**



**Caption 1**

4-chamber cine showing apical displacement of the tricuspid valve septal leaflet and atrialization of the right ventricle.

**Figure/Table 2**



**Caption 2**

3-chamber cine showing septal hypertrophy with systolic anterior motion of the mitral valve causing LV outflow tract flow acceleration.

**Figure 3**



**Caption 3**

Apical short axis cine showing LV hypertrabeculation compatible with LV non-compaction (LVNC).

### **Bibliographic References**

Postma AV, van Engelen K, van de Meerakker J, Rahman T, Probst S, Baars MJ, Bauer U, Pickardt T, Sperling SR, Berger F, et al.. Mutations in the sarcomere gene MYH7 in Ebstein anomaly. *Circ Cardiovasc Genet*. 2011; 4:43–50. doi: 10.1161/CIRCGENETICS.110.957985

Speaker: J. Uppal,

Category: Ebstein's Anomaly, Hypertrophic Cardiomyopathy, Non-Compaction

000138

## Cardiac adaptation to acute haemodynamic stress in patients with type 2 diabetes

A. Chowdhary \* (1); S. Thirunavukarasu (1); N. Jex (1); F. Jonathan (1); P. Swoboda (1); H. Xue (2); P. Kellman (2); J. Greenwood (1); S. Plein (1); E. Levelt (1)

(1) Leeds institute of cardiovascular and metabolic medicine, University of Leeds, Leeds, United Kingdom; (2) National institutes for health, NHLBI, Bethesda, United States of America

### Abstract

**BACKGROUND:** Due to varying cardiac workloads, efficient demand-supply matching is crucial for maintaining normal cardiac function. Cardiac metabolism is profoundly affected by changes in cardiac workload. There is scarcity of non-invasive studies evaluating how the heart adapts to hemodynamic stress in type 2 diabetes (T2D) patients. Using cardiovascular magnetic resonance (CMR) and <sup>31</sup>Phosphorus MR spectroscopy (<sup>31</sup>P-MRS) we assessed changes in cardiac energetics, perfusion, strain, systolic and diastolic function in response to acute increases in cardiac workload with dobutamine stress in T2D patients and healthy volunteers (HV). We hypothesized that cardiac energetics are further impaired acutely during dobutamine stress and that this will have consequences on the systolic and diastolic function in diabetes patients.

**METHODS:** 38 T2D patients and 18 matched HV were recruited. Participants with ischemic heart disease were excluded. The CMR protocol consisted of rest and dobutamine stress cine imaging, perfusion imaging (motion corrected, automated in-line perfusion mapping), velocity-encoded mitral in-flow imaging and late gadolinium enhancement imaging at 3T (Figure-1, scan protocol). Intravenous dobutamine was delivered peripherally, at incremental doses between 10 and 40 µg/kg/min as necessary to achieve the 65% of the age-predicted maximal heart rate. Average infusion time was 18min.

**RESULTS:** Clinical and biochemical characteristics, and rest and dobutamine stress CMR/<sup>31</sup>P-MRS results are provided in Table-1.

During dobutamine stress, increases in rate pressure product were similar in diabetes patients and controls. Rest and peak stress LV ejection fraction (LVEF), global longitudinal strain (GLS), and mitral in-flow E/A ratio were all lower in diabetes patients compared to HV. This was despite both groups showing similar increases in LVEF and GLS, and similar reductions in diastolic function with dobutamine stress. Patients with diabetes showed LV concentric remodelling. Moreover, stress myocardial blood flow (MBF) and myocardial perfusion reserve was lower in T2D patients, when rest MBF was similar in both groups.

Compared to HV, rest phosphocreatinine (PCr)/ATP ratio was 21% lower in T2D patients, with a further, 4% reduction during stress. However, there was a more pronounced reduction in the stress PCr/ATP in HV (24% relative reduction), although stress PCr/ATP remained numerically higher in HV compared to T2D patients. There was a significant correlation between the rest diastolic function (mitral valve in-flow E/A ratio) and energetics ( $r=0.41$ ,  $p=0.02$ ), and rest MBF and LVEF ( $r=0.33$ ,  $p=0.01$ ).

**CONCLUSIONS:** This is the most comprehensive CMR and 31P-MRS study exploring the cardiac response to acute hemodynamic stress in diabetes patients compared to controls to date. Patients with diabetes showed lower systolic and diastolic function and energetics both at rest and during peak stress, and lower stress global myocardial blood flow compared to non-diabetic controls. The acute changes in energetics or perfusion were not associated with the cardiac contractile or diastolic function response to acute haemodynamic stress. Contrary to expected, more pronounced reductions in energetics were detected in the controls compared to diabetes patients. This may suggest that a chronic metabolic energetic deficit in diabetes patients activates compensatory mechanisms potentially, including increased cellular fuel uptake and utilization rates, to minimize reductions in the PCr/ATP ratio.

**Figure/Table 1**

	<b>HV</b> <b>(n=18)</b>	<b>T2D</b> <b>(n=38)</b>	<b>P value</b>
Age (yrs)	62 ± 7	64 ± 10	0.5
Male %	39%	62%	0.09
Systolic blood pressure (mmHg)	124 ± 17	130 ± 17	0.3
Heart rate (beats/min)	60 ± 10	68 ± 8	0.01*
Body mass index (kg/m2)	25 ± 3	27 ± 4	0.28
Fasting glucose (mmol/L)	4.9 ± 0.4	9.7 ± 2.6	<0.0001*
Glycated haemoglobin (mmol/mol)	35 ± 3	63 ± 12	<0.00001*
BNP (pg/ml)	59 ± 31	114 ± 141	0.09
<b>CARDIAC STRUCTURAL CHANGES</b>			
LV end diastolic volume (ml)	149 ± 41	129 ± 31	0.08
LV end diastolic volume index (ml/m2)	84 ± 18	66 ± 15	0.001*
LV end systolic volume index (ml/m2)	31 ± 10	26 ± 8	0.03*
LV mass (g)	87 ± 29	101 ± 27	0.08
LV mass index (g/m2)	49 ± 13	52 ± 10	0.4
LV mass/ LV end diastolic volume (g/ml)	0.58 ± 0.09	0.79 ± 0.17	0.00001*
LA maximum volume (ml)	61 ± 30	55 ± 23	0.5
<b>REST AND STRESS SYSTOLIC FUNCTION</b>			
Cardiac Contractility (mmHg/ml/m2)	4.51 ± 1.76	5.65 ± 1.81	0.03*
LV ejection fraction (rest) (%)	66 ± 5	62 ± 6	0.03*
LV ejection fraction (stress) (%)	80 ± 5	75 ± 7	0.009*
Δ LV ejection fraction (%)	14 ± 6	13 ± 5	0.6
LA ejection fraction (rest) (%)	64 ± 15	58 ± 13	0.22
LA ejection fraction (stress) (%)	69 ± 14	56 ± 16	0.006*
<b>STRESS PERFUSION</b>			
Increase in RPP, %	105 ± 31	120 ± 51	0.5
MBF stress (ml/g/min)	2.06 ± 0.48	1.68 ± 0.72	0.04*
MBF rest (ml/g/min)	0.67 ± 0.11	0.69 ± 0.16	0.8
MPR	3.11 ± 0.72	2.53 ± 1.10	0.04*
<b>REST AND STRESS MYOCARDIAL STRAIN</b>			



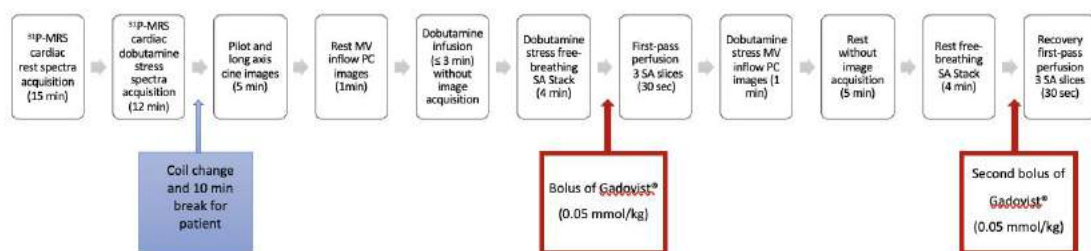
GLS rest (%)	21 ± 3	16 ± 4	0.0001*
MAPSE rest (mm)	16 ± 2	11 ± 3	0.00001*
GLS stress (%)	24 ± 3	19 ± 4	0.001*
MAPSE stress (mm)	14 ± 2	14 ± 5	0.8
<b>REST AND STRESS DIASTOLIC FUNCTION (MV inflow flow assessments)</b>			
E/A rest	1.31 ± 0.53	1.03 ± 0.46	0.07
E/A stress	1.02 ± 0.28	0.78 ± 0.30	0.01*
<b>REST AND STRESS MYOCARDIAL ENERGETICS</b>			
Increase in RPP, %	103 ± 36	123 ± 57	0.3
PCr/ATP rest	2.01 ± 0.40	1.58 ± 0.42	0.01*
PCr/ATP stress	1.53 ± 0.37	1.51 ± 0.39	0.9
Δ PCr/ATP	0.48 ± 0.40	0.02 ± 0.37	0.03*

Values are mean ± SD and number (%) for categorical variables. \* signifies  $p \leq 0.05$ ; T2D indicates type 2 diabetes; HV, healthy volunteers; n, number; yrs, years; mmHg, millimeters of mercury; min, minute; kg, kilogram; m, metre; mmol/L, millimoles per litre; mmol/mol, millimoles per mole; pg/ml, picogram per millilitre; BNP, B type natriuretic peptide; LV, left ventricle; ml, millilitres; g, gram; LA, left atrium; RV, right ventricle; MBF, myocardial blood flow; MPRI, myocardial perfusion reserve index; GLS, global longitudinal strain; MAPSE, mitral annular plane systolic excursion; MV, mitral valve; PCr/ATP, phosphocreatinine to adenosine triphosphate ratio.

**Caption 1**

**Table 1: Demographics, biochemical and CMR characteristics**

**Figure/Table 2**



**Caption 2**

**Figure 1: 31P Magnetic Resonance Spectroscopy and Cardiac Magnetic resonance protocol**

Speaker: A. Chowdhary

Category: Spectroscopy, Diabetes, Dobutamine

# Characterization of Myocardial Injury on Cardiovascular Magnetic Resonance Imaging in Patients Diagnosed with Coronavirus Disease-2019

M. Vidula \* (1); J. Rajewska-Tabor, (2); J. J. Cao (3); Y. Kang, (1); J. Craft (4); W. Mei, (4); P. Chandrasekaran (5); D. Clark (6); A.-M. Poenar, (7); M. Gorecka, (8); M. Malahfji (9); E. Cowan, (10); J. Kwan, (11); S. Reinhardt, (11); S. Al-Tabatabaee, (12); P. Doebelin, (12); A. Villa, (13); I. Karagodin, (14); N. Alvi (14); P. Christia, (15); N. Spetko, (16); M. P. Cassar (17); C. Park, (18); L. Nambiar, (19); A. Turgut, (20); M. Roosta Azad (21); M. Lambers, (22); M. Salerno (23); J. Kim, (24); M. Elliott, (25); B. Raman, (17); S. Neubauer, (17); C. Tsao, (16); G. Larocca, (15); A. R. Patel (26); A. Chiribiri (27); S. Kelle (12); L. Baldassarre (28); D. J. Shah (10); S. Hughes (29); M. Tong (30); M. Pyda (31); O. Simonetti (5); S. Plein (7); Y. Han (1)

(1) Medicine/Cardiology, University of Pennsylvania, Philadelphia, United States of America; (2) Department of magnetic resonance, University of Medical Sciences, Poznan, Poland; (3) Cardiology, St. Francis Hospital & Heart Center, Roslyn, United States of America; (4) Cardiology, St Francis Hospital, The Heart Center, Roslyn, United States of America; (5) Davis Heart and Lung Research Institute, The Ohio State University, Columbus, United States of America; (6) Cardiology, Vanderbilt University Medical Center, Nashville, United States of America; (7) Licamm, Leeds institute of Cardiovascular and Metabolic Medicine, Leeds District, UK, United Kingdom; (8) Biomedical imaging science department, Leeds Institute of Cardiovascular and Metabolic Medicine, Leeds, United Kingdom; (9) Cardiology, Houston Methodist Heart & Vascular Center, Tomball, United States of America; (10) Cardiology, Houston Methodist Hospital, Houston, United States of America; (11) Cardiology, Yale University, New Haven, United States of America; (12) Cardiology, German Heart Center Berlin, Berlin, Germany; (13) School of biomedical engineering & imaging sciences, King's College London, London, United Kingdom; (14) Cardiology, The University of Chicago, Chicago, United States of America; (15) Cardiology, Mount Sinai Hospital, New York, United States of America; (16) Cardiology, Beth Israel Deaconess Medical Center (BIDMC), Boston, United States of America; (17) Cardiology, University of Oxford, Oxford, United Kingdom; (18) Medicine, Weill Cornell Medicine, New York, United States of America; (19) Cardiology, Weill Cornell Medicine, New York, United States of America; (20) Cardiology, University of Virginia, Charlottesville, United States of America; (21) Cardiology, Contilia Heart and Vascular Centre, Essen, Germany; (22) Cardiology, Contilia Heart and Vascular Centre, Essen, Germany; (23) Cardiology, radiology, and medical imaging, University of Virginia, Charlottesville, United States of America; (24) Medicine, Weill Cornell Medical College, New York, United States of America; (25) Cardiology, Atrium Health Carolinas Medical Center, Charlotte, United States of America; (26) Medicine and radiology, UChicago Medicine, Chicago, United States of America; (27) Biomedical Engineering and Imaging Sciences, King's College London Waterloo Campus, London, United Kingdom; (28) Cardiovascular medicine, Yale University, New Haven, United States of America; (29) Division of cardiovascular medicine, Vanderbilt University Medical Center, Nashville, United States of America; (30) Internal medicine, The Ohio State University, Columbus, United States of America; (31) Department of magnetic resonance, University of Medical Sciences, Poznań, Poland

## Abstract

**Background:** The objective of this study was to characterize patterns of myocardial injury by cardiovascular magnetic resonance (CMR) in a large, international, multicenter cohort of patients with coronavirus disease-2019 (COVID-19).

**Methods:** This retrospective, multicenter study consisted of 1,047 patients with PCR-confirmed COVID-19 who underwent CMR (89.8% clinical scans, 10.2% research scans; median time from a positive PCR test to CMR: 112 days [interquartile range: 60–181 days]) at 12 sites in the United States, 3 sites in the United Kingdom, 2 sites in Germany, and 1 site in Poland. Data collected included demographics, clinical characteristics, CMR-derived morphologic and functional parameters, late gadolinium enhancement (LGE) patterns, and diagnoses of myocarditis and myocardial infarction (MI) by CMR.

**Results:** Baseline characteristics of the entire cohort are shown in Table 1. In the overall cohort (mean age  $47.4 \pm 16.5$  years, 47.5% women, 36.3% hospitalized), 38.8% had LGE, 29.0% were diagnosed with myocarditis (acute: 8.1%, prior: 13.2%, possible: 7.6%), and 7.3% were diagnosed with MI (acute: 1.9%, prior: 4.7%, possible: 0.7%). Patterns of myocarditis were detected at similar rates in hospitalized and ambulatory patients (29.9% vs 28.5%,  $p=0.42$ ), but rates of MI were higher in the hospitalized cohort (13.4% vs 3.8%,  $p<0.0001$ ). Patients with known obstructive coronary artery disease (CAD) were more likely to have evidence of MI (71.1%) than patients with either nonobstructive disease (14.3%) or without known CAD (2.2%,  $p<0.0001$ ), and less likely to have evidence of myocarditis (15.9% vs 37.5% vs 41.6%,  $p=0.004$ ). Compared to the troponin-negative cohort, the troponin-positive cohort was more likely to have evidence of myocarditis (38.7% vs 28.5%,  $p<0.0001$ ) and MI (24.3% vs 3.1%,  $p<0.0001$ ). Similarly, higher rates of myocarditis (37.6% vs 26.8%,  $p<0.0001$ ) and MI (20.8% vs 3.9%,  $p<0.0001$ ) were detected in patients with elevated natriuretic peptides than in patients without elevated natriuretic peptides. Representative images of a patient with acute myocarditis are shown in Figure 1, and images of a patient with an acute MI are shown in Figure 2.

**Conclusions:** In a large, international, multicenter CMR study of COVID-19 patients with high clinical suspicion for myocardial injury, the diagnosis of myocarditis or MI is frequent. The patterns of injury differ in various patient subgroups, defined by hospitalization status, history of CAD, and laboratory evidence of myocardial injury or stress. While COVID-19 infection may not be the definitive cause of myocardial injury in these patients, these findings further our understanding of the characteristics and patterns of myocardial injury in patients diagnosed with COVID-19, and future studies are needed to better understand the prognostic significance of these findings.

**Figure/Table 1**

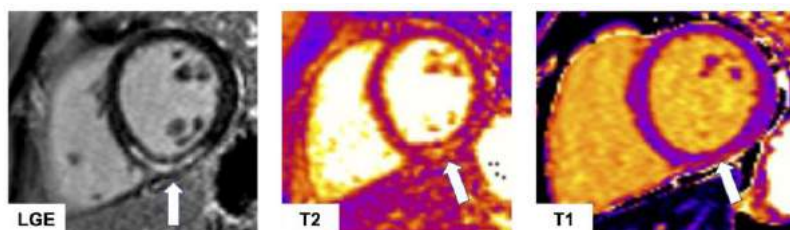
Clinical Characteristics	N with Available Data	Results (n [%] or mean $\pm$ standard deviation)
<b>Demographics</b>		
Age (years)	1047	$47.4 \pm 16.5$
Female	1047	497 (47.5%)
Race	913	

White		692 (75.8%)
Black		136 (14.9%)
Hispanic	807	51 (6.3%)
Hospitalized	1040	377 (36.3%)
Intubated	1034	55 (5.3%)
<b>Comorbidities</b>		
Hypertension	988	322 (32.6%)
Hyperlipidemia	965	264 (27.4%)
Diabetes	977	147 (15.0%)
Current smoker	821	46 (5.6%)
Known coronary anatomy	364	
Obstructive disease		45 (12.4%)
Nonobstructive disease		49 (13.5%)
Preexisting cardiomyopathy	961	101 (10.5%)
Preexisting respiratory condition	952	195 (20.5%)
<b>Laboratory Studies</b>		
Troponin elevation	709	191 (26.9%)
Natriuretic peptide elevation	584	193 (33.0%)

### Caption 1

Table 1. Baseline characteristics of the entire cohort.

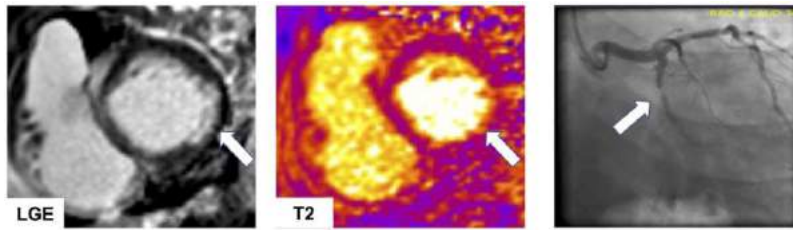
### Figure/Table 2



### Caption 2

Figure 1. Images of a patient with acute myocarditis in the setting of a recent COVID-19 infection, demonstrating subepicardial to midmyocardial enhancement in the mid inferior and inferoseptal walls (left panel, arrow), with corresponding elevation in native T2 times (middle panel, arrow) and native T1 times (right panel, arrow).

### Figure 3



### Caption 3

Figure 2. Images of a patient with an acute infarct in the setting of an active COVID-19 infection. There is subendocardial enhancement in the basal inferolateral wall (left panel, arrow), with corresponding elevation in native T2 times (middle panel, arrow). Coronary angiography (right panel) revealed a proximal left circumflex occlusion (arrow).

Speaker: M. Vidula

Category: Myocarditis, Acute Myocardial Infarction, Chronic Myocardial Infarction

000140

## Fluid-Structure Stability Analysis to Predict Aortic Dilation

T. Zhao (1); G. Elisha (1); E. Johnson \* (2); S. Halder (1); B. Smith (3); B. Allen (2); M. Markl (2); N. Patankar (1)

(1) Mechanical engineering, Northwestern University, Evanston, United States of America;  
(2) Radiology, Northwestern University, Chicago, United States of America; (3) Physical medicine and rehabilitation, Northwestern University, Chicago, United States of America

### Abstract

**Background-** Guidelines for clinical management of patients with aortic dilation recommend regular imaging, with maximal diameter and/or interval diameter changes being key metrics for identifying patients at higher risk for complications, such as dissection [1]. However, it remains a challenge to distinguish between patients with long-term stable aortic dilatation and those who may experience further growth and may require surgical intervention. Here, we present a novel analysis of 4D flow MRI in the thoracic aorta that identifies fluid structure instabilities predictive of later complications in a cohort of aortopathy patients.

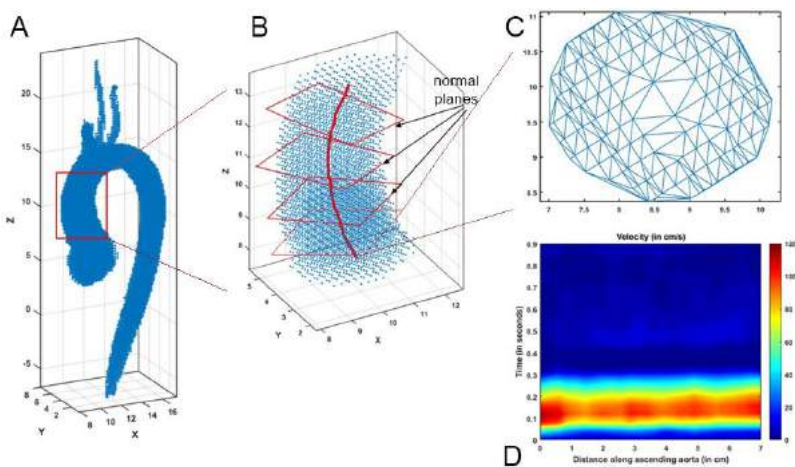
**Methods-** An institutional MRI database was queried to identify a patient cohort with suspected isolated aortopathy and tricuspid aortic valve and a healthy subject cohort without disease. All subjects were included in this study with IRB supervision and approval. Imaging was performed by 4D flow MRI at 1.5T or 3T with  $(1.2\text{--}3.1\text{ mm})^3$ , 33-45 ms resolution and full thoracic aorta coverage. A flow stability parameter  $N\omega$  was derived from Navier stokes equations relating physical fluid pressure, cross-sectional area, and velocity to identify the threshold at which linear perturbations will cause unbounded growth to area [2,3]. Pressure, area and velocity values used to compute  $N\omega$  were calculated or taken directly from segmented aortic 4D flow data (fig. 1). Values of  $N\omega$  above zero indicate theoretical fluid structure instability and expected potential for growth. Aortic measurements for patients from all available imaging (CT, MR) performed within 5 years after the date of the 4D flow MRI were collated, with standardized assessments of sinus of valsalva (SOV) and maximal ascending aortic (MAA) diameters. Interval growth events were identified as a change in maximal dimension above 3mm/year between successive time points. Surgical interventions that involved replacement or repair of the aortic valve or ascending aorta were also annotated. In the patient cohort, the potential for  $N\omega > 0$  to predict future adverse events (interval growth/dilation or intervention) was evaluated. Group statistical comparisons used Wilcoxon rank sum tests, and true/false positives/negatives and receiver-operator curve (ROC) analysis were used to assess predictive performance.

**Results-** A total of 217 subjects were included, comprising 117 patients and 100 healthy subjects. Of the 117 patients, 72 had adequate follow-up data for evaluation of  $N\omega$  predictive performance. In this group, 22 subjects had interval growth  $> 3\text{mm}$  in both/either MAA and/or SOV recorded at some time after the 4D flow MRI, and 6 subjects underwent aortic valve and/or wall repair (fig. 2). The  $N\omega > 0$  threshold for prediction of future adverse events achieved sensitivity/specificity of 0.91 and 0.98. Area under the curve from ROC analysis for  $N\omega$  was 0.97 for predicting growth or surgical intervention within five years. The  $N\omega$  values for patients (med. -1.24, IQR [-2.43, 1.04]) were generally higher than for healthy volunteers (med. -2.26, IQR [-3.13, -1.10]) with significance ( $p < 0.001$ ; fig. 3). However, patients were

not matched to the healthy subjects for age ( $46.4\pm15.5$  yr vs.  $58.5\pm11.7$  yr) or sex (24% F vs. 51% F).

**Conclusions-** The fluid-structure stability parameter, derived from physical first principles, is highly predictive of future aortic dilation and aortic surgery in a cohort of patients being imaged for suspected aortopathy. Comparison to healthy subjects showed higher (less stable) values for the parameter in patients, but an age- and sex-matched comparison would be more conclusive for establishing group differences. Expanding the cohort size for the patients studied here and extending analysis to bicuspid patients would help establish calculation of the fluid-structure stability parameter as a valuable clinical metric for management of aortopathy.

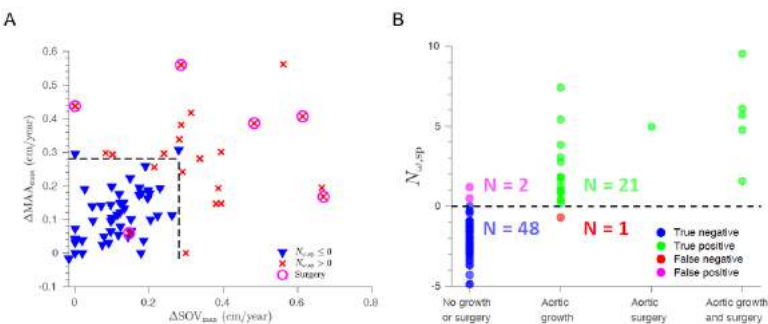
Figure/Table 1



Caption 1

Figure 1. Processing of 4D flow MRI for calculation of stability parameter  $N\omega$  proceeds from segmented thoracic aorta (A), with a centre-line and cutplanes through the ascending aorta (B), and cross-sectional meshing by Delaunay triangulation (C) with a velocity map in length along the aorta and time through the cardiac cycle (D) extracted from the 4D flow MRI.

Figure/Table 2

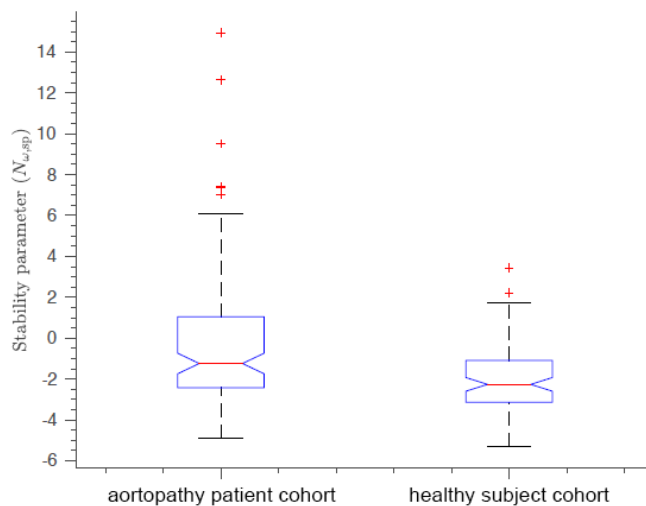




## Caption 2

Figure 2. Maximal interval aortic growth (dilation) rates (A) observed in the patient cohort follow-up data for 72 subjects, labelled by stability parameter  $N\omega$  sign (positive/negative) and surgical intervention. True/false positive/negative prediction performance (B) for using  $N\omega$  to predict future dilation or surgical aortic valve/wall repair.

## Figure 3



## Caption 3

Figure 3. Comparison of stability parameter  $N\omega$  in suspected-aortopathy and healthy subject cohorts ( $n=117,100$ ); the distribution of the patient cohort parameter value is higher than that of the healthy subject cohort ( $p<0.001$ ).

## Bibliographic References

[1] Otto CM, Nishimura RA, Bonow RO, Carabello BA, Erwin JP, Gentile F, et al. 2020 ACC/AHA Guideline for the Management of Patients With Valvular Heart Disease. Journal of the American College of Cardiology. 2021 Feb;77(4):e25–197. , [2] Azer K, Peskin CS. A One-dimensional Model of Blood Flow in Arteries with Friction and Convection Based on the Womersley Velocity Profile. Cardiovasc Eng. 2007 Jun 26;7(2):51–73., [3] Wang X-F, Nishi S, Matsukawa M, Ghigo A, Lagrée P-Y, Fullana J-M. Fluid friction and wall viscosity of the 1D blood flow model. Journal of Biomechanics. 2016 Feb;49(4):565–71.

Speaker: E. Johnson

Category: 4D Flow, Aorta, Fluid Dynamics

000141

## Evaluation of aortic valve regurgitation by cardiovascular magnetic resonance using 2D and 4D flow analysis

P. Gerhardt \* (1); N. Shehu (1); I. Ferrari (1); M. Hüllebrandt (2); A. Hennemuth (2); E. Hendrich (3); P. Ewert (1); H. Stern (1); C. Meierhofer (1)

(1) Kinderkardiologie, Deutsches Herzzentrum München, München, Germany; (2) Mevis, Fraunhofer Institute for Digital Medicine MEVIS, Berlin, Germany; (3) Radiologie, Deutsches Herzzentrum München, München, Germany

### Abstract

#### Background

Incomplete closure of the aortic valve causes aortic regurgitation (AR) and leads to a volume shift from the aorta back into the left ventricle. This ongoing volume overload of the left ventricle is a risk for ventricular dilation, functional impairment and provokes the development of heart failure. Cardiovascular magnetic resonance (CMR) directly measures backward flow through the aortic valve. Since several measurement methods as 2D or 4D phase-contrast CMR are available less is known about the most reliable level in the ascending aorta (Figure 1). The aim of this study was to evaluate the appropriate level for ROI placement for 2D and 4D flow for the most accurate measurement of aortic regurgitation.

#### Methods

We analyzed thirty 2D and 4D flow datasets from patients with aortic valve regurgitation, median age 31 years, range 8-56) were analyzed. Flow measurements for gold standard 2D CMR were performed at 3 different levels of the aorta, 4D flow was measured along the entire thoracic aorta and 3 ROIs were positioned at the same levels as in 2D in post processing. We defined three different levels; the aortic valve, the aortic bulb and the proximal aorta ascendens for flow evaluation. We also recorded the occurrence of interfering parameters, such as vortices and stenosis. Two experienced investigators analyzed all data.

#### Results

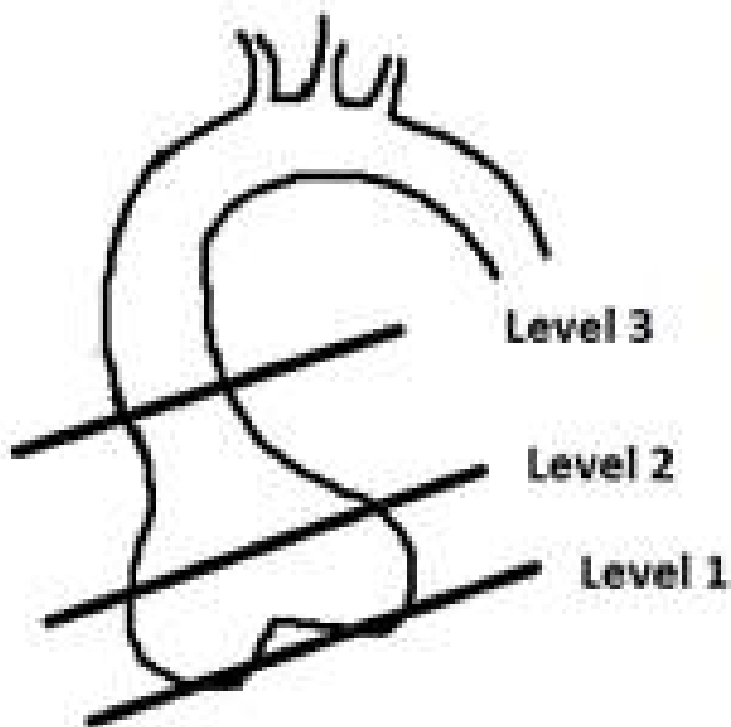
AR at all defined levels by 2D flow was median 31% (range 1-79) and 18% (range 1-70) by 4D acquisition. AR by 2D flow at the level of the aortic valve was median 26% (range 1-40), at the level of the aortic bulb 33% (range 4-51), and at the level of the ascending aorta 32% (range 1-79), AR by 4D flow was median 18% (range 1-46), 17% (range 1-70), and 16 % (range 1-41), respectively. Linear regression for 2D and 4D showed the best correlation for the level of the aortic valve ( $r^2$  0.53). Furthermore, correlation of antegrade 2D and 4D flow was at the same level ( $r^2$  0.83). Pronounced vortices showed a marked negative influence on the acquisition of retrograde flow with most accurate measurements on the level of the aortic

valve (65 % vs. 48% and 44% at the level of the aortic bulb and mid ascending aorta, respectively, Table 1).

## Conclusions

AR was measured most reliable at the level of the aortic valve when comparing gold standard 2D flow with 4D flow CMR. Patients with pronounced vortices were significantly more often underestimated compared to patients with "straight" flow (Figure 2).

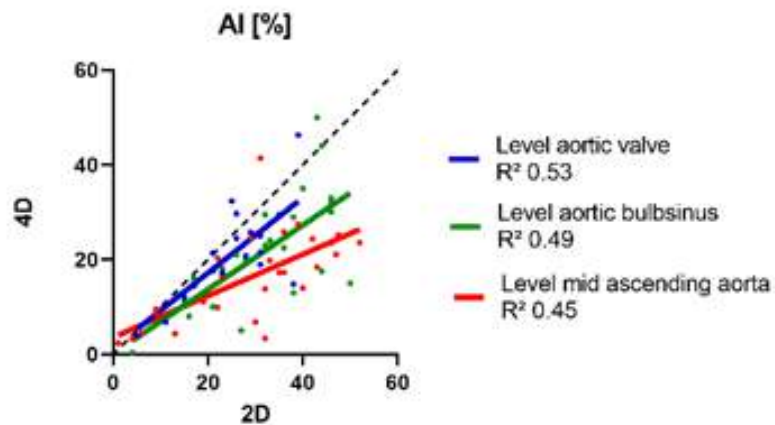
## Figure/Table 1



## Caption 1

Figure 1: Level of ROIs in the aorta

## Figure/Table 2



**Caption 2**

Figure 2: Correlation of AR [%] 4D and 2D flow at 3 different levels

**Figure 3**

Level	Aortic valve		Aortic bulb		Mid ascending aorta	
n	23		25		32	
Vortex	None/low	Strong	None/low	Strong	None/low	Strong
AR correct n(%)	11 (48%)	4 (17%)	7 (28%)	5 (20%)	13 (41%)	1 (3%)
AR underestimated n (%)	1 (4%)	7 (%)	2 (8%)	11 (44%)	3 (9%)	15 (47%)
Correct in total	65%		48%		44%	

**Caption 3**

Table 1: Influence of vortices on AR measurement

Speaker: P. Gerhardt

Category: 4D Flow, Aortic Valve, Aortic Regurgitation

**000144**

## **Longitudinal evaluation of atrial function in patients with tetralogy of Fallot**

B. Ittleman \* (1); J. Steele, (1); A. Bader (2)

(1) Pediatric Cardiology, Yale University, New Haven, United States of America; (2) Radiology, Yale University, New Haven, CT, USA, New Haven, United States of America

### **Abstract**

#### **Background:**

Atrial function as measured by strain and strain rate is emerging as a sensitive early marker of diastolic dysfunction in patients with congenital heart disease (1). Cardiac MRI (CMR) has advantages when evaluating atrial function compared to echocardiography, including, improved spatial resolution and chamber quantification. In patients with repaired tetralogy of Fallot (rTOF) left and right atrial function has been shown to be abnormal compared to age matched controls (2,3). This study's aims were to longitudinally evaluate the progression of atrial function in patients with rTOF, assess if atrial function improved after pulmonary valve replacement (PVR) and determine whether a relationship exists between atrial function and development of new tachyarrhythmias or sudden cardiac death (SCD).

#### **Methods:**

Patients from our center with rTOF who had multiple CMRs over a thirteen-year period were identified. CMR examinations were retrospectively reviewed and right and left atrial size and function were measured in the two and four chamber views and assessed for changes over time and after PVR. Left and right atrial reservoir, conduit, and pump strain and strain rates were determined using by tissue tracking. Changes in atrial function were examined to determine if there was improvement after PVR and if a relationship with primary endpoints of new tachyarrhythmia or SCD exists.

#### **Results:**

Forty-two patients with rTOF were identified (55% male). Median age of TOF repair was 2.5 years and median age of PVR was 20 years (table 1). A gradual decline in atrial function was seen in patients with rTOF which did not recover after PVR (Figure 1) despite improvements in right ventricular size (median 144 mL/m<sup>2</sup> pre valve and 105 mL/m<sup>2</sup> post valve) and maintained systolic function. Notably right atrial pump strain (median 15.3 pre valve and 8.2 post valve) and left atrial conduit strain (median 32.5 pre valve and 21 post valve) had the biggest decreases after valve placement (Table 1). Additionally, left and right atrial size continued to increase after PVR. Five patients reached the primary endpoint of a new tachyarrhythmia; however, this finding did not reach statistical significance.

## Conclusions:

Prior studies have established that atrial function is abnormal in patients with rTOF. In our cohort we observed progressive decline of left and right atrial function over time which did not improve after PVR despite improved ventricular size and maintained function. Five patients reached a primary endpoint of new tachyarrhythmia. Additional studies are needed to further elucidate the implications of declining atrial function in this population and its potential relationship with adverse events.

## Figure/Table 1

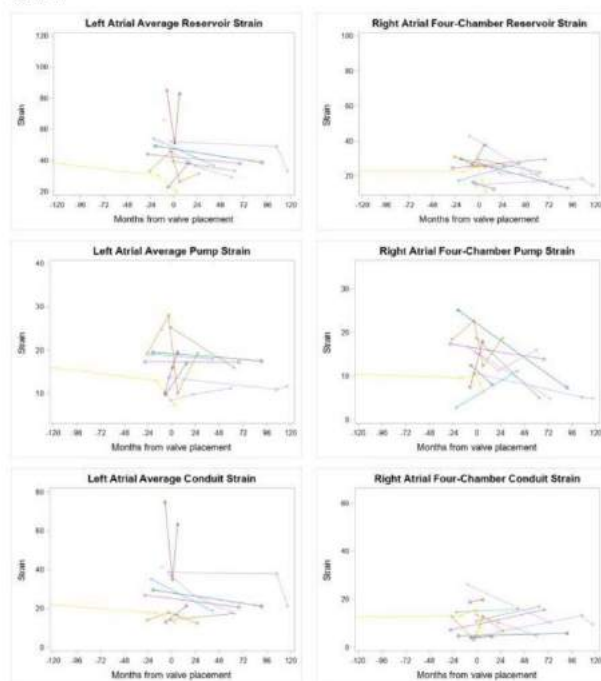
Table 1 Demographic parameters and CMR Characteristics before and after pulmonary valve replacement (n=11)		Median (1st, 3rd quartile)
Male, n (%)	23 (55)	
Age at corrective surgery (years)	2.5	
Surgical PVR, n (%)	6 (55)	
Age at PVR (years)	20 (14.5, 24.5)	
CMR Timing:	Pre PVR	Post PVR
Time between pre and post CMR (months)	62 (15, 89.5)	62 (15, 89.5)
Age at MRI (years)	20 (12, 24.5)	23 (16, 27)
RVEDV (ml)	225 (152, 255)	176 (164, 266)
RVEDVi (ml/m <sup>2</sup> )	144 (135, 169)	105 (85, 129)
RV EF (%)	40 (37.5, 50.5)	42 (41, 48)
RA size (ml)	48.4 (37.3, 61.9)	67.2 (50.3, 74)
RA indexed size (cm <sup>2</sup> )	16.1 (13.9, 20.5)	20.4 (17.7, 23)
RA reservoir strain	26.1 (21, 29.3)	20.1 (15.8, 24.6)
RA conduit strain	11 (4.6, 15.2)	11.7 (9.4, 15.1)
RA pump strain	15.3 (10.5, 18.1)	8.2 (5.7, 11.3)
RA reservoir strain rate	1.7 (1.3, 1.9)	1.1 (0.9, 1.3)
RA conduit strain rate	-1 (1.4, 0.8)	-1.5 (-1.8, -1)
RA pump strain rate	-1.8 (-2.2, -1.25)	-1.3 (-1.6, -1)
LVEDV (ml)	125 (112, 152)	157 (124, 163)
LVEDVi (ml/m <sup>2</sup> )	83 (73, 94)	79 (70, 82.5)
LV EF (%)	51 (54, 56)	54 (51, 56.5)
LA size (ml)	36.3 (32.2, 52)	44.4 (35.3, 58.8)
LA indexed size (cm <sup>2</sup> )	13.6 (13, 17.7)	16.1 (13.8, 19.1)
LA reservoir strain	47.7 (44.4, 53.8)	37.4 (34.2, 38.6)
LA conduit strain	32.5 (20.2, 38.2)	21 (17.8, 25.5)
LA pump strain	18.2 (11, 23.4)	16.1 (10.2, 17.2)
LA reservoir strain rate	2.4 (1.9, 3.5)	1.7 (1.6, 1.9)
LA conduit strain rate	-3.7 (-4.7, -2.6)	-2.7 (-3.1, -2.1)
LA pump strain rate	-2.4 (-2.6, -2.1)	-2.1 (-2.4, -1.6)

## Caption 1

PVR pulmonary valve replacement; CMR cardiac magnetic resonance imaging; RVEDV right ventricular end diastolic volume; RVEDi indexed right ventricular end diastolic volume; LVEDV left ventricular end diastolic volume; LVEDVi indexed left ventricular end diastolic volume

## Figure/Table 2

Figure 1.



## Caption 2

Measurements of left and right atrial strain by CMR pre and post pulmonary valve replacement. 0 on the x-axis annotates time of valve replacement. Each patient is color coded with symbols representing timing or CMR.

## Bibliographic References

1. Ta, H.T., Alsaied, T., Steele, J.M. et al. Atrial Function and Its Role in the Non-invasive Evaluation of Diastolic Function in Congenital Heart Disease. *Pediatr Cardiol* 41, 654–668 (2020). <https://doi.org/10.1007/s00246-020-02351-w>, 2. Shelby, K, Quanling, S, Navya, J, et al. Abnormal right atrial performance in repaired tetralogy of Fallot: A CMR feature tracking analysis. *Int. J. Cardiol.* 248, 136-142 (2017). <https://doi.org/10.1016/j.ijcard.2017.06.121>, 3. Ta, H.T., Truong, V.T., Alsaied, T. et al. Left Atrial Strain in the Repaired Tetralogy of Fallot Population: Comparisons to Biventricular Function, Native T1 Values, Exercise Parameters and Healthy Controls. *Pediatr Cardiol* 42, 1102–1110 (2021). <https://doi.org/10.1007/s00246-021-02587-0>

Speaker: B. Ittleman

Category: Congenital Heart Disease, Pediatric , Cardiac Strain



**Automated detection of cardiac resting phases for self-gated free-running whole-heart imaging**

G. Rossi \* (1); N. Masala (1); M. Stuber (2); J. Yerly (2); C. Roy (1); J. Bastiaansen (1)

(1) Department of radiology, Lausanne University Hospital (CHUV) and University of Lausanne (UNIL), Lausanne, Switzerland; (2) Department of radiology, Lausanne University Hospital (CHUV), CIBM, and University of Lausanne (UNIL), Lausanne, Switzerland

**Abstract**

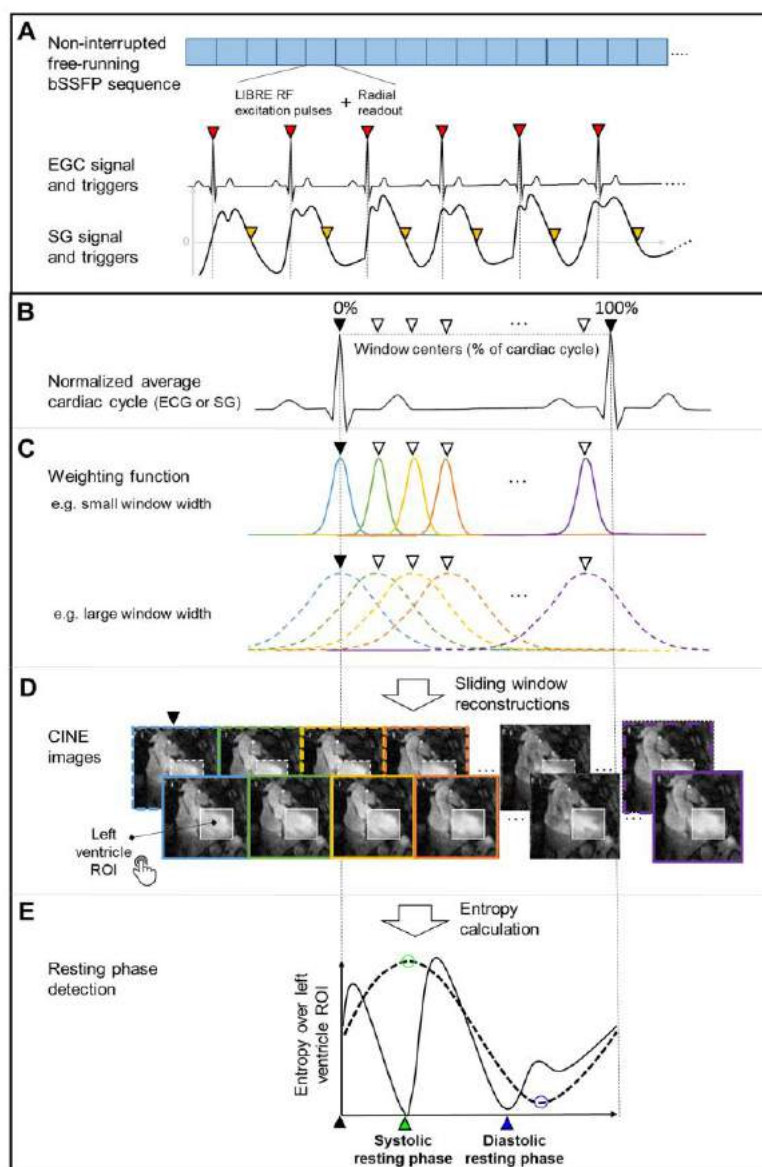
**Background.** Reliable motion compensation strategies are required for high quality 3D MRI of the heart, commonly translating into time inefficient examinations with a complex workflow (e.g. ECG setup, respiratory navigators). In the free-running framework [1], continuously acquired whole-heart data are retrospectively reconstructed as cardiac motion-resolved images, using either ECG- or cardiac self-gating (SG). This results in a considerably simplified workflow and eliminates the need for a-priori identification of trigger windows [1,2]. Still, identifying cardiac phases of interest (e.g. systolic and diastolic resting phases) requires additional manual post-processing and in the case of SG, the trigger point can vary between subjects resulting in an unpredictable shift relative to the ECG R-wave (Fig.1A). In this work, we test the hypothesis that by intentionally inducing and then measuring cardiac-motion blur in free-running data, cardiac resting phases can be automatically identified.

**Methods.** Data were acquired in 10 healthy volunteers (age: 25-38 y; 6 M) with written informed consent on a 1.5T MAGNETOM Aera (Siemens Healthcare, Erlangen, Germany) using a prototype free-running acquisition [3]. To automatically identify cardiac resting phases, preliminary 3D cardiac motion-resolved (CINE) images are created wherein cardiac-motion blur is intentionally induced using a sliding window reconstruction beginning at either the ECG R-wave or at the SG trigger [1] (Fig.1A-D). We posit that the quantifiable change in blur along the cardiac cycle (i.e. image entropy over an ROI containing the left ventricle) or “entropy footprint” relates to the underlying cardiac motion with local extrema representing resting phases (Fig.1E). Entropy footprints for ECG-gated and SG 3D CINE images for two sliding window sizes ( $w=5\%$  and  $50\%$  of the RR interval) were compared to visually inspected RCA and LV motion. Finally, in one dataset the automated resting phase detection was used to define the center of reconstruction windows (Fig.3B) to produce systolic and diastolic respiratory motion-compensated 3D CMRA images using fNAV [4,5].

**Results.** Entropy footprints (Fig.2A-B) showed a repeatable pattern over subjects, with entropy variation strictly related to LV motion for small  $w$  (Fig.3A). For SG CINE images, an expected subject-dependent shift corresponding to the shift between ECG and SG triggers was observed (Fig.2B). Correspondence was found between automatically detected local minima (for small  $w$ ) closest to the global extrema (for large  $w$ ) and the visually identified resting phases. Absolute errors (ECG small and large  $w$ ; SG small and large  $w$ ; in ms) were of ( $12\pm 8$  and  $55\pm 45$ ;  $10\pm 8$  and  $65\pm 54$ ) for systole and ( $57\pm 51$  and  $70\pm 33$ ;  $51\pm 46$  and  $63\pm 43$ ) for diastole. The reduced accuracy for diastole is attributable to its longer duration and to concurrent isovolumetric processes. Using automated resting phase detection, high quality systolic and diastolic 3D CMRA images (Fig.3C-D) were obtained.

**Conclusions.** In this work, we showed that image entropy information from sliding window 3D CINE reconstructions can be used for automated identification of specific cardiac phases regardless of the source of the cardiac signal. The method could be exploited for preliminary identification of reconstruction windows for static resting phase reconstructions (e.g. for coronary imaging or inline ejection fraction computation), or for automated definition of trigger points for dynamic reconstructions, simultaneously increasing reconstruction efficiency and easing comparative analysis of different datasets.

**Figure/Table 1**

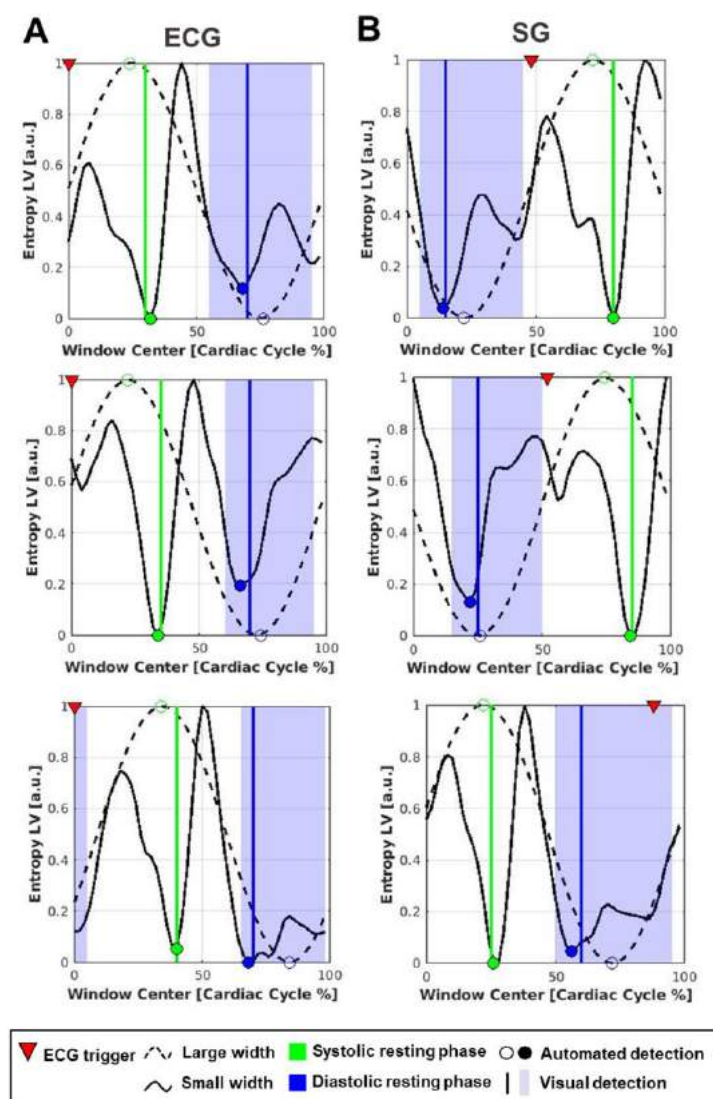


**Caption 1**

**Figure 1.** Entropy-based detection of cardiac resting phases. ECG, or SG cardiac signals extracted from the data can be used for cardiac motion-compensation of free-running data

(A). Preliminary sliding window CINE reconstructions (D) with fixed number of frames (B) and varying window width (C) allow for automatic detection of cardiac resting phases (E).

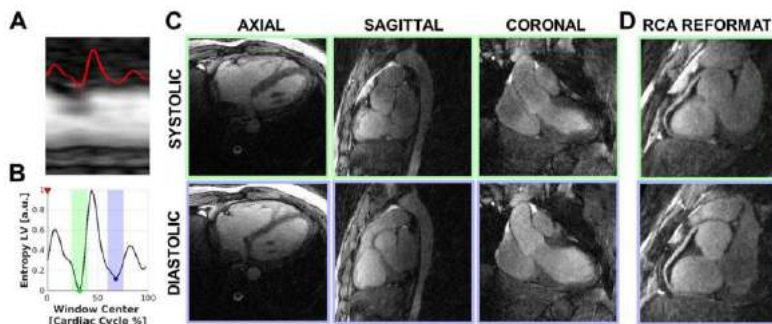
Figure/Table 2



Caption 2

**Figure 2.** Examples of entropy footprints obtained in 3 subjects for ECG (A) and SG (B) CINE images for large (dotted) and small (solid) window widths. Automatically (circles) and visually detected systolic (green line) and diastolic (blue line: center based on RCA, blue area: extent based on LV) resting phases are reported.

**Figure 3**



**Caption 3**

**Figure 3.** **A:** Relationship between entropy footprint (red) and LV motion (M-mode image from ECG CINE sliding-window reconstruction). **B-D:** Resting phase reconstructions (**C**) and RCA reformats (**D**) obtained from data within windows of  $\pm 8\%$  centered at the automatically detected systolic (green) and diastolic (blue) resting phases (**B**).

### Bibliographic References

[5] Rossi, G.M.C., Masala, N., Bastiaansen, J.A.M, Bustin, A., Yerly, J., Heerfordt, J., Piccini, D., Stuber, M., & Roy, C.W. (2020). Focused navigation (fNAV) for cardiac and respiratory motion-compensated free-running 3D whole-heart coronary MRA. *Proc. Intl. Soc. Mag. Reson. Med.* 29 0188 (2021)., [4] Roy, C. W., Heerfordt, J., Piccini, D., Rossi, G., Pavon, A. G., Schwitter, J., & Stuber, M. (2021). Motion compensated whole-heart coronary cardiovascular magnetic resonance angiography using focused navigation (fNAV). *Journal of Cardiovascular Magnetic Resonance*, 23(1), 1-17., [3] Masala, N., Bastiaansen, J. A., Di Sopra, L., Roy, C. W., Piccini, D., Yerly, J., ... & Stuber, M. (2020). Free-running 5D coronary MR angiography at 1.5 T using LIBRE water excitation pulses. *Magnetic resonance in medicine*, 84(3), 1470-1485., [2] Coppo, S., Piccini, D., Bonanno, G., Chaptinel, J., Vincenti, G., Feliciano, H., & Stuber, M. (2015). Free-running 4D whole-heart self-navigated golden angle MRI: initial results. *Magnetic resonance in medicine*, 74(5), 1306-1316., [1] Di Sopra, L., Piccini, D., Coppo, S., Stuber, M., & Yerly, J. (2019). An automated approach to fully self-navigated free-running cardiac and respiratory motion-resolved 5D whole-heart MRI. *Magnetic resonance in medicine*, 82(6), 2118-2132.

Speaker: G. Rossi

Category: 3D, Motion Correction, Coronary Angiography



**000148**

## **Extensive myopericarditis post-mRNA COVID-19 vaccine**

Y. Kim \* (1); S. Clifford (2); S. Huber (2)

(1) Department of cardiology, Yale New Haven Hospital, New Haven, United States of America; (2) Department of radiology, Yale New Haven Hospital, New Haven, United States of America

### **Abstract**

#### **Description of Clinical Presentation:**

30 year-old man with no prior medical history developed chest pain four days following the second dose of the coronavirus disease 2019 (COVID-19) mRNA-1273 ModernaTX vaccine. He had no prior COVID-19 infection. He presented to the emergency room with gradually worsening substernal chest pain, associated with headache and nausea that started during a 5-hour flight. Vital signs and physical exam were unremarkable with no muffled heart sounds or friction rub noted. Labs were notable for troponin I elevated to 12.65 ng/ml (reference 0-0.08 ng/ml), troponin T 1.38 ng/ml (reference <0.01ng/ml), and D-dimer of 0.33 mg/L (<0.5mg/L). The rest of his labs were unremarkable. COVID-2 RNA assay was negative. ECG showed normal sinus rhythm with diffuse ST elevations.

#### **Diagnostic Techniques and Findings:**

Given patient's young age and clinical presentation of chest pain, transthoracic echocardiogram was performed. It showed normal bi-ventricular function, left ventricular ejection fraction of 67% and normal wall motion. There was no pericardial effusion. Chest radiograph was unremarkable. Decision was made to proceed with cardiac MRI (cMRI) given ECG changes and prior reports of myocarditis in patients post vaccination. Standard cMRI was performed on Siemens 1.5T Avanto scanner including cine steady-state free precession, T2 fat saturated black blood and late gadolinium enhancement (LGE) imaging. Patient received 0.2 mmol/kg of intravenous gadolinium (gadoterate meglumine). cMRI showed normal systolic function without regional wall motion abnormalities. There was no pericardial effusion. On T2 images there was diffuse edema involving almost the entire myocardium (Figure 1, 2). The T2 skeletal muscle to myocardium single intensity ratio ranged from 2.5-2.8. There was diffuse patchy LGE involving multiple areas of the myocardium and pericardium but with relative sparing of the basal septum (Figure 1,2). The findings support acute myocarditis diagnosis according to the 2018 updated Lake Louise criteria.

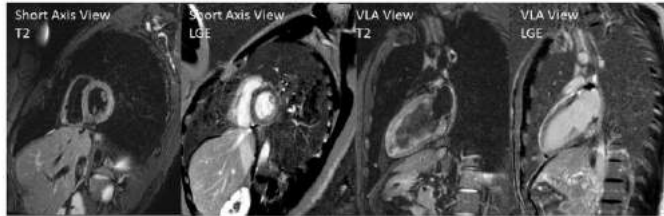
#### **Learning Points from this Case:**

Myocarditis in patients who were recently vaccinated with mRNA COVID-19 is rare with only 1,226 cases reported from December 2020 to June 2021, however recognizing clinical presentation is important for management and treatment plan. Cardiac MRI is a powerful tool to help clinicians diagnose post vaccine myocarditis and reduce utilization of other diagnostic tools. Presence of T2 signal with associated LGE in the myocardium and pericardium is diagnostic of myopericarditis in the correct clinical context. In this patient, cMRI was able to rapidly identify myocarditis as the etiology of patient's chest pain and evaluate the extent of the myocardial involvement. Such rapid diagnosis also limits unnecessary testing for other etiologies such as ischemic and thromboembolic. After patient was initiated on treatment with

NSAIDs and colchicine, his chest pain resolved within 48 hours. He was counseled on physical exertion limitations and will be followed with outpatient cMRI in 4 weeks.

### Figure/Table 1

Figure 1: Short axis and VLA views: T2 and LGE

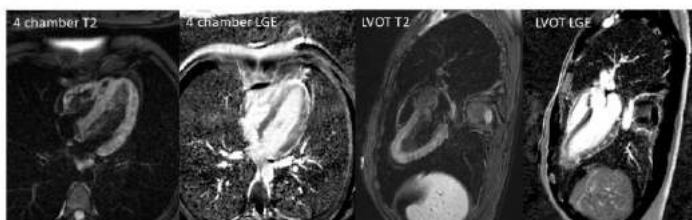


### Caption 1

T2 images show diffuse edema involving almost the entire myocardium. Post-contrast images with diffuse patchy late gadolinium enhancement (LGE) of almost the entire myocardium and pericardium with relative sparing of the basal septum.

### Figure/Table 2

Figure 2: 4 chamber and LVOT views: T2 and LGE



### Caption 2

T2 images show diffuse edema involving almost the entire myocardium. Post-contrast images with diffuse patchy late gadolinium enhancement (LGE) of almost the entire myocardium and pericardium with relative sparing of the basal septum.

### **Bibliographic References**

4. Diaz GA, Parsons GT, Gering SK, et al. Myocarditis and Pericarditis after vaccination for COVID-19. JAMA. 2021. , 3. Shaw KE, Cavalcante JL, Han BK, Goss M. Possible Association Between COVID-19 Vaccine and myocarditis. JACC Cardiovascular Imaging. 2021, 14(9): 1856–1861., 2. Starekova J, Bluemke DA, Bradham WS, Grist TM, S ML, Reeder SB. Myocarditis Associated with mRNA COVID-19 Vaccination. RSNA. 2021. Accessed on September 18, 2021. <https://doi.org/10.1148/radiol.2021211430>., 1.

Center for Disease Control. United States of America Department of Health and Human Services COVID-19 Vaccine Safety Technical (VaST) Work Group Report, June 28, 2021. Accessed on September 18, 2021. <https://www.cdc.gov/vaccines/acip/work-groups-vast/report-2021-06-28.html>

Speaker: Y. Kim

Category: Myocarditis, Pericardial Disease, Late Gadolinium Enhancement



000149

## The predictive value of the heart rate response to breathing maneuvers for inducible myocardial perfusion deficits

M. Khaki \* (1); M. Benovoy (2); J. Luu (1); E. Hillier (3); M. Sami (1); M. Friedrich (4)

(1) Faculty of medicine and health sciences, McGill University, Montreal, Canada; (2) Cardiac imaging, Circle Cardiovascular Imaging, Calgary, Canada; (3) Faculty of medicine and health sciences, McGill University Health Centre Glen Site (MUHC), Decarie Boulevard, Montreal, Canada; (4) Departments of medicine and diagnostic radiology, McGill University Health Centre (MUHC), Montreal, Canada

### Abstract

#### Background:

Simple breathing maneuvers with hyperventilation (HV) and breath-holds (BH), coupled with Oxygenation-Sensitive Cardiovascular Magnetic Resonance (OS-CMR) imaging have been shown to reflect coronary vascular function. A retrospective study of heart rate (HR) response to HV in OS-CMR showed that the blunted HR increase in response to HV may allow for identifying patients with coronary artery disease (CAD). Our study aims to define an optimal threshold for HR response to the breathing maneuvers that can be used to rule out myocardial ischemia in patients with suspected CAD.

#### Methods

We assessed 61 patients with suspected CAD (age  $\geq 35$  years) and 14 healthy volunteers. Using a pulse sensor (EKG-Flex/Pro sensor-SA9306M, Thought Technology Ltd.; Montreal, Canada), beat-to-beat HR was recorded while performing a 4-min breathing maneuver that included 2 minutes of normal breathing (NB), followed by 1 min of deep HV at a pace of 30 breaths/min, and a subsequent maximal voluntary BH. On the same day, patients underwent clinically indicated adenosine first-pass myocardial perfusion imaging. A significant inducible perfusion deficit as clinically reported served as the reference. We analyzed raw HR data using a MATLAB-based automated analysis tool. We calculated heart rate recovery during the breath-hold (HRR-BH) defined as the percentage of HR recovery during BH relative to peak HR during HV ( $(\text{Peak HR-HV} - \text{Min HR-BH} / \text{Peak HR-HV}) * 100$ ).

#### Results

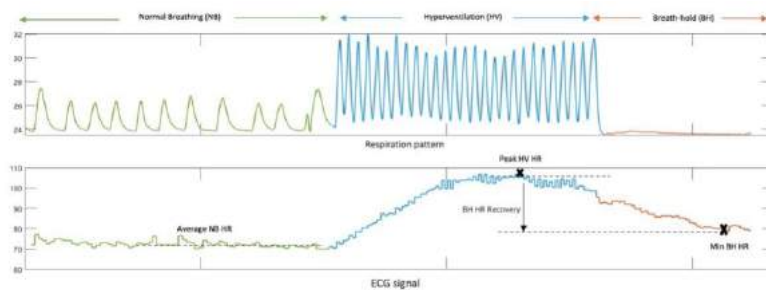
After excluding 8 patients and 1 control due to incomplete CMR scans or uninterpretable pulse tracings, 53 patients and 13 controls were included in the analysis. A diagnosis of myocardial ischemia was made in 43 patients (58% male;  $64 \pm 10$  years). Patients with ischemia had a significantly smaller response (HRR-BH;  $13.9 \pm 6.8$ ) than the control group ( $30.1 \pm 8.8$ ;  $p < .0001$ ) and the non-ischemic group ( $21.7 \pm 10.7$ ;  $p = 0.02$ ) (Figure 2A). Men had a higher HRR-BH in both control and non-ischemic groups, while women in the ischemic group had a greater HRR-BH (Fig. 2B). Overall, age showed an inverse correlation with HRR-BH in patients ( $r = -0.42$ ;  $p = 0.0003$ ), which was not the case in healthy controls ( $r = 0.11$ ,  $p = 0.73$ ) (Fig. 2C). As HRR-BH was not significantly different between control and non-ischemic groups, we combined them into a single group for identifying the appropriate cut-

off. The area under the ROC curve for HRR-BH was 0.85 (95%; CI 0.74-0.95) (Fig. 3). The best overall discrimination ability for HRR-BH was achieved with a cut-off of  $\geq 26\%$  recovery from baseline, which had a sensitivity of 95.3%, specificity of 52.1%, a negative predictive value (NPV) of 85.7%, and a positive predictive value (PPV) of 78.8%, independently of relevant clinical information.

## Conclusion

HR recovery following a simple vasoactive breathing maneuver demonstrated a high negative predictive value in predicting inducible myocardial perfusion deficits and therefore could serve as an efficient pre-imaging screening tool or as a complementary marker in combination with stress perfusion or breathing-enhanced CMR protocols. A larger prospective study is warranted.

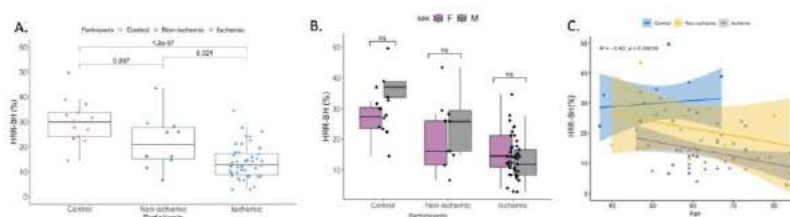
**Figure/Table 1**



**Caption 1**

The respiration pattern and the corresponding HR response in a healthy control.

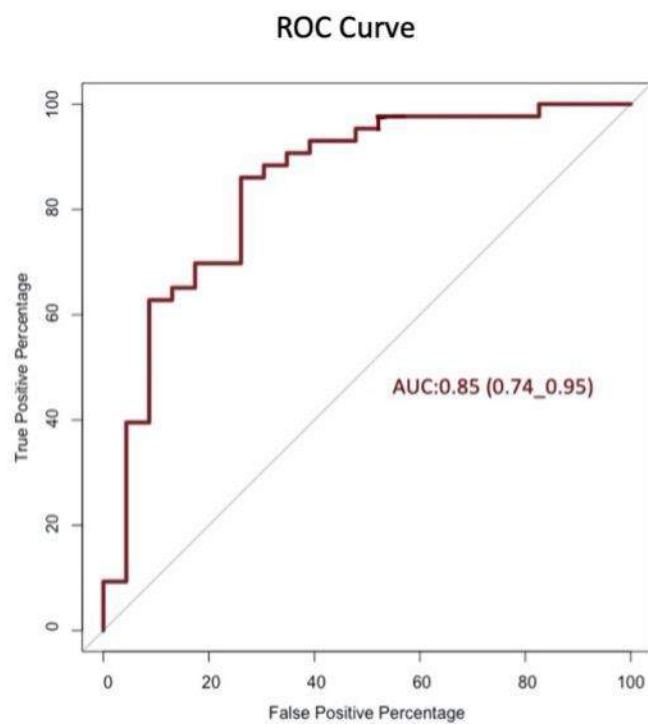
**Figure/Table 2**



**Caption 2**

**A.** The comparison of the breath-hold heart rate recovery (HRR-BH) between three groups using one-way ANOVA with Post Hoc test. **B.** The relationship between age and HRR-BH, overall ( $r=-0.42$ ) and at the group-level (the ribbon around the fitted lines indicates 95% CI). **C.** The comparison of the HRR-BH as a function of sex. ns: non-significant.

**Figure 3**



**Caption 3**

Relative Operating Characteristic (ROC) representing the diagnostic performance of the HRR-BH.

Speaker: M. Khaki

Category: coronary Artery Disease, First-Pass Perfusion, ECG

000151

## Non-Linear Accelerator of Event Prediction

R. Biederman \* (1); M. Doyle, (1); G. Rayarao (1); N. Hussain, (1)

(1) Cardiac mri, Allegheny Health Network, Pittsburgh, United States of America

### Abstract

#### Background:

In patients with pulmonary arterial hypertension, prediction of adverse events (AE) is hampered by the wide variety of conditions that can precipitate AEs. Consider that both elevation and lowering of pulmonary arterial pressures are associated with disease progression and similarly there is wide dispersion of left and right ventricular functional conditions that lead to AEs. Thus, given the dissociation of linear progression of physiology with initiation of an AE, we sought to identify inherently non-linear cardiovascular properties to predict AEs. Previously we introduced measures of left and right heart impedance, which vary in a saw-tooth manner with ejection fraction, making them ideal candidates to predict AE's due to their non-linear variation with linear progression of EF.

#### Methods:

Patients (n=41) with pulmonary artery hypertension underwent a CMR protocol to assess left and right ventricular function from a set of parallel short-axis cine images and a set of long-axis images, with MPA and aorta flow assessed using phase velocity mapping. These data were used to measure the left and right ejection fraction and left and right impedance. Data were obtained in the baseline and returning patients (n=35, 85%) yielding 76 unique data sets. Adverse events considered were: myocardial infarction, angina, hypotension, atrial fibrillation and orthostatic syncope, with 12 (29%) patients suffering at least one AE. Binary logistic models were constructed to identify predictors of AE ( $p < 0.05$  for variable inclusion) and receiver operator curves were derived for each model.

#### Results:

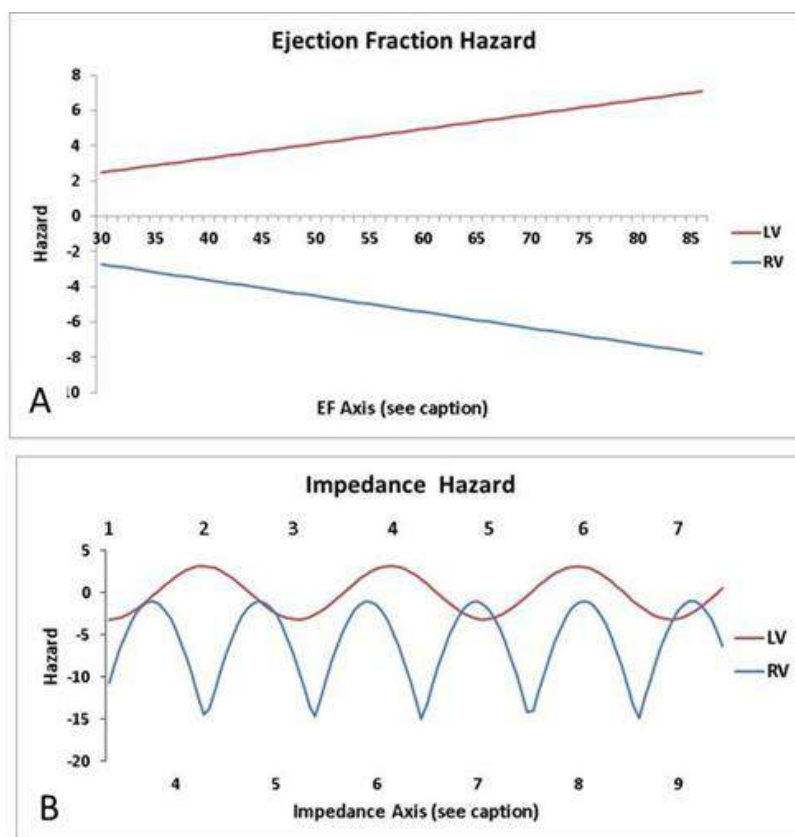
The left and right ejection fractions model showed that as the left ventricular EF linearly increased, hazard increased, while as right ventricular EF linearly increased, hazard decreased, Figure 1A. In contrast the left and right impedance model show that hazard changes in a sinusoidal manner for left and right impedance values, Figure 1B. The corresponding receiver operator curves are shown in Figures 2A and 2B, respectively. When medication was entered into the model (Letairis and Treprostinil in this case), the area under the ROC curves increased (Figures 3A and 3B). The impedance and medicine model generated a sensitivity of 92% with a specificity of 88%, while the ejection fraction and medicine model generated a sensitivity of 92% with a specificity of 59%.

#### Conclusions:

In patients with pulmonary artery hypertension, variables that linearly relate to outcomes, such as ejection fraction, only weakly account for the observed adverse events. When

employing the CMR-measured impedance, which varies in a sinusoidal manner with events, the prediction of adverse events improved, allowing prediction with high sensitivity and specificity. This novel impedance index may shed light on thitherto hidden cardiac physiology.

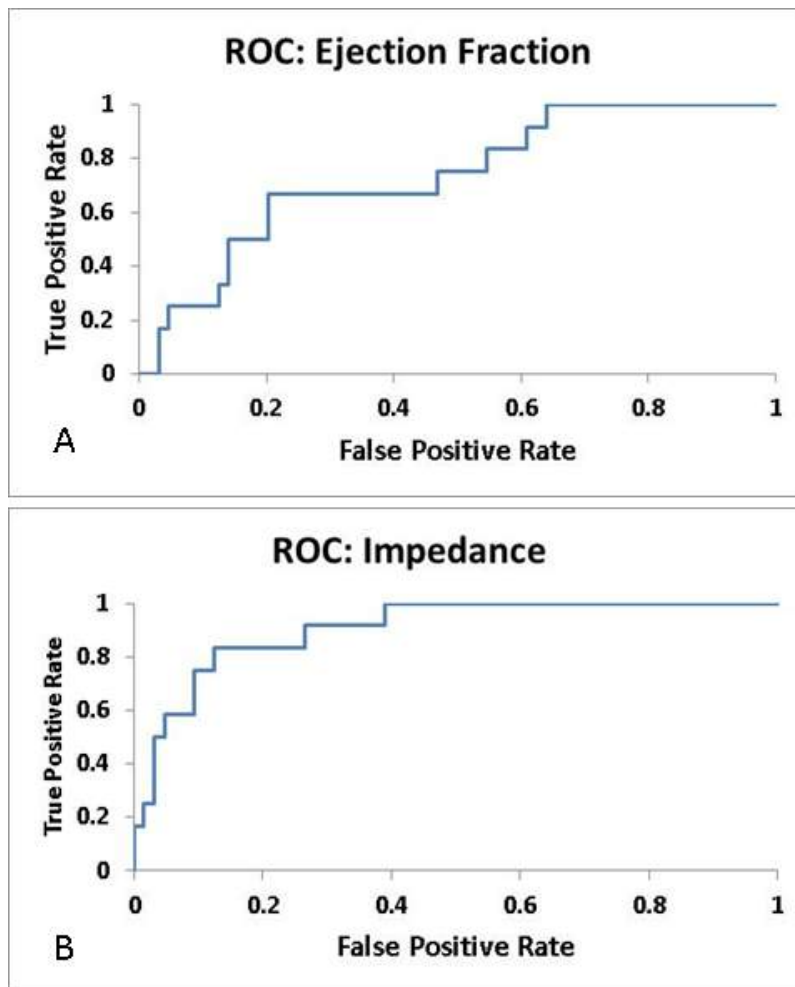
**Figure/Table 1**



**Caption 1**

Figure 1: A) Hazard Components due to left (red) and right (blue) ejection fraction. The X axis is the left and right ejection fraction. B) Components of hazard due to left (red) and right (blue) impedance values. The left impedance cycle is plotted along the lower X axis and the right impedance cycle is plotted along the upper X axis.

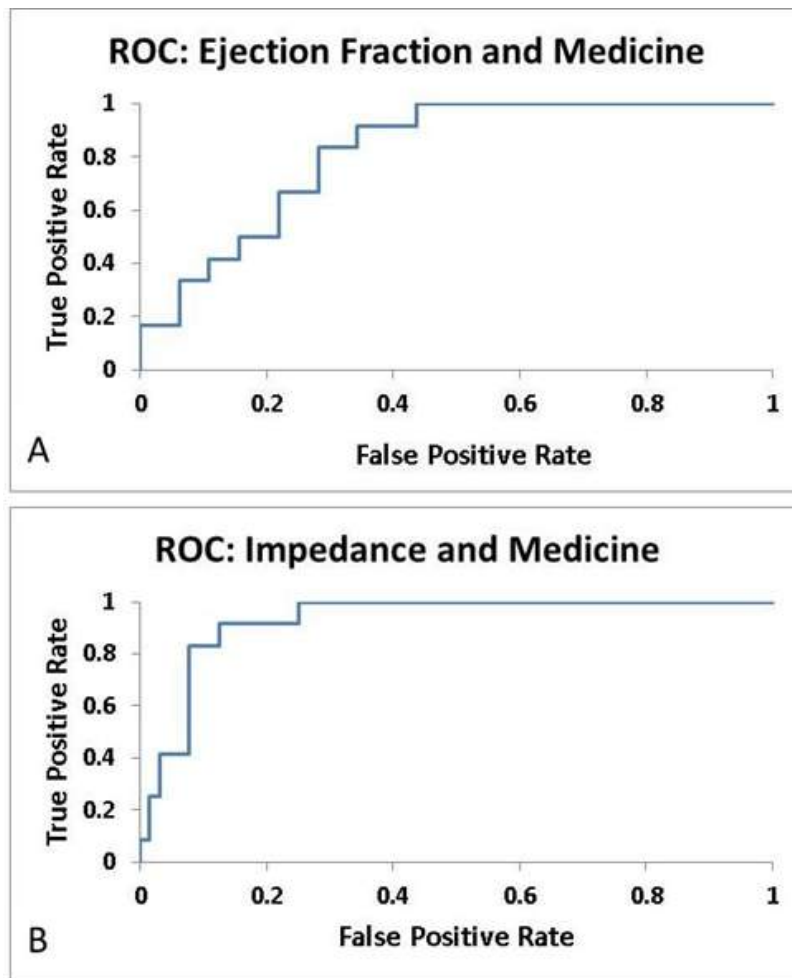
**Figure/Table 2**



## Caption 2

Figure 2: A) the receiver operator curve for the ejection fraction model is plotted AUC =0.73 (95% CI, 0.6 0.87) and B) the receiver operator curve for the impedance model is plotted AUC =0.91 (95% CI, 0.84 0.98).

## Figure 3



### Caption 3

Figure 3: A) the receiver operator curve for the ejection fraction and medication model is plotted AUC =0.82 (95% CI, 0.71 0.93) and B) the receiver operator curve for the impedance model and medication is plotted AUC =0.93 (95% CI, 0.87 0.99).

Speaker: R. Biederman

Category: Pulmonary Hypertension, Flow, Aorta

000152

## **Impact of Adverse Geometric and Tissue Remodeling on Myocardial Strain among patients with Friedreich's Ataxia – Multiparametric Assessment via Cardiac Magnetic Resonance**

M. E. Janjua \* (1); K. Tak, (2); R. Meier, (2); J. Kim, (2); S. Hyde (3); H. Bowe (3); N. Hasan (3); A. Ruda (3); O. E. Pagovich (3); R. G. Crystal, (3); J. Weinsaft (2)

(1) Medicine, Medbay (Weill Cornell Medicine - Qatar), Doha, Qatar; (2) Medicine, Weill Cornell Medicine, New York, United States of America; (3) Genetic medicine, Weill Cornell Medicine, New York, United States of America

### **Abstract**

**Introduction:** Cardiac magnetic resonance (CMR) is used to widely screen for cardiomyopathy - which is a leading cause of death in Friedreich's Ataxia (FA). CMR feature tracking (strain) provides added insight into left ventricular (LV) function: Impact of adverse geometric and tissue remodeling on myocardial strain in FA cardiomyopathy is unknown.

**Methods:** The population comprised FA patients and age/gender controls (matched 1:2 to FA patients) who underwent CMR (1.5T) via a prospective protocol that included cine-(SSFP) for LV structure/function, parametric T1 mapping for diffuse fibrosis, and late gadolinium enhancement (LGE) for focal fibrosis. Longitudinal LV, RV, and LA strain were measured in long (4 chamber) and circumferential/radial strain (basal, mid, apical LV) in LV short axis. Strain was compared between FA and controls, as well as between FA patients with and without adverse tissue remodeling based on focal fibrosis on LV-CMR.

**Results:** 45 subjects (30 FA, 15 controls) prospectively underwent CMR. FA patients had more advanced LV remodeling as evidenced by greater LV mass ( $p=0.006$ ), despite smaller chamber size ( $p<0.001$ ). Despite equivalent systolic function based on EF, global longitudinal strain (GLS) and time to peak strain (TTP) were lower with FA (both  $p<0.05$ ) paralleled by a trend towards decreased global radial strain (GRS): LV mass inversely correlated with GLS ( $r=-0.587$ ,  $p<0.001$ ) and GRS ( $r=-0.418$ ;  $p=0.004$  [**Figure**]). LA strain and strain rate were near 2-fold lower in FA patients vs. controls (both  $p<0.001$ ), paralleled by correlation between LV mass and LA strain ( $r=-0.485$ ,  $p<0.001$ ). Among FA patients, 27% ( $n=8$ ) had focal LGE ( $2.02 \pm 1.60\%$  LV myocardium), among whom LV mass was higher ( $p=0.01$ ), and post contrast T1 tended to be lower ( $p=0.08$ ) vs. patients without LGE (**Table**). All LV strain indices were lower in patients with LGE (all  $p\leq 0.01$ ): As in the overall cohort, subgroup analysis in FA patients showed impaired LV radial ( $r=-0.506$ ), and LV ( $r=-0.612$ ) and LA longitudinal ( $r=-0.502$ ) strain correlated with adverse LV remodeling quantified based on LV mass (all  $p<0.01$ ).



**Conclusion:** Among FA patients, adverse LV structural and tissue-based remodeling on CMR is associated with impaired myocardial strain. Magnitude of strain impairment is increased with LGE-CMR evidenced myocardial fibrosis and correlates with LV mass, suggesting CMR strain as a marker of high-risk FA phenotype.

**Figure/Table 1**

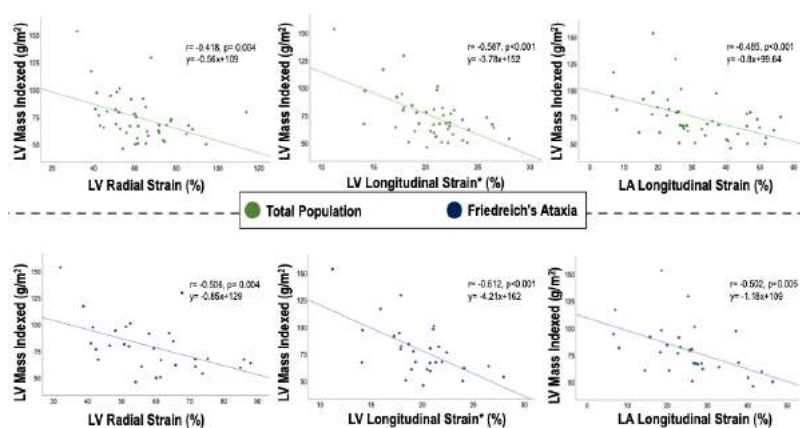
	Overall (n=30)	Fibrosis (LGE) - (n=22)	Fibrosis (LGE) + (n=8)	p
<b>Population Characteristics</b>				
Age	25 ± 4	25 ± 4	24 ± 3	0.67
Heart Rate	77 ± 14	79 ± 13	73 ± 19	0.36
Male Gender (%)	47	41	63	0.31
Total # of repeats	1613 ± 323	1562 ± 300	1754 ± 363	0.15
<b>CMR</b>				
<i>LV Structure and Function</i>				
LV Myocardial Mass (g/m <sup>2</sup> )	79 ± 24	73 ± 20	97 ± 27	<b>0.01</b>
LV End Diastolic Volume (mL/m <sup>2</sup> )	65 ± 13	64 ± 11	65 ± 18	0.91
LV End Systolic Volume (mL/m <sup>2</sup> )	24 ± 14	23 ± 14	30 ± 12	0.22
LV Ejection Fraction (%)	64 ± 10	68 ± 5	54 ± 12	<b>0.01</b>
<i>LV Parametric T1 Mapping</i>				
Native Myocardial T1	985.86 ± 69.72	988.06 ± 53.71	978.93 ± 111.86	0.77
Post Contrast Myocardial T1	403.46 ± 73.50	416.98 ± 67.11	360.99 ± 81.69	0.08
Extracellular Volume Fraction	0.27 ± 0.05	0.27 ± 0.05	0.30 ± 0.06	0.18
<i>LV Myocardial Strain</i>				
Global Longitudinal Strain	-19.70 ± 3.51	-20.78 ± 2.79	-16.74 ± 3.80	<b>0.003</b>
Longitudinal Strain Time to Peak	283.23 ± 36.03	277.55 ± 33.05	298.88 ± 41.48	0.16
Global Longitudinal Strain Rate	-0.07 ± 0.02	-0.08 ± 0.01	-0.06 ± 0.02	<b>0.002</b>
Global Radial Strain	58.81 ± 14.45	63.36 ± 13.04	46.32 ± 10.56	<b>0.003</b>
Global Radial Strain Rate	0.23 ± 0.07	0.26 ± 0.05	0.16 ± 0.04	<b>&lt;0.001</b>
Global Circumferential Strain	-29.32 ± 6.43	-31.15 ± 4.99	-24.27 ± 7.55	<b>0.007</b>
Global Circumferential Strain Rate	-0.12 ± 0.04	-0.13 ± 0.03	-0.08 ± 0.04	<b>0.003</b>
<i>LA Myocardial Strain</i>				
Global Longitudinal Strain	25.44 ± 10.25	27.48 ± 9.79	19.85 ± 9.96	0.07
Global Longitudinal Strain Rate	0.08 ± 0.04	0.09 ± 0.04	0.07 ± 0.04	0.14
<i>RV Myocardial Strain</i>				
Global Longitudinal Strain	-25.07 ± 5.23	-26.66 ± 4.48	-20.71 ± 4.82	<b>0.004</b>
Global Longitudinal Strain Rate	-0.09 ± 0.02	-0.09 ± 0.02	-0.09 ± 0.03	0.27
<i>RA Myocardial Strain</i>				
Global Longitudinal Strain	29.93 ± 9.07	32.25 ± 7.53	23.56 ± 10.38	<b>0.02</b>

Global Longitudinal Strain Rate	$0.10 \pm 0.03$	$0.11 \pm 0.03$	$0.08 \pm 0.04$	<b>0.048</b>
---------------------------------	-----------------	-----------------	-----------------	--------------

## Caption 1

Table. LV Strain and Chamber Remodeling Among Friedreich's Ataxia Patients with and without Fibrosis on Late Gadolinium Enhancement CMR

## Figure/Table 2



## Caption 2

Myocardial strain in relation to left ventricular mass. Correlation coefficients as quantified among the overall study population (top [Friedreich's Ataxia patients and age/gender matched controls]), and in analyses restricted to FA patients (bottom). Note that in both cohorts magnitude of impaired LV radial (left) and longitudinal (center) strain correlated with adverse LV geometric remodeling as quantified by myocardial mass, paralleling similar results in analyses relating LA strain to LV mass (right; all  $p < 0.01$ )

Speaker: M. E. Janjua

Category: Cardiomyopathy, Nonischemic Cardiomyopathy, Ventricular Remodeling

000153

## Deep Learning for fully automated 3D aortic segmentation of 4D flow MRI on type B aortic dissection

A. Maroun \* (1); H. Berhane (1); S. Chu (1); O. Kilinc (1); E. Weiss (1); J. Baraboo (1); M. Pradella (2); C. Mehta (3); C. Malaisrie (3); A. Hoel (4); M. Markl (1); B. Allen (1)

(1) Department of radiology, Northwestern University Feinberg School of Medicine, Chicago, United States of America; (2) Radiology, Northwestern University Feinberg School of Medicine, Chicago, United States of America; (3) Division of cardiac surgery, Northwestern University Feinberg School of Medicine, Chicago, United States of America; (4) Vascular surgery, Northwestern University Feinberg School of Medicine, Chicago, United States of America

### Abstract

**Background:** Type B aortic dissection (TBAD) is a life-threatening disease caused by a tear of the aortic intimal layer, with the subsequent formation of a true (TL) and a false lumen (FL). 4D flow MRI assessment of in vivo aortic hemodynamic parameters in the TL and FL has shown potential to improve risk-stratification. In fact, flow stasis and kinetic energy, can help identify patients at increased risk of aortic dilation [1,2]. However, evaluation of volumetric 4D-flow MRI aortic flow dynamics requires manual, cumbersome data analysis, including 3D TL and FL segmentation, limiting reproducibility and clinical translation. The purpose of this study was to evaluate the performance of an in-house deep learning-based segmentation tool, trained on non-dissected aortas, for a fully automated 3D TL and FL segmentation.

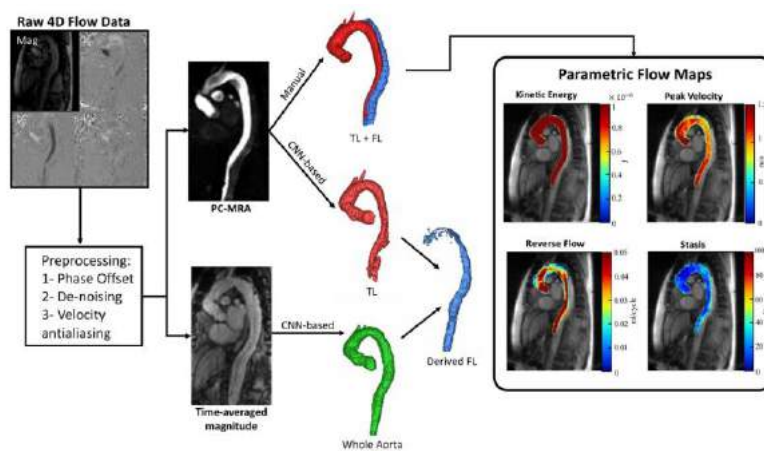
**Methods:** 25 patients with TBAD (age =  $56 \pm 12$  years; 16 male) who underwent standard-of-care aortic 4D flow MRI (sagittal-oblique 3D volume) were retrospectively included. 4D flow MRI data analysis includes preprocessing (eddy current correction, velocity antialiasing) and calculation of an aortic 3D Phase Contrast MR Angiogram (PC-MRA). Fully automated 3D aortic segmentation was based on a previously developed and tested convolutional neural network (CNN), trained on 4D flow derived PC-MRA data of 1018 non-dissection subjects [3]. No re-training on TBAD data was performed for this study. CNN-based automated 3D segmentations were generated using PC-MRA and time averaged 4D flow magnitude data (Fig.1). CNN-based segmentation was compared to manual PC-MRA-based 3D TL and FL segmentations performed by an observer with 1 year of experience and Dice scores were calculated to assess performance. After manual removal of aortic branches, voxelwise calculation of kinetic energy (KE), peak velocity, flow stasis, and reverse flow (RF) was carried out, and agreement was analyzed using Bland-Altman plots. To assess human vs machine performance, interobserver variability of manual analysis was assessed on a subset of 10 dissection patients.

**Results:** CNN demonstrated good performance for the TL with a median Dice score of 0.72 [0.57–0.83] and fair performance for the FL 0.45 [0.35-0.55], compared to 0.87 [0.84-0.91] and 0.81 [0.79-0.88] in the interobserver analysis (Fig.2). In 3 cases, severe TL narrowing caused an interruption of the TL automated segmentation. Other common errors include FL incorporation into the automated TL segmentation due to high FL flow values on PC-MRA images. For hemodynamic parameters, significant bias was only observed for FL RF in the CNN-based segmentation ( $p=0.02$ ). For the TL, CNN-based segmentation showed moderate

agreement for peak velocity and KE with limits of agreement (LOA) of 29% and 38%, respectively, compared to 11% and 17% in the interobserver analysis (Fig.3). For the FL, CNN-based segmentation demonstrated fair agreement for flow stasis and RF with LOA of 35% and 56%, respectively, whereas KE and peak velocity had a LOA of 177% and 99%. FL interobserver analysis yielded lower LOAs for the 4 parameters (9-33%).

**Conclusions:** CNN-based aortic segmentation showed promising results for TBAD segmentation and reasonable agreement for relevant flow parameters, considering that no-retraining was performed. It is notable that the results were substantially affected by 3 outliers, attesting that the study was limited by a small sample size. Future work should focus on re-training the CNN on TBAD data and incorporating manual tools for fast and accurate corrections.

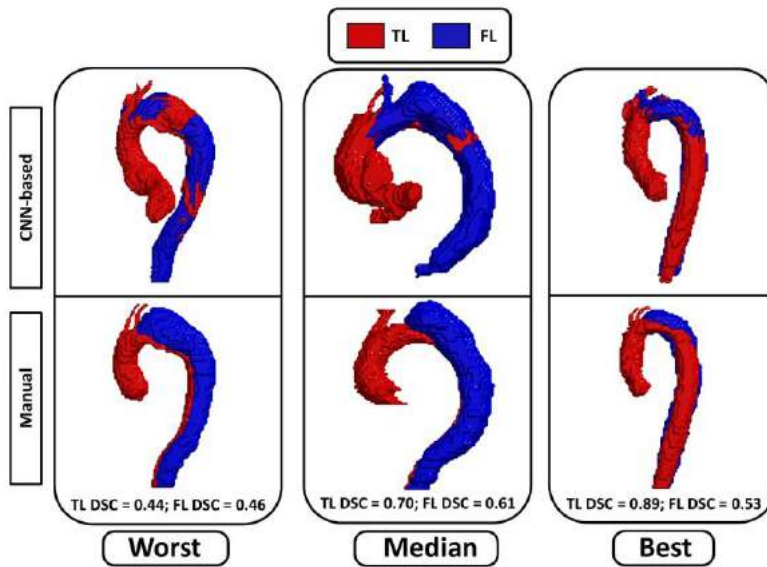
**Figure/Table 1**



**Caption 1**

Figure 1. 4D flow MRI analysis workflow. Generated PC-MRA images were used to perform a full manual 3D segmentation and a CNN-based TL segmentation, whereas CNN-based whole aorta segmentation was depicted by time-averaged magnitude images. FL 3D segmentation was subsequently deduced by subtracting the TL from the whole aorta.

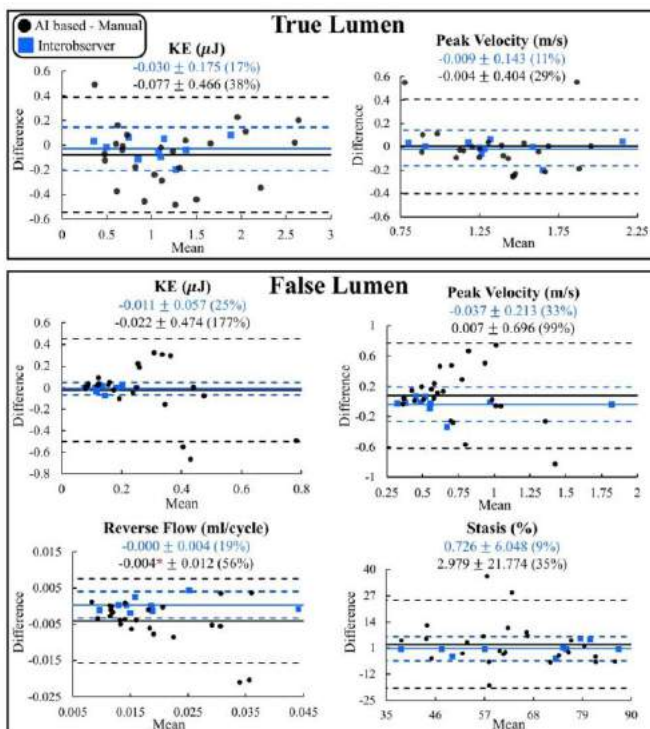
**Figure/Table 2**



**Caption 2**

Figure 2. Representative 3D segmentations for dissection patients with the worst, median, and best Dice scores (DSC) for AI based (top) compared to manual (bottom) 3D segmentation. In each panel, the TL 3D segmentation is shown in red, and the FL 3D segmentation is shown in blue.

**Figure 3**



### Caption 3

Figure 3. Interobserver variability and CNN-based vs. manual segmentation Bland Altman plots. Bias  $\pm$  LOA are shown in blue for the interobserver analysis, and black for the CNN-based vs. manual analysis (\* indicates  $p < 0.05$ ). Percent difference was defined as the LOA divided by the mean of the reference manual segmentation.

### Bibliographic References

2. Zilber ZA, Boddu A, Malaisrie SC, Hoel AW, Mehta CK, Vassallo P, Burris NS, Roldán-Alzate A, Collins JD, François CJ, Allen BD. Noninvasive Morphologic and Hemodynamic Evaluation of Type B Aortic Dissection: State of the Art and Future Perspectives. *Radiol Cardiothorac Imaging*. 2021 Jun 24;3(3):e200456. doi: 10.1148/ryct.2021200456. PMID: 34235440; PMCID: PMC8250421., 3. Berhane H, Scott M, Elbaz M, Jarvis K, McCarthy P, Carr J, Malaisrie C, Avery R, Barker AJ, Robinson JD, Rigsby CK, Markl M. Fully automated 3D aortic segmentation of 4D flow MRI for hemodynamic analysis using deep learning. *Magn Reson Med*. 2020 Oct;84(4):2204-2218. doi: 10.1002/mrm.28257. Epub 2020 Mar 13. PMID: 32167203; PMCID: PMC7724647., 1. Jarvis K, Pruijssen JT, Son AY, Allen BD, Soulat G, Vali A, Barker AJ, Hoel AW, Eskandari MK, Malaisrie SC, Carr JC, Collins JD, Markl M. Parametric Hemodynamic 4D Flow MRI Maps for the Characterization of Chronic Thoracic Descending Aortic Dissection. *J Magn Reson Imaging*. 2020 May;51(5):1357-1368. doi: 10.1002/jmri.26986. Epub 2019 Nov 12. PMID: 31714648; PMCID: PMC7166194.

Speaker: A. Maroun

Category: 4D Flow, Aortic Dissection, Segmentation

000154

## Mapping Hypertrophy: T1 to the Rescue

J. P. Mazur, (1); K. M. Mikrut, \* (1); K. M. Zareba, (1)

(1) Division of cardiovascular medicine, The Ohio State University Wexner Medical Center, Columbus, United States of America

### Abstract

#### Description of clinical presentation:

A 62-year-old male with history of polysubstance abuse presented with lower extremity edema and shoulder pain. He was found to have acute kidney injury (creatinine 1.73 mg/dL) and hyperkalemia (K 6.0 mmol/L). His admission electrocardiogram (EKG) revealed sinus bradycardia at 42 bpm with premature atrial contractions and a right bundle-branch block. During the admission the patient had sinus pauses up to 4 seconds with heart rate down to 28 bpm. The patient felt fatigued, but denied history of syncope. He had a mild troponin elevation (peak high sensitivity troponin 71ng/L, normal < 52 ng/L).

#### Diagnostic techniques and their most important findings:

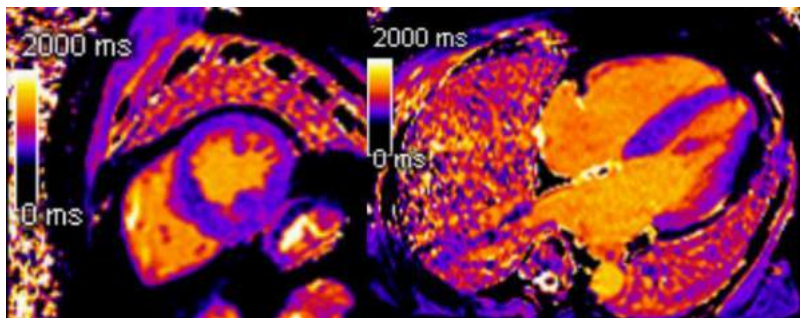
Transthoracic echocardiography demonstrated left ventricular hypertrophy (LVH) up to 1.6 cm in the septum, preserved left ventricular ejection fraction with no wall motion abnormalities. Exercise stress test demonstrated an inadequate chronotropic response and non-specific ST-T wave changes at peak exercise. The patient denied a history of hypertension and remained normotensive throughout admission. CMR was performed on a 1.5 T scanner to evaluate the LVH and demonstrated preserved biventricular function with severe LVH up to 2.0 cm in the septum. Myocardial native T1 signal was significantly decreased at 879 ms in the septum with a normal septal extracellular volume fraction (ECV) of 25% (normal local values: native myocardial T1 920 - 1084 ms; ECV <31%) (Figure 1). The lateral wall native myocardial T1 was 1031 ms and ECV was 37% at the site of significant fibrosis. Significantly elevated T2 signal was noted in the basal lateral wall (T2 of 60 ms, normal <51 ms) and to a lesser extent the septum (Figure 2). LGE imaging demonstrated dense areas of midwall fibrosis in the basal septal and lateral walls (Figure 3). T2\* mapping did not demonstrate cardiac iron overload (41 ms, normal <20 ms). Together these findings were highly suspicious for Anderson-Fabry Disease (AFD). Patient's alpha-galactosidase A level was severely decreased at 0.001 U/L (normal 0.074 - 0.457 U/L). The patient was discharged prior to genetic testing. He has not returned for scheduled follow up.

#### Learning points from this case:

AFD is a rare entity but should be considered in patients with LVH. CMR is very useful in patients with AFD as it can define LVH patterns, the extent of fibrosis, and demonstrate evolution of disease. Multiple stages of cardiac AFD are hypothesized: 1) the initial accumulation phase characterized by normal to reduced myocardial T1 values without LVH; followed by 2) the inflammation and myocyte hypertrophy phase with low native T1, normal ECV, LGE with or without LVH, and inflammation demonstrated by elevated myocardial T2 and troponin values; and finally 3) the fibrosis and impairment phase with pseudonormalization of native T1 and extensive LGE. In our patient the interventricular septum demonstrated low native T1 values, normal ECV with the presence of LGE which

corresponds to the inflammation and hypertrophy phase of AFD. In the lateral wall dense LGE, pseudonormalized T1 with high ECV were noted which corresponds to the fibrosis and impairment phase. Multiple stages of disease progression were noted in our patient, the most advanced in the lateral wall as commonly observed in AFD. Myocardial edema/inflammation was noted in both the earlier and later phases in this patient consistent with the belief that AFD causes a chronic inflammatory state in the myocardium.

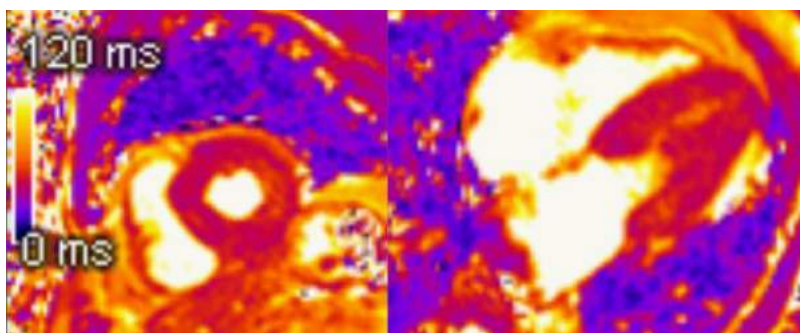
**Figure/Table 1**



**Caption 1**

Significantly depressed myocardial native T1 signal in the septum on short axis and horizontal long axis imaging as compared to the basal lateral wall.

**Figure/Table 2**

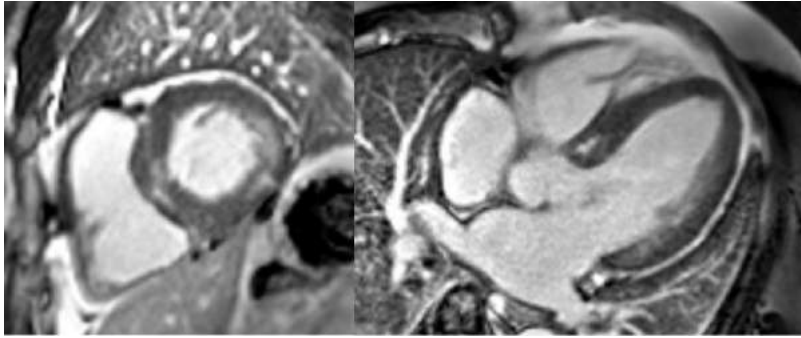


**Caption 2**

Evidence of myocardial edema / inflammation on T2 mapping, particularly in the basal lateral wall.

**Figure 3**





### **Caption 3**

Prominent dense midwall myocardial fibrosis in the lateral and septal walls on phase sensitive inversion recovery late gadolinium enhancement imaging.

Speaker: K. M. Mikrut,

Category: Anderson Fabry, Mapping Techniques, Cardiomyopathy

**000156**

## **Ventricular hemodynamic forces are altered in patients with precapillary pulmonary hypertension**

K. Pola \* (1); E. Bergström (1); J. Töger (1); G. Rådegran, (2); P. Arvidsson (1); M. Carlsson (1); H. Arheden (1); E. Ostenfeld (1)

(1) Clinical physiology, department of clinical sciences lund, Lund University, Skåne University Hospital, Lund, Sweden; (2) Cardiology, department of clinical sciences lund, section of heart failure and valvular disease, Lund University, Skåne University Hospital, Lund, Sweden

### **Abstract**

#### **Background**

Precapillary pulmonary hypertension (PHprecap) is a vascular condition with elevated pulmonary vascular pressure and resistance (1), which influence both morphology and function of the heart as well as outcome. Patients with PHprecap are often diagnosed at a late stage and may rapidly deteriorate. To improve outcome, new means of monitoring early treatment effect or deterioration would be of great value. Hemodynamic forces (HDF) computed from cardiac magnetic resonance imaging (CMR) and 4D flow have the potential to be used as an early marker of cardiac dysfunction (2,3). However, it is currently unknown whether HDF can reflect the ventricular functional performance in PHprecap. Therefore, the aim of this study was to investigate whether HDF differ in the right (RV) and left ventricle (LV) in patients with PHprecap compared to healthy controls.

#### **Methods**

Patients with PHprecap (pulmonary arterial hypertension, n=12, and chronic thromboembolic pulmonary hypertension, n=5, total n=17) and age-matched controls (n=11) underwent CMR at 1.5T (MAGNETOM Aera, Siemens Healthcare, Erlangen, Germany) (Table 1). Biventricular HDF were computed over the cardiac cycle using a prototype 4D-flow sequence and the Navier-Stokes equations (4). HDF were then analyzed in three orthogonal directions for each ventricle (RV: apex-base, diaphragm-outflow tract, and septum-free wall; and LV: apex-base, inferior-anterior, and lateral wall-septum), using an analysis module implemented in Segment v2.2 R7052 (Medviso, Lund, Sweden) (Figure 1) (5). Measurements of HDF were calculated using root mean squares and indexed to stroke volume of each ventricle.

#### **Results**

Right ventricular HDF in the apex-base direction did not differ between the groups in systole but were larger in patients than controls in diastole (Table 1, Figure 2). RV HDF were larger in patients compared to controls in the diaphragm-outflow tract and septum-free wall directions, both in systole and diastole.

Left ventricular HDF (Table 1, Figure 2) were larger in patients than controls in the apex-base and inferior-anterior directions, both in systole and diastole, but did not differ in the lateral wall-septum direction.

## Conclusion

Patients with PHprecap have higher HDF both in the RV and LV. The larger forces in systole imply altered biventricular contraction in PHprecap, and the increased diastolic forces suggest a modified filling mechanism. The differences in forces between patients and controls cannot be explained by differences in intraventricular blood volume output, as forces were indexed to stroke volume. The potential for HDF in monitoring treatment effect and detecting early cardiac deterioration remains to be investigated.

## Acknowledgements

We thank Ning Jin at Siemens Medical Solutions USA Inc., Cleveland, Ohio, USA for providing the 4D flow sequence as a work-in-progress package. We also thank the SCAPIS study for allowing access to data to identify 7 healthy controls.

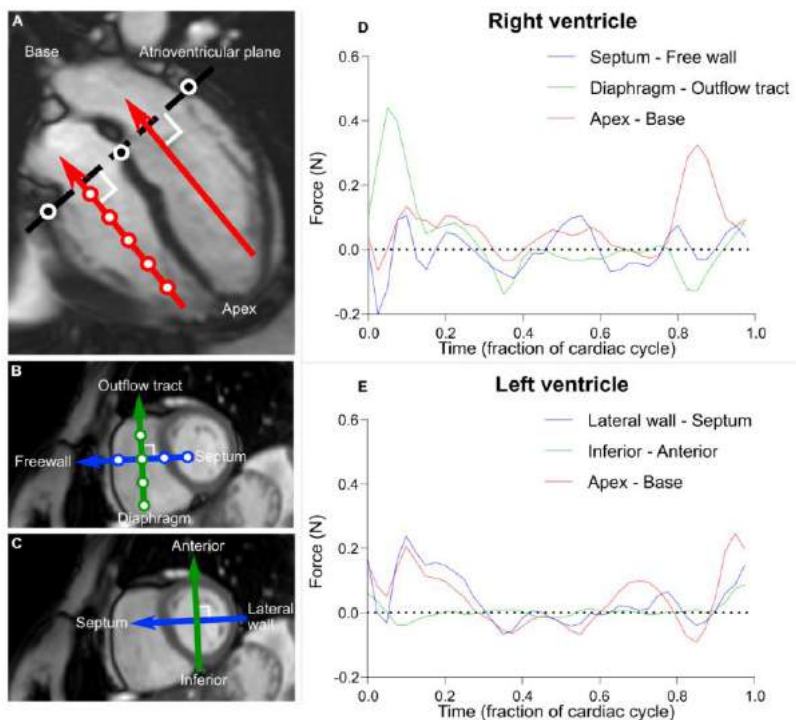
**Figure/Table 1**

	Patients	Controls	p-value
<b><u>Subject characteristics</u></b>			
N	17	11	-
- Pulmonary arterial hypertension	12	-	-
- Chronic thromboembolic pulmonary hypertension	5	-	-
Women; n, (%)	13 (76%)	6 (55%)	0.4
Age (years)	68 [16]	60 [19]	0.05
RV stroke volume (mL)	79 [34]	83 [27]	0.2
RV ejection fraction (%)	40 [21]	52 [5]	0.01
LV stroke volume (mL)	63 [21]	90 [24]	0.03
LV ejection fraction (%)	52 [10]	53 [7]	0.7
Mean pulmonary artery pressure (mmHg)	41 [20]	-	-
Pulmonary artery wedge pressure (mmHg)	8 [2]	-	-
Pulmonary vascular resistance (WU)	7 [6]	-	-
<b><u>Hemodynamic forces (N/L)</u></b>			
<b><i>Right ventricle</i></b>			
- Apex-Base, systole	1.0 [0.43]	1.1 [0.45]	0.6
- Apex-Base, diastole	1.4 [0.80]	0.89 [0.30]	0.0003
- Diaphragm-RVOT, systole	2.0 [0.77]	1.3 [0.51]	0.03
- Diaphragm-RVOT, diastole	0.73 [0.41]	0.40 [0.24]	0.009
- Septum-Free wall, systole	0.62 [0.39]	0.37 [0.25]	0.004
- Septum-Free wall, diastole	0.55 [0.39]	0.36 [0.12]	0.002
<b><i>Left ventricle</i></b>			
- Apex-base, systole	2.3 [1.0]	1.4 [0.36]	0.002
- Apex-base, diastole	1.6 [0.70]	1.1 [0.60]	0.03
- Inferior-Anterior, systole	0.66 [0.37]	0.40 [0.23]	0.01
- Inferior-Anterior, diastole	0.44 [0.25]	0.21 [0.070]	0.03
- Lateral wall-Septum, systole	1.8 [0.79]	1.4 [0.57]	0.07
- Lateral wall-Septum, diastole	0.53 [0.20]	0.37 [0.27]	0.08

Caption 1

**Table 1. Subject characteristics and hemodynamic forces.** Data is expressed as median and interquartile range [IQR] or absolute numbers and proportion in parentheses (%). LV, left ventricular; RV, right ventricular; RVOT, right ventricular outflow tract.

Figure/Table 2

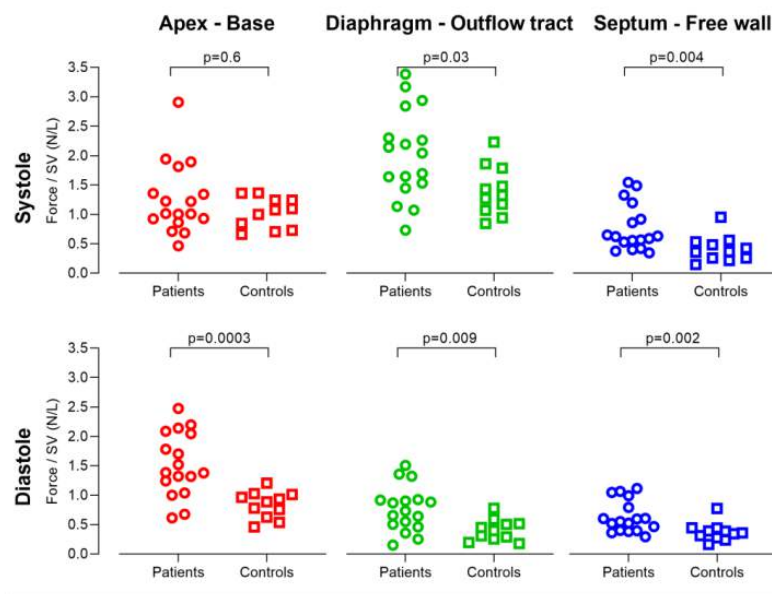


Caption 2

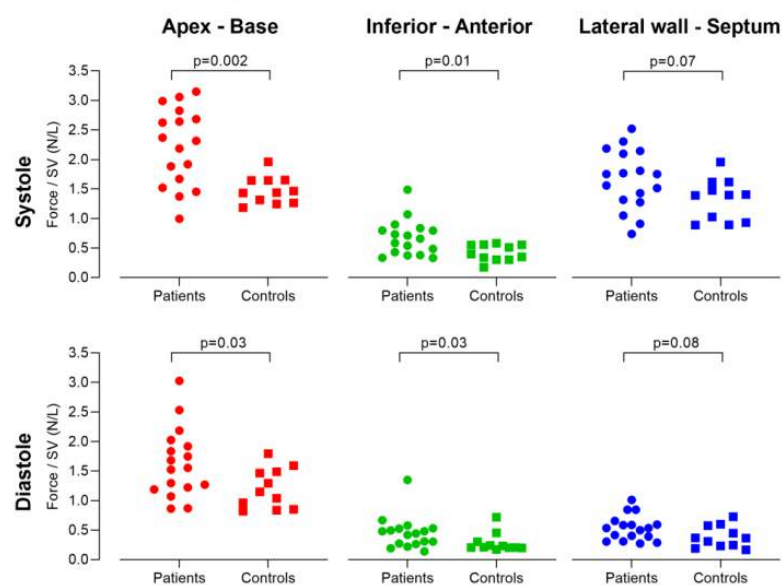
**Figure 1. Ventricular directions and example of hemodynamic force curves for one patient.** Left column: intraventricular directions in long-axis (A), short-axis right (B) and left (C) ventricular view. Right panel: hemodynamic force curves of the right (D) and left (E) ventricle.

Figure 3

### Right Ventricular Hemodynamic Forces



### Left Ventricular Hemodynamic Forces



### Caption 3

**Figure 2.** Hemodynamic forces indexed to stroke volume during systole and diastole in patients with PHprecap (circles) compared to healthy controls (squares). Intraventricular directions: apex-base (left column, red), diaphragm-outflow tract and inferior-anterior (middle column, green), and septum-free wall and lateral wall-septum (right column, blue).

## **Bibliographic References**

5) Heiberg E, Sjögren J, Ugander M, Carlsson M, Engblom H, Arheden H. Design and validation of Segment - freely available software for cardiovascular image analysis. *BMC Med Imaging*. 2010;10:1–13. , 4) Töger J, Arvidsson PM, Bock J, Kanski M, Pedrizzetti G, Carlsson M, et al. Hemodynamic forces in the left and right ventricles of the human heart using 4D flow magnetic resonance imaging: Phantom validation, reproducibility, sensitivity to respiratory gating and free analysis software. *PLoS One*. 2018;13(4):1–22. , 3) Lapinskas T, Pedrizzetti G, Stoiber L, Düngen HD, Edelmann F, Pieske B, et al. The Intraventricular Hemodynamic Forces Estimated Using Routine CMR Cine Images: A New Marker of the Failing Heart. *JACC Cardiovasc Imaging*. 2019;12(2):377–9. , 2) Arvidsson PM, Töger J, Carlsson M, Steding-Ehrenborg K, Pedrizzetti G, Heiberg E, et al. Left and right ventricular hemodynamic forces in healthy volunteers and elite athletes assessed with 4D flow magnetic resonance imaging. *Am J Physiol - Hear Circ Physiol*. 2017;312(2):H314–28. , 1) Galiè N, Humbert M, Vachiery JL, Gibbs S, Lang I, Torbicki A, et al. 2015 ESC/ERS Guidelines for the diagnosis and treatment of pulmonary hypertension. *Eur Heart J*. 2016;37(1):67–119.

Speaker: K. Pola

Category: Pulmonary Hypertension, 4D Flow, Ventricular Dysfunction

000157

## Improved computation of Lagrangian tissue displacement and strain for cine DENSE MRI using a regularized spatiotemporal least squares method

S. Ghadimi \* (1); F. Epstein (1)

(1) Biomedical engineering, University of Virginia, Charlottesville, United States of America

### Abstract

**Background:** In DENSE, the phase of each pixel of tissue in space and time provides an independent measurement of absolute tissue displacement relative to the time when the initial displacement-encoding pulses were applied upon detection of the ECG R-wave. In other words, DENSE intrinsically measures the Eulerian displacement of each pixel. Previously for DENSE, estimation of Lagrangian displacement used two steps: first a spatial interpolation was used, and, second, least squares fitting through time to a Fourier or polynomial model was employed [1,2]. However, there is no strong rationale for such a through-time model. Here, we develop a method to compute the Lagrangian displacement using a least squares minimization to enforce fidelity with the acquired Eulerian displacement data while simultaneously providing model-independent regularization in space and time, enforcing only spatiotemporal smoothness (Fig 1).

**Methods:** To estimate Lagrangian displacement from the measured Eulerian displacements, we formulate the following minimization problem (Eq. 1):

$$\text{Min}(\|(Ax_a - y_a)\|^2 + \lambda \|(Bx_a)\|^2 + \mu \|x_a - x_{a-1}\|^2) \quad (1)$$

where  $x_a$  is the desired Lagrangian displacement trajectories for frame  $a$ ,  $\|(Ax_a - y_a)\|^2$  enforces fidelity with the measured  $y_a$  Eulerian displacements, and  $A$  is the spatial bilinear interpolator. Eq. 1 also includes the spatial regularization term,  $\|(Bx_a)\|^2$  where  $B$  represents the sum of the squares of the second spatial derivatives (wrt to  $x$  and  $y$ ). Finally, for Eq. 1,  $\|x_a - x_{a-1}\|^2$  provides a model-independent method to enforce smoothness in time, and  $\lambda$  and  $\mu$  are weighting factors. We solve Eq. 1 and compute  $x_a$  using regularized spatiotemporal least squares (RSTLS) as shown in Fig. 2B. To evaluate the RSTLS method, we compared it to the prior two-step method for analysis of short-axis DENSE images from 32 healthy volunteers (95 slices). We used deep-learning methods for segmentation of the left ventricle and phase unwrapping [3]. The unwrapped phase data were converted to Eulerian displacement by dividing by the displacement encoding frequency. For the RSTLS and two-step methods, we computed the the mean absolute percent error (MAPE) relative to the measured Eulerian displacement field. We also quantified the peak early diastolic strain rate (PEDSR), a parameter likely to be over-smoothed by a through-time polynomial model.

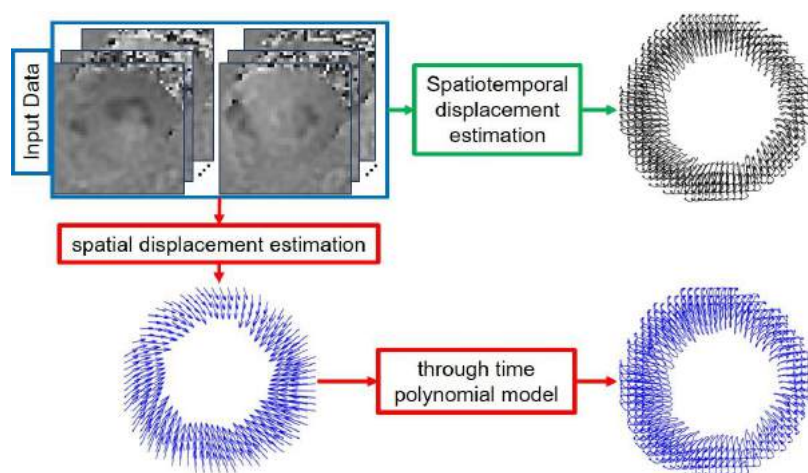
**Results:** Fig. 2C illustrates over-smoothing of displacement trajectories using the two-step method and better depiction of fine details like post-systolic shortening in displacement data using the RSTLS method. Fig. 3 demonstrates similar findings in strain-time curves, including over-smoothing of post-systolic shortening and early diastole, as well as oscillation artifacts in diastasis, using the two-step method, which are eliminated using the RSTLS method. For RSTLS vs. the two-step method, the MAPE was lower ( $0.64 \pm 0.71$  mm vs 0.78

$\pm 0.87$  mm,  $p < 0.05$ ), the PEDSR was higher ( $2.14 \pm 0.37\%$  vs.  $1.7 \pm 0.19\%$ ,  $p < 0.05$ ) and the strain rate during diastasis was lower ( $0.13 \pm 0.01$  s<sup>-1</sup> vs  $0.38 \pm 0.03$  s<sup>-1</sup>,  $p < 0.05$ ).

**Conclusion:** Compared to the two-step method, RSTLS avoids over-smoothing and model-based artifacts, and better depicts fine details such as post-systolic shortening, PEDSR, and diastasis. Less robustness to noise may be a disadvantage of RSTLS.

This work was supported by R01 HL147104.

**Figure/Table 1**



**Caption 1**

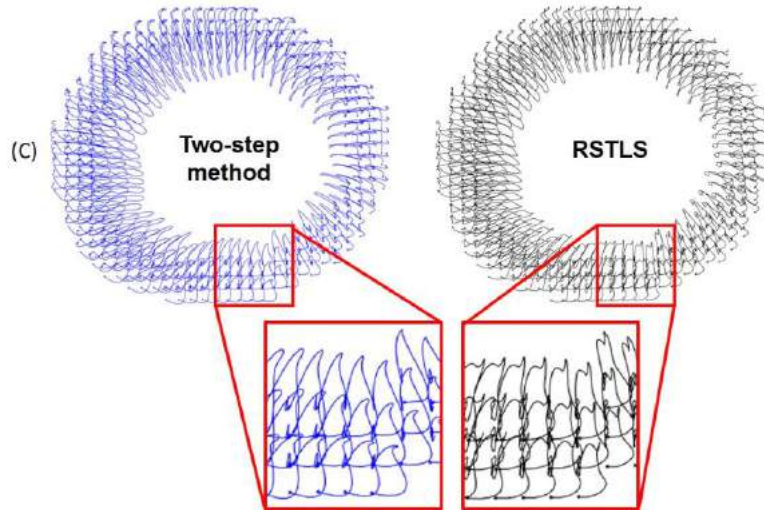
Previously, computation of Lagrangian trajectories for DENSE was performed using a two-step method (red pathway). Alternatively, we propose a regularized spatiotemporal least squares method for simultaneous spatiotemporal estimation without imposition of a through-time model (green pathway).

**Figure/Table 2**



$$(A) \quad \text{Min}(\|Ax_a - y_a\|^2 + \lambda\|Bx_a\|^2 + \mu\|x_a - x_{a-1}\|^2)$$

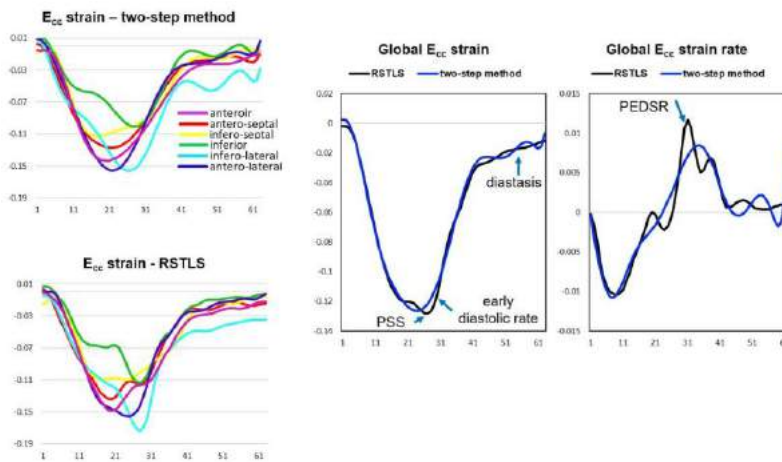
$$(B) \quad x_a = (\hat{A}^T \hat{A})^{-1} (\hat{A}^T \hat{y}_a), \quad \text{where } \hat{A} = \begin{bmatrix} A \\ \sqrt{\lambda} B \\ \sqrt{\mu} \end{bmatrix}, \quad \hat{y}_a = \begin{bmatrix} y_a \\ 0 \\ \sqrt{\mu} x_{a-1} \end{bmatrix}$$



**Caption 2**

(A) Minimization equation to compute Lagrangian displacement. (B) The Lagrangian displacement obtained using RSTLS. (C) An example comparing 2D Lagrangian displacement trajectories computed using the two-step method and the RSTLS method from a healthy subject. The RSTLS method captures fine details like post-systolic shortening that are over-smoothed using the two-step method.

**Figure 3**



**Caption 3**

In a healthy subject, RSTLS better captures strain features such as post-systolic shortening, early diastole, and diastasis, that are over-smoothed or have artifacts when computed using the two-step method. Ecc is circumferential shortening.

### **Bibliographic References**

[3] Ghadimi, S. et al. Fully-automated global and segmental strain analysis of DENSE cardiovascular magnetic resonance using deep learning for segmentation and phase unwrapping. *J. Cardiovasc. Magn. Reson.* 23, 1–13 (2021)., [2] Young, A. A., Li, B., Kirton, R. S. & Cowan, B. R. Generalized spatiotemporal myocardial strain analysis for DENSE and SPAMM imaging. *Magn. Reson. Med.* 67, 1590–1599 (2012)., [1] Spottiswoode, B. S. et al. Tracking myocardial motion from cine DENSE images using spatiotemporal phase unwrapping and temporal fitting. *IEEE Trans. Med. Imaging* 26, 15–30 (2007).

Speaker: S. Ghadimi

Category: DENSE, Cardiac Strain, Image Analysis

000159

## Evaluation of single ventricle morphology in an elderly patient using cardiac MRI

Y. Kim \* (1); S. Clifford (2); S. Huber (2); J. Steele (3)

(1) Department of cardiology, Yale New Haven Hospital, New Haven, United States of America; (2) Department of radiology, Yale New Haven Hospital, New Haven, United States of America; (3) Department of pediatrics. department of radiology., Yale New Haven Hospital, New Haven, United States of America

### Abstract

55 year-old man with history of double-inlet left ventricle (DILV) with L-malposition of the great arteries, and no history of prior surgical intervention presented to our clinic as a new referral. He was recently diagnosed with atrial fibrillation and started on medical treatment with sotalol. On physical exam, BP 123/76, HR 57 and O2 80%. Cardiovascular exam was notable for single second heart sound and a grade 2/6 systolic ejection murmur along the left sternal border. The remainder of the exam was unremarkable.

### Diagnostic Techniques and Findings:

At his prior institutions, the patient had been previously followed by echocardiography (TTE) and cardiac catheterization. Given his new arrhythmia, the decision was made to pursue Cardiac MRI (CMR) for improved functional and hemodynamic assessment. CMR confirmed double inlet left ventricle with double outlet right ventricle, D-looped ventricles and L-malposed great arteries (Figure 1). The single ventricle is severely dilated, indexed end diastolic and end systolic volumes of 249ml/m<sup>2</sup> and 124ml/m<sup>2</sup> respectively, and a normal single ventricle systolic function. The left and right atrioventricular valves are normal without apical displacement of the right atrioventricular valve, as is typical of DILV (Figure 1). The pulmonary valve is hypoplastic and partially bicuspid (Figure 2). Phase contrast imaging showed the pulmonic valve peak velocity to be 5 m/s, consistent with severe stenosis. There was trivial regurgitation. Given patient's baseline hypoxia to 80% on room air, detailed assessment of shunt fraction and collateral flow calculations were performed showing a Qp:Qs of 0.8 - 0.9 with no significant collateral flow, and abnormal right and left pulmonary artery (PA) branch flow differential (right PA 74% and left PA 26%). The main pulmonary artery is hypoplastic with post-stenotic dilation. Tissue characterization was normal without late gadolinium enhancement.

### Learning Points from this Case:

We present a rare case of an older adult with single ventricle physiology who was felt to be sufficiently balanced to defer intervention in his era of childhood. A detailed hemodynamic evaluation was performed using CMR. Adult patients with congenital heart disease (CHD) with and without prior surgical repairs require close hemodynamic monitoring over their lifespan. TTE can provide valuable information, however it is limited in evaluation of right sided cardiac structures and distal pulmonary arteries in adult patients. Invasive and radionuclide lung perfusion tests carry increased risk of complications and cumulative radiation exposure and do not carry the benefit of hemodynamic and flow assessment that CMR provides. CMR use has evolved rapidly and has become a powerful modality for assessment of structural pathology, function and hemodynamics in adult patients with CHD. This is especially useful for assessment of valvular regurgitation or stenosis, and evaluation of

branch pulmonary arteries with estimation of total right and left lung flows. In this case, we were able to identify peak velocity across pulmonic valve at 5 m/s, estimate aortic valve regurgitant fraction, obtain Qp:Qs ratio, and estimate right and left pulmonary artery branch flow via a non-invasive approach. This case demonstrates that CMR is a reliable non-invasive way to obtain functional and hemodynamic assessment in patients with congenital heart disease who require further evaluation than had previously been available.

### Figure/Table 1

Figure 1: Axial and 4 chamber FISP

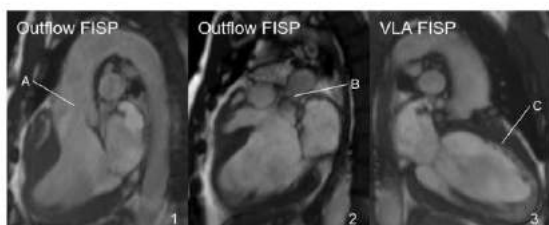


### Caption 1

Axial images demonstrating aortic valve anterior (A) and leftward to the pulmonic valve (B)  
1. Trileaflet aortic valve. Pulmonic valve is hypoplastic and partially bicuspid. 2. Aortic and pulmonic valve is systole. 3. Four chamber view of single ventricle (C) with right and left (D, E) atrioventricular valves which are normal in appearance without apical displacement.

### Figure/Table 2

Figure 2: Outflow and VLA FISP



## Caption 2

1. Outflow and VLA images demonstrating aortic (A) outflow tract with mildly dilated aortic root. 2 pulmonic outflow tract (B) with thickening of the pulmonic valve annulus and leaflets and post-stenotic dilation. There is severe pulmonic valve stenosis. 3. Redemonstration of normal left atrioventricular valve and single dilated ventricle.

## Bibliographic References

Kang IS, Redington AN, Benson LN, Macgowan C, Valsangiacomo ER et al. Differential Regurgitation in branch pulmonary arteries after repair of Tetralogy of Fallot. A phase-contrast cine magnetic resonance study. *Circulation*. 2003;107:2938-2943., Sridharan S, Derrick G, Taylor AM. Assessment of differential branch pulmonary blood flow: a comparative study of phase contrast magnetic resonance imaging and radionuclide lung perfusion imaging. *Heart*. 2006;92(7):963-968. , Burchill LJ, Huang J, Tretter JT, Khan AM, Crean AM et al. Noninvasive Imaging in Adult Congenital Heart Disease. *Circulation Research*. 2017;120:995–1014., Motoki N., Ohuchi H., Miyazaki A., Yamada O. Clinical profiles of adult patients with single ventricular physiology. *Circulation*. 2009;73:1711–1716. doi: 10.1253/circj.CJ-08-1155, Pundi K.N., Johnson J.N., Dearani J.A., Pundi K.N., Li Z., Hinck C.A., Dahl S.H., Cannon B.C., O’Leary P.W., Driscoll D.J., et al. 40-Year Follow-Up After the Fontan Operation: Long-Term Outcomes of 1,052 Patients. *J. Am. Coll. Cardiol*. 2015;66:1700–1710. doi: 10.1016/j.jacc.2015.07.065

Speaker: Y. Kim

Category: Single Ventricle, Blood Flow, Pulmonary Stenosis

000160

## **Quantification of Blood Flow and Velocity in a Swine Model of Pulmonary Hypertension using 4D Flow MRI**

D. Seiter \* (1); B. Allen, (2); D. M. Tabima, (3); T. A. Hacker, (4); T. H. Oechtering, (5); N. C. Chesler, (6); O. Wieben, (1)

(1) Medical Physics, University of Wisconsin-Madison, Madison, WI, USA, Madison, United States of America; (2) Surgery, University of Wisconsin-Madison, Madison, WI, USA, Madison, United States of America; (3) Biomedical engineering, University of Wisconsin-Madison, Madison, WI, USA, Madison, United States of America; (4) Medicine, University of Wisconsin-Madison, Madison, WI, USA, Madison, United States of America; (5) Radiology, University of Wisconsin-Madison, Madison, WI, USA, Madison, United States of America; (6) Biomedical engineering, University of California Irvine, Irvine, United States of America

### **Abstract**

**Background:** Pulmonary venous hypertension (PVH) is a common consequence of left heart failure and is caused by elevated left atrial pressure. PVH is associated with increased mean pulmonary artery pressure (mPAP) as well as vascular changes that lead to increased pulmonary vascular resistance (PVR), both of which can be measured using right heart catheterization (RHC). (1,2) As the disease progresses from isolated post-capillary to combined post- and pre-capillary PH (Cpc-PH), mortality rate rises due to right heart failure. In this pilot study, we evaluate severe PVH independent of left heart failure using 4D Flow MRI, aiming to focus on the vascular and right heart effects of Cpc-PH.

**Methods:** Invasive pulmonary vein banding (PVB) (3) was performed on four male white pigs (9.78, 0.9kg) using a non-occlusive banding of the inferior pulmonary venous (IPV) confluence. A sham operation without band placement was performed on two male pigs of similar weight (10kg, 11.7kg). Each pig was scanned and underwent RHC 12-16 weeks after banding using cine bSSFP for cardiac function, CE MRA for vascular anatomy, and radially undersampled 4D flow MRI (4) (3.0 T MRI scanner [GE Healthcare Discovery MR750, Waukesha, WI], TR=6.3ms, TE=2.1ms, Isotropic Resolution=1.95mm<sup>3</sup>, tip=8 degrees, Total Scan Time=13min). Swine PVB02, PVB04, and Sham 2 were scanned two to three times between 8-16 weeks post surgery, allowing longitudinal analysis. Planes were placed to measure velocities and flow in the vessels of interest using Enight (Ansys, Canonsburg PA) and processed using custom software in Matlab (Mathworks, Natick MA). Flow path line visualizations were also created in Enight.

**Results:** At week 16, swine body weights were: banded, 50.94.13 kg, shams, (58.7kg, 54.6kg). PVB01 was banded at the confluence of left and right inferior pulmonary veins (LIPV, RIPV), while the other 3 PVB swine had a band placed on the RIPV alone. Flow pathline visualization for PVB01, Sham 1, and PVB03 is shown in Figure 1, illustrating the effects of the band in each placement. Both images are scaled to the same color bar: velocities in induced stenoses are much higher than sham at the same location. All banded animals developed severe Cpc-PH quantified by increase mPAP compared with the shams, but the swine with RIPV bands experienced lower pressures and were able to partially compensate for reduced RIPV flow through the LIPV compared with PVB01, see Table 1. Longitudinal

comparison of mPAP and IPV mean flow is shown for swine scanned multiple times in Figure 2.

**Conclusion:** In this study, we used 4D Flow MRI in a novel swine model of severe PH due to pulmonary vein narrowing. The surgical banding procedure is challenging, involving working through a small (~5-6 cm) incision to locate and band the vessels. 4D Flow MRI allowed confirmation of success of the difficult procedure and provided quantification of blood flow and velocity. Longitudinal data shows that as flow increases with swine age, mPAP rises to pathological levels due to banding. The banding model thus causes PH to develop over time, offering unique insight into disease progression. Our intention in using this model is to induce Cpc-PH without impacting the left heart, enabling study of PH focused on vascular and right heart changes. Future work will increase the number of subjects, include histopathology, and analyze PH-specific hemodynamics in the main pulmonary artery using flow visualizations.

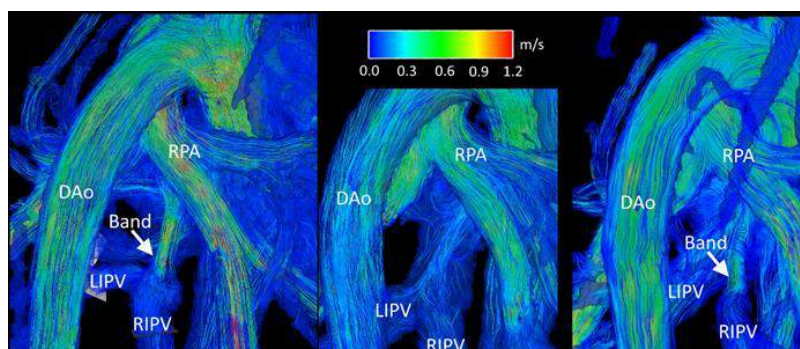
**Figure/Table 1**

	Banded Vessel	IPVs Mean Flow (L/min) (left, right)	IPVs Peak Velocity(cm/s) (left, right)	MPA MeanFlow (L/min)	RV EF(%)	mPAP(mmHg)	PVR(mmHg-min/L)
PVB01	IPV	0.43, 0.44	11.60, 10.80	2.94	28	50.67	11.94
PVB02	RIPV	1.96, 0.35	38.85, 28.23	4.66	67	27.67	1.70
PVB03	RIPV	1.10, 0.31	34.91, 14.72	2.27	54	27.67	2.95
PVB04	RIPV	1.23, 0.13	40.20, 16.30	2.40	63	30.00	2.27
Sham1	~	0.87, 1.29	23.50, 31.40	4.50	65	19.00	0.08
Sham2	~	1.13, 1.34	22.26, 34.46	4.06	69	19.67	0.72

**Caption 1**

Final MRI scan and catheter data from all subjects.

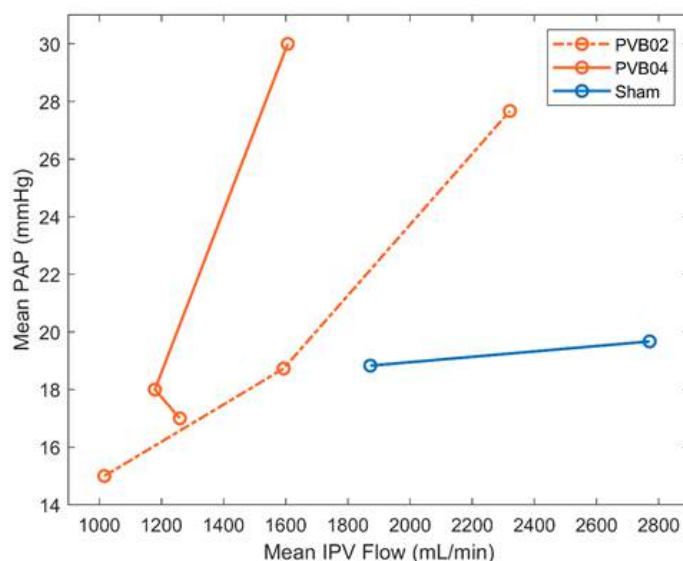
**Figure/Table 2**



## Caption 2

Figure 1: Side by side pathline visualization of PVB01 banded on the IPV confluence (Left), and Sham 1 (center), and PVB03 banded on the RIPV only (Right). Descending aorta (DAo), Right Pulmonary Artery (RPA), and Left and Right Inferior Pulmonary Veins (LIPV, RIPV) are labelled for reference. Band placement is shown.

## Figure 3



## Caption 3

Figure 2: Growth-related flow increase is associated with mPAP increase in PVB swine. The banded (PVB) swine show data points from 8-, 12-, and 16-weeks post-surgery, plotted bottom left to top right. The sham data points are from 8- and 16-weeks.

## Bibliographic References

1. Assad TR, Hemnes AR, Larkin EK, et al. Clinical and Biological Insights Into Combined Post- and Pre-Capillary Pulmonary Hypertension. *J Am Coll Cardiol*. 2016;68(23):2525-2536. doi:10.1016/j.jacc.2016.09.942, 2. Vonk Noordegraaf A, Groeneveldt JA, Bogaard HJ. Pulmonary hypertension. *Eur Respir Rev*. 2016;25(139):4-11. doi:10.1183/16000617.0096-2015, 3. Pereda D, García-Alvarez A, Sánchez-Quintana D, et al. Swine model of chronic postcapillary pulmonary hypertension with right ventricular remodeling: Long-term characterization by cardiac catheterization, magnetic resonance, and pathology. *J Cardiovasc Transl Res*. 2014;7(5):494-506. doi:10.1007/s12265-014-9564-6, 4. Johnson KM, Lum DP, Turski PA, Block WF, Mistretta CA, Wieben O. Improved 3D



phase contrast MRI with off-resonance corrected dual echo VIPR. Magn Reson Med. 2008;60(6):1329-1336. doi:10.1002/mrm.21763, 5. Reiter G et al. Blood flow vortices along the main pulmonary artery measured with MR imaging for diagnosis of pulmonary hypertension. Radiology. 2015;275(1):71-79. doi:10.1148/RADIOL.14140849

Speaker: D. Seiter

Category: 4D Flow, Pulmonary Hypertension, Animal Experimentation

## An Inline Deep-Learning Based Free-Breathing and ECG-Free Cine for Exercise CMR

M. morales \* (1); S. Assana (1); X. Cai (2); K. chow (3); H. Haji-valizadeh (1); E. Sai (1); J. Rodriguez (1); S. Berg, (1); N. Whitehead (1); P. Pierce (1); B. Goddu (1); W. Manning (1); R. Nezafat (1)

(1) Department of medicine (cardiovascular division), Beth Israel Deaconess Medical Center (BIDMC), Boston, United States of America; (2) Mr collaboration, Siemens Medical Solutions USA, Inc., Boston, United States of America; (3) Healthineers, Siemens Healthcare Diagnostics, Chicago, United States of America

### Abstract

**INTRODUCTION:** Provocative stress testing is an important tool to detect cardiac disease which are often undetectable at rest. While pharmaceutical stress CMR cine imaging offers the most accurate and reproducible assessment of cardiac function, guidelines advise physical exercise as the preferred method for stress<sup>1</sup>. However, standard ECG-segmented cine imaging during exercise is challenging. Alternatively, free-breathing ECG-free real time cine can be achieved by combining highly accelerated imaging with compressed sensing (CS) image reconstruction. Nevertheless, reconstruction times with CS can be long and not truly real time. Thus, we sought to develop an inline deep-learning (DL) based free-breathing and ECG-free cine imaging approach for evaluation of left-ventricular (LV) function.

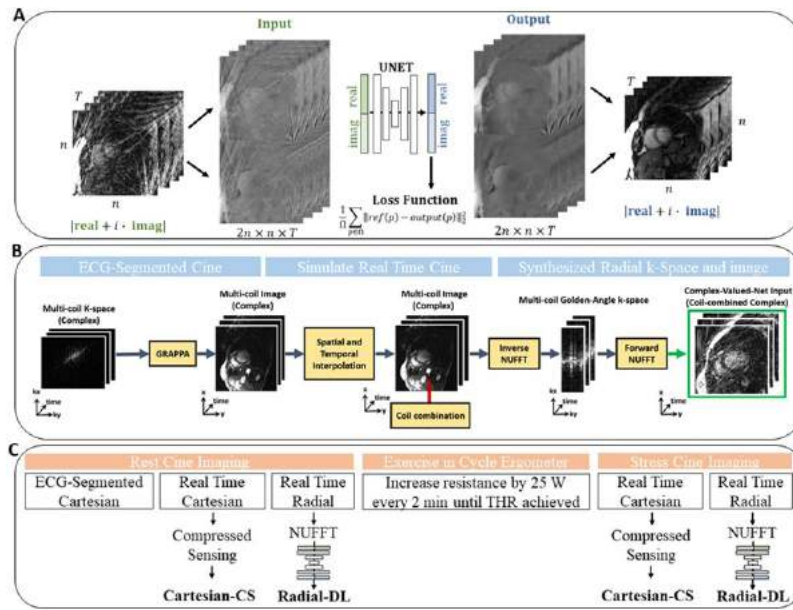
**METHOD:** We implemented a prototype real time cine tiny golden angle (N=5)2 radial acquisition: FOV=288 mm<sup>2</sup>, resolution=2 mm<sup>2</sup>, slice thickness=8 mm, TE/TR=1.52/3.14 ms, flip angle=43°, lines per frame=12, temporal resolution=37.7 ms. We also implemented a 3D U-net model to suppress artifacts from this accelerated sequence (Fig. 1A). We used ECG-segmented Cartesian k-space data from 503 patients for training. Ground-truth: GRAPPA-reconstructed and interpolated to resolution=2 mm<sup>2</sup> and 37.7 ms. Input: synthesized aliased images from highly undersampled radial k-space acquisition (Fig. 1B). Subjects were prospectively recruited for evaluation (*n*=20). All underwent 3T imaging at rest: ECG-segmented cine followed by real-time cine with Cartesian and radial sampling patterns (MAGNETOM Vida, Siemens Healthcare, Germany). Some subjects (*n*=11, including 4 patients with suspected coronary disease) were then exercised using a MR-compatible cycle ergometer (Lode, Netherlands) and a continuous workload ramp protocol. after reaching target heart rate ( $[202 - \text{age}] \times 0.85$ ) or exhaustion, subjects underwent imaging at exercise stress: real-time cine with Cartesian and radial sampling patterns. Cartesian data was CS-reconstructed using inline vendor-provided reconstruction. We implemented and tested in several patients the DL reconstruction inline using the Siemens Framework for Image Reconstruction (FIRE) prototype. We used gridded and coil combined images generated in-scanner as inputs to the DL model. Real time cine are hereinafter referred to as Cartesian-CS and radial-DL (Fig. 1C).

**RESULTS:** Rest and stress cine images are shown in Fig. 2. One reader evaluated cine data at rest (ECG-segmented, Cartesian-CS, radial-DL) and stress (Cartesian-CS, radial-DL). Metrics were graded on a 5-point Likert scale (1- non-diagnostic to 5-best). Evaluations at rest were: ( $4.5 \pm 0.6$ ,  $3.9 \pm 0.4$ ,  $2.0 \pm 0.5$ ) for artifact level; ( $4.1 \pm 1.6$ ,  $3.9 \pm 0.7$ ,  $2.1 \pm 0.9$ ) for LV wall sharpness; ( $4.5 \pm 0.9$ ,  $4.0 \pm 0.5$ ,  $2.8 \pm 0.9$ ) for LV temporal fidelity. Evaluations at stress

were  $(3.5 \pm 0.5, 2.0 \pm 0.4)$ ,  $(2.9 \pm 0.9, 1.5 \pm 0.8)$ , and  $(3.5 \pm 0.7, 2.5 \pm 0.7)$ , accordingly. Biases in LV parameters at rest between ECG-segmented and real time cine (Cartesian-CS, radial-DL) were:  $-5.9 \pm 6.3$  mL,  $-3.1 \pm 7.5$  mL for end-diastolic volume;  $-2.9 \pm 3.5$  mL,  $-6.8 \pm 4.2$  mL for end-systolic volume;  $0.6 \pm 2.2\%$ ,  $4.8 \pm 3.0\%$  for ejection fraction;  $-5.6 \pm 5.0$  g,  $-1.4 \pm 5.5$  g for myocardial mass. Fig. 3 shows representative inline reconstruction images of two patients.

**CONCLUSION:** Combination of highly accelerated radial acquisition with DL enables the fast reconstruction of real-time cine images. Our study demonstrated the feasibility of such methodology for exercise stress CMR and was implemented inline.

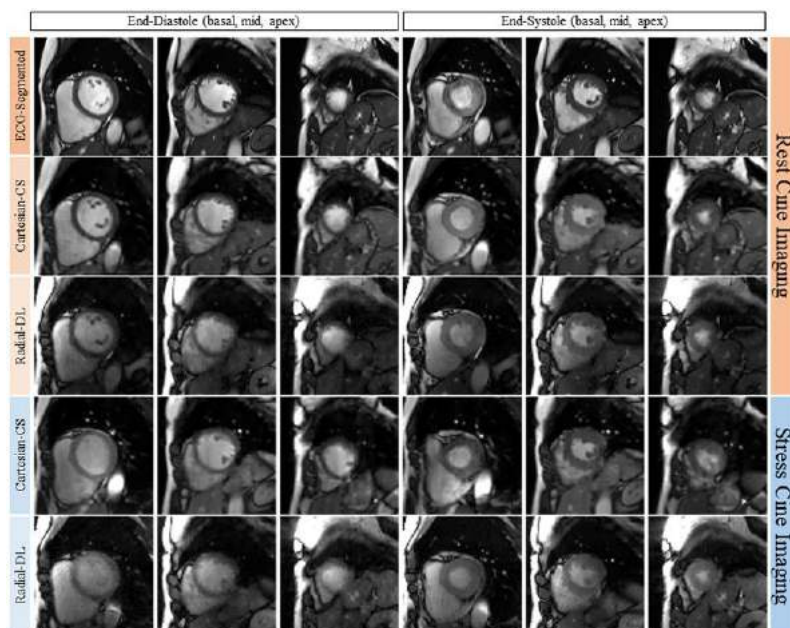
**Figure/Table 1**



**Caption 1**

Figure 1. (A) DL Model: designed to suppress streaking artifacts from complex images (B) Train Data: ECG-segmented raw k-space data were retrospectively acquired and used to synthesize fully- and under-sampled training pairs. (C) Exercise protocol: All subjects were imaged at rest. Eleven subjects were imaged after a continuous exercise ramp protocol.

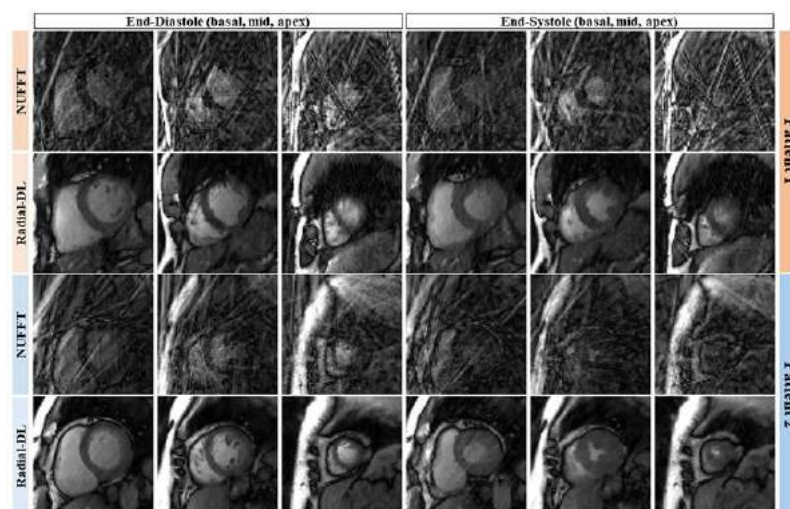
**Figure/Table 2**



**Caption 2**

Figure 2. From top to bottom, representative reconstructions of ECG-segmented, real-time Cartesian-CS, and real-time radial-DL (proposed) cine data at rest; real-time Cartesian-CS and real-time radial-DL cine data during exercise stress. Images correspond to a patient with suspected coronary disease and are shown at end-diastolic and end-systolic phases.

**Figure 3**



**Caption 3**

Figure 3. Representative Inline reconstructions for two cardiac patients. Coil-combined NUFFT images generated by the scanner (first and third rows) were used as inputs to the proposed deep learning model. The model generated images (Radial-DL) show substantial suppression of artifacts within the scanner (second and fourth rows).

### **Bibliographic References**

2. 1 Craven, T. P., Tsao, C. W., La Gerche, A., Simonetti, O. P. & Greenwood, J. P. Exercise cardiovascular magnetic resonance: development, current utility and future applications. *Journal of Cardiovascular Magnetic Resonance* 22, 1-20 (2020). 2 Wundrak, S. et al. Golden ratio sparse MRI using tiny golden angles. *Magnetic resonance in medicine* 75, 2372-2378 (2016), 1. Craven, T. P., Tsao, C. W., La Gerche, A., Simonetti, O. P. & Greenwood, J. P. Exercise cardiovascular magnetic resonance: development, current utility and future applications. *Journal of Cardiovascular Magnetic Resonance* 22, 1-20 (2020)

Speaker: M. morales

Category: Exercise, Real Time, Golden Angle

**Self-gating for Fetal Cardiac MRI**

M. Hott \* (1); H. von Kleist (2); A. J. Powell (1); A. Barker (3); R. Friesen (4); L. Browne (3); M. H. Moghari (3)

(1) Department of cardiology, Harvard Medical School, Boston Children's Hospital, Boston, United States of America; (2) Helmholtz zentrum münchen, Technische Universität München, München, Germany; (3) Department of radiology, University of Colorado and Children's Hospital Colorado, Aurora, United States of America; (4) Department of cardiology, University of Colorado and Children's Hospital Colorado, Aurora, United States of America

**Abstract**

**Background:** Echocardiography is the gold standard for fetal diagnosis of congenital heart disease CHD, but there is a growing interest in the complementary role MRI could play in diagnosis (1). Currently non-gated static MRI images of the fetal heart and extracardiac vessels can be obtained in most fetuses but gated acquisitions capable of resolving intracardiac malformations and calculating ventricular volumes have remained elusive (2). Doppler ultrasound gating (3) was introduced to facilitate external triggering of the fetal heart signal, but gating may be susceptible to loss of ECG signal related to fetal motion. Self-gating replaces the need for an external device by detecting the fetal heart rate from k-space data (4). In this study, the efficacy of a self-gating method in acquiring cine images of the fetal heart in patients undergoing clinically indicated fetal MRIs was evaluated.

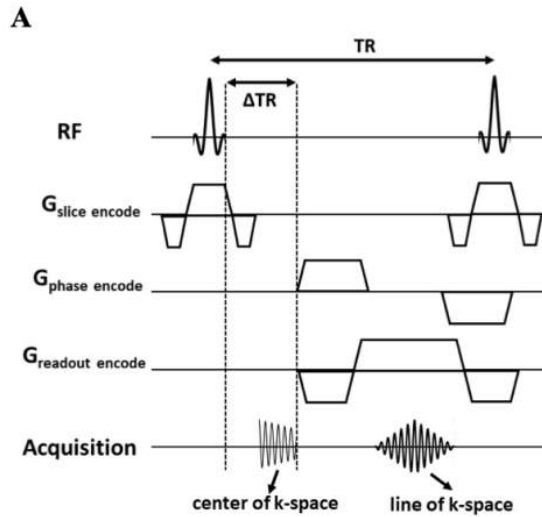
**Methods:** A cine balanced steady-state free precession (bSSFP) sequence with Cartesian trajectory was modified to extend each TR by recording the center of k-space prior to acquiring one Cartesian k-space line (Figure 1) (5). The signals of center points were then transformed into the frequency domain and underwent independent component analysis and second order blind identification analysis (Figure 2A). The component that best represents fetal cardiac motion was selected based on power spectral density (Figure 2B). After transforming the chosen component back into the time domain, cardiac cycles were detected and used to bin image data into appropriate cardiac phases inline on the scanner. A fetal patient study was performed to evaluate the performance of self-gating in fetal cardiac MRI. A stack of axial, horizontal-long-axis (HLA), and short-axis (SA) cine images were acquired using the modified bSSFP sequence while mothers were holding their breaths. All images were reconstructed inline on the scanner using SENSE (Figure 1B). Images were qualitatively scored by two cardiac imagers for sharpness of the blood pool, the myocardial interface, and the endocardial ventricular borders. Scoring was based on a 4-point scale [1. Poor, 2. Fair, 3. Good, 4. Excellent], and whether images were diagnostically conclusive for evaluation of ventricular size and function. Interobserver variability was measured using an Intraclass Correlation Coefficient (ICC) analysis. The relationship between scores and gestational week (GW) was assessed using Pearson's correlation coefficient (CC).

**Results:** Nine fetal singletons were recruited to participate in the study (median age 27 (21-36) GWs). One singleton at 27 GWs could not be imaged due to persisting fetal bulk motion. Images for the other eight fetal patients were attributed good scores ( $3.18 \pm 0.75$ ) by two cardiac imagers. The raters were in strong agreement and not statistically different (ICC:0.80,

p-value:0.02). Investigating the relationship between GW and scores showed moderate correlation (CC:0.65) with good scores starting at 23 GWs, the lowest score 2 at 21 GWs and the highest score 4 at 25 and 31 GWs. All evaluated images were labelled diagnostically conclusive by both observers. Figure 3 shows examples of self-gated images at end-systole and end-diastole acquired from two fetal patients.

**Conclusion:** We evaluated the efficacy of a self-gated bSSFP cine sequence for fetal cardiac MRI. We showed that self-gated cine images of the fetal heart could be used for the assessment of ventricular function across a range of second and third trimester GWs. Our future goal is to perform quantitative measurements of volume and function and extend this technique for flow measurements.

**Figure/Table 1**



**B**

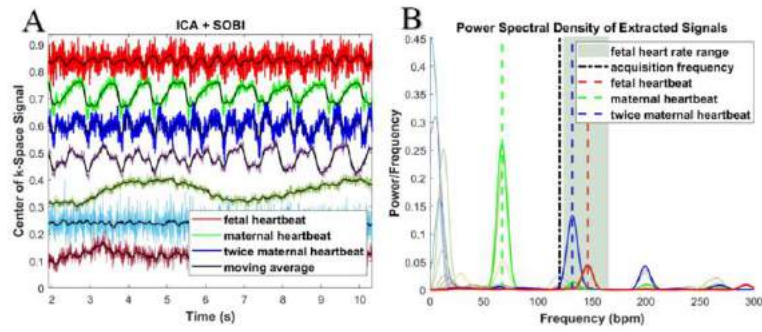
Imaging parameters	Modified bSSFP sequence
K-space trajectory	Cartesian
Cardiac gating	Retrospective self-gating
Acquired spatial resolution (mm <sup>2</sup> )	1.8 × 1.8
Reconstructed resolution (mm <sup>2</sup> )	0.78 × 0.78
Slice thickness (mm)	8
Slice gap (mm)	-4
Field of view (mm <sup>2</sup> )	250-300 × 275-300
TR/TE (ms)	3.3/2.1
Number of acquired center points	200
Flip angle (°)	60
Acquired heart phases	20
Reconstructed heart phases	30
Parallel imaging (SENSE)	2
Scan time (seconds)	5-10 breath holds, 11 seconds each

### Caption 1

(A) The pulse sequence diagram of the self-gating cine balanced steady-state free precession (bSSFP) sequence shows the extension in  $\Delta TR$  to readout the center point of k-space ahead of acquiring a Cartesian k-space line. (B) Imaging parameters of the self-gating cine bSSFP sequence.

**Figure/Table 2**

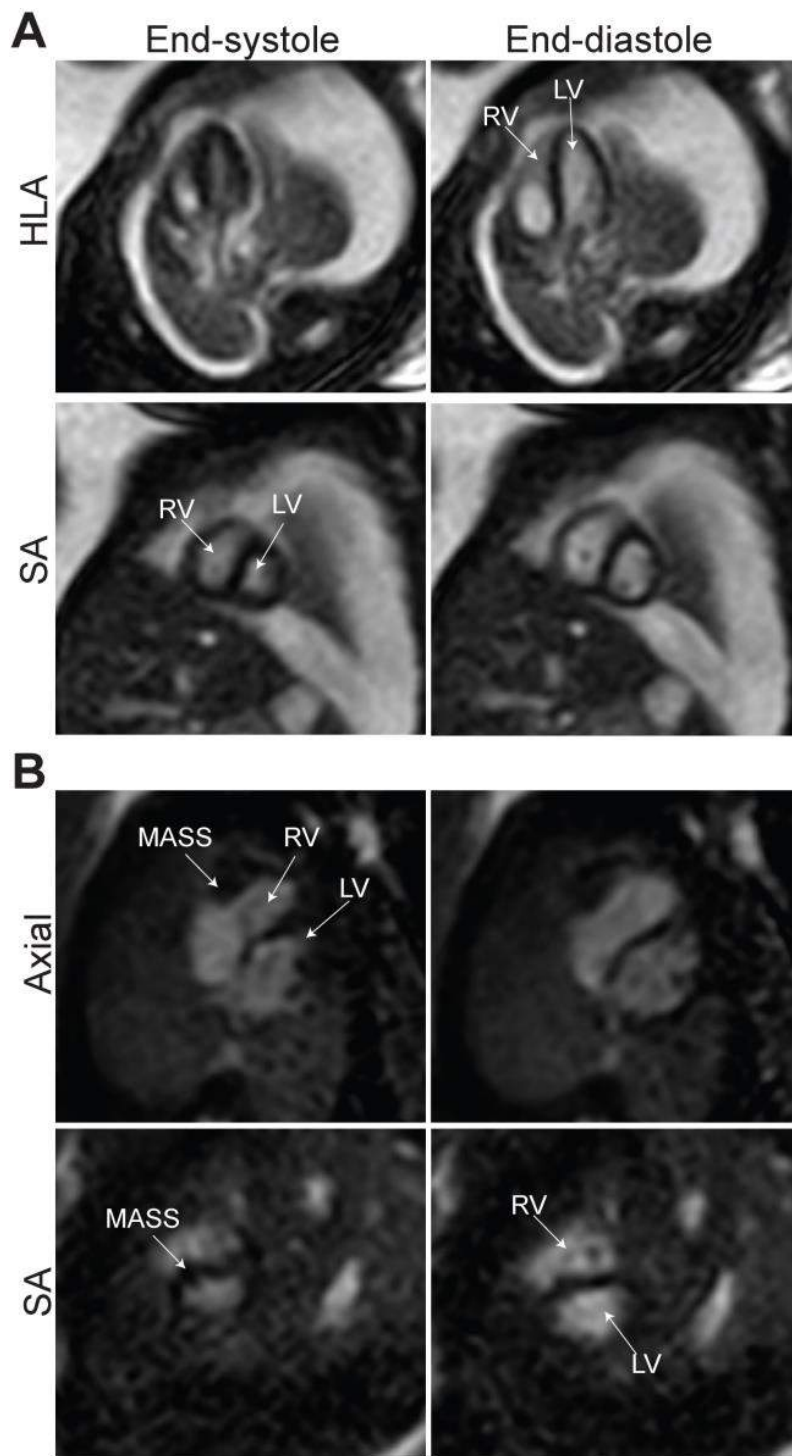




## Caption 2

(A) Extracted motion components from the center point of k-space after independent component analysis (ICA) and second order blind identification (SOBI) analysis. (B) Power spectral density of the extracted components showing peaks for the maternal heart rate (67 bpm), twice the maternal heart rate (132 bpm), and the fetal heart rate (146 bpm).

## Figure 3



### Caption 3

(A) horizontal-long-axis (HLA) and short-axis (SA) images at end-systolic and end-diastolic cardiac phase from a fetus at 31 GWs with large bilateral pleural effusions. (B) Axial and SA images at end-systolic and end-diastolic cardiac phase from a fetus with multiple cardiac masses at 29 GWs.

### **Bibliographic References**

1. Meyer-Wittkopf M, Cook A, McLennan A, Summers P, Sharland GK, Maxwell DJ. Evaluation of three-dimensional ultrasonography and magnetic resonance imaging in assessment of congenital heart anomalies in fetal cardiac specimens. *Ultrasound Obstet Gynecol* 1996;8(5):303-308., 2. Wielandner A, Mlczech E, Prayer D, Berger-Kulemann V. Potential of magnetic resonance for imaging the fetal heart. *Seminars in fetal & neonatal medicine* 2013;18(5):286-297., 3. Kording F, Yamamura J, de Sousa MT, Ruprecht C, Hedstrom E, Aletras AH, Ellen Grant P, Powell AJ, Fehrs K, Adam G, Kooijman H, Schoennagel BP. Dynamic fetal cardiovascular magnetic resonance imaging using Doppler ultrasound gating. *J Cardiovasc Magn Reson* 2018;20(1):17., 4. Larson AC, White RD, Laub G, McVeigh ER, Li D, Simonetti OP. Self-gated cardiac cine MRI. *Magn Reson Med* 2004;51(1):93-102., 5. Buehrer M, Curcic J, Boesiger, P Kozerke S. Prospective self-gating for simultaneous compensation of cardiac and respiratory motion. *Magn Reson Med* 2008;60(3):683-690.

Speaker: M. Hott

Category: Self-Gating, Fetal, Cardiac Function

000165

## **Rapid Strain Encoded MRI (SENC) During In-magnet Exercise**

Y. Liu \* (1); C. Crabtree (2); Y. Pan (3); J. Heyniger (4); A. Buxton (3); X. Cai (5); N. jin (6); J. Varghese (1); R. Ahmad (3); O. Simonetti (1)

(1) Davis heart and lung research institute, The Ohio State University, Columbus, United States of America; (2) Department of human sciences, The Ohio State University, Columbus, United States of America; (3) Department of biomedical engineering, The Ohio State University, Columbus, United States of America; (4) Cardiovascular medicine, The Ohio State University Wexner Medical Center, Columbus, United States of America; (5) Mr collaboration, Siemens Medical Solutions USA, Inc., Boston, United States of America; (6) Mr collaboration, Siemens Medical Solutions, Malvern, United States of America

### **Abstract**

#### **Background**

Pharmaceutical and exercise stress are used in conjunction with imaging to reveal pathological processes. Exercise stress is preferred as it elicits physiological stress and reproduction of exertional symptoms, and exercise capacity itself has diagnostic and prognostic value. While treadmill CMR has been shown to achieve higher heart rates during imaging [1], it requires patient transfer from treadmill to the MRI table and precludes simultaneous imaging during exercise. Strain encoded MRI (SENC) has been shown to be sensitive to abnormal function during low-dose dobutamine infusion [2]. In this study, we explore the feasibility of SENC measurement of global longitudinal strain (GLS) in the left ventricle (LV) during sub-maximal exercise stress using an in-magnet stepper exercise device (Cardiostepper, Ergospect GmbH, Austria).

#### **Methods**

Prototype real time (RT) SSFP cine (temporal resolution ~42ms) [3] and prototype SENC [4] data were collected on a 1.5T clinical scanner (MAGNETOM Sola, Siemens Healthcare, Erlangen, Germany) in subjects at rest and during stepper exercise at a cadence of 60 steps/min. Seven short-axis (SAX) slices and three groups of long-axis (LAX) cine covering the LV were acquired first to quantify cardiac function; then basal, midventricular and apical SAX SENC series were acquired to measure longitudinal strain. Resting SENC was acquired with breathholding, while SENC and cine were acquired with free-breathing during exercise. Quantification was performed to measure GLS from SENC using MyoStrain 5.2 (MyoCardial Solutions, NC, USA) and cardiac output (CO) from cine (NeoSoft LLC, WI, USA). Rest and stressed heart rates and exercise time were recorded. The Borg self-assessment scale was used to measure the level of difficulty of exercise.

#### **Results**

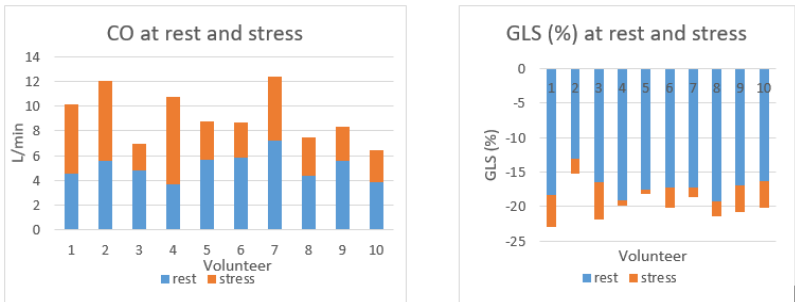
All 10 healthy volunteers (age 26.9 +/-6.9y, 6M4F) completed the exercise comfortably (self-assessed Borg scale 9 and 11, very light and fairly light on 6-20 scale) to reach a target heart rate of at least 110 beats/min. All cine and SENC images were of diagnostic quality (Figures 2 and 3). Heart rate increased on average 50.3 +/-14.8 beats/min, and average exercise time was

14.9 +/- 3.9 minutes. CO increased by an average of 4.5 +/-1.8 L/min, or 87%; average GLS (%) increased 2.8% from 17.1% at rest (Figure 1). While significant increase in both CO and GLS were observed, no significant correlation was found between the CO increase and GLS change, nor between heart rate increase and GLS.

Conclusions

Use of in-bore exercise equipment allows CMR data acquisition during exercise with the heart rate held at a relatively constant, elevated level. Quantitative real-time cardiac MRI methods are feasible to use during in-magnet exercise. Preliminary normal values of SENC GLS during sub-maximal exercise were established in a limited number of healthy volunteers.

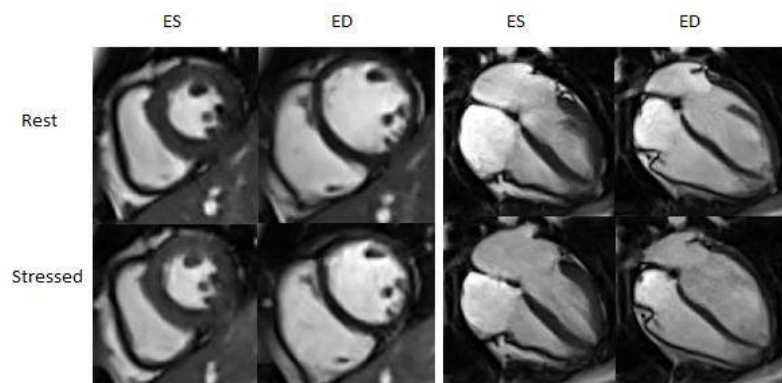
Figure/Table 1



Caption 1

Figure 1. CO (left) and GLS (%) (right) increase (orange) during exercise and at rest (blue) for all volunteers.

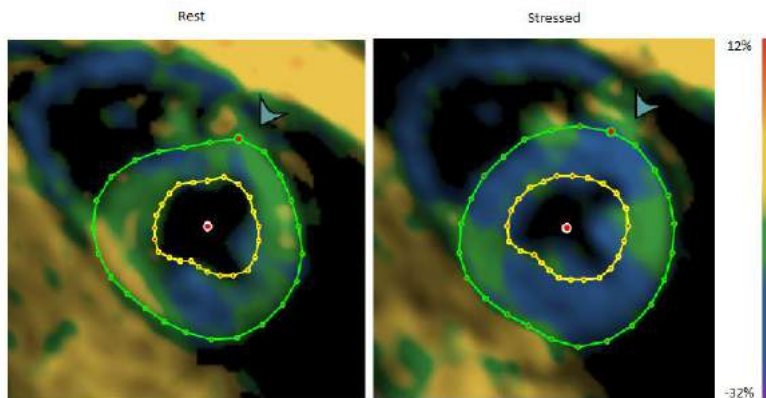
Figure/Table 2



Caption 2

Figure 2. Representative end systolic (left) and end diastolic (right) frames of short axis view at rest (top) and during exercise (bottom); In the right panel, the ES and ED frames of the 4-chamber LAX view is shown.

**Figure 3**



**Caption 3**

Figure 3. Typical SAX SENC images of the same slice location with placed regions-of-interest overlaid on the peak strain frame at rest (left) and during exercise (middle), the GLS is clearly increased during exercise; the color bar representing the strain range is also shown (right).

### Bibliographic References

4. Pan, Li, et al. "Real-time imaging of regional myocardial function using fast-SENC." *MRM* 55.2 (2006): 386-395., 3. Chen, Chong, et al. "Sparsity adaptive reconstruction for highly accelerated cardiac MRI." *MRM* 81.6 (2019): 3875-3887., 2. Korosoglou, Grigorios, et al. "Strain-encoded CMR for the detection of inducible ischemia during intermediate stress." *JACC: Cardiovascular Imaging* 3.4 (2010): 361-371., 1. Lafountain, Richard A., et al. "Cardiopulmonary exercise testing in the MRI environment." *Physiological measurement* 37.4 (2016): N11.

Speaker: Y. Liu

Category: Cardiac Function, Cardiac Strain, Exercise Stress

000166

## Real-time CMR Feature Tracking for Quantitative Assessment of Left Ventricle Wall Motion in Heart Failure Patients

Y. Li \* (1); J. Craft (1); J. Cheng (1); K. Gliganic (1); W. Schapiro (1); J. J. Cao (1)

(1) Cardiac imaging, St. Francis Hospital & Heart Center, Roslyn, United States of America

### Abstract

**Background:** Heart failure (HF) is a complex clinical syndrome caused by systolic and/or diastolic dysfunction in the ventricle (1). Because CMR offers high reproducibility in volumetric measurements, it has become the choice of imaging modality for evaluating HF with systolic dysfunction that typically induces a lower ejection fraction (EF) than normal ( $<50\%$ ). However, as volumetric measurements are not sensitive to diastolic dysfunction, CMR is not effective for evaluating HF with preserved EF ( $\geq 50\%$ ) (2). The presented work aimed to seek a quantitative measure complementary to volumetric indices for improved HF evaluation with CMR by analyzing left ventricle (LV) wall motion with feature tracking in real-time CMR images (3,4).

**Methods:** Standard retrospective cine permits the visualization of cardiac motion consistently existing over several cardiac cycles (5). In contrast, real-time CMR can image not only long-lasting motion, but also short-lived motion that may vary from one cardiac cycle to another (4). In this work, we sought to use feature tracking (3) to analyze real-time LV wall motion. To that end, real-time images were collected over a series of sequential cardiac cycles. Feature tracking was used to measure radial and circumferential motion of LV endocardial borders on the short-axis plane. With correlation analysis between the radial and circumferential velocity measurements, a CMR index, torsion correlation was calculated to evaluate how well LV twisting would coordinate with radial motion along the time. In a CMR study, we demonstrated that torsion correlation would provide a quantitative measure complementary to volumetric indices for improved HF evaluation.

**Results:** We recruited 16 healthy volunteers, 8 HF patients with  $EF < 50\%$  and 10 HF patients with preserved EF. Figure 1 provides image examples and volumetric measurements with retrospective cine and real-time CMR in these subjects. Both retrospective cine and real-time CMR indicated significant difference in volumetric measurements between the healthy volunteers and the HF patients with  $EF < 50\%$ . In contrast, no difference was found between the healthy volunteers and the HF patients with preserved EF.

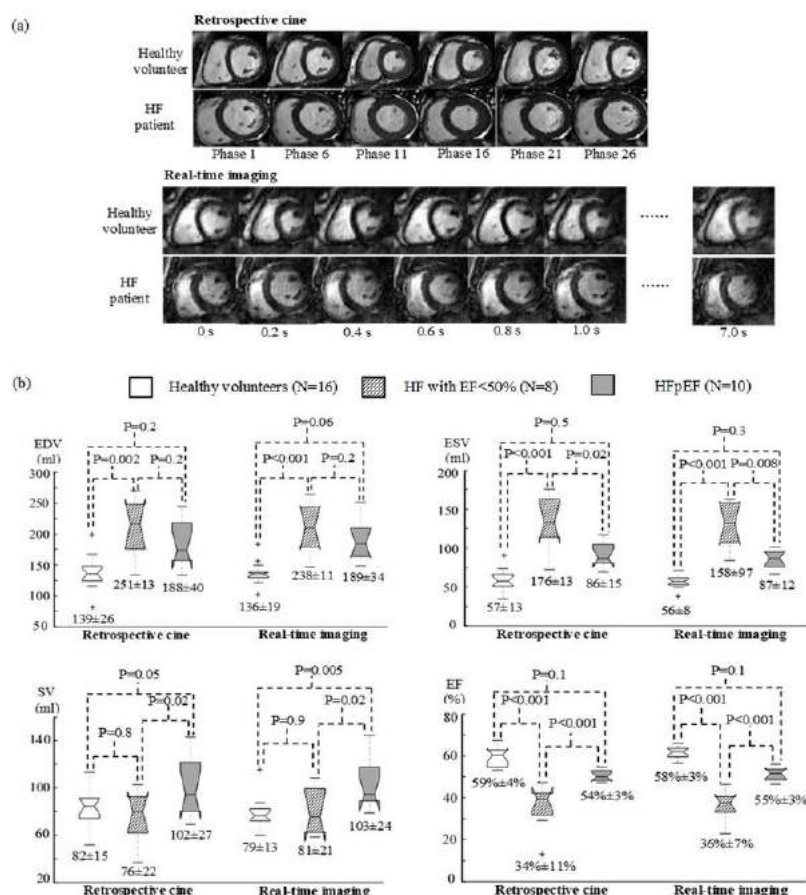
Figure 2 provides examples of feature tracking and correlation analysis in retrospective cine and real-time images. With real-time feature tracking, short-lived LV wall motion was observed which varied from one cardiac cycle to another. In contrast, feature tracking with retrospective cine showed only the long-lasting motion which occurred in every cardiac cycle. In correlation analysis with real-time CMR, considerable difference existed among the healthy volunteer, the HF patient with  $EF < 50\%$  and the HF patient with preserved EF. This difference was not found in correlation analysis with retrospective cine.

The one-way ANOVA statistics (Figure 3a) indicated that the HFpEF patients and healthy volunteers presented difference in torsion correlation calculated with real-time CMR

( $P<0.001$ ). This difference, however, was not found with retrospective cine. In the scatter plots of EF against torsion correlation with real-time CMR (Figure 3b), the HF patients with  $EF<50\%$  and those with preserved EF were both differentiated from the healthy volunteers.

**Conclusion:** Real-time CMR feature tracking enables correlation analysis between LV radial and circumferential wall motion over a series of sequential cardiac cycles. This analysis can provide quantitative LV function assessment complementary to volumetric measurements and offer the potential for improved HF evaluation with CMR.

**Figure/Table 1**

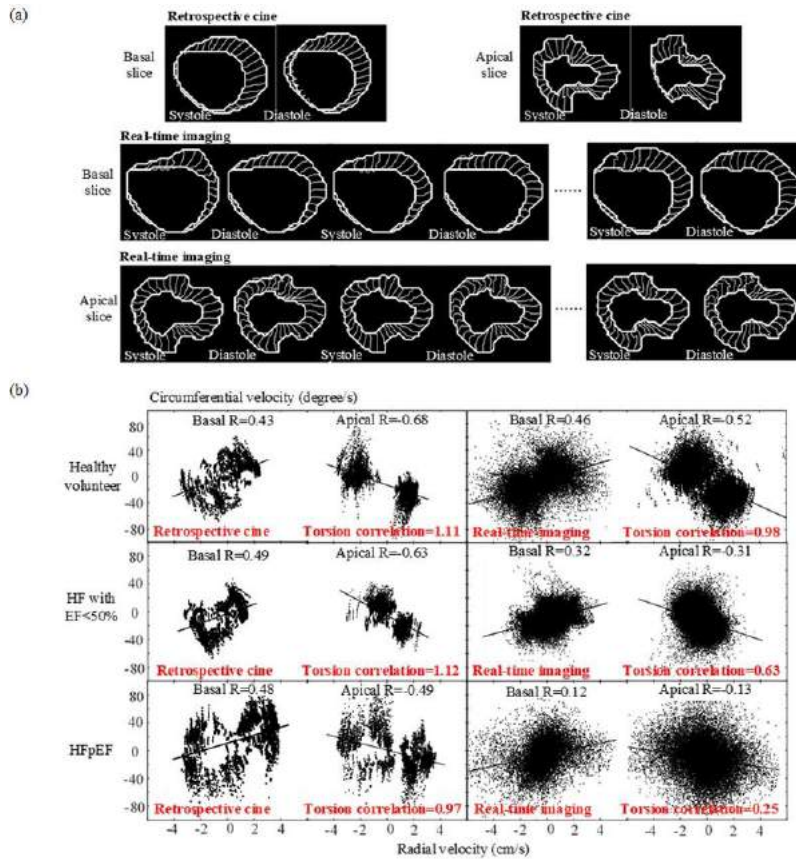


**Caption 1**

Figure 1. (a) Retrospective cine and real-time CMR image examples in a healthy volunteer and a HF patient. (b) Box plots for EDV, ESV, SV and EF measurements in the healthy volunteers and HF patients. The numbers above the boxes provide the P values from ANOVA statistics and those below the boxes are the mean and standard deviation.

**Figure/Table 2**

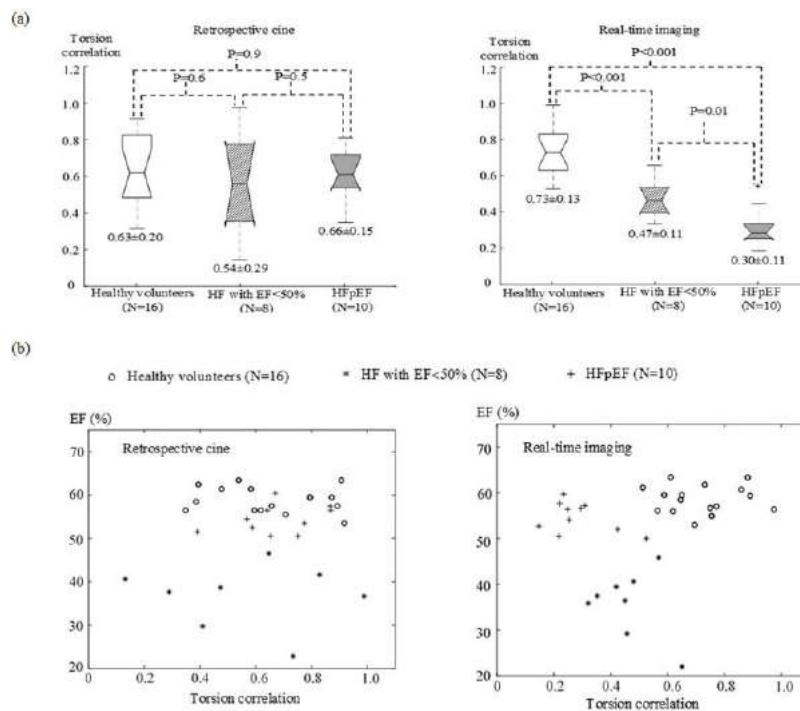




**Caption 2**

Figure 2. (a) Feature tracking examples with retrospective cine and real-time CMR. The basal and apical slices presented opposite circumferential motion due to twisting. (b) Correlation analysis in a healthy volunteer, a HF patient with EF<50%, and a patient with HFpEF. Three subjects presented considerable difference in correlation analysis with real-time CMR.

**Figure 3**



### Caption 3

Figure 3. (a) Box plots for torsion correlation measurements with ANOVA P values (above the boxes) and mean  $\pm$  standard deviation (below the boxes). (b) Scatter plots of EF against torsion correlation. The HFpEF patients and healthy volunteers were differentiated in the plots from real-time CMR while they were mixed in those from retrospective cine.

### Bibliographic References

1. Yancy CW, Jessup M, Bozkurt B, Butler J, Casey DE, Jr., Colvin MM, et al. 2017 ACC/AHA/HFSA Focused Update of the 2013 ACCF/AHA Guideline for the Management of Heart Failure: A Report of the American College of Cardiology/American Heart Association Task Force on Clinical Practice Guidelines and the Heart Failure Society of America. *Circulation* (2017) 136(6):e137-e61. Epub 2017/04/30. doi: 10.1161/CIR.0000000000000509. PubMed PMID: 28455343.
2. Leong DP, De Pasquale CG, Selvanayagam JB. Heart failure with normal ejection fraction: the complementary roles of echocardiography and CMR imaging. *JACC Cardiovasc Imaging* (2010) 3(4):409-20. Epub 2010/04/17. doi: 10.1016/j.jcmg.2009.12.011. PubMed PMID: 20394903.
3. Pedrizzetti G, Claus P, Kilner PJ, Nagel E. Principles of cardiovascular magnetic resonance feature tracking and echocardiographic speckle tracking for informed clinical use. *J Cardiovasc Magn Reson* (2016) 18(1):51. Epub 2016/08/27. doi: 10.1186/s12968-016-0269-7. PubMed PMID: 27561421; PubMed Central PMCID: PMC4500424.
4. Zhang S, Uecker M, Voit D, Merboldt K-D, Frahm J. Real-time cardiovascular magnetic resonance at high temporal resolution: radial FLASH with nonlinear inverse reconstruction. *Journal of Cardiovascular Magnetic Resonance* (2010) 12(1):39.
5. Bucciarelli-Ducci C, Flamm SD, Kim RJ, Nagel E.

Standardized cardiovascular magnetic resonance imaging (CMR) protocols: 2020 update.  
Journal of Cardiovascular Magnetic Resonance (2020) 22(1):1-18.

Speaker: Y. Li

Category: Heart Failure Preserved Ejection Fraction, Feature Tracking, Real Time

000167

## Highly Accelerated Free-Breathing Real-Time 2D Flow Imaging using Compressed Sensing and Shared Velocity Encoding

F. Xiong \* (1); N. jin (2); A. L. Emrich (3); S. R. Hall (3); J. M. Ruddy (3); J. Aldinger (4); G. Young (4); U. J. Schoepf (4); D. Giese (5); T. Emrich (4); A. Varga-Szemes (4)

(1) Cardiovascular mr r&d, Siemens Medical Solutions USA, Inc., Charleston, United States of America; (2) Cardiovascular mr r&d, Siemens Medical Solutions USA, Inc., Chicago, United States of America; (3) Department of surgery, Medical University of South Carolina, Charleston, United States of America; (4) Department of radiology and radiological science, Medical University of South Carolina, Charleston, United States of America; (5) Mr cardiovascular predevelopment, Siemens Healthcare GmbH, Erlangen, Germany

### Abstract

**Background:** 2D phase contrast (PC) MRI is an established clinical tool for evaluating cardiovascular blood flow. Conventional approaches often rely on retrospectively ECG-synchronized and segmented CINE acquisitions of multiple heartbeats with respiratory control, which leads to lower acquisition efficiency and restricted usage in cardiac arrhythmias [1]. As a promising alternative, 2D real-time (RT) PC MRI utilizes single-shot k-space data acquisition to overcome problems due to irregular heartbeats or poor respiratory control. However, the current RT techniques either suffer from poor temporal/spatial resolutions or require extensive offline reconstruction. In this study, we demonstrate the feasibility of a highly accelerated, free-breathing RT PC technique empowered by compressed sensing (CS) and shared velocity encoding (SVE) [2-4] which allows a scan time less than 5s and fast inline image reconstruction.

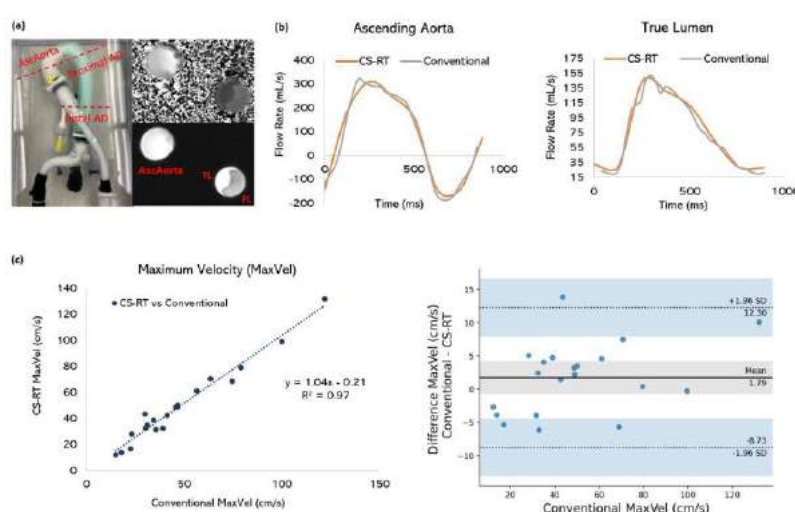
**Methods:** Phantom studies (n=8) were performed using a pulsatile flow phantom (80 bpm) with silicone models of Type B aortic dissection (AD) on a 3T clinical scanner (MAGNETOM Vida, Siemens Healthcare, Erlangen, Germany). The MRI protocol included conventional segmented (GRAPPA R=2, spatial resolution 2x2x6mm<sup>3</sup>, temporal resolution 35.2ms) and prototype CS-RT (CS R=8, spatial resolution 2.5x2.5x6mm<sup>3</sup>, temporal resolution 52ms) PC techniques. Through-plane flow measurements were done at three locations (ascending, proximal and distal descending aorta). Flow parameters including the maximum velocities (MaxVel) and flow rates (MaxFlow), and the total forward blood flow (Vol/min) were calculated with a commercial software (cvi42, Circle Cardiovascular Imaging). The same PC protocols were tested in healthy volunteers (n=4). The 2-tailed, paired t-tests and Bland-Altman analyses were used to evaluate for differences between flow parameters. Correlation between the two methods was assessed using linear regression with further evaluation using the intraclass correlation coefficient (ICC).

**Results:** CS-RT enabled similar flow quantification to conventional 2D flow MR both in-vitro and in-vivo with >80% reduction in scan time (2±1s vs 19±3s). Comparisons of the flow measurements at all locations in AD phantoms demonstrated an excellent correlation and agreement (MaxVel r: 0.97; ICC: 0.99, p<.001; MaxFlow r: 0.96; ICC: 0.99, p<.001; Vol/min r: 0.91; ICC: 0.97, p<.001). No significant difference was found between the two techniques (mean differences: MaxVel -1.79cm/s, p=0.15; MaxFlow 2.37ml/s, p=0.65; Vol/min -0.23l/min, p=0.21). In healthy volunteers, a similarly good correlation and agreement

(MaxVel r:0.93; ICC: 0.91,  $p<.001$ ; MaxFlow r: 0.88; ICC: 0.93,  $p<.001$ ; Vol/min r: 0.86; ICC: 0.92,  $p<.001$ ) were observed. However, CS-RT underestimated the maximum velocities within an acceptable margin [5] (mean differences: MaxVel -13.60cm/s (12.14%),  $p<0.001$ ; MaxFlow -45.47ml/s (12.46%),  $p=0.01$ ; and Vol/min 0.33l/min (7%),  $p=0.21$ ).

**Conclusions:** The highly accelerated CS-RT PC technique provides >80% scan time efficiency improvement and is feasible for evaluation of cardiovascular flow patterns without requiring breath-holding. Although CS-RT 2D flow slightly underestimates the maximum flow velocities, it allows for a quick flow assessment when arrhythmia or poor respiratory control is present.

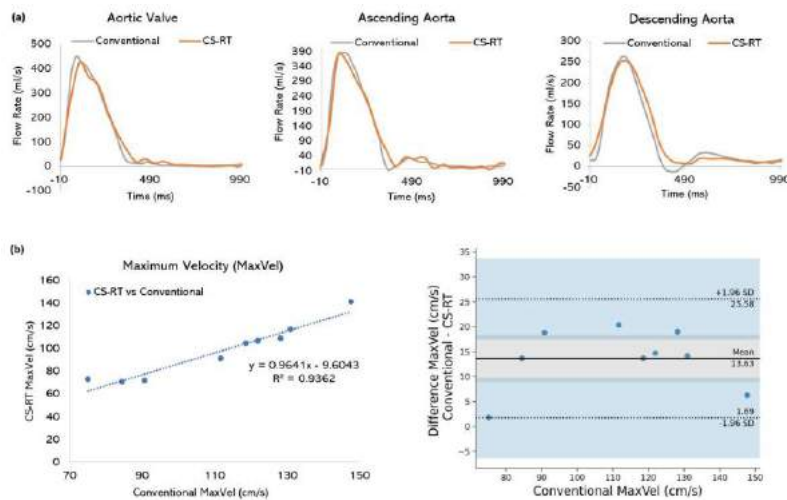
**Figure/Table 1**



**Caption 1**

Figure 1: Flow analysis in a pulsatile phantom with conventional and CS-RT 2D flow techniques. (a) Silicone aortic dissection (AD) model with typical 2D imaging planes at ascending aorta, proximal and distal AD, and the correspondent magnitude and phase images at proximal AD. (b) Representative flow curve in ascending aorta and true lumen. (c) Linear regression and Bland-Altman analyses comparing the maximum velocities.

**Figure/Table 2**



## Caption 2

Figure 2: Flow analysis in volunteers with conventional and CS-RT 2D flow techniques. (a) Representative flow curve in aortic valve, ascending and descending aorta. (b) Linear regression and Bland-Altman analyses comparing the maximum velocities.

## Bibliographic References

[5] Ma, L. E., Markl, M., Chow, K., Huh, H., Forman, C., Vali, A., Greiser, A., Carr, J., Schnell, S., Barker, A. J., & Jin, N. . Aortic 4d flow MRI in 2 minutes using compressed sensing, respiratory controlled adaptive K-space reordering, and Inline Reconstruction. *Magnetic Resonance in Medicine*, 81(6), 3675–3690. <https://doi.org/10.1002/mrm.27684> (2019)., [4] Greiser A, Forman C, Wetzl J, Tillmanns C, Stalder AF, Schmidt M, Zenge M, Mueller E; Clinical Evaluation and Optimization of Highly Accelerated 2D and 4D Phase Contrast Flow Imaging Applications using Sparse Sampling and Iterative Reconstruction; #6076 ISMRM 23 (2015)., [3] Greiser A., Zenge M., Schmidt M., Speier P., Mueller E.; Highly Accelerated Phase Contrast Imaging using Compressed Sensing and Iterative Reconstruction for High Resolution Short Breathhold Flow Acquisitions; #3851 Proc. ISMRM 22 (2014). , [2] Greiser A., Zenge M., Schmidt M., Gulsun A., Stalder A.F.; Application of Highly Accelerated Cartesian Phase Contrast Imaging Using Compressed Sensing and Iterative Reconstruction to Real-Time and Vector Encoded Flow Imaging; #3854 Proc. ISMRM 22 (2014). , [1] Sun, A., Zhao, B., Li, Y. et al. Real-time phase-contrast flow cardiovascular magnetic resonance with low-rank modeling and parallel imaging. *J Cardiovasc Magn Reson* 19, 19 (2017). <https://doi.org/10.1186/s12968-017-0330-1>

Speaker: F. Xiong

Category: Accelerated Imaging, Blood Flow, Free Breathing

000168

## Impact of pulmonary haemodynamics on exercise performance in patients after the arterial switch operation

E. Warmerdam \* (1); T. Takken, (2); H. van Assen (3); J. Westenberg, (3); P. Ooij, (4); G. Krings, (5); A. Roest, (6); F. Rijnberg, (7); H. Lamb, (3); M. Voskuil, (1); T. Leiner (8); H. Grotenhuis (5)

(1) Cardiology, UMC Utrecht, Utrecht, Netherlands; (2) Physiology, Wilhelmina Childrens Hospital / UMCU, Utrecht, Netherlands; (3) Radiology, Leiden University Medical Center (LUMC), Leiden, Netherlands; (4) Radiology, Wilhelmina Childrens Hospital / UMCU, Utrecht, Netherlands; (5) Pediatric cardiology, Wilhelmina Childrens Hospital / UMCU, Utrecht, Netherlands; (6) Pediatric cardiology, Leiden University Medical Center (LUMC), Leiden, Netherlands; (7) Cardiothoracic surgery, Leiden University Medical Center (LUMC), Leiden, Netherlands; (8) Radiology, UMC Utrecht, Utrecht, Netherlands

### Abstract

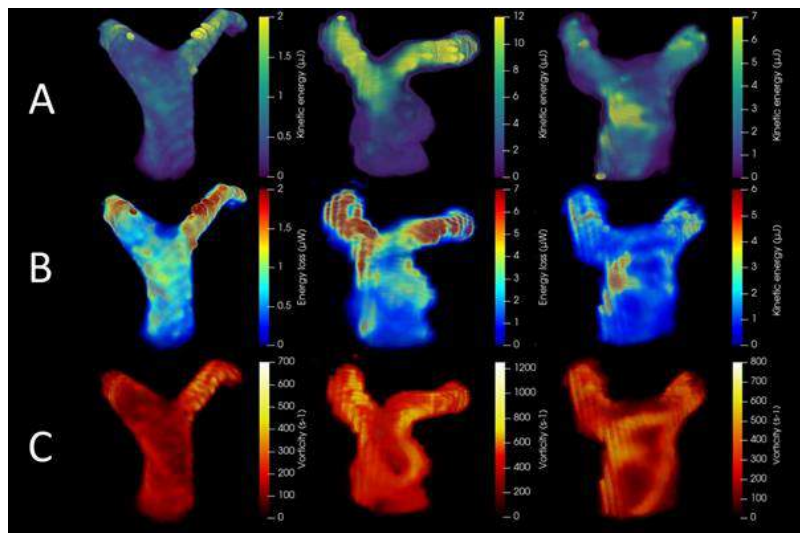
**Background** Pulmonary stenosis (PS) and decreased exercise capacity are common complications after the arterial switch operation (ASO) for transposition of the great arteries. Four-dimensional flow (4D flow) cardiac magnetic resonance (CMR) provides a comprehensive quantitative haemodynamic evaluation. We investigated the relation between pulmonary artery (PA) haemodynamics as measured with 4D flow CMR and exercise capacity after ASO.

**Methods** A prospective study in patients after ASO was performed between December 2018 and October 2020. All patients underwent cardiopulmonary exercise testing (CPET) and CMR, including 4D flow acquisition. From CPET, predicted peak oxygen uptake corrected for sex, age and weight (predVO<sub>2</sub>peak/kg) was calculated for each patient. Decreased exercise capacity was defined as predVO<sub>2</sub>peak/kg < 80%. 4D flow CMR was used to calculate energy loss, kinetic energy, helicity and vorticity in the main, right, and left PA.

**Results** A total of 36 patients were included with a mean age of 20±8 years. Decreased predVO<sub>2</sub>peak/kg was found in 42% of patients. In the main PA, energy loss was found to be moderately associated with predVO<sub>2</sub>peak/kg (p=0.0499). In the left PA, energy loss, kinetic energy, and vorticity were found to have a moderate association with predVO<sub>2</sub>peak/kg (p=0.0196, p=0.0283, p=0.0056, respectively). No associations were found between flow parameters in the right PA and predVO<sub>2</sub>peak/kg.

**Conclusion** A substantial number of TGA patients has a decreased exercise capacity, associated with abnormal 4D flow parameters in the LPA and MPA. Energy loss, kinetic energy and vorticity in the PAs of TGA patients are moderately associated with exercise capacity.

### Figure/Table 1



**Caption 1**

. Four-dimensional flow CMR results at peak-systole in the pulmonary arteries from three patients with transposition of the great arteries. Panel A shows a visual representation of the kinetic energy. Panel B shows a visual representation of the energy loss. Panel C shows a visual representation of vorticity, in the pulmonary arteries. In all three patients, there is similarity in the patterns of kinetic energy, energy loss and vorticity.

Speaker: E. Warmerdam

Category: 4D Flow, Exercise



000170

**Novel insights into in-utero arch morphology in suspected coarctation of the aorta: statistical shape analysis in 112 fetuses using three-dimensional fetal cardiac MRI**

M. van Poppel \* (1); U. Hermida (2); D. Lloyd (3); J. K. Steinweg (1); A. De Vecchi (2); R. Razavi (1); P. Lamata (2); K. Pushparajah (1)

(1) Cardiovascular imaging, King's College London, London, United Kingdom; (2) Biomedical engineering, King's College London, London, United Kingdom; (3) Perinatal imaging & health, Evelina London Children's Hospital, Westminster Bridge Road, London, United Kingdom

**Abstract**

**Background:** Coarctation of the aorta (CoA) is a common and potentially life-threatening heart defect. Antenatal diagnosis of CoA remains difficult with high false positive rates despite improvements in fetal echocardiography. Motion corrected three-dimensional (3D) fetal cardiac magnetic resonance imaging (CMR) is an adjunct imaging modality for antenatal diagnosis of cardiovascular anomalies [1] and has shown potential to improve antenatal prediction of duct-dependent CoA using morphological measurements [2]. It remains challenging however to fully capture the complexity of 3D arch geometry. The aim of this study was to apply novel statistical shape analysis techniques to 3D fetal CMR allowing objective and comprehensive assessment of the arch anatomy in-utero.

**Methods:** Between July 2015 and April 2021 women carrying a fetus with suspected CoA were offered fetal CMR examination, consisting of multiple two-dimensional single-shot fast spin echo sequences. Motion-corrected slice-volume registration [1] was used to generate high resolution 3D volumes of which subsequently 3D meshes were extracted using semi-automatic segmentation and manual refinements of the region of interest. Cases with severe congenital diaphragmatic hernia or abnormal ventriculoarterial connection were excluded from further analysis. Arterial duct (AD) and aortic centreline points and their maximum inscribed radius were automatically extracted and used, with a principal component analysis (PCA), to build a statistical shape model capturing relevant shape variations. A linear discriminant analysis [3] was performed to find the optimal anatomical axis of variation to distinguish between CoA and false positive (FP) cases, in which each case is represented by a single score (i.e. Z-score).

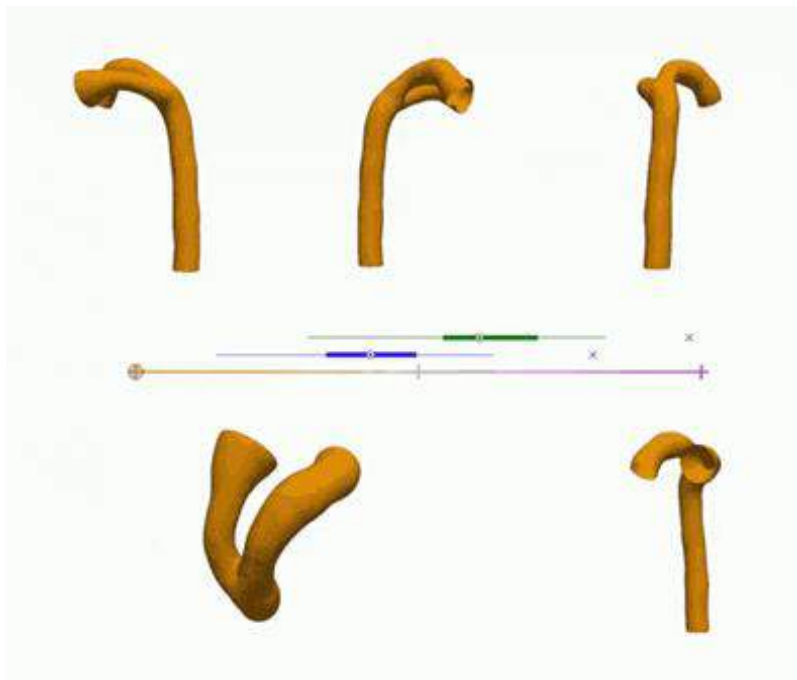
**Results:** In total 112 patients (median gestational age 32 weeks, IQR 31-33) were included for statistical shape analysis. Additional minor heart anomalies were suspected in 81/112 (72%). Outcome data was available for 106/112 patients, and duct-dependent CoA requiring surgical repair in neonatal period was confirmed in 43 (41%), one fetus in the FP group developed late CoA. PCA resulted in the first 10 anatomical modes explaining 86% of shape variation in the population. Their optimal linear combination (based on 106 cases) classified cases with an AUC of 0.89. In addition to expected vessel size differences and proximal displacement of isthmus, the extreme shapes give detailed insight in the course and position of the aortic

isthmus, AD and descending aorta (Figure 1) e.g., FP cases tend to have tortuous AD before it inserts into the side of the isthmus/descending aorta compared to CoA cases where the isthmus insertion is seen into the superior aspect of an unbent AD.

**Conclusion:** This study demonstrated feasibility of applying a novel statistical shape analysis pipeline to fetal CMR data allowing detailed exploration of arch anatomy in-utero providing novel insights into the complex spatial relationship of the great arteries, with potential to improve antenatal diagnosis of fetuses with suspected neonatal CoA.

*\*the first two authors have contributed equally to this work and share first authorship. The last two authors share last authorship.*

**Figure/Table 1**



**Caption 1**

Axis of anatomical variation that best discriminates between confirmed CoA and FP cases. Boxplots represent the CoA (green) and FP (blue) Z-score distributions across the axis. Orange cross and 3D shape show -3SD from the mean shape (grey cross); purple cross and shapes +3SD.

### **Bibliographic References**

3. Varela M, Bisbal F, Zacur E, Berruezo A, Aslanidi OV, Mont L, Lamata P. Novel computational analysis of left atrial anatomy improves prediction of atrial fibrillation recurrence after ablation. *Front Physiol* 2017;8(FEB):68, 2. Lloyd DFA, van Poppel MPM, Pushparajah K, Vigneswaran TV, Zidere V, Steinweg J, van Amerom JFP, Roberts TA, Schulz A, Charakida M, Miller O, Sharland G, Rutherford M, Hajnal JV, Simpson JM, Razavi R. Analysis of 3-Dimensional Arch Anatomy, Vascular Flow, and Postnatal Outcome in Cases of Suspected Coarctation of the Aorta Using Fetal Cardiac Magnetic Resonance Imaging. *Circ Cardiovasc Imaging*. 2021 Jul;14(7):e012411, 1. Lloyd DFA, Pushparajah K, Simpson JM, van Amerom JFP, van Poppel MPM, Schulz A, Kainz B, Deprez M, Lohezic M, Allsop J, Mathur S, Bellsham-Revell H, Vigneswaran T, Charakida M, Miller O, Zidere V, Sharland G, Rutherford M, Hajnal JV, Razavi R. Three-dimensional visualisation of the fetal heart using prenatal MRI with motion-corrected slice-volume registration: a prospective, single-centre cohort study. *Lancet*. 2019 Apr 20;393(10181):1619-1627

Speaker: M. van Poppel

Category: Coarctation, Fetal, 3D

**000171**

**Identifying prognostic CMR features throughout the cardiac cycle using time-resolved machine learning feature extraction**

S. Alabed \* (1); J. Uthoff (2); P. Garg (1); F. Alandejani (1); K. Dwivedi (1); A. Rothman (1); R. Condliffe (1); J. Wild (1); D. Kiely (1); H. Lu (2); A. Swift (1)

(1) Infection, immunity & cardiovascular disease, The University of Sheffield, Sheffield, United Kingdom; (2) Computer science, The University of Sheffield, Sheffield, United Kingdom

**Abstract**

**Background**

Pulmonary arterial hypertension (PAH) is a rare but serious disease associated with high mortality if left untreated (1). Evaluating prognosis is key to identifying high-risk patients and optimising their management strategies (2,3). A recent machine learning model using multilinear principal component analysis (MPCA) successfully detected PAH features on CMR (4). MPCA is a linear and transparent feature extraction method that allows visualisation of the extracted features and therefore is interpretable. This study aims to assess the prognosis in PAH through features extracted using MPCA throughout the cardiac cycle.

**Methods**

723 patients were included; 516 in the training and 207 in the validation cohort. Patients were 74% female aged  $59 \pm 16$  years and included PAH secondary to connective tissue disease 46%, idiopathic PAH 27%, congenital heart disease 16% and other subtypes (11%).

Short-axis and 4-chamber cine imaging were used in machine learning after registering images to each other using three anatomical landmarks, masking surrounding tissues, and downscaling image size as described previously (5). The prediction model was trained through 10-fold cross-validation on the development cohort (n=516). For each split during training, MPCA features were extracted and ranked for prognostic capability using Fisher's Discriminant Analysis in a stepwise feature inclusion method. Performance was tested using the tuning-set (n ~50) of cases. The feature set with the highest average fold-performance was used to train the final support vector machines on the development cohort. This model was then applied to the left out validation cohort (n=207). Trained features were visualised to obtain spatially relevant feature maps. To visually inspect the impact of specific regions on high- and low-risk of mortality prediction, a two-step procedure of thresholding and clustering was implemented. Voxels containing high absolute values of MPCA features were thresholded and overlaid on individual subjects' original CMR scans.

**Results**

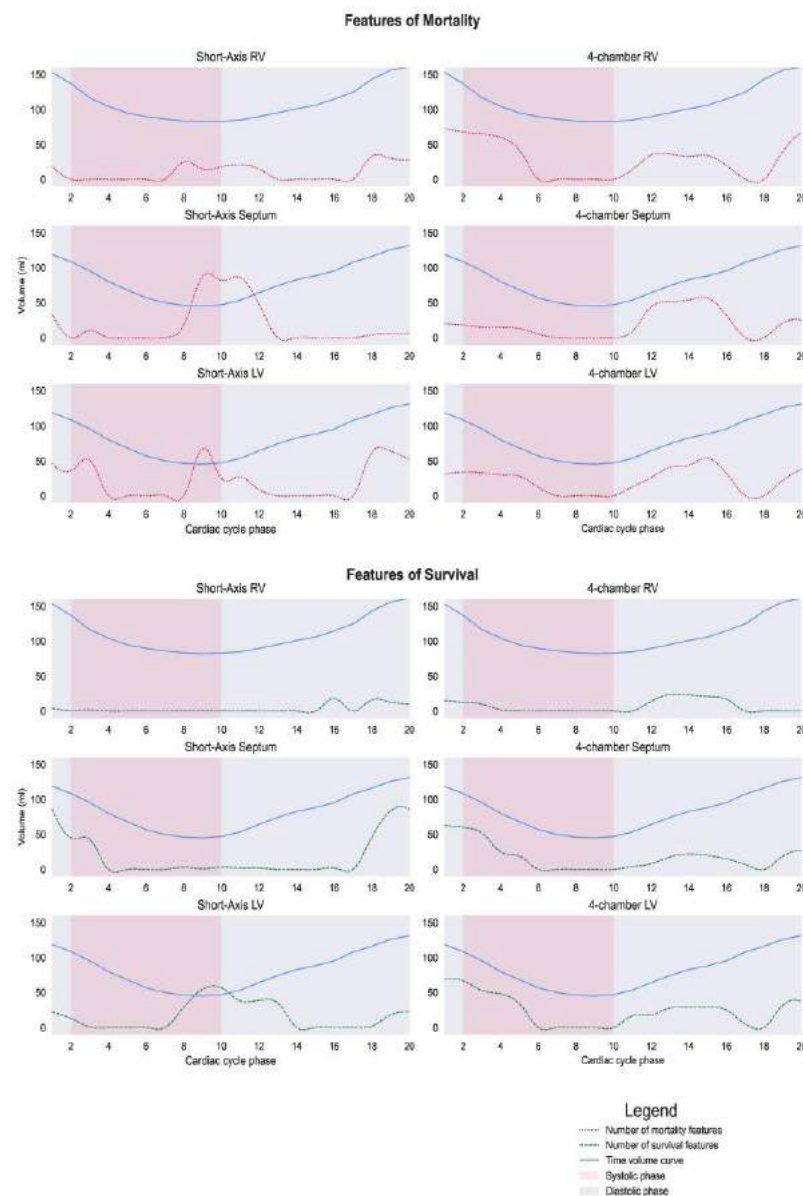
The one-year mortality rate in the validation cohort was 10%, with an overall mortality rate of 29% over the total follow-up period. Univariate Cox regression analysis of the combined short-axis and 4-chamber MPCA-based predictions was statistically significant (Hazard Ratios 2.1, 95% CI 1.3, 3.4,  $p = 0.002$ ). The c-index of the MPCA model was  $c = 0.72$ ,

indicating good predictive performance compared to standard CMR RV ejection fraction ( $c = 0.58$ ) and RV end-systolic volume ( $c = 0.65$ ). The MPCA features extracted on the short-axis views showed that abnormalities in the interventricular septum (end-systole phase) and LV chamber (end-diastole phase) indicated a higher risk of mortality (Figure 1 and 2). On 4-chamber views, the most predictive mortality features were at the RV during early systole. Parameters predicting survival were normal LV and interventricular septum in diastole on short-axis and 4-chamber images; the RV was a poor predictor of survival.

## Conclusion

The MPCA-based machine learning is an explainable approach that allows visualisation of cardiac features associated with both one-year mortality and with survival. The time-resolved assessment helped to understand the temporal and anatomical relevance of the extracted features throughout the cardiac cycle.

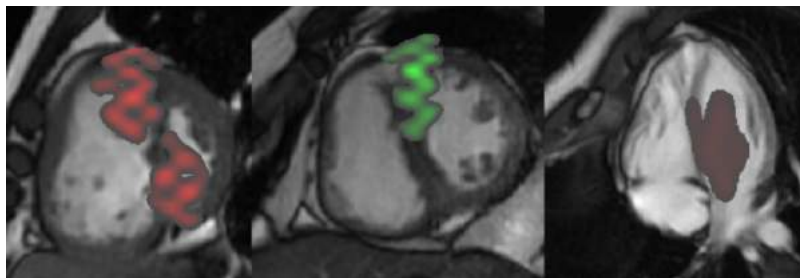
**Figure/Table 1**



### Caption 1

Time-resolved cardiac features of poor prognosis and survival throughout the cardiac cycle on short-axis and 4-chamber views. The most prognostic cardiac features were at the septum at end-systole and early-diastole on both the short-axis and 4-chamber views, RV during systole and LV during diastole on 4-chamber views.

### Figure/Table 2



### Caption 2

Visualisation of mortality and survival features on short-axis and 4-chamber images in three different patients with PAH. Left image: Septum and LV features of high risk of mortality at end-systole. Middle image: Features of survival visualised at the septum at end-diastole. Right image: 4-chamber view showing high-risk features in the septum and LV in diastole.

### Bibliographic References

1) Kiely DG, Elliot CA, Sabroe I, Condliffe R. Pulmonary hypertension: diagnosis and management. *BMJ* 2013; 346: f2028, 2) Kiely DG, Levin D, Hassoun P, et al. EXPRESS: Statement on imaging and pulmonary hypertension from the Pulmonary Vascular Research Institute (PVRI). *Pulmonary Circulation* 2019; : 2045894019841990., 3) Galiè N, Humbert M, Vachiery J-L, et al. 2015 ESC/ERS Guidelines for the diagnosis and treatment of pulmonary hypertension: The Joint Task Force for the Diagnosis and Treatment of Pulmonary Hypertension of the European Society of Cardiology (ESC) and the European Respiratory Society (ERS): Endorsed by: Association for European Paediatric and Congenital Cardiology (AEPC), International Society for Heart and Lung Transplantation (ISHLT). *Eur Respir J* 2015; 46: 903–75., 4) Swift AJ, Lu H, Uthoff J, et al. A machine learning cardiac magnetic resonance approach to extract disease features and automate pulmonary arterial hypertension diagnosis. *European Heart Journal Cardiovascular Imaging* 2021; Vol. 22, No.

2, pp. 236–245. DOI:10.1093/ehjci/jeaa001., 5) Uthoff J, Alabed S, Swift AJ, Lu H. Geodesically smoothed tensor features for pulmonary hypertension prognosis using the heart and surrounding tissues. Medical Image Computing and Computer Assisted Intervention – MICCAI 2020. MICCAI 2020. Lecture Notes in Computer Science, vol 12262. Springer, Cham. [https://doi.org/10.1007/978-3-030-59713-9\\_25](https://doi.org/10.1007/978-3-030-59713-9_25)

Speaker: S. Alabed

Category: Prognosis, Pulmonary Hypertension, Image Analysis

000179

## Multilevel Evaluation of Four Convolutional Neural Network Architectures for Ventricular Function Quantification from Short-Axis Cine Images

C. Ammann \* (1); T. Hadler (1); J. Gröschel (1); J. Schulz-Menger (1)

(1) Working group on cardiovascular magnetic resonance, Charité – Universitätsmedizin Berlin, ECRC, MDC, Helios Klinikum Berlin Buch, DZHK, Berlin, Germany

### Abstract

**Background:** CMR is accepted as the gold standard for the quantification of cardiac function, volume and mass, for which precise contouring of the heart chambers is essential. Recently, various convolutional neural networks (CNNs) have shown great potential at automating time-consuming medical segmentation tasks. CNNs have demonstrated that they can achieve an overall accuracy in the range of inter-observer errors for cardiac short-axis quantification with respect to clinical parameters. However, at the same time they make human atypical mistakes that are anatomically implausible and damage their trustworthiness. Segmentation results from CNNs and human experts alike vary the most for the basal and apical slices.

**Aim:** This work aims to provide a detailed quantitative and qualitative assessment of the performance of four popular CNN architectures.

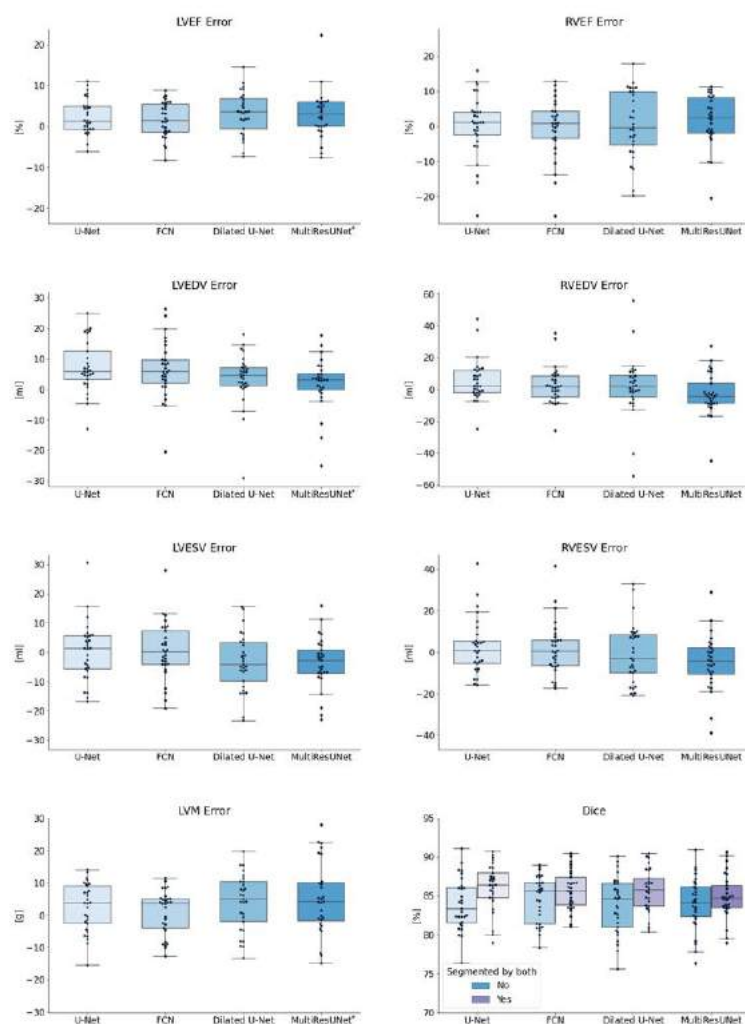
**Methods:** Our implementations of the U-Net, FCN, Dilated U-Net and MultiResUNet were trained on short-axis bSSFP cine images (1.5T Avanto fit, Siemens) in end-diastole of 117 patients from the clinical routine that have been manually segmented by an experienced reader. The networks share comparable hyperparameters and were trained for 1.000 epochs each using the average of binary cross-entropy and dice loss. When designing the training pipeline, emphasis was put on extensive data augmentation and on retaining subpixel information of the ground truth contours by training on double resolution and augmenting the contour polygons before generating the pixel masks. Segmentation results were evaluated against the original expert contours for 29 test cases using an unpublished software “Lazy Luna”, which allows for an automated, quantitative assessment of clinical results, a comparison of the underlying segmentations by metrics as well as a visualization of segmentation differences for qualitative analysis.

**Results:** We found no relevant differences between the four investigated CNNs in terms of quantitative clinical results and segmentation metrics (Figure 1, Table 2). Overall, the outcomes show good agreement with the manual results, however outliers illustrate significant differences between all four CNNs and the manual segmentation for selected slices. This includes false positives and negatives for the segmentation decision as well as poor Dice values, indicating segmentation difficulty. Qualitative analysis revealed recurring errors made by all networks in basal and apical slices on challenging cases, where the partial volume effect, difficult detection of valves, and poor contrast due to apical fat complicate an exact and reproducible delineation of the cavity. Visual backtracking of these errors allowed us to characterize segmentation mistakes (Figure 3). Modifications to CNN architecture, such as stepwise upsampling and skip connections, dilated convolutions or multi-residual blocks and paths, added no relevant value to the segmentation performance for our dataset.



Conclusion: Multilevel evaluation of CNN performance revealed comparable quantitative results as well as similar qualitative segmentation errors for all networks. Eliminating anatomically implausible segmentations and failures is vital to increase acceptance and confidence in CNNs in clinical routine.

**Figure/Table 1**



\*One slice for the left ventricle in end-diastole was excluded for the MultiResUNet due to a failed segmentation.

**Caption 1**

Boxplots of clinical parameter errors and Dice values for all test cases showing quantile 1, median and quantile 3 compared to the expert contours. The last plot offers two Dice boxplots per network, one for the Dice values for all images, and another for Dice values restricted to images segmented by both reader and network.

**Figure/Table 2**

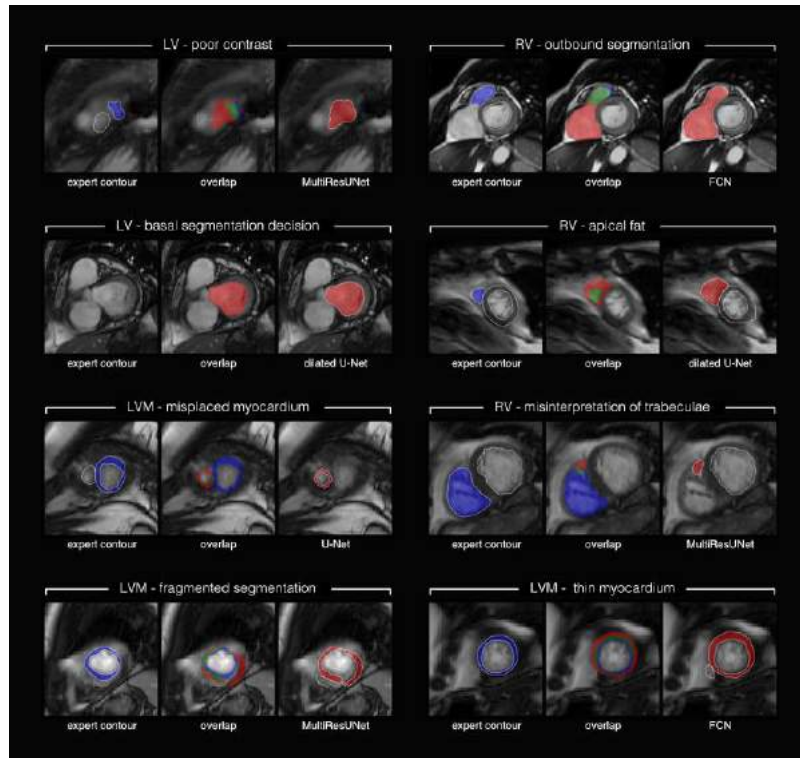
	U-Net mean ( $\pm$ o)	FCN mean ( $\pm$ o)	Dilated U-Net mean ( $\pm$ o)	MultiResUNet mean ( $\pm$ o)
<b>LVEF (error) [%]</b>	2.4 $\pm$ 4.3*	1.6 $\pm$ 4.3*	3.2 $\pm$ 5.3*	3.4 $\pm$ 6.2*
<b>LVEDV (error) [ml]</b>	7.4 $\pm$ 8.5*	6.4 $\pm$ 9.4*	3.4 $\pm$ 8.6*	5.1 $\pm$ 19.1
Dice (all slices) [%]	91.1 $\pm$ 21.8	90.8 $\pm$ 22.6	92.1 $\pm$ 20.1	92.1 $\pm$ 20.4
Dice (segmented by both) [%]	95.2 $\pm$ 5.2	95.3 $\pm$ 5.2	94.8 $\pm$ 8.3	95.3 $\pm$ 6.1
Hd [mm]	3.2 $\pm$ 1.6	3.4 $\pm$ 3.3	3.3 $\pm$ 2.1	3.2 $\pm$ 2.2
<b>LVESV (error) [ml]</b>	0.2 $\pm$ 10.0	0.5 $\pm$ 9.8	-3.5 $\pm$ 9.7	-3.7 $\pm$ 8.8*
Dice (all slices) [%]	88.5 $\pm$ 24.0	87.3 $\pm$ 25.4	87.4 $\pm$ 25.0	89.5 $\pm$ 22.1
Dice (segmented by both) [%]	91.4 $\pm$ 9.8	90.7 $\pm$ 11.7	88.7 $\pm$ 16.0	90.9 $\pm$ 11.7
Hd [mm]	4.0 $\pm$ 2.6	4.3 $\pm$ 3.8	4.9 $\pm$ 5.8	4.0 $\pm$ 2.6
<b>LVM (error, in ED) [g]</b>	2.5 $\pm$ 7.5	0.9 $\pm$ 6.9	3.9 $\pm$ 8.7*	7.9 $\pm$ 18.9*
Dice (all slices) [%]	79.7 $\pm$ 23.1	79.0 $\pm$ 24.2	79.8 $\pm$ 23.3	80.5 $\pm$ 22.6
Dice (segmented by both) [%]	81.2 $\pm$ 12.0	80.5 $\pm$ 14.0	80.0 $\pm$ 15.3	81.3 $\pm$ 12.7
<b>RVEF (error) [%]</b>	0.2 $\pm$ 8.9	-0.5 $\pm$ 8.5	0.5 $\pm$ 9.6	1.8 $\pm$ 7.3
<b>RVEDV (error) [ml]</b>	5.4 $\pm$ 13.2*	2.5 $\pm$ 11.8	1.5 $\pm$ 19.4	-2.9 $\pm$ 13.3
Dice (all slices) [%]	88.7 $\pm$ 23.7	89.0 $\pm$ 22.6	87.5 $\pm$ 25.2	87.7 $\pm$ 24.8
Dice (segmented by both) [%]	91.9 $\pm$ 10.0	91.6 $\pm$ 9.9	91.3 $\pm$ 11.0	91.5 $\pm$ 9.3
Hd [mm]	6.5 $\pm$ 9.0	6.9 $\pm$ 9.3	6.6 $\pm$ 7.7	6.5 $\pm$ 7.8
<b>RVESV (error) [ml]</b>	2.6 $\pm$ 13.4	1.7 $\pm$ 12.8	-0.8 $\pm$ 14.5	-5.0 $\pm$ 13.3
Dice (all slices) [%]	83.0 $\pm$ 29.8	84.3 $\pm$ 27.6	84.0 $\pm$ 28.5	84.1 $\pm$ 27.9
Dice (segmented by both) [%]	85.5 $\pm$ 15.2	83.9 $\pm$ 17.7	85.5 $\pm$ 15.6	82.9 $\pm$ 19.1
Hd [mm]	9.4 $\pm$ 11.5	9.4 $\pm$ 11.6	8.7 $\pm$ 10.5	9.5 $\pm$ 10.5
<b>Segmentation decision precision<sup>1</sup> [%]</b>	95.4	95.4	96.5	97.2
<b>Segmentation decision recall<sup>2</sup> [%]</b>	96.2	97.2	95.7	95.6

Legend: LVEF: left ventricular ejection fraction, LVEDV: left ventricular end-diastolic volume, LVESV: left ventricular end-systolic volume, LVM: left ventricular myocardial mass, RVEF: right ventricular ejection fraction, RVEDV: right ventricular end-diastolic volume, RVESV: right ventricular end-systolic volume, Hd: Hausdorff distance, <sup>1</sup>precision: correctly segmented / (correctly segmented + incorrectly segmented), <sup>2</sup>recall: correctly segmented / (correctly segmented + incorrectly not segmented), \*p < 0.05

## Caption 2

Comparison of the four evaluated CNN architectures with respect to clinical parameters, segmentation metrics and segmentation decision metrics. Best results underlaid in blue.

Figure 3



### **Caption 3**

Qualitative comparison of segmentation results for challenging examples. Blue area: manual segmentation, red area: network segmentation, green area: segmentation agreement.

### **Bibliographic References**

Bai W, Sinclair M, Tarroni G, Oktay O, Rajchl M, Vaillant G, et al. Automated cardiovascular magnetic resonance image analysis with fully convolutional networks. *J Cardiovasc Magn Reson.* 2018., Sander J, de Vos BD, Isgum I. Automatic segmentation with detection of local segmentation failures in cardiac MRI. *Sci Rep.* 2020., Bernard O, Lalande A, Zotti C, Cervenansky F, Yang X, Heng PA, et al. Deep Learning Techniques for Automatic MRI Cardiac Multi-Structures Segmentation and Diagnosis: Is the Problem Solved? *IEEE Trans Med Imaging.* 2018., Schulz-Menger J, Bluemke DA, Bremerich J, Flamm SD, Fogel MA, Friedrich MG, et al. Standardized image interpretation and post-processing in cardiovascular magnetic resonance - 2020 update : Society for Cardiovascular Magnetic Resonance (SCMR): Board of Trustees Task Force on Standardized Post-Processing. *J Cardiovasc Magn Reson.* 2020.

Speaker: C. Ammann

Category: Segmentation, Ventricular Function, Image Analysis

000180

## **Non-ECG-triggered, free-breathing myocardial T1, T2, T2\*, and fat-fraction mapping with MR Multitasking**

T. Cao \* (1); N. Wang (1); H.-L. Lee, (1); X. Mao (1); Y. Xie, (1); A. Christodoulou (1); D. Li (1)

(1) Biomedical imaging research institute, Cedars-Sinai Medical Center, Los Angeles, United States of America

### **Abstract**

#### **Background**

Myocardial T1, T2, and T2\* mapping can detect fibrosis, edema, and iron overload, respectively<sup>1</sup>. Fat-fraction (FF) is a biomarker for chronic myocardial infarction and nonischemic cardiomyopathies. Comprehensive quantification of the parameters is appealing for myocardial tissue characterization and risk assessment. However, it typically requires four separate breath-holding and ECG-triggered scans, resulting in long scan time, potential image misregistration, and patient fatigue. To overcome these limitations, we have developed a free-breathing, non-ECG-triggered technique for simultaneous myocardial T1, T2, T2\*, and FF mapping based on MR Multitasking framework<sup>2</sup> and evaluated its performance against reference methods.

#### **Methods**

The pulse sequence (Fig. 1) includes hybrid T2prep/IR (T2-IR) preparation modules with different preparation durations, followed by radial FLASH readout modules. Acquisitions alternate between a training data readout at the 0° spoke and multi-echo imaging data readouts with golden angle increments. A variable TR (VTR) approach collects only a single echo for training data, preserving temporal resolution and imaging efficiency (Fig. 1B).

Based on the MR Multitasking framework<sup>2</sup>, the underlying image is modeled as a high dimensional tensor with two spatial dimensions and separate T2-IR prep duration, inversion time, echo time, cardiac motion, and respiratory motion dimensions. Spatiotemporal correlation allows accelerated acquisition and efficient reconstruction of the entire high-dimensional image.

Ten healthy volunteers were imaged on a 3T scanner (MAGNETOM Vida, Siemens Healthcare). Multitasking parameters included FA=5°, FOV=270x270mm<sup>2</sup>, slice thickness=8mm, in-plane resolution=1.7x1.7mm<sup>2</sup>, TR/TE1/ΔTE=16.6ms/1.6ms/1.3ms for imaging data (11 echoes), TR/TE=3.6ms/1.6ms for training data, 3 short-axis slices, scan time=2.5min/slice. Reference T1 maps with MOLLI, T2 maps with T2-prep FLASH, T2\* maps with multi-echo GRE (FA=20°), and FF maps with 6-point Dixon (FA=5°) were acquired at diastole and end-expiration. Reference and Multitasking scans were performed twice at the mid-ventricular slice to assess repeatability.

#### **Results and Discussion**

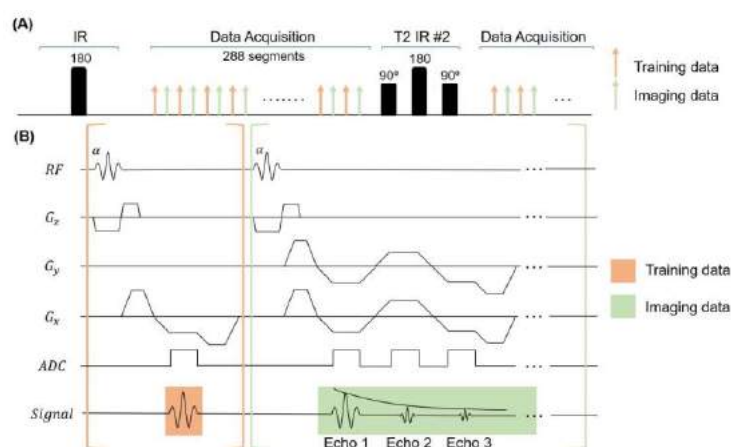
Fig. 2A shows mapping results in a representative healthy volunteer. The proposed technique produced co-registered maps resembling reference maps. Average values in each of the AHA 16 segments are in Fig. 2B. Spatial homogeneity was quantified by root-mean-square (RMS) inter-segment standard deviation (ISSD), which indicated little spatial variability in T1 (<90 ms), T2 (<4 ms), and FF (<6 %) maps. Both methods revealed low T2\* values in the infero-lateral segment, which could be related to susceptibility artifacts. Paired t-tests in Fig 2C indicated small but statistically significant differences in T1 and T2 measurements, yet Multitasking measurements are still close to previous literature range<sup>3-5</sup> (T1: 1100-1314 ms, T2: 38-46 ms, T2\*: 20.5-24 ms, FF: 1-1.5 %). Bland-Altman plots in Fig 2D show good limits of agreement.

The repeatability measurements for both methods are shown in Fig. 3A-B. The Bland-Altman plots for Multitasking repeated measurements are in Fig. 3C. Both methods demonstrated very low RMS within-segment standard deviation (WSSD), indicating good repeatability.

## Conclusion

With a single 2.5-min acquisition, our proposed technique achieves simultaneous T1, T2, T2\*, and FF mapping without breath-hold or ECG-triggering. Further clinical validation is warranted.

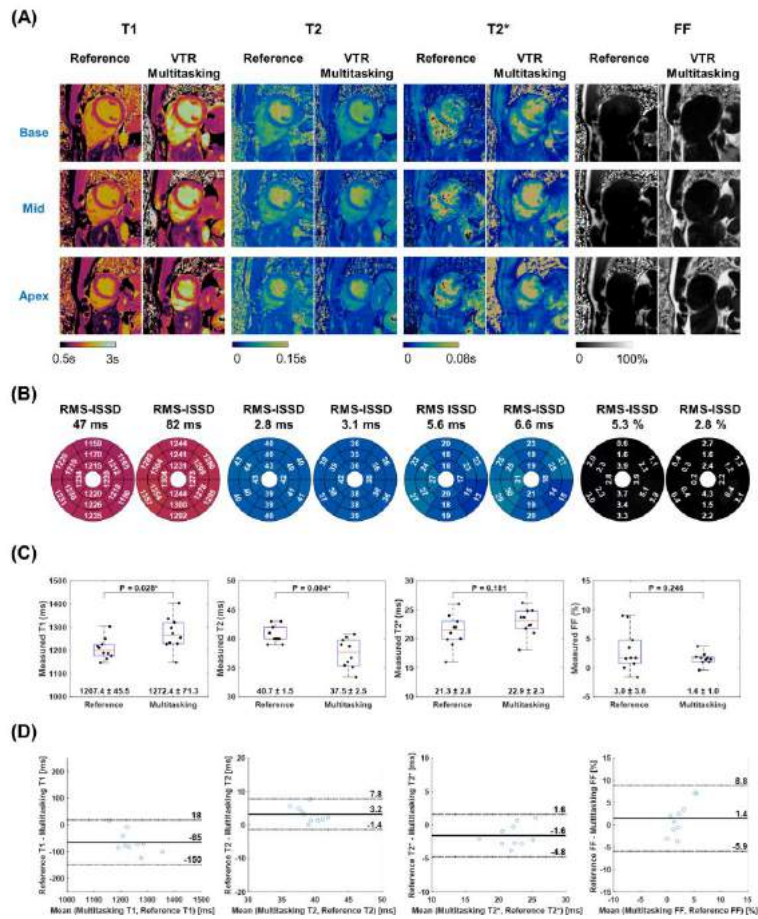
## Figure/Table 1



## Caption 1

Figure 1. Sequence diagram. Hybrid T2IR preparation modules with different preparation times are followed by radial multi-echo FLASH readout modules. Acquisition alternates between a short-TR, single-echo training data readout and a longer-TR, multi-echo imaging data readout module.

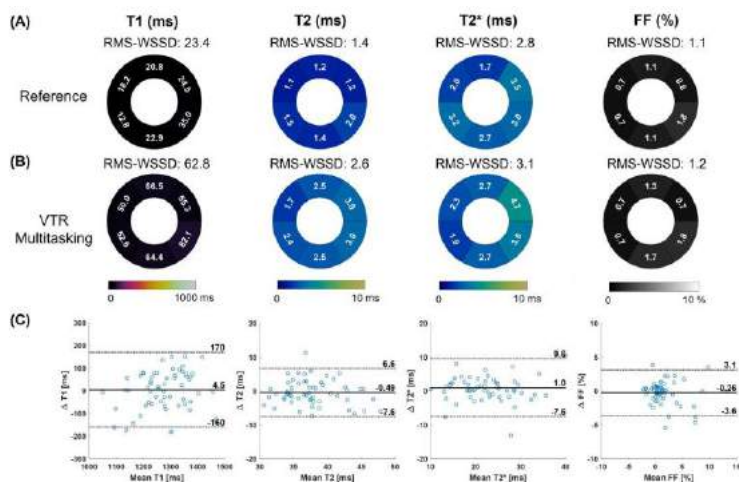
## Figure/Table 2



**Caption 2**

Figure 2. (A) Reference and multitasking maps on a healthy volunteer. (B) The average bullseye plot for parametric maps. (C) Paired t-test for different methods. (D) Bland-Altman plots for different methods.

**Figure 3**



### Caption 3

Figure 3. (A) Bullseye plot for reference measurement repeatability. (B) Bullseye plot for Multitasking measurement repeatability. (C) Bland-Altman plot for Multitasking measurement repeatability.

### Bibliographic References

1. Ugander M, Bagi PS, Oki AJ, Chen B, Hsu LY, Aletras AH, Shah S, Greiser A, Kellman P, Arai AE. Myocardial edema as detected by pre-contrast T1 and T2 CMR delineates area at risk associated with acute myocardial infarction. *JACC: Cardiovascular Imaging*. 2012 Jun;5(6):596-603.
5. Jaubert O, Cruz G, Bustin A, Schneider T, Lavin B, Koken P, Hajhosseiny R, Doneva M, Rueckert D, Botnar RM, Prieto C. Water-fat Dixon cardiac magnetic resonance fingerprinting. *Magnetic resonance in medicine*. 2020 Jun;83(6):2107-23.
4. Roy C, Slimani A, de Meester C, Amzulescu M, Pasquet A, Vancraeynest D, Vanoverschelde JL, Pouleur AC, Gerber BL. Age and sex corrected normal reference values of T1, T2 T2\* and ECV in healthy subjects at 3T CMR. *Journal of Cardiovascular Magnetic Resonance*. 2017 Dec;19(1):1-2.
3. von Knobelsdorff-Brenkenhoff F, Prothmann M, Dieringer MA, Wassmuth R, Greiser A, Schwenke C, Niendorf T, Schulz-Menger J. Myocardial T1 and T2 mapping at 3T: reference values, influencing factors and implications. *Journal of Cardiovascular Magnetic Resonance*. 2013 Dec;15(1):1-1.
2. Christodoulou AG, Shaw JL, Nguyen C, Yang Q, Xie Y, Wang N, Li D. Magnetic resonance multitasking for motion-resolved quantitative cardiovascular imaging. *Nature biomedical engineering*. 2018 Apr;2(4):215-26.

Speaker: T. Cao

Category: Parametric Mapping, Free Breathing, Rapid Imaging

000183

## The impact of gestational diabetes on the myocardium

S. Thirunavukarasu \* (1); A. Faiza (2); A. Chowdhary (1); N. Jex (1); H. Xue (3); P. Swoboda (1); P. Kellman (3); J. Greenwood (4); S. Plein (4); T. Everett (2); E. Scott (5); E. Levelt (1)

(1) leeds institute of cardiovascular and metabolic medicine, University of Leeds, Leeds, United Kingdom; (2) Fetal medicine, Department of Fetal Medicine, Leeds, United Kingdom; (3) National institutes of health, National Heart Lung & Blood: Sloand Elaine M MD, Bethesda, United States of America; (4) Licamm, Leeds institute of Cardiovascular and Metabolic Medicine, Leeds District, UK, United Kingdom; (5) Department of clinical and population science, Leeds Institute of Cardiovascular and metabolic medicine, Leeds, United Kingdom

### Abstract

**Background-** Gestational diabetes (GDM) is associated with an increased risk of cardiovascular (CV) mortality and morbidity in later life. In women with pregnancies complicated by GDM, pregnancy-associated cardiometabolic stresses may play an important role in the developmental programming of CV disease in later life both for the women and the offspring. The magnitude of maternal myocardial changes in structure, function and tissue characteristics or energetics with the onset of GDM has not been characterized.

**Objectives-** We sought to investigate if women with GDM exhibit adverse cardiac alterations in myocardial energetics, function or tissue characteristics and peripheral endothelial function which might make them more susceptible to adverse CV events in later life.

**Methods-** Thirty-nine healthy pregnant (HP) women, thirty women with GDM (primigravida singleton pregnancies for all), and fifteen age-matched nulliparous healthy female controls were recruited. Participants underwent 31phosphorus magnetic resonance spectroscopy (31P-MRS) and cardiovascular magnetic resonance (cine imaging, velocity-encoded mitral in-flow imaging, T1 mapping) (CMR) at 3T.

**Results-** Clinical and biochemical characteristics are provided in Table-1, CMR/31P-MRS results in Table-2. Plasma triglyceride and insulin levels were higher, and hemoglobin was lower in both pregnancy groups. Despite the similar gestational age, the BMI was significantly higher in the GDM group compared the HP. There were no significant differences in blood pressure measurements, NTproBNP, or glucose levels between the three groups. The mean resting heart rate was higher in the two pregnancy groups compared to nulliparous controls (GDM:91±14bpm, HP:86±23bpm, Controls:61±9bpm, p=0.001). The GDM group showed significant reductions in myocardial energetics (GDM:1.9±0.6, HP:2.5±0.5, Controls:2.7±0.5; p<0.001) and significant increases in left ventricular mass (GDM:102±19g, HP:88±16g, Controls:82±11g, p=0.0006) compared to HP and nulliparous controls. Moreover, across the two pregnant groups, left-ventricular ejection fraction (GDM:57±6%, HP:60±5%, Controls:62±4%, p=0.02) and global longitudinal strain (GDM: -18±3%, HP: -20±3%, Controls: -21±2%, p=0.03) were only significantly reduced in the GDM group compared to nulliparous controls. Both pregnancy groups exhibited similarly higher mitral inflow E/A ratio compared to nulliparous controls. Myocardial native T1 was also similarly increased in both pregnancy groups (GDM:1308±38ms, HP:1326±34ms,



Controls:  $1298 \pm 47$  ms;  $p=0.04$ ). There were significant correlations of the PCr/ATP with LVEF ( $r=0.34$ ,  $p=0.02$ ) and with GLS ( $r=0.26$ ,  $p=0.05$ ).

**Conclusions-** This study has demonstrated for the first time that GDM is associated with a significant increase in LV mass and significant reductions in cardiac energetics, strain and systolic function. These adverse phenotypic features may be important components of the worsened CV outcomes in women with GDM in the longer term. Importantly, this study showed that CMR was well-tolerated in pregnancy and may play a significant role in assessing myocardial involvement in women with adverse pregnancy outcomes such as GDM.

## Figure/Table 1

**Table 1- Clinical characteristics and the biochemistry**

Variable	Non-pregnant participants (n=15)	Healthy Pregnancy (n=39)	Gestational diabetes (n=30)	P value
Age, y	30 $\pm$ 5	31 $\pm$ 4	31 $\pm$ 5	0.2
Gestational date at CMR, wks	-	29 $\pm$ 2	31 $\pm$ 2	0.5
BMI, kg/m <sup>2</sup>	23 $\pm$ 4@#	27 $\pm$ 4#*	33 $\pm$ 5@*	0.000
Heart rate, bpm	61 $\pm$ 9@#	86 $\pm$ 23#	91 $\pm$ 14@	0.001
Systolic BP, mmHg	112 $\pm$ 7	116 $\pm$ 12	121 $\pm$ 13	0.1
Diastolic BP, mmHg	73 $\pm$ 6	72 $\pm$ 7	76 $\pm$ 9	0.2
Hemoglobin, g/L	134 $\pm$ 7#@	122 $\pm$ 9#	122 $\pm$ 9@	0.001
Haematocrit, L/L	0.42 $\pm$ 0.02#@	0.37 $\pm$ 0.03#	0.37 $\pm$ 0.03@	0.03
Total cholesterol, mmol/L	4.8 $\pm$ 1.1	6.8 $\pm$ 1.7	6.4 $\pm$ 1.1	0.3
HDL, mmol/L	1.9 $\pm$ 0.4#	2.2 $\pm$ 0.5#*	1.9 $\pm$ 0.4*	0.004
LDL, mmol/L	2.4 $\pm$ 0.5#	3.6 $\pm$ 1.2#*	3.3 $\pm$ 1.2*	0.005
TG, mmol/L	0.9 $\pm$ 0.4@#	2.4 $\pm$ 1.0#*	3.1 $\pm$ 0.8@*	0.000
Creatinine, umol/L	55 $\pm$ 6@#	46 $\pm$ 11#	45 $\pm$ 8@	0.000
eGFR, ml/min/1.73m <sup>2</sup>	90 $\pm$ 0	90 $\pm$ 0	90 $\pm$ 0	1
Urine Alb/creatinine ratio	-	1.6 $\pm$ 2	1.8 $\pm$ 3.2	0.9
HBA1c, mmol/mol	32 $\pm$ 3	31 $\pm$ 6*	33 $\pm$ 3*	0.02
Glucose, mmol/L	5.1 $\pm$ 0.5	5.1 $\pm$ 1.4	5.1 $\pm$ 0.7	0.9
Insulin, pmol/L	73 $\pm$ 66@#	222 $\pm$ 163#	213 $\pm$ 176@	0.012
NT- proBNP, ng/L	55 $\pm$ 15	55 $\pm$ 32	46 $\pm$ 17	0.3
FFA), mmol/L	-	0.3 $\pm$ 0.1	0.4 $\pm$ 0.2	0.6

<b>D-3-Hydroxybutyrate, mmol/L</b>	-	0.1±0.04	0.2±0.2	0.6
------------------------------------	---	----------	---------	-----

### Caption 1

# p<0.05 versus healthy pregnant subjects with Bonferroni correction

a p < 0.05 versus gestational diabetes subjects with Bonferroni correction.

\* p < 0.05 versus healthy pregnant subjects and gestational diabetes subjects with Bonferroni correction.

### Figure/Table 2

**Table 2- CMR findings of the study cohort**

<b>Variable</b>	<b>Non-pregnant participants (n=15)</b>	<b>Healthy Pregnancy (n=39)</b>	<b>Gestational diabetes (n=30)</b>	<b>P value</b>
<b>LV end diastolic volume (ml)</b>	134±20	142±23	136±24	0.4
<b>LV end diastolic volume index (ml/m2)</b>	79±10@	75±13*	67±11@*	0.003
<b>LV end systolic volume (ml)</b>	52±10	59±12	59±14	0.2
<b>LV end systolic volume index (ml/m2)</b>	31±5	31±6	29±7	0.3
<b>LV stroke volume (ml)</b>	82±11	83±15	77±13	0.2
<b>LV ejection fraction (%)</b>	62±4@	60±5	57±6@	0.02
<b>LV mass (g)</b>	82±11@	88±16*	102±19@*	0.0006
<b>LV mass index (g/m2)</b>	49±7	47±8	50±7	0.2
<b>Cardiac output (l/min)</b>	5.8±1.1	6.6±1	6.2±0.9	0.1
<b>Cardiac index (l/min/m2)</b>	3.4±0.6	3.5±0.5*	3.1±0.4*	0.002
<b>Wall thickness (mm)</b>	5.5±1.2@	5.6 ± 1.2*	7.1±1.5@*	0.0002
<b>RV end diastolic volume (ml)</b>	148±21	156±27	145±31	0.3
<b>RV end diastolic volume index (ml/m2)</b>	87±12@	83±14*	72±15@*	0.002
<b>RV end systolic volume (ml)</b>	67±15	71±16	68±22	0.8
<b>RV end systolic volume index (ml/m2)</b>	40±8	38±8	34±11	0.1
<b>RV stroke volume (ml)</b>	79±11	85±17	77±13	0.1

<b>RV ejection fraction (%)</b>	55±5	55±6	54±7	0.6
<b>LA biplane end-systolic volumes (mL)</b>	51±15	46±12	48±15	0.5
<b>Biplane LA EF (%)</b>	51±15	46±12	48±15	0.7
<b>Global longitudinal strain (-), %</b>	21±2@	20±3	18±3@	0.03
<b>Mean native T1 relaxation time (ms)</b>	1298±47@	1326±34	1308±38@	0.04
<b>T2 relaxation time, (ms)</b>	42±2@	40±3	39±3@	0.02
<b>MAPSE</b>	16±2@	14±3	14±2@	0.01
<b>E/A ratio</b>	1.5±0.5@#	1.7±0.4#	1.7±0.4@	<0.001
<b>PCR/ATP</b>	2.7±0.5@	2.5±0.5*	1.9±0.6@*	<0.001
<b>Deceleration time DT (ms)</b>	164±40	151±37	179±75	0.2

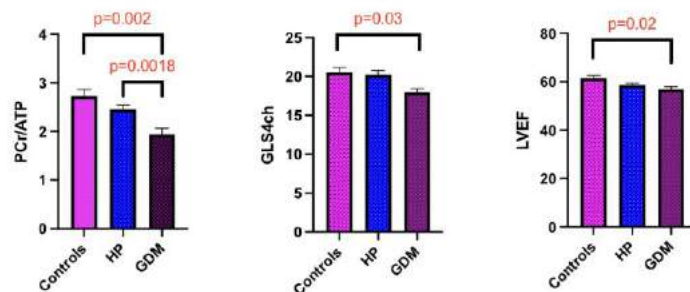
## Caption 2

# p<0.05 versus healthy pregnant subjects with Bonferroni correction

a p < 0.05 versus gestational diabetes subjects with Bonferroni correction.

\* p < 0.05 versus healthy pregnant subjects and gestational diabetes subjects with Bonferroni correction.

## Figure 3



## Caption 3

Figure 1: Differences in cardiac energetics, strain and systolic function between women with gestational diabetes, healthy pregnancies and the nulliparous controls; (A) PCR/ATP ratio, (B) Global longitudinal strain %, (C) Left ventricular ejection fraction.

(Error bars indicate standard error of the mean)

Speaker: S. Thirunavukarasu

Category: Spectroscopy, Diabetes, Cardiovascular Risk

000187

## Free-Running 5D Flow MRI: Impact of Respiratory State Resolution in on Image Quality and Flow Quantification

E. Weiss \* (1); C. Rigsby (2); J. Robinson (3); J. Baraboo (4); L. Ma (5); M. B. L. Falcão (6); C. Roy (7); M. Stuber (8); M. Markl (4)

(1) Department of radiology, Northwestern University Feinberg School of Medicine, Chicago, United States of America; (2) Medical imaging, Ann & Robert H. Lurie Children's Hospital of Chicago, Chicago, United States of America; (3) Pediatric cardiology, Ann & Robert H. Lurie Children's Hospital of Chicago, East Chicago Avenue, Chicago, United States of America; (4) Department of radiology, Northwestern University Feinberg School of Medicine, East Superior Street, Chicago, IL, USA, Chicago, United States of America; (5) Radiology, Northwestern University Feinberg School of Medicine, Chicago, United States of America; (6) Department of radiology, CHUV Centre hospitalier universitaire vaudois, Lausanne, Switzerland; (7) Department of radiology, Lausanne University Hospital, Lausanne, Switzerland; (8) Department of diagnostic and interventional radiology, CHUV Centre hospitalier universitaire vaudois, Lausanne, Switzerland

### Abstract

**Background:** Free running 5D flow MRI is a novel technique that enables fully self-gated (cardiac and respiration) measurement of respiratory resolved blood flow. This may be particularly useful in patients with venous abnormalities, such as those with a Fontan connection, where respiration is a known driver of flow [1]. While previous studies have used 4 respiratory state (RS) bins, it is not clear how many bins are necessary to characterize respiratory driven flow. The reduction of the number of RS bins to 2 or 3 would allow for reduced scan time and/or improved image quality (increased number of k-space per bin). The purpose of this study was to systematically investigate the impact of number of RS on image quality and ability to measure respiration driven flow changes.

**Methods:** 5D flow MRI [2], a radially sampled, fully self-gated scan, was acquired in 5 patients with congenital heart disease who received ferumoxytol for a clinically indicated CMR study. All data sets were reconstructed with 2, 3 and 4 RS bins (9 bins per patient) where each reconstructed bin is a full 4D flow data set (TR=40ms, spatial resolution=2x2x2mm). 5D flow data analysis included background phase correction, velocity anti-aliasing and quantification of net flow across 2D planes at the following anatomic locations: main pulmonary artery (MPA) or left and right pulmonary arteries (LPA and RPA) in subject 2, ascending aorta (AAo), descending aorta (DAo) at the level of the MPA, inferior vena cava (IVC), and superior vena cava (SVC), bilaterally if applicable. The range of the net flow (max flow–min flow) was measured for each vessel in each reconstruction. Image quality was qualitatively assessed between reconstructions.

**Results:** One patient was excluded due to poor image quality. The remaining cohort (10.8±5.3y, 1 female) is described in Table 1. Example images for subject 4 are shown in Fig 1a-f. These demonstrate improved image quality, as evidenced by qualitatively sharper vessel boundaries, when reconstructed with fewer RS bins. With respect to respiratory resolved net flow, the trend for respiration driven changes was consistent within each patient

across the 3 reconstructions (ex. Fig1h-i). Across all subjects and vessels, there was a significant decrease in the range captured between the 4 bin and the 2 bin reconstructions (3.2mL  $p<0.001$ , Fig2), but flow changes were similar between the 4 bin and 3 bin reconstructions (1.4mL decrease,  $p=0.054$ , fig2). Similar findings were observed when only caval veins and MPA, which have expected respiratory driven flow, were included in the comparison (4.1mL,  $p=0.005$ , Fig2).

**Conclusions:** The number of RS reconstructed impacts the ability to measure respiration driven flow. Two RS bins were insufficient whereas respiratory driven net flow differences for 3 bins were equivalent to 4 bins in our small feasibility study cohort. Using 3 RS bins instead of 4 allows for a shorter scan time or increased data per bin to improve image quality which was qualitatively seen in all patients. Future studies in larger cohorts are needed to assess reconstruction impact on other flow metrics such as peak velocity.

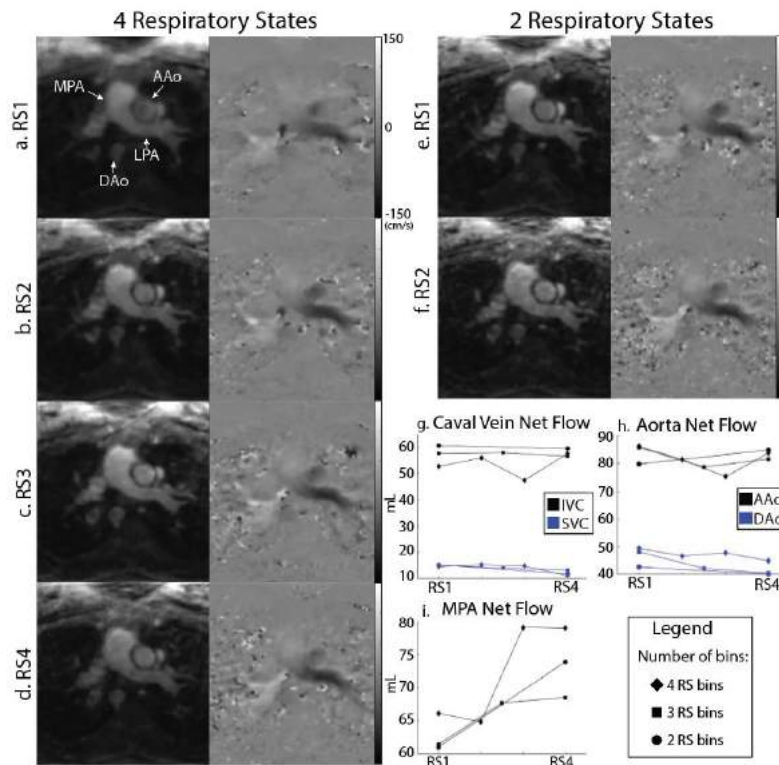
**Figure/Table 1**

Subject	GA	Age (yrs)	Gender	Anatomy
1	Y	2.9	M	Partial anomalous pulmonary venous return and large superior sinus venosus septal defect with left to right shunting
2	N	13.9	M	Hypoplastic left heart syndrome status-post Fontan procedure and coarctation of the aorta
3	N	13.7	M	Loeys-Dietz Syndrome status-post valve sparing aortic root replacement for aortic root dilation
4	N	12.5	F	Closed superior sinus venosus ASD, partial anomalous pulmonary venous return status-post warden procedure, left SVC patent and drains to coronary sinus

**Caption 1**

Table 1. Summary of cohort included in analysis. (GA=general anesthesia).

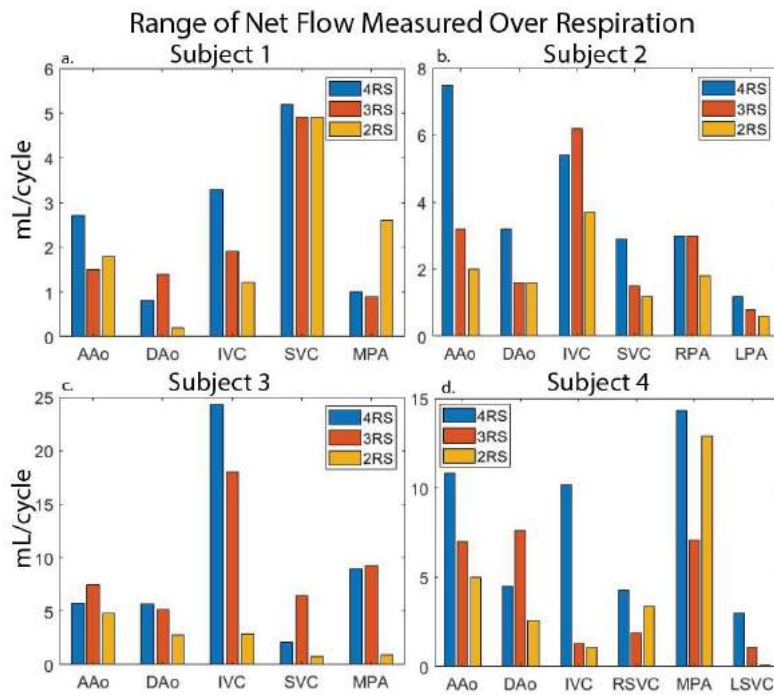
**Figure/Table 2**



## Caption 2

Fig 1. Magnitude and right-left phase images for subject 4 (RS1=end-expiration). reconstructed using 4 (a-d) and 2 bins (e-f). There was increased sharpness in the 2 RS bin reconstructions. Increased MPA flow was visualized as respiration progressed. Absolute net flow values are reported for each bin in each reconstruction (g-i).

## Figure 3



**Caption 3**

Figure 2. The range of net flow (max flow–min flow) measured across the respiratory cycle for each vessel measured in all 4 patients (a-d) across all 3 reconstructions.

### Bibliographic References

van der Woude, S. F., Rijnberg, F. M., Hazekamp, M. G., Jongbloed, M. R., Kenjeres, S., Lamb, H. J., ... & Wentzel, J. J. (2021). The influence of respiration on blood flow in the Fontan circulation: insights for imaging-based clinical evaluation of the total cavopulmonary connection. *Frontiers in Cardiovascular Medicine*, 8.

Speaker: E. Weiss

Category: 4D Flow, Congenital Heart Disease, Respiratory Self-gating



**Catheter Tracking Error Characterization for CMR-Guided Interventions**

A. Gupta \* (1); L. Biswas, (2); J. Soni, (2); B. Coles, (1); S. Ferguson, (2); G. Wright, (3); N. Ghugre, (3)

(1) Medical biophysics, University of Toronto - St. George Campus, Toronto, Canada; (2) Physical science platform, Sunnybrook Research Institute, Toronto, Canada; (3) Schulich heart program, Sunnybrook Research Institute, Toronto, Canada

**Abstract**

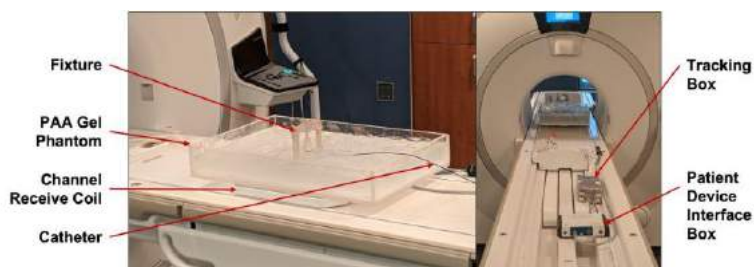
**Background.** Cardiovascular magnetic resonance (CMR) imaging is a promising image guidance modality for minimally invasive cardiac interventions. Some examples of such catheter-based interventions include radiofrequency (RF) ablation treatment for ventricular tachycardia, and therapy delivery involving biologics (cells, genes, biomaterials) for the treatment of myocardial infarction. Studies in the past have had success with CMR-guided RF ablations in left ventricular myocardium [1] and have also shown feasibility with transendocardial cell delivery [2], but have not characterized the errors associated with CMR-guided catheter positioning within the heart. Recent electrophysiology (EP) work has shown that a targeting accuracy of <5mm is desired for RF ablations, since re-entry circuits are generally situated within 5mm of infarct border zones [3]. Additionally, prior work demonstrated that a 1cm injection spacing pattern maximized the retention of injected pluripotent stem cell-derived cardiomyocytes in non-human primate hearts [4]. Given these results, a target of constraining tracking error to <5mm is warranted. Hence, the aim of our study was to characterize the errors associated with CMR-guided catheter tracking under static conditions, using a phantom setup and two different types of pulse sequences.

**Methods.** The tracking setup is shown in Figure 1. The catheter has two microcoils embedded at its distal end, which allows for active tracking under CMR. Using both conventional 3-projection [5] (Flip angle = 5°; FOV = 30 x 30 x 30cm; acquisition size = 512; TR = 9ms) and Hadamard multiplexed (HM) [5] (Flip angle = 5°; FOV = 17.3 x 17.3 x 17.3cm; acquisition size = 256; TR = 2ms) active tracking sequences in a 1.5-T CMR scanner, we tracked the catheter tip (extrapolated from the coil positions – see Fig 2) at 16 positions within a saline and polyacrylic acid gel. The 16 positions were mainly constrained to the (+X, +Z) octant of the bore, within the boundaries of X<100mm and Z<80mm. These were chosen to encompass the likely location of the heart during a scan. A fixture was used to maintain tip alignment with the Z-axis at each position. Separate studies demonstrated relative orientation independence of measures. We acquired both ground truth (GT) imaging data and 15 seconds of real-time tracking data at each position. Error was calculated as the absolute difference between the GT coordinate and the mean tracked coordinate.

**Results.** GT coronal and sagittal slices of the catheter tip at one position are presented (Fig 2), along with two heat maps of catheter tip tracking error (Fig 3). With the conventional sequence, the mean error was  $3.33 \pm 0.02$ mm, while the min and max errors were  $0.91 \pm 0.003$ mm and  $11.67 \pm 0.08$ mm, respectively. With HM, the mean error was  $1.64 \pm 0.08$ mm, while the min and max errors were  $0.60 \pm 0.04$ mm and  $3.37 \pm 0.12$ mm, respectively. The error observed with HM was kept below our target constraint of 5mm.

**Conclusions.** For active catheter tracking under static conditions, employing HM was preferable to using the conventional sequence as the former is, by design, insensitive to off-resonance errors due to static magnetic field inhomogeneities. Our next step is to characterize the tip tracking error under dynamic conditions (using a motion phantom) to simulate cardiac and respiratory motion. In vivo conditions will introduce additional error sources, notably relative tissue motion; however, our study confirms that static tracking errors should not be limiting for the 5mm target accuracy, encouraging next steps toward in vivo translation for applications including CMR-guided cardiac EP and delivery of biologics.

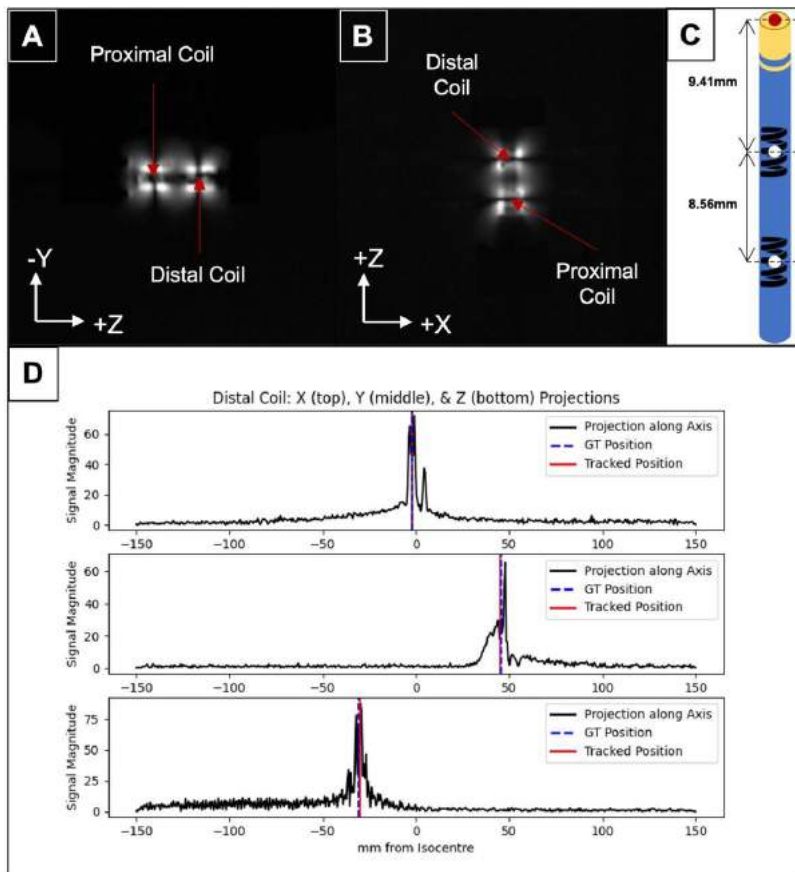
**Figure/Table 1**



**Caption 1**

Active catheter tracking setup in the Imaging Research Centre for Cardiac Intervention (IRCCI) at Sunnybrook Research Institute. The Patient Device Interface and Tracking boxes are required for passing all signals (microcoil tracking, temperature, impedance, intracardiac electrograms) from the catheter to the scanner bed.

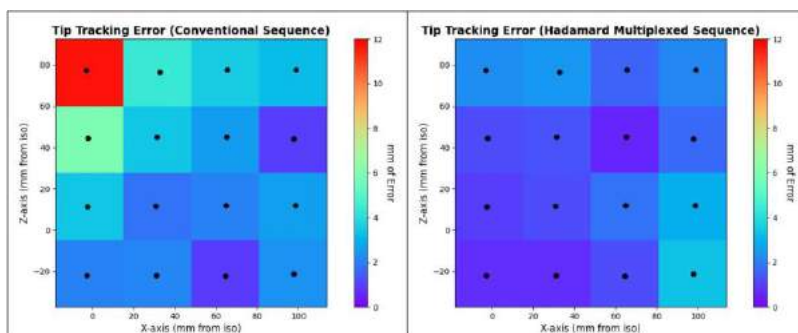
**Figure/Table 2**



**Caption 2**

(A) GT sagittal and (B) coronal slices of proximal and distal coils embedded at the catheter tip, with (C) graphic to scale. (D) Distal coil projections along X, Y, & Z axes from one position. Following centroid-based peak localization for both coils, the tip location was calculated given the known distance and co-linear geometry of the coils relative to the tip.

**Figure 3**



**Caption 3**

Tracking error heat maps generated from manipulating X & Z positions of the catheter tip. The Y position was maintained at -4.5mm throughout. The black markers indicate the 16 tracked positions within the gel phantom. The error exceeded our 5mm target at (X, Z) = (-3mm, 77mm) & (-2mm, 45mm) positions while using the conventional sequence.

### **Bibliographic References**

[1] Chubb, H. et al. Cardiac Electrophysiology Under MRI Guidance: an Emerging Technology. *Arrhythmia Electrophysiol. Rev.* 6, 85 (2017)., [2] Dick, A. J. et al. Magnetic Resonance Fluoroscopy Allows Targeted Delivery of Mesenchymal Stem Cells to Infarct Borders in Swine. *Circulation* 108, 2899–2904 (2003)., [3] Piers, S. R. D. et al. CMR–Based Identification of Critical Isthmus Sites of Ischemic and Nonischemic Ventricular Tachycardia. *JACC Cardiovasc. Imaging* 7, 774–784 (2014)., [4] Chong, J. J. H. et al. Human Embryonic Stem Cell-Derived Cardiomyocytes Regenerate Non-Human Primate Hearts. *Nature* 510, 273–277 (2014)., [5] Dumoulin, C. L., Souza, S. P. & Darrow, R. D. Real-time position monitoring of invasive devices using magnetic resonance. *Magn. Reson. Med.* 29, 411–415 (1993).

Speaker: A. Gupta

Category: Accuracy and Effectiveness, Ablation, Interventional CMR

000191

## **Coronary microvascular function, cardiac energetics and contractility in ideal body weight type 2 diabetes**

A. Chowdhary \* (1); S. Thirunavukarasu (1); N. Jex (1); P. Swoboda (1); H. Xue (2); P. Kellman (2); J. Greenwood (1); S. Plein (1); E. Levelt (1)

(1) Leeds institute of cardiovascular and metabolic medicine, University of Leeds, Leeds, United Kingdom; (2) National institutes for health, NHLBI, Bethesda, United States of America

### **Abstract**

#### **Background**

Coronary microvascular dysfunction (CMD) and myocardial energetic compromise have each been proposed as pivotal features of the diabetic cardiomyopathy process and both are also evident in obese individuals without diabetes. While myocardial energetic compromise has been demonstrated in lean T2D patients (LnT2D) previously, we sought to assess whether or not diabetes affects coronary microvascular function in individuals with ideal body weight.

#### **Methods**

A total of seventy-two participants (27 overweight T2D patients [O-T2D], 15 LnT2D, 15 lean healthy volunteers [LnHV] and 15 overweight healthy volunteers [O-HV]) without established cardiovascular disease were recruited (table 1). Participants underwent magnetic resonance imaging (CMR) for assessment of subcutaneous, epicardial and visceral adipose tissue areas (SAT, EAT and VAT respectively), rest and adenosine stress myocardial blood flow (MBF), cardiac structure and function. <sup>31</sup>Phosphorus-magnetic resonance spectroscopy (MRS) was utilized for measuring myocardial energetic status (phosphocreatine to ATP ratio [PCr/ATP]).

#### **Results**

Table 2 denotes the CMR and MRS results. Stress MBF was reduced only in O-T2D (LnHV:2.07±0.47ml/g/min, O-HV:2.08±0.42ml/g/min, LnT2D:2.16±0.36ml/g/min, O-T2D:1.65±0.26ml/g/min; p=0.0003). While O-T2D patients showed greater visceral adiposity, accumulation of visceral fat was also evident in LnT2D patients at similar levels to O-HV (LnHV:127±53cm<sup>2</sup>, O-HV:181±60cm<sup>2</sup>, LnT2D:182±99cm<sup>2</sup>, O-T2D:310±60cm<sup>2</sup>; p<0.0001). Despite normal myocardial perfusion, LnT2D showed significant reductions in myocardial PCr/ATP and left ventricular ejection fraction similar to O-T2D compared to both control groups (LnHV:2.20±0.41, O-HV:2.11±0.37, LnT2D:1.68±0.11, O-T2D:1.45±0.21; p<0.0001). Neither lean nor overweight T2D patients showed any significant cardiac structural alterations compared to the control groups.

#### **Conclusions**

Type 2 diabetes patients with ideal body weight do not show alterations in myocardial perfusion but show significant reductions in myocardial energetics and function.

**Figure/Table 1**

	<b>LnHV</b>	<b>(n=15)<sup>O-</sup> HV (n=15)</b>	<b>LnT2D (n=15)</b>	<b>(n=15)<sup>O-</sup> T2D (n=27)</b>	<b>ANOVA/Chi-square</b>
Age (yrs)	63 ± 7	66 ± 8	63 ± 12	66 ± 10	0.8
Sex (M, %)	10 (67)	8 (53)	9 (60)	23 (85)	0.08
Duration of diabetes (yrs)	-	-	13.4 ± 6.3	11.3 ± 3.2	0.2
Systolic BP, mmHg	130 ± 13	133 ± 13	126 ± 17	131 ± 14	0.5
Diastolic BP, mmHg	77 ± 7	76 ± 7	72 ± 8	75 ± 6	0.06
Heart rate, bpm	63 ± 10	67 ± 11	69 ± 13	66 ± 10	0.7
Height, cm	171 ± 9	169 ± 8	168 ± 10	172 ± 9	0.5
Weight, kg	70 ± 10 <sup>€§</sup>	83 ± 8 <sup>€#</sup>	68 ± 10 <sup>#</sup>	88 ± 11 <sup>§</sup>	<b>&lt;0.0001</b>
BMI, kg/m2	23 ± 2 <sup>€†</sup>	29 ± 2 <sup>≠</sup>	24 ± 1 <sup>§</sup>	30 ± 2	<b>&lt;0.0001</b>
Waist circumference, cm	90 ± 7 <sup>€†</sup>	105 ± 6 <sup>≠</sup>	92 ± 11 <sup>§</sup>	109 ± 8	<b>&lt;0.0001</b>
Waist over hip ratio	0.95 ± 0.08 <sup>€†</sup>	1.01 ± 0.06 <sup>≠</sup>	0.94 ± 0.10 <sup>§</sup>	1.02 ± 0.04	<b>0.0001</b>
Haemoglobin, g/L	141 ± 9	148 ± 8	140 ± 11	148 ± 16	0.08
Creatinine, umol/L	71 ± 11	71 ± 11	87 ± 7	81 ± 12	0.06
eGFR, ml/min/1.73m2	82 ± 8	81 ± 6	82 ± 11	75 ± 12	0.3
Total cholesterol, mmol/L	5.85 ± 0.65 <sup>†</sup>	5.17 ± 1.35	4.71 ± 1.19	4.54 ± 1.27	0.03
HDL, mmol/L	1.94 ± 0.58 <sup>€¶†</sup>	1.53 ± 0.38	1.61 ± 0.45 <sup>§</sup>	1.24 ± 0.23	<b>&lt;0.0001</b>
LDL, mmol/L	3.35 ± 0.38	2.99 ± 1.10	2.41 ± 0.97	2.45 ± 1.35	0.1
TG, mmol/L	1.22 ± 0.65 <sup>†</sup>	1.49 ± 0.64	1.60 ± 0.82	2.59 ± 1.70	<b>0.002</b>
Fasting blood glucose, mmol/L	4.9 ± 0.6 <sup>¶†</sup>	5.2 ± 0.4 <sup>≠*</sup>	8.7 ± 2.9	9.2 ± 4.1	<b>0.0002</b>
HbA1c, mmol/mol	37 ± 3 <sup>¶†</sup>	38 ± 2 <sup>≠*</sup>	58 ± 8	64 ± 20	<b>&lt;0.0001</b>
Insulin, pmol/L	25 ± 15 <sup>†</sup>	67 ± 35	41 ± 29 <sup>§</sup>	114 ± 99	<b>0.002</b>
C peptide, pmol/L	432 ± 205 <sup>†</sup>	745 ± 300	553 ± 265	1023 ± 698	<b>0.005</b>

HOMA-IR	$0.79 \pm 0.49^{\dagger}$	$2.21 \pm 1.23^*$	$2.40 \pm 2.02 \S$	$6.22 \pm 5.73$	<b>0.001</b>
TG/HDL	$0.76 \pm 0.63^{\dagger}$	$1.05 \pm 0.48^*$	$1.14 \pm 0.84\S$	$2.27 \pm 1.83$	<b>0.002</b>
Medications, n (%)					
ACE-I	-	-	4 (20)	14 (52)	0.2
ARB	-	-	3 (20)	3 (11)	0.1
Beta blocker	-	-	0 (0)	5 (19)	<b>0.02</b>
CCB	-	-	3 (20)	3 (11)	0.1
Aspirin	-	-	6 (40)	7 (26)	0.6
Statin	-	-	10 (67)	19 (70)	0.09
Metformin	-	-	10 (67)	15 (56)	<b>0.002</b>
Sulphonylurea	-	-	4 (27)	8 (30)	0.07
GLP-1RA	-	-	0 (0)	0 (0)	-
Gliptins	-	-	4 (27)	6 (22)	0.05
SGLT2i	-	-	1 (6)	2 (7)	0.4
Thiazolidinediones	-	-	3 (20)	1 (3)	0.06

Values in bold signify € signifies  $p < 0.05$  between LnHV and O-HV, § signifies  $p < 0.05$  between LnT2D and O-T2D, ¶ signifies  $p < 0.05$  between LnHV and LnT2D, \* signifies  $p < 0.05$  between O-HV and O-T2D, † signifies  $p \leq 0.05$  between LnHV and O-T2D, ≠ signifies  $p \leq 0.05$  between O-HV and LnT2D. Values are mean  $\pm$  SD or median (IQR) for continuous variables and number (%) for categorical variables.

## Caption 1

**Table 1: Demographics, biochemical characteristics and medications.**

## Figure/Table 2

	<b>LnHV</b>	(n=15) <b>O-HV</b>	(n=15) <b>LnT2D</b>	(n=15) <b>O-T2D</b>	(n=27)	<b>ANOVA</b>
LV end-diastolic volume (ml)	152 ± 33	140 ± 30	125 ± 28	149 ± 23		0.06
LV end diastolic volume index (ml/m2)	82 ± 13	72 ± 13	70 ± 12	74 ± 14		0.3
LV end systolic volume (ml)	56 ± 13	52 ± 16	50 ± 14§	64 ± 16		<b>0.01</b>
LV end systolic volume index (ml/m2)	31 ± 6	27 ± 7	29 ± 7	31 ± 7		0.2
LV stroke volume (ml)	95 ± 22¶	88 ± 16≠	75 ± 17	84 ± 13		<b>0.01</b>
LV ejection fraction (%)	63 ± 4†	63 ± 4*	60 ± 5	57 ± 6		<b>0.0009</b>
LV mass (g)	93 ± 27	95 ± 29	79 ± 19	96 ± 19		0.1
LV mass index (g/m2)	52 ± 12	52 ± 11	48 ± 10	49 ± 10		0.2
LV mass /LV end diastolic volume(mg/ml)	0.65 ± 0.12	0.72 ± 0.15	0.69 ± 0.21	0.67 ± 0.13		0.4
RV end diastolic volume (ml)	161 ± 36¶	153 ± 43	122 ± 30	146 ± 23		<b>0.01</b>
RV end diastolic volume index (ml/m2)	87 ± 14¶†	78 ± 18	69 ± 12	72 ± 10		<b>0.001</b>
RV end systolic volume (ml)	67 ± 22	61 ± 24	54 ± 17	65 ± 15		0.6
RV stroke volume (ml)	93 ± 19	92 ± 21	69 ± 17	81 ± 13		0.8
RV ejection fraction (%)	60 ± 7	60 ± 5	56 ± 6	56 ± 8		0.06
Native T1 (ms)	1207 ± 81	1166 ± 84	1148 ± 111	1210 ± 69		0.07
Extracellular volume (%)	23 ± 3	22 ± 3	23 ± 2	22 ± 3		0.5
Cell Volume (ml/m2)	70 ± 18	74 ± 17	64 ± 20	76 ± 17		0.6
Peak circumferential strain, negative (%)	21.3 ± 2.7†	21.9 ± 2.2*	21.7 ± 3.3§	18.3 ± 3.0		<b>0.0005</b>
Global longitudinal strain, negative (%)	15.1 ± 3.1†	15.2 ± 3.7*	13.4 ± 2.7	11.1 ± 2.8		<b>0.002</b>



PDSR circum (1/s)	1.18 ± 0.25	1.15 ± 0.18	1.22 ± 0.29§	0.95 ± 0.19	<b>0.03</b>
LA maximum volume (ml)	57 ± 24	61 ± 20	61 ± 16	68 ± 22	0.6
LA maximum volume indexed (ml/m <sup>2</sup> )	33 ± 13	32 ± 11	34 ± 8	32 ± 16	0.8
LA ejection fraction (%)	57 ± 9	63 ± 13	55 ± 8	54 ± 11	0.09

#### Myocardial Perfusion

Stress myocardial blood flow (ml/g/min)	2.07 ± 0.47 ¶	2.08 ± 0.42≠	2.16 ± 0.36§	1.65 ± 0.26	<b>0.0003</b>
Rest myocardial blood flow (ml/g/min)	0.64 ± 0.08	0.72 ± 0.15	0.74 ± 0.13	0.66 ± 0.14	0.08
Myocardial perfusion reserve index	3.18 ± 0.84	3.17 ± 0.59	2.98 ± 0.66	2.58 ± 0.58	0.5
Stress rate pressure product (bpm*mmHg)	11942 ± 3256	11764 ± 3102	11464 ± 2100	10652 ± 3452	0.3
Rest rate pressure product (bpm*mmHg)	8339 ± 1585	8265 ± 1723	8645 ± 1599	8487 ± 1897	0.7
Increase in rate pressure product (%)	39	38	37	31	0.7

#### Adipose tissue measurements and myocardial energetics

Subcutaneous adipose tissue (cm <sup>2</sup> )	106 ± 31€	169 ± 55	147 ± 71	140 ± 37	<b>0.04</b>
Visceral adipose tissue (cm <sup>2</sup> )	127 ± 53†	181 ± 60*	182 ± 99§	310 ± 60	<b>&lt;0.0001</b>
Epicardial adipose tissue (cm <sup>2</sup> )	14 ± 6†	17 ± 5*	18 ± 8§	34 ± 13	<b>&lt;0.0001</b>
PCr/ATP	2.20 ± 0.41¶†	2.11 ± 0.37≠*	1.68 ± 0.11	1.45 ± 0.21	<b>&lt;0.0001</b>

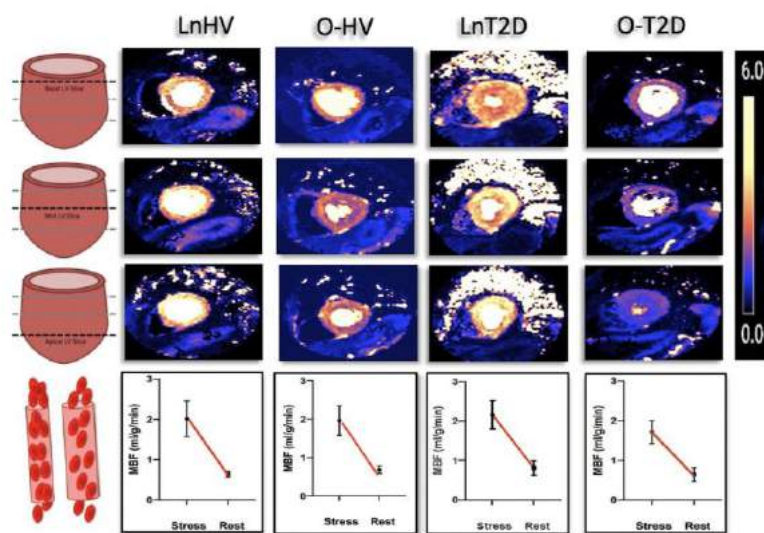
Values in bold signify p<0.05. € signifies p<0.05 between LnHV and O-HV, § signifies p<0.05 between LnT2D and O-T2D, ¶ signifies p<0.05 between LnHV and LnT2D, \* signifies p<0.05 between O-HV and O-T2D, † signifies p≤0.05 between LnHV and O-T2D, ≠ signifies p≤0.05 between O-HV and LnT2D. Values are mean ± SD for continuous variables and number (%) for categorical variables. LnHV indicates lean healthy volunteers; O-HV, obese/overweight healthy volunteers; LnT2D, lean type 2 diabetes; O-T2D, overweight type

2 diabetes; ANOVA, analysis of variance; LV, left ventricular; ml, milliliter; ml/m<sup>2</sup>, milliliters per square meter of body surface area; g, gram; g/m<sup>2</sup>, gram per square meter of body surface area; RV, right ventricular; ms, milliseconds; PDSR, peak diastolic strain rate; s, seconds; LA, left atrial; min, minute; bpm, beats per minute; mmHg, millimetres of mercury; cm<sup>2</sup>, centimetre square; PCr/ATP, phosphocreatine adenosine triphosphate ratio.

**Caption 2**

**Table 2: MRI and 31P-MRS parameters**

**Figure 3**



**Caption 3**

**Figure-3: Myocardial blood flow maps at peak stress**

Representative myocardial blood flow maps acquired at basal, mid-ventricular and apical levels during peak stress along with graphs showing the reduction in myocardial blood flow at peak stress and rest in LnHV, O-HV, LnT2D and O-T2D. 1

Speaker: A. Chowdhary

Category: Diabetes, Spectroscopy, Microvascular disease

000192

## Abnormal Right and Left Ventricular Cardiac MRI Derived Strain in Children with COVID-19 Myocarditis

E. Rhee \* (1); J. Dobrila (2); H. Kaur (3); M. Marshall (4); M. Patel (5); L. Xiong (5); R. Kharouf (5); D. Adebo (5); S. uppu (6)

(1) Pediatric cardiology, Inova Fairfax Hospital, Gallows Road, Falls Church, United States of America; (2) Pediatric and congenital cardiac surgery, University of texas health science center at Houston, Houston, United States of America; (3) Medical student, University of texas health science center at Houston, Houston, United States of America; (4) Pediatric cardiology, University of Texas Health Science Center at Houston, Fannin Street, Houston, United States of America; (5) Pediatric cardiology, University of texas health science center at Houston, Houston, United States of America; (6) Congenital cardiology, University of texas health science center at Houston, Houston, United States of America

### Abstract

**Background:** Cardiac MRI (CMR) derived left ventricular (LV) longitudinal and circumferential strain is known to be abnormal in subjects with clinical myocarditis[1,2]. CMR strain is a useful additional tool that can help identify those with subclinical myocarditis and may help with longitudinal follow-up[1,3,4]. CMR derived right ventricular (RV) strain in acute myocarditis has not been studied. We sought to assess feasibility of RV CMR strain in acute myocarditis, and compare LV and RV CMR strain with COVID-19 myocarditis subjects.

**Methods:** Retrospective single institutional review of children with acute myocarditis who underwent CMR after 2016 was performed (n=52), this group included COVID-19 myocarditis subjects after 2020 (n=17). Children with no evidence of myocarditis served as controls (n=25). Those with congenital heart disease and technically limited images for CMR strain analysis were excluded (n=25). Biventricular longitudinal, circumferential and radial peak strains were derived using Circle cvi42. Short axis images were used for circumferential and radial strain. Data between cases and controls were compared using an independent sample t-test. One-way ANOVA with post hoc analysis was used to compare characteristics of COVID-19, non-COVID-19 myocarditis and controls.

**Results:** 38 myocarditis and 14 controls met inclusion criteria (age range 7.3-17.9 yrs). Table 1 shows baseline patient and CMR characteristics between the groups. RV strain was obtained in 51 subjects. All CMR derived peak strain values except for RV longitudinal strain were abnormal in myocarditis group (Table 1). One-way ANOVA revealed that there was a statistically significant difference with RV and LV strain between COVID-19, non-COVID-19 myocarditis and controls (Table 2 and Figure).

**Conclusion:** CMR derived RV strain is feasible in children with myocarditis using routine clinical CMR sequences. Interestingly children with COVID-19 myocarditis have abnormal RV and LV strain except for LV longitudinal strain when compared to non-COVID-19 myocarditis and controls.

**Figure/Table 1**

Table 1: Baseline characteristics between Controls and Myocarditis			
	Control	Myocarditis	p
N	14	38	
Median Age (years, IQR)	15.6 (7.3 – 17.4)	15.1 (7.7 – 17.9)	0
Male: Female	9:5	30:8	
Mean BSA (m2)	1.75	1.73	0
Mean LV EF (%)	66	59.5	0
Mean RV EF (%)	63	58.2	0
Mean LV EDVi (ml/m2)	76.1	84.7	0
Mean RV EDVi (ml/m2)	77.2	82.5	0
CMR evidence of myocarditis	0	26	
Mean RV longitudinal strain	-18.4 ± 3.1	-16.9 ± 4.6	0
Mean RV circumferential strain	-15.7 ± 3.4	-12.4 ± 3.9	0
Mean RV radial strain	+28.9 ± 9.3	+20.8 ± 6.9	0
Mean LV longitudinal strain	-15.9 ± 1.8	-13.9 ± 2.9	0
Mean LV circumferential strain	-19.6 ± 2.9	-16.7 ± 3.3	0
Mean LV radial strain	+35.1 ± 8.8	+27.6 ± 7.2	0

**Caption 1**

BSA - body surface area; LV - left ventricle; RV - right ventricle; EF - ejection fraction; EDVi - indexed end-diastolic volume. Data expressed as mean  $\pm$  SD.

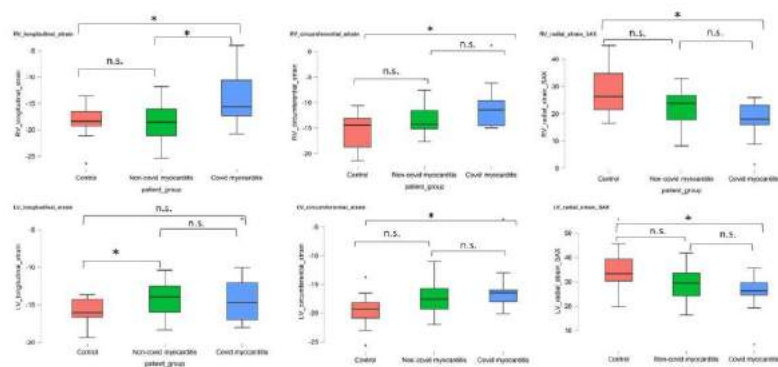
**Figure/Table 2**

Table 2: One-way ANOVA (Welch's) for Controls, non-COVID-19, and COVID-19 myocarditis			
Strain	Control	Non-COVID-19 myocarditis	COVID-19
RV longitudinal	-18.4 $\pm$ 3.1	-18.6 $\pm$ 3.7	-14.2 $\pm$ 4.7
RV circumferential	-15.7 $\pm$ 3.4	-13.4 $\pm$ 3.1	-10.7 $\pm$ 4.5
RV radial	+28.9 $\pm$ 9.3	+22.6 $\pm$ 6.5	+17.6 $\pm$ 6.0
LV longitudinal	-15.9 $\pm$ 1.8	-14.1 $\pm$ 2.3	-13.8 $\pm$ 3.9
LV circumferential	-19.6 $\pm$ 2.9	-17.2 $\pm$ 2.9	-15.9 $\pm$ 3.9
LV radial	+35.1 $\pm$ 8.8	+28.8 $\pm$ 7.1	+25.4 $\pm$ 7.1

**Caption 2**

Data expressed as mean  $\pm$  SD; F - F-value.

**Figure 3**



### Caption 3

**Figure: Boxplots comparing strain among controls, COVID-19 and non-COVID-19 myocarditis (Games-Howell Post Hoc test. \* for  $p < 0.05$ , n.s. not significant)**

### Bibliographic References

Weigand J, Nielsen JC, Sengupta PP, Sanz J, Srivastava S, Uppu S. Feature Tracking-Derived Peak Systolic Strain Compared to Late Gadolinium Enhancement in Troponin-Positive Myocarditis: A Case-Control Study. *Pediatr Cardiol*. 2016;37: 696–703. doi:10.1007/s00246-015-1333-z 2. Urmeneta Ulloa J, Martínez de Vega V, Salvador Montañés O, Álvarez Vázquez A, Sánchez-Enrique C, Hernández Jiménez S, et al. Cardiac magnetic resonance in recovering COVID-19 patients. Feature tracking and mapping analysis to detect persistent myocardial involvement. *Int J Cardiol Heart Vasc*. 2021;36: 100854. doi:10.1016/j.ijcha.2021.100854 3. Chen X, Hu H, Pan J, Shu J, Hu Y, Yu R. Performance of cardiovascular magnetic resonance strain in patients with acute myocarditis. *Cardiovasc Diagn Ther*. 2020;10: 725–737. doi:10.21037/cdt-20-221 4. Kobayashi R, Dionne A, Ferraro A, Harrild D, Newburger J, VanderPluym C, et al. Detailed assessment of left ventricular function in multisystem inflammatory syndrome in children, using strain analysis. *CJC Open*. 2021;3: 880–887. doi:10.1016/j.cjco.2021.02.012, Urmeneta Ulloa J, Martínez de Vega V, Salvador Montañés O, Álvarez Vázquez A, Sánchez-Enrique C, Hernández Jiménez S, et al. Cardiac magnetic resonance in recovering COVID-19 patients. Feature tracking and mapping analysis to detect persistent myocardial involvement. *Int J Cardiol Heart Vasc*. 2021;36: 100854. doi:10.1016/j.ijcha.2021.100854, Chen X, Hu H, Pan J, Shu J, Hu Y, Yu R. Performance of cardiovascular magnetic resonance strain in patients with acute myocarditis. *Cardiovasc Diagn Ther*. 2020;10: 725–737. doi:10.21037/cdt-20-221, Kobayashi R, Dionne A, Ferraro A, Harrild D, Newburger J, VanderPluym C, et al. Detailed assessment of left ventricular function in multisystem inflammatory syndrome in children, using strain analysis. *CJC Open*. 2021;3: 880–887. doi:10.1016/j.cjco.2021.02.012

Speaker: E. Rhee

Category: Pediatric , Cardiac Strain, Myocarditis

000194

## Hybrid PET/CMR Response Monitoring in Myocardial Infarction using a Dual-Condition Protocol

F. Habach \* (1); J. Barry, (2); M. Larsen, (2); M. Jamieson, (3); A. Singnurkar, (3); M. Laflamme (4); N. Ghugre, (1)

(1) Physical sciences, Sunnybrook Research Institute, Toronto, Canada; (2) Schulich heart research program, Sunnybrook Research Institute, Toronto, Canada; (3) Nuclear medicine, Sunnybrook Research Institute, Toronto, Canada; (4) McEwen stem cell institute, University Health Network, Toronto, Canada

### Abstract

**Background:** Myocardial infarction (MI) remains the most significant cause of heart failure worldwide.[1] Several novel treatments are on the horizon, including acellular biomaterial scaffolds, gene, and stem cell-based treatments.[2] For successful clinical translation, Cardiac Magnetic Resonance Imaging (CMR) can elucidate structure, function and viability, and evaluate treatment efficacy. In addition, Positron Emission Tomography (PET) can offer metabolic information, as well as status on inflammatory processes.[3] Clinically, glycolytic suppression is typically used to isolate inflammatory or ischemic activity. Additionally, glucose loading can provide further information by inducing metabolite uptake within the myocardium. [3] Combining fasting and glucose loading protocols (dual-condition) in one imaging session could have the advantages of reduced scan time and cost, while also providing better PET/CMR co-registration. The objective of this work was to develop a hybrid PET/CMR imaging protocol that will accurately and simultaneously reflect myocardial structure, function and metabolism using a novel dual-condition protocol, in an experimental model of MI.

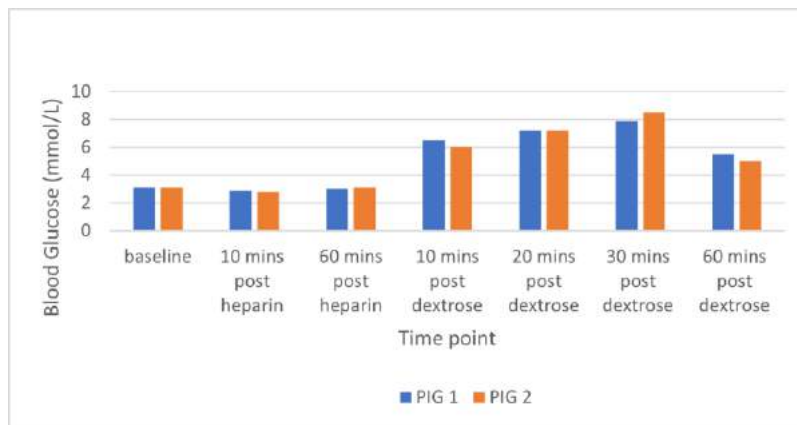
**Methods:** A whole-body clinical PET/MR scanner (Siemens mMR) and a validated porcine model [4] of MI (90 min LAD occlusion/reperfusion) was utilized. Fasting was induced by a 24 hour fast and injection of a heparin bolus (2000 IU). Glucose loading was induced by a 30-minute constant dextrose infusion (0.8 mL/min/kg). Physiological blood glucose measurements in fasted/glucose loaded states were studied in offline experiments (n=2). Imaging was performed at baseline, 10-, 31-, and 45-days post-MI (n=2). For CMR, a CINE sequence was used to assess anatomy and function and 3D Late Gadolinium Enhancement (LGE) (1x1x2 mm res.) was used to delineate scar tissue. For PET, a 1-hour dynamic list-mode acquisition (2 mm iso. res.) was performed concurrently with CMR, immediately following [18F]-FDG dosing (2.5 mCi) in the fasted state. Next, with a second FDG dose (7.5 mCi), a 1.5-hour acquisition was performed following glucose loading. PET standard uptake values (SUVs) were computed and corrected for the second imaging session by appropriate activity subtraction. 3D LGE was co-registered with 3D [18F]-FDG-PET images for SUV comparison within infarct and healthy myocardial regions.

**Results:** Offline physiological experiments showed changes in blood glucose post heparin ( $-0.25 \pm 0.05$  mmol/L) and post-dextrose infusion ( $+5.1 \pm 0.3$  mmol/L). (Figure 1). Co-registered 3D LGE and [18F]-FDG-PET showed strong spatial correlations between infarct location and inflammatory cell activity (Figure 2). Glucose loading induced almost 6-fold increase in tracer uptake immediately after dextrose infusion (Figure 3).



**Conclusions:** Dual dose protocol shows promise in inducing different metabolic states within the same imaging session. Developing the PET/CMR framework opens the possibility of its widespread use as an *in vivo* non-invasive imaging modality for probing mechanisms of new cardiac reparative therapies, for both pre-clinical efficacy testing and clinical implications for response monitoring in patients suffering from MI-related heart failure.

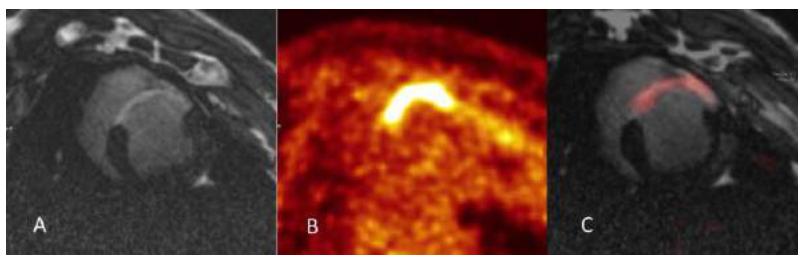
**Figure/Table 1**



**Caption 1**

**Figure 1.** Offline physiological experiments measure blood glucose levels following heparin injection during fasted state, and dextrose infusion during glucose loading. 2000 IU bolus of heparin was administered followed by 0.8 mL/kg/min of dextrose for 30 minutes.

**Figure/Table 2**

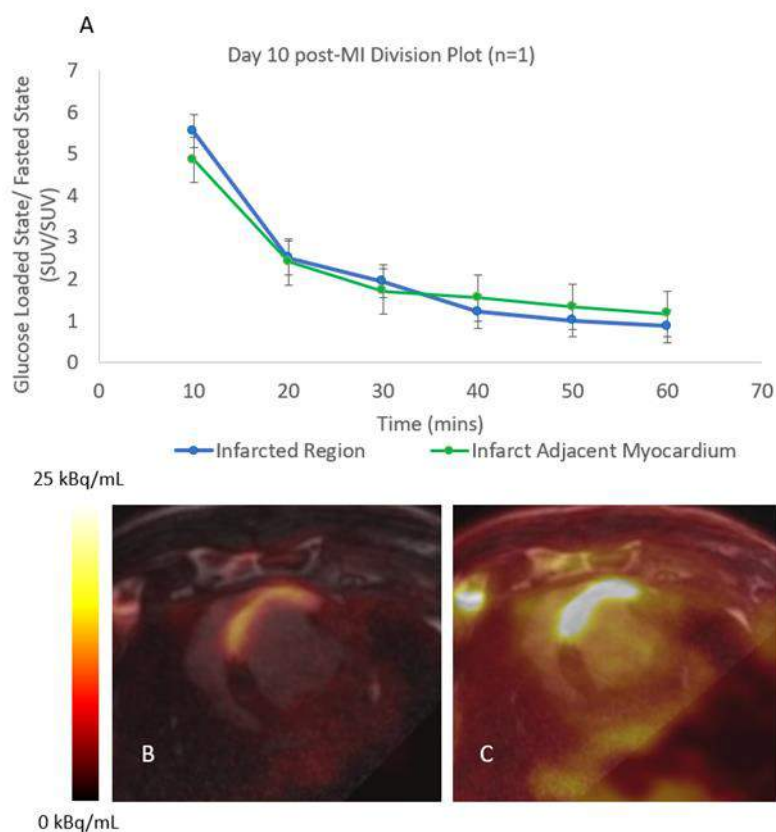


**Caption 2**

**Figure 2.** Left ventricular short axis view of infarcted porcine heart (10 days post-MI). **A)** 3D Late Gadolinium Enhancement (LGE) image of infarcted scar tissue ( $FOV = 300\text{ mm}$ ,  $TI = 200\text{ ms}$ ). **B)** 18F-FDG-PET image of inflammatory cell activity within the infarct region. (*Acq.*

*Time = 10 mins, FOV = 258 mm, FDG Dose = 2.5 mCi). C) Co-registered LGE and 18FDG-PET images.*

**Figure 3**



**Caption 3**

**Figure 3:** A) Division plot of glucose loading induced FDG uptake over fasted state FDG uptake within infarcted region, and infarct adjacent myocardium. B) short axis view of 10 day induced infarct within left ventricular wall, fasted state. C) short axis view of 10 day induced infarct within left ventricular wall, glucose loaded state.

### Bibliographic References

- Romagnuolo, R., et al. Human Embryonic Stem Cell-Derived Cardiomyocytes Regenerate the Infarcted Pig Heart but Induce Ventricular Tachyarrhythmias. *Stem Cell Rep.* 12(5), 967-981 (2019). <https://doi.org/10.1016/j.stemcr.2019.04.005>, 3. Shelbert, H. R. Measurements of myocardial metabolism in patients with ischemic heart disease. *Am. J. Cardiol.* 82(5), 61K-67K (1998). [https://doi.org/10.1016/S0002-9149\(98\)00539-6](https://doi.org/10.1016/S0002-9149(98)00539-6), 2. Hastings, L. C. et al. Drug and cell delivery for cardiac regeneration. *Adv. Drug Deliv. Rev.* 84, 85-106 (2015).

<https://doi.org/10.1016/j.addr.2014.08.006>, 1. Public Health Agency of Canada. Canadian Chronic Disease Surveillance System (CCDSS), Data Tool 2000–2016, 2018 Edition. Public Health Agency of Canada (2019).

Speaker: F. Habach

Category: Acute Myocardial Infarction, Metabolism, Tissue Characterization

000201

## CMR confirms conduction defect in fatty acid oxidation compromised heart

E.-S. Ibrahim (1); J. Jarzembowski, (2); S. Kumar, \* (2)

(1) Department of radiology, Medical College of Wisconsin, Milwaukee, United States of America; (2) Department of pathology, Medical College of Wisconsin, Milwaukee, United States of America

### Abstract

**Background:** Healthy heart is a metabolically dynamic organ requiring large energy resource, and fatty acid oxidation (FAO) pathway predominantly supports this energy demands. Any disruption to this capability would result in dysfunction and ultimately organ failure. Gene mutations, physiological perturbations and stress would interrupt this metabolic flexibility resulting in impaired signaling, energy insufficiency, contractile dysfunction, and heart failure. Disorders of FAO pathways could range from mild and manageable to severe and life-threatening. In many cases, the subclinical cardiac dysfunction is overlooked in this disorder even after an echocardiograph evaluation because cardiac dysfunction may be devoid of structural damage, along with only subtle cardiac dysfunction. However, if left untreated, this disorder could progress into major cardiac complications and heart failure. In this study, we use CMR to evaluate the heart function in mitochondrial trifunctional protein (MTP) mutant rats, where clinical symptoms of this disorder overlap with other less severe FAO deficiencies and are frequently misdiagnosed.

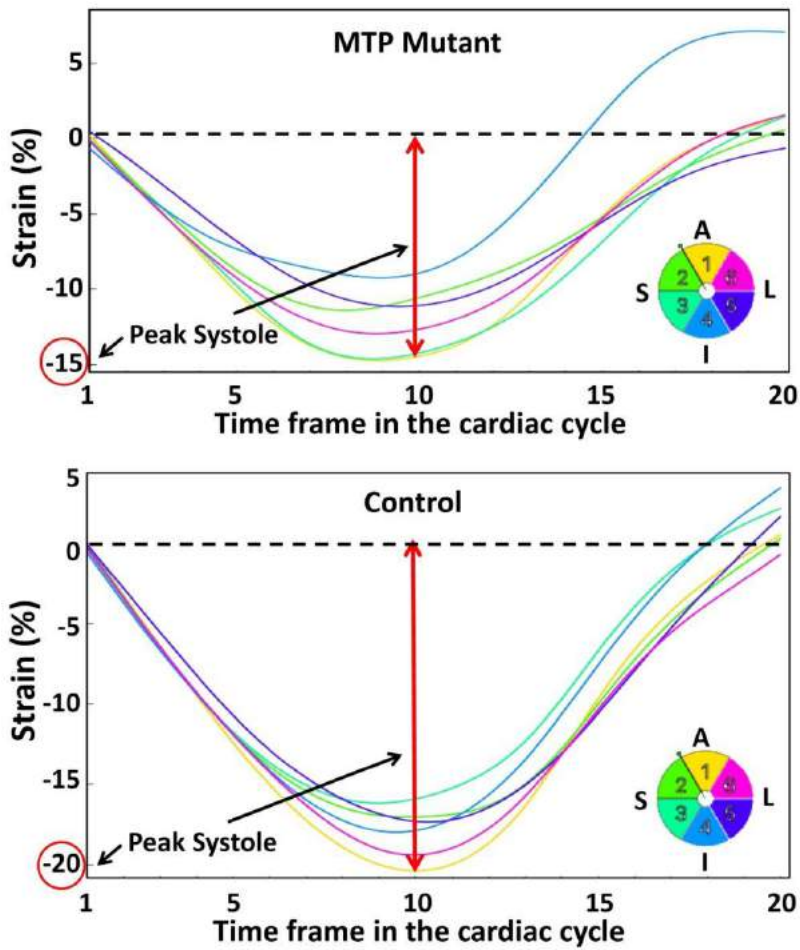
**Methods:** Seven rats (3 MTP alpha variant heterozygous mutant Sprague-Dawley rats and 4 wild type controls) were imaged using an optimized CMR exam when they were 7 weeks of age. The CMR exam included both acquiring cine and tagging images covering the heart. The cine images were analyzed using the cvi42 software package to measure ejection fraction (EF), while the tagged images were analyzed using the SinMod-based InTag software package to measure myocardial circumferential, radial, and longitudinal strain components. The results are represented as mean $\pm$ SEM. Statistical analysis was conducted to determine significance of the measurement differences between the mutant and control rats ( $P < 0.05$  considered significant).

**Results:** The CMR results revealed 10% reduction in EF ( $60.5 \pm 2.3\%$  in control vs.  $54.3 \pm 1.5\%$  in MTP mutant rats). CMR also revealed reduced myocardial strain in the MTP mutant rats, compared to the control rats, in all strain directions (**Figures 1-2**), although the reductions in the circumferential and longitudinal strains were more than that in radial strain. Global longitudinal, circumferential, and radial strains in the MTP mutant rats were  $-15.7 \pm 0.3\%$ ,  $-12.3 \pm 0.7\%$ , and  $22.3 \pm 2.4\%$ , respectively, vs. corresponding values of  $-16.3 \pm 5\%$ ,  $-13.0 \pm 0.9\%$ , and  $23.0 \pm 0\%$  in the control rats. The differences in strain measurements between the two groups were not statistically significant. Regional wise, most reductions in strain were in the basal and mid-ventricular segments compared to apical segments (**Table 1**).

**Conclusion:** CMR is a valuable tool for detecting subtle changes in cardiac function in the MTP mutant rats. Especially, CMR strain imaging revealed subclinical cardiac dysfunction in the MTP mutant rats with the degree of strain reduction depending on strain direction and regional location. Therefore, a comprehensive CMR functional exam would be valuable for

early detection of MTP mutation-induced cardiac dysfunction and potential development into heart failure.

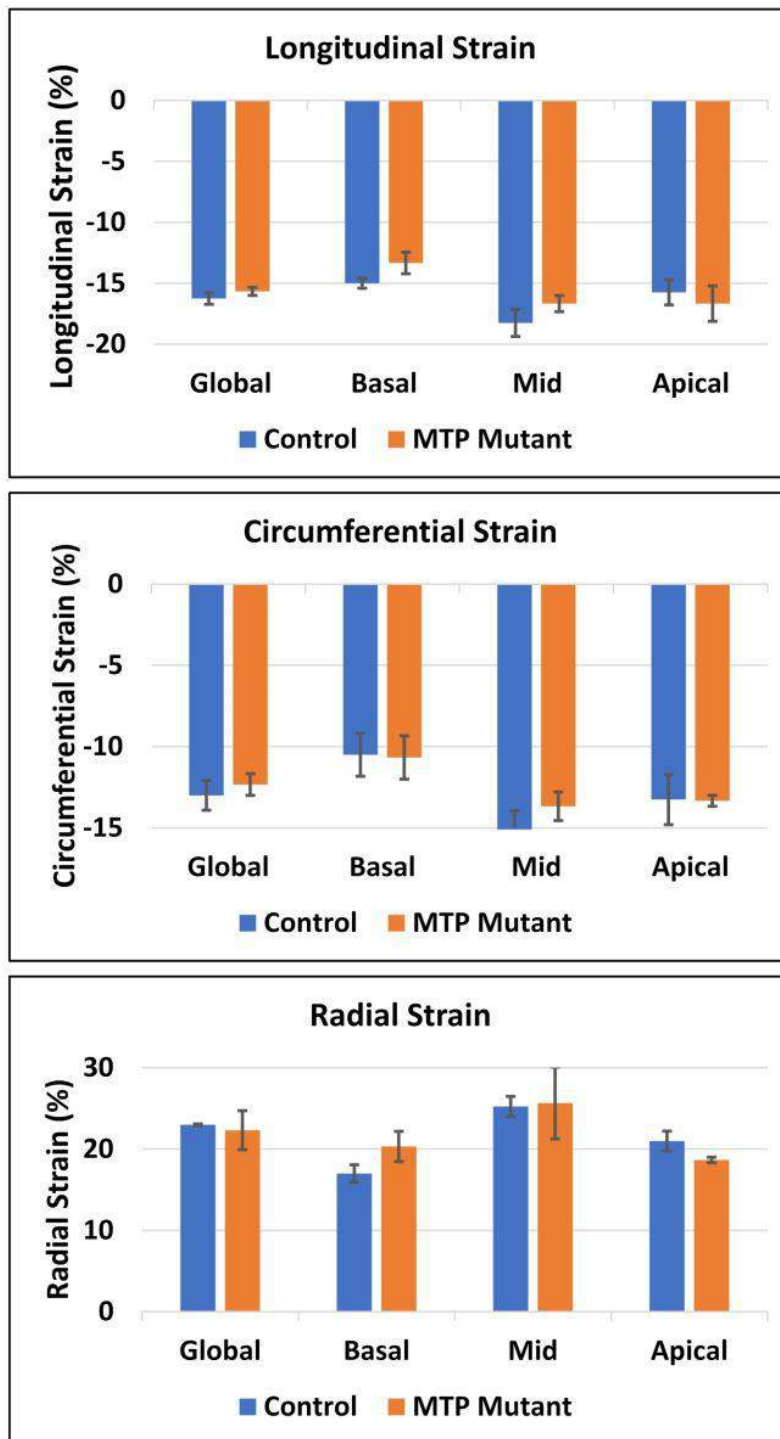
Figure/Table 1



Caption 1

**Figure 1.** Circumferential segmental strain curves through the cardiac cycle measured from a mid-ventricular short-axis slice in MTP mutant (up) and control (bottom) rats, showing recued peak systolic strain (red arrow) in the mutant rat. A, anterior; I, inferior; L, lateral; S, septal.

Figure/Table 2



**Caption 2**

**Figure 2.** Longitudinal (top), circumferential (middle), and radial (bottom) peak-systolic strain measurements (mean  $\pm$  SEM) in control (blue) and mutant (orange) rats, showing lower values in the mutant rats, especially in the longitudinal and circumferential directions.

**Figure 3**

Parameter	Control	MTP Mutant
Ell, Basal (%)	-15.0±0.4	-13.3±0.9
Ell, Mid (%)	-18.3±1.1	-16.7±0.7
Ell, Apical (%)	-15.8±1.0	-16.7±1.5
Ell, Global (%)	-16.3±0.5	-15.7±0.3
Ecc, Basal (%)	-10.5±1.3	-10.7±1.3
Ecc, Mid (%)	-15.3±1.3	-13.7±0.9
Ecc, Apical (%)	-13.3±1.5	-13.3±0.3
Ecc, Global (%)	-13.0±0.9	-12.3±0.7
Err, Basal (%)	17.0±1.1	20.3±1.9
Err, Mid (%)	25.3±1.3	25.7±4.4
Err, Apical (%)	21.0±1.2	18.7±0.3
Err, Global (%)	23.0±0	22.3±2.4

**Caption 3**

**Table 1.** Measurements (mean±SEM) of different strain components at different levels in the LV in MTP mutant and control rats. Ell, Ecc, Err: longitudinal, circumferential, and radial strains, respectively.

### **Bibliographic References**

EH Ibrahim et al. Magn Reson Imaging 2020; 73:130-137., D Marsden et al. Genetics in Medicine 2021; 23:816-829., JL Merritt et al. Rev Endocr Metab Disord 2020; 21:479-493.

Speaker: S. Kumar,

Category: Animal Experimentation, Cardiac Function, Statin

000204

**Free breathing, non-contrast, simultaneous and co-registered 3D coronary magnetic resonance angiography and plaque imaging in patients with non-ST-segment elevation myocardial infarction**

R. Hajhosseiny \* (1); A. Hartley, (2); G. Cole, (2); C. Munoz (1); A. Sethi, (3); R. Al-Lamee (2); D. Gopalan (4); R. Kaprielian (3); K. Kunze (5); R. Neji (5); C. Prieto (1); R. Khamis (2); R. M. Botnar (1)

(1) School of Biomedical Engineering and Imaging Sciences, King's College London, London, United Kingdom; (2) National heart and lung institute, Imperial College London, Hammersmith Campus, London, United Kingdom; (3) Department of cardiology, Imperial College Healthcare NHS Trust, London, United Kingdom; (4) Department of radiology, Imperial College Healthcare NHS Trust, London, United Kingdom; (5) MR Research Collaborations, Siemens Healthcare Limited, Frimley, United Kingdom

**Abstract**

**Background:** Rupture of an atherosclerotic plaque is the main trigger of myocardial infarction. Coronary high-risk plaque identified on cardiovascular magnetic resonance (CMR) is significantly associated with future coronary events, independent of coronary lumen stenosis (1). However, CMR plaque imaging is clinically limited by low spatial resolution, misregistration artefacts, respiratory motion related image quality degradation and unpredictable acquisition times. We have developed a novel 3D free-breathing non-contrast CMR sequence that allows for simultaneous high-resolution visualisation of the coronary arteries and high-risk plaque on co-registered bright and black blood images (2,3). Here, we investigate the feasibility of this technique in patients with non-ST-segment elevation myocardial infarction (NSTEMI)

**Methods:** The 3D sequence interleaves the acquisition of a T2prep-IR prepared bright-blood dataset with a T1 weighted (T1w) dataset without magnetization preparation (3) (iT2prep-BOOST). The bright-blood T2prep-IR dataset enables visualisation of the coronary lumen. Subtraction of the T2prep-IR dataset from the T1w dataset results in a coregistered black-blood dataset that enables visualisation of the coronary vessel wall, thrombus and intraplaque haemorrhage. 2D image-based navigation and respiratory binning enables 2D translational motion correction and 3D non-rigid motion estimation. The final image is obtained using a 3D non-rigid motion compensated iterative sense reconstruction for each contrast before subtraction. Reconstruction is implemented inline on the scanner. The proposed approach enables 100% scan efficiency and predictable scan times (<15 minutes). The acquired spatial resolution is 1.2x1.2x1.2 mm<sup>3</sup> with 3-fold undersampling. The proposed framework was compared against the gold standard modalities of invasive X-ray coronary angiography and optical coherence tomography (OCT)/intravascular ultrasound (IVUS) in a cohort of 15 patients who presented to our unit with NSTEMI. For visualisation purposes only, a second black-blood image was obtained with phase-sensitive inversion recovery (PSIR)-like reconstruction of the T2prep-IR and T1w datasets which was used for image fusion with the vessel wall (subtraction-based black-blood as described above) dataset.



**Results:** Figures 1 and 2 demonstrate the images of a 54-year-old male patient with type 2 diabetes mellitus, hypertension and 35-year smoking history. He presented to our heart assessment centre with 48 hours of worsening chest pain. Peak high-sensitivity troponin was elevated at 2218 ng/L. His electrocardiogram was normal. We were able to directly visualise culprit plaque rupture and acute intra-coronary thrombus of the proximal right coronary artery as well as bystander disease of the proximal to mid left anterior descending artery using iT2prep-BOOST. Figure 3 demonstrates the images of a 51-year-old male with a 30-year smoking history and strong family history of coronary artery disease who presented to our centre with 12 hours of chest pain at rest. His peak high-sensitivity troponin was elevated at 13459 ng/L with T wave inversions in the inferior electrocardiogram leads. We were able to directly visualise culprit vessel stenosis, plaque rupture and acute intra-coronary thrombus with iT2prep-BOOST.

**Conclusions:** In summary, the proposed iT2prep-BOOST framework has the potential to simultaneously visualise coronary artery stenosis as well as culprit and bystander coronary plaque in patients with NSTEMI.

**Figure/Table 1**

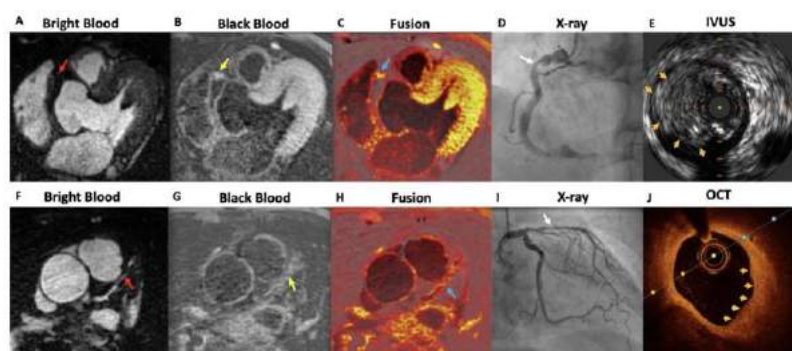


**Figure 1:**

**A-** Bright blood coronary magnetic resonance angiography showing a severe/critical proximal right coronary artery (RCA) stenosis (red arrow). **B-** Acute intracoronary thrombus of the proximal RCA on simultaneous contrast free black blood vessel wall images (yellow arrow). **C-** Fusion of the black blood vessel wall images with the PSIR black blood dataset for anatomical correlation (blue arrow). **D-** Severe/critical proximal RCA stenosis on invasive X-ray angiography (white arrow). **E-** Acute intracoronary thrombus on intravascular ultrasound (IVUS) (orange arrows). **F-** Bright blood coronary magnetic resonance angiography showing severe proximal to mid left anterior descending (LAD) artery stenosis (red arrow). **G-** Diffuse atherosclerosis on black blood vessel wall images (yellow arrow). **H-** Fusion of the black blood vessel wall images with the PSIR black blood dataset for anatomical correlation (blue arrow). **I-** Diffuse severe proximal to mid LAD stenosis on invasive X-ray angiography (white arrow). **J-** Diffuse high signal fibrotic atherosclerosis on optical coherence tomography (OCT) (orange arrows).

**Caption 1**

**Patient 1.** Direct visualisation of culprit plaque rupture and acute intra-coronary thrombus of the proximal right coronary artery as well as bystander disease of the proximal to mid left anterior descending artery using iT2prep-BOOST.

**Figure/Table 2**

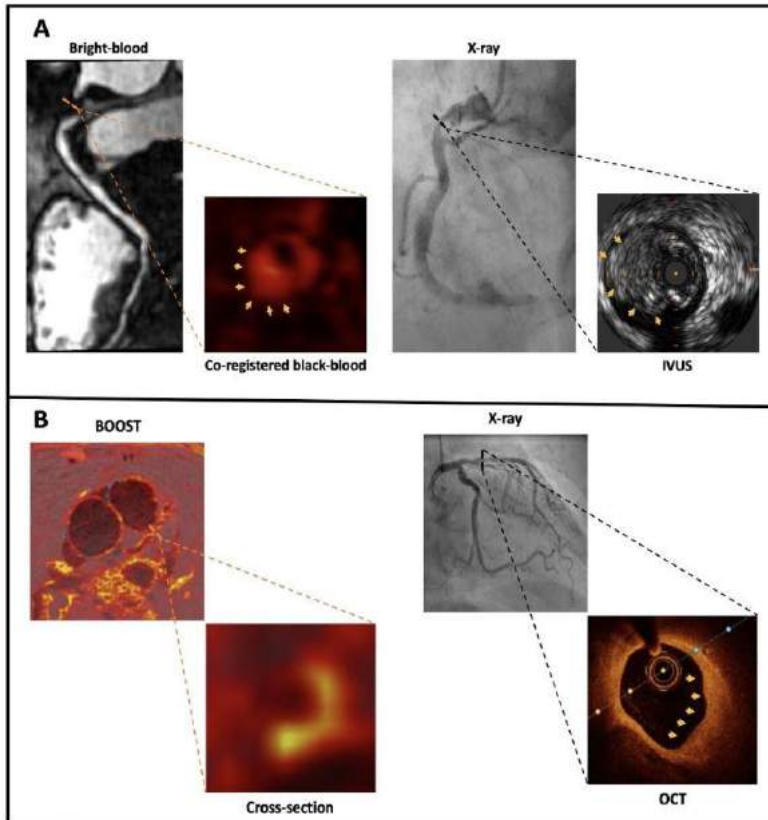


**Figure 2:**  
**A.** Images on the left represent the multiplanar reformat bright blood coronary magnetic resonance angiography of the right coronary artery (RCA), demonstrating a severe/critical stenosis of the proximal segment, with corresponding acute intraluminal thrombus as seen on the cross-sectional view of the vessel on simultaneous co-registered T1 weighted black-blood images (yellow arrows). Images on the right demonstrate the corresponding severe stenosis of the proximal RCA on invasive X-ray angiography and acute intracoronary thrombus as seen on intravascular ultrasound (IVUS) (yellow arrows). This represents direct visualisation of culprit plaque rupture and acute intraluminal thrombus with non-contrast CMR.

**B.** Images on the left demonstrate increased vessel wall signal intensity in the proximal to mid left anterior descending artery (LAD) as visualised on the longitudinal and 3D multiplanar reformatted cross-sectional view of the vessel on co-registered IT2Prep-BOOST imaging. Images on the right represent the corresponding severe proximal to mid LAD stenosis on invasive X-ray angiography and high signal fibrotic atherosclerosis on optical coherence tomography (OCT) (yellow arrows). This represents direct visualisation of bystander atherosclerotic plaque with non-contrast CMR.

## Caption 2

**Patient 1.** Cross sectional views of culprit vessel intra-coronary thrombus formation in the right coronary artery (A) and bystander coronary disease of the left anterior descending artery (B).

## Figure 3

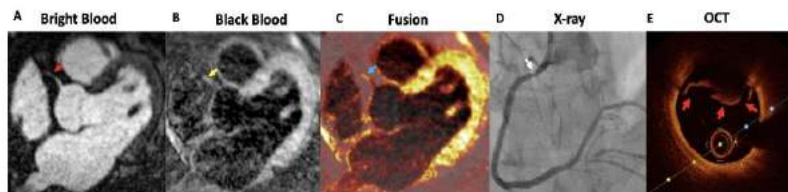


**Figure 3:**

**A-** Bright blood coronary magnetic resonance angiography showing a severe proximal right coronary artery (RCA) stenosis (red arrow). **B-** Acute intracoronary thrombus of the proximal RCA on simultaneous contrast free black blood vessel wall images (yellow arrow). **C-** Fusion of the black blood vessel wall images with the PSIR black blood dataset for anatomical correlation (blue arrow). **D-** Severe proximal RCA stenosis on invasive X-ray angiography (white arrow). **E-** Acute intracoronary thrombus on optical coherence tomography (OCT) (red arrows).

### Caption 3

**Patient 2.** Direct visualisation of culprit plaque rupture and acute intra-coronary thrombus of the proximal right coronary artery using iT2prep-BOOST.

### Bibliographic References

1. Noguchi T, Kawasaki T, Tanaka A, et al. High-Intensity Signals in Coronary Plaques on Noncontrast T1-Weighted Magnetic Resonance Imaging as a Novel Determinant of Coronary Events. *J. Am. Coll. Cardiol.* 2014;63:989–999.
2. Ginami G, Neji R, Phinikaridou A, Whitaker J, Botnar RM, Prieto C. Simultaneous bright- and black-blood whole-heart MRI for noncontrast enhanced coronary lumen and thrombus visualization. *Magn. Reson. Med.* 2018;79:1460–1472.
3. Milotta G, Ginami G, Cruz G, Neji R, Prieto C, Botnar RM. Simultaneous 3D whole-heart bright-blood and black blood imaging for cardiovascular anatomy and wall assessment with interleaved T 2 prep-IR. *Magn. Reson. Med.* 2019;82:312–325.

Speaker: R. Hajhosseiny

Category: Coronary Angiography, Coronary Vessel Wall, Acute Coronary Syndrome

000205

## **Myocardial fibrosis is associated with adverse cardiac remodelling and predicts worse outcomes in hypertensive heart disease**

N. Iyer \* (1); T.-T. Le, (1); M. Kui, (2); J. Bryant (1); B. Ang, (1); D.-F. Toh, (1); M. Ugander, (3); C. Chin (2)

(1) National heart research institute singapore, National Heart Centre Singapore, Singapore, Singapore; (2) Department of cardiology, National Heart Centre Singapore, Singapore, Singapore; (3) Kolling institute, The University of Sydney, Camperdown, Australia

### **Abstract**

#### **Background**

Arterial hypertension can induce significant cardiac remodelling with resultant adverse cardiovascular outcomes. Myocardial fibrosis is a pathological hallmark of heart failure and cardiac complications. We aim to examine the association between myocardial fibrosis on cardiovascular magnetic resonance (CMR) and patients with hypertension; and determine the prognostic implications of myocardial fibrosis in this cohort.

#### **Methods**

The cohort consisted of 800 asymptomatic patients with essential hypertension from the REMODEL observational study (clinicaltrials.gov identifier: NCT02670031). The CMR protocol included cine, strain, native T1- and ECV-mapping, and late gadolinium enhancement (LGE) imaging at 1.5T (Siemens Aera 1.5T, Siemens Healthineers, Erlangen, Germany). Patients were classified based on the presence/absence of non-myocardial infarction (MI) pattern LGE. Patients with MI pattern LGE were excluded. The primary outcome was a composite of all-cause mortality, acute coronary syndrome, strokes and decompensated heart failure.

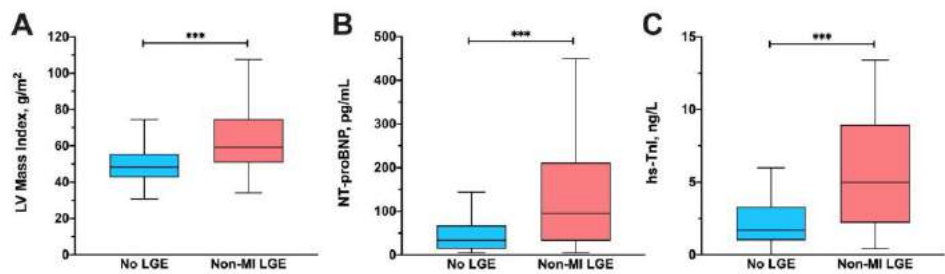
#### **Results**

Compared to patients without LGE (n=641), patients with non-MI pattern LGE (n=142) demonstrated more advanced cardiac remodelling, with increased left ventricular (LV) mass index and elevated biochemical markers of myocardial injury (NT-proBNP and hs-TnI) (Figure 1). These associations remained significant after adjusting for age, sex and systolic blood pressure. Over 39.1[30.0-50.3] months (2551.3 patient-years), 24 adverse events occurred (0.9 events/100 patient-years). Patients with non-MI pattern LGE had a nearly eight-fold increase in adverse events compared to patients without LGE (3.7 events/100 patient-years vs. 0.47 events/100 patients-years, respectively; log-rank  $P < 0.0001$ ) (Figure 2). Findings remained significant after adjusting for age, sex, systolic blood pressure and LV mass.

Conclusions

Non-ischemic myocardial fibrosis on CMR is associated with adverse features of cardiac remodeling, myocardial injury, and predicts worse outcomes in patients with hypertension.

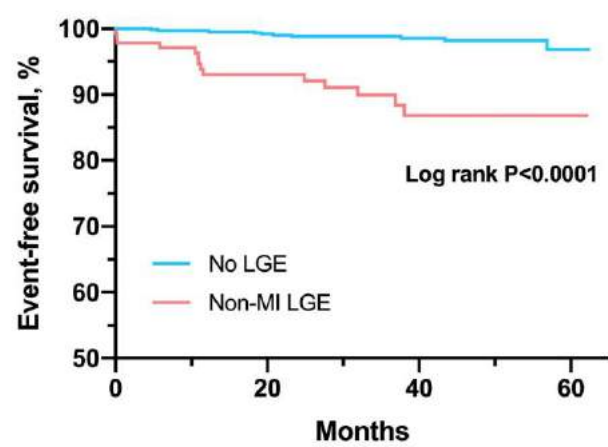
Figure/Table 1



Caption 1

Figure 1. Compared with those without LGE, hypertensive patients with non-MI pattern LGE had increased left ventricular mass index (A), N-terminal pro b-type natriuretic peptide (B) and high-sensitivity cardiac troponin I (C). Results are presented in box-and-whiskers plot (Tukey method).

Figure/Table 2



Caption 2

Figure 2. Event-free survival associated with the presence or absence of non-MI pattern LGE.

Speaker: N. Iyer

Category: Hypertension, Fibrosis, Outcomes

000208

## Understanding human myocardial ageing using CMR-ECGI: Myocardial inflammation and diffuse fibrosis associate with electrophysiological derangements

M. Webber \* (1); G. Joy (1); D. Falconer (1); X. Tao (2); I. Pierce (3); A. Hughes (1); J. Moon (4); P. Lambiase (3); P. Kellman (5); Y. Rudy (6); M. Orini (1); G. Captur (1)

(1) Institute of cardiovascular science, University College London, London, United Kingdom; (2) École nationale supérieure des arts et industries textiles, ENSAIT, Roubaix; (3) Barts heart centre, Barts Health NHS Trust, London, United Kingdom; (4) Cardiac mri, Barts heart Center, London, United Kingdom; (5) National institutes for health, NHLBI, Bethesda, United States of America; (6) Department of biomedical engineering, Washington University in St. Louis, St. Louis, United States of America

### Abstract

**Background:** Susceptibility to sudden arrhythmic death increases with age and can be predicted by biomarkers noninvasively derived by electrocardiographic imaging (ECGI) such as activation time (AT), repolarisation time (RT) and activation recovery interval (ARI). To understand how the ageing myocardial substrate multi-parametrically assessed by cardiovascular magnetic resonance (CMR) influences cardiac electrophysiology (EP), a noninvasive, re-usable and affordable ECGI solution was needed. We recently developed the CMR-ECGI vest to study the EP landscape of the ageing heart under physiological conditions.

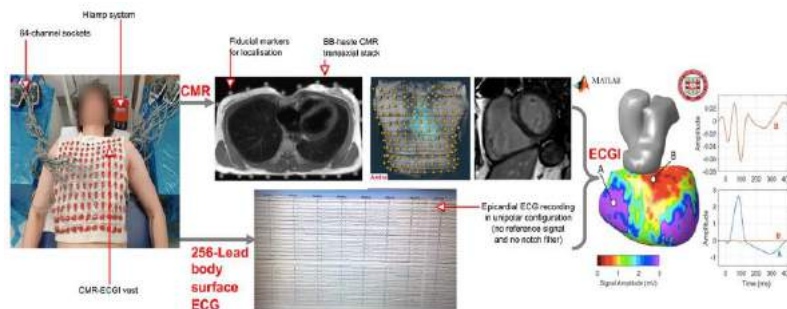
**Methods:** CMR-ECGI at 3 Tesla was prospectively performed on all participants (Figure 1). 256-Lead body surface potentials were recorded at a sampling frequency of 2048Hz, for 5 minutes at rest in the supine position and then co-registered with CMR-derived heart-torso geometries. Epicardial unipolar potentials were reconstructed using state-of-the-art ECGI algorithms and local ATs and RTs were computed using standard methods to derive panoramic cardiac EP maps (Figure 2).

**Results:** 50 Participants were recruited: 33 older persons from a population-based cohort (all 75 years; 52% male) and 17 young healthy volunteers (38±13 years, 59% male). CMR-derived tissue characteristics differed between old and young (respectively, T1 1295±51ms vs 1280±46ms,  $p=0.12$ ; T2 46.5±3.4ms vs 43.5±3.4ms,  $p=0.002$ ; extracellular volume [ECV] 26.96±2.36% vs 23.31±4.31%,  $p=0.004$ ; stress myocardial blood flow [SMBF] 2.16±0.65mL.g<sup>-1</sup>.min<sup>-1</sup> vs 2.77±0.67mL.g<sup>-1</sup>.min<sup>-1</sup>,  $p=0.003$ ). All ECGI biomarkers were prolonged in older compared to younger hearts (respectively, mean AT 41.42±17.95ms vs 32.94±4.83ms,  $p=0.007$ ; mean RT 323.7±28.10ms vs 299.5±18.10ms,  $p=0.002$ ; mean ARI 280.3ms±19.11 vs 265.1±19.67ms,  $p=0.01$ ; mean local gradient of activation time [LGAT] 0.59±0.09ms/mm vs 0.53±0.10ms/mm,  $p=0.03$ ) (Figure 3). Apart from left ventricular ejection fraction, no other standard CMR size/function parameter or presence of late gadolinium enhancement, were associated with ECGI parameters, whereas native T1, T2 and ECV were all associated with RT prolongation (respectively, Spearman's correlation coefficient ( $r_s$ ) 0.38,  $p=0.007$ ;  $r_s$ 0.34,  $p=0.02$ ;  $r_s$ 0.57,  $p<0.001$ ) and with ARI prolongation (respectively,  $r_s$ 0.29,  $p=0.03$ ;  $r_s$ 0.39,  $p=0.005$ ;  $r_s$ 0.58,  $p<0.001$ ).



**Conclusions:** Ageing alters the normal electrophysiological sequence of activation and repolarization in the human heart and alterations are associated with low-grade myocardial inflammation and diffuse fibrosis. High-throughput CMR-ECGI could provide deeper insights into the pathophysiology of arrhythmogenesis beyond conventional measures of cardiac structure and function.

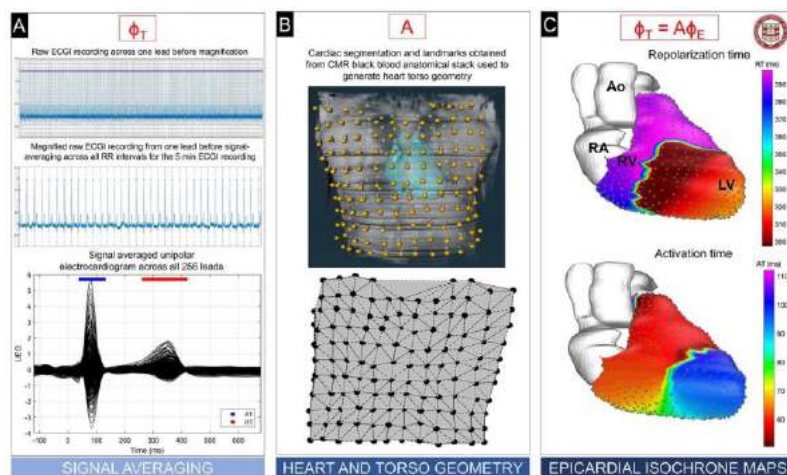
**Figure/Table 1**



**Caption 1**

ECGI is performed for 5 mins at rest. CMR transaxial BB anatomical stack is used to locate fiducial markers for co-registration. Activation time isochrone map shown for a 75-year with midwall late gadolinium enhancement corresponding to a zone of fractionation in the unipolar electrograms. BB=black blood.

**Figure/Table 2**

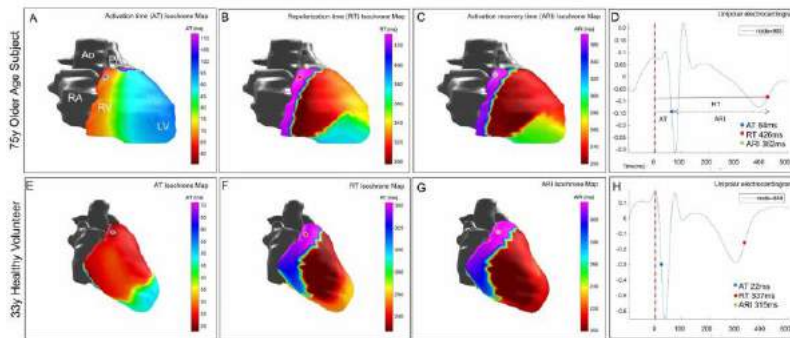


**Caption 2**

The inverse solution of electrocardiography  $\phi_T = A\phi_E$ . ' $\phi_T$ ' Torso electrical potentials (obtained from the ECGI vest) are combined with 'A' the geometric matrix of the heart and

torso surface (obtained from CMR) to compute ' $\phi E$ ' epicardial potentials which are projected onto the heart surface in the form of isochrone maps using state of the art algorithms (YR labs).

**Figure 3**



**Caption 3**

Activation and recovery time isochrone maps arising from CMR-ECGI in a healthy 75 year old (A-D) and a healthy 27 year old volunteer (E-H) Unipolar electrocardiograms are shown highlighting the point of initial activation. Note the prolonged activation time, repolarisation time and activation recovery interval of the older participant compared to the young control.

Speaker: M. Webber

Category: Electrophysiology, Sudden Cardiac Death, Biomarkers



000210

## Occult Cardiac Dysfunction in Adolescent Long COVID Patients by Strain Encoded Imaging

T. Fick \* (1); K. Hor, (1); M. Lee, (1); J. Williams, (1); S. Rajpal, (1); K. L'italien, (1); S. Lee, (1)

(1) Pediatric Cardiology, Nationwide Children's Hospital, Columbus, United States of America

### Abstract

#### Background

There is emerging evidence of myocardial involvement after SARS-CoV-2 infection. This has ranged from evidence of direct infection on autopsy or biopsy-based studies to subclinical myocarditis seen by cardiac magnetic resonance imaging (CMR) in the asymptomatic collegiate athletes. Post-acute sequelae of COVID-19, or “long COVID” (LC) is an emerging disease entity seen with persistence or development of symptoms after acute infection, but its pathophysiology is unknown. Cardiac symptoms such as dyspnea on exertion, chest pain, and decreased exertional tolerance are commonly reported in LC. Occult myocardial involvement has been reported after SARS-CoV-2 infection and may also be playing a role in LC. We sought to use Strain-ENCodeD (SENC) deformation analysis to describe strain findings in a cohort of LC patients to assess for occult myocardial disease.

#### Methods

Retrospective review of patients who underwent CMR for acute symptomatic COVID-19 (SX) or LC. SX was defined as <30 days and LC defined as >60 days from positive SARS-CoV-2 test. No subjects met Lake Louise Criteria for myocarditis. We compared strain data to a cohort of normal controls obtained pre-pandemic. All studies were performed using 3.0 T Siemens Skyra scanner (Siemens Healthineers, Germany). We utilized SENC imaging to assess for global longitudinal (GLS) and circumferential strain (GCS) using MyoStrain (Myocardial Solutions, Morrisville, NC). Reduced strain was defined as absolute magnitude <17% and statistical significance set at  $p < 0.05$ .

#### Results

We collected data on 34 patients with LC (50% males), 6 patients with SX (38% males) and compared these patients with 18 healthy controls. The SX and LC cohorts were similar in age (LC mean age  $16.5 \pm 2.3$  years old, SX mean age  $15.9 \pm 2.1$  years old). Table 1 summarizes the ejection fraction and strain data. Left ventricular ejection function was preserved with no statistical difference between the three groups. All three groups had preserved LVGCS with no difference amongst the groups. However, both LC ( $-17.8 \pm 2.1$ ,  $p < 0.0001$ ) and SX patients ( $-17.6 \pm 2.4$ ,  $p < 0.0001$ ) had statistically lower LVGLS magnitude than control group ( $-20.2 \pm 1.7$ ) with 11/35 (31%) LC patients having abnormal LVGLS (Figure 1). When comparing LVGLS between the LC and SX groups, there was no statistical difference.

#### Conclusion

SX and LC patients have significant decreased LVGLS compared to controls. These differences are seen in both groups of COVID-19 patients despite a longer period from infection in the LC group. Follow-up studies are necessary to determine if these findings persist.

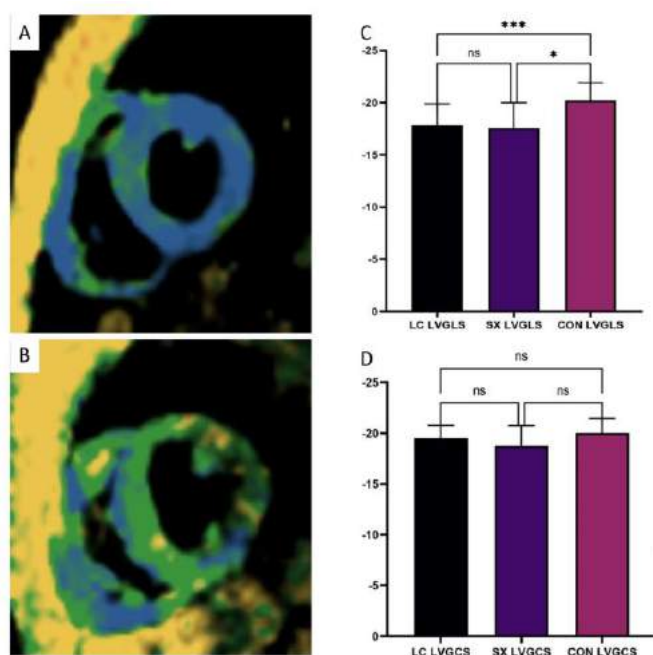
**Figure/Table 1**

	Average Age	% Male	LVEF (%)	Ave LV GLS	Ave LV GCS
<b>Long Covid</b>	16.5	50	59.7	-17.8	-19.5
	( $\pm 2.3$ )*		( $\pm 3.1$ )	( $\pm 2.1$ )*	( $\pm 1.3$ )
<b>Symptomatic Covid</b>	15.9	50	57.6	-17.6	-15.9
	( $\pm 2.1$ )*		( $\pm 4.2$ )	( $\pm 2.4$ )*	( $\pm 2.0$ )
<b>Control</b>	19.3	50	61.1	-20.2	-20
	( $\pm 1.1$ )		( $\pm 5.2$ )	( $\pm 1.7$ )	( $\pm 1.4$ )

**Caption 1**

**Table 1:** Table representation of ejection fraction and strain data for LC, SX and control patients. \* statistically significant against controls \*\* statistically significant against LC

**Figure/Table 2**



## Caption 2

Figure 1. Upper left panel shows normal strain in control patient as compared to lower left panel showing abnormal strain in a SX patient. Upper right panel shows LV GLS between the three groups and lower right shows LV GCS between the groups. Note no difference in LV GLC between SX and LC patients.

## Bibliographic References

Joy G, Artico J, Kurdi H, Seraphim A, Lau C, Thornton GD, et al. Prospective Case-Control Study of Cardiovascular Abnormalities 6 Months Following Mild COVID-19 in Healthcare Workers. *JACC Cardiovasc Imaging*. 2021., Havervall S, Rosell A, Phillipson M, Mangsbo SM, Nilsson P, Hober S, et al. Symptoms and Functional Impairment Assessed 8 Months After Mild COVID-19 Among Health Care Workers. *JAMA*. 2021;325(19):2015-6., Kim JH, Levine BD, Phelan D, Emery MS, Martinez MW, Chung EH, et al. Coronavirus Disease 2019 and the Athletic Heart: Emerging Perspectives on Pathology, Risks, and Return to Play. *JAMA Cardiol*. 2021;6(2):219-27., Huang L, Zhao P, Tang D, Zhu T, Han R, Zhan C, et al. Cardiac Involvement in Patients Recovered From COVID-2019 Identified Using Magnetic Resonance Imaging. *JACC Cardiovasc Imaging*. 2020;13(11):2330-9., Carvalho-Schneider C, Laurent E, Lemaignan A, Beaufils E, Bourbao-Tournois C, Laribi S, et al. Follow-up of adults with noncritical COVID-19 two months after symptom onset. *Clin Microbiol Infect*. 2021;27(2):258-63.

Speaker: T. Fick

Category: Myocarditis, Nonischemic Cardiomyopathy, Strain

000211

## Inline Implementation of a High-Resolution Myocardial Perfusion Imaging Framework with Integrated Motion Compensation: A Feasibility Study

K. Kunze \* (1); N. Mellor (2); T. Moon (2); K. Pushparajah (3); R. Neji (1); A. Chiribiri (3)

(1) MR Research Collaborations, Siemens Healthcare Limited, Frimley, United Kingdom;  
(2) Evelina london children's hospital, Guy's and St Thomas' NHS Foundation Trust, London, United Kingdom; (3) Biomedical Engineering and Imaging Sciences, King's College London, London, United Kingdom

### Abstract

**Background:** Current clinical myocardial perfusion MR techniques are hampered by a lack of spatial resolution. Both cardiac and respiratory motion are a challenge to image quality, and usually result in the need for breath held exams and very fast single-shot acquisitions, with acquisition durations of single slices also being the limiting factor for anatomical coverage. To increase spatial resolution and/or shorten single-shot acquisition times, a high acceleration factor is desirable. This however is only achievable with some regularization across the dynamic series, which leads to blurring in case of motion between frames. This work describes a feasibility study for a high-resolution perfusion imaging framework using an integrated motion compensation within the temporal regularization in a fast, GPU-supported inline reconstruction.

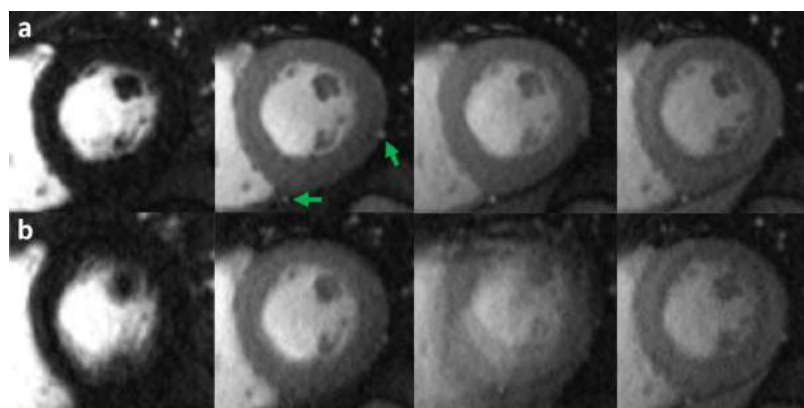
**Methods:** A 2D single-shot, saturation-recovery MR perfusion sequence prototype was implemented featuring a dedicated sampling pattern with linear undersampling and incoherent undersampling of low and high spatial frequencies, respectively. A prototype reconstruction was implemented inline on the scanner with GPU support, featuring a preliminary reconstruction of all frames at reduced resolution without temporal regularization, an estimation of non-rigid motion fields between all frames (1), and a final reconstruction with motion fields incorporated into a temporal regularization term (2,3). The described sequence and reconstruction were applied in 3 patients with suspected Myocarditis (ages 12/16/17 years) on a 3T Scanner (MAGNETOM Vida, Siemens Healthcare, Erlangen, Germany), with the following parameters: 1.3mm<sup>2</sup> acquired resolution, 8mm slice thickness, 3-4 slices per heartbeat, acceleration factor 5.5-6.0, FLASH readout, TE/TR 1.19/2.71ms, BW 707 Hz/px, TI 110ms, FA 15deg, chemical-shift selective fat saturation, single slice readout time 105ms (excluding sat pulses, delay times and FatSat). The sequence was applied in free breathing during a bolus injection (0.15 mmol/kg Gadobutrol) for 90 dynamics and reconstructed with (MC) and without (NMC) integrated motion compensation. Additionally, a clinical reference sequence was applied directly afterwards for 40 dynamics (acquired/reconstructed resolution 2.3x1.9/1.9x1.9mm<sup>2</sup>, TPAT acceleration factor 2, TE/TR 1.03/2.16ms, BW 1003 Hz/px, TI 95ms, single slice readout time 125ms).

**Results:** Image reconstruction time for the high-resolution acquisition was 20-30s per slice. Image quality for MC was excellent in all three cases despite heavy respiratory and cardiac motion as revealed by the comparison of MC and NMC reconstructions. Fig. 1 shows a comparison of MC and NMC images in one patient at different points during the dynamic series. Fig. 2 shows MC, TPAT and LGE images of the same patient, the latter confirming acute myocarditis and validating the contrast pattern seen in both MC and TPAT images

during the last frames. Fig. 3 shows a second patient with both cardiac and respiratory motion, leading to significant blurring in NMC, but no comparable degradation in MC images.

**Conclusion:** A high-resolution myocardial perfusion approach based on a fast inline reconstruction with integrated motion compensation was successfully employed in patients with suspected myocarditis, showing excellent ability to handle both cardiac and respiratory motion at a resolution of  $1.3\text{mm}^2$ .

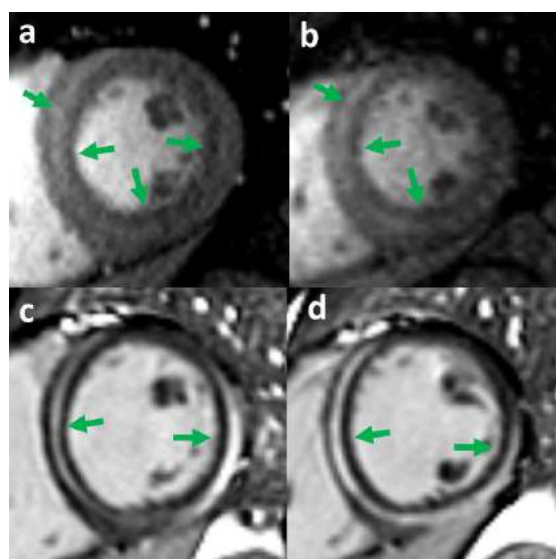
**Figure/Table 1**



**Caption 1**

Example case (17y), upper row shows MC (a), lower row NMC (b) reconstructions. The columns show peak RV/LV, peak myocardium, end of the first pass, and last dynamic respectively. Breathing motion led to heavy blurring in NMC reconstruction in the bottom row. Coronaries are highlighted as an example of a well-resolved, small structure.

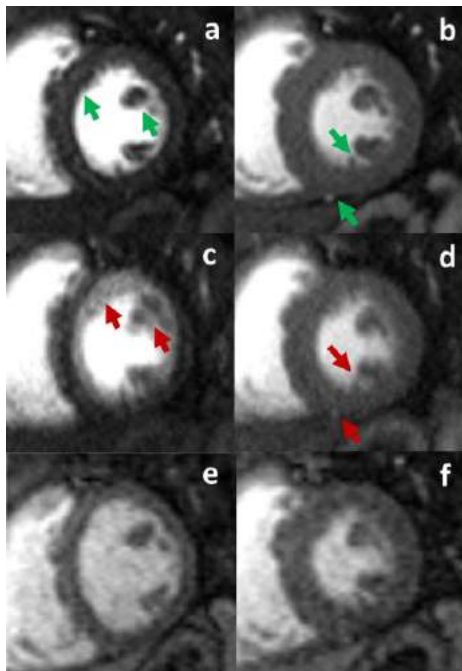
**Figure/Table 2**



## Caption 2

Same case as Fig 1, upper row shows the last dynamic (~80s post injection) of the high-res images with MC (a) versus the first dynamic of the reference sequence run directly after it (b). Both a) and b) are beginning to show a ring-shaped contrast enhancement pattern. The bottom row (c/d) shows the corresponding LGE scans taken 10 minutes after injection.

## Figure 3



## Caption 3

Example case (12y) with respiratory motion and mis-triggering. Top: MC high-resolution, mis-triggered diastolic frame (a) and systolic frame without adjacent mis-triggering (b). c) and d) show the same frames as a) and b) for NMC, exhibiting severe blurring motion. Bottom: Mis-triggered diastolic (e) and systolic (f) images from the reference TPAT series.

## Bibliographic References

- 1) Xue H, Zuehlsdorff S, Kellman P, et al. Unsupervised inline analysis of cardiac perfusion MRI. In Proceedings of the International Conference on Medical Image Computing and Computer-Assisted Intervention, 2009, 741-749., 3) Muehlberg F, Stoetzner A, Forman C, et al. Comparability of compressed sensing-based gradient echo perfusion sequence SPARSE and conventional gradient echo sequence in assessment of myocardial ischemia. European Journal of Radiology, 2020, 131:109213. , 2) McElroy S, Kunze KP, Nazir S, et al. Stress first pass myocardial perfusion using simultaneous multi-slice (SMS) SSFP with iterative reconstruction and integrated motion compensation. Proceedings of the Annual

SCMR Meeting, 2021.

Speaker: K. Kunze

Category: First-Pass Perfusion, Nonlinear Reconstruction, 3D

000214

## Image-based validation of a new Doppler-based index for coarctation severity assessment

A. Ghorbanniahassankiadeh, \* (1); J. LaDisa (2); E.-S. Ibrahim, (3)

(1) Biomedical engineering, Medical College of Wisconsin, Wauwatosa, United States of America; (2) Pediatrics, Medical College of Wisconsin, Wauwatosa, United States of America; (3) Radiology, Medical College of Wisconsin, Wauwatosa, United States of America

### Abstract

**Background:** Coarctation of the aorta (CoA) is the third most common cardiovascular defect among children with congenital heart disease. CoA severity is assessed via blood pressure gradient (BPG) estimated using simplified Bernoulli equation (SBE) from Doppler echocardiography (echo), but simplifications of the SBE limit diagnostic accuracy. In a rabbit model mimicking discrete juxtaductal human CoA[1], catheter versus Doppler comparison of BPG revealed a diastolic continuous-flow pressure gradient (CFPG) that is independently associated with CoA severity. The objective of the current work was to create subject-specific fluid structure interaction (FSI) models from MRI data of CoA rabbits to assess the potential influence of the anesthesia, minimum alveolar isoflurane concentration (MAC) 1%, used with CoA rabbits for our CFPG analysis.

**Methods:** Anesthetized rabbits were scanned in the supine, head-first position on a GE 3T MRI Premier scanner (GE Healthcare, Waukesha, WI) using an 18-channel knee coil and peripheral gating. Gadolinium-enhanced (Gd; Omniscan gadodiamide; GE Healthcare, Princeton, NJ) MR angiography (MRA) was performed (injection rate: 2 ml/s) to elucidate the flow domain for FSI modeling. Phase-contrast (PC-MRI) images were acquired across the ascending aorta, proximal and distal descending aorta, coarctation site, and carotid arteries. Twenty 2D velocity-encoded and phase (through-plane direction: 80 cm/s) magnitude images were acquired per cardiac cycle (temporal resolution: 15-30 ms). Other parameters included 12x12-cm field of view, a 256x224 acquisition matrix, TR of 8.5 ms, TE of 1.7 ms, flip angle of 20 degrees, and 3 mm slice thickness. FSI models were reconstructed from MRA data for representative rabbits (mild and severe CoA vs control rabbits). Ascending aortic PC-MRI waveforms were mapped to the inlet faces of each model and Windkessel boundary conditions were imposed to replicate flow and BP measured from PC-MRI and catheter measurements, respectively<sup>1</sup>. Cyclic strain was replicated within 5% of the imaging data. After matching physiologic results during Isoflurane at a 1 MAC, Windkessel parameters were adjusted until the mean BP increased by 65-70% to represent recovery to conscious state[2, 3] while assuming no significant isoflurane-induced change in cardiac output[4].

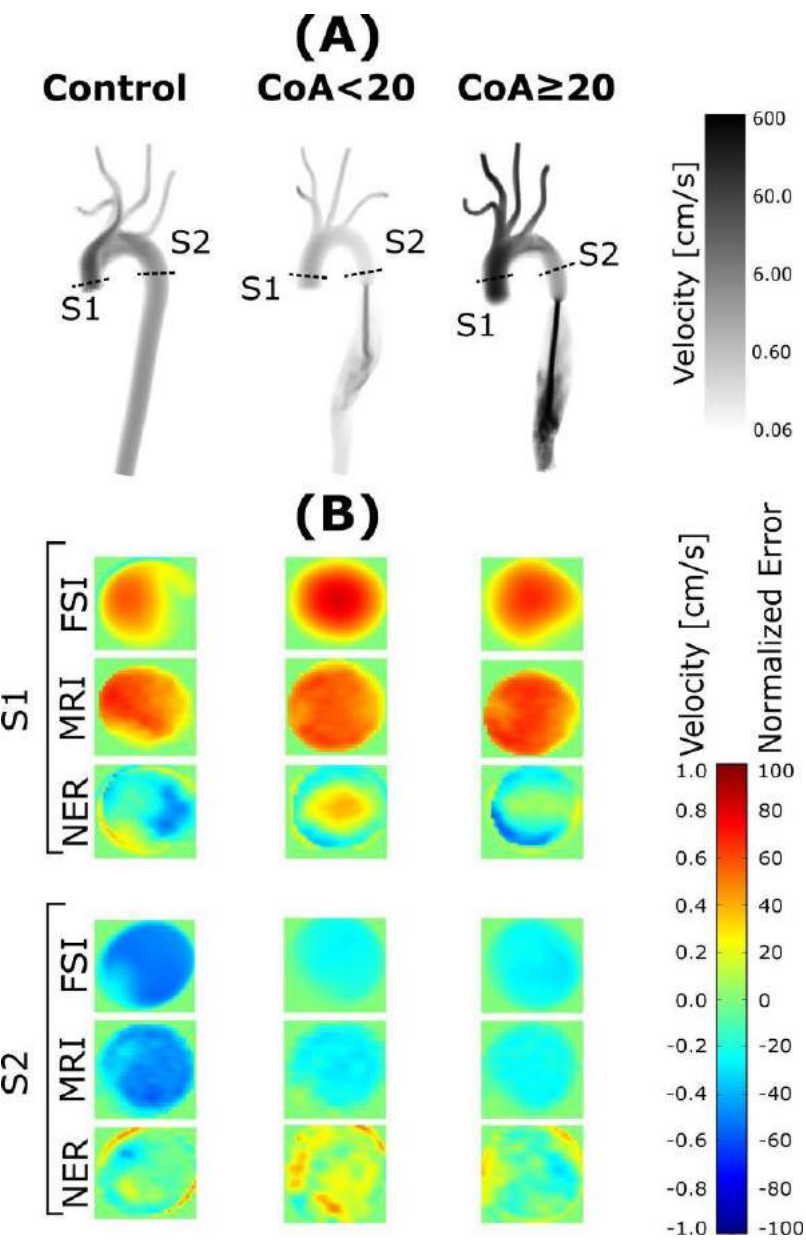
**Results:** Relative to Control, FSI results from CoA rabbits showed lower velocity in the aortic arch, a velocity jet up to ~500 cm/s due to the CoA, and turbulent deceleration associated with tortuosity and post-stenotic dilatation (Figure). 2D through-plane velocity comparison between PC-MRI and FSI simulations, as well as the corresponding normalized velocity difference map, showed good agreement (difference ≈18%). Strong agreement in peak jet velocities was also observed between measured results and FSI simulations (difference <0.80



m/s). Peak CoA velocity under simulated conscious conditions revealed no significant differences compared with the anaesthetized condition.

Conclusions: These findings suggest (1) CFPG results from our anaesthetized CoA rabbits are expected to remain unchanged under conscious conditions, (2) the utility of CFPG may be assessed computationally beyond the discrete juxtaductal configuration studied to date, and (3) differences in results between humans and rabbits from our newly derived CFPG are likely due to factors other than those from anesthesia.

Figure/Table 1



Caption 1

Figure - FSI results comparing representative CoA and Control rabbits during Isoflurane (MAC = 1). (A) Volume rendered peak blood flow velocity. (B) Blood flow velocity comparison between PC-MRI and FSI results at peak systole for slice locations S1 and S2. Color maps correspond to through-plane velocity magnitude as well as the normalized error (NER) from FSI results quantified as percent difference relative to PC-MRI data.

### **Bibliographic References**

[1] Menon A, Eddinger TJ, Wang H, Wendell DC, Toth JM and LaDisa JF, Jr. Altered hemodynamics, endothelial function, and protein expression occur with aortic coarctation and persist after repair. , [2] Owen TL. Effect of age on blood pressure and small vessel reactivity in male rabbits. *Blood Vessels*. 1986;23:271-8., [3] Pipkin FB. Cardiovascular responses in rabbits of different ages to hypertensin and adrenaline. *Q J Exp Physiol Cogn Med Sci*. 1971;56:210-20., [4] Preckel B, Schlack W, Comfere T, Obal D, Barthel H and Thamer V. Effects of enflurane, isoflurane, sevoflurane and desflurane on reperfusion injury after regional myocardial ischaemia in the rabbit heart in vivo. *Br J Anaesth*. 1998;81:905-12.

Speaker: A. Ghorbanniahassankiadeh,

Category: Phase Contrast , Computational Fluid Dynamics, Congenital Heart Disease

000215

## On the Influence of Respiratory State on Pilot Tone Derived Cardiac Triggers

M. Bacher \* (1); P. Speier (1); M. B. L. Falcão (2); C. Roy (2); M. Prša (3); T. Rutz (4); M. Stuber (2)

(1) DL CARD, Siemens Healthineers, Erlangen, Germany; (2) Department of radiology, Lausanne University Hospital (CHUV) and University of Lausanne (UNIL), Lausanne, Switzerland, Lausanne, Switzerland; (3) Woman-mother-child department, Lausanne University Hospital (CHUV) and University of Lausanne (UNIL), Lausanne, Switzerland, Lausanne, Switzerland; (4) Department of cardiology, Lausanne University Hospital (CHUV) and University of Lausanne (UNIL), Lausanne, Switzerland

### Abstract

#### Background

Pilot Tone (PT)[1] is a novel, electromagnetic sensing technique capable of remotely sensing respiratory and cardiac motion that has gained popularity in recent years. The PT signal is closely correlated to total cardiac volume[2] and can be used both in real-time or retrospectively to trigger or gate MR acquisitions. We have previously used PT in lieu of self-gating[3] for its high temporal resolution and sequence-independence in a free-running acquisition strategy. PT signals are used to bin the acquired data into respiratory and cardiac bins. Here we aim to investigate how the trigger points derived from the cardiac PT signal change depending on the respiratory position.

#### Methods

We scanned 12 volunteers (a: 27 $\pm$ 3y, 7 male, 8 female) and eight patients (a: 24 $\pm$ 16y, 5 male, 3 female) at 1.5T (MAGNETOM Sola, Siemens Healthcare GmbH, Erlangen, Germany) using a prototype free-running acquisition[3]. From raw PT data (one channel per receive coil) the respiratory and cardiac PT signals  $s_{PT,resp}$  and  $s_{PT,card}$  were extracted using Blind Source Separation (BSS) (PCA for  $s_{PT,resp}$ , ICA for  $s_{PT,card}$ ). The cardiac signal was filtered using our Kalman-Filter processing chain[4], where cardiac triggers are detected as zero-crossings of the signals 1st derivative (Fig. 1a). The respiratory signal  $s_{PT,resp}$  was used to bin the data into three respiratory bins (see Fig. 1b). For each of these bins, triggers were extracted from  $s_{PT,card}$  and matched with ECG R-peaks as ground truth (Fig. 1c). The temporal difference between ECG R-peak and PT triggers,  $\Delta_{trig}$  (see Fig. 1) was determined and, to account for the effect of R-R duration changing with respiratory state (respiratory sinus arrhythmia),  $\Delta_{trig}$  was normalized to the mean R-R interval in its corresponding bin and is thus given in percent of the mean R-R interval. This normalization also allows for the pooling of results over subjects. Respiratory bins were then tested for significant differences in  $\Delta_{trig,norm}$  using ANOVA. To characterize respiratory amplitude, we used navigators on the liver dome, derived from reconstructed 3D datasets. In total, we analyzed 8550 individual heartbeats in the volunteer- and 3742 heartbeats in the patient cohort.

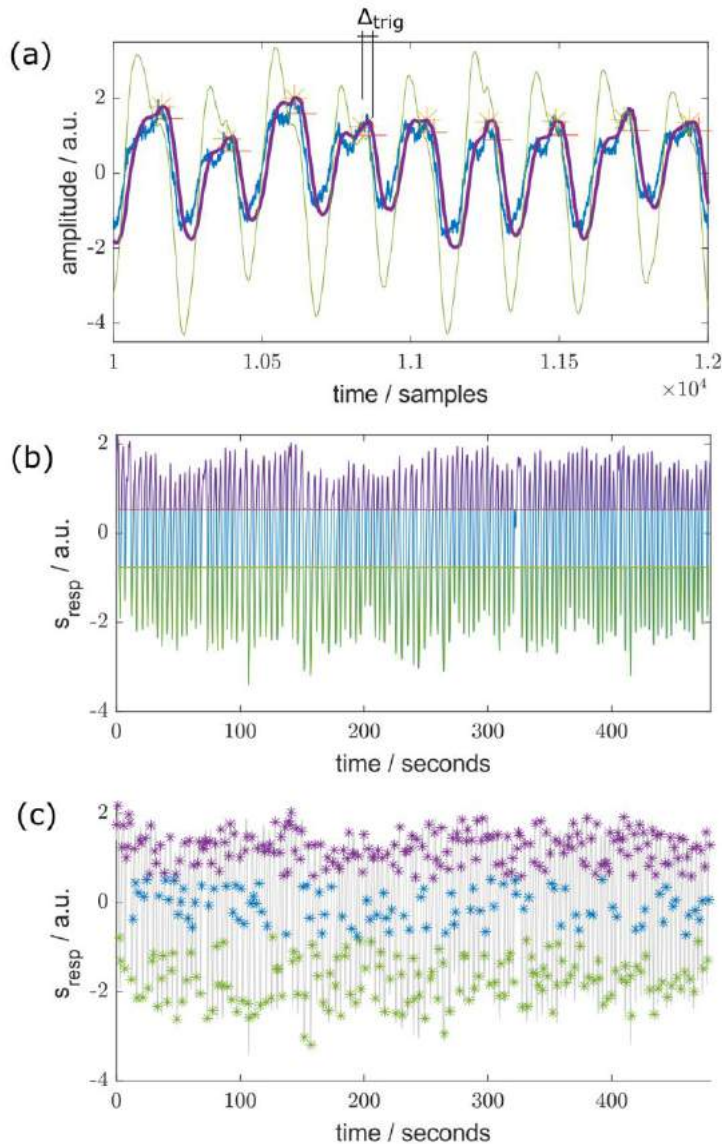
#### Results

We found significant differences in  $\Delta_{\text{trig,norm}}$  between all respiratory states in the volunteer cohort (Fig. 3) but no significant difference was observed in the patient cohort. Normalized trigger delays are given in Tab.1. Respiratory amplitude was significantly higher in the volunteer cohort ( $16.1 \pm 4.9 \text{ mm}$ ) than in the patient cohort ( $9.1 \pm 1.8 \text{ mm}$ ).

## Conclusions

We found that in subjects with higher respiratory amplitude, trigger points are slightly shifted with respect to R-peak, whereas this effect is not significant when the respiratory amplitude is lower. Falcão et al.[3] found no significant difference in image quality when using PT derived motion data compared to self-gating, but when going to higher temporal resolutions, these small changes will potentially need to be considered. The observed differences in  $\Delta_{\text{trig,norm}}$  are readily explained by the fact that BSS techniques are statistical in nature and healthy subjects tend to spend more time in expiration. Thus, these datapoints are weighted more strongly in the separation algorithm when training on free-breathing data. This could be mitigated by introducing data weighting based on respiratory state during this training phase.

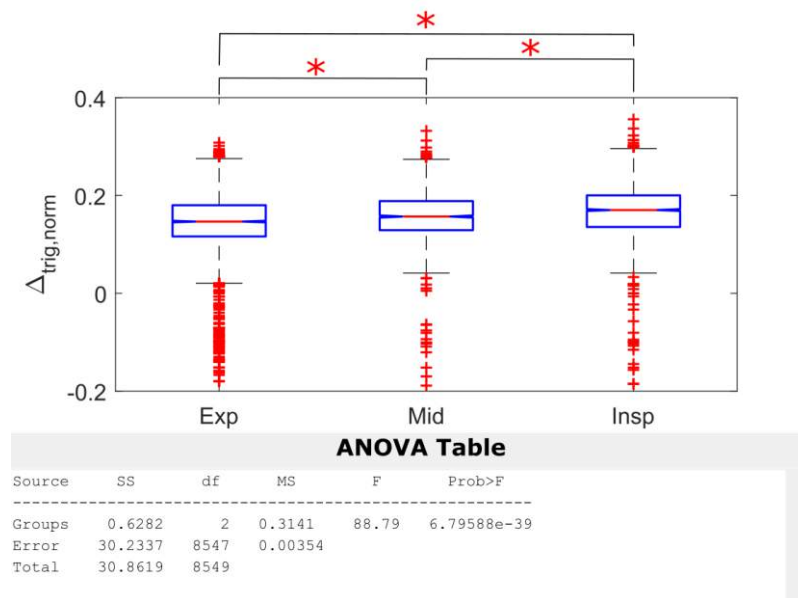
**Figure/Table 1**



## Caption 1

Figure 1: (a) Raw cardiac signal (blue), Kalman Filtered (purple), 1st derivative (green). PT triggers (red +, zero-crossings of the 1st derivative) plotted against ECG R-peaks (yellow \*). (b) Binning of datapoints into respiratory bins (green: Expiration, Blue: Mid-respiratory and Purple: Inspiration). (b) PT derived trigger points found for each bin in (a)

## Figure/Table 2



## Caption 2

Figure 2: ANOVA results shown as boxplot for the volunteer cohort. Delta\_trig, norm differ significantly between groups at the P<0.005 confidence level (red asterisks). Outliers are plotted as red +. No significant differences were observed between respiratory states in the patient cohort.

## Figure 3

	Insp	Mid	Exp
	in % of mean R-R interval		
	Volunteers		

mean	0.16	0.16		0.15
std. dev.	0.06	0.05		0.06
<b>Patients</b>				
mean	0.18	0.17		
std. dev.	0.07	0.07		

### Caption 3

Table 1: Means and standard deviation of dtrig,norm in Expiration, Mid-respiration and inspiration stratified by volunteer and patient cohort. dtrig,norm is given in percent of the mean R-R interval in the corresponding respiratory state.

### Bibliographic References

[4] Bacher M, Gatehouse P, Wage R, et al. Performance Analysis of a Fully Automatic Real-Time Capable Pilot Tone Cardiac Triggering Framework. Proc. from 23rd Annu. SCMR Sci. Sess. 2020;63:412–414., [3] Falcão MBL, Di Sopra L, Ma L, et al. (in press) Pilot Tone navigation for respiratory and cardiac motion resolved free-running 5D flow Magnetic Resonance Imaging. Magn. Reson. Med. 2021., [2] Bacher M, Dornberger B, Bollenbeck J, Stuber M, Speier P. Listening in on the Pilot Tone: A Simulation Study. In: Joint Annual Meeting of the ISMRM & ESMRMB, Virtual. ; 2021. p. 1364., [1] Speier P, Fenchel M, Rehner R. PT-Nav: a novel respiratory navigation method for continuous acquisitions based on modulation of a pilot tone in the MR-receiver. In: Magnetic Resonance Materials in Physics, Biology and Medicine. Vol. 28. ; 2015. pp. 97–98. doi: 10.1007/s10334-015-0487-2.

Speaker: M. Bacher

Category: Respiratory Motion, Navigator, Gating

000216

## Reduced Myocardial Strain is Associated with Myocardial Inflammation and Fibrosis on Cardiovascular Magnetic Resonance Imaging in Collegiate Athletes Recovering From SARS-CoV-2 Infection

J. Heyniger \* (1); J. Varghese, (2); P. Chandrasekaran (1); K. Gil, (1); S. Lee, (3); M. Lee, (3); K. Hor, (3); C. Daniels, (1); S. Rajpal (1); O. Simonetti (4)

(1) Cardiovascular medicine, The Ohio State University, Columbus, United States of America; (2) Department of radiology, The Ohio State University, Columbus, United States of America; (3) Pediatric cardiology, Nationwide Children's Hospital, Columbus, United States of America; (4) Davis heart and lung research institute, Ohio State University, Columbus, United States of America

### Abstract

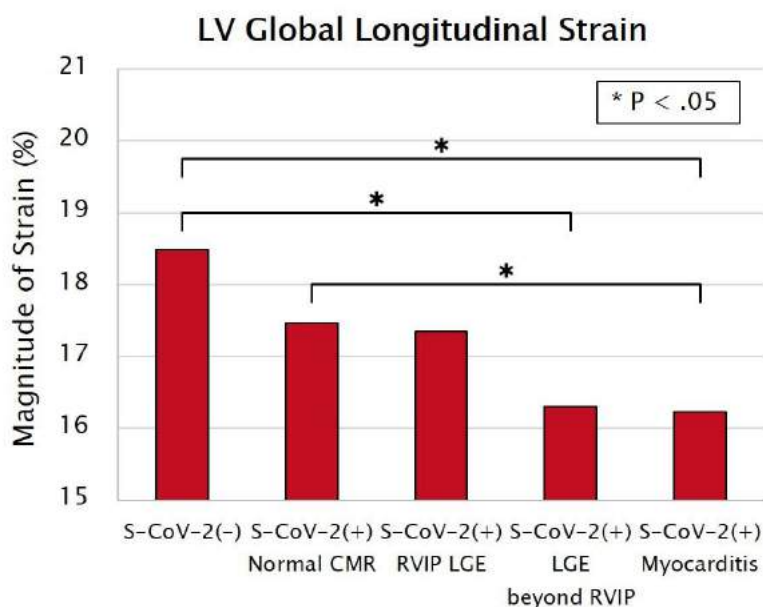
**Background:** The ongoing COVID-19 pandemic has raised concerns over its potential association with myocarditis, an inflammatory disease of the heart muscle most often caused by viral infection (1). Myocarditis is a significant cause of sudden cardiac death (SCD) in competitive athletes (2) and continued exercise can lead to arrhythmic events, including SCD (3). Our group has developed a cardiac screening protocol that includes a comprehensive cardiovascular magnetic resonance (CMR) scan to identify high risk athletes following a SARS-CoV-2 (S-CoV-2) infection before returning to competitive play. These scans included a technique called Strain Encoded Magnetic Resonance (SENC) to measure myocardial strain, the deformation of the heart muscle during contraction. SENC has been previously validated and shown to produce highly reproducible measurements of global longitudinal strain (GLS) and global circumferential strain (GCS) (4).

**Methods:** The CMR screening results were used to stratify patients into the following groups: no CMR abnormalities, late gadolinium enhancement (LGE) isolated to the Right Ventricular Insertion Point (RVIP), LGE beyond the RVIP, and Myocarditis defined by presence of both LGE and elevated T2. We sought to determine the functional significance of these CMR markers by comparing the left ventricular (LV) strain between these groups. We analyzed SENC data from S-CoV-2 positive patients, as well as athletes who never tested positive and had no S-CoV-2 antibodies to serve as negative controls.

**Results:** We enrolled 16 S-CoV-2 negative control athletes (Group 1). Among 204 S-CoV-2 positive athletes analyzed, 138 had no abnormalities on CMR (Group 2), 29 had isolated right ventricular insertion point (RVIP) LGE (Group 3), 27 had LGE beyond RVIP (Group 4), and 11 athletes had myocarditis (Group 5). There was a deterioration in GLS as CMR abnormalities progressed from control athletes to those with LGE and myocarditis. GLS was significantly lower in Groups 4 and 5 compared with negative controls, as well as Group 5 compared to Group 1, ( $p < 0.05$ , Figure 1). Longitudinal MyoHealth, the percentage of myocardial segments with normal longitudinal strain ( $>17\%$ ), showed a similar worsening from controls to those with CMR markers of fibrosis and inflammation. The Longitudinal MyoHealth was significantly lower in both Groups 4 and 5 compared to both Groups 1 and 2, ( $p < 0.05$ , Figure 2). There was no significant difference in GCS or LV ejection fraction between the 5 groups.

**Conclusions:** SARS-CoV-2 infection in collegiate athletes leads to subtle abnormalities in cardiac function detected by GLS that correlate with abnormal mapping and LGE suggestive of myocardial inflammation and fibrosis. The clinical significance of these abnormalities remains to be determined.

**Figure/Table 1**

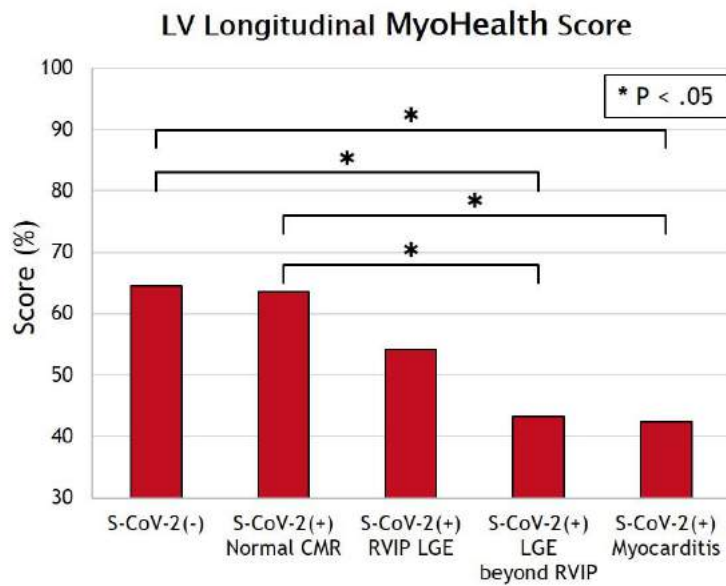


**Caption 1**

**Fig. 1.** Global Longitudinal Strain for each group. Statistical testing was completed via one-way ANOVA with a Tukey-Kramer post hoc test.

**Figure/Table 2**





## Caption 2

**Fig. 2.** Longitudinal MyoHealth® score for each group. Statistical testing was completed via one-way ANOVA with a Tukey-Kramer post hoc test.

## Bibliographic References

1. Fung G, Luo H, Qiu Y, Yang D, McManus B. Circ Res. 2016;118(3):496-514. , 2. Maron BJ, Udelson JE, Bonow RO, et al. Circulation. 2015;132(22):e273-e280. , 3. Tilles JG, Elson SH, Shaka JA, Abelman WH, Lerner AM, Finland M. Proc Soc Exp Biol Med. 1964;117(3):777-782. , 4. Giusca S, Korosoglou G, Zieschang V, et al. Sci Rep. 2018;8(1).

Speaker: J. Heyniger

Category: Strain, Athlete, Myocarditis

000217

## Improving the accuracy of left ventricular functional assessment in Hypertrophic Cardiomyopathy (HCM)

G. Dasegowda \* (1); S. Viswamitra, (2); D. Sinha (2)

(1) Radiology, Massachusetts General Hospital, Boston, United States of America; (2) Radiology, Sri Sathya Sai Institute of Higher Medical Sciences, Bengaluru, India

### Abstract

**Background:** Calculation of stroke volume and ejection fraction is critical in HCM. We evaluated the impact of papillary muscle and trabeculated myocardium in the assessment of ventricular functional parameters in Cardiovascular Magnetic Resonance (CMR) imaging of Hypertrophic Cardiomyopathy (HCM) as compared to aortic flow to determine the most accurate method.

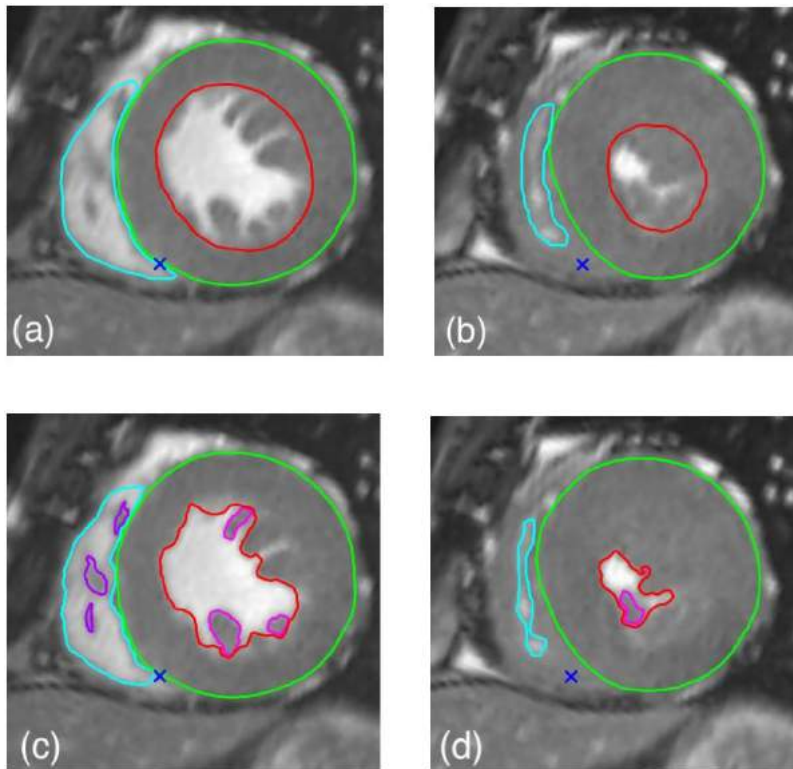
**Methods and Materials:** 46 contiguous patients (mean age  $46 \pm 14$  years) diagnosed with HCM by echocardiography who underwent CMR between 2018 and 2021 were included in this retrospective study. Cine CMR images were obtained on a 1.5 T (Siemens Aera, Erlangen, Germany) using a breath hold ECG triggered Steady-State Free Precession (Tru-FISP) sequence with slice thickness of 8mm. The endocardial and epicardial contours were drawn in the end-diastolic and end-systolic phase using SuiteHeart, Neosoft (WI, USA). In the inclusion method, which is the default method for auto contouring, the contouring included the papillary muscle and trabeculated myocardium as part of the LV cavity in both systole and diastole. In the exclusion method, the papillary muscle and trabeculated myocardium were excluded from the LV cavity (Fig 1). The functional parameters assessed for both methods were left ventricular ejection fraction (LVEF), Stroke Volume (SV), LV mass index, aortic flow. Correlation with aortic flow was performed on a subset of these patients (n=20) in whom there was absent or trivial mitral regurgitation as seen on echocardiography. Paired t-test and Pearson's correlation coefficient was used to analyse correlation. P value  $< 0.05$  was considered significant.

**Results:** We observed that there was a significant difference between both the methods.  $LVEF(i) = 55 \pm 9$  and  $LVEF(e) = 72 \pm 10$  with mean difference of 17 ( $p < 0.0001$ ).  $SV(i) = 74 \pm 18$  ml and  $SV(e) = 64 \pm 16$  ml with mean difference of 10 ( $p = 0.0081$ ). LV mass index(i) =  $98 \pm 35$  gm/m<sup>2</sup> and LV mass index(e) =  $124 \pm 42$  gm/m<sup>2</sup> with difference of 26 ( $p = 0.0019$ ). Correlation coefficients of the stroke volume with aortic flow in patients with absent or trivial MR were  $r = 0.93$  (exclusion method) and  $r = 0.73$  (inclusion method), both p value  $< 0.0001$ .

**Conclusions:** In patients with HCM, our study demonstrates that exclusion of the papillary muscles from the left ventricular cavity significantly improves the correlation of stroke

volume with the aortic flow. Thus, by extension, exclusion would also improve accuracy of the measurements of the left ventricular volume and mass, which showed significant differences between the two measurements in our study. We suggest that the exclusion method of analysis, as described, be used to improve accuracy in HCM.

**Figure/Table 1**



**Caption 1**

Figures demonstrating the two methods: Inclusion method of contouring at end-diastole(a) and end-systole (b); Exclusion method of contouring at end-diastole (c) and end-systole (d).

Speaker: G. Dasegowda

Category: Hypertrophic Cardiomyopathy, Ventricular Function, Papillary Muscle

000219

## **Feasibility of dark-blood late gadolinium enhancement evaluation in young patients with congenital and acquired heart disease**

C. Gonzalez de Alba \* (1); L. J. Malone, (2); L. Browne (2); B. Fonseca (1); R. Friesen (1); D. Irrer (1); M. H. Moghari (2)

(1) Department of pediatrics, Children's Hospital Colorado, University of Colorado Anschutz Medical Campus, Aurora, United States of America; (2) Department of radiology, University of Colorado and Children's Hospital Colorado, Aurora, United States of America

### **Abstract**

**Background:** Late gadolinium enhancement sequences have become common in pediatric cardiovascular magnetic resonance (CMR) exams to assess for myocardial scar/fibrosis. Bright-blood late gadolinium enhancement (BB-LGE) by conventional phase sensitive inversion recovery (PSIR) is a commonly utilized sequence, with inversion time (TI) chosen to primarily null the myocardium signal, leaving a bright blood pool and dark myocardium [1]. One downside of BB-LGE is the similar T1 value of scar/fibrosis and the left ventricular blood pool, making subendocardial areas of fibrosis difficult to assess. A gray-blood LGE (GB-LGE) has been described, which targets additional nulling of the LV blood pool, leaving it gray along with a dark myocardium [2]. This technique has shown to improve ischemic scar detection over BB-LGE in adult patients [3]. We set out to evaluate the feasibility of GB-LGE technique in a young population with congenital and acquired heart disease, and compare it to conventional BB-LGE.

**Methods:** Baseline patient demographic data, magnetic field strength and functional analysis are present in Table 1. Twenty-four patients scheduled for clinically indicated CMR studies at our institution including LGE imaging were selected to undergo both BB-LGE and GB-LGE. Approximately 8-10 minutes following gadolinium administration, a Look-Locker sequence was performed to select the TI to null the myocardium (BB-LGE) and conventional PSIR sequences were obtained (short and horizontal long axis stacks). The Look-Locker sequence was repeated with TI selected to null the blood pool (GB-LGE) followed by repeat short and horizontal long axis PSIR stacks. BB-LGE and GB-LGE PSIR images were reviewed separately at a week apart by 2 readers with additional CMR subspecialty training, blinded to initial clinical interpretation. Studies were analyzed for overall image quality, confidence in scar detection, confidence in detection of LGE, LGE class, inter and intra-observer agreement for presence of scar and intraclass correlation coefficient for total scar burden. This study was approved by our institutional IRB.

**Results:** Median age of the study population was 16 years of age (interquartile range: 3). Eight to 13% of patients had ischemic-type scar, while 35 – 46% had non-ischemic scar (Table 2). Overall confidence in myocardial scar detection by BB or GB-LGE was not statistically different between readers ( $p = 0.18$  and  $p = 1$ ). Grading of image quality was not statistically different between both techniques ( $p = 1$ ,  $p = 0.24$ ). There was no difference in detection of total myocardial scar burden between both techniques ( $p = 0.06$  and  $p = 0.2$ ). There was a good inter-observer agreement for presence of scar on BB-LGE (kappa = 0.79, 95% CI 0.56 to 1) and GB-LGE studies (kappa = 0.78, 95% CI 0.55 to 1), as well as excellent intraobserver agreement for both readers (kappa = 1, 95% CI 1 and kappa = 0.82 95% CI 0.59 to 1). The

interclass correlation coefficient for total scar burden was excellent for the BB-LGE (ICC = 0.98, 95% CI 0.97 to 0.99) and GB-LGE (ICC = 0.95, 95% CI 0.89 to 0.98).

Conclusions: GB-LGE is a feasible technique in young patients with congenital and acquired heart disease with no significant difference in image quality compared to conventional BB-LGE technique and good inter-observer agreement between both techniques. Though scar detection was not statistically different between both techniques, this is likely due to a lower proportion of ischemic type LGE in younger patients compared to the adult population.

**Figure/Table 1**

Age at study (years)	16 (3)
Gender	
• Female (n, %)	11 (46%)
• Male (n, %)	13 (54%)
Weight (kg)	62 (19)
Height (cm)	165 (19)
Body surface area (m <sup>2</sup> )	2 (0.34)
Field strength	
• 1.5 T	4 (17%)
• 3 T	20 (83%)
Left ventricular end-diastolic volume - indexed (mL/m <sup>2</sup> )	85 (21)
Left ventricular end-systolic volume - indexed (mL/m <sup>2</sup> )	39 (12)
Cardiac index (L/min/m <sup>2</sup> )	3 (0.8)
Left ventricular ejection fraction (%)	57 (5)
Right ventricular ejection fraction (%)	52 (6)
Diagnoses (n, %)	
• Myocarditis	6 (25%)
• Turner syndrome	4 (17%)
• Aortic pathology	4 (17%)
• Ischemic pathology (Kawasaki, LAD thrombus)	2 (8%)
• Other diagnoses	8 (33%)

**Caption 1**

*Title: Table 1. Baseline patient demographics and volumetric data (N=24)*

*Bottom caption: Data is presented as median and interquartile range in parenthesis.*

**Figure/Table 2**

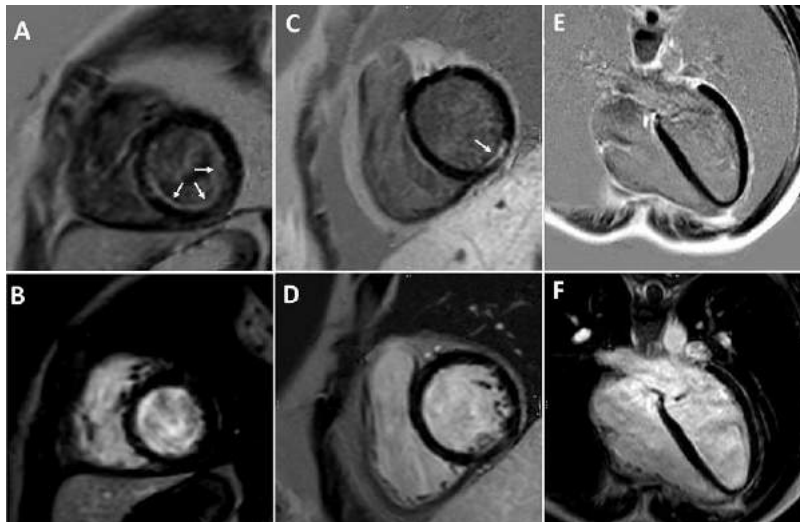
	Reader 1		Reader 2	
	BB-LGE (n = 24) (%)	GB-LGE (n = 24) (%)	BB-LGE (n=24) (%)	GB-LGE (n=23) (%)
No scar	11 (46%)	11 (46%)	11 (46%)	12 (52%)
Ischemic scar	2 (8%)	2 (8%)	3 (12%)	3 (13%)
Non-ischemic scar	11 (46%)	11 (46%)	10 (42%)	8 (35%)
Mixed	0	0	0	0

## Caption 2

*Title: Table 2. Late gadolinium enhancement classification.*

*Bottom caption: BB: Bright-blood, GB: Gray-blood, LGE: Late gadolinium enhancement*

## Figure 3



## Caption 3

Figure 1. Panels A & B: Endocardial fibroelastosis (arrows) is best seen on GB-LGE (Panel A) compared to BB-LGE (Panel B). Panels C & D: LGE (arrow) is best differentiated from blood pool in GB-LGE (Panel C) compared to BB-LGE (Panel D). Panels E & F: Myocardium is best differentiated from lung tissue on GB-LGE (Panel E) compared to BB-LGE (Panel F).

## Bibliographic References

3. Holtackers RJ, Van De Heyning CM, Nazir MS, Rashid I, Ntalas I, Rahman H, Botnar RM, Chiribiri A. Clinical value of dark-blood late gadolinium enhancement cardiovascular magnetic resonance without additional magnetization preparation. J Cardiovasc Magn Reson. 2019 Jul 29;21(1):44. doi: 10.1186/s12968-019-0556-1. , 2. Holtackers RJ, Chiribiri A, Schneider T, Higgins DM, Botnar RM. Dark-blood late gadolinium enhancement without additional magnetization preparation. J Cardiovasc Magn Reson. 2017;19(1):64., 1.
- Kellman P, Arai AE, McVeigh ER, Aletras AH. Phase-sensitive inversion recovery for detecting myocardial infarction using gadolinium-delayed hyperenhancement. Magn Reson Med. 2002;47(2):372–83.

Speaker: C. Gonzalez de Alba

Category: Late Gadolinium Enhancement, Congenital Heart Disease, Fibrosis

000221

## Prediction of Respiration-Induced Cardiac Motion using Pilot Tone and Machine Learning

Y. Pan \* (1); Y. Liu (1); N. jin (2); P. Speier (3); R. Ahmad (4); O. Simonetti (1)

(1) Davis Heart and Lung Research Institute, The Ohio State University, Columbus, United States of America; (2) Research and collaboration department, Siemens Medical Solutions USA, Inc, Malvern, United States of America; (3) DI card, Siemens Healthineers, Erlangen, Germany; (4) Department of biomedical engineering, The Ohio State University, Columbus, United States of America

### Abstract

**Background:** While cardiac MRI has many advantages as a diagnostic tool, data acquisition is relatively slow and prone to motion induced artifacts. Respiratory motion artifacts can be problematic in individuals with cardiovascular disease due to difficulty with breath-holding. Navigator and Pilot Tone (PT) based respiratory motion tracking have been developed to prospectively correct for patient-specific respiratory motion [1, 2]. These methods typically utilize linear or polynomial models to predict respiratory motion of the heart in real time. In this study, a machine learning based motion model (MLM) is proposed and its performance is compared against a polynomial fitting model (PFM).

**Methods:** Training and testing scans were acquired in nine healthy volunteers ( $36 \pm 15$  years, 5 females) on a 1.5T clinical system (MAGETOM Sola, Siemens Healthcare, Erlangen, Germany). Training data were ECG triggered, single-shot bSSFP images acquired during free-breathing over 100 repetitions (heartbeats) to capture multiple respiratory cycles. For testing data, parameters and slice position were the same as training data but scanned over an additional 50 repetitions. Data were acquired in the sagittal plane in six volunteers, and in both sagittal and coronal planes in three volunteers. The PT signal was sampled every 500 microseconds throughout each scan.

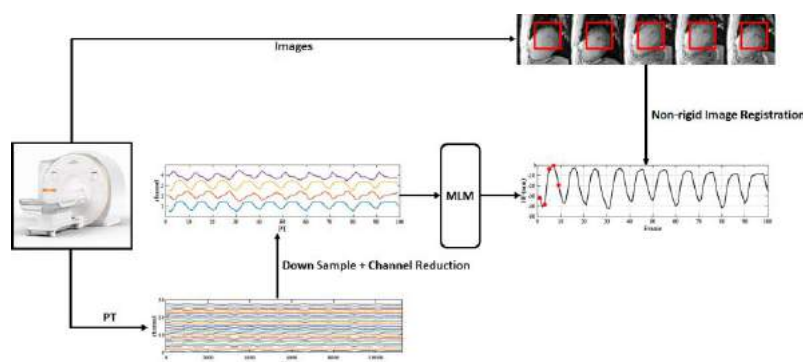
Neural network training and motion estimation were performed in MATLAB (MathWorks, Natick, Massachusetts, USA) (Figure 1). To estimate respiratory motion, all images were registered to an end-expiratory frame using non-rigid image registration [3]. For faster processing, the PT signal was down-sampled to two samples per heartbeat, and physical channels were reduced to two virtual channels using PCA. Respiratory motion observed from training images and PT data were then fed through a bi-directional long short-term memory network [4]. From training data, 80 images were used to train the MLM and 20 images were used as cross validation to determine how many preceding PT samples were required for optimal network performance. Model performance was then evaluated by calculating normalized root mean square error (NRMSE), where motion prediction was compared against the motion observed from images as ground truth. For comparison, the PFM described in the previous study [1] was also trained and evaluated.

**Results:** Cross validation and testing performance for both models are shown in Table 1. MLM had average NRMSE of 0.27 for cross validation and 0.54 for testing across all volunteers, and PFM had average NRMSE of 0.55 and 1.15. The overall performance of MLM was better than PFM in both cross validation and testing. Figure 2 a) and b) shows the

Bland Altman plot between observed and predicted respiratory motion in millimeters. The difference between observation and MLM prediction was  $-1.19 \text{ mm} \pm 7.76$  for MLM and  $-0.41 \text{ mm} \pm 13.73$  for PFM. Correlation coefficient was 0.83 and 0.55 for MLM and PFM, respectively. Although MLM had slightly higher bias than PLM, no statistical significance was found between prediction and observation in either model. Figure 2 c) shows an example from one volunteer, where MLM resulted in less prediction error compared to PLM.

**Conclusion:** An MLM utilizing PT signal to predict patient specific respiratory motion during cardiac MRI was implemented and tested. The technique was shown to reduce NRMSE compared to PFM. Further investigation is needed to evaluate the ability of this model to prospectively correct for respiratory motion in CMR applications.

**Figure/Table 1**



**Caption 1**

Work flow of motion estimation and testing. Free breathing single shot images and the PT signal were collected simultaneously. All images were registered to an end expiratory frame to estimate respiratory motion. The processed PT signals were then fed through MLM and compared with respiratory motion estimated from images as ground truth.

**Figure/Table 2**

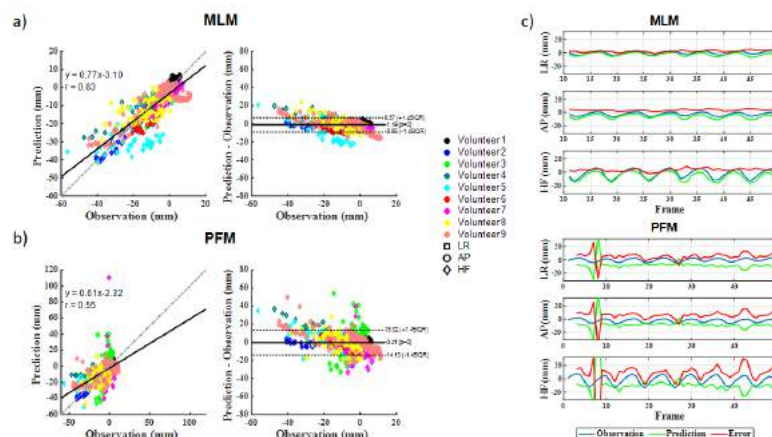
Volunteer	Cross Validation		Testing	
	MLM	PFM	MLM	PFM
V1	<b>0.24</b>	0.55	<b>0.76</b>	1.09
V2	<b>0.13</b>	0.22	0.2	0.2
V3	<b>0.24</b>	0.45	<b>0.65</b>	3.05
V4	<b>0.19</b>	0.57	<b>0.37</b>	0.66
V5	<b>0.43</b>	0.55	0.64	<b>0.53</b>
V6	<b>0.16</b>	0.36	<b>0.48</b>	0.6
V7	<b>0.28</b>	0.86	<b>0.75</b>	2.89
V8	<b>0.31</b>	0.54	<b>0.45</b>	0.65
V9	<b>0.45</b>	0.86	<b>0.55</b>	0.68
Mean	<b>0.27</b>	0.55	<b>0.54</b>	1.15



## Caption 2

Respiratory motion model performance comparison between machine learning based model (MLM) and polynomial fitting model (PFM). Normalized root mean square error (NRMSE) values were calculated as an evaluation of model performance. Lower NRMSE represents a better prediction. Overall, MLM was shown to reduce NRMSE compared to PFM.

Figure 3



## Caption 3

Correlation and Bland-Altman plots comparing observed and predicted motion from MLM and PFM, and example of respiratory motion prediction in all three directions. In a) and b), each data point represents heart motion in a single direction with respect to an end expiratory frame. In c), observed motion is shown in blue, predicted motion in green, and error in red.

## Bibliographic References

Zhang, S., et al. Bidirectional long short-term memory networks for relation classification. in Proceedings of the 29th Pacific Asia conference on language, information and computation. 2015., Chofd'Hotel, C., G. Hermosillo, and O. Faugeras. Flows of diffeomorphisms for multimodal image registration. in Proceedings IEEE International Symposium on Biomedical Imaging. 2002. IEEE., Ludwig, J., et al., Pilot tone-based motion correction for prospective respiratory compensated cardiac cine MRI. Magn Reson Med, 2021. 85(5): p. 2403-2416., Bush, M.A., et al., Patient specific prospective respiratory motion correction for efficient, free-breathing cardiovascular MRI. Magn Reson Med, 2019. 81(6): p. 3662-3674.

Speaker: Y. Pan

Category: Motion Correction, Free Breathing, Respiratory Motion

000223

**Novel atrial 4D Flow Hemodynamic Signature Index (HSI) associates inversely with stroke volume and directly with LA size independent of age, gender and CHA<sub>2</sub>DS<sub>2</sub>-VASc score in atrial fibrillation patients**

T. Nallamotheu \* (1); M. Pradella (1); D. Lee (2); D. Kim (1); M. Markl (1); P. Greenland (3); R. Passman (2); M. Elbaz (1)

(1) Radiology, Northwestern University Feinberg School of Medicine, Chicago, United States of America; (2) Medicine (cardiology), Northwestern University Feinberg School of Medicine, Chicago, United States of America; (3) Preventive medicine, Northwestern University Feinberg School of Medicine, Chicago, United States of America

**Abstract**

**Background:** Atrial fibrillation (AF) is the most common sustained arrhythmic disorder. Recent 4D Flow CMR studies showed the presence of complex left atrial (LA) flow patterns in AF patients, including vortex flow, stasis, and jets. The interacting dynamics of such patterns may associate with disease severity. However, current 4D flow metrics (e.g., peak velocity, stasis, vorticity, kinetic energy, energy loss) can only measure partial individual flow patterns separately, potentially under-evaluating the flow complexity and association with cardiac dysfunction. Recently, a novel 4D hemodynamic signature index (HSI) was proposed that derives a unique profile of the patient's entire 4D LA flow dynamics[1,2]. HSI is computed directly from 4D Flow CMR through mathematical interrogation of the associations between millions of flow vector-pairs in the LA to comprehensively quantify complex composite flow alterations. This study aimed to utilize the new HSI metric to 1) identify significant differences in LA flow signatures between AF patients and healthy controls; 2) assess HSI association with global cardiac dysfunction and clinical parameters in AF patients.

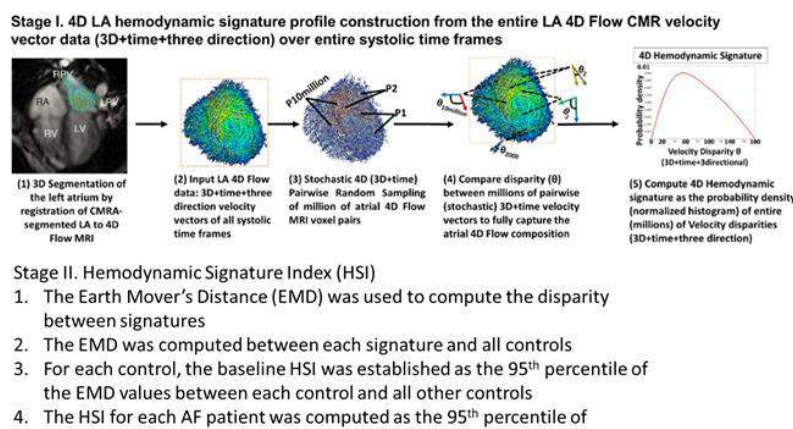
**Methods:** This retrospective IRB-approved study included 144 subjects—93 patients with AF (68 male, age 63±11 years) and 51 healthy volunteers (24 male, age 75±9 years; p<0.001 for age)—underwent standard CMR including 4D Flow. LA 4D HSI computation is comprised of 2 stages (Fig 1)[1,2]. Stage I obtains the subject's flow signature of millions of pairwise vector disparities over systole. Stage II obtains the HSI for each subject as a measure of the difference of its flow signature from all controls. Spearman correlation, and regression analysis were performed to assess associations of clinical parameters to the HSI: LA size, left ventricular stroke volume (SV), age, gender, and CHA<sub>2</sub>DS<sub>2</sub>-VASc score.

**Results:** AF Patients showed distinct differences in the derived flow signature profile relative to healthy volunteers (Fig. 2a). Compared to controls, AF patients had a higher density of high vector disparities (mismatch), indicating higher heterogeneity in 3D LA flow dynamics. This effect was quantified by the elevated HSI in AF patients (p<0.001). HSI showed significant inverse correlation with SV (Fig. 3a, rho=-0.32, p=0.04; N=44) and positive correlation with LA size (Fig. 3b, rho=0.28, p=0.006; N=93). Univariate regression analysis showed that HSI had a negative linear association with SV (B=-0.06 mL-1, p=0.03, N=44) and a positive linear association with LA size (B=2.7e-05 mm-3, p=0.004, N=93). Age, gender, and CHA<sub>2</sub>DS<sub>2</sub>-VASc score were neither correlated nor independent predictors. A multiple regression containing all variables showed only SV (B=-0.11 mL-1, p=0.004) and

LA size ( $B=4.3e-05 \text{ mm}^{-3}$ ,  $p=0.003$ ) as significant predictors of the HSI independent of age, gender, and CHA<sub>2</sub>DS<sub>2</sub>-VASc score (adjusted  $R^2=0.28$ ,  $N=44$ ).

**Conclusion:** The results of this study demonstrate significant differences in the novel 4D flow HSI metric in AF patients versus controls. HSI is a comprehensive measure of the relative spatiotemporal heterogeneity in 3D LA flow dynamics from 4D Flow CMR. Increased HSI values in AF patients were associated inversely with LV SV and directly with LA size independent of age, gender, and CHA<sub>2</sub>DS<sub>2</sub>-VASc score. This may suggest clinical association of this new index to severity of cardiac dysfunction in AF. The HSI mathematical definition is inherently normalized to LA volume, emphasizing that the found associations are inherent to detected LA flow changes and not confounded by measurement bias to LA volume. Larger studies are needed to assess the HSI association to clinical outcomes.

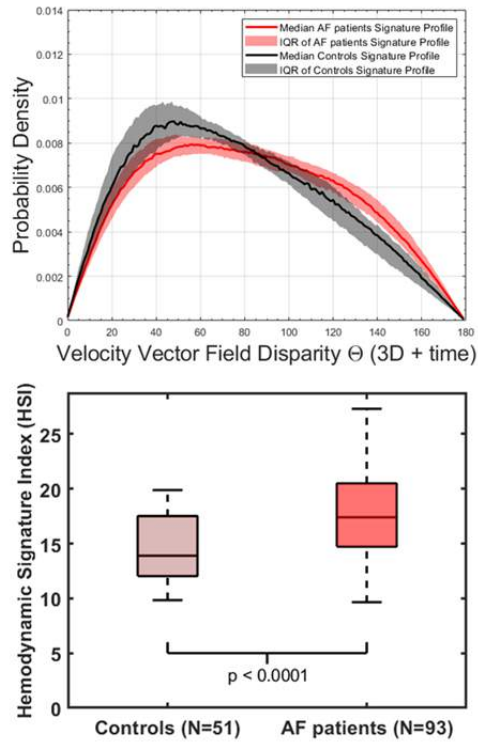
## Figure/Table 1



## Caption 1

Figure 1: Methods. Stage I: The signature profile is computed as a probability density function of values of angular disparity between stochastically sampled vector pairs throughout the left atrium and systole. Stage II: The HSI is computed as a disparity metric between each signature profile and all control signatures.

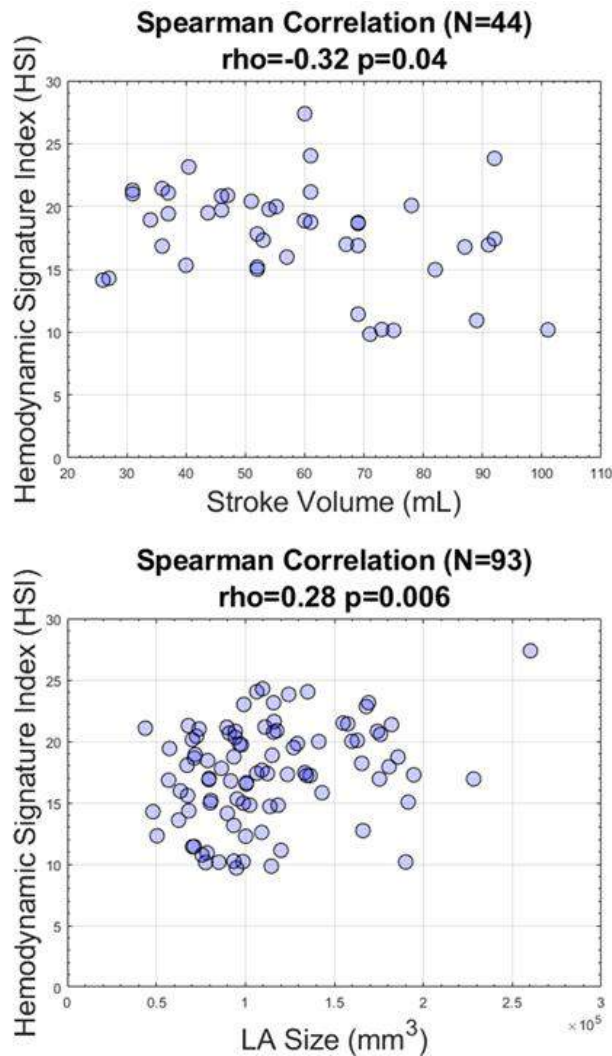
## Figure/Table 2



## Caption 2

Figure 2: 4D Hemodynamic signatures and HSI. **(a)** Median and interquartile range of signatures for all AF patients (red, N=93) and all controls (gray, N=51). **(b)** Box plot of HSI for all controls vs. all AF patients. AF HSI is significantly elevated ( $p < 0.0001$ ).

## Figure 3



### Caption 3

Figure 3: Association of HSI with clinical parameters. **(a)** Correlation of HSI with stroke volume (SV) ( $\rho = -0.32$ ,  $p = 0.04$ ,  $N = 44$ ). A negative linear association was found ( $B = -0.06$  mL<sup>-1</sup>,  $p = 0.03$ ,  $N = 44$ ). **(b)** Correlation of HSI with LA size ( $\rho = 0.28$ ,  $p = 0.006$ ,  $N = 93$ ). A positive linear association was found ( $B = 2.7 \times 10^{-5}$  mm<sup>-3</sup>,  $p = 0.004$ ,  $N = 93$ ).

### Bibliographic References

Funding: This research is supported in part by the Transformational Project Award AHA 20TPA35490311 from the American Heart Association (AHA)., [1] Elbaz M.S.M., Malaisrie C., McCarthy P., Markl M. (2021) Stochastic 4D Flow Vector-Field Signatures: A New Approach for Comprehensive 4D Flow MRI Quantification. In: de Bruijne M. et al. (eds) Medical Image Computing and Computer Assisted Intervention – MICCAI 2021. MICCAI 2021. Lecture Notes in Computer Science, vol 12905. Springer, Cham. [https://doi.org/10.1007/978-3-030-87240-3\\_21](https://doi.org/10.1007/978-3-030-87240-3_21), [2] Nallamothu T, DiCarlo A, Lee D, Kim D,

Arora R, Markl M, Greenland P, Passman R and Elbaz M. (2021) Novel Stochastic 4D Flow Signatures of time-resolved 3D left atrial flow-field alterations in atrial fibrillation. In Proceedings: 29th Scientific Meeting, International Society for Magnetic Resonance in Medicine (ISMRM). 2021.

Speaker: T. Nallamotheu

Category: Atrial Fibrillation , 4D Flow, Image Analysis

000224

## Automatic data selection for the reconstruction of static whole-heart images in systolic and diastolic phases for free-running acquisitions

L. Romanin \* (1); C. Roy (2); J. Heerfordt (1); P. Milan (3); R. Tobias (4); T. Estelle (5); M. Stuber (6); D. Piccini (7)

(1) Department of diagnostic and interventional radiology, Lausanne University Hospital and Advanced clinical imaging technology, Siemens Healthcare AG, Lausanne, Switzerland; (2) Department of diagnostic and interventional radiology, Lausanne University Hospital (CHUV) and University of Lausanne (UNIL), Lausanne, Switzerland; (3) Woman-mother-child department, Lausanne University Hospital (CHUV), Lausanne, Switzerland; (4) Service of cardiology, centre de resonance magnétique cardiaque (crmc), Lausanne University Hospital (CHUV), Lausanne, Switzerland; (5) Department of diagnostic and interventional radiology, Lausanne University Hospital (CHUV), Lausanne, Switzerland; (6) Department of diagnostic and interventional radiology, Lausanne University Hospital (CHUV) and Centre for Biomedical Imaging (CIBM), Lausanne, Switzerland; (7) Advanced clinical imaging technology, Siemens Healthcare AG, Lausanne, Switzerland

### Abstract

**Background:** Due to the long acquisition times in MRI, efficient cardiac and respiratory motion extraction strategies are needed to reconstruct motion-compensated whole-heart images. Recently, a fully automated self-gated signal extraction was proposed for free-running acquisitions (1). However, it has also been demonstrated that using a SIMilarity-driven Multi-dimensional Binning Algorithm (SIMBA) (2) explicit extraction of physiological signals is not necessary to reconstruct a static motion-consistent cardiac image. One limitation is the difficulty of preselecting a specific phase before reconstruction. In this study we compare different dimensionality reduction techniques to explore whether we could use distances in the low-dimensional space to map physiological states. These analyses are first performed using a numerical phantom simulation, and then the derived approach applied to ferumoxytol-enhanced scans of 10 patients with congenital heart disease.

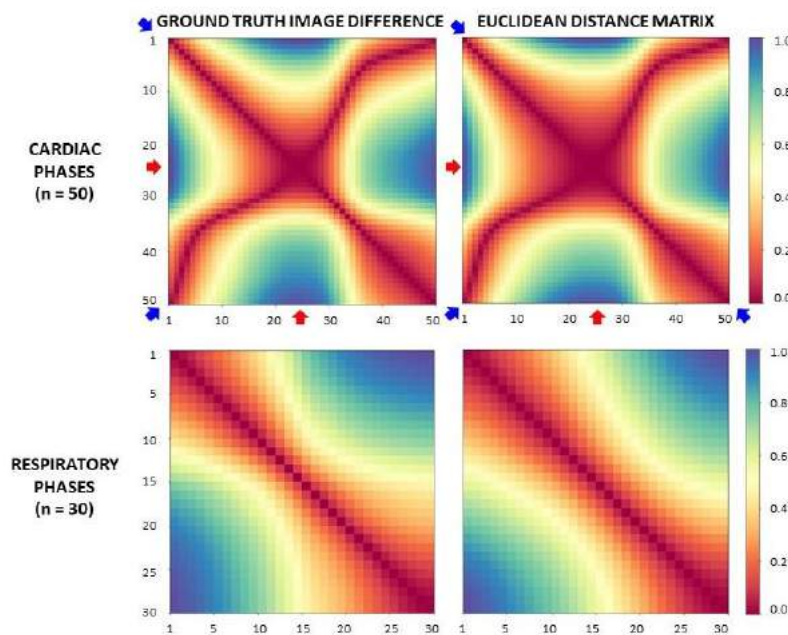
**Methods:** The numerical phantom used in this study is derived from the XCAT framework and generates high-resolution 3D volumes of the chest for up to 50 cardiac and 30 respiratory motion states (3). Data acquisition and processing were performed as in the original paper (2). For dimensionality reduction of the data, two linear methods, principal component analysis (PCA) and multi-dimensional scaling (MDS), and two non-linear methods, isometric mapping (Isomap) and local linear embedding (LLE), were compared (4). Euclidean distance matrices (EDMs) were computed, for respiratory and cardiac phases separately, to characterize the distribution of the data projected in the low-dimensional space, after dimensionality reduction. These matrices were compared to ground-truth image difference matrices (IDMs) obtained by taking the mean absolute image difference between pairs of the original phantom images. The structural similarity index (SSIM) between the two matrices was used as a measure of SIMBA's capability to map image differences to linear distances between points in the low-dimensional space. The method was judged to be that with the highest SSIM value and lower computational time. Finally, a 3D volume reconstruction of the two most distant clusters, among the most populated ones, was performed, and the two static images visually compared.

For both images, the percentage of the reconstructed data in systole and diastole was determined using the QT interval as the duration of systole (5).

**Results:** For all four dimensionality reduction methods, we can visually observe a similar pattern between the ground truth IDMs and the EDMs (Figure 1). Isomap is the method giving the highest SSIM while PCA gives the lowest SSIM (Table 2). For the patient's datasets, reconstruction of the two most distant clusters results in a first image with  $70\pm 8\%$  systolic and  $30\pm 8\%$  diastolic data, and a second image with  $34\pm 13\%$  systolic and  $66\pm 13\%$  diastolic data (Figure 3).

**Conclusions:** In this work we could demonstrate that there is a correspondence between distances of points in the low-dimensional space and physiological states. Given this result, we could exploit EDMs to show that it is possible to select two different images of the heart corresponding to a mostly diastolic and a mostly systolic phases. However, we still observe mixing of phases and biases related to the acquisition scheme, that need to be addressed. Future steps involve investigating a more precise mapping in the low-dimensional space with the goal of obtaining 3D end-diastolic and 3D end-systolic images.

**Figure/Table 1**



**Caption 1**

Comparison between ground truth IDMs and EDMs of points in the low-dimensional space for the Isomap mapping. For cardiac phases, if we take for instance the first point ( $n=1$ ), the beginning of the R-wave, it is most similar to adjacent phases and to diastolic phases ( $n=[1;5]\cup[45;50]$ , blue arrows), but most different to systolic phases ( $n=[20;30]$ , red arrows).

**Figure/Table 2**

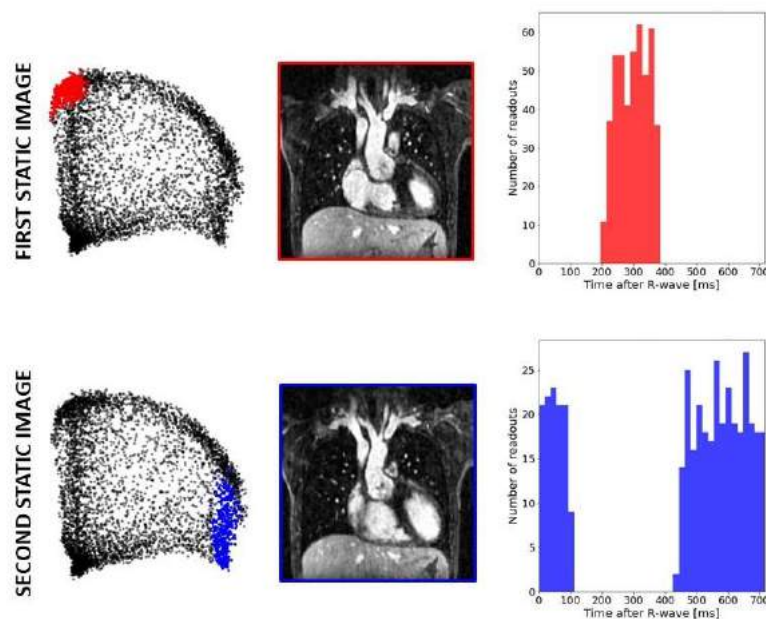


		STRUCTURAL SIMILARITY INDEX (SSIM) BETWEEN EUCLIDEAN DISTANCE MATRIX AND GROUND TRUTH IMAGE DIFFERENCE MATRIX		
DIMENSIONALITY REDUCTION METHOD		Respiratory Phases [a. u.]	Cardiac Phases [a. u.]	Time of Computation [sec]
LINEAR DIMENSIONALITY REDUCTION METHODS	Principal Component Analysis (N = 20)	0.22	0.75	0.06
	Multi-dimensional Scaling (N=10)	0.95	0.94	262
NON-LINEAR DIMENSIONALITY REDUCTION METHODS	Isometric Mapping (N = 12)	0.95	0.94	186
	Local Linear Embedding (N = 5)	0.67	0.92	1226

## Caption 2

Comparison of the dimensionality reduction methods. Four methods are compared in terms of structural similarity indices between the image difference map and the Euclidean distance matrix, and in terms of total computational time. N is the number of components chosen optimizing the phases mapping and giving reasonable computational times.

## Figure 3



## Caption 3

Selection and reconstruction of static images of a ferumoxytol-enhanced dataset. Left column: the data selected in the low-dimensional space. Center column: the reconstructed static images. Right column: histograms showing the cardiac selection with respect to the reference ECG time.

### **Bibliographic References**

[5] Roes SD, JMRI 2008, 27:1046-1053, [4] Pedregosa F, JMLR 12 2011, 2825-2830 , [2] Heerfordt J, MRM 2021, 86:213–229 , [1] Di Sopra L, MRM 2019, 82:2118–2132, [3] Roy CW, JCMR 2021, 23

Speaker: L. Romanin

Category: Whole Heart , Ferumoxytol, Motion Correction

000225

## Physiologic insight into the origin of pulmonary artery systolic blood pressure using cardiac MR image data

R. Biederman \* (1); G. Rayarao (1); M. Doyle, (1); N. Hussain, (1)

(1) Cardiac mri, Allegheny Health Network, Pittsburgh, United States of America

### Abstract

**Background:** Prediction of pulmonary arterial pressures (PAP) by CMR has been achieved with excellent accuracy using 4D flow characteristics. However, while prediction is accurate, insight in the physiologic conditions producing the elevated systolic blood pressure remain elusive. We introduce a means to predict the PAP from routine image data easily obtained by CMR that identifies the physical conditions associated with pressure conditions. We employ the previously described impedance between the LV and the aorta (IMPLV) and between the RV and the main pulmonary artery (IMPRV) which are combined with physiologic variables to predict PAP.

**Methods:** Patients (n=40, 82% F),  $51 \pm 12$  yrs) with a diagnosis of pulmonary artery hypertension underwent evaluation by CMR to assess the blood flow through the aorta and PA at the interface to the LV and RV, respectively. Phase velocity mapping at single plane through the aorta was obtained during free breathing conditions (acquisition time ~2 min) to calculate the IMPLV using the formula:

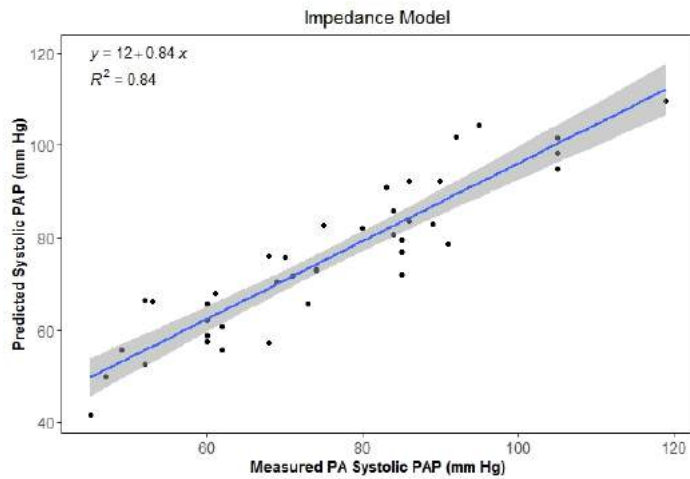
$$\text{IMP} = (\text{end systolic ejection time}) \times (\text{mean blood velocity}) / (\text{vessel diameter})$$

Similarly the flow was measured through the MPA to assess IMPRV. Systolic PAP was measured during a right heart catheterization examination performed within one month of the CMR examination. A multiple linear regression model was generated to predict systolic PAP, with parameters retained with a significance  $<0.05$ .

**Results:** The parameters that best predicted the systolic PAP were sinusoidal transforms of IMPLV and IMPRV along with age and RV Mass ( $r = 0.92$ ,  $p < 0.001$ ), Fig 1. The standard major-axis line was fitted to the data ( $p < 0.001$ ). The corresponding physiologic components of pressure are shown in Figure 2. Each component is plotted on an axis corresponding to the full range of the respective variable encountered in the data.

**Conclusions:** This is the first demonstration of the utility of a CMR-measured left and right ventricular impedance to directly predict systolic PAP. Of central importance is the distinguishing feature that no calibration of the data is required, thus, unlike typical Echo-derived estimates of PAP or newer implanted pressure monitors, no estimate of CVP or RAP is required. The pressure varies linearly with age and RV mass, but sinusoidally with impedance, indicating the non-linear nature of this novel CMR-measured metric of cardiovascular function.

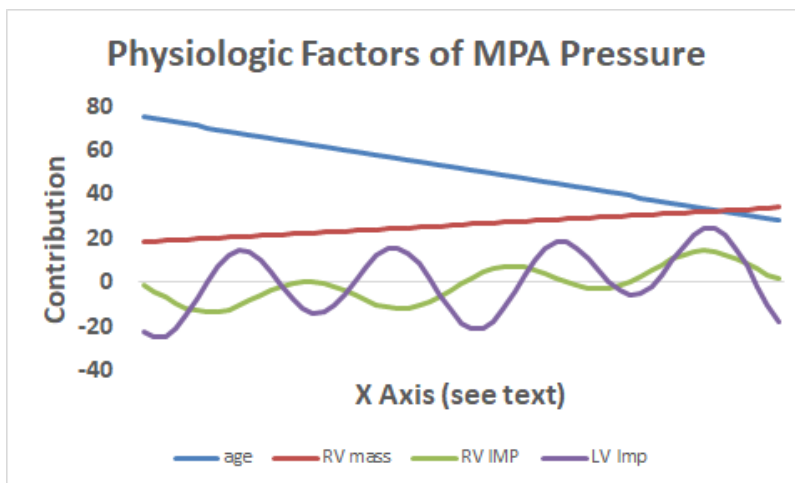
**Figure/Table 1**



### Caption 1

The model prediction of main pulmonary artery systolic blood pressure is plotted against the right heart catheterization measured pressure.

### Figure/Table 2



### Caption 2

The model generated components of systolic blood pressure are plotted against the composite X axis: age 20-80, RV mass 60-130, RV impedance 1-9, LV impedance 1-18 over 4 cycles.

Speaker: R. Biederman

Category: Pulmonary Hypertension, Flow, Atrial Function

000227

**CMR shows that Eplerenone promotes anti-inflammatory epicardial adipose tissue and preserves coronary microvascular function in mice fed a high-fat high-sucrose diet**

S. Shah \* (1); M. Wolf (2); F. Epstein (1)

(1) Biomedical engineering, University of Virginia, CHARLOTTESVILLE, United States of America; (2) Cardiovascular medicine, University of Virginia, Charlottesville, United States of America

**Abstract**

**Background:** Coronary microvascular disease and heart failure with preserved ejection fraction (HFpEF) in patients with comorbidities of obesity and diabetes are largely attributed to a chronic proinflammatory state. Epicardial adipose tissue (EAT), the fat depot directly on the heart surface, has been described as a transducer of metabolic inflammation to the coronary vasculature as, in obesity, it undergoes a phenotypic shift where M1-polarized macrophages accumulate and the EAT secretes proinflammatory cytokines [1]. An increased EAT volume has previously been associated with HFpEF [2]; however, the fatty acid composition (FAC) of EAT also contributes to its proinflammatory state, as saturated fatty acids (SFAs) promote M1 macrophage polarization whereas polyunsaturated fatty acids (PUFAs) promote an anti-inflammatory state [3]. Prior work in mice has shown that mineralocorticoid receptor (MLR) antagonism reduces inflammation in abdominal and epididymal adipose tissue [4]. We hypothesized that CMR of obese mice treated with the MLR antagonist, Eplerenone (EPL), would shift the EAT FAC towards an anti-inflammatory state and preserve myocardial perfusion reserve.

**Methods:** Untreated (n=6) and EPL-treated (n=6) C57Bl/6 male mice fed a high-fat high-sucrose diet (HFHSD) were studied. HFHSD (40% kcal fat, 40% kcal sucrose) was initiated at 10 weeks of age and continued for 10 weeks. In the treatment group, EPL (100 mg/kg/day) was added to the HFHSD. CMR was performed using a 7T system and included FAC imaging, T1 mapping, and myocardial perfusion reserve (MPR) imaging of a mid-ventricular short-axis slice. FAC-MRI was performed using an interleaved multi-echo gradient-echo sequence with 9 echoes, initial TE of 2.0ms, echo spacing 0.3ms, averages 8, and resolution  $0.2 \times 0.2 \text{ mm}^2$ . EAT FAC maps were computed using an IDEAL method to estimate the SFA, PUFA, and monounsaturated fatty acid (MUFA) fractions [5]. Rest and adenosine arterial spin labeling was performed at baseline and 10 weeks post diet to quantify MPR. T-tests were used to test for significant differences between SFA, PUFA, and MUFA fractions as well as EAT T1 between untreated and EPL-treated mice. A two-way ANOVA was used to test for significant differences in MPR between groups and time-points.

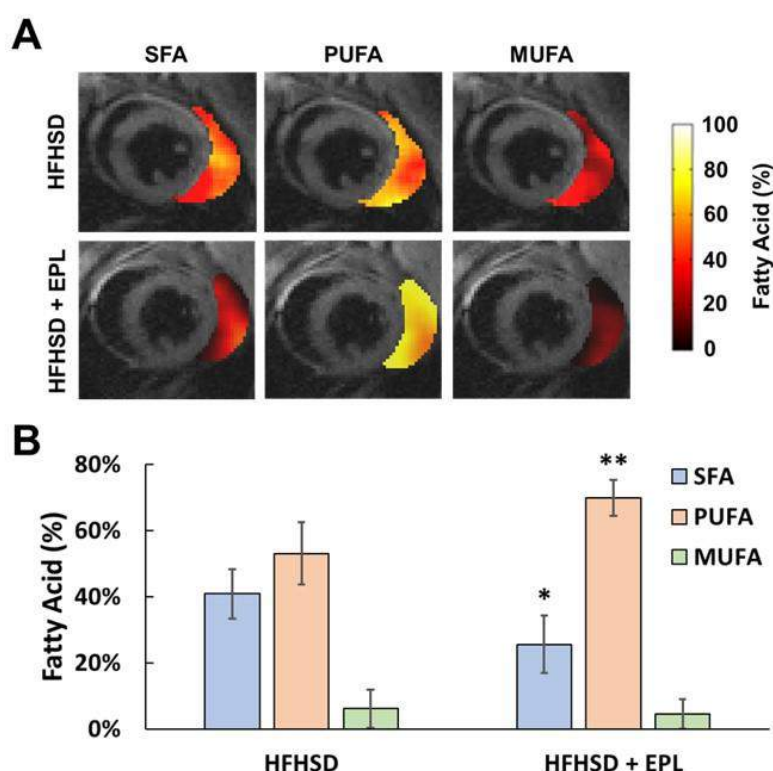
**Results:** EAT SFA% was reduced ( $26 \pm 9\%$  vs  $41 \pm 7\%$ ,  $p < 0.01$ ), PUFA% was increased ( $70 \pm 5\%$  vs  $53 \pm 9\%$ ,  $p < 0.01$ ), and MUFA% was unchanged ( $5 \pm 4\%$  vs  $6 \pm 6\%$ ) in EPL-treated vs untreated mice (Figure 1). EAT T1 was increased in EPL-treated mice ( $1276 \pm 100$  vs  $1079 \pm 89$ ,  $p < 0.01$ , Figure 2). Lastly, MPR was significantly higher in EPL-treated mice post-diet ( $1.87 \pm 0.07$  vs  $1.44 \pm 0.07$ ,  $p < 0.01$ , Figure 3).

**Conclusions:** CMR in HFHSD mice showed increased EAT SFAs and a shortened EAT T1, which may represent biomarkers of proinflammatory adipose tissue, and these correlated with

impaired coronary microvascular function ( $\text{MPR} = 1.44 \pm 0.07$ ). EPL treatment led to decreased EAT SFAs and a longer EAT T1, which may represent biomarkers of anti-inflammatory adipose tissue, and these correlated with improved coronary microvascular function ( $\text{MPR} = 1.87 \pm 0.07$ ). Together, these results suggest that CMR of EAT FAC, EAT T1 and MPR enable investigation of the role of EAT as a metabolic transducer of coronary microvascular inflammation and dysfunction, including for the evaluation of therapies that may dampen the deleterious cardiovascular effects of proinflammatory EAT.

This work was supported by R01EB001763.

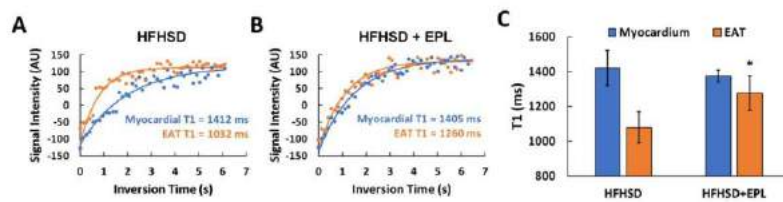
**Figure/Table 1**



**Caption 1**

**Figure 1.** (A) Example EAT FAC maps show a shift towards SFA reduction and PUFA accumulation in EAT in EPL-treated mice. (B) EPL significantly altered the EAT fatty acid composition as SFAs were significantly reduced ( $*p < 0.01$ ) and PUFAs significantly increased ( $**p < 0.01$ ) after 10 weeks on HFHSD.

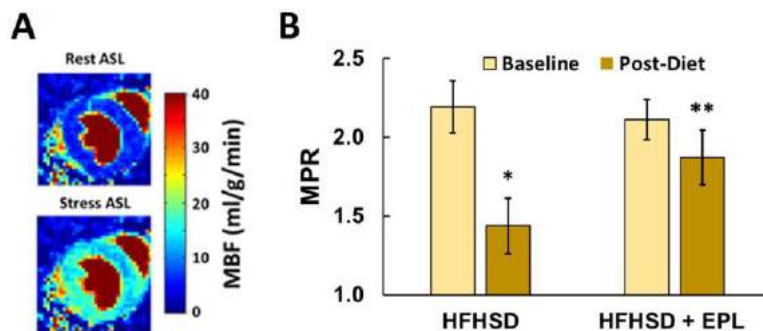
**Figure/Table 2**



## Caption 2

**Figure 2.** Example myocardial and EAT T1 relaxation curves in untreated (A) and EPL-treated (B) mice respectively. (C) EPL significantly lengthened the EAT T1 (\* $p<0.01$ ) after 10 weeks of HFHSD.

## Figure 3



## Caption 3

**Figure 3.** (A) Example rest and adenosine stress myocardial blood flow (MBF) maps in an untreated mouse at baseline. (B) MPR was significantly reduced post-diet in untreated mice (\* $p<0.01$ ) while MPR was greater in EPL-treated mice (\*\* $p<0.01$  vs HFHSD post-diet).

## Bibliographic References

5. Berglund, Johan, Håkan Ahlström, and Joel Kullberg. "Model-based mapping of fat unsaturation and chain length by chemical shift imaging—phantom validation and in vivo feasibility." *Magnetic resonance in medicine* 68.6 (2012): 1815-1827., 4. Wada, Tsutomu, et al. "Eplerenone prevented obesity-induced inflammasome activation and glucose intolerance." *Journal of Endocrinology* 235.3 (2017): 179-191., 3. Rocha, Daniela Mayumi, Josefina Bressan, and Helen Hermana Hermsdorff. "The role of dietary fatty acid intake in inflammatory gene expression: a critical review." *Sao Paulo Medical Journal* 135 (2017): 157-168., 2. Koepp, Katlyn E., et al. "Hemodynamic and functional impact of epicardial adipose

tissue in heart failure with preserved ejection fraction." JACC: Heart Failure 8.8 (2020): 657-666., 1. Patel, Vaibhav B., et al. "Epicardial adipose tissue as a metabolic transducer: role in heart failure and coronary artery disease." Heart failure reviews 22.6 (2017): 889-902.

Speaker: S. Shah

Category: Epicardial Fat, Inflammation, Microvascular disease



000228

**A case of restrictive right ventricular physiology after biventricular repair of pulmonary atresia with intact ventricular septum**

S. Duong \* (1); J. Cohen, (1); K. Stern, (1)

(1) Pediatrics, Mount Sinai Hospital, New York, United States of America

**Abstract**

**Clinical Presentation:** This is a 14 year old male with membranous valvar pulmonary atresia and intact ventricular septum. He underwent catheter-based perforation and balloon dilation of the pulmonary valve as a neonate; and then transannular patch repair of his right ventricular outflow tract with ASD closure at 3 months. Postoperatively he has a residual PFO and small coronary sinus septal defect, and has done overall clinically very well with no further cardiac intervention and no cardiac medications. On recent clinic visits he has a  $\text{spO}_2$  of 94-97% at rest and 90% during exercise. He has appropriate exercise tolerance with  $\text{VO}_2$  max of 42 ml/kg/min (80% predicted), and  $\text{VE}/\text{VCO}_2$  was abnormal at 33.6, indicating respiratory inefficiency likely due to V/Q mismatch from decreased pulmonary blood flow. Liver transient elastography was 9 kPa (F2 fibrosis) which may reflect subclinical fibrosis or congestion, however he has no clinical or biochemical evidence of liver disease.

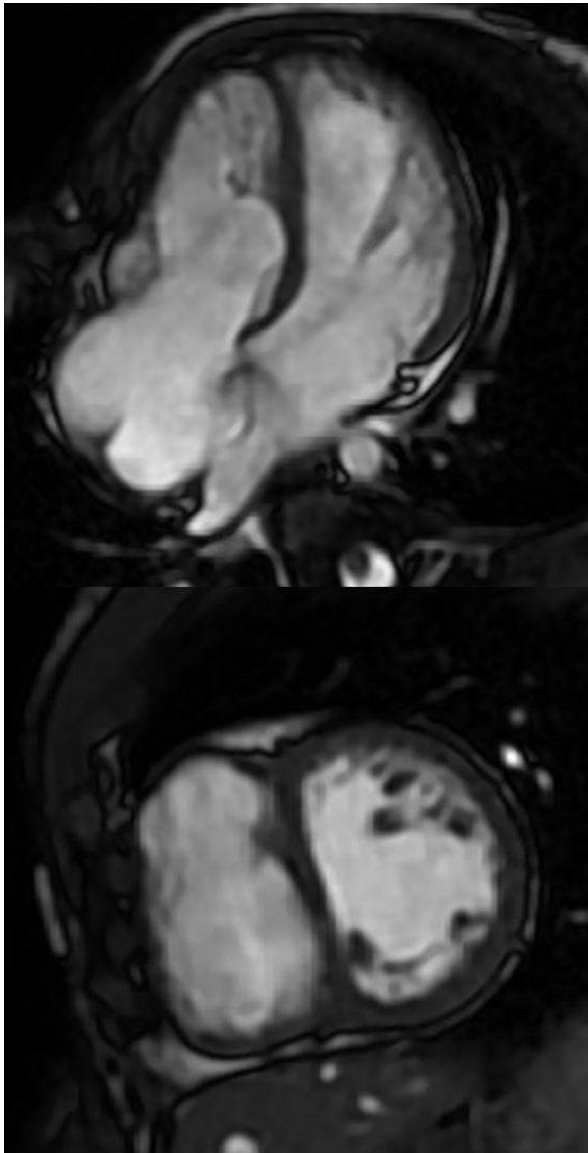
**Diagnostic Methods and Results:** A cardiac MRI was performed on a 1.5T Signa HDxt GE scanner. Balanced SSFP cine imaging was performed for anatomy and ventricular function. Free-breathing phase contrast imaging performed for measurement of Qp:Qs ratio and pulmonary regurgitant fraction. Gadolinium contrast enhanced angiography (0.15 mmol/kg gadobutrol) followed by single-shot phase sensitive inversion recovery for myocardial delayed enhancement.

MRI was significant for a mildly foreshortened RV with normal RV size ( $\text{RV EDVi} = 96 \text{ ml/m}^2$ ,  $Z = +1.0$ ) and function ( $\text{RVEF} 56\%$ ). There was mild LV dilation ( $\text{LV EDVi} = 112 \text{ ml/m}^2$ ,  $Z = +2.6$ ) and mildly depressed LV function ( $\text{LV EF} = 47\%$ ). There was pronounced early diastolic bowing of the interventricular septum into the left ventricle and this area was relatively thinner than the rest of the septum. The atrial septum bowed from right-to-left in diastole. The IVC and os of the coronary sinus appear dilated, and the right atrium appeared qualitatively dilated but measured upper limits of normal ( $73 \text{ ml/m}^2$ ). There was prominent flow reversal in the hepatic veins and IVC during at end diastole. There was moderate pulmonary regurgitation (regurgitation fraction=36%) and pronounced antegrade flow in the main and branch pulmonary artery during end-diastole. The Qp:Qs was 0.74. Myocardial delayed enhancement was observed in the RV subendocardium of the basal interventricular septum and the moderator band.

**Learning points:** Patients with pulmonary atresia with intact ventricular septum that undergo a biventricular repair are at risk of restrictive RV physiology due to underdevelopment of the right ventricle. Poor RV compliance causes right-to-left atrial level shunting of blood with Qp:Qs <1 and  $\text{spO}_2$  desaturation. The stiff RV is unable to “accept” any more volume at end diastole, thus antegrade flow is seen in the branch pulmonary arteries at end diastole and prominent retrograde flow may be seen in the IVC/hepatic veins. Elevated filling pressures also lead to dilation of the right atrium. The diastolic bowing of the interventricular septum into the LV suggests increased RV filling pressures. RV fibrosis, visualized as delayed enhancement, has been observed in this population and likely contributes to the restrictive

physiology. While this patient is clinically well, the evidence of restrictive RV physiology and abnormal liver elastography raise concern about long-term sequelae of increased central venous pressure. Cardiac MRI findings add important insight into the physiology and may inform decisions to intervene to reduce RV diastolic volume load, such as pulmonary valve replacement, and reduce hypoxia, such as atrial septal defect closure; though evidence-based guidelines for interventions in this population are not well described.

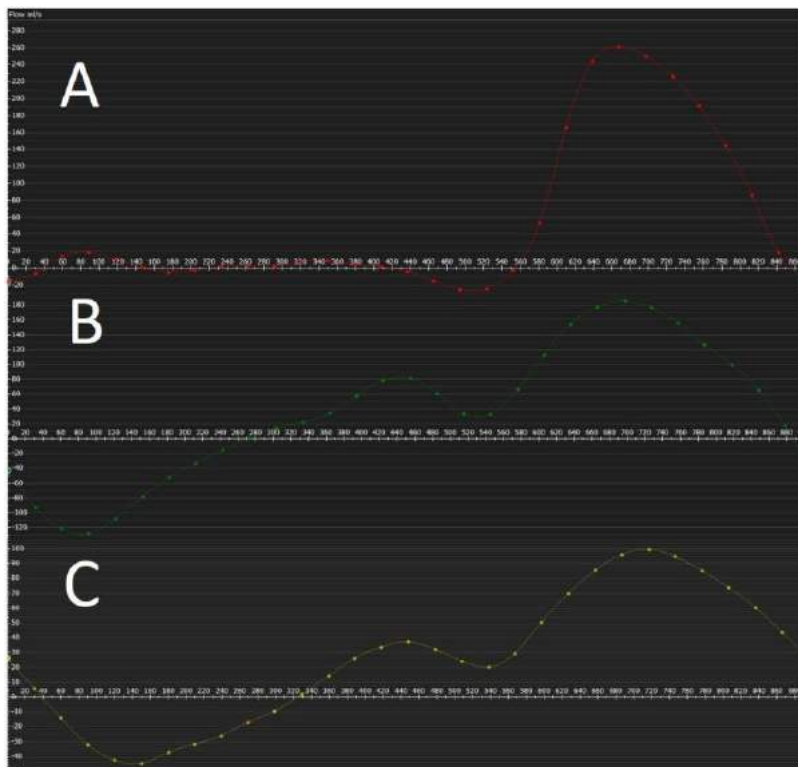
**Figure/Table 1**



**Caption 1**

Four-chamber (Top panel) and ventricular short axis (Bottom Panel) bright blood SSFP in diastole. Note the relatively smaller right ventricle, with interventricular septum bowing into the LV during diastole suggestive of increased right ventricular diastolic pressure.

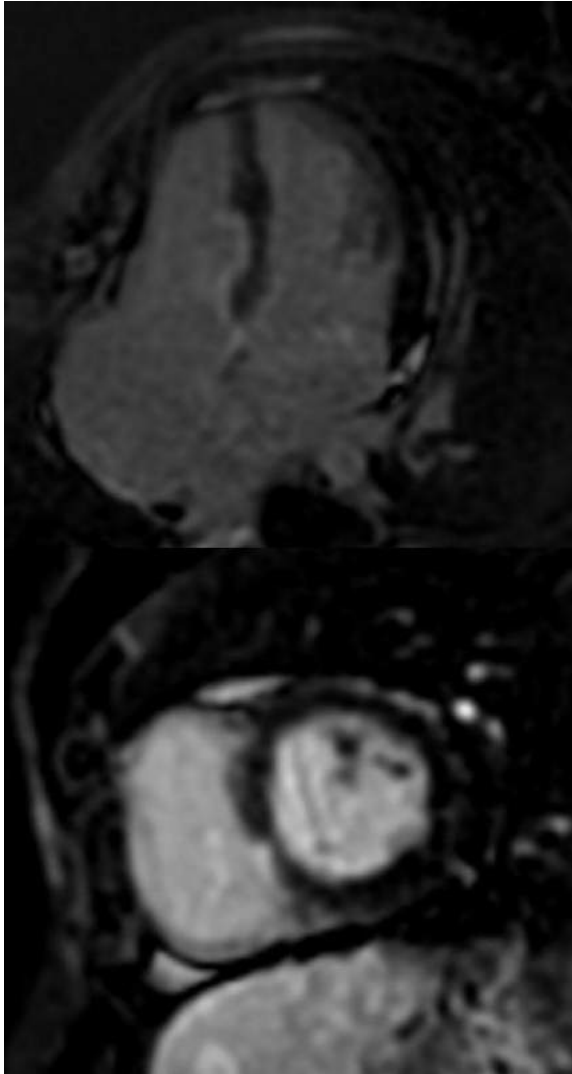
**Figure/Table 2**



**Caption 2**

Phase contrast flow imaging of the aorta (panel A), main pulmonary artery (panel B), right pulmonary artery (panel C). Note significant pulmonary regurgitation in early diastole, and antegrade pulmonary blood flow in the main and branch pulmonary arteries during late diastole consistent with restrictive right ventricular physiology

**Figure 3**



### **Caption 3**

Myocardial delayed enhancement imaging in the four-chamber (top panel) and ventricular short axis (bottom panel) showed right ventricular subendocardial enhancement at the basal ventricular septum and moderator band.

### **Bibliographic References**

Redington, Andrew N., Daniel Penny, Michael L. Rigby, and Alison Hayes. "Antegrade Diastolic Pulmonary Arterial Flow as a Marker of Right Ventricular Restriction after Complete Repair of Pulmonary Atresia with Intact Septum and Critical Pulmonary Valvar Stenosis." *Cardiology in the Young* 2, no. 4 (October 1992): 382–86.  
<https://doi.org/10.1017/S1047951100007988>, Liang, Xue-Cun, WWM Lam, EWY Cheung, AKP Wu, Sophia J. Wong, and Yiu-Fai Cheung. "Restrictive Right Ventricular Physiology and Right Ventricular Fibrosis as Assessed by Cardiac Magnetic Resonance and Exercise

Capacity After Biventricular Repair of Pulmonary Atresia and Intact Ventricular Septum.” *Clinical Cardiology* 33, no. 2 (February 23, 2010): 104–10. <https://doi.org/10.1002/clc.20711>., Li, Vivian Wing-Yi, Edwina Kam-Fung So, Wenxi Li, Pak-Cheong Chow, and Yiu-Fai Cheung. “Interplay between Right Atrial Function and Liver Stiffness in Adults with Repaired Right Ventricular Outflow Obstructive Lesions.” *European Heart Journal - Cardiovascular Imaging*, no. 344 (December 26, 2020). <https://doi.org/10.1093/ehjci/jeaa344>.

Speaker: S. Duong

Category: Congenital Heart Disease, Right Ventricle, Children

000229

## Data-consistent non-Cartesian deep subspace learning for ultrafast CMR multitasking reconstruction

Z. Chen \* (1); Y. Chen (1); T. Cao (1); Y. Xie (1); D. Li (1); A. Christodoulou (1)

(1) Biomedical Imaging Research Institute, Cedars-Sinai Medical Center, Los Angeles, United States of America

### Abstract

#### Background

CMR multitasking (MT) is a promising approach for quantitative imaging without breath-holds or ECG monitoring [1], but slow iterative non-Cartesian reconstruction is a barrier to clinical adoption. Clinically feasible reconstruction time is feasible using deep subspace learning [2], but the initial study used only a simple single-pass network with limited precision of quantitative maps. Data-consistent (DC) deep learning networks can improve image reconstruction quality [3], but are less well developed for non-Cartesian imaging and for subspace imaging methods such as MT. Here we developed a non-Cartesian DC deep subspace learning method trained on 96 T1 CMR MT datasets, and evaluated its reconstruction speed, T1 precision and T1 accuracy against iterative methods and against a naïve network without DC layer.

#### Methods

Network design: The proposed network consists of two parts: a U-Net and a DC layer. For the DC layer, we developed a non-Cartesian preconditioned gradient descent subspace DC module. A novel preconditioner was used for efficient gradient descent. The network and DC layer operate within a subspace described by the multitasking model [1]. The U-Net part was pretrained without DC layer, and we directly add the DC layer without further training.

Dataset overview: A total of 123 T1 CMR MT datasets were collected from Siemens 3T scanners. We used 96 cases for training, 12 cases for validation and 15 cases (including 3 cardiomyopathy patients) for testing. The matrix size of spatial subspaces is  $320 \times 320 \times 32$ .

Evaluation methods: The performance of the proposed DC network with one gradient step was compared against a naïve network consisting of the same U-Net without DC layer. The iteratively reconstructed labels were used as reference. The PSNR, SSIM and NRMSE of T1-weighted images were calculated at two inversion times (bright blood and dark blood contrast); the whole cardiac cycle (20 frames) at the end-expiration (EE) respiratory phase was used for calculation. Accuracy and precision of EE, end-diastolic septal T1 were compared against the corresponding T1 values from iterative reconstruction using Bland-Altman plots.

#### Results

Reconstruction times were 10 min for iterative reconstruction, 1 sec for the naïve network and 5 sec for the proposed network. Table 1 shows the quantitative metrics of the networks'

reconstructed dynamic images. The proposed network outperforms the naïve U-Net in all metrics. One example case of testing T1 maps from both networks and from iterative reconstruction are shown in Figure 1. The error maps clearly show the proposed network have smaller pixelwise T1 error than the naïve U-Net. Bland-Altman plots of the T1 fitting results among the whole testing set are shown in Figure 2. Neither network showed statistically significant bias in T1, but the proposed network was more precise in T1 mapping than the naïve U-Net, improving the limits of agreement by 40%.

## Conclusion

Non-Cartesian DC deep subspace learning accelerates CMR multitasking reconstruction on the order of 100x, and produces 40% higher precision than the same network without data consistency. Future studies will validate the method in a patient cohort.

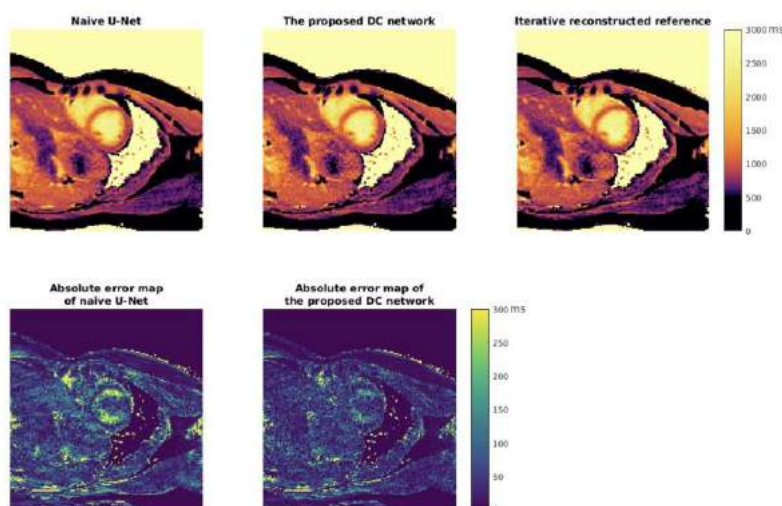
**Figure/Table 1**

		Naïve U-Net	The proposed DC network
PSNR	Bright blood	32.2±4.6	<b>34.9±3.3</b>
	Dark blood	35.2±5.3	<b>38.0±3.2</b>
SSIM	Bright blood	0.830±0.064	<b>0.887±0.041</b>
	Dark blood	0.891±0.042	<b>0.929±0.023</b>
NRMSE	Bright blood	0.198±0.082	<b>0.152±0.044</b>
	Dark blood	0.132±0.086	<b>0.096±0.031</b>

**Caption 1**

**Table 1.** Quantitative metrics of the reconstructed dynamic images using different networks compared with iterative reconstruction images among the testing set.

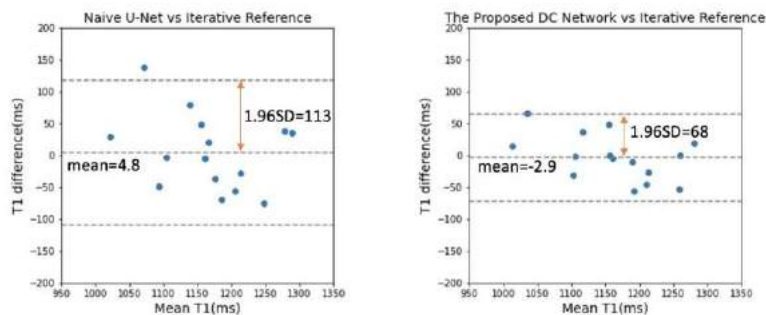
**Figure/Table 2**



## Caption 2

**Figure 1.** An example case of testing T1 maps from both networks and iterative reconstruction. The corresponding error maps are shown in the bottom. Error maps clearly show that the proposed network have smaller error than naive U-Net. The error map of the proposed network also has fewer structural features than naive U-Net's error map.

## Figure 3



## Caption 3

**Figure 2.** Bland-Altman plots of the T1 fitting results among the whole testing set. The septal region is used to calculate the average T1 value in each case.

## Bibliographic References

[1] A. G. Christodoulou et al., "Magnetic resonance multitasking for motion-resolved quantitative cardiovascular imaging," *Nature biomedical engineering*, vol. 2, no. 4, pp. 215-226, 2018. [Online]. Available: <https://escholarship.org/content/qt6ff194z4/qt6ff194z4.pdf?t=qaewub.>, [2] Y. Chen, J. L. Shaw, Y. Xie, D. Li, and A. G. Christodoulou, "Deep learning within a priori temporal feature spaces for large-scale dynamic MR image reconstruction: Application to 5-D cardiac MR Multitasking," in *International Conference on Medical Image Computing and Computer-Assisted Intervention*, 2019: Springer, pp. 495-504. , [3] J. Schlemper, J. Caballero, J. V. Hajnal, A. N. Price, and D. Rueckert, "A deep cascade of convolutional neural networks for dynamic MR image reconstruction," *IEEE transactions on Medical Imaging*, vol. 37, no. 2, pp. 491-503, 2017. [Online]. Available: <https://spiral.imperial.ac.uk:8443/bitstream/10044/1/51669/9/08067520.pdf>.

Speaker: Z. Chen

Category: Parametric Mapping, Non-Cartesian, Rapid Imaging



000231

## **The impact of automated post processing with and without user correction on the assessment of serial CMR examinations**

J. Weber \* (1); M. Passick, (1); N. Ngai (1); Q. Zhou (1); J. J. Cao (1)

(1) Research, St. Francis Hospital & Heart Center, Roslyn, United States of America

### **Abstract**

**Background:** The advent of automated software for CMR post-processing has led to vast improvements in the reproducibility of volumetrics and ejection fractions (EF) allowing for improved accuracy in detecting serial changes which can be critical clinically assessing response to therapy. However, user input is still necessary at times. In this report, we used fully automated, user-corrected, and user-dependent post processing to compare the reproducibility and detectable changes in serial clinical examinations for patients with cardiomyopathy and with chemotherapy.

**Methods:** This was a prospective study that included patients with 2 serial CMR examinations. The participants were clinical patients referred for cardiomyopathy evaluation or for chemotherapy induced cardiotoxicity assessment. All provided written consents. SSFP cine short-axis stack was used (with long-axis reference) to calculate left ventricular (LV) volumes and EF. Three sets of volumes were calculated using fully automated software (suiteHEART version 5.0.1, NeoSoft LLC, Pewaukee, WI) except for the identification of ED/ES phases, user-corrected approach modifying contours generated from automated software, and user-dependent post processing using a manual software (QMASS v. 7.2, Medis Medical Imaging, The Netherlands). For each analysis a random subset was used to assess reproducibility agreement by intra-class correlation (ICC). The standard error of measurement (SEM) was used to establish cut-points for minimum detectable difference (MDD) among serially analyzed cases and were compared across the three analysis methods.

**Results:** There were 95 subjects referred for the evaluation of cardiomyopathy with serial CMRs and 11 oncology patients enrolled before and after chemotherapy. On average, serial studies occurred  $14 \pm 9$  months apart from each other. The mean age was  $54 \pm 13$  and 70% were male (Table 1). While ICC values were excellent for all 3 analysis methods, the SEM and derived MDD were the best (smallest detectable difference) from the automated post-processing method, followed by the user-corrected and user-dependent methods (Table 2). Based on the MDD of LVEF for each post-processing method of 0.4%, 1.7% and 4.2%, the serial changes were detected in 96%, 80% and 49% of cardiomyopathy patients, 82%, 64% and 64% in chemotherapy patients, respectively. (Table 3). Within each post-processing method, detectable differences did not significantly differ by EF greater or less than 50% or by the presence or absence of regional wall motion abnormalities (RWMA).

**Conclusion:** Automated post-processing of CMR, whether fully automated or with user correction, results in a narrower margin of error and enhanced detection of small serial changes when compared with manual post processing. Additional research is warranted to successfully balance reproducibility and accuracy when using automated post-processing methods.

**Figure/Table 1****Baseline characteristics**

	<i>Mean (SD)</i>
Age	54 (13)
Male gender	75 (77)
Height (in)	68 (4)
Weight (lbs)	193 (38)
BSA	2.01 (0.23)
Diabetes (%)	18 (19)
Hypertension (%)	41 (42)
Hyperlipidemia (%)	49 (51)
Family history of CAD (%)	38 (40)
History of MI (%)	9 (9)
Cath (%)	52 (55)
Heart Failure (%)	35 (36)
Renal disease (%)	4 (4)
Any smoking (%)	28 (29)

**Post-processed volumes**

	<b>Automated</b>	<b>Semi-Automated</b>	<b>Manual</b>
	<i>Mean (SD)</i>	<i>Mean (SD)</i>	<i>Mean (SD)</i>
LV end-diastolic vol (mL)	176 (46)	174 (45)	168 (44)
LV end-Systolic vol (mL)	89 (36)	88 (35)	85 (35)
LV stroke vol (mL)	87 (20)	86 (19)	82 (26)
LV ejection fraction (%)	51 (10)	51 (9)	51 (10)
RV end-diastolic vol (mL)	158 (48)	151 (44)	146 (41)
RV end-Systolic vol (mL)	78 (30)	70 (25)	71 (27)
RV stroke vol (mL)	81 (29)	81 (23)	74 (22)
RV ejection fraction (%)	51 (11)	54 (7)	52 (8)

**Caption 1**

Table 1. Baseline characteristics

**Figure/Table 2****Reproducibility**

	<b>Automated</b>		
	<i>ICC (95% CI)</i>	<i>SEM (95% CI)</i>	<i>MDD</i>
<b>LV end-diastolic volume</b>	0.99 (0.98, 1)	0.42 (0.37, 0.46)	1.2 mL
<b>LV end-systolic volume</b>	1 (1, 1)	0.10 (0.09, 0.11)	0.3 mL

<b>LV ejection fraction</b>	0.99 (0.97, 1)	0.13 (0.11, 0.14)	0.4 %
	<b>Semi-Automated</b>		
<b>LV end-diastolic volume</b>	0.99 (0.96, 0.99)	1.1 (0.9, 1.2)	3.1 mL
<b>LV end-systolic volume</b>	1 (0.99, 1)	0.2 (0.21, 0.27)	0.6 mL
<b>LV ejection fraction</b>	0.96 (0.9, 0.99)	0.6 (0.54, 0.69)	1.7 %
	<b>Non-automated</b>		
<b>LV end-diastolic volume</b>	0.98 (0.95, 0.99)	1.4 (1.2, 1.5)	3.9 mL
<b>LV end-systolic volume</b>	0.96 (0.96, 0.96)	1.5 (1.3, 1.7)	4.2 mL
<b>LV ejection fraction</b>	0.95 (0.9, 0.98)	1.5 (1.3, 1.6)	4.2 %

## Caption 2

Table 2. Reproducibility metrics of automated, semi-automated, and non-automated post processing methods.

Abbreviations: ICC = Intra-class correlation; SEM = Standard error of measurement; MDD = Minimum detectable difference

## Figure 3

<b>Detected serial changes*</b>	Automated		Semi-Automated		Non-automated	
	LVEF≥50%	LVEF<50%	LVEF≥50%	LVEF<50%	LVEF≥50%	LVEF<50%
LV end-diastolic volume (%)	53 (96)	38 (97)	56 (98)	38 (100)	53 (93)	35 (92)
LV end-systolic volume (%)	53 (96)	38 (97)	57 (100)	38 (100)	43 (75)	30 (79)
LV ejection fraction (%)	54 (98)	36 (92)	44 (77)	32 (84)	25 (44)	22 (57)
	Automated		Semi-Automated		Non-automated	
	RWMA absent	RWMA present	RWMA absent	RWMA present	RWMA absent	RWMA present
LV end-diastolic volume (%)	53 (96)	38 (97)	54 (98)	40 (100)	52 (95)	36 (90)
LV end-systolic volume (%)	54 (98)	37 (95)	55 (100)	55 (100)	39 (71)	34 (85)
LV ejection fraction (%)	55 (100)	35 (90)	41 (75)	35 (89)	23 (42)	24 (60)

## Caption 3

Table 3. Detected serial changes of volumes and EF among post-processing methods

\*Described as Number (%) of serial changes detected during post-processing

Abbreviation: RWMA = regional wall-motion abnormalities

Speaker: J. Weber

Category: Automated Processing, Segmentation, Cine Imaging

000233

## Early evaluation of subclinical cardiotoxicity in chest tumor patients receiving immune checkpoint inhibitors by cardiovascular magnetic resonance: a prospective observational study

J. Liu \* (1); Y. Cao (1); K. Zhu (2); S. Yao (3); M. Yuan (1); X. Kong (1); X. Liu (1); Y. Li (1); Y. Cui (1); X. Han (1); X. Zhou (4); R. Meng (2); H. Shi (1)

(1) Department of radiology, wuhan union hospital, wuhan, China; (2) Cancer center, wuhan union hospital, wuhan, China; (3) Department of rehabilitation medicine, wuhan tongji hospital, wuhan, China; (4) Mr collaboration, Siemens Healthineers Ltd., shanghai, China

### Abstract

#### Background

Limited data exists on the subclinical effects of cardiotoxicity in chest tumor patients receiving immune checkpoint inhibitors (ICIs) [1-3]. Therefore, we aimed to evaluate the manifestations of subclinical cardiotoxicity in this patient cohort using cardiovascular magnetic resonance (CMR), and their relationship with baseline CMR and clinical parameters.

#### Methods

A prospective, longitudinal study was conducted in chest tumor patients ( $n = 60$ ). Following informed consent, patients underwent serial CMR (1.5T scanner, MAGNETOM Altea, Siemens Healthineers, Erlangen, Germany) at three time points: baseline, 3 weeks (1st follow-up), and 3 months (2nd follow-up) after initiation of ICI therapy (Figure 1). Patients who underwent at least 2 CMR examinations (baseline and 1st follow-up CMR data) were included in the analysis. The following CMR parameters were assessed: functional parameters and global strains of left ventricle (LV) and right ventricle (RV), T1 mapping and derived extracellular volume fraction (ECV), and T2 mapping and late gadolinium enhancement (LGE). According to the recent task force criteria [4-5], an LV ejection fraction (LVEF) with a  $> 10\%$  decrease compared with baseline LVEF was defined as reduced LVEF, while a reduced RV ejection fraction (RVEF) was defined as  $< 45\%$ .

#### Results

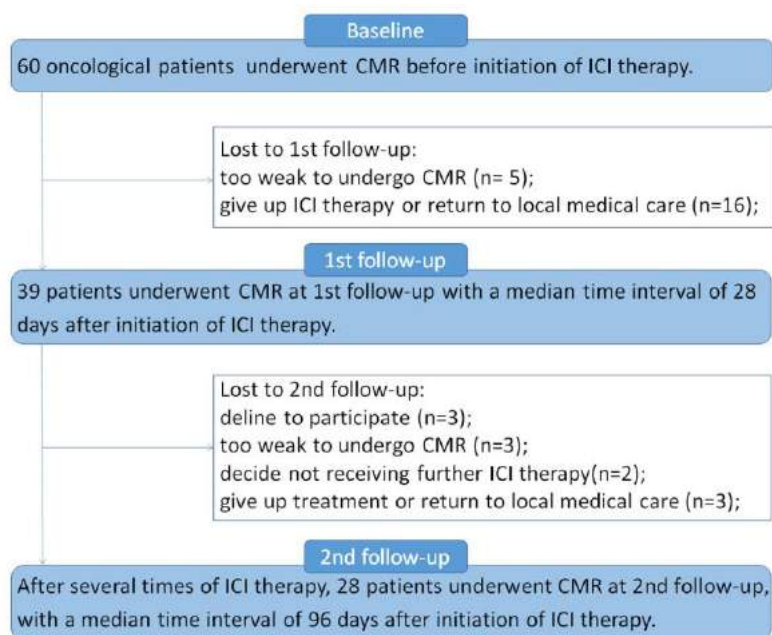
Thirty-nine patients ( $n = 39$ , age =  $60.3 \pm 10.0$  years, 28 males) successfully underwent baseline and first follow-up CMR. Of these, 24 (61.5%) had at least one risk factor. Most patients (92.3%) had lung cancer, and all patients received ICI monotherapy. Compared with baseline data, LVEF, RVEF, LV global radial strain and circumferential strain, and RV global radial strain showed significant decrease at 1st follow-up (Figure 2, Table 1). There were 28 patients (age =  $60.3 \pm 9.3$  years, 21 males) with CMR data at 2nd follow-up, and LVEF, RVEF, and global strains of both ventricles showed further reduction. Native T1, post-contrast T1, ECV, and T2 values revealed no statistically significant differences ( $p > 0.05$ ). The presence of CV risk factor represented a predictor of LVEF reduction  $> 10\%$  at 1st

follow-up ( $p = 0.020$ ). A baseline LVEF  $< 53\%$  emerged as significant for predicting both reduction of LVEF  $> 10\%$  ( $p = 0.030$ ) and RVEF  $< 45\%$  ( $p = 0.040$ ) at 2nd follow-up.

## Conclusion

At the early stage of ICI therapy, bi-ventricular dysfunction is the main manifestation of subclinical myocardial injury in patients with chest tumors. A baseline LVEF  $< 53\%$  may be associated with further reduction in bi-ventricular dysfunction in this patient population.

**Figure/Table 1**



**Caption 1**

Flow chart of the study cohort. *ICI* immune checkpoint inhibitor, *CMR* cardiovascular magnetic resonance.

**Figure/Table 2**

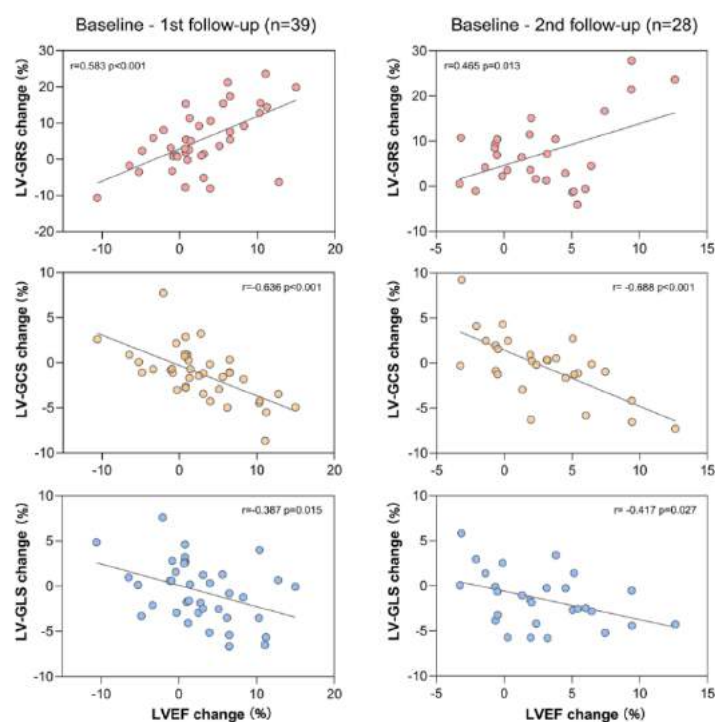
	Baseline (n=39)	1st follow-up (n=39)	p value	2nd follow-up (n=28)	p value#
Times of ICI therapy	-	1	-	3 (3, 4)	-
Time interval since First ICI therapy, days	-	28 (26, 30)	-	96 (96, 105)	-
Heart rate	76.5 ± 12.0	77.2 ± 13.9	0.778	72.3 ± 12.5	0.016
<b>Laboratory results</b>					

Lactate dehydrogenase, u/l	187.0 (152.0, 224.0)	184.0 (155.0, 220.5)	0.915	180.0 (146.0, 219.0)	0.179
Creatine kinase, u/l	52.5 (38.0, 72.8)	49.0 (33.5, 66.0)	0.392	52.0 (37.0, 69.5)	0.446
Creatine kinase-mb, ng/ml	0.5 (0.3, 0.7)	0.5 (0.3, 0.8)	0.729	0.5 (0.3, 0.7)	0.797
High-sensitivity cardiac troponin i, ng/l	1.3 (0.8, 2.8)	1.8 (0.8, 3.2)	0.300	1.6 (1.0, 2.4)	0.837
<b>Abnormal electrocardiograph</b>	14 (35.9)	14 (35.9)	1.000	9 (32.1)	0.479
<b>CMR parameters</b>					
Left ventricular end-diastolic volume, ml	117.6 ± 25.4	113.7 ± 25.2	0.499	117.5 ± 25.0	0.162
Left ventricular end-systolic volume, ml	56.3 ± 13.7	57.9 ± 13.9	0.610	59.4 ± 14.0	0.874
Left ventricular stroke volume, ml	61.3 ± 16.6	55.8 ± 16.7	0.149	58.1 ± 15.8	0.022
Left ventricular ejection fraction, %	52.4 ± 7.1	49.4 ± 6.7	0.005	48.6 ± 6.8	0.001
Cardiac output, l/min	4.6 ± 1.1	4.2 ± 1.1	0.107	4.1 ± 0.9	<0.001
Cardiac index, l/min/m <sup>2</sup>	2.6 ± 0.6	2.4 ± 0.6	0.119	2.4 ± 0.5	<0.001
Right ventricular end-diastolic volume, ml	108.5 ± 24.6	106.2 ± 27.1	0.589	110.4 ± 26.0	0.599
Right ventricular end-systolic volume, ml	57.8 ± 16.8	58.3 ± 15.7	0.870	64.5 ± 14.4	0.149
Right ventricular stroke volume, ml	50.7 ± 12.0	47.9 ± 14.3	0.302	45.8 ± 14.5	0.028
Right ventricular ejection fraction, %	47.9 ± 5.3	44.9 ± 7.0	0.014	40.9 ± 7.5	<0.001
LV-GRS, %	38.3 ± 8.8	32.9 ± 9.9	<0.001	31.6 ± 9.2	<0.001
LV-GCS, %	-18.3 ± 2.9	-17.1 ± 2.6	0.003	-17.0 ± 3.4	0.005
LV-GLS, %	-13.9 ± 3.0	-13.4 ± 2.8	0.320	-11.8 ± 2.2	0.008
RV-GRS, %	34.1 ± 12.1	28.7 ± 8.3	0.025	25.2 ± 8.1	<0.001
RV-GCS, %	-12.4 ± 3.9	-12.1 ± 4.7	0.727	-11.4 ± 4.0	0.207
RV-GLS, %	-15.8 ± 5.4	-15.4 ± 5.3	0.720	-13.1 ± 5.2	0.023
Native T1, ms	1022.5 ± 39.1	1016.6 ± 47.2	0.358	1012.2 ± 40.4	0.316
Post-contrast T1, ms	452.2 ± 37.1	460.3 ± 41.6	0.188	461.2 ± 31.5	0.186
extracellular volume, %	28.3 ± 2.8	28.6 ± 4.3	0.566	27.7 ± 3.1	0.560
T2, ms	46.2 ± 3.4	46.1 ± 3.3	0.810	46.3 ± 3.4	0.588

**Caption 2**

Continuous variables were described as mean  $\pm$  standard deviation, median (interquartile range), or n (%). #data at 2nd follow-up were compared with data of the same patient cohort at baseline using paired samples t test or Wilcoxon signed-rank test. *CMR* cardiovascular magnetic resonance, *ICI* immune checkpoint inhibitor, *LV* left ventricle, *RV* right ventricle, *GRS* global radial strain, *GCS* global circumferential strain, *GLS* global longitudinal strain, *LGE* late gadolinium enhancement.

**Figure 3**



**Caption 3**

Correlation between changes in LVEF and changes in global strain values of left ventricle at two time points during follow-up. *LVEF* left ventricular ejection fraction.

## Bibliographic References

- 1.Saunderson CE, Plein S, Manisty CH. Role of cardiovascular magnetic resonance imaging in cardio-oncology. *Eur Heart J Cardiovasc Imaging*. 2021;22:383-96., 2.Higgins AY, Arbune A1, Soufer A, Ragheb E, Kwan JM, Lamy J, et al. Left ventricular myocardial strain and tissue characterization by cardiac magnetic resonance imaging in immune checkpoint inhibitor associated cardiotoxicity. *PLoS One*. 2021;16:e0246764., 3.Zhang L, Awadalla M,



Mahmood SS, Nohria A, Hassan MZ, Thuny F, et al. Cardiovascular magnetic resonance in immunecheckpoint inhibitor-associated myocarditis. *Eur Heart J*. 2020;41:1733–43., 4. Plana JC, Galderisi M, Barac A, Ewer MS, Ky B, Crosbie MS, ET al. Expert consensus for multimodality imaging evaluation of adult patients during and after cancer therapy: a report from the American Society of Echocardiography and the European Association of Cardiovascular Imaging. *J Am Soc Echocardiogr*. 2014;27:911-39., 5. Etoom Y, Govindapillai S, Hamilton R, Manlhiot C, Yoo SJ, Farhan M, et al. Importance of CMR within the Task Force Criteria for the diagnosis of ARVC in children and adolescents. *J Am Coll Cardiol*. 2015;65:987-95.

Speaker: J. Liu

Category: Late Gadolinium Enhancement, Cardiac Function, Cardiac Strain

000236

## Comorbid diabetes worsens myocardial energetics, perfusion and contractility in patients with severe aortic stenosis

N. Jex \* (1); A. Chowdhary (1); S. Thirunavukarasu (1); H. Procter (2); F. Jonathan (1); H. Xue (3); P. Kellman (3); P. Swoboda (1); J. Greenwood (1); S. Plein (1); E. Levelt (1)

(1) Leeds institute of cardiovascular and metabolic medicine, University of Leeds, Leeds, United Kingdom; (2) Cardiology, Leeds General Infirmary, Leeds, United Kingdom; (3) National institutes of health, National Heart Lung & Blood: Sloan and Elaine M MD, Bethesda, United States of America

### Abstract

**Background-** Aortic stenosis (AS) and type 2 diabetes mellitus (DM) are increasingly frequent comorbidities in aging populations, and diabetes is associated with increased morbidity and mortality after aortic valve replacement (AVR). Although distinct pathological entities, AS and DM share common features of impaired myocardial energetics and coronary microvascular dysfunction. The mechanisms for the adverse prognostic association between AS and DM are incompletely understood but are likely to include the collective impact of DM and AS on myocardial metabolism and perfusion.

**Objectives-** Utilizing <sup>31</sup>Phosphorus magnetic resonance spectroscopy (<sup>31</sup>P-MRS) and cardiovascular magnetic resonance (CMR), we tested the hypotheses that the collective impact of severe AS and DM on the myocardium aggravates myocardial energetic impairment, contractile dysfunction and impairs coronary microvascular function.

**Methods-** Seventy-three severe AS patients with (DAS, n=25) and without DM (IsoAS, n=48) undergoing AVR were prospectively recruited. A further 15 isolated DM and 15 healthy volunteers served as control groups. Severe AS patients with left ventricular systolic dysfunction (LVEF <50%), coronary artery disease (CAD), prior cardiac surgery, moderate or above valvular heart disease other than AS, renal impairment (estimated glomerular filtration rate [eGFR] below 30 mL/min/1.73m<sup>2</sup>) or insulin treatment were excluded. All subjects underwent <sup>31</sup>P-MRS followed by a comprehensive CMR protocol including cine imaging, native pre- and post-contrast T1 mapping, stress and rest adenosine perfusion and late gadolinium enhancement (LGE).

**Results-** Clinical and biochemical characteristics are provided in Table-1, CMR/<sup>31</sup>P-MRS results in Table-2. Patients were matched for age, sex, and blood pressure across the groups with DM control and DAS patients matched for HBA1c. All AS patients matched for surgical scores and frailty scores (EURO score and Rockwood score respectively). NTproBNP levels were similarly elevated in both AS groups. Left ventricular (LV) volumes and ejection fraction (EF) were similar between groups, with no significant difference in LV mass or wall thickness between the DAS and IsoAS groups. DAS patients showed greater reductions in myocardial PCr/ATP (HV: 2.17±0.5, DM Control: 1.58±0.21, IsoAS Control: 1.7±0.42, DAS: 1.39±0.25, p<0.0001) and global stress myocardial blood flow (MBF) than IsoAS patients (HV: 2.14±0.66ml/min/g, DM: 1.81±0.39ml/min/g, IsoAS: 1.66±0.5ml/min/g, DAS: 1.24±0.3ml/min/g, p<0.0001). Moreover, the DAS group displayed the most significant reductions in global longitudinal strain and left atrial function. Rest MBF was similar across

the cohorts, while the myocardial perfusion reserve was reduced in both severe AS groups, though showing more significant reductions in DAS.

**Conclusion-** This study provides the first mechanistic evidence of the combined effect of AS and DM on cardiac energetics, perfusion, and function. Co-morbidity with diabetes leads to significant deterioration in GLS, left atrial function, myocardial energetics, and coronary microvascular function in patients with severe AS. These adverse phenotypic features may be important components of the worsened AVR clinical outcomes attributable to combined presence of AS and DM. Emphasising diabetes comorbidity among the surgical risk stratification of AS patients may improve prognostic accuracy of risk scores and consequently clinical outcomes.

**Figure/Table 1**

**Table 1: Clinical Characteristics and biochemistry**

Variable	HV n=15	DM n=15	IsoAS n=48	DAS n=23	p value
Age, y	71±4	71±7	71±9	72±7	0.99
Female, n(%)	4(26)	5(33)	17(35)	5(22)	0.24
BMI, kg/m <sup>2</sup>	26±2¶	27±3§	28±3€	31±4	<0.0001
Heart rate, bpm	62±10	65±11	70±14	71±14	0.07
Systolic BP, mmHg	136±9	127±15	132±17	131±21	0.87
Diastolic BP, mmHg	76±5	72±6	76±8	73±10	0.24
Haemoglobin, g/L	149±10¶†	148±14§	131±21*	131±19	<0.0001
Creatinine, umol/L	73±8	71±16	79±18	83±19	0.07
eGFR, ml/min/1.73m <sup>2</sup>	84±8¶	77±16	78±12	72±15	0.01
Total cholesterol, mmol/L	5.3±1.1¶	4.71±1.2	5±1.5€	4.3±1.1	0.003
HDL, mmol/L	1.7±0.4¶	1.6±0.5§	1.5±0.4	1.3±0.3	0.002
LDL, mmol/L	2.9±1¶	2.4±0.9	2.9±1.3	2.3±1	0.02
TG, mmol/L	1.3±0.6	1.6±0.5	1.4±0.7	1.8±1.1	0.05
HbA1c, mmol/mol	37±3¶≠	60±11*	37±4€	59±16	<0.0001
Insulin, pmol/L	39±31¶≠	114±99*	56±55€	148±136	<0.0001
NT- proBNP, ng/L	67±72¶†	132±100§	1579±3237*	1430±2264	<0.0001
<b>AS clinical details</b>					
AV Peak Velocity, m/s	-	-	4.5±0.5	4.5±0.5	0.89
MV Doppler E:A	-	-	0.76±0.2	1.1±0.9	0.02
TDI average e/e'	-	-	12.4±4	14±5	0.45
6 min walk test, m	-	-	411±112	385±101	0.23

<b>Rockwood Score</b>	-	-	2.17±0.8	2.22±0.4	0.36
<b>EURO score II (%)</b>	-	-	1.13±0.7	1.14±0.5	0.27
<b>Cardiovascular history</b>					
<b>Stroke TIA, n(%)</b>	-	0(0)	3(6)	1(4)	0.54
<b>HTN, n(%)</b>	-	0(0)	17(35)	13(56)	0.09
<b>PAF, n(%)</b>	-	0(0)	7(15)	1(4)	0.2

€signifies p<0.05 between DAS and isoAS , § signifies p<0.05 between DAS and DM

¶ signifies p<0.05 between DAS and HV, \* signifies p<0.05 between IsoAS and DM

† signifies p≤0.05 between IsoAS and HV, ≠ signifies p≤0.05 between DM and HV

### Caption 1

Table 1: Clinical characteristics and biochemistry

### Figure/Table 2

Table 2: CMR and 31P-MRS findings

	<b>HV</b>	<b>DM</b>	<b>IsoAS</b>	<b>DAS</b>	<b>p value</b>
	n=15	n=15	n=48	n=25	
<b>LV end-diastolic volume indexed to BSA, mL/m<sup>2</sup></b>	78±15	75±13	83±24	84±21	0.64
<b>LV end-systolic volume indexed to BSA, mL/m<sup>2</sup></b>	28±6	31±8	33±23	36±20	0.4
<b>LV mass, g</b>	102±25¶	93±13	146±39*†	153±64 §	<b>&lt;0.0001</b>
<b>LV mass to LV end-diastolic volume, g/mL</b>	0.66±0.11¶	0.65±0.11§	0.93±0.19*†	0.88±0.26	<b>&lt;0.0001</b>
<b>LV stroke volume, mL</b>	95±22	81±14	96±22	99±20§	<b>0.046</b>
<b>LV ejection fraction, %</b>	64±3	57±7	62±13	60±11	<b>0.046</b>
<b>LV maximal wall thickness, mm</b>	10±1¶	11±2*	14±3†	15±2	<b>&lt;0.0001</b>
<b>RV end-diastolic volume indexed to BSA, mL/m<sup>2</sup></b>	83±12	73±11	80±18	78±21	0.21

<b>RV end-systolic volume indexed to BSA, ml/m<sup>2</sup></b>	32±7	34±10	37±15	37±17	0.78
<b>RV stroke volume, ml</b>	97±17	78±15	83±20	82±22	<b>0.047</b>
<b>RV ejection fraction, %</b>	62±5	55±9	55±10	53±10	0.07
<b>LA biplane end-systolic volumes, mL</b>	72±20	73±26	103±52	98±44	<b>0.03</b>
<b>Biplane LA EF, %</b>	59±11¶	53±11	44±17	40±18	<b>0.009</b>
<b>Global longitudinal strain, negative (-), %</b>	16±4¶	13±8	13±4	11±4	<b>0.003</b>
<b>Peak systolic circumferential strain, (-), %</b>	21±2	18±6	18±5	18±5	0.14
<b>Peak longitudinal diastolic strain rate, s<sup>-1</sup></b>	0.79±0.18	0.8±0.25	0.82±0.31	0.66±0.2	0.2
<b>Mean native T1, (ms)</b>	1209±79	1153±53	1244±84*	1269±82§	<b>0.0003</b>
<b>Extra cellular volume, (%)</b>	24±3	23±3	25±2	25±4	<b>0.04</b>
<b>Myocardial Energetics</b>					
<b>PCr/ATP ratio</b>	2.17±0.5¶	1.58±0.21≠	1.7±0.42†	1.39±0.25€	<b>&lt;0.0001</b>
<b>Myocardial Perfusion</b>					
<b>Increase in RPP, %</b>	25	29	23	25	0.5
<b>Stress MBF, ml/min/g</b>	2.14±0.66¶	1.81±0.39§	1.66±0.5	1.24±0.3€	<b>&lt;0.0001</b>
<b>Rest MBF, ml/min/g</b>	0.66±0.11	0.73±0.18	0.72±0.17	0.67±0.22	0.77
<b>MPR</b>	3.83±1.8¶	2.62±0.82§	2.46±0.78†	1.78±0.48€	<b>&lt;0.0001</b>

€ signifies p<0.05 between DAS and isoAS , § signifies p<0.05 between DAS and DM

¶ signifies p<0.05 between DAS and HV, \* signifies p<0.05 between IsoAS and DM

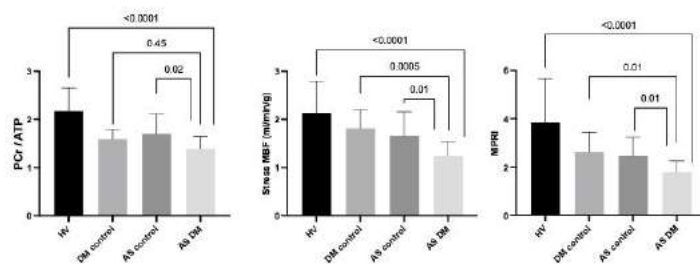
† signifies p≤0.05 between IsoAS and HV, ≠ signifies p≤0.05 between DM and HV

Values are mean ±standard deviations or percentages. AS indicates severe aortic stenosis; BSA, body surface area; LV, Left ventricle; RV, right ventricle; DM, type 2 diabetes mellitus; LV, left ventricular; LA, left atrial; LA EF, left atrial ejection fraction; PCr, phosphocreatine; ATP, adenosine tri-phosphate; RPP, rate pressure product; MBF, myocardial blood flow; MPR, myocardial perfusion reserve

## Caption 2

Table 2: CMR and 31P-MRS Findings

## Figure 3



### Caption 3

**Figure 1:** Differences in myocardial PCr/ATP ratio, global stress myocardial blood flow and myocardial perfusion reserve between healthy volunteers, patients with isolated DM, patients with isolated severe AS and patients with severe AS and DM;

Speaker: N. Jex

Category: Aortic stenosis, Diabetes, Spectroscopy

000245

## **Ferumoxytol-enhanced 4D flow quantification of a large coronary artery fistula in a neonate with pulmonary atresia, intact ventricular septum**

J. Mandell \* (1); L. Olivieri (2); M. Donofrio (2); Y.-H. Loke (2)

(1) Pediatric Cardiology, University of Rochester Medical Center, Rochester, United States of America; (2) Cardiology, Children's National Hospital, Washington, United States of America

### **Abstract**

#### **Description of Clinical Presentation**

JO is a full term female neonate prenatally diagnosed with a small right ventricle (RV), ductal dependent pulmonary flow and to-and-fro flow in the right ventricular outflow tract (RVOT) of unclear etiology. Post-natal echocardiogram established the diagnosis of pulmonary atresia with an intact ventricular septum (PA-IVS) and a suspected large coronary artery fistula arising from the RVOT. A cardiac CT on day of life (DOL) 2 confirmed the coronary artery fistula connecting the right ventricle and the left main coronary os. The branch pulmonary arteries were confluent, arising from a patent ductus arteriosus. A cardiac catheterization was performed on DOL 6 to define the coronary anatomy demonstrating a single left coronary artery giving rise to left anterior descending, circumflex, and right coronary arteries, ending in the large fistulous connection to the RV. There was extensive discussion regarding the possibility of flow reversal in the fistula causing a runoff lesion placing the neonate at risk of coronary steal and ischemia. A cardiac magnetic resonance (CMR) study was done to assess the fistula and quantify systemic and pulmonary blood flow.

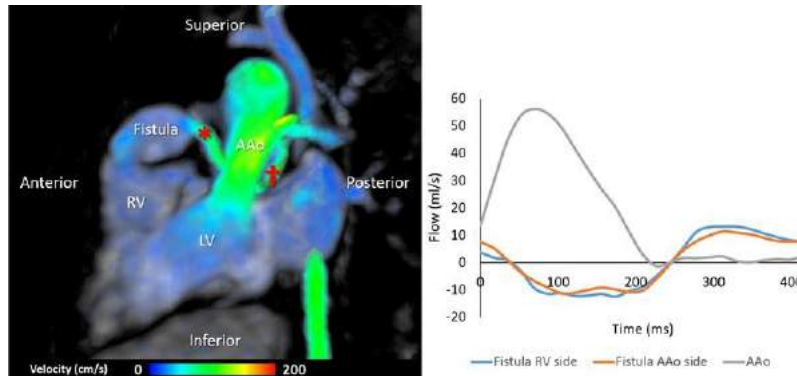
#### **Diagnostic Techniques and Their Most Important Findings**

CMR was performed under general anesthesia on a Siemens Aera 1.5T scanner. At the time of the study, the patient was 12 days old with a weight of 2.7 kg and body surface area of 0.18 m<sup>2</sup>. 4D flow imaging following Ferumoxytol contrast administration using Siemens WIP 785A was acquired (isotropic resolution 1.3 mm, flip angle 15 degrees, TR 40.3 ms, TE 2.5 ms, Venc 200 cm/s). Standard 2D phase contrast imaging was also performed for verification. 4D Flow quantification was performed using Arterys (San Francisco, CA) and flow from 2D phase contrast was measured with Medis (The Netherlands), both after background correction. Further visualization was performed using iTFlow (Cardio Flow Design, Japan) for pathline tracing of fistula and aorta flow. Short axis cine volumetry was used to quantify left and right ventricular cardiac output using Medis. The coronary artery fistula measured between 3.5-5 mm in diameter, similar in size to the branch pulmonary arteries. Aorta and branch pulmonary artery flows were reported clinically to calculate a systemic flow of 1.7 L/min/m<sup>2</sup> and pulmonary flow of 4.4 L/min/m<sup>2</sup>. Coronary fistula flow measured at both aorta and RV ends was identical at 0.3 L/min during systole (towards aorta) and 0.3 L/min during diastole (towards RV) with no net flow over the cardiac cycle (Figure 1). Flow measurements were corroborated by additional flows shown in Figure 2 as well as 2D phase contrast in the aorta, branch pulmonary arteries, and inferior and superior vena cava (mean difference 0.06 ± 0.05 ml/s). Additionally, no flow reversal was seen in the proximal ascending aorta, distal to the fistula. Pathline tracing supported to-and-fro flow in the fistula without significant runoff (Figure 3).

## Learning Points from this case

We demonstrate the use of 4D flow CMR with ferumoxytol contrast in a small neonate (2.7 kg). As ferumoxytol enhances signal-to-noise ratio, higher spatial resolution (down to 1.3 mm voxel size) can be achieved by 4D flow, allowing for measurements in small vessels that are consistent with other conventional CMR measurements. In this case, the CMR study was able to provide valuable insight into this unusual physiology in PA-IVS which could not be determined by other methods.

**Figure/Table 1**

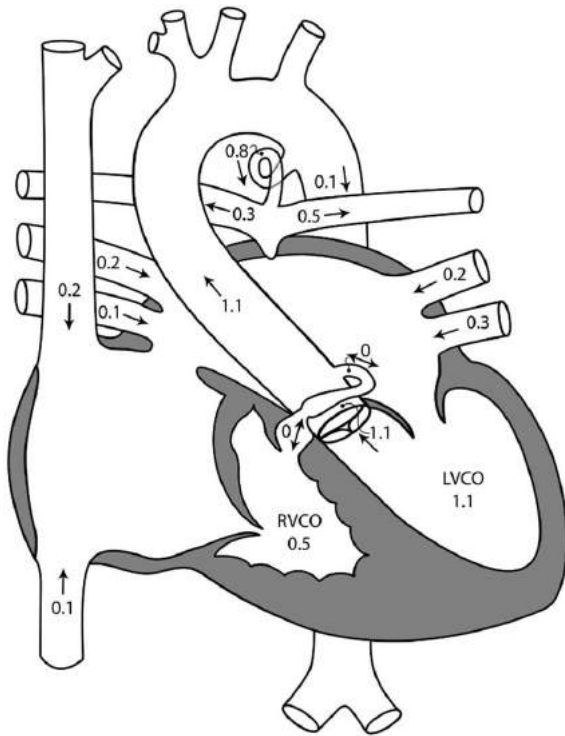


**Caption 1**

Figure 1: Left) Sagittal projection of 4D flow (Arterys) during peak systole with color representing velocity. Location of coronary fistula flow measurements are shown at right ventricular (RV) side (\*) and ascending aorta (AAo) side (†). Right) Flow profiles of the AAo and coronary fistula are shown.

**Figure/Table 2**

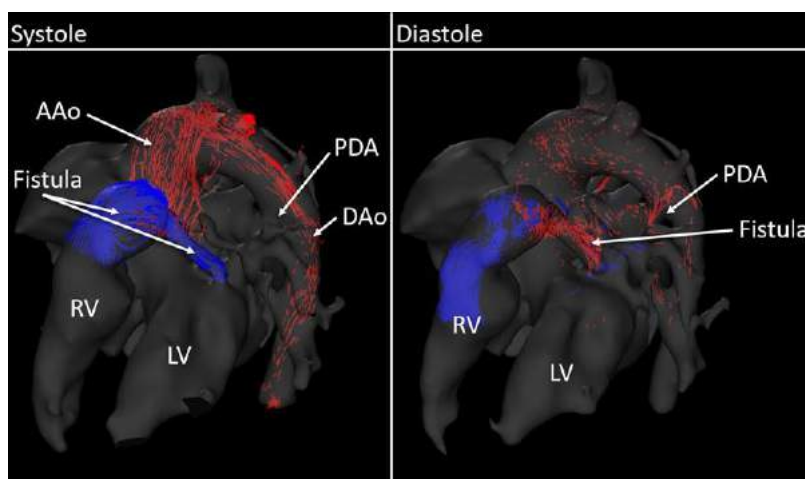




**Caption 2**

Figure 2: Schematic of anatomy with measured flows from 4D flow. All numbers are net flow (L/min) and arrows indicate direction of flow. Right and left ventricular cardiac output (RVCO, LVCO, respectively) are shown.

**Figure 3**



**Caption 3**

Figure 3: Pathline tracing (iTFlow); Particles seeded in right ventricle (RV)-fistula connection (blue) flow towards ascending aorta (AAo) in systole, then reverse into RV during diastole. AAo flow (red) fills the patent ductus arteriosus (PDA) and pulmonary arteries in diastole with a small amount entering the fistula, though not reaching the RV.

Speaker: J. Mandell

Category: 4D Flow, Ferumoxytol, Congenital Heart Disease

**Assessment of myocardium native T1 and perfusion using exercise CMR with a new MRI-compatible supine ergometer**

B. He \* (1); X. Zhou (2); F. Gao (1)

(1) Department of radiology, West China Hospital, Sichuan University, Chengdu, China;  
(2) Mr collaboration, Siemens Healthineers Ltd., Shanghai, China

**Abstract**

**Background:** Exercise imaging is known to have a higher sensitivity than pharmacological stressors to detect subclinical cardiac diseases (1, 2). This study aimed to show a new custom-made MRI-compatible ergometer and assess the reproducibility of measurements for myocardial native T1 and myocardial blood flow (MBF) at rest and exercise.

**Methods:** Ten healthy volunteers (5 females) underwent CMR scanning twice in a 3 T MR scanner (MAGNETOM Skyra, Siemens Healthcare, Erlangen, Germany). The whole imaging protocol is shown in Figure 1a. Native T1 maps at mid-ventricular short-axis locations were acquired by utilizing a modified Look-Locker inversion recovery (MOLLI) sequence with motion correction and a 5b(3b)3b scan scheme (3). Stress and rest perfusion images were acquired with a time interval of 15 min in between. The myocardial native T1 and MBF measurements were performed on the mid-ventricular short-axis slice positions. The native T1 maps were acquired at 1st and 3rd minute after the start of exercise; and MBF was acquired at 4th minute. The subjects alternately depressed pedals for 4 minutes at 60 Hz within the MR cavity. The MRI-compatible ergometer was set on the patient table as shown in Figure 1b. The reproducibility of the two tests was determined by the intra-group correlation coefficient (ICC) and coefficient of variation (CoV). The consistency of tests was analyzed by Bland-Altman method.

**Results:** The mean exercise intensity was 15.6 W, with an exercise duration of 5 minutes. Exercise induced a 27% increase in systolic blood pressure and an increase of 74% and 65% in heart rate at the 1st and 3rd minutes. The rate pressure product increased 121% and 108% at the 1st and 3rd minutes (all  $p < 0.001$ ). The exercise native T1 values at 1st and 3rd minutes were  $1302 \pm 64$  ms and  $1315 \pm 61$  ms, respectively, which were significantly larger than resting T1 ( $p < 0.05$ ). The effect of exercise stress from test and retest was shown in Figure 2. It was demonstrated that exercise T1 value at the 1st and 3rd minutes had strong reliability (ICC=0.75 and 0.89) and excellent reproducibility (CoV = 3.0% and 2.0%). Mean global rest MBF, exercise MBF and MPR were  $0.9 \pm 0.1$  ml/min/100g,  $1.6 \pm 0.3$  ml/min/100g, and  $1.8 \pm 0.2$ , respectively. Test-retest reliability of stress MBF was moderate [CoV 10.7%, ICC 0.84 (0.28;0.96)]. Test-retest reliability of MPR was good [ICC, 0.92 (0.68;0.98)]. The test–retest reproducibility is shown in Figure 3. Female subjects had higher positive changes in native T1 and MBF, compared to male.

**Conclusions:** Excellent reproducibility was shown in the assessment of native myocardial T1, MBF and MPR using our new custom-made MRI-compatible ergometer. The use of this device in an MR scanner may offer great potential in clinical practice to accurately and noninvasively assess cardiovascular function under stress.

Figure/Table 1

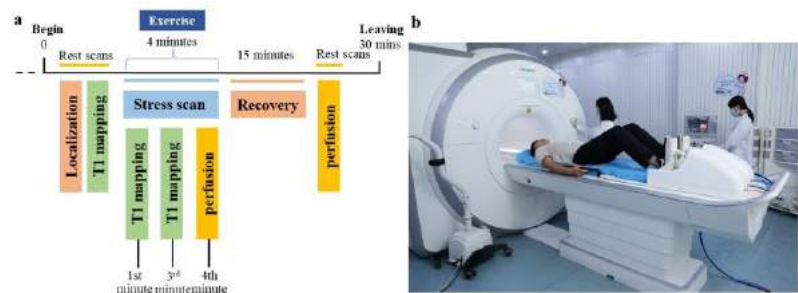


Figure 1. CMR imaging

protocol and healthy-subject protocol.

Caption 1

Supine pedal exercise was performed with a customer-made MRI-compatible ergometer on the MR table.

Figure/Table 2

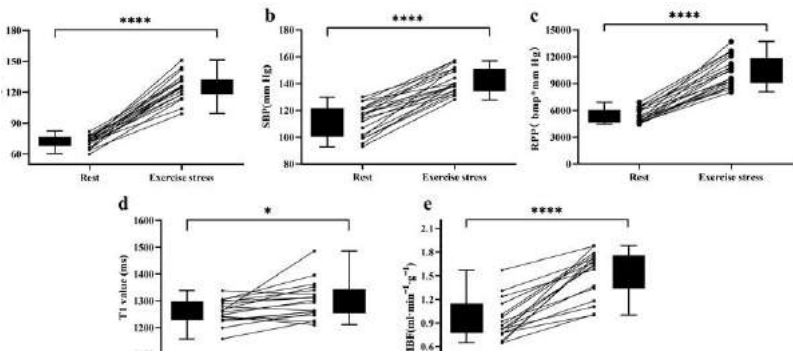


Figure 2. The effect of

exercise stress from test and retest.

Caption 2

The effect on heart rate (HR)(a), systolic blood pressure (SBP)(b), rate-pressure product (RPP)(c), native T1(d) and myocardial blood flow (MBF)(f) in all subjects. All mean values of the respective parameters increased significantly during the exercise stress, compared to counterparts at rest.

Figure 3

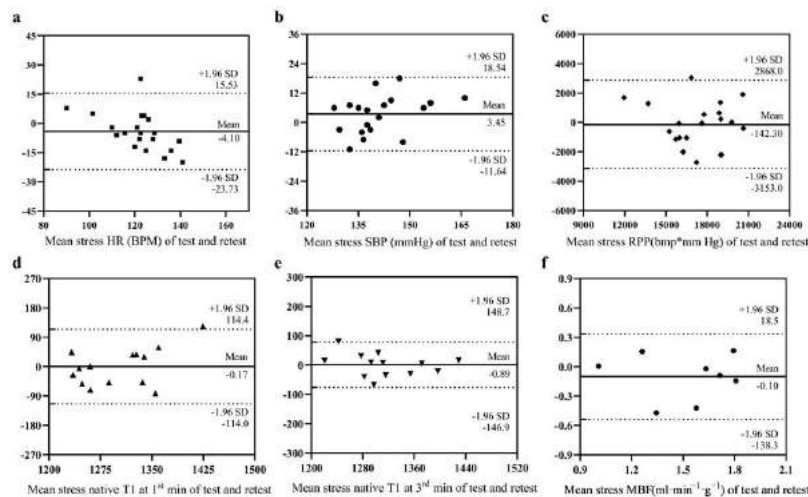


**Figure 3. Bland-Altman**

plots.

### Caption 3

Test–retest reproducibility of heart rate (HR)(a), systolic blood pressure (SBP) (b), rate-pressure product (RPP) (c), and native T1 using exercise stress with motion correction in all healthy young volunteers at 1st (d) and 3rd (e) mins. and stress MBF(f).

### Bibliographic References

3.Kellman P, Wilson JR, Xue H, Ugander M, Arai AE. Extracellular volume fraction mapping in the myocardium, part 1: evaluation of an automated method. *J Cardiovasc Magn Reson.* 2012;14(1):63. 2.Gibbons RJ, Balady GJ, Bricker JT, Chaitman BR, Fletcher GF, Froelicher VF, et al. ACC/AHA 2002 guideline update for exercise testing: summary article. A report of the American College of Cardiology/American Heart Association Task Force on Practice Guidelines (Committee to Update the 1997 Exercise Testing Guidelines). *J Am Coll Cardiol.* 2002;40(8):1531-40. 1.Heiberg J, Asschenfeldt B, Maagaard M, Ringgaard S. Dynamic bicycle exercise to assess cardiac output at multiple exercise levels during magnetic resonance imaging. *Clin Imaging.* 2017;46:102-7.

Speaker: B. He

Category: Exercise Stress, Native T1, First-Pass Perfusion

000247

## Uncertainty Assessment for Deep Learning-based Segmentation of Stress Perfusion CMR Using Patch-Level Training and Test-time Analysis

D. Yalcinkaya \* (1); K. Youssef (1); B. Heydari (2); L. Zamudio (1); R. Dharmakumar (1); B. Sharif (1)

(1) Krannert cardiovascular research center, Indiana University School of Medicine, Indianapolis; UCLA Dept. of Bioengineering, Los Angeles, United States of America; (2) Dept. of cardiac sciences, Stephenson Cardiac Imaging Centre, Calgary, Canada

### Abstract

#### Background

Deep neural networks (DNNs) may suffer from miscalibration where model confidence and accuracy deviate from each other [1]. As in other applications of deep learning (DL) in medical imaging, caution is warranted on the potential overconfidence that may be incorrectly implied in segmentations of CMR datasets generated by DNNs. An accompanying uncertainty assessment of the DL-based pipeline may therefore help add an interpretable measure of confidence which, in turn, may help prevent the end-user from interpreting the results without any nuance. Uncertainty assessment for DNNs has been studied in multiple modalities [2] including CMR [3]. We introduce a spatiotemporal (2D+time) patch-based DL method using a novel test-time sliding-patch analysis approach to concurrently segment stress perfusion CMR images and extract an “uncertainty map” in the process.

#### Methods

Stress/rest perfusion CMR data in 96 volunteer patients with suspected ischemia was obtained at 3T (vendor-provided SR-prepared FLASH) for training and validation. For testing, 40 stress CMR studies acquired on a different 3T scanner at an external site with a different pulse sequence (SR-prepared bSSFP) were used. Fig 1A describes the data processing pipeline for our proposed patch-level approach dubbed patch3-UNet: a DNN based on “vanilla” 3D UNet [4] jointly processes dynamic time frames for each spatiotemporal patch and detects the myocardial pixels within each 2D patch. As seen in Fig 1B, a pixel belongs to multiple patches and hence, at test time, is analyzed multiple times thanks to our sliding window approach. Subsequently, the collection of test-time solutions are merged together to obtain the uncertainty map (Fig 1B).

#### Results

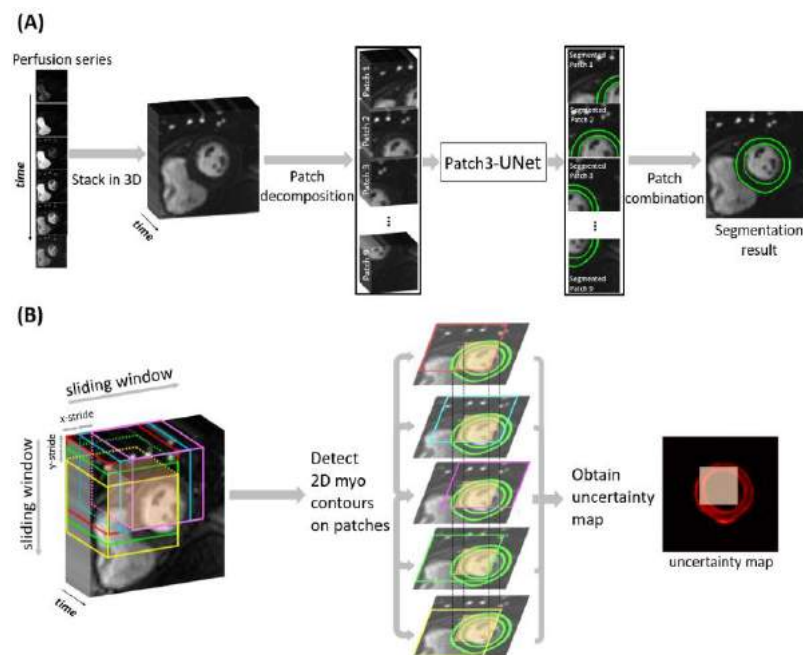
Fig 2A shows a challenging test case with a very small LV blood pool in a patient with hypertrophic cardiomyopathy. Although our network (patch3-UNet) successfully segments this slice, the accompanying uncertainty map demonstrates that the network struggles in the septal and inferior sectors. This is consistent with the fact that it is also difficult for an expert reader to determine the location of the endo/epi contours in these sectors due to the small LV/RV bloodpool. Fig 2B shows another challenging example with a thin layer of epicardial fat along the lateral wall (green arrows). The uncertainty map shows that patch3-UNet is highly uncertain in the inferolateral wall (resulting in non-contiguous segmentation) which

also corresponds to the most challenging sector to segment due to thin layer of epicardial fat. Here, the uncertainty map can be used to alert the end-user to correct this specific sector, or to exclude it. Fig 3A shows representative results for a patient with single-vessel CAD. Here we evaluated the effect of different data augmentation settings on the level of uncertainty. As can be seen, advanced augmentation [5] led to reduced uncertainty. Fig 3B summarizes the performance (n=40).

## Conclusion

Our proposed test-time sliding-patch analysis approach enables concurrent assessment of uncertainty for DL-derived segmentation maps. Further, our proof-of-concept results showed that the resulting uncertainty map has practical value in interpreting the results in challenging cases and advanced data augmentation reduces the overall uncertainty. Our results suggest that uncertainty assessment enables a more reliable integration of DL-based analysis of stress CMR into clinical practice.

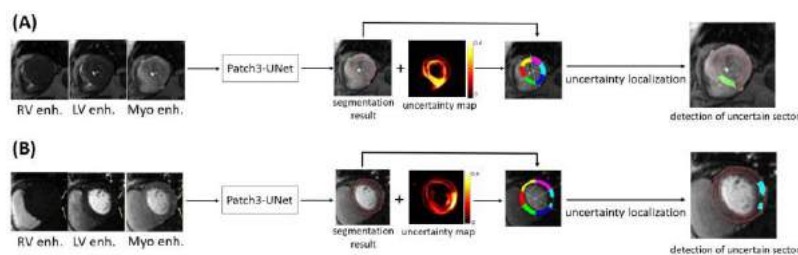
**Figure/Table 1**



**Caption 1**

(A) Perfusion images are decomposed into spatiotemporal patches by applying a spatial sliding window. A UNet detects the myocardial pixels on patches (patch3-UNet), and then patches are combined together. (B) For the same orange volume, multiple myocardium (myo) segmentation solutions are obtained with test-time sliding-patch analysis and incorporated to create the uncertainty map.

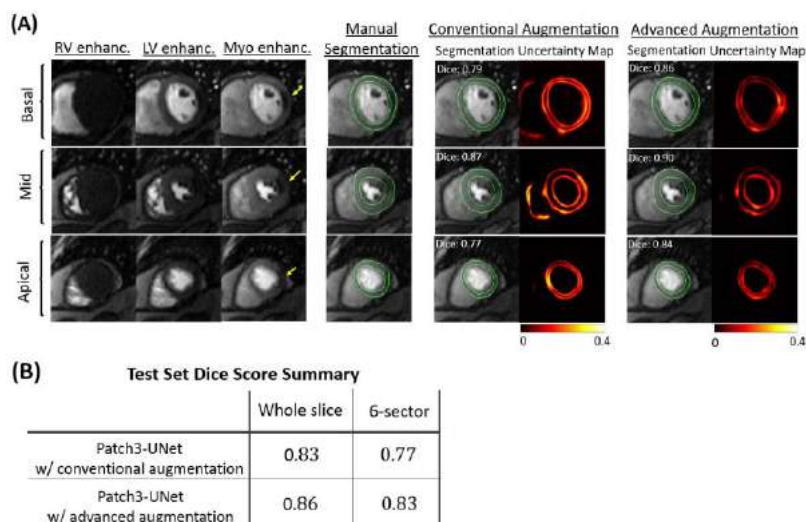
**Figure/Table 2**



**Caption 2**

Uncertainty assessment and localization on two challenging slices (see text for details). Patch3-UNet outputs the myocardial contours and uncertainty map. The network can also segment RV and subsequently RV insertion point is detected. So, the segmentation is split into 6 sectors. Uncertainty is localized as the sector that has the highest total variation in the uncertainty map.

**Figure 3**



**Caption 3**

(A) Stress perfusion time frames in a patient with stress-induced perfusion deficit (yellow arrows) are shown with the segmentation and uncertainty map results of two patch3-UNet with different augmentation settings. A higher value in the uncertainty maps implies high uncertainty. (B) Summary of the mean Dice scores across 40 stress perfusion CMR exams (120 myocardial slices). Patch3-UNet with advanced augmentation resulted in higher Dice.



## Bibliographic References

5. Yalcinkaya D, Youssef K, Beaulieu T, Unal HB, Dharmakumar R, Sharif B. Deep Learning-based Segmentation of Myocardial Perfusion CMR: The Role of Patch-based Training and Advanced Data Augmentation. SCMR 24th Scientific Sessions, Feb 2021, San Diego, CA. AbstractID#942182, 4. Ronneberger O, Fischer P, Brox T. U-Net: Convolutional Networks for Biomedical Image Segmentation. Proceedings of MICCAI. 2015;9351:234–241. doi:10.1007/978-3-319-24574-4\_28, 3. Do HP, Guo Y, Yoon AJ, Nayak KS. Accuracy, uncertainty, and adaptability of automatic myocardial ASL segmentation using deep CNN. Magn Reson Med. 2020 May;83(5):1863-74., 2. Roy AG, Conjeti S, Navab N, Wachinger C, Alzheimer's Disease Neuroimaging Initiative. Bayesian quicknat: model uncertainty in deep whole-brain segmentation for structure-wise quality control. NeuroImage. 2019 Jul 15;195:11-22., 1. Guo C, Pleiss G, Sun Y, Weinberger KQ. On Calibration of Modern Neural Networks. Proceedings of ICML 2017. arXiv:1706.04599

Speaker: D. Yalcinkaya

Category: First-Pass Perfusion, Automated Processing, Segmentation

000250

**Correlation between left ventricular fractal dimension and impaired strain assessed by cardiac MRI feature tracking in patients with left ventricular noncompaction and normal left ventricular ejection fraction**

S. Yu \* (1); X. Chen, (1); K. Yang, (1); J. Wang (1); K. Zhao, (2); W. Dong, (1); W. Yan, (1); S. Zhao, (1); G. Su, (3)

(1) MR center, Fuwai hospital, Beijing, China; (2) Paul c. lauterbur research center for biomedical imaging, Shenzhen Institutes of Advanced Technology, Chinese Academy of Sciences, SZ University Town, Beijing, China; (3) Department of cardiology, Jinan Central Hospital, Shandong First Medical University , Jinan, China

**Abstract**

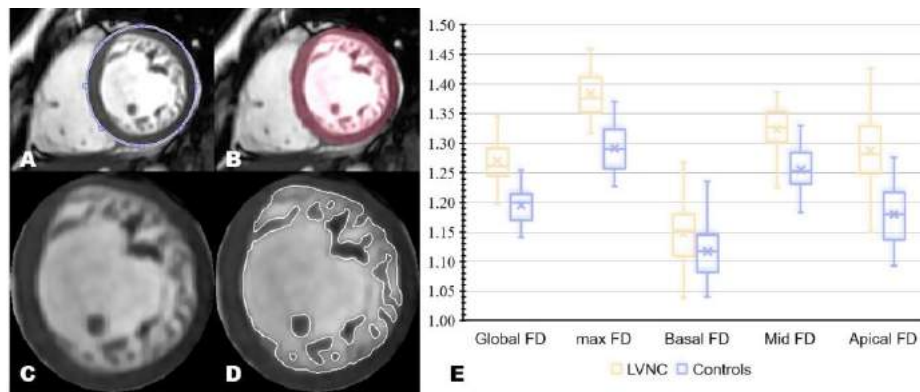
**Background:** Patients with extremely prominent excessive trabeculation but without reduced left ventricular ejection fraction (LVEF) are common in our clinical experience, and it is unclear whether they have a pathologic condition. Therefore, we aimed to investigate the correlation between the extent of excessive trabeculation assessed by fractal dimension (FD) and myocardial contractility assessed by cardiac MRI feature tracking in patients with left ventricular noncompaction (LVNC) and normal LVEF.

**Methods:** Forty-one LVNC patients with normal LVEF ( $\geq 50\%$ ) and 41 healthy controls were retrospectively included. All patients fulfilled three available diagnostic criteria on MRI: 1) the presence of noncompacted and compacted LV myocardium with a two-layered appearance, with at least involvement of the LV apex; 2) end-diastolic NC/C ratio  $>2.3$  on long-axis views and  $\geq 3$  on short-axis views; 3) noncompacted mass  $>20\%$  of the global LV mass. No pathologic (pressure/volume load, e.g., hypertension) or physiologic (e.g., pregnancy and vigorous physical activity) remodelling factors leading to excessive trabeculation existed. Cardiac MRI feature tracking was performed on cine images to determine left ventricular (LV) peak strains in three directions: global radial strain (GRS), global circumferential strain (GCS) and global longitudinal strain (GLS). The complexity of excessive trabeculation was quantified by fractal analysis on short-axis cine stacks.

**Results:** Compared with controls, patients with LVNC had impaired GRS, GCS and GLS (GRS,  $31.06\%$  [ $27.36\%$ ,  $33.84\%$ ] versus  $35.92\%$  [ $31.27\%$ ,  $41.21\%$ ]; GCS,  $-18.11 \pm 2.67\%$  versus  $-20.24 \pm 2.16\%$ ; GLS,  $-15.20 \pm 2.25\%$  versus  $-16.28 \pm 2.36\%$ ; all  $p < 0.05$ ). The global, maximal and regional FD values of the LVNC population were all significantly higher than those of the controls (Figure 1, all  $p < 0.05$ ). Global FD was positively correlated with the end-diastolic volume index, end-systolic volume index and stroke volume index ( $r = 0.483$ ,  $0.505$  and  $0.335$ , respectively, all  $p < 0.05$ ), but negatively correlated with GRS and GCS ( $r = -0.458$  and  $0.508$ , respectively, both  $p < 0.001$ ). Moreover, apical FD was also weakly associated with LVEF and GLS ( $r = -0.249$  and  $0.252$  respectively, both  $p < 0.05$ ).

**Conclusion:** In patients with LVNC, LV systolic dysfunction was detected early by cardiac MRI feature tracking despite the presence of normal LVEF and was associated with excessive trabecular complexity assessed by FD.

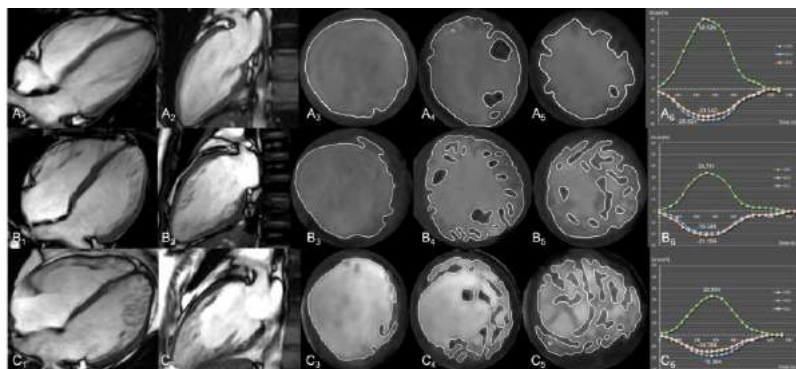
**Figure/Table 1**



**Caption 1**

Fractal analysis. (A) Region of interest (ROI) allocation; (B) ROI confirmation; (C) ROI segmentation; (D) Outline identification; (E) Global and regional fractal dimension (FD) values of patients with left ventricular noncompaction (LVNC) and healthy controls.

**Figure/Table 2**



**Caption 2**

Representative examples of healthy control (cluster A) and patients with different degrees of excessive trabeculation (cluster B-C): cine images at end diastole (A1-2, B1-2, C1-2); basal, medial, apical fractal dimension (A3-5, 1.054, 1.206, 1.156; B3-5, 1.094, 1.407, 1.448; C3-5, 1.116, 1.403, 1.511); GRS, GCS and GLS (A6, B6, C6)

Speaker: S. Yu

Category: Fractal Dimension, Cardiac Strain, Non-Compaction

000251

## A medical device-grade T2 phantom for quality assurance of inflammation imaging by CMR

M. Fornasiero \* (1); I. Pierce (2); M. Webber (3); H. Seo (4); K. E. Keenan (5); K. Stupic (5); R. Brühl (6); B. Ittermann (7); W. Pang (8); A. Hughes (3); R. Nezafat (9); P. Kellman (10); J. Moon (11); G. Captur (3)

(1) , University College London, Gower Street, London, UK, London, UK, United Kingdom; (2) Barts heart centre, Barts Health NHS Trust, London, United Kingdom; (3) Institute of cardiovascular science, University College London, London, United Kingdom; (4) Centre for inherited heart muscle conditions, Royal Free Hospital, London, United Kingdom; (5) Physical measurement laboratory, NIST, Boulder, United States of America; (6) In vivo mri, PTB Physikalisch-Technische Bundesanstalt Braunschweig und Berlin, Berlin, Germany; (7) Biomedical magnetic resonance, PTB Physikalisch-Technische Bundesanstalt Braunschweig und Berlin, Berlin, Germany; (8) Board and management team, Resonance Health, Burswood, Australia; (9) Cardiology, Beth Israel Deaconess Medical Center (BIDMC), Boston, United States of America; (10) National institutes for health, NHLBI, Bethesda, United States of America; (11) Cardiac mri, Barts Heart Center, London, United Kingdom

### Abstract

#### Introduction

T2 mapping quantifies myocardial oedema, typically reflecting inflammation. Use is growing, but there are no quality control systems so single-center T2 mapping times are not generalizable and longitudinal studies cannot reliably track interval change.

#### Aim

Expertise from the T1 Mapping and Extracellular Volume phantom (T1MES) program was utilized to fabricate a dedicated T2 mapping phantom to medical device standards.

#### Method

A collaboration including a specialist MRI small-medium enterprise, clinicians, physicists, and national metrology institutes was formed. A T2 mapping phantom (**Fig 1i**) was designed to cover clinically relevant T1 and T2 times for healthy and inflamed native and post-contrast myocardium across field-strengths (**Fig 1iii,v**). Refinement required three iterations (two initial prototypes).

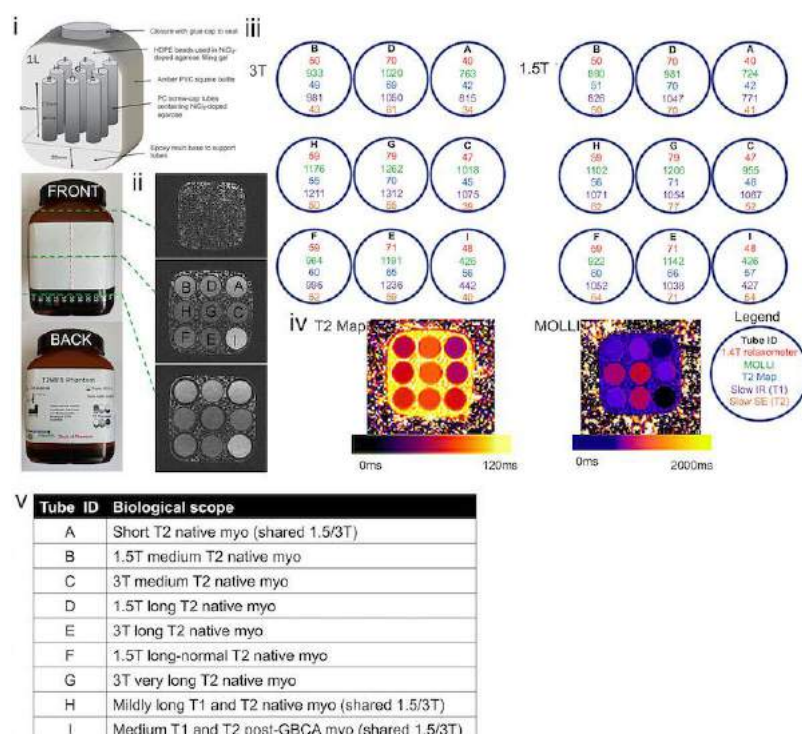
## Results

The phantom is agarose gel-based with nickel chloride useable at both 1.5 and 3 Tesla. Its nine differently-doped tubes are embedded in a gel/beads matrix, covering the clinically meaningful myocardial T2 range (42 to 71ms). The phantom was free of air bubbles and susceptibility artifacts (**Fig 1ii**) and maps were free from off-resonance artifacts (**Fig 1iv**). The main gel high-density polyethylene beads were effective at flattening the  $B_0$  and  $B_1$  fields (**Fig 2i,ii**). Measured T1 and T2 times showed coefficients of variation of  $\leq 1\%$  between repeat scans indicating good short-term reproducibility. Temperature dependency experiments at the metrology institutes (**Fig 2iii**) confirmed that between 13–40°C, short-T1/2 tubes were more stable with temperature than long-T1/2 tubes.

## Conclusion

The T2 mapping phantom is the first to replicate clinically relevant T1/T2 times across myocardial health and disease. Regulatory approval is pending via the Food and Drug Administration (FDA) database and Conformité Européene (CE) marking with pending reproducible mass manufacture for longitudinal cohort studies and inflammation imaging.

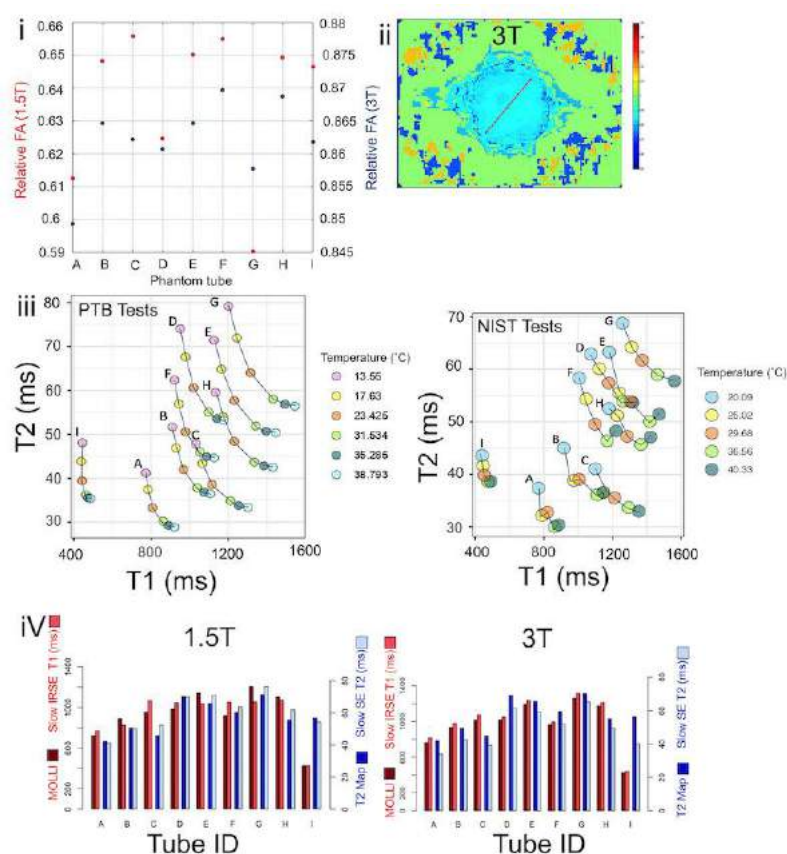
**Figure/Table 1**



**Caption 1**

**i)** Phantom structure. **ii)** Phantom views including isocentre line and liquid crystal display thermometer. **iii)** Tube T1/T2 times at 3T and 1.5T with: slow reference times T1/T2 (purple|orange) and clinical times (green|blue). T2 measured using a 1.4T relaxometer (red). **iv)** Exemplar T2 and T1 maps (Siemens 3T Prisma). **v)** Relaxometry scopes explained.

**Figure/Table 2**



**Caption 2**

**i)**  $B_0$  field homogeneity at 1.5T (red), 3T (blue): small frequency shifts. **ii)** Diagonal profile across the T2 phantom  $B_1$  field map, showing excellent  $B_1$  homogeneity. **iii)** Temperature tests carried out at German Physikalisch-Technische Bundesanstalt and National Institute of Standards and Technology. **iv)** Reference T1/T2 times compared to clinical sequences

Speaker: M. Fornasiero

Category: Accuracy and Effectiveness, Parametric Mapping, Inflammation

000253

**Flow patterns and regional stiffness in the false lumen of patients with chronic type B aortic dissection and their relationship with aortic growth rate. A 4D flow CMR study**

A. Ruiz-Muñoz (1); A. Guala \* (1); L. Dux-Santoy (2); G. Teixidó-Turà (1); S. Maria Luz (1); J. Garrido-Oliver (1); F. Valente (1); G. Casas (1); R. Fernandez-Galera (1); L. Galian-Gay (1); L. Gutierrez (1); T. González-Alujas (1); I. Ferreira-González (3); A. Evangelista-Masip (1); J. F. Rodriguez Palomares (1)

(1) Department of cardiology, Hospital Vall d'Hebron, VHIR. Universitat Autònoma de Barcelona. CIBER-CV, Barcelona, Spain; (2) Department of cardiology, Hospital Vall d'Hebron, Vall d'Hebron Research Institute, Universitat Autònoma de Barcelona, Barcelona, Spain; (3) Department of cardiology, Hospital Vall d'Hebron, VHIR. Universitat Autònoma de Barcelona. CIBERESP, Barcelona, Spain

**Abstract**

**BACKGROUND**

Patency of the false lumen in chronic aortic dissection (AD) is associated with aortic dilation and long-term aortic events. However, predictors of adverse outcomes in this population are still limited. The aim of this study was to evaluate the relationship between aortic growth rate and anatomical variables, flow patterns and regional aortic stiffness in patients with chronic type B aortic dissection.

**METHODS**

Forty-one patients with a chronic, patent false lumen in the descending aorta after an AD, no genetic connective tissue disorders and with an imaging follow-up including two computed tomography angiograms (CTA) acquired at least 3 years apart underwent a contrast-enhanced 4D flow CMR and an MR angiography (MRA). The 4D flow CMR study was used to analyse flow patterns and aortic stiffness in the false lumen of these patients. Retrograde flow in systole and diastole, wall shear stress (WSS) and in-plane rotational flow (IRF) were calculated at 8 equidistant planes in the distal descending aorta (DAo), from the pulmonary bifurcation to the diaphragmatic level, and averaged values were used (1–3). Aortic stiffness in the FL was assessed in terms of pulse wave velocity (PWV), which was calculated from the third supraortic trunk to the diaphragmatic level (4). The percentage of thrombus in the FL was calculated as the ratio of thrombus volume and FL volume on MRA. Dominant entry tear area was quantified on the baseline CTA (Figure 1). Aortic growth rate (GR) was defined as the difference between final and baseline aortic diameters as measured on CTA divided by follow-up duration.

**RESULTS**

Anatomical features, flow dynamics and regional stiffness in the false lumen are shown in Table 1. Twenty-five patients have repaired type A AD with residual entry tear and 16 have type B AD. Mean follow-up duration was of  $59 \pm 32$  months. In bivariate analysis, WSS, IRF and PWV were positively related to aortic growth rate, while dominant entry tear area and

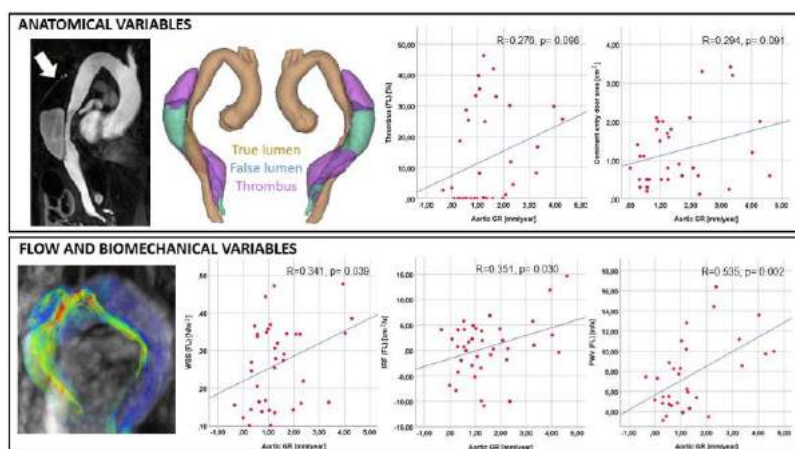


percentage of thrombus in the FL showed a positive tendency with growth rate (Table) (Figure). In multivariate analysis IRF, PWV, dominant entry tear area and thrombus in the FL were positively and independently associated with FL growth rate (Table). Retrograde systolic and diastolic flow were not related to aortic growth rate while WSS showed a nearly-significant positive association (Table).

## CONCLUSIONS

Rotational flow, regional aortic stiffness and percentage of thrombus in the false lumen are positively and independently related to aortic growth rate in chronic type B aortic dissection. The assessment of these parameters may help to identify patients at higher risk of adverse clinical events.

**Figure/Table 1**



**Caption 1**

Figure 1. Anatomical features, flow dynamics and biomechanics in the false lumen. MR angiography and segmentations of regions of interest (top-left), and velocity map on 4D flow CMR (bottom-left). Scatter plots showing correlations between aortic growth rate and anatomical (top), flow and biomechanical variables (bottom).

**Figure/Table 2**

**Table. Anatomical, haemodynamic and biomechanical parameters. Bivariate analysis and multivariate model.**

	Overall (n=41)	Bivariate analysis	Multivariate analysis
<b>Anatomical variables</b>			
Dominant entry tear area [cm <sup>2</sup> ]	1.2 ± 0.9	0.091	<b>0.014</b>
Thrombus in FL [%]	13 ± 15	0.098	<b>0.028</b>
<b>Haemodynamics in the FL</b>			
Retrograde flow in systole [mL]	1.5 ± 1.1	0.252	-
Retrograde flow in diastole [mL]	9.0 ± 5.1	0.850	-
Wall shear stress (magnitude) [N/m <sup>2</sup> ]	0.26 ± 0.11	<b>0.039</b>	0.056
In-plane rotational flow [cm <sup>2</sup> /s]	0.62 ± 5.49	<b>0.030</b>	<b>0.014</b>
<b>Biomechanics in the FL</b>			
Pulse wave velocity [m/s]	7.6 ± 3.5	<b>0.002</b>	<b>0.001</b>

## Bibliographic References

1. Ruiz-Muñoz A, Guala A, Rodriguez-Palomares J, Dux-Santoy L, Servato L, Lopez-Sainz A, et al. Aortic flow dynamics and stiffness in Loeys–Dietz syndrome patients: a comparison with healthy volunteers and Marfan syndrome patients. *Eur Hear J - Cardiovasc Imaging*. 2021;34:1–9. , 2. Dux-Santoy L, Guala A, Sotelo J, Uribe S, Teixidó-Turà G, Ruiz-Muñoz A, et al. Low and Oscillatory Wall Shear Stress Is Not Related to Aortic Dilation in Patients With Bicuspid Aortic Valve: A Time-Resolved 3-Dimensional Phase-Contrast Magnetic Resonance Imaging Study. *Arterioscler Thromb Vasc Biol*. 2020;40(1):e10–20. , 3. Guala A, Rodriguez-Palomares J, Galian-Gay L, Teixido-Tura G, Johnson KM, Wieben O, et al. Partial Aortic Valve Leaflet Fusion Is Related to Deleterious Alteration of Proximal Aorta Hemodynamics: A 4-Dimensional Flow Magnetic Resonance Imaging Study. *Circulation*. 2019;139(23):2707–9. , 4. Guala A, Rodriguez-Palomares J, Dux-Santoy L, Teixidó-Turà G, Maldonado G, Galian L, et al. Influence of Aortic Dilation on the Regional Aortic Stiffness of Bicuspid Aortic Valve Assessed by 4-Dimensional Flow Cardiac Magnetic Resonance: Comparison With Marfan Syndrome and Degenerative Aortic Aneurysm. *JACC Cardiovasc Imaging*. 2019;12(6):1020–9.

Speaker: A. Guala

Category: 4D Flow, Aorta, Imaging Biomarkers

000254

## The diagnostic value of corrected pulmonary transit time in left heart disease according to hemodynamic phenotype

C. Gong \* (1); X. Guo (1); W. Ke (2); Y. Chen (1)

(1) Department of cardiology, West China Hospital, Chengdu, China; (2) Department of geriatrics, West China Hospital, Chengdu, China

### Abstract

**Background:** The concurrent pulmonary hypertension (PH) was remarkably associated with the deterioration of the left heart disease (LHD) patient's symptoms, the reduction of exercise capacity, and poor prognosis. Moreover, LHD-PH patients could be divided into 2 subgroups of LHD-Combined post- and pre-capillary (Cpc) PH patients and LHD-Isolated post-capillary (Ipc) PH patients, and the identification of a pre-capillary component in the LHD-PH patients was of great influence on the therapy and outcome. However, the current diagnosis of PH and classification of LHD-PH subgroups relied on purely invasive hemodynamic definitions. Cardiovascular magnetic resonance (CMR)-based corrected pulmonary transit time (PTTc) exhibited good correlation with hemodynamics in different cardiovascular diseases. This study aimed to investigate the non-invasive diagnostic value of PTTc in LHD and LHD-PH patients according to hemodynamic phenotype.

**Methods:** We prospectively recruited fifty-four LHD patients who underwent both clinically indicated right heart catheterization (RHC) and a 3.0T CMR examination. The diagnosis of PH was on the base of mean pulmonary artery pressure (mPAP) > 20 mmHg. Furtherly, LHD-PH individuals were separated according to the newest criteria of 6th World Symposium on Pulmonary Hypertension: LHD-IpcPH: pulmonary arterial wedge pressure, PAWP > 15 mmHg and pulmonary vascular resistance, PVR < 3 WU, and LHD-CpcPH: PAWP > 15 mmHg and PVR ≥ 3 WU. CMR first-pass perfusion images of the 4-chamber long-axis plane were analyzed to determine the PTT, which calculated as the time interval between the peak of two signal intensity/time curves in right ventricular (RV) and left ventricular (LV) cavity and corrected for the heart rate (PTTc). Statistics analysis mainly included student t test, Pearson's correlation analysis, logistic regression analysis, and Receiver operating characteristic (ROC) curve analysis.

**Results:** PTTc was significantly prolonged in LHD-PH patients than LHD-no PH ( $16.50 \pm 8.06$  vs.  $8.46 \pm 2.33$  s,  $P < 0.001$ ), and in LHD-Cpc PH patients than LHD-Ipc PH patients ( $18.64 \pm 7.81$  vs.  $10.84 \pm 5.82$  s,  $P = 0.005$ ). The prolonged PTTc correlated well with increased PVR ( $R = 0.489$ ,  $P < 0.001$ ), mPAP ( $R = 0.548$ ,  $P < 0.001$ ), PAWP ( $R = 0.595$ ,  $P < 0.001$ ), ventricular dilation (LV end-diastolic volume index (EDVi),  $R = 0.534$ ,  $P < 0.001$ ; RV EDVi,  $R = 0.689$ ,  $P < 0.001$ ), and cardiac dysfunction (LV ejection fraction (EF),  $R = -0.783$ ,  $P < 0.001$ ; RV EF,  $R = -0.814$ ,  $P < 0.001$ ). PAWP, RV EDVi, and RV EF independently predict the PTTc ( $P < 0.01$ ). Furthermore, ROC exhibited PTTc with a cut-off of 10.62s allowed LHD-PH patients to be distinguished from LHD-no PH patients (area under curve 0.836, sensitivity 72.50%, specificity 85.71%,  $P < 0.001$ ), and a cut-off of 10.71s was able to differentiate LHD-Cpc PH patients from LHD-Ipc PH patients (area under curve 0.815, sensitivity 86.21%, specificity 72.73%,  $P < 0.001$ ).

**Conclusion:** PTTc could serve as a helpful non-invasive marker in the diagnosis of PH in LHD patients and the identification of a precapillary component in LHD-PH patients. This finding might facilitate improved the selection for invasive RHC evaluation, assessment of prognosis, and the management for therapy of LHD patients.

**Figure/Table 1**

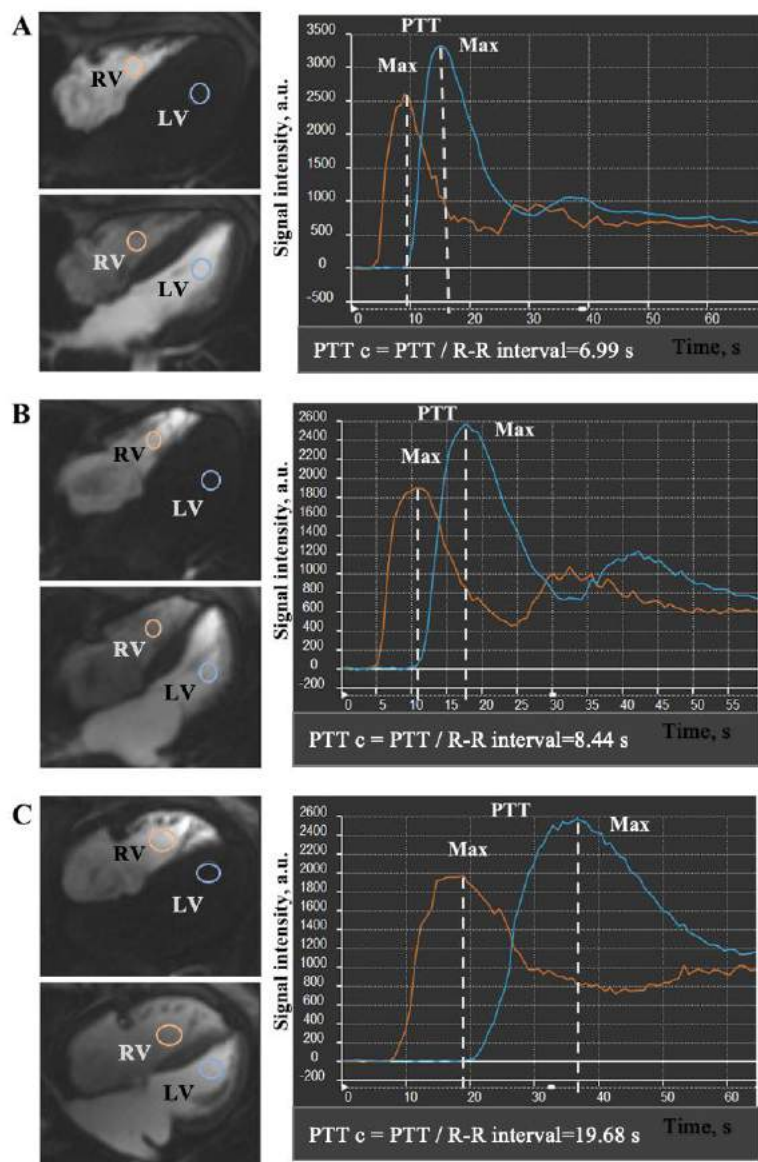
	<b>LHD-no PH (N=14)</b>	<b>LHD-PH (N=40)</b>	<b>P value</b>	<b>LHD-Ipc PH(N=11)</b>	<b>LHD-Cpc PH(N=29)</b>	<b>P value</b>
<b>Demographics</b>						
Age, years	50.79 ± 14.83	47.73 ± 12.93	0.467	48.27 ± 16.13	47.5 ± 11.83	0.872
Female, n (%)	8 (57.14)	13 (32.50)	0.123	4 (36.36)	9 (31.04)	1.000
BSA, m <sup>2</sup>	1.63 ± 0.18	1.62 ± 0.18	0.880	1.59 ± 0.22	1.63 ± 0.17	0.515
BMI, kg/m <sup>2</sup>	23.81 ± 3.14	22.18 ± 3.21	0.106	21.14 ± 3.72	22.58 ± 2.97	0.212
SBP, mmHg	114.69 ± 13.46	108.10 ± 19.96	0.273	110.09 ± 20.40	107.35 ± 20.10	0.703
DBP, mmHg	75.15 ± 16.14	70.80 ± 13.71	0.346	69.73 ± 12.03	71.21 ± 14.48	0.765
HR, bpm	73.92 ± 17.27	79.18 ± 19.68	0.410	79.64 ± 13.47	79.00 ± 21.86	0.929
WHO class, n	1/5/8/0	4/15/18/3	0.690	2/4/5/0	2/11/13/3	0.540
<b>Laboratory</b>						
Hct, %	0.40 ± 0.07	0.41 ± 0.07	0.550	0.40 ± 0.07	0.42 ± 0.08	0.549
Cr, µmol/l	83.75 ± 26.12	85.90 ± 20.98	0.770	80.55 ± 24.57	87.93 ± 19.54	0.326
eGFR, ml/min/m <sup>2</sup>	80.87 ± 27.80	87.71 ± 21.32	0.345	94.62 ± 23.18	85.08 ± 20.38	0.210
Log Tnt, pg/mL	1.67 ± 0.37	1.75 ± 0.46	0.557	1.64 ± 0.32	1.80 ± 0.50	0.350
Log NT-pro BNP, pg/mL	3.31 ± 0.47	3.59 ± 0.33	<b>0.019</b>	3.55 ± 0.25	3.61 ± 0.36	0.670
<b>Invasive hemodynamics</b>						
mRAP, mmHg	2.00 ± 1.47	11.39 ± 6.59	<b>&lt;0.001</b>	10.36 ± 7.24	11.79 ± 6.41	0.551
sPAP, mmHg	23.00 ± 6.90	55.70 ± 17.52	<b>&lt;0.001</b>	42.09 ± 8.93	60.86 ± 17.28	<b>0.002</b>
mPAP, mmHg	13.79 ± 4.74	35.60 ± 10.29	<b>&lt;0.001</b>	26.46 ± 4.30	39.07 ± 9.77	<b>&lt;0.001</b>
dPAP, mmHg	8.57 ± 4.60	25.33 ± 8.91	<b>&lt;0.001</b>	19.00 ± 4.31	27.72 ± 9.08	<b>0.004</b>
PAWP, mmHg	7.57 ± 3.76	23.93 ± 7.42	<b>&lt;0.001</b>	19.82 ± 2.40	25.48 ± 8.09	<b>0.029</b>
TPG, mmHg	5.31 ± 2.81	11.68 ± 5.52	<b>&lt;0.001</b>	6.64 ± 3.39	13.59 ± 4.95	<b>&lt;0.001</b>

DPG, mmHg	3.33 ± 3.14	3.75 ± 3.84	0.733	-0.82 ± 2.93	2.24 ± 5.66	0.098
PVR, Wood units	1.79 ± 1.09	4.88 ± 2.48	<b>&lt;0.001</b>	2.05 ± 0.81	5.99 ± 1.97	<b>&lt;0.001</b>
PVRi, Wood units/m2	3.33 ± 2.04	8.50 ± 4.53	<b>&lt;0.001</b>	3.30 ± 1.17	10.48 ± 3.66	<b>&lt;0.001</b>
SVR, Wood units	25.85 ± 9.18	27.15 ± 9.96	0.682	25.56 ± 8.35	27.80 ± 10.63	0.538
SVRi, Wood units/m2	42.53 ± 13.82	46.46 ± 17.28	0.462	41.10 ± 12.73	48.56 ± 18.54	0.229
PVRi/SVRi	0.08 ± 0.04	0.19 ± 0.14	<b>0.012</b>	0.09 ± 0.05	0.23 ± 0.15	<b>0.006</b>
CI, L /min/ m2	2.10 ± 0.62	1.61 ± 0.55	<b>0.013</b>	1.90 ± 0.61	1.50 ± 0.50	<b>0.038</b>
SvO2, %	68.17 ± 6.37	57.26 ± 10.63	<b>0.002</b>	61.27 ± 12.61	55.68 ± 9.53	0.141
<b>LV volume and function</b>						
LV EDVi, mL/m2	87.94 ± 48.68	118.08 ± 50.25	<b>0.019</b>	90.17 ± 26.03	130.21 ± 53.74	<b>0.007</b>
LV ESVi, mL/m2	43.66 ± 42.01	82.54 ± 45.31	<b>0.001</b>	54.24 ± 25.47	95.40 ± 46.89	<b>0.003</b>
LV SVi, mL/m2	40.98 ± 10.96	32.13 ± 10.77	<b>0.012</b>	35.93 ± 8.96	30.61 ± 11.22	0.191
LV EF, %	54.19 ± 14.54	29.35 ± 14.37	<b>&lt;0.001</b>	42.05 ± 12.10	24.47 ± 12.13	<b>&lt;0.001</b>
LV massi, g/m2	106.96 ± 34.70	98.08 ± 35.22	0.467	95.10 ± 32.05	99.23 ± 36.90	0.758
<b>RV volume and function</b>						
RV EDVi, mL/m2	67.76 ± 22.17	90.81 ± 35.62	<b>0.042</b>	67.79 ± 38.99	100.03 ± 30.30	<b>0.013</b>
RV ESVi, mL/m2	30.77 ± 12.36	63.11 ± 31.74	<b>&lt;0.001</b>	39.21 ± 32.21	72.66 ± 26.56	<b>0.003</b>
RV SVi, mL/m2	36.99 ± 13.90	27.91 ± 10.92	<b>0.024</b>	28.57 ± 8.01	27.66 ± 11.99	0.826
RV EF, %	54.27 ± 10.25	33.11 ± 13.48	<b>&lt;0.001</b>	46.52 ± 11.78	27.95 ± 10.24	<b>&lt;0.001</b>
<b>Perfusion</b>						
PTTc, s	8.46 ± 2.33	16.50 ± 8.06	<b>&lt;0.001</b>	10.84 ± 5.82	18.64 ± 7.81	<b>0.005</b>

### Caption 1

**Table 1.** Clinical and CMR characteristics in different LHD subgroup patients according to hemodynamics profiles.

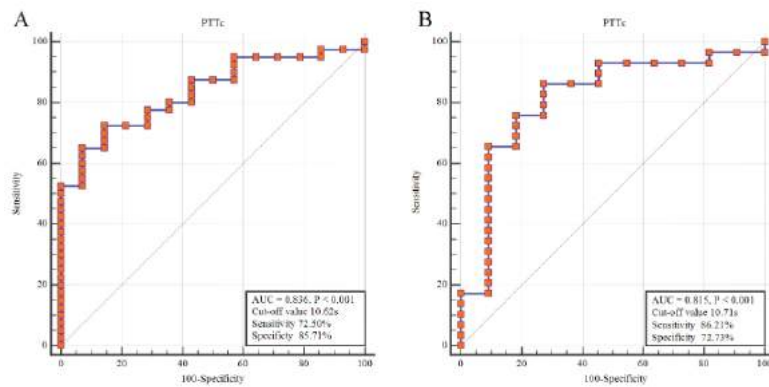
Figure/Table 2



Caption 2

**Figure 1.** Illustrative examples of the calculation of PTTc in the first-pass perfusion signal intensity/time curves in a LHD without PH patient (A), LHD-Ipc PH patient (B), and LHD-Cpc PH patient (C), respectively. LV left ventricle; RV Right ventricle.

Figure 3



### Caption 3

**Figure 2.** Receiver operating characteristic (ROC) curves of PTTc for discriminating LHD-PH patients from LHD-no PH patients (A), and LHD-Cpc PH patients from LHD-Ipc PH patients (B).

### Bibliographic References

- Vachieri JL, Tedford RJ, Rosenkranz S, Palazzini M, Lang I, Guazzi M, et al. Pulmonary hypertension due to left heart disease. *Eur Respir J.* 2019 Jan;53(1).
- Bursi F, McNallan SM, Redfield MM, Nkomo VT, Lam CS, Weston SA, et al. Pulmonary pressures and death in heart failure: a community study. *J Am Coll Cardiol.* 2012 Jan 17;59(3):222-31.
- Johns CS, Wild JM, Rajaram S, Tubman E, Capener D, Elliot C, et al. Identifying At-Risk Patients with Combined Pre- and Postcapillary Pulmonary Hypertension Using Interventricular Septal Angle at Cardiac MRI. *Radiology.* 2018 Oct;289(1):61-8.
- Colin GC, Pouleur AC, Gerber BL, Poncelet PA, de Meester C, D'Hondt AM, et al. Pulmonary hypertension detection by computed tomography pulmonary transit time in heart failure with reduced ejection fraction. *Eur Heart J Cardiovasc Imaging.* 2020 Oct 20;21(11):1291-8.
- Cao JJ, Li L, McLaughlin J, Passick M. Prolonged central circulation transit time in patients with HFpEF and HFrEF by magnetic resonance imaging. *Eur Heart J Cardiovasc Imaging.* 2018 Mar 1;19(3):339-46

Speaker: C. Gong

Category: Pulmonary Hypertension, First-Pass Perfusion, pulmonary Vascular Resistance (PVR)

000255

**Additional value of CMR feature tracking parameters of the left ventricle for the evaluation of the risk of complex ventricular arrhythmias and sudden cardiac death in patients with Mitral Valve Prolapse and Mitral Annular Disjunction**

M. Guglielmo \* (1); D. Arangalage (2); M. Bonanni (3); G. Angelini (4); L. V. Paiocchi (5); L. A. Leo (5); M. Valgimigli (5); G. Pontone (6); F. Faletra (5); G. Pedrazzini (5); P. Monnay (7); A. G. Pavon (8)

(1) Cardiovascular Imaging, UMC, Heidelberglaan, Utrecht, Netherlands; (2) Département de cardiologie, hôpital bichat, Bichat, Paris; (3) Department of experimental medicine, university of rome "tor vergata", University of Rome "Tor Vergata", Rome, Italy; (4) Division of university cardiology, cardiothoracic department, policlinico university hospital, University of Bari Aldo Moro, Bari, Italy; (5) Division of cardiology, Istituto Cardiocentro Ticino, Lugano, Switzerland; (6) Cardiovascular imaging, Monzino Cardiology Center, Milano, Italy; (7) Center for cardiac magnetic resonance, Lausanne University Hospital, Lausanne, Switzerland; (8) Service of cardiology, Istituto Cardiocentro Ticino, Via Tesserete, Lugano, Switzerland

**Abstract**

**Background:**

Mitral valve prolapse (MVP) with mitro-annular disjunction (MAD) has been associated with complex ventricular arrhythmias (c-VA) and sudden cardiac death (SCD) but risk stratification in this subset of patients remains insufficiently characterized. The aim of this study was to investigate the association between deformation parameters assessed by feature tracking (FT) cardiac magnetic resonance (CMR) in patients with MVP and MAD (MVP-MAD) and c-VA and/or SCD.

**Methods:**

We included 23 patients ( $47 \pm 13$  years; 43 % males) with MVP-MAD, of whom 17 (74 %) presented with c-VA and 6 (26%) with SCD, as well as 20 age- and sex-matched controls ( $50 \pm 18$  years; 57% males). All patients underwent CMR with assessment of MAD length, late gadolinium enhancement (LGE), extracellular volume (ECV), global and regional longitudinal (LS), and circumferential strain (CS). RATIO-CS was defined as the ratio between regional CS in the basal inferolateral and mid-inferolateral walls (fig.1).

**Results**

In MVP-MAD patients, non-ischemic LGE of the LV inferior and inferolateral wall was observed in 21 patients (50%). As compared to controls, MVP-MAD patients showed lower global LS ( $-18.7 \pm 4.1$  vs  $-24.7 \pm 5.7$   $p < 0.001$ ), higher native T1 relaxation time and ECV of the left ventricle (LV) inferolateral wall ( $1104 \pm 63$ ms vs  $1083 \pm 66$ ms  $p < 0.029$  and  $0.31 \pm 0.03$  vs  $0.27 \pm 0.04$   $p < 0.003$ ), lower CS and LS of the LV mid and inferolateral segments ( $p < 0.005$ ).

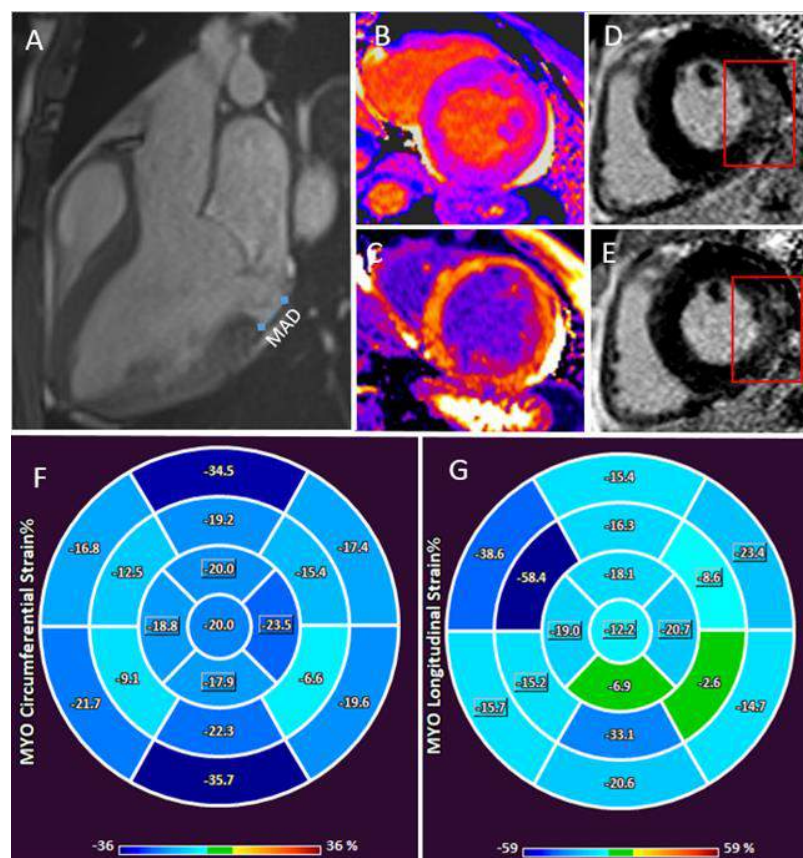


Logistic univariate regression analysis showed an increased risk of c-VA in case of LGE presence (OR: 9.52 [2.28-39.7]  $p=0.002$ ), a high number of LV segments with LGE (OR: 1.78 [1.21-2.63]  $p=0.004$ ), GLS (OR: 1.58 [1.21-2.07]  $p<0.001$ ), decreased inferolateral mid ventricular wall CS (OR: 1.41 [1.16-1.72]  $p<0.001$ ), decreased basal and mid-ventricular inferolateral wall LS (OR: 1.11 [1.00-1.23]  $p=0.047$  and OR: 1.62 [1.22-2.13]  $p<0.001$  respectively), increased native T1 times (OR: 1.01 [1.00-1.02]  $p=0.039$ ), increased ECV of the basal infero-lateral wall (OR: 4.93e+07 [1.22-1.98e+15]  $p=0.047$ ) and decreased RATIO-CS (OR: 7.48 [1.87-30.00]  $p=0.005$ ) (table 1). In multivariate analysis the presence of a lower LS in the basal inferolateral wall remained an independent predictor of c-VA (OR: 1.62 [1.22-2.13.00]  $p=0.0007$ ) and RATIO-CS remained an independent predictor of SCD (OR: 7.73 [1.78-33.60]  $p=0.006$ ).

## Conclusion:

Lower inferolateral LS and RATIO CS are respectively associated with c-VA and SCD in MVP-MAD patients. FT may provide additional value for risk stratification on top of standard CMR parameters in this subset of patients.

**Figure/Table 1**



**Caption 1**

FIG.1: CMR of a patient with aborted SCD. Panel A) 3-chamber view showing MAD, pre contrast T1 mapping (Panel B) and post contrast T1 mapping (Panel C) with higher relaxation times and ECV, Panel D and E

**Figure/Table 2**

	<b>OR</b>	<b>95% CI</b>	<b>P</b>
<b>Mitral Regurgitant Fraction</b>	89.400	0.6650-12000.00	0.0723
<b>LGE</b>	<b>9.520</b>	<b>2.280-39.700</b>	<b>0.00197</b>
<b>Number of segments</b>	<b>1.780</b>	<b>1.210-2.63</b>	<b>0.0035</b>
<b>MAD</b>	1.180	0.9750-1.44	0.0876
<b>Pre contrast mean T1</b>	1.010	9.97e-01-1.03	0.130
<b>Pre contrast T1 inferolateral wall</b>	<b>1.01</b>	<b>1.00-1.02</b>	<b>0.0386</b>
<b>Pre contrast T1 inferior wall</b>	1.010	0.9950-1.0200	0.256
<b>Mean ECV</b>	124000.000	0.000828-1.87e+13	0.222
<b>ECV inferior wall</b>	6540000.00000	0.0118000-3.64e+15	0.127
<b>ECV infero-lateral wall</b>	<b>4.93e+07</b>	<b>1.2200000-1.98e+15</b>	<b>0.0474</b>
<b>GLS</b>	<b>1.58</b>	<b>1.21-2.07</b>	<b>0.000925</b>
<b>RLS Basal Inferior wall</b>	1.02	0.950-1.100	0.545
<b>RLS Mid-ventricular Inferior wall</b>	1.05	0.977-1.13	0.185
<b>RLS Basal infero-lateral wall</b>	<b>1.11</b>	<b>1.00-1.23</b>	<b>0.0470</b>
<b>RLS Mid-ventricular Inferolateral wall</b>	<b>1.62</b>	<b>1.22-2.13</b>	<b>0.000753</b>
<b>GCS</b>	1.13	0.987-1.29	0.0775
<b>RCS basal infero-lateral wall</b>	<b>9.520</b>	<b>2.280-39.700</b>	<b>0.00197</b>
<b>RCS mid-ventricular infero-lateral wall</b>	<b>1.41</b>	<b>1.16-1.72</b>	<b>0.000563</b>
<b>RCS basal inferior wall</b>	1.000	1.000-1.010	0.0675
<b>RCS mid-ventricular inferior wall</b>	3.580	0.8760-14.60	0.0759
<b>RATIO-CS</b>	<b>7.480</b>	<b>1.870-30.000</b>	<b>0.00451</b>

**Caption 2**

Table 1: univariate statistics. LGE: late gadolinium enhancement, MAD: mitro-annular disjunction, ECV: extracellular volume, GLS: global longitudinal strain, RLS: regional longitudinal strain, GCS: global circumferential strain;

Speaker: M. Guglielmo

Category: Mitral Valve, Arrhythmia, Feature Tracking

000256

## Deep Neural Network Based Diagnosis of Ischemic Versus Non-Ischemic Dilated Cardiomyopathy Using 3D Myocardial Deformation Analysis of Routine Cine MRI

A. Satriano \* (1); A. Cornhill (1); D. Labib (1); M. Magyar-Ng, (1); Y. Mikami (1); S. Dykstra (1); J. Flewitt (1); A. Howarth (1); C. Lydell (2); N. Fine (1); R. Greiner, (3); J. A. White (1)

(1) Cumming school of medicine, department of cardiac sciences, University of Calgary, Calgary, Canada; (2) Cumming school of medicine, department of radiology, University of Calgary, Calgary, Canada; (3) Department of computing science, University of Alberta, Edmonton, Canada

### Abstract

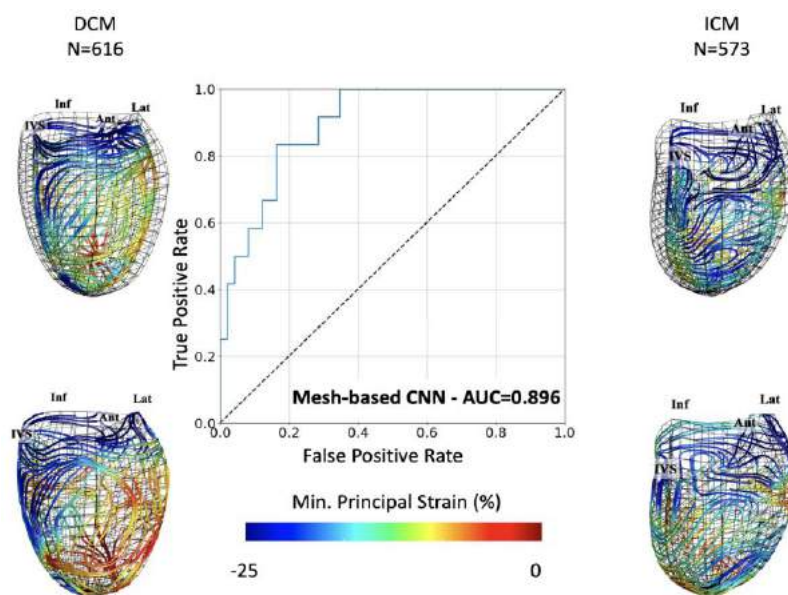
**Background:** Expanding innovations in 3-dimensional myocardial deformation analysis (3D-MDA) of routine 2-D cine imaging and deep neural network (DNN)-based modelling have made possible the classification of cardiomyopathy etiology without contrast-based techniques. In this study we evaluated these combined techniques to deliver automated classification of ischemic versus non-ischemic etiology (ICM vs NIDCM) in a large series of patients with dilated cardiomyopathy.

**Methods:** A total of 1,189 patients with ischemic or idiopathic non-ischemic dilated cardiomyopathy were identified from the Cardiac Imaging Registry of Calgary (CIROC). Of these, 573 (48%) had ischemic cardiomyopathy. Diagnosis was confirmed by both clinical criteria and LGE imaging. 3D-MDA was performed using validated software to deliver nodal coordinates of endocardial and epicardial mesh layers throughout the cardiac cycle encoded to a standardized anatomic model. Auxiliary data was provided in the form of layer-specific regional peak-systolic strain amplitude (in both geometry-dependent and principal strain directions), timing, systolic and diastolic rate. These were collectively presented as inputs to multiple, phase- and layer-specific ResNet models where the encodings of patient-specific inputs were concatenated to provide a common input to a series of fully-connected neural network layers for binary classification. Of the available population dataset, 80% was used for model training and 20% for validation, following stratification to ensure a balanced distribution of etiology. Model performance was assessed by area under the ROC curve – AUC. Success was defined as correct classification of disease etiology.

**Results:** Recruited subjects had a mean age of 58.9 +/- 13.2 years (276 females: age 59.2 +/- 12.8 years, 913 male: age 58.8 +/- 13.4, p=0.6). By traditional statistical modelling, the single most predictive variable for disease classification was global longitudinal subepicardial strain (ICM: -4.6 +/- 1.8%, NIDCM: -4.2 +/- 1.7%, AUC=0.57). Volumetric clinical variables did not add diagnostic value (LVEF: AUC=0.57; LVEDVI: AUC=0.53). A final DNN model, considering all multi-phase, multi-layer data inputs, provided an AUC of 0.896 (sensitivity: 0.83, specificity: 0.84) (Figure 1) for correct classification of disease etiology in the hold-out validation cohort.

**Conclusions:** DNN-based classification of disease etiology in patients with dilated cardiomyopathy is feasible from 3D-MDA derived data from contrast-free MR-based imaging. Leveraging mesh-based, time-dependent, and layer-specific data, superior classification performance of ischemic versus non-ischemic etiology is achieved versus traditional strain-based measures. The present study demonstrates the capacity of biomechanical data to inform modern deep neural networks to diagnose cardiomyopathy etiology from routinely captured 2D cine MRI data.

**Figure/Table 1**



**Caption 1**

**Figure 1.** 3D myocardial deformation analysis (3D-MDA) shown as Minimum Principal Strain Lines and amplitudes for ICM and DCM phenotypes. AUC is reported for the mesh-based deep neural network model trained for the classification of ischemic versus non-ischemic etiology.

Speaker: A. Satriano

Category: Ischemic Cardiomyopathy, Dilated Cardiomyopathy, 3D

000257

## The Final Device Frontier; Does Mixing Matter?

R. Biederman \* (1); L. Gevenosky (1); M. Doyle, (1)

(1) Cardiac mri, Allegheny Health Network, Pittsburgh, United States of America

### Abstract

**Introduction:** Over the last decade, intensive efforts have been aimed at improving the acceptability of pacemakers and ICDs in the MRI environment. Various labs have evaluated construction, safety, efficacy, reproducibility and more recently, clinical impact value in legacy devices. In parallel, there has been an extensive well-founded effort by the major vendors to develop MRI compatible devices. This latter effort is poised to revolutionize our utilization of such devices. Yet, remaining are only a few legitimate reasons for hesitation in universal use of any PM/ICD in the MRI bore. However, mixing vendor manufacturer leads and generators remains a major concern while in the bore.

**Hypothesis:** We hypothesize that mixed leads and generators has no different safety signal than common devices whether CIED or non-CIED.

**Methods:** We undertook a retrospective analysis of our database to determine the safety signal in those patients in whom mixed vendor leads and devices were present. Comparisons of impedance, amplitude, threshold and battery voltage and patient safety, etc. were performed.

**Results:** From September 2010 through September 2021, representing 1582 patients with CIED (82%) and non-CIED (18%) were scanned. The majority of the mixed population were, naturally obtained from the non-CIED population (98%) not having significant time for need for generator replacement. Accordingly, approximately 10% of these underwent mixed MRI imaging to include: 71% neurologic, 15% orthopedic and 14% cardiovascular indications. In comparison of safety signals between standard and mixed lead/generator implants, there were no differences in any implant parameters either pre-MRI study or post-interrogation (p=NS). Similarly, there were no patient events in the peri-MRI scan or reported in the 30 day post-MRI scan (p=NS). Importantly, especially for EP considerations, there were no additional complications in the interrogation mechanics. Finally, utilizing a similar approach to manipulation of the MRI parameters for maximum safety contingent on the dependent/non-dependent patient status was employed regardless of lead/generator configuration yielded no complications.

**Conclusion:** Employing a similar approach to MRI scanning in those patients with mixed vendor lead/generator configurations yielded no difference in a multitude of safety, interrogation, devices and efficacy parameters. This suggests, despite inherent concerns for incompatibility between vendors while in the magnetic field, no such fears are warranted.

Speaker: R. Biederman

Category: Pacemaker, Implantable Cardiac Device, Safety

000262

**Mycotic pseudoaneurysm from stented part of LAD communicating with lingula - an unusual cause for hemoptysis**

L. Robinson Vimala \* (1)

(1) Radiodiagnosis , Christian Medical College, Vellore, India

**Abstract**

**Clinical presentation:** 41-year-old gentleman, known case of anterior wall MI had undergone PCI with LAD stent in 2017. He presented with a history of cough and small volume hemoptysis for the past 1.5 years.

**Diagnostic techniques & their most important findings:**

Cardiac MRI performed revealed ill-defined soft tissue seen surrounding the LAD stent in the pericardial space with few necrotic areas within, which is extending into the inferior lingula.

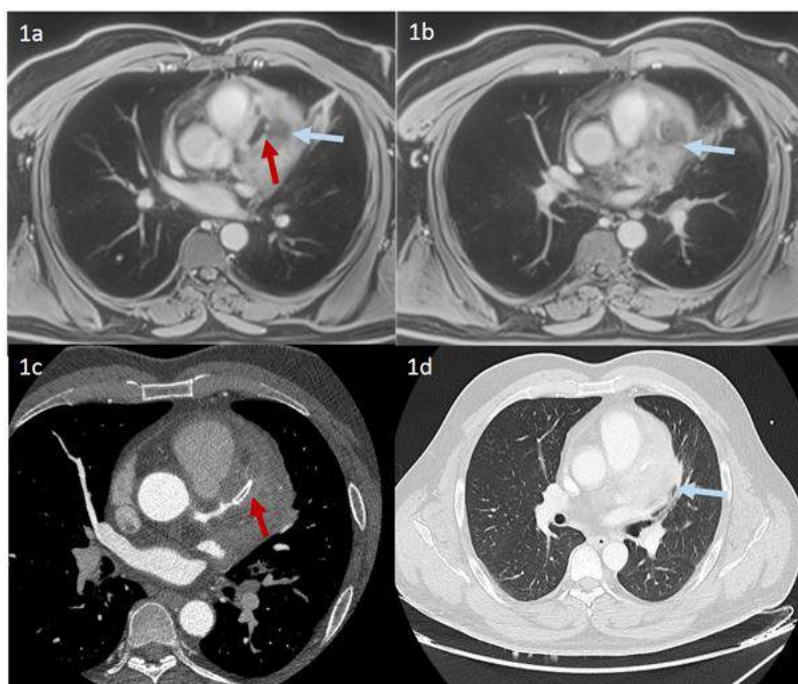
CT coronary angiogram performed confirmed the same findings and blocked LAD stent. LAD distal to the stent is re-formed by collaterals. He underwent catheter coronary angiography which confirmed distal LAD stent occlusion. Hence, he underwent recanalization and PCI to LAD.

Post-procedure he continued to have fever spikes and hemoptysis. Hence repeat cardiac MRI and CT coronary angiogram was performed which revealed interval development of active leak from LAD stented part, into a walled cavity of pseudoaneurysm in the adjacent epicardial space with an increase in surrounding soft tissue thickening, which is extending into the pericardial space and adjacent lingula. The findings were confirmed on the catheter angiogram also.

He underwent infected stent removal, debridement, and coronary artery bypass grafting (LIMA to LAD). Peroperatively, there was a large pseudoaneurysm of the proximal LAD with extrusion of the stents into the hematoma having frank pus formed over the proximal LAD. Repeated cultures of sputum, pus culture from the site of infection grew *Pseudomonas aeruginosa* which was pansusceptible to the standard antibiotic panel. His post-op period was uneventful and was discharged after 2 weeks.

**Figure/Table 1**

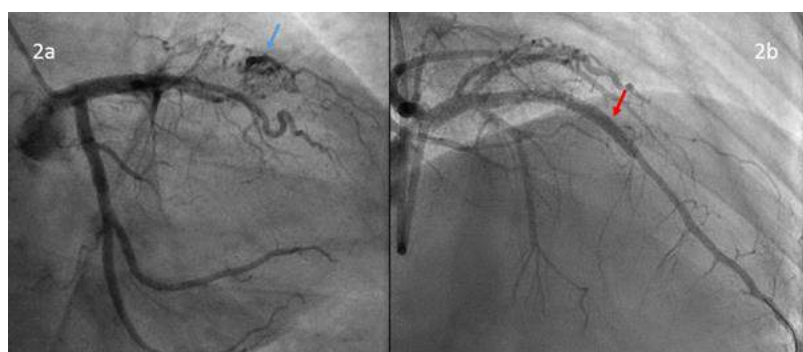




### Caption 1

Figure 1-a & b: Axial TRUFI image demonstrates soft tissue thickening with a hypointense center in the epicardial space (blue arrow) surrounding the LAD stent (red arrow) extending into the pericardial space and into adjacent inferior lingula. c & d: CT coronary angiogram also demonstrates the same findings and occluded LAD stent.

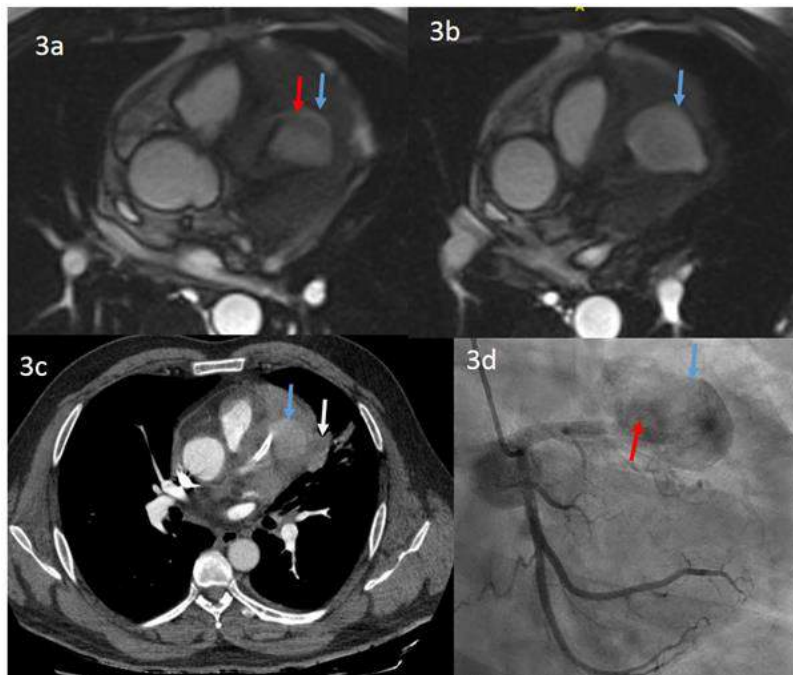
### Figure/Table 2



### Caption 2

Figure 2-a: Coronary catheter angiogram confirms the LAD stent occlusion and distal LAD supplied through collaterals (blue arrow). b: Flow restored through LAD stent (red arrow).

**Figure 3**



**Caption 3**

Figure 3-a & b: Axial TRUFI image demonstrates interval development of active leak from LAD stented part (red arrow), into a walled cavity of pseudoaneurysm in the adjacent epicardial space with an increase in surrounding soft tissue thickening, which is extending into the pericardial space and adjacent lingula. c & d: CT and catheter coronary angiogram respectively, also demonstrates contrast leaking from LAD stent (red arrow) forming a pseudoaneurysm (blue arrow) and collapse consolidation in lingula (white arrow).

### **Bibliographic References**

Gloria Santangelo, Andrea Buono, Antonio Silvestro, Manuela Giglio, Maurizio Tespili, Alfonso Ielasi, Multimodal Imaging of Post-Stenting Mycotic Coronary Pseudoaneurysm Complicated by Device Fracture and Myocardial Abscess. J Am Coll Cardiol Case Rep. 2020 Sep, 2 (11) 1667–1670., Edla Arjun Padmakumar Pankaj Jariwala. Mycotic aneurysm of the left anterior descending coronary artery induced by 'mother-and-child' catheter assisted percutaneous coronary angioplasty. Indian Heart J. Sep-Oct 2017;69(5):663-665.

Speaker: L. Robinson Vimala

Category: coronary Artery Disease, Coronary Angiography, Pseudoaneurysm

000263

## MINOCA case study: The importance of multimodality imaging

T. Swinn \* (1); A. Dastidar (1); E. Sammut, (2)

(1) Cardiology, North Bristol NHS Trust, Bristol, United Kingdom; (2) School of medicine, University of Bristol, Bristol, United Kingdom

### Abstract

#### Description of clinical presentation

41-year-old female with a past medical history including heavy cocaine use and cigarette smoking, asthma, obesity, and depression was admitted following seizures secondary to a mixed overdose of venlafaxine, cetirizine, and omeprazole. She was intubated on arrival in the Emergency Department and admitted to the Intensive Care Unit. Admission ECG showed normal sinus rhythm with no pathological changes. On day 4 of the admission, the patient developed ST elevation in V2-V4 and T-wave inversion in V3-V5 whilst intubated. Serum troponin T was 3913ng/l, rising to 4521ng/l 4 hours later.

#### Diagnostic techniques and their most important findings

The patient underwent urgent invasive coronary angiography with optical coherence tomography (OCT) on the day of ECG changes. Coronary arteries were unobstructed apart from a mild hazy lesion in the proximal left anterior descending (LAD) artery (*figure 1*). This lesion was not flow limiting (TIMI score 3). OCT to the proximal LAD lesion showed mild-moderate stenosis 55% with no clear plaque rupture. Coronary artery spasm was observed in distal LAD. Aspirin and clopidogrel were started for a presumed diagnosis of myocardial infarction with normal coronary arteries (MINOCA). The patient was successfully extubated 4 days later and self-discharged before further imaging.

The patient returned 19 days after initial admission reporting chest pain at rest. A voltage-gated CT scan of her thorax showed a pulmonary embolus in a right lower lobe segmental artery. This was treated with apixaban.

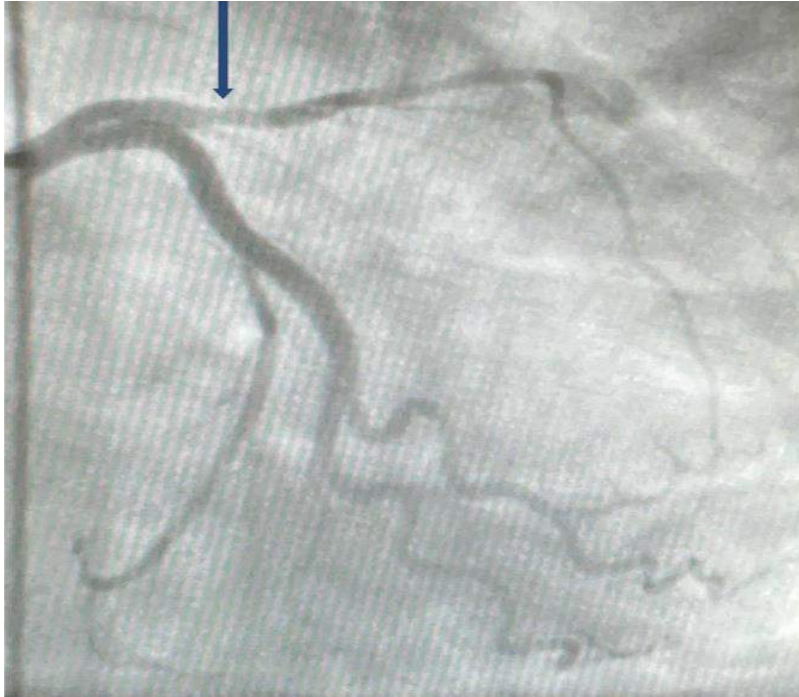
A cardiac MRI scan (myocardial viability protocol with gadolinium contrast) was performed 23 days after the ECG changes. This demonstrated a moderate-to-severely dilated and impaired left ventricle (end-diastolic volume 250ml, ejection fraction 37%). There were extensive akinetic regional wall motion abnormalities in the LAD territory with myocardial thinning. There was near-transmural myocardial late enhancement in these areas, worst towards the apex (*figure 2*). Atria size, valve morphology and function, and right ventricle size and function were normal. An embolic cause for the MINOCA was suspected and hence a bubble echo was requested.

An echocardiogram with bubble contrast demonstrated a large patent foramen ovale with no resting shunt (*figure 3*).

#### Learning points from this case

The CMR imaging above led to the diagnosis of a suspected paradoxical embolic myocardial infarction with spontaneous recanalization (MINOCA). This case required fluoroscopy, OCT, CT, MRI, and ultrasound to reach this diagnosis and highlights the importance of careful selection of imaging techniques to answer specific clinical questions. Each modality used provided complementary information and, when viewed together, led to a complex diagnosis and the correct care.

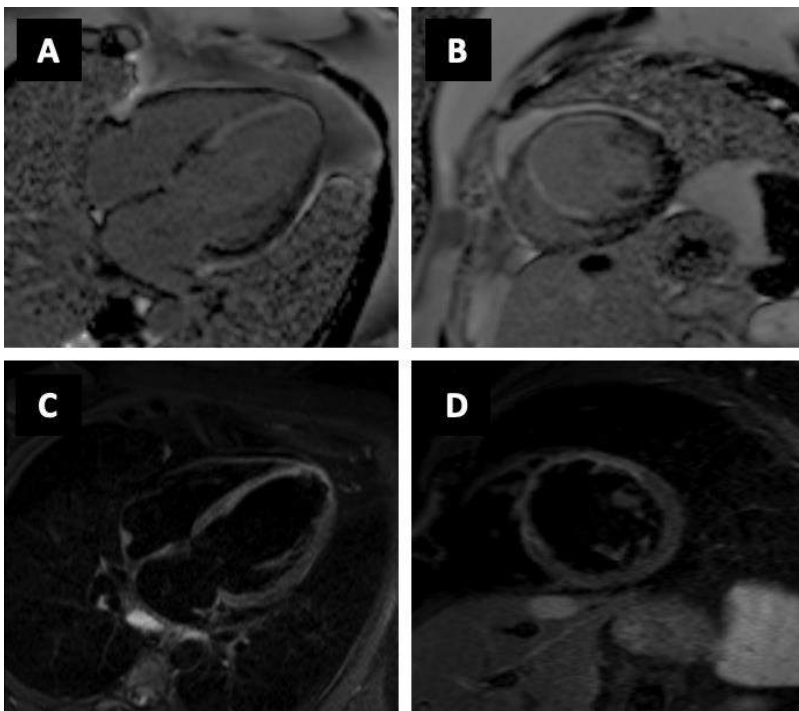
### Figure/Table 1



### Caption 1

Invasive coronary angiogram shows a non-flow-limiting 55% stenosis in the proximal LAD. Coronary arteries otherwise unobstructed.

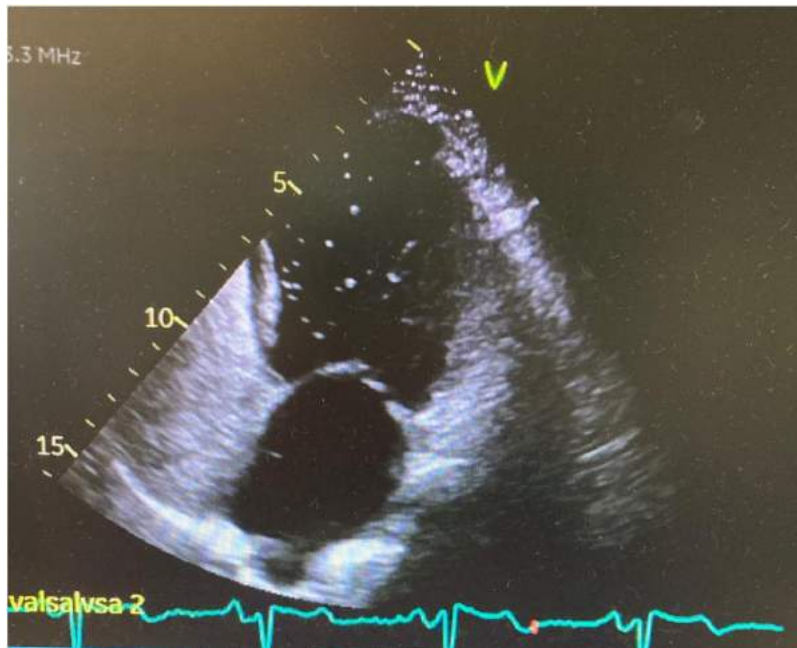
### Figure/Table 2



## Caption 2

Panels A and B show late gadolinium enhancement imaging of 4 chamber and mid ventricular short axis slices demonstrating extensive full thickness scar in LAD territory. Panels C and D demonstrate corresponding STIR imaging with increased signal in area of scar suggestive of an acute event.

## Figure 3



## Caption 3

Echocardiogram with bubble contrast demonstrates contrast entering the left atrium and left ventricle

Speaker: T. Swinn

Category: Angiography, Thrombus, Acute Myocardial Infarction

000266

## Radial artifact reduction in cardiac cine imaging using region-optimized virtual coil selection

C. Chen \* (1); Y. Liu (2); N. jin (3); O. Simonetti (4); R. Ahmad (5)

(1) , Université d'État de l'Ohio, Columbus, United States of America; (2) Davis Heart and Lung Research Institute, Ohio State University, Columbus, United States of America; (3) Research and collaboration department, Siemens Medical Solutions USA, Inc, Malvern, United States of America; (4) Davis heart and lung research institute, Ohio State University, Columbus, United States of America; (5) Department of bioengineering, The Ohio State University, Columbus, United States of America

### Abstract

#### Background

Radial k-space sampling has drawn continuous interest in cardiac MRI due to its motion robustness. However, it is sensitive to the scanner imperfections, which can lead to inconsistencies in k-space trajectories and degrade image quality. A number of methods have been proposed to perform the trajectory correction [1,2,3]; however, they do not fully suppress the artifacts, especially from the outer region of the images. In this work, we propose to apply region-optimized virtual (ROVir) [4] coil selection to suppress the signal and hence the artifact originating from the areas outside of the region of interest (ROI) in cardiac real-time (RT) cine imaging.

#### Methods

Five healthy volunteers were imaged under free-breathing conditions using a prototype radial balanced SSFP sequence on a 1.5 T scanner (MAGNETOM Sola, Siemens Healthcare, Erlangen, Germany). Images were acquired using 12-channel body array combined with 12 channels in the posterior spin array coil, resulting in 24 channels. Three views (short-axis, 2-chamber and 4-chamber) were collected for each volunteer using radial trajectory with a constant angle increment (tiny golden angle = 23.63 degree). The other scan parameters are: flip angle 62-72 degree, slice thickness 6-9 mm, FOV (with oversampling) 560-640 mm, readout size (RO) 320, TR 2.74-2.91 ms, TE 1.32-1.39 ms, 12 spokes/frame, and 50 frames.

The images were reconstructed retrospectively using a SENSE-based compressed sensing method with 3D undecimated wavelet transform [5]. The regularization weight was manually tuned using one dataset. Figure 1 (a) shows the ROI and the “interference region” used to generate ROVir coils. The ROI is defined as a circle of radius  $RO/4$  in the center of FOV, and there is a transition band between the ROI and the interference region. As shown in Figure 1 (b), the last four ROVir coils, highlighted with the red dashed box, were discarded before the reconstruction as they mostly captured the signal from the interference region. For comparison, we also reconstructed the datasets using all 24 original coils. Finally, the images reconstructed using both methods were visually scored in terms of the level of artifacts (5: no artifact; 4: minor artifact; 3: significant artifact but diagnostic; 2: severe artifacts but barely diagnostic; 1: non-diagnostic due to extreme artifacts) by an expert reviewer.



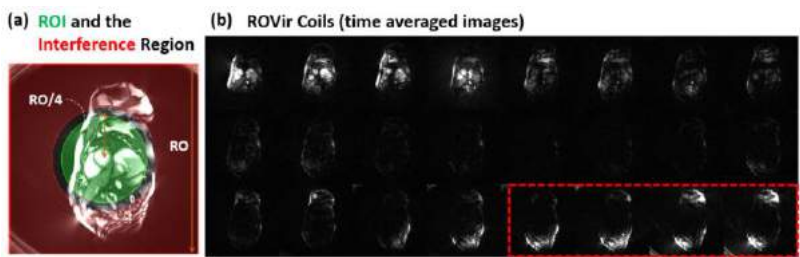
Results

Figure 2 illustrates the reconstructed RT cine images from three different volunteers. As expected, there is a visible suppression of the signal in the interference region. More importantly, as highlighted by the yellow arrow in the temporal profile, the radial artifacts were also reduced significantly. The results from visual scoring are listed in Table 1. The images reconstructed using selected ROVir coils received higher values ( $4.5\pm0.5$ ) than the ones using original coils ( $3.6\pm0.5$ ).

Conclusion

Using a reduced number of region-optimized virtual (ROVir) coils, the radial artifacts originating from the outer region of FOV are suppressed significantly. This technique can be applied at the preprocessing stage and thus can suppress the radial artifact without prolonging the reconstruction time.

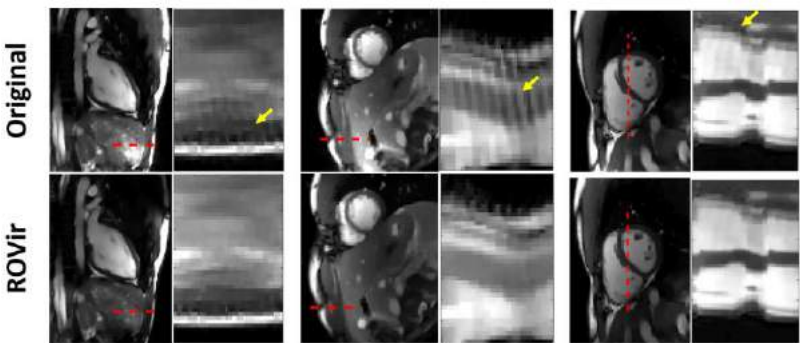
Figure/Table 1



Caption 1

Figure 1. Application of ROVir to suppress signal from the region outside of ROI. (a) The ROI (marked in green) and the interference region (marked in red) are automatically selected based on the size of the image. (b) The time-averaged individual coil images after ROVir. The last four coils, highlighted with the red dashed box, were discarded before the reconstruction to reduce the radial artifacts.

Figure/Table 2



## Caption 2

Figure 2. Radial-based RT cine images from three different volunteers. The top row are the images reconstructed using all the original coils, and the bottom row are the ones using the selected ROVir coils. The temporal profiles along the red dashed lines are shown, with the yellow arrows highlighting the radial artifacts.

## Figure 3

#slice	#1	#2	#3	#4	#5	#6	#7	#8	#9	#10	#11	#12	#13	#14	#15	#16	#17	Average
Original	4	3	4	3	4	4	4	4	3	3	3	3	4	3	4	4	4	3.6 ± 0.5
ROVir	5	4	5	4	5	5	5	5	4	4	4	4	5	4	5	4	5	4.5 ± 0.5

## Caption 3

Table 1. Scores in terms of the level of artifacts (5: no artifact; 4: minor artifact; 3: significant artifact but diagnostic; 2: severe artifacts but barely diagnostic; 1: non-diagnostic due to extreme artifacts). The images of 17 slices from 5 volunteers were scored, with the higher score in bold font for each slice.

## Bibliographic References

[5] Kayvanrad MH et al., Magnetic Resonance Imaging 32 (2014) 1353-1364, [4] D Kim et al., Magnetic Resonance in Medicine 86 (1), 197-212 (2021), [3] S Rosenzweig et al., Magnetic Resonance in Medicine 81 (3), 1898--1906 (2019)., [2] KT Block et al., ISMRM 19:2816, 2011. , [1] P Speier et al., ISMRM 14:2379, 2006.

Speaker: C. Chen

Category: Free Breathing, Non-Cartesian, Real Time



000267

## **Feasibility and Preliminary Results of the Use of Dynamic Contrast Enhanced (DCE) MRI in Abdominal Aortic Aneurysms (AAA) as a Marker for Diseases Progression**

A. Zhou \* (1); H. Dong (1); J. Leach (1); C. Zhu (2); D. Saloner (1); M. Hope (1); D. Mitsouras (1)

(1) Radiology and biomedical imaging, University of California San Francisco, San Francisco, United States of America; (2) Radiology, University of Washington, Seattle, United States of America

### **Abstract**

#### **Background**

AAA, a dilatation of the abdominal aorta to >3cm diameter, has a pooled global prevalence of 4.8% [1]. Unrepaired AAAs sometimes progress to rupture, with 80–90% mortality [2]. Dmax remains the most clinically relevant predictor of progression and is used to time repair. Nonetheless, 10% of AAA rupture before repair thresholds are reached (generally, Dmax>5.5cm), and 40% of ruptured AAA are below repair thresholds at last surveillance [3]. AAA wall microvasculature has been identified as a source of inflammatory cells and matrix metalloproteinases that lead to loss of wall strength and AAA progression [4]. DCE MRI has been previously used to quantify vessel wall microvascular density in carotid atherosclerotic disease [5]. The aim of this study was to explore DCE MRI for AAA risk stratification under the hypothesis that it relates to AAA inflammation.

#### **Methods**

DCE was acquired at 3T in 18 AAA subjects using a 3D fast gradient-echo (VIBE) sequence (1.5x1.5x5mm resolution, 20-26 slices; temporal resolution 13-15s, up to 30 phases). Two axial slices were selected for analysis. We measured normalized relative enhancement area-under-the-curve AUC and slope at selected times after contrast arrival (52s and 234s for AUC, and 26s and 78s for slope), based on preliminary histogram evaluations. These measurements were extracted for the whole wall and each of its four quadrants (left/anterior/right/posterior). Dmax and intraluminal thrombus thickness (ILTth) were measured from the DCE MRI, and AAA growth rate was retrospectively estimated from each patients' prior studies (MRI or CT) from the preceding 2 years. We used Pearson's correlation to associate Dmax, ILTth, and past growth rate with the above-described DCE parameters.

#### **Results**

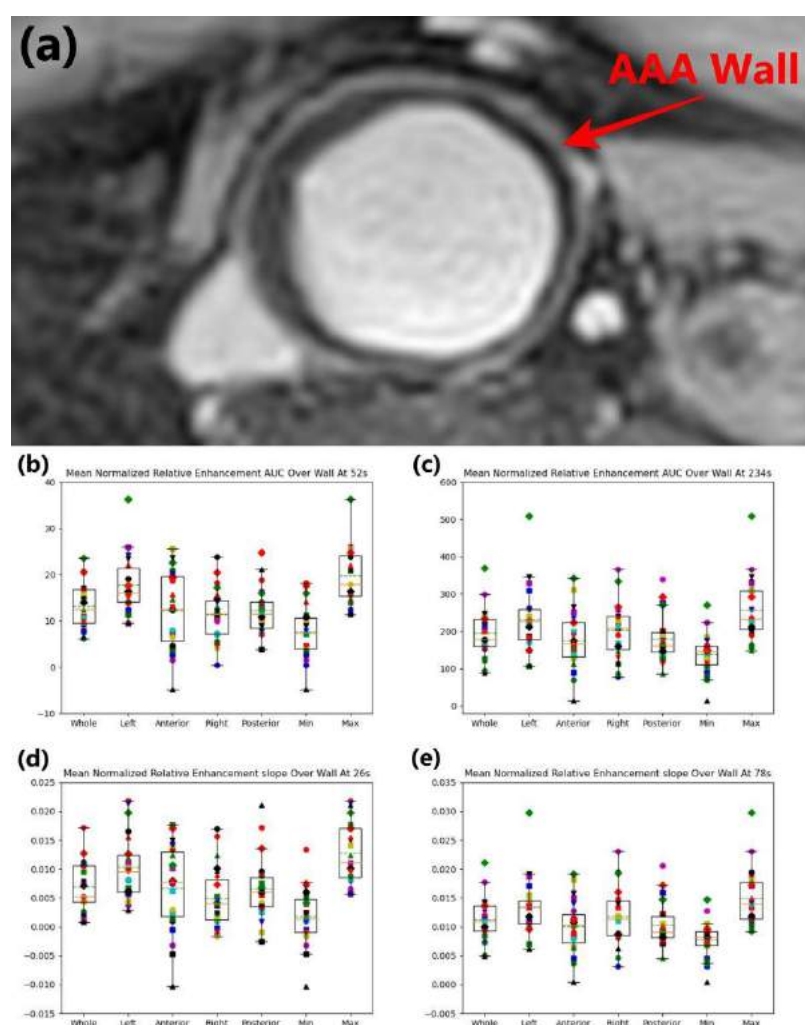
The mean wall normalized relative enhancement AUCs and slopes of each patient across the whole wall and in each quadrant revealed wide inter- and intra-subject variations for all measurements (Figure 1 (b)-(e)). Comparison of the minimum versus maximum AUCs and slopes across quadrants (Figure 1, last two columns) suggests significant differences in contrast uptake across the wall circumference in each subject, and is verified by a paired t-test (all  $p < 0.0001$ , Figure 2). Statistically significant correlations with AAA past growth rate were observed for all the whole wall, minimum and maximum quadrant AUC at 234s, and slope at 78s as well. (whole wall: Pearson  $r=0.54$ ,  $p=0.026$  for AUC at 234s, maximum quadrant:

Pearson  $r=0.51$ ,  $p=0.038$  for AUC at 234s, minimum quadrant: Pearson  $r=0.51$ ,  $p=0.038$  for AUC at 234s; whole wall: Pearson  $r=0.57$ ,  $p=0.018$  for slope at 78s, maximum quadrant: Pearson  $r=0.57$ ,  $p=0.018$  for slope at 78s, minimum quadrant: Pearson  $r=0.53$ ,  $p=0.030$  for slope at 78s). However, None of these correlated with AAA maximum diameter No correlations to ILTth were observed for any DCE measurements.

## Conclusions

DCE MRI revealed differential contrast uptake in the AAA wall for each individual and between individuals. Late AUC and slope correlated with AAA past growth rate, while early AUC and slope did not correlate with AAA growth rate. Future prospective studies are needed to determine if DCE MRI can improving AAA risk stratification.

**Figure/Table 1**

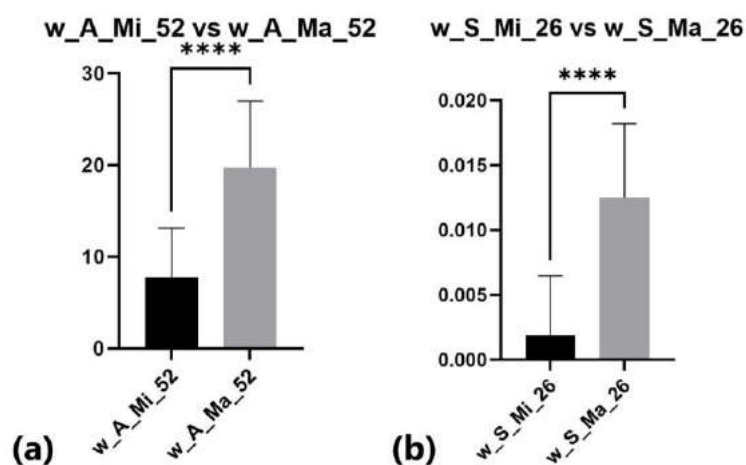


**Caption 1**

Fig. 1. (a) DCE MRI image showing the cross section of one AAA Plots: Wall mean normalized relative enhancement AUC and slope over the whole wall and four quadrants. (b)

AUC at 52 seconds; (c) AUC at 234 seconds; (d) Slope at 26 seconds; (e) Slope at 78 seconds. Last two are respectively the minimum and maximum of four quadrants mean.

**Figure/Table 2**



**Caption 2**

Fig. 2. Paired t-test between minimum and maximum wall quadrants. (a) AUC at 52s. (b) Slope at 26s.

### Bibliographic References

[1] Koch AE, Haines GK, Rizzo RJ, et al. Human abdominal aortic aneurysms. Immunophenotypic analysis suggesting an immune-mediated response. *The American journal of pathology*. 1990;137(5):1199-1213., [2] Bengtsson H, Bergqvist D. Ruptured abdominal aortic aneurysm: A population-based study. *Journal of Vascular Surgery*. 1993;18(1):74-80., [3] Ahmad M, Mistry R, Hodson J, Bradbury AW. How Quickly Do Asymptomatic Infrarenal Abdominal Aortic Aneurysms Grow and What Factors Affect Aneurysm Growth Rates? Analysis of a Single Centre Surveillance Cohort Database. *European Journal of Vascular and Endovascular Surgery*. 2017;54(5)., [4] Reeps C, Pelisek J, Seidl S, et al. Inflammatory Infiltrates and Neovessels Are Relevant Sources of MMPs in Abdominal Aortic Aneurysm Wall. *Pathobiology*. 2009;76(5)., [5] Kerwin WS, O'Brien KD, Ferguson MS, Polissar N, Hatsukami TS, Yuan C. Inflammation in Carotid Atherosclerotic Plaque: A Dynamic Contrast-enhanced MR Imaging Study. *Radiology*. 2006;241(2).

Speaker: A. Zhou

Category: Abdominal Aorta, Aneurysm, Aorta

000269

## **A Case of Fulminant Cardiac Sarcoidosis**

D. Tong, (1); A. Canan \* (2); S. Yan, (3); W. Roberts (4); J. De Lemos (1)

(1) Cardiology, UT Southwestern Medical Center, Dallas, United States of America; (2) Radiology, UT Southwestern Medical Center, Dallas, United States of America; (3) Pathology, UT Southwestern Medical Center, Dallas, United States of America; (4) Pathology, Baylor University Medical Center, part of Baylor Scott & White Health, Dallas, United States of America

### **Abstract**

#### **Description of Clinical Presentation**

A 39-year-old man without significant past medical history presented with progressive malaise and dyspnea on exertion for a few weeks. His initial physical exam was significant for borderline low blood pressure 90/70mmHg and mildly distended jugular vein. EKG showed sinus tachycardia with frequent runs of non-sustained ventricular tachycardia (Fig1A). Labs showed mild renal and hepatic dysfunction, significantly elevated NT-proBNP, and mildly increased serum lactate. Transthoracic echography demonstrated severely impaired biventricular systolic function (LVEF 17%) with global hypokinesis and septal and inferior wall akinesis (Fig1B). The patient was referred for cardiac magnetic resonance (CMR) for evaluation of the etiology of the newly diagnosed cardiomyopathy.

#### **Diagnostic Techniques and Their Most Important Findings**

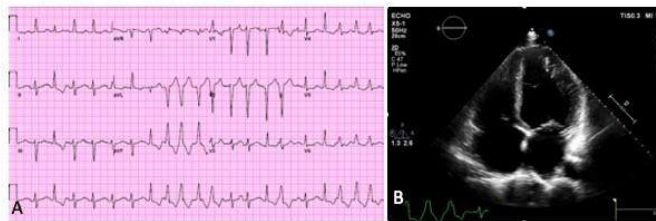
Cine CMR images confirmed severe biventricular systolic dysfunction. Late gadolinium enhancement (LGE) images showed extensive subendocardial and subepicardial and focal areas of transmural LGE in the anterior, septal and inferior walls of the left ventricle (LV), extending into the right ventricular anterior wall (Fig2B&C). However, T2 parametric mapping was normal (45ms) (Fig2D). Additionally, significant mediastinal lymphadenopathy was also detected (Fig2A). The imaging findings, together with clinical presentation, are highly suggestive for possible cardiac sarcoidosis (CS), which was confirmed by pathological study of the endomyocardial biopsy (EMB) (Fig3A). Meanwhile, the patient's clinical condition continued to worsen despite supportive treatment, and he suffered cardiogenic shock with sustained ventricular tachycardia. He was placed on veno-arterial extracorporeal membrane oxygenation (VA-ECMO), and received an urgent heart transplant 5 days later. Classical pathological changes of sarcoidosis were detected in the explanted heart (Fig3B), with similar distribution pattern demonstrated by CMR study.

#### **Learning Points from this Case**

Although the definite diagnosis of CS is based on histology, the patchy, predominantly epicardial LV distribution pattern often makes EMB biopsy low yield<sup>1</sup>. CMR provides valuable information regarding tissue characterization, severity, and stages of the underlying

pathology, and therefore has become an important diagnostic and prognostic modality in the evaluation of CS2. In this case, the widely distributed extensive subepicardial and subendocardial LGE changes indicate significant myocardial involvement, which likely correlates with patient's fulminant clinical course. The normal T2 mapping in this patient suggests lack of significant myocardial edema and a late stage of the disease. This case emphasizes the use of CMR in the identification of potential causes of new onset heart failure and diagnosis of cardiac sarcoidosis.

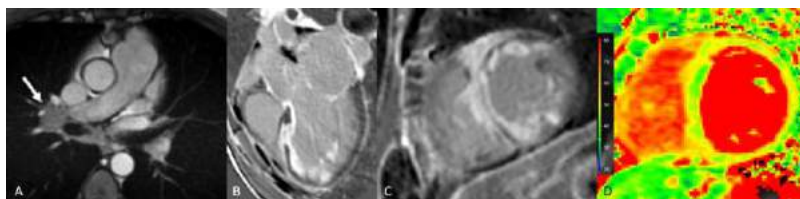
**Figure/Table 1**



**Caption 1**

**Fig 1: A.** Electrocardiogram (EKG) showing sinus tachycardia with frequent short runs of nonsustained ventricular tachycardia. **B.** Transthoracic echocardiography showing dilated cardiac chamber and impaired cardiac function.

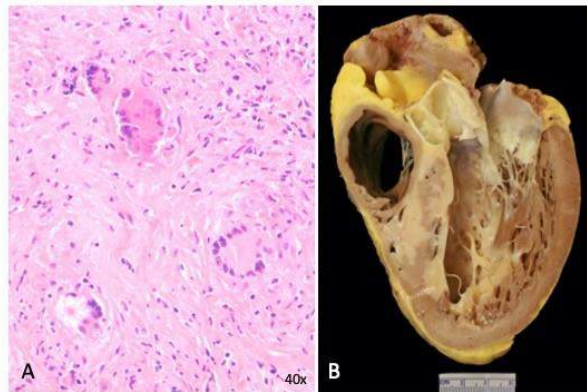
**Figure/Table 2**



**Caption 2**

**Fig 2: A.** Enlarged right hilar lymph node (arrow) on axial bright blood image. 3 chamber (**B**) and short axis (**C**) phase sensitive inversion recovery images demonstrating extensive subendocardial and supepicardial LGE with extension into the RV anterior wall. **D.** T2 color map in short axis orientation showing normal T2 values of the LV myocardium (45 ms).

**Figure 3**



**Caption 3**

**Fig 3:** **A.** H&E staining of the endomyocardial tissue showing noncaseating granulomas with multinucleated giant cells. **B.** Gross pathology of the explanted heart showing whitish-yellow sarcoid lesion infiltrating septum, LV inferior wall and the apex.

### **Bibliographic References**

Smedema, J.P., Ainslie, G. & Crijns, H. Review: Contrast-enhanced magnetic resonance in the diagnosis and management of cardiac sarcoidosis. *Prog Cardiovasc Dis* 63, 271-307 (2020)., Hamzeh, N., Steckman, D.A., Sauer, W.H. & Judson, M.A. Pathophysiology and clinical management of cardiac sarcoidosis. *Nat Rev Cardiol* 12, 278-288 (2015).

Speaker: A. Canan

Category: Cardiomyopathy, Sarcoidosis, Parametric Mapping

000271

## **Superiority of Stress Perfusion CMR Compared with Gated SPECT: Results from GadaCAD2**

A. Arai \* (1); J. Schulz-Menger (2); D. J. Shah (3); Y. Han (4); P. Bandettini (5); A. Abraham, (6); P. Woodard (7); J. Selvanayagam (8); C. Hamilton-Craig, (9); J. Carr (10); L. Teo (11); R. S. Tan (12); C. Kramer (13); B. Wintersperger (14); M. Harisinghani (15); S. Flamm (16); M. Friedrich (17); I. Klem (18); S. Raman (19); D. Haverstock (20); Z. Liu (20); G. Brueggenwerth (21); M. Santuiste (22); D. Pennell (23); D. Berman (24)

(1) Cardiology, Consultant, Kensington, United States of America; (2) Working group on cardiovascular magnetic resonance, Charité – Universitätsmedizin Berlin, Berlin, Germany; (3) Cardiology, Houston Methodist Hospital, Houston, United States of America; (4) Cardiovascular division, Hospital of the University of Pennsylvania, Philadelphia, United States of America; (5) NHLBI, Bethesda, MD, USA, National Institutes of Health, Bethesda, United States of America; (6) Cardiology, Royal Perth Hospital, Perth, Australia; (7) Department of radiology, Washington University School of Medicine, Washington, United States of America; (8) Cardiology, Flinders University, Adelaide, Australia; (9) Cardiology, The University of Queensland, Saint Lucia, Australia; (10) Radiology, Feinberg School of Medicine, Chicago, United States of America; (11) Department of diagnostic imaging, National University Health System, Singapore, Singapore; (12) Cardiology, National Heart Centre Singapore, Singapore, Singapore; (13) Cardiology, University of Virginia, Charlottesville, United States of America; (14) Dept of Medical Imaging, Toronto General Hospital, Toronto, Canada; (15) Radiology, Massachusetts General Hospital, Boston, United States of America; (16) Section of cardiovascular imaging, Cleveland Clinic Main Campus, Cleveland, United States of America; (17) Departments of Medicine and Diagnostic Radiology, Division of Experimental Medicine, Centre Universitaire de Santé McGill Site Glen, Montréal, Canada; (18) Cardiology, Duke University, Durham, United States of America; (19) Cardiology, Indiana University School of Medicine, West 10th Street, Indianapolis, United States of America; (20) Statistics and data insights, Bayer, Whippany, NJ, United States of America; (21) Digital diagnostics gcis - general clinical imaging services, Bayer AG, Berlin, Germany; (22) Med & clin affairs radiology, Bayer, Whippany, NJ, United States of America; (23) Cardiac mri, Royal Brompton Hospital, London, United Kingdom; (24) Cardiology, Cedars-Sinai Medical Center, Los Angeles, United States of America

### **Abstract**

**Background:** GadaCAD2 was one of two nearly identical international, multicenter, prospective, controlled, Phase 3 clinical trials that led to FDA approval of gadobutrol in the USA for stress perfusion and late gadolinium enhancement in adults with known or suspected coronary artery disease (CAD). A secondary objective of the study was to determine if stress perfusion CMR was non-inferior to SPECT for detecting significant CAD.

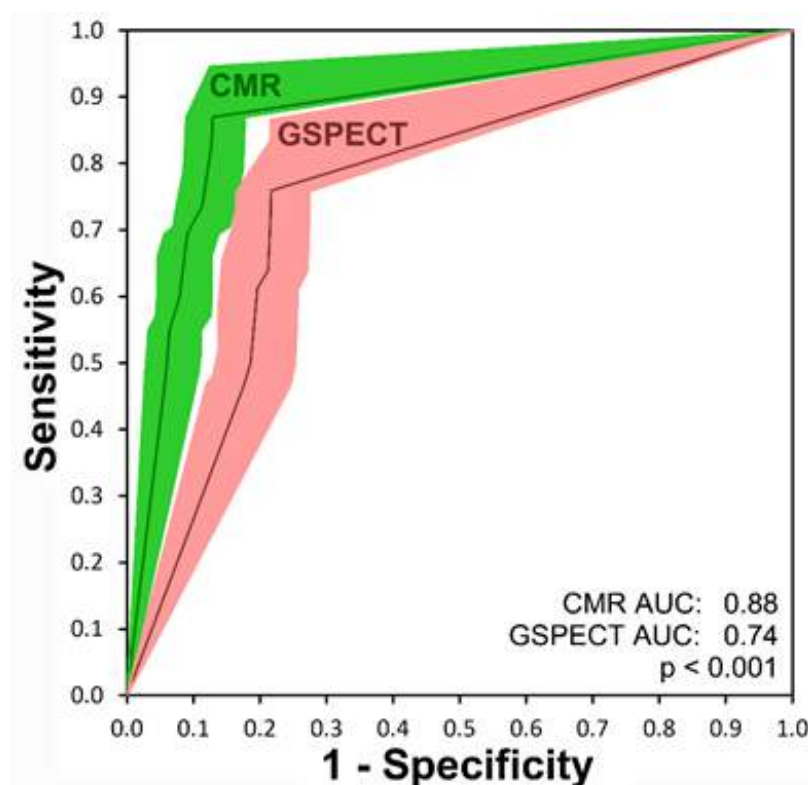
**Methods:** Participants with known or suspected CAD consented to a research vasodilator stress perfusion CMR scan with specified methods and comparison with a gated SPECT performed using standard clinical protocols. For CMR, adenosine or regadenoson served as

vasodilators. The dose of gadobutrol was 0.1 mmol/kg body weight. The standard of reference was a 70% stenosis defined by quantitative coronary angiography (QCA). Analysis was per patient. CMR, SPECT, and QCA were evaluated by independent central core lab readers blinded to clinical information.

**Results:** Participants in GadaCAD2 were predominantly male (61.4% male; mean age  $58.9 \pm 10.2$  years) and were recruited from the USA (75.0%), Australia or New Zealand (14.7%), Singapore (5.7%), and Canada (4.6%). Among participants with analyzable CMR, gated SPECT, and QCA, the prevalence of significant CAD was 24.5% (n=72 of 294). The sensitivity of CMR for a 70% QCA stenosis was non-inferior to gated SPECT (0.74 vs 0.64,  $p=0.12$ ). The AUC for stress perfusion CMR was significantly higher than gated SPECT (0.88 vs 0.74,  $p<0.001$ ) with almost no overlap of the 95% confidence limits (figure 1). Stress perfusion CMR was statistically superior to gated SPECT for specificity ( $p=0.002$ ), positive predictive value ( $p<0.001$ ), and negative predictive value ( $p=0.041$ ).

**Conclusions:** Vasodilator stress perfusion CMR, as performed with gadobutrol 0.1 mmol/kg body weight, had superior diagnostic accuracy for the detection of significant CAD as compared with gated SPECT. These findings extend and confirm previous comparisons of CMR and SPECT with a study design that is multi-center, controlled, and predominantly US-based.

**Figure/Table 1**



**Caption 1**



Figure 1. Receiver operating characteristic curves with 95% confidence limits comparing CMR & gated SPECT

**Figure/Table 2**

Study	Sample Size	CAD (+)	CAD (-)	Sensitivity	Specificity	AUC	PPV	NPV	TP	TN	FP	FN
GadaCAD2 Gated SPECT	294	72	222	0.64	0.79	0.74	0.49	0.87	46	175	47	26
GadaCAD2 CMR	294	72	222	0.74	0.89	0.88	0.68	0.91	53	197	25	19
CMR vs gated SPECT Two-sided P value:				0.127	0.002	<0.001	<0.001	0.041	0.022			

**Caption 2**

Table 1. Comparison of diagnostic accuracy of gated SPECT versus stress perfusion CMR in GadaCAD2

## Bibliographic References

Arai, AE, Schultz-Menger J, Berman, D, et al. Gadobutrol-Enhanced Cardiac Magnetic Resonance Imaging for Detection of Coronary Artery Disease. JACC 2020, 76 (13): 1536-47

Speaker: A. Arai

Category: Stress CMR, Perfusion, Gadolinium

000273

## Validation of accelerated 4D flow MRI in Qp/Qs quantification with adult healthy volunteers

T. Fujiwara \* (1); E. K. Englund (1); H. M. Mehdi. (1); B. Fonseca (2); L. Browne (1); A. Barker (3)

(1) Department of radiology, Children's Hospital Colorado, University of Colorado Anschutz Medical Campus, Aurora, United States of America; (2) Department of pediatrics, Children's Hospital Colorado, University of Colorado Anschutz Medical Campus, Aurora, United States of America; (3) Department of radiology/department of bioengineering, Children's Hospital Colorado, University of Colorado Anschutz Medical Campus, Aurora, United States of America

### Abstract

**Background:** The ratio of pulmonary to systemic blood flow (Qp/Qs) is used to detect existence and amount of shunt flow between systemic and pulmonary circulation in patients with congenital heart diseases. 2D phase-contrast (PC) MRI at the ascending aorta and main pulmonary artery is used routinely in clinical practice, however this ratio can also be obtained from 4D flow (time resolved, three-dimensional PC-MRI) (Horowitz, et al. 2021). With accelerated acquisitions, 4D flow can acquire three-dimensional velocity field of the great vessels in a relatively short scan time (4-10 minutes), providing not only insight into Qp/Qs, but also advanced flow metrics (e.g., wall shear stress, Barker et al. 2012). However, the accelerated 4D flow compromise signal-to-noise (SNR), which may lead to inaccurate quantification. In particular, quantifying Qp/Qs is challenging due to accumulated error from time integral over a cardiac cycle in net flow calculation. Here, we tested 4D flow scans with different acceleration factors in adult healthy volunteers to validate Qp/Qs measurement.

**Methods:** Eight healthy volunteers were scanned using a 3T Philips Ingenia scanner (Philips Healthcare, Best, Netherlands) to acquire free-breathing 2D-PC and 4D flow data. The volunteer's demographics are shown in Table 1. 2D-PC at the ascending aorta and main pulmonary arteries were performed as a gold-standard. Mildly accelerated (SENSE) and highly accelerated (Compressed SENSE) 4D flow datasets were acquired, with coverage of the great vessels (the aorta and pulmonary arteries, Table 1 and Fig. 1). Eddy current correction, noise masking, and anti-aliasing were applied using custom MATLAB (MATLAB R2019b, Natick, MA) scripts. The aorta and pulmonary arteries were automatically segmented from PC-MRA with a convolutional neural network (dense U-net, Berhane et al. 2020), and any minor errors were detected and corrected by a human observer in 3D slicer, open-source image processing software. Net flow at the aorta and main pulmonary artery were quantified in Enight (Ansys Inc., Canonsburg, PA). Centerlines were manually defined on the ascending aorta and main pulmonary trunk. Three measurement planes were then placed on each centerline at approximately the same location as 2D-PC (Fig. 1). Net flows at the three planes were then averaged to obtain Qp (pulmonary flow volume), Qs (systemic flow volume) and their ratio (Qp/Qs). 2D-PC data were analyzed in Circle (cvi 42; Circle Cardiovascular Imaging, Calgary, Alberta, Canada) to obtain gold-standard measurements. Qs, Qp, and Qp/Qs was compared between 2D-PC and the two 4D flow acquisitions using a one-way ANOVA with a significance level of 0.05. In addition, Bland-Altman analysis was conducted for Qp/Qs. Statistical analysis was performed in MATLAB R2019b.

**Results:** Mean scan time was 9:39 min (mild acceleration) and 4:07 min (high acceleration). Flow measurements are shown in Table 1. A non-significant underestimation of Qp and Qs exist when the 4D flow sequences were compared to the 2D-PC data. Qp/Qs values were  $1.05 \pm 0.12$  (2D-PC),  $0.97 \pm 0.08$  (mild acceleration), and  $0.94 \pm 0.08$  (high acceleration). No statistical significance was observed among the three groups in Qs, Qp and Qp/Qs quantification ( $p=0.47$ ,  $0.13$  and  $0.08$ , respectively). Bland-Altman analysis presented no significant biases (Fig.2).

**Conclusions:** We validated Qp/Qs quantification with differently accelerated 4D flow MRI and effects of acceleration factors were not found in this limited population. Future directions are to increase the number of volunteers and to validate in a pediatric cohort.

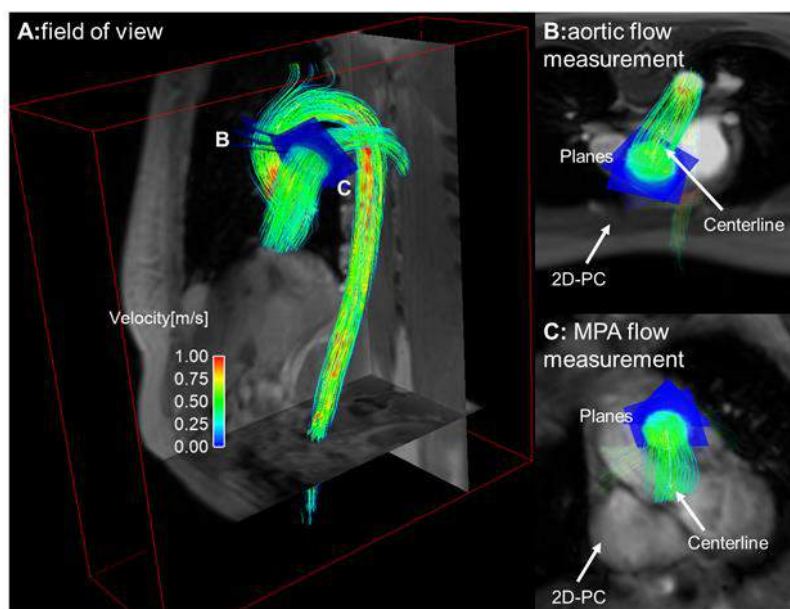
**Figure/Table 1**

Demographics			
male/female	5/3		
Age [y]	36.0 $\pm$ 2.0		
Height [cm]	170.0 $\pm$ 10.7		
Weight [kg]	68.8 $\pm$ 10.1		
BSA [m <sup>2</sup> ]	1.8 $\pm$ 0.2		
Scan parameters	2D phase-contrast	Mildly accelerated 4D flow	Highly accelerated 4D flow
Acceleration factors	2x SENSE	SENSE [1.5-2x (phase), 1.5x (slice)]	6x Compressed SENSE
flip angle [deg]	10	7	7
Echo time [ms]	2.56-2.87	2.39-2.41	2.39-2.41
Repetition time [ms]	4.16-4.52	4.02-4.06	4.03-4.06
Venc [cm/s]	150	150	150
Temporal resolution [ms]	22-28	28-36	29-38
Pixel/voxel size [mm <sup>2</sup> /mm <sup>3</sup> ]	1.17 $\times$ 1.17	1.56-2.18 $\times$ 1.56-2.18 $\times$ 2.47-2.52	1.56-2.18 $\times$ 1.56-2.18 $\times$ 2.48-2.53
Field of view [mm <sup>3</sup> ]	141 $\times$ 134-141	275-384 $\times$ 275-384 $\times$ 101-126	275-384 $\times$ 275-384 $\times$ 103-124
Acquisition matrix	120 $\times$ 114-120	160-192 $\times$ 160-192 $\times$ 41-50	144-176 $\times$ 144-176 $\times$ 41-50
Cardiac phases	40	30	30
Scan time [min]	0:39-1:25	6:46-12:31	2:48-5:27
Flow analysis			
Qs [ml/cycle]	81.7 $\pm$ 15.5	74.0 $\pm$ 14.9	73.8 $\pm$ 12.5
Qp [ml/cycle]	85.0 $\pm$ 11.4	71.9 $\pm$ 17.2	70.1 $\pm$ 16.2
Qp/Qs [ - ]	1.05 $\pm$ 0.12	0.97 $\pm$ 0.08	0.94 $\pm$ 0.08

**Caption 1**

Table 1 Subject demographics [mean±std], scan parameters [min-max] and flow analysis results [mean±std].

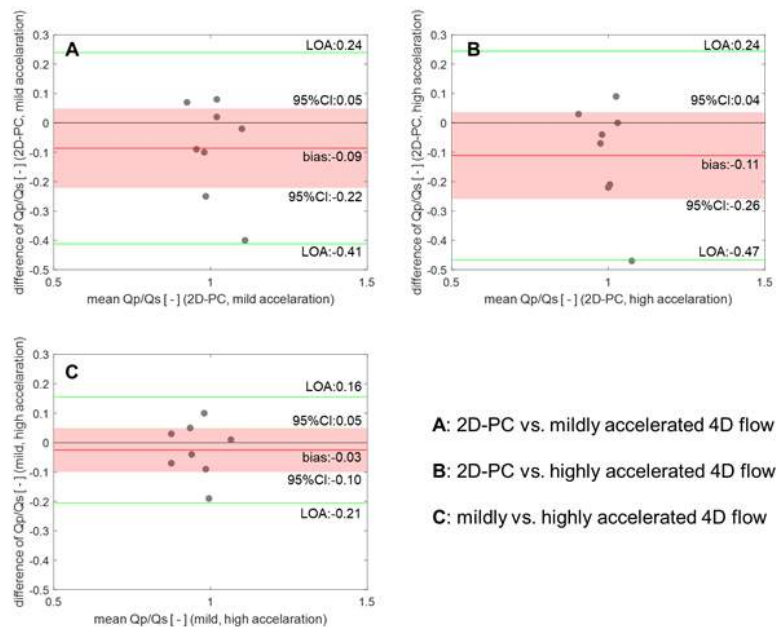
**Figure/**Table 2



**Caption 2**

Fig. 1 (A) Field of view of 4D flow data and streamline visualization. (B,C) 2D phase-contrast (2D-PC) slices of the ascending aorta and the main pulmonary artery (MPA) were used to identify their location in the 4D flow volume. Three measurement planes were placed on the manually defined vessel centerlines at approximately the same location as the 2D-PC.

**Figure 3**



**Caption 3**

Fig. 2 Bland-Altman plots for Qp/Qs quantification. Biases and limits of agreements (LOA) are drawn by red and green lines, respectively. 95% confidence intervals (95% CI) for biases are shown by red shaded areas.

### Bibliographic References

Berhane H, Scott M, Elbaz M, Jarvis K, McCarthy P, Carr J, Malaisrie C, Avery R, Barker AJ, Robinson JD, Rigsby CK and Markl M. Fully automated 3D aortic segmentation of 4D flow MRI for hemodynamic analysis using deep learning. *Magn Reson Med*. 2020;84:2204-2218., Barker AJ, Markl M, Burk J, Lorenz R, Bock J, Bauer S, Schulz-Menger J and von Knobelsdorff-Brenkenhoff F. Bicuspid aortic valve is associated with altered wall shear stress in the ascending aorta. *Circ Cardiovasc Imaging*. 2012;5:457-66., Horowitz MJ, Kupsky DF, El-Said HG, Alshawabkeh L, Kligerman SJ and Hsiao A. 4D Flow MRI Quantification of Congenital Shunts: Comparison to Invasive Catheterization. *Radiol Cardiothorac Imaging*. 2021;3:e200446.

Speaker: T. Fujiwara

Category: 4D Flow, Accelerated Imaging, Compressed Sensing

000274

## CMR derived pulmonary transit time as a predictor of outcomes in patients with heart failure

J. Farley \* (1); L. Brown (1); P. Garg (2); A. Wahab (1); J. Klassen (1); N. Jex (1); S. Thirunavukarasu (1); A. Chowdhary (1); N. Sharrack (1); M. Gorecka, (1); H. Xue (3); E. Levelt (1); E. Dall'Armellina (1); P. Kellman (3); J. Greenwood (1); S. Plein (1); P. Swoboda (1)

(1) Leeds institute of cardiovascular and metabolic medicine, University of Leeds, Leeds, United Kingdom; (2) Infection, immunity & cardiovascular disease, The University of Sheffield, Sheffield, United Kingdom; (3) National institutes for health, NHLBI, Bethesda, United States of America

### Abstract

**Background:** Pulmonary transit time (PTT) is the time taken for blood to pass through the pulmonary circulation. It is possible to measure PTT from arterial input function (AIF) images of dual phase first-pass perfusion imaging without requirement for additional imaging or contrast administration. PTT has been validated against invasive cardiac catheterisation correlating with both cardiac output and filling pressure (both important prognostic markers in heart failure). We hypothesised that prolonged PTT is associated with clinical outcomes in patients with heart failure.

**Methods:** We recruited outpatients with a recent diagnosis of heart failure with LVEF <50% on referral echocardiogram, aged >18 years and referred for investigation into the aetiology of heart failure. Exclusion criteria were previous myocardial infarction (MI), revascularisation or angina, hypertrophic cardiomyopathy, amyloidosis, suspected myocarditis or advanced renal failure. Patients were followed up by review of medical records for major adverse cardiovascular events (MACE) to include cardiovascular death, heart failure hospitalisation, non-fatal MI and non-fatal stroke.

PTT was measured from low resolution AIF dynamic images of both the LV and RV during rest perfusion. A convolutional neural network approach was used to segment both cavities and measure signal intensity over time. Gadolinium contrast curves over time were calculated from signal intensity data and the PTT measured as the time (in seconds) between the centroid of the left (LV) and right ventricle (RV) indicator dilution curves.

**Results:** A total of 251 patients were prospectively recruited. Following CMR, 17 patients (6.8%) were excluded from this study due to suboptimal LV fit during automated PTT assessment. This left a total of 234 patients. Patients were followed-up over a median of 617 days. During this time, 21 patients (9.0%) encountered MACE of which 18 patients had a heart failure hospitalisation, 3 had a non-fatal MI, 1 had a non-fatal stroke, and 4 had cardiovascular death. Receiver operator analysis was used to identify a cut-off of >12.4s which was associated with MACE. Patients with PTT >12.4s were older, more frequently male and had higher prevalence of atrial fibrillation than those with PTT<12.4s (Table 1). Univariate Cox regression analysis showed factors including age, heart rate, ischaemic late gadolinium enhancement, LV ejection fraction (EF), RV EF and PTT>12.4s all to be associated with MACE (Table 2). On multivariate stepwise Cox regression, the optimal model

included only PTT>12.4s, age and heart rate. PTT>12.4s had significant association with MACE (Hazard ratio 3.95; 95% confidence interval 1.66-9.40, P=0.002) which remained significant even after adjustment for age and heart rate (Hazard ratio 2.84; 95% confidence interval 1.14-9.7.02, P=0.02), Figure 1.

**Conclusions:** PTT >12.4s was an independent predictor of MACE in patients with a recent diagnosis of heart failure. PTT has the potential to be a prognostic marker in heart failure because it is influenced by both cardiac output and LV filling pressure both of which are important for outcomes in heart failure. Future studies are required to establish if PTT and therefore outcomes can be altered by medical or device therapy.

**Figure/Table 1**

	PTT < 12.4 s (n = 190)	PTT > 12.4 s (n = 44)	P Value
Age (years)	63 (54-71)	70 (58-77)	0.005*
Male sex	127 (67)	39 (89)	0.01*
HR (bpm)	71 (63-82)	77 (65-91)	0.22
SBP (mmHg)	121 (110-137)	119 (105-134)	0.14
DBP (mmHg)	74 (70-81)	75 (69-83)	0.71
NYHA I	117 (62)	28 (65)	0.94
NYHA II	61 (32)	13 (30)	
NYHA III	10 (5)	2 (5)	
AF	66 (34)	27 (61)	0.001*
Current smoker	33 (18)	7 (16)	0.81
Previous smoker	71 (38)	16 (36)	0.88
Betablocker	149 (80)	33 (75)	0.50
Statin	74 (40)	21 (48)	0.32
ACE-inhibitor/ angiotensin receptor blocker	160 (86)	36 (82)	0.53
Mineralocorticoid receptor antagonist	44 (24)	15 (34)	0.15
Diuretic	79 (42)	25 (57)	0.08
HF admission in previous 12 months	45 (25)	13 (30)	0.50

Values are median (interquartile range) or n (%). \*Signifies p<0.05; HR indicates heart rate; SBP, systolic blood pressure; DBP, diastolic blood pressure; NYHA, New York Heart Association Functional Class; AF, atrial fibrillation; HF, heart failure

**Caption 1**

Table 1: Clinical characteristics of patients according to PTT

**Figure/Table 2**

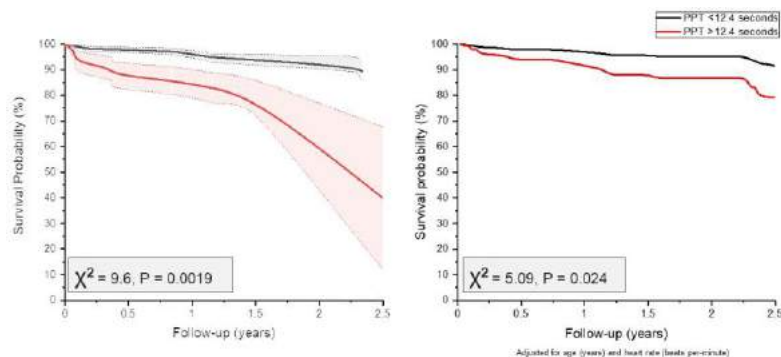
Covariate	Beta	SE	Wald	Exp(b)	95% CI of Exp(b)	P value
Age	0.7015	0.2879	5.9362	2.02	1.1470 to 3.5458	0.0148*
Sex	0.3217	0.4521	0.5063	1.38	0.5687 to 3.3464	0.4767
Hypertension	0.5479	0.4437	1.5249	1.73	0.7249 to 4.1270	0.2169
AF	-0.2245	0.464	0.234	0.80	0.3217 to 1.9839	0.6286
Heart rate	0.4418	0.1954	5.1092	1.56	1.0605 to 2.2815	0.0238*
Inducible ischaemia	0.5771	0.6288	0.8421	1.78	0.5192 to 6.1080	0.3588
Non-ischaemic LGE	-0.1249	0.4833	0.0668	0.88	0.3423 to 2.2757	0.796
Ischaemic LGE	0.9515	0.441	4.6552	2.59	1.0911 to 6.1469	0.031*
LVEDV	0.2516	0.2031	1.5351	1.29	0.8638 to 1.9149	0.2154
LV mass	0.1664	0.2111	0.6212	1.18	0.7808 to 1.7863	0.4306
LVEF	-0.6613	0.2343	7.9691	0.52	0.3261 to 0.8170	0.0048*
RVEDV	0.3841	0.196	3.8395	1.47	0.9999 to 2.1563	0.0501
RVEF	-0.484	0.2134	5.1434	0.62	0.4057 to 0.9364	0.0233*
PTT > 12.4 s	1.3733	0.4424	9.6345	3.95	1.6588 to 9.3978	0.0019*
PBVI	0.0382	0.2256	0.0287	1.039	0.6677 to 1.6167	0.8654

\*Signifies  $p \leq 0.05$ ; AF indicates atrial fibrillation; LGE, late gadolinium enhancement; LVEDV, left ventricular end diastolic volume; LVEF, left ventricular ejection fraction; RVEDV, right ventricular end diastolic volume; RVEF, right ventricular ejection fraction; PTT, pulmonary transit time; PBVI, pulmonary blood volume indexed

## Caption 2

Table 2: Univariate cox-regression analysis of predictors of MACE

## Figure 3



## Caption 3

Figure 1: MACE free survival probability according to PTT (unadjusted left and adjusted for age and heart rate right).

Speaker: J. Farley

Category: Heart Failure, Prognosis, Arterial Input Function



000276

## Quantification of In Vivo Ascending Thoracic Aortic Aneurysm Mechanical Properties using DENSE MRI: Difference in Surgical and Non-Surgical Patients

H. Dong \* (1); H. Haraldsson (1); J. Leach (1); A. Zhou, (1); M. Ballweber (1); C. Zhu, (1); Y. Xuan (2); Z. Wang (2); M. Hope (1); L. Ge (2); F. Epstein (3); D. Saloner (1); E. Tseng (2); D. Mitsouras (1)

(1) Radiology and biomedical imaging, University of California San Francisco, San Francisco, United States of America; (2) Surgery, University of California San Francisco, San Francisco, United States of America; (3) Biomedical engineering, University of Virginia, Charlottesville, United States of America

### Abstract

#### *Background:*

Rupture and dissection are life-threatening sequela of ascending thoracic aortic aneurysms (aTAAs). Current guidelines recommend surgical intervention when aTAA size exceeds 5.5cm [1]. Nonetheless, only 40% of acute type A dissections occur in aTAA that meet the diameter threshold for surgical repair [2]. Aortic stiffness is associated with various cardiovascular comorbidities as well as with mural ECM composition, rendering it relevant for predicting the progression of aneurysms [3]. Displacement encoding with stimulated echoes (DENSE) is a non-invasive phase-contrast MRI technique that measures tissue displacement during its deformation, from which local stretch or strain is derived to gauge the stiffness [4].

The aim of this patient study was to measure aTAA wall stretch using in vivo DENSE, and to establish differences in wall stretch between patients who underwent surgical repair versus those for whom surveillance was continued. Finally, we sought to study the relationship between the DENSE-derived stretch and aTAA diameter used clinically.

#### *Methods:*

Thirteen male aTAA patients were included in this prospective Institutional Review Board-approved study. Six patients underwent surgical repair while seven patients continued imaging surveillance (See Table 1). The clinical decision to proceed to surgery was made by vascular surgeons, and was independent of the data or results from this study.

Data were acquired at 1.5T or 3T (Avanto or Skyra, Siemens Healthcare, Erlangen, Germany). A single slice was prescribed orthogonal to the vessel centerline at the level of maximum aTAA diameter in the tubular portion of the ascending aorta. An ECG-triggered, respiratory navigator-gated DENSE spiral acquisition [4] measuring tissue displacement in all 3 spatial dimensions was performed to estimate the wall stretch ( $\lambda_{\text{DENSE}}$ ) between systolic and diastolic loading conditions (See Figure 1) [5]. Moreover, we calculated the aTAA to the descending thoracic aorta (DTA) wall stretch ratio:  $\gamma_{\text{DENSE}} = \lambda_{\text{DENSE}}$  of aTAA /  $\lambda_{\text{DENSE}}$  of DTA.

#### *Results:*

The mean aTAA wall stretch ( $\lambda_{\text{DENSE}}$ ) was lower for the surgical group than for the non-surgical group. However this difference was not significant ( $p=0.085$ ; Figure 2a).

The mean stretch ratio ( $\gamma_{\text{DENSE}}$ ) was statistically significantly lower in the surgical group than the non-surgical group ( $p<0.01$ ; Figure 2b), indicating aTAAs in the surgical group were stiffer than the unaffected remote descending thoracic aorta when compared to those that continued surveillance.

DENSE stretch and stretch ratio were not statistically significantly correlated with aTAA diameter (See Figure 2c and d). This adds to robust evidence that diameter may be inadequate to gauge the mechanical properties of an aneurysm.

### Conclusions:

A novel measurement, the DENSE-derived aTAA to descending aorta stretch ratio, distinguishes aTAA patients scheduled for surgical repairs. The measurement also did not correlate to aTAA diameter, demonstrating potential value toward risk stratification by providing information independent of aTAA diameter.

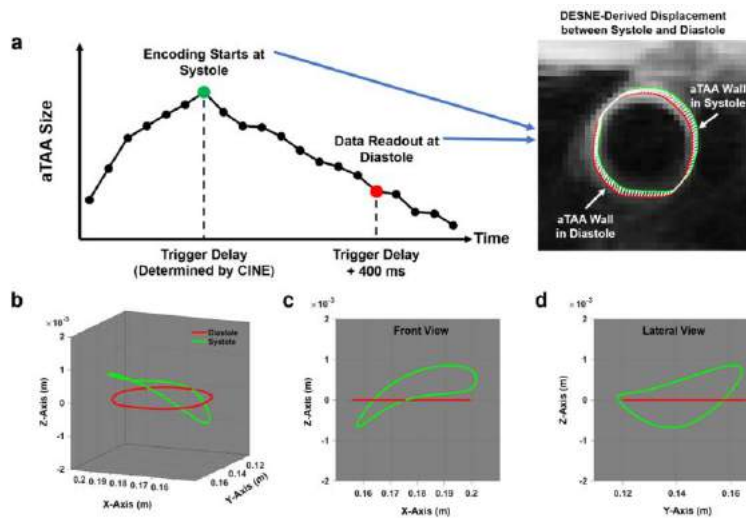
**Figure/Table 1**

Table 1. Demographics			
	Surgical Group	Non-Surgical Group	P-Value
Age	64.5±6.6	64.5±11.1	0.9
Height (cm)	182.9±12.1	182.9±5.3	1.0
Weight (kg)	90.5±20.6	81.6±10.8	0.3
BMI	26.3±4.7	25.5±3.2	0.3
BSA	2.2±0.3	2.0±0.1	0.4
aTAA Diameter	5.1±0.5	4.9±1.0	0.6
Diameter/Height	0.0289±0.0032	0.0278±0.0056	0.6
BAV	3	0	0.1
TAV	3	7	
Hypertension	4	5	1.0
Hyperlipidemia	3	5	0.6
Diabetes	0	2	0.5
Smoking	2	3	1.0

**Caption 1**

Table 1. Demographics

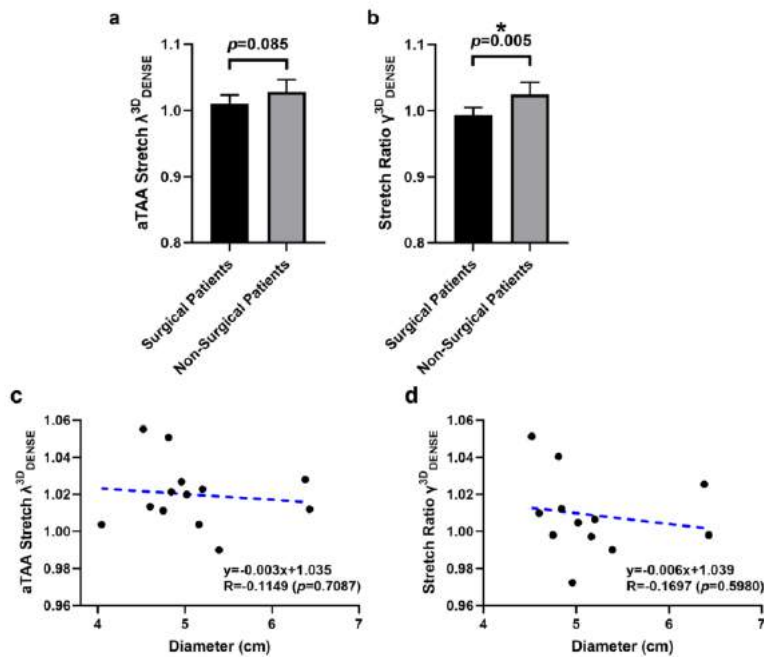
**Figure/Table 2**



**Caption 2**

Figure 1. DENSE-Derived Wall Displacement. DENSE encodes a displacement between systole and diastole to calculate aTAA wall stretch between the cardiac phases (a). Three-dimensional DENSE encoding was performed, allowing quantification of the through-plane displacement along the z-axis in addition to the in-plane displacement in the xy-plane (b-d).

**Figure 3**



**Caption 3**

Figure 2. aTAA Wall Stretch (a); aTAA to Descending Thoracic Aorta Wall Stretch Ratio (b). Correlation between aTAA Diameter and DENSE-Derived Wall Stretch (c); Correlation between aTAA Diameter and DENSE-Derived Wall Stretch Ratio (d).

### **Bibliographic References**

1. Davies RR, Goldstein LJ, Coady MA, et al. Yearly rupture or dissection rates for thoracic aortic aneurysms: simple prediction based on size. *Ann Thorac Surg.* 2002;73(1):17-28. doi:10.1016/S0003-4975(01)03236-2, 2. Hagan PG, Nienaber CA, Isselbacher EM, et al. The International Registry of Acute Aortic Dissection (IRAD): New Insights Into an Old Disease. *JAMA.* 2000;283(7):897-903. doi:10.1001/JAMA.283.7.897, 3. Dong H, Russell DS, Litsky AS, et al. In Vivo Aortic Magnetic Resonance Elastography in Abdominal Aortic Aneurysm. *Invest Radiol.* 2020;Publish Ah(7):Publish Ahead of Print. doi:10.1097/RLI.0000000000000660, 4. Zhong X, Spottiswoode BS, Meyer CH, Kramer CM, Epstein FH. Imaging three-dimensional myocardial mechanics using navigator-gated volumetric spiral cine DENSE MRI. *Magn Reson Med.* 2010;64(4):1089-1097. doi:10.1002/MRM.22503, 5. Haraldsson H, Hope M, Acevedo-Bolton G, et al. Feasibility of asymmetric stretch assessment in the ascending aortic wall with DENSE cardiovascular magnetic resonance. *J Cardiovasc Magn Reson* 2014 161. 2014;16(1):1-8. doi:10.1186/1532-429X-16-6

Speaker: H. Dong

Category: Aneurysm, DENSE, Biomarkers

000277

## Simultaneous Multislice Cardiac MR Multitasking for Non-ECG, Free-breathing, T1-T2 Myocardial Mapping

X. Mao \* (1); H.-L. Lee, (1); T. Cao (1); F. Han (2); Y. Xie (1); D. Li (1); A. Christodoulou (1)

(1) Biomedical imaging research institute, Cedars-Sinai Medical Center, Los Angeles, United States of America; (2) Mr r&d and collaboration, Siemens Medical Solutions USA, Inc, Los Angeles, United States of America

### Abstract

**Background:** Myocardial T1/T2 mapping is promising for assessing focal and diffuse myocardial pathologies, but it takes 6 breath holds to obtain 3 T1 and 3 T2 short-axis slices (roughly 6 minutes). CMR Multitasking has shown promise for non-ECG and free-breathing T1-T2 mapping, performing 2D single-slice imaging in a 1.5 min scan<sup>1</sup>. Simultaneous multi-slice (SMS) imaging<sup>2</sup> is a powerful technique to efficiently expand slice coverage without incurring the full-time penalty of sequential slice acquisition. In this work, we integrated radial SMS and 3-slice self-gating/training data acquisition into T1-T2 Multitasking to provide co-registered multiparametric maps in a 3-min, free-breathing, non-ECG MRI scan. We evaluated its performance in a phantom and n=10 healthy volunteers.

**Methods:** Sequence Design: Interleaved inversion recovery (IR) and T2prep-IR pulses were employed to generate the T1 and T2 contrasts (Figure 1). A CAIPIRINHA-type phase modulation pattern was applied to the excitation pulses to achieve a multi-band factor of 3. A continuous-acquisition radial FLASH sequence alternated between imaging data and training data in successive readouts. Imaging data were incremented by the golden angle and cycled between the 3 phase modulation patterns; training data were collected at the 0° radial spoke from all 3 slices with no phase modulation. The excitation flip angle alternated between 3° and 10° in successive IR periods to allow B1+ corrected T1 mapping<sup>3</sup>.

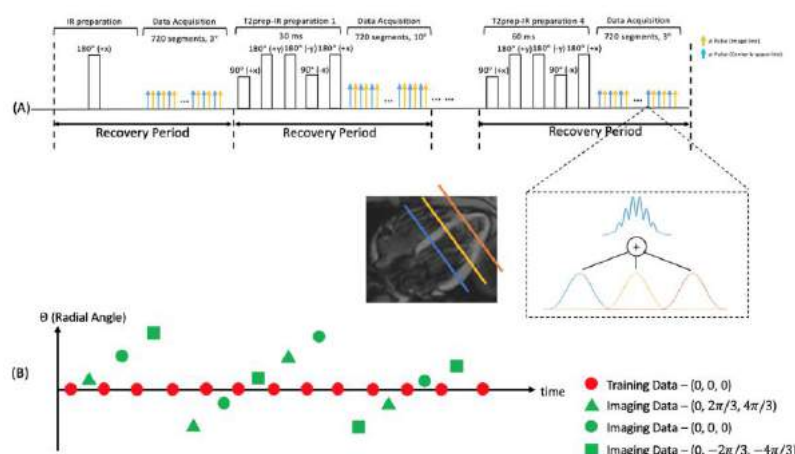
Data Collection: An ISMRM/NIST phantom and ten healthy consenting volunteers (3 males, 7 females, age 36.7±12.3) were imaged on a 3T scanner (MAGNETOM Vida, Siemens Healthcare). Multitasking pulse sequence parameters were TR/TE=3.5 ms/1.7 ms, recovery period=2.5 s, FOV=270x270mm<sup>2</sup>, resolution=1.7x1.7x8.0 mm<sup>3</sup>, 3 slices, scan time=3 min, 20 cardiac bins, 6 respiratory bins. MOLLI and T2-prep FLASH measurements (1.4x1.4x8.0 mm<sup>3</sup>) were acquired at both systole and diastole using an end-expiration breath-hold. For the phantom study, the IRSE T1 and SE T2 (1.7x1.7x8.0 mm<sup>3</sup>) were used as references.

**Results:** Multitasking-SMS measurements and IRSE/SE measurements showed excellent agreement with ICC=0.986, and 0.999 for T1 and T2, respectively (Figure 2). Multitasking-SMS overestimated T1 values in the range of T1>2000ms (higher than the myocardial T1 range), but achieved greater agreement (ICC=0.997) in the more relevant range of T1≤2000ms. 2D Multitasking-SMS T1 and T2 mapping results from one healthy subject are shown in Figure 3A-B. Figure 3C further shows the T1/T2 values in 16 AHA segments across all 10 healthy subjects in the bull's eye plot. Bland-Altman plots show the bias and limits of agreement between Multitasking-SMS and reference measurements (Figure 3D) and repeated Multitasking-SMS measurements (Figure 3E). Multitasking-SMS T1/T2 maps reported slightly higher myocardial T1/T2 values (1275±91.1/46.8±2.7 ms) than the reference T1/T2

values ( $1248 \pm 22.9 / 43.2 \pm 1.5$  ms) in 10 healthy controls. Multitasking T1/T2 measurements were repeatable with a coefficient of variation of 6.3% and 5.1%, respectively.

**Conclusion:** Co-registered T1 and T2 maps were simultaneously acquired at 3 short-axis slices using an SMS-accelerated Multitasking technique in a 3-min scan. The myocardial T1, T2 values were slightly higher than the reference MOLLI and T2-prep FLASH measurements but were still within the reported normal range<sup>4</sup>. This method shows potential for reducing exam time for quantitative CMR without ECG or breath-holds.

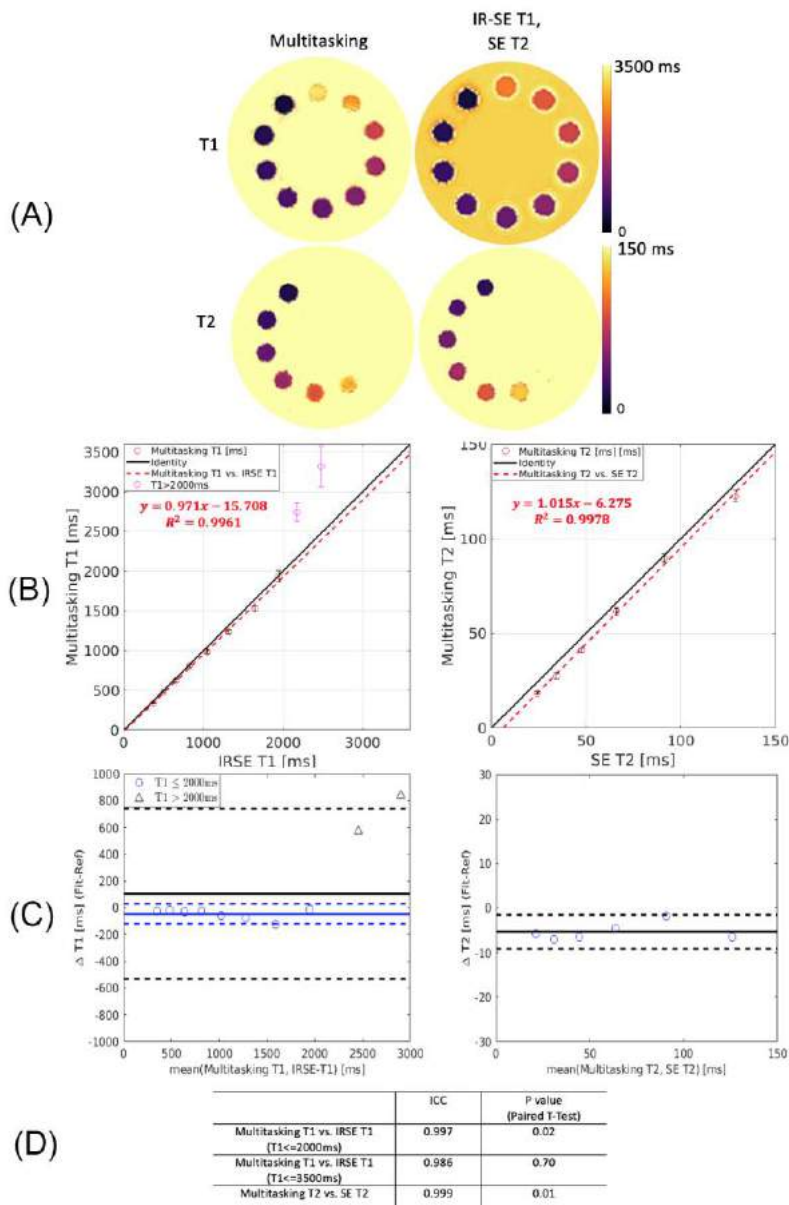
**Figure/Table 1**



**Caption 1**

**Figure. 1** Schematic diagram of the proposed 2D MR Multitasking sequence with SMS-acceleration, where 5 different preparations (0, 30ms, 40ms, 50ms, 60ms) are repeated throughout the scan. Each FLASH excitation pulse can excite 3 slices simultaneously.

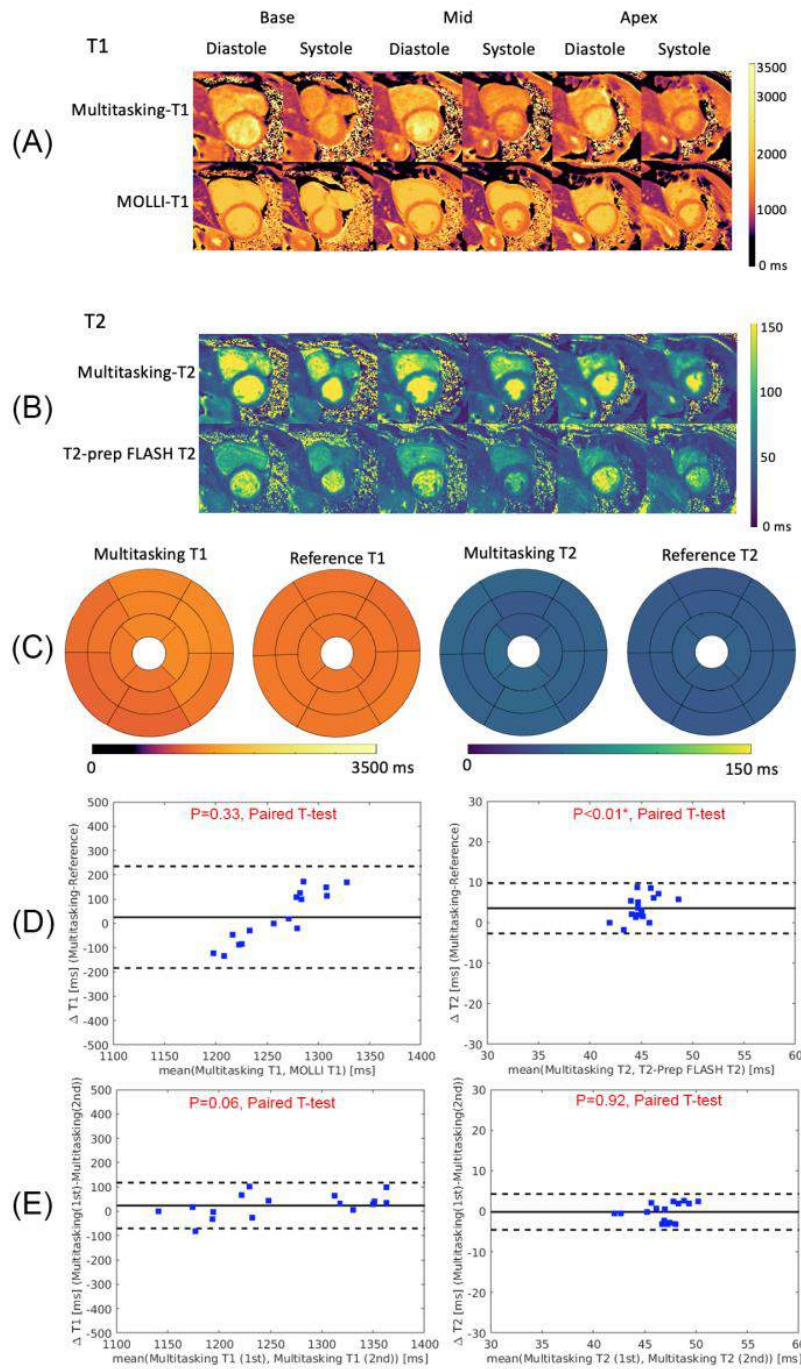
**Figure/Table 2**



## Caption 2

**Figure. 2** A, T1/T2 measurements of the phantom using Multitasking-SMS and reference methods B, Linear regression between Multitasking-SMS and reference (T1<=2000ms, T2<=150ms). C, The bias and limits of agreement was  $-62.8 \pm 118.2$ ms (T1<=2000ms) for T1 and  $5.3 \pm 3.8$ ms for T2 (T2<=150ms). D, ICC and Paired T-test results.

## Figure 3



**Caption 3**

**Figure. 3** A-B, 2D Multitasking-SMS and reference T1/T2 maps of the same volunteer (F, 40). C, The 16-segment AHA model for the Multitasking-SMS T1/T2 maps and the reference T1/T2 maps in all 10 scanned subjects. D-E, Bland-Altman plots between Multitasking-SMS and reference measurements, and repeated Multitasking-SMS measurements.



## **Bibliographic References**

[4] Weingärtner, S., Meßner, N. M., Budjan, J., Loßnitzer, D., Mattler, U., Papavassiliu, T., ... & Schad, L. R. (2017). Myocardial T1-mapping at 3T using saturation-recovery: reference values, precision and comparison with MOLLI. *J Cardiovasc Mag Reson*, 18(1), 84., [3] Serry, F., Ma, S., Mao, X., Han, F., Xie, Y., Han, H., Li, D., & Christodoulou, A. (2021). Dual flip angle (2FA) IR-FLASH with spin history mapping for B1+-insensitive T1 mapping: Application to T1 cardiovascular magnetic resonance multitasking, *Magn Reson Med*, doi: 10.1002/mrm.28935, [2] Yutzy, S. R., Seiberlich, N., Duerk, J. L., & Griswold, M. A. (2011). Improvements in multislice parallel imaging using radial CAIPIRINHA. *Magn Reson Med*, 65(6), 1630-1637., [1] Christodoulou, A. G., Shaw, J. L., Nguyen, C., Yang, Q., Xie, Y., Wang, N., & Li, D. (2018). Magnetic resonance multitasking for motion-resolved quantitative cardiovascular imaging. *Nature Biomed Eng*, 2(4), 215-226.

Speaker: X. Mao

Category: Simultaneous Multislice Excitation, Parametric Mapping, Free Breathing

**000278**

## **Multiparametric CMR with T1/T2 Mapping in Friedreich's Ataxia**

V. Chan \* (1); E. Nguyen (1); G. R. Karur (1); P. Thavendiranathan (2); R. Wald (2); K. Hanneman (1)

(1) Joint Department of Medical Imaging, University Health Network, Toronto, Canada; (2) Division of cardiology, University Health Network, Toronto, Canada

### **Abstract**

#### Description of Clinical Presentation

A 26-year-old male with genetically-proven Friedreich's ataxia (FA) diagnosed 17 years ago was referred for cardiac MRI. Past medical history was significant for obesity (BSA 2.24m<sup>2</sup>, BMI 33.3 kg/m<sup>2</sup>) and ataxia requiring ambulation with a walker. He had no chest pain, shortness of breath, syncope or palpitations. An electrocardiogram in 2014 demonstrated normal sinus rhythm with possible left ventricular hypertrophy (LVH).

#### Diagnostic Techniques and Their Most Important Findings

Several cardiac MRI studies between 2014 and 2021 demonstrated normal biventricular size and global systolic function. However, there was slight progression of concentric LVH that worsened over time. The maximal end diastolic wall thickness at the basal to mid interventricular septum had progressed from 13 mm (2014), to 14 mm (2017) and finally to 16 mm (2021). No late gadolinium enhancement was identified to suggest the presence of myocardial fibrosis, scar or infiltration. However, native T1 and T2 values were both low, likely reflecting myocardial iron accumulation in the setting of FA.

#### Learning Points from this case

FA is a rare early onset degenerative disease with an autosomal recessive pattern caused by an insufficient amount of the nuclear-encoded mitochondrial protein frataxin, whose deficit results in iron metabolism dysregulation and mitochondrial dysfunction (1). In FA, decreased iron-sulphur cluster and heme formation leads to mitochondrial iron accumulation, and ensuing oxidative damage that primarily affects sensory neurons, endocrine glands and the myocardium (2). Cardiomyopathy is the leading cause of death (3). Cardiac findings on imaging include progressive myocardial thickening and declining LV ejection fraction (4). FA cardiomyopathy is unlike hemochromatosis in which the heart can accumulate large amounts of iron before manifesting cardiac failure (5). Retention of iron in inflammatory cells may be more important in the pathogenesis of FA cardiomyopathy than the small granular inclusions in cardiomyocytes or the amount of total heart iron. Where myocardial iron overload in hemochromatosis causes fibrosis without inflammation (5), attachment of monocytes to, and penetration of cardiomyocyte plasma membranes with strong iron expression in the inflammatory infiltrate may be unique for FA cardiomyopathy. Cardiac MRI plays an important role in assessing patients with FA. Besides being able to accurately and reproducibly measure biventricular volumes, ventricular systolic function and LV mass,

parametric mapping techniques can quantify myocardial iron accumulation. Native T1 values are typically elevated in the setting of fibrosis, infiltration and edema, and are low in the presence of fat/lipids and iron. High native T2 values are more specific for myocardial edema while values are low in the setting of iron overload. Therefore combined T1 and T2 mapping provides complementary information and is useful in characterizing myocardial tissue changes. Cardiac MRI has an established role in the assessment of ventricular volumes, function and fibrosis in patients with FA. Parametric mapping may add value by quantifying myocardial iron accumulation. Further study is needed to evaluate the prognostic significance of these findings.

## **Figure/Table 1**

### **Caption 1**

The most recent cardiac MRI in 2021 was performed at 3T and demonstrated (A) concentric left ventricular hypertrophy with maximum wall thickness of 16 mm on cine SSFP, (B) no late gadolinium enhancement, and (C) low T1 (1100 ms) and (D) T2 values (33 ms) in keeping with myocardial iron.

### **Bibliographic References**

5. Olson LJ, et al. Cardiac iron deposition in idiopathic hemochromatosis: Histological and analtic assessment of 14 hearts from autopsy. J Am Coll Cardiol 10:1239-43., 4. Michael S, et al. Iron and iron-responsive proteins in the cardiomyopathy of Friedreich's ataxia, Cerebellum. 2006;5:257-67., 3. Andermann E et al. Genetic and family studies in Friedreich's ataxia. Can J Neurol Sci 1976;3:287-301, 2. Boddaert N et al. Selective iron cheleation in Friedreich's ataxia: Biologic and clinical implications. Blood, 2007, 110(1): 401-8., 1. Llorens JV, et al. The role of iron in Friedreich's Ataxia: Insights from studies in human tissues and cellular and animal models. Frontiers in Neuroscience, 2019;13:75.

Speaker: V. Chan

Category: Parametric Mapping, Native T1, T2

**000280**

## **Aortic Regurgitation Staging with Transthoracic Echocardiogram vs Cardiac MRI**

O. Jandali \* (1); J. Gonzalez (2); G. Wesbey (3); J. Allem (2); A. Robinson (2)

(1) Internal Medicine GME, Scripps Health, La Jolla, United States of America; (2) Cardiology, Scripps Clinic, La Jolla, United States of America; (3) Radiology, Scripps Clinic, La Jolla, United States of America

### **Abstract**

#### **Clinical Presentation:**

This is an 82 year old male with a past medical history of Essential Hypertension, 1st Degree AV Block, non-specific Intraventricular conduction delay on remote EKG, and Hyperlipidemia who presented for his annual primary care visit reporting atypical chest pain. Physical exam was notable for diastolic murmur at the left sternal border. EKG demonstrated new left bundle branch block.

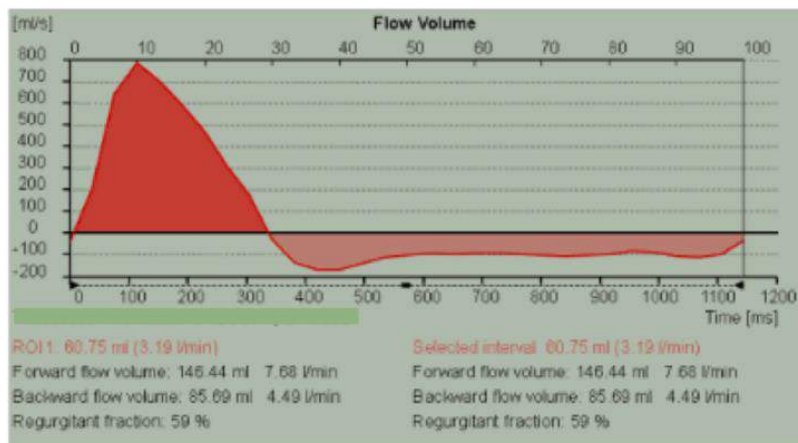
#### **Diagnostic Techniques and Their Most Important Findings**

Transthoracic Echocardiogram showed moderately dilated LV with mildly decreased LV EF 46% with global hypokinesis and visually moderate aortic insufficiency with a dilated ascending aorta. Coronary Angiogram showed no obstructive CAD. Cardiac MRI confirmed mildly reduced LV systolic function, LVEF 47%, clarified the LV cavity enlargement as severe and demonstrated severe aortic regurgitation with regurgitant fraction of 59% (Figure 1) and severe LV dilation (LVEDVI 201 ml/m<sup>2</sup>). It additionally showed akinesia and thinning of basal infero-lateral wall consistent with prior MI with nonviable complete transmural LGE of the basal infero-lateral wall segment as well as ascending aorta aneurysmal dilation, and septal motion consistent with LBBB.

#### **Learning Points from This Case**

This is a case where TTE identified moderate LV enlargement but underestimated both the severity of underlying aortic regurgitation and LVE. CMR was able to clarify the severity of the aortic regurgitation. CMR should be considered when staging AR, particularly in cases where the severity of aortic regurgitation is unclear or borderline.

#### **Figure/Table 1**



### Caption 1

Phase Contrast CMR Velocity-Time Integral calculation of Aortic valve regurgitant volume (VENC=200cm/sec)

Speaker: O. Jandali

Category: Aortic Regurgitation, Left Ventricle, Valvular Heart Disease

**000281**

## **Cardiac Magnetic Resonance for Acute Cardiac Transplant Rejection: Imaging-Pathologic Correlation**

P. Reddy \* (1); S. Thomas (2); P. Araoz, (3)

(1) Department of cardiovascular medicine, Mayo Clinic, Rochester, United States of America; (2) Department of pathology, Mayo Clinic, Rochester, United States of America; (3) Department of radiology, Mayo Clinic, Rochester, United States of America

### **Abstract**

#### **Clinical Presentation:**

49-year-old female who underwent heart transplantation in November 2012 for familial non-ischemic lamin-related cardiomyopathy. All endomyocardial biopsies post-transplant were only remarkable for grade 1R rejection without serious clinical complications. On routine follow-up echocardiogram in November 2020, she was notably tachycardic (145) bpm with increased wall thickness (13 mm), which prompted donor-specific antibody testing. The antibody levels were noted to be significantly elevated at 26,000, compared to less than 300 on her prior visit. Endomyocardial biopsy was then performed. Although the biopsy was suspicious for antibody-mediated rejection based on complement immunofluorescence studies, the tissue was scant and largely obscured by fibrosis deeming it non-diagnostic. She was then admitted for a repeat biopsy and had a cardiac MRI during that hospitalization. Her biopsy confirmed grade 2 antibody-mediated rejection. She was treated with plasmapheresis and high-dose steroids. Despite treatment, her antibody levels did not decrease. Repeat MRI was performed one week later and showed decreased ejection fraction (28%) along with diffuse myocardial edema. Subepicardial delayed enhancement (DE) and a subendocardial DE in the inferolateral segment were noted. Her immunosuppression was further adjusted with an increase in prednisone and initiation of rituximab.

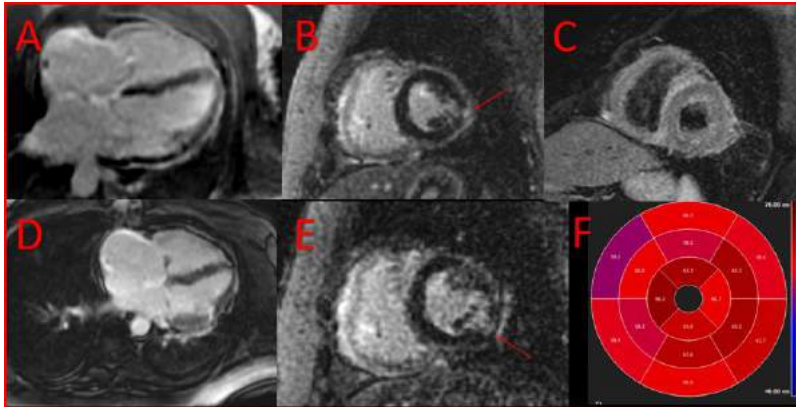
#### **Diagnostic Techniques:**

This case highlights the use of cardiac MRI in monitoring and identifying transplant rejection with pathologic correlation. Serial longitudinal MRI performed for this patient over the course of 6 months emphasize the changes seen with acute allograft rejection. Myocardial edema on T2 mapping was diffusely elevated on her initial presentation on 11/2020. These changes persisted on 1-month follow-up and later resolved on the MRI from 05/2021. Her ejection fraction also normalized (55%) on the most recent study. Delayed enhancement remained the same, including the vascular scar from allograft vasculopathy in the inferolateral wall. Figures 1-3.

#### **Learning points:**

1. T2 mapping for assessment of myocardial edema has evidence in longitudinal follow-up of transplant rejection<sup>1</sup>
2. Delayed enhancement changes may persist despite clinical improvement.
3. Due to the patchy nature of transplant rejection, a right ventricular endomyocardial biopsy may not always be representative of the underlying process. MRI imaging may fill this gap.
4. Serial cardiac MRI may decrease the need for endomyocardial biopsy in patients recovering from rejection on intensified immunosuppression or may be an adequate substitute if a biopsy is contraindicated.

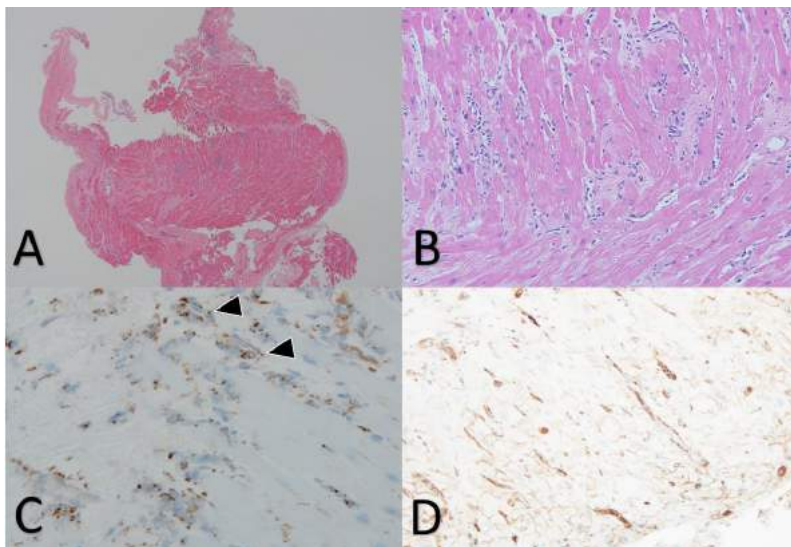
**Figure/Table 1**



**Caption 1**

**Figure 1:** Cardiac MRI 11/16/20 (A-C) **A.** 4-chamber DE showing mild pericardial enhancement. **B.** Short-axis DE. **C:** Qualitative mild diffuse edema on T2-weighted imaging. Cardiac MRI 11/20/20 (D-F) **D/E.** New area of subendocardial vascular DE. **F.** T2 Parametric map - diffusely elevated

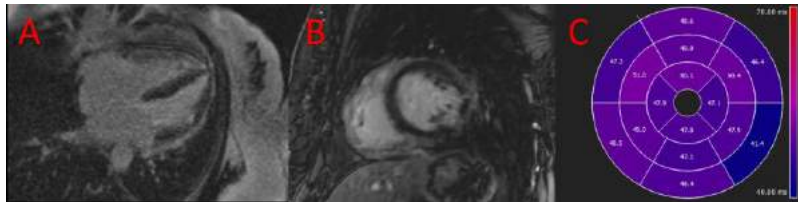
**Figure/Table 2**



## Caption 2

**Figure 2:** Diagnostic endomyocardial biopsy **A.** low power view of interstitium and foci of chronic inflammation, **B.** high power pattern of hypercellular interstitium and endothelial swelling, **C.** CD68 immunohistochemistry highlighting intravascular macrophages (arrowheads), **D.** C4d immunohistochemistry highlighting capillary complement deposition.

## Figure 3



## Caption 3

**Figure 3:** Cardiac MRI 05/2021 **A/B.** Persistent DE in the inferolateral segments. **C.** T2 parametric map with normalized T2 myocardial values.

## Bibliographic References

2. Vermes E, Pantaléon C, Auvet A, et al. Cardiovascular magnetic resonance in heart transplant patients: diagnostic value of quantitative tissue markers: T2 mapping and extracellular volume fraction, for acute rejection diagnosis. J Cardiovasc Magn Reson. 2018;20(1):59. Published 2018 Aug 27. doi:10.1186/s12968-018-0480-9, 1. Han D, Miller RJH, Otaki Y, et al. Diagnostic Accuracy of Cardiovascular Magnetic Resonance for Cardiac Transplant Rejection: A Meta-analysis [published online ahead of print, 2021 Jul 7]. JACC Cardiovasc Imaging. 2021;S1936-878X(21)00427-7. doi:10.1016/j.jcmg.2021.05.008

Speaker: P. Reddy

Category: Heart Transplant, Cardiac Allograft Vasculopathy, Heart Failure



000282

## Use of Right Ventricular Diastolic Wall Motion to measure Hemodynamic Forces in repaired Tetralogy of Fallot

Y.-H. Loke \* (1); F. Capuano (2); S. Kollar (3); P. Kitslaar (4); M. Cibis (4); E. Balaras (5); J. Reiber (4); G. Pedrizzetti (6); L. Olivieri (7)

(1) Cardiology, Children's National Hospital, Michigan Avenue Northwest, Washington, DC, USA, Washington, United States of America; (2) Department of fluid mechanics, Universidad Politècnica de Catalunya, Barcelona, Spain; (3) Pediatric cardiology, Children's National Hospital, Washington, United States of America; (4) Medical imaging, Medis Medical Imaging, Leiden, Netherlands; (5) Laboratory for computational physics and fluid mechanics, School of Engineering and Applied Science, Washington, United States of America; (6) Dipartimento di ingegneria e architettura, University of Trieste, Trieste, Italy; (7) Cardiology, Children's National Hospital, Washington, United States of America

### Abstract

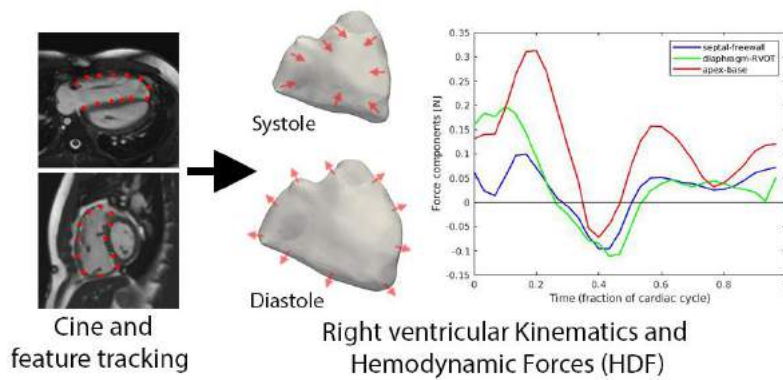
**Background:** Patients with repaired Tetralogy of Fallot (rTOF) will develop right ventricle (RV) dysfunction from chronic pulmonary insufficiency (PI). Cardiac magnetic resonance (CMR) biomarkers informs timing of pulmonary valve replacement (PVR), but do not clarify the direct impact of PI on myocardial biomechanics. 4D flow studies have shown that RV hemodynamic forces (HDF) are altered in rTOF. In this study, we derived HDF in rTOF, exclusively using RV wall motion from conventional cine.

**Methods:** This was a retrospective study using CMR of a cohort of rTOF patients and normal controls. Feature-tracking (QStrain, Medis) was used to capture RV wall motion from cine imaging. A novel diffeomorphic mapping technique (Figure 1) was used to calculate 3D RV kinematic models and global HDF vector generated throughout the cardiac cycle. The magnitude of HDF in diastole was further separated into three directions for analysis: Apical-to-Basal, Septum-to-Free Wall, and Right Ventricular Outflow Tract (RVOT)-to-Diaphragm. HDF parameters were indexed to RV volume. Conventional CMR parameters including RV ejection fraction (RV-EF%) and pulmonary regurgitant fraction (RF%) were collected.

**Results:** 68 rTOF studies (body surface area  $1.67 \pm 0.37$ , age  $21 \pm 11$ ) and 20 control studies (body surface area  $1.5 \pm 0.54$ , age  $14 \pm 6$ ) were included. The rTOF cohort had RV-EF%  $49 \pm 6\%$ , RF%  $27 \pm 17\%$ , and RV end-diastolic volume  $137 \pm 75$  mL/m<sup>2</sup>. When compared to controls, rTOF patients had increased HDF in all three directions (Figure 2). RF% correlated with both the Apical-to-Basal and RVOT-to-Diaphragm HDF in diastole (Figure 3). RV-EF% modestly correlated with Apical-to-Basal HDF ( $r = 0.2438$ ,  $p = 0.045$ ) and Septum-to-Free Wall HDF ( $r = 0.2703$ ,  $p = 0.0258$ ).

**Conclusions:** rTOF have altered HDF, a global parameter that can be captured by RV diastolic wall motion without need to analyze 4D flow details. PI in rTOF patients is correlated to diastolic HDF exerted along the direction of the basal and RVOT directions. Quantification of HDF further specifies the impact of PI on RV myocardial biomechanics and may be a potential biomarker to inform PVR timing.

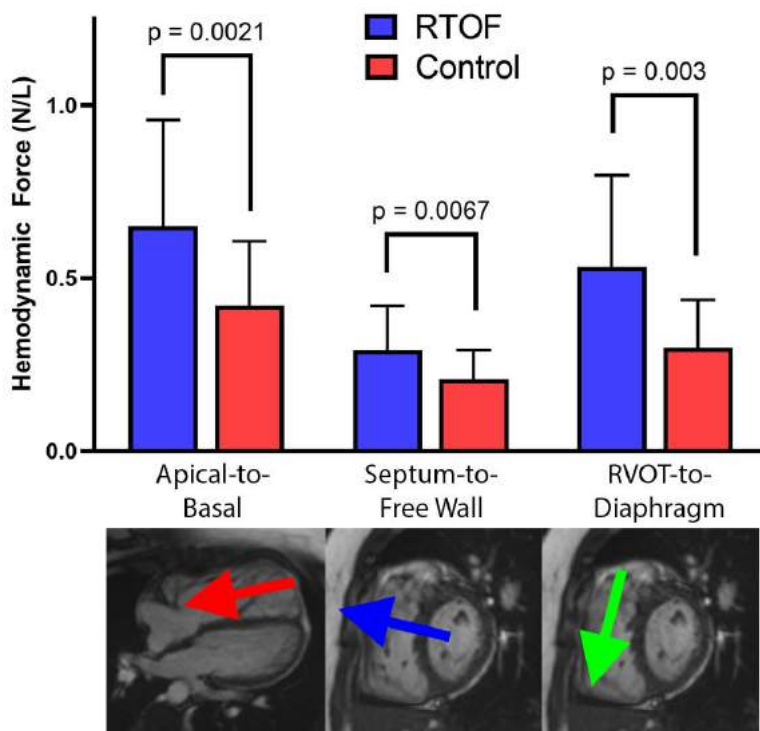
### Figure/Table 1



**Caption 1**

Figure 1. Methodology to calculate the Hemodynamic Forces (HDF) in the right ventricle.

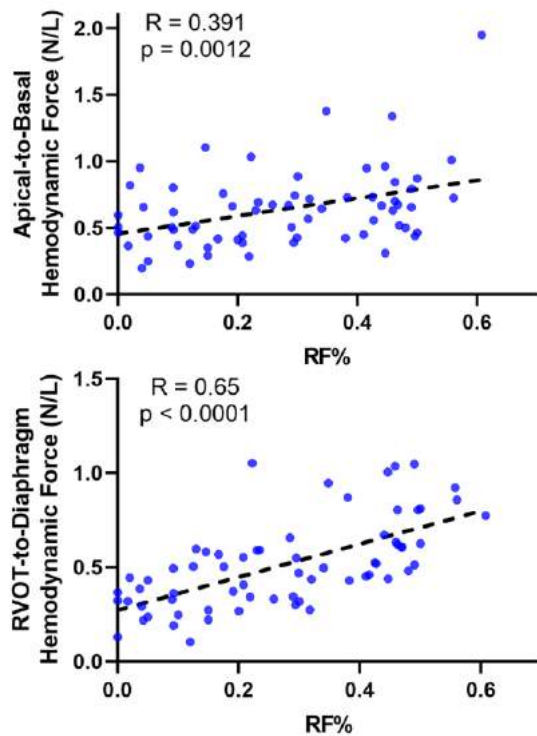
**Figure/Table 2**



**Caption 2**

Figure 2. Repaired Tetralogy of Fallot (RTOF) patients have higher hemodynamic forces in apical-to-basal, septum-to-free wall and right ventricular outflow tract (RVOT)-to-diaphragm directions.

**Figure 3**



**Caption 3**

Figure 3. Pulmonary regurgitant fraction (RF%) correlated with higher hemodynamic forces in apical-to-basal and right ventricular outflow tract (RVOT)-to-diaphragm directions.

### **Bibliographic References**

Pia Sjöberg et al. Altered biventricular hemodynamic forces in patients with repaired tetralogy of Fallot and right ventricular volume overload because of pulmonary regurgitation. *Am J Physiol Heart Circ Physiol* . 2018 Dec 1;315(6):H1691-H1702. doi: 10.1152/ajpheart.00330.2018. Epub 2018 Sep 28.

Speaker: Y.-H. Loke

Category: Tetralogy of Fallot, Cardiac Strain, Right Ventricle

**Microvascular Function in Patients Recovered from COVID-19 Infection**

I. Karagodin \* (1); S. Wang (2); A. Singh, (2); L. Landeras, (3); D. Gorre, (3); H. Patel, (2); N. Alvi (4); J. Gutbrod, (2); M. Tang, (2); H. Wang (5); M. Benovoy, (6); M. Janich (5); H. Benjamin, (7); J. Chung, (3); A. R. Patel (8)

(1) , NorthShore Evanston Hospital, Evanston, United States of America; (2) Cardiology, UChicago Medicine, Chicago, United States of America; (3) Radiology, UChicago Medicine, Chicago, United States of America; (4) Cardiovascular medicine, AMITA Health Adventist Medical Center Hinsdale, Hinsdale, United States of America; (5) Cardiac imaging, GE Healthcare, Chicago, United States of America; (6) Cardiac imaging, Circle Cardiovascular Imaging, Calgary, Canada; (7) Orthopedic surgery, UChicago Medicine, Chicago, United States of America; (8) Medicine and radiology, UChicago Medicine, Chicago, United States of America

**Abstract**

**Background:** The novel SARS-CoV-2 virus, which leads to coronavirus 2019 (COVID-19) infection, is known to cause vascular dysfunction via a host of mechanisms including platelet and endothelial activation. While COVID-19 is known to adversely affect the cardiovascular system, there is a paucity of data relating to its effects on myocardial perfusion. In this prospective, single-center, cross-sectional cohort study, we aimed to use multiparametric cardiac magnetic resonance (CMR) imaging to investigate differences in qualitative and quantitative myocardial perfusion (a biomarker of microvascular function) in patients recovered from COVID-19 infection compared to non-infected control subjects.

**Methods:** We conducted a prospective, single-center study of 27 patients recovered from COVID-19 infection (mean 165 +/- 103 days from PCR-confirmed diagnosis) and 12 controls using multiparametric regadenoson-based stress perfusion CMR as the primary imaging modality. All patients underwent echocardiograms within one month of CMR. CMR image acquisition and analysis were performed per Society of Cardiovascular Magnetic Resonance (SCMR) guidelines, with LGE interpretation performed by two blinded CMR experts. Discrepancies were arbitrated by a third blinded expert. LGE in the right ventricular insertion point was considered as negative. COVID subjects with native T1, T2, and extra-cellular volume fraction (ECV) values more than 2 standard deviations (SD) from control subject values were classified as abnormal. Myocardial blood flow during rest and stress was quantified via the Fermi deconvolution method using CFI42 software (Circle Cardiovascular Imaging; Alberta, CA) and corrected for resting rate-pressure product. Quantitative and qualitative myocardial perfusion, T1 and T2 relaxation times, ECV, electrocardiographic and echocardiographic abnormalities, and prevalence of LGE were compared between groups.

**Results:** There were no significant differences in terms of age, gender, BMI, or co-morbidities between cases and controls. No significant differences were observed in myocardial perfusion parameters: resting myocardial blood flow (MBF) 0.87 +/- 0.37 vs. 0.80 +/- 0.45 mL/g/min, p = 0.66; stress MBF 2.42 +/- 0.76 vs. 2.37 +/- 0.91 mL/g/min, p = 0.87; global myocardial perfusion reserve (MPR) 3.14 +/- 1.0 vs. 4.0 +/- 2.3, p = 0.18; normalized resting MBF 1.05 +/- 0.37 vs. 0.85 +/- 0.38 mL/g/min, p = 0.17; normalized stress MBF 3.06

+/- 1.16 vs. 2.65 +/- 1.04 mL/g/min,  $p = 0.35$ ; and normalized resting MPR 4.21 +/- 2.26 vs. 4.79 +/- 3.18,  $p = 0.56$ . In addition, there were no significant differences in T1 time (1020 +/- 71 vs. 1011 +/- 57 ms,  $p = 0.69$ ), T2 time (52.1 +/- 3.3 ms vs. 53.3 +/- 5.0 ms,  $p = 0.41$ ), ECV (29.8 +/- 5.5% vs. 30.0 +/- 4.1%,  $p = 0.92$ ), prevalence of qualitative perfusion defects (4/27 = 15% vs. 1/12 = 8%,  $p = 1.0$ ), LGE (6/27 = 22% vs. 1/12 = 8%,  $p = 0.4$ ), electrocardiographic abnormalities (5/27 = 19% vs. 2/12 = 17%,  $p = 1.0$ ), or echocardiographic abnormalities (5/25 = 20% vs. 1/7 = 14%,  $p = 1.0$ ) (**Table 1**).

**Conclusion:** Patients who have recovered from COVID-19 infection do not demonstrate significant quantitative or qualitative differences in myocardial perfusion compared to non-infected controls, even when normalized for blood pressure and heart rate. These results suggest that either: a) coronary vasculature is able to maintain homeostasis using autoregulatory mechanisms despite endothelial involvement of SARS CoV-2 virus, or b) endothelial function normalizes over time following recovery from COVID-19 infection.

**Figure/Table 1**

**Table 1**

Characteristic	COVID-Recovered Patients (n = 27)	Controls (n = 12)	p
<b>Patient Characteristics</b>			
Age, years	41.4 +/- 14.1	48.3 +/- 14.7	0.17
Gender (% female)	52% (14/27)	17% (2/12)	0.08
Body Mass Index (BMI)	30.0 +/- 7.1	26.3 +/- 4.1	0.11
Coronary Artery Disease	13% (3/27)	8% (1/12)	1.0
Diabetes Mellitus	15% (4/27)	17% (2/12)	1.0
Hypertension	30% (8/27)	25% (3/12)	1.0
Chronic Kidney Disease	7% (2/27)	8% (1/12)	1.0
Hyperlipidemia	22% (6/27)	50% (6/12)	0.13
Underlying Lung Disease	19% (5/27)	8% (1/12)	0.65
<b>CMR Findings</b>			
LVEF (%)	57.8 +/- 8.6	59.1 +/- 8.2	0.66
RVEF (%)	52.2 +/- 6.5	55.3 +/- 4.1	0.13

T1 time (ms)	1020 +/- 71	1011 +/- 57	0.69
T2 time (ms)	52.1 +/- 3.3	53.3 +/- 5.0	0.41
Extracellular Volume (ECV) (%)	29.8 +/- 5.5	30.0 +/- 4.1	0.92
Abnormal T1 (%) (>2SD from control)	4/27 (15%)	N/A	N/A
Abnormal T2 (%) (>2SD from control)	0/27 (0%)	N/A	N/A
Abnormal ECV (%) (>2SD from control)	3/27 (11%)	N/A	N/A
Late Gadolinium Enhancement (LGE)	22% (6/27)*	8% (1/12)	0.40
Qualitative Perfusion Defects	15% (4/27)**	8% (1/12)	1.0
<b>Quantitative Myocardial Perfusion Parameters</b>			
Rest MBF (mL/g/min)	0.87 +/- 0.37	0.80 +/- 0.45	0.66
Stress MBF (mL/g/min)	2.42 +/- 0.76	2.37 +/- 0.91	0.87
MPR	3.14 +/- 1.0	4.0 +/- 2.3	0.18
Normalized Rest MBF (mL/g/min)***	1.05 +/- 0.37	0.85 +/- 0.38	0.17
Normalized Stress MBF (mL/g/min)***	3.06 +/- 1.16	2.65 +/- 1.04	0.35
Normalized MPR***	4.21 +/- 2.26	4.79 +/- 3.18	0.56
<b>Laboratory, Electrocardiographic, and Echocardiographic Findings</b>			
High-Sensitivity Troponin (ng/L)	9.1 +/- 5.5	7.1 +/- 1.7	0.37
NT-pro-B-type natriuretic peptide (ntproBNP) (pg/mL)	74.4 +/- 119.3	42.1 +/- 53.8	0.50
High-Sensitivity C-Reactive Protein (CRP) (mg/L)	3.3 +/- 5.6	1.4 +/- 1.3	0.43
D-Dimer (ug/mL)	0.58 +/- 0.97	0.33 +/- 0.06	0.58
Electrocardiographic Abnormalities	19% (5/27)	17% (2/12)	1.0
Echocardiographic Abnormalities	20% (5/25)	14% (1/7)	1.0

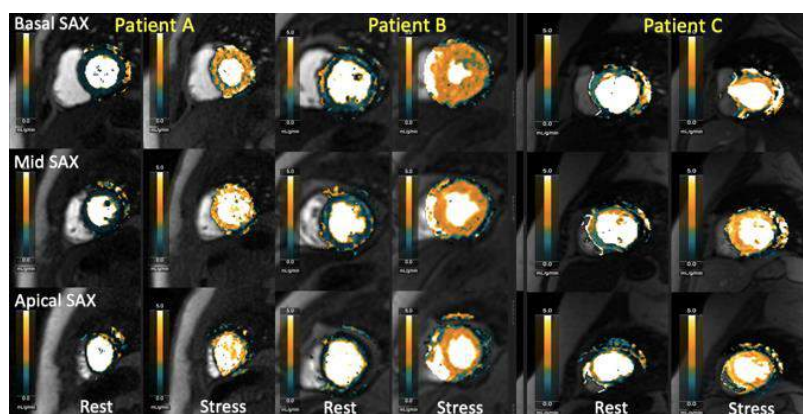
Abbreviations: CMR = cardiac magnetic resonance; LVEF = left ventricular ejection fraction, RVEF = right ventricular ejection fraction, LGE = late gadolinium enhancement, MBF = myocardial blood flow, MPR = myocardial perfusion reserve

\*Two patients with LGE likely attributed to history of myocardial infarction rather than COVID-19 related injury

\*\*Two patients with perfusion defects likely attributed to history of CAD rather than COVID-19 related injury

\*\*\*Normalized to resting rate pressure product to account for resting hemodynamic impact on myocardial blood flow and perfusion reserve.

**Figure/Table 2**



**Caption 2**

Representative examples of (A) Healthy Control with normal MBF and MPR, B) COVID-19 recovered patient with no history of CAD with normal MBF and MPR, and C) COVID-19 recovered patient with history of ischemic cardiomyopathy with low rest and stress MBF in the mid to basal inferior and inferolateral walls. SAX = short-axis

Speaker: I. Karagodin

Category: Perfusion, Small Vessel Disease, Vascular Abnormality

000286

## **4D Flow MRI-Enhanced Computational Fluid Dynamics for Flow Dynamics Assessment in Patients Pre- and Post-Aortic Coarctation Repair**

L. Shahid \* (1); J. Rice, (1); H. Berhane (2); C. Rigsby (3); J. Robinson (4); L. Griffin (3); M. Markl (2); A. Roldan (1)

(1) Mechanical engineering, University of Wisconsin-Madison, Madison, United States of America; (2) Radiology, Northwestern University Feinberg School of Medicine, Chicago, United States of America; (3) Medical imaging, Ann & Robert H. Lurie Children's Hospital of Chicago, Chicago, United States of America; (4) Pediatric cardiology, Ann & Robert H. Lurie Children's Hospital of Chicago, East Chicago Avenue, Chicago, United States of America

### **Abstract**

Coarctation of the aorta (COA) is a congenital heart disease characterized by a narrowing in the aortic arch or proximal descending aorta. COA can induce abnormal pressure gradients at the site of the narrowing resulting in hypertension, ventricular dysfunction, aneurysmal lesions, or even rupture. Treatment procedures for COA include surgery, intravascular stent placement, and balloon angioplasty. Improved diagnostic imaging can guide clinicians in treatment planning and assessment of its success. 4D Flow MRI allows for the visualization and quantification of COA patient-specific hemodynamic information.<sup>1</sup> Despite recent developments in 4D Flow MRI, shortcomings include phase-offset errors, limited spatio-temporal resolution, velocity aliasing, inaccuracy in assessment of slow flow, and distortion of images due to metal artifact (e.g., stents). To address these limitations, Computational Fluid Dynamics (CFD) has high potential to enhance 4D Flow MRI.<sup>2</sup> The purpose of this study is to implement and validate a patient-specific 4D flow MRI enhanced CFD pipeline using Adaptive Mesh Refinement (AMR) in a cohort of pediatric patients with native COA and after COA repair.

In-vivo 4D Flow MRI and CE-MRI/CT were performed before and after COA repair for five pediatric patients (age of  $10 \pm 4$  years, median follow-up duration of  $5 \pm 3$  years) following an IRB-approved HIPAA-compliant protocol. 3D patient-specific anatomies of the thoracic aorta were generated by 3D segmentation of CE-MRA/CTA using commercial software (Mimics and 3-matic, Materialise NV, Leuven, Belgium). Flow rates at the ascending and descending aorta, brachiocephalic, left common carotid, and left subclavian arteries were extracted from 4D Flow MRI data (EnSight, Ansys, Inc., Canonsburg, PA, USA). The flow rate at the ascending aorta was imposed as the inlet boundary condition, and the other outflow rates were used for validation. A three-element Windkessel model was used to impose patient-specific outlet boundary conditions.<sup>3</sup> CFD simulations based on patient-specific anatomies were executed using CONVERGE CFD (Convergent Science Inc., Madison, WI, USA). Sub-grid scale (SGS)-based AMR is a novel numerical method that was implemented during the CFD simulations. AMR refines the computational grid size in regions of large velocity gradients,<sup>4</sup> in this case stenoses.

Ten 4D Flow MRI scans were performed on the patient cohort. Patient 1's mycotic aneurysm was not visible due to low velocity relative to high VENC, in-stent blood flow was not captured for patients 2 and 4 due to susceptibility artifact (red boxes in Figure 1). Ten CFD simulations were successfully completed using patient-specific anatomies and flow conditions



(Figure 2). The spatial resolution of CFD varied between 1 mm<sup>3</sup> to (1/8)<sup>3</sup> mm<sup>3</sup> (due to AMR) while the MRI spatial resolution was 1.5 mm<sup>3</sup>. The temporal resolution of CFD was 10 ms compared to  $37.0 \pm 3.6$  ms for MRI. The fractional volumetric flow rates at the four outlets from CFD results were directly compared to in-vivo 4D Flow MRI data, and the maximum difference between MRI and CFD for each case is reported in Table 1 as  $\Delta q$ . The average  $\Delta q$  was found to be  $9.6 \pm 3.0$  %.

Image-based CFD provided quantitative flow results that agreed well with 4D Flow MRI, consistent with previously conducted validation studies.<sup>5</sup> This method enhanced MRI outcomes by visualizing aneurysmal and in-stent hemodynamics. AMR improved the spatio-temporal resolution of CFD simulations while maintaining reasonable runtimes. The spatio-temporal resolution was improved due to the execution of AMR. Future studies are warranted to investigate the potential of the computationally enhanced method as a predictive tool for treatment planning and post-intervention assessment.

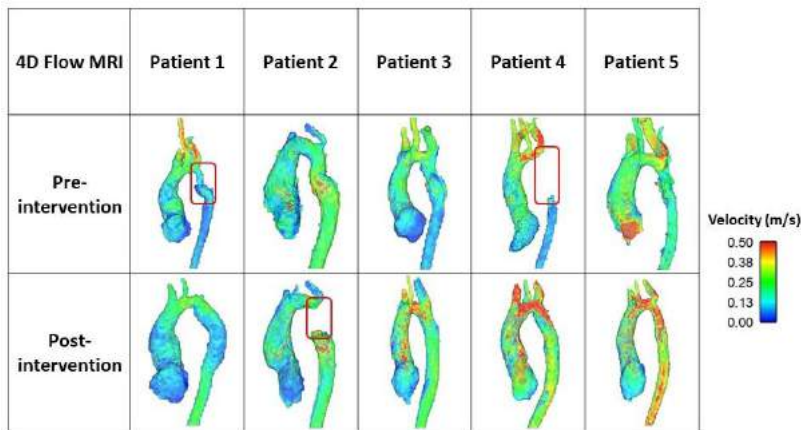
**Figure/Table 1**

Patient	Intervention	Age	Gender	Intervention Procedure	$\Delta q$ = Maximum difference in fractional volumetric flow between MRI and CFD (%)
1	Pre	6	F	Placement of a 16 mm gel weave interposition graft.	3.9
	Post	8			11.8
2	Pre	13	M	Stent placement, 4010 XL delivered with 22 mm stent.	12.8
	Post	16			11.9
3	Pre	7	M	Resection with extended end-to-end anastomosis and patent ductus arteriosus ligation.	9.1
	Post	15			7.9
4	Pre	10	M	Previously had stent placement, reintervention with 16 mm gel weave end-to-end interposition graft.	21.0*
	Post	15			12.7
5	Pre	14	M	Ebstein anomaly and dysplastic mitral valve. Repair with interposition graft.	7.4
	Post	20			9.2

Caption 1

Table 1: Patient demographic and intervention procedures. The fractional volumetric flow rates were calculated from 4D Flow MRI and CFD for each patient case. Severe aliasing was reported for Patient 4 pre-intervention, hence 4D Flow MRI data is unreliable for this case.

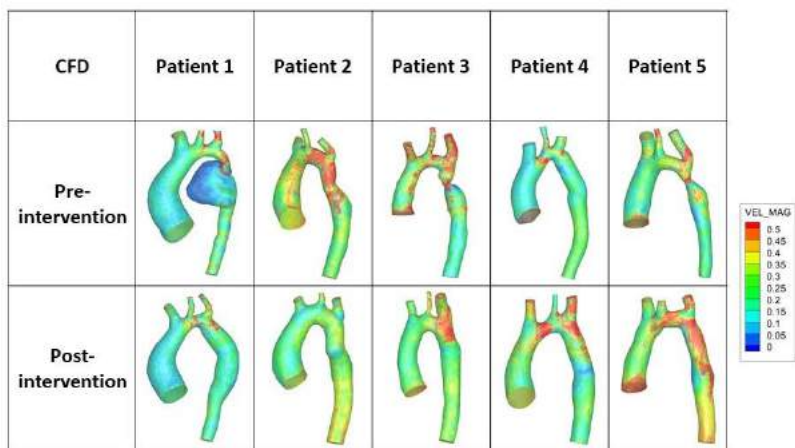
Figure/Table 2



Caption 2

Figure 1: 3D velocity profiles from in-vivo 4D Flow MRI studies on all five patients, pre- and post-COA repair. 4D Flow MRI failed to detect blood flow in mycotic aneurysm (Patient 1) and stent (Patients 2 and 4). The problematic regions are indicated by a red box.

Figure 3



Caption 3

Figure 2: 3D velocity profiles from CFD simulations with AMR on all five patients, pre- and post-COA repair. CFD successfully predicted the aneurysmal (Patient 1) and in-stent blood flow (Patient 2 and 4).

### **Bibliographic References**

1. Hope MD, Meadows AK, Hope TA, et al. Clinical evaluation of aortic coarctation with 4D flow MR imaging. *Journal of Magnetic Resonance Imaging*. 2010;31(3):711-718. doi:10.1002/jmri.22083,
2. Marsden AL, Esmaily-Moghadam M. Multiscale Modeling of Cardiovascular Flows for Clinical Decision Support. *Applied Mechanics Reviews*. 2015;67(3). doi:10.1115/1.4029909,
3. Zambrano BA, McLean NA, Zhao X, et al. Image-based computational assessment of vascular wall mechanics and hemodynamics in pulmonary arterial hypertension patients. *Journal of Biomechanics*. 2018;68(2018):84-92. doi:10.1016/j.jbiomech.2017.12.022,
4. Pewowaruk R, Li Y, Rowinski D, Roldán-Alzate A. Solution adaptive refinement of cut-cell Cartesian meshes can improve FDA nozzle computational fluid dynamics efficiency. *International Journal for Numerical Methods in Biomedical Engineering*. 2021;37(4). doi:10.1002/cnm.3432,
5. Roldán-Alzate A, Frydrychowicz A, Niespodzany E, et al. In vivo validation of 4D flow MRI for assessing the hemodynamics of portal hypertension. *Journal of Magnetic Resonance Imaging*. 2013;37(5):1100-1108. doi:10.1002/jmri.23906

Speaker: L. Shahid

Category: 4D Flow, Computational Fluid Dynamics, Coarctation

000287

## Objective and Automated Detection of Motion-induced Subendocardial Dark Rim Artifacts in Cardiac Perfusion MRI Enabled by Deep Learning

H. B. Unal \* (1); K. Youssef (1); L. Zamudio (1); D. Yalcinkaya (1); R. Dharmakumar (1); B. Sharif (1)

(1) Krannert cardiovascular research center, Indiana University School of Medicine, Indianapolis; UCLA Dept. of Bioengineering, Los Angeles, United States of America

### Abstract

**BACKGROUND:** The subendocardial dark-rim artifact (DRA) remains an important challenge in the routine clinical use of stress perfusion CMR since it reduces the diagnostic accuracy in patients with suspected ischemia by mimicking the appearance of perfusion defects in the subendocardial wall. DRAs are primarily induced by Gibbs ringing [1] and/or cardiac motion [2]. Several methods have been proposed to suppress DRAs by post-processing [3] or by using non-Cartesian trajectories [4,5]. To the best of our knowledge, however, a fully automatic method to detect DRAs does not exist. In this work, we propose a deep-learning-enabled approach to automatically detect motion-induced DRAs by analyzing multiple reconstructions of the same time frame.

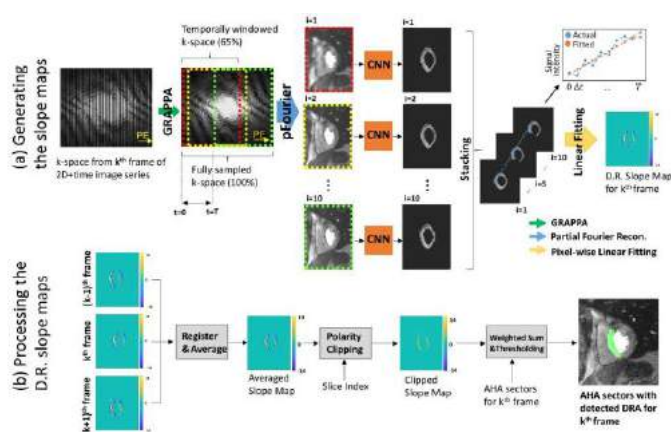
**METHODS:** As shown in Fig. 1, the conventionally acquired Cartesian k-space data (e.g., with GRAPPA acceleration) for a given time-frame is first reconstructed into a fully sampled k-space matrix. Then, multiple reconstructions of the same time-frame are generated ( $i=1,2,\dots, 10$  shown in Fig 1a) by sliding the selected temporal window in k-space. Next, all reconstructed image series are segmented automatically with a Unet-based deep neural network. The subendocardial pixels are cropped and stacked (across the recon. index  $i=1,\dots,10$ ) and the pixel-wise signal intensity is fitted to a line, resulting in a “dynamic recon (DR) slope map” for each frame. Finally, the DR slope maps from neighboring frames are combined and processed (Fig. 1b) to detect the DRA across all sectors (AHA 6-sector model). To test our method, stress/rest perfusion data from 13 healthy volunteers and patients with suspected ischemia and 2 canines (SR-prepared FLASH at 3T) were analyzed.

**RESULTS:** Fig. 2 shows representative results from volunteer studies. Case 1 is a healthy volunteer with DRA in both septal and inferior sectors. As shown, our proposed technique accurately detected the myocardial sectors with DRA after processing the DR slope map. Case 2 is a patient with known distal LAD disease with a DRA in the septal wall. In this case, our method detected the septal sectors with DRA without falsely identifying the true defect as artifact. Case 3 is a patient with true global subendocardial ischemia and no DRAs. As expected, our technique does not detect any DRA in this case. Figure 3 shows a representative result from animal studies (see caption). To assess the overall DRA detection performance, we performed receiver-operating-characteristic analysis by varying the detection threshold (Fig. 1b). The area under the ROC curve (AUC) for per-sector and per-slice detection were both 0.83.

**CONCLUSIONS:** We have proposed a fully automatic technique to objectively detect the subendocardial DRA in perfusion CMR studies. . In this proof-of-concept study, our deep-learning-enabled method achieved an AUC of 0.83 for per-sector detection of subendocardial

DRA. To our knowledge, this is the first work to enable fully-automatic DRA detection in perfusion CMR. Our future work involves evaluating the developed method in a larger datasets of patients with suspected ischemia.

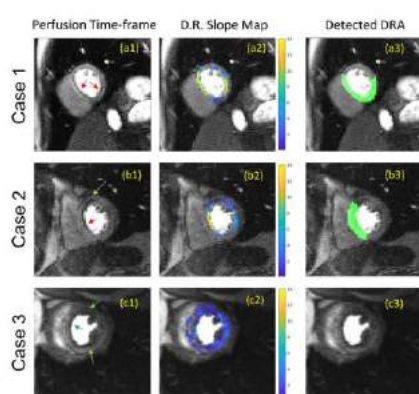
**Figure/Table 1**



**Caption 1**

Proposed algorithm for automatic detection of subendocardial DRA. (a) Multiple reconstructions with different temporal windows are segmented and stacked. Slope maps are generated with pixel-wise linear fitting. (b) Neighboring slope maps are processed to obtain AHA sectors with detected DRA.

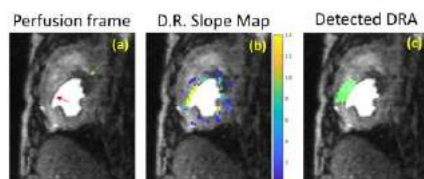
**Figure/Table 2**



**Caption 2**

Representative results from volunteer studies. DRAs and true perfusion defects are shown with red and green arrows, respectively. Case 1 is a healthy volunteer with DRAs. Case 2 has known distal LAD disease as well as septal DRA. Case 3 is a patient with suspected heart failure. The algorithm detects DRAs in all presented cases successfully.

**Figure 3**



**Caption 3**

Representative adenosine-stress perfusion CMR time frame from animal studies (canines with single-vessel epicardial stenosis). (a) DRA region and hypoperfused area are shown with red and green arrows respectively. (b) Slope map highlights DRA region. (c) The proposed method detects the location of DRA accurately.

### Bibliographic References

[2] Storey P, Chen Q, Li W, Edelman RR, Prasad PV. Band artifacts due to bulk motion. *Magn Reson Med*. 2002;48(6). doi:10.1002/mrm.10314, [1] Di Bella EV, Parker DL, Sinusas AJ. On the dark rim artifact in dynamic contrast-enhanced MRI myocardial perfusion studies. *Magn Reson Med*. 2005;54(5). doi:10.1002/mrm.20666, [3] Kellner E, Dhital B, Kiselev VG, Reiser M. Gibbs-ringing artifact removal based on local subvoxel-shifts. *Magn Reson Med*. 2016;76(5):1574-1581. doi:10.1002/mrm.26054, [5] Sharif B et al. Towards elimination of the dark-rim artifact in first-pass myocardial perfusion MRI: removing Gibbs ringing effects using optimized radial imaging. *Magn Reson Med*. 2014;72(1). doi:10.1002/mrm.24913, [4] Salerno M et al. Improved First-Pass Spiral Myocardial Perfusion Imaging with Variable Density Trajectories. *Magn Reson Med*. 2013;70. doi: 10.1002/mrm.24569

Speaker: H. B. Unal

Category: Stress CMR, Subendocardium, First-Pass Perfusion

000291

## Cardiovascular magnetic resonance to differentiate veteran athlete's heart with cavity dilatation and mild dilated cardiomyopathy

W. Javed \* (1); M. Farooq (1); L. Brown (1); F. Jonathan (1); H. Xue (2); E. Levelt (1); E. Dall'Armellina (1); J. Greenwood (3); P. Kellman (4); S. Plein (3); P. Swoboda (1)

(1) Leeds institute of cardiovascular and metabolic medicine, University of Leeds, Leeds, United Kingdom; (2) National heart lung, and blood institute, National Institutes of Health, Bethesda, United States of America; (3) Licamm, Leeds institute of Cardiovascular and Metabolic Medicine, Leeds District, UK, United Kingdom; (4) National institutes for health, NHLBI, Bethesda, United States of America

### Abstract

**Introduction-** Endurance athletic training leads to several cardiac adaptations including ventricular dilatation and mildly reduced left ventricular (LV) ejection fraction (EF) at rest. In clinical practice, this phenotype may be difficult to differentiate from early dilated cardiomyopathy (DCM), particularly in older subjects with additional risk factors. DCM is often a progressive disease initially manifesting as either LV dilatation or mild EF impairment in isolation which if untreated, progresses to the characteristic presentation of significant LV dilatation and impairment 1. We aimed to determine the optimal cardiovascular magnetic resonance (CMR) tissue characteristic which best differentiates athletic ventricular dilatation and mild DCM.

**Methods-** We prospectively recruited 75 male participants: 37 asymptomatic endurance athletes and 38 patients with mild DCM. Inclusion criteria for both cohorts consisted of age 50-80 years old, LVEF 45-54% and either dilated LV or RV indexed to body surface area (BSA). Athletes (all cyclists or triathletes) trained  $\geq 10$  hours per week for  $\geq 15$  years and currently regularly competed. Exclusion criteria for DCM patients included symptoms of chest pain, prior coronary revascularisation, inducible ischaemia or myocardial infarction on CMR. All participants underwent identical CMR protocol (Siemens Prisma 3.0T) including volumetric assessment, pre-and post-contrast T1 mapping, motion corrected quantitative stress perfusion and late gadolinium enhancement (LGE). Indexed cardiac volumes were used to identify those with cavity dilatation from age-adjusted reference ranges 2. Regions with hyperenhancement on LGE were excluded from mapping analysis. Statistical analysis between groups was performed using unpaired t-test and receiver-operator curve (ROC) analysis.

**Results-** Athletes had lower body mass index (BMI), heart rate and blood pressure. They also exhibited lower incidence of pre-existing cardiac disease including hypertension, hyperlipidaemia and atrial fibrillation. LV end-diastolic volumes index (EDVi) was not significantly different between athletes and mild DCM patients ( $112 \pm 14$  vs  $103 \pm 30$  ml/m<sup>2</sup>,  $P=0.13$ ). However, LV EF ( $57 \pm 6$  vs  $50 \pm 4$  %,  $P<0.001$ ) and RV EDVi ( $114 \pm 17$  vs  $82 \pm 22$  ml/m<sup>2</sup>,  $P<0.001$ ) were both greater in athletes than mild DCM patients (Table 1). There was no difference in the prevalence of non-ischaemic pattern LGE in both groups (18 (49%) vs 20 (53%),  $P=0.82$ ). Native T1 ( $1250 \pm 21$  vs  $1329 \pm 114$  ms,  $P<0.001$ ) and extracellular volume (ECV) ( $23.1 \pm 1.7$  vs  $25.2 \pm 2.9$  %,  $P<0.001$ ) were both lower in athletes than mild DCM patients. Furthermore, athletes had higher myocardial perfusion reserve (MPR) than mild

DCM patients ( $3.83 \pm 1.24$  vs  $2.87 \pm 0.97$ ,  $P=0.001$ ). On ROC analysis, native T1 (area under curve (AUC) 0.94,  $P<0.001$ ), ECV (AUC 0.71,  $P<0.001$ ) and MPR (AUC 0.73,  $P<0.001$ ) were all able to differentiate athletes and mild DCM (Figure 1). The presence of non-ischaemic LGE was not discriminatory (AUC 0.52,  $P=0.77$ ). Native T1 was significantly better at discriminating than both ECV and MPR ( $P<0.001$  vs both).

**Conclusion-** Native T1, ECV and MPR were all discriminatory between veteran endurance athlete's heart and patients with mild DCM. Non-ischaemic fibrosis had high prevalence in both groups and was not discriminatory. Recognition of this pattern of tissue characteristics may be useful in clinical practice to differentiate these two overlapping phenotypes although further validation, particularly in longitudinal studies, is required.

**Figure/Table 1**

	<b>Athletes with dilated LV cavity</b>	<b>Mild dilated cardiomyopathy</b>	<b>P-value</b>
<b>N</b>	37	38	
<b>Age</b>	$59.6 \pm 7.5$	$63.1 \pm 8.0$	0.06
<b>Body mass index (kg/m<sup>2</sup>)</b>	$24.0 \pm 2.1$	$27.4 \pm 4.5$	$< 0.001$
<b>Heart Rate (BPM)</b>	$52 \pm 9$	$68 \pm 16$	$< 0.001$
<b>Systolic blood pressure (mmHg)</b>	$116 \pm 22$	$127 \pm 18$	0.003
<b>Diastolic blood pressure (mmHg)</b>	$72 \pm 8$	$78 \pm 9$	0.001
<b>Hypertension</b>	0	19 (50%)	$<0.001$
<b>Hyperlipidaemia</b>	0	15 (40%)	$<0.001$
<b>Atrial fibrillation</b>	0	15 (40%)	$<0.001$
<b>Diabetes</b>	0	3 (8%)	0.24
<b>Stroke or transient ischaemic attack</b>	0	6 (16%)	0.03
<b>LV EDVi (ml/m<sup>2</sup>)</b>	$112 \pm 14$	$103 \pm 30$	0.13
<b>LV EF (%)</b>	$57 \pm 6$	$50 \pm 4$	$< 0.001$
<b>LV mass index (g/m<sup>2</sup>)</b>	$81 \pm 9$	$68 \pm 22$	0.002
<b>RV EDVi (ml/m<sup>2</sup>)</b>	$114 \pm 17$	$82 \pm 22$	$< 0.001$
<b>RV EF (%)</b>	$54 \pm 8$	$53 \pm 10$	0.42
<b>Non-ischaemic pattern LGE</b>	18 (49%)	20 (53%)	0.82
<b>Native T1 (ms)</b>	$1250 \pm 21$	$1329 \pm 114$	$< 0.001$
<b>ECV (%)</b>	$23.1 \pm 1.7$	$25.2 \pm 2.9$	$< 0.001$
<b>Stress MBF (ml/g/min) *</b>	$2.13 \pm 0.68$	$1.99 \pm 0.65$	0.38
<b>Rest MBF (ml/g/min)</b>	$0.57 \pm 0.14$	$0.73 \pm 0.30$	0.003
<b>MPR*</b>	$3.83 \pm 1.24$	$2.87 \pm 0.97$	0.001

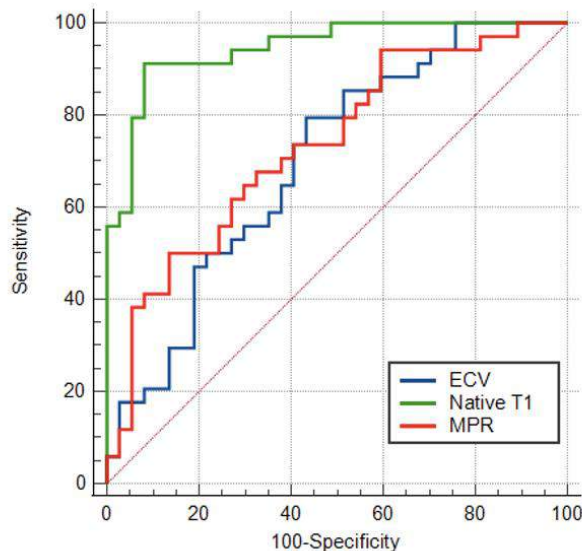
**Caption 1**



### **Table 1; Comparison of athletes with dilated LV cavity and mild DCM patients**

\*2 athletes and 1 DCM patient were excluded because of inadequate stress.

**Figure/Table 2**



**Caption 2**

**Figure 1; Receiver Operator Curve Analysis to discriminate mild DCM from veteran athletes with dilated LV cavity**

### **Bibliographic References**

2. Kawel-Boehm N, Hetzel SJ, Ambale-Venkatesh B, et al. Reference ranges ("normal values") for cardiovascular magnetic resonance (CMR) in adults and children: 2020 update. J Cardiovasc Magn Reson. 2020;22(1):87. doi:10.1186/s12968-020-00683-3., 1. Japp AG, Gulati A, Cook SA, Cowie MR, Prasad SK. The Diagnosis and Evaluation of Dilated Cardiomyopathy. J Am Coll Cardiol. 2016;67(25):2996-3010. doi:10.1016/j.jacc.2016.03.590.

Speaker: W. Javed

Category: Athlete, Dilated Cardiomyopathy, Tissue Characterization

000292

## Left Atrial Sphericity and Pressure in Relation to Atrial Strain and Strain Rate in Patients with Atrial Fibrillation

L. H. Hopman \* (1); P. Bhagirath (1); M. J. Mulder (1); A. M. Van Der Laan (1); A. Demirkiran (1); A. C. van Rossum (1); C. P. Allaart (1); M. J. Gotte (1)

(1) Cardiology, Amsterdam UMC, locatie VUmc, Amsterdam, Netherlands

### Abstract

#### Introduction

Left atrial (LA) sphericity is a novel, geometry-based parameter that has been used to visualize and quantify LA geometrical remodeling in patients with atrial fibrillation (AF). Increased sphericity is part of the LA remodeling process and may be caused by different pathological conditions. Currently, it is assumed that a more spherical shape of the LA is associated with an increase in atrial wall stretch, which may affect atrial function. However, this hypothesis remains to be evaluated.

This study examined the association between LA sphericity and LA longitudinal strain measured by feature tracking in patients with AF.

#### Method

A total of 135 AF patients underwent cardiovascular magnetic resonance (CMR) imaging in sinus rhythm prior to their pulmonary vein isolation (PVI) procedure. LA sphericity was calculated by segmenting the LA (excluding the pulmonary veins and the LA appendage) on a 3D contrast enhanced MR angiogram and comparing the resulting shape with a perfect sphere. LA global reservoir strain, conduit strain, contractile strain, and corresponding strain rates were derived from cine CMR images using feature tracking. Mean LA pressure was assessed during the PVI procedure in a subset of patients (n=78).

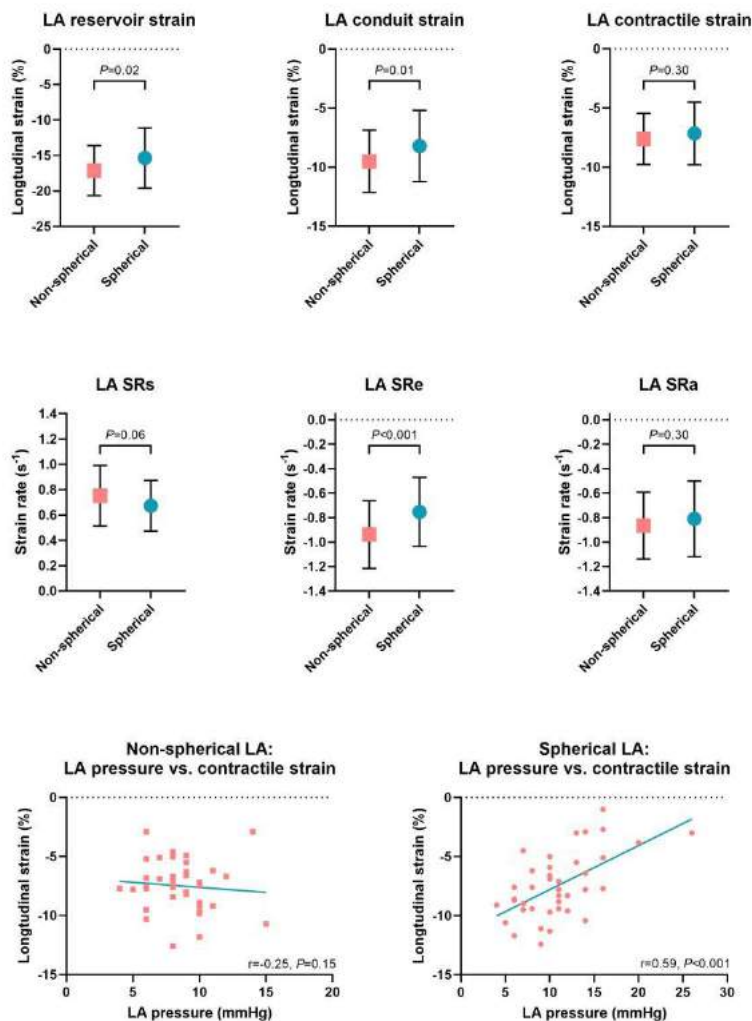
#### Results

Patients with a spherical LA (dichotomized by the median value; >79.13%) had a lower LA reservoir strain and conduit strain compared to patients with a non-spherical LA ( $-15.4 \pm 4.2\%$  vs.  $-17.1 \pm 3.5\%$ ,  $P=0.02$  and  $-8.2 \pm 3.0\%$  vs.  $-9.5 \pm 2.6\%$ ,  $P=0.01$ , respectively). LA strain rate during early ventricular diastole (SRe) was also different between both groups ( $-0.7 \pm 0.3$  vs.  $-0.9 \pm 0.3$ ,  $P<0.001$ ). In contrast, no difference was found for LA contractile strain ( $-7.2 \pm 2.6\%$  vs.  $-7.6 \pm 2.2\%$ ,  $P=0.30$ ). In patients with a spherical LA, there was a correlation between LA contractile strain and LA pressure ( $r=0.59$ ,  $P<0.001$ ) while this correlation was not observed in patients with a non-spherical LA ( $r=-0.25$ ,  $P=0.15$ ).

## Conclusion

LA passive function, measured using feature tracking CMR, is significantly impaired in AF patients with a more spherical LA compared to patients with a non-spherical LA shape. In patients with a spherical LA, LA pressure was correlated with LA contractile function indicating that an increased LA wall stretch ultimately can impact LA contractile function if LA pressure rises.

Figure/Table 1



Speaker: L. H. Hopman

Category: Left Atrium, Atrial Fibrillation , Strain

000296

**The value of cardiovascular magnetic resonance feature tracking in evaluating left ventricular myocardial dysfunction in arrhythmogenic right ventricular cardiomyopathy**

Y. Gao \* (1); W. Qian (1); W. Liu (1); X. Zhou (2); S. Liao (3); Y. Zhu (1); X. Zhu (1); Y. Xu (1)

(1) Department of radiology, The First Affiliated Hospital of Nanjing Medical University, No 300, Guangzhou Road, Nanjing, China; (2) Mr collaboration, Siemens Healthineers Ltd., Shanghai, China; (3) Department of cardiology, The First Affiliated Hospital of Nanjing Medical University, No 300, Guangzhou Road, Nanjing, China

**Abstract**

**Background:** A proportion of patients with arrhythmogenic right ventricular cardiomyopathy (ARVC) involved with left ventricular (LV) do not have fibrosis detectable by cardiac magnetic resonance (CMR) late gadolinium enhancement (LGE). The aim of this study was to explore the value of CMR feature tracking (FT) in evaluating LV myocardial dysfunction in ARVC.

**Materials and methods:** A total of 32 ARVC patients and 30 healthy controls were retrospectively enrolled. ARVC patients were divided into 2 subgroups: the presence of LGE group (LGE+, n=17) and the absence of LGE group (LGE-, n=15). Conventional biventricular functional parameters were calculated in all subjects. LV global peak strain (GPS) and peak systolic strain rate (GPSSR) in radial, circumferential and longitudinal directions were assessed, respectively. Moreover, the LV standard deviation of time to peak strain (TTP-SD) in three directions were also recorded.

**Results:** Compared with the controls, LV GPS and GPSSR in three directions were all significantly impaired in the LGE+ group (all  $p < 0.05$ ). However, only the LV longitudinal GPSSR were reduced in the LGE- group ( $-0.66 \pm 0.21$  vs.  $-0.82 \pm 0.24$ ;  $p = 0.038$ ). Compared with the LGE- group, all LV GPS and GPSSR parameters except for radial GPSSR were significantly impaired in the LGE+ group (all  $p < 0.05$ ). LV radial GPS, using a cut-off value less than 32.25% (AUC: 0.855) was the best discriminator between the 2 subgroups by multivariate logistic regression analysis (OR: 1.194, 95% CI: 1.033-1.380;  $P = 0.016$ ). In the synchronous contraction analyses, the radial and circumferential TTP-SD of the LGE+ group were significantly larger than that of the controls.

**Conclusions:** The reduced LV global strain and strain rate were associated to the presence of LV LGE. Subtle systolic dysfunction could be detected by CMR-FT in ARVC patients with the absence of LV LGE.

Speaker: Y. Gao

Category: ARVC, Feature Tracking, Late Gadolinium Enhancement

**000297**

## **Fetal blood flow assessment in early third trimester using motion-robust fetal whole heart 4D flow cine MRI**

J. K. Steinweg \* (1); T. Roberts (1); M. van Poppel (1); D. Lloyd (1); A. Price (1); J. V. Hajnal (1); R. Razavi (1); K. Pushparajah (1)

(1) School of biomedical engineering & imaging sciences, King's College London, London, United Kingdom

### **Abstract**

#### **Background**

Fetal cardiac imaging has a significant impact on patient management and counselling in congenital heart disease (CHD), but encompasses a multitude of challenges, including very small structures encapsulated in the womb, rapid fetal heart rate (140 to 180/min), unpredictable fetal motion and maternal respiration. Emerging new techniques in fetal CMR can overcome some limitations of fetal echocardiography and aid to map fetal circulation, thus providing important insights into pathophysiology and prognostication in CHD (Sun et al., 2021). However, most common techniques using metric-optimised gating or external ultrasound-gating require precise slice-plane selection and are susceptible to motion especially in earlier gestations, limiting their wider adoption.

#### **Methods**

In this single centre prospective study, we applied a novel motion-robust reconstruction framework for 4D magnitude and flow data with full temporal resolved cardiac cycle (Roberts et al., 2020). Acquisition combined k-t SENSE accelerated balanced steady-state free precession sequences (repetition time (TR)/echo time (TE) 3.8/1.9 ms; flip angle 60 degree; voxels 2x2x6mm; acceleration factor 8; temporal resolution ~81ms) (van Amerom et al., 2019) with continuous stable state 2D acquisition using linear frequency SWEEP through multiple non-coplanar stacks (Jackson et al., 2019). Final 1.25mm isotropic resolution allows assessment of anatomy and function in one volumetric data set.

Primary objective is to trial feasibility of 4D flow cine acquisition during routine clinical fetal CMR scans. Secondary objective is to assess antenatal differences in cardiac volumetrics and function in major congenital lesions.

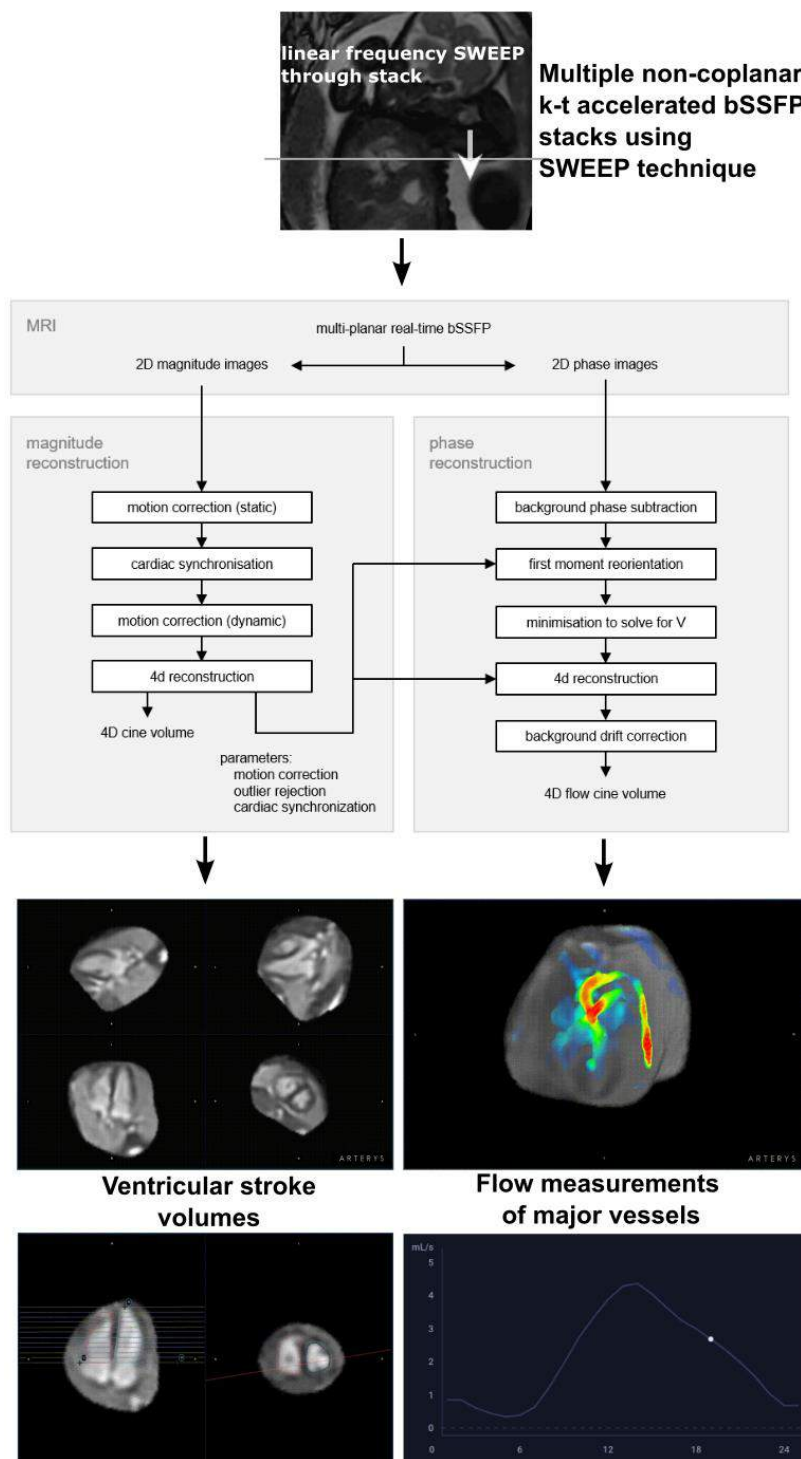
#### **Results**

Data was acquired from 59 women carrying a fetus with antenatal diagnosis of CHD and 6 pregnant controls with current research ethics. Gestational age at scan was 29 – 35 weeks (median 32). Acquisition is feasible in less than 15 min (median number of 5 stacks) in a clinical CMR setting. Reconstruction of 4D magnitude cine volume and flow cine volumes was available in cases with at least 3 and 4 non-coplanar bSSFP stacks, respectively. Initial analysis shows correlation between stroke volumes acquired from 4D magnitude cine volumes and vessel flow measurements derived from phase encoded data in the same imaging data sets, allowing a comprehensive approach to individual fetal pathophysiology.

## Conclusion

4D flow cine MRI allows antenatal structural and functional assessment of fetal circulation in pre-clinical practice in early third trimester. These new tools bare new insights to elucidate antenatal pathophysiology in CHD and may establish new normal physiological values to aid individual risk stratification before birth.

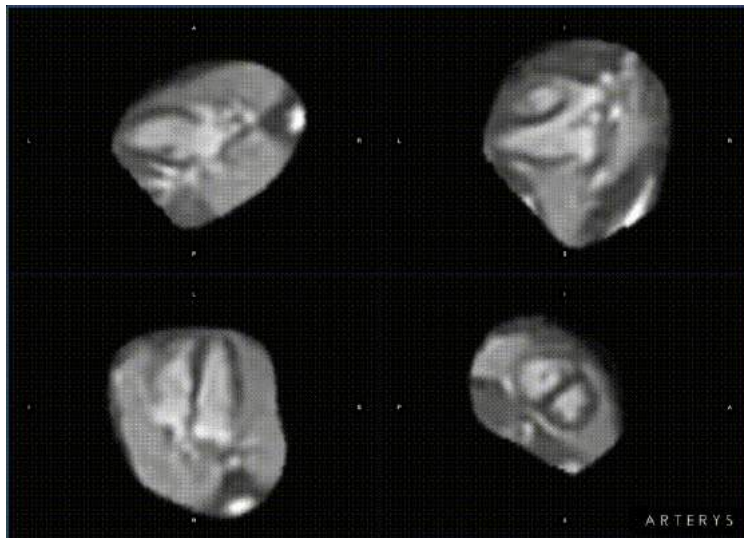
**Figure/Table 1**



### Caption 1

Acquisition and processing overview (adapted from Roberts et al., 2020)

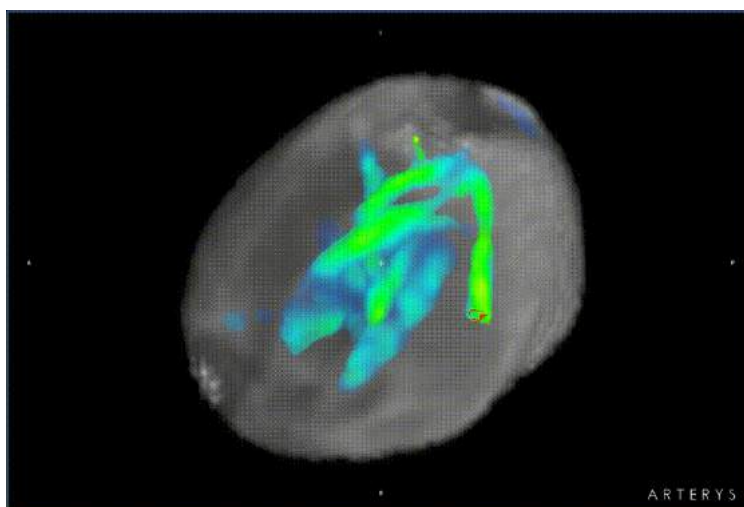
### Figure/Table 2



### Caption 2

4D magnitude cine volume from 32-week gestation scan of normal control, HR 152/min  
(Two Chamber, Three Chamber, Four Chamber and Short Axis View)

### Figure 3



### Caption 3

4D flow cine volume from 32-week gestation scan of normal control, HR 152/min

(seen from anterior left)

### Bibliographic References

van Amerom, J. F. P., Lloyd, D. F. A., Deprez, M., Price, A. N., Malik, S. J., Pushparajah, K., Poppel, M. P. M., Rutherford, M. A., Razavi, R., & Hajnal, J. V. (2019). Fetal whole-heart 4D imaging using motion-corrected multi-planar real-time MRI. *Magnetic Resonance in Medicine*, mrm.27798. <https://doi.org/10.1002/mrm.27798>, Sun, L., Lee, F.-T., van Amerom, J. F. P., Freud, L., Jaeggi, E., Macgowan, C. K., & Seed, M. (2021). Update on fetal cardiovascular magnetic resonance and utility in congenital heart disease. *Journal of Congenital Cardiology*, 5(1), 4. <https://doi.org/10.1186/s40949-021-00059-x>, Jackson, L. H., Price, A. N., Hutter, J., Ho, A., Roberts, T. A., Slator, P. J., Clough, J. R., Deprez, M., McCabe, L., Malik, S. J., Chappell, L., Rutherford, M. A., & Hajnal, J. V. (2019). Respiration resolved imaging with continuous stable state 2D acquisition using linear frequency SWEEP. *Magnetic Resonance in Medicine*, 82(5), 1631–1645. <https://doi.org/10.1002/mrm.2783>, Roberts, T. A., van Amerom, J. F. P., Uus, A., Lloyd, D. F. A., van Poppel, M. P. M., Price, A. N., Tournier, J.-D., Mohanadass, C. A., Jackson, L. H., Malik, S. J., Pushparajah, K., Rutherford, M. A., Rezavi, R., Deprez, M., & Hajnal, J. V. (2020). Fetal whole heart blood flow imaging using 4D cine MRI. *Nature Communications*, 11(1), 4992. <https://doi.org/10.1038/s41467-020-18790-1>

Speaker: J. K. Steinweg

Category: 4D Flow, Fetal, Congenital Heart Disease



000298

## **Amplification of imaging signature from off-the-shelf nitinol guidewires during MRI-guided catheterization using a U-Net**

B. Basar \* (1); C. G. Bruce, (1); A. Jaimes (1); K. O'Brien (1); H. Mandelkow, (2); R. Lederman (1); H. Xue (3); A. Campbell-Washburn (1)

(1) Mri technology program, National Institutes of Health, Bethesda, United States of America; (2) Ninds, National Institutes of Health, Bethesda, United States of America; (3) Nhlbi, National Institutes of Health, Bethesda, United States of America

### **Abstract**

**Background:** MRI-guidance offers improved tissue visualization, however the safety and conspicuity of commercial guidewires remains challenging. Lower MRI field strength reduces RF-induced device heating [1], but also reduces the susceptibility artifacts induced by nitinol devices. Previous studies have used machine learning to improve tracking of needles [2]. These efforts have relied on labeled training data, which are difficult to obtain for poorly visible guidewires. We propose a method that combines an isotropic 3D+time baseline acquisition with a deep neural network (U-Net) [3] for contrast matching and demonstrate proof-of-concept for enhancing the guidewire signature during real-time imaging.

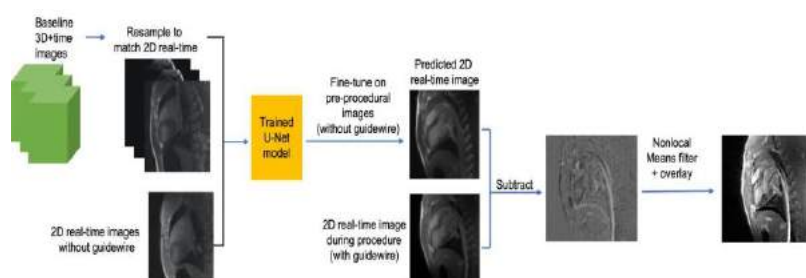
**Methods:** Animal experiments were performed according to local ethical guidelines. A nitinol guidewire (Glidewire, Terumo, Japan) was used for heart catheterization in swine on a prototype 0.55T MRI system (MAGNETOM Aera, Siemens Healthcare, Erlangen, Germany). An isotropic 3D+time sequence was acquired during pre-procedural imaging. A standard 2D bSSFP sequence was used for interactive real-time imaging during guidewire navigation. Figure 1 demonstrates the proposed pipeline. The 3D+time baseline acquisition was resampled using affine transform to match the orientation of the real-time frames. The baseline image with the most similar respiratory motion state to the real-time image was selected by computing the maximum correlation coefficient. A 2D U-Net was trained on 5700 pairs of matching frames acquired from six pigs to predict real-time image contrast. Images with a guidewire were excluded from the training set, which was split 80/20 for training/validation. The network was trained for 150 epochs with a learning rate of 0.001 and mean absolute error (MAE) as the cost function. The model performance was assessed using MAE and cosine similarity between predicted and real-time images. The model was trained using Tensorflow2.4 on NIH High Performance Computing cluster Biowulf [4]. The trained model was fine-tuned for 10 epochs on test day using pre-procedural data. During a procedure, the predicted images were subtracted from real-time frames to isolate the guidewire signal. The difference image was passed through a onlocal means filter, then overlaid on the real-time image to amplify the guidewire signature.

**Results:** The proposed 2D U-Net model consisted of four convolutional layers, 3x3 kernels, and an Adam optimizer. The average test error was 0.04/0.89 (MAE/cosine similarity) across three subjects before fine-tuning. Following fine-tuning, the test error decreased to 0.01/0.98. Figure 2 demonstrates the U-Net performance without a guidewire. Figure 2A-2C show example images of the input, target, and predicted images. A subtraction of a real-time frame and its matching resampled 3D frame performs poorly as it is dominated by contrast differences (Figure 2D). Residual contrast differences are also visible following subtraction of

the U-Net predicted image and real-time frame prior to model fine-tuning (Figure 2E). The contrast differences are resolved by fine-tuning, and the resulting difference image is mostly noise in the absence of a guidewire (Figure 2F). During a procedure, the subtraction of the predicted frames from the real-time frames can better isolate the subtle guidewire signal, which can then be overlaid on the real-time frame (Figure 3).

**Conclusion:** In this proof-of-concept study, we implemented a pipeline that utilizes a 2D U-Net to match the contrast of 3D+time baseline images and a 2D real-time image from MRI-guided catheterization, enabling the improved visualization of guidewires at 0.55T.

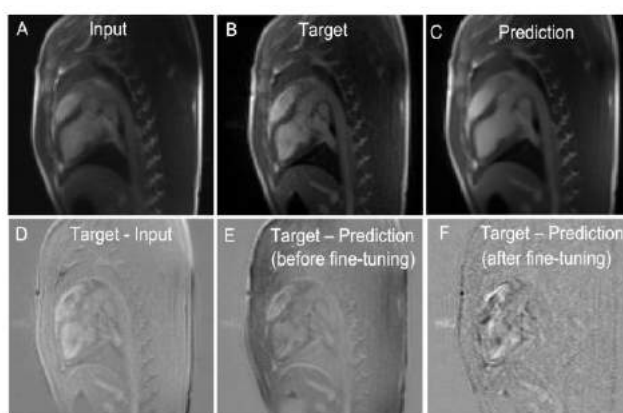
**Figure/Table 1**



**Caption 1**

The input to the U-Net is pairs of matching resampled and real-time frames. On test day, the trained model is fine-tuned on pre-procedural data (without guidewire). At test time, the fine-tuned model predicts real-time frames. The difference of the real-time frame and the predicted frames delineates the guidewire signal, which is overlaid on the real-time frame.

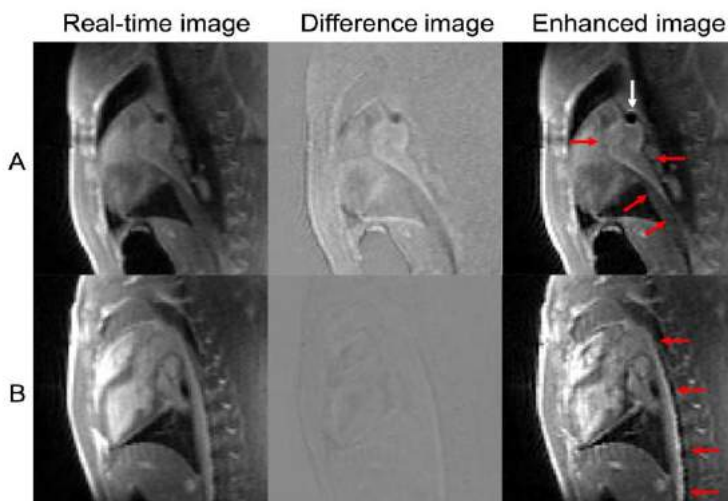
**Figure/Table 2**



## Caption 2

The baseline (A) and real-time(RT) (B) frames differ in contrast. The model predicts the baseline frame in RT contrast (C). A direct subtraction of the RT and the baseline frames (D), as well as the subtraction of the prediction from RT frame before fine-tuning (E) yield poor results. After fine-tuning (F), the subtraction image is mostly noise as desired.

**Figure 3**



## Caption 3

(A) Right heart catheterization example with the guidewire looped in the right atrium and extended distal to the air-filled balloon (white arrow). (B) Left heart catheterization example with substantial guidewire signal amplification after processing. Red arrows point to the amplified guidewire signal.

## Bibliographic References

4. <http://hpc.nih.gov>, 3. David Ojika, Bhavesh Patel, G. Athony Reina, Trent Boyer, Chad Martin and Prashant Shah. "Addressing the Memory Bottleneck in AI Model Training", Workshop on MLOps Systems, Austin TX (2020) held in conjunction with Third Conference on Machine Learning and Systems (MLSys)., 2. A. Mehrtash et al., "Automatic Needle Segmentation and Localization in MRI With 3-D Convolutional Neural Networks: Application to MRI-Targeted Prostate Biopsy," in IEEE Transactions on Medical Imaging, vol. 38, no. 4, pp. 1026-1036, April 2019, doi: 10.1109/TMI.2018.2876796., 1. Campbell-Washburn AE, Ramasawmy R, Restivo MC, Bhattacharya I, Basar B, Herzka DA, et al. Opportunities in interventional and diagnostic imaging by using high-performance low-field-strength MRI. Radiology. (2019) 293:384–93. doi: 10.1148/radiol.2019190452

Speaker: B. Basar

Category: Interventional CMR, Automated Processing, Animal Experimentation

000303

## **Cardiac magnetic resonance based predictors of ventricular arrhythmia recurrence following catheter ablation for ventricular tachycardia: initial experience**

P. Bhagirath \* (1); M. Kemme, (1); P. Postema (1); C. Allaart, (1); M. Gotte, (1)

(1) Cardiology, Amsterdam UMC, locatie VUmc, Amsterdam, Netherlands

### **Abstract**

#### **Background**

Catheter ablation can stop incessant ventricular arrhythmias (VA) and limit damaging and distressing shocks from implantable cardioverter defibrillators (ICD). In addition, patients do not have to undergo intensive therapy with anti-arrhythmic drugs which often has serious side-effects and causes physical limitations. However, the current procedural efficacy and long-term success rates of ablation therapy are limited. An important cause for this is the shortcoming in detailed substrate assessment and the lack of comprehension regarding how the presence of substrate leads to altered electrical behavior of the myocardium.

Therefore, to improve catheter ablation procedures, a more detailed and personalized characterization of the arrhythmic substrate using CMR is required.

#### **Methods**

Patients with an ischemic cardiomyopathy who had undergone a VT-ablation were included for a retrospective analysis. 2D late gadolinium enhancement (LGE) images were analyzed using commercially available software (ADAS-VT) to quantify the extent of variation in scar composition and quantify the number of conduction pathways (Figure 1).

The predictive value of these parameters in differentiating between stable and unstable electro-pathological substrate was investigated by correlating these variables with the occurrence of arrhythmias during the follow-up period after VT-ablation.

#### **Results**

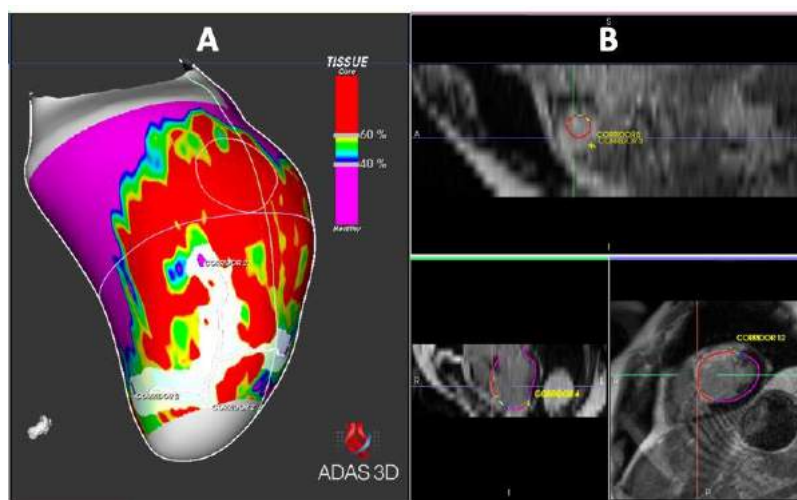
12 patients (mean age  $74 \pm 7.1$  years, 100% male) with a mean follow-up of  $3.4 \pm 1.4$  years were included for analysis. 7 patients (58%) had recurrence of VT during the follow-up period. For the entire cohort mean homogeneous and heterogeneous scar values were  $10.73 \pm 7.84$  g and  $21.47 \pm 18$  g respectively. Patients with recurrent VT had a larger area of homogeneous fibrosis ( $14.9 \pm 6.9$  vs  $4.79 \pm 4.6$ ,  $p=0.017$ ). No significant difference between the two groups was observed for the amount of heterogenous fibrosis ( $27.6 \pm 6.8$  vs  $12.8 \pm 7$ ,  $p=0.17$ ).

An average of  $5 \pm 3.8$  conduction pathways of viable myocardium were observed for the entire population. No significant difference in the number of pathways was observed between the two groups ( $p=0.776$ ).

## Conclusion

Substrate assessment and risk-stratification using LGE may significantly improve the prediction of ventricular arrhythmia recurrence in patients with ischemic cardiomyopathy undergoing VT ablation. These findings could be used to guide patient selection towards ablation and/or device therapy.

## Figure/Table 1



## Caption 1

Panel a depicting the 3D shell with color coded tissue characteristics (red is homogeneous enhancement, transition zone is heterogeneous and purple is healthy myocardium). A sleeve of viable myocardial tissue in the scar area is depicted as corridor 2. Column b depicts the 2D LGE images in orthogonal views with endocardial contours.

Speaker: P. Bhagirath

Category: Arrhythmia, Late Gadolinium Enhancement, Gray Zone

**000304**

### **3D Late Gadolinium Enhancement using Generative Adversarial Network**

S. Yoon \* (1); X. Cai (2); A. AMYAR (1); E. Sai (1); A. Paskavitz (1); J. Cirillo (1); W. Manning (1); R. Nezafat (1)

(1) Cardiology, Beth Israel Deaconess Medical Center (BIDMC), Boston, United States of America; (2) Mr collaboration, Siemens Medical Solutions USA, Inc., Boston, United States of America

#### **Abstract**

##### **Introduction:**

Despite advances in free-breathing 3D LGE, 2D LGE remains the most widely used technique because 3D LGE requires a longer acquisition time. Compressed sensing (CS) has been used to reduce scan time in 3D LGE [1]; however, reconstruction time is relatively long. Further reduction in scan time has also recently been demonstrated using deep learning (DL) [2]. However, this approach requires training using a fully sampled k-space dataset, which is not available in 3D LGE. In this study, we implemented and evaluated performance of a super-resolution generative adversarial network (SRGAN) for 3D LGE imaging, in which training can readily be performed using available 3D LGE images.

##### **Method:**

The SRGAN consists of three networks: (1) generative, (2) discriminative, and (3) pre-trained VGG network (**Fig 1**). The generative network consists of 23 dense residual blocks, an up-sampling layer that increases spatial resolution by a factor of 4 in the phase encoding direction, and two convolutional layers. The discriminative network consists of 10 convolutional layers. A pre-trained VGG network was used for the perceptual loss calculation. For network training, we retrospectively identified 363 patients in whom 3D LGE data was collected at our center. Free-breathing 3D LGE images were collected at 3T (MAGNETOM Vida, Siemens Healthcare, Erlangen, Germany). The dataset was divided into 291 patients for training/validation and 72 for testing. For each dataset, we extracted the GRAPPA-reconstructed and coil-combined complex images from the vendor reconstruction pipeline and converted into k-space by Fourier Transform. To synthesize the training/testing dataset, we cropped the center 25% of the k-space data (**Fig 2**). We retain the acquired data along the readout direction, and only reduce the k-space data along the phase encoding direction, resulting in a simulated scan time reduction by 4 times. We used the original resolution and a reduced resolution image along the phase encoding direction to train SRGAN. Original resolution and reduced resolution images were inputted to the model, and the output was a super-resolved image. The generative network generated super-resolved images during the training process, while the discriminative network evaluated whether the generated images were distinguishable from the original resolution images. The generative network and discriminative network were trained alternately for 300 epochs using Adam optimizer. The batch size was 32, and the learning rate was 0.001. We implemented the model with Pytorch framework and trained on a DGX-1 workstation (NVIDIA Santa Clara, California).

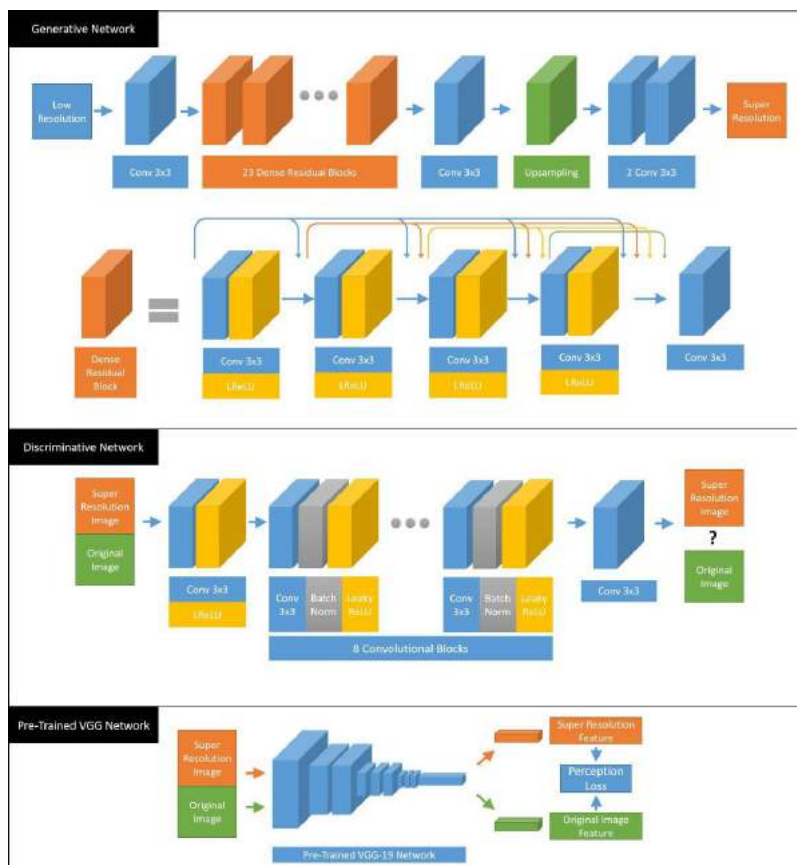
## Results:

Original and super-resolved images are shown in Fig 3. The SRGAN yielded images (right column) with similar sharpness as the original data (left column) from input images with limited spatial resolution along the phase encoding direction (middle column). Notably, even though our model was only trained with 4ch LGE images, SRGAN yielded similar image quality enhancement in other orientations.

## Conclusion:

In this study, we demonstrated the potential of SRGAN to reduce image acquisition time for 3D LGE through synthesized data acquisition. Further studies are warranted to evaluate the performance of this model in prospectively undersampled 3D LGE data.

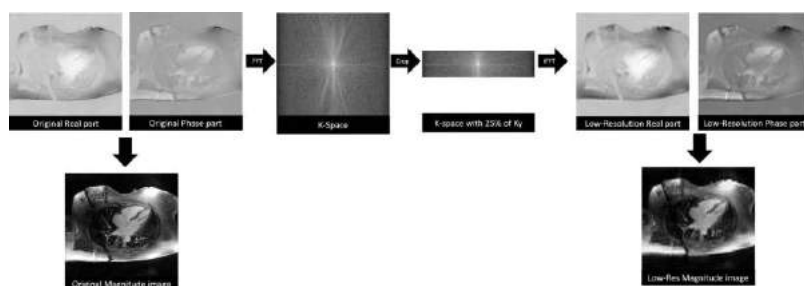
Figure/Table 1



Caption 1

Figure 1. The implemented SRGAN for 3D LGE imaging. The generative network generates the super-resolved output from the low-resolution input. The discriminative network captures discrepancies between the original image and the super-resolved output image. The image features help the learning focused on the texture and shape of the image.

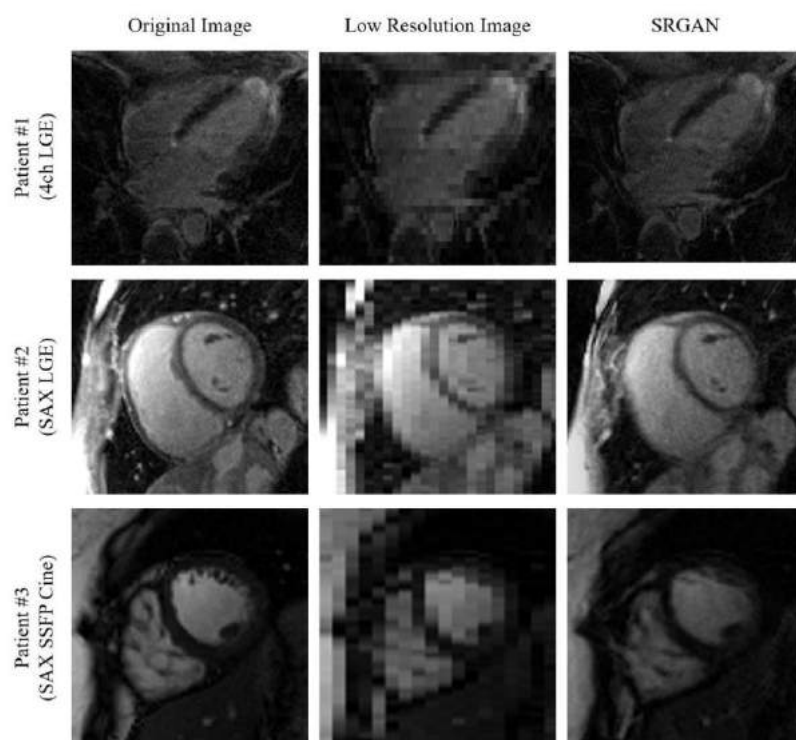
**Figure/Table 2**



**Caption 2**

Figure 2. Data preprocessing for synthesizing training and testing dataset for SRGAN. To generate a low-resolution image retrospectively, k-space was restored from the original complex image through Fourier transform. Afterwards, 25% of the low-frequency region of the phase encoding direction of the k-space is selected to generate a low-resolution image.

**Figure 3**



**Caption 3**



Figure 3. Example 3D LGE images from 3 different patients, showing original images, original under-sampled and corresponding SRGAN images. SRGAN was successful in recovering the lower resolution along the ky direction.

### **Bibliographic References**

[1] Basha, Tamer A., et al. "Clinical performance of high-resolution late gadolinium enhancement imaging with compressed sensing." *Journal of Magnetic Resonance Imaging* 46.6 (2017): 1829-1838., [2] El-Rewaify, Hossam, et al. "Deep complex convolutional network for fast reconstruction of 3D late gadolinium enhancement cardiac MRI." *NMR in Biomedicine* 33.7 (2020): e4312

Speaker: S. Yoon

Category: Late Gadolinium Enhancement, Accelerated Imaging, Image Analysis

000306

## Tissue Based Predictors of Right Ventricular Dysfunction in Patients with Coronary Artery Disease –A 8116 Patient Multicenter Stress Perfusion Study

P. Villar-Calle (1); J. Kochav (2); K. Vadaketh (3); R. Meier, (4); K. Tak, (5); J. Johannesen (1); O. Khalique (6); R. Judd (7); R. Kim (8); D. J. Shah (9); J. Heitner (10); A. Farzaneh far (11); C. Shenoy (12); J. Weinsaft (13); J. Kim \* (1)

(1) Medicine, Weill Cornell Medicine, New York, United States of America; (2) Cardiology, Columbia University Irving Medical Center, New York, United States of America; (3) Medicine, NewYork-Presbyterian Hospital/Weill Cornell Medical Center, New York, United States of America; (4) Medicine, Weill Cornell Medical College, New York, United States of America; (5) Medicine, Cornell University Medical College, New York, United States of America; (6) Cardiology, Columbia University Irving Medical Center, Roslyn, United States of America; (7) Medicine, Duke University, Durham, NC, United States of America; (8) Medicine, Duke Cardiovascular Magnetic Resonance (MRI) Center, Durham, United States of America; (9) Cardiology, Houston Methodist Hospital, Houston, United States of America; (10) Cardiology, NewYork-Presbyterian / Weill Cornell Medical Center, New York, United States of America; (11) Cardiology, Duke University - Main Campus, Durham, Durham, United States of America; (12) Cardiology, University of Minnesota Medical Center, Minneapolis, United States of America; (13) Cardiology, Weill Cornell Medical College, Scarsdale, United States of America

### Abstract

**Background:** RV dysfunction is known to impact prognosis but its determinants in patients with coronary artery disease are poorly understood. Limited understanding of causal factors of RV dysfunction undermines ability to apply targeted coronary revascularization to augment RV performance and to test new therapies for the RV. To date, stress CMR has been used to assess ischemia and infarction in relation to the LV; however the impact of myocardial tissue properties on RV function is unknown.

**Methods:** Vasodilator stress cardiac magnetic resonance was performed in adult patients ( $\geq 18$  years of age) with known or suspected coronary artery disease at 7 sites between May 2005 and October 2018. Stress CMR was performed on 1.5T or 3.0T scanners. Myocardial infarction was identified on LGE-CMR and transmural extent was graded on a per segment basis. Ischemia was assessed on stress CMR based on impaired first-pass perfusion and localized by using segment partitions corresponding to cine and LGE analyses.

**Results:** A total of 8117 patients (mean age  $60.1 \pm 14.1$  years; 55 % male) were studied. RV dysfunction was present in 711 patients (8.8 %). Among patients with RV dysfunction, 38 % ( $n=271$ ) had moderate or greater RV dysfunction. RV dysfunction patients had greater LV remodeling (LVEDV  $209.75 \pm 96.11$  ml vs.  $146.04 \pm 53.19$  ml,  $p<0.001$ ), lower LVEF ( $36.45 \pm 16.53\%$  vs.  $57.38 \pm 12.53\%$ ,  $p<0.001$ ), greater global ischemic burden ( $8.35 \pm 17.57\%$  vs.  $6.46 \pm 14.93\%$  LV,  $p=0.001$ ) and larger infarct size ( $6.77 \pm 11.30\%$  vs.  $2.93 \pm 6.99\%$  LV,  $p<0.001$ ) [Table]. 38% of affected patients had substantial viable myocardium ( $<50\%$  infarct thickness) in ischemic territories. Regarding injury pattern, RV dysfunction was associated with ischemia and infarction in all territories: anterior MI extent (HE score:  $1.34 \pm 3.20$  vs.

0.63 ± 2.18, p<0.001, ischemia score: 1.51 ± 3.45 vs. 1.15 ± 3.14, p=0.004), inferior MI extent (HE score: 2.19 ± 3.89 vs. 0.89 ± 2.40, p<0.001, ischemia score: 1.90 ± 3.67 vs. 1.46 ± 3.33, p=0.001), and lateral MI extent (HE score: 1.71 ± 3.45 vs. 0.74 ± 2.22, p<0.001, ischemia score: 1.23 ± 2.92 vs. 0.93 ± 2.57, p=0.003), suggesting that ischemia and infarction mediated RV dysfunction is a global LV-related process. During follow-up (median 5.1 [2.4, 8.4] years), 1407 deaths (17.3%) occurred. Kaplan-Meier analysis for patients stratified by RV dysfunction demonstrates strong prognostic utility of RV performance for all-cause mortality (p<0.001) (**Figure**). RV dysfunction conferred increased mortality risk (HR: 1.82, 95% CI 1.57 – 2.11, p<0.001) even after controlling for LV function, infarction and ischemia.

**Conclusion:** RV dysfunction in patients with suspected CAD is associated with potentially reversible LV processes, including ischemic and predominantly viable myocardium, which confers increased mortality risk independent of LV function and tissue substrate.

**Figure/Table 1**

**Table A. Tissue-Based Markers of Right Ventricular Dysfunction**

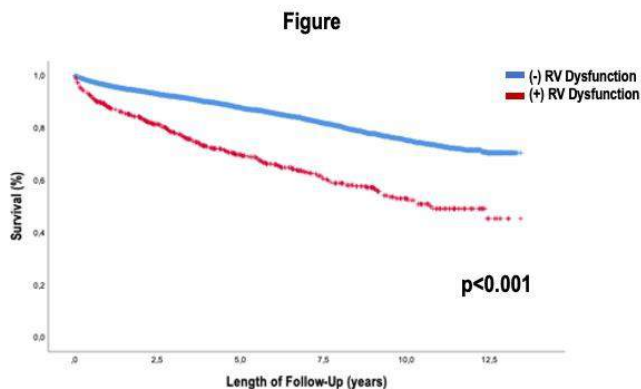
	RV Function		P
	Dysfunction (-) (n=7406)	Dysfunction (+) (n=711)	
<b>Global</b>			
LVEDV (ml)	146.0 ± 53.2	209.8 ± 96.1	<0.001
LVEF (%)	57.4 ± 12.5	36.5 ± 16.5	<0.001
RVEDV (ml)	130.6 ± 46.3	175.0 ± 63.3	<0.001
RVEF (%)	55.6 ± 9.8	35.9 ± 10.0	<0.001
Global Infarct Size (% LV)	2.9 ± 7.0	6.8 ± 11.3	<0.001
Global Ischemia Extent (% LV)	6.5 ± 14.9	8.4 ± 17.6	0.001
Global Ischemia Summed Score	3.6 ± 7.3	4.6 ± 8.3	<0.001
Global Ischemic and Viable Segments	1.5 ± 2.9	2.0 ± 3.4	<0.001
Ischemic and Dysfunctional Segments	0.4 ± 1.5	1.1 ± 2.7	<0.001
<b>Regional</b>			
<b>Anterior</b>			
MI Extent (Summed HE Score)	0.6 ± 2.2	1.3 ± 3.2	<0.001
Summed Ischemia Score	1.2 ± 3.1	1.5 ± 3.5	0.004
Ischemic Segments	0.3 ± 0.9	0.4 ± 1.1	0.002
Ischemic and Viable Segments	0.5 ± 1.2	0.7 ± 1.4	0.001
Ischemic and Dysfunctional Segments	0.1 ± 0.6	0.4 ± 1.1	<0.001
<b>Inferior</b>			
MI Extent (Summed HE Score)	0.9 ± 2.4	2.2 ± 3.9	<0.001
Summed Ischemia Score	1.5 ± 3.3	1.9 ± 3.7	0.001
Ischemic Segments	0.5 ± 1.2	0.6 ± 1.3	0.041
Ischemic and Viable Segments	0.6 ± 1.3	0.8 ± 1.5	0.001
Ischemic and Dysfunctional Segments	0.2 ± 0.7	0.5 ± 1.2	<0.001
<b>Lateral</b>			
MI Extent (Summed HE Score)	0.7 ± 2.2	1.7 ± 3.5	<0.001
Summed Ischemia Score	0.9 ± 2.6	1.2 ± 2.9	0.003
Ischemic Segments	0.3 ± 0.9	0.4 ± 1.0	0.008
Ischemic and Viable Segments	0.4 ± 1.0	0.5 ± 1.2	0.001
Ischemic and Dysfunctional Segments	0.1 ± 0.5	0.3 ± 0.9	<0.001

**Figure/Table 2**

Table B. Tissue-Based Markers of Right Ventricular Dysfunction

	RV Function				P
	Normal (n=7406)	Mild RV Dysfunction (+) (n=440)	Moderate RV Dysfunction (+) (n=196)	Severe RV Dysfunction (+) (n=75)	
<b>Global</b>					
LVEDV (ml)	146.0 ± 53.2	190.2 ± 86.5	240.5 ± 103.1	242.7 ± 101.3	<0.001
LVEF (%)	57.4 ± 12.5	40.7 ± 15.9	30.6 ± 15.2	26.8 ± 14.7	<0.001
RVEDV (ml)	130.6 ± 46.3	158.6 ± 55.5	181.7 ± 64.3	211.1 ± 66.6	<0.001
RVEF (%)	55.6 ± 9.8	41.6 ± 7.5	32.8 ± 6.8	24.1 ± 6.7	<0.001
Global Infarct Size (% LV)	2.9 ± 7.0	6.7 ± 11.2	6.4 ± 11.4	8.1 ± 11.6	<0.001
Global Ischemia Extent (% LV)	6.5 ± 14.9	8.2 ± 17.1	7.7 ± 16.4	11.1 ± 22.5	0.005
Global Ischemia Summed Score	3.6 ± 7.3	4.9 ± 8.8	4.1 ± 7.6	4.5 ± 7.7	0.001
Global Ischemic and Viable Segments	1.5 ± 2.9	2.0 ± 3.4	1.8 ± 3.3	2.3 ± 3.7	<0.001
Ischemic and Dysfunctional Segments	0.4 ± 1.5	1.00 ± 2.4	1.2 ± 2.7	1.8 ± 3.8	<0.001
<b>Regional</b>					
<b>Anterior</b>					
MI Extent (Summed HE Score)	0.6 ± 2.2	1.4 ± 3.3	1.2 ± 3.0	1.3 ± 3.0	<0.001
Summed Ischemia Score	1.2 ± 3.1	1.6 ± 3.7	1.4 ± 3.1	1.3 ± 3.0	0.030
Ischemic Segments	0.3 ± 0.9	0.4 ± 1.0	0.4 ± 1.1	0.6 ± 1.3	0.005
Ischemic and Viable Segments	0.5 ± 1.2	0.6 ± 1.4	0.7 ± 1.5	0.7 ± 1.5	0.010
Ischemic and Dysfunctional Segments	0.1 ± 0.6	0.3 ± 1.0	0.4 ± 1.2	0.6 ± 1.5	<0.001
<b>Inferior</b>					
MI Extent (Summed HE Score)	0.9 ± 2.4	2.1 ± 3.7	2.1 ± 4.0	3.1 ± 4.4	<0.001
Summed Ischemia Score	1.5 ± 3.3	2.1 ± 3.9	1.5 ± 3.0	2.0 ± 3.6	0.002
Ischemic Segments	0.5 ± 1.2	0.6 ± 1.4	0.5 ± 1.1	0.7 ± 1.4	0.1
Ischemic and Viable Segments	0.6 ± 1.3	0.8 ± 1.5	0.6 ± 1.2	1.0 ± 1.6	0.002
Ischemic and Dysfunctional Segments	0.2 ± 0.7	0.5 ± 1.2	0.5 ± 1.1	0.6 ± 1.4	<0.001
<b>Lateral</b>					
MI Extent (Summed HE Score)	0.7 ± 2.2	1.7 ± 3.5	1.5 ± 3.3	2.2 ± 3.9	<0.001
Summed Ischemia Score	0.9 ± 2.6	1.3 ± 3.0	1.2 ± 2.8	1.2 ± 2.4	0.028
Ischemic Segments	0.3 ± 0.9	0.3 ± 1.0	0.4 ± 1.0	0.6 ± 1.3	0.008
Ischemic and Viable Segments	0.4 ± 1.0	0.5 ± 1.2	0.5 ± 1.2	0.6 ± 1.3	0.007
Ischemic and Dysfunctional Segments	0.1 ± 0.5	0.2 ± 0.8	0.3 ± 0.9	0.6 ± 1.2	<0.001

Figure 3



Caption 3

Kaplan-Meier survival analysis for known or suspected coronary artery disease patient groups partitioned based on presence or absence of right ventricular dysfunction. As shown mortality risk increased among patients with right ventricular dysfunction.

Speaker: J. Kim

Category: coronary Artery Disease, Right Ventricle, Stress CMR

000307

## **Circumferential wall shear stress correlates with future co-localized progressive dilation in bicuspid aortic valve patients**

A. Guala \* (1); L. Dux-Santoy (1); G. Teixidó-Turà (2); A. Ruiz-Muñoz (1); K. Johnson (3); O. Wieben (3); L. Galian (2); F. Valente (2); M. L. Servato (2); L. Gutierrez (2); T. González-Alujas (2); J. Garrido-Oliver (2); A. Sao-Avilés (2); I. Ferreira-González (4); A. Evangelista (2); J. F. Rodriguez Palomares (2)

(1) Department of cardiology, Hospital Vall d'Hebron, Vall d'Hebron Research Institute, Universitat Autònoma de Barcelona, Barcelona, Spain; (2) Department of cardiology, Hospital Vall d'Hebron, VHIR. Universitat Autònoma de Barcelona. CIBER-CV, Barcelona, Spain; (3) Departments of medical physics and radiology, University of Wisconsin-Madison, Madison, United States of America; (4) Department of cardiology, Hospital Vall d'Hebron, VHIR. Universitat Autònoma de Barcelona. CIBERESP, Barcelona, Spain

### **Abstract**

### **Background**

Bicuspid aortic valve (BAV) is the most common congenital heart defect and it is associated with dilation of the ascending aorta (AAo). Despite the high prevalence, little evidence is available regarding the aetiology of this disease, with cross-sectional studies pointing to either abnormal blood flow and thus wall shear stress (WSS) [1,2], which was linked to aortic wall degeneration [3], or to intrinsic alteration of the aortic stiffness [4]. A technique providing 3D maps of aortic progressive dilation rate from 2 contrast-enhanced computed tomography angiograms (CTA) was recently introduced and validated, showing marked improvement in performance compared to current standard [5]. We tested whether local WSS is related to faster dilation rates in BAV patients free from aortic valve disease.

### **Methods**

Forty BAV patients with native aortic valve and aorta, free from moderate and severe aortic valve stenosis (maximum velocity at the aortic valve < 3m/s) or regurgitation (regurgitant fraction < 16%) underwent a baseline 4D flow CMR study followed by two CTA. WSS was computed at 64 pre-specified standardized ascending aortic regions, automatically obtained dividing the ascending aorta into 8 longitudinal sections and 8 circumferential regions (I = inner, L = left, O = outer and R=right) [2]. WSS was projected into axial and circumferential directions, following an established methodology [1,2]. Progressive dilation rate was assessed in terms of increase in diameter as measured in the two CTA divided by follow-up duration, i.e. growth rate (GR) [mm/year], with a recently-validated technique based on elastic registration [5]. GR was extracted at the same 64 pre-specified ascending aortic locations. A two-tailed p-value < 0.05 was considered statistically significant.

### **Results**

Demographic and clinical characteristics of the cohort are shown in Table 1 while maps of WSS and growth rate are included in Figure 1. Median follow-up duration was  $44.8 \pm 2.6$

months. Growth rate (Figure 1A) was heterogeneous in the ascending aorta, with faster progression (up to 0.26 mm/year) located in the outer mid AAo region and in the inner region of the proximal-mid AAo. WSS (magnitude) and its axial component showed to be maximum in the right region of the mid AAo (Figure 1B and 1D, respectively) while circumferential WSS showed highest values in the outer region of the mid AAo (Figure 1C), in correspondence with the location of fastest GR. Statistically-significant association between GR and circumferential WSS matched region with fast progressive dilation was fastest, while WSS magnitude and its axial component resulted in limited associations with GR maps.

## Conclusions

Circumferential wall shear stress is related to fast progressive dilation of the ascending aorta in bicuspid aortic valve patients. If confirmed by further prospective studies, the assessment of WSS may be considered in the clinical follow-up of these patients.

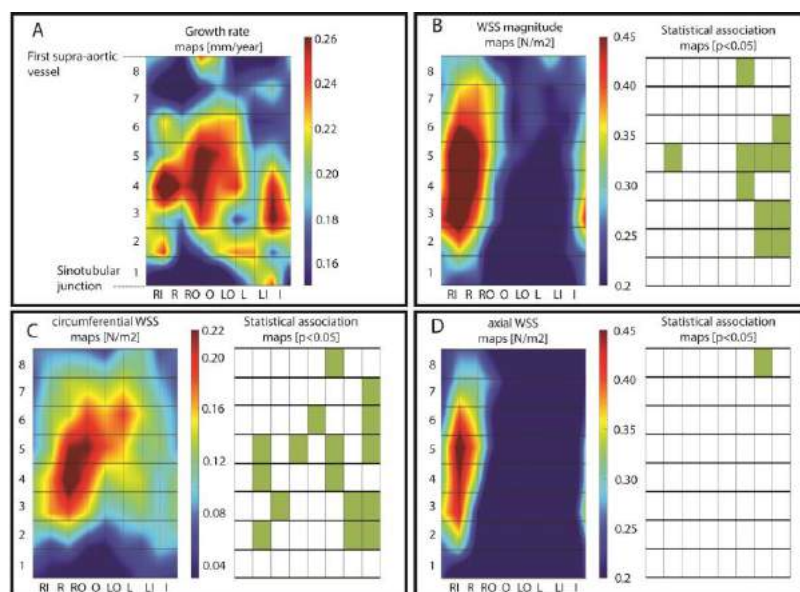
**Figure/Table 1**

	Mean $\pm$ SD
<b>N</b>	40
<b>Age [years]</b>	51 $\pm$ 13
<b>Sex [% of male]</b>	72
<b>BSA [m<sup>2</sup>]</b>	1.86 $\pm$ 0.19
<b>SBP [mmHg]</b>	134 $\pm$ 17
<b>DBP [mmHg]</b>	77 $\pm$ 11
<b>AAo diameter [mm]</b>	41.4 $\pm$ 7.3
<b>BAV type [%RL]</b>	80

**Caption 1**

Table 1: Demographic and clinical characteristics of the cohort. BSA = body surface area; SBP and DBP = systolic and diastolic blood pressure, respectively; AAo = ascending aorta, BAV = bicuspid aortic valve.

**Figure/Table 2**



## Caption 2

Figure 1. Ascending aorta growth rate map (A) and maps of wall shear stress (WSS) magnitude (B) and its circumferential (C) and axial (D) components, along with the statistical significance ( $p < 0.05$ ) maps for their associations with local growth rate.

## Bibliographic References

[2] Guala A, Rodriguez-Palomares J, Galian-Gay L, Teixido-Tura G, Johnson KM, Wieben O, Sao Avilés A, Evangelista A. Partial Aortic Valve Leaflet Fusion Is Related to Deleterious Alteration of Proximal Aorta Hemodynamics. *Circulation*. 2019 Jun 4;139(23):2707-2709. doi: 10.1161/CIRCULATIONAHA.119.039693. , [4] Guala A, Rodriguez-Palomares J, Dux-Santoy L, Teixido-Tura G, Maldonado G, Galian L, Huguet M, Valente F, Gutiérrez L, González-Alujas T, Johnson KM, Wieben O, Sao Avilés A, Garcia-Dorado D, Evangelista A. Influence of Aortic Dilation on the Regional Aortic Stiffness of Bicuspid Aortic Valve Assessed by 4-Dimensional Flow Cardiac Magnetic Resonance: Comparison With Marfan Syndrome and Degenerative Aortic Aneurysm. *JACC Cardiovasc Imaging*. 2019 Jun;12(6):1020-1029. doi: 10.1016/j.jcmg.2018.03.017. , [1] Rodríguez-Palomares JF, Dux-Santoy L, Guala A, Kale R, Maldonado G, Teixido-Tura G, Galian L, Huguet M, Valente F, Gutiérrez L, González-Alujas T, Johnson KM, Wieben O, García-Dorado D, Evangelista A. Aortic flow patterns and wall shear stress maps by 4D-flow cardiovascular magnetic resonance in the assessment of aortic dilatation in bicuspid aortic valve disease. *J Cardiovasc Magn Reson*. 2018 Apr 26;20(1):28. doi: 10.1186/s12968-018-0451-1. , [3] Guzzardi DG, Barker AJ, van Ooij P, Malaisrie SC, Puthumana JJ, Belke DD, Mewhort HE, Svystonyuk DA, Kang S, Verma S, Collins J, Carr J, Bonow RO, Markl M, Thomas JD, McCarthy PM, Fedak PW. Valve-Related Hemodynamics Mediate Human Bicuspid Aortopathy: Insights From Wall Shear Stress Mapping. *J Am Coll Cardiol*. 2015 Aug 25;66(8):892-900. doi: 10.1016/j.jacc.2015.06.1310. , [5] Lydia Dux-Santoy, Jose F. Rodríguez-Palomares, Gisela Teixido-Tura, Aroa Ruiz-Muñoz, Guillem Casas, Filipa Valente, Maria Luz Servato, Laura Galian-Gay, Laura Gutierrez, Teresa Gonzalez-Alujas, Rubén Fernández-Galera, Arturo Evangelista, Ignacio Ferreira-González, Andrea Guala. Registration-based semi-automatic assessment of aortic diameter growth rate from contrast-enhanced computed tomography outperforms manual quantification. In press *European Radiology* 2021. Doi: 10.1007/s00330-021-08273-2.

Speaker: A. Guala

Category: 4D Flow, Bicuspid Aortic Valve, Aneurysm

000308

## **Preventing Sudden Death: A Diagnosis of Cystic Tumor of the Atrioventricular Node by Cardiac Magnetic Resonance**

Y. J. Kim \* (1); M. Hill (2); A. Brener (2); M. Massad (3); C. Gans (2); N. T. Nazir (2)

(1) University of Illinois College of Medicine at Chicago, West Polk Street, Chicago, IL, USA, University of Illinois College of Medicine at Chicago, Chicago, United States of America; (2) Cardiology, University of Illinois College of Medicine at Chicago, Chicago, United States of America; (3) Cardiothoracic surgery, University of Illinois College of Medicine at Chicago, Chicago, United States of America

### **Abstract**

#### **Description of Clinical Presentation:**

A 46-year-old female underwent abdominal computed tomography to evaluate pain at the incision site of an abdominoplasty two years prior. A 2-cm oval hyperdensity at the intra-atrial septum was incidentally appreciated (Figure 1) and confirmed by transthoracic echocardiography (Figure 2a). Biventricular function and chamber size were normal, with no evidence of valvular disease. Initially, the patient was free of cardiopulmonary symptoms, however developed rapidly worsening exertional dyspnea and hypoxemia and was hospitalized for further evaluation.

#### **Diagnostic Techniques and Their Most Important Findings:**

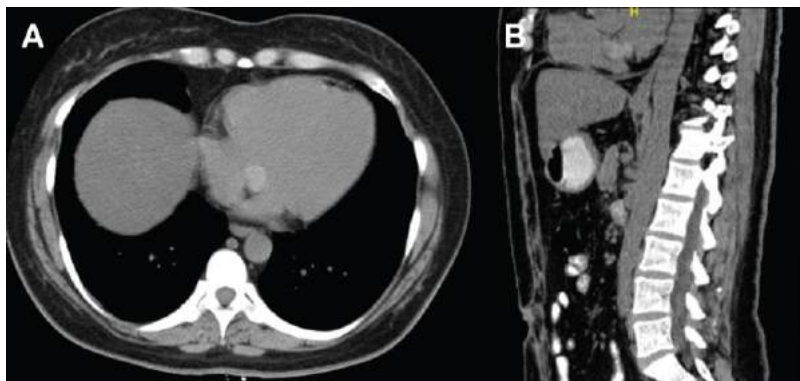
Electrocardiography was notable for first-degree atrioventricular (AV) block, stable compared to five years prior. Transesophageal echocardiography again demonstrated an immobile mass, at the junction of atrial and ventricular septa, extending into the right atrium (Figure 2b). Cardiac magnetic resonance (CMR) imaging was performed on a 3.0 Tesla scanner (Philips Achieva) and demonstrated a well-circumscribed, cyst-like mass in the interatrial septum measuring 1.9 x 2.0 cm (Figure 3a). On late gadolinium sequencing (gadoteridol [Prohance], 0.19 mmol/kg), the lesion was hyperintense in comparison to myocardium, and myocardial delayed enhancement imaging was normal (Figure 3b). Follow-up T2-weighted fat saturation and short-tau inversion recovery (STIR) sequences were obtained on a 1.5 Tesla scanner (Siemens Aera), showing patchy areas of varying intensity within the mass likely secondary to fibrous and fluid content (Figure 3c). Cystic tumor of the AV node (CTAVN) was suspected. Given the patient's progressive dyspnea and potential sequelae of this condition including complete heart block or lethal arrhythmia, she was referred for open surgical excision. Surgery was complicated by intraoperative mitral regurgitation requiring mechanical mitral valve replacement, and complete heart block with junctional escape rhythm requiring epicardial pacemaker placement. Histopathology of the specimen confirmed a diagnosis of CTAVN with endodermal remnants.

#### **Learning Points from this Case:**



CTAVN are rare congenital cardiac tumors located in the atrial septum that comprise only 2.7% of cardiac tumors (1). Patients can be asymptomatic or present with symptoms such as syncope, palpitations, dyspnea, or chest pain. Feared sequelae of this condition include complete heart block or sudden cardiac death due to arrhythmia. CTAVNs are histologically benign and may either be endodermal in origin or contain elements resembling solid cell nests of the thyroid. Earlier reports of CMR to evaluate CTAVN describe high signal intensity both on T1-weighted and T2-weighted MRI. However, low signal intensity on T2-weighted images has also been described (2); this discrepancy may be related to heterogeneous intracystic contents. CTAVN also enhance on late gadolinium sequencing (3). The T2-STIR sequences in our case reflect similar findings and patchy areas of signal intensity suggestive of fibrous and fluid components. In summary, CMR is an essential diagnostic tool in identifying CTAVN. Familiarity with this entity and appropriate sequencing protocols are critical to ensure timely diagnosis and proper management of this potentially deadly condition.

**Figure/Table 1**



**Caption 1**

**Figure 1.** A) Axial and B) sagittal chest computed tomography (CT) imaging demonstrating a 2-cm oval hyperdensity at the intra-atrial septum located at the base of the tricuspid valve.

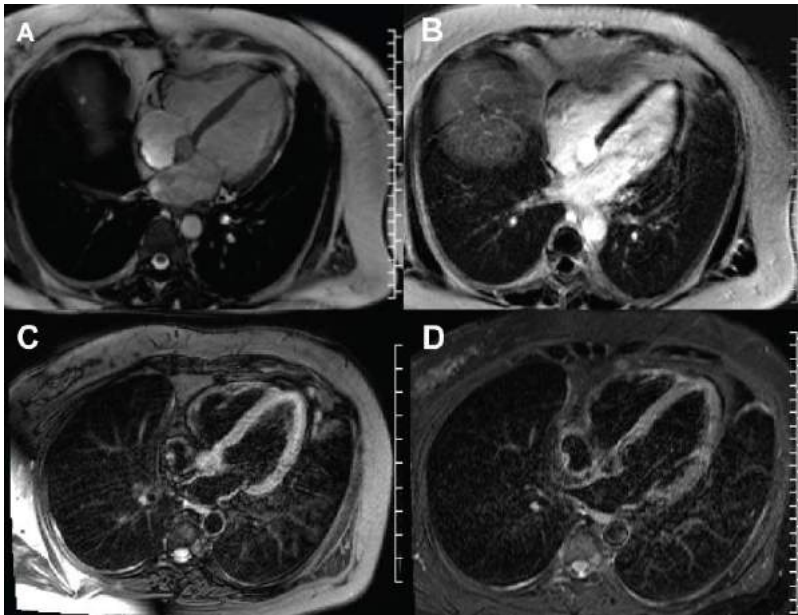
**Figure/Table 2**



## Caption 2

**Figure 2.** A) Transthoracic and B) transesophageal echocardiography confirming a 2-cm oval mass at the intra-atrial septum located at the base of the tricuspid valve.

## Figure 3



## Caption 3

**Figure 3.** Cardiac magnetic resonance imaging A) Four chamber view with mass at level of AV node. B) Late gadolinium enhancement on inversion recovery sequencing showing increased intensity of mass and no myocardial uptake. C) T2-weighted fat saturation and D) STIR sequences with heterogeneous uptake, reflecting fibrous and fluid content.

## Bibliographic References

1. Luc JGY, Phan K, Tchantchaleishvili V. Cystic tumor of the atrioventricular node: a review of the literature. *J Thorac Dis* 2017;9:3313–3318., 2. Suzuki K, Matsushita S, Suzuki H, Kuroda K, Inaba H, Arakawa A, et al. Cystic Tumor of the Atrioventricular Node. *J Thorac Imag.* 2014;29:W97–9., 3. Tran TT, Starnes V, Wang X, Getzen J, Ross BD. Cardiovascular magnetic resonance diagnosis of cystic tumor of the atrioventricular node. *J Cardiovasc Magn Reson.* 2009;11:13.

Speaker: Y. J. Kim

Category: Cardiac Mass, Clinical Utility, Cardiac Surgery

000309

## Impact of Choice of Deep Learning Architectures in Accelerated Cardiac T1 Mapping with MyoMapNet

A. AMYAR \* (1); R. Guo (1); S. Assana (1); X. Cai (2); K. Chow (3); B. Goddu (1); P. Pierce (1); J. Rodriguez (1); R. Nezafat (1)

(1) Department of medicine (cardiovascular division), Beth Israel Deaconess Medical Center (BIDMC), Boston, United States of America; (2) Mr collaboration, Siemens Medical Solutions USA, Inc., Boston, United States of America; (3) Healthineers, Siemens Healthcare Diagnostics, Chicago, United States of America

### Abstract

**Background:** In conventional T1 mapping, a series of T1 weighted images is collected and fit to a 2 or 3-parameter model of the signal recovery to estimate voxel-wise T1 values. We have recently demonstrated that a fully connected neural network (FC) can be used instead of conventional fitting model for T1 estimation [1]. In MyoMapNet [1], we collected four T1 weighted images after a single inversion recovery (Look-Locker (LL4)), which was then used in an FC to estimate T1 values. However, the optimal deep learning (DL) architecture has not been studied. We sought to investigate the performance of DL models in MyoMapNet.

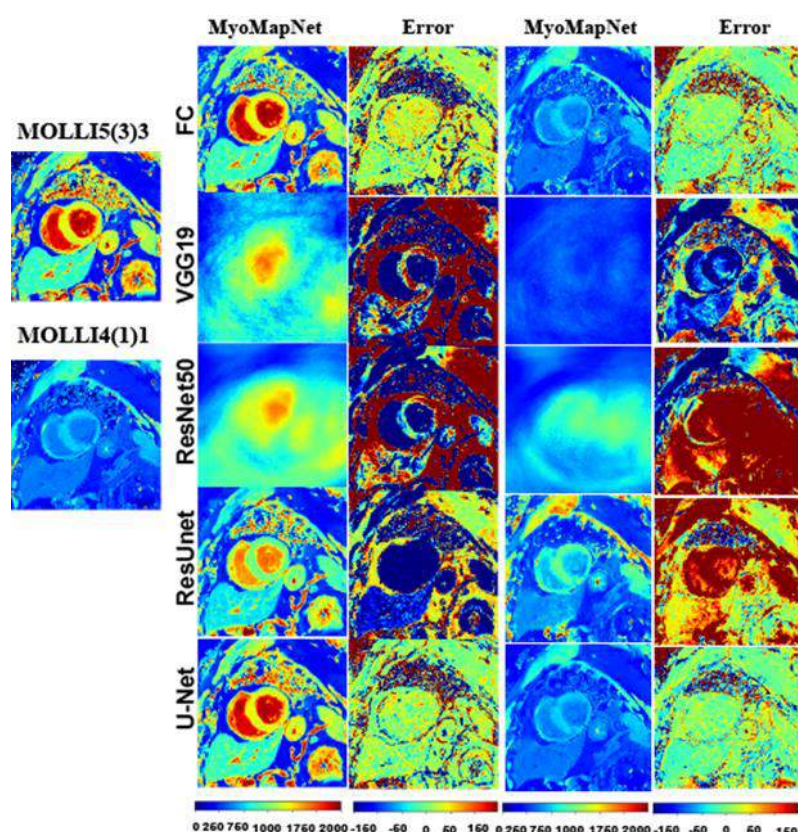
**Methods:** We implemented and tested three different classes of DL architectures for MyoMapNet: (a) a fully connected neural network, (b) convolutional neural networks (VGG19, ResNet50), and (c) encoder-decoder networks with skip connections (U-Net, ResUNet). Modified Look-Locker (MOLLI) images from 749 patients undergoing a clinical cardiac MRI at 3T (MAGNETOM Vida, Siemens Healthineers, Germany) were extracted. Native and post-contrast images were collected using MOLLI5(3)3 and MOLLI4(1)3(1)2 with the following imaging parameters: readout sequence = bSSFP, field of view (mm<sup>2</sup>) = 360×325, voxel size (mm<sup>3</sup>) = 1.7×1.7×8, flip angle = 35°, TR (ms) = 2.5, TE (ms) = 1.02, bandwidth (Hz/Pixel) = 1093, GRAPPA acceleration rate = 2, lines of k-space per shot = 75. This retrospectively collected dataset was divided into a training/validation (N=607/78) and a testing dataset (N=61). To synthesize accelerated cardiac T1 mapping, we extracted the first four T1 weighted images from a conventional MOLLI acquisition. Using the training/validation dataset, we trained each model using the mean absolute error cost function for 3000 epochs with an early stopping of 70 to avoid overfitting. We used a batch size of 64 and Adam optimizer with a learning rate of 0.01. During training, we used the mean difference between MOLLI and the estimated T1 values for the myocardium and blood pool to choose the best model. To further evaluate the performance of each model in prospectively collected data, we collected LL4 images both native and post-contrast in addition to the conventional MOLLI sequence in 28 subjects. Finally, we integrated the two top-performing models for inline reconstruction of T1 mapping such that MyoMapNet T1 maps were readily available upon completion of the scan on the scanner.

**Results:** **Figure 1** shows representative native and post-contrast T1, and maps in a patient acquired by MOLLI5(3)3 and different DL models. **Figures 2 and 3** show Bland-Altman plots of T1 values for the testing dataset and prospectively collected LL4, respectively. There were no significant differences between MOLLI, U-Net, and FC ( $P>0.05$ ); however, there was 10% improvement in T1 precision by U-Net vs. FC, with a standard deviation (std) of 56

ms vs 63 ms for the myocardium, and 25 ms vs 50 m for the blood pool for native T1. Similar results were observed for post-contrast, with a std of 25 ms vs 30 ms for the myocardium and 12 ms vs 18 ms for the blood pool.

**Conclusion:** U-Net and FC enable fast myocardial T1 mapping from only four T1-weighted images collected by the LL4 sequence with similar accuracy as MOLLI. While accuracy was similar between U-Net and FC, our finding shows an improvement in T1 precision in U-Net.

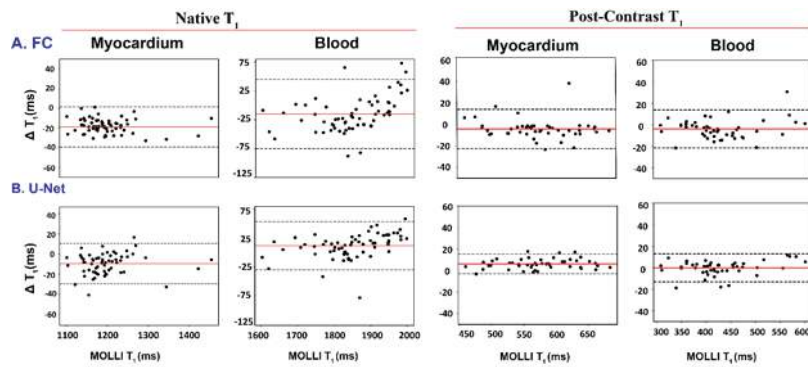
**Figure/Table 1**



**Caption 1**

Native and post-contrast T1 maps generated using MOLLI and MyoMapNet with 5 different DL architectures calculated from the first four T1 weighted images, extracted from corresponding MOLLI sequence and their differences. The VGG and ResNet50 failed to estimate T1 maps and resulted in blurry images. ResUNet was able to create anatomically correct images but with significant error in T1 estimates. Both U-Net and FC resulted in similar image quality to MOLLI.

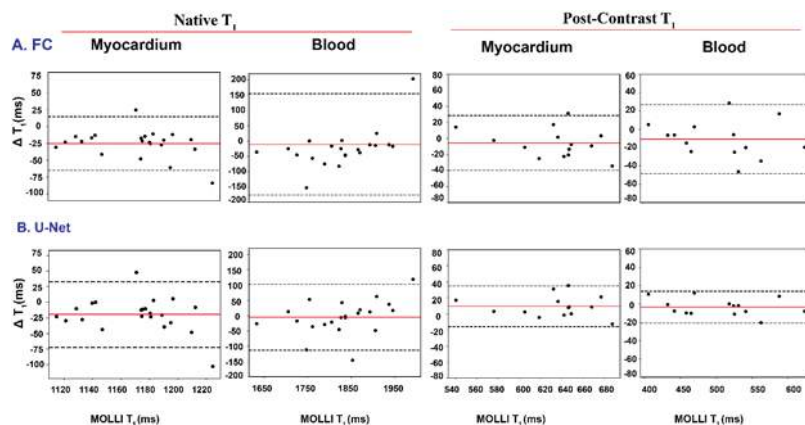
**Figure/Table 2**



**Caption 2**

Bland-Altman plots demonstrating the agreement between MOLLI (5(3)3 for native, 4(1)3(1)2 for post-contrast) and MyoMapNet for myocardium and blood T1 values for FC and U-Net models in the testing dataset (N= 61). DL-estimated MyoMapNet T1 maps were calculated from the first four T1 weighted images of the MOLLI acquisition.

**Figure 3**



**Caption 3**

Bland-Altman plots demonstrating the agreement between MOLLI and MyoMapNet for myocardium and blood T1 values for FC and U-Net models from LL4 sequence (N= 28).

## Bibliographic References

EI-Rewaidy, H., et al., MyoMapNet: Accelerated Modified Look-Locker Inversion Recovery Myocardial T1 Mapping via Neural Networks. arXiv preprint arXiv:2104.00143, 2021.

Speaker: A. AMYAR

Category: Mapping Techniques, Accelerated Imaging, Accuracy and Effectiveness



000310

## Accelerated Dark Blood MRI of the Heart, Lungs and Great Vessels using Unbalanced 3D Steady-State Free Precession

R. Edelman \* (1); N. Leloudas, (1); J. Pang, (2); I. Koktzoglou (1)

(1) Radiology, NorthShore University HealthSystem, Evanston, United States of America;  
(2) Mri, Siemens Medical Solutions Usa, Inc., Chicago, United States of America

### Abstract

**Background:** We recently described a novel dark blood brain imaging technique called unbalanced T1 Relaxation-Enhanced Steady-State (uT1RESS) which uses a highly efficient 3D unbalanced steady-state free precession (3D uSSFP) readout to suppress the blood pool signal (1). The technique was modified for dark blood imaging of the chest using ECG gating with an option for compressed sensing (CS). We hypothesized that ECG-gated 3D uSSFP would provide a robust method for dark blood imaging of the heart, lungs, and great vessels, and evaluated breath-hold and navigator-gated versions of the technique in a series of patients undergoing cardiac MRI. We also compared breath-hold 3D uSSFP with a standard dark blood imaging technique, variable flip angle turbo spin-echo (VFA-TSE or SPACE).

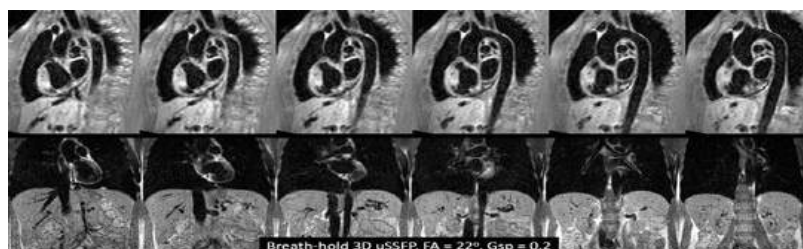
**Methods:** The study was approved by the hospital IRB. 31 adult subjects were imaged at 1.5 Tesla using 3D uSSFP with GRAPPA (acceleration factor = 2) but no CS, including 5 healthy adult volunteers and 26 patients (age range 44 to 86 years old). An additional 3 subjects were imaged using CS but no GRAPPA with an acceleration factor of 4. For breath-hold acquisitions, the 3D uSSFP pulse sequence used a high sampling bandwidth, asymmetric readout, and 1 shot along the phase-encoding direction, whereas 3 shots were acquired for navigator-gated scans. To minimize signal dephasing from bulk motion, ECG gating was used to synchronize the data acquisition to the diastolic phase of the cardiac cycle. To further reduce motion sensitivity, the moment of the dephasing gradient was set to one-fifth of the moment of the readout gradient. For compressed sensing, a variable density Poisson distribution was used to avoid coherent sampling artifacts (2). In 8 subjects, breath-hold 3D uSSFP was compared with breath-hold VFA-TSE acquired with and without blood suppression of 50 or 100 mT/ms along three coordinate axes. Images were reviewed by a single reader with more than 10 years of experience interpreting cardiovascular MRI studies and scored subjectively according to a 4-point scale. For quantitative analysis, tissue signal and standard deviation were measured in the air anterior to the chest wall, subcutaneous fat, paraspinal muscles, within the lungs, and within the posterior wall and lumen of the descending aorta.

**Results:** Image quality for breath-hold 3D uSSFP was good-to-excellent in all subjects (Figures 1 and 2). Compressed sensing with an acceleration factor of 4 allowed the acquisition of 48 3D partitions in a single breath-hold vs. 24 without CS (Figure 3). The image quality score (mean  $\pm$  SD) was  $3.86 \pm 0.36$ . aCNR measurements were as follows: aortic wall-to-lumen  $95.4 \pm 56.5$ ; aortic wall-to-lung =  $94.8 \pm 56.7$ ; aortic wall-to-fat =  $-13.2 \pm 69.0$ ; aortic wall-to-muscle =  $19.1 \pm 41.4$ ; aortic lumen-to-lung =  $-0.6 \pm 5.2$ ; aortic lumen-to-fat =  $-108.6 \pm 63.7$ ; aortic lumen-to-muscle =  $-76.3 \pm 56.8$ . 3D uSSFP consistently outperformed VFA-TSE (respective image quality scores were  $3.87 \pm 0.35$  and  $2.62 \pm 0.92$

( $P=0.013$ ). Vascular and lung pathology (aortic aneurysms, dissections, mediastinal cyst, lung nodules) was well demonstrated by 3D uSSFP.

*Conclusions:* Our initial results suggest that breath-hold, ECG-gated 3D uSSFP consistently provides good-to-excellent image quality for dark blood evaluation of the lungs and great vessels, while a free-breathing, navigator-gated implementation offers the potential for dark blood morphological evaluation of the heart. Moreover, the use of compressed sensing enables at least a twofold increase in spatial coverage.

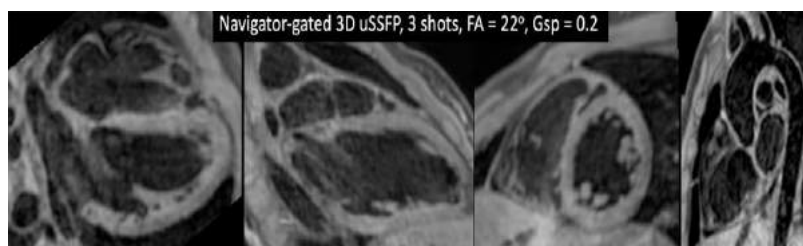
**Figure/Table 1**



**Caption 1**

Fig. 1. Healthy subject. Oblique sagittal (top) and coronal (bottom) breath-hold 3D uSSFP (6 images shown out of 24 acquired), acquired with flip angle (FA) =  $22^\circ$  and gradient spoiler factor (Gsp) = 0.2. There is uniform blood pool suppression in the chest and abdominal vessels without evidence of banding artifacts from off-resonance effects.

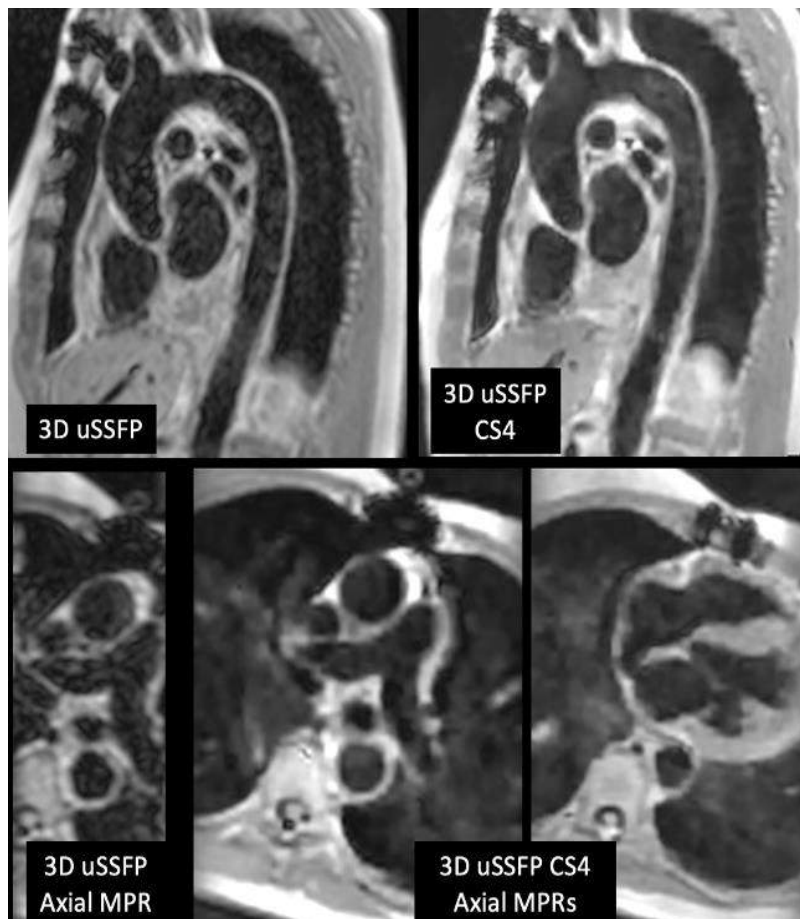
**Figure/Table 2**



**Caption 2**

Fig. 2. Example of free-breathing, navigator-gated 3D uSSFP. Scans were acquired in a sagittal orientation with multiplanar reconstructions performed in standard cardiac orientations. There is uniform blood pool suppression without evidence of motion artifacts, allowing detailed evaluation of cardiac and aortic morphology.

**Figure 3**



### Caption 3

Figure 3. Example of using compressed sensing (acceleration factor = 4) for increased spatial coverage (48 3D partitions per breath-hold with CS vs. 24 3D partitions without CS). Top row: Image quality is similar for scans acquired without CS (left) and with CS (right). Bottom row: Multiplanar reformations show twofold improved spatial coverage using CS.

### Bibliographic References

1. Edelman R, et al. Twofold improved tumor-to-brain contrast using a novel T1 relaxation-enhanced steady-state (T1RESS) MRI technique. *Sci Adv.* 2020;6(44). Epub 2020/10/30. , 2.
- Yamamoto T, et al. Magnetic resonance angiography with compressed sensing: An evaluation of moyamoya disease. *PloS one.* 2018;13(1):e0189493. Epub 2018/01/20.

Speaker: R. Edelman

Category: Accelerated Imaging, Vessel Wall, 3D



000312

# **Intra-aortic segmental flow energetics and vorticity associate with aortopathy severity in bicuspid aortic valve patients: Novel 4D CMR virtual Catheter evaluation in 440 patients**

M. Elbaz \* (1); A. Gupta (1); T. Agirlar Trabzonlu (1); H. Berhane (2); R. Bonow (3); J. Carr (4); C. Malaisrie (5); P. McCarthy (6); M. Markl (7)

(1) Radiology, Northwestern University Feinberg School of Medicine, Chicago, United States of America; (2) Biomedical engineering, Northwestern University, Chicago, United States of America; (3) Cardiology, Northwestern Memorial Hospital, Chicago, United States of America; (4) Radiology, Feinberg School of Medicine, Chicago, United States of America; (5) Division of cardiac surgery, Northwestern University Feinberg School of Medicine, Chicago, United States of America; (6) Cardiac surgery, Northwestern University Feinberg School of Medicine, Chicago, United States of America; (7) Department of radiology, Northwestern University Feinberg School of Medicine, East Superior Street, Chicago, IL, USA, Chicago, United States of America

## **Abstract**

**Background:** Recent 4D Flow CMR studies showed association of aortic flow changes with aortopathy in Bicuspid aortic valve (BAV) patients. While important, these studies focused primarily on the forces near the wall. However, under the hypothesis that aortopathy may be a result of progressive aortic hemodynamic overload, intra-aortic 3D flow changes within the aortic center (i.e. farther from the wall) might precede (and contribute to) the forces' buildup near the wall. However, studying the role of intra-aortic flow within the aortic center in aortopathy has been hindered by technical challenges including the variability in aortic shapes and sizes and lack of a physical boundary in the aortic center to define a consistent intra-aortic flow interrogation volume. Recently, a novel automated 4D CMR virtual catheter (vCath) technique has been developed that allows reproducible quantification of 3D intra-aortic flow from 4D Flow CMR including kinetic energy (KE), viscous energy loss rate (EL), vorticity [1]. The aims of this study were to utilize the 4D CMR vCath to quantify 3D intra-aortic KE, EL, vorticity within the aortic center in 1) three segments: Ascending aorta (AAo), Arch and Descending aorta (DAo). 2) association with aortic dilation and stenosis severity.

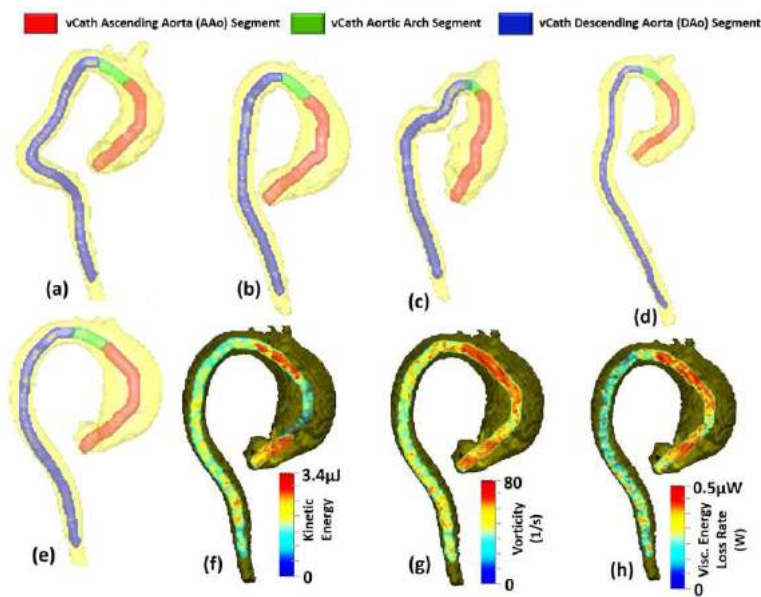
**Methods:** This retrospective IRB-approved study included 440 BAV patients ([328 men, age:  $49 \pm 14$ yr; 342 with R-L, 98 Type0 Sievers fusion pattern]) with 4D Flow CMR. Per patient, an automated vCath model was constructed using published methods [1]. The vCath was then divided into three 3D aortic segments: AAo, Arch, DAo (Fig. 1). For each segment, the time-peak over the cardiac cycle of the volumetric total of each flow metric normalized to the segment volume was calculated: (KE\_AAo, KE\_Arch, KE\_D Ao); (EL\_AAo, EL\_Arch, EL\_D Ao); (Vorticity\_AAo, Vorticity\_Arch, Vorticity\_D Ao). Using multivariate regression, we tested separately for each of the intra-aortic flow metrics, the association of segmental vCath flow measures to two outcomes: MAA diameter and AS severity by CMR (ordinal).

**Results:** Fig 1. Shows example vCath models in 5 patients. AS severity was positively correlated with EL\_AAo ( $p=0.68$ ), Vorticity\_AAo ( $p=0.67$ ), KE\_AAo( $p=0.42$ ), EL\_Arch ( $p=0.42$ ), Vorticity\_Arch ( $p=0.38$ ); and inversely correlated with KE\_D Ao ( $p=-$

0.36), KE\_Arch ( $\rho=-0.19$ ) (Fig. 2). MAA diameter was inversely correlated with KE\_DAO ( $\rho=-0.37$ ), KE\_Arch ( $\rho=-0.36$ ), KE\_AAo ( $\rho=-0.20$ ), Vorticity\_DAO ( $\rho=-0.15$ ), EL\_DAO ( $\rho=-0.11$ ) (Fig. 3). Predictors of AS severity were KE\_AAo ( $\beta=0.002$  J/m<sup>3</sup>,  $p<0.001$ ), KE\_DAO ( $\beta=-0.001$  J/m<sup>3</sup>,  $p<0.001$ ); EL\_AAo ( $\beta=0.002$  W/m<sup>3</sup>,  $p<0.001$ ); EL\_Arch ( $\beta=0.004$  W/m<sup>3</sup>,  $p<0.001$ ) Vorticity\_AAo ( $\beta=0.014$  1/s,  $p<0.001$ ), Vorticity\_Arch ( $\beta=-0.003$  W/m<sup>3</sup>,  $p=0.01$ ). Predictors of MAA diameter were KE\_AAo ( $\beta=-0.004$  J/m<sup>3</sup>,  $p=0.004$ ), KE\_Arch ( $\beta=-0.01$  J/m<sup>3</sup>,  $p<0.001$ ); EL\_AAo ( $\beta=-0.005$  W/m<sup>3</sup>,  $p=0.01$ ), EL\_DAO ( $\beta=-0.02$  W/m<sup>3</sup>,  $p=0.01$ ), Vorticity\_AAo ( $\beta=-0.03$  1/s,  $p$ ). All were independent of age, gender, Sievers type.

**Conclusions:** In 440 BAV patients, the automated 4D CMR vCath modeling allowed consistent quantification of segmental intra-aortic 3D flow KE, EL, vorticity. Segmental 3D intra-aortic energetics and vorticity within the aorta center associated with disease severity (MAA diameter & AS severity) independent of age, gender, Sievers fusion type. These results may reveal an important role of 3D flow changes within the aortic center in aortopathy. Hence, 4D CMR vCath may help extend 4D Flow CMR utility to study the role of intra-aortic flow changes within the aortic center in aortopathy development. Future longitudinal studies should assess whether intra-aortic flow changes may be an earlier predictor of aortopathy.

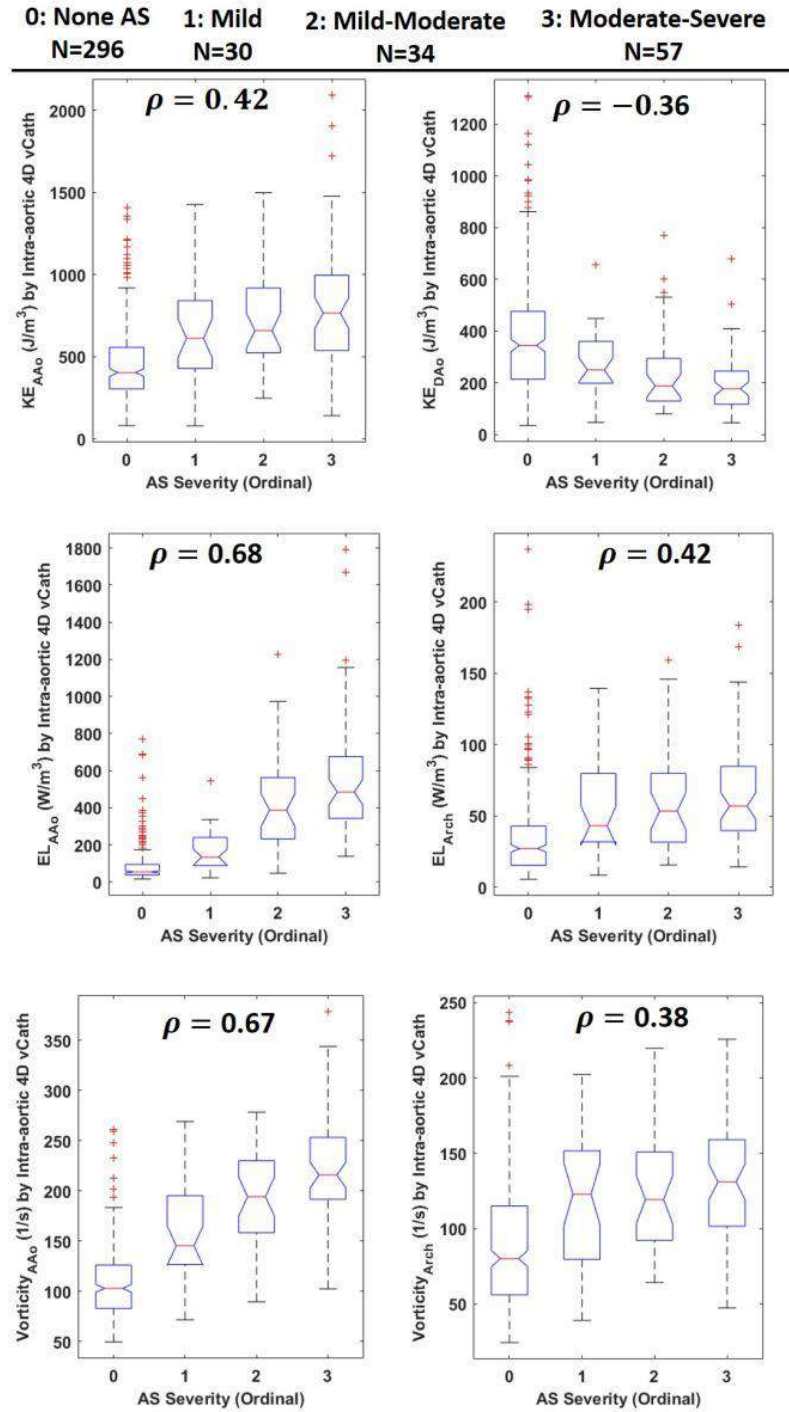
**Figure/Table 1**



**Caption 1**

**Fig. 1:** Example results of the successful intra-aortic segmental 4D vCath construction in 5 patients with different aortic shapes, and sizes (a-e), and example of vCath 3D mapping of Kinetic energy, viscous energy loss rate and vorticity (f-h) along the aorta in the patient in (e).

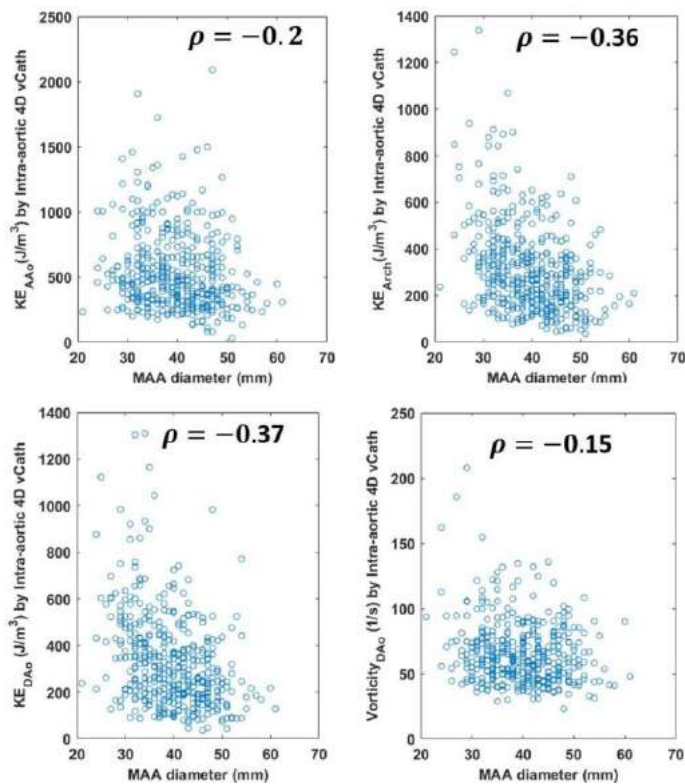
**Figure/Table 2**



**Caption 2**

**Fig. 2:** Segmental Intra-aortic flow correlations with aortic valve (AS) severity (ordinal): 0: None AS (N=296); 1: Mild AS (N=30); 2: Mild-Moderate (N=34); 3: Moderate-Severe (N=57). All presented Spearman correlations had p-value<0.001. Kruskal-Wallis test showed significant differences (p<0.001) between the AS groups for all presented metrics.

**Figure 3**



**Caption 3**

**Fig. 3:** Scatter plots demonstrating inverse correlations between Mid-ascending (MAA) diameter and vCath segmental Intra-aortic flow metrics of Kinetic energy, and Vorticity.

All presented Spearman correlations showed  $p\text{-value} \leq 0.002$ .

### Bibliographic References

References: [1] Elbaz, Mohammed SM, Michael B. Scott, Alex J. Barker, Patrick McCarthy, Chris Malaisrie, Jeremy D. Collins, Robert O. Bonow, James Carr, and Michael Markl. "Four-dimensional virtual catheter: noninvasive assessment of intra-aortic hemodynamics in bicuspid aortic valve disease." *Radiology* 293, no. 3 (2019): 541-550., Funding: This work is supported by grant R21 HL150498 from the National Heart, Lung, and Blood Institute of the National Institutes of Health (NIH-NHLBI).

Speaker: M. Elbaz

Category: 4D Flow, Image Analysis, Bicuspid Aortic Valve

000313

## **Comparison of 4D Flow-Measured Aortic Haemodynamic Parameters Between BAV and TAV in the presence of severe AS**

C. Richards \* (1); A. Parker, (1); A. Alfuhied, (1); K. Parke, (1); G. Mccann, (1); A. Singh, (1)

(1) Department of cardiovascular sciences, University of Leicester, Leicester, United Kingdom

### **Abstract**

#### **Background**

Altered haemodynamic flow patterns in the aorta are potentially associated with tissue remodelling leading to bicuspid valve (BAV)-related aortopathy.(1-2) Using 4D-flow cardiovascular magnetic resonance (CMR), we correlated haemodynamic flow parameters with aortic dilatation between BAV and tricuspid valve (TAV) phenotypes in patients with severe aortic stenosis (AS).(3-4)

#### **Method**

4D-flow CMR was performed on 26 patients (mean age  $71 \pm 6$  years) with severe AS (aortic valve area  $\leq 1$  cm<sup>2</sup>) and 9 healthy volunteers (mean age  $58 \pm 4$  years) on a 3T scanner. In-plane peak velocity, reverse flow volume, pulse wave velocity (PWV) and maximum wall shear stress (WSS) were quantified independently by two observers at 5 levels between the aortic root and descending aorta. Helicity was visually scored (none, mild, moderate, and severe) by the rotational angle of blood flow within the vessel (Figure-1). Ascending (AA) and descending (DA) aortic diameters and distensibilities and AA areas were determined at the level of the pulmonary artery bifurcation. Analysis of covariance was used to correct for age and diastolic blood pressure when comparing variables between groups.

#### **Results**

Inter-observer variability for the 4D-flow measures was good to excellent (intraclass correlation coefficient 0.8–0.9). Peak velocity, reverse flow volume and WSS at the aortic root and proximal AA levels, as well as the AA diameter and area were significantly higher in the overall AS patient group compared to the controls. AA diameters were also significantly larger in BAV ( $n = 5$  right-left coronary phenotype,  $n = 4$  right-non-coronary phenotype) compared to TAV ( $n = 17$ ). However, there were no significant differences in aortic distensibility, PWV, WSS or any other 4D-flow measures between subgroups following age correction (Table-1). Severe helicity was significantly increased overall in the AS cohort compared to the healthy volunteers but the difference between BAV and TAV was not significant.

## Conclusion

Our data suggest that in the presence of severe AS and after accounting for age, differences in aortic flow haemodynamics or stiffness parameters are no longer significant between BAV and TAV phenotypes. BAV-related flow patterns alone are therefore not likely to account for the proximal aortic dilatation and bicuspid aortopathy.

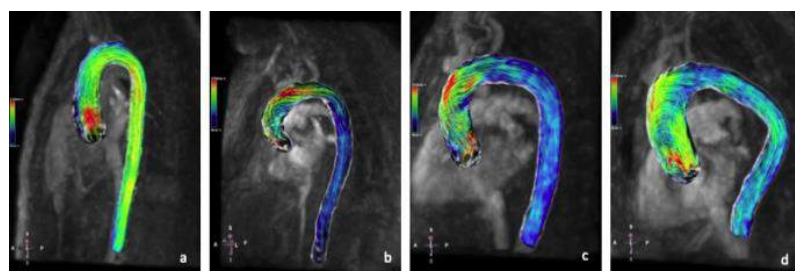
**Figure/Table 1**

Variable	Mean $\pm$ Standard Deviation		ANCOVA p-value
	BAV (n = 9)	TAV (n = 17)	
Peak Velocity (cm/s)	330.95 $\pm$ 67.41	319.28 $\pm$ 64.75	0.38
Total Flow Volume (ml)	65.96 $\pm$ 26.79	66.42 $\pm$ 17.97	0.61
Reverse Flow Volume (ml)	6.74 [3.09, 11.14]	3.18 [0.58, 6.31]	0.57
Pulse Wave Velocity (m/s)	5.84 $\pm$ 1.57	8.32 $\pm$ 3.76	0.38
Wall Shear Stress (Pa)	0.42 $\pm$ 0.16	0.40 $\pm$ 0.12	0.97
AAo Diameter (mm)	39.66 $\pm$ 1.73	34.08 $\pm$ 0.89	< 0.05
AAo Area (cm <sup>2</sup> )	12.03 $\pm$ 1.08	9.06 $\pm$ 0.47	0.08
Severe helicity	6 (67%)	9 (53%)	0.52
Ascending Aortic Distensibility (10 $\cdot$ 3 $\times$ mmHg <sup>-1</sup> )	3.7 [2.1, 4.7]	1.6 [1.0, 2.1]	0.452
Descending Aortic Distensibility (10 $\cdot$ 3 $\times$ mmHg <sup>-1</sup> )	3.9 [1.8, 5.2]	2.0 [1.4, 2.4]	0.219

**Caption 1**

Summary of key flow parameters and dimensions at the aortic root of BAV and TAV subgroups of AS patients.

**Figure/Table 2**



## Caption 2

Visual categorisation of degree of helicity; (a) none, (b) mild ( $\leq 180^\circ$ ), (c) moderate ( $180^\circ - 360^\circ$ ), and (d) severe ( $\geq 360^\circ$ ).

## Bibliographic References

4. Singh A, Horsfield MA, Bekele S, Greenwood JP, Dawson DK, Berry C, Hogrefe K, Kelly DJ, Houston JG, Guntur Ramkumar P, Uddin A, Suzuki T, McCann GP. Aortic stiffness in aortic stenosis assessed by cardiovascular MRI: a comparison between bicuspid and tricuspid valves. *European Radiology*. 2019;29(5):2340–9., 3. Stankovic Z, Allen BD, Garcia J, Jarvis KB, Markl M. 4D flow imaging with MRI. *Cardiovascular Diagnosis & Therapy*. 2014;4(2):173–92., 2. Hassanabad AF, Feindel CM, Verma S, Fedak PWM. Evolving Surgical Approaches to Bicuspid Aortic Valve Associated Aortopathy. *Frontiers in Cardiovascular Medicine*. 2019;6:19. , 1. Ward C. Clinical significance of the bicuspid aortic valve. *Heart*. 2000;83(1):81–5.

Speaker: C. Richards

Category: 4D Flow, Aortic Valve, Blood Flow

000314

## Four-Dimensional Strain Characterization of Cardiomyopathy in Duchenne Muscular Dystrophy Over Time Using Cardiac Magnetic Resonance Imaging

C. Earl \* (1); V. Pyle (1); F. Damen (1); S. Clark (2); J. Soslow (3); L. Markham (4); C. Goergen (1)

(1) Biomedical Engineering, Purdue University, West Lafayette, United States of America; (2) Biomedical engineering, Indiana University School of Medicine, West Lafayette, United States of America; (3) Department of pediatric cardiology, Vanderbilt University Medical Center, Nashville, United States of America; (4) Pediatric cardiology, Indiana University School of Medicine, Indianapolis, United States of America

### Abstract

**Background:** Cardiomyopathy (CM) is the most common cause of mortality in patients with Duchenne muscular dystrophy (DMD) but the age of onset and clinical progression are varied. Early diagnosis and treatment has been shown to improve both quality and length of life (1). Currently, there are no standard imaging biomarkers that predict the onset or pace of CM progression. Our objective was to evaluate how localized kinematic parameters change over time utilizing spatiotemporal analysis of 4D (3D plus time) cardiac magnetic resonance (CMR) in DMD CM. We hypothesized that regional metrics derived from our novel 4D strain analysis would correlate with left ventricular ejection fraction (LVEF) and decrease over time, providing insight for future DMD CM characterization studies.

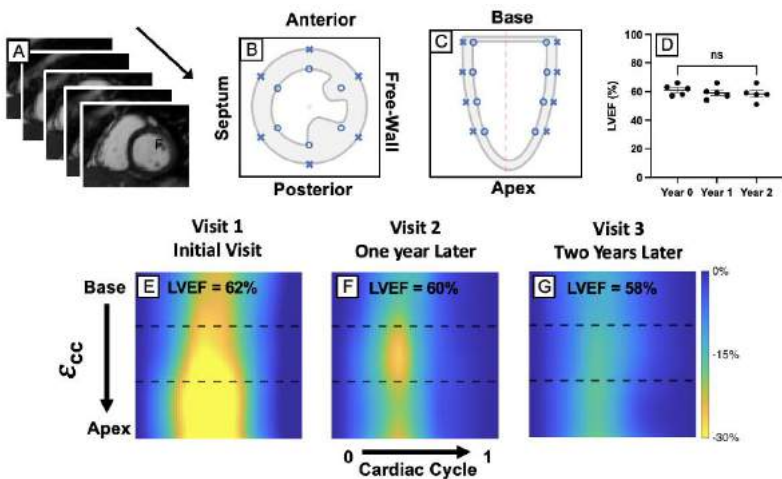
**Methods:** Sequential short axis cine CMR images of DMD patients (n=10) with a range of CM severity were compiled into 4D sequences. In a subset of patients without initial overt LV dysfunction (LVEF>55%; n=5) further image analysis was performed on scans 1 and 2 years after initial scan to evaluate kinematic changes over time. For all 4D sequences, epi- and endocardial borders were segmented across one cardiac cycle for kinematic analysis using a custom-built MATLAB graphical user interface (MathWorks, Natick, MA). We calculated Green-Lagrange circumferential strain ( $\epsilon_{cc}$ ) at 60 equally spaced short axis slices and across 60 time points to generate a spatiotemporal map (Figure 1). We also evaluated a novel “hybrid strain index” combining basal  $\epsilon_{cc}$  with posterior free-wall longitudinal strain. Spearman’s rho was used to determine statistical correlation and Kruskal-Wallis one-way analysis of variance was used to determine statistical difference between timepoints.

**Results:** DMD subjects had a median age of 11 years (8-24); 3 had LVEF<55% and 7 had late gadolinium enhancement. For all subjects at the initial timepoint (n=10), regional peak averages of  $\epsilon_{cc}$  decreased with LVEF for basal ( $\rho=-0.94$ ,  $p<.001$ ) and mid-LV ( $\rho=-0.84$ ,  $p=.004$ ), but not at the apex ( $\rho=-0.55$ ,  $p=.106$ ). The hybrid strain index also decreased with LVEF ( $\rho=0.89$ ,  $p<.001$ ). In the subset of patients examined over time (n=5) LVEF did not change significantly (Figure 1D), however, regional peak averages of  $\epsilon_{cc}$  decreased significantly at the base ( $p=0.0098$ ), but not significantly in the mid-LV ( $p=0.0502$ ) or at the apex ( $p=0.0743$ ; Figure 2).



**Conclusion:** 4D spatiotemporal analysis of CMR images in DMD patients allows for robust comparison of regional kinematic parameters that correlate with LVEF and decrease significantly over time. Identification of an imaging marker of CM progression prior to abnormal LVEF could guide proactive therapeutic intervention and/or power clinical trials aimed to improve outcomes and responses to therapy in this vulnerable population.

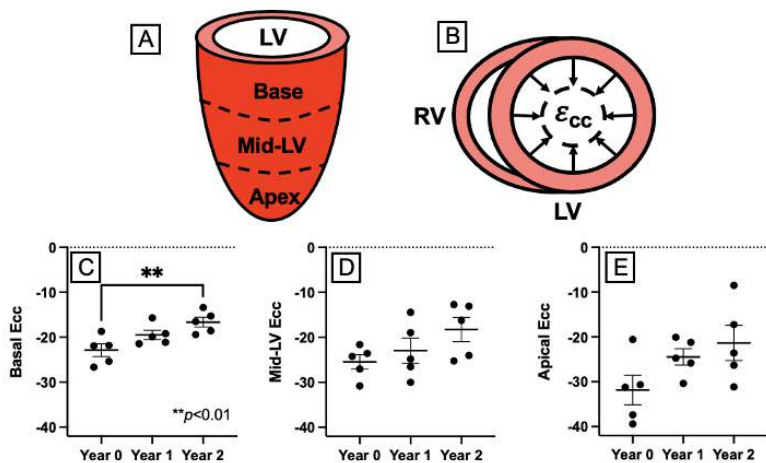
**Figure/Table 1**



**Caption 1**

**Figure 1:** 4D CMR spatiotemporal analysis of DMD cardiomyopathy. A) Sequential short axis cine-MRI used for analysis B,C) Schematic of spatiotemporal tracking for deformation analysis. D) LVEF (%) over time as measured by CMR E,F,G) Initial (E), year 1 (F), and year 2 (G) patient spatiotemporal  $\epsilon_{cc}$  maps.

**Figure/Table 2**



## Caption 2

**Figure 2:** Regional assessment of DMD cardiomyopathy over time. analysis A,B) Schematic of circumferential strain ( $\epsilon_{cc}$ ) C,D,E) Basal (D), mid-LV (E), and apical (F) peak average  $\epsilon_{cc}$  estimates over time.

## Bibliographic References

Mcnally EM, Kaltman JR, Benson DW, Canter CE, Cripe LH, Duan D, Finder JD, Groh WJ, Hoffman EP, Judge DP, Kertesz N, Kinnett K, Kirsch R, Metzger JM, Pearson GD, Rafael-Fortney JA, Raman SV, Spurney CF, Targum SL, Wagner KR, Markham LW. Contemporary Cardiac Issues in Duchenne Muscular Dystrophy. *Circulation*. 2015;131(18):1590-1598.

Speaker: C. Earl

Category: Duchenne Muscular Dystrophy, Cardiac Strain, 3D

000316

## **Longitudinal Precedes Circumferential Strain Abnormality in Sickle Cell Anemia: A Cardiovascular Magnetic Resonance Feature-Tracking Study**

H. Jacobs \* (1); S. Lee, (1); C. Stiver, (1); J. Williams, (1); S. Creary, (2); A. Villella, (2); M. Lee, (1); K. Hor, (1)

(1) Pediatric cardiology, Nationwide Children's Hospital, Columbus, United States of America; (2) Pediatric hematology and oncology, Nationwide Children's Hospital, Columbus, United States of America

### **Abstract**

#### **Background**

Sickle Cell Disease (SCD) is an autosomal recessive hemolytic disease that affects 1 in 360 African American live births. Sickle cell anemia (SCA) is the most common variant of SCD leading to chronic transfusions. Chronic transfusions result in iron overload and deposition of iron in the heart and liver leading to diastolic dysfunction. Systolic dysfunction with decline in global function as assessed by ejection fraction is a late finding. Studies in non-ischemic cardiomyopathy (NICMD) demonstrate incremental predictive values of additional strain parameters over left ventricular ejection fraction (LVEF) to predict cardiovascular events. Prior transthoracic echocardiography (TTE) studies demonstrate abnormal global longitudinal strain (GLS) in SCA patients, an indicator of early occult cardiac dysfunction. We hypothesized that both GLS and GCS are abnormal ( $\geq -17$ ) compared to controls and that GLS decline precedes that of GCS in patients with SCA with preserved LVEF.

Our objective is to quantify myocardial deformation from cine cardiac magnetic resonance (CMR) images using Feature-Tracking (FT) based technique in patients with SCA compared healthy control subjects.

#### **Methods**

Single institution retrospective study of SCA patients and control subjects with CMR evaluation. GLS and GCS were obtained from three long axis views and three short axis views using a commercially available CMR-FT software (Medis Medical Imaging, Qstrain 3.2, Leiden, Netherlands). Demographic and clinical CMR data including LVEF was collected for statistical analysis using Student's T-test.

#### **Results**

28 SCA patients were identified with complete CMR dataset (age  $16.1 \pm 4.9$  years) and 11 age-matched control subjects (age  $18.5 \pm 0.7$  years,  $p = 0.06$ ). Indexed LV end diastolic volume (LVEDVI) was larger in SCA patients compared to control ( $109.2 \pm 18.2$  vs  $96.8 \pm 14.1$ ,  $p = 0.03$ ) with no difference in LVEF ( $59.3 \pm 5.6\%$  vs  $58.4 \pm 5.7\%$ ,  $p = 0.3$ ). SCA patients had lower GLS and GCS magnitude (GLS  $-14.8 \pm 2.8$  vs  $-20.3 \pm 1.5$ ,  $p < 0.0001$  and GCS  $-17 \pm 3.6$  vs  $-20.1 \pm 1.5$ ,  $p = 0.004$ ) compared to control. There were no difference between GLS and GCS in control subjects but GLS magnitude was significantly lower than GCS in patients with SCA ( $-14.8 \pm 2.8$  vs  $-17 \pm 3.6$ ,  $0.009$ ).

## **Conclusion**

Our study confirmed prior studies that GLS is abnormal compared to control group but also found that GCS magnitude was significantly lower compared to control. In addition, we found that GLS decline precedes GCS decline in SCA patients with preserved LVEF. The use of multiple strain parameters have been shown to have incremental predictive value in NICMD to predict cardiovascular events. This may suggest that using CMR-FT to evaluate myocardial strain can be used as an early diagnostic tool to assess for occult dysfunction and perhaps lead to earlier intervention to decrease cardiovascular events. Future larger longitudinal studies are needed to determine rate of progression and patient outcomes.

## **Bibliographic References**

Sundd, P, Gladwin MT, et al. Pathophysiology of Sickle Cell Disease. Annual Review of Pathology: Mechanisms of Disease 2019; 14:1, 263-292, Voskaridou E, Christoulas D, et al. Sickle-cell disease and the heart: review of the current literature. British Journal of Haematology 2012; 157, 664-673, Murphy CJ, Oudit GY, et al. Iron-overload cardiomyopathy: pathophysiology, diagnosis and treatment. Journal of Cardiac Failure 2010; 16:11, 888-900, Whipple NS, Naik RJ, et al. Ventricular global longitudinal strain is altered in children with sickle cell disease. British Journal of Haematology 2018; 183:5, 796-806, Schuster A, Hor KN, et al. Cardiovascular magnetic resonance myocardial feature tracking: concepts and clinical applications. Circulation. Cardiovascular Imaging 2016; 9:4

Speaker: H. Jacobs

Category: Sickle Cell Disease, Strain, T2\*

000317

## Cine Image Based Cardiac Disease Classification Using a Graph Based Deep Learning Approach

A. Varga-Szemes \* (1); T. Chitiboi (2); U. J. Schoepf (1); A. Jacob (2); S. Ghosal (2); F. Xiong (3); P. Sharma (2); J. Aldinger (1); T. Emrich (1)

(1) Department of radiology and radiological science, Medical University of South Carolina, Charleston, United States of America; (2) Digital technology & innovation, Siemens Medical Solutions USA, Inc, Princeton, United States of America; (3) Cardiovascular mr r&d, Siemens Medical Solutions USA Inc., Charleston, South Carolina, Charleston, United States of America

### Abstract

**Background:** CMR has a pivotal role in diagnostic decision making in patients with cardiovascular diseases. Current image analysis techniques are mostly reliant on qualitative visual assessment and crude quantitative measures of cardiac structure and function. In recent years, the wide availability of high computational power has triggered the development of artificial intelligence (AI) technologies in medical imaging. AI approaches to image-based diagnosis rely on algorithms that learn from past clinical examples through identification of hidden and complex imaging patterns [1]. Existing work demonstrates the value of image-based cardiovascular diagnosis with AI for several conditions [2-3]. In the current study, we aimed to develop and test a deep learning (DL) algorithm for cardiovascular disease classification based on cine image datasets.

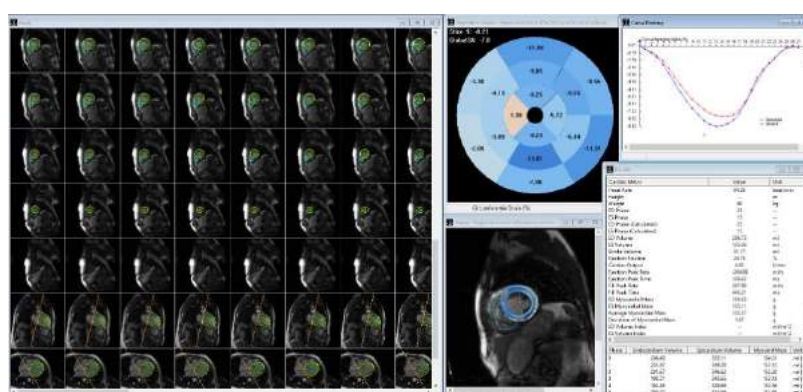
**Methods:** Image datasets of 570 consecutive patients who had previously undergone clinically indicated CMR at our institution were retrospectively identified. The cohort included normal patients (n=277), patients with dilated cardiomyopathy (DCM, n=77), hypertrophic CM (HCM, n=65), ischemic heart disease (IHD, n=134), and myocarditis (n=17). Expert annotation was performed by a reader with 12 years of experience in CMR and used as reference. Cine images in short and long axis were segmented using a DL approach [4] (Figure 1) and 26 volume, strain, and wall thickness measures were computed. A disease classification network (DCN) was developed and trained using graph attention networks [5] (Figure 2). Three variations of the DCN were trained using: (i) a full set of 26 features from the DL method; (ii) a subset of four features from the DL method (end-diastolic, end-systolic, stroke volumes, and ejection fraction); and (iii) the same four features from manual annotation. The DCNs were evaluated by five-fold cross-validation. Classification performance was assessed using receiver operating characteristic (ROC) curves and F1 score, which were calculated for each individual class.

**Results:** All 570 cases were successfully segmented using the fully automated algorithm. The full-feature DCN provided superior accuracy for disease identification represented by higher area under the curve (AUC) values and F1 scores compared to the partial feature DCN and manual-based DCN (Table 1). The full-feature DCN was able to reach 0.92 AUC for the

discrimination of patients from normal controls. Similar accuracy was found for the identification of patients with DCM and HCM (both AUCs 0.94). Slightly lower AUC (0.82) was found for IHD, likely due to the heterogeneity of imaging findings and limitations of the cine acquisition in this disease. The lowest AUC (0.65) was measured for myocarditis, likely due to unspecific cine features.

**Conclusions:** The fully automated deep learning algorithm shows high accuracy for cardiac disease classification based on cine images only. Such algorithm has the potential to improve the efficiency of the reading process, especially by identifying and filtering out patients with normal cardiac anatomy and function.

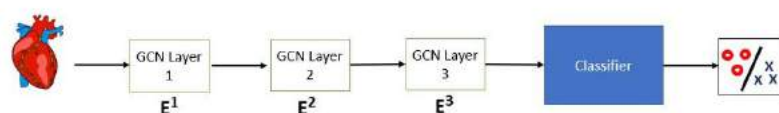
**Figure/Table 1**



**Caption 1**

**Figure 1** – From left to right, automatic segmentation result for an IHD patient, end-systolic circumferential strain bulls-eye plot and overlay on mid-ventricular slice, global and local circumferential strain curves and automatically extracted volumetric features.

**Figure/Table 2**



**Caption 2**

**Figure 2** – Graph-based convolutional neural network for multi-class classification. GCN 1-3 are consecutive graph convolutional network layers, E1 – 3 are the attention weights, and the Classifier subnetwork is a 2-layer linear regression network with soft-max.

**Figure 3**

Classification	Full-Feature AI		[EDV, ESV, SV, EF] AI		[EDV, ESV, SV, EF] manual		Subjects	Controls
	ROC-AUC	F1 Score	ROC-AUC	F1 Score	ROC-AUC	F1 Score		
Normal vs. abnormal	0.92	0.82	0.80	0.65	0.89	0.47	277	293
DCM vs. non-DCM	0.94	0.65	0.94	0.63	0.93	0.65	77	493
HCM vs. non-HCM	0.94	0.70	0.67	0.20	0.76	0.31	65	505
IHD vs. non-IHD	0.82	0.41	0.72	0.04	0.76	0.09	134	436
Myo vs. non-myocard	0.65	0.09	0.76	0.20	0.75	0.18	17	553

**Caption 3**

**Table 1** – Classification using the graph-based approach comparing full-feature DCN, DCN with four preselected features, and DCN with same manual features

### Bibliographic References

[1] Martin-Isla C, Campello VM, Izquierdo C, Raisi-Estabragh Z, Baeßler B, Petersen SE, Lekadir K. Image-Based Cardiac Diagnosis With Machine Learning: A Review. *Front Cardiovasc Med*. 2020 Jan 24;7:1. doi: 10.3389/fcvm.2020.00001. PMID: 32039241, [2] Leiner T, Rueckert D, Suinesiaputra A, Baeßler B, Nezafat R, Išgum I, Young AA. Machine learning in cardiovascular magnetic resonance: basic concepts and applications. *J Cardiovasc Magn Reson*. 2019 Oct 7;21(1):61. doi: 10.1186/s12968-019-0575-y. PMID: 31590664, [3] Ruijsink B, Puyol-Antón E, Oksuz I, Sinclair M, Bai W, Schnabel JA, Razavi R, King AP. Fully Automated, Quality-Controlled Cardiac Analysis From CMR: Validation and Large-Scale Application to Characterize Cardiac Function. *JACC Cardiovasc Imaging*. 2020 Mar;13(3):684-695. doi: 10.1016/j.jcmg.2019.05.030. Epub 2019 Jul 17. PMID: 31326477, [4] Chitiboi T, Georgescu B, Wetzl J, Borgohain I, Geppert C, Piechnik SK, Neubauer S, Petersen S, Sharma P. Deep Learning-based Strain Quantification from CINE Cardiac MRI. *ISMRM 2020*. [5] Veličković P, Cucurull G, Casanova A, Romero A, Lio P, Bengio Y. Graph attention networks. *arXiv preprint arXiv:1710.10903*. 2017 Oct 30.

Speaker: A. Varga-Szemes

Category: Automated Processing, Cine Imaging, Image Analysis

## Diagnostic and Prognostic Utility of Quantitative Perfusion CMR for Differentiation of Cardiac Neoplasm and Thrombus

T. Ruiz Maya (1); K. Tak, (2); R. Meier, (3); J. Kim, (3); R. Kim, (4); J. Grizzard (5); R. Steingart, (1); J. Weinsaft (6); A. Chan \* (7); C. Park, (8)

(1) Cardiology, Memorial Sloan Kettering Cancer Center, New York, United States of America; (2) Medicine, Cornell University Medical College, New York, United States of America; (3) Medicine, Weill Cornell Medical College, New York, United States of America; (4) Medicine, Duke University, Durham, United States of America; (5) Radiology, Virginia Commonwealth University Health, Midlothian, United States of America; (6) Cardiology, Weill Cornell Medical College, Scarsdale, United States of America; (7) Medicine/cardiology, Memorial Sloan Kettering Cancer Center, New York, United States of America; (8) Medicine, Weill Cornell Medicine, New York, United States of America

### Abstract

**Background:** CMR is widely used to differentiate cardiac neoplasm (CNEO) and thrombus (CTHR) based on tissue properties stemming from vascularity. LGE-CMR is a validated reference to differentiate CNEO and CTHR: Perfusion CMR can also assess vascularity via quantification of dynamic contrast uptake. To date, utility of perfusion CMR to differentiate CNEO and CTHR - including prognostic significance perfusion pattern in patients with CMASS - is unknown.

**Methods:** The population comprised adult cancer patients who underwent contrast-enhanced CMR (0.2 mmol/kg gadolinium). CNEO and CTHR were defined using the reference of LGE-CMR via established criteria (presence or absence of contrast enhancement): Affected (CMASS+) patients were matched (1:1) to unaffected (CMASS-) controls of equivalent cancer type/stage. Perfusion CMR (gradient echo) was analyzed (blinded to LGE), for which contrast intensity upslope (time intensity function) was used to quantify dynamic patterns of contrast enhancement within masses. Follow-up was performed for all cause mortality.

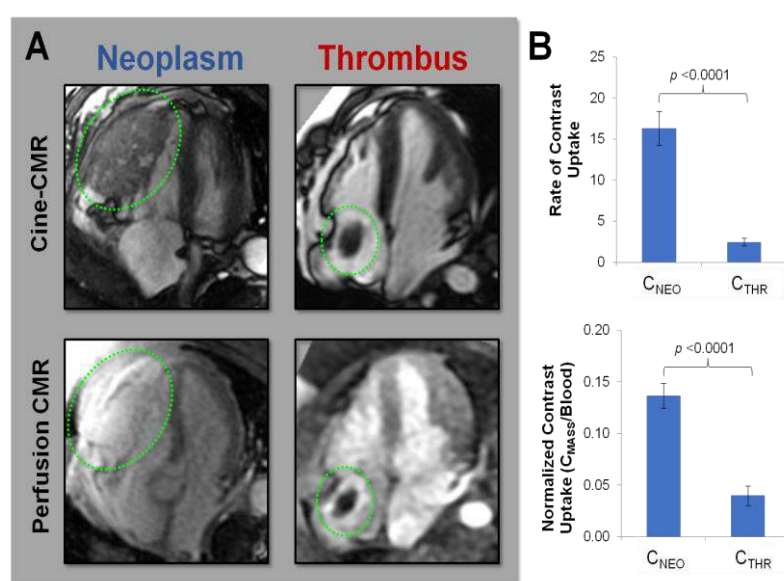
**Results:** 306 patients ( $56.9 \pm 16$  yo; 57%M) were studied – inclusive of CMASS+ patients (CNEO=108, CTHR=45) and matched controls with systemic cancer (leading etiologies: sarcoma [20.3%], GI [15.7%], GU [12.4%]). Clinical characteristics (CAD, atherosclerosis risk factors, anti-cancer treatments) were similar between CMASS patients and controls ( $p=NS$ ). Regarding CMASS location, CNEO varied (LV 30% | RV 30% | LA 29% | RA 34% | pericardium 26%) whereas CTHR which were typically right-sided and associated with indwelling catheters (RA 98% | LV 2%). On first-pass perfusion CMR, regions with CNEO (defined by LGE) demonstrated dynamic increments contrast enhancement, whereas persistent hypoenhancement was evident in regions with CTHR (**Fig 1A**). Consistent with this, quantitative first-pass perfusion analysis showed that rates of absolute contrast enhancement were >10-fold higher among CNEO vs. CTHR ( $16.3 \pm 2.1$  vs  $2.5 \pm 0.5$ ,  $p < 0.0001$ ), paralleling similar marked differences when contrast enhancement was normalized to blood pool ( $0.14 \pm 0.01$  vs  $0.04 \pm 0.001$ ,  $p < 0.0001$ ) (**Fig 1B**). ROC analysis was used to establish optimal partition indices to differentiate CNEO from CTHR (**Fig 2**), for which results demonstrated good overall performance (AUC 0.83-0.89;  $p < 0.001$  [accuracy 80-84%]). As



shown in **Fig 3**, use of perfusion CMR partitions to differentiate CNEO from CTHR also stratified prognosis: Patients with perfusion-CMR defined CNEO had higher risk for death than did matched controls (HR=1.49[1.06-2.09],  $p=0.02$ ), which was equivalent to that using LGE-CMR (HR=1.71[1.21–2.41],  $p=0.003$ ): Similarly, comparison between CMASS groups demonstrated higher mortality with CNEO as defined by both perfusion (HR=2.03[1.19-3.46],  $p=0.009$ ) and LGE (LGE: HR=3.43[1.95-6.03],  $p<0.001$ ). Conversely, patients with CTHR had similar mortality to matched controls, irrespective of whether CTHR was defined via LGE (HR=0.85[0.45-1.63],  $p=0.63$ ) or perfusion CMR (HR=1.18[0.61–2.31],  $p=0.61$ )

**Conclusions:** Quantitative perfusion CMR provides a novel means to differentiate CNEO from CTHR based on tissue properties stemming from vascularity. Among systemic cancer patients, cardiac masses that enhance on perfusion-CMR confer increased risk for death.

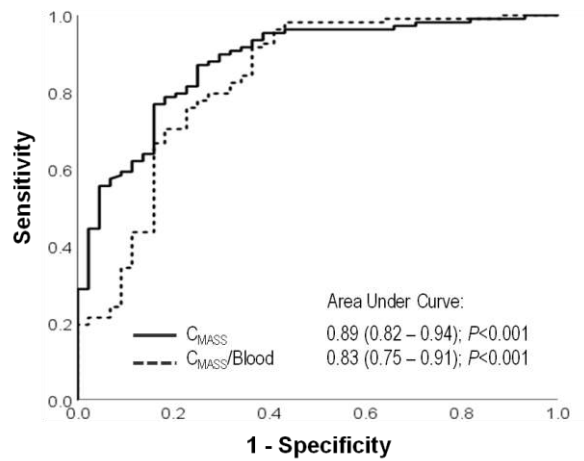
**Figure/Table 1**



**Caption 1**

Figure 1. (A) First pass perfusion CMR demonstrating diffuse contrast uptake in CNEO whereas no significant uptake in CTHR. (B) Quantitative perfusion CMR showing rate of contrast uptake from time-intensity curve within CNEO vs CTHR as well as normalization to contrast uptake of blood pool within left ventricular cavity.

**Figure/Table 2**

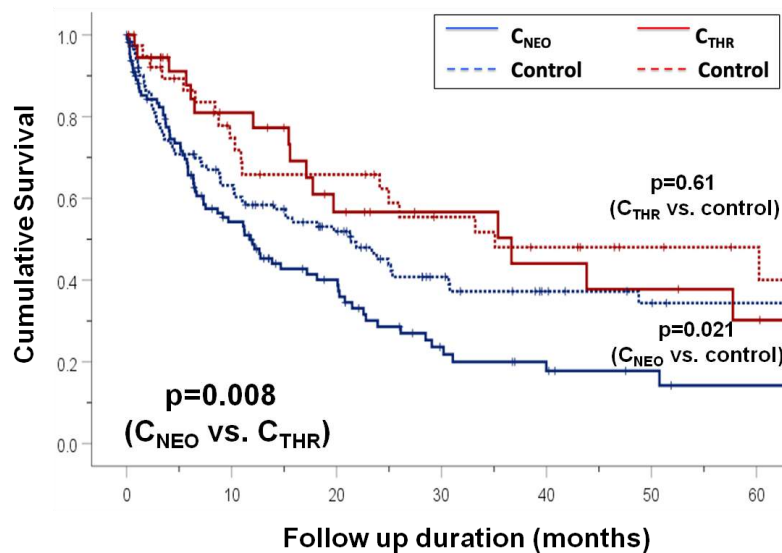


	Sensitivity	Specificity	PPV	NPV	Accuracy
$C_{MASS}$	82% (36/44)	79% (85/108)	61% (36/59)	91% (85/93)	80% (121/153)
$C_{MASS}/blood$	64% (29/45)	92% (99/108)	76% (29/38)	86% (99/115)	84% (128/153)

**Caption 2**

Figure 2. ROC Analysis of quantitative perfusion CMR of cancer-associated cardiac masses compared to LGE CMR. Sensitivity, specificity, positive predictive value, negative predictive value, and accuracy of detecting CNEO compared to LGE-CMR.

**Figure 3**



**Caption 3**

Figure 3. Kaplan-Meier curves comparing survival among patients with quantitative perfusion CMR-evidenced CNEO, CTHR, and their respective matched controls. Perfusion CMR-evidenced CNEO and CTHR were identified based on ROC curve cut offs.

Speaker: A. Chan

Category: Cardiac Mass, Perfusion, Prognosis

000319

## Noninvasive Differentiation of Cardiac Amyloidosis Subtype Using Cardiac Magnetic Resonance and Light Chain Biomarkers: Is it Too Good to Be True?

J. Slivnick \* (1); N. Alvi (2); C. Singulane (1); S. Scheetz (1); A. Goyal, (3); A. Wallner (3); H. Patel (1); N. Sarswat (1); K. Addetia (1); O. Simonetti (4); K. M. Zareba, (5); A. R. Patel (1)

(1) Cardiovascular Medicine, UChicago Medicine, Chicago, United States of America; (2) Cardiovascular medicine, AMITA Health Adventist Medical Center Hinsdale, Hinsdale, United States of America; (3) Cardiovascular medicine, The Ohio State University Wexner Medical Center, Columbus, United States of America; (4) Davis heart and lung research institute, The Ohio State University, Columbus, United States of America; (5) Division of cardiovascular medicine, The Ohio State University Wexner Medical Center, Columbus, United States of America

### Abstract

**Background:** Cardiac amyloidosis (CA) is most commonly caused by deposition of immunoglobulin light chain (AL-CA) or transthyretin (ATTR-CA) proteins. While cardiac magnetic resonance (CMR) is frequently obtained in the evaluation of suspected CA, current guidelines recommend that CA subtype should be determined using invasive tissue biopsy or a combination of light chain biomarkers and pyrophosphate (PyP) nuclear scan(1). However, these methods add additional downstream cost and/or are invasive. We aimed to determine whether a combination of a pattern of late gadolinium enhancement (LGE) which is typical for CA and negative light chain biomarkers could accurately identify ATTR-CA.

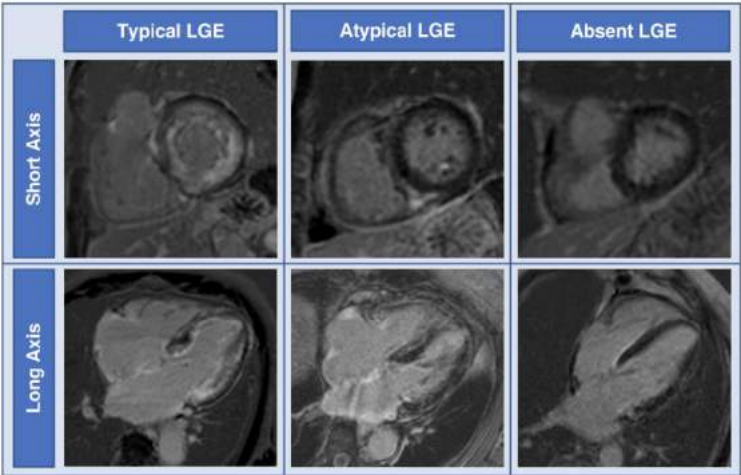
**Methods:** Patients with AL-CA or ATTR-CA who had a typical CA pattern of LGE were retrospectively identified at The Ohio State University and University of Chicago (Figure 1). Typical LGE pattern was defined as subendocardial-to-transmural LGE within hypertrophied myocardium with either diffuse circumferential involvement, of  $\geq 6$  wall segments involvement, or inability to obtain adequate LGE images due to abnormal gadolinium kinetics based on Look-Locker imaging. Patients with non-contrast studies, atypical LGE pattern, or incomplete CA subtyping were excluded. We assessed the prevalence of ATTR-CA and AL-CA amongst patients with and without positive light chain biomarkers—defined as presence of an m-protein on serum or urine protein electrophoresis with immunofixation or kappa/lambda light chain ratio  $\leq 0.26$  or  $\geq 1.65$  (or  $\geq 2.5$  in CKD III or higher). In those who underwent technetium pyrophosphate (PyP) or methyl diphosphonate (Tc-MDP) scan, we assessed whether Tc-PyP/MDP results led to correct or incorrect reclassification of CA subtype.

**Results:** 153 patients met inclusion criteria (mean age  $70 \pm 11$  yrs, 73% male, 55% ATTR-CA, 46% AL-CA). Of the 62 patients with typical LGE and negative light chains, 61 had ATTR-CA (PPV=98%, Figure 2). Overall, the absence of light chains was 73% sensitive and 99% specific for ATTR-CA. Out of the 153, 47 patients also underwent Tc-PyP (n=41) or MDP (n=6). The nuclear scan (2 Tc-PyP and 2 MDP) suggested that 4 of the patients with typical LGE pattern and negative light chains did not have ATTR-CA. However, based on either endocardial biopsy (n=3) or genetic testing (n=1), all 4 cases were confirmed to have ATTR-CA despite having a negative Tc-PyP/MDP scan. The most common reasons for false

negative Tc-PyP/MDP was ongoing treatment with tafamidis or use of the older Tc-MDP tracer.

**Conclusions:** In this multicenter study, the absence of serum light chains in patients with a typical LGE pattern for CA was highly specific for the diagnosis of ATTR-CA. Although current guidelines recommend a combination of Tc-PyP imaging and serum light chains to non-invasively diagnose ATTR-CA, our study demonstrates that this may not be necessary in those patients who have a typical CA LGE pattern in the absence of light chains. We propose a potential future diagnostic algorithm incorporating CMR in figure 3. Additionally, our data suggest that systematically pursuing Tc-PYP imaging in these patients may result in the incorrect reclassification of ATTR-CA patients as not having ATTR-CA resulting in delays in accurate diagnosis and access to therapy. Our findings should be validated in a prospectively designed study aimed at specifically addressing this issue.

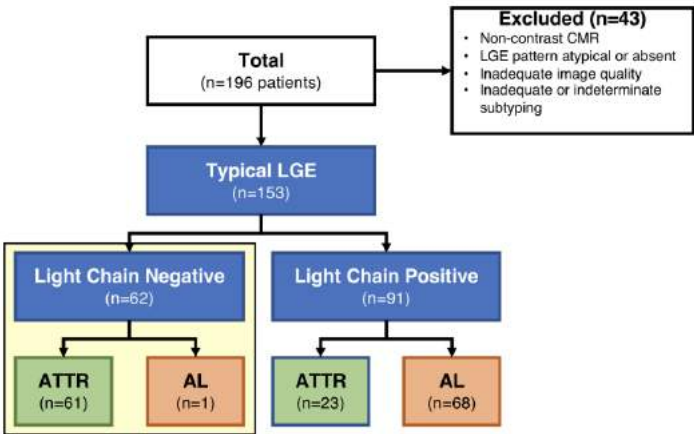
Figure/Table 1



Caption 1

Figure 1: Diagram showing examples of typical, atypical, and absent LGE within our cardiac amyloidosis cohort.

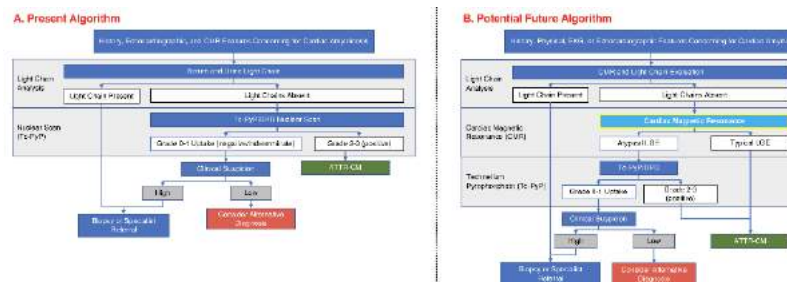
Figure/Table 2



## Caption 2

Figure 2: Schematic illustrating distribution of AL-CA and ATTR-CA amongst patient with and without positive light chains.

## Figure 3



## Caption 3

Figure 3: depicting the current recommended diagnostic algorithm for patients with suspected CA (panel A) as well as a potential future algorithm based on our findings (Panel B). Adapted from J Am Heart Assoc. 2021 May 4;10(9):e019840.

## Bibliographic References

1. Dorbala S, Ando Y, Bokhari S, et al. ASNC/AHA/ASE/EANM/HFSA/ISA/SCMR/SNMMI Expert Consensus Recommendations for Multimodality Imaging in Cardiac Amyloidosis: Part 1 of 2-Evidence Base and Standardized Methods of Imaging. J Card Fail. Nov 2019;25(11):e1-e39.

Speaker: J. Slivnick

Category: Amyloidosis , Cardiomyopathy, Late Gadolinium Enhancement

000320

## Radial k-space Sampling Produces Better Image Quality than Cartesian for Real-time Cine MRI in Patients with a Cardiac Implantable Electronic Device

K. Hong, \* (1); H. Yang (2); J. Collins (3); A. R. Patel (4); D. Lee (5); D. Kim (2)

(1) Radiology, Northwestern University Feinberg School of Medicine, 이스트 수퍼리어 스트리트, Chicago, United States of America; (2) Radiology, Northwestern University Feinberg School of Medicine, Chicago, United States of America; (3) Radiology, Mayo Clinic Rochester MN, Rochester, United States of America; (4) Medicine and radiology, University Of Virginia, Lee Street, Charlottesville, United States of America; (5) Division of cardiology, internal medicine, Northwestern University Feinberg School of Medicine, Chicago, United States of America

### Abstract

**Background:** While breath-held (BH) cardiac cine MRI using Cartesian k-space sampling and balanced steady-state free precession readout is the golden standard for assessment of cardiac function in non-device patients [1], it is not applicable for patients with a cardiac implantable electronic device (CIED) due to off-resonance artifacts. BH cine MRI with gradient echo (GRE) readout is the current standard for CIED patients, but it, too, may yield non-diagnostic image quality in CIED patients with limited breath-holding capacity and/or arrhythmia. To compensate for those issues, free-breathing, real-time (FB-RT) cine MRI using Cartesian k-space sampling, gradient echo readout (GRE), and compressed sensing (CS) algorithm was developed and evaluated in patients with a CIED [2]. Its image quality, however, was often suboptimal due to limited acceleration afforded by Cartesian k-space sampling. We hypothesize that radial k-space sampling produces better image quality than Cartesian k-space sampling for FB-RT cine with GRE readout. In this study, we sought to compare the image quality produced by FB-RT cine between Cartesian and radial k-space sampling patterns in patients with a CIED.

**Methods:** We enrolled 2 patients (a 61 year-old male, a 61 year-old female) with a CIED and 7 non-device patients (male/female=4/3,  $46.7 \pm 15.1$  year-old) with a CIED taped below the left clavicle (~12 cm away from the heart). The 16-fold accelerated Cartesian k-space sampling with GRE readout was previously described [2]. We developed a matching 16-fold accelerated radial k-space sampling with tiny golden angles ( $32.0397^\circ$ ) and GRE readout. FB-RT cine scans were performed to cover the whole left ventricle in short-axis planes during post-contrast. The relevant imaging parameters included: FOV=400x400 mm<sup>2</sup>, slice thickness=8 mm, reconstruction matrix=192x192, spatial resolution=2.1x2.1 mm<sup>2</sup>, flip angle=15°, TE/TR=1.46/2.95 ms for Cartesian and 1.46/3.34 ms for radial, receiver bandwidth=744 Hz/pixel, 12 k-space lines per frame (acceleration factor=16), temporal resolution=35.4 ms for Cartesian and 40.1 ms for radial. Please refer to [2,3] for other parameters. **Image Reconstruction:** We reconstructed cine images using SPARSE-SENSE [2,3] with a temporal total variation as the sparsifying transform, 36 iterations, and empirically derived normalized regularization weights: 0.01 for Cartesian and 0.001 for radial sampling. **Image Analysis:** For quantitative analysis, we utilized a metric embedded in Matlab: perception-based image quality evaluator (PIQE)[4], which requires no reference and mainly evaluates the level of noise, distortion, and blurriness ([0,20]-excellent;[21,35]-

good;[36,50]-fair;[51,80]-poor;[81,100]-bad). PIQE was evaluated in each cine frame, and its values were averaged across multiple cardiac frames and slices per patient.

**Results:** Figures 1 and 2 compared FB-RT cine images between Cartesian and radial in patients with a CIED and non-device patients with a taped CIED, respectively. Summarizing the results from all datasets, radial cine yielded significantly ( $p<0.05$ ) lower mean PIQE than Cartesian cine (i.e., better image quality). In Table 1, mean PIQE was classified as excellent for all 9 radial datasets, whereas only 2 Cartesian datasets were classified as excellent.

**Conclusions:** This preliminary study shows that FB-RT GRE cine MRI with radial k-space sampling produces better image quality than matching Cartesian sampling in patients with a CIED. Future study is warranted to compare visual assessment by clinical raters and cardiac functional parameters with segmented BH cine with GRE as the reference.

**Figure/Table 1**

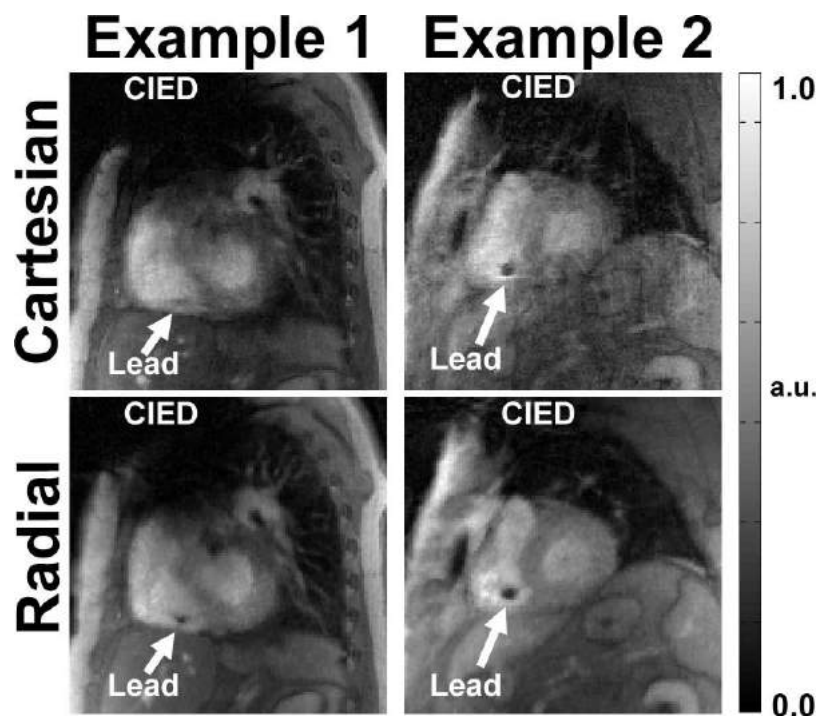
Patient ID	Cartesian Cine	Radial Cine	<i>p</i> -value
CIED Pt #1	28.9 ± 4.4 (G)	14.5 ± 2.2 (E)	<0.001
CIED Pt #2	33.1 ± 3.8 (G)	13.4 ± 3.3 (E)	<0.001
Taped CIED Pt #1	35.0 ± 5.2 (G)	12.7 ± 2.0 (E)	<0.001
Taped CIED Pt #2	13.6 ± 9.8 (E)	9.8 ± 4.2 (E)	<0.001
Taped CIED Pt #3	26.7 ± 7.5 (G)	14.3 ± 4.2 (E)	<0.001
Taped CIED Pt #4	18.0 ± 3.4 (E)	10.1 ± 2.6 (E)	<0.001
Taped CIED Pt #5	24.7 ± 6.6 (G)	12.7 ± 2.3 (E)	<0.001
Taped CIED Pt #6	30.3 ± 6.6 (G)	11.1 ± 4.0 (E)	<0.001
Taped CIED Pt #7	32.3 ± 7.3 (G)	10.9 ± 2.6 (E)	<0.001

**Caption 1**

**Table 1.** A comparison of mean PIQE between Cartesian vs. radial k-space sampling patterns per patient. Values present mean ± standard deviation.  $p<0.05$  is considered statistically significant (pair-wise t-test). E=excellent; G=good; F=fair; P=poor; B=bad.

**Figure/Table 2**

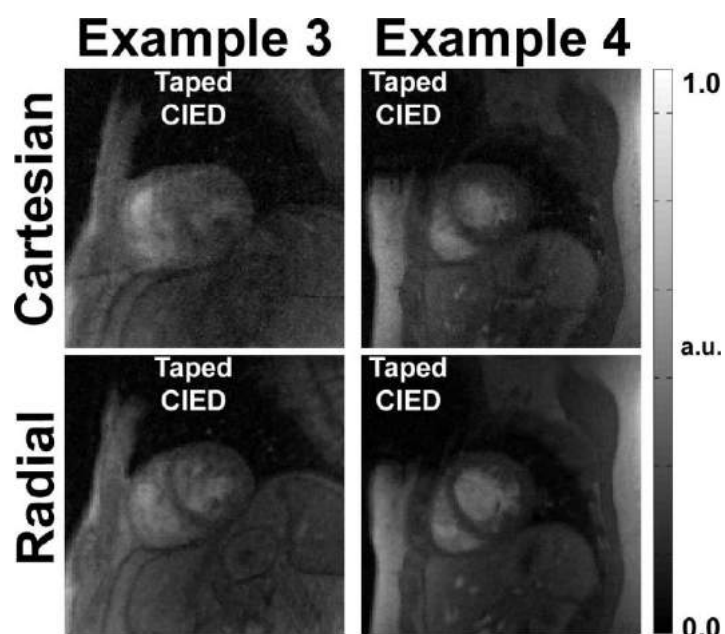




**Caption 2**

**Figure 1.** Representative Cartesian (top row) vs. radial (bottom row) cine images in patients with a CIED: Example 1 (column 1) and Example 2 (column 2). The corresponding PIQE of Example 1 and 2 was 21.5 (good) and 34.6 (good) for Cartesian and 12.8 (excellent) and 18.3 (excellent) for radial, respectively.

**Figure 3**



### Caption 3

**Figure 2.** Representative Cartesian (top row) vs. radial (bottom row) cine images of a non-device patient with a taped CIED: Example 3 (column 1) and Example 4 (column 2). The corresponding PIQE of Example 3 and 4 was 35.1 (good) and 32.3 (good) for Cartesian and 9.6 (excellent) and 7.5 (excellent) for radial, respectively.

### Bibliographic References

4. Venkatanath N, Praneeth D, Chandrasekhar BM, Channappayya SS, Medasani SS. Blind Image Quality Evaluation Using Perception Based Features. IEEE, In Proceedings of the 21st National Conference on Communications (NCC) 2015., 3. Haji-Valizadeh H, Rahsepar AA, Collins JD, Bassett E, Isakova T, Block T, Adluru G, DiBella EVR, Lee DC, Carr JC, Kim D, Binders CKDOMw, Nicotinamid ESG. Validation of highly accelerated real-time cardiac cine MRI with radial k-space sampling and compressed sensing in patients at 1.5T and 3T. Magn Reson Med 2018;79(5):2745-2751., 2. Hong S, Hong K, Culver AE, Pathrose A, Allen BD, Wilcox JE, Lee DC, Kim D. Highly Accelerated Real-Time Free-Breathing Cine CMR for Patients With a Cardiac Implantable Electronic Device. Acad Radiol 2020., 1. American College of Cardiology Foundation Task Force on Expert Consensus D, Hundley WG, Bluemke DA, Finn JP, Flamm SD, Fogel MA, Friedrich MG, Ho VB, Jerosch-Herold M, Kramer CM, Manning WJ, Patel M, Pohost GM, Stillman AE, White RD, Woodard PK. ACCF/ACR/AHA/NASCI/SCMR 2010 expert consensus document on cardiovascular magnetic resonance: a report of the American College of Cardiology Foundation Task Force on Expert Consensus Documents. Circulation 2010;121(22):2462-2508.

Speaker: K. Hong,

Category: Cardiac Implantable Electronic Devices, Cine Imaging, Real Time

000321

## Accuracy of free-breathing SASHA in identifying T1 and T2 elevations found on conventional mapping in pediatric orthotopic heart transplant patients

D. Patel \* (1); V. Cleveland (1); K. Hamman (1); S. Irizarry (1); J. Kanter (1); T. Downing (1); J. Berger (1); A. Christopher (2); R. Cross, (1); K. Chow (3); L. Olivieri (1)

(1) Cardiology, Children's National Hospital, Washington, United States of America; (2) Cardiology, UPMC Children's Hospital of Pittsburgh, Pittsburgh, United States of America; (3) Mr r&d collaborations, Siemens Medical Solutions Usa, Inc., Chicago, United States of America

### Abstract

**Background:** Cardiovascular magnetic resonance is a promising modality for evaluation of graft rejection and health, given its quantitative, volumetric assessment of fibrosis and edema. Quantitative T1/T2 parametric mapping reveals patterns of T1/T2 elevation (“hotspots”) in myocardial diseases, such as rejection, reinforcing that these pathologic changes are not uniform in nature. Breath-held (BH) Modified Look-Locker Inversion (BH MOLLI) T1 mapping and T2-prepared balanced steady-state free-precession (BH T2p-bSSFP) can be used to identify regional myocardial disease, which may be useful in guiding endomyocardial biopsy (EMB). However, the sequence requires good breath-holding, so free-breathing (FB) techniques may impart an advantage, particularly in a pediatric population. The primary aim of this study was to evaluate the ability of FB multi-parametric SATuration recovery single-SHot Acquisition (mSASHA) T1 and T2 to identify hotspots present on conventional BH T1 and T2 maps in pediatric orthotopic heart transplant (OHT) patients. A secondary aim was to measure the distance between hotspots using FB and BH approaches.

**Methods:** In a prospective IRB approved study, and with consent/assent, pediatric OHT patients underwent clinically indicated EMB and noncontrast 1.5T CMR (MAGNETOM Aera, Siemens Healthcare, Erlangen, Germany) with BH MOLLI T1 and T2p-bSSFP mapping and prototype FB mSASHA T1 and T2 in 8 short-axis slices. Maps with poor image quality or significant motion were excluded. Both FB and BH T1 and T2 maps were segmented using semi-automated thresholding software (ITK-SNAP, v3.6) to identify hotspots, demonstrated in Figure 1. Both the presence/absence and location coordinates of hotspot centers were collated and compared using 3D software (3-matic, Materialise, Leuven, Belgium).

**Results:** Forty children with OHT were included (age  $12.0 \pm 4.8$  y, graft age  $6.0 \pm 4.4$  y, HR  $81 \pm 11$  bpm, BSA  $1.5 \pm 0.4$  m<sup>2</sup>, and LVEF  $64.1 \pm 5.4\%$ ). Seven (17.5%) FB T1 maps and no FB T2 maps were discarded due to motion artifact or poor image quality. Mapping results from both sequences are summarized in Table 1. T1 hotspots were identified in 24/40 patients using BH MOLLI, and 19 of those 24 using FB mSASHA (79.2% sensitivity). T2 hotspots were identified in 10/40 patients using BH maps, and 8 of those 10 using FB mSASHA (80% sensitivity). Of the 9 T1 and 30 T2 BH cases with no hotspots, FB maps also demonstrated no hotspots (100% specificity for T1 and T2). There was overlap noted in 3D space between all FB and BH located hotspots and a consistent offset (average  $4.9 \pm 2.4$ mm on T1 maps and  $5.3 \pm 1.6$ mm on T2 maps) in the circumferential cardiac direction (Figure 2), thought to be secondary to difference in acquisition times between BH and FB maps.

**Conclusion:** FB mSASHA T1/T2 maps can identify hotspots present on conventional BH T1/T2 maps in pediatric OHT patients, with high sensitivity, specificity, and overlap in 3D space. Further optimization is needed to improve image quality and motion artifact in the pediatric population. Free-breathing mapping may improve patient comfort and enable OHT assessment in younger patient populations who are unable to hold their breath.

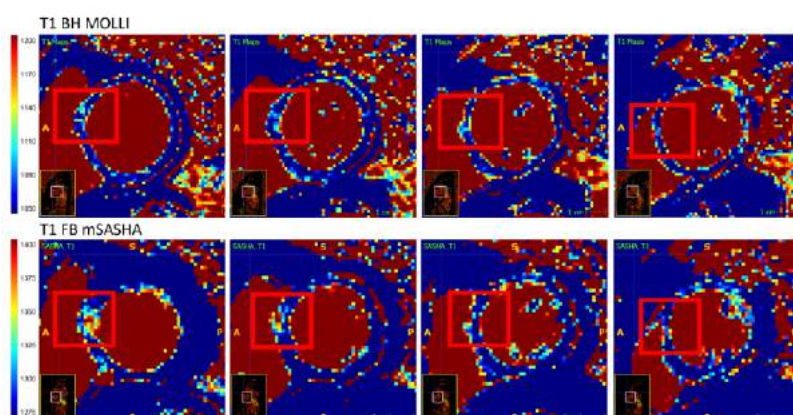
**Figure/Table 1**

	T1 (n=40)		T2 (n=40)	
Maps excluded due to artifact	7 (17.5%)		0 (0%)	
Hotspot Identification	BH MOLLI (33 total)		BH T2p-bSSFP (40 total)	
	Hotspot Present	No Hotspot	Hotspot Present	No Hotspot
Hotspot present on mSASHA	19	0	8	0
No hotspot on mSASHA	5	9	2	30
Match rate:	79.2%	100%	80%	100%

**Caption 1**

Table 1. Mapping results from breath held (BH) and free breathing (FB) maps

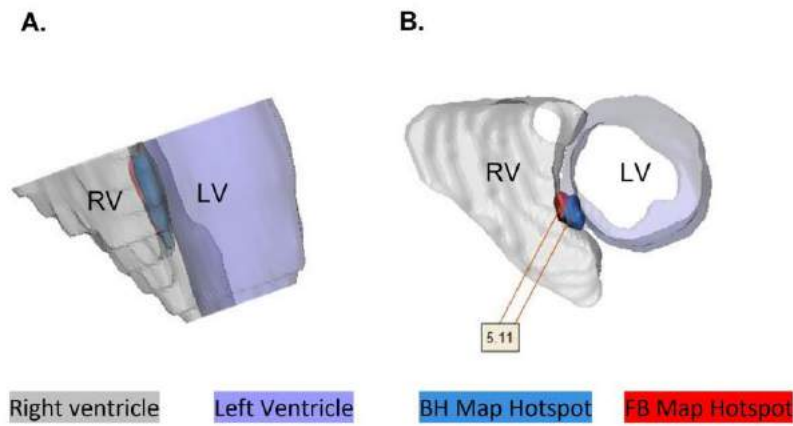
**Figure/Table 2**



**Caption 2**

Figure 1. T1 BH (breath-held) MOLLI and T1 FB (free breathing) mSASHA parametric maps as viewed in ITK-SNAP segmentation software, with appropriate thresholding applied. A hotspot is identified (in red box) in the basal to mid anteroseptal regions.

**Figure 3**



### Caption 3

Figure 2. 3D representation of hotspot (also demonstrated in Figure 1), located in basal to mid anteroseptal region, relative to segmented right ventricle and left ventricle in anteroposterior view (A) and short-axis view (B). Hotspot identified on FB maps is located about 5.11 mm from hotspot identified on BH maps in the circumferential cardiac direction.

Speaker: D. Patel

Category: Parametric Mapping, Heart Transplant, Mapping Techniques

000324

## Quantification of Left Atrial Function by the Area-Length Method Overestimates Left Atrial Emptying Fraction

S. Liu \* (1); A. DiCarlo (2); J. Baraboo (2); A. Maroun (1); D. Lee (3); R. Passman (4); M. Markl (2); P. Greenland (5); M. Pradella (6)

(1) Department of Radiology, Northwestern University Feinberg School of Medicine, Chicago, United States of America; (2) Department of radiology, Northwestern University Feinberg School of Medicine, East Superior Street, Chicago, IL, USA, Chicago, United States of America; (3) Division of cardiology, internal medicine, Northwestern University Feinberg School of Medicine, Chicago, United States of America; (4) Department of cardiology, Northwestern University Feinberg School of Medicine, Chicago, United States of America; (5) Preventive medicine, Northwestern University Feinberg School of Medicine, Chicago, United States of America; (6) Radiology, Northwestern University Feinberg School of Medicine, East Superior Street, Chicago, IL, USA, Chicago, United States of America

### Abstract

### BACKGROUND

The biplane area-length method is commonly used in cardiac MRI (CMR) to assess left atrial (LA) volume (LAV) and function. Studies have shown that this method allows for good estimation of maximum LA volume (LAV<sub>max</sub>) compared to 3D assessment, which is based on short axis (SAX) cine steady state free precession (SSFP) [1]. However, there is only limited data available on its estimation of minimum LAV (LAV<sub>min</sub>) or volume before atrial contraction (LAV<sub>preA</sub>) [1, 2]. As a result, the effect on the calculation of LA emptying fractions (LAEF) using the biplane method compared to 3D assessment is not well investigated [3]. This is relevant because associations between LAEF and clinical endpoints, such as outcome after myocardial infarction, have been reported [4]. In this study, we sought to compare volumetric and functional LA parameters obtained from the area-length method with 3D assessment as the reference standard in a healthy aging cohort.

### METHODS

Participants underwent a dedicated cardiac MRI on a 1.5T system (Siemens, Germany). The MRI protocol included standard two- and four-chamber SSFP cine imaging, as well as SAX SSFP cine series covering the whole LA (spatial resolution: 1.8x1.8x6mm, temporal resolution: ~40ms). The biplane area-length method analysis was based on manually defined 2D LA contours on two- and four-chamber series using a commercial software (cvi42, version 5.9.0, Circle, Canada) (Fig. 1A). For 3D assessment, LA contours were manually delineated for each LA SAX 2D slice and cardiac time point (Fig. 1B). At the atrioventricular junction, the LA was contoured only if there was less than 50% of left ventricular myocardium visible. All 2D SAX contours were combined into a time-resolved 3D LA volume dataset using MATLAB (MathWorks, USA). The pulmonary veins and the left atrial appendage were excluded in both methods [1]. LAV<sub>max</sub>, LAV<sub>min</sub>, and LAV<sub>preA</sub> were identified in the respective volume-time curves to calculate total, active, and passive LAEF (Fig. 1C) [1]. Wilcoxon signed-rank tests and Bland-Altman plots were used for comparison.

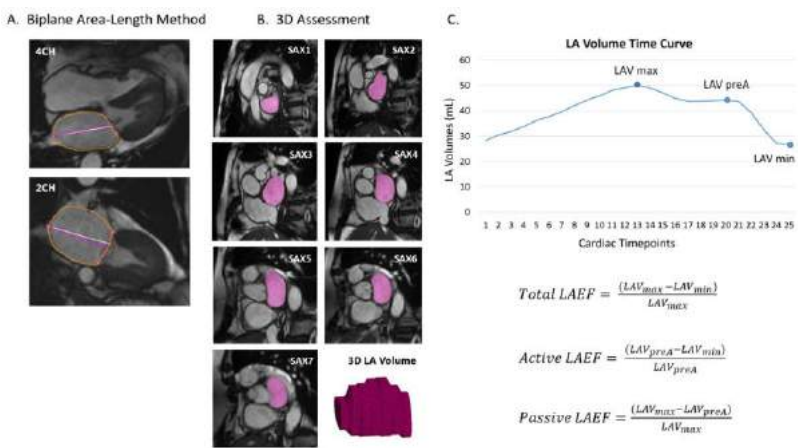
RESULTS

We included 80 participants in this ongoing study, mean age  $73.2\pm7.7$  years (42 female). Standard volumetric assessment showed that LAVmin ( $p<0.001$ , bias: -9.5 mL), LAVmax ( $p<0.001$ , bias: -12.0 mL) and LAVpreA ( $p<0.001$ , bias: -10.9 mL) were significantly smaller using the biplane method compared to the 3D assessment (Table 1). Furthermore, the biplane method reported significantly higher LAEFtotal ( $p<0.001$ , bias: 7.0%), LAEFactive ( $p<0.001$ , bias: 6.8%), and LAEFpassive ( $p<0.001$ , bias: 3.6%) (Fig. 2). The limits of agreement for each LAEF parameter were wide, represented in high percentage errors for LAEFtotal (60.5%), LAEFactive (92.7%), and LAEFpassive (160.0%).

CONCLUSION

Our results of 3D LAEF are similar to reported 3D mean values in a small sample of 20 volunteers in the same age group [5]. Yet, we observed wide limits of agreement with high percentage error, which indicates both overestimation and underestimation on an individual level. These findings suggest a potential lack of precision using the biplane area-length method, which might be relevant for future studies evaluating LA function. We will include more participants and conduct interobserver assessment to validate our data.

Figure/Table 1



Caption 1

Fig 1. (A) LA contours on two- and four-chamber images at max LAV. (B) LA contours on SAX images and a 3D volume representation of the LA. (C) Determination of maximum (LAVmax), minimum (LAVmin), and LAV before atrial contraction (LAVpreA) using the LA volume time curve for each method, and the equations used to calculate LAEF parameters.

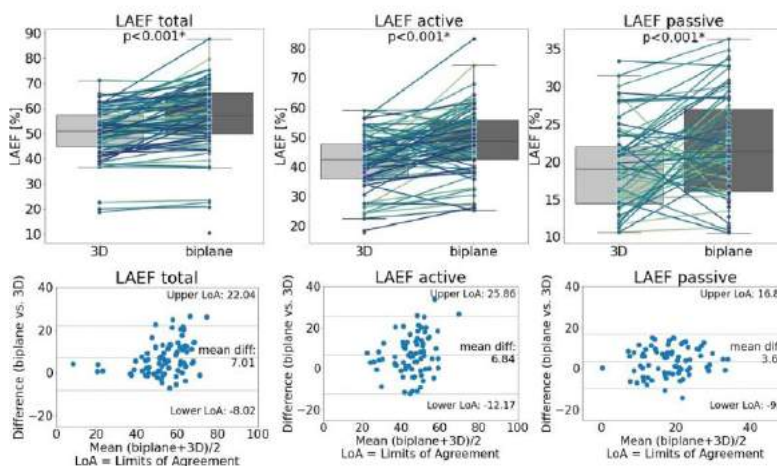
Figure/Table 2

Parameter	Biplane	3D	P-value	Bias	LoA	% Error
LAV min (mL)	26.9 ± 19.0	35.1 ± 18.5	p<0.001	-9.5	-31.9–13.0	127.9
LAV max (mL)	59.5 ± 23.7	68.8 ± 21.6	p<0.001	-12.0	-47.6–23.7	103.6
LAV preA (mL)	44.7 ± 16.1	56.1 ± 15.7	p<0.001	-10.9	-33.7–11.9	81.3
LAEF total (%)	57.0 ± 13.5	49.6 ± 11.3	p<0.001	7.0	-8.0–22.0	60.5
LAEF active (%)	48.9 ± 11.3	41.1 ± 10.2	p<0.001	6.8	-12.2–25.9	92.7
LAEF passive (%)	20.3 ± 7.9	16.5 ± 7.3	p<0.001	3.6	-9.6–16.8	160.0

**Caption 2**

Table 1. Mean values with standard deviation for LAV and LAEF parameters as calculated by the biplane and 3D methods. LoA = Limits of Agreement. % Error (Percentage Error) = (upper LoA – lower LoA) / (mean from 3D method).

**Figure 3**



**Caption 3**

Fig 2. Bland-Altman plots comparing biplane and 3D methods for each LAEF parameter. Overall, the biplane method overestimated the LAEFs significantly; however, limits of agreement were wide, resulting in high percentage errors (LAEF total: 60.5%, LAEF active: 92.7%, LAEF passive: 160.0%). This indicates variance on an individual level.

## Bibliographic References

1. Zemrak F, Ambale-Venkatesh B, Captur G, Chrispin J, Chamera E, Habibi M, Nazarian S, Mohiddin SA, Moon JC, Petersen SE et al: Left Atrial Structure in Relationship to Age, Sex, Ethnicity, and Cardiovascular Risk Factors: MESA (Multi-Ethnic Study of Atherosclerosis).



Circ Cardiovasc Imaging 2017, 10(2)., 2. Bashir A, Rabbat M, Biswas S, Wilber D, Sanagala T, Syed MA: Left atrial volume assessment by area-length method compared to multislice volumetric method using cardiovascular magnetic resonance imaging. Journal of Cardiovascular Magnetic Resonance 2013, 15(Suppl 1):E97-E97., 3. Wandelt LK, Kowallick JT, Schuster A, Wachter R, Stumpfing T, Unterberg-Buchwald C, Steinmetz M, Ritter CO, Lotz J, Staab W: Quantification of left atrial volume and phasic function using cardiovascular magnetic resonance imaging-comparison of biplane area-length method and Simpson's method. Int J Cardiovasc Imaging 2017, 33(11):1761-1769., 4. Schuster A, Backhaus SJ, Stiermaier T, Navarra JL, Uhlig J, Rommel KP, Koschalka A, Kowallick JT, Lotz J, Gutberlet M et al: Left Atrial Function with MRI Enables Prediction of Cardiovascular Events after Myocardial Infarction: Insights from the AIDA STEMI and TATORT NSTEMI Trials. Radiology 2019, 293(2):292-302., 5. Maceira AM, Cosin-Sales J, Prasad SK, Pennell DJ: Characterization of left and right atrial function in healthy volunteers by cardiovascular magnetic resonance. Journal of Cardiovascular Magnetic Resonance 2016, 18(1):64.

Speaker: S. Liu

Category: Left Atrium, Cardiac Function, Cine Imaging

000325

## **An Unusual Cardiac Mass Diagnosed by Cardiac Magnetic Resonance**

T. Patel \* (1); P. Norton (2); C. Kramer (3); M. Salerno (4)

(1) Cardiac imaging, University of Virginia, CHARLOTTESVILLE, United States of America; (2) Radiology, University of Virginia, Charlottesville, United States of America; (3) Cardiology, radiology and medical imaging, University of Virginia, Charlottesville, United States of America; (4) Cardiology, radiology, and medical imaging, University of Virginia, Charlottesville, United States of America

### **Abstract**

#### **Description of Clinical Presentation:**

11 year old male without risk factors presented with a 10lb weight loss and abdominal pain, and was found to be in acute heart failure with a BNP >400. Initial imaging with an echocardiogram was notable for a 4.5cm cardiac mass in the right atrium, moderate pericardial effusion, and mild-moderately reduced LV systolic function. Given the location and age of the patient, the mass was thought to be a sarcoma and he was referred for cardiac magnetic resonance (CMR) for further evaluation.

#### **Diagnostic Techniques and Their Most Important Findings:**

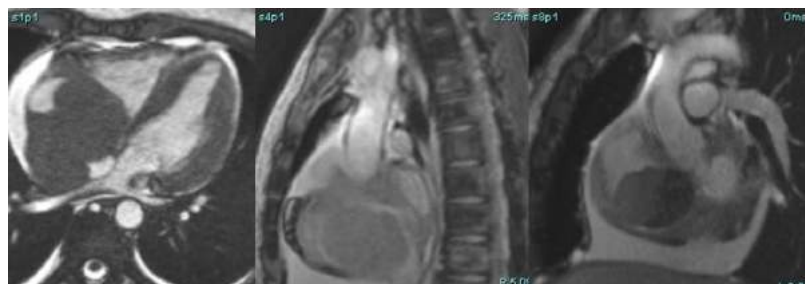
Steady-state free precession (SSFP) cine images revealed mildly reduced LV function, moderately reduced RV function and a severely dilated right atrium with a lobulated 6.4cm x 4cm mass (Figure 1). The mass extended into the tricuspid valve causing a mass effect on adjacent structures including the inferior right pulmonary vein, IVC, and SVC. Tissue characterization was notable for hyperintense T2 signal and isointense T1 signal (Figure 2). LGE showed heterogeneous uptake within the mass with a rim of enhancement (Figure 3). The patient underwent biopsies of the mass which was found to show aggressive B-cell lymphoma and was subsequently started on chemotherapy. A follow-up CMR showed an interval reduction in the right atrial mass to 4.7 x 3.5cm and improvement in biventricular systolic function (Figure 3). Pt is currently in remission after completing chemotherapy.

#### **Learning Points from this Case**

Cardiac tumors are rare but can be associated with adverse outcomes. Metastatic tumors are more common than primary cardiac tumors. In children, the majority of primary cardiac tumors are benign with rhabdomyomas and fibromas making up 80% of all cardiac tumor cases. Sarcomas are the most common primary malignant tumor in children. Cardiac sarcomas typically appear as a single lesion with variable tissue characterization. Primary cardiac lymphomas are very rare and typically involve the right heart. Cardiac lymphomas are hypo- to isointense on T1-weighted images, isointense on T2-weighted images, and exhibit heterogeneous LGE. Lymphomas are also notorious for extending into neighboring structures including IVC, myocardium, and pericardium. In this case, there was extension into other

structures, but the extent was underestimated in terms of involvement of pericardium and IVC. Differentiation or recognition of cardiac lymphoma is important as the treatment is chemotherapy rather than resection. This case illustrates the importance of considering cardiac lymphomas in the differential of cardiac masses, especially when extension of the mass to adjacent structures is seen, in the pediatric population to guide management.

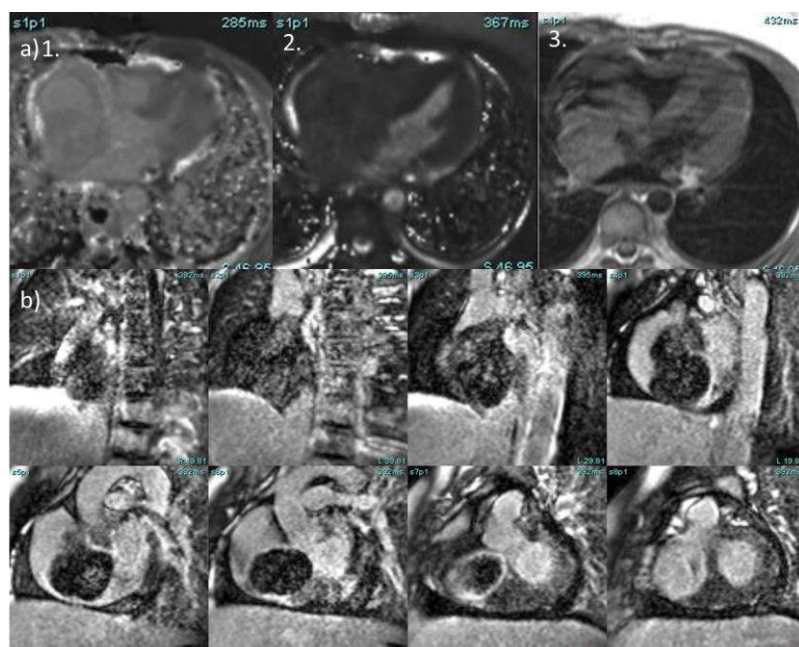
**Figure/Table 1**



**Caption 1**

Figure 1: SSFP cine of a right atrial lobulated mass measuring 6.4cm x 4cm. The first image is pre contrast while the second two are post contrast showing some uptake of gadolinium in the mass.

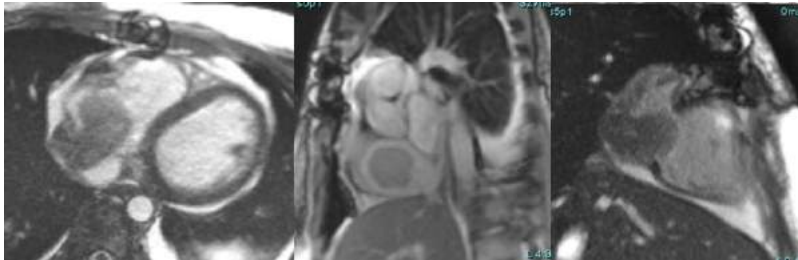
**Figure/Table 2**



**Caption 2**

a) Parametric mapping of the right atrial mass shows 1. Similar T1 times as the myocardium 2. Increased T2 times as compared to the myocardium and 3. increased T2w signal. These images also show tumor extension into the atrial wall. b) LGE showed heterogeneous uptake within the mass with a potential rim of enhancement

**Figure 3**



**Caption 3**

Figure 3: Follow-up CMR showing an interval reduction in the right atrial mass to 4.7 x 3.5cm.

### **Bibliographic References**

1. Ting Y. Tao, Noushin Yahyavi-Firouz-Abadi, Gautam K. Singh, and Sanjeev Bhalla. Pediatric Cardiac Tumors: Clinical and Imaging Features. *RadioGraphics* 2014 34:4, 1031-1046
2. Lam KY, Dickens P, Chan AC. Tumors of the heart: a 20-year experience with a review of 12,485 consecutive autopsies. *Arch Pathol Lab Med* 1993;117(10):1027–1031
3. Jeudy J, Kirsch J, Tavora F et al. Cardiac lymphoma: radiologic-pathologic correlation. *RadioGraphics* 2012;32(5):1369–1380
4. Agarwala B, Rubin CM. Intracardiac lymphoma in a child: successful treatment with chemotherapy alone. *Pediatr Cardiol* 2000;21(4):401–402
5. van Beek EJ, Stolpen AH, Khanna G, Thompson BH. CT and MRI of pericardial and cardiac neoplastic disease. *Cancer Imaging* 2007;7:19–26

Speaker: T. Patel

Category: Cardiac Mass, Parametric Mapping, Late Gadolinium Enhancement

000327

## Recurrent Neural Networks for Cardiac Cine MRI Segmentation with Sparse Annotations

H. Yang \* (1); A. Pathrose, (1); B. Benefield (2); D. Shen (1); A. DiCarlo (1); A. K. Katsaggelos (3); O. S. Cossairt (4); D. Lee (2); D. Kim (1)

(1) Department of radiology, Northwestern University Feinberg School of Medicine, Chicago, United States of America; (2) Department of cardiology, Northwestern University Feinberg School of Medicine, Chicago, United States of America; (3) Department of electrical and computer engineering, Northwestern University, Evanston, United States of America; (4) Department of computer science, Northwestern University, Evanston, United States of America

### Abstract

**Background:** Cardiac cine MRI is the gold standard test for evaluation of global cardiac functional parameters such as ejection fraction (EF)[1]. During image processing, only end-diastolic (ED) and end-systolic (ES) frames are labeled by clinicians, thereby ignoring all other cardiac frames which may have valuable diagnostic and prognostic information. The main obstacle for tapping into said information is the requisite manual labor to draw “circles” for all frames. Deep learning methods have been shown capable of automatically segmenting cardiac MR images[2]. They usually require large-scale, fully-annotated datasets for training the network. However, the available annotations for cine images are temporally sparse. Moreover, applying a network to segment each time frame separately ignores the temporal continuity in the sequential data. In this study, we sought to develop a recurrent neural network to automatically segment cardiac cine images for all cardiac phases given ED and ES annotations only.

**Methods:** This study used cardiac cine MRI datasets with ED and ES annotations from 600 patients; 280 patients from the DETERMINE trial; 320 patients from the Multi-Centre, Multi-Vendor & Multi-Disease Cardiac Image Segmentation Challenge (M&Ms)[3]. Data from 450 patients were used for training the network.

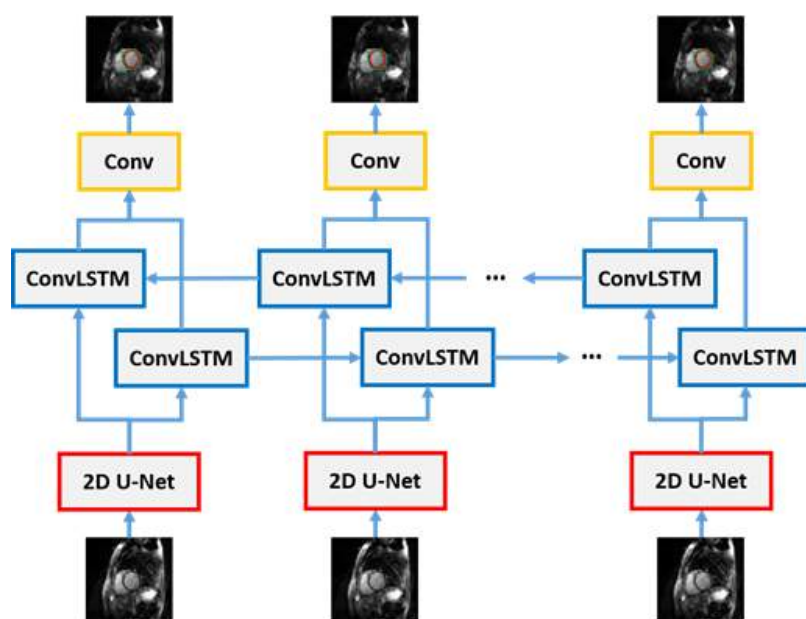
We combined a bi-directional convolutional LSTM (Bi-ConvLSTM) and a 2D U-Net based on the network architecture proposed by Bai et al[4] (Fig 1). The loss function consists of cross-entropy loss, DICE loss, and Hausdorff distance loss. For training the network, the loss function was evaluated only for the labeled ED and ES frames. To test the network performance, one medical research fellow with 3 years of experience labeled the endocardial contours for all time frames in 6 test subjects. We also implemented a 2D U-Net[5] as a reference. Temporal continuity of predicted volume variation was measured using the L1-norm of the derivative of the time-area curve for which a smaller value indicates smoother change and better continuity.

**Results:** In the 6 subjects that we obtained manual annotations for all time frames, the proposed Bi-ConvLSTM produced slightly better DICE scores than the 2D U-Net for endocardial segmentation for all cardiac phases ( $0.873 \pm 0.091$  vs  $0.867 \pm 0.099$ ,  $p=0.02$ ) and epicardial segmentation for ED and ES frames ( $0.862 \pm 0.082$  vs  $0.857 \pm 0.080$ ,  $p=0.15$ ); it performed slightly worse for endocardial segmentation for ED and ES frames ( $0.956 \pm 0.035$

vs  $0.959 \pm 0.022$ ,  $p=0.22$ ). The inter-rater (rater 1 vs rater 2) DICE score for endocardial segmentation for ED and ES frames was  $0.860 \pm 0.105$ . Evaluated over all 150 test subjects, Bi-ConvLSTM shows better temporal continuity than the U-Net (Fig 2). The L1-norm of the derivative of the temporal curve shows significant superiority of Bi-ConvLSTM over the U-Net ( $45.71 \pm 25.09$  vs  $50.76 \pm 33.06$ ,  $p < 0.001$ ) in terms of temporal continuity. Despite the lower DICE score, Bi-ConvLSTM predicted the volumetric parameters (EF, SV, EDV, ESV) slightly better than the U-Net (Fig 3).

**Conclusions:** Bi-ConvLSTM is capable of resolving volume change for all cardiac phases with better temporal continuity than the U-Net and providing slightly more accurate prediction of the ejection fraction and other volumetric parameters of cardiac function.

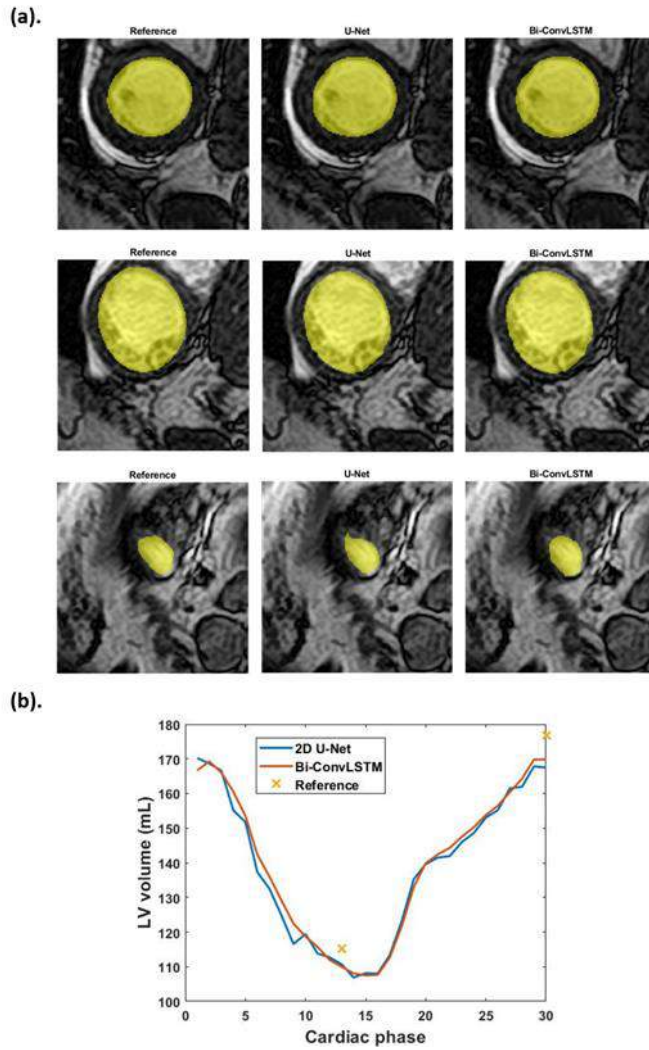
**Figure/Table 1**



**Caption 1**

Network architecture. A bi-directional convolutional long short-term memory network (Bi-ConvLSTM) was combined with a 2D U-Net which extracts features from the time frame. Conv: 2D convolutional layer.

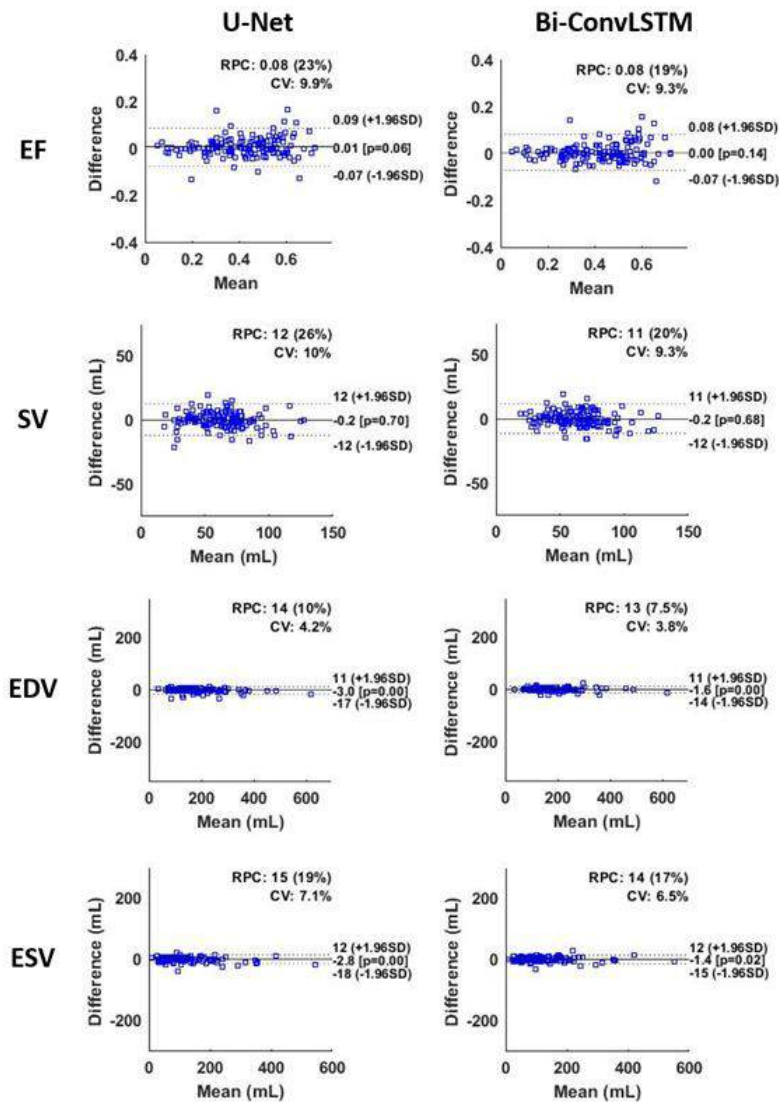
**Figure/Table 2**



## Caption 2

Endocardial segmentation. (a). Results from multiple slices show that both U-Net and Bi-ConvLSTM are able to provide high-quality segmentation for individual time frames. (b). Temporal curve of LV volume shows that Bi-ConvLSTM achieves better temporal continuity throughout cardiac phases than U-Net.

**Figure 3**



### Caption 3

Bland-Altman analysis over all 150 test subjects shows that Bi-ConvLSTM has slightly better agreement with reference than U-Net for measuring ejection fraction (EF), stroke volume (SV), end-diastolic volume (EDV), and end-systolic volume (ESV). RPC: reproducibility coefficient and % of values. CV: coefficient of variation (SD of mean values in %).

Speaker: H. Yang

Category: Cine Imaging, Ejection Fraction, Image Analysis



000328

## The Interdependence of Atrial Fibrosis and Strain on Atrial Pressure and Volumes: A Study of Left Atrial Remodeling in Atrial Fibrillation

J. Lamy \* (1); T. Roy (1); R. Chamoun (1); S. Huber (2); S. Niederer (3); H. Mojibian (2); L. Baldassarre (4); J. Meadows (2); J. Akar (4); D. Peters (1)

(1) Radiology and biomedical imaging, Yale University, New Haven, United States of America; (2) Radiology and biomedical imaging, Yale New Haven Hospital, New Haven, United States of America; (3) Biomedical engineering & imaging sciences, King's College London, London, United Kingdom; (4) Cardiology, Yale New Haven Hospital, New Haven, United States of America

### Abstract

**Background.** Atrial fibrillation (AF) is the most common arrhythmia, with a forecast for 12.1 million affected people by 2030, in the USA alone (1). The simple hypothesis that pressure overload causes pathological remodeling of the left atrium (LA) is the basis of numerous studies (2). LA myocardium is thin and therefore prone to dilatation. Cardiovascular magnetic resonance (CMR) can image multiple features of the LA's pathological remodeling: changes in volumes and function (through cine images) and LA fibrosis with 3D late gadolinium enhancement (LGE). In this work, we investigated the role of pressure-related volume changes, and the presence of atrial fibrosis, in determining atrial strains.

**Methods.** One hundred and seven consecutive patients with AF underwent a standard CMR exam including a free-breathing high resolution 3D LGE acquisition of the atrium3 and long-axis cines (2 and 4-chamber). Within 30 days after CMR, an AF ablation procedure was performed including invasive mean left atrial pressure (LAP) measurement). Among the 107 subjects, 40 were excluded, either due to non-sinus rhythm during CMR (N=23), non-diagnostic cine (N=10), or because of more than mild mitral regurgitation (N=7). Volumes, EFs, strains and strain rates during the reservoir, conduit and active phases were measured and LA fibrosis content (LGE content (mL) normalized by BSA) was assessed (3), when available, from LGE volumes (n=41). Since atrial strain is conceptually dependent on atrial volume, we further analyzed relationships, in patients with normal (N=32) and enlarged LA (N=35) (defined here as LA minimum indexed volume>30ml/cm<sup>2</sup>)

**Results.** Subject characteristics are presented in Table 1. The significant functional correlations to pressure and LA fibrosis are presented in Table 2. While LAP (n=67) was associated with increased LA volumes in the whole cohort (r=0.32, p=0.01), and especially in patients with elevated LA volume (r=0.41, p<0.01), it was not associated with any LA strain metric or with LA fibrosis (Table 2). Increasing atrial pressure was associated with increased LV longitudinal strain (at the time of the atrial kick, Table 2) in patients with normal volumes. As expected, LA Strains and volumes were indeed very strongly correlated (r=0.82, Figure 1A). In the general population, LA LGE content (n=41) was associated with higher LA volumes, lower LA systolic function (strains, strain rates, LAEF) and BMI (Table 2). However, in patients with normal LA volumes, increased LA fibrosis was much more strongly correlated to reduced strains (Figure 1B), compared to the relationship in patients with an enlarged LA.

**Conclusion.** LA strain is often proposed as a LA remodeling surrogate, potentially indicating changes in LA fibrosis (4) or LA pressure (5). However, LA volume was better associated to pressure in our AF cohort and no metric of atrial function was a potential pressure surrogate. Furthermore, LA strain is an approximate surrogate of LA fibrosis, but is most useful in subjects with normal LA volumes, since LA volume itself so strongly impacts strains.

**Figure/Table 1**

	<b>All subject (67)</b>
<b><i>Patient description</i></b>	
<b>Age (y)</b>	61 ± 8
<b>Sex(M/F)</b>	45/22
<b>BMI (kg/m<sup>2</sup>)</b>	31.7 ± 5.7
<b>BSA (m<sup>2</sup>)</b>	2.17 ± 0.27
<b><i>LV indices</i></b>	
<b>LV mass (g)</b>	118 ± 37
<b>LVEF (%)</b>	55 ± 11
<b>LVESVi (ml/m<sup>2</sup>)</b>	35 ± 15
<b>LVEDVi (ml/m<sup>2</sup>)</b>	76 ± 18
<b><i>LV strains</i></b>	
<b>LV global strain (%)</b>	-20.0 ± 5.4
<b>LV strain (pre-atrial kick) (%)</b>	-6.4 ± 2.2
<b><i>LA indices</i></b>	
<b>LAEF (%)</b>	40 ± 17
<b>LAESVi (ml/m<sup>2</sup>)</b>	54 ± 16
<b>LAEDVi (ml/m<sup>2</sup>)</b>	33 ± 17
<b>LAP (mm Hg)</b>	12.2 ± 5.3
<b>Sqrt(LGE/BSA) (ml/m<sup>2</sup>)</b>	0.40 (.28 - .67)
<b><i>LA strains</i></b>	
<b>LA reservoir strain (%)</b>	21.0 ± 10.4
<b>LA conduit strain (%)</b>	14.8 ± 4.4
<b>LA booster strain (%)</b>	11.7 ± 4.9

**Caption 1**

**Table 1: Patient characteristics**

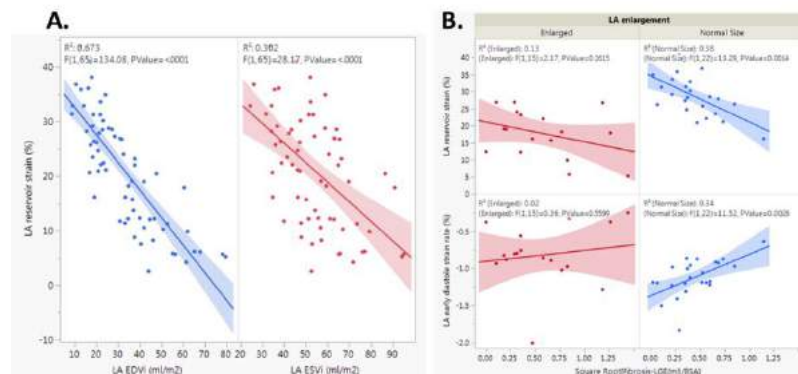
**Figure/Table 2**

All						
Correlations subject LAEDVi<30LAEDVi≥30						
w/ LA LGE (67)						
	r	p	r	p	r	p
BMI	.36	.0217	-	n.s.	-	n.s.
LA reservoir strain	-.46	.0028	-.61	.0014	-	n.s.
LA conduit strain	-	n.s.	-.57	.0038	-	
LA early systole strain rate	-.39	.0134	-.51	.0107	-	n.s.
LA early diastole strain rate	.34	.0327	.59	.0026	-	n.s.
LA EDVi	.45	.0037	-	n.s.	.65	.0045
LA ESVi	.33	.0385	-	n.s.	.66	.0039
LA booster volume	.36	.0229	-	n.s.	.57	.0045
LA EF	-.40	.0098	-.57	.0036	-	n.s.
Correlations w/ LA Pressure						
BMI	.27	.0284	-	n.s.	-	n.s.
LA ESVi	.32	.009	-	n.s.	.43	.0105
LA booster volume	.28	.0242	-	n.s.	.34	.048
LV strain (pre-atrial kick)	-	n.s.	.40	.0218	-	n.s.

**Caption 2**

**Table 2: Functional correlates of LA fibrosis and pressure**

**Figure 3**



**Caption 3**

**A.**Scatter plot showing LA volumes versus the LA longitudinal reservoir strain. **B.** LA fibrosis versus the LA longitudinal reservoir and early diastolic strain rate in patients with normal and enlarged LA. In patients with enlarged LA, fibrosis is not correlated with strain; conversely in patients with normal LA size, the relationship is strong.

## Bibliographic References

5. Henein M, Tossavainen E, Söderberg S, Grönlund C, Gonzalez M, Lindqvist P. Left atrial strain rate estimates PCWP. *Int Cardiovasc Forum J.* 2013;1(1):25-30., 4. Lisi M, Mandoli GE, Cameli M, et al. Left atrial strain by speckle tracking predicts atrial fibrosis in patients undergoing heart transplantation. *Eur Heart J - Cardiovasc Imaging.* 2021;(jeab106)., 3. Quail M, Grunseich K, Baldassarre LA, et al. Prognostic and functional implications of left atrial late gadolinium enhancement cardiovascular magnetic resonance. *J Cardiovasc Magn Reson.* 2019;21(1):2., 2. Blume GG, Mcleod CJ, Barnes ME, et al. Left atrial function: physiology, assessment, and clinical implications. *Eur J Echocardiogr.* 2011;12(6):421-430. , 1. Colilla S, Crow A, Petkun W, Singer DE, Simon T, Liu X. Estimates of Current and Future Incidence and Prevalence of Atrial Fibrillation in the U.S. Adult Population. *Am J Cardiol.* 2013;112(8):1142-1147.

Speaker: J. Lamy

Category: Cardiac Strain, Atrial Fibrillation , Remodelling

000329

## Framework for predictive modeling of risk of sudden cardiac death in AAOCA from advanced imaging using experimental and computational modeling approaches

Y. Farsiani \* (1); A. Razavi (2); J. Parthasarathy, (1); S. Molossi (3); C. Mery (4); L. Dasi, (2); R. Krishnamurthy (1)

(1) Radiology, Nationwide Children's Hospital, Columbus, United States of America; (2) Biomedical engineering, Georgia Institute of Technology, Atlanta, United States of America; (3) Pediatrics-cardiology, Baylor College of Medicine, Houston, United States of America; (4) Department of pediatrics, Dell Children's Medical Center, Austin, United States of America

### Abstract

**Background:** Anomalous aortic origin of a coronary artery (AAOCA) is the most frequent detectable cause of sudden cardiac death (SCD) in children/young adults. The mechanisms underlying SCD are unclear, making risk stratification and management challenging. Biomechanical modeling using precision medicine strategies offers a valid and innovative approach to studying AAOCA by focusing on the patient-specific pathological mechanism for SCD. In this study, we evaluate the accuracy of a combined experimental and computational patient-specific framework for the non-invasive hemodynamic evaluation of AAOCA derived from advanced coronary imaging.

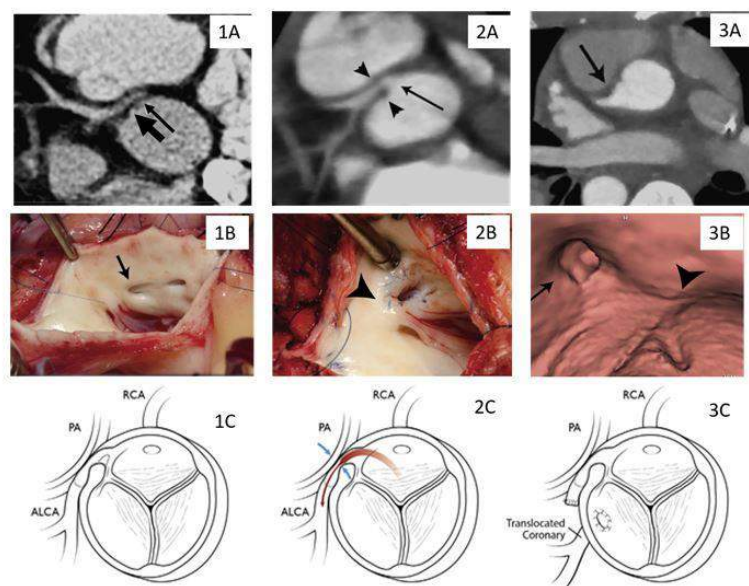
**Methods:** Experimental biomechanical and computational models were created from a patient with an anomalous left coronary artery that presented with aborted SCD, underwent unroofing and later required coronary reimplantation for repeat SCD (Figure 1). Models were created at three time points: preoperatively, after unroofing, and after coronary reimplantation. The experimental assessment used 3D printed aortocoronary flow models (Figure 2) connected to a left heart pulse duplicator, with models precisely featuring morphological biomarkers derived from imaging. Computational fluid dynamics (CFD) aortocoronary model was created using standard techniques. Fractional flow reserve (FFR), coronary flow rates, pressure drop, and velocities were calculated at rest and simulated exercise. Experimental and computational results were compared with available clinical findings and catheterization based FFR.

**Results:** Surgical data showed that unroofing partially resolved ischemia from ostial stenosis and a short intramural course, but did not resolve obstruction related to a thickened intercoronary pillar, which required subsequent translocation to restore normal coronary flow. Catheterization showed resting FFR of 0.7 preoperatively, 0.8 after unroofing, and >0.9 after coronary reimplantation. Experimental modeling showed pre-operative FFR of 0.78, 0.81 and 0.95 for the 3 time-points respectively, in good agreement with clinical data. CFD analysis showed a corresponding pressure drop of  $\cong 12$  mmHg in the preoperative model that decreased successively after unroofing (8 mmHg) and after translocation (6 mmHg).

**Conclusions:** This study shows the feasibility of experimental and computational approaches to provide noninvasive hemodynamic assessment from advanced imaging data. Biomechanical modeling provided comparable results to those obtained from invasive cardiac catheterization. These techniques warrant further evaluation to further understand their utility

for predictive modeling of risk of SCD, surgical planning, and prognostication after AAOCA surgery.

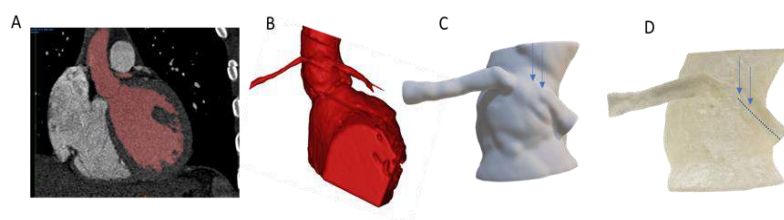
**Figure/Table 1**



**Caption 1**

Patient with AAOCA-L. Preoperative (1A) and intraoperative (1B) views show a slit-like ostium (thin arrow) with an intramural segment traveling behind the thick pillar (thick arrow). initial unroofing (2A and 2B) shows an increased ostium size but compression by the pillar. After reimplantation (3A, 3B) show a wide-open ostium away from the pillar.

**Figure/Table 2**



**Caption 2**

Process flow 3D Printed pre-operative model creation (A): DICOM CTA segmentation of aorta and coronaries, (B ) 3D virtual model of AAOCA blood pool, (C) 3D Pre print model of AAOCA lumen (D): 3D printed AAOCA model with visualization of intramural course

Speaker: Y. Farsiani

Category: Imaging Biomarkers, Coronary Arteries, Sudden Cardiac Death

000333

## Cardiac Magnetic Resonance Imaging as a Surveillance Method for Chronic Graft Failure in Pediatric Heart Transplant Recipients

K. Watanabe \* (1); N. Arva, (2); J. Arzu, (3); M. Sojka, (1); P. Tannous, (1); C. Rigsby (4); M. Markl (5); J. Robinson (1); S. Alsaffar, (1); N. Husain (1)

(1) Cardiology, Ann & Robert H. Lurie Children's Hospital of Chicago, Chicago, United States of America; (2) Pathology, Ann & Robert H. Lurie Children's Hospital of Chicago, Chicago, United States of America; (3) Preventative medicine, Northwestern University Feinberg School of Medicine, Chicago, United States of America; (4) Medical imaging, Ann & Robert H. Lurie Children's Hospital of Chicago, Chicago, United States of America; (5) Department of radiology, Northwestern University Feinberg School of Medicine, East Superior Street, Chicago, IL, USA, Chicago, United States of America

### Abstract

**Background:** Chronic graft failure (CGF) is one of the top causes of mortality in pediatric heart transplant (PHT). The cause of CGF is multifactorial with pathology including coronary artery vasculopathy (CAV) and microvessel disease (MVD) (Figure 1). Unfortunately, subclinical progression of CGF is difficult to monitor. Endomyocardial biopsy (EMB) can detect fibrosis and MVD in patients with CGF, but is invasive and costly. We sought to evaluate associations between the histopathologic changes of CGF as seen on EMB and Cardiac Magnetic Resonance Imaging (CMR) findings as a non-invasive surveillance procedure

**Method:** This retrospective study included PHT patients who underwent standard-of-care comprehensive structure-function CMR between 9/2015 and 6/2021. We included patients who had EMB within 6 months of CMR and excluded those with moderate to severe rejection on EMB. Comprehensive CMR included CINE SSFP imaging for assessment of global cardiac function, volumes and mass, T2 mapping as a measure of myocardial edema, pre- and post gadolinium-contrast T1 mapping to detect tissue fibrosis, and myocardial stress perfusion imaging (Figure 2). Myocardial perfusion reserve index (MPRI) for the base and mid-ventricle slices was analyzed by comparing the relative uptake during stress and rest perfusion and was calculated as the ratio between the maximum upslope of the first-pass myocardial perfusion time-intensity curve divided by the maximum upslope of the first-pass LV cavity time-intensity curve. On EMB, fibrosis was qualitatively graded on a scale of 0-5 (Figure 3a) and MVD was quantified as number of capillaries with stenotic wall thickening (due to either endothelial cell swelling or medial hypertrophy) per fields of view (Abnl vessel/FOV) (Figure 3b). Spearman rank correlation analysis was performed to investigate relationships between CMR variables and EMB findings. CMR variables were also compared using Wilcoxon rank sum test between patients with CAV vs. no CAV.

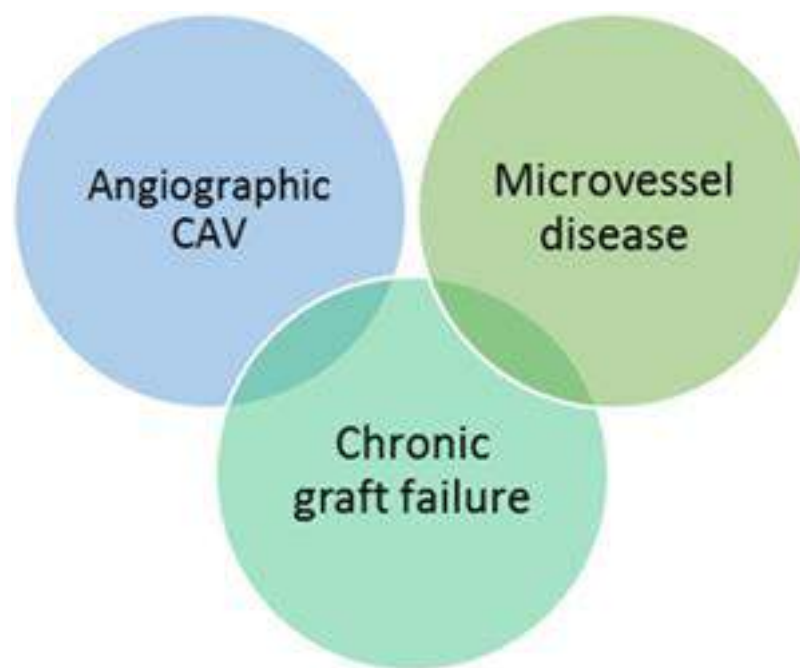
**Results:** Thirty-three PHT were included with a median age at CMR 16.1 years (IQR, 12.2-19.5) and time from transplant 7.2 years (4.2-11.1). In our cohort, 8/33 (24%) had angiographic diagnosis of CAV per International Society of Heart Lung Transplantation (ISHLT) guidelines, although only 2/8 had greater than ISHLT CAV grade 1. Fibrosis score and Abnl vessel/FOV were elevated in the CAV group vs. no CAV group, [1.0 (IQR, 1.0-3.0) vs 3.0 (2.8-3.0)  $p=0.04$ ] and [0.9 (0.7-1.4) vs 1.7 (0.9-2.7)  $p=0.04$ ], respectively. When



comparing CMR and fibrosis score, increased fibrosis score was associated with increased global T1 ( $\rho$  0.38,  $p$ = 0.03), global T2 ( $\rho$  0.40,  $p$ = 0.03), peak T2 ( $\rho$  0.41,  $p$ = 0.02) and extracellular volume (ECV) ( $\rho$  0.30,  $p$ =0.09). With greater Abnl vessel/FOV there was higher global T1 ( $\rho$  0.33,  $p$ = 0.07). Furthermore, in those with any angiographic CAV, MPRI was lower (0.9 (0.9-1.2) CAV group vs 1.3 (1.2-1.5) no CAV group;  $p$ =0.08).

Conclusion: Presence of CAV is associated with EMB histopathological changes of fibrosis and MVD in PHT recipients. Abnormalities in CMR tissue characterization and perfusion are noted in those with fibrosis on EMB and angiographic CAV. These data suggest that CMR could aid in monitoring of CGF non-invasively and longitudinal follow up studies in larger cohorts which include a wider spectrum of disease progression may aid in further refining the role of CMR in graft surveillance.

**Figure/Table 1**



**Caption 1**

Figure 1. Relationship of CAV, MVD and CGF

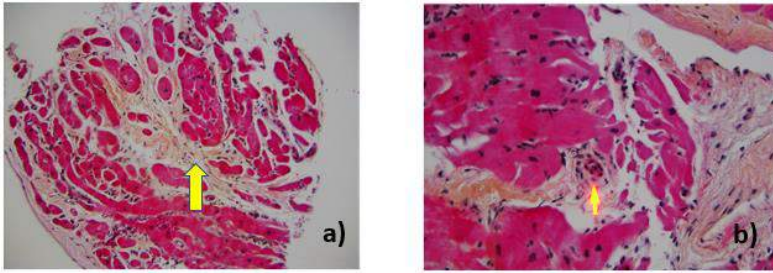
**Figure/Table 2**



**Caption 2**

Figure 2. CMR protocol

**Figure 3**



### Caption 3

Figure 3. a) EMB specimen with moderate fibrosis identified by the arrow b) Arrow identifying microvessel with stenotic wall thickening

Speaker: K. Watanabe

Category: Perfusion, Heart Transplant, Pediatric

000336

## Left Ventricular Function Analysis Performed by Regionalized Wall Stress in a Swine Model

J. Ref \* (1); A. Kathuria (2); A. Anilkumar (2); A. Grijalva (2); A. Hindosh (2); J. Lancaster (3); S. Daugherty (3); J. Koevary (3); M. Moulton (4); S. Goldman (3); R. Avery (5)

(1) Sarver Heart Center, North Campbell Avenue, Tucson, AZ, USA, University of Arizona College of Medicine – Tucson, North Campbell Avenue, Tucson, United States of America; (2) College of medicine, The University of Arizona, Tucson, United States of America; (3) Dept. of cardiology, The University of Arizona, Tucson, United States of America; (4) Dept. of cardiotoracic surgery, University of Nebraska Medical Center, Omaha, United States of America; (5) Dept. of radiology, Northwestern Memorial Hospital, Chicago, United States of America

### Abstract

**Introduction:** Regional noninvasive method using CMR to define wall stress is promising as a time-sensitive and accessible approach implementable for research and clinical protocols. Regional wall stress localizes measurements to specific myocardial anatomy to detect coronary abnormalities and LV remodeling. Modified Laplace's law has been implemented to assess regional differences in LV anatomy during different timepoints because of its robust capability to assess cardiac function [1].

Regional systolic (ESWS) and diastolic (EDWS) wall stress using CMR derived volumes and LV wall thickness along the antero-septal wall were calculated. With LAD occlusion/reperfusion, the myocardial damage is localized along the antero-septal vascular territory and identified on CMR. Regional wall stress calculations provide baseline values, cardiac damage-associated values, and potentially cardiac recovery associated values. Since total LV wall stress calculations are often cumbersome and time-consuming, we have investigated regional wall stress to rapidly standardize myocardial damage to further evaluate LV function following LAD occlusion.

**Methods:** Male Yucatan mini swine underwent LAD balloon occlusion/reperfusion technique (90 min). Cardiac MRI is performed prior to MI and 1 month after MI. Wall stress is done in short axis (SAX) EKG-gated balanced steady state free precession cine images. SAX cines at baseline and 1-month post-MI studies were compared at equal anatomical position. Two observers took 10 wall thickness measurements near anterior right ventricular insertion point including the mid anterior and mid septal wall at end-systole (ES) and end-diastole (ED). The left ventricle area in both ED and ES were calculated using a closed polygon tool (Miele-lxiv, Florence, Italy) to calculate LV radii. Hemodynamic LV End-diastolic pressure (LVEDP) and LV systolic pressure (LVSP) measurements were obtained by solid state pressure tipped micromanometer catheter prior to CMR. Modified Laplace's Law [2] is then used to calculate wall stress:  $\sigma = Pr / (h(2 + h/r))$  where P = intracavity pressure, r = ventricular radius, h = wall thickness

**Results:** 16 Yucatan mini swine were evaluated at both baseline and 1 month post-MI. Average infarct size was  $24 \pm 3\%$ , EDWS increased ( $P < 0.01$ ) from  $18 \pm 3$  kPa to  $61 \pm 10$  kPa, ESWS increased from  $8 \pm 1$  kPa to  $13 \pm 2$  kPa LV, Diastolic Wall Thickness decreased ( $P < 0.01$ )

from  $7\pm 1$  to  $6\pm 1$  mm, Systolic Wall Thickness decreased ( $P<0.01$ ) from  $13\pm 1$  to  $8\pm 1$  mm, Diastolic Ventricular Radius increased ( $P<0.05$ ) from  $15\pm 1$  to  $17\pm 1$  mm, and Systolic Ventricular Radius increased ( $P<0.01$ ) from  $9\pm 1$  to  $12\pm 1$  mm. LVEDP and LVESP showed no significant changes.

**Conclusion:** LV regional wall stress derived by the modified Laplace's Law correlated with both pressure and physical changes of LV chamber size and transmural myocardial thickness. Limitations of this model include only transmural estimates of passive circumferential myocardial wall stress. However, further study, suggests this may be a rapid way of detecting changes in regional coronary blood flow, myocardial oxygen consumption and LV remodeling.

### **Bibliographic References**

[2] Zhang Z, Tendulkar A, Sun K, Saloner DA, Wallace AW, Ge L, Guccione JM, Ratcliffe MB. Comparison of the Young-Laplace law and finite element-based calculation of ventricular wall stress: implications for postinfarct and surgical ventricular remodeling. *Ann Thorac Surg*. 2011 Jan;91(1):150-6. doi: 10.1016/j.athoracsur.2010.06.132. PMID: 21172505; PMCID: PMC3058250., [1] Li JK. Comparative cardiac mechanics: Laplace's Law. *J Theor Biol*. 1986 Feb 7;118(3):339-43. doi: 10.1016/s0022-5193(86)80064-9. PMID: 3713216.

Speaker: J. Ref

Category: Stress, Ischemic Heart Disease, MR Post-Processing

000339

## Relevance of Right Versus Left Ventricular Function and Fibrosis for Patient Reported Shortness of Breath: Findings from 9,057 patients of the CIROC Registry

E. Nabet \* (1); S. Dykstra (2); S. Islam, (1); J. Flewitt (2); A. Satriano (2); S. Rivest (2); S. Manoushagian (1); C. Lydell (2); A. Howarth (2); N. Fine (2); J. A. White (2); J. Gaztanaga (1)

(1) Cardiology, NYU Langone Hospital Long Island, Mineola, United States of America; (2) Cumming school of medicine, department of cardiac sciences, University of Calgary, Calgary, Canada

### Abstract

#### Background:

Markers of left ventricular (LV) function and fibrosis are recognized predictors of adverse events in patients with known or suspected cardiovascular (CV) disease. However, growing data supports that the right ventricle (RV) plays a key role in patient well-being and future risk of cardiovascular events. We sought to evaluate whether RV health (function, volumes, and RV insertion-site fibrosis) is an important and independent predictor of patient self-reported shortness of breath in patients with established cardiovascular disease.

#### Methods:

Matched cardiac MRI and patient-reported health information were obtained from 9,057 consecutively enrolled patients of the Cardiovascular Imaging Registry of Calgary (CIROC). All patients executed a self-administered shortness of breath survey at time of MRI designed to mirror classification assignments of the NYHA. Univariate and multivariable logistic regression models were fitted to identify associations between NYHA class  $\geq$ II and MRI-based features, inclusive of LV and RV volumes, LV mass, atrial volume, LV- and RV-specific patterns of late gadolinium enhancement (LGE), and valve disease severity. RV-specific fibrosis was defined as RV insertion (RVI) site fibrosis extending from within an RV pedicle across the epicardial contour of the LV myocardium (Figure 1). The respective influence of RVEF and LVEF on shortness of breath was studied by six pre-defined phenotypic categories representative of bi-ventricular EF severity, as shown in Table 2.

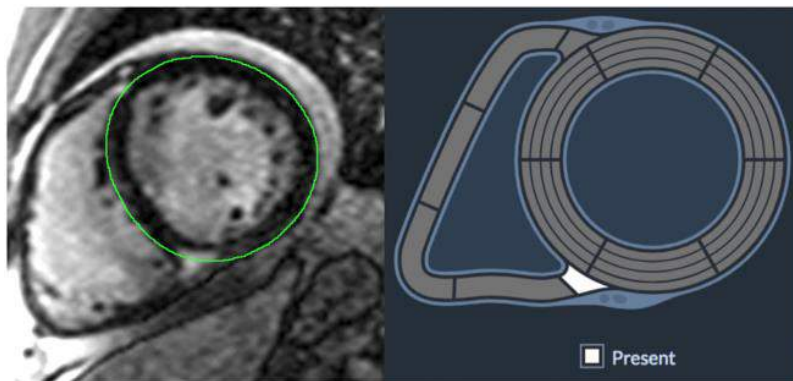
#### Results:

The mean age was 55.5 years (38.9% female) with a median LVEF of 58.7% (interquartile range-IQR 49.3-64.3) and median RVEF of 55.5% (IQR 50.0-61.0). NYHA  $\geq$ II was described in 2,875 subjects (31.7%). As shown in Table 2, following adjustment for baseline variables only EF phenotypes with RVEF<40% were independently associated with NYHA $\geq$ II status. In this model, RVI site fibrosis was also an independent predictor with an adjusted OR of 1.27 ( $p=0.001$ ). RVEF<40% as a solitary phenotypic marker provided an adjusted OR of 2.29 ( $p<0.0001$ ) for NYHA  $\geq$ II with RVI fibrosis also independently associated (OR 1.27,  $p=0.001$ ). An identical model evaluating LVEF<40% failed to show significance ( $p=0.48$ ). Similarly, no LV-specific LGE fibrosis pattern was associated with NYHA  $\geq$ II.

#### Conclusions:

RVEF and RVI site fibrosis are superior predictors of patient-reported NYHA functional status compared to LVEF and LV patterns of fibrosis. These findings demonstrate the influence of RV health on clinically relevant patient-reported measures of health.

**Figure/Table 1**



**Caption 1**

Figure 1. Example standardized coding of Right Ventricular Insertion (RVI) site fibrosis pattern in a patient of the CIROC Registry. Fibrosis seen extending from within an RV pedicle across the epicardial contour of the LV myocardium.

**Figure/Table 2**

Variables	OR (95% CI)	P-value
Age (per 5 years)	1.07 (1.04-1.09)	<0.0001
Female gender	2.15 (1.88-2.46)	<0.0001
Race		
Caucasian	reference	
Aboriginal/American Indian/Alaska native	1.21 (0.86-1.71)	0.276
Asian	0.70 (0.58-0.85)	<0.001
African American	0.86 (0.61-1.20)	0.971
Hispanic	1.21 (0.96-1.54)	0.115
Other	0.90 (0.64-1.26)	0.537
Smoked past 10 years	1.71 (1.52-1.92)	<0.0001
Alcohol use $\geq$ moderate	0.85 (0.75-0.97)	0.015
Known coronary artery disease	1.20 (1.02-1.41)	0.026
Hypertension	1.18 (1.05-1.33)	0.007
History of Heart Failure	1.61 (1.35-1.91)	<0.0001
BSA (kg/m <sup>2</sup> ) (per 1 unit)	2.92 (2.26-3.76)	<0.0001
Heart Rate (per 10 units)	1.19 (1.14-1.24)	<0.0001
SBP (per 10 units)	0.94 (0.91-0.97)	<0.001
EF Phenotype Categories		
LVEF $\geq$ 50 / RVEF $>$ 40	reference	
LVEF $\geq$ 50 / RVEF $<$ 40	1.98 (1.20-3.26)	0.008
LVEF 41-49 / RVEF $>$ 40	0.84 (0.69-1.02)	0.083
LVEF 41-49 / RVEF $<$ 40	2.07 (1.24-3.44)	0.005
LVEF $\leq$ 40 / RVEF $>$ 40	0.95 (0.74-1.22)	0.682
LVEF $\leq$ 40 / RVEF $<$ 40	2.11 (1.50-2.97)	<0.0001
LVESV_i (per 10 units)	1.04 (1.01-1.07)	0.007
LVCO (per 1 unit)	0.90 (0.86-0.94)	<0.0001
LGE - RVI site fibrosis	1.27 (1.11-1.45)	0.001

## Caption 2

Table 2. Multivariable logistic regression model, for shortness of breath, defined as NYHA  $\geq$ II. Variable selection executed via LASSO method.

Speaker: E. Nabet

Category: Right Ventricle, Ejection Fraction, Late Gadolinium Enhancement



**000340**

## **A rare cause of Acute myocardial infarction in patient with bicuspid aortic valve**

M. J. Rafiee \* (1); F. Babaki (2); M. Chetrit (3); M. Friedrich (4)

(1) Research institute, cardiovascular imaging service, McGill University Health Centre Glen Site (MUHC), Montreal, Canada; (2) Medicine, University of Montreal, Montréal, Canada; (3) Research institute, cardiovascular imaging service, McGill University Health Centre Glen Site (MUHC), Montréal, Canada; (4) Departments of Medicine and Diagnostic Radiology, Division of Experimental Medicine, Centre Universitaire de Santé McGill Site Glen, Montréal, Canada

### **Abstract**

#### **Abstract**

#### **Clinical presentation:**

A 37 -year-old man with known bicuspid aortic valve presented to the emergency with acute onset chest pain with radiating to his left shoulder, mild exertional dyspnea after bicycling. The pain was lasted few hours and then spontaneously resolved. He did not report fever, chills, cough, nausea, vomiting, palpitation or syncope.

His physical exam revealed normal vital signs and a 3/6 early systolic murmur at the right parasternal area on cardiac auscultation. He had high troponin with a maximum of 20258 ng/l (normal, 17.5 ng/l).

#### **Diagnostic Techniques and Findings:**

ECG showed left ventricular hypertrophy with Q waves in the inferior limbs.

Transthoracic echocardiography demonstrated Hypokinesia of the basal to mid inferior wall with preserved LV global systolic function. BAV with moderate fibrocalcifications of the cusps, Mild to moderate AS, Moderate AI. CT angiography of the thoracic aorta showed fusiform aneurysm of ascending aorta without evidence of dissection (**Fig 1 A,B,C,D**). The result of coronary catheterization was normal.

Diagnosis of myocardial infection with non-obstructive coronary artery disease (MINOCA) was the first hypothesis and he was sent for cardiac MRI evaluation.

A 1.5 T MRI revealed Acute transmural infarction (AMI) of the mid inferior and inferolateral segments with microvascular obstruction (**Figure 2 A,B,C,D**). The patient underwent Bentall procedure because aneurysmal dilatation of the ascending aorta and significant AI. The surgeon found extensively calcified aortic valve cusps with an area of severe raw surface on the calcium, probably explaining the source of embolization to the coronary artery.

#### **Discussion and Learning points:**

The most common cause of the AMI is atherosclerotic disease. However, 5% to 6 % of the patients have normal or near-normal coronary arteries on angiography and currently classified as myocardial infarction with nonobstructive coronary arteries (MINOCA) (1).

Coronary embolism (CE) is a rare cause of MINOCA. Shibata et al showed that the prevalence of CE as a nonatherosclerotic cause of AMI based on the histological, angiographic and other diagnostic imaging findings criteria was 2.9% (2). Spontaneous calcific material embolization to the coronary arteries is a rare clinical manifestation of the calcified aortic valve (3). Left coronary system is more commonly being involved by embolism than right system due to the more flow into the LAD (4). Cardiac MRI (CMR) has emerged as a robust and non-invasive imaging modality for the evaluation of acute chest pain. Given its safety, inter and intra-observer consistency, accuracy and ability to myocardial characterization, CMR is a pivotal diagnostic modality in the evaluation of patients presenting with MINOCA (5) .

A coronary artery embolism is a rare cause of acute myocardial infarction. The possibility of calcific embolism should be considered as a cause of AMI in patients with calcified aortic valve and normal coronary angiography. The clinicians must be vigilant to identify this etiology Besides suggestive clinical context, using cardiac MRI as a single-scan assessment may be helpful to define uncommon etiology of the MINOCA.

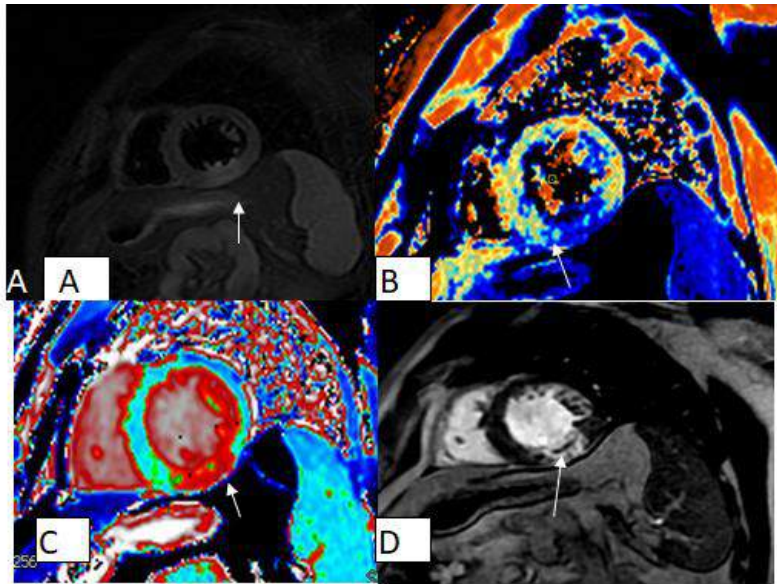
**Figure/Table 1**



**Caption 1**

Figure1 (A) Coronary angiography reveals normal and non stenotic right coronary artery (B ) Axial CT angiography at level of aortic valve shows calcified bicuspid aortic valve (arrow) (c) 3D (VRT) CT angiography of the thoracic aorta reveals: Fusiform aneurysm of the ascending aorta with a maximum diameters 52x49 mm., (D) Transthoracic aorta shows: Bicuspid aortic valve with moderate fibrocalcification cusps (arrow)

**Figure/Table 2**



## aption 2

Figure 2. CMR findings of the inferior wall AMI. (A) Short axis T2-weighted fat suppressed image shows high signal intensity suggestive edema in the inferior LV wall (arrow) (B) Short axis T2 map reveals significantly increased T2 values in the mid inferior wall (arrow) (C) Short axis T1-map image shows regionally increased T1 values in the mid inferior wall (arrow) (D) Late enhancement image after Gadolinium injection at the level of mid inferior wall shows transmural enhancement with central non-enhanced core consists with microvascular obstruction (arrow).

## Bibliographic References

1. Jacqueline E. Tamis- Holland et al, Contemporary Diagnosis and Management of Patients with Myocardial Infarction in the Absence of Obstructive Coronary Artery Disease Circulation. 2019;139: e891–e908
2. Prevalence, Clinical Features, and Prognosis of Acute Myocardial Infarction Attributable to Coronary Artery Embolism, Circulation. 2015; 132:241-250
3. Holley KE, Bahn RC, McGoon DC, Mankin HT. Calcific embolization associated with valvotomy for calcific aortic stenosis. Circulation 1963; 28:175–81
4. Prizel KR, Hutchins GM, Bulkley BH. Coronary artery embolism and myocardial infarction. Ann Intern Med 1978; 88:155–61
5. Agewall S, Beltrame JF, Reynolds HR, et al. ESC working group position paper on myocardial infarction with non-obstructive coronary arteries. Eur Heart J 2017; 38:143-53

Speaker: M. J. Rafiee

Category: Acute Coronary Syndrome, Aortic Valve, Bicuspid Aortic Valve

000342

**Left ventricular myocardial deformation and tissue characterization assessed by cardiovascular magnetic resonance and its determinants in type 2 diabetes mellitus patients with preserved ejection fraction**

Z. Li \* (1); D. Han (1); J. Deng (1); W. Gao (1); W. Chen (1)

(1) Department of Radiology, First Affiliated Hospital of Kunming Medical University, Kunming, China

**Abstract**

**Background:** Early detection of subclinical myocardial dysfunction in patients with type 2 diabetes mellitus (T2DM) is essential for recommending therapeutic interventions that can prevent or reverse heart failure, thereby improving the prognosis in such patients. This study aims to quantitatively evaluate left ventricular (LV) myocardial deformation and tissue characteristics using cardiovascular magnetic resonance (CMR) imaging in type 2 diabetes mellitus patients with preserved ejection fraction, and to investigate the association between CMR and clinical parameters.

**Methods:** 67 patients were enrolled in this study, including 17 T2DM only patient (G1), 18 diabetic patients with Hypertension (G2), 32 with hypertension (HT), and 44 sex-, age-matched controls (Cs). All subjects undergo CMR examinations (1.5T, MAGNETOM Amira, Siemens, Best, Netherlands). The values of native T1, post-contrast T1 and ECV were measured from the basal, mid and apical part of the left ventricular myocardial according to AHA 17-segmentation via the modified Look-Locker inversion recovery technique. The left ventricular global longitudinal strain (GLS) was evaluated using routine cine images and tissue-tracking analysis software (CVI42, Circle Cardiovascular imaging, Calgary, AB, Canada). The baseline clinical and biochemical indices were collected before the CMR examination.

**Results:** The global ECV were significantly higher in all diabetic patients than in the Cs ( $30.75 \pm 3.65\%$  vs.  $26.33 \pm 2.81\%$ ;  $p < 0.05$ ). And T2DM patient had reduced LV longitudinal strain (GLS) compared with Cs ( $-16.51 \pm 2.53\%$  vs.  $-19.66 \pm 3.21\%$ ,  $p < 0.001$ ). Moreover, G2 had increased global ECV value than that of both the G1 ( $31.92 \pm 3.05\%$  vs.  $29.59 \pm 3.90\%$ ,  $p = 0.032$ ) and the HT ( $31.92 \pm 3.05\%$  vs.  $29.22 \pm 6.58\%$ ,  $p = 0.042$ ). And the GLS was significantly reduced in G2 than in G1 ( $-15.75 \pm 2.29\%$  vs.  $-17.27 \pm 2.57\%$ ,  $p < 0.05$ ) and the HT group ( $-15.75 \pm 2.29\%$  vs.  $-17.54 \pm 3.097\%$ ,  $p < 0.05$ ). In the diabetic patient group, the independent determinants of the ECV value were HbA1C ( $\beta = 2.286$ ,  $p = 0.013$ ), SBP ( $\beta = 0.038$ ,  $p = 0.013$ ) (model  $R^2 = 0.353$ ), and the independent determinant of the GLS was the HbA1C value ( $\beta = 2.186$ ,  $P = 0.027$ ) (model  $R^2 = 0.168$ ).

**Conclusions:** T2DM patients with preserved ejection fraction had significantly increased ECV and deteriorated LV GLS which might be related to poor glycemic control, especially in patients with hypertension. HbA1c is an independently predictor of myocardial extracellular interstitial expansion and strain damage, which may be helpful for the clinical decision-making of blood glucose control.

**Figure/Table 1**

	Control (n=44)	T2DM (n=35)	G1 (n=17)	G2 (n=18)	HT (n=32)
<b>Clinical characteristics</b>					
Age/year	49 (11)	53(11)	52 (11)	54 (12)	48 (12)
Male/(n)	27	22	10	12	20
Height/(m)	1.66 (0.09)	1.68(0.08)	1.66 (0.08)	1.65 (0.08)	1.65 (0.07)
Weight/(kg)	63.56(11.12)	70.00(64.50,78.00)a	68.52 (11.90)	71.00(66.00,86.00)a	72.29 (9.34)a
BMI/(kg/m <sup>2</sup> )	23.02 (3.22)	25.51(23.08,28.16) a	24.53(3.40)	27.06(24.24,29.04)a, b	26.27 (3.25)a
BSA/m <sup>2</sup>	1.70 (0.18)	1.86(0.27)a	1.83 (0.31)a	1.88 (0.24)a	1.82 (0.14)a
SBP/mmHg	118.36 (10.80)	133.08(14.65)a	124.82 (11.03)	140.88 (13.49)a, b	139.96 (29.87)a, b
DBP/mmHg	76.93 (9.33)	82.60(12.42)	76.64 (10.16)	88.22 (11.93)a, b	90.62 (22.89)a, b
HR/bpm	76 (13)	71(12)	69(10)	73(13)	76 (14)
Diabetes duration/y	-	6.65(4.49)	6.41 (3.35)	6.88 (5.45)	-
HCT /%	43.77 (3.73)	42.77(4.80)	41.35 (4.32)	44.11 (4.96)	42.66 (4.92)
hemoglobin/(g/L)	148.00 (15.10)	142.94(15.99)	139.29 (17.05)	146.38 (14.55)	145.43 (18.54)
GSP/(mmol/L)	278.70 (49.03)	338.19(71.90) a	333.59 (63.16)a	343.13 (82.92)a	260.75 (21.58)b, c
HbA1C/%	5.57 (0.33)	8.09(1.86)a	8.50 (2.13)a	7.65 (1.49)a	5.75 (0.43)b, c
Glu(mmol/L)	4.91 (0.49)	7.11(6.13,9.13)a	6.67(5.74,9.66)a	7.62 (2.39)a	5.11(0.62)b, c
TC/(mmol/L)	4.34 (0.89)	4.51(1.05)	4.54 (1.15)	4.49 (0.97)	4.44 (1.00)
F-CHO/(mmol/L)	1.49 (0.36)	1.63(0.44)	1.56 (0.38)	1.69 (0.49)	1.55 (0.38)
LDL-C/(mmol/L)	2.49 (0.72)	2.71(0.92)	2.88 (0.95)	2.54 (0.88)	2.65 (0.77)
HDL-C/(mmol/L)	1.23 (0.41)	0.98(0.21)a	0.95 (0.19)a	1.02 (0.23)a	1.03 (0.20)a
TG/(mmol/L)	1.88(0.90,2.23)	1.61(1.30,2.38)	1.81 (0.91)	2.11 (1.44)	1.67(1.26,2.39)
<b>CMR characteristics</b>					
Myo-Mass/g	83.86 (22.97)	117.05(87.84,172.50)a	95.60(80.10,171.41)	130.17 (89.24,207.90)a	120.00(94.45,141.05)a

Myo-Mass index/(g/m2)	49.26 (39.90,57.90)	62.68(48.92,88.77)a	54.32(46.30,85.64)a	68.79(50.96,91.90)a	67,30(56.65,77.25)a
LVEDV/ml	129.11 (23.23)	136.68(108.49,167.64)	135.30 (107.99,147.93)	159.50 (128.60,177.48)a	131.58 (28.36)
LVESV/ml	52.03 (13.84)	47.74(33.42,72.50)	43.80 (30.70,59.20)	55.65 (34.05,88.49)	52.88 (19.73)
LVSV/ml	77.41 (15.00)	90.22(28.96)a	89.00 (34.75)	91.38 (23.19)a	79.57 (19.66)
LVEDVi/(ml/m2)	76.53 (13.31)	75.65(65.85,83.88)	71.61(66.70,80.89)	81.84 (22.69)	72.15 (15.97)
LVESVi/(ml/m2)	30.74 (6.76)	27.50(18.66,39.77)	26.63(18.33,31.11)	30.23(19.00,44.70)	28.42 (11.71)
LVSVi/(ml/m2)	45.98 (9.46)	48.37(13.45)	48.77 (15.20)	47.99 (12.00)	43.52 (10.29)
LVEF/%	60.27 (6.21)	61.77(13.69)	63.25 (13.85)	60.38 (13.79)	61.15 (10.47)
LVGLS/%	-19.66 (3.21)	-16.51(2.53)a	-17.27 (2.57)a	-15.75 (2.29)a, b	-17.54 (3.09)a, c
LVGRS/%	33.15 (8.01)	32.41(6.00)	32.60 (6.75)	32.22 (5.36)	32.37 (4.56)
LVGCS/%	-23.74 (3.31)	-23.24 (3.25)	-23.14 (3.01)	-23.34 (3.49)	-22.66 (3.00)
Apex Native T1/ms	1027.53 (33.58)	1027.36(48.08)	1025.00 (55.34)	1029.87 (40.65)	1025.28 (48.97)
Mid Native T1/ms	1031.54 (28.96)	1052.26(39.67)a	1046.70 (47.89)	1057.82 (29.77)a	1060.90 (41.37)a
Base Native T1/ms	1037.00 (26.35)	1062.78(44.08)a	1067.56 (55.63)	1058.00 (29.53)a	1070.31 (42.00)a
Global Native T1/ms	1035.02 (26.65)	1060.17(43.63)a	1051.64 (46.65)	1068.70 (39.93)a	1059.46 (34.74)a
Apex Post T1/ms	446.65 (61.12)	443.30(51.47)	443.05 (62.06)	443.56 (39.29)	439.40 (58.76)
Mid Post T1/ms	460.47 (58.28)	453.76(45.07)	456.23 (50.98)	451.29 (39.71)	458.87 (58.74)
Base Post T1/ms	465.84 (58.20)	457.50(50.20)	462.31 (57.62)	452.68 (42.87)	459.28 (58.55)
Global Post T1/ms	456.25 (59.64)	446.50(41.14)	452.29 (47.12)	440.70 (34.63)	438.03 (67.95)
Apex ECV/%	26.60 (2.63)	28.76(2.10)a	28.81 (2.46)a	28.71 (1.77)a	27.76 (2.49)
Mid ECV/%	25.78 (2.35)	29.70(3.18)a	28.99 (3.78)a	30.41 (2.35)a, b	28.12 (2.03)a, c
Base ECV/%	25.93 (2.43)	30.03(3.30)a	28.43 (3.33)a	31.63 (2.44)a, b	28.53 (2.48)a, c

<b>Global ECV/%</b>	<b>26.33 (2.81)</b>	<b>30.75(3.65)a</b>	<b>29.59 (3.90)a</b>	<b>31.92 (3.05)a, b</b>	<b>29.22 (6.58)a, c</b>
---------------------	---------------------	---------------------	----------------------	-------------------------	-------------------------

### Caption 1

Mean (SD) or median (25th, 75th percentiles) for non-parametric data.

*a* *P* value versus Cs, *b* *P* value versus G1, *c* *P* value G2.

*P* <0.05 is considered to indicate statistical significance.

### Figure/Table 2

	<b>Unstandardized <math>\beta</math></b>	<b>Standardized <math>\beta</math></b>	<b>P value</b>
<b>GECV</b>			
<b>SBP/mmHg</b>	<b>0.099</b>	<b>0.038</b>	<b>0.013</b>
<b>HbA1C/%</b>	<b>6.055</b>	<b>2.286</b>	<b>0.013</b>
<b>GLS</b>			
<b>HbA1C/%</b>	<b>5.113</b>	<b>2.186</b>	<b>0.027</b>

### Caption 2

Table2 multivariate regression analysis for GECV and GLS in T2DM patients

### Bibliographic References

Wang ZT, Wang CH, Chen YS, Sun JY, Zhu T, Zhang Y, Gao FB. [Magnetic Resonance Imaging Tissue Feature Tracking for Cardiac Amyloidosis]. Sichuan Da Xue Xue Bao Yi Xue Ban 2019;50(4):466-470., Foussier C, Barral PA, Jerosh-Herold M, Gariboldi V, Rapacchi S, Gallon A, Bartoli A, Bentatou Z, Guye M, Bernard M, Jacquier A. Quantification of diffuse myocardial fibrosis using CMR extracellular volume fraction and serum biomarkers of collagen turnover with histologic quantification as standard of reference. Diagn Interv Imaging 2021;102(3):163-169., 6. Chery G, Kamp N, Kosinski AS, Schmidler GS, Lopes RD, Patel M, Al-Khatib SM. Prognostic value of myocardial fibrosis on cardiac magnetic

resonance imaging in patients with ischemic cardiomyopathy: A systematic review. *Am Heart J* 2020;229:52-60., 2. Dillmann WH. Diabetic Cardiomyopathy. *Circ Res* 2019;124(8):1160-1162., 1. Li Y, Teng D, Shi X, Qin G, Qin Y, Quan H, Shi B, Sun H, Ba J, Chen B, Du J, He L, Lai X, Li Y, Chi H, Liao E, Liu C, Liu L, Tang X, Tong N, Wang G, Zhang JA, Wang Y, Xue Y, Yan L, Yang J, Yang L, Yao Y, Ye Z, Zhang Q, Zhang L, Zhu J, Zhu M, Ning G, Mu Y, Zhao J, Teng W, Shan Z. Prevalence of diabetes recorded in mainland China using 2018 diagnostic criteria from the American Diabetes Association: national cross sectional study. *Bmj* 2020;369:m997.

Speaker: Z. Li

Category: Diabetes, Mapping Techniques, Feature Tracking



**000343**

## **Multimodality CMR-FDG PET Surveillance of Primary B-Cell Cardiac Lymphoma**

K. McSurdy \* (1); C. Dass, (2); Y. Toyoda, (3); A. Bains, (4); M. Gannon (5); M. Bromberg, (6); W. Vandecker (5); P. Patil (5)

(1) Department of internal medicine, Temple University Hospital, Philadelphia, United States of America; (2) Department of radiology, Temple University Hospital, Philadelphia, United States of America; (3) Department of surgery/cardiovascular surgery, Temple University Hospital, Philadelphia, United States of America; (4) Department of pathology and laboratory medicine, Temple University Hospital, Philadelphia, United States of America; (5) Department of internal medicine/cardiology, Temple University Hospital, Philadelphia, United States of America; (6) Department of internal medicine/hematology and oncology, Temple University Hospital, Philadelphia, United States of America

### **Abstract**

#### **Clinical Presentation**

A 72 year-old female with a history of hypertension and hyperlipidemia presented to the emergency department with chest pain. Echocardiography revealed an irregular, homogenous echogenicity obstructing the right ventricular outflow tract (RVOT) with extension to the pulmonic valve and a small pericardial effusion. She underwent right heart catheterization and pericardiocentesis with cytology yielding atypical cells but no frank malignant cells were seen. Endomyocardial biopsy was attempted but could not be completed due to poor visualization and obstruction. Avidity on fluorodeoxyglucose-positron emission tomography (FDG-PET) and tissue characterization by cardiac magnetic resonance (CMR) revealed an infiltrative mass, strongly suggesting malignancy. Imaging findings and refractory symptoms of chest pain and dyspnea led to coronary angiography revealing non-obstructive CAD and pursuit of surgical resection. Surgical exploration revealed extensive cardiac tumor originating from the right ventricle, extending to the ventricular septum, left ventricle, pulmonary artery and aorta with moderate adhesions to the pericardium (Figure 1A). Surgical pathology revealed a primary, diffuse large B-cell lymphoma (DLBCL) (Figure 1B). She underwent modified R-CHOP chemotherapy and subsequent surveillance by serial CMR and FDG-PET imaging has not shown obvious residual or recurrent disease.

#### **Diagnostic Techniques & Important Findings**

Faced with the diagnostic challenge of a new cardiac mass and limited visualization, CMR provided wide field-of-view imaging of the mass extent (Figure 2A). It demonstrated an enhancing, infiltrative right ventricular mass with a discrete, lobulated mass extending across the pericardium and to the RVOT, proximal pulmonary artery and aortopulmonary groove with tumor thrombus in the pulmonary trunk. Dephasing flow was seen in the RVOT, consistent with obstruction. Correlative imaging of the cardiac mass by FDG-PET demonstrated significant FDG avidity (Figure 2B).

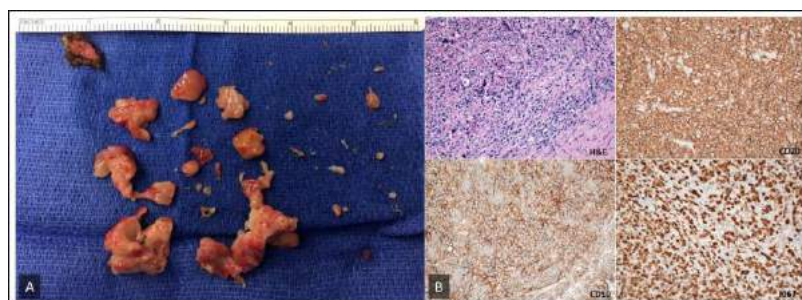
Following surgical resection and three cycles of chemotherapy, CMR in tandem with FDG-PET played a primary role in surveillance. Follow-up CMR showed significant interval resolution of the infiltrative mass with scarring in the RVOT consistent with post-surgical changes, but maintained FDG activity on concurrent PET. Residual tumor concern and high-

risk for perforation with endomyocardial biopsy led to additional cycles of chemotherapy. CMR six months later showed further resolution (Figure 3A) with minimal FDG activity on PET that was felt to be related to inflammatory changes rather than residual tumor (Figure 3B).

## Learning Points

Primary cardiac lymphoma is an exceedingly rare type of non-Hodgkin's lymphoma that involves both the heart and pericardium and accounts for less than 0.01% of cardiac tumors. With limited median survival less than 1 year, prompt recognition, treatment and surveillance of recurrence are paramount. This case highlights the importance of CMR in establishing the diagnosis of infiltrative cardiac mass, particularly one suspicious for lymphoma. Further, we demonstrate the diagnostic utility of multi-modality imaging with FDG-PET and CMR, combining evaluation of cardiac function and tissue characterization by CMR with FDG-PET for assessment of malignant potential. The value of this multi-modality diagnostic approach has been further demonstrated by ongoing cardiac tumor surveillance.

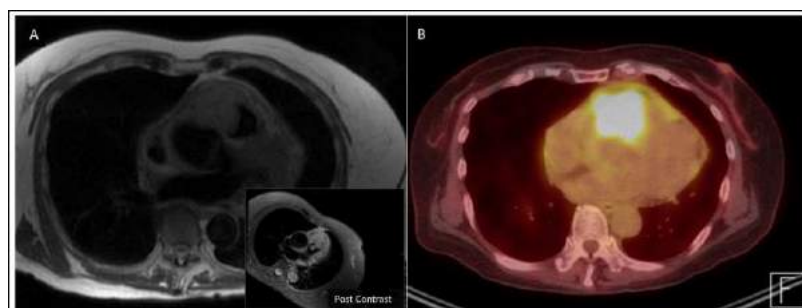
## Figure/Table 1



## Caption 1

**Figure 1.** (A) Gross surgical specimens of resected cardiac DLBCL. (B) Microscopic surgical pathology: H&E demonstrating infiltrating sheets of large neoplastic lymphocytes with predominantly a centroblastic morphology, tumor cells marking CD20 and CD10 with high proliferation index by immunofluorescence ki67.

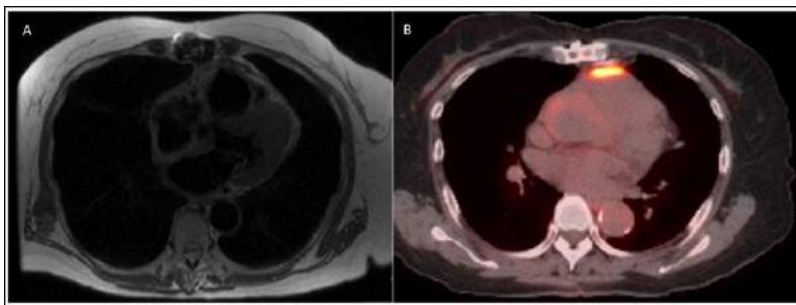
## Figure/Table 2



## Caption 2

**Figure 2.** (A) Pre-Treatment CMR showing an enhancing, infiltrative cardiac mass extending into the RVOT on dark-blood imaging. (B) Correlative Pre-Treatment FDG-PET demonstrating marked uptake by the cardiac mass.

## Figure 3



## Caption 3

**Figure 3.** (A) Post-Treatment CMR showing interval resolution of the cardiac mass seen previously. (B) Correlative Post-Treatment FDG-PET showing minor FDG uptake, likely associated with post-surgical inflammation at site of surgical patch.

## Bibliographic References

G. L. Ceresoli, A. J. M. Ferreri, E. Bucci, C. Ripa, M. Ponzoni, and E. Villa, "Primary cardiac lymphoma in immunocompetent patients: diagnostic and therapeutic management," *Cancer*, vol. 80, no. 8, pp. 1497–1506, 1997. , Chim, C. S., et al. "Primary cardiac lymphoma." *American journal of hematology* 54.1 (1997): 79-83. , K. Y. Lam, P. Dickens, and A. C. L. Chan, "Tumors of the heart. A 20-year experience with a review of 12,485 consecutive autopsies," *Archives of Pathology and Laboratory Medicine*, vol. 117, no. 10, pp. 1027–1031, 1993.

Speaker: K. McSurdy

Category: Cardiac Mass, Right Ventricle, Tumor

000344

## Fully Automated Inline 2D Flow Analysis

N. jin \* (1); K. chow (2); A. Pruitt (3); Y. Liu (4); O. Simonetti (5); M. Tong (6)

(1) Cardiovascular mr r&d, Siemens Medical Solutions USA, Inc, Malvern, United States of America; (2) Cardiovascular mr r&d, Siemens Medical Solutions Usa, Inc., Chicago, United States of America; (3) Biomedical engineering, The Ohio State University, Columbus, United States of America; (4) Davis Heart and Lung Research Institute, Ohio State University, Colmbus, United States of America; (5) Davis heart and lung research institute, The Ohio State University, Columbus, United States of America; (6) Internal medicine, The Ohio State University, Columbus, United States of America

### Abstract

**Background:** 2D phase-contrast (PC) MRI is commonly used to evaluate cardiovascular hemodynamics. However, flow quantification results are not readily available on the scanner due to the complexity of offline post-processing. Manual delineation of the vessel of interest can be time consuming, and background phase correction (BPC) by polynomial surface fitting of stationary tissue [1] can require manual adjustment further complicating routine clinical workflow. The aim of this study was to develop an automated framework to fully integrate a 2D flow analysis on the scanner with BPC using automatic rejection of temporally invariant outliers (ARTO) [2] and vessel segmentation using deep learning (DL) [3]. The objective was to automatically provide flow quantification results immediately following 2D PC data acquisition. We validated the quantitative results using commercial software.

**Methods:** This framework (**Fig. 1**) was implemented in the Siemens Image Calculation Environment (ICE) and prototype Framework for Image Reconstruction Environment (FIRE) [4], which provides a flexible interface between ICE and third-party code running in open-source repositories using the streaming ISMRM raw data format [5]. Magnitude and phase images were reconstructed and sent to an ICE functor for BPC with ARTO, which iteratively removes outlier pixels. Pre-trained DL segmentation algorithms for 2D PC aorta (AO) and main pulmonary artery (MPA) images were implemented in PyTorch and executed within a containerized Python 3.9 environment in FIRE. Flow analysis reports including flow quantification, peak velocity and flow curves, were generated on the scanner and stored as DICOMs.

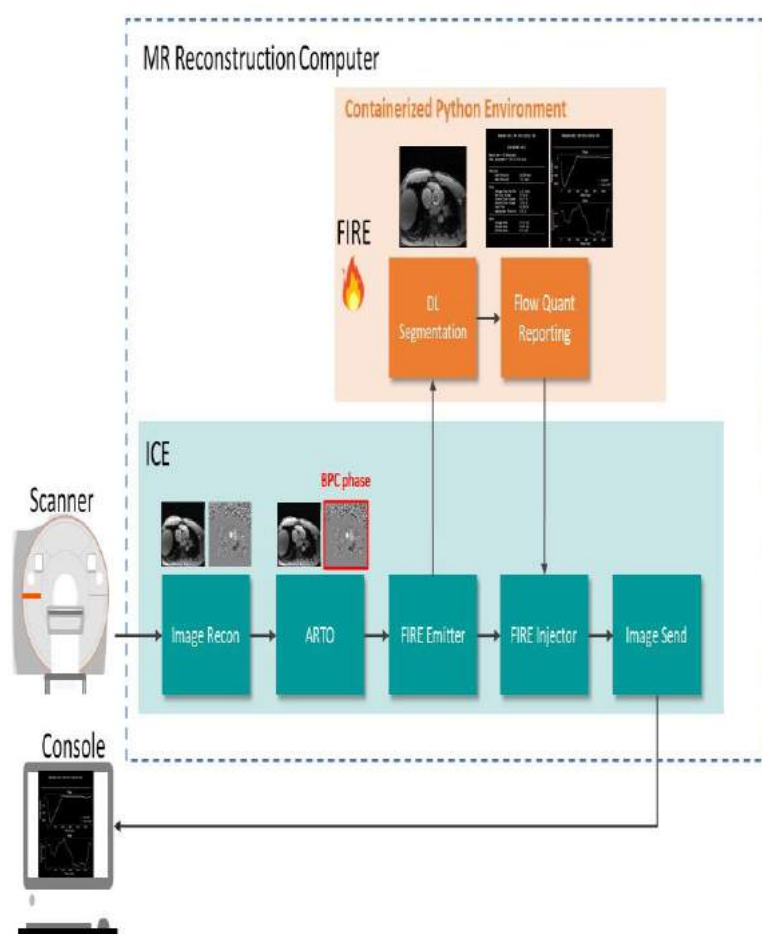
We tested this technique in 24 patients (14 female,  $42.1 \pm 20.0$  years old) referred for clinical cardiac MR on a 1.5T clinical scanner (MAGNETOM Sola, Siemens Healthcare, Erlangen, Germany). 2D flow images were acquired in AO orientation for all patients and in MPA orientation for one patient using the prototype 2D segmented PC sequence with retrospective ECG triggering (GRAPPA R=2, temporal resolution = 33.2 ms, VENC = 150-350 cm/s). All flow data were also post-processed using cvi42 (Circle Cardiovascular Imaging Inc. Calgary, Canada) with manual BPC to compare the quantitative flow parameters.

**Results:** The automated inline 2D flow analysis was successful in all scans and took under 10 seconds for each dataset. **Fig. 2** shows the representative output of inline flow results of AO and MPA from one patient with severe atrial septal defect (ASD) ( $Q_p/Q_s = 2.76$ ). No significant difference was found between the flow analysis results from inline flow and cvi42

(net flow: mean difference (MD) =  $1.00 \pm 3.51$  ml,  $p = 0.17$ ; peak flow rate: MD =  $1.81 \pm 8.51$  ml/s,  $p = 0.30$ ; peak velocity: MD =  $-4.14 \pm 12.07$  cm/s,  $p = 0.10$ ) with very strong correlations (**Fig. 3**).

**Conclusion:** We developed a rapid, fully automated framework for inline 2D flow analysis on the scanner, providing BPC, vessel segmentation and accurate flow quantification without any user interaction. With flow quantification results streamlined a few seconds after the scan, post-hoc image analysis is not required. The operator can immediately view the results during the scan and make timely decisions about whether additional acquisitions are required.

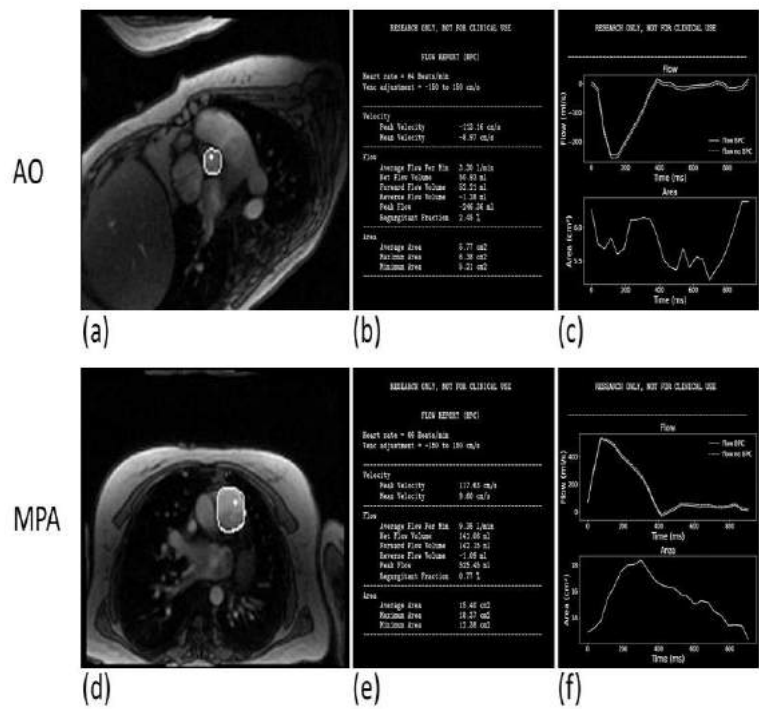
**Figure/Table 1**



**Caption 1**

**Figure 1.** Inline 2D flow analysis framework implemented on Siemens ICE and prototype FIRE. ARTO functor performed BPC and sent images to a Python container via FIRE emitter for DL image segmentation and flow analysis. Results were sent back as DICOMs via FIRE injector to be viewed on the console.

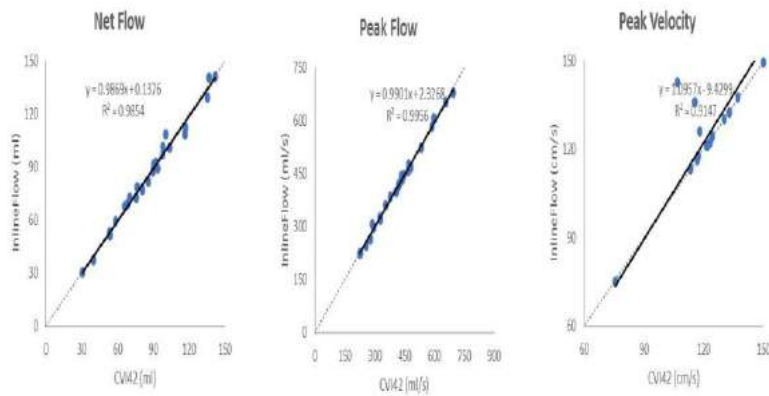
Figure/Table 2



Caption 2

**Figure 2.** Representative outputs of inline flow results from one patient with severe ASD. **(a, d)** Magnitude images in the systolic phase with automated vessel segmentation with the white dot indicated the position of peak velocity. **(b, c, e, f)** Inline flow reports, including quantitative results **(b and e)** and plots of flow and area curve **(c and f)**

Figure 3



### Caption 3

**Figure 3.** Linear regression analysis showed a very strong correlation between the net flow, peak flow rate and peak velocity measured by inline flow and cvi42.

### Bibliographic References

1. Chernobelsky et al., Baseline correction of phase contrast images improves quantification of blood flow in the great vessels. J Cardiovasc Magn Reson. 2007;9:681–685., 2. Pruitt et al., A method to correct background phase offset for phase-contrast MRI in the presence of steady flow and spatial wrap-around artifact. Magn Reson Med. 2019 Apr;81(4):2424-2438, 3. Jin et al., Automatic Vessel Segmentation for 2D Phase Contrast MR using Deep Learning. ISMRM 2021, 4. Chow et al. Prototyping Image Reconstruction and Analysis with FIRE. SCMR 2021, 5. Inati et al., ISMRM Raw data format: A proposed standard for MRI raw datasets. Magn Reson Med.2017;77(1):411-421

Speaker: N. jin

Category: Flow, Automated Processing, Image Analysis

000347

## High-altitude chronic hypoxia prevents myocardial dysfunction in type 2 diabetic rats

Y. Wan \* (1); D. Zhu (1); B. He (1); L. Wang (1); C. Chen (1); X. Zhou (2); F. Gao (1)

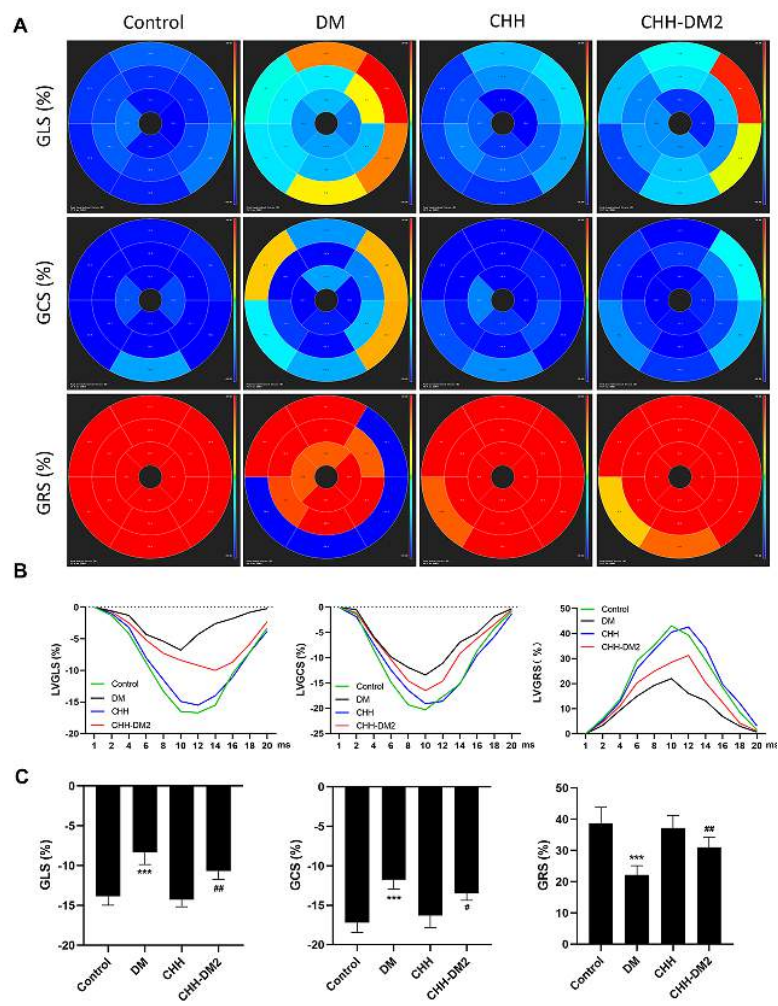
(1) Radiology, West China Hospital of Sichuan University, Chengdu, China; (2) Mr collaboration, Siemens Healthineers Ltd, Shanghai, China

### Abstract

**Background**High altitude chronic hypoxia (CHH) had favorable impact on the lower prevalence of diabetes together with the better glucose tolerance(1-3). However, whether they prevent diabetic cardiomyopathy are not established. This study aimed to investigate the effects of high-altitude chronic hypoxia on left ventricular (LV) function in rats with type 2 diabetes mellitus.**Methods**Sprague-Dawley rats were randomly divided into control (altitude 500 m), DM (diabetes mellitus and altitude 500 m), CHH (altitude 4250 m), CHH-DM2 (altitude 4250 m and DM for 2 weeks), CHH-DM4 (altitude 4250 m and DM for 4 weeks), and CHH-DM8 (altitude 4250 m and DM for 8 weeks) groups. Short-axis, 2-chamber and 4-chamber magnetic resonance cine images of all the groups were acquired using a 7.0T small animal scanner (Bruker, Ettlingen, Germany). Left ventricular cardiac function and global myocardial strain were evaluated at 2, 4, and 8 weeks by commercial software CVI42 (Circle Cardiovascular Imaging Inc., Calgary, Canada). Subsequently, biochemical indexes, histological and level of hypoxia induced factor (HIF)-1 $\alpha$  were evaluated. **Results**Left ventricular ejection fraction (LVEF), global longitudinal (GLS), circumferential (GCS), and radial (GRS) strains significantly decreased in the DM group compared with the controls. However, left ventricular cardiac function and global myocardial strain was significantly better in the CHH-DM2 group compared with the DM group, both in terms of LVEF (Figure 1). The CHH-DM4 and CHH-DM8 groups also showed cardioprotection, with the maximum level of efficacy (Table 1). Mechanistically, prolonged chronic hypoxia intervention at high altitude further reduced cardiac apoptosis, autophagy and oxidative stress, and further increased HIF-1 $\alpha$  expression. **Conclusions**High-altitude chronic hypoxia exerted cardioprotective effects by improving LV function, increasing global myocardial strain and attenuating cardiac hypertrophy in type 2 diabetic rats. These benefits indicate it may be a potential treatment strategy for diabetic cardiomyopathy.

### Figure/Table 1





**Caption 1**

Figure 1: The global myocardial strain of left ventricle in the four groups.

**Figure/Table 2**

Parameters	Control group	DM group	CHH-DM2 group	CHH-DM4 group	CHH-DM8 group
LVEF (%)	62.81±2.02	52.21±4.36***	57.64±3.16 <sup>#</sup>	61.26±4.13 <sup>###</sup>	62.07±3.69 <sup>###</sup>
GLS (%)	-15.15±1.07	-9.83±1.89***	-11.74±1.42 <sup>#</sup>	-13.9±1.78 <sup>###</sup>	-14.02±2.48 <sup>###</sup>
GCS (%)	-21.05±3.48	-13.35±4.26***	-17.02±1.33 <sup>#</sup>	-18.34±1.69 <sup>###</sup>	-19.04±1.08 <sup>###</sup>
GRS (%)	45.28±11.71	23.25±7.56***	28.26±6.7 <sup>#</sup>	37.40±6.11 <sup>###</sup>	36.12±4.06 <sup>###</sup>

## Caption 2

Table 1 Left ventricular strain parameters detected at week 2, 4, 8.

### Bibliographic References

1. Santos JL, Pérez-Bravo F, Carrasco E, Calvillán M, Albala C. Low prevalence of type 2 diabetes despite a high average body mass index in the Aymara natives from Chile. *Nutrition* 2001;17:305-9., 2. Marlatt KL, Greenway FL, Kyle Schwab J, Ravussin E. Two weeks of moderate hypoxia improves glucose tolerance in individuals with type 2 diabetes. *Int J Obes (Lond)* 2020;44:744-7., 3. Lin X, Ye M, Mo W, Zhao H. The effects of chronic hypoxia on the endocrine-related parameters in elderly rats with type 2 diabetes mellitus. *Am J Transl Res* 2021;13:3198-205.

Speaker: Y. Wan

Category: Ventricular Dysfunction, Strain, Diabetes

**000348**

## **The Case of the -Itis': Arthritis, Pericarditis, and Myocarditis**

C. Shen \* (1); J. Brown, (2); G. Wesbey, (3); J. Gonzalez, (1); A. Patel, (1); A. Robinson \* (1)

(1) Cardiology, Scripps Clinic, La Jolla, United States of America; (2) Biochemistry, University of California San Diego, La Jolla, United States of America; (3) Radiology, Scripps Clinic, La Jolla, United States of America

### **Abstract**

#### **Description of Clinical Presentation:**

A 64-year-old woman with history of complete heart block status post dual-chamber pacemaker placement and seropositive rheumatoid arthritis treated with methotrexate and hydroxychloroquine presented with gradually progressive exertional intolerance and chest pain. She experienced a dull ache-like sensation at her sternum associated with shortness of breath, occurring intermittently and often exacerbated by activity. As an outpatient over a period of a few months, she underwent testing with coronary angiography that found no significant epicardial disease, pulmonary function testing that showed mild restrictive lung disease, and chest CT that did not show an interstitial lung disease. In addition, echocardiogram showed preserved ejection fraction 59% and normal mean pulmonary artery pressure 21 mmHg but with inferior wall hypokinesis. Finally, her symptoms increased to the point that in a single month, she presented to the emergency department on four separate occasions, and troponin levels drawn were consistently and mildly elevated 0.113-0.166. On review of troponin levels from 4 years prior, they were also mildly elevated.

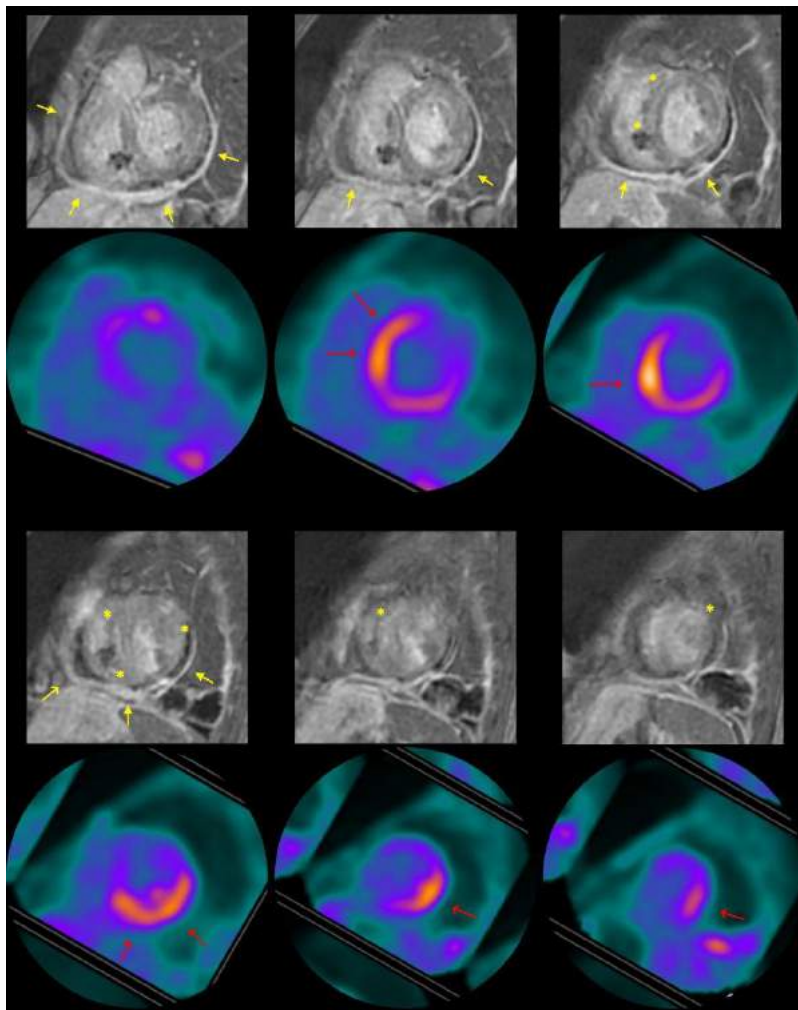
#### **Diagnostic Techniques and Their Most Important Findings:**

Finally, she underwent cardiac MRI showing extensive, patchy myocardial late gadolinium enhancement as well as circumferential pericardial thickening and enhancement with a small pericardial effusion consistent with myocarditis and pericarditis. PET FDG showed moderate septal and inferior/inferolateral FDG activity, consistent with myocardial inflammation. She was initiated on steroid therapy and abatacept for rheumatoid arthritis with improvement in symptoms.

#### **Learning Points from this Case:**

A 64-year-old woman with third degree heart block, elevated troponin, and chest discomfort had progressive exertional intolerance ultimately found to be secondary to peri- and myocarditis associated with rheumatoid arthritis. Extra-articular manifestations of rheumatoid arthritis are uncommon but can include cardiac conduction abnormalities, pericarditis, and myocarditis. Myocarditis is an uncommon complication of rheumatoid arthritis but may respond to immunosuppressive therapies. CMR can be useful in the work-up of chest pain and myocardial injury with no coronary obstruction, identifying the cause of idiopathic heart block and in evaluating for cardiac complications of rheumatologic conditions.

**Figure/Table 1**



**Caption 1**

Matched short axis CMR (1st and 3rd rows) and FDG (2nd and 4th rows) demonstrating pericardial thickening and enhancement (yellow arrows), patchy myocardial late gadolinium enhancement (yellow asterisks) and FDG avidity (red arrows).

**Bibliographic References**

Mavrogeni S, Dimitroulas T, Sfrikakis PP, Kitas GD. Heart involvement in rheumatoid arthritis: multimodality imaging and the emerging role of cardiac magnetic resonance. *Semin Arthritis Rheum*. 2013 Dec;43(3):314-24. doi: 10.1016/j.semarthrit.2013.05.001. Epub 2013 Jun 17. PMID: 23786873.

Speaker: C. Shen, A. Robinson

Category: Myocarditis, Pericardial Disease, Late Gadolinium Enhancement

000352

**Comparison of cardiac function, structure, myocardial deformation, myocardial fibrosis in peripartum cardiomyopathy and dilated cardiomyopathy**

H. Fu \* (1); H. XU (2); Y. Guo (3)

(1) Radiology, West China Second University Hospital, Sichuan University, Chengdu, China; (2) Radiology department, West China Second University Hospital, Sichuan University, Chengdu, China, Chengdu, China; (3) West china second university hospital, sichuan university, chengdu, china, Department of Radiology, Chengdu, China

**Abstract**

**Abstract**

**Background :** Similarities and differences in imaging phenotype between peripartum cardiomyopathy(PPCM) and dilated cardiomyopathy(DCM) haven't been studied.

**Purpose:** This study aimed to compare cardiac structure, function, deformation, and myocardial fibrosis between PPCM and DCM, and to explore the uniformity of segmental deformation dysfunction furtherly.

**Methods:** 102 PPCM patients, 38 age-matched female DCM patients, and 21 healthy puerperas were retrospectively enrolled. Cardiac magnetic resonance(CMR) was performed. Parameters of cardiac function, structure, deformation, and fibrosis were compared between PPCM and DCM. Degree of deformation dysfunction was compared among segments.

**Results:** PPCM and age-matched female DCM patients have similar biventricular function and structure, global and segmental myocardial strain(all  $p>0.05$ ). Prevalence and total number of segments with LGE in PPCM was lower than that in DCM(34.3% vs 55.3%,  $p=0.024$ ; 272/1632 vs 188/608,  $p<0.001$ ). Despite no significant difference was found in global LGE extent, basal LGE extent in DCM patients was more severe than PPCM patients( $13.02\pm19.40$  vs  $4.85\pm12.60$ ,  $p=0.020$ ). Besides, average number of segments with LGE( $2.65\pm4.86$  vs  $4.95\pm6.48$ ,  $p=0.053$ ) and middle LGE extent tended to be more prominent in DCM patients( $11.60\pm18.61$  vs  $5.08\pm12.12$ ,  $p=0.05$ ). LGE mainly located in basal and middle part of left ventricle and its distribution in segments was homogeneous in PPCM and DCM. Compared with DCM patients, myocardial deformation dysfunction presented in a more heterogenous way in PPCM.

**Conclusion:** PPCM and DCM shared similar cardiac function, structure, and deformation. Myocardial fibrosis in PPCM seemed to be less prevalent than DCM. PPCM patients presented with a more inhomogeneous segmental myocardial deformation dysfunction.

**Figure/Table 1**

<b>Table 1. Comparison of global and segmental myocardial deformation and LGE in left ventricle</b>			
Parameters	PPCM	DCM	P
Global PRS	10.0(6.5,16.9)	10.2(7.2,17.5)	0.600
Global PCS	-8.7(-13.2,-5.8)	-10.4(-13.7,-7.3)	0.366
Global PLS	-6.3(-9.4,-4.1)	-6.7(-9.6,-4.9)	0.582
Basal PRS	17.1(11.2,29.0)	20.1(11.6,32.6)	0.453
Basal PCS	-8.9(-11.9,-6.3)	-8.3(-11.1,-6.6)	0.590
Basal PLS	-5.4(-7.5,-3.0)	-4.6(-6.4,-2.8)	0.208
Middle PRS	9.0(5.4,15.1)	9.7(6.2,18.3)	0.408
Middle PCS	-8.5(-12.9,-5.6)	-9.6(-14.2,-6.3)	0.318
Middle PLS	-5.8(-9.9,-4.0)	-6.0(-9.7,-3.5)	0.896
Apical PRS	8.1(4.1,15.0)	7.9(4.0,12.6)	0.448
Apical PCS	-10.2(-16.3,-6.9)	-12.3(-16.6,-8.2)	0.241
Apical PLS	-8.1(-12.1,-5.4)	-8.9(-12.9,-6.8)	0.157
Global LGE extent, %	10.48±55.51	12.02±18.41	0.87
Basal LGE extent, %	4.85±12.60	13.02±19.40	0.020*
Middle LGE extent, %	5.08±12.12	11.60±18.61	0.050
Apical LGE extent, %	1.15±3.38	2.70±6.44	0.163
Presence of LGE, n	35(34.3%)	21(55.3%)	0.024*
Average segments of LGE	2.65±4.86	4.95±6.48	0.053
Total segments of LGE	272/1632	188/608	<0.001*
Abbreviations: Peak Radial Strain, PRS; Peak Circumferential Strain, PCS; Peak Longitudinal Strain, PLS; Late Gadolinium Enhancement, LGE.			

**Caption 1**

**Comparison of global and segmental myocardial deformation and LGE in left ventricle**

**Figure/Table 2**

<b>Table 2. Uniformity of myocardial deformation dysfunction and fibrosis among basal, middle, and apical part of LV for PPCM and DCM</b>				
	Basal	Middle	Apical	P
The difference of PRS compared with healthy puerperas				
PPCM	38.5(26.7,44.4)#*	27.8(21.8,31.4)#&	24.0(17.2,28.0)*&	<0.001
DCM	35.5(23.0,44.0)#*	27.1(18.5,30.6)#	24.3(19.6,28.2)*	<0.001
The difference of PCS compared with healthy puerperas				
PPCM	9.6(6.7,12.3)*#	13.6(9.3,16.6)#	14.8(8.8,18.0)*	<0.001
DCM	10.3(7.5,12.0)	12.5(7.9,15.8)	12.6(8.3,16.7)	0.057

The difference of PLS compared with healthy puerperas				
PPCM	7.2(5.1,9.5)*#	9.4(5.2,11.2)#	10.1(6.1,12.8)*	<0.001
DCM	8.0(6.2,9.8)	9.2(5.5,11.7)	9.3(5.3,11.4)	0.892
Extent of LGE				
PPCM	4.85±12.60%*	5.08±12.12%&	1.15±3.38%*&	<0.001
DCM	13.02±19.40%*	11.60±18.61%&	2.70±6.44%*&	0.001
Abbreviations: as shown in Table 4. # means statistical difference between basal and middle part; * means statistical difference between basal and apical part; & means statistical difference between apical and middle part.				

## Caption 2

**Uniformity of myocardial deformation dysfunction and fibrosis among basal, middle, and apical part of LV for PPCM and DCM**

## Figure 3

## Caption 3

Comparison of LGE extent in segments between PPCM and age-matched female DCM patients

Speaker: H. Fu

Category: Cardiac Function, Cardiac Strain, Cardiomyopathy



000354

## Significantly elevated hepatic extracellular volume in adult patients with Fontan circulation and its correlation with impaired functional capacity

S. Kongrat \* (1); T. Lueangklanlayanakhun (1); V. Prakongwong, (1); W. Prasertkulchai (1); T. Tangchareon (1)

(1) Division of cardiology, department of internal medicine, Faculty of Medicine Ramathibodi Hospital, Mahidol University, Bangkok, Thailand

### Abstract

**Background:** Fontan - associated liver disease is a major concern in patients who underwent this procedure. Regularly imaging of the liver is currently recommended in Fontan patients but not in other congenital heart disease. The extracellular volume of the liver can be obtained during the CMR scanning and studies showed the high liver ECV in Fontan patients but the correlation between the liver ECV and the functional capacity of Fontan patients has not yet been reported.

**Objective:** 1). To compare ECV of the liver between Fontan patients and other congenital heart diseases with significant pulmonic or tricuspid regurgitation. 2) to evaluate the correlation between the liver ECV in adult Fontan patients and their functional capacity and clinical characteristics.

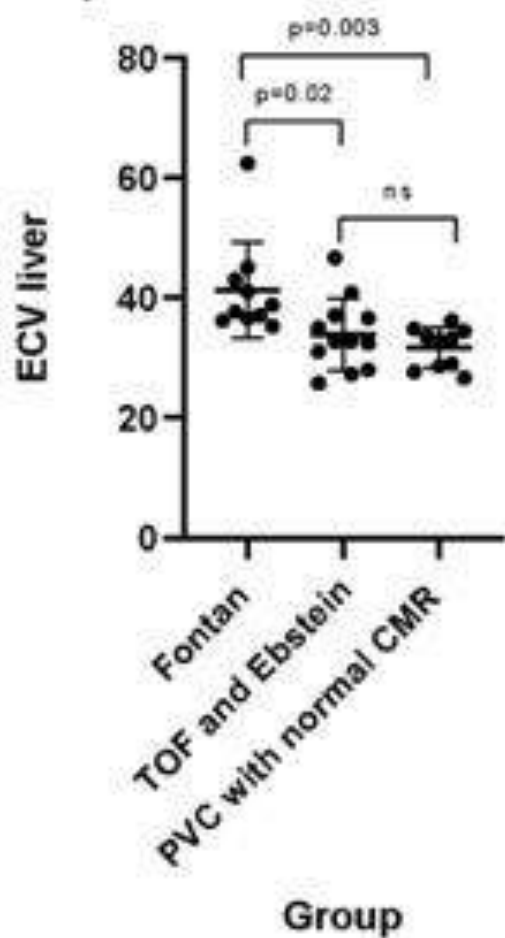
**Methods:** A retrospective analysis of cardiovascular magnetic resonance imaging of patients with history of Fontan surgery from 2017-2020 were conducted. Clinical characteristics and ECV of the liver were evaluated and compared between patients and control group. The functional capacity was evaluated from the 6-minute walk distance (6 MWD). The correlation between the ECV of the liver and the functional capacity were analyzed.

**Results:** Total 32 patients were enrolled in the study; 10 Fontan patients, 12 Ebstein's anomaly or tetralogy of Fallot patients with significant Pulmonic or Tricuspid regurgitation and 10 control group. The liver ECV were significantly higher in Fontan patients compared with non-Fontan and control group (41.3% in Fontan group, 33.9% in non-Fontan ACHD and 31.7% in control group with  $p = 0.02$  and  $0.003$  in Fontan vs. non-Fontan ACHD and Fontan vs. control group respectively). In Fontan patients, there was a significant correlation between the liver ECV and the liver blood biochemistry with  $r=0.91$ ,  $p = 0.01$  for AST/ALT ratio and  $r=0.85$ ,  $p = 0.002$  for AST. The liver ECV inversely correlated with the six-minute walk distance ( $r= -0.69$ ,  $p =0.03$ ). There was no significant correlation between liver ECV and systemic ventricular ejection fraction in Fontan patients ( $r = -0.16$ ,  $p = 0.66$ ). However, there were inversely correlation between liver ECV and systemic ventricular function in the whole cohort ( $r = -0.4$ ,  $p = 0.02$ ).

**Conclusion:** The liver ECV in patients who underwent Fontan operation significantly showed inversed correlation with their functional capacity. These findings suggest of the liver ECV measured by CMR as a potential marker for adverse outcomes.

Figure/Table 1

### Compare ECV liver in each group



Caption 1

Figure 1 Demonstrated significant differences of ECV liver in Fontan patients, non-Fontan ACHD and control group

Figure/Table 2

Clinical	Fontan (N= 10)	TOF with severe PR or Ebstein with severe TR (N = 12)	PVC with normal CMR findings (N=10)
Age (years)	23.6 ± 4.5	33.9 ± 5.6	31.7 ± 3.3
Male	6 (60%)	7 (58.3%)	6 (60%)
Age of Fontan surgery (years)	12.8 ± 7.4	-	-
Duration after surgery to CMR (years)	9.7 ± 8.7	-	-
Serum Albumin	38.9 ± 7.6	-	-
Serum AST (U/L)	39.2 ± 27.2	-	-
Serum ALT (U/L)	26.7 ± 10.3	-	-
AST/ALT	1.8 ± 1.9	-	-
Systemic ventricular function (%)	47.9 ± 14.5	53.7 ± 8.8	60.9 ± 8.8*
Six-minute walk distance (m)	332.9 ± 69.8	-	-
ECV (%)	41.3±8.1	33.9±5.9 <sup>#</sup>	31.7±3.4 <sup>†</sup>

## Caption 2

**Figure 2 Baseline characteristics in Fontan patients, non-Fontan ACHD group and control group. \*significant difference between Fontan and control,  $p = 0.01$  #, † significant difference between Fontan, non-Fontan ACHD group and control group  $p = 0.02$ ,  $p = 0.003$  respectively**

## Figure 3

Clinical characteristics	Pearson correlation coefficient	p-value
Age	- 0.06	0.88
Age of Fontan surgery	-0.57	0.09
Duration after Fontan to CMR	0.58	0.1
US liver findings	-0.01	0.98
<u>Six-minute walk distance</u>	<u>-0.69</u>	<u>0.03</u>
<u>Serum albumin</u>	<u>-0.7</u>	<u>0.02</u>
<u>AST</u>	<u>0.85</u>	<u>0.002</u>
ALT	-0.51	0.13
<u>AST/ALT ratio</u>	<u>0.91</u>	<u>0.01</u>
Total bilirubin	0.04	0.91
Systemic ventricular function	-0.16	0.66

## Caption 3

**Figure 3 Demonstrated inversely correlation between ECV liver and six-minute walk distance, serum albumin and significant correlation with AST and AST/ALT ratio**

Speaker: S. Kongrat

Category: Fontan, Extracellular Volume Fraction , Function

000355

## The performance of CMR derived first-pass perfusion parameters in detection of the left ventricle diastolic dysfunction: Validation with Cardiac Catheterization

X. Guo \* (1); C. Gong (2); C. Yucheng (2)

(1) , , , China; (2) Department of cardiology, West China Hospital, Chengdu, China

### Abstract

**Background** The non-invasive assessment of left ventricular (LV) diastolic dysfunction is still a challenging issue. Clinical haemodynamic parameters via cardiac catheterization are considered to be gold standard. Echocardiography is noninvasive and is widely used to evaluate cardiac diastolic function based on comprehensive evaluations, however, the estimation of LV filling pressures and negative predictive value may lack precision. Therefore, a reliable non-invasive method to detect LV diastolic dysfunction would be desirable. The quantitative parameters derived from cardiac magnetic resonance (CMR) first-pass perfusion imaging had an advantage of hemodynamic evaluation. We aimed to investigate the diagnostic accuracy of values from CMR for invasive measured LV diastolic dysfunction in patients with left heart disease (LHD) using invasive catheterization.

**Methods** We retrospectively enrolled 77 LHD patients who underwent CMR and catheterization. LV diastolic dysfunction was defined as invasively measured pulmonary capillary wedge pressure (PCWP) or LV end-diastolic pressure (LVEDP) > 12 mmHg. Pulmonary transit time (PTT) was measured as the time for blood to pass from LV to right ventricular (RV) assessed by first-pass perfusion imaging. Pulmonary transit beat (PTB) was the number of cardiac cycles of the interval and pulmonary blood volume indexed to body surface area (PBVi) was the product of PTB and RV stroke volume index (RVSVi).

**Results** Of 77 LHD patients, 53 (68.83%) patients were found to have impaired LV diastolic function. Among them, 30 (38.96%) were diagnosed with light chain cardiac amyloidosis, 25 (32.47%) with idiopathic dilated cardiomyopathy (DCM), 14 patients (18.18%) suffering from hypertrophic cardiomyopathy and 8 patients (10.39%) with other disease including myocarditis and coronary heart disease. Compared to controls, patients with LV diastolic dysfunction showed significantly longer PTT, larger PTB and PBVi ( $p < 0.05$ ). At multivariable logistic regression analyses, only PTT and PTB were independent predictors of LV diastolic dysfunction ( $P < 0.05$ ). At the best cut-off point of 11.9s, PTT yielded best diagnostic performance for the diagnosis of LV diastolic dysfunction ( $AUC = 0.83$ ,  $P < 0.001$ ). Reproducibility of parameters derived from first-pass perfusion is shown in Table 5. ICC for interobserver and intraobserver reproducibility for PTTc and PTB was high ( $\geq 0.90$ ), suggesting good reproducibility while PBVi with lower ICC revealed worsened reproducibility.

**Conclusion** PTT is a novel non-invasive quantitative marker of diastolic dysfunction in LHD patients validated by catheterization, which provides the functional assessment and hemodynamic congestion grade. In addition, PTTc displayed good diagnostic accuracy (83%) for the detection of diastolic dysfunction at the best cut-off level of 11.9s and high specificity (100%) for a rule-out test.

**Figure/Table 1**

	Normal diastolic function (n=24)	Diastolic dysfunction (n=53)	<i>p</i>
<b>Baseline characteristics</b>			
Male, n (%)	13(54.2)	34(64.2)	0.405
SBP, mmHg	125.33±5.30	105.44±3.61	<b>0.005</b>
DBP, mmHg	80.67±5.52	69.96±2.48	0.011
HR, bpm	76.78±7.86	74.52±2.63	0.195
BMI, kg/m <sup>2</sup>	23.29±1.06	21.95±0.60	0.497
BSA, m <sup>2</sup>	1.57±0.06	1.60±0.04	0.920
NYHA III-IV, n (%)	15(62.5)	29(54.7)	0.523
NT-proBNP, pg/mL	3658.89±1694.58	5621.85±888.55	0.094
Tnt, pg/mL	57.52±14.28	116.29±29.06	0.169
Crea, µmol/l	155.89±65.39	88.15±4.03	0.183
eGFR, ml/min/m <sup>2</sup>	81.80±10.38	84.49±3.99	0.737
Hct, %	0.39±0.03	0.41±0.01	0.814
Hb, g/l	125.33±8.78	135.04±4.68	0.812
Urea, mmol/l	7.62±1.32	6.74±0.67	0.979
Uric acid, µmol/l	376.33±50.75	460.04±31.40	0.065
Triglyceride, mmol/l	1.50±0.19	1.25±0.12	0.166
Cholesterol, mmol/l	4.30±0.44	33.59±20.71	0.345
LDH, IU/L	287.67±37.32	267.00±19.58	0.878
HBDH, IU/L	233.56±34.07	220.85±15.44	0.900
β-HB, mmol/l	0.11±0.03	1.03±0.83	0.399
<b>CMR parameters</b>			
LVEDV, mL	141.42±28.05	208.74±26.21	0.291
LVESV, mL	71.04±24.28	154.27±23.85	0.136
LVEF, %	53.96±5.27	31.05±2.72	<b>0.004</b>
LVmass, g	146.85±21.46	163.40±13.02	0.769
RVEDV, mL	113.37±13.57	152.27±14.58	0.198
RVESV, mL	51.53±6.68	106.90±12.80	<b>0.003</b>
RVEF, %	53.16±3.56	34.21±2.60	<b>&lt;0.001</b>
LV long-axis Strain	-8.14±0.78	-4.57±0.50	<b>0.001</b>
LV long-axis Strain Rate	-0.55±0.05	-0.35±0.03	<b>0.002</b>

PTTc, s	8.47±0.47	15.08±1.05	<b>&lt;0.001</b>
PTB, bpm	8.97±0.59	17.89±1.39	<b>&lt;0.001</b>
PBVi, mL/m2	300.35±23.11	476.63±47.33	<b>0.001</b>
<b>Hemodynamic features</b>			
mRAP, mmHg	1.67±0.29	11.04±1.28	<b>&lt;0.001</b>
sPAP, mmHg	23.67±2.52	52.82±3.10	<b>&lt;0.001</b>
mPAP, mmHg	13.22±1.67	33.37±1.74	<b>&lt;0.001</b>
dPAP, mmHg	7.78±1.64	23.56±1.52	<b>&lt;0.001</b>
Qpi, L /min/ m2	2.00±0.19	1.55±0.09	<b>0.031</b>
Qsi, L /min/ m2	2.27±0.23	1.60±0.11	<b>0.019</b>
SVRi, Wood units/m2	45.08±5.01	49.49±3.64	0.748
PVRi, Wood units/m2	4.26±1.32	8.46±0.94	<b>0.015</b>
PVRi/SVRi	0.09±0.03	0.20±0.03	<b>0.038</b>

Abbreviation: LHD left heart disease; LAP pulmonary capillary wedge pressure; SBP systolic blood pressure; DBP diastolic blood pressure; HR heart rate; BMI body mass index; BSA body surface area; NYHA New York Heart class; NT-pro BNP N-terminal pro-brain natriuretic peptide; Tnt Troponin T; eGFR estimated glomerular filtration rate; Hct hematocrit; Hb hemoglobin; LDH Lactic dehydrogenase; HBDH Hydroxybutyrate dehydrogenase;  $\beta$ -HB  $\beta$ -Hydroxybutyric acid. CMR cardiac magnetic resonance; LAP pulmonary capillary wedge pressure; PTTc pulmonary transit time corrected; LV left ventricle; RV Right ventricle; EDV end-diastolic volume; ESV end-systolic volume; EF ejection fraction; mRAP mean right atrial pressure; sPAP systolic pulmonary artery pressure; mPAP mean pulmonary artery pressure; dPAP diastolic pulmonary artery pressure; Qpi pulmonary circulation blood flow index; Qsi systemic circulation blood flow index; PVRi pulmonary vascular resistance index; SVRi systemic vascular resistance index.

## Caption 1

**Table 1: baseline characteristics, CMR and cardiac catheterization values between patients with and without diastolic LV dysfunction.**

## Figure/Table 2

Model	Parameters	Univariate analysis		multivariable analysis	
		OR (95% CI)	P	OR (95% CI)	P
	Age	0.980 (0.945-1.016)	0.266		
	Male	1.514 (0.568-4.033)	0.407		

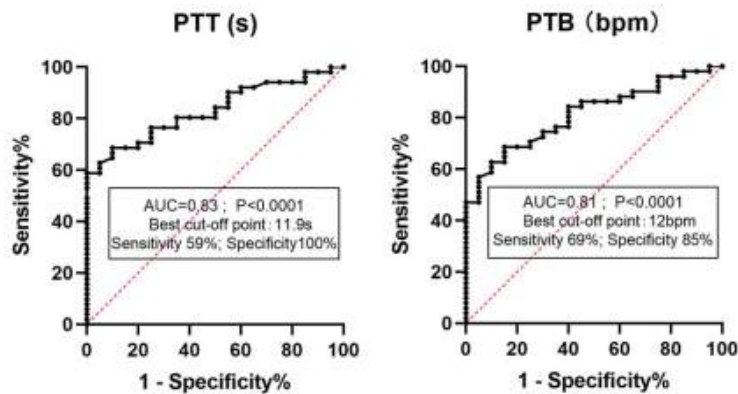
	NYHA III-IV	0.725 (0.270-1.947)	0.523		
	SBP	0.963 (0.936-0.991)	<b>0.009</b>		
	DBP	0.953 (0.917-0.991)	<b>0.015</b>		
	LVEF	0.953 (0.920-0.986)	<b>0.006</b>		
	RVEF	0.931 (0.891-0.973)	<b>0.001</b>		
	RVESV	1.015 (1.002-1.029)	<b>0.029</b>		
	LV long-axis Strain	1.338 (1.110-1.612)	<b>0.002</b>		
	LV long-axis Strain Rate	57.402 (3.492-943.650)	<b>0.005</b>		
	PTTc	1.424 (1.142-1.776)	<b>0.002</b>		
	PTB	1.292 (1.097-1.520)	<b>0.002</b>		
	PBVi	1.003 (1.000-1.006)	<b>0.048</b>		
Model 1	LV Strain			1.268 (1.023-1.571)	<b>0.030</b>
	PTTc			1.427 (1.081-1.884)	<b>0.012</b>
Model 2	LV Strain			1.231 (1.007-1.505)	<b>0.042</b>
	PTB			1.339 (1.052-1.705)	<b>0.018</b>
Model 3	LV Strain			1.263 (1.015-1.572)	<b>0.036</b>
	RVEF			0.913 (0.859-0.970)	<b>0.003</b>
	PBVi			1.002 (0.997-1.007)	0.369

**Note: The three multivariate models are the results of PTT, PTB and PBVi adjusted by the above indexes Adjusted for all entered covariates in model 1, 2 and 3 separately.**

## **Caption 2**

**Table 2: Univariate and multivariate logistic regression analysis of left ventricular diastolic dysfunction**

## **Figure 3**



### Caption 3

**Figure 1:** ROC curves of PTTc and PTB for diagnosing patients with left ventricular diastolic dysfunction

### Bibliographic References

5. Kindermann M. How to diagnose diastolic heart failure: a consensus statement on the diagnosis of heart failure with normal left ventricular ejection fraction by the Heart Failure and Echocardiography Associations of the European Society of Cardiology. *Eur Heart J* 2007; 28: 2686; author reply 2686-2687., 4. Harjola VP, Mullens W, Banaszewski M et al. Organ dysfunction, injury and failure in acute heart failure: from pathophysiology to diagnosis and management. A review on behalf of the Acute Heart Failure Committee of the Heart Failure Association (HFA) of the European Society of Cardiology (ESC). *Eur J Heart Fail* 2017; 19: 821-836., 3. Ponikowski P, Voors AA, Anker SD et al. 2016 ESC Guidelines for the diagnosis and treatment of acute and chronic heart failure: The Task Force for the diagnosis and treatment of acute and chronic heart failure of the European Society of Cardiology (ESC). Developed with the special contribution of the Heart Failure Association (HFA) of the ESC. *Eur J Heart Fail* 2016; 18: 891-975., 2. Obokata M, Reddy YNV, Borlaug BA. Diastolic Dysfunction and Heart Failure With Preserved Ejection Fraction: Understanding Mechanisms by Using Noninvasive Methods. *JACC Cardiovasc Imaging* 2020; 13: 245-257., 1. Nagueh SF. Left Ventricular Diastolic Function: Understanding Pathophysiology, Diagnosis, and Prognosis With Echocardiography. *JACC Cardiovasc Imaging* 2020; 13: 228-244.

Speaker: X. Guo

Category: Cardiac Magnetic Resonance Elastography, Ventricular Dysfunction, Cardiomyopathy



000360

## Liver T1 mapping in prognosis of pulmonary hypertension patients

J. Guo \* (1); J. Wang (1); J. He (1); L. Wang (1); Y. Xu (1); J. Guo (1); K. Wan (2); X. Zhou (3); Y. Chen (1)

(1) Cardiology, West China Hospital clinics, Chengdu Shi, China; (2) Geriatrics, West China Hospital clinics, Chengdu Shi, China; (3) Mr collaboration, Siemens Healthineers Ltd., shanghai, China

### Abstract

**Background:** Prognostic significance of liver involvement in PH patients is still unclear. Native T1 and ECV values of the liver measured by cardiac magnetic resonance were shown to be predictive in other cardiovascular diseases.

**Methods:** We prospectively included 188 PH patients and 64 healthy volunteers who underwent cardiovascular magnetic resonance examination between October 2013 to December 2019 in West China Hospital, Sichuan University. Three regions of interests (ROIs) were carefully delineated in the same location in pre- and post-contrast T1 mapping sequence in liver parenchyma. Fat and blood vessels in the liver were not included in ROIs. Native T1 and ECV values were measured and compared between PH patients and healthy volunteers. Patients included underwent regular follow-up at month 3, 6, 12 and 1 year thereafter by telephone call or clinical visits in accordance with guidelines. The primary endpoint was defined as all-cause mortality, lung transplantation and atrial septostomy according to the REVEAL Registry. The secondary endpoint was defined as a combination of all-cause mortality, lung transplantation and heart failure related readmission. Statistical analysis were performed using independent sample t test, Pearson's and Spearman's rank correlation, logistic regression analysis.

**Results:** During the median follow-up of 33.33 months (interquartile range: 19.98-50.10 months), 31 patients (16.5%) met primary endpoint and 80 patients (42.6%) met secondary endpoint. Both native T1 and ECV values of the liver were significantly higher in PH patients than healthy volunteers. Besides, native T1 and ECV values of liver were all related with functional and volume parameters of right-sided heart. In univariate cox regression, increased native T1 value of liver indicated higher risk of suffering from primary endpoint [hazard ratio (HR) 1.005, 95% confidence interval (CI) 1.002-1.007,  $p < 0.001$ ] and secondary endpoint [hazard ratio (HR) 1.010, 95% confidence interval (CI) 1.006-1.014,  $p < 0.001$ ]. Higher ECV value of liver also indicated higher risk of suffering from primary endpoint [hazard ratio (HR) 1.026, 95% confidence interval (CI) 1.001-1.053,  $p < 0.001$ ] and secondary endpoint [hazard ratio (HR) 1.069, 95% confidence interval (CI) 1.033-1.106,  $p < 0.001$ ]. Besides, the addition of native T1 value of liver to total right atrial ejection fraction (RAEF) and right ventricular ejection fraction (RVEF) significantly improved the prognosis prediction performance for cox models.

**Conclusions:** Native T1 and ECV values of liver in PH patients were significantly higher than those of healthy volunteers, and may also considered to be important parameters for disease severity evaluation and prognostic prediction.

## Figure/Table 1

**Table 2. Correlation between liver native T1 value, ECV value of the liver and other clinical parameters.**

	Correlation with T1 value		Correlation with ECV value	
	r value	p value	r value	p value
NT-pro BNP, pg/ml	0.357	< 0.001	0.371	< 0.001
6MWD, m	-0.249	0.001	-0.105	0.192
TBIL, $\mu$ mol/L	0.133	0.072	0.241	0.001
DBIL, $\mu$ mol/L	0.251	0.001	0.428	< 0.001
IBIL, $\mu$ mol/L	0.010	0.897	0.122	0.108
RVEF, %	-0.231	0.002	-0.246	0.001
RVEDVi, ml/m <sup>2</sup>	0.174	0.018	0.303	< 0.001
RVESVi, ml/m <sup>2</sup>	0.197	0.007	0.290	< 0.001
RV longitudinal strain, %	0.139	0.067	0.205	0.009
Total RAEF, %	-0.214	0.004	-0.260	0.001
Passive RAEF, %	-0.130	0.085	-0.002	0.976
Active RAEF, %	-0.271	< 0.001	-0.312	< 0.001
TAPSE, mm	-0.113	0.137	-0.167	0.033
SvO <sub>2</sub> , %	-0.211	0.007	-0.089	0.269
Mean right atrial pressure, mmHg	0.404	< 0.001	0.333	< 0.001
Mean pulmonary arterial pressure, mmHg	0.074	0.322	0.042	0.587
Cardiac index, L/min/m <sup>2</sup>	-0.161	0.038	-0.073	0.364

6MWD: 6-minute walk distance; TBIL: total bilirubin; RVEF: right ventricular ejection fraction; RVEDVi: right ventricular end-diastolic volume index; RVESVi: right ventricular end-systolic volume index.

## Caption 1

Table 2. Correlation between liver native T1 value, ECV value of the liver and other clinical parameters.

## Figure/Table 2

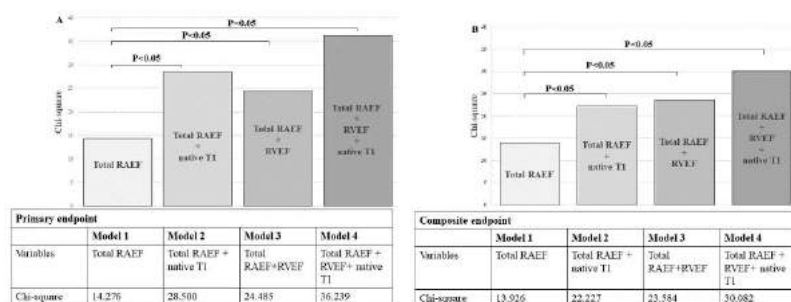
**Table 3. Univariate cox regression analysis of composite endpoint and major endpoint in all PH patients.**

	Composite endpoint		Major endpoint	
	HR (95% CI)	p value	HR (95% CI)	p value
Mean native T1 value of the liver, ms	1.005(1.002-1.007)	< 0.001	1.010 (1.006-1.014)	< 0.001
ECV value of the liver	1.026 (1.001-1.053)	0.044	1.069 (1.033-1.106)	< 0.001

## Caption 2

Table 3. Univariate cox regression analysis of composite endpoint and major endpoint in all PH patients.

**Figure 3**



**Caption 3**

Figure 3. Incremental prognostic value of native T1 value of liver over CMR parameters to primary and composite endpoint

## Bibliographic References

- Benza, R.L., et al., Predicting survival in pulmonary arterial hypertension: insights from the Registry to Evaluate Early and Long-Term Pulmonary Arterial Hypertension Disease Management (REVEAL). *Circulation*, 2010. 122(2): p. 164-72.
- Tonelli, A.R., et al., Prevalence and prognostic value of left ventricular diastolic dysfunction in idiopathic and heritable pulmonary arterial hypertension. *Chest*, 2012. 141(6): p. 1457-1465.
- Gan, C., et al., Impaired left ventricular filling due to right-to-left ventricular interaction in patients with pulmonary arterial hypertension. *Am J Physiol Heart Circ Physiol*, 2006. 290(4): p. H1528-33.
- Olsson, K.M., et al., Decompensated right heart failure, intensive care and perioperative management in patients with pulmonary hypertension: Updated recommendations from the Cologne Consensus Conference 2018. *Int J Cardiol*, 2018. 272s: p. 46-52.
- Rosenkranz, S., et al., Systemic Consequences of Pulmonary Hypertension and Right-Sided Heart Failure. *Circulation*, 2020. 141(8): p. 678-693.

Speaker: J. Guo

Category: Pulmonary Hypertension, Prognosis, T1

000361

## Myocardial Tissue Oxygenation and Microvascular Blood Volume Measurement Using a Contrast-BOLD Model

J. Dendy \* (1); S. Hughes (1); J. Soslow (2); D. Clark (1); J. Gore (3)

(1) Division of cardiovascular medicine, Vanderbilt University Medical Center, Nashville, United States of America; (2) Department of pediatric cardiology, Vanderbilt University Medical Center, Nashville, United States of America; (3) Vanderbilt university institute of imaging science, Vanderbilt University, Nashville, United States of America

### Abstract

#### Background

Blood oxygenation level dependent (BOLD) MRI can measure microvascular tissue changes in the myocardium.[1-3] We propose a method of quantitatively measuring changes in microvascular volume (MBV) and blood oxygenation induced by pharmacologic challenges. Comparison of MBV and blood oxygenation allows for evaluation of myocardial supply and demand changes associated with drug therapy and has great potential for noninvasive assessment of myocardial microvascular disease.

#### Methods

We postulate that at high fields there is a contribution to transverse relaxation rates from static susceptibility effects of the intravascular blood which scales with the blood volume and depends on the oxygenation state of the blood. We model the gradient relaxation rate  $R2^*$  as  $R2^* = R2' + kV(\chi_B - \chi_T)$ , where  $R2'$  is the relaxation rate in the absence of vasculature, and  $kV(\chi_B - \chi_T)$  is the contribution from blood in the microcirculation. In the presence of an intravascular contrast agent such as iron oxide, the rate increases to  $R2_{MION}^* = R2' + kV(\chi_{MION} + \chi_B - \chi_T)$ , where  $\chi_{MION}$  is the magnetic susceptibility of the agent. Administration of a vasoactive substance causes changes in both the blood volume and oxygenation, such that  $R2_{VASO}^* = R2' + k(V + \Delta V)(\Delta\chi_{VASO} + \chi_B - \chi_T)$ . For the same dose of vasoactive agent in the presence of the intravascular MION contrast agent  $R2_{MION+VASO}^* = R2' + k(V + \Delta V)(\Delta\chi_{VASO} + \chi_{MION} + \chi_B - \chi_T)$ .  $R2^*$  measurements thereby provide enough information to obtain a map of MBV and tissue oxygenation changes.

#### Methods

Twelve healthy rats were imaged using a 4.7T Varian system with a 63 mm quadrature transmit/receive imaging coil.  $R2^*$  maps were acquired with and without infusion of adenosine at a rate of 0.3 mg/kg\*min and dobutamine at a rate of 40 mcg/kg\*min. In addition,  $R2^*$  maps were acquired after the administration of MION (10 mg/kg of iron oxide total), with and without adenosine or dobutamine (Figure 1).

#### Results

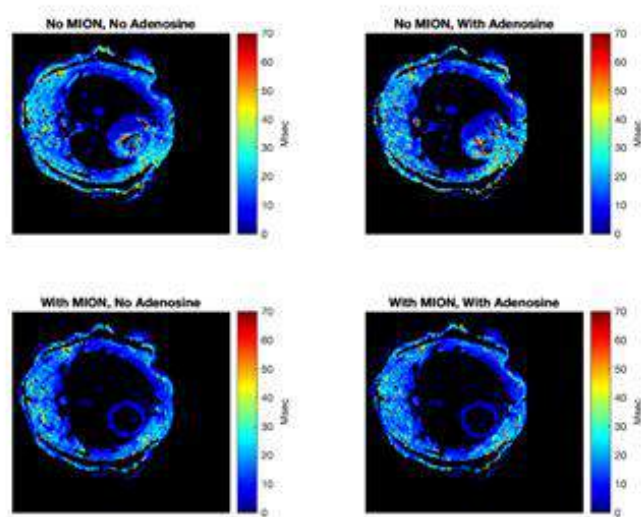
Total MBV increased by 10.84% with adenosine and by 25.67% with dobutamine ( $P < 0.05$ ). Both adenosine and dobutamine demonstrated significant differences between

endocardial and epicardial MBV changes ( $P < 0.05$ ; Figure 2). Total myocardial oxygenation saturation increased by 6.59% with adenosine and by 1.64% with dobutamine ( $P = 0.27$ ). The differences between epicardial and endocardial oxygenation changes were significant with each drug (adenosine  $P < 0.05$ , dobutamine  $P < 0.05$ ; Figure 3).

## Conclusions

Our results suggest that adenosine causes a minimal change in microvascular blood volume, with a significant increase in tissue oxygen saturation. One possible interpretation of these results is that adenosine essentially causes a “washout effect,” increasing oxygen supply beyond the oxygen requirements of the myocardial tissue. Conversely, dobutamine infusion is shown to result in a larger increase in myocardial microvascular volume, with a negligible change in tissue oxygenation. The microvascular blood volume increases to the degree needed to provide supply-demand match, and thus there is no change in tissue oxygenation in healthy myocardium.

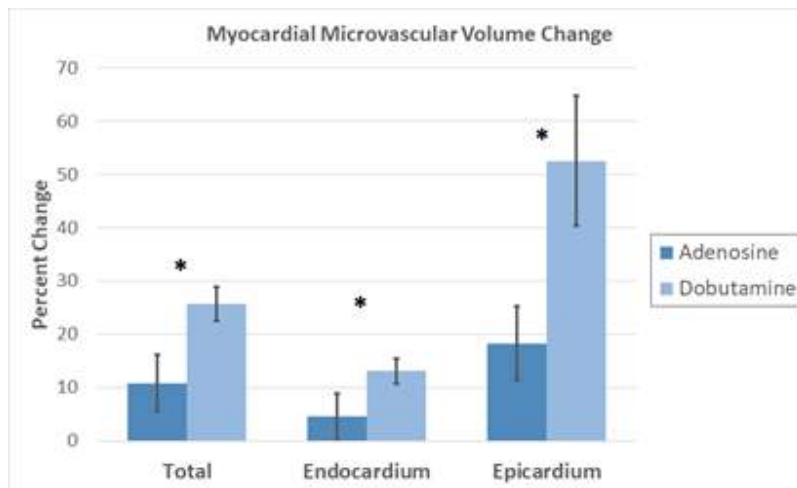
## Figure/Table 1



## Caption 1

Figure 1. R2\* Maps of Rat Myocardium. A. At rest. B. During adenosine infusion. C. After MION administration, without adenosine. D. After MION administration, during adenosine infusion.

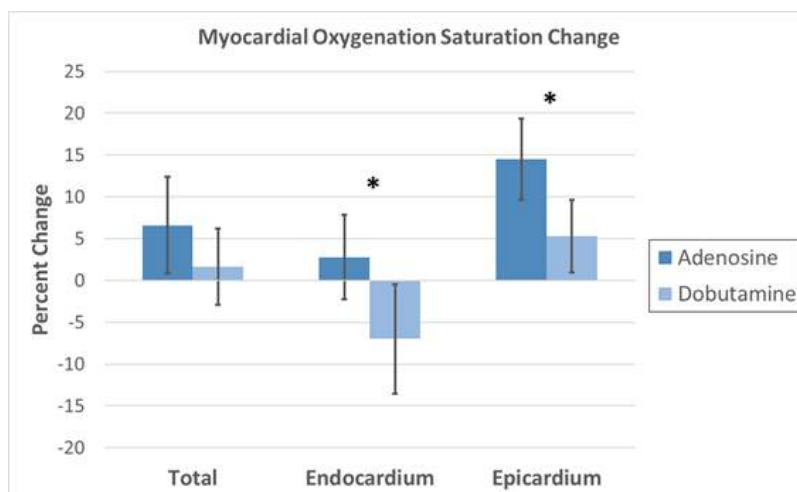
## Figure/Table 2



**Caption 2**

Figure 2. Percent Change in Microvascular Volume During Infusion of Adenosine and Dobutamine (\* represents statistical significance)

**Figure 3**



**Caption 3**

Figure 3. Percent Change in Tissue Oxygenation Saturation During Infusion of Adenosine and Dobutamine (\* represents statistical significance)

Speaker: J. Dendy

Category: BOLD , Microvascular disease, Mapping Techniques

000363

## Detection of early signs of right ventricular systolic impairment in Ebstein's anomaly by cardiac magnetic resonance feature tracking

C. Furtmüller, \* (1); F. Baessato (1); N. Shehu (1); I. Ferrari, (1); B. Reich, (1); N. Nagdyman (1); S. Martinoff, (2); H. Stern, (1); P. Ewert, (1); C. Meierhofer (1)

(1) Congenital heart disease and pediatric cardiology, Deutsches Herzzentrum München, München, Germany; (2) Radiology, Deutsches Herzzentrum München, München, Germany

### Abstract

#### Background

Cardiovascular magnetic resonance feature-tracking analysis (CMR-FT) provides a quantitative assessment of myocardial contraction with potential for diagnostic and prognostic ability in a wide spectrum of diseases. Ebstein's anomaly (EA) is a rare congenital heart disease characterized by apical displacement of the tricuspid valve. It is however deemed a disorder of development affecting the global right ventricular myocardium. Aim of our study is to describe the complex contractile mechanics of the functional right ventricle (RV) in patients affected by EA through CMR-FT.

#### Methods

Fifty surgery-free EA patients who had undergone a complete CMR protocol at our institution between January 2017 and December 2020 were selected for the retrospective study. A historical control group of twenty-five healthy subjects was also included. CMR-FT analysis was performed at a dedicated workstation by manually tracing RV endo- end epicardial borders on steady-state-free-precession (SSFP) cine images. RV strain derived values such as global peak systolic radial (GRS) and circumferential (GCS) strain were obtained from short-axis cine images (basal, mid, apical), while global peak systolic longitudinal strain (GLS) was calculated on a long-axis slice. The magnitude of apical displacement of the tricuspid valve was measured on a 4-chamber cine image.

#### Results

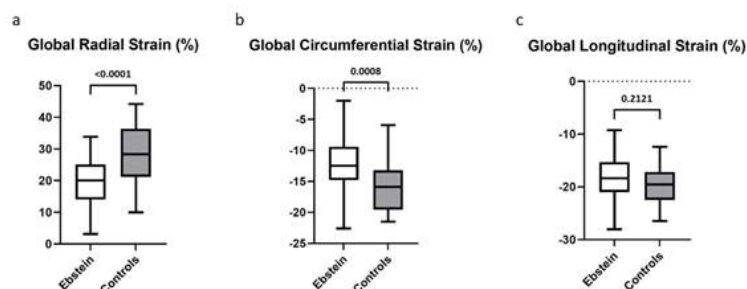
EA patients presented significantly impaired GRS and GCS in respect to controls ( $19.2 \pm 7.6$  vs.  $29.2 \pm 9.5$ ,  $p < 0.0001$  and  $-12.2 \pm 4.5$  vs.  $-15.9 \pm 3.9$ ,  $p = 0.0008$ , respectively), whereas no statistical difference was observed for GLS (Figure 1). In a subgroup analysis, GRS was significantly compromised in patients with a severely displaced tricuspid valve ( $>16$  mm/m<sup>2</sup>) compared to milder forms ( $16.9 \pm 8.3$  vs.  $21.5 \pm 6.2$ ,  $p = 0.03$ ) and to controls ( $29.2 \pm 9.5$ ,  $p$  value among the three groups  $< 0.0001$ ). Among EA patients with a preserved EF (RVEF  $> 52\%$ ), twelve (48%) vs. six (24%) controls already showed compromised GRS and GCS.

#### Conclusions

The contractile pattern of the functional RV in EA is characterised by prevalent alterations in the short-axis direction as indicated by reduced GRS and GCS. Strain values might be

reduced prior to routine used functional parameters like RVEF and can possibly serve as an early predictor of myocardial dysfunction in EA patients.

**Figure/Table 1**



**Caption 1**

**Figure 1** Both global radial and circumferential strain (a, b) are significantly reduced in Ebstein's anomaly in respect to controls ( $p < 0.0001$ ), showing a prevalent impairment of myocardial contraction of the functional right ventricle in the short-axis direction. In opposition, longitudinal function is not significantly reduced (c).

Speaker: C. Furtmüller,

Category: Ebstein's Anomaly, Feature Tracking, Congenital Heart Disease



000364

## Chest Pain in the Cardiac Amyloidosis Patient: Think Small... Vessel

J. Slivnick \* (1); S. Wang (2); N. Alvi (3); A. Zahid (1); S. Scheetz (1); H. Wang (4); M. Benevoy (5); J. Gutbrod (1); A. R. Patel (1)

(1) Cardiovascular Medicine, UChicago Medicine, Chicago, United States of America; (2) Cardiac imaging, UChicago Medicine, Chicago, United States of America; (3) Cardiovascular medicine, AMITA Health Adventist Medical Center Hinsdale, Hinsdale, United States of America; (4) Healthcare, GE Healthcare, Wauwatosa, United States of America; (5) Director, Circle Cardiovascular Imaging Inc., Montreal, Canada

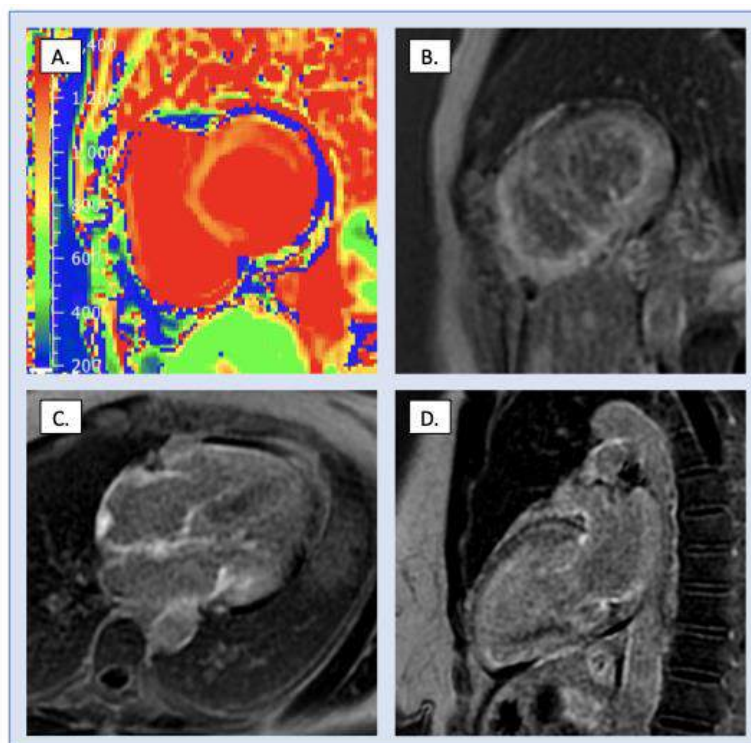
### Abstract

**Clinical Presentation:** A 57 year-old female with a history of smoldering multiple myeloma with light chain cardiac amyloidosis on chemotherapy and prior stem cell transplantation who presented for evaluation of chest discomfort. The chest pain was left-sided, lasted from seconds to minutes, and could occur either at rest or with stress. Of note, one month ago, the patient had had a mild COVID-19 infection not requiring hospitalization. Her exam was unremarkable, and a 12-lead ECG showed low limb voltage with septal infarct pattern, unchanged from prior.

**Diagnostic Techniques:** Due to her atypical chest pain and history of cardiac amyloidosis, a stress cardiac magnetic resonance was performed. All images were acquired on a 1.5T MR scanner (GE SIGNA Artist, GE Healthcare, Waukesha, WI) with SR prep SPGR sequence. A modified dual sequence with one AIF slice and three myocardial slices were obtained along the short axis of the left ventricle. SPGR based proton density imaging for improved surface coil intensity correction were acquired at the first two frames. Cine imaging showed mild, left ventricular hypertrophy with normal left ventricular ejection fraction (57%). On T1 mapping, pre-contrast T1 relaxation time and extracellular volume were elevated at 1,129 ms (figure 1A) and 55% respectively, consistent with diffuse interstitial infiltration. Late gadolinium enhancement (LGE) imaging demonstrated striking, diffuse LGE involving most myocardial segments with near-transmurality in the base (figure 1B-D). On first pass perfusion, there was a circumferential, subendocardial perfusion defect in the basal and mid-ventricle which was not present on rest (solid arrow, figure 2). Quantitative myocardial perfusion mapping was performed using CircleCVI using the deconvolution technique and demonstrated a global reduction in myocardial blood flow most pronounced in the subendocardium, a pattern consistent with microvascular disease (dashed arrows, figure 2). Stress myocardial perfusion reserve (1.49, normal >2.3) was also markedly impaired.

**Learning Points:** In this case, we demonstrate a case of cardiac amyloidosis complicated by microvascular disease shown on CMR using visual and quantitative perfusion analysis. Previous studies have shown a high prevalence of microvascular disease in patients with cardiac amyloidosis(1,2). While visual analysis requires the presence of a subendocardial perfusion defect, quantitative myocardial blood flow analysis can also identify global impairment in perfusion reserve—as was seen in this patient—and may therefore be more sensitive(3).

### Figure/Table 1



**Caption 1**

Figure 1: Cardiac Magnetic Resonance (CMR) findings. Panel A: T1 map demonstrating diffusely elevated myocardial T1 relaxation times consistent with diffuse interstitial infiltration. Panels B-D: Late gadolinium enhancement (LGE) imaging showing diffuse, near transmural LGE involving nearly all myocardial segments as well as the right ventricle and bilateral atria.

**Figure/Table 2**

		Visual		Quantitative	
		Rest	Stress	Rest	Rest
Healthy					
Amyloid					

## **Caption 2**

Figure 2: Stress perfusion images in our patient with cardiac amyloidosis (bottom panel) as well as a control patient for comparison (top panel). In the cardiac amyloidosis patient, there is a circumferential perfusion defect on first pass perfusion imaging. Quantitative myocardial perfusion demonstrating globally impaired stress myocardial perfusion most prominently involving the subendocardium.

## **Bibliographic References**

1. Dorbala S, Vangala D, Bruyere J, et al. Coronary microvascular dysfunction is related to abnormalities in myocardial structure and function in cardiac amyloidosis. *JACC Heart Fail.* Aug 2014;2(4):358-67. , 2. Li R, Yang ZG, Wen LY, et al. Regional myocardial microvascular dysfunction in cardiac amyloid light-chain amyloidosis: assessment with 3T cardiovascular magnetic resonance. *J Cardiovasc Magn Reson.* Apr 06 2016;18:16., 3. Lanza GA, Buffon A, Sestito A, et al. Relation between stress-induced myocardial perfusion defects on cardiovascular magnetic resonance and coronary microvascular dysfunction in patients with cardiac syndrome X. *J Am Coll Cardiol.* Jan 2008;51(4):466-72.

Speaker: J. Slivnick

Category: Amyloidosis , Stress CMR, First-Pass Perfusion

000365

## Evaluation of left ventricular remodeling in patients with a history of preeclampsia: Assessment with cardiac magnetic resonance

H. Zhang \* (1); Y. Guo (2)

(1) , West China Second University Hospital, Sichuan University, Chengdu, China; (2) West china second university hospital, sichuan university, chengdu, china, Department of Radiology, Chengdu, China

### Abstract

**Background:** Preeclampsia is a severe form of gestational hypertension, and cardiovascular impairment is one of its most severe complications. Cardiac magnetic resonance (CMR) provides accurate and reproducible assessment of biventricular geometry and function. However, relevant research on evaluation of postnatal left ventricular remodeling and myocardial strain of preeclampsia using CMR is rare. Therefore, in this study, we aim to investigate the left ventricular geometry and function, especially left ventricular hypertrophy (LVH) in patients with a history of preeclampsia, and further explore possible risk factors of LVH in these patients.

**Methods:** A total of 103 women with history of preeclampsia who delivered in our hospital within 5 years were enrolled in the study group whereas 30 normotensive women with a history of an uneventful pregnancy were selected as controls. Patients were subgrouped as mild or severe preeclampsia based on their severity, and as preterm (gestational week  $< 34$ ) or term (gestational week  $\geq 34$ ) based on the gestational week of the initial diagnosis. CMR was performed and cine sequence was used to evaluate the geometry, function, myocardial mass and thickness. Left ventricular wall thickness was determined by M/V, which is calculated by dividing left ventricular mass index (LVMI) by left ventricular end diastolic volume index (LVDEVI). The normal range of LVMI and M/V calculated from the control group was applied to the study group, and LVH was classified accordingly as concentric remodeling, concentric hypertrophy and eccentric hypertrophy. The clinical characteristics, left ventricular geometry and function, as well as patterns of LVH were compared, and possible risk factors of LVH were explored.

**Results:** The preeclampsia group had lower LVEDV and LVDEVI, and higher LVM, LVMI and M/V than did the control group. LVM and LVMI of the preterm group were higher than those of the term group (all  $p < 0.05$ ). There was no significant difference of LVMI and M/V between mild and severe group. Based on the normal range of LVMI and M/V calculated from the data of the control group, there were 58 cases (56.31%) of non-LVH, and 45 cases (43.69%) of LVH, with 28 cases (27.18%) of concentric remodeling, 15 cases (14.56%) of concentric hypertrophy and 2 cases of eccentric hypertrophy (1.94%). End diastolic wall thickness of all the 16 segments in the preeclampsia group were significantly higher than those of the control group, with no case of asymmetrical hypertrophy. LVEF of both the preeclampsia group and control group were within the normal range, with no significant difference between the 2 groups. LVEF of mild group was higher than that of the control group and severe group. Multivariable analysis showed that obesity (OR=10.68,  $P=0.03$ ) and

time interval between performing CMR and delivery (OR=0.92, P=0.01) were independently associated with LVH.

**Conclusions :** Nearly half of the patients with a history of preeclampsia within 5 years have LVH, mainly in the form of concentric remodeling and concentric hypertrophy. Obesity is independently associated with LVH, therefore, perinatal and postnatal weight management of patients with a history of preeclampsia is important. Time interval between performing CMR and delivery is negatively associated with LVH, indicating LVH might be reversible in patients with preeclampsia.

Speaker: H. Zhang

Category: Ventricular Remodeling, Cardiac Mass, Nonischemic Cardiomyopathy

000366

## Cardiac Remodeling after Tricuspid Valve Repair in Patients with Ebstein Anomaly: a CMR study

S. Yu \* (1); X. Chen, (1); K. Yang, (1); J. Song, (1); K. Ji, (1); S. Zhao, (1)

(1) MR center, Fuwai hospital, Beijing, China

### Abstract

#### Background

Tricuspid valve reconstruction in patients with Ebstein anomaly provides effective reduction of right heart volume overload and improved symptoms. However, data on serial assessments of cardiac structural and functional remodeling are scarce. We aimed to evaluate immediate and follow-up cardiac remodeling by cardiac magnetic resonance (CMR) after tricuspid valve repair in Ebstein anomaly, and also to investigate preoperative predictors and cut-offs of reverse RV remodeling.

#### Methods

In this retrospective study, we analyzed CMR parameters of the whole heart in patients with Ebstein anomaly before tricuspid valve surgery, at discharge and follow-up from December 2015 to December 2020.

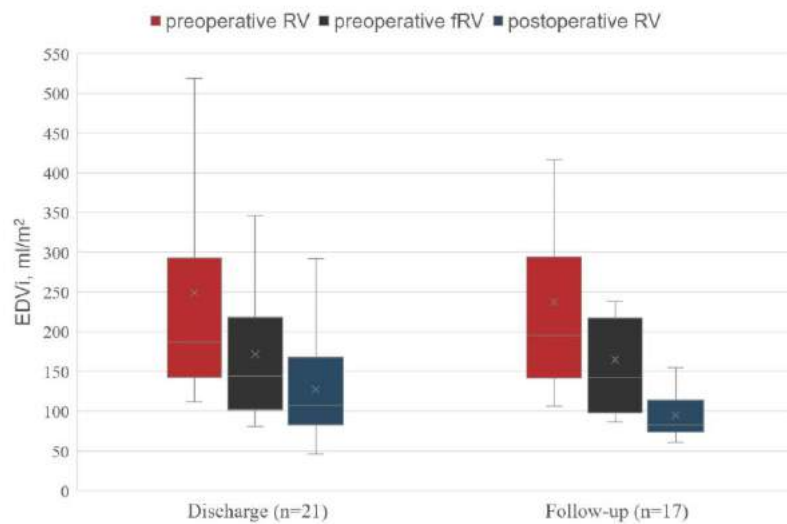
#### Results

Twenty-nine patients who underwent surgical treatment and finished both pre- and postoperative CMR examinations were included. Of those, 21 patients performed postoperative CMRs at discharge (median, 8 d), 17 patients underwent follow-up CMRs at a median of 187 days after surgery, and 11 patients had two postoperative CMR examinations at median of 9 days and 189 days, respectively. In general, indexed right heart volume promptly decreased immediately after surgery and decreased further at follow-up; indexed left ventricular end-diastolic volume, stroke volume as well as global longitudinal strain (absolute value) increased from preoperative to midterm follow-up. However, right ventricle global longitudinal strain and right atrial reservoir strain were significantly impaired after surgery. Fifteen patients achieved normalization of diastolic and systolic RV volumes after surgery. Indexed RV end-diastolic volume showed the highest discriminative value for predicting RV normalization (area under the curve:0.867; sensitivity, 93%; specificity, 71%;  $p<0.05$ ) with an optimal cut-off of 221 mL/m<sup>2</sup>.

#### Conclusion

Volume overload of right heart improved immediately and sustained thereafter. Left ventricular volumes and longitudinal deformation increased at follow-up. Tricuspid valve reconstruction before indexed RV end-diastolic volume reaches 221 mL/m<sup>2</sup> yields good chances of reverse RV remodeling.

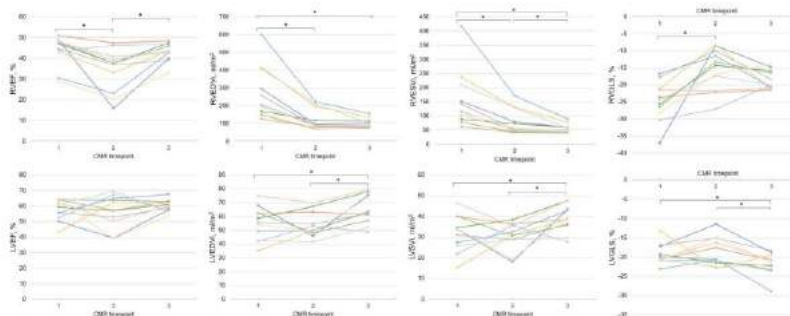
#### Figure/Table 1



**Caption 1**

Right ventricular end-diastolic volume changes after surgery. EDVi, indexed end-diastolic volume; fRV, functional right ventricle; RV, right ventricle.

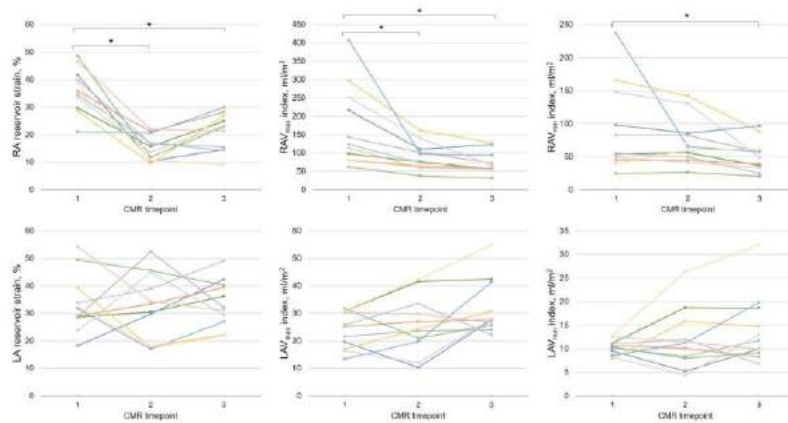
**Figure/Table 2**



**Caption 2**

Serial assessments of biventricular remodeling (n=11). LVEDVi, indexed left ventricular end-diastolic volume; LVEF, left ventricular ejection fraction; LVGLS, left ventricular global longitudinal strain; LVSVi, indexed left ventricular stroke volume; RVEDVi, indexed right ventricular end-diastolic volume; RVEF, right ventricular ejection fraction; RVESVi, indexed right ventricular end-systolic volume; RVGLS, right ventricular global longitudinal strain.

**Figure 3**



**Caption 3**

Serial assessments of biatrial remodeling (n=11). LA, left atrial; LAVmax, maximal left atrial volume; LAVmin, minimal left atrial volume; RA, right atrial; RAVmax, maximal right atrial volume; RAVmin, minimal right atrial volume.

Speaker: S. Yu

Category: Ebstein's Anomaly, Cardiac Function, Cardiac Strain



000367

## Quiescent-Interval Slice-Selective (QISS) MRA Accurately Estimates Intravascular Stent Dimensions Prior to Intervention in Patients with Peripheral Artery Disease

T. Emrich \* (1); J. Decker, (2); U. J. Schoepf (1); F. Xiong (3); T. Todoran (4); J. Aldinger (1); R. Edelman (5); I. Koktzoglou (5); A. Varga-Szemes (1)

(1) Department of radiology and radiological science, Medical University of South Carolina, Charleston, United States of America; (2) Department of diagnostic and interventional radiology, University Hospital Augsburg, Augsburg, Germany; (3) Cardiovascular mr r&d, Siemens Medical Solutions USA Inc., Charleston, South Carolina, Charleston, United States of America; (4) Department of medicine, Medical University of South Carolina, Charleston, United States of America; (5) Radiology, NorthShore University HealthSystem, Evanston, United States of America

### Abstract

**Background:** Procedural planning prior to revascularization in peripheral artery disease (PAD) is important for analyzing relevant lesions as it provides information on the location, degree and length of stenoses, as well as the diameter of the affected arteries (1-3). Quiescent-interval slice-selective (QISS) MRA is a robust non-contrast alternative for pre-procedural assessment of PAD patients (4,5). Therefore, the purpose of this study was to evaluate the feasibility of QISS MRA for pre-procedural stent size estimation in patients with PAD compared to computed tomography angiography (CTA).

**Methods:** PAD patients (n=33, 68±9 years, 18 men) who had previously undergone QISS MRA, CTA, and DSA of the lower extremity run-off in a prospective research study were included in this retrospective analysis. All patients underwent MR imaging on 1.5T and 3T systems (MAGNETOM Avanto and Skyra, Siemens Healthcare, Erlangen, Germany). A QISS MRA protocol was performed using an electrocardiographically gated prototype pulse sequence (20). Typical pulse sequence parameters were: field of view 400 × 260, acquired voxel size 1.0 × 1.0 × 3.0 mm, reconstructed voxel size 0.5 × 0.5 × 3.0 mm, echo time 1.4 ms, repetition time 3.5 ms, flip angle 90°, and bandwidth 658 Hz/pixel. Stenotic lesion length and diameter were quantified to estimate the dimensions of the stent necessary to reinstate blood flow in the respective arteries (Figure 1). Measured dimensions were corrected for the closest stent size available. Estimated dimensions were compared between QISS MRA and CTA, and validated against the stent size used for intervention. The Friedman test with subsequent pairwise paired Wilcoxon signed-rank test was used for analysis

**Results:** Estimated stent diameters derived from stenosis diameters showed no significant difference in QISS MRA compared to CTA and the physical stent diameters used as reference standard (p = 0.483). Mean estimated stent length was lower in QISS MRA (45.8 ± 27.8 mm) and in CTA (46.4 ± 29.3 mm) compared to the physical stent length (50.4 ± 34.0 mm). These differences were significant for overall stent length assessment (Friedman  $X^2 = 11.96$ ), as well as for pairwise comparison of QISS MRA to physical stent dimension and CTA to physical

stent dimension (Table 1). When the measured lengths of stenoses were adjusted to the next available stent length, no significant differences were found between QISS MRA ( $51.7 \pm 33.2$  mm), CTA ( $50.7 \pm 33.2$  mm), and physical stent length ( $50.4 \pm 34.0$  mm; Friedman  $X^2 = 2.38$ ,  $p = 0.303$ ). There was strong correlation in stent diameter, length and adjusted length among the three modalities (all  $r \geq 0.95$ ).

**Conclusions:** This study has shown that QISS MRA represents a reliable method for pre-procedural lesion assessment and stent size estimation in PAD patients. Both stent diameter and length could adequately be estimated especially with further adjustment to the nearest dimensions of available stents. These results suggest QISS MRA as a feasible alternative to CEMRA and CTA for pre-interventional assessment in PAD patients with contraindications to intravenous contrast media.

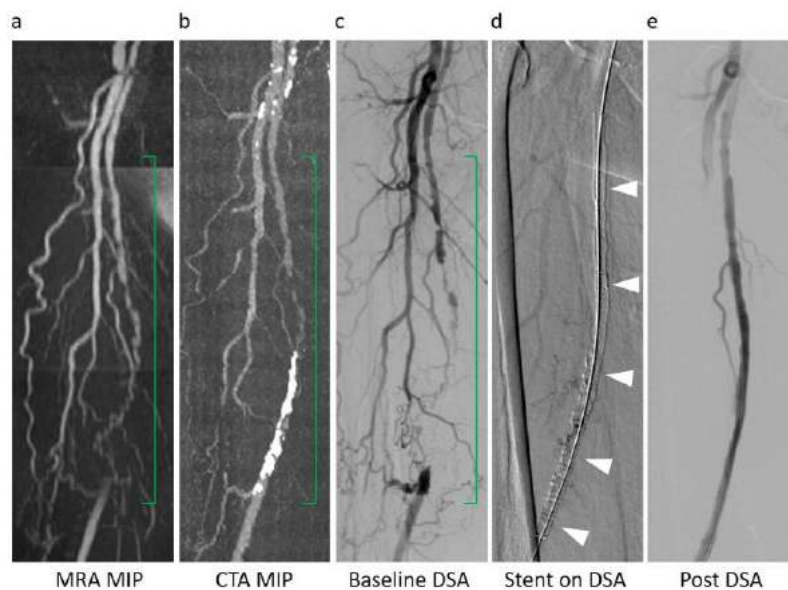
**Figure/Table 1**

Table 1							
	QISS MRA	CTA	Physical stent	Friedman $X^2$	p	Subgroup analysis	p
Diameter (mm)	8.9 ± 2.9	8.8 ± 3.0	8.8 ± 3.8	1.45	0.483	QISS MRA/CTA	0.740
						QISS MRA/DSA	0.651
						CTA/DSA	0.862
Length (mm)	45.8 ± 27.8	46.4 ± 29.3	50.4 ± 34.0	11.96	0.003	QISS MRA/CTA	0.675
						QISS MRA/DSA	0.002
						CTA/DSA	<0.001
Adjusted length (mm)	51.7 ± 33.2	50.7 ± 33.2	50.4 ± 34.0	2.38	0.303	QISS MRA/CTA	0.444
						QISS MRA/DSA	0.883
						CTA/DSA	0.436
QISS MRA, quiescent-interval single-shot magnetic resonance angiography; CTA, computed tomography angiography; DSA, digital subtraction angiography (represents physical stent size)							

**Caption 1**

**Table 1** – Estimated stent diameters and lengths by QISS MRA and CTA, compared to physical stent dimensions. Data are displayed as mean  $\pm$  standard deviation

**Figure/Table 2**



## Caption 2

**Figure 1:** 75-year-old man with advanced PAD. Corresponding QISS MRA MIP (A), CTA MIP (B), and baseline DSA (C) show stenosis and occlusion of the mid third of the right superficial femoral artery with distal reconstitution. Pre- and post-occlusion vessel diameters (MRA 6.5 and 6.8 mm, CTA 6.4 and 6.5 mm) and lesion length (MRA 247 mm and CTA 234 mm) were in good agreement with the physical stent diameter and length used to treat the lesion (Complete SE®, 7.0 × 150 mm and 7.0 × 100 mm, total length of 250 mm). Post-interventional DSA (E) shows reinstated flow in the affected artery.

## Bibliographic References

1. Itoga NK, Kim T, Sailer AM, Fleischmann D, Mell MW: Lower Extremity CT Angiography Can Help Predict Technical Success of Endovascular Revascularization in the Superficial Femoral and Popliteal Artery. *J Vasc Surg* 2017; 66:835-843.e1., 2. Pollak AW, Norton PT, Kramer CM: Multimodality imaging of lower extremity peripheral arterial disease: current role and future directions. *Circ Cardiovasc Imaging* 2012; 5:797–807., 3. Thukkani AK, Kinlay S: Endovascular intervention for peripheral artery disease. *Circ Res* 2015; 116:1599–1613., 4. Edelman RR, Sheehan JJ, Dunkle E, Schindler N, Carr J, Koktzoglou I: Quiescent-interval single-shot unenhanced magnetic resonance angiography of peripheral vascular disease: Technical considerations and clinical feasibility. *Magn Reson Med* 2010; 63:951–958., 5. Wu G, Yang J, Zhang T, et al.: The diagnostic value of non-contrast enhanced quiescent interval

single shot (QISS) magnetic resonance angiography at 3T for lower extremity peripheral arterial disease, in comparison to CT angiography. J Cardiovasc Magn Reson 2016; 18:71.

Speaker: T. Emrich

Category: Peripheral Artery Disease, Angiography, Stenosis

000368

## Characteristics and clinical value of diffuse myocardial fibrosis in Eisenmenger syndrome

C. Gong \* (1); W. Ke (2); Y. Chen (1)

(1) Department of cardiology, West China Hospital, Chengdu, China; (2) Department of geriatrics, West China Hospital, Chengdu, China

### Abstract

**Background:** Right ventricular dysfunction is one of the risk indicators for adverse prognosis in Eisenmenger syndrome (ES) patients; nonetheless, the mechanisms do not well defined. Myocardial fibrosis has been considered as the common etiology of ventricular dysfunction in different cardiovascular diseases. However, there was no associations between focal myocardial fibrosis detected by Cardiac magnetic resonance (CMR) late gadolinium enhancement (LGE) and disease severity, ventricular remodeling, and survival in ES patients. T1 mapping by CMR has emerged as a well-established and robust technique of quantification of diffuse myocardial fibrosis, capable of identification of myocardial involvement not detectable by LGE. This study aimed to detect the prevalence of diffuse myocardial fibrosis and explore the potential association with clinical severity, hemodynamics, right ventricular (RV) remodeling, and risk stratification profile in ES patients.

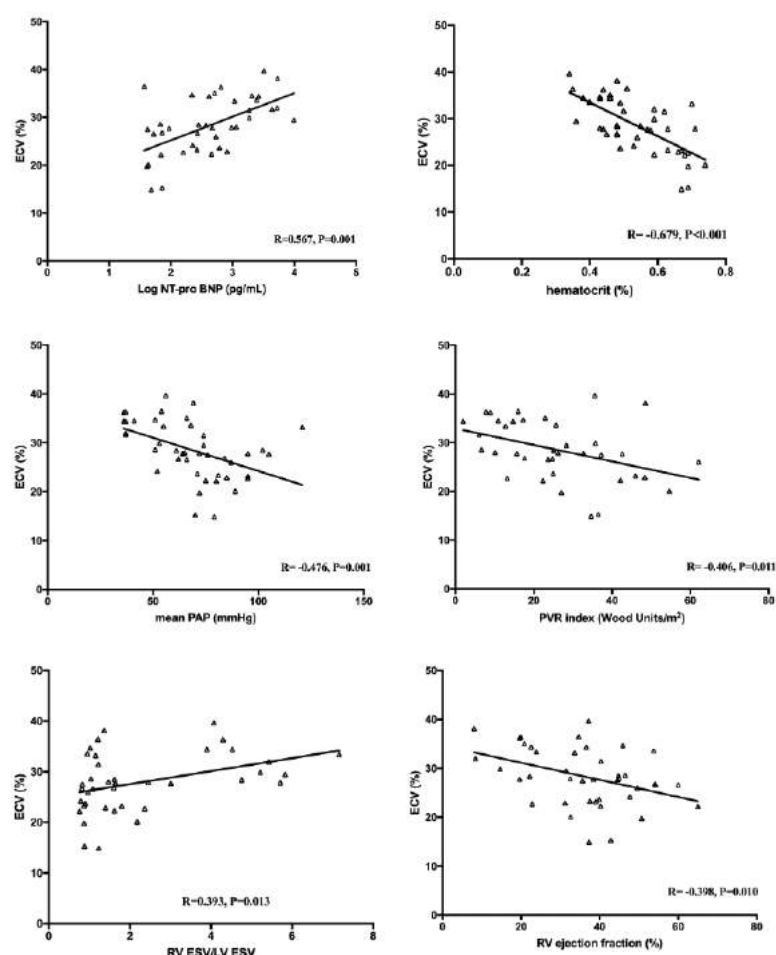
**Methods:** Forty-five adults with ES and thirty healthy volunteers were included, all of which underwent a contrast enhanced CMR at a 3T scanner. LGE images were qualitatively assessed for the presence of myocardium hyperintensity and deemed present only when focal myocardial enhancement was visible in both short and matching long-axis views by two independent observers. Regions of interest of septal myocardium sampling was manually contoured as large as possible with a strict exclusion of any LGE, epicardial fat, trabeculations and near wall blood in the mid-ventricular left ventricular (LV) short-axis slice pre- and post-T1 mapping images to determine the diffuse myocardial fibrosis.

**Results:** LGE was identified in forty-three of ES patients in the anterior and inferior ventricular insertion point (VIP) (95.56%), among which 12 (27.91%) involved septum. Others included RV myocardium in 10 (22.22%), LV myocardium in 3 (6.67%), RV papillary muscles in 3 (6.67%), and LV papillary muscles in 1 (2.22%). Excluding anterior and inferior VIP, ES patients were furtherly divided into LGE-positive and LGE-negative two subgroups, and no significantly difference between subgroups was observed about the clinical characteristics, hemodynamics, and CMR morphology and function. Extracellular volume (ECV) was significantly higher in ES patients than normal controls ( $28.55\% \pm 5.90\%$  vs.  $25.55\% \pm 2.15\%$ ,  $P = 0.004$ ). Increased ECV showed good correlations with biomarkers as Log N-terminal pro-brain natriuretic peptide ( $R = 0.567$ ,  $P = 0.001$ ) and hematocrit ( $R = -0.679$ ,  $P < 0.001$ ), RV afterload as mean pulmonary arterial pressure ( $R = 0.476$ ,  $P = 0.001$ ) and pulmonary vascular resistance index ( $R = 0.406$ ,  $P = 0.011$ ), and RV remodeling as RV/LV end-systolic volume ( $R = 0.393$ ,  $P = 0.013$ ) and RV ejection fraction ( $R = -0.398$ ,  $P = 0.010$ ). Moreover, ECV with a cut-off of 29.04% performed well in differentiating high-risk from low- and intermediate-risk profile ES patients (area under curve 0.857, specificity 78.13%, sensitivity 100.00%,  $P = 0.001$ ). Besides, there was no difference found in ECV

between LGE-positive and LGE-negative groups ( $P > 0.05$ ); however, ECV was significantly higher in patients with negative LGE than normal controls ( $P < 0.05$ ).

**Conclusion:** Diffuse myocardial fibrosis is a common feature of ES and related to biomarkers of heart failure, increased RV afterload, maladaptive RV remodeling, and worse risk stratification, which could serve as an important severity imaging marker in ES.

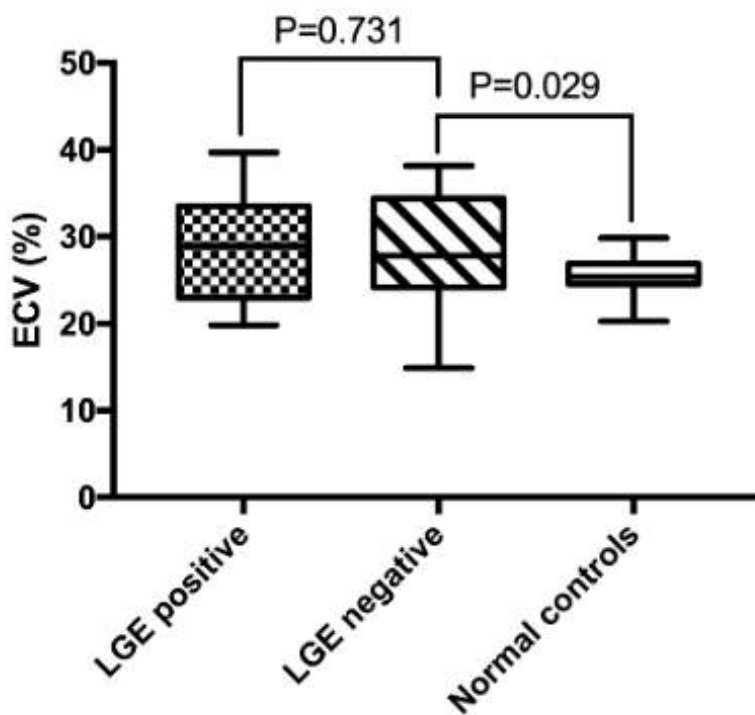
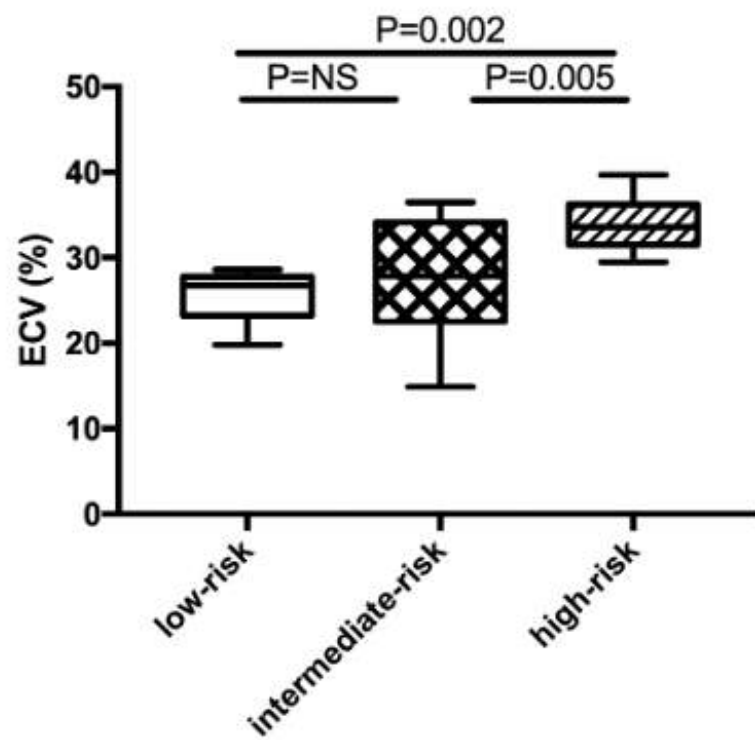
**Figure/Table 1**



**Caption 1**

**Figure 1.** Correlation of septal myocardial ECV with biomarkers, RV afterload and RV remodeling. ECV extracellular volume; NT-pro BNP N-terminal pro-brain natriuretic peptide; PAP pulmonary artery pressure; PVR pulmonary vascular resistance; RV right ventricular; LV Left ventricular; ESV end-systolic volume.

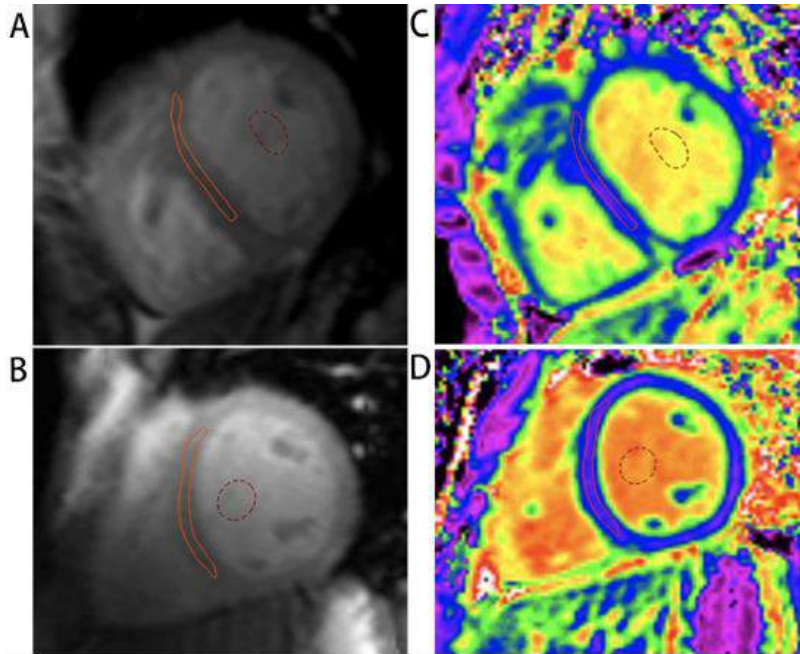
**Figure/Table 2**



Caption 2

**Figure 2.** Septal myocardial ECV among ES patients with different risk profiles, and among LGE positive, LGE negative and normal controls groups. ECV extracellular volume; LGE late gadolinium enhancement; ES Eisenmenger syndrome.

**Figure 3**



**Caption 3**

**Figure 3.** The representative contours of ROI on the native T1 and ECV mapping images of normal controls (A. native T1 mapping; C. ECV mapping) and ES patients (B. native T1 mapping; D. ECV mapping). The orange solid line contour represents the septum, and the red dotted contour represents the blood pool. ROI, region of interest; ECV, extracellular volume; ES Eisenmenger syndrome.

### Bibliographic References

- Broberg CS, Prasad SK, Carr C, Babu-Narayan SV, Dimopoulos K and Gatzoulis MA. Myocardial fibrosis in Eisenmenger syndrome: a descriptive cohort study exploring associations of late gadolinium enhancement with clinical status and survival. *J Cardiovasc Magn Reson.* , • Broberg CS, Chugh SS, Conklin C, Sahn DJ and Jerosch-Herold M. Quantification of diffuse myocardial fibrosis and its association with myocardial dysfunction in congenital heart disease. *Circ Cardiovasc Imaging.* 2010;3:727-34., • Arvanitaki A, Giannakoulas G, Baumgartner H and Lammers AE. Eisenmenger syndrome: diagnosis, prognosis and clinical management. *Heart.* 2020;106:1638-1645.

Speaker: C. Gong

Category: Congenital Heart Disease, Fibrosis, Extracellular Volume Fraction



000369

**Simultaneous multi slice quantitative myocardial perfusion with stress CMR: validation against invasive anatomical and physiological assessment**

M. S. Nazir \* (1); X. Milidonis (1); S. McElroy (1); M. Ryan (1); M. Yazdani (1); K. Kunze (2); R. Hajhosseiny (3); V. Vergani (1); D. Stäb (4); P. Speier (5); R. Neji (2); D. Perera (6); S. Plein (7); S. Roujol (1); A. Chiribiri (1)

(1) Biomedical Engineering and Imaging Sciences, King's College London Waterloo Campus, London, United Kingdom; (2) Siemens healthineers, Siemens - Frimley, Frimley, United Kingdom; (3) Biomedical Engineering and Imaging Sciences, King's College London, London, United Kingdom; (4) Mr research collaborations, Siemens Healthcare Pty Ltd, Melbourne, Australia; (5) Magnetic resonance, Siemens Healthcare GmbH, Erlangen, Germany; (6) Cardiovascular medicine, King's College London Waterloo Campus, London, United Kingdom; (7) Licamm, Leeds institute of Cardiovascular and Metabolic Medicine, Leeds District, UK, United Kingdom

**Abstract**

Background

Stress perfusion cardiovascular magnetic resonance (CMR) has been shown to have high diagnostic accuracy for coronary artery disease (CAD). However, routine stress perfusion CMR lacks complete spatial coverage, which may underestimate ischemia. There are now methods to achieve quantitative high-resolution whole heart coverage myocardial perfusion, and allow quantification of absolute myocardial blood flow (MBF). (1) The objective of this study was to determine the diagnostic accuracy of stress MBF derived from high resolution, whole heart simultaneous multi slice (SMS) myocardial perfusion CMR for the detection of significant CAD defined by invasive angiography (ICA) and fractional flow reserve (FFR).

Methods

Thirty-eight patients (14 female, mean age  $61 \pm 11$  years) with suspected CAD underwent adenosine stress first-pass SMS contrast enhanced myocardial perfusion imaging at 1.5T. (1) Six myocardial slices in short axis were acquired in each patient. Patients were scanned with a dual-sequence SMS-bSSFP perfusion acquisition following administration of adenosine for a minimum of three minutes. Typical myocardial perfusion acquisition parameters: TR/TE/ $\alpha$ : 2.84ms/1.42ms/50°, voxel size: 1.9x1.9mm<sup>2</sup>, slice thickness: 10mm, SMS factor: 2, in-plane acceleration factor: 3.5, FOV: 360x270mm, bandwidth 1532 Hz/pixel. Absolute stress MBF was derived. Visual analysis of the dynamic perfusion series was undertaken by two expert CMR readers. Diagnostic accuracy was determined based the presence of significant CAD defined by ICA and FFR using Area under the Curve (AUC) from receiver operator characteristic (ROC) curves.

## Results

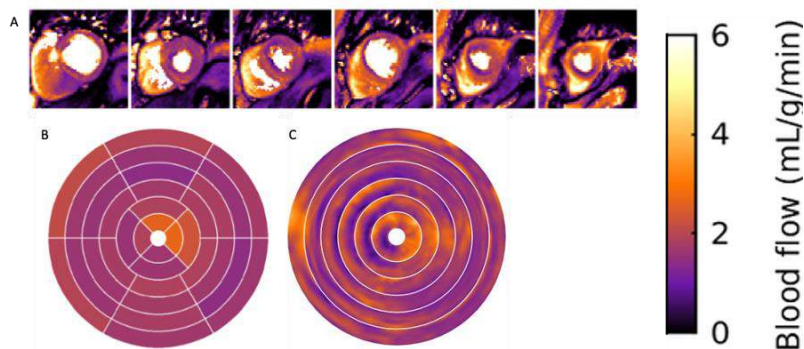
At the patient level, there was significantly lower stress MBF in patients with CAD compared to those without CAD (2.03 [1.82 – 2.37] vs 2.68 [2.31 – 2.93] ml/g/min,  $p<0.001$ ). There was a high diagnostic accuracy for the detection of CAD for quantitative stress MBF, with AUC 0.84 (95% CI 0.68 – 0.94,  $p<0.001$ ), and for visual analysis with AUC 0.89 (95% CI: 0.75 – 0.97),  $p<0.0001$ ). These were not significantly different ( $p=0.52$ ). The optimal MBF for detection of CAD was  $\leq 2.50$  ml/g/min, with a sensitivity of 100% (95% confidence interval [CI]: 77% to 100%) and specificity 71% (95% CI: 49% to 87%).

Typical cases are shown in Figure 1 and Figure 2.

## Conclusions

High-resolution quantitative whole heart myocardial perfusion imaging shows good diagnostic accuracy for detection of significant CAD, with comparable accuracy compared to expert visual analysis. This technique could be considered for widespread clinical use without the need for expert analysis of visual dynamic perfusion images.

### Figure/Table 1



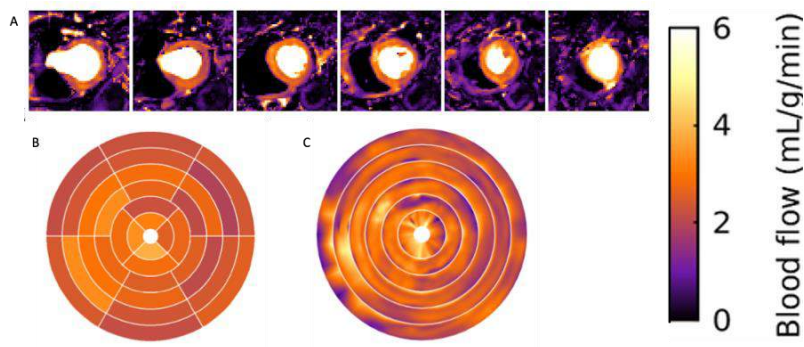
### Caption 1

**Figure 1.** Quantitative myocardial perfusion maps in a patient with chest pain, hypertension, type 2 diabetes mellitus and a family history of ischaemic heart disease. Global MBF was calculated as 1.85ml/g/min. Invasive coronary angiography confirmed a severe stenosis in the proximal left anterior descending artery.

A: Left to right: basal to apical slice perfusion maps.

B: AHA segmentation on a polar map demonstrating a 32-segment model with segmental maps of absolute myocardial flow. C: Perfusion map demonstrating the transmural perfusion gradient in the radial direction.

## Figure/Table 2



## Caption 2

**Figure 2.** Whole heart quantitative myocardial perfusion maps in a patient with a moderate stenosis in the LAD. Global myocardial blood flow was 2.70ml/g/min. Invasive FFR to this vessel was 0.92, indicating that this vessel was not haemodynamically significant.

A: Left to right: basal to apical slice perfusion maps.

B: AHA segmentation on a polar map demonstrating a 32-segment model with segmental maps of absolute myocardial flow. C: Perfusion map demonstrating the transmural perfusion gradient in the radial direction.

## Bibliographic References

1. Nazir MS, Neji R, Speier P, Reid F, Stäb D, Schmidt M, et al. Simultaneous multi slice (SMS) balanced steady state free precession first-pass myocardial perfusion cardiovascular magnetic resonance with iterative reconstruction at 1.5 T. J Cardiovasc Magn Reson. 2018;20(1):84.

Speaker: M. S. Nazir

Category: First-Pass Perfusion, Quantification, Simultaneous Multislice Excitation

000370

## The dynamic change of left atrial volume and function and the clinical implications in patients with non-ischemic dilated cardiomyopathy

Y. Li \* (1); Y. Xu (1); X. Zhou (2); Y. Chen (1)

(1) Department of cardiology, West China Hospital of Sichuan University, Chengdu, China;  
(2) Mr collaboration, Siemens Healthineers Ltd., Shanghai, China

### Abstract

**Background** Patients with non-ischemic dilated cardiomyopathy (DCM) are characterized by ventricular dilation and dysfunction. Although previous study showed that left atrial (LA) dysfunction was a biomarker of poor prognosis, the dynamic change and prognostic implications of LA volume and function were unknown.

**Methods** A total of 168 DCM patients with guideline-directed medical therapy underwent sequential cardiovascular magnetic resonance (CMR) examinations (median interval: 14.6 months, interquartile range: 12.5 – 19.1 months). LA remodeling was defined as the LA volume index increment or LA empty fraction decrease compared with LA volume and function reference value in our previously published study. The LA reverse remodeling was defined as more than 15% decrease in LA maximal volume index. LA adverse remodeling was an increase of LA maximal volume index greater than 10%. The major adverse cardiovascular events (MACE) were a composite of cardiac death, heart transplantation, and heart failure readmission. Statistical analyses were performed mainly using paired t-test, logistic regression analysis, Kaplan-Meier analysis, and log-rank test.

**Results** 120 (71%) patients showed LA remodeling at baseline CMR. In multivariate logistic regression analysis, heart rate, Log transformed N-terminal prohormone of brain natriuretic peptide, and left ventricular end-diastolic volume index showed independent predictors of LA remodeling. At follow-up CMR examination, LA volume and function did not show an obvious difference among patients without LA remodeling in the first CMR. For patients with LA remodeling, LA reverse remodeling occurred in 75 patients, and 17 patients showed LA adverse remodeling. During a median follow-up of 25.3 months (interquartile range: 11.7 – 31.9 months), 27 patients reached MACE. Kaplan-Meier curves demonstrated that patients without LA remodeling have the lowest risk of adverse clinical outcome, while the incidence of MACE was highest among patients with LA adverse remodeling (Log-rank  $P < 0.001$ ).

**Conclusion** Most DCM patients presented LA remodeling at baseline. Patients without LA remodeling showed stable LA volume and function in the follow-up, with the best clinical outcomes. Patients with LA adverse remodeling identify a high-risk cohort.

**Figure/Table 1**

**Table.** Univariate and multivariate logistic regression analysis for prediction of LA remodeling.

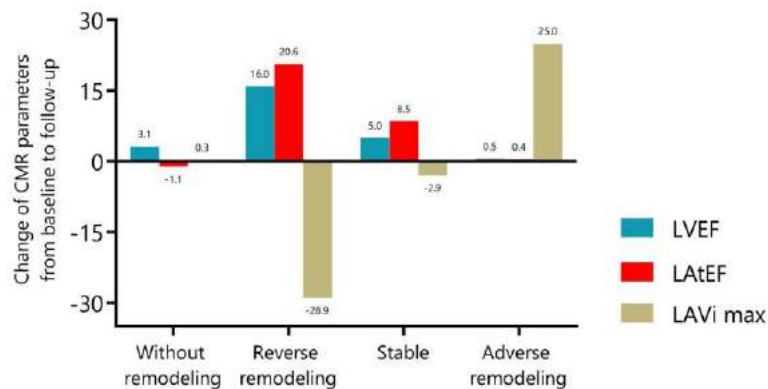
Parameters	Univariate analysis		Multivariate analysis	
	OR (95% CI)	<i>P</i> value	OR (95% CI)	<i>P</i> value
Male gender	2.23 (1.11 - 4.70)	<b>.02</b>		
Age	1.01 (0.99 - 1.04)	.37		
HF duration	1.99 (0.99 - 1.01)	.73		
NYHA class	3.08 (1.86 - 5.11)	<b>&lt; .001</b>		
SBP	0.99 (0.97 - 1.01)	.17		
HR	1.04 (1.02 - 1.07)	<b>&lt;.001</b>	1.03 (1.00 - 1.07)	<b>.04</b>
BMI	0.96 (0.89 - 1.04)	.35		
Log (NT-proBNP)	12.37 (4.79 - 31.94)	<b>&lt;.001</b>	5.74 (2.13 - 15.45)	<b>.001</b>
LVEF	0.87 (0.83 - 0.91)	<b>&lt;.001</b>		
LVmassi	1.03 (1.01 - 1.05)	<b>.001</b>		
LVEDVi	1.03 (1.02 - 1.04)	<b>&lt;.001</b>	1.02 (1.01 - 1.04)	<b>.01</b>
RVEF	0.93 (0.91 - 0.96)	<b>&lt; .001</b>		
LGE	1.03 (0.53 - 2.02)	.92		

### Caption 1

Abbreviations: HF, heart failure; NYHA, New York Heart Association; SBP, systolic blood pressure; HR, heart rate; BMI, body mass index; Log (NT-proBNP), Log transformed N-terminal pro-B-type natriuretic peptide; LVmassi, left ventricular mass index; LVEDVi, left ventricular end-diastolic volume index; RVEF, right ventricular ejection function; LGE; late gadolinium enhancement

### Figure/Table 2

**Figure 1.** The extent of left atrial and ventricular volume and function change between the first and second cardiac magnetic resonance examinations



## Caption 2

Without remodeling: both left atrial volume and function are within normal reference in the first CMR.

Reverse remodeling: more than 15% decrease in LA maximal volume index between two CMR examinations.

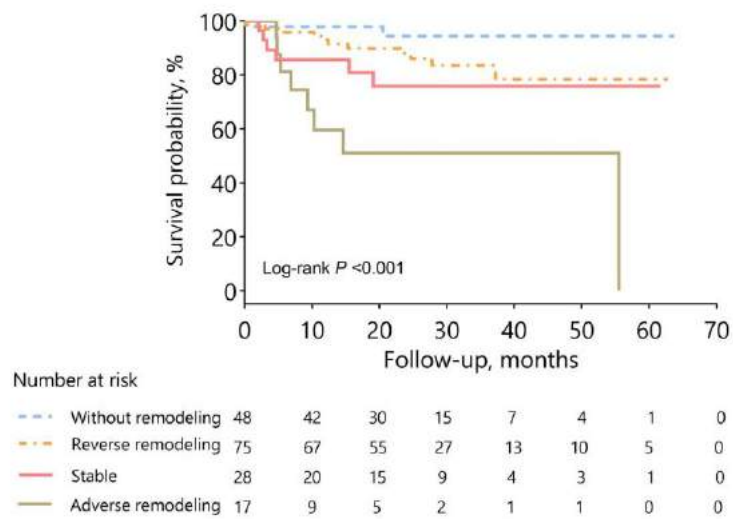
Stable: the decrease in LA maximal volume index less than 15% and the increase in LA maximal volume index less than 10% between two CMR examinations.

Adverse remodeling: more than 15% increase in LA maximal volume index between two CMR examinations.

Abbreviations: LVEF, left ventricular ejection fraction; LAtEF, left atrial total ejection fraction; LAVi max, left atrial maximal volume index; CMR, cardiac magnetic resonance

## Figure 3

**Figure 2.** Kaplan-Meier curve of the incidence of major adverse cardiovascular events for different groups



Speaker: Y. Li

Category: Dilated Cardiomyopathy, Left Atrium, Prognosis

000372

## Clinical Validation of Spiral Acquisition with Respiratory correction and Cardiac Self-gating (SPARCS) using bSSFP and GRE sequences at 1.5T

X. Wang \* (1); R. Zhou (2); J. Wang (1); M. Van Houten (1); M. Salerno (3)

(1) Biomedical Engineering, University of Virginia, Charlottesville, United States of America;  
(2) School of Artificial Intelligence, Beijing University of Posts and Telecommunications, Beijing, China; (3) Department of medicine, University of Virginia Health System, Charlottesville, United States of America

### Abstract

**Background:** Segmented bSSFP cardiac cine CMR is the gold standard technique for assessing cardiac function, however this technique requires ECG gating and breath-holding (BH) which can be difficult for some patients. We previously developed bSSFP and spoiled GRE based cine imaging using Spiral Acquisition with Respiratory correction and Cardiac Self-gating (SPARCS) at 1.5T and validated the strategy on volunteers [1,2]. The goal of this project was to clinically validate the SPARCS techniques against segmented bSSFP in patients with cardiovascular disease.

**Methods:** 9 patients were imaged using standard segmented breath-held ECG-gated Cartesian bSSFP cine imaging and the bSSFP and GRE SPARCS techniques on a 1.5T scanner (MAGNETOM Aera, Siemens Healthcare, Erlangen, Germany). Cine images were graded by an experienced cardiologist from 1 to 5 (1-poor, 5-excellent). GRE and bSSFP SPARCS cine data were acquired continuously for 8s per slice and 10 slices were acquired for whole heart coverage. Spatial resolution and temporal resolution were  $1.5 \times 1.5 \times 8 \text{ mm}^3$  and 40ms. Table 1 shows the sequence parameters for the different techniques [2]. Self-gated cardiac signals were derived from band-pass filtered principal component analysis of gridding an  $8 \times 8$  central region of k-space over each spiral arm across all the coils [2]. Respiratory motion correction was performed by rigid registration over heart ROI for each RR [3]. Motion corrected k space data was binned into different cardiac phases using the self-gating cardiac signal. L+S reconstruction ( $L = 0.008$ ,  $S = 1e-5$ ) was performed to reconstruct the images [4]. The left ventricular ejection fraction (EF) was quantified by each technique, and Bland-Altman analysis was performed between the SPARCS techniques and the segmented bSSFP technique.

**Results:** Clinical indications for the CMR studies in the 9 patients included cardiac sarcoidosis, palpitation, hypertrophic cardiomyopathy, and non-ischemic cardiomyopathy). Figure 2 shows images in a patient with suspected hypertrophic cardiomyopathy acquired with the BH segmented bSSFP and SPARCS GRE and bSSFP techniques. Image quality scores for these 3 techniques were 5, 3.5, and 3.9 respectively. While the SPARCS techniques had a lower image quality than the breath-held technique ( $p < 0.05$ ), there was no difference in image quality between the SPARCS GRE and bSSFP techniques ( $p = 0.3$ ). Figure 3 shows Bland-Altman plots for the comparison of EF between the techniques. The mean EF of the BH segmented bSSFP, SPARCS bSSFP and SPARCS GRE were 55%, 53%, and 57% respectively with no significant bias in the mean EF by bSSFP ( $p = 0.21$ ) or GRE ( $p = 0.15$ ) compared to the BH technique.



**Conclusion:** We demonstrated that both bSSFP and GRE SPACRS produce similar assessment of EF as compared to gold-standard BH segmented SSFP imaging at 1.5T in patients with cardiovascular disease. Cine images with whole heart coverage can be acquired during free breathing without ECG gating within 90s with good image quality.

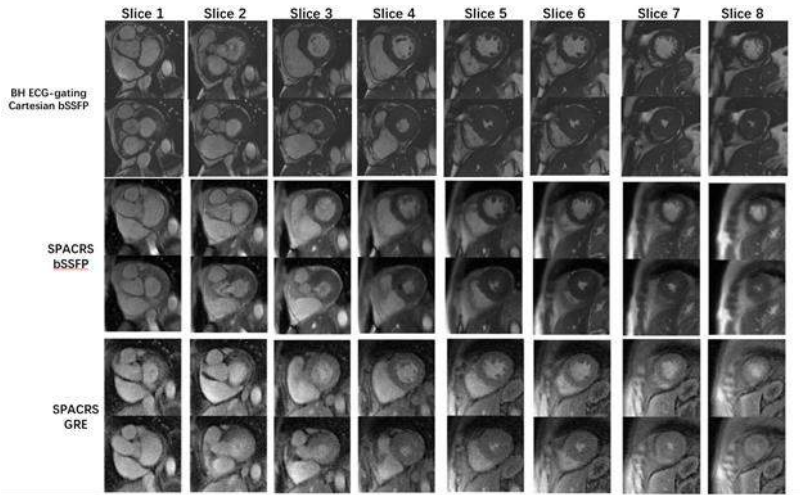
**Figure/Table 1**

SPARCS Sequences	bSSFP	GRE
Spatial resolution [mm <sup>3</sup> ]	1.5 x 1.5 x 8	
Temporal resolution [ms]	~40ms	
TR [ms]	5.10	7.78
TE [ms]	1	1
Flip Angle [degree]	60	15
Spiral out length [ms]	1.44	4.99
Spiral type	Linear variable density	Dual Density
Spiral starting density	0.15x	0.2x
Spiral ending density	0.0375x	0.026x

**Caption 1**

Table 1: bSSFP and GRE sequences parameters

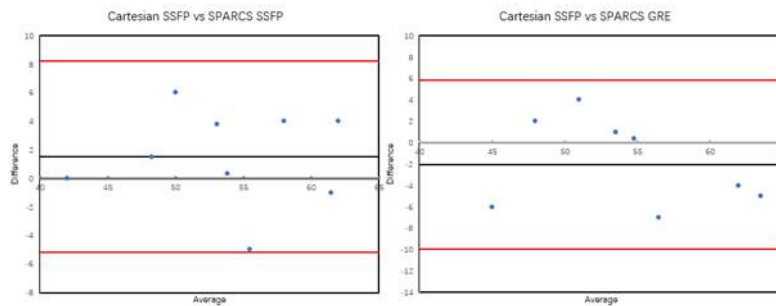
**Figure/Table 2**



**Caption 2**

Figure 1: CMR cine images acquired with SPACRS GRE and bSSFP techniques and the BH ECG gated Cartesian bSSFP reference technique at end systole and end diastole for patient being evaluated for hypertrophic cardiomyopathy.

**Figure 3**



**Caption 3**

Figure 2: Bland-Altman plot comparing EF derived from the BH segmented bSSFP technique as compared to the SPARCS bSSFP and GRE techniques.

### Bibliographic References

1. Zhou R, Yang Y, Wang Z, et al. bSSFP and GRE based cine imaging using Spiral Acquisition with Respiratory correction and Cardiac Self-gating (SPARCS) at 1.5T. In: Proceedings of the SCMR 23rd Annual Scientific Sessions, Orlando, Florida, USA, 2020. Abstract 749677., 2. Zhou R, Weller DS, Yang Y, Jacob M, Kramer CM, Ahmed AH. Free-breathing cine imaging with motion-corrected reconstruction at 3T using SPiral Acquisition with Respiratory correction and Cardiac Self-gating (SPARCS). Magn. Reson. Med. 2019;1–15. , 3. Zhou R, Huang W, Yang Y, Chen X, Weller DS, Kramer CM, et al. Simple motion correction strategy reduces respiratory-induced motion artifacts for k-t accelerated and compressed-sensing cardiovascular magnetic resonance perfusion imaging. J. Cardiovasc. Magn. Reson. Journal of Cardiovascular Magnetic Resonance; 2018;20:1–13. , 4. Otazo R, Candès E, Sodickson DK. Low-rank plus sparse matrix decomposition for accelerated dynamic MRI with separation of background and dynamic components. Magn. Reson. Med. 2015;73:1125–36.

Speaker: X. Wang

Category: Cardiac Function, Respiratory Self-gating, Motion Correction

000378

**The effect of left ventricular function and infarct size on the temporal evolution of invasive microvascular function indices after reperfused ST-segment elevation myocardial infarction**

A. Demirkiran \* (1); L. Robbers (1); N. Hoeven (1); H. Everaars (1); L. H. Hopman (1); G. Janssens (1); H. Berkhof (2); J. Lemkes (1); M. Leeuwen (3); A. Nap (1); R. Loon (1); G. Waard (1); A. C. van Rossum (1); N. Royen (4); R. Nijveldt (4)

(1) Cardiology, Amsterdam UMC, locatie VUmc, Amsterdam, Netherlands; (2) Epidemiology and biostatistics, Amsterdam UMC, locatie VUmc, Amsterdam, Netherlands; (3) Cardiology, Isala Hospital, Zwolle, Netherlands; (4) Cardiology, Radboud University Medical Center, Nijmegen, Netherlands

**Abstract**

*Background and purpose:*

Despite the successful restoration of primary percutaneous coronary intervention (PCI), the restoration of the microvascular flow fails in up to 50% of the reperfused ST-segment elevation myocardial infarction (STEMI) patients. The dynamic interplay between the evolution of microvascular function and the left ventricular function and infarct size remains unclarified. This study aims to explore the relationship between the temporal change in microvascular function indices and left ventricular ejection fraction (LVEF) and infarct size (IS).

*Methods:*

This study included 101 STEMI patients who underwent angiography for primary PCI and at 1-month follow-up. During both procedures, coronary microcirculation function in the culprit artery was measured and included coronary flow reserve (CFR) and the index of microcirculatory resistance (IMR). Cardiovascular magnetic resonance imaging was performed 2 to 7 days after PCI and at 1-month, and provided the information of LVEF and IS.

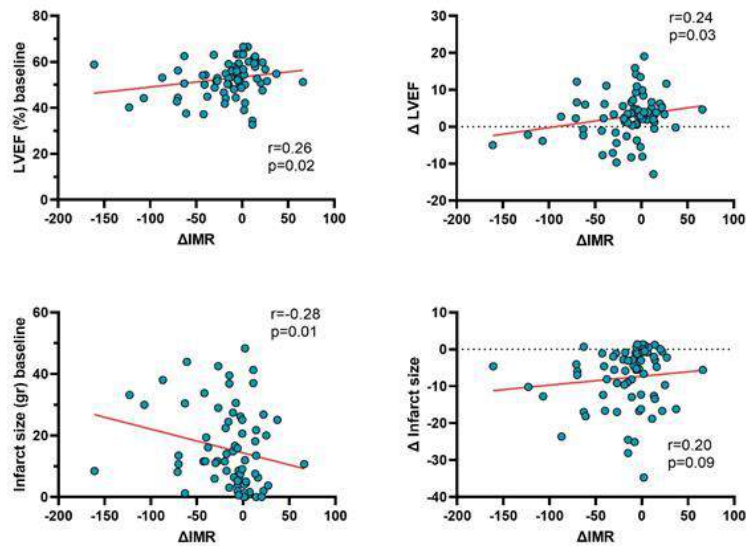
*Results:*

Over 1-month, mean CFR and IMR demonstrated a significant change (both,  $p < 0.001$ ). A significant correlation was observed between the absolute change of IMR over 1-month ( $\Delta$ IMR) and LVEF and IS at baseline (figure 1). No correlation was observed between  $\Delta$ CFR and LVEF and IS at baseline. IMR demonstrated a significant change only in patients with larger infarctions (above median) whilst CFR changed significantly both in patients with smaller and larger infarctions.  $\Delta$ IMR demonstrated a correlation with the absolute change in LVEF over 1-month ( $\Delta$ LVEF) and a tendency for correlation with  $\Delta$ IS.  $\Delta$ CFR showed no correlation with both  $\Delta$ LVEF and  $\Delta$ IS.

*Conclusion(s):*

In reperfused STEMI patients, baseline IS has an important effect on the recovery of hyperemic microvascular resistance. Furthermore,  $\Delta$ IMR is related to the improvement in functional outcome over 1-month.

**Figure/Table 1**



Speaker: A. Demirkiran

Category: Cardiac Function, Infarct Size, Microvascular disease

## Is T1 relaxation a biomarker of pro-inflammatory epicardial adipose tissue?

J. Bresticker \* (1); S. Shah (1); B. French (1); A. Marette (2); M. Wolf (3); F. Epstein (1)

(1) Biomedical Engineering, University of Virginia, Charlottesville, United States of America;  
(2) Department of medicine, Laval University, Québec, Canada; (3) Cardiovascular medicine, University of Virginia, Charlottesville, United States of America

### Abstract

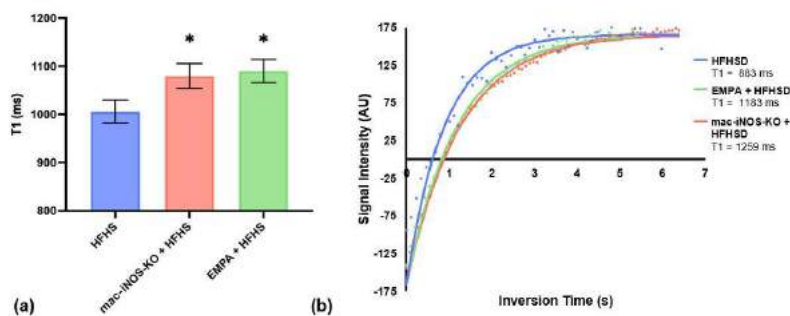
**Background:** Obesity promotes the accumulation and inflammation of epicardial adipose tissue (EAT). The EAT has been characterized as a transducer of systemic inflammation, likely contributing to coronary microvascular disease (CMD) and heart failure with preserved ejection fraction (HFpEF) [1]. Obesity triggers macrophages in adipose tissue to undergo a phenotypic shift from an anti-inflammatory M2 polarization to a more pro-inflammatory M1 polarization [2]. The EAT fatty acid composition (FAC) likely influences M1/M2 polarization, as saturated fatty acids activate the pro-inflammatory TLR4 receptor [3]. M1 polarized macrophages express elevated levels of inducible nitric oxide synthase (iNOS), generating nitric oxide ( $\cdot\text{NO}$ ) [2]. Select antidiabetic drugs (e.g. sodium glucose co-transporter 2 (SGLT2) inhibitors and metformin) have been shown to reduce EAT volume and reduce systemic inflammation [4]. Additionally, we have shown that treatment with a mineralocorticoid receptor antagonist reduces M1-polarized macrophages, prolongs EAT T1, and reduces CMD in mice fed a high-fat high-sucrose diet (HFHSD) [5]. We hypothesized that the  $\cdot\text{NO}$  from M1-polarized macrophage iNOS leads to T1 shortening in EAT.

**Methods:** To test the hypothesis that  $\cdot\text{NO}$  from M1-macrophage iNOS leads to EAT T1 shortening, macrophage-specific iNOS knockout (mac-iNOS KO) mice were studied. To further test whether a therapy known to reduce EAT inflammation and M1 polarization shows prolonged EAT T1, mice treated with an SGLT2 inhibitor, Empagliflozin (EMPA), were studied. Mac-iNOS KO mice were generated by crossing C57Bl/6J mice homozygous for floxed iNOS with LysM-Cre mice. Mac-iNOS KO (n=13), EMPA-treated (n=12, 30 mg/kg/day), and wild-type control (n=12) mice were fed a high-fat high-sucrose diet (HFHSD) (40% kcal fat, 40% kcal sucrose) initiated at 10 weeks of age. Cardiac MRI was performed at 8-10 weeks on diet and included a mid-ventricular short-axis slice imaged using T1 mapping and FAC MRI. FAC MRI was performed using an interleaved multi-echo gradient-echo sequence with 9 echoes, initial TE of 2.0 ms, echo spacing of 0.3 ms, 8 averages, and  $0.2 \times 0.2 \text{ mm}^2$  resolution. EAT FAC maps were computed using the IDEAL method to estimate the saturated fraction (SF) and unsaturated fraction (UF) of fatty acids. One-way ANOVA with post-hoc tests was used to assess differences between groups.

**Results:** EAT T1 was increased in mac-iNOS KO and EMPA-treated vs controls ( $1079.9 \pm 93.5$  vs  $1090.1 \pm 83.2$  vs  $1005.8 \pm 83.0$  ms,  $p < 0.05$ , respectively) (Fig. 1). EAT SF and UF were unchanged in mac-iNOS KO mice vs controls (Fig. 2). EAT SF was decreased ( $0.24 \pm 0.12$  vs  $0.39 \pm 0.09$ ,  $p < 0.05$ ) and UF was increased ( $0.76 \pm 0.12$  vs  $0.61 \pm 0.09$ ,  $p < 0.05$ ) in EMPA mice vs controls (Fig. 2). Mac-2 immunostaining showed that SGLT2 inhibition greatly reduced macrophage accumulation in EAT (Fig. 3).

**Conclusion:** Coupled changes in EAT FAC and EAT T1 may reflect the underlying biology of adipose tissue inflammation whereby saturated fatty acids trigger M1-macrophage polarization and activate iNOS. We investigated this relationship using cardiac MRI of EMPA-treated and mac-iNOS KO mice fed a HFHSD. EMPA-treated mice showed a decrease in EAT SF, reduced macrophages on histology, and a prolonged EAT T1. Additionally, mac-iNOS KO mice showed prolonged EAT T1. These results suggest that EAT T1 may be reduced by  $\cdot\text{NO}$  from M1-polarized macrophage iNOS and, accordingly, that T1 may be a biomarker of proinflammatory EAT. This work was supported by R01EB001763.

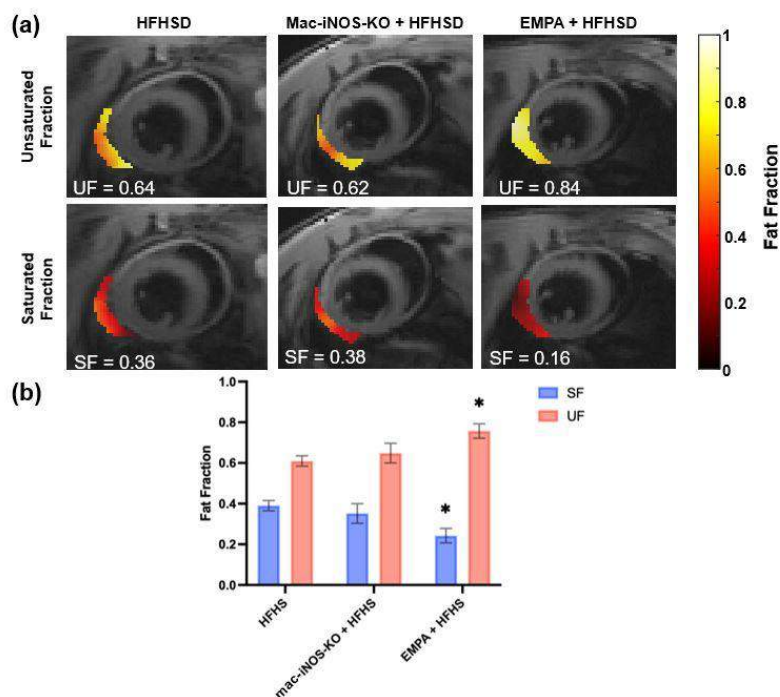
**Figure/Table 1**



**Caption 1**

(a) T1 relaxation was significantly prolonged in mac-iNOS KO (\* $p < 0.05$ ,  $n = 13$ ) and EMPA-treated (\* $p < 0.05$ ,  $n = 12$ ) mice after 8-10 weeks on HFHSD compared to controls ( $n = 14$ ). Error bars indicate standard error of the mean. (b) Example EAT T1 relaxation curves reveal differences in T1 recovery time between mac-iNOS KO and EMPA-treated mice vs controls.

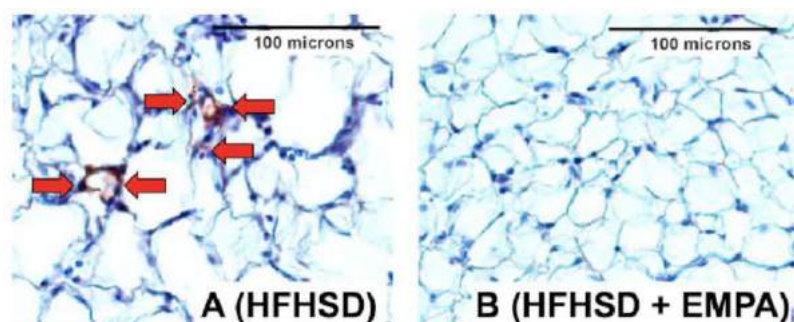
**Figure/Table 2**



## Caption 2

(a) Example UF and SF maps of EAT illustrate increased UF and decreased SF in EMPA-treated mice. (b) EMPA shifts the EAT to an anti-inflammatory phenotype as the SF was reduced ( $*p < 0.05$ ,  $n = 12$ ) and the UF was increased ( $*p < 0.05$ ,  $n = 12$ ) after 8-10 weeks on HFHSD. Mac-iNOS KO mice ( $n = 6$ ) showed no difference in EAT FAC after 8-10 weeks on HFHSD.

## Figure 3



## Caption 3

Mac-2 staining in (A) untreated HFHSD and (B) EMPA-treated HFHSD mice shows that EMPA reduces M1-polarized macrophages (brown, red arrows) and decreases adipocyte size. The “crown-like-structures” confirm M1 polarization.

## Bibliographic References

4.) Bouchi R;Terashima M;Sasahara Y;Asakawa M;Fukuda T;Takeuchi T;Nakano Y;Murakami M;Minami I;Izumiyama H;Hashimoto K;Yoshimoto T;Ogawa Y; “Luseogliflozin Reduces Epicardial Fat Accumulation in Patients with Type 2 Diabetes: a Pilot Study.” Cardiovascular Diabetology, U.S. National Library of Medicine, <https://pubmed.ncbi.nlm.nih.gov/28253918/>., 3.) Lee, Joo Y., et al. “Saturated Fatty Acids, but Not Unsaturated Fatty Acids, Induce the Expression of Cyclooxygenase-2 Mediated through Toll-like Receptor 4.” Journal of Biological Chemistry, vol. 276, no. 20, 2001, pp. 16683–16689., <https://doi.org/10.1074/jbc.m011695200>., 2.) Lumeng, Carey N., et al. “Obesity Induces a Phenotypic Switch in Adipose Tissue Macrophage Polarization.” Journal of Clinical Investigation, vol. 117, no. 1, 2007, pp. 175–184., <https://doi.org/10.1172/jci29881>., 1.) Packer, Milton. “Epicardial Adipose Tissue May Mediate Deleterious Effects of Obesity and Inflammation on the Myocardium.” Journal of the American College of Cardiology, vol. 71, no. 20, 2018, pp. 2360–2372., <https://doi.org/10.1016/j.jacc.2018.03.509>., 5.) Shah, Soham, et al. “CMR shows that Eplerenone promotes anti-inflammatory epicardial adipose tissue and preserves coronary microvascular function in mice fed a high-fat high-sucrose diet” [abstract]. Society of Cardiovascular Magnetic Resonance Imaging 25th Annual Scientific Sessions; 2022 Feb 2-5; Fort Lauderdale, FL, USA, submitted.

Speaker: J. Bresticker

Category: Epicardial Fat, T1 , Inflammation



000383

## **Redefining hypertrophic cardiomyopathy using deep phenotyping of mutation carriers; a hybrid diffusion tensor-perfusion CMR-ECGImaging study**

G. Joy \* (1); M. Webber (1); C. Kelly (2); I. Pierce (3); R. D. Adam (3); I. Teh (2); J. Schneider (2); A. Das (2); R. Hughes (1); H. Kotwal, (3); S. Horgan (3); C. Nguyen (4); P. Kellman (5); Y. Rudy (6); M. Orini (1); P. Lambiase (1); G. Captur (1); E. Dall'Armellina (7); J. Moon (1); L. R. Lopes (1)

(1) Institute of cardiovascular science, University College London, London, United Kingdom; (2) Licamm, Leeds institute of Cardiovascular and Metabolic Medicine, Leeds District, UK, United Kingdom; (3) Cardiology, Barts Health NHS Trust, London, United Kingdom; (4) Cardiovascular research center, Massachusetts General Hospital, Boston, United States of America; (5) National heart lung, and blood institute, National Institutes of Health, Bethesda, United States of America; (6) Department of biomedical engineering, Washington University in St. Louis, St. Louis, United States of America; (7) Leeds institute of cardiovascular and metabolic medicine, University of Leeds, Leeds, United Kingdom

### **Abstract**

#### **Background**

Hypertrophic cardiomyopathy is defined clinically by unexplained hypertrophy, genetically by pathogenic sarcomeric protein mutations and histologically by myocyte disarray, small vessel disease and fibrosis. These lead to electrical abnormalities and risk of sudden death, and may predate overt hypertrophy. We hypothesised that it would now be possible to identify subclinical manifestations of gene expression concurrently in early (genotype positive (G+) pre-hypertrophy (LVH-) subjects.

#### **Methods**

The study was conducted by a consortium of four academic teams in genotyping, cardiac diffusion tensor imaging (cDTI), perfusion mapping and ECG Imaging (ECGI). 3T cDTI using a motion-compensated spin-echo sequence was acquired in 3 short-axis slices. Quantitative adenosine stress perfusion was performed using standard clinical protocols. A novel ECGI vest (256 unipolar electrodes) was used to quantify conduction & repolarisation dynamics intervals. Standard structure, function, late gadolinium enhancement (LGE) and extra-cellular volume (ECV) mapping were also performed.

#### **Results**

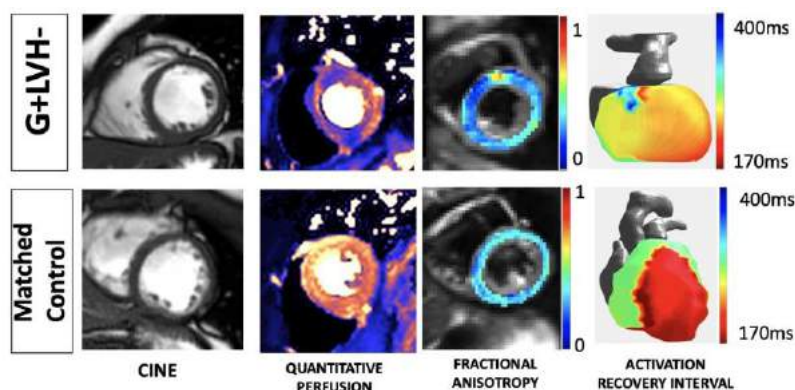
The first 40 mutation carriers (G+LVH-) from 38 families and 17 matched healthy controls (HC) have undergone the study protocol. Median age of carriers was 38(24–41) years, 65%(26) female, 73%(29) white. Mutations included 27(68%) *MYBPC3*, 8(20%) *MYH7*,

2(5%) *TNNI3*, 2(5%) *TNNT2*, 1(1%) *FHOD3*. There was no significant difference in ejection fraction or maximum wall thickness between G+LVH- and HC. The feasibility of combining four novel methodologies concurrently has been achieved. In preliminary results, in G+LVH- (vs HC), there were more perfusion defects (37% vs 0 p=0.004). cDTI parameters (eg Fractional Anisotropy (FA), Mean diffusivity (MD)) and ECGI parameters (eg Activation Recovery Interval, ARI) were successfully measured. Compared to HC, there was prolongation of average ARI ((a surrogate for action potential duration) (227(211-247) vs 213(198-231)ms p=0.027) and Repolarization Time (RT) (249(233-275) vs 238(218-246)ms p=0.029). In G+ LVH-, perfusion defects associated with prolonged ARI (r=0.37 p=0.027) and ECV associated with prolonged RT (r=0.36 p=0.033). The full data will be analysed once the prespecified sample size (n=75) is achieved.

## Conclusion

Multiple imaging and electrophysiological abnormalities develop before hypertrophy. Using a combination of advanced CMR (structure, function, LGE, ECV, perfusion mapping, cDTI) and ECGI, all major aspects of the HCM phenotype can now be measured in early disease, promising major new insights into HCM phenotype development and risk, and novel biomarkers to monitor the effect of disease modifying therapies.

**Figure/Table 1**



**Caption 1**

**Figure** - Above – a 23 year old Female MYBPC3 carrier, Below- a 22 year old female healthy volunteer. Several abnormalities are seen including perfusion defects, lower FA (0.29 vs 0.36) and higher median ARI (266ms vs 199ms) despite the absence of LVH or LGE.

Speaker: G. Joy

Category: Hypertrophic Cardiomyopathy, Perfusion, ECG

000384

# Characteristics of Native Right Ventricular Outflow Tract in Repaired Tetralogy of Fallot Assessment by Cardiovascular Magnetic Resonance Predicting Successful Balloon Expandable Transcatheter Pulmonary Valve Replacement

M. Lee \* (1); S. Lee, (2); B. Boe, (3); J. Williams, (2); K. Hor, (2)

(1) , , Columbus, United States of America; (2) Pediatric cardiology, Nationwide Children's Hospital, Columbus, United States of America; (3) Pediatric cardiology, Nationwide Children's Hospital, Children's Drive, Columbus, OH, USA, Columbus, United States of America

## Abstract

**Background:** Balloon expandable transcatheter pulmonary valve replacement (BETPVR) has been successfully implanted into right ventricular to pulmonary artery conduits (RV-PA). Patients with repaired tetralogy of Fallot (rTOF) typically underwent surgical PVR. BETPVR in native right ventricular outflow tracts (nRVOT) became more common to avoid risks associated with surgical PVR. Cardiovascular magnetic resonance imaging (CMR) has been integral in demonstrating indications and for timing of PVR. nRVOT morphology is heterogenous compared to RV-PA conduits (Figure 1A). Since 2013, our center has utilized CMR 3-dimensional angiography (CMRA) images for evaluation of nRVOT to determine BETPVR candidacy. The purpose of this study is to describe the characteristics of nRVOT anatomy leading to successful or failed BETPVR implantation.

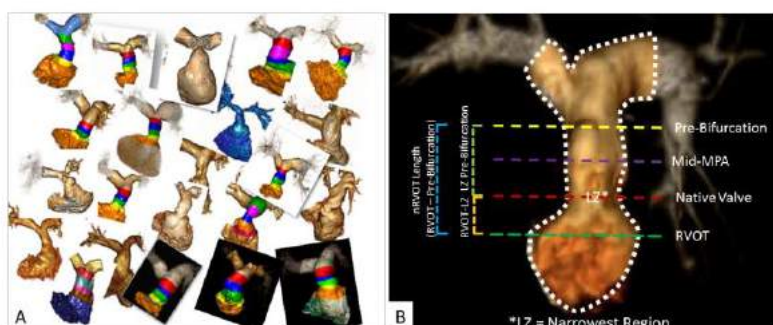
**Methods:** Single center retrospective review was performed of patients with attempted BETPVR between 2013-2018 with CMRA. We divided the nRVOT into 4 regions (RVOT, Native Valve, Mid-MPA and Pre-bifurcation (Figure 1B). Location of narrowest dimension was localized to one of these regions and determined as the likely landing zone (LZ) of the BETPVR. Total nRVOT length was measured from the RVOT to Pre-Bifurcation. To determine room for seating of the BETPV two additional lengths were measured (RVOT to LZ, and LZ to Pre-bifurcation) (Figure 1B). nRVOT assessment for BETPVR feasibility based on known parameters of commercially BETPVs was performed and blinded to catheterization results, with reasons for failure documented.

**Results:** 38 rTOF with nRVOT underwent attempted BETPVR. Demographics and nRVOT measurements are provided in Table 1. 28/38 (73.7%) had successful BETPVR and of these CMR correctly predicted 27/28 (96.1%). 1 patient with LZ in the RVOT was thought to be too low but TPVR was able to be implanted higher. Location of LZ at or near the mid-MPA was the most common with 21/28 (75%) patients followed by Native Valve 7/28 (25%) location. All patients had adequate nRVOT length ( $41.8 \pm 10$  mm), LZ to RVOT ( $19.7 \pm 6.9$  mm), and LZ to Pre-bifurcation ( $21.7 \pm 9.1$  mm). 10/38 (26.3%) had failed BETPVR attempt. Of these 6/10 (60%) were successfully predicted to not be good candidates and all 6 had the LZ near the bifurcation with a short LZ to Pre-bifurcation of  $9.4 \pm 7.9$  mm and of these, 3 had branch PAs stents, 2 had borderline LZ size and 1 had short LZ to Pre-Bifurcation length of 9.2 mm. 4/10 (40%) were predicted to have successful BETVPR and all had adequate total nRVOT ( $40.5 \pm 5.8$  mm), RVOT to LZ ( $14.1 \pm 4$  mm) and LZ to Pre-Bifurcation ( $26.3 \pm 12.9$  mm) lengths as well as LZ to accommodate BETPVR. However, 2 had coronary compression

on balloon sizing; 1 had branch PA stents and the catheter could not be advanced. One had predominant PS and instead underwent balloon pulmonary valvuloplasty.

Conclusion: Our approach using CMRA imaging had a high rate of success predicting BETPVR implantation. The characteristics of these patients included LZ within parameters of commercially available BETPV and LZ near the mid-MPA with adequate length on either side of the valve. The most striking characteristic of patients with failed BETPVR attempt was location of the LZ at the Pre-bifurcation with a short length from LZ to Pre-Bifurcation. The most difficult challenges using CMRA imaging were borderline patients with dynamic nRVOT and coronary artery compression with balloon sizing. Future studies with 3D whole heart imaging and/or 4D flow may resolve many of these issues.

**Figure/Table 1**



**Caption 1**

Figure 1A-B: Heterogeneity and nRVOT Measurement Location. (A) rTOF native RVOT morphology is heterogeneous with larger variation including location of narrowing and lengths. (B) Segmentation of nRVOT into 4 regions and measurement of lengths including total nRVOT, RVOT to landing zone, and landing zone to pre-bifurcation.

**Figure/Table 2**

Table 1: Demographics and nRVOT Measurements

Demographic/nRVOT Parameter	Successful (n = 28)	Unsuccessful (n = 10)
Age, years (mean $\pm$ SD)	27.6 $\pm$ 16.6	29 $\pm$ 16.1
Gender (n, %)		
Female	16 (57%)	5 (50%)
Male	12 (43%)	5 (50%)

BSA, m2 (mean $\pm$ SD)	1.7 $\pm$ 0.4	1.7 $\pm$ 0.4
PVR Indication (n, %)		
Regurgitation	22 (79%)	9 (90%)
Mixed	6 (21%)	1 (10%)
Smallest landing zone (n, %)		
RVOT	6 (21%)	2 (20%)
Native valve	1 (4%)	1 (10%)
Mid-MPA	<b>21 (75%)</b>	1 (10%)
Pre-bifurcation	--	<b>6 (60%)</b>
RVOT Length, mm (mean $\pm$ SD)	42 $\pm$ 10	41 $\pm$ 8
Landing zone to RVOT, mm (mean $\pm$ SD)	20 $\pm$ 7	25 $\pm$ 11
Landing zone to Pre-bifurcation, mm (mean $\pm$ SD)	22 $\pm$ 9	16 $\pm$ 13

Speaker: M. Lee

Category: Congenital Heart Disease, Tetralogy of Fallot, Pulmonary Valve Replacement

000388

## Predicting adverse clinical outcome by CMR using a machine learning algorithm

Q. Zhou \* (1); M. Passick, (1); J. Craft (2); J. Weber, (3); N. Ngai (1); S. Jonathon (1); J. J. Cao (4)

(1) Research, St. Francis Hospital & Heart Center, Roslyn, United States of America; (2) Cardiology, St Francis Hospital, The Heart Center, Roslyn, United States of America; (3) Cardiac imaging, St Francis Hospital, Dematteis Research Center, Greenvale; (4) Cardiology, St Francis Hospital, The Heart Center, Roslyn

### Abstract

**Background:** CMR is highly valuable in clinically diagnosis and outcome prediction. Many CMR variables when assessed individually are important in the outcome prediction. However, their collective value of outcome prediction is unclear. In addition, the relative importance of each variable has not been fully investigated. In this study we sought to utilize machine learning algorithms to optimize outcome prediction using common clinical CMR variables.

**Methods:** This is a mixed prospective and retrospective cohort of patients referred for clinical CMR evaluation. The XGBoost model with a Bayesian optimizer was developed to test 5 models based on combinations of 3 groups of variables: demographic data, common clinical CMR variables, and CMR strains (longitudinal, circumferential and radial) by feature tracking. The clinical outcome was the composite of hospitalized heart failure and all-cause mortality. AUC was used to evaluate the model performance. Shapley values were used to evaluate the importance features predicting outcomes.

**Results:** A total of 987 subjects were included in the analysis. The average age was  $68 \pm 17$  years. Mean left ventricular ejection fraction (LVEF) was  $50 \pm 15\%$ . Late gadolinium enhancement (LGE) was present in 279 (28%) subjects. After a mean follow up duration of 4 years the composite outcome occurred in 267 (27%) subjects. The demographics, CMR measurements including strains are listed in Table 1 below.

The CMR variables significantly outperformed the demographic variables in outcome prediction with AUC 0.856 vs 0.750 ( $p < 0.001$ , Table 2). Based on the Shapley values the top 5 most important features of CMR variables were LAVmin, LV stroke volume, LVEF, LAEF and LGE (model 2; Figure 1A). The addition of strain parameters did not seem to further enhance the model performance with AUC of 0.854. However, it shifted the order of Shapley value where the longitudinal strain rose to be the most important feature followed by LV stroke volume, LAVmin, LVEF and LAEF (model 3; Figure 1B). When all 3 groups of variables were combined the model performance was enhanced significantly with AUC of 0.890 ( $p = 0.027$  comparing model with 2 group variables). The order of top 5 feature importance in this final model was age, longitudinal strain, LAVmin, LAEF and LVEF (model 5; Figure 1C).

**Conclusions:** Using machine learning algorithm the collective common CMR variables perform well in clinical outcome prediction. Adding strain variables does not seem to significantly enhance the model performance. However, it shifted the order of relative

importance of CMR variables where longitudinal strain becomes the most important feature. The model performs at its best when all variables are included.

**Figure/Table 1**

	Variables	All subjects (N = 987) Mean $\pm$ SD or N (%)	Subjects with outcome (N = 267) Mean $\pm$ SD or N (%)
Demographics	Age (years)	68 $\pm$ 17	78 $\pm$ 13
	Female (%)	603 (61)	167 (63)
	BMI	30 $\pm$ 11.1	28 $\pm$ 9
	Hypertension (HTN) (%)	291 (29)	133 (50)
	DM (%)	107 (11)	59 (22)
	Hyperlipidemia (%)	291 (29)	103 (39)
	FH (%)	164 (17)	48 (18)
	CAD history (%)	148 (15)	50 (19)
	LVEDV (ml/m <sup>2</sup> )	86 $\pm$ 27	94 $\pm$ 35
Clinical MRI variables	LVESV (ml/m <sup>2</sup> )	43 $\pm$ 31	57 $\pm$ 39
	LVEF (%)	50 $\pm$ 15	42 $\pm$ 18
	LV <sub>mass</sub> (g/m <sup>2</sup> )	62 $\pm$ 21	75 $\pm$ 25
	LVSV (ml)	84 $\pm$ 53	80 $\pm$ 79
	RVESV (ml/m <sup>2</sup> )	73 $\pm$ 19	74 $\pm$ 25
	RVESV (ml/m <sup>2</sup> )	33 $\pm$ 19	38 $\pm$ 25
	RVEF (%)	52 $\pm$ 11	47 $\pm$ 15
	RVSV (ml)	76 $\pm$ 35	68 $\pm$ 43
	LAV <sub>max</sub> (ml/m <sup>2</sup> )	44 $\pm$ 27	54 $\pm$ 42
	LAV <sub>min</sub> (ml/m <sup>2</sup> )	27 $\pm$ 25	40 $\pm$ 41
	LAEF (%)	40 $\pm$ 20	30 $\pm$ 20
	LGE Prevalence (%)	279 (28)	115 (43)
	LGE Score	7 $\pm$ 7	9 $\pm$ 10
	AS (%)	70 (7)	46 (17)
	MS (%)	10 (1)	9 (3)
	AR (%)	117 (12)	57 (21)
	MR (%)	307 (31)	126 (48)
	TR (%)	312 (32)	107 (40)
	PR (%)	52 (5)	30 (11)
	RWMA (%)	262 (27)	125 (47)
Strains	Longitudinal (%)	-11 $\pm$ 5	-8 $\pm$ 5
	Radial (%)	23 $\pm$ 11	17 $\pm$ 11
	Circumferential (%)	-14 $\pm$ 5	-11 $\pm$ 6

**Caption 1**

Baseline characteristics

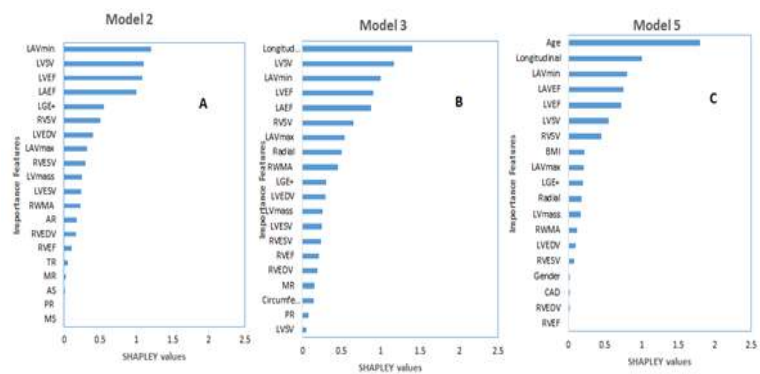
**Figure/Table 2**

	Composite outcome	Composite
<b>Model 1</b>	Demographic	0.750
<b>Model 2</b>	Clinical MRI variables	0.856
<b>Model 3</b>	Clinical MRI variables + strain	0.854
<b>Model 4</b>	Clinical CMR variables + Demographic	0.888
<b>Model 5</b>	Clinical MRI variables + strain + Demographic	0.890

**Caption 2**

Comparing model performance using AUC for outcome prediction.

**Figure 3**



### Caption 3

Importance Features for predicting outcome based on model 2, 3 and 5

Speaker: Q. Zhou

Category: Late Gadolinium Enhancement, Image Analysis, Left Ventricle



000389

**Aetiology and prognostic significance of non-infarct pattern late gadolinium enhancement in patients with coronary artery disease: a cardiovascular magnetic resonance prospective outcomes study**

R. Jones \* (1); D. Hammersley, (2); A. J. Baksi, (3); R. Owen, (4); G. Rea, (2); P. Theotokis, (2); F. Simard, (3); R. Buchan, (3); S. Hatipoglu (3); B. Almogheer, (3); F. Musella, (3); A. Azzu, (3); A. Lota (3); U. Tayal (2); A. De Marvao (2); A. Vazir, (3); B. Halliday (2); J. Ware (2); D. Pennell (3); S. Prasad (5)

(1) Genetics & Imaging, NHLI Guy Scadding Building, Cale Street, London, United Kingdom; (2) Genetics & imaging, National Heart & Lung Institute, London, United Kingdom; (3) Cardiovascular magnetic resonance unit, Royal Brompton Hospital, Guy's and St Thomas' NHS Foundation Trust, London, UK, United Kingdom; (4) Medical statistics, London School of Hygiene & Tropical Medicine, London, United Kingdom; (5) Cardiovascular magnetic resonance unit, Royal Brompton Hospital, Guy's and St Thomas' NHS Foundation Trust, London, UK, United Kingdom

**Abstract**

**Background:** Patterns of late gadolinium enhancement typically associated with dilated cardiomyopathy (DCM) are increasingly being recognised in coronary artery disease (CAD) populations (Figure 1). Long-term prospective cardiovascular magnetic resonance (CMR) studies may enhance our understanding of the prevalence, aetiology and prognostic significance of this novel phenotype.

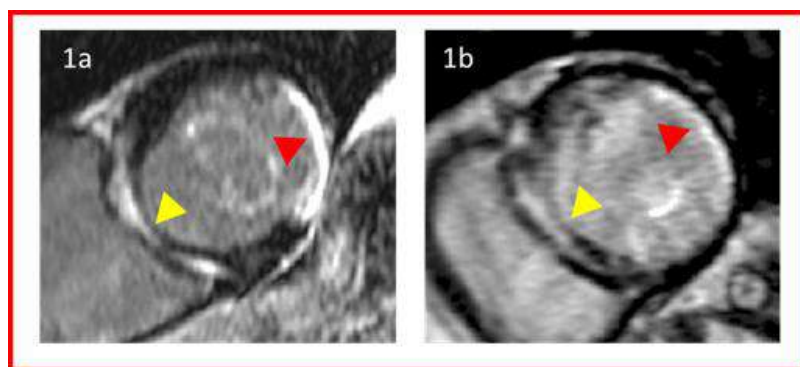
**Methods:** Patients with stable CAD were prospectively recruited into a CMR registry between 2009 and 2016. A diagnosis of CAD was defined by either the presence of severe epicardial CAD, previous coronary revascularisation or history of prior myocardial infarction (confirmed on CMR). Non-infarct pattern late gadolinium enhancement (NI-LGE) was confirmed by two independent level 3 CMR readers and subcategorised as either mid-wall, subepicardial or in multiple patterns and present in the ventricular septum, left ventricular free wall or in both locations. The primary endpoint was all-cause mortality. Secondary endpoints included a composite of cardiovascular mortality, major heart failure event or major arrhythmic event. Clinical outcomes were adjudicated by a panel of experienced cardiologists blinded to the imaging data. Univariable and multivariable analyses of the primary and secondary endpoints were examined using Cox regression modelling.

**Results:** 453 patients (mean age 64 years, mean left ventricular ejection fraction [LVEF] 47%, 95% with evidence of severe CAD) were followed for a median of 6.4 years. 63 (14%) patients had evidence of NI-LGE with involvement of the ventricular septum in 55 (12%) individuals. Patients with NI-LGE had elevated indexed LV end-diastolic volumes (131mls/m<sup>2</sup> vs 103mls/m<sup>2</sup>, P<0.001), elevated indexed LV end-systolic volumes (82mls/m<sup>2</sup> vs 50mls/m<sup>2</sup>, P<0.001) and a lower LVEF (38% vs 48%, P<0.001) as compared to patients without NI-LGE (Table 1). Patients with NI-LGE had a similar number of severely diseased coronary vessels (p=0.46) but a decreased prevalence of prior myocardial infarction diagnoses (56% vs 76%, P<0.001), lower number of infarcted myocardial segments (3 vs 5, P<0.001) and reduced absolute infarct LGE mass (12g vs 19g, P=0.001, Table 1) as compared to

individuals without NI-LGE. Cumulative incidence of the primary endpoint stratified by presence or absence of NI-LGE suggested that patients with this CMR biomarker had an increased risk of the primary endpoint (10-year risk 64% vs 42% for patients with and without NI-LGE,  $P<0.001$ , Figure 2a). Additionally, cumulative incidence of the primary and secondary endpoints stratified by presence or absence of septal NI-LGE suggested that patients with this pattern of LGE had increased risk of both outcomes (Figure 2b and 2d). However, on multivariable analyses neither NI-LGE or septal mid-wall LGE were associated with the primary endpoint (Figure 2e).

**Conclusions:** NI-LGE in patients with CAD is likely a marker of significant adverse LV remodelling but does not appear to be an independent prognostic indicator after adjustment for baseline covariates. The greater LV dilatation despite reduced burden of myocardial infarction in this group suggests a possible concomitant cardiomyopathic process however the aetiological ground truth remains unclear. In conclusion, patients with CAD and CMR evidence of non-infarct pattern myocardial fibrosis represent an advanced disease subgroup and intensive optimisation of prognostic therapies is likely indicated.

**Figure/Table 1**



**Caption 1**

**Figure 1: LGE-CMR images demonstrating NI-LGE from unique patients with coronary artery disease.**

Myocardial infarction pattern LGE (red arrows) and non-infarct pattern LGE (yellow arrows).

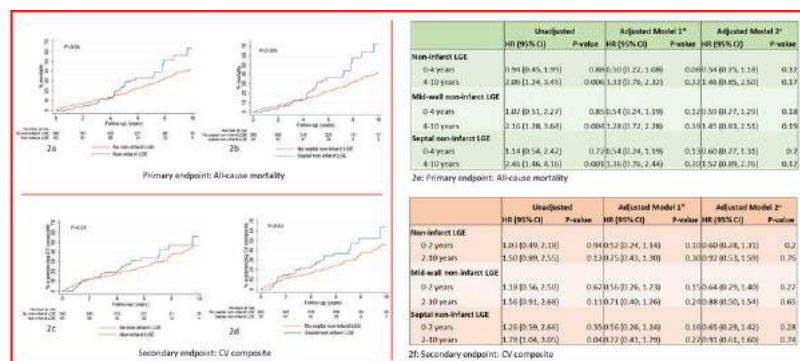
**Figure/Table 2**

Table 1: Baseline characteristics				
Variable	All patients (N=453)	Non-infarct pattern LGE		P-value
		No (N=390)	Yes (N=63)	
<b>Clinical demographics</b>				
Age (years)	64.4 (9.9)	64.1 (9.9)	66.8 (9.5)	0.04
Female	63 (13.9)	62 (15.9)	1 (1.6)	0.002
BMI (kg/m <sup>2</sup> )	27.8 (5.0)	27.9 (5.1)	27.5 (4.2)	0.63
Significant CAD	426 (95.1)	366 (95.1)	60 (95.2)	0.95
CAD type				0.46
Single vessel	135 (31.7)	118 (32.2)	17 (28.3)	
2 vessels	123 (28.9)	108 (29.5)	15 (25.0)	
3 vessels	168 (39.4)	140 (38.3)	28 (46.7)	
Prior MI	330 (72.8)	295 (75.6)	35 (55.6)	<0.001
History of PCI	228 (50.3)	202 (51.8)	26 (41.3)	0.12
History of CABG	126 (27.8)	108 (27.7)	18 (28.6)	0.89
Hypertension	239 (52.8)	204 (52.3)	35 (55.6)	0.63
Diabetes	130 (28.7)	112 (28.7)	18 (28.6)	0.98
Hypercholesterolemia	368 (81.2)	317 (81.3)	51 (81.0)	0.95
<b>CMR volumetric measurements</b>				
LVEF (%)	46.9 (16.6)	48.3 (16.0)	38.4 (18.2)	<0.001
LV mass indexed (g/m <sup>2</sup> )	79.1 (24.4)	76.7 (22.5)	93.6 (30.3)	<0.001
LVESVi (ml/m <sup>2</sup> ), median (IQR)	52.9 (29.4-81.3)	49.7 (29.2-75.1)	82.3 (41.0-118.1)	<0.001
LVEDVi (ml/m <sup>2</sup> )	107.1 (40.8)	103.2 (38.2)	131.2 (48.2)	<0.001
<b>LGE characterisation</b>				
NI-LGE location				
Septal	37 (8.7)	0 (.)	37 (58.7)	
LV free-wall	8 (1.7)	0 (.)	8 (12.7)	
Both	18 (28.6)	0 (.)	18 (28.6)	
NI-LGE pattern				
Linear mid-wall	46 (73.0)	0 (.)	46 (73.0)	
Sub-epicardial	5 (7.9)	0 (.)	5 (7.9)	
Multiple patterns	12 (19.0)	0 (.)	12 (19.0)	
Infarct pattern LGE	394 (87.0)	349 (89.5)	45 (71.4)	<0.001
Multi-territory infarct-pattern LGE	124 (31.5)	106 (30.4)	18 (40.0)	0.19
No. infarcted segments, median (IQR)	5.0 (3.0-8.0)	5.0 (3.0-8.0)	3.0 (0.0-6.0)	<0.001
Total LGE mass (g), median (IQR)	19.1 (7.8-31.6)	19.2 (7.8-31.7)	17.8 (8.9-31.6)	0.83
Infarct LGE mass (g), median (IQR)	18.2 (6.9-30.6)	19.2 (7.8-31.7)	11.5 (0.0-23.3)	0.001
NI-LGE mass (g), median (IQR)	0.0 (0.0-0.0)	0.0 (0.0-0.0)	5.2 (2.7-9.2)	<0.001

## Caption 2

Table 1: Baseline characteristics.

Figure 3



Caption 3

**Figure 2: Primary and secondary endpoints.** 2a-d: Kaplan-Meier plots. 2e-f. Cox proportional Hazard models. \*Model 1 adjusted for LVEF, age, diuretic, diastolic blood pressure, QTc interval, diabetes, LAVi and history of CABG following backwards stepwise procedure. ×Model 2 adjusted for LVEF, age and sex.

Speaker: R. Jones

Category: Ischemic Cardiomyopathy, Late Gadolinium Enhancement, Dilated Cardiomyopathy

000390

## **Ferumoxytol-enhanced 3D cine using Heart-NAV motion compensation during free breathing**

M. Ganigara, \* (1); M. Nagiub, (1); R. Vamsee, (1); A. Tandon (1); D. Young, (1); L. Browne (2); T. Hussain (1); M. H. Moghari, (2); J. Greer (1)

(1) Pediatrics, UT Southwestern Medical Center, Dallas, United States of America; (2) Radiology, University of Colorado Anschutz Medical Campus, Aurora, United States of America

### **Abstract**

**Background:** Ventricular volumes are measured using contiguous 2D cine bSSFP slices across the heart, requiring acquisitions in multiple orientations. 3D cine acquisitions (1-3) enable multiplanar reformatting for a full evaluation in a single scan, but cannot be acquired within a breath hold. Heart-NAV (3) is a prospectively-respiratory gated free breathing technique for 3D cine acquisitions that tracks the heart-liver border using intermittently acquired superior-inferior projections of the chest, and depends on contrast administration to track the diaphragm by enhancing the heart/liver border. While the rapid clearance of gadolinium (Gd) from the blood pool can significantly reduce this contrast, blood pool agents such as ferumoxytol may improve Heart-NAV respiratory compensation by minimizing contrast clearance. The purpose of this study was to demonstrate 3D cine imaging using Heart-NAV following ferumoxytol administration, and to quantitatively compare metrics of cardiac function against the clinical standard 2D cine.

**Methods:** 20 patients were scanned on a 1.5T Philips Ingenia (median age: 16, range: 1-24) years, 10 male), 5 under general anesthesia. Ferumoxytol (Feraheme, 4 mg/kg) was administered  $41 \pm 23$  minutes before 3D cine imaging using a slow infusion over 15 mins. 3D cines were acquired using a spoiled GRE, flip angle =  $25^\circ$ , 20 heart phases (interpolated to 30), resolution =  $2 \times 2 \times 2.4$  mm (reconstructed to 1.2 mm isotropic), with Compressed SENSE factor = 4. The average scan time across patients was  $3:51 \pm 0:55$  mins (range: 1:05 to 4:58 mins). 3D cines were reconstructed to short-axis on the scanner console with the slice thickness matched to the corresponding breath-held 2D cine. Ventricle contours were analyzed using commercially available software (CVI42, Circle Cardiovascular Imaging). An additional patient who received a Heart-NAV 3D cine with Gd was included for qualitative comparison.

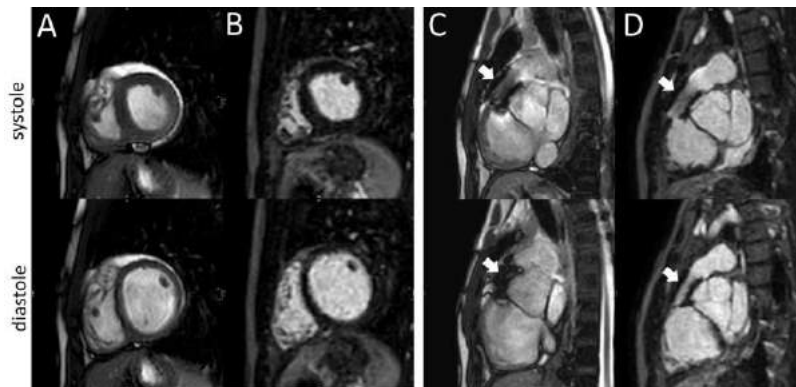
**Results:** Figure 1 shows 2D cines with the corresponding reformatted 3D Heart-NAV cines at end-systole and end-diastole in the same patient. This patient had stent which prohibited visualization of the main pulmonary artery in the clinical 2D bSSFP cine. The reduced sensitivity of the 3D spoiled GRE cine to off-resonance enabled visualization inside of the stent with ferumoxytol enhancement. Figure 2 shows end-diastolic 3D Heart-NAV images acquired using ferumoxytol (A) and Gd (B) in two additional patients, showing a higher contrast blood/myocardium border with ferumoxytol.

Figure 3 shows the quantitative comparison between 2D bSSFP cine and 3D Heart-NAV spoiled GRE cine datasets. Ventricular volumes had high correlation and low bias, below 3.3 mL across all comparisons by Bland Altman analysis. The estimates of LV mass did not agree

as well, likely due to the less distinct epicardial border with the 3D spoiled GRE. However, the high contrast blood/myocardium border streamlined the measurement of ventricular volumes (Figure 1, A,B). The average contrast ratio and contrast to noise ratios (3) were 3.3 and 9.0 for the 2D cine and 4.4 and 12.3 for the 3D cine.

**Conclusion:** Ferumoxytol enhanced 3D Heart-NAV spoiled GRE cines resulted in high-contrast blood/myocardium borders, which allowed accurate estimation of ventricular volumes, and provided excellent visualization of the anatomy.

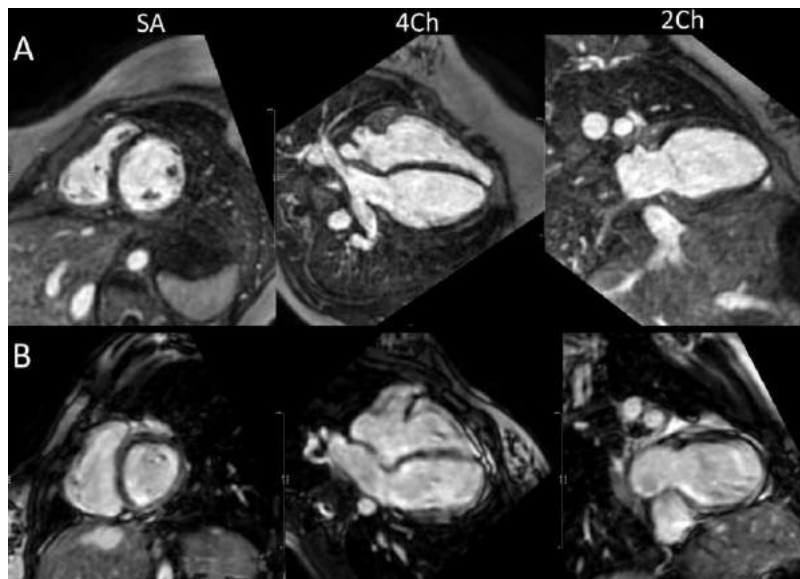
**Figure/Table 1**



**Caption 1**

Short axis (A,B) and right ventricular outflow track (C,D) views acquired using 2D bSSFP cine (A, C) and 3D Heart-NAV spoiled GRE cine (B, D) in the same patient. The white arrows show a stent in the main pulmonary artery, which obscured visualization with the bSSFP (C), while ferumoxytol-enhanced spoiled GRE enabled excellent visualization near the stent (D).

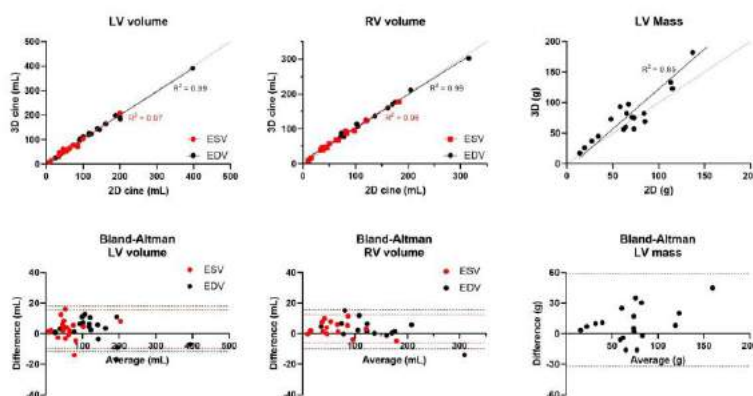
**Figure/Table 2**



**Caption 2**

3D Heart-NAV spoiled GRE cine with ferumoxytol (A) and Gd (B) at end-diastole in two patients. Images were acquired 76mins after ferumoxytol administration and 29 mins after Gd administration. Despite the shorter delay before imaging, Gd enhancement was less effective and resulted in blurring as it is quickly cleared from the blood pool.

**Figure 3**



**Caption 3**

Agreement between 2D and 3D cine measurements. LV and RV volumes showed excellent correlation at end-systole and end-diastole. Bias for EDV and ESV was 3.1 and 2.9 mL for the LV and 2.9 and 3.3 mL for the RV. 95% confidence intervals are indicated by the dotted lines. 3D LV mass estimation suffered due to the obscure epicardial border (bias = 13.5 g).

### **Bibliographic References**

2. Han F, Rapacchi S, Khan S, Ayad I, Salusky I, Gabriel S, Plotnik A, Finn JP, Hu P. Four-dimensional, multiphase, steady-state imaging with contrast enhancement (MUSIC) in the heart: a feasibility study in children. *Magn Reson Med* 2015;74(4):1042-1049., 3.  
Moghari MH, Barthur A, Amaral ME, Geva T, Powell AJ. Free-breathing whole-heart 3D cine magnetic resonance imaging with prospective respiratory motion compensation. *Magnetic resonance in medicine* 2018;80(1):181-189., 1. Usman M, Ruijsink B, Nazir M, Cruz G, Prieto C. Free breathing whole-heart 3D CINE MRI with self-gated Cartesian trajectory. *Magnetic resonance imaging* 2017;38:129-137.

Speaker: M. Ganigara,

Category: 3D, Cine Imaging, Ferumoxytol



000395

## Performance of Deep Learning Disease Classification and Risk Stratification in Patients with Hypertrophic Cardiomyopathy and Cardiac Amyloidosis

J. Cockrum \* (1); D. Chen (2); M. Nakashima (3); T. H. Hwang (3); M. Hanna (4); K. Kanj (4); R. Basnet (5); M. Benovoy (5); S. Kapadia (4); L. Svensson (6); B. Griffin (7); S. Flamm (7); R. Grimm (7); W. Tang (4); D. Kwon (4)

(1) Cleveland clinic lerner college of medicine, Cleveland Clinic, Cleveland, United States of America; (2) Business intelligence, Cleveland Clinic Main Campus, Cleveland, United States of America; (3) Quantitative health sciences, Cleveland Clinic Main Campus, Cleveland, United States of America; (4) Cardiovascular medicine, Cleveland Clinic Main Campus, Cleveland, United States of America; (5) Cardiac imaging, Circle Cardiovascular Imaging, Calgary, Canada; (6) Heart and vascular institute, Cleveland Clinic Main Campus, Cleveland, United States of America; (7) Section of cardiovascular imaging, Cleveland Clinic Main Campus, Cleveland, United States of America

### Abstract

**Background:** Cardiovascular magnetic resonance (CMR) imaging is an important diagnostic tool in the evaluation of cardiac amyloidosis (CA) and hypertrophic cardiomyopathy (HCM). Differentiating HCM from CA can be difficult, particularly when distinct late gadolinium (LGE) patterns are not present. CMR cine imaging provides morphological, functional, and textural information which contain important diagnostic utility for identifying etiologies of left ventricular hypertrophy. Deep learning (DL) has been used to improve diagnostic and prognostic utility of diagnostic procedures. This study assesses the efficacy of DL methods compared to left ventricular morphology (LVM) measurements in diagnosing CA vs HCM and risk stratifying CA patients using CMR cine images.

**Methods:** 454 patients with a diagnosis of hypertrophic cardiomyopathy (HCM) (n = 260, 57%) or cardiac amyloidosis (n = 194, 43%) who underwent CMR imaging at a single institution between 2008 and 2018 were selected for analysis. Patients were randomly assigned to training (n=317, 70%) and testing (n=137, 30%) subgroups. A DL (DenseNet121) model was trained using short axis CMR cine images acquired after the administration of gadolinium. A Random Forest model was also trained using LVM measurements automatically extracted from cine images using third party software (cvi42, Circle Cardiovascular Imaging): ejection fraction, LV end diastolic volume (EDV), LV end systolic volume (LV ESV), myocardial mass, and peak wall thickness. Additionally, the LVM measurements were combined with the output of the last convolutional layer of the DL model to form a hybrid DL model using both CMR cine images and LV morphology measurements as features. The accuracy, F1 score, and area under the curve (AUC) of the receiver operating characteristics (ROC) curve were calculated for each model and compared. DL imaging features and LVM measurements were each subsequently fed into a random survival forest (RSF) model to predict mortality in the subset of patients with CA (n = 194). A C-statistic was calculated for each model and compared. Finally, CA patients were stratified into high and low risk groups based on the RSF predictions, and a Wilcoxon Log-Rank Test was used to compare survival curves for each model.

**Results:** Deep learning (DenseNet121) model using CMR cine images had the highest diagnostic accuracy (91%), with an AUC of 0.97 and F1 score of 0.88. LVM measurements were added to create a hybrid DL model, the diagnostic performance was similar with an accuracy of 88% and AUC of 0.95 ( $p = 0.215$ ). The Random Forest model using LVM measurements had the lowest diagnostic accuracy (86%) and statistically significantly lower AUC (0.89,  $p = 0.009$ ), compared to the base DL model. The RSF model utilizing image features from the DL model and the RSF model using LVM measurements had a C-statistic of 0.61 and 0.56, respectively. RSF using image features from the DL model resulted in a significant difference between the high and low risk survival curves ( $p = 0.03$ ), while the RSF using LVM measurements did not ( $p = 0.31$ ).

**Conclusions:** DL models using CMR cine images more accurately categorized HCM and CA and improved risk prediction than traditional machine learning using LVM measurements alone. Utilizing DL methods to increase the diagnostic accuracy and prognostic ability of CMR cine images has potential important ramifications for appropriately diagnosing patients with CA vs HCM, and selecting appropriate management.

**Figure/Table 1**

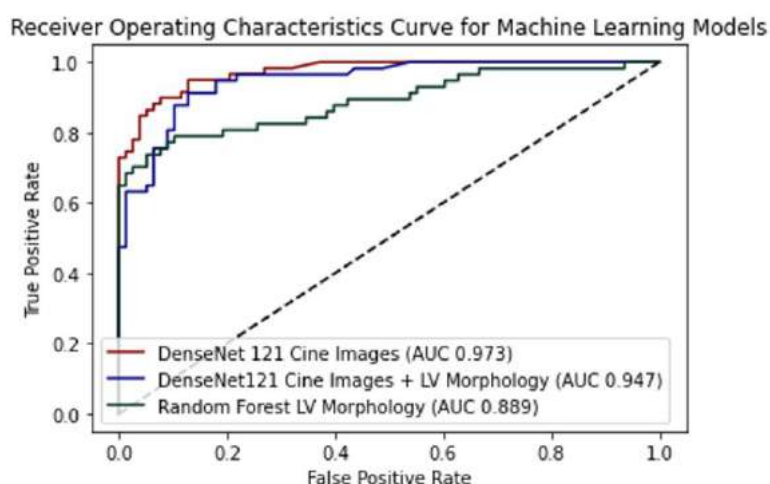
	Random Forest using LV Morphology	DenseNet121 using CMR cine images	DenseNet121 using CMR cine images and LV Morphology
Accuracy	0.859	0.912	0.888
AUC (95% CI)	0.889* (0.828 – 0.949)	0.973* (0.951 – 0.994)	0.947 (0.913 – 0.982)
F1	0.816	0.898	0.869

**Caption 1**

Metrics comparing the performance of each model for the diagnosis of cardiac amyloidosis.

\* $p = 0.009$

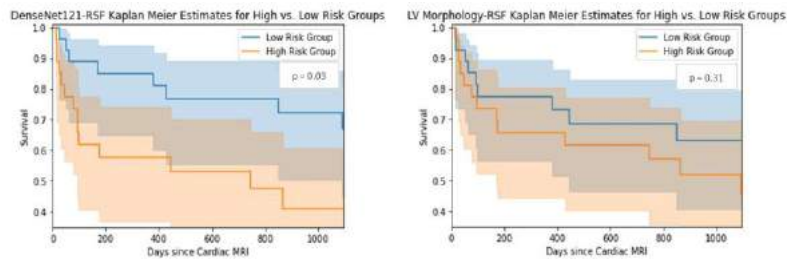
**Figure/Table 2**



## Caption 2

Receiver operating characteristics curve for each machine learning model for the diagnosis of cardiac amyloidosis.

## Figure 3



## Caption 3

Kaplan-Meier survival curves for high and low risk amyloid patients as determined by (left) random survival forest trained using image features extracted using deep learning model and (right) random survival forest trained using LV morphology measurements.

Speaker: J. Cockrum

Category: Amyloidosis , Cine Imaging, Hypertrophic Cardiomyopathy

000398

## Is the Agreement between Magnetic Resonance and Echocardiographic Measurements of Left Ventricular Ejection Fraction Biased by Patient's Sex?

L. Lee \* (1); S. Wang (2); H. Patel, (1); S. Liu, (3); V. M.-A. Mor-Avi (1); R. Lang, (1); A. R. Patel (4)

(1) Cardiology, UChicago Medicine, Chicago, United States of America; (2) Cardiac imaging, UChicago Medicine, Chicago, United States of America; (3) Cardiology, Riverside Medical Center, Kankakee, United States of America; (4) Medicine and radiology, UChicago Medicine, Chicago, United States of America

### Abstract

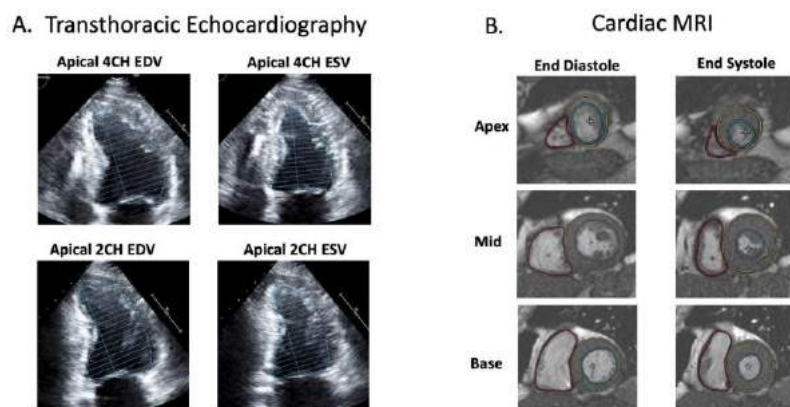
**Background.** Recent focus on gender biases in medical sciences has revealed that historically many research studies focused preferentially on male patients, often resulting in findings that cannot be directly extrapolated to women. While differences between male and female cardiac anatomy and physiology are becoming better recognized, it is not fully understood how sex-related anatomical differences, such as breast tissue prominence, affect the ability of different cardiac imaging modalities to accurately detect cardiac abnormalities. This study was aimed to determine whether agreement between cardiac magnetic resonance (CMR) and echocardiographic evaluations of left ventricular (LV) ejection fraction (EF) is affected by the patient's sex.

**Methods.** We retrospectively studied 408 consecutive patients (age  $50 \pm 17$  years; BMI  $27.6 \pm 7.1$  kg/m<sup>2</sup>; 187 men, 221 women) who underwent same day CMR and echocardiographic quantitative evaluation of LVEF (sample tracing, Figure 1). Inter-technique agreement between LVEF measurement was assessed using linear regression with Pearson's correlation and Bland-Altman analysis of biases and limits of agreement. Additionally, the number of patients in whom the inter-modality difference in LVEF exceeded 5% was determined for each sex group. The difference in the prevalence of such discordance was tested using the chi-squared analysis.

**Results.** No significant differences in BMI was noted between men ( $28 \pm 6$  kg/m<sup>2</sup>) and women ( $27 \pm 8$  kg/m<sup>2</sup>) (Table 1). CMR and echocardiography derived LVEF values correlated highly ( $r=0.86$ ) with only minimal difference between sexes (Figure 2). Bland-Altman analysis showed biases of -4% (CI: -20 to 12%) for men and -3% (CI: -19 to 14%) for women. The proportion of individuals with inter-technique differences in LVEF >5% was higher for men (114/187, 62%) than women (108/221, 49%), without reaching statistical significance (chi-square=1.57,  $p=0.19$ ).

**Conclusion.** In a large sample of male and female patients who underwent same day CMR and echocardiographic examinations, there is no significant bias in the inter-modality agreement in the quantitative evaluation of LV systolic function.

**Figure/Table 1**



**Caption 1**

Figure 1. Sample tracings for calculation of left ventricular ejection fraction (LVEF) by (A) transthoracic echocardiography (biplane method of disks) and (B) cardiac MRI. EDV = end-diastolic volume; ESV = end-systolic volume; 4CH = 4 chamber; 2CH = 2 chamber.

**Figure/Table 2**

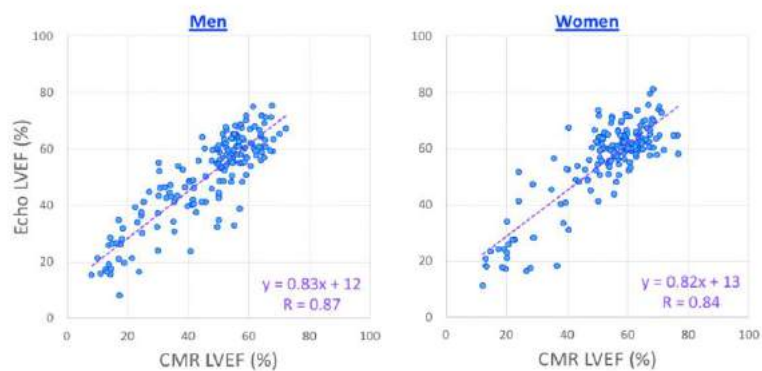
**Table 1: Baseline Clinical Characteristics**

	Male (n)	Male (%)	Female (n)	Female (%)	P value
<b>DEMOGRAPHICS</b>					
Total Patients	187	45.8%	221	54.2%	
Age (years) $\pm$ SD	51 $\pm$ 16		49 $\pm$ 17		0.30
BMI (kg/m <sup>2</sup> ) $\pm$ SD	28 $\pm$ 6		27 $\pm$ 8		0.33
Caucasian	98	52.4%	105	47.5%	0.57
African American	74	39.6%	96	43.4%	0.61
Other Ethnicity	15	8.0%	20	9.0%	0.73
<b>BASELINE MEDICAL HISTORY</b>					
Coronary Artery Disease	59	31.6%	23	10.4%	0.000016
Heart Failure	75	40.1%	54	24.4%	0.015
Cerebrovascular Disease	4	2.1%	2	0.9%	0.31
Arrhythmia	40	21.4%	42	19.0%	0.63
CABG	14	7.5%	6	2.7%	0.034
Any Valve Surgery	2	1.1%	11	5.0%	0.030
Heart Transplant	12	6.4%	3	1.4%	0.009
ICD Implanted	4	2.1%	0	0.0%	0.031
Any Smoking	90	48.1%	72	32.6%	0.036

## Caption 2

Table 1. Baseline Demographics and Clinical Characteristics.

## Figure 3



## Caption 3

Figure 2. CMR and echocardiography derived left ventricular (LVEF) values correlated highly overall ( $r=0.86$ ) with only minimal difference between sexes.

Speaker: L. Lee

Category: Echocardiography, Multi-Modality, Ventricular Function

**000401**

## **Ischemic Cardiomyopathy secondary to Spontaneous Coronary Artery Dissection in a Young Female: Role of Cardiac MRI**

S. Sharma \* (1); R. Rajagopal (1); A. Kaushik, (2)

(1) Diagnostic and interventional radiology, All India Institute of Medical Sciences(AIIMS), Jodhpur, Jodhpur, India; (2) Cardiology, All India Institute of Medical Sciences(AIIMS), Jodhpur, Jodhpur, India

### **Abstract**

#### **Description of Clinical Presentation**

A 31-year-old female presented to the Cardiology department of our institution with a history of chest pain for 9 months and new-onset dyspnoea and orthopnoea. She had past history of multiple miscarriages, headaches from 9-10 years, and right-sided vision loss from 8-9 years. She had been investigated at multiple places outside our institution for her previous complaints but was not able to find the cause of her ailments. Her lipid and thyroid profile and homocysteine levels were within normal limits. No history of hypertension, diabetes, trauma, or past intervention was elucidated.

#### **Diagnostic Techniques and Their Most Important Findings**

The patient initially underwent a chest radiograph in our department which revealed cardiomegaly and pleural effusion. Suspicion of anterior myocardial infarction was raised on electrocardiography. Transthoracic echocardiography showed global hypokinesia with severe left ventricular (LV) systolic dysfunction (left ventricular ejection fraction: 15-18%).

Contrast-enhanced Cardiac MRI (GE Discovery 750W 3T) was undertaken which revealed grossly dilated left atrium and ventricle with mild mitral regurgitation and severe LV systolic dysfunction. Left ventricular wall thinning, resting perfusion defects and late gadolinium enhancement were noted involving subendocardium in anterior, anteroseptal, and anterolateral segments at mid-ventricular level (hypokinetic segments) and transmurally in septal and anterior segments at the apical level and in LV apex (akinetic segments). Findings were consistent with "ischemic cardiomyopathy" with infarcts in the territory of the left anterior descending (LAD) artery.

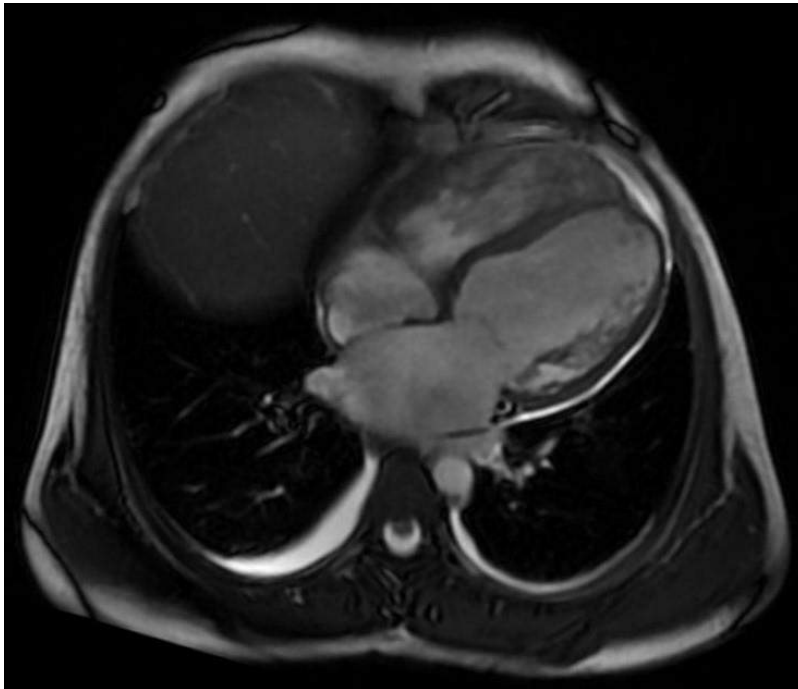
The subsequently done coronary angiography revealed spontaneous coronary artery dissection in mid LAD with 70-80% stenosis. Due to the presence of a large percentage of non-viable myocardium and the risks associated with intervention with severe LV systolic dysfunction, the patient was explained the poor prognosis and was kept on medical management.

#### **Learning Points from The Case**

1. Spontaneous coronary artery dissection (SCAD) is an important but often unidentifiable cause of myocardial infarction in young patients, especially in females with no traditional risk factors for coronary artery disease.

2. Diagnosis of SCAD requires a high index of suspicion. Unidentified and untreated cases have a poor prognosis with subsequent non-salvageable myocardial infarcts (as was seen in our case) and poor rates of survival.
3. Cardiac MRI is instrumental in establishing the accurate diagnosis of ischemic cardiomyopathy and confirming the presence and exact location of myocardial infarcts. In fact, the possibility of coronary artery disease and further decision to undertake coronary angiography was raised on Cardiac MRI in our case.
4. Understanding the patterns of late gadolinium enhancement on cardiac MRI is extremely useful in identifying the causes of cardiomyopathies.

**Figure/Table 1**

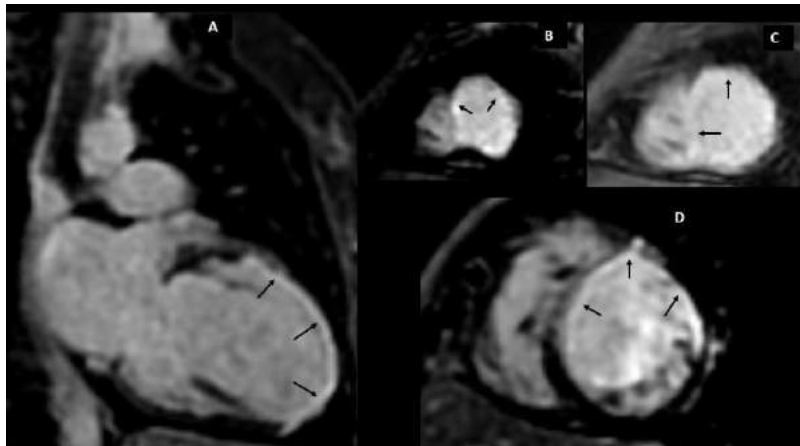


**Caption 1**

Figure 1: Axial 4chamber view (FIESTA sequence) of Cardiac MRI shows dilated left atrium and left ventricle with bilateral pleural effusion

**Figure/Table 2**





## Caption 2

2 chamber (A) and short-axis views (B-D) of Cardiac MRI (SPGR sequence) show late gadolinium enhancement involving LV apex (B: transmural), septal and anterior segments at apical level (C: transmural), and anterior, anteroseptal, and anterolateral segments at mid-ventricular level (D: subendocardium): LAD territory infarcts.

## Bibliographic References

Tweet MS, Eleid MF, Best PJM, Lennon RJ, Lerman A, Rihal CS, et al. Spontaneous coronary artery dissection: Revascularization versus conservative therapy. *Circ Cardiovasc Interv.* 2014;7(6):777–86. , Hayes SN, Kim CESH, Saw J, Adlam D, Arslanian-Engoren C, Economy KE, et al. Spontaneous coronary artery dissection: Current state of the science: A scientific statement from the American Heart Association. *Circulation.* 2018; 137:523–57.

Speaker: S. Sharma

Category: Acute Coronary Syndrome, Acute Myocardial Infarction, Accuracy and Effectiveness

000405

## Right/ left ventricular blood pool T2 ratio: associations with dyspnoea and outcomes in patients with newly diagnosed heart failure

B. Chambers (1); J. Farley \* (2); D. Broadbent (3); M. Spurr (4); L. Brown (2); N. Jex (2); S. Thirunavukarasu (2); A. Chowdhary (2); N. Sharrack (2); M. Gorecka, (2); E. Levelt (2); E. Dall'Armellina (2); J. Greenwood (2); S. Plein (2); P. Swoboda (2)

(1) Cardiology department, Leeds General Infirmary, Leeds, United Kingdom; (2) Leeds institute of cardiovascular and metabolic medicine, University of Leeds, Leeds, United Kingdom; (3) Department of medical physics, Leeds General Infirmary, Leeds, United Kingdom; (4) Department of cardiovascular research, Leeds General Infirmary, Leeds, United Kingdom

### Abstract

**Background:** T2 relaxation time of blood is influenced by the degree of oxygenation. The oxygen saturation can be estimated by the Luz-Meiboom model where  $T2_{max}$  is the T2 time of fully oxygenated blood and K is a constant:  $1/T2 = 1/T2_{max} + K(1-SaO_2)^2$ . From a T2 map the LV and RV blood pools can be imaged simultaneously and the T2 of oxygenated (left ventricular (LV)) and mixed venous (right ventricular (RV)) blood can be estimated. This technique has been validated in a pig model, with excellent correlation ( $R^2 = 0.89$ ) between T2 mapping and invasive measurement (1). Mixed venous oxygen saturation is an important prognostic marker in patients with heart failure. However, at present it can only be measured by invasive catheterisation. We aimed to investigate whether RV/LV blood pool T2 ratio is associated with symptoms and outcomes in patients with newly diagnosed heart failure.

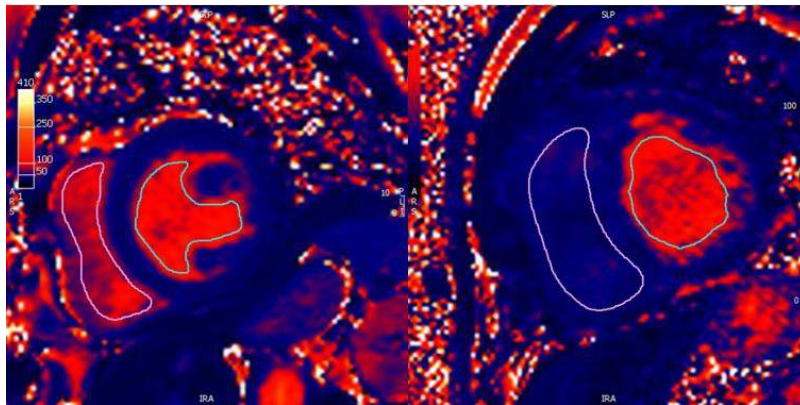
**Methods:** We recruited outpatients with a recent diagnosis of heart failure with LVEF <50% on referral echocardiogram, aged >18 years and referred for investigation into the aetiology of heart failure. Exclusion criteria were previous myocardial infarction, revascularisation or angina, hypertrophic cardiomyopathy, amyloidosis, suspected myocarditis or advanced renal failure. Patients were followed up by review of medical records for major adverse cardiovascular events (MACE) to include cardiovascular death, heart failure hospitalisation, non-fatal MI and non-fatal stroke. Short axis T2-maps at mid ventricular and basal levels were manually segmented by drawing contours in the blood pool avoiding areas of trabeculation and artefact (Figure 1). The T2 ratio (%) was calculated as mean of mid and basal RV blood pool divided by mean of mid and basal LV blood pool.

**Results:** A total of 269 patients with newly diagnosed heart failure were recruited. Median age was 64 (interquartile range (IQR) 54-72) and 179/269 (66%) were male. Median T2 ratio was 56% (IQR 49-63%) with median LV ejection fraction of 41% (IQR 32-49%). There was a linear correlation between LVEF and T2 ratio ( $\rho = 0.45$ ,  $P < 0.001$ ). 94 (35%) patients reported significant dyspnoea on exertion. In these patients T2 ratio was significantly lower (55% (IQR 52-57%) vs 57% (IQR 55-59%)  $P = 0.03$ ). During median follow up of 599 days, 20 patients encountered MACE of which 15 had a heart failure hospitalisation, 3 had a non-fatal stroke, and 3 had cardiovascular death. Receiver operator analysis was used to identify a cut-off of <52% which was associated with MACE (Figure 2). On univariate Cox regression analysis, lower T2 ratio had a significant association with MACE on follow up (Hazard ratio

(HR) 0.93, 95% confidence interval (CI) 0.89-0.98,  $P=0.005$ ). However, after adjustment for LVEF this was no longer significant (HR 0.95 (95% CI 0.92-1.0,  $P=0.10$ ).

**Conclusions:** RV/LV T2 blood pool ratio can be calculated easily from T2 maps and in this cohort of patients with recently diagnosed heart failure had significant association with patient reported exertional breathlessness on exertion. T2 ratio was significantly correlated with LVEF but did not have an independent association with MACE. Further studies are needed to establish whether T2 ratio can be used to investigate mechanisms of dyspnoea and MACE in different patient populations.

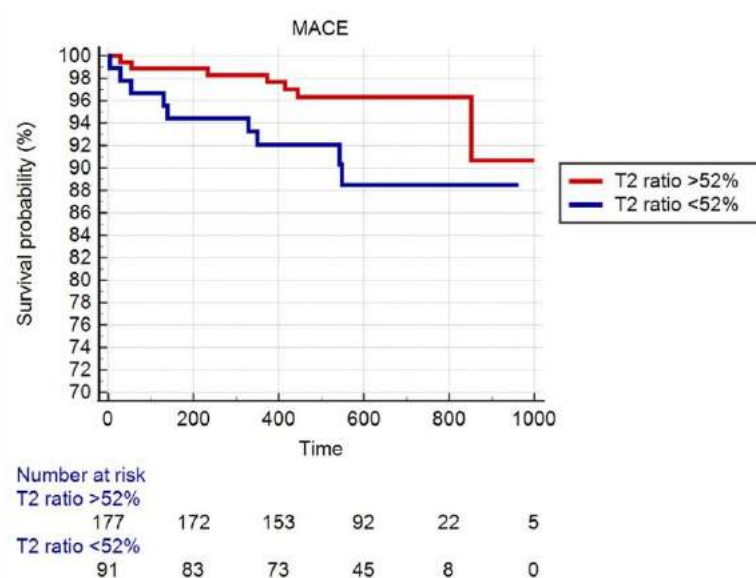
#### Figure/Table 1



#### Caption 1

Figure 1 shows T2 maps from 2 patients with heart failure with contours of LV blood pool (cyan) and RV blood pool (pink). Left sided panel is from a patient with DCM (LVEF 36%, T2 ratio 77%) who had no events on follow up. Right sided panel is from another patient with DCM (LVEF 12%, T2 ratio 47%) who had a subsequent heart failure hospitalisation.

#### Figure/Table 2



## Caption 2

Figure 2 shows that patients with a T2 ratio <52% had significantly worse MACE free survival than those with T2 ratio >52% (P=0.027 by Log-Rank Test)

## Bibliographic References

- 1) Varghese J, Potter LC, LaFountain R, et al. CMR-based blood oximetry via multi-parametric estimation using multiple T2 measurements. J Cardiovasc Magn Reson. 2017 Nov 9;19(1):88.

Speaker: J. Farley

Category: Parametric Mapping, Heart Failure, Outcomes

000406

## Diagnostic accuracy of SMS-bSSFP DCE-MRI lung perfusion for screening of pulmonary thrombo-embolism

H. Hasaneen \* (1); X. Milidonis (1); M. Hajhosseiny (2); C. Cirillo (3); F. Bosio (1); T. Castiello (1); K. Alfakih (4); G. Benedetti (5); S. M. Mak (5); P. Marino (6); B. Mukherjee (7); S. Roujol (1); S. McElroy (1); A. Chiribiri (1); A. Villa (1)

(1) Biomedical engineering and imaging sciences, King's College London, London, United Kingdom; (2) Radiology, East and North Hertfordshire NHS Trust, London, United Kingdom; (3) Cardiology, Oxford University Hospitals NHS Foundation Trust, Oxford, United Kingdom; (4) Cardiology, Lewisham and Greenwich NHS Trust, London, United Kingdom; (5) Radiology, Guy's and St Thomas' NHS Foundation Trust, London, United Kingdom; (6) Lane fox respiratory unit, Guy's and St Thomas' NHS Foundation Trust, London, United Kingdom; (7) Respiratory medicine, Guy's and St Thomas' NHS Foundation Trust, London, United Kingdom

### Abstract

**Background:** Pulmonary embolism (PE) is a potentially fatal condition that is one of the most common causes of cardiovascular mortality worldwide (1). Despite being treatable with complete resolution of emboli in most of the affected subjects, some may retain clots causing vascular obstruction and fibrosis resulting in chronic thrombo-embolic disease (CTED) or chronic thrombo-embolic pulmonary hypertension (CTEPH). A V/Q scan is the recommended modality of choice for screening for CTEPH under ESC/ERS guidance (2), with invasive catheter angiography being the gold standard for diagnosis of chronic thrombo-embolism (CTE). In daily practice, however, CT pulmonary angiogram (CTPA) and V/Q SPECT are commonly used for screening and characterisation of pulmonary arterial abnormalities. MRI has been emerging as an alternative modality through continuous technical advancements allowing for the ultimate exploitation of the advantages inherent in MRI as excellent soft tissue characterisation, being radiation-free and using a relatively low-nephrotoxic contrast agents. Dynamic contrast enhanced-MRI (DCE-MRI) is one of the main MR techniques for lung perfusion assessment that has gained wider adoption being more clinically and technically established. It has risen as an alternative for evaluation of CTE with comparable accuracy to perfusion scintigraphy in screening for CTEPH (3, 4). In this study, we sought to assess the utility and diagnostic accuracy of a novel free-breathing sequence; simultaneous multi slice (SMS)-bSSFP DCE-MRI lung perfusion in the diagnosis of CTE against CTPA and/or V/Q SPECT as reference standard.

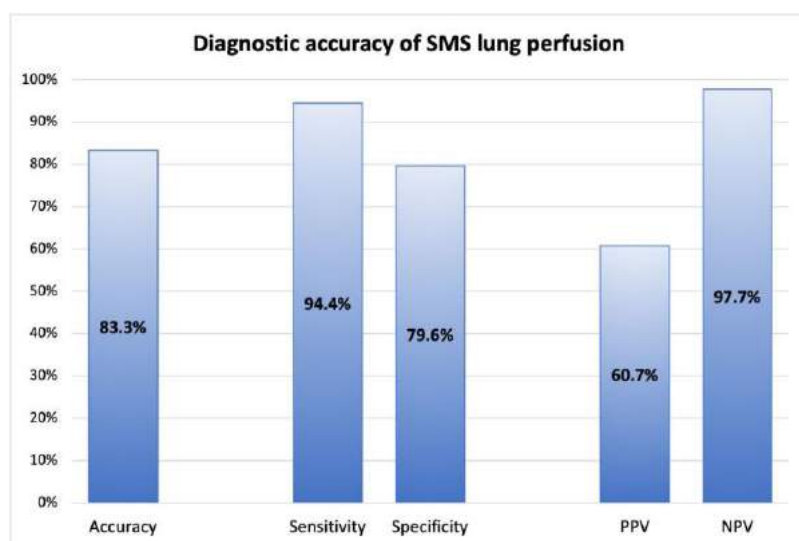
**Methods:** Consecutive patients referred for cardiovascular MRI (CMR) with history of COVID-19 and/or pulmonary hypertension (PH) who have undergone SMS-bSSFP DCE-MRI and had CTPA and/or V/Q SPECT within 6 months of the CMR study were retrospectively identified and included. Scans were acquired on a 1.5T MR scanner (MAGNETOM Aera, Siemens Healthcare, Erlangen, Germany) using a free breathing SMS-bSSFP sequence acquiring 16 coronal slices covering the entire lungs every 2 seconds. A dual-bolus protocol was used. Scans were analysed visually for the presence of perfusion defects suggestive of CTE (one or more segmental or subsegmental perfusion defect), as described previously (3). Diagnostic accuracy of DCE-MRI lung perfusion was compared to

CTPA and/or V/Q SPECT to calculate sensitivity, specificity, negative and positive predictive values.

**Results:** 79 patients (36.7% females, average age  $56.8 \pm 15$  years) fulfilling the inclusion criteria were identified. 7 patients were excluded due to disagreement in the results of CTPA and V/Q SPECT. 72 final patients were included in the analysis. SMS-bSSFP DCE-MRI lung perfusion showed an overall diagnostic accuracy of 83.3% against CTPA and/or V/Q SPECT, with PPV=60.7% and NPV=97.7%, as illustrated in figures 1 and 2. The high NPV highlights the potential use of SMS-bSSFP DCE-MRI lung perfusion as a good screening test for suspected pulmonary CTE.

**Conclusion:** Free breathing SMS-bSSFP DCE-MRI lung perfusion is a highly accurate adjunct for CTED/CTEPH screening. When combined with other established and emerging techniques e.g., functional assessment and 4D flow respectively, it can be a valuable technique in cardiopulmonary-MRI, providing both structural and functional evaluation of the heart and lungs in one single scan.

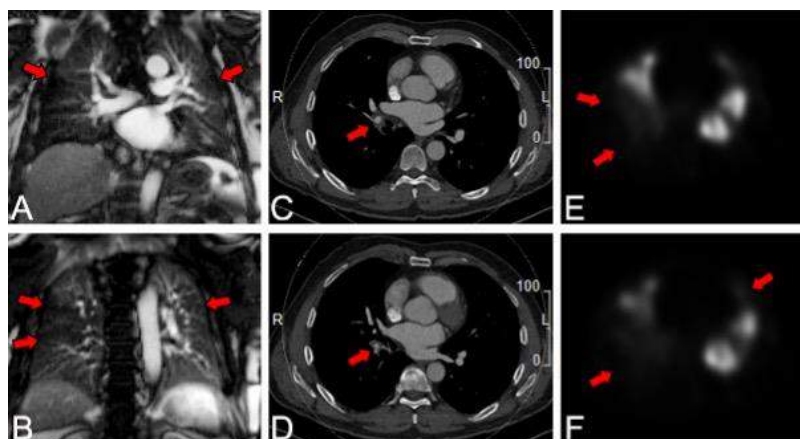
**Figure/Table 1**



**Caption 1**

**Figure (1):** Overall diagnostic accuracy of SMS-bSSFP DCE-MRI lung perfusion in the diagnosis of pulmonary chronic thrombo-embolism compared to CTPA and/or V/Q SPECT (PPV; positive predictive value, NPV; negative predictive value)

**Figure/Table 2**



## Caption 2

**Figure (2):** Bilateral CTED, more on the right lung; (A and B) SMS-bSSFP DCE-MRI showing wedge-shaped perfusion defects, (C and D) DE-CTPA showing (C) stenosis of a segmental branch of the right lower lobe pulmonary artery and (D) web in the right basal trunk, (E and F) V/Q SPECT showing perfusion defects in both lower lung lobes and lingula.

## Bibliographic References

1. Konstantinides SV, Meyer G, Becattini C, Bueno H, Geersing G-J, Harjola V-P, et al. 2019 ESC Guidelines for the diagnosis and management of acute pulmonary embolism developed in collaboration with the European Respiratory Society (ERS) The Task Force for the diagnosis and management of acute pulmonary embolism of the European Society of Cardiology (ESC). *European heart journal*. 2020;41(4):543-603.
2. Galiè N, Humbert M, Vachiery J-L, Gibbs S, Lang I, Torbicki A, et al. 2015 ESC/ERS guidelines for the diagnosis and treatment of pulmonary hypertension: the joint task force for the diagnosis and treatment of pulmonary hypertension of the European Society of Cardiology (ESC) and the European Respiratory Society (ERS): endorsed by: Association for European Paediatric and Congenital Cardiology (AEPC), International Society for Heart and Lung Transplantation (ISHLT). *European heart journal*. 2016;37(1):67-119.
3. Johns CS, Swift AJ, Rajaram S, Hughes PJ, Capener DJ, Kiely DG, et al. Lung perfusion: MRI vs. SPECT for screening in suspected chronic thromboembolic pulmonary hypertension. *Journal of Magnetic Resonance Imaging*. 2017;46(6):1693-7.
4. Rajaram S, Swift AJ, Telfer A, Hurdman J, Marshall H, Lorenz E, et al. 3D contrast-enhanced lung perfusion MRI is an effective screening tool for chronic thromboembolic pulmonary hypertension: results from the ASPIRE Registry. *Thorax*. 2013;68(7):677-8.

Speaker: H. Hasaneen

Category: Simultaneous Multislice Excitation, Lung Disease, Pulmonary Hypertension



**Influence of Spatial Resolution for Imaging Intramyocardial Hemorrhage with T2\* Maps**

X. Zhang \* (1); H.-J. Yang, (1); R. Dharmakumar (2)

(1) Biomedical imaging research institute, Cedars-Sinai Medical Center, Los Angeles, United States of America; (2) Krannert cardiovascular research center, Indiana University School of Medicine, Indianapolis, United States of America

**Abstract**

**Background:** T2\* CMR is the preferred method for detecting and characterizing hemorrhagic myocardial infarction (MI); however, the influence of spatial resolution on T2\*-based characterization of hemorrhagic remnants has not been investigated. While partial volume effects are not of major concern in the acute phase of MI, the wall thinning that accompanies chronic MI can challenge the characterization of hemorrhagic remnants within the infarct wall (1,2). We hypothesized that in the presence of myocardial wall thinning in chronic MI, hemorrhagic remnants are not accurately quantified due to strong partial voluming. We investigated our hypothesis in a pig model. To remove confounding factors (motion, flow, and off-resonance artifacts) present in-vivo, we used excised pig hearts.

**Methods: Animals Studies, CMR Acquisitions & Analysis:** Reperfused LAD infarcts were created in 10 pigs. Animals were euthanized at 8 weeks post MI and the hearts were collected and imaged on a 3T whole body MRI system using 3D multi-gradient echo sequences with various in-plane and through-plane spatial resolutions. For scan parameters see Table 1A (*Ideal* acquisitions correspond to scans performed while ignoring practical limitations such as scan duration, whereas *Practical* acquisitions are performed with realistic parameter sets). In total, 28 *Ideal* and 20 *Practical* data sets were available for analysis (Table-1B). Endo- and epi-cardial contours were used to delineate the myocardial region. Subsequently a mean-2SD criterion was used to delineate the hemorrhage core. The data from the *Ideal* group with a spatial resolution of 0.3x0.3x2 mm<sup>3</sup> served as the ground truth with the remaining datasets serving as variables. Receiver operating characteristic (ROC) curve and its area under curve (AUC) were computed. Two-way ANOVA was performed on AUCs of all hearts at all in-plane and through-plane resolutions.

**Results:** Representative images from two animals (Swine 1 and Swine 2) are shown in Figure 1. Note that in both animals, the band of hemorrhagic remnants disappeared with coarser resolution. ROC analysis of both animals from *Ideal* datasets showed a trend toward lower AUC for both coarser in-plane and through-plane resolutions for swine 1 (Fig. 1C) and swine 2 (Fig. 1D). ROC analysis across all *Ideal* datasets showed that AUC is strongly dependent on both in-plane and through-plane resolution (Fig. 2A and 2C). Interestingly, ROC analysis of *Practical* datasets showed that through-plane resolution plays a prominent role in identifying hemorrhage than in-plane resolution (Fig. 2B and 2D). In *Practical* acquisitions, optimal AUC was observed from 1.6x1.6x2 to 0.8x0.8x8 mm<sup>3</sup> anti-diagonally. This behavior is further evident in Fig. 2E, where peak AUC was achieved for voxel sizes between 5.12 to 6.76 mm<sup>3</sup>. Notably we also found that MIs with thinner (less transmural) hemorrhagic regions were more vulnerable to changes in spatial resolution with respect to detection of hemorrhage (note the worse ROC performance from Swine 1 compared to Swine 2), see Fig. 2F. This is also evidenced by lower R2 of transmural and AUC for *Practical* vs. *Ideal* acquisitions,

respectively (Fig. 2G), indicating the thinner the band of hemorrhage the more sensitive are they to changes in spatial resolution for detection with T2\* CMR.

**Conclusion:** We conclude that the accuracy of detecting hemorrhagic remnants with T2\* maps at 3T within chronic MIs is strongly dependent on spatial resolution. Specifically, the optimal detection of hemorrhagic remnants with T2\* CMR requires imaging voxels to between 5 and 7 mm3.

**Figure/Table 1**

**A**

	mGRE	Ideal	Practical
TR (ms)	33	788	80
TEs (ms)	3.69, 7.38, 11.07, 14.76, 18.45, 22.14, 25.82, 29.52	4.95, 13.7, 22.45, 31.2, 39.95	2.55, 5.80, 9.90, 15.56, 21.22
Flip Angle (degree)	15	60	18
Bandwidth (Hz/pixel)	870	250	780
Average number	2	16	1
iPAT factor	NA	NA	2
Partial Fourier	NA	NA	6/8
ECG gated	No	No	Yes
Slice thickness (mm)	1	2,4,6,8	

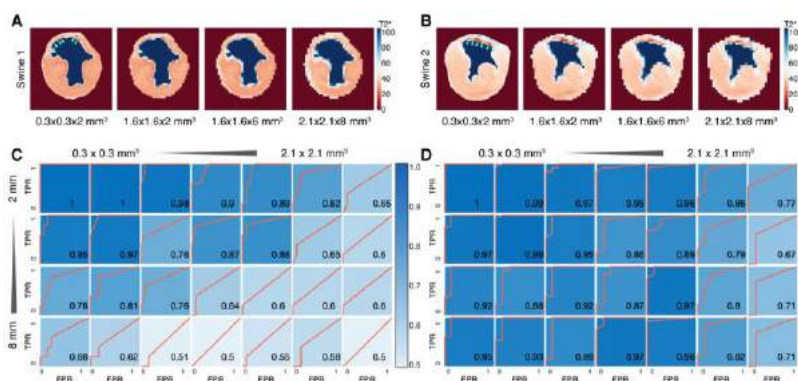
**B**

	In-plane Resolution (mm <sup>2</sup> )						
Ideal	0.3x0.3	0.6x0.6	0.8x0.8	1.0x1.0	1.3x1.3	1.6x1.6	2.1x2.1
Practical	NA		0.8x0.8	1.0x1.0	1.3x1.3	1.6x1.6	2.1x2.1

**Caption 1**

**Table 1. A)** Ex-vivo scan parameters for of multi-gradient echo acquisitions, *Ideal* group and *Practical* group respectively. **B)** In-plane resolution set between *Ideal* group (0.3x0.3 - 2.1x2.1 mm<sup>2</sup>) and *Practical* group (0.8x0.8 - 2.1x2.1 mm<sup>2</sup>). Total imaging data sets: for *Ideal* group 4x7 = 28, and for *Practical* group 4x5 = 20.

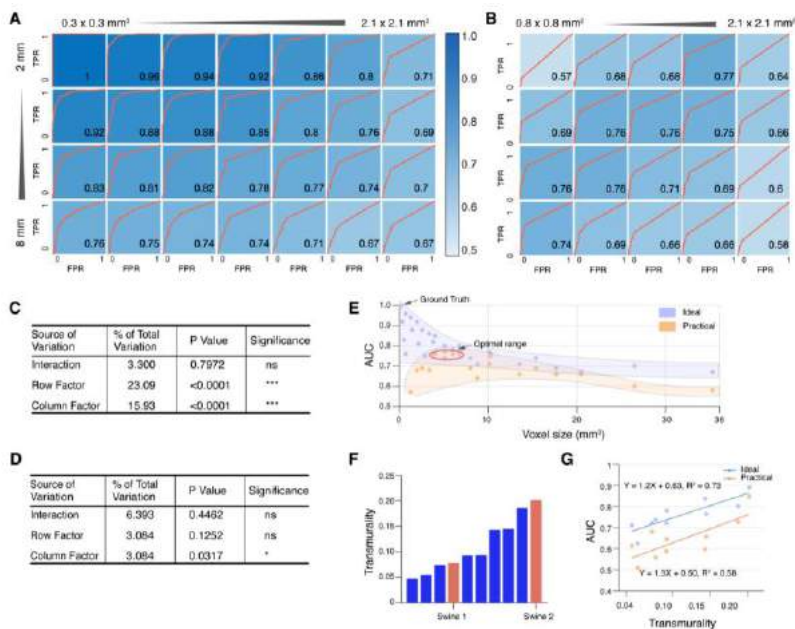
**Figure/Table 2**



**Caption 2**

**Figure 1.** Representative examples **A)** Swine 1 and **B)** Swine 2 using *Ideal* acquisitions of T2\* maps with 4 representative spatial resolution: Left to right are 0.3x0.3x2, 1.6x1.6x2, 1.6x1.6x6 and 2.1x2.1x8 mm3. IMH is denoted by arrowheads. **C)** and **D)** correspond to ROC analysis for swine 1 and swine 2 respectively acquired using *Ideal* parameters.

**Figure 3**



**Caption 3**

**Figure 2.** ROC curves with AUC for **A)** *Ideal* and **B)** *Practical*. Two-way ANOVA shows effect of spatial resolutions for **C)** *Ideal* and **D)** *Practical*. **E)** Scatter plot of voxel size vs. AUC: optimal voxel size range for *Practical* identified. **F)** Transmurality of IMH for all subjects. **G)** Linear regression of transmurality vs. AUC for *Ideal* and *Practical*.

**Bibliographic References**

2. Takigawa M, Martin R, Cheniti G, et al. Detailed comparison between the wall thickness and voltages in chronic myocardial infarction. J Cardiovasc Electrophysiol. 2019;30:195-204.,  
1. Dipan JS, Kim HW, James O, et al. Prevalence of Regional Myocardial Thinning and Relationship With Myocardial Scarring in Patients With Coronary Artery Disease. J Am Med Assoc. 2013 March 6; 309(9): 909–918

Speaker: X. Zhang

Category: Chronic Myocardial Infarction, Intramyocardial Hemorrhage, T2\*

000414

## Deep Learning-based Segmentation of Biventricular Tissue Phase Mapping in Pediatric Patients

N. Brown \* (1); H. Berhane (2); A. pathrose (2); M. Markl (2); C. Rigsby (3); J. Robinson (4); N. Husain (1)

(1) Pediatric cardiology, Ann & Robert H. Lurie Children's Hospital of Chicago, Chicago, United States of America; (2) Radiology, Northwestern University, Chicago, United States of America; (3) Medical imaging, Ann & Robert H. Lurie Children's Hospital of Chicago, Chicago, United States of America; (4) Cardiology, Ann & Robert H. Lurie Children's Hospital of Chicago, Chicago, United States of America

### Abstract

#### Background:

CMR assessment of myocardial deformation using various techniques has become a useful tool for evaluating subclinical myocardial dysfunction. Tissue phase mapping (TPM) is one of these techniques which uses phase-contrast cine MR for the multidirectional assessment of left ventricular (LV) and right ventricular (RV) myocardial velocities [1]. Although its feasibility has been demonstrated in various congenital and acquired heart diseases, clinical application is limited by prolonged post-processing times and inter-reader variability related to manual segmentation of myocardial contours [2, 3]. Within our research group, a deep learning (DL) tool was recently developed to automate TPM LV and RV segmentation. Utilization of this tool in a cohort of adult heart transplant patients led to a significant reduction in post-processing time with good accuracy compared to manual segmentation [4]. We hypothesized that this tool would demonstrate similar accuracy and improvement in post-processing in a cohort of pediatric patients.

#### Methods:

We retrospectively evaluated 8 patients with Duchenne muscular dystrophy and 8 normal controls (total 16 patients, age 8-21 years, 3 female) who had TPM performed as part of their CMR study (Figure 1). TPM datasets were processed using the DL tool and compared to manual segmentations. Global and segmental peak velocities in longitudinal ( $V_z$ ) and radial ( $V_r$ ) directions were quantified for both the LV and RV with regional analysis based on an extended 16+10 (LV+RV) AHA segment model. The accuracy of DL segmentation masks was evaluated using Dice scores for mask overlap, and linear regression and Bland-Altman analyses for manual vs. DL agreement of peak radial and longitudinal velocities ( $V_r$  and  $V_z$ ). Approximate post-processing times were also noted for manual vs. DL segmentation.

#### Results:

Median Dice scores were higher for the LV than the RV and were better for the base than the apex (LV base 0.71, LV apex 0.56, RV base 0.46, RV apex 0.22; Figure 2). Myocardial velocities correlated well between manual and DL segmentation for both LV and RV ( $R \geq 0.88$  for all; Figure 3). There was no significant bias between the two methods by Bland-Altman analysis with narrow limits of agreement for the LV (maximum  $\pm 2$  cm/s) and moderate DL performance for the RV (maximum  $\pm 5$  cm/s for the RV). Manual segmentation took on average 1 hour to complete, whereas DL segmentation took less than 10 minutes.

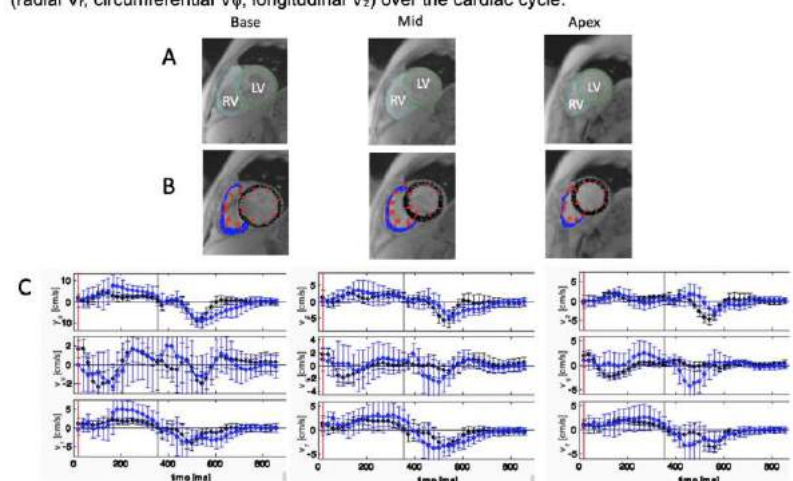
## Conclusion:

This initial feasibility study shows that a DL tool can be applied to a pediatric population for automated segmentation of TPM. Substantial reduction in post-processing time was noted along with good correlation between myocardial velocities derived from manual segmentations. Further refinements are ongoing to improve accuracy of the DL tool in the pediatric population in order to increase the clinical applicability of CMR-derived TPM.

## Figure/Table 1

Figure 1: TPM Analysis

A) Ventricular contouring on acquired TPM images B) Velocity vectors during ventricular systole  
C) Velocity-time curves showing the temporal evolution of both RV and LV motion components (radial  $V_r$ , circumferential  $V_\phi$ , longitudinal  $V_z$ ) over the cardiac cycle.



## Caption 1

Legend: LV (black), RV (blue). Box and whiskers at each time point represent mean velocity and range across all 16+10 (LV+RV) AHA segments, respectively.

## Figure/Table 2

Figure 2: Side-by-side comparison of LV/RV masks and Dice scores for manual vs. DL-based TPM analysis

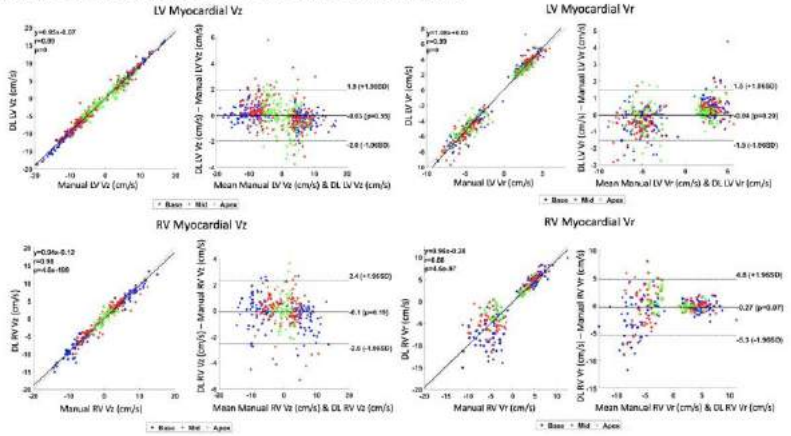
	Manual	DL	Overlap	RV Dice Scores	LV Dice Scores
Base				0.46 (0.41-0.51)	0.71 (0.62-0.73)
Mid				0.38 (0.27-0.49)	0.66 (0.61-0.73)
Apex				0.22 (0.17-0.23)	0.56 (0.42-0.61)

Caption 2

Legend: Representative masks from one patient. Manual: RV (cyan), LV (yellow). DL: RV (blue), LV (red). Overlap: manual (blue), DL (red), overlap (grey). Dice scores represented as median (interquartile range).

Figure 3

Figure 3: Linear Regression and Bland-Altman Plots



Caption 3

Legend: Linear regression and Bland-Altman plots for manual vs DL myocardial velocities for all 16 patients (DMD and controls). All 16+10 (LV+RV) AHA segments are plotted and color-coded as base (blue), mid (red), and apex (green). Positive scores represent systolic velocities, and negative scores represent diastolic velocities.

### **Bibliographic References**

1. Föll, D., et al., Magnetic Resonance Tissue Phase Mapping of Myocardial Motion. *Circulation: Cardiovascular Imaging*, 2010. 3(1): p. 54-64. doi:10.1161/CIRCIMAGING.108.813857, 2. Li, A., et al., Altered regional myocardial velocities by tissue phase mapping and feature tracking in pediatric patients with hypertrophic cardiomyopathy. *Pediatr Radiol*, 2020. 50(2): p. 168-179. 10.1007/s00247-019-04549-4, 3. Berhane, H., et al., Myocardial velocity, intra-, and interventricular dyssynchrony evaluated by tissue phase mapping in pediatric heart transplant recipients. *J Magn Reson Imaging*, 2020. 51(4): p. 1212-1222. 10.1002/jmri.26916, 4. Shen, D., et al., Automated segmentation of biventricular contours in tissue phase mapping using deep learning. *NMR in Biomedicine*. n/a(n/a): p. e4606. <https://doi.org/10.1002/nbm.4606>

Speaker: N. Brown

Category: MR Post-Processing, Automated Processing, Nonischemic Cardiomyopathy

000415

## Excellent performance of the electrocardiographic QRS-T angle against CMR in identifying left ventricular hypertrophy phenotype cardiomyopathies

D. Nayyar \* (1); R. Hughes (2); H. Shiwani, (2); S. Rosmini (2); K. Patel, (2); M. Fontana, (3); K. Knott, (4); J. Moon (4); G. A. Figtree, (1); T. A. Treibel, (4); M. Ugander, (1); R. Kozor, (1)

(1) The kolling institute, University of Sydney, Sydney, Australia; (2) Barts heart centre, St Bartholomew's Hospital, London, United Kingdom; (3) Cardiac imaging, Royal Free London NHS Foundation Trust, London, United Kingdom; (4) Cardiac imaging, St Bartholomew's Hospital, London, United Kingdom

### Abstract

**Background:** Current electrocardiography (ECG) criteria for diagnosing left ventricular hypertrophy (LVH) have poor sensitivity and varying specificity. The 12-lead ECG-derived spatial peaks QRS-T angle measures the three-dimensional spatial discordance between depolarization (QRS) and repolarization (T), and has shown improved diagnostic performance in diagnosing LVH. Cardiac magnetic resonance (CMR) allows accurate measurement of left ventricular (LV) mass and volumes. Our aim was to assess the diagnostic performance of the QRS-T angle in identifying LVH phenotype cardiomyopathies.

**Methods:** A retrospective observational study was performed comparing healthy volunteers with paired 12-lead ECG and CMR to patients with LVH of varying etiology including hypertension, aortic stenosis (AS), hypertrophic cardiomyopathy (HCM), Fabry disease, and amyloidosis. We used established methods based on manually measuring the peak QRS magnitude in leads I, II and V1-6 to estimate the QRS-T angle using Kors' regression-related transform (1,2). LV global wall thickness (GT) is the mean wall thickness of the whole LV in end-diastole, and was calculated according to the previously validated formula,  $GT [mm] = 0.05 + 1.60 * LVM[g]^{0.84} * LVEDV[ml]^{-0.49}$  (3).

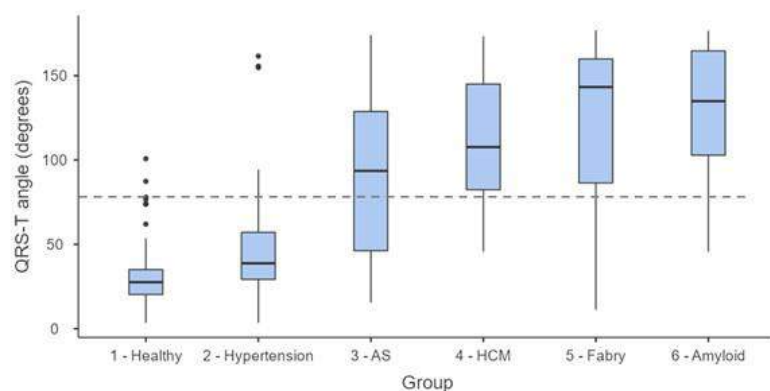
**Results:** Subjects (n=290, mean age  $58 \pm 17$  years, 41% female) included healthy volunteers (n=50, 56% female), hypertension (n=40, 48% female), AS (n=50, 36% female), HCM (n=50, 64% female), Fabry (n=50, 40% female), and amyloidosis (n=50, 6% female). Receiver operating characteristic (ROC) analysis found an area under the curve (AUC) of 0.90 for using the QRS-T angle to differentiate healthy or hypertension from the other LVH phenotype cardiomyopathies (QRS-T angle threshold  $\geq 79$  degrees, sensitivity 76%, specificity 93%, positive predictive value 64%, negative predictive value 96%). Diagnostic performance was worse for the QRS vector magnitude (AUC 0.66), Cornell voltage (AUC 0.68) and Sokolow-Lyon voltage (AUC 0.59). In a subgroup of subjects with complete CMR data (n=257), there was a modest correlation between the QRS-T angle and both LV mass ( $R^2=0.40$ ) and GT ( $R^2=0.49$ ), and far weaker correlations between the QRS vector magnitude, Cornell voltage, or Sokolow-Lyon voltage, and LV mass and GT ( $R^2=0.04-0.15$ ). LV mass/QRS vector magnitude demonstrated excellent performance for differentiating between amyloidosis and the other groups (AUC=0.90, threshold  $\geq 109$  g/mV, sensitivity 82%, specificity 79%, positive predictive value 51%, negative predictive value 95%).

**Conclusions:** The ECG QRS-T angle had excellent diagnostic performance for differentiating any LVH phenotype cardiomyopathy from healthy or hypertension. Furthermore, LV



mass/QRS vector magnitude demonstrated excellent diagnostic performance for differentiating between amyloidosis and all other groups. The QRS-T angle and QRS vector magnitude can easily be estimated from a routine 12-lead digital or paper ECG, and have additional clinical utility in conjunction with CMR in diagnosing and differentiating LVH phenotypes.

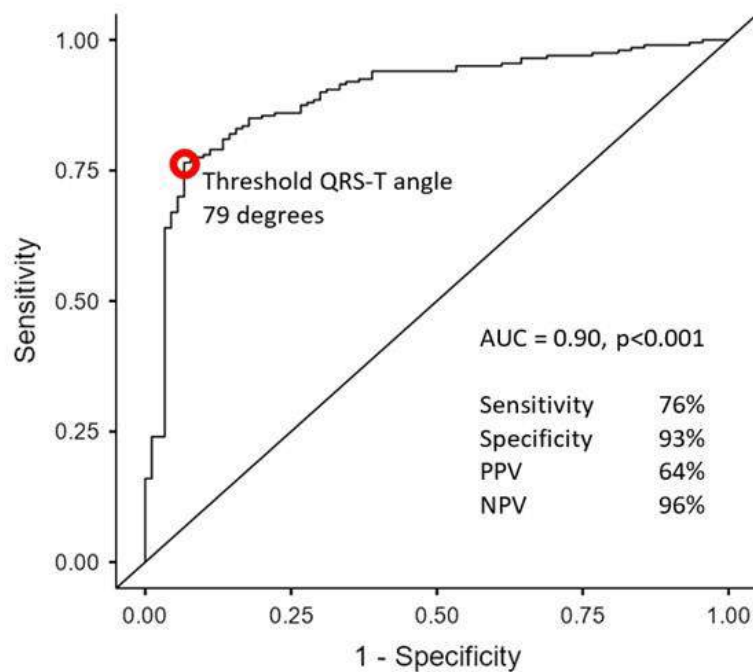
**Figure/Table 1**



**Caption 1**

**Figure 1:** Box-plot comparing QRS-T angle for each patient group. The dotted line indicates the optimal cut-off (79 degrees) for differentiating healthy or hypertension from the other left ventricular hypertrophy phenotype cardiomyopathies based on the Youden index. AS; aortic stenosis, HCM; Hypertrophic cardiomyopathy.

**Figure/Table 2**



## Caption 2

**Figure 2:** Receiver operating characteristic curve of QRS-T angle for differentiating between healthy or hypertension from the other left ventricular hypertrophy phenotype cardiomyopathies. AUC; area under the curve.

## Bibliographic References

3. Lundin M, Heiberg E, Nordlund D, Gyllenhammar T, Steding-Ehrenborg K, Engblom H, et al. Mean wall thickness improved characterization and prognosis in left ventricular hypertrophy [abstract]. Proceedings of the 22nd Annual Meeting of the Society for Cardiovascular Magnetic Resonance; 2019 Feb 6-9. [Bellevue, WA, US. Abstract ID#549719].
1. Kors J, van Herpen G, Sittig A, van Bommel J. Reconstruction of the Frank vectorcardiogram from standard electrocardiographic leads: diagnostic comparison of different methods. *Eur Heart J* 1990;11: 1083–92.
2. Cortez D, Sharma N, Devers C, Devers E, Schlegel T. Visual transform applications for estimating the spatial QRS-T angle from the conventional 12-lead ECG: Kors is still most Frank. *J Electrocardiol*. 2014 Jan-Feb;47(1):12-9.

Speaker: D. Nayyar

Category: Cardiomyopathy, ECG, Left Ventricle

000416

**Comparison of Dual-Bolus versus Dual-Sequence Techniques in Automated Pixel-Wise Quantitative Myocardial Perfusion Imaging by Cardiovascular Magnetic Resonance (CMR): A Study from the AQUA Consortium**

P. Kim \* (1); H. Wang (2); Y. Tada, (1); M. Benovoy, (3); A. Arai (4); M. Janich (5); T. Y. Law, (6); K. H. Lam, (6); H. F. Sze, (6); T. H. Sin, (6); W. W. V. Tse, (6); H. S. Tang, (6); A. H. T. Fong, (6); C.-W. Lee, (7); X. Guo, (3); A. R. Patel (8); I. M. Saeed (9); M. Friedrich (10); M.-Y. NG (6)

(1) Medicine, University of California San Diego, La Jolla, United States of America; (2) Cardiac imaging, GE Healthcare, Waukesha, WI, USA, United States of America; (3) Cardiac imaging, Circle Cardiovascular Imaging, Calgary, Canada; (4) Cardiology, Consultant, Kensington, United States of America; (5) Cardiac imaging, GE Healthcare, Munich, United States of America; (6) Radiology, The University of Hong Kong, Hong Kong, Hong Kong; (7) Cardiac imaging, GE Healthcare, Taipei, Taiwan; (8) Cardiology, UChicago Medicine, Chicago, United States of America; (9) Cardiology, Inova Fairfax Hospital, Falls Church, United States of America; (10) Departments of Medicine and Diagnostic Radiology, Division of Experimental Medicine, Centre Universitaire de Santé McGill Site Glen, Montréal, Canada

**Abstract**

**Background**

Absolute quantification of myocardial blood flow from first pass perfusion CMR requires an accurate arterial input function (AIF). To prevent the signal saturation in the AIF image that results in a non-linear signal concentration curve, 1:10 diluted and full concentration doses of gadolinium injection are commonly performed as the dual bolus technique (DB). In contrast, the novel dual sequence technique (DS) uses both a short saturation and subsequent long saturation recovery myocardial perfusion images in one image acquisition.<sup>1–3</sup> However, few clinical studies comparing both techniques have been performed.<sup>2,4,5</sup> This study aimed to compare myocardial blood flow (MBF) measurements by DB and DS techniques in a multi-center study by the AQUA investigators.

**Methods**

48 total patients (42 patients with suspected coronary artery disease and 6 heart-transplant patients) from University of Hong Kong (HKU) and University of California, San Diego (UCSD) underwent stress, using either adenosine or regadenoson, and rest myocardial perfusion imaging. A 1:10 diluted bolus was immediately followed by a full concentration bolus (0.075 mmol/kg) acquisition for both stress and rest myocardial perfusion. All images were acquired on 3-Tesla MRI scanners (GE SIGNA Premier and GE SIGNA 750) using saturation recovery prep spoiled gradient recalled sequence. Also, a modified DS technique with one AIF basal slice and three myocardial slices were performed along the short axis of the left ventricle for both diluted and full concentration boluses. The fully quantitative MBF analyses for DB and DS were performed via the Fermi deconvolution method using Circle CVI42 software. The relationship between stress MBF by DB and DS, both global and

regional (AHA 16-segment model), was assessed with Pearson's correlation coefficient or Spearman rank correlation, when normality could not be assumed. Bland-Altman plots comparing DB versus DS for global and regional MBF were also performed.

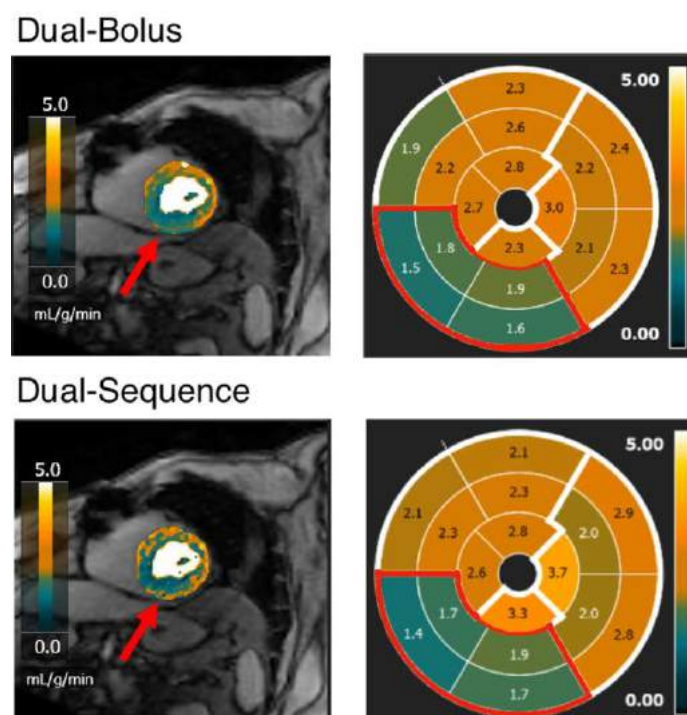
## Results

Quantitative perfusion results (Fig 1) show a very strong correlation for regional ( $r = 0.89$ ) and global ( $r = 0.93$ ) MBF comparing DB versus DS that is statistically significant ( $p < 0.0001$ , Fig 2). Bland-Altman plots (Fig 3) also show a very small absolute difference between DB and DS for regional ( $0.11 \pm 0.4$  ml/g/min) and global ( $0.10 \pm 0.3$  ml/g/min) MBF. Further comparisons of DB vs DS were performed separately for each site (HKU and UCSD) and similarly showed very strong correlations that were statistically significant (results not shown).

## Conclusions

DS technique shows a very high correlation to DB MBF that is statistically significant in our multi-center study. These results support the use of the DS technique that is fully automated and also simpler to perform, while obtaining MBF values that are similar to the established DB technique. As DS is now a multi-vendor technique, this study also supports wider adoption of DS quantitative myocardial perfusion. The AQUA investigators are performing ongoing studies to corroborate these results in more patients and across different cardiovascular diseases.

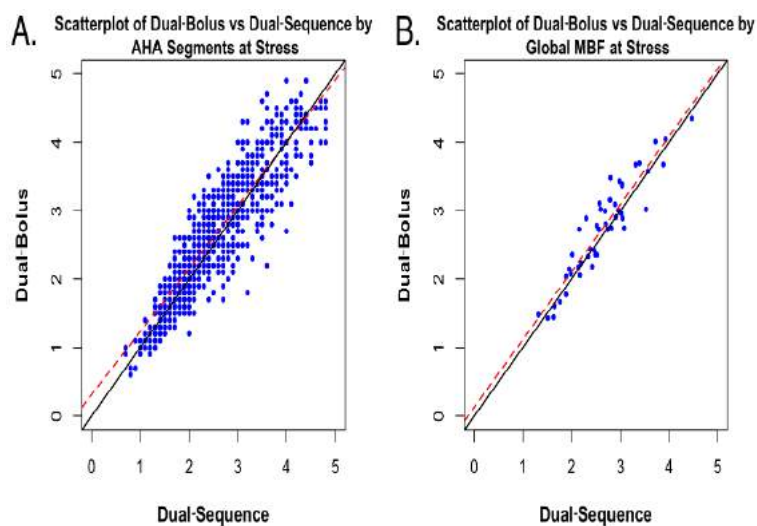
**Figure/Table 1**



**Caption 1**

Quantitative MBF comparing DB (first row) and DS (second row) are shown. Pixel-wise maps of the basal slice (first column) and 16-segment polar maps (second column) are similar between DB and DS. This patient shows reduced MBF of the myocardial segments supplied by the right coronary artery (red arrows).

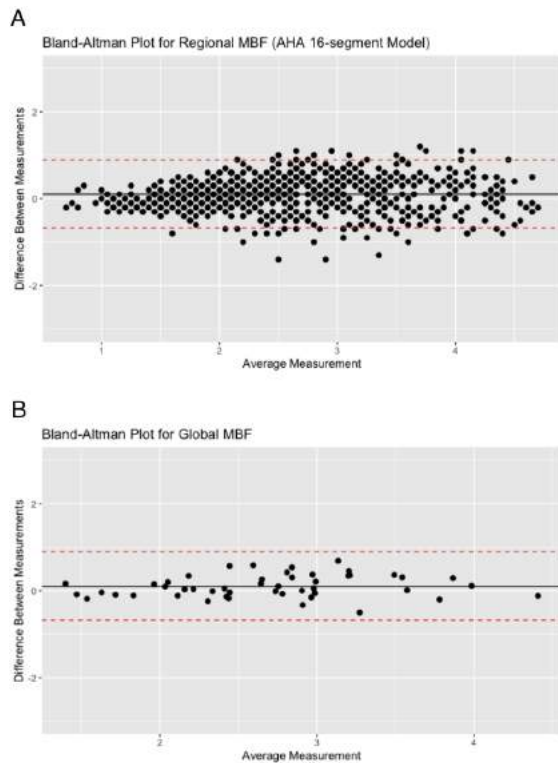
**Figure/Table 2**



**Caption 2**

Scatterplots (blue points) and simple linear regression lines (red dashed line) are shown comparing DB versus DS using both (A) regional and (B) global MBF. The identity line is the black straight line shown in both scatterplots. The linear regression lines show very high correlation for both regional and global MBF that are statistically significant ( $p < 0.0001$ ).

**Figure 3**



### Caption 3

Bland-Altman Plots comparing DB versus DS using both (A) regional and (B) global MBF. The mean differences for both regional (0.11 ml/g/min) and global (0.10 ml/g/min) MBF are small. The majority of the data points fall between the 95% confidence intervals (red dashed lines) for both plots.

### Bibliographic References

Biglands JD, Ripley DP, Broadbent DA, Higgins DM, Swoboda PP, McDiarmid AK, Garg P, Plein S, Buckley DL. A comparison of dual-bolus and dual-sequence quantitative myocardial perfusion techniques. *Journal of cardiovascular magnetic resonance: official journal of the Society for Cardiovascular Magnetic Resonance*. 2015;17(1):P50., Christian TF, Aletras AH, Arai AE. Estimation of absolute myocardial blood flow during first-pass MR perfusion imaging using a dual-bolus injection technique: comparison to single-bolus injection method. *Journal of magnetic resonance imaging: JMRI*. 2008;27(6):1271–1277., Hsu L-Y, Jacobs M, Benovoy M, Ta AD, Conn HM, Winkler S, Greve AM, Chen MY, Shanbhag SM, Bandettini WP, Arai AE. Diagnostic Performance of Fully Automated Pixel-Wise Quantitative Myocardial Perfusion Imaging by Cardiovascular Magnetic Resonance. *JACC. Cardiovascular imaging*. 2018;11(5):697–707., Kellman P, Hansen MS, Nielles-Vallespin S, Nickander J, Themudo R, Ugander M, Xue H. Myocardial perfusion cardiovascular magnetic resonance: optimized dual sequence and reconstruction for quantification. *Journal of cardiovascular magnetic resonance: official journal of the Society for Cardiovascular Magnetic Resonance*.

2017;19(1):43., Gatehouse PD, Elkington AG, Ablitt NA, Yang G-Z, Pennell DJ, Firmin DN. Accurate assessment of the arterial input function during high-dose myocardial perfusion cardiovascular magnetic resonance. Journal of magnetic resonance imaging: JMRI. 2004;20(1):39–45.

Speaker: P. Kim

Category: coronary Artery Disease, Perfusion, Stress CMR

J. Hamilton \* (1)

(1) Radiology, University of Michigan, Ann Arbor, United States of America

**Abstract**

**Background:** MR Fingerprinting (MRF) is a technique for multiparametric mapping that traditionally uses dictionary-based matching [1]. Recently, neural networks have been applied for parameter estimation without a dictionary to shorten computation times and reduce artifacts. One such method was demonstrated for cardiac MRF using a fully-connected network trained on single-voxel timecourses produced by a Bloch equation simulation [2]. Convolutional neural networks (CNNs) trained on image patches from in vivo MRF scans may achieve better image quality by exploiting spatial correlations, as shown in brain applications [3]. However, obtaining sufficient training data for cardiac MRF is challenging because the cardiac rhythm affects the sequence timings and signal timecourses, and thus many training scans are potentially needed. We propose a reconstruction for cardiac MRF based on the “deep image prior” (DIP) framework, which uses a CNN to reconstruct T1, T2, and M0 maps with reduced noise and aliasing artifacts without additional training data beyond a single undersampled scan.

**Methods:** The DIP framework uses the structure of a deep CNN to remove noise and artifacts, rather than learning from a large training set [4]. We modify the DIP framework for cardiac MRF by using a randomly initialized U-Net, which takes a random noise tensor as input (that remains fixed during training), and outputs T1, T2, and M0 maps consistent with the acquired k-space data (Figure 1). The U-Net is trained in a self-supervised manner. At each iteration, the maps are used to simulate a time series of MRF images, multiplied by coil sensitivities, and sampled using a 48-fold undersampled spiral k-space trajectory with golden angle rotation. The U-Net is updated using a loss function that is the mean squared error between the reconstructed and acquired k-space data after density compensation. Calculation of the forward model is accelerated in two ways. First, a pre-trained “fingerprint generator” network outputs signal timecourses for any T1, T2, and cardiac rhythm to avoid time-consuming Bloch simulations, as described previously [5]. Second, images are projected to a low-dimensional subspace of rank  $K=5$  to reduce the number of NUFFT operations each iteration. 2D MRF scans were collected in 5 healthy subjects at 1.5T (Sola, MAGNETOM Siemens) at a medial short-axis slice during a 15-heartbeat breathhold with a 254ms diastolic gating window and 705 TRs, called the “long acquisition”. Time points were retrospectively discarded to simulate a 5-heartbeat breathhold with a 150ms gating window with 140 TRs, called the “short acquisition”. Maps were reconstructed using 1) NUFFT gridding and dictionary matching, 2) low-rank subspace reconstruction and dictionary matching, and 3) the proposed DIP method. Conventional mapping was also performed using MOLLI and T2-prep bSSFP. T1/T2 values in the myocardial septum were measured.

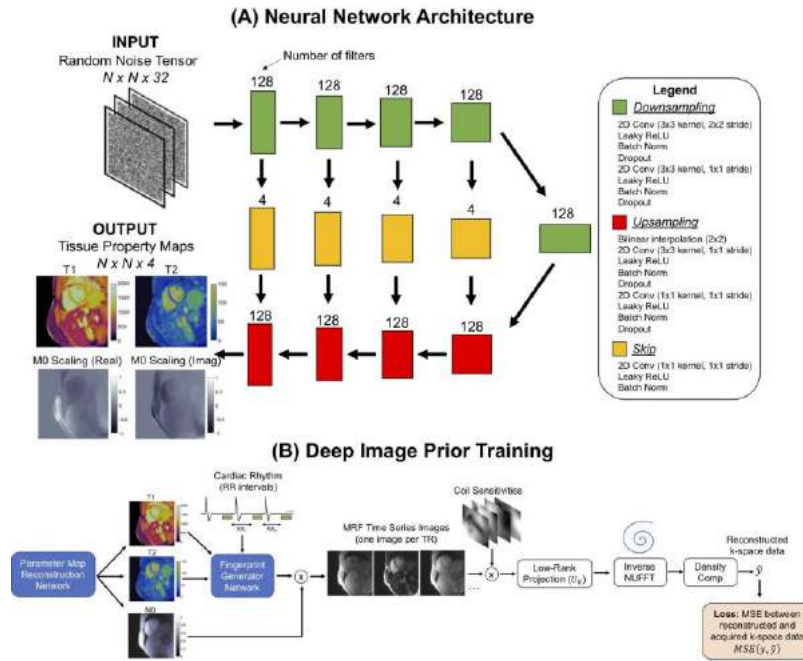
**Results:** Representative maps are shown in Figure 2. The DIP reconstruction successfully reduced noise and aliasing artifacts, with a visible improvement over the comparison methods for the shortened MRF acquisition. T1 and T2 values in the myocardial septum from all subjects are given in Table 1. Lower standard deviations were observed using the DIP



reconstruction. The DIP reconstruction yielded a closer agreement among T1 and T2 values from the long and short MRF acquisitions (Table 1C), likely due to the reduced aliasing artifacts.

**Conclusions:** Using a U-Net trained on a single undersampled dataset, the proposed deep image prior reconstruction for 2D cardiac MRF can reduce noise and aliasing artifacts, which is leveraged to shorten the breathhold time and ECG acquisition window.

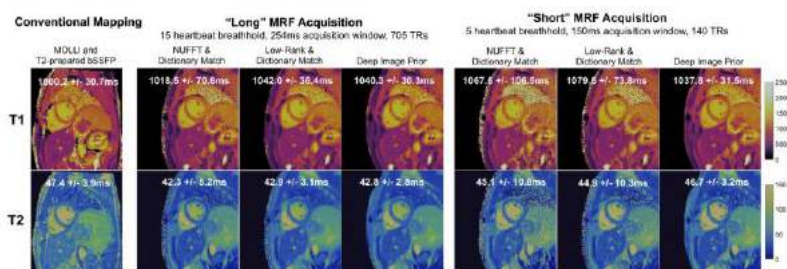
**Figure/Table 1**



**Caption 1**

**Figure 1:** (A) A randomly initialized U-Net is trained in a self-supervised manner on a single undersampled MRF dataset to output T1, T2, and M0 maps. (B) On each epoch of training, the maps are used to calculate the forward encoding model (including a pretrained neural network to output signal evolutions from the maps); the loss is calculated in k-space.

**Figure/Table 2**



## Caption 2

**Figure 2:** Maps in a healthy subject using conventional mapping, MRF with a 15-heartbeat breathhold and 254ms gating window, and MRF with a 5-heartbeat breathhold and 150ms gating window. MRF maps were obtained in three ways: 1) NUFFT and dictionary matching, 2) low-rank reconstruction and dictionary matching, and 3) deep image priors.

## Figure 3

(A)  $T_1$  (ms)

Subject	NUFFT + Dictionary		Low Rank + Dictionary		Deep Image Prior		MOLLI
	705 TRs	140 TRs	705 TRs	140 TRs	705 TRs	140 TRs	
1	1023 $\pm$ 66	1068 $\pm$ 107	1050 $\pm$ 31	1059 $\pm$ 78	1047 $\pm$ 18	1037 $\pm$ 23	1000 $\pm$ 31
2	1107 $\pm$ 97	1099 $\pm$ 200	1073 $\pm$ 39	962 $\pm$ 75	1046 $\pm$ 18	1035 $\pm$ 39	991 $\pm$ 50
3	1026 $\pm$ 90	1118 $\pm$ 155	1054 $\pm$ 46	1044 $\pm$ 98	1028 $\pm$ 25	1068 $\pm$ 41	980 $\pm$ 30
4	1069 $\pm$ 75	1104 $\pm$ 185	1077 $\pm$ 40	1062 $\pm$ 71	1074 $\pm$ 42	1054 $\pm$ 33	1010 $\pm$ 43
5	1037 $\pm$ 82	1138 $\pm$ 179	1026 $\pm$ 24	1046 $\pm$ 63	1024 $\pm$ 23	1027 $\pm$ 27	1016 $\pm$ 50

(B)  $T_2$  (ms)

Subject	NUFFT + Dictionary		Low-Rank + Dictionary		Deep Image Prior		T2-prep bSSFP
	705 TRs	140 TRs	705 TRs	140 TRs	705 TRs	140 TRs	
1	42.3 $\pm$ 5.4	46.1 $\pm$ 10.0	42.5 $\pm$ 3.1	45.9 $\pm$ 10.1	42.7 $\pm$ 2.7	46.9 $\pm$ 1.8	47.2 $\pm$ 3.9
2	41.3 $\pm$ 4.2	46.2 $\pm$ 12.4	41.0 $\pm$ 2.2	46.1 $\pm$ 7.1	39.9 $\pm$ 1.9	41.2 $\pm$ 3.2	47.0 $\pm$ 3.9
3	36.7 $\pm$ 4.5	61.6 $\pm$ 21.0	38.2 $\pm$ 2.7	41.5 $\pm$ 9.0	38.3 $\pm$ 3.0	45.1 $\pm$ 3.9	38.3 $\pm$ 3.0
4	36.0 $\pm$ 3.1	33.3 $\pm$ 9.7	38.4 $\pm$ 1.9	41.3 $\pm$ 5.7	37.1 $\pm$ 1.7	37.4 $\pm$ 2.3	45.5 $\pm$ 2.9
5	36.9 $\pm$ 4.9	48.2 $\pm$ 15.3	40.7 $\pm$ 1.6	42.9 $\pm$ 8.2	39.5 $\pm$ 1.6	38.5 $\pm$ 2.1	48.3 $\pm$ 4.1

(C) Bland-Altman Statistics (Short vs Long Acquisition)

	NUFFT + Dictionary	Low-Rank + Dictionary	Deep Image Prior
<b>T1</b>	<b>52.9ms</b> (-34.4, 140.2)ms	<b>-21.4ms</b> (-123.2, 80.5)ms	<b>0.4 ms</b> (-45.5, 46.4)ms
<b>T2</b>	<b>8.4ms</b> (-11.8, 28.7)ms	<b>3.4ms</b> (1.3, 5.4)ms	<b>2.3ms</b> (-3.8, 8.5)ms

## Caption 3

**Table 1:** (A) Septal  $T_1$  and (B)  $T_2$  from all subjects using long and short MRF scans with different reconstructions, and conventional mapping. (C) Bland-Altman statistics comparing  $T_1$  and  $T_2$  from short vs long MRF acquisitions. Values reported as bias (95% lower, 95% upper limit of agreement). Positive bias indicates higher values using the short acquisition.

## Bibliographic References

[5] Hamilton JI, Seiberlich N. Machine Learning for Rapid Magnetic Resonance Fingerprinting Tissue Property Quantification. Proc IEEE. 2020;108(1):69-85., [4] Lempitsky V, Vedaldi A, Ulyanov D. Deep Image Prior. In: Proceedings of the IEEE Computer Society Conference on Computer Vision and Pattern Recognition. IEEE Computer Society; 2018:9446-9454., [3] Fang Z, Chen Y, Liu M, et al. Deep Learning for Fast and Spatially-

Constrained Tissue Quantification from Highly-Accelerated Data in Magnetic Resonance Fingerprinting. IEEE Trans Med Imaging. 2019;38(10):2364-2374., [2] Hamilton JI, Currey D, Rajagopalan S, Seiberlich N. Deep learning reconstruction for cardiac magnetic resonance fingerprinting T1 and T2 mapping. Magn Reson Med. 2021;85(4):2127-2135., [1] Ma D, Gulani V, Seiberlich N, et al. Magnetic resonance fingerprinting. Nature. 2013;495(7440):187-192.

Speaker: J. Hamilton

Category: Parametric Mapping, Nonlinear Reconstruction, Tissue Characterization

000419

## Comparison of Clinical and CMR Biomarkers in Children Presenting with Acute Chest Pain and Elevated Troponins – Pre-COVID and Post COVID Vaccine

A. Gulhane \* (1); B. Soriano (2); M. Ferguson (3); E. Romberg, (4); L. Stanescu (4); S. Bhutta (1); R. Otto, (4); E. Caris, (5); S. Mallenahalli Chikkabyrappa, (5); M. Portman (5); H. Litt (6); S. Buddhe (5)

(1) Radiology, University of Washington, Seattle, United States of America; (2) Pediatrics, Seattle Children's Hospital, Seattle, United States of America; (3) Pediatric radiology, Seattle Children's Hospital, Seattle, United States of America; (4) Radiology, Seattle Children's Hospital, Seattle, United States of America; (5) Cardiology, Seattle Children's Hospital, Seattle, United States of America; (6) Radiology, University of Pennsylvania, Philadelphia, United States of America

### Abstract

**Background:** Myocarditis presenting as isolated acute chest pain with elevated troponins in previously asymptomatic children is rare. Recently this has been reported in association with COVID-19 vaccines. We aim to compare clinical biomarkers and CMR imaging features in children who presented with these symptoms in the pre-COVID era and post COVID vaccine.

**Methods:** This is a single center retrospective study. Children presenting with isolated chest pain and elevated troponin were divided into two groups – pre-COVID group (Group I – 09/11/2012 to 09/29/2019) and post-COVID vaccine (group II- 05/04/2021 to 08/13/2021, children presenting within 2-3 days post vaccine). Clinical and baseline CMR (performed within 30 days of symptoms) data were collected. CMR data including tissue mapping, late gadolinium enhancement (LGE) quantification and strain analysis were performed using cvi42® (Circle Cardiovascular Imaging).

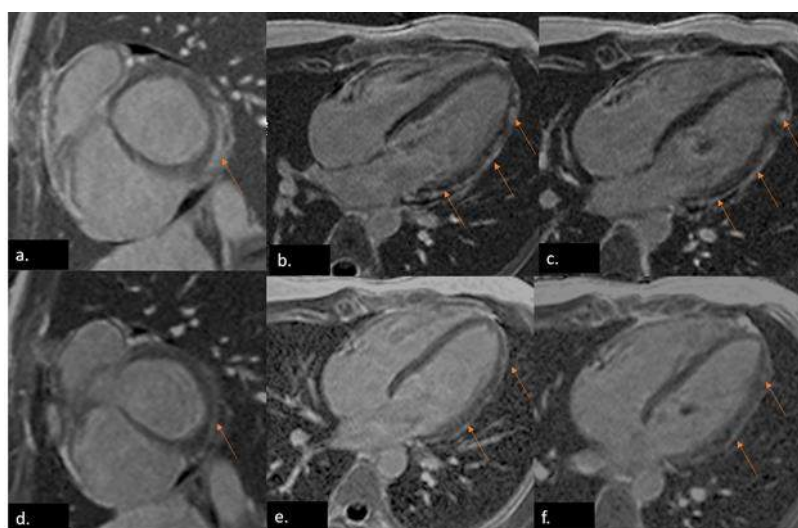
### Results:

Group I included 21 and group II 17 patients. There was no significance difference in mean age (15.4 vs 14.8 years), sex (males 85% vs 94%), highest average troponin value (12 vs 9.2 ng/mL), ECG ST segment abnormalities (47.6% vs 52.9% patients), LVEF (  $54.0 \pm 8.9\%$  vs  $54.5 \pm 5.0\%$  ) in group I and II respectively. On CMR, subepicardial LGE was present in majority of patients (90% in group I vs. 82% in group II). Enhanced myocardial volume (%LGE) was higher in group I ( $25.3 \pm 13.9\%$ ) compared to ( $10.3 \pm 8.9\%$ ) in group II. Significant difference with higher iEDV (indexed end-diastolic volume), BNP ( $221 \pm 297$  vs  $38 \pm 25$  pg/ml) and %LGE was noted in group I, BSA was higher in group II (P <0.05). Although elevated in both groups, patients in group II had lower mean native T1 values (all patients) compared to group I (available in 13 patients) ( $1070 \pm 30$  vs.  $1102 \pm 85.46$  msec) (p=0.15). T2 values were only available in the post-vaccine group and found to be mildly elevated to  $54 \pm 4$ ms Abnormal LV strain was noted in both groups with no significant difference between groups (LV global longitudinal strain  $-16.8 \pm 3.1$  in group I vs  $-16.0 \pm 1.48$  in group II, p=0.33).

2/3 patients with follow up CMR (average duration 14.4 months) showed persistent LV LGE in group I and stable LVEF. However, follow up CMR in 3 patients in group II (average duration 3 months) showed complete/near complete resolution of LGE and improved LVEF in all 3 patients.

**Conclusions:** Previously healthy children presenting with isolated acute chest pain and elevated troponins after COVID vaccine, though rare, appear to have no significant difference in most demographics and troponins levels compared to patients presenting with similar symptoms prior to COVID 19 pandemic. Post vaccine group had lower enhanced myocardial volume with no significant differences in other CMR parameters. Long term multicenter studies are needed to see if these smaller elevation in T1, T2, and BNP as well as return to normal of LVEF and disappearance of LGE in all of the limited follow-up cases would suggest a more benign course in children post-COVID vaccine. Follow up CMR imaging would be vital in predicting long term outcomes.

**Figure/Table 1**



**Caption 1**

17yr male presented 2 days after receiving COVID vaccine with acute chest pain, elevated troponins of 11.1ng/ml. LVEF was 51%, Native T1 value 1123ms and ECV 0.31. CMR LGE PSIR (a,b,c) showing subepicardial LGE upto 7.8%. Near complete resolution of LGE on follow up CMR after 3.6 months (d,e,f).

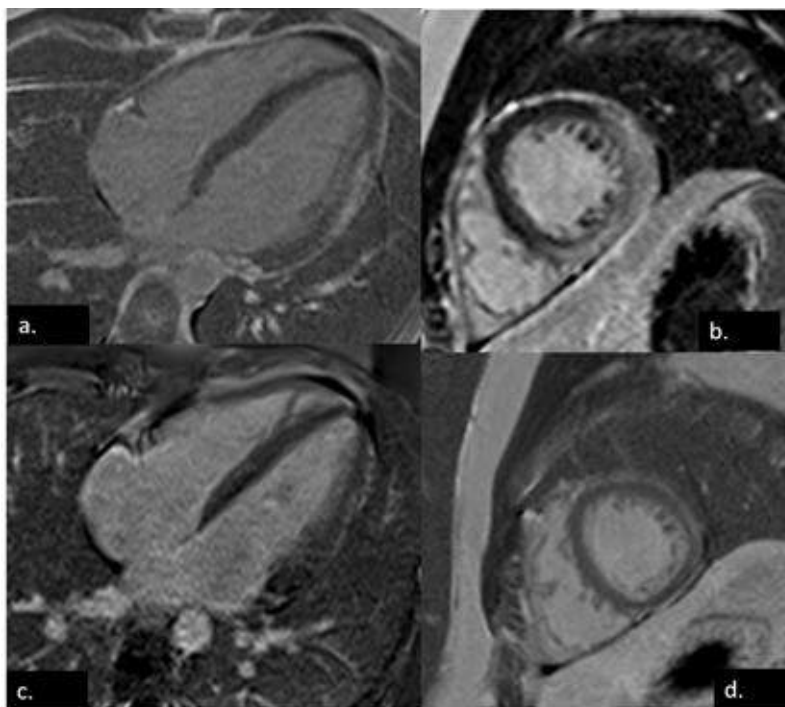
**Figure/Table 2**

	<b>Pre Covid</b>		
<b>Demographics</b>	<b>Myocarditis</b>	<b>Post Covid Vaccine</b>	<b>P value</b>
	<b>(n=21)</b>	<b>Myocarditis (n=17)</b>	

Age	15.4 ± 1.6	14.8 ± 1.5	0.2451
Sex (Males)	85.71%	94%	0.4079
Body surface area (m2)	1.34 ± 0.2	1.69 ± 0.22	< <b>0.0001</b>
CMR dates	09/11/2012 to 09/29/2019	05/04/2021 to 08/13/2021	-
ECG			
ST segment abnormalities	10/21	9/17	0.7471
Non-specific	11/21	5/17	
Normal	-	3/17	0.1594
Highest troponin value (ng/ml)	12 ± 8.5	9.2 ± 4.8	0.2345
BNP (pg/ml)	221 ± 297	38 ± 25	<b>0.0161</b>
<b>CMR findings</b>	<b>Pre Covid myocarditis (n=21)</b>	<b>Post Covid vaccine myocarditis (n=17)</b>	<b>P value</b>
EDV (ml)	160 ± 41	153 ± 29	0.5567
iEDV (ml/m2)	118 ± 22	89 ± 11	< <b>0.0001</b>
SV (ml)	73 ± 24	82 ± 15	0.1867
iSV (ml/m2)	64 ± 16	48 ± 7.3	<b>0.0005</b>
EF			
Normal	16/21	11/17	0.4435
Mild decline	2/21	4/17	0.2455
Moderate decline	3/21	2/17	0.8216
LVEF (%)	54.03 ± 8.9 (n=21)	54.51 ± 5.00	0.8440
Edema	21/21	16/17	0.2661
LGE site			

Subepicardial	19	14	0.4676
Midmyocardial to subepicardial	2	1	0.6773
No enhancement	0	2	0.1111
LGE % volume (5std)	25.29 ± 13.88 (n= 21)	10.32 ± 8.87	<b>P = 0.0005</b>
Native T1 mapping global average (ms)	1102 ± 85.46 (n=13)	1070 ± 30	<b>P = 0.1594</b>
ECV average	0.29± 0.05 (n=13)	0.26 ± 0.02	0.0319
Global longitudinal strain (GLS)%	-16.8 ± 3.1 (n=21)	-16.0 ± 1.48	0.3356
Global circumferential strain (GCS)%	-18.2 ± 5.5 (n=21)	-18.1 ± 2.2	0.9443
Global radial strain (GRS)%	29.6 ± 17.8 (n=21)	29.4 ± 3.8	0.9641

**Figure 3**



**Caption 3**

17 yr. male presented to ED days pre-COVID pandemic with acute chest pain, elevated troponin of 14.2ng/ml and nonspecific ECG findings. LGE CMR showed 22% subepicardial LGE in inferior and lateral LV wall, LVEF 57%, native T1 value 1171 ms and ECV 0.31. Treatment with IVIG and steroids showed significant resolution of LGE 6 months later.

### **Bibliographic References**

Peng J, Zhao X, Zhao L, et al. Normal Values of Myocardial Deformation Assessed by Cardiovascular Magnetic Resonance Feature Tracking in a Healthy Chinese Population: A Multicenter Study. *Front Physiol.* 2018;9:1181. Published 2018 Sep 3. doi:10.3389/fphys.2018.01181

Speaker: A. Gulhane

Category: Imaging Biomarkers, Myocarditis, Children



**Low-Rank Deep Image Prior Reconstruction for Real-Time Cine Imaging at 1.5 and 0.55 Tesla**

J. Hamilton \* (1)

(1) Radiology, University of Michigan, Ann Arbor, United States of America

**Abstract**

**Background:** Deep learning can enable accelerated cine MRI with reduced noise and artifacts [1], which may be especially useful to counter lower SNR, suboptimal coil geometry, and lower coil count on 0.55T scanners. Neural networks usually require training on many datasets. However, these are not readily available at 0.55T, are time-consuming to acquire, and may produce hallucinations. An alternative paradigm is deep image priors (DIP) [2], whereby a randomly initialized network is trained to reconstruct a single undersampled dataset using a forward model of the imaging physics. While DIP has been applied to real-time cine MRI at 1.5T [3], here we propose to combine the advantages of DIP with low-rank subspace modeling for free-breathing ungated non-Cartesian cine MRI at both 1.5T and 0.55T.

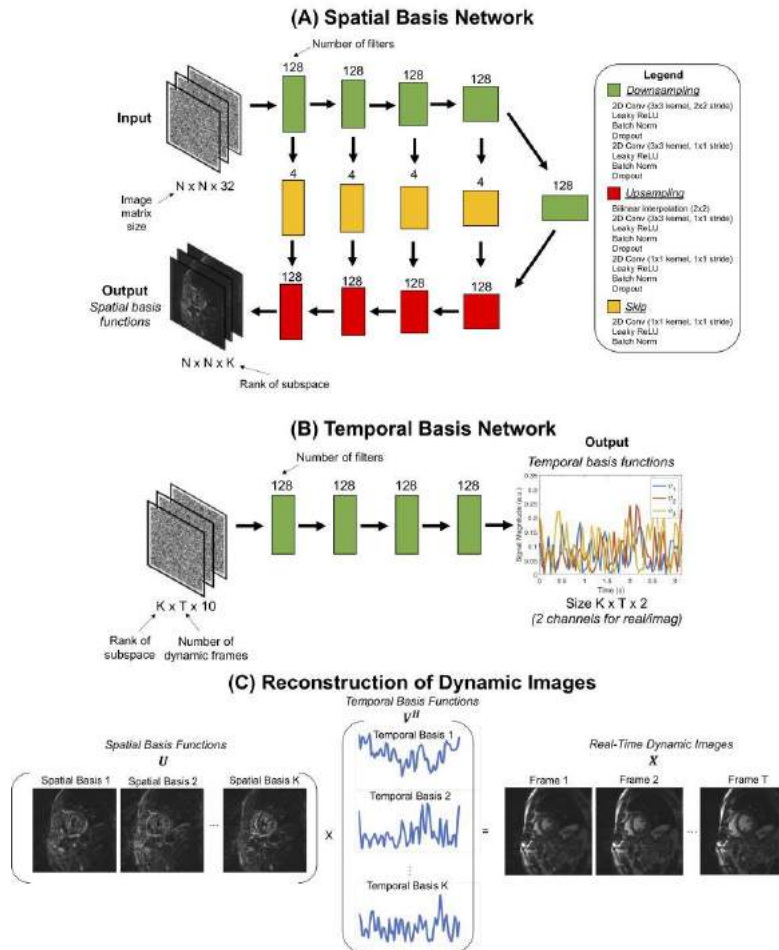
**Methods:** The DIP framework uses the structure of a convolutional neural network (CNN) to remove noise and artifacts, rather than learning on a large training set [2]. We adapted the DIP framework for real-time non-Cartesian cine MRI with low-rank subspace modeling. Using a single undersampled dataset, randomly initialized networks are trained to output dynamic images consistent with the acquired k-space data (Figure 1). Two subnetworks are used, a U-Net that outputs spatial basis functions and a CNN that outputs temporal basis functions of rank  $K$ , which are multiplied to yield dynamic images. The input to each subnetwork is a random noise tensor. During training, 5 of the output image frames are randomly selected as a mini-batch, multiplied by coil sensitivities, and sampled in k-space using an inverse NUFFT operation. The loss function is the MSE between reconstructed and acquired k-space data after density compensation. All experiments used 2D bSSFP scans with 192x192 matrix, 300mm<sup>2</sup> FOV, 50ms/frame, and 1.6x1.6x8.0mm<sup>3</sup> resolution. First, a breathheld and ECG-gated Cartesian cine dataset collected at 1.5T was retrospectively undersampled using golden angle radial sampling with 18 spokes per frame ( $R=16.7$  with respect to Cartesian). Low-rank DIP with rank  $K=20$  was compared to NUFFT gridding, compressed sensing with temporal total variation (GRASP) [4], and compressed sensing with low-rank modeling (GRASP-Pro, 64x64 initial reconstruction, rank 20) [5] using nRMSE and SSIM. Second, real-time free-breathing ungated data were collected in 1 volunteer and 2 patients at 1.5T (golden angle radial, 18 spokes/frame, FA=70deg, TR=3.1ms,  $R=16.7$ ) and 3 volunteers at 0.55T (variable density spiral, 6 arms/frame,  $R=8$ , FA=110deg, TR=8.1ms). Single-slice ejection fraction (EF) measurements were compared among all methods.

**Results:** In simulations, low-rank DIP was superior (SSIM/nRMSE 0.965/0.035) to NUFFT gridding (0.812/0.200), GRASP (0.960/0.043) and GRASP-Pro (0.953/0.044). Real-time images in a patient with suspected pericarditis at 1.5T and a healthy subject at 0.55T are shown in Figure 2. Low-rank DIP suppressed undersampling artifacts and noise; qualitative improvement was especially prominent at 0.55T. EF measurements are reported in Table 1.

Real-time EF values using low-rank DIP agreed with those using GRASP and GRASP-Pro at both field strengths and with the reference breathheld and gated EF values at 1.5T.

**Conclusions:** A low-rank deep image prior reconstruction that is trained using a single undersampled dataset can enable real-time non-Cartesian cine imaging at 1.5T and 0.55T.

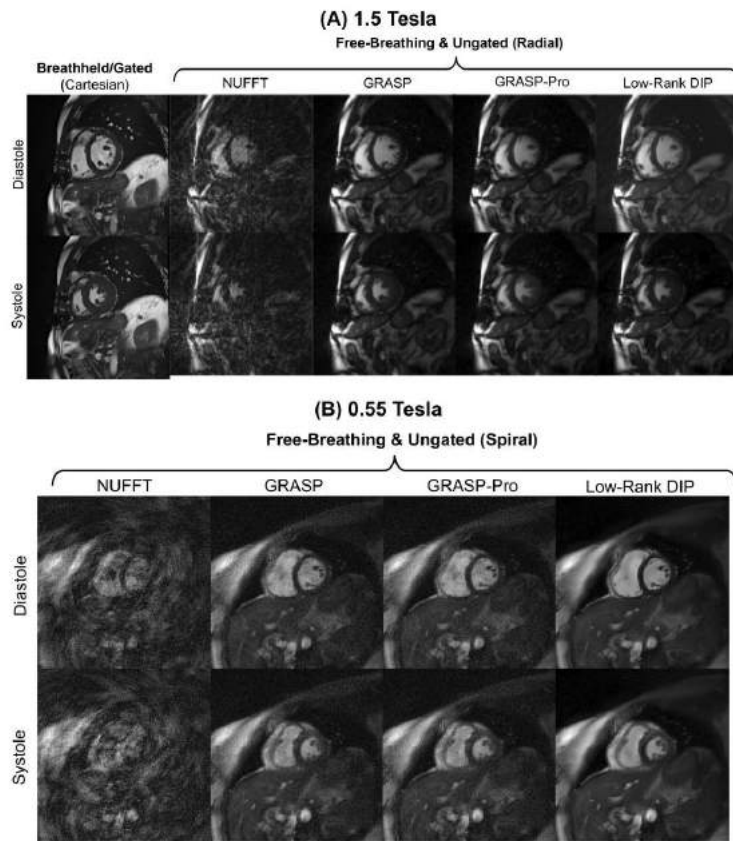
**Figure/Table 1**



**Caption 1**

**Figure 1:** (A) A U-Net takes a random noise tensor as input and outputs spatial basis functions. (B) A network with 4 convolutional layers outputs the temporal basis functions. (C) The spatial and temporal basis functions are multiplied to yield dynamic images. Both subnetworks are trained to ensure the images are consistent with acquired k-space data.

**Figure/Table 2**



## Caption 2

**Figure 2:** (A) Real-time cine images at 1.5T in a patient with suspected pericarditis using golden angle radial sampling ( $R=16.7$ , 50ms/frame,  $1.6 \times 1.6 \times 8.0 \text{ mm}^3$ ) using NUFFT gridding, GRASP, GRASP-Pro, and low-rank DIP. (B) Real-time cine images at 0.55T in a healthy subject with golden angle spiral sampling ( $R=8$ , 50ms/frame,  $1.6 \times 1.6 \times 8.0 \text{ mm}^3$ ).

## Figure 3

**(A) 1.5 Tesla**

Subject	Breathheld/Gated Cartesian	Real-Time GRASP	Real-Time GRASP-Pro	Real-Time Low-Rank DIP
1	73.2%	71.4%	71.8%	71.1%
2	63.1%	60.3%	61.1%	59.5%
3	73.7%	72.8%	70.8%	72.4%

**(B) 0.55 Tesla**

Subject	Real-Time GRASP	Real-Time GRASP-Pro	Real-Time Low-Rank DIP
4	62.5%	63.7%	61.6%
5	54.4%	56.2%	55.1%
6	71.4%	67.8%	73.4%

### Caption 3

**Table 1:** Single-slice EF measurements. (A) EF from 3 subjects at 1.5T using a reference breathheld and ECG-gated Cartesian cine scan, and real-time cine imaging with golden angle radial sampling reconstructed using GRASP, GRASP-Pro, and low-rank DIP. (B) EF from 3 different subjects at 0.55T using real-time cine with golden angle spiral sampling.

### Bibliographic References

[5] Feng L, Wen Q, Huang C, Tong A, Liu F, Chandarana H. GRASP-Pro: imProving GRASP DCE-MRI through self-calibrating subspace-modeling and contrast phase automation. *Magn Reson Med*. 2020;83(1):94-108., [4] Feng L, Grimm R, Block KT obias, et al. Golden-angle radial sparse parallel MRI: combination of compressed sensing, parallel imaging, and golden-angle radial sampling for fast and flexible dynamic volumetric MRI. *Magn Reson Med*. 2014;72(3):707-717., [3] Yoo J, Jin KH, Gupta H, Yerly J, Stuber M, Unser M. Time-Dependent Deep Image Prior for Dynamic MRI. *IEEE Trans Med Imaging*. 2021:1., [2] Lempitsky V, Vedaldi A, Ulyanov D. Deep Image Prior. In: *Proceedings of the IEEE Computer Society Conference on Computer Vision and Pattern Recognition*. IEEE Computer Society; 2018:9446-9454., [1] Sandino CM, Lai P, Vasanaawala SS, Cheng JY. Accelerating cardiac cine MRI using a deep learning-based ESPIRiT reconstruction. *Magn Reson Med*. 2021;85(1):152-167.

Speaker: J. Hamilton

Category: Nonlinear Reconstruction, Cine Imaging, Real Time

**Impact of Respiratory Phases on Cardiac Output Quantification**

P. Chandrasekaran \* (1); C. Chen (2); K. Gil, (3); M. Tong (3); O. Simonetti (3); R. Ahmad (2)

(1) Davis Heart and Lung Research Institute, The Ohio State University, Columbus, United States of America; (2) Biomedical engineering, The Ohio State University, Columbus, United States of America; (3) Cardiovascular medicine, The Ohio State University, Columbus, United States of America

**Abstract**

**Background:** Real-time (RT) free-breathing cardiac MRI acquisition is routinely used in patients with poor respiratory control or arrhythmias. With advanced acquisition and reconstruction techniques, the image quality of RT is now comparable to that of breath-held segmented imaging. However, for accurate quantification of cardiac output, the effect of respiratory phase should be considered [1]. The purpose of this research is to evaluate the impact of respiratory phase on cardiac output measured with RT cine and flow.

**Methods:** Short-axis (SAX) stacks of breath-held segmented cine were acquired at the end expiratory phase in 23 patients (12 female,  $50 \pm 15$  years). Free-breathing RT cine, based on a balanced steady-state free-precession sequence, was performed for 10 slices in the same patient cohort in the same orientation. Breath-held segmented flow and free breathing RT flow was performed in the aortic view in 58 (32 female,  $47 \pm 16$  years) patients. All the patients were scanned on a 1.5 T scanner (MAGNETOM Sola, Siemens Healthcare, Erlangen, Germany). Some of the acquisition parameters are summarized in Table 1. The RT images were reconstructed inline using a Gadgetron [2] based implementation of SCoRe [3, 4], which is a parameter-free SENSE-based reconstruction method.

Respiratory signal was extracted using a principal component analysis based semi-automated method, with manual sign correction for RT flow images and automatic sign correction for RT cine images [5]. Using this respiratory signal, a random heartbeat and a heartbeat corresponding to the peak expiratory (PE) phase were extracted from the RT image series.

The heartbeats from the breath-held acquisition as well as random and PE heartbeats from RT were used to analyze left ventricular (LV) and right ventricular (RV) function and aortic hemodynamics. We extracted ejection fraction (EF) for both chambers from cine images, and peak flow rate and peak velocity from flow images. The images were analyzed semi-automatically in NeoSoft (Pewaukee, WI, USA).

**Results:** Figure 1 shows the agreements of the RT heartbeats with the reference for EF in both ventricles. Figure 2 shows the agreements of the RT heartbeats with the segmented reference for peak velocity and peak flow rate. For cardiac function using cine imaging, the quantification at PE shows a better agreement with the reference compared to that at a random respiratory phase. The limits of agreement (LOA) improve from (-1.42, 11.03) to (-2.92, 7.3) for LVEF (%) and from (-5.71, 13.33) to (-5.61, 7.53) for RVEF (%). The bias reduces from 4.81 to 2.19 for LVEF and from 3.81 to 0.93 for RVEF. Likewise, in flow imaging, the limits of agreement change from (-7.95, 33.74) to (-11.93, 28.43) for peak velocity (cm/s) and from

(-47.67, 91.09) to (-66.34, 78.4) for peak flow rate (ml/s) and bias reduces from 12.89 to 8.25 for peak velocity and from 21.71 to 6.03 for peak flow rate.

**Conclusion:** In this study, we compared RT cine and flow at random and peak expiration phases with breath-held segmented reference. The impact of respiratory phase on cardiac function was observed in both cine and flow parameters, with PE heartbeat offering a better agreement with the breath-held standard.

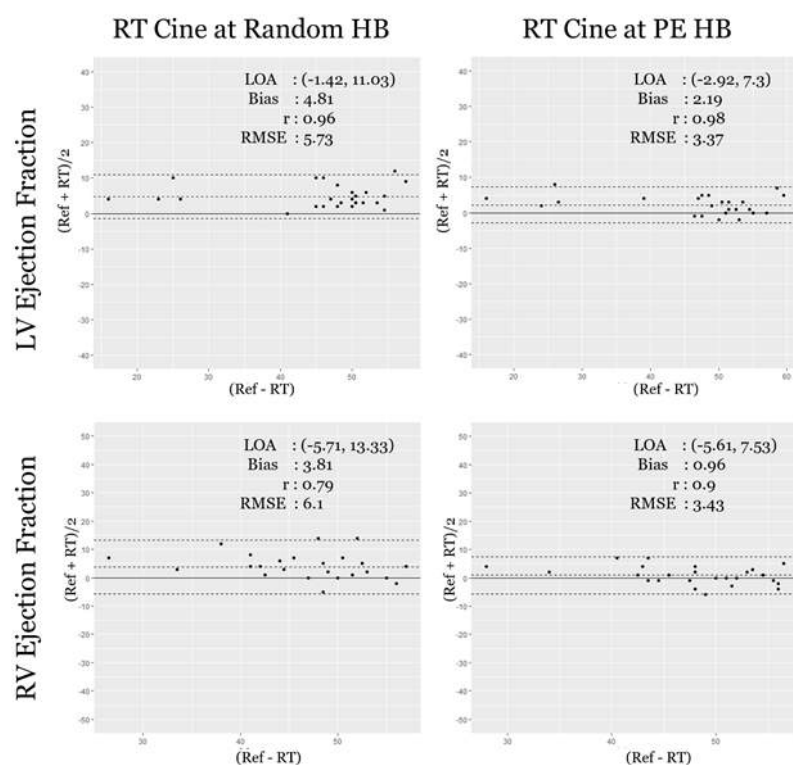
**Figure/Table 1**

	No. of Patients	Sequence	TR (ms)	TE (ms)	Acceleration Factor	Spatial Resolution	Temporal Resolution (ms)	Flip Angle	Scan Time
BH Seg. Cine (Reference)	26	balanced SSFP	2.59 – 2.93	1.09 – 1.21	2	(1.4 – 2) x (1.3 – 2) mm <sup>2</sup>	44 – 72	55° – 72°	(5 – 7) heartbeats
RT Cine			2.61 – 2.81	1.14 – 1.23	6.5 – 9.3	(2 – 2.8) x (2.1 – 3) mm <sup>2</sup>	46.9 – 50.9	70°	10 s/slice
BH Seg. Flow (Reference)	58	GRE	4.23 – 4.83	2.26	2	2 x 2.9 mm <sup>2</sup>	42 – 76	15°	(6 – 10) heartbeats
RT Flow			4.38 – 4.52	2.34 – 2.54	15.7 – 18	(2.6 – 2.7) x (2 – 3.3) mm <sup>2</sup>	52 – 54	12°	10 s/slice

**Caption 1**

Table 1: Acquisition parameters for cine and flow imaging. Here, BH stands for breath-held.

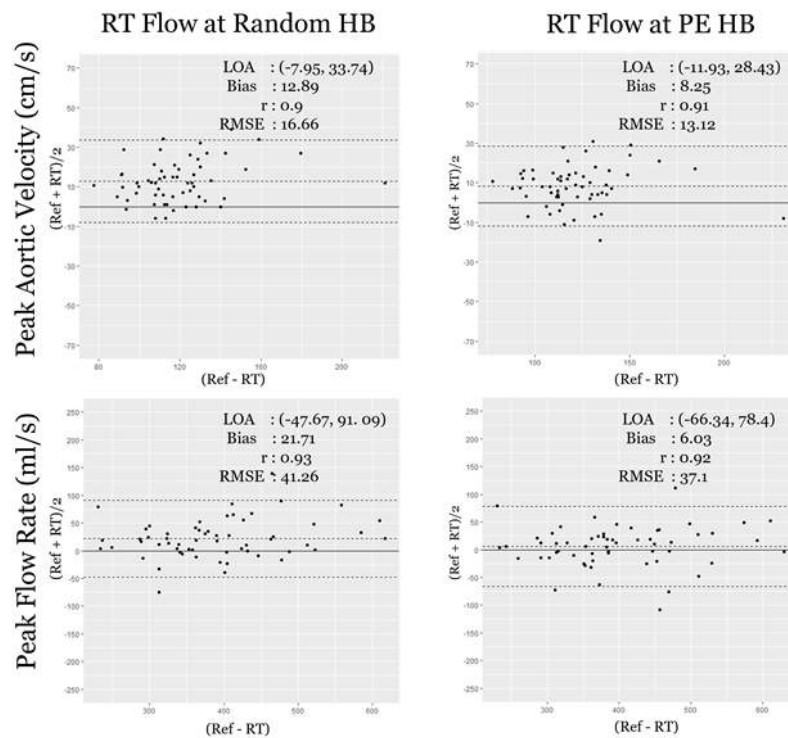
**Figure/Table 2**



**Caption 2**

Figure 1: Cardiac function quantification results from breath-held segmented (Ref) and real-time (RT) cine. The top row shows the Bland-Altman plots of left ventricular ejection fraction (LVEF) for heartbeats at random and peak expiration phases. The bottom row shows this comparison for right ventricular ejection fraction (RVEF).

**Figure 3**



**Caption 3**

Figure 2: Cardiac flow quantification results from breath-held segmented (Ref) and real-time (RT) flow images. The top row shows the Bland-Altman plots of peak aortic velocity (cm/s) for heartbeats at random and peak expiration phases. The bottom row shows this comparison for peak flow rate (ml/s).

### Bibliographic References

[5] C. Chen et.al, IEEE 17th ISBI 2020. p. 1–4., [4] C. Chen et.al, SCMR2020 #751158., [1] Guido Claessen et al., Am J Physiol Heart Circ Physiol 2014 Mar;306(6):H816-24., [2] Michael Schacht Hansen et al., Magn Reson Med. 69:1768–1776 (2013)., [3] C. Chen et al., Magn Reson Med. 81:3875–3887 (2019).

Speaker: P. Chandrasekaran

Category: Respiratory Motion, Real Time, Cardiac Output



**Synthetic Multicontrast LGE from Post-Contrast Cardiac MR Fingerprinting Maps**

I. Rashid \* (1); V. Rajagopalan (2); S. Al-Kindi (2); S. Rajagopalan (2); N. Seiberlich (3); J. Hamilton (3)

(1) Cardiology, Case Western Reserve University, Euclid Avenue, Cleveland, United States of America; (2) Cardiology, University Hospitals Cleveland Medical Center, Cleveland, United States of America; (3) Radiology, University of Michigan, ANN ARBOR, United States of America

**Abstract**

**Background:** Conventional late gadolinium enhancement (LGE) imaging is lengthy and operator-dependent, with scar conspicuity depending on proper selection of inversion time (TI) [1]. Synthetic LGE has been proposed using post-contrast MOLLI T1 maps [2] but has been limited to bright-blood imaging, where it can be difficult to identify subendocardial scar [3,4]. We introduce a Synthetic Multicontrast LGE method where images with different contrast weightings are derived from a single post-contrast MR Fingerprinting (MRF) scan.

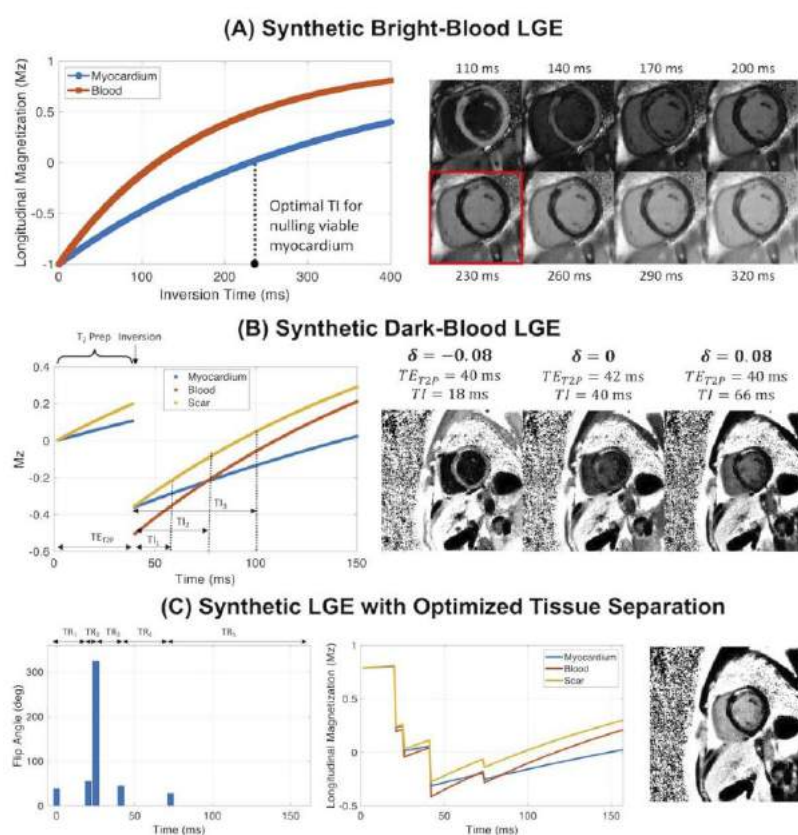
**Methods:** Fifteen patients with ischemic cardiomyopathy were scanned at 1.5T (Aera, Siemens MAGNETOM). Conventional LGE was performed 10min post-injection (1.4x1.4x8.0mm<sup>3</sup>, TR/TE 2.4/1.2ms, IR-bSSFP, FA 45deg) following a TI scout. Post-contrast 2D MRF scans (1.6x1.6x8.0mm<sup>3</sup>, FA 4-25deg, TR/TE 5.3/1.4ms) were collected at a medial short-axis slice during a breathhold [5]. T1 and T2 maps were obtained using a low-rank subspace reconstruction and dictionary matching. Bloch simulations were performed using the maps to generate synthetic multicontrast LGE images as follows (Figure 1). First, magnitude inversion recovery (MagIR) images were simulated from the T1 map with automated TI selection to null viable myocardium. Second, T2-prepared inversion recovery (T2IR) images were simulated using both T1 and T2 maps. Scan parameters were automatically selected using T1 and T2 measured for each patient in viable myocardium and blood. Different degrees of blood suppression were obtained using a tunable coefficient  $\delta$ , with  $\delta < 0$  yielding dark blood and gray viable myocardium, and vice versa for  $\delta > 0$ , similar to related work [4]. Third, a novel optimized contrast image was derived from both T1 and T2 maps, designed to separate signals from blood, viable myocardium, and scar. This image was calculated by optimizing an arbitrary sequence of  $n$  flip angles and TRs (we empirically use  $n=5$ ). The theoretical contrast between blood, viable myocardium, and scar for each type of synthetic image was calculated in Bloch simulations using T1 and T2 values representative of each tissue (obtained from patient MRF measurements). One blinded cardiologist reader scored all images on a 5-point scale for overall diagnostic confidence. The same reader identified the presence or absence of scar on each image, and sensitivity was calculated on a per-image basis.

**Results:** Synthetic multicontrast LGE images are shown for three ischemic cardiomyopathy patients (Figure 2). As shown in Figure 3A, synthetic MagIR yielded the highest theoretical contrast between myocardium/scar but poorest contrast between blood/scar; the opposite was true for synthetic T2IR sequences, whereas the synthetic optimized contrast achieved a balance of myocardium/scar and blood/scar contrast. Figure 3B shows ratings for diagnostic confidence, with mean scores of 3.3 (reference), 3.6 (MagIR), 2.7 (dark-blood T2IR), 2.5

(gray-blood T2IR), and 3.2 (optimized contrast). Scar was identified for 13/15 patients using reference LGE. Of these patients, the sensitivity for scar using each synthetic image was 0.77 (10/13) MagIR, 0.62 (8/13) dark-blood T2IR, 0.69 (9/13) gray-blood T2IR, and 0.92 (12/13) optimized contrast. On one occasion, standard LGE failed to identify subendocardial anteroseptal scar that was correctly identified with synthetic optimized contrast. On another occasion, subendocardial scar was not identified with optimized synthetic contrast due to the presence of a bright blood pool artifact.

**Conclusions:** Post-contrast MRF can be used to derive LGE images with multiple bright and dark blood contrast weightings from one scan that holds promise for clinical translation.

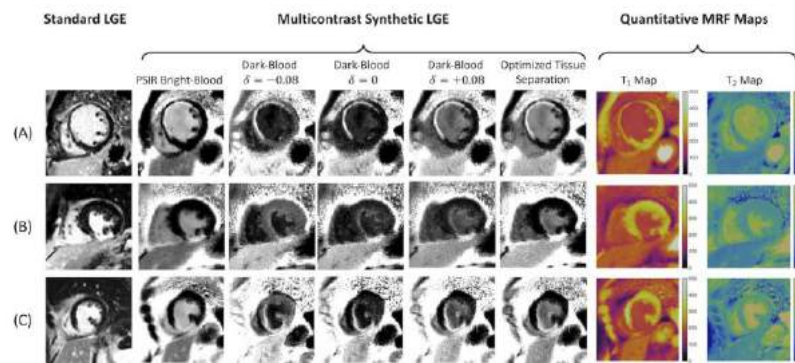
**Figure/Table 1**



**Caption 1**

**Figure 1:** (A) A magnitude inversion recovery image is simulated using the T1 map. (B) Post-contrast T1 and T2 are used to simulate T2-prep inversion recovery scans; the level of blood suppression is controlled by  $\delta$ . (C) A synthetic image with improved separation of scar, viable myocardium, and blood is obtained by optimizing an arbitrary sequence of RF pulses.

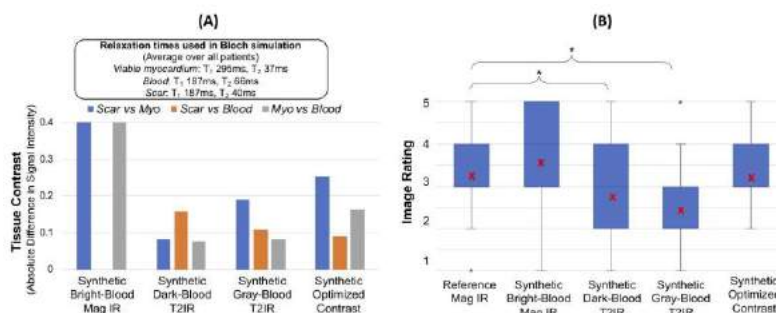
**Figure/Table 2**



**Caption 2**

**Figure 2:** Acquired reference LGE images (left), synthetic multicontrast images (middle), and quantitative post-contrast MRF T1 and T2 maps (right) in three patients with ischemic cardiomyopathy. Patients A and C have subendocardial scarring that is prominent on the synthetic dark-blood images and synthetic images with optimized tissue separation contrast.

**Figure 3**



**Caption 3**

**Figure 3:** (A) The theoretical contrast (defined as the absolute difference in longitudinal magnetization) between different tissues using each synthetic image contrast was calculated using Bloch equation simulations based on post-contrast T1 and T2 values measured in patients. (B) Image quality ratings. Mean scores indicated by red X.  $p < 0.05$  indicated by \*.

## Bibliographic References

[5] Hamilton JI, Pahwa S, Adedigba J, et al. Simultaneous Mapping of T1 and T2 Using Cardiac Magnetic Resonance Fingerprinting in a Cohort of Healthy Subjects at 1.5T. J Magn Reson Imaging. 2020;52(4):1044-1052., [4] Kellman P, Xue H, Olivieri LJ, et al. Dark blood

late enhancement imaging. Journal of Cardiovascular Magnetic Resonance. 2016;18(1):77., [3] Basha T, Roujol S, Kissinger K V, Goddu B, Manning WJ, Nezafat R. Black blood late gadolinium enhancement using combined T(2) magnetization preparation and inversion recovery. Journal of Cardiovascular Magnetic Resonance. 2015;17:O14., [2] Varga-Szemes A, van der Geest RJ, Spottiswoode BS, et al. Myocardial Late Gadolinium Enhancement: Accuracy of T1 Mapping-based Synthetic Inversion-Recovery Imaging. Radiology. 2016;278(2):374-382., [1] Simonetti OP, Kim RJ, Fieno DS, et al. An improved MR imaging technique for the visualization of myocardial infarction. Radiology. 2001;218(1):215-223.

Speaker: I. Rashid

Category: Late Gadolinium Enhancement, Rapid Imaging, Parametric Mapping

000425

## Multiband cine DENSE MRI using a self-calibrated slice-low-rank reconstruction for single-breathhold myocardial strain imaging of the left ventricle

C. Sun \* (1); Y. Wang (2); F. Epstein (2)

(1) Biomedical engineering, University of Virginia, Columbia, United States of America; (2) Biomedical engineering, University of Virginia, Charlottesville, United States of America

### Abstract

**Background:** Accurate and reproducible whole-slice and segmental circumferential strain assessed rapidly in three short-axis slices would provide valuable diagnostic and prognostic information and facilitate an efficient clinical workflow. For DENSE, typically three short-axis slices are acquired with each slice requiring one breathhold (14 heartbeats). Previously, parallel imaging and low-rank methods showed promising results for accelerating DENSE[2]. Building on these, we sought to develop a MB cine DENSE method to acquire three short-axis slices with 2D displacement encoding in a single breathhold.

**Methods:** We developed a spiral cine DENSE sequence with variable flip angle MB excitation, outer volume suppression (OVS), and golden angle-rotation (Figure 1A). We employed CAIPIRINHA phase modulation with MB=4[3] to simultaneously excite three slices using a four spiral interleave acquisition (called MB3+). For the reconstruction, we implemented a self-calibration method to fit non-Cartesian slice-GRAPPA (NCSG) kernels[3] and coil sensitivity maps for each slice (Figure 1B, step 2). The reconstruction employed a non-cartesian slice-low-rank approach based on a recently-developed Cartesian slice-L+S method[4], which enforces MB data consistency, uses in- and through-plane coil information and exploits golden-angle rotation to reduce slice separation artifacts (Figure 1B, step 3). We evaluated the single-breathhold MB DENSE method in 4 human volunteers, where 3 slices with 2D displacement encoding were simultaneously acquired in a single breathhold (14 heartbeats). The slice-low-rank reconstructed images were compared to non-iterative NCSG reconstructed images[3,4] and reference single-band DENSE images at matched slice locations. MRI was performed on a 3T system (Prisma, Siemens) using 24-30 RF receiver channels.

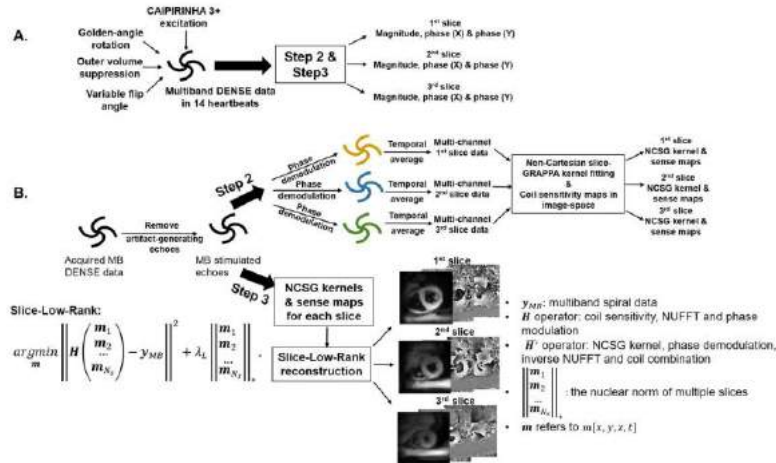
**Results:** Figure 2A illustrates example results from one volunteer, where NCSG, iterative slice-low-rank and reference single-band cine DENSE images at a basal location are shown. Slice-low-rank shows better image quality and is more similar to reference images than NCSG. Figure 2B illustrates example slice-low-rank results and, adjacently, single-band reference images. MB images show image quality similar to single-band images at basal, mid-ventricular and apical locations for both magnitude and phase. Example circumferential strain maps (Ecc) and segmental strain-time curves also show a close correspondence between the single-band and MB slice-low-rank methods (Figure 3A). Correlation and Bland-Altman plots in Figure 3B, and intraclass correlation of 0.98 quantitatively show excellent agreement between single-breathhold MB DENSE and single-band DENSE for all segments and all three slices of four volunteers.

**Conclusions:** The proposed MB spiral cine DENSE acquisition and self-calibrated slice-low-rank reconstruction with MB3+ phase modulation and golden-angle rotation provides single-

breathhold strain imaging of the left ventricle with excellent agreement compared to single-band cine DENSE strain. When combined with fully-automated deep-learning strain analysis[5], these methods can provide accurate and reproducible global and segmental strain imaging within an efficient clinical workflow, requiring the addition of just a single breathhold to any 3T CMR protocol.

**Acknowledgements:** NIH R01HL147104.

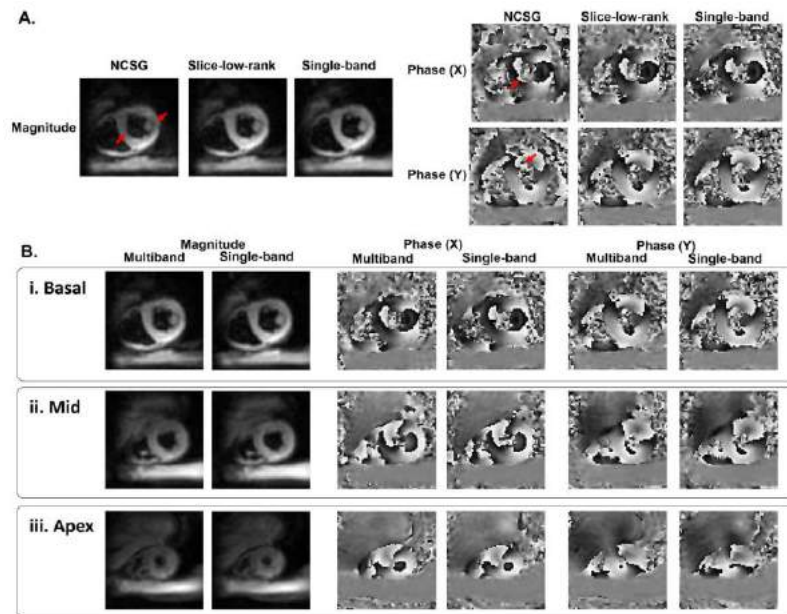
**Figure/Table 1**



**Caption 1**

Schematic diagram of the proposed multiband DENSE acquisition and reconstruction. (A) The pipeline of one single breathhold MB spiral cine DENSE acquisition and reconstruction, and (B) the spiral cine DENSE self-calibration method (step 2) and the reconstruction method (step 3).

**Figure/Table 2**

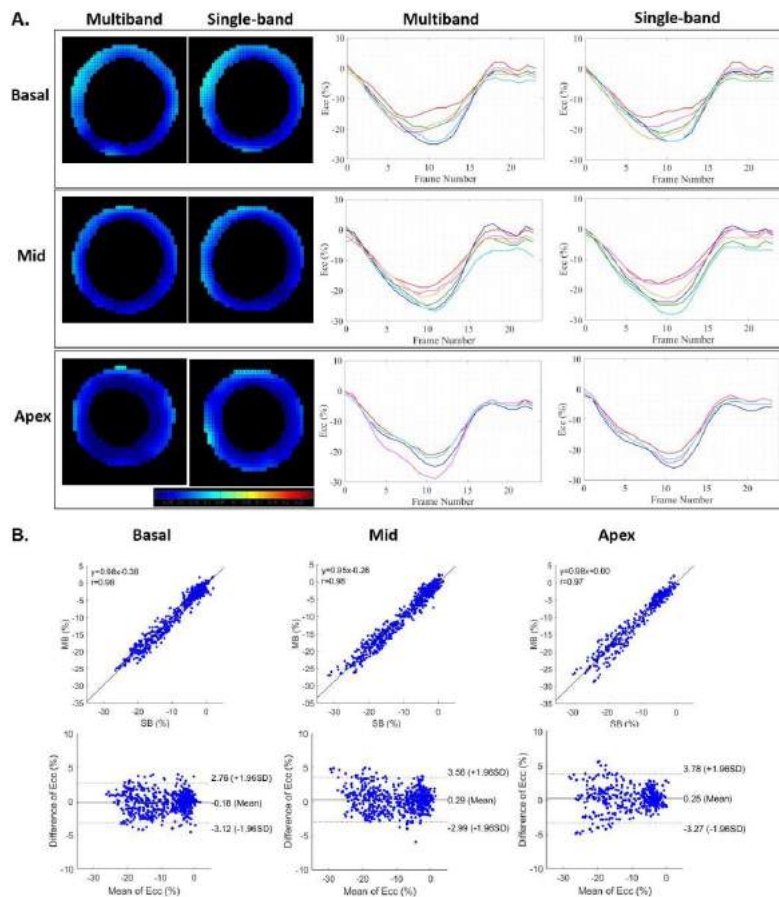


## Caption 2

(A) Comparison of NCSG MB, slice-low-rank MB, and single-band cine DENSE images at a basal location. Red arrows indicate the artifacts. (B) Example images of slice-low-rank reconstructed images and single-band images of three short-axis slices at basal, mid-ventricular, and apical locations. Magnitude and phase images show similar image quality.

**Figure 3**





### Caption 3

(A) Comparison of strain maps and strain-time curves of three short-axis slices at basal, mid-ventricular, and apical locations using single-breathhold multiband and single-band acquisitions. (B) Correlation plots and Bland-Altman plots comparing strain (Ecc) computed from multiband and single-band acquisitions for all segments and slices of four volunteers.

### Bibliographic References

[1] Zhong X, Spottiswoode BS, Meyer CH, Kramer CM, Epstein FH. Imaging three-dimensional myocardial mechanics using navigator-gated volumetric spiral cine DENSE MRI. *Magn Reson Med* 2010;64(4):1089-1097. [2] Chen X, Yang Y, Cai X, Auger D, Meyer CH, Salerno M, Epstein FH. Accelerated two-dimensional cine DENSE cardiovascular magnetic resonance using compressed sensing and parallel imaging. *J Cardiovasc Magn Reson* 2016;18(1):38. [3] Sun C, Yang Y, Cai X, Salerno M, Meyer CH, Weller D, Epstein FH. Non-Cartesian slice-GRAPPA and slice-SPIRiT reconstruction methods for multiband spiral cardiac MRI. *Magnetic Resonance in Medicine*, 83, 1235-1249, 2020. [4] Sun C, Robinson A, Schumann C, Weller D, Salerno M, Epstein FH. Multiband first-pass myocardial perfusion MRI using a slice-low-rank plus sparse model. *ISMRM 28th Annual Meeting, Virtual meeting*, 2020, p.1097. [5] Ghadimi S, Auger DA, Feng X, Sun C, Meyer CH, Bilchick KC, Cao JJ,



Scott AD, Oshinski JN, Ennis DB, Epstein FH. Fully-automated global and segmental strain analysis of DENSE cardiovascular magnetic resonance using deep learning for segmentation and phase unwrapping. J Cardiovasc Magn Reson 2021;23(1):20.

Speaker: C. Sun

Category: Simultaneous Multislice Excitation, DENSE, Rapid Imaging

000427

## Accelerated aortic 4D flow magnetic resonance imaging using compressed sensing in type B aortic dissection: Initial results

O. Kilinc \* (1); S. Chu (1); E. Weiss (1); J. Baraboo (1); A. Maroun (1); N. jin (2); K. chow (3); X. Bi (3); R. Davids (3); C. Mehta (4); C. Malaisrie (4); A. Hoel (5); M. Markl (1); B. Allen (1)

(1) Radiology, Northwestern University Feinberg School of Medicine, Chicago, United States of America; (2) Cardiovascular imaging, Siemens Medical Solutions USA, Inc., Cleveland, United States of America; (3) Cardiovascular imaging, Siemens Medical Solutions USA, Inc., Chicago, United States of America; (4) Cardiac surgery, Northwestern University Feinberg School of Medicine, Chicago, United States of America; (5) Vascular surgery, Northwestern University Feinberg School of Medicine, Chicago, United States of America

### Abstract

**Background:** 4D flow MR imaging can quantify *in vivo* aorta hemodynamic parameters. However, standard aorta 4D flow acquisitions can take 10-15 minutes, limiting their translation into clinical practice. Compressed sensing (CS) acceleration can significantly reduce scan time, but the effects of undersampling and CS reconstruction on 4D flow hemodynamic parameter quantification is not well understood. We aimed to evaluate the reliability of highly accelerated CS 4D flow MRI for the quantification of aortic flow dynamics in healthy volunteers and patients with chronic type B aortic dissection (cTBAD).

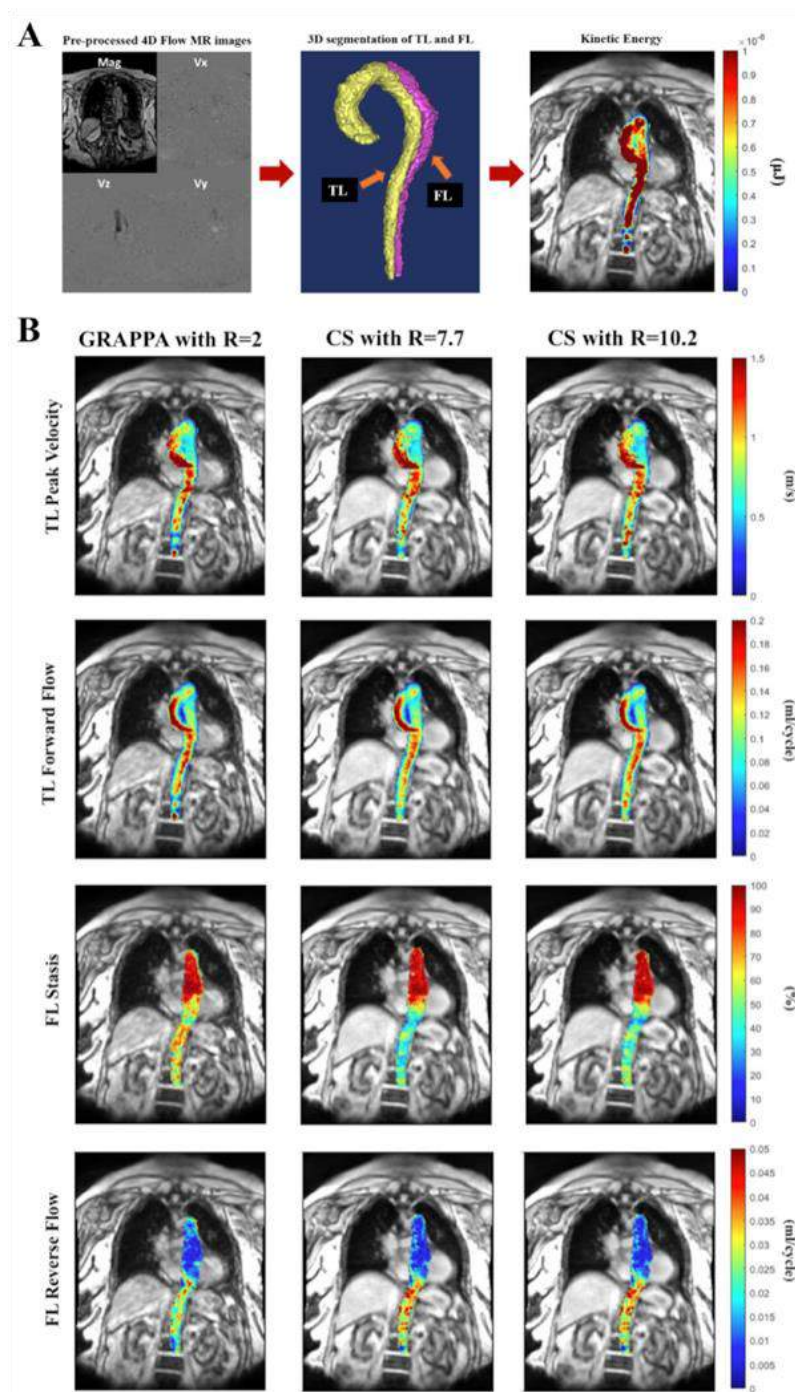
**Method:** Three patients with medically managed cTBAD (61±11.5 years old; 2 female) and 2 volunteers (28-year-old male, 21-year-old female) were prospectively recruited. All subjects underwent 3 non-contrast, free-breathing 4D flow scans - one conventional GRAPPA-accelerated (R=2) and two CS-accelerated scans with R=7.7 and 10.2. All images were acquired on a 1.5T MRI system (MAGNETOM Sola, Siemens Healthcare, Erlangen, Germany) using retrospective ECG-gating, the same spatial (~2.5 mm<sup>3</sup>) and temporal (40 ms) resolution, and venc (160 cm/s). All subjects were re-scanned 5-10 days after the first scan for interscan reliability assessment. Each 4D flow data set was preprocessed, and the true lumen (TL) and false lumen (FL) were manually segmented (Mimics, Materialise, Belgium) as illustrated in figure 1. Voxel-wise forward flow (FF), peak velocity (PV) and kinetic energy (KE) were calculated in TL and FL (patients) and in entire aorta (volunteers). Voxel-wise FL reverse flow (RF) and flow stasis were also measured (Fig. 1). Voxel-wise parameters were averaged within the aorta through the cardiac cycle to yield a single value and compared groupwise between each 4D flow acquisition using paired t-test or Wilcoxon rank sum as appropriate. Variability between acquisitions and reproducibility of each acquisition type between scan 1 and 2 were also assessed using Pearson correlation coefficient and Bland-Altman analysis.

**Results:** Groupwise comparisons showed no difference between CS-acceleration sequences and GRAPPA for any hemodynamic parameter ( $p>0.05$  for all, Fig. 2). Mean KE, FF, and PV showed significant positive correlation between both CS-accelerated sequences and GRAPPA in TL ( $p<0.01$ ). Mean KE and stasis were strongly correlated between both CS-accelerated sequences and GRAPPA in FL (KE  $p<0.05$ , stasis  $<0.01$ ). In FL; mean PV and FF showed a nonsignificant positive correlation trend between both CS sequences and GRAPPA (PV;  $r=$

0.449 and 0.367, FF;  $r=0.776$  and  $0.670$ , for CS10.2 and CS7.7 respectively) and RF between CS7.7 and GRAPPA ( $r=0.419$ ). Inter-sequence comparisons and reliability analyses of each CS-accelerated sequence showed low bias and limits of agreements in Bland-Altman plots with relatively lower percentage levels in TL FF and FL stasis measurements for both CS10.2 and CS7.7 compared to GRAPPA (Fig. 3).

**Conclusion:** While limited by a small sample size, the current pilot study demonstrates that highly accelerated CS 4D flow with reduced scans times of ~3-4 minutes has the potential to provide accurate and reproducible quantification of TL/FL advanced hemodynamics in cTBAD patients.

**Figure/Table 1**



**Caption 1**

**Figure 1:** A) 4D flow MRI data analysis workflow: pre-processing of raw 4D flow MR images followed by manual 3D segmentation of aorta B) TL forward flow, peak velocity and FL stasis and reverse flow maps in one subject with chronic type-B aortic dissection and comparison of maps generated by conventional and CS 4D flow scans can be seen.

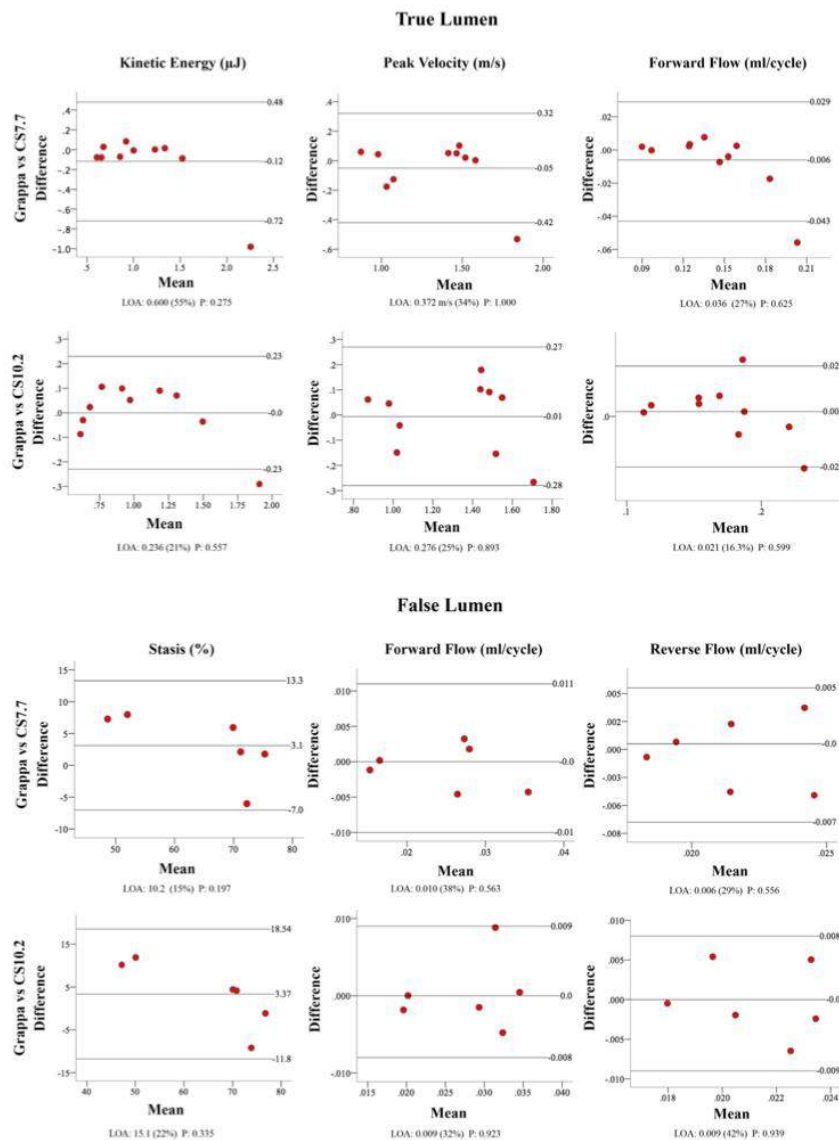
**Figure/Table 2**

True Lumen Comparisons		GRAPPA	CS7.7	GRAPPA	CS10.2
Kinetic Energy ( $\mu\text{J}$ )	Mean	1.046 $\pm$ 0.377	1.163 $\pm$ 0.600	1.046 $\pm$ 0.377	1.047 $\pm$ 0.436
	P- value	0.275*		0.557*	
	Correlation	0.921**		0.971**	
Peak Velocity (m/s)	Mean	1.300 $\pm$ 0.278	1.350 $\pm$ 0.242	1.300 $\pm$ 0.278	1.306 $\pm$ 0.297
	P- value	1.000*		0.893	
	Correlation	0.851**		0.894**	
Forward Flow (ml/cycle)	Mean	0.138 $\pm$ 0.027	0.144 $\pm$ 0.040	0.138 $\pm$ 0.027	0.136 $\pm$ 0.002
	P- value	0.625		0.599	
	Correlation	0.936**		0.948**	
False Lumen Comparisons		GRAPPA	CS7.7	GRAPPA	CS10.2
Kinetic Energy ( $\mu\text{J}$ )	Mean	0.194 $\pm$ 0.063	0.222 $\pm$ 0.081	0.194 $\pm$ 0.063	0.222 $\pm$ 0.105
	P- value	0.181		0.302	
	Correlation	0.877**		0.896**	
Peak Velocity (m/s)	Mean	0.610 $\pm$ 0.121	0.713 $\pm$ 0.098	0.610 $\pm$ 0.121	0.683 $\pm$ 0.148
	P- value	0.125		0.310	
	Correlation	0.367		0.449	
Forward Flow (ml/cycle)	Mean	0.028 $\pm$ 0.006	0.027 $\pm$ 0.005	0.028 $\pm$ 0.006	0.027 $\pm$ 0.005
	P- value	0.563*		0.923	
	Correlation	0.670		0.776	
ReverseFlow (ml/cycle)	Mean	0.021 $\pm$ 0.002	0.021 $\pm$ 0.002	0.021 $\pm$ 0.002	0.021 $\pm$ 0.003
	P- value	0.556		0.939	
	Correlation	0.419		-0.042	
Stasis (%)	Mean	66.46 $\pm$ 8.99	63.30 $\pm$ 12.19	66.46 $\pm$ 8.99	63.09 $\pm$ 14.67
	P- value	0.197		0.335	
	Correlation	0.944**		0.933**	

**Caption 2**

**Figure 2:** Summary of groupwise comparisons and mean and standard deviations for each parameter for each acquisition type (\* indicates Wilcoxon signed-rank test for nonparametric population. \*\* indicates statistical significance in Pearson correlation coefficients.).

**Figure 3**



**Caption 3**

**Figure 3:** Bland-Altman plots comparing the measurements of the conventional and CS 4D flow scans. We can see the low bias values and limits of agreements in all comparisons with lower percentage levels of TL forward flow and FL stasis analysis for both CS10.2 and CS7.7 compared to GRAPPA.

## Bibliographic References

Pathrose, A., et al., Highly accelerated aortic 4D flow MRI using compressed sensing: Performance at different acceleration factors in patients with aortic disease. *Magn Reson Med*, 2021. 85(4): p. 2174-2187., Ma, L.E., et al., Aortic 4D flow MRI in 2 minutes using compressed sensing, respiratory controlled adaptive k-space reordering, and inline

reconstruction. Magn Reson Med, 2019. 81(6): p. 3675-3690. , Jarvis. K., et al., Parametric Hemodynamic 4D Flow MRI Maps for the Characterization of Chronic Thoracic Descending Aortic Dissection. J Mag Reson Imaging, 2020. 51(5): p.1357-1368.

Speaker: O. Kilinc

Category: 4D Flow, Aortic Dissection, Compressed Sensing

000428

## RR-Resolved 5D flow for Decoding the Impact of Cardiac Rhythm on Left Atrial Flow Dynamics in Atrial Fibrillation and Stroke

J. Baraboo \* (1); E. Weiss (2); L. Ma (1); J. Hwang (1); S. Gunasekaran (1); M. B. L. Falcão (3); C. Roy (4); M. Stuber (5); R. Passman (6); D. Kim (7); M. Markl (1)

(1) Department of radiology, Northwestern University Feinberg School of Medicine, East Superior Street, Chicago, IL, USA, Chicago, United States of America; (2) Department of radiology, Northwestern University Feinberg School of Medicine, Chicago, United States of America; (3) Department of radiology, CHUV Centre hospitalier universitaire vaudois, Lausanne, Switzerland; (4) Department of radiology, Lausanne University Hospital, Lausanne, Switzerland; (5) Department of diagnostic and interventional radiology, CHUV Centre hospitalier universitaire vaudois, Lausanne, Switzerland; (6) Department of cardiology, Northwestern University Feinberg School of Medicine, Chicago, United States of America; (7) Room 1600 , Université Northwestern, Evanston, United States of America

### Abstract

**Background:** Atrial fibrillation (AF) is the most common sustained cardiac arrhythmia. Impaired left atrium (LA) hemodynamics, slow blood flow velocities and blood stasis, have been implicated in increased risk for LA thrombus formation and cardioembolic stroke [Handke, Lowe]. RR-resolved 5D flow is a novel MRI technique to acquire time-varying 3D anatomic and velocity measures for varied RR-interval durations during cardiac arrhythmia (fig 1)[Ma]. LA peak velocities and blood stasis can be measured across a range of RR interval durations to assess the impact of changes of heart rates on atrial hemodynamics. The purpose of this study was to apply RR-resolved 5D flow MRI in a cohort of AF patients with and without a history of stroke. We hypothesize that AF patients with prior stroke will have greater impaired RR-resolved LA hemodynamics (lowered peak velocities, higher LA stasis) than AF patients who have not had a stroke.

**Methods:** 24 AF patients ( $68 \pm 8$  years old, 5 female) undergoing cardiac MRI with RR-resolved 5D Flow were retrospectively enrolled (venc = 100 cm/s, FOV =  $250 \times 250 \times 250$  mm<sup>3</sup>, TE/TR = 2.93/4.70 ms, flip angle =  $7^\circ$ , temporal resolution = 40 ms, spatial resolution =  $2.5 \times 2.5 \times 2.5$  mm<sup>3</sup>). 8 AF patients had a history of stroke and 16 had no stroke history. RR-resolved 5D flow reconstruction included sorting k-space data based on RR-interval where each RR bin had the same number of RR-intervals (RR1 to RR4, fig 1). The RR distribution coefficient of variation (RR-std/RR-mean, CoV) was calculated per patient. RR-resolved 5D flow data analysis included background phase correction, velocity anti-aliasing, and manual 3D segmentation of the LA (Mimics, Materialise, Belgium). Blood stasis was calculated per voxel as the percentage of cardiac time with absolute LA velocity < 10 cm/s and then averaged over the segmented LA region to determine mean stasis. Peak velocities were calculated as the mean of the top 5% of velocities. T-test or Wilcoxon ranksum test was used to determine significant differences ( $\alpha = .05$ ).

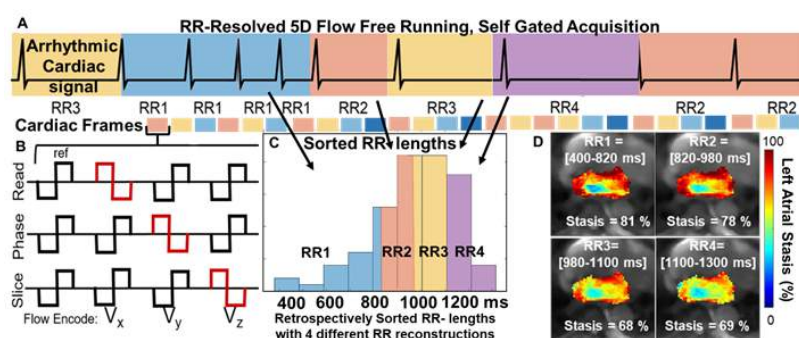
**Results:** The RR variability during acquisition was similar between stroke and no-stroke groups (RR distribution CoV not significantly different between groups,  $0.18 \pm 0.10$  vs  $0.14 \pm .07$ ,  $p = 0.34$ ). RR-resolved 5D flow derived mean stasis and peak velocities demonstrated



trends, though non-significant, for lowered peak velocities (represented in fig 2) and higher stasis per RR bin comparison for the stroke history AF subgroup compared to the no stroke AF subgroup (fig 3). Stasis and peak velocity percent differences between groups ranged from 4% to 16%. Largest differences were observed for RR1 bin between AF stroke history vs no stroke history for peak velocity ( $0.21 \pm 0.04$  m/s vs  $0.24 \pm .05$  m/s, 16% percent difference,  $p = 0.10$ ) and stasis ( $69 \pm 12\%$  vs  $66 \pm 14\%$ , 11% percent difference,  $p = 0.17$ , fig 3).

**Conclusions:** We demonstrated a trend towards lowered LA peak velocities and higher stasis in AF patients with a stroke history compared to those with no stroke history. Largest, though still non-significant, percent differences were in shorter RR intervals (RR1 bin) likely to be either rejected or averaged with less discriminatory heartbeat hemodynamics by other non RR-interval resolved acquisitions. This study was limited due CoV heterogeneity with more patients needed for further rhythm (maintaining sinus vs undergoing arrhythmia during acquisition) stratification and examination.

**Figure/Table 1**

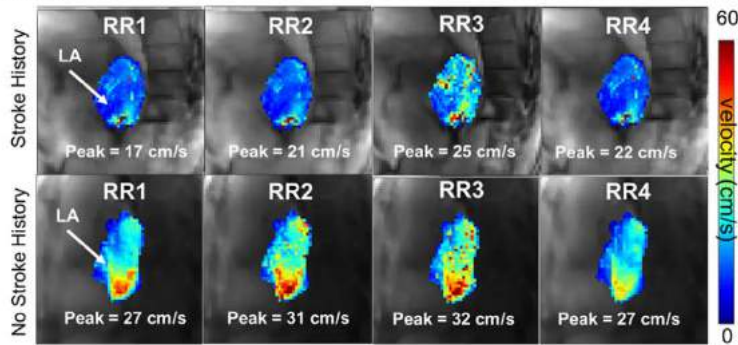


**Caption 1**

**Figure1.** A) RR-Resolved 5D Flow is a free running acquisition that retrospectively determines RR interval duration and cardiac time frames. B) 3D time varying velocity is encoded through bipolar gradients. C) RR-durations are sorted into 4 RR-bins (RR1 to RR4) for reconstruction. D) Stasis (shown: 2D axial maps) and peak velocity are derived per bin.

**Figure/Table 2**

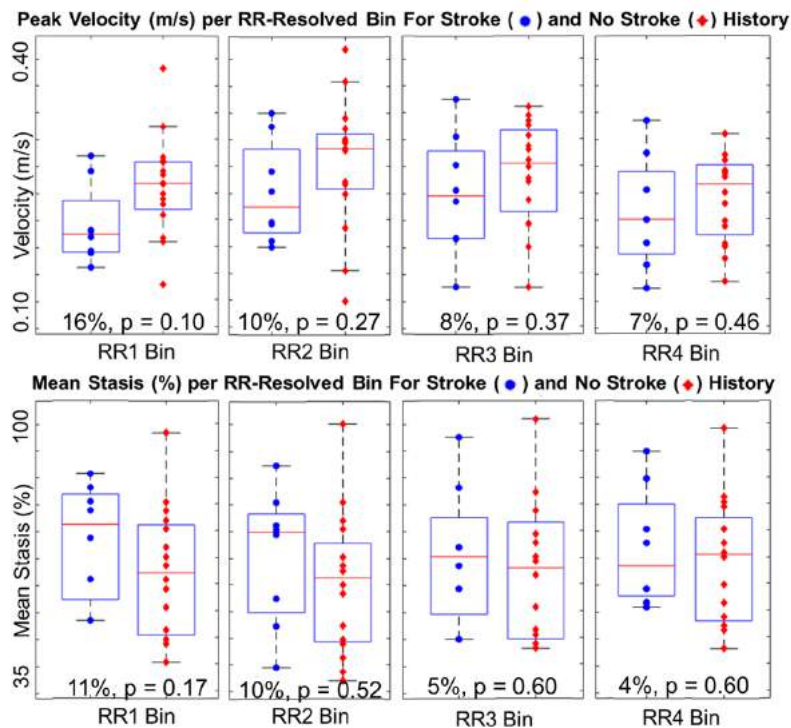
Velocity MIPs for RR-resolved 5D flow for 2 Patients with different Stroke History



Caption 2

**Figure2.** RR-resolved left atrial (LA) peak velocity maps (sagittal maximum intensity projections) for AF patients with stroke history (top) and no stroke (bottom). Most pronounced differences in LA velocities were seen for the shortest RR-interval duration (RR1 bin) with diminishing differences for longer RR-intervals (RR2-4 bins).

Figure 3



Caption 3

**Figure3.** Left atrial peak velocity (top) and mean stasis (bottom) boxplots per RR bin for AF patients with stroke history (n = 8, blue circles) and with no stroke history (n = 16, red diamonds). Absolute mean percent differences are shown with p-values. Peak velocities trended lower and stasis trended higher for AF patients with prior stroke.

### **Bibliographic References**

Ma L, Yerly J, Sopra L Di, et al. Using 5D flow MRI to decode the effects of rhythm on left atrial 3D flow dynamics in patients with atrial fibrillation. *Magn Reson Med*. 2021;85(6):3125-3139. doi:10.1002/MRM.28642, Lowe GDO. Virchow's Triad Revisited: Abnormal Flow. *Pathophysiol Haemost Thromb*. 2003;33(5-6):455-457. doi:10.1159/000083845, Handke M, Harloff A, Hetzel A, Olschewski M, Bode C, Geibel A. Left Atrial Appendage Flow Velocity as a Quantitative Surrogate Parameter for Thromboembolic Risk: Determinants and Relationship to Spontaneous Echocontrast and Thrombus Formation—A Transesophageal Echocardiographic Study in 500 Patients with Cerebral Ischemia. *J Am Soc Echocardiogr*. 2005;18(12):1366-1372. doi:10.1016/J.ECHO.2005.05.006

Speaker: J. Baraboo

Category: Atrial Fibrillation , 4D Flow, Left Atrium

000430

## CMR diagnosis of eosinophilic myocarditis with bi-ventricular thrombi in a child with hypereosinophilia syndrome

M. Elizabeth \* (1); K. Talina (2); M. Arshid (1); P. Umakumaran (1); K. Osman (1); A. VAIKOM HOUSE (1)

(1) Pediatrics, Oklahoma Children's Hospital, Oklahoma City, United States of America; (2) Radiology, Oklahoma Children's Hospital, Oklahoma City, United States of America

### Abstract

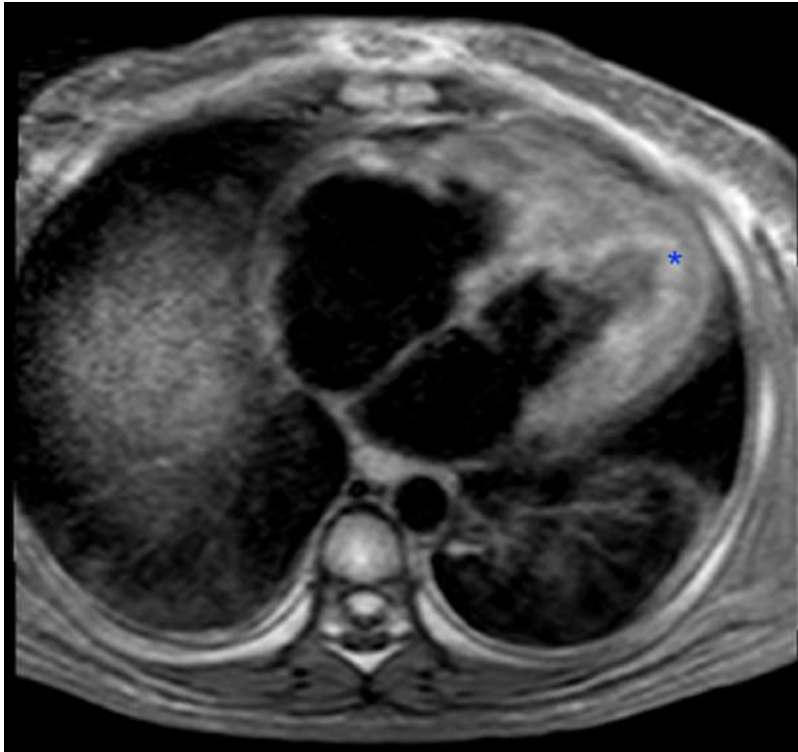
**Background:** An 11-year old previously healthy male presented to the ER with several weeks of fatigue, abdominal pain, nausea and vomiting. On exam he was tachycardic, with a new 2/6 holosystolic murmur at the apex, S3 gallop, and hepatosplenomegaly. Initial laboratory findings showed markedly elevated white blood cell count (75.99 K/mm<sup>3</sup>) with hypereosinophilia (56.99 K/mm<sup>3</sup>), elevated Troponin I (2.368 ng/mL), and elevated BNP (974 pg/mL). Electrocardiogram demonstrated sinus tachycardia with wide complex QRS, bifascicular block, and repolarization abnormality. Echocardiogram revealed severe tricuspid regurgitation, severe mitral regurgitation, and biventricular hypertrophy with hyperdynamic systolic function, left ventricular apical hypokinesia and impaired diastolic function. The constellation of peripheral eosinophilia, increased left ventricular wall thickness, and preserved systolic function raised the suspicion of eosinophilic myocarditis and CMR was performed confirming eosinophilic myocarditis with large apical bi-ventricular thrombi. Secondary causes for hypereosinophilia were excluded and the diagnosis of idiopathic hypereosinophilic syndrome with eosinophilic myocarditis was made. He was treated with steroids in addition to weekly vincristine and hydroxyurea with improved eosinophil count (5-7 K/mm<sup>3</sup>). He also was trialed on mepolizumab with no benefit. For the cardiac thrombi, he was treated with lovenox and transitioned to rivaroxaban with reduction in the thrombus burden. He has had two bone marrow biopsies that have not shown overt dysplasia. He is currently maintained on benralizumab, vincristine, prednisone with improvement in peripheral eosinophilia, LGE burden and improvement in thrombus burden.

**Technique:** Steady-state free precession cine imaging showed hypokinesia involving the apical segments and biventricular apical masses. There was preserved LV ejection fraction. Extensive myocardial inflammation and edema was demonstrated on T1 and T2 weighted sequences. 2D-PSIR late gadolinium enhancement sequences revealed extensive subendocardial enhancement and large layering LV apical thrombus and smaller RV apical thrombus. Following therapy, repeat CMR at 6 months showed improvement in the LGE and thrombus burden.

**Learning points:** In patients with hypereosinophilia presenting with heart failure, the diagnosis of eosinophilic myocarditis should be considered. CMR plays a key role in diagnosis and can identify presence of ventricular thrombus, obliteration of ventricular cavity, and degree of fibrosis. In this case, the layered LV thrombus was missed on initial echo and visualized on CMR. Patients with EM should be identified promptly and managed by a multidisciplinary team including cardiology and allergy/immunology specialists. Immunosuppression with high-dose steroids, anticoagulation and heart failure management is the general treatment strategy of choice. Additional chemotherapeutic agents including anti-IL-5 agents may be needed in refractory cases. Ventricular thrombi are a well-

known complication and there should be a low threshold for suspicion for plastered apical thrombi when ventricular wall hypokinesia is noted

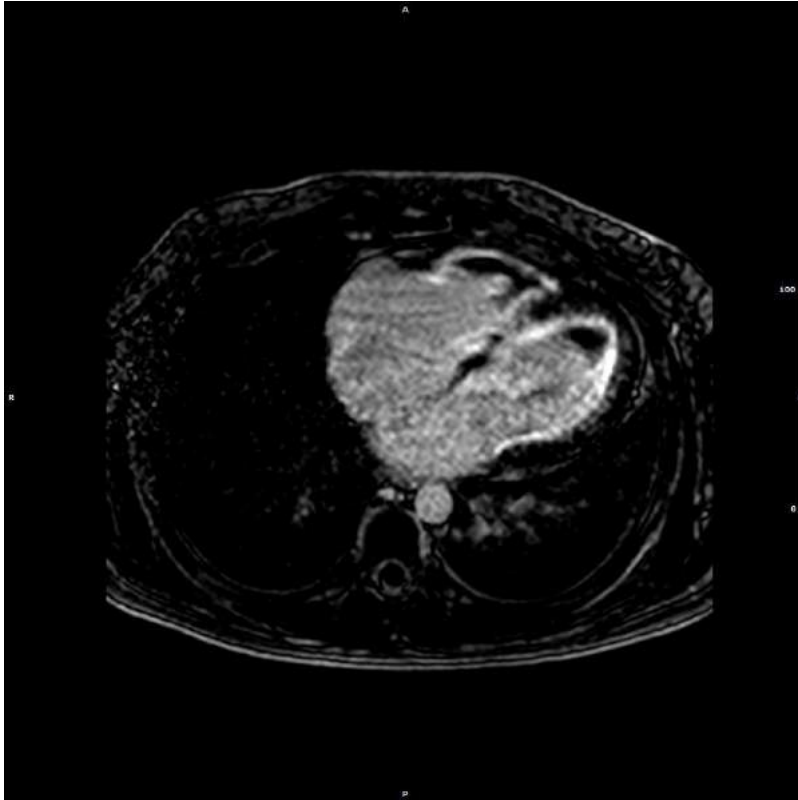
**Figure/Table 1**



**Caption 1**

Initial MRI at presentation - Axial STIR image with hyperenhancement of ventricular myocardium(asterisk) consistent with myocardial edema.

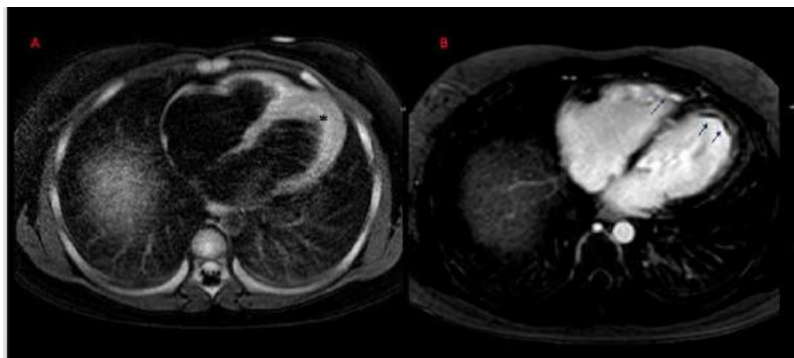
**Figure/Table 2**



**Caption 2**

Initial MRI at presentation - LGE imaging showing extensive sub-endocardial enhancement in both ventricles and apical thrombi in bilateral ventricles.

**Figure 3**



**Caption 3**

Follow up MRI with axial STIR image (panel A) showing improvement in myocardial edema(asterisk) and axial PSISR image (panel B) showing resolution of right ventricular thrombus, significant improvement in LGE burden (arrows) in both ventricles and reduction in left ventricular thrombus size.

Speaker: M. Elizabeth

Category: Eosinophilic Myocarditis, Pediatric , Heart Failure

000431

## Texture analysis of myocardial native T1 mapping discriminates between hypertensive heart disease and non-apical hypertrophic cardiomyopathy

Y. Mei \* (1); J. Liu (1); H. Liu (2); H. Shi (1)

(1) Department of radiology, wuhan union hospital, wuhan, China; (2) Ge healthcare, GE Healthcare, Shanghai, China

### Abstract

#### Background

About 13-31% of hypertrophic cardiomyopathy (HCM) patients manifest symmetrical hypertrophy and the non-apical subtype of HCM may be more difficulty to be distinguished from hypertensive heart disease (HHD) in morphology[1-2]. Texture analysis (TA) based on native T1 mapping can find differences in spatial localization of fibrosis by measuring associated spatial distributions of pixel intensity levels without gadolinium-based contrast agents[3-5].

#### Methods

This retrospective study included 32 non-apical HCM, 18 apical HCM and 44 HHD patients who had undergone CMR plain scan with native T1 mapping in three short-axis slices (basal, middle, apical) using a 1.5T scanner (MAGNETOM Aera, Siemens Healthcare, Erlangen, Germany). The contours of three short-axis slices were semi-automatically generated and manually corrected using 3D slicer (version 4.11), and then imported the contour file into a commercially available software (A.K, version version 3.1.0.R, Artificial Intelligence Kit, GE Healthcare, US) for texture analysis. Six texture analysis methods (replace outliers by quantiles, standardization, Mann Whitney U test, correlation analysis, gradient boosting decision tree and logistic regression with five fold cross validation) were performed for step-wise dimension reduction and feature selection. Cardiac function and strain parameters were analyzed based on a stack of short-axis slices and three long-axis slices. The global T1 value was calculated by measuring the septal myocardial sampling within the mid-ventricular short-axis slice.

#### Results

The selected texture features, consisting of 4 gray level co-occurrence matrix (GLCM) features (joint average, joint energy, joint entropy, imc2), first order feature (minimum), gray level size zone matrix (GLSZM) feature (size zone non-uniformity) and gray level dependence matrix (GLDM) feature (small dependence high gray level emphasis), provided a diagnostic accuracy of 80.3% [confidence interval (CI) : 0.766-0.932] to differentiate non-apical HCM from HHD patients. And the combination of these texture features with cardiac function and strain parameters [left ventricular ejection fraction (LVEF), left ventricular wall thickness and global circumferential strain (GCS)] showed better area under the curve (AUC) compared with using texture features alone (0.972 vs. 0.864,  $p < 0.01$ ) For distinguishing between apical HCM and HHD patients, the AUCs were as follows: 0.801 for TA and 0.899 for TA adding in cardiac function and strain

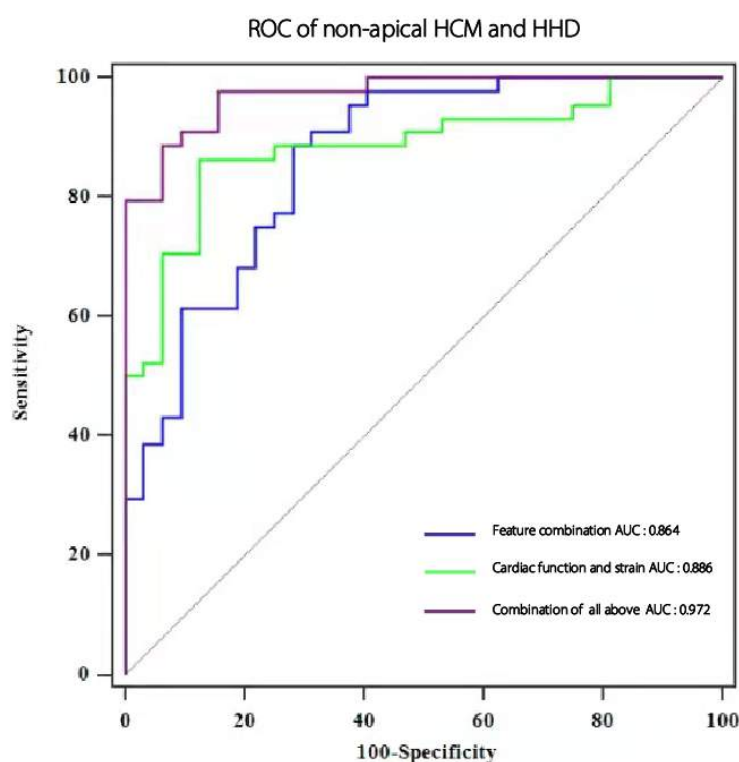


analysis ( $p<0.05$ ). And two of these TA features, GLCM feature (joint entropy) and GLDM feature (small dependence high gray level emphasis) also work for differentiating apical HCM and HHD.

## Conclusion

TA of native T1 mapping shows high accuracy in differentiating non-apical HCM from HHD. Combining TA with some cardiac function and strain parameters can provide incremental value over using TA alone.

**Figure/Table 1**



**Caption 1**

**Figure 1** ROC analyse indicating the accuracy of the texture features of the native T1 map, combination of cardiac function and strain analysis and combination of all above to differentiate non-apical HCM and HHD patients. HCM, hypertrophic cardiomyopathy; HHD, hypertensive heart disease

**Figure/Table 2**

HHD (n=44)	Non-apical HCM (n=32)	Apical HCM (n=18)	Statistics	p- Value	p- Value( non- apical	p- Value(a pical HCM	p- Value( non- apical
---------------	--------------------------	----------------------	------------	-------------	--------------------------------	-------------------------------	--------------------------------

						HCM vs. HHD)	vs. HHD)	HCM vs. apical HCM)
Age	50.18±14.06	46.53±13.97	52.33±10.25	1.24	0.294	0.266	0.727	0.13
Gender(Male/Female)	35/9	27/5	15/3	0.322	0.851	0.592	0.991	0.76
Body surface area(m <sup>2</sup> )	1.88±0.22	1.81±0.20	1.90±0.15	1.361	0.261	0.218	0.572	0.106
<b>Cardiovascular Magnetic Resonance</b>								
LV end-diastolic volume(ml)	184.00(130.29, 268.78)	142.56(118.73, 171.95)	137.14(128.23, 166.24)	5.277	0.071	0.035*	0.117	0.716
LV end-systolic volume(ml)	119.83(54.96, 206.62)	61.01(47.48, 93.52)	55.20(44.57, 65.75)	11.19	0.004*	0.008*	0.006*	0.275
LV stroke volume(ml)	68.00(50.92, 81.48)	74.98(66.41, 88.70)	87.50(81.59, 97.51)	18.146	<0.001*	0.025*	<0.001*	0.008*
LV ejection fraction(%)	35(24, 57)	55(47, 63)	63(60, 65)	21.965	<0.001*	0.001*	<0.001*	0.017*
LV cardiac output(L/min)	4.57(3.70, 5.76)	4.98(4.27, 6.47)	5.27(4.78, 6.10)	6.932	0.031*	0.077	0.016*	0.249
LV cardiac index(L/(min·m <sup>2</sup> ))	2.33(1.94, 3.03)	2.75(2.42, 3.37)	2.83(2.49, 3.21)	9.484	0.009*	0.008*	0.043*	0.816
Heart rate(bpm)	71.25(59.50, 85.75)	67.35(59.66, 72.31)	59.60(53.96, 68.10)	6.608	0.037*	0.201	0.021*	0.063
LV mass index(mg/m <sup>2</sup> )	74.13(52.81, 99.58)	65.02(50.93, 92.50)	72.22(51.31, 89.16)	0.696	0.706	0.427	0.664	0.731
Maximal LVWT(mm)	13.64(12.33, 15.30)	16.46(15.07, 17.19)	13.53(12.04, 17.52)	11.13	0.004*	<0.001*	0.332	0.327
Global native T1(ms)	1055.00(1029.80, 1086.60)	1068.50(1042.05, 1089.20)	1043.50(1010.20, 1068.15)	3.538	0.171	0.258	0.243	0.066
<b>Strain analysis</b>								
GRS(%)	16.66(9.28, 33.04)	25.91(19.11, 36.95)	33.06(24.48, 40.22)	11.253	0.004*	0.013*	0.005*	0.109
GCS(%)	-11.90(-19.18, -8.05)	-17.55(-20.08, -13.06)	-20.94(-22.78, -16.77)	13.001	0.002*	0.028*	0.002*	0.026*
GLS(%)	-6.43±3.49	-8.18±2.96	-8.51±3.31	3.838	0.025*	0.025*	0.035*	0.649

**Caption 2**

HCM, hypertrophic cardiomyopathy; HHD, hypertensive heart disease; LV, left ventricular; LVWT, left ventricular wall thickness; GRS, global radial strain; GCS, global circumferential strain; GLS, global longitudinal strain

**Figure 3**

	AUC	95% CI	Sensitivity	Specificity
<b>Non-apical HCM vs. HHD</b>				
Texture Analysis	0.864	0.766-0.932	0.864	0.719
Cardiac function and strain analysis	0.886	0.792-0.947	0.841	0.875
Combination of all above	0.972	0.906-0.996	0.886	0.937
<b>Apical HCM vs. HHD</b>				
Texture Analysis	0.801	0.680-0.891	0.778	0.750
Cardiac function and strain analysis	0.871	0.762-0.943	0.833	0.864
Combination of all above	0.899	0.796-0.961	0.889	0.818
<b>Non-apical HCM vs. apical HCM</b>				
Texture Analysis	0.878	0.755-0.954	0.778	0.906
Cardiac function and strain analysis	0.760	0.619-0.870	0.778	0.719
Combination of all above	0.875	0.751-0.952	0.778	0.906

**Caption 3**

AUC, area under the ROC curve; CI, confidence interval; HCM, hypertrophic cardiomyopathy; HHD, hypertensive heart disease

### Bibliographic References

- [1]. Shapiro LM, McKenna WJ. Distribution of left ventricular hypertrophy in hypertrophic cardiomyopathy: a two-dimensional echocardiographic study. J Am Coll Cardiol 1983;2:437e44., [2]. Nakamura T, Sugihara H, Kinoshita N, et al. Can serum carnitine levels distinguish hypertrophic cardiomyopathy from hypertensive hearts? Hypertension 2000;36:215e9., [3]. Gillies RJ, Kinahan PE, Hricak H Radiomics: Images are more than pictures, They are data. Radiology 2016;278(2):563-77., [4]. Baessler B, Mannil M, Oebel S, Maintz D, Alkadhi H, Manka R Subacute and chronic left ventricular myocardial scar: Accuracy of texture analysis on nonenhanced cine MR images. Radiology 2018;286(1):103-12., [5]. Baeßler B, Mannil M, Maintz D, Alkadhi H, Manka R Texture analysis and machine

learning of non-contrast T1-weighted MR images in patients with hypertrophic cardiomyopathy—Preliminary results. Eur J Radiol 2018;102(November 2017):61-7.

Speaker: Y. Mei

Category: Cardiomyopathy, Hypertensive Heart Disease, Cardiac Function

000432

## Assessment of aortic hemodynamics by accelerated dual-venic 4D flow MRI in patients with type B aortic dissection: Initial results

O. Kilinc \* (1); S. Chu (1); J. Baraboo (1); E. Weiss (1); A. Maroun (1); N. jin (2); K. chow (3); X. Bi (3); R. Davids (3); C. Mehta (4); C. Malaisrie (4); A. Hoel (5); M. Markl (1); B. Allen (1)

(1) Radiology, Northwestern University Feinberg School of Medicine, Chicago, United States of America; (2) Cardiovascular imaging, Siemens Medical Solutions USA, Inc., Cleveland, United States of America; (3) Cardiovascular imaging, Siemens Medical Solutions USA, Inc., Chicago, United States of America; (4) Cardiac surgery, Northwestern University Feinberg School of Medicine, Chicago, United States of America; (5) Vascular surgery, Northwestern University Feinberg School of Medicine, Chicago, United States of America

### Abstract

**Background:** 4D Flow MR imaging (MRI) allows quantification of in vivo aorta hemodynamics. There is a wide dynamic range of velocities measured between true lumen (TL) and false lumen (FL) in type B aortic dissection (TBAD) and single-venic (SV) 4D flow MRI may limit the characterization of hemodynamic parameters. Dual-venic (DV) 4D flow MRI is capable of measuring larger velocity dynamics ranges. We aim to assess the impact of DV 4D flow MRI on hemodynamic characterization of aorta in chronic TBAD (cTBAD) patients and volunteers. We hypothesize that DV acquisition has higher velocity-to-noise ratio (VNR), will better capture low velocity features, and provide similar quantification of peak velocity (PV) in TL and FL.

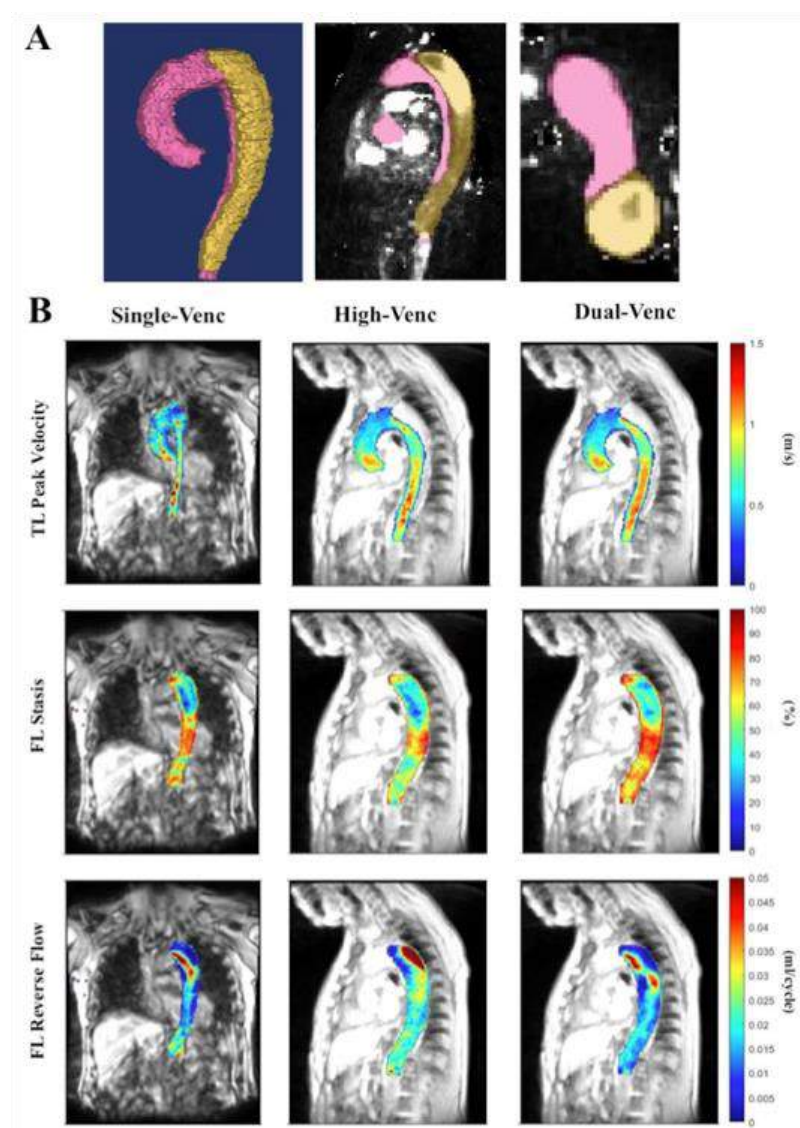
**Methods:** A total of 3 patients with cTBAD (61±11.5 years old; 2 female) and 2 volunteers (28-year-old male, 21-year-old female) were scanned with non-contrast, free-breathing 4D flow scans using SV (GRAPPA, R=2) and DV with compressed sensing (R=7.7) prototype. All images were acquired on a 1.5T MRI system (MAGNETOM Sola, Siemens Healthcare, Erlangen, Germany) using retrospective ECG-gating, 160 cm/s for SV and 80/160 cm/s for DV, the same spatial (~ 2.5 mm<sup>3</sup>) and 2 views per segment for SV and 1 for DV to obtain similar temporal resolution (40 ms). DV data was reconstructed by combining low and high-venic (HV) data using a model-based Bayesian unfolding algorithm. HV data from DV acquisition was analyzed separately. A second scan was performed 5-10 days after the first scan for the repeatability assessment. After manual segmentations, the following parameters were calculated voxel-wise: forward flow (FF), PV, kinetic energy (KE) in TL and FL (patients) and in entire aorta (volunteers) and FL reverse flow (RF) and flow stasis in patients (Fig. 1). Parameters were averaged over the segmented volume throughout the cardiac cycle and means were compared between SV, DV, and HV using paired t-test or Wilcoxon rank sum tests as appropriate. Pearson correlation and Bland-Altman analysis were also used for all comparisons. VNR was calculated as mean velocity in entire aorta divided by the velocity standard deviation in spine.

**Results:** The KE in TL; PV, and FF in FL did not show significant difference in any groupwise comparison ( $p>0.05$ , Fig. 2). HV to SV comparison showed no significant difference in any FL parameter. KE and PV in TL showed significant positive correlation in all groupwise comparisons. FF in TL was significantly correlated between SV and DV

acquisitions ( $r=0.890$ ). Stasis, KE, and PV in FL were significantly correlated between DV and HV (Fig. 2). KE in TL and stasis, FF and RF in FL showed low, clinically insignificant limits of agreements with variable percentages on Bland-Altman plots (Fig. 3). The VNR in entire aorta was higher by an average of 28% in DV compared to HV. All acquisition types showed strong ( $>0.800$ ) significant correlation between two scans for all TL parameters.

**Conclusion:** This study demonstrates the feasibility of accelerated DV 4D flow MRI in patients with cTBAD. In our cTBAD patient population, DV hemodynamic aortic parameters were similar to SV for KE, PV, and FF. RF and stasis differences in FL are consistent with the higher VNR in DV suggesting DV may better characterize lower velocity flow features relative to SV.

**Figure/Table 1**



**Caption 1**

**Figure 1: A:** Manual segmentations of true and false lumen and their 3D appearance in a patient with chronic type B aortic dissection. **B:** True lumen peak velocity, false lumen stasis and reverse flow maps for each acquisition type. GRAPPA 4D flow was acquired in coronal and DV CS was acquired in sagittal oblique orientation.

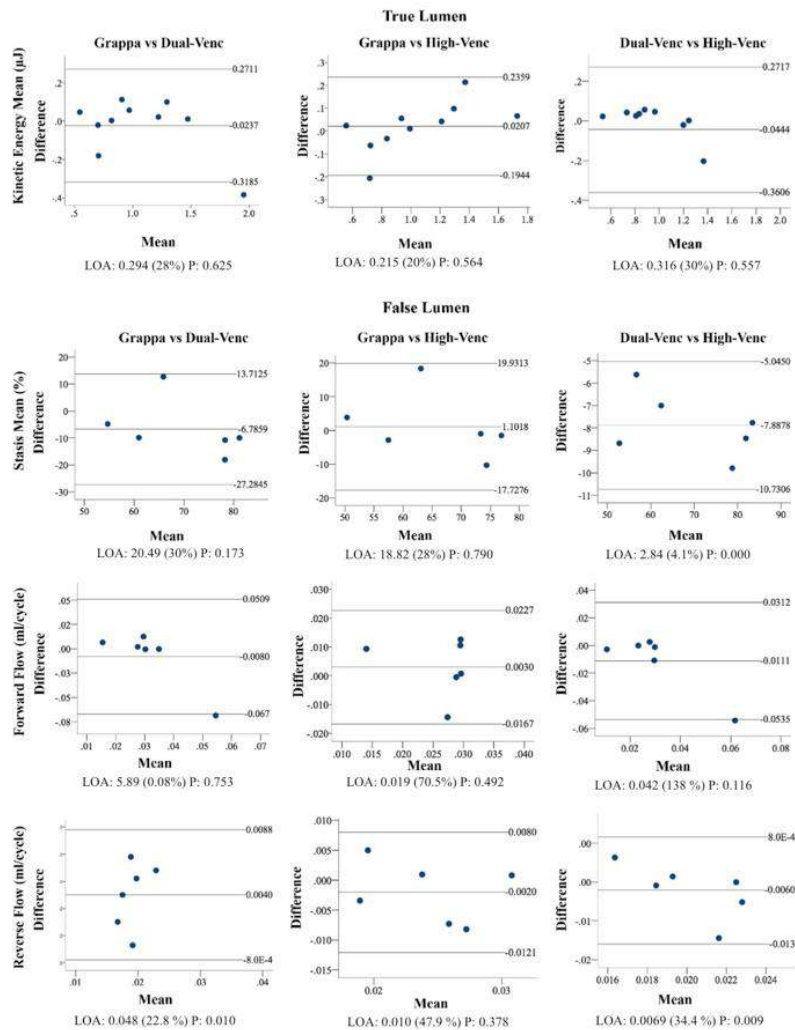
**Figure/Table 2**

True Lumen Comparisons		GRAPPA	Dual-Venc	GRAPPA	High-Venc	Dual-Venc	High-Venc
Kinetic Energy ( $\mu\text{J}$ )	Mean	1.046 $\pm$ 0.397	1.070 $\pm$ 0.471	1.046 $\pm$ 0.397	1.026 $\pm$ 0.329	1.070 $\pm$ 0.471	1.026 $\pm$ 0.329
	P- value	0.625		0.564		0.557	
	Correlation	0.954**		0.972**		0.981**	
Peak Velocity (m/s)	Mean	1.300 $\pm$ 0.293	1.233 $\pm$ 0.273	1.300 $\pm$ 0.293	1.194 $\pm$ 0.253	1.233 $\pm$ 0.273	1.194 $\pm$ 0.253
	P- value	0.030		0.009		0.015	
	Correlation	0.960**		0.941**		0.991**	
Forward Flow (ml/cycle)	Mean	1.138 $\pm$ 0.029	1.143 $\pm$ 0.037	1.138 $\pm$ 0.029	0.045 $\pm$ 0.008	0.143 $\pm$ 0.037	0.045 $\pm$ 0.008
	P- value	0.390		0.000		0.000	
	Correlation	0.890**		0.389		0.112	
False Lumen Comparisons		GRAPPA	Dual-Venc	GRAPPA	High-Venc	Dual-Venc	High-Venc
Kinetic Energy ( $\mu\text{J}$ )	Mean	0.194 $\pm$ 0.069	0.264 $\pm$ 0.282	0.194 $\pm$ 0.069	0.292 $\pm$ 0.268	0.264 $\pm$ 0.282	0.292 $\pm$ 0.268
	P- value	0.563*		1.000*		0.063*	
	Correlation	-0.009		0.003		1.000**	
Stasis (%)	Mean	66.4 $\pm$ 9.85	73.2 $\pm$ 13.9	66.4 $\pm$ 9.85	65.3 $\pm$ 13.2	73.2 $\pm$ 13.9	65.3 $\pm$ 13.2
	P- value	0.173		0.790		0.000	
	Correlation	0.664		0.693		0.996**	
Peak Velocity (m/s)	Mean	0.610 $\pm$ 0.133	0.727 $\pm$ 0.342	0.610 $\pm$ 0.133	0.711 $\pm$ 0.321	0.727 $\pm$ 0.342	0.711 $\pm$ 0.321
	P- value	0.466		0.510		0.209	
	Correlation	0.042		-0.002		0.999**	
Forward Flow (ml/cycle)	Mean	0.028 $\pm$ 0.007	0.036 $\pm$ 0.026	0.028 $\pm$ 0.007	0.024 $\pm$ 0.008	0.036 $\pm$ 0.026	0.024 $\pm$ 0.008
	P- value	0.753*		0.492		0.116*	
	Correlation	-0.322		0.201		0.719	
Reverse Flow (ml/cycle)	Mean	0.021 $\pm$ 0.002	0.017 $\pm$ 0.001	0.021 $\pm$ 0.002	0.023 $\pm$ 0.003	0.017 $\pm$ 0.001	0.023 $\pm$ 0.003
	P- value	0.010		0.378		0.009	
	Correlation	0.844		-0.156		0.441	

**Caption 2**

**Figure 2:** Groupwise sequence comparisons for numerous flow parameters in true lumen and false lumen. Pearson correlation coefficients can also be seen for each comparison (\* indicates nonparametric sample requiring Wilcoxon rank sum test. \*\* indicates statistical significance in Pearson correlation coefficients).

**Figure 3**



**Caption 3**

**Figure 3:** Bland-Altman plots of several groupwise comparisons in true lumen and false lumen. Percent difference was defined as the limit of agreement divided by the mean value of each parameter from reference scan (GRAPPA) or the average of all values of both sequences if there is no reference sequence.

### Bibliographic References

Schnell. S., et al., Accelerated Dual-Venc 4D flow MRI for neurovascular applications. J Magn Reson Imaging, 2017. 46(1): p.102–114., Binter. C., et al., Bayesian multipoint velocity encoding for concurrent flow and turbulence mapping. Magn Reason Med. 2013. 69(5): P.1337-1345., Jarvis. K., et al., Parametric Hemodynamic 4D Flow MRI Maps for the Characterization of Chronic Thoracic Descending Aortic Dissection. J Mag Reson Imaging, 2020. 51(5): p.1357-1368.



Speaker: O. Kilinc

Category: 4D Flow, Aortic Dissection, Velocity

000433

## CMR Criteria for successful bi-ventricular repair in hypoplastic left heart complex

A. VAIKOM HOUSE \* (1); A. Saprungruang (2); S. Behere (1); M. Seed (3); C. Lam (4); B. David (5); E. Jaeggi, (3); S.-J. Yoo (6)

(1) Pediatrics, Oklahoma Children's Hospital, Oklahoma City, United States of America; (2) Pediatrics, SickKids Foundation, University Avenue, TORONTO, Canada; (3) Pediatrics, The Hospital for Sick Children, Toronto, Canada; (4) Diagnostic imaging, SickKids, Toronto, Canada; (5) Cardiothoracic surgery, The Hospital for Sick Children, Toronto, Canada; (6) Diagnostic imaging, Hospital for Sick Children, Toronto, Canada

### Abstract

**Background:** Patients with 'borderline left ventricle (LV)' in hypoplastic left heart complex (HLHC) where the aortic and mitral valves are small, but without significant stenosis could be considered for biventricular repair. Criteria for successful biventricular repair in hypoplastic left heart complex is scant and based on echocardiographic criteria that are known to be inaccurate when the LV is crescentic in shape. We sought to retrospectively identify CMR criteria that are associated with successful biventricular repair in neonates with 'borderline LV' in the absence of severe aortic or mitral stenosis.

**Methods:** This single center retrospective study included all patients from January 2003 to July 2021 with borderline left heart complex referred for cardiac MRI for assessment of LV size at birth. Other variants of 'borderline LV' including critical aortic stenosis, unbalanced atrioventricular septal defect, large ventricular septal defect or any pulmonary outflow tract obstruction or anomalous pulmonary venous connections were excluded. Failed biventricular repair (Group1) was defined as death, heart transplantation or conversion to single-ventricle palliation. Successful primary biventricular repair (Group 2) was described as establishing biventricular circulation as the index operation. Staged biventricular repair (Group 3) was defined as accomplishing biventricular circulation in a staged manner with initial hybrid procedure followed by complete biventricular repair. Comparisons between groups for the categorical variables were made using Fisher's exact test. Comparisons of the continuous variables were made using the ANOVA followed by post-hoc T-test. A logistic fit of dichotomous outcome (primary or staged biventricular repair vs failed biventricular repair) by indexed left ventricular end-diastolic volume (LVEDVi) was performed and a receiver operating characteristic (ROC) curve was generated. Statistical analysis performed on JMP Pro 14.

**Results:** 30 unique patients with hypoplastic left heart complex were identified. Demographics and MRI parameters are summarized in Table1. 19/30 (63%) underwent successful primary biventricular repair, median follow up of 9.2 years (range 0.06-11.41 years). 6/30 (20%) patients underwent staged biventricular repair, median follow up 2.7 years (range 0.2-7.3 years). 5/30 (17%) patients failed biventricular repair, median follow up 1.2 years (range 0.3-6.0 years). Successful primary or staged biventricular repair (Group 2 or 3) was associated with a larger CMR LVEDVi ( $p=0.003$ ), larger ascending aortic flow ( $p=0.019$ ) and the presence of ascending aortic flow greater than SVC flow ( $p=0.011$ ). An LVEDVi cut off of 18.4 mL/m<sup>2</sup> had a sensitivity of 96% and a specificity of 80% to predict a successful primary or staged biventricular repair

**Conclusions:** In patients with hypoplastic left heart complex, larger LVEDVi, larger ascending aortic flow and ascending aortic flow greater than SVC flow at initial neonatal MRI were more likely to have a successful biventricular repair. An LVEDVi cut off of 18.4 ml/m2 had a sensitivity of 96% and a specificity of 80% to predict a successful biventricular repair.

**Figure/Table 1**

	Group 1 (Failed Biventricular Repair)		Group 2 (Primary Biventricular Repair)		Group 3 (Staged Biventricular Repair)		
	Median (25th%-75th%)	Mean (SD)	Median (25th%-75th%)	Mean (SD)	Median (25th%-75th%)	Mean (SD)	
<b>MRI</b>							<b>p-value*</b>
Birth_weight(kg)	3.26 (3.20, 3.60)	3.47 (0.63)	3.34 (3.10, 3.65)	3.35 (0.31)	3.20 (2.89, 3.88)	3.40 (0.69)	0.9536
Gestation age(weeks)	39.0 (39.0, 39.6)	39.1 (0.75)	38.6 (38.0, 39.7)	38.7 (1.42)	38.6 (38.0, 40.0)	38.8 (1.09)	0.9016
Age_at_exam(days)	2.00 (2.00, 4.00)	2.80 (1.30)	2.00 (1.00, 5.00)	3.11 (3.05)	1.50 (1.00, 4.00)	3.50 (4.85)	0.8103
WEIGHT (kg)	3.30 (3.20, 3.60)	3.33 (0.34)	3.30 (3.00, 3.68)	5.90 (11.0)	3.62 (3.00, 4.30)	3.64 (0.69)	0.7043
BSA (m2)	0.21 (0.21, 0.23)	0.21 (0.01)	0.20 (0.20, 0.21)	0.20 (0.01)	0.22 (0.21, 0.24)	0.23 (0.02)	0.0612
LVEDVi(ml/m2)	17.4 (17.2, 17.4)	18.6 (5.58)	29.0 (28.0, 33.8)	30.0 (3.63)	21.5 (18.4, 27.0)	24.1 (8.64)	0.0030
RVESVi(ml/m2)	6.00 (5.60, 6.00)	6.28 (2.27)	13.6 (12.0, 14.0)	12.9 (2.74)	9.80 (8.00, 12.0)	12.7 (7.88)	0.0026
LVSVi(ml/m2)	11.8 (11.0, 13.6)	12.1 (3.66)	17.1 (14.4, 19.0)	17.1 (2.76)	11.3 (9.70, 13.0)	11.6 (2.77)	0.0010
LVEF	63.0 (63.0, 68.0)	65.7 (8.30)	57.5 (50.0, 62.0)	56.9 (6.69)	52.5 (48.0, 57.0)	50.3 (11.6)	0.0426
RVEDVi(ml/m2)	84.0 (81.0, 124)	97.8 (27.3)	80.6 (60.0, 109)	84.3 (29.0)	105 (87.3, 124)	114 (37.6)	0.1559
RVESVi(ml/m2)	48.0 (33.0, 50.0)	43.8 (13.4)	44.5 (35.4, 58.0)	46.2 (15.8)	59.9 (44.0, 85.0)	67.0 (26.9)	0.1849
RVSVi(ml/m2)	48.0 (42.4, 69.6)	54.0 (17.4)	36.1 (24.0, 49.0)	38.0 (15.8)	42.8 (40.0, 47.0)	47.6 (13.4)	0.1777
RVEF	59.0 (53.6, 60.0)	55.1 (7.87)	47.5 (41.0, 50.0)	44.8 (7.61)	43.5 (38.0, 48.0)	42.7 (7.66)	0.0363
QAsc_aortic(l)/min/m2	1.05 (0.71, 1.90)	1.25 (0.62)	2.10 (1.74, 2.30)	2.05 (0.43)	1.52 (0.90, 1.98)	1.50 (0.55)	0.0196
Q_SVC(l)/min/m2	2.00 (1.40, 2.24)	1.84 (0.52)	1.40 (1.20, 1.64)	1.45 (0.34)	1.33 (1.08, 1.52)	1.60 (0.84)	0.2632
Q_Dao(l)/min/m2	1.00 (1.00, 1.52)	1.13 (0.41)	1.22 (1.05, 1.48)	1.26 (0.34)	0.91 (0.62, 1.70)	1.08 (0.55)	0.5718
QPA(l)/min/m2	1.21 (1.07, 2.10)	1.49 (0.73)	1.57 (1.30, 2.72)	1.99 (0.91)	2.06 (1.02, 3.83)	2.22 (1.40)	0.4416
QPA(l)/min/m2	2.48 (1.54, 2.86)	2.35 (0.83)	2.18 (1.45, 3.48)	2.56 (1.27)	2.80 (1.81, 3.71)	2.72 (1.28)	0.9266
Qa(l)/min/m2	3.00 (2.96, 3.35)	2.97 (0.75)	2.74 (2.27, 3.14)	2.76 (0.55)	2.14 (1.92, 3.10)	2.68 (1.22)	0.4007
QPCS	1.19 (0.90, 1.60)	1.30 (0.56)	1.40 (1.00, 2.10)	1.67 (0.84)	2.55 (0.57, 3.36)	2.28 (1.53)	0.5198

**Caption 1**

Table 1 : Patient demographics and MRI variables compared by group.

Speaker: A. VAIKOM HOUSE

Category: Hypoplastic Left Heart Syndrome , Congenital Heart Disease, Isolated Left Ventricular Apical Hypoplasia

000434

## **CMR appearances in patients with muscular dystrophies and correlation with echocardiography**

A. Mohata \* (1); R. Vimal (2); K. Richa (1); G. Suraj (1); A. Kumar (1)

(1) Department of Cardiothoracic Imaging, Narayana Institute of Cardiac Sciences, Bengaluru, India; (2) Radiology, Narayana Institute of Cardiac Sciences, Bengaluru, India

### **Abstract**

#### **CMR appearances in patients with muscular dystrophies and correlation with echocardiography**

### **BACKGROUND:**

Muscular dystrophies encompass a diverse group of congenital disorders that are primarily characterized by progressive loss of muscle mass and ensuing limb weakness. Muscular dystrophy associated cardiomyopathy is a cause of sudden cardiac death in young patients. Early detection of associated cardiac involvement is important as early initiation of specific cardioprotective therapy can improve quality of life and improve life expectancy. Cardiac Magnetic Resonance (CMR) is emerging as the imaging of choice in non-invasive assessment of these patients.

### **METHODS:**

Retrospective review of all the cardiac MR examinations conducted in our tertiary referral centre over the last 3 years. All scans were performed on a 3 Tesla MRI scanner (Ingenia Philips Healthcare, Netherlands).

Standard imaging sequences were used to determine anatomical and functional information. T1 mapping was used to identify early myocardial involvement and LGE (Late gadolinium enhancement) imaging was done to study the enhancement characteristics. CMR and echocardiographic findings were correlated.

### **RESULTS:**

A total of 17 patients with genetically proven congenital muscular dystrophies had CMR examinations during this period. The average age of patients was 12.5 years with a range from 7 to 28 years. All the patients in our study were males. Of the 17 cases, 14 patients were diagnosed Duchenne muscular dystrophy (82%), while 3 were Becker muscular dystrophy (18%).

All patients in our study had deranged global longitudinal strain. About 53% of patients had raised native T1 values. The average LVEF (left ventricular ejection fraction) was 55.4% and average RVEF (right ventricular ejection fraction) was seen to be 55.1%. A total of 7 patients (41.1%) showed late gadolinium enhancement, all of which were of non-ischemic pattern.

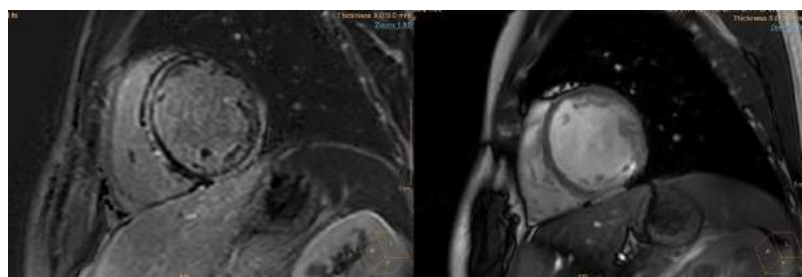
Presence of delayed enhancement had good correlation with presence of regional wall motion abnormalities on echocardiography.

All patients with positive findings on CMR had abnormalities on echocardiographic examination, the commonest being altered global longitudinal strain. Global longitudinal strain assessed on CMR had good correlation with echocardiography. The average LVEF on echocardiography is 59.4% and all patients had good right ventricular function.

## CONCLUSIONS:

CMR is a good non-invasive imaging modality to evaluate cardiac involvement in congenital muscular dystrophies. It shows a good correlation with echocardiography. Use of novel methods such as parametric mapping and strain imaging can increase the sensitivity and aid in the betterment of the quality of life. In addition, it also provides for detailed assessment including right ventricular function and enhancement properties.

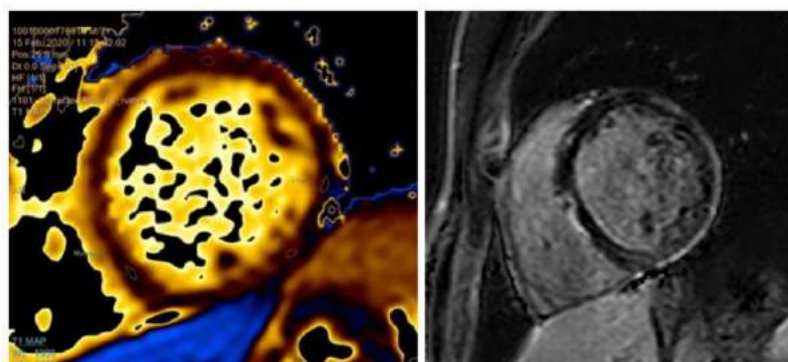
**Figure/Table 1**



**Caption 1**

Late gadolinium enhancement and short axis images in Duchenne muscular dystrophy

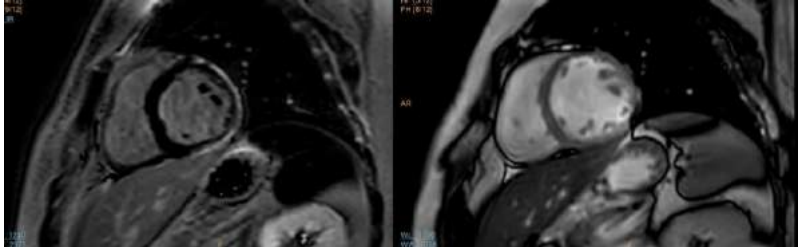
**Figure/Table 2**



**Caption 2**

T 1mapping and late gadolinium enhancement images in Duchenne muscular dystrophy

**Figure 3**



**Caption 3**

Late gadolinium enhancement and short axis images in Becker muscular dystrophy

Speaker: A. Mohata

Category: Muscular Dystrophy, Parametric Mapping, Cardiac Strain

000435

## Native T1 and Contrast Excretion in Normal Pericardial Fluid and Pericardial Effusions at 1.5T

S. Thalén \* (1); J. Ramos (2); P. Sorensson, (3); H. Engblom, (2); M. Ugander, (4)

(1) Clinical Physiology, Karolinska Institute, Stockholm, Sweden, Sweden; (2) Clinical physiology, Karolinska Institute, Stockholm, Sweden; (3) Medicine, Karolinska Institute, Stockholm, Sweden; (4) Kolling institute, The University of Sydney, Camperdown, Australia

### Abstract

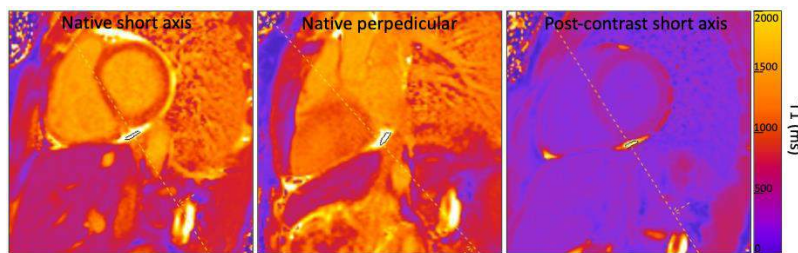
**Background:** T1 mapping has shown promise in characterizing pericardial effusions, and also shown that gadolinium-based contrast agents administered during a cardiovascular magnetic resonance (CMR) exam are excreted into pericardial effusion fluid (1,2). The potential diagnostic utility of contrast excretion dynamics in pericardial fluid is unknown. This study aimed to measure pericardial fluid T1 before and after contrast administration (gadoteric acid, 0.2 mmol/kg) in healthy volunteers in order to establish normal values and further compare them to a clinical cohort of patients with pericardial effusion.

**Methods:** Healthy volunteers (n=30) were recruited and compared to a clinical cohort consisted of 69 patients with at least 5 mm of pericardial effusion previously characterized (2). CMR T1 maps were acquired using a 1.5T MAGNETOM Aera scanner and a prototype MOLLI sequence using a 5s(3s)3s acquisition scheme. A short-axis (SA) stack encompassing the heart was acquired and a perpendicular (P) slice was prescribed through any pocket of pericardial fluid. A reliable measurement had a region of interest size >10 mm<sup>2</sup>, coefficient of variation <10%, and relative difference <5% between P and SA. The following variables were analysed and compared: native T1,  $\Delta T1$  defined as the difference between native T1 and post-contrast T1 and  $\Delta R1$  defined as  $1/\text{post-contrast T1} - 1/\text{native T1}$ . An example T1 map is shown in figure 1. Normal reference ranges were calculated as mean  $\pm$  1.96\*SD.

**Results:** In healthy volunteers, 26/30 (87%) had a sufficient amount of pericardial fluid to enable reliable measurement. Native T1 of pericardial fluid in SA and P slices did not differ ( $3262 \pm 163$  vs  $3267 \pm 173$  ms,  $p=0.75$ ).  $\Delta T1$  was  $1710 \pm 344$  ms and  $\Delta R1$   $0.37 \pm 0.15$  s<sup>-1</sup>. Results when applying the established normal reference ranges to the clinical cohort are shown in figure 2. Native T1 was normal in 28/69 (41%) of patients, above normal in 2/69 (3%) and below normal 39/69 (57%), and  $\Delta R1$  was normal in 53/69 (77%) of patients, above normal in 14/69 (20%) and below normal in 2/69 (3%).

**Conclusion:** T1 can be reliably measured in a normal pocket of pericardial fluid in healthy volunteers, and normal reference values are presented. Furthermore, T1 mapping shows promising ability to differentiate normal pericardial fluid from pericardial effusion fluid in patients. Roughly half of the effusions had a below normal native T1, consistent with higher protein content, and 20% had an above normal  $\Delta R1$ , indicating a higher contrast concentration despite dilution effects in a larger volume of pericardial fluid, suggesting an inflammatory and exudative etiology.

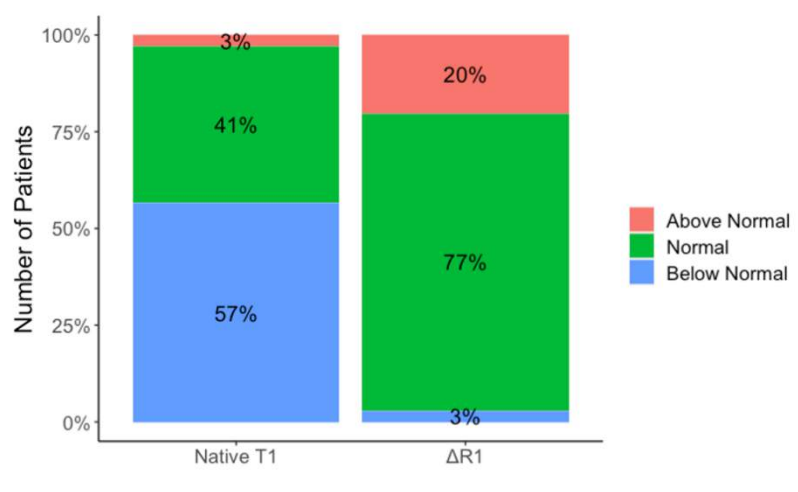
### Figure/Table 1



**Caption 1**

**Figure 1.** Example T1 maps taken before contrast administration in short axis (left) and perpendicular (middle) slice orientation, and in short-axis post contrast (right).

**Figure/Table 2**



**Caption 2**

**Figure 2.** Stacked barplots showing the percentage of clinical patients above, within and below the normal reference ranges determined from the healthy volunteers.

## Bibliographic References

1. Rosmini S, Seraphim A, Knott K, Brown JT, Knight DS, Zaman S, et al. Non-invasive characterization of pleural and pericardial effusions using T1 mapping by magnetic



resonance imaging. Eur Heart J Cardiovasc Imaging. 2021 Jul 30;jeab128. , 2. Thalén S, Maanja M, Sigfridsson A, Maret E, Sörensson P, Ugander M. The dynamics of extracellular gadolinium-based contrast agent excretion into pleural and pericardial effusions quantified by T1 mapping cardiovascular magnetic resonance. J Cardiovasc Magn Reson Off J Soc Cardiovasc Magn Reson. 2019 14;21(1):71.

Speaker: S. Thalén

Category: Contrast, Pericardial Effusion, Native T1

000436

## **4D flow MRI energetics in the Fontan circulation correlate with exercise capacity and MRI derived liver fibrosis**

F. Rijnberg, \* (1); J. Westenberg, (2); H. van Assen (2); J. Juffermans (2); L. Kroft, (2); P. van den boogaard (2); C. Terol Espinosa De Los Monteros (3); E. Warmerdam (4); T. Leiner (5); H. Grotenhuis (6); M. Jongbloed (7); M. Hazekamp (1); A. Roest (3); H. Lamb (2)

(1) Cardiothoracic surgery, Leiden University Medical Center (LUMC), Leiden, Netherlands; (2) Radiology, Leiden University Medical Center (LUMC), Leiden, Netherlands; (3) Pediatric cardiology, Leiden University Medical Center (LUMC), Leiden, Netherlands; (4) Pediatric cardiology, UMC Utrecht, Utrecht, Netherlands; (5) Radiology, UMC Utrecht, Utrecht, Netherlands; (6) Pediatric Cardiology, Wilhelmina Childrens Hospital / UMCU, Utrecht, Netherlands; (7) Cardiology, Leiden University Medical Center (LUMC), Leiden, Netherlands

### **Abstract**

#### **Background**

Blood flow efficiency in the TCPC has been associated with exercise capacity and liver fibrosis using in silico computational fluid dynamic modelling(1, 2). Nowadays, 4D flow MRI allows for assessment of in vivo blood flow energetics, including kinetic energy (KE) and viscous energy loss rate (EL). This study explores the relationship between in vivo 4D flow MRI derived blood flow energetics in the total cavopulmonary connection (TCPC) with exercise capacity and MRI derived liver fibrosis.

#### **Methods**

Fontan patients were prospectively evaluated using a comprehensive cardiovascular and liver MRI protocol, including 4D flow imaging of the TCPC, between 2018-2021. Peak VO<sub>2</sub> was determined using cardiopulmonary exercise testing (CPET). Iron-corrected whole liver T1 mapping was performed as a marker of liver fibrosis. KE and EL in the TCPC were computed from 4D flow MRI and normalized for inflow. Furthermore, blood flow energetics were compared between standardized segments of the TCPC after normalization for inflow and/or segment length(3).

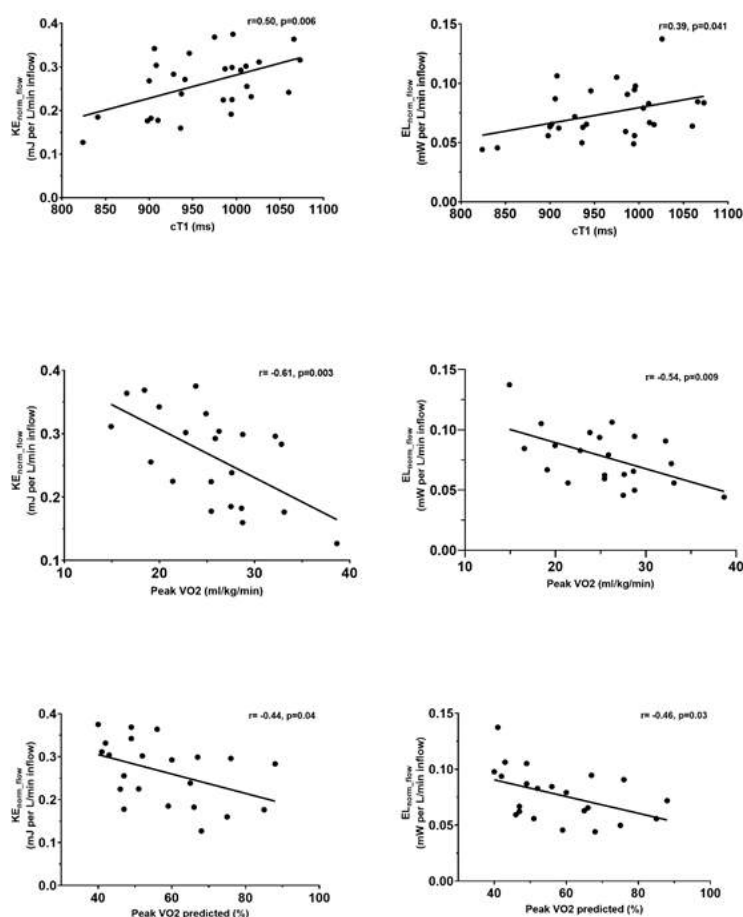
#### **Results**

Sixty-two Fontan patients were included (53% male, mean age 17.3 years (SD 5.1 years). Maximal effort CPET was obtained in 50 patients (peak VO<sub>2</sub> 27.1±6.2 ml/kg/min, 56±12% of predicted). Both KE and EL in the entire TCPC (n=28) were significantly correlated with cT1 (r=0.50, p=0.006 and r=0.39, p=0.04, respectively, Figure 1A-B), peak V02 (r=-0.61, p=0.003 and r=-0.54, p=0.009, respectively, Figure 2A-B) and predicted peak V02 (r=-0.44, p=0.04 and r=-0.46, p=0.03, respectively, Figure 3A-B). An example of two representative cases is shown in Figure 2. Segmental analysis indicated that the Fontan tunnel and left pulmonary artery were associated with most adverse energetics (Table 1).

## Conclusions

In vivo 4D flow MRI derived kinetic energy and viscous energy loss rate in the TCPC correlates with exercise capacity and MRI derived liver fibrosis. 4D flow MRI therefore has great potential as a non-invasive screening tool for identification of patients with adverse TCPC flow efficiency to guide treatment strategies during follow-up.

**Figure/Table 1**

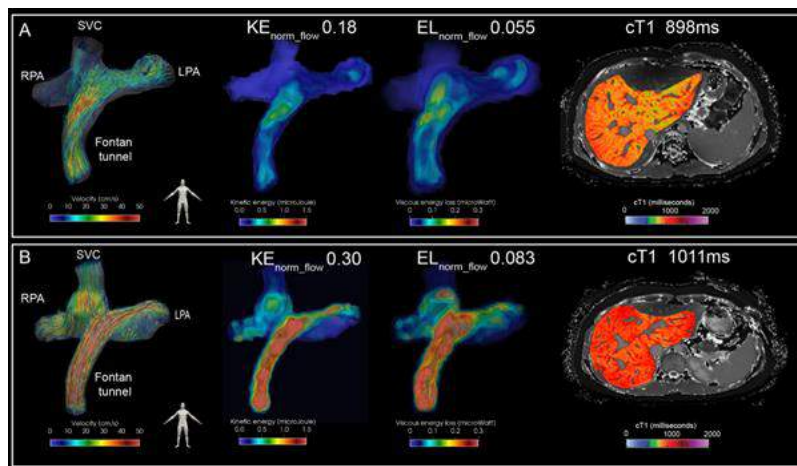


**Caption 1**

Correlation analysis between KE (left) and EL (right) with cT1 liver mapping (upper panel), peak VO2 (middle panel) and predicted peak VO2 (lower panel) are shown.

KE; kinetic energy, EL; viscous energy loss rate

**Figure/Table 2**



**Caption 2**

Streamline representation of blood flow in the TCPC is shown for 2 Fontan patients (left panel). Corresponding spatial distribution of KE and EL is shown (middle panels). The time-averaged normalized energetics values are indicated above. Whole liver cT1 mapping is shown for a transversal slice (right panel).

KE; kinetic energy, EL; viscous energy loss rate, cT1; iron-corrected T1 mapping, RPA/LPA; right/left pulmonary artery, SVC; superior vena cava.

**Figure 3**

**Table 1.** 4D flow MRI derived energetics in the TCPC

4D flow MRI	n	KE <sub>norm_flow</sub>	EL <sub>norm_flow</sub>
Total TCPC	28	0.26(0.01)	0.075(0.022)
<i>Segmental analysis</i>		<b>KE<sub>norm_flow+length</sub></b>	<b>EL<sub>norm_flow+length</sub></b>
Fontan tunnel	35	0.034(0.011)	0.0087(0.0029)
SVC	31	0.023(0.0069)	0.0065(0.0024)
LPA	46	0.040(0.018)	0.012(0.0054)
RPA	49	0.031(0.0095)	0.0081(0.0032)
Fontan confluence	56	0.094*(0.041)	0.031*(0.013)

Values indicate mean (SD). \* KE<sub>norm\_flow</sub> and EL<sub>norm\_flow</sub>. LPA/RPA; left/right pulmonary artery, SVC; superior vena cava, TCPC; total cavopulmonary connection, KE; kinetic energy, EL; viscous energy loss rate

### **Bibliographic References**

3. Friso M Rijnberg, Joe F Juffermans, Mark G Hazekamp, Willem A Helbing, Hildo J Lamb, Arno A W Roest et al. Segmental assessment of blood flow efficiency in the total cavopulmonary connection using 4D flow MRI: vortical flow is associated with increased viscous energy loss, *European Heart Journal Open*, 2021;, oeab018, <https://doi.org/10.1093/ehjopen/oeab018>, 2. Trusty PM, Wei ZA, Rychik J, Graham A, Russo PA, Surrey LF, et al. Cardiac Magnetic Resonance-Derived Metrics Are Predictive of Liver Fibrosis in Fontan Patients. *Ann Thorac Surg*. 2020;109(6):1904-11., 1. Khiabani RH, Whitehead KK, Han D, Restrepo M, Tang E, Bethel J, et al. Exercise capacity in single-ventricle patients after Fontan correlates with haemodynamic energy loss in TCPC. *Heart*. 2015;101(2):139-43.

Speaker: F. Rijnberg,

Category: 4D Flow, Congenital Heart Disease, VO2

000437

## SW cardioprotective therapy by using shock waves: in vivo MR validation after myocardial infarction in porcine model

L. Petrusca \* (1); M. Viallon (2); K. Moulin (2); L. Augeul (3); N. Mewton (4); P. Croisille (2)

(1) Univ Lyon, insa-lyon, université claudes bernard lyon 1, ujm-saint etienne, cnrs, inserm, creatis, Creatis Laboratory, Lyon; (2) Univ Lyon, insa-lyon, université claudes bernard lyon 1, ujm-saint etienne, cnrs, inserm, creatis, St Etienne North Hospital, Radiology Department, Villeurbanne; (3) Inserm umr-1060, laboratoire carmen, université lyon 1, faculté de médecine, rockefeller, lyon, CarMeN Laboratory, Lyon; (4) Centre d'investigation clinique de lyon, hôpital louis pradel, hospices civils de lyon, lyon, fr, Hospices Civils de Lyon, Lyon

### Abstract

**Background:** The new frontier in the treatment of acute myocardial infarction (AMI) has shifted from the rapid restoration of an effective reperfusion of the occluded artery, toward the effective protection of myocardium at risk for infarction in the territory downstream of occlusion, by mean of so-called “cardioprotection” strategies[1]. Several Phase II clinical studies were conducted to test various cardioprotective targeted interventions to reduce infarct size. For now, no therapy has demonstrated its effectiveness and/or been successfully transposed to the routine therapeutic care in patients with AMI[2]. Here, we propose to investigate the effects of shock waves (SW) therapy as a non-invasive cardioprotective innovative approach to trigger healing molecular mechanisms in acute phase of AMI.

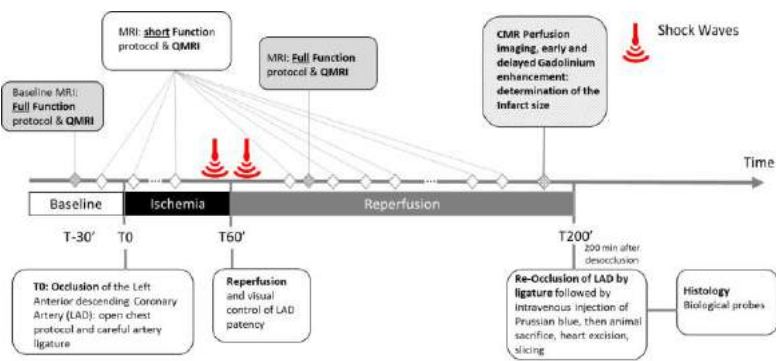
**Materials and Methods:** SW therapy benefit was evaluated in an ischemia-reperfusion (IR) open chest model in swine after using quantitative CMR (Fig1). AMI was induced during 50 minutes in 14 farm pigs, randomized in 2 equivalent groups: with SW therapy and without (control). In the therapy group, SW applications was initiated at the end of the ischemia using the DUOLITH device, (Storz Medical, Switzerland) and prolonged during early reperfusion (600 +1200 shots @0.07 mJ/mm<sup>2</sup>, f=5Hz). Quantitative CMR acquisitions (1.5T magnet, Aera, Siemens healthcare) was performed at multiple time-points, including baseline (B), Ischemia (I), Early and Late Reperfusion (ER, LR: @3hours) and after Gadolinium administration. The MR protocol included native T1, T2 mapping, global & regional function quantification, post-Gd T1 mapping, early & late Gd enhancement (EGE & LGE). The mean values of MR indexes were determined in the lesion, blood and remote myocardium. Before animal sacrifice, uniprimer blue was administrated after reocclusion for area at risk determination.

**Results:** A significant change in the ejection fraction (LVEF) was observed at the end of reperfusion in the treated SW group (+59.9%) versus (+52.3%) in control group compared to ischemia. Tissue changes as revealed by T1,T2 relaxation times show moderate evolution in both groups during ischemia step in the lesion area (+9.6%, +8.6% in control, +5.4% and -1.1% in SW group), while a strong increase of T1 and T2 is detected at the reperfusion step (+22.5%, +23.6 in control and +26.9% and +24.4% in SW group). A reduction of the global strain is coherently observed during ischemia in both groups, while the strain values are strongly and significantly increased during ER in the treated group compared to the control group (radial/circumferential/longitudinal: +4.7%/+2.6%/-16% in the control group

versus +39.7%/+34%/+17.5% in SW group). MVO obstruction was detected in both groups (N=2 in each group).

**Discussion:** Our protocol involving full quantitative evaluation of tissue biomarkers and function after AMI demonstrate an improvement in global and regional cardiac function, indicating a noticeable positive effect of the SW therapy after AMI during early reperfusion. A trend toward higher T1 and T2 values that did not reach significance indicate slight additional edema in the SW group. This study open new question on the role of edema and deserves further experimental investigations including chronic follow-up.

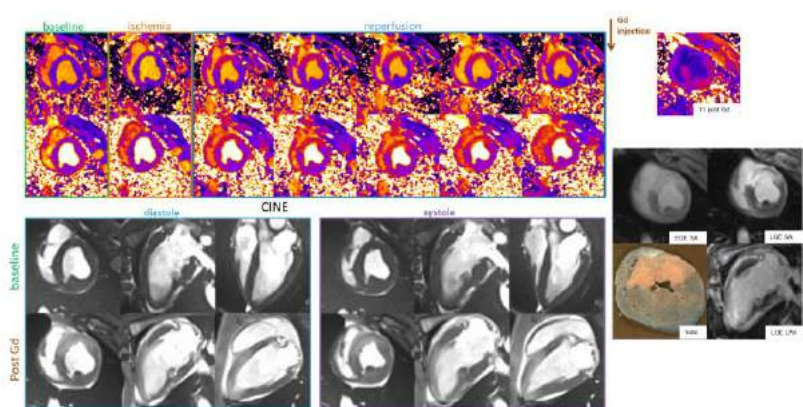
Figure/Table 1



Caption 1

Figure 1. MR and SW therapy multi-step protocol of acute ischemia reperfusion pig model at open chest

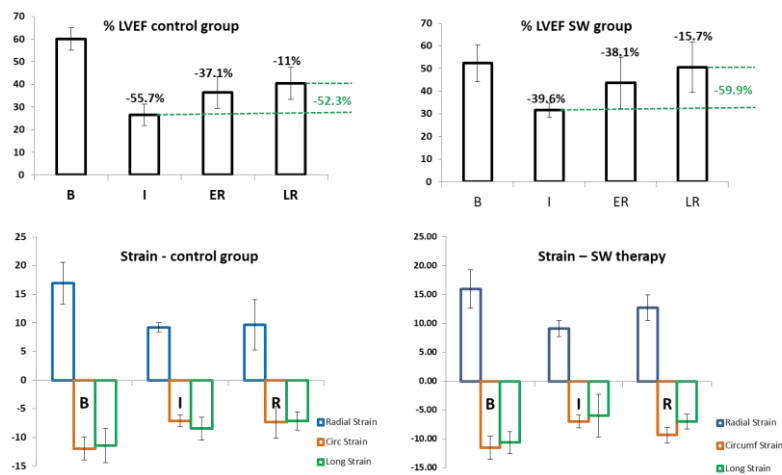
Figure/Table 2



Caption 2

Figure 2. Example of T1 and T2 dynamics in baseline, during ischemia and reperfusion in a pig model. CINE images are displayed in 3 orthogonal axes, in diastole and systole. EGE and LGE maps are shown in short and long axis, together with a macroscopic picture of the lesion after blue injection.

**Figure 3**



**Caption 3**

Figure 3. % of LVEF ejection fraction in 4 different steps of the protocol (B, I, ER and LR) in control and SW therapy group. Strain (radial, circumferential and longitudinal) evolution is illustrated in both configurations (lower part of the figure)

Speaker: L. Petrusca

Category: Acute Myocardial Infarction, Animal Experimentation, Medical Treatment



000442

## **Magnetic resonance myocardial T1-rho mapping: comparison to T1 mapping, T2 mapping and late gadolinium enhancement imaging**

A. Bustin \* (1); X. Pineau (2); S. Sridi (2); P. Jaïs (1); M. Stuber (3); H. Cochet (1)

(1) Ihu liry, electrophysiology and heart modeling institute, Université de Bordeaux – INSERM U1045, Bordeaux; (2) Department of cardiovascular imaging, Hôpital Cardiologique du Haut-Lévêque, CHU de Bordeaux, Bordeaux; (3) Department of diagnostic and interventional radiology, Lausanne University Hospital and University of Lausanne, Lausanne, Switzerland

### **Abstract**

#### **Background:**

Magnetic resonance myocardial T1 rho (T1 $\rho$ ) mapping has emerged as a promising tool for detecting myocardial injuries without exogenous contrast agents (1-3). Yet, the tissue determinants driving T1 $\rho$  changes are still unclear, and the applicability of the technique to the broad spectrum of acute and chronic myocardial injuries remains uncharted territory. The aims of this study were to identify clinical correlates of myocardial T1 $\rho$ , and to examine how myocardial T1 $\rho$  mapping performs against conventional pre- and post-contrast techniques under various clinical scenarios.

#### **Methods:**

A total of 113 subjects were enrolled between October 2020 and December 2020. The population comprised 69 patients (51 males, age  $54 \pm 16$ yo) with known ischemic (N=18) and non-ischemic (N=51) heart disease and 44 healthy controls (22 males, age  $44 \pm 16$ yo). CMR was performed using a 1.5T Siemens MAGNETOM Aera scanner. Breath-held T1 $\rho$  mapping (pre-contrast, Fig.1), conventional T2 mapping (T2-prepared bSSFP, pre-contrast), T1 mapping (MOLLI, pre- and post-contrast), ECV quantification, and late gadolinium enhancement (LGE, 15min after injection of 0.2mmol/kg gadoteric acid) were performed in short-axis (2). Injured areas were defined by an expert as regions with LGE, while remote areas were defined as regions with no LGE. The agreement between T1 $\rho$  map, T2 map, ECV and LGE was assessed at a segmental level on the left ventricle (LV). Quantitative analysis was achieved by tracing regions of interest on T1 $\rho$ , T2, and ECV maps within remote and injured areas.

#### **Results:**

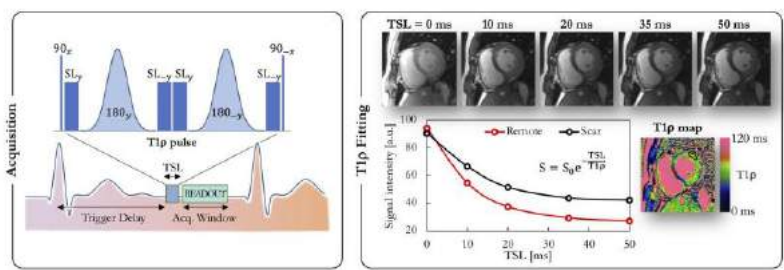
In healthy controls, mean myocardial T1 $\rho$  was  $47 \pm 2$ ms. Compared to males, females showed higher T1 $\rho$  ( $48 \pm 2$ ms vs.  $46 \pm 2$ ms,  $P < 0.01$ ), T2 ( $47 \pm 2$ ms vs.  $45 \pm 3$ ms,  $P = 0.03$ ) and ECV ( $26 \pm 2\%$  vs.  $24 \pm 2\%$ ,  $P < 0.01$ ). T1 $\rho$  positively related with age ( $R = 0.4$ ,  $P < 0.01$ ), and significantly increased from basal to apical LV levels ( $P < 0.01$ ). In patients with acute focal myocardial injuries (N=9 with focal T2 elevation), T1 $\rho$  significantly increased ( $69 \pm 7$ ms vs.  $48 \pm 2$ ms in remote,  $P < 0.01$ ). In patients with focal fibrosis (N=27 with positive LGE and negative T2), T1 $\rho$  significant increased ( $64 \pm 5$ ms vs.  $47 \pm 2$ ms in remote,  $P < 0.01$ ). In patients with diffuse myocardial involvement (N=8 with ECV  $> 30\%$ ), T1 $\rho$  significantly increased

( $52\pm6\text{ms}$  vs.  $47\pm2$  in controls,  $P<0.01$ ) with a moderate positive correlation with ECV ( $R=0.312$ ,  $P<0.01$ ). Examples of patients with ischemic and non-ischemic cardiomyopathies are shown in Figures 2 and 3.

Conclusions:

Myocardial T1 $\rho$  values are gender and age dependent. The technique appears to be equally sensitive to acute, chronic, focal, and diffuse myocardial injuries, and may thus be a contrast-free adjunct to CMR for gaining new and quantitative insight into acute and chronic myocardial structural disorders.

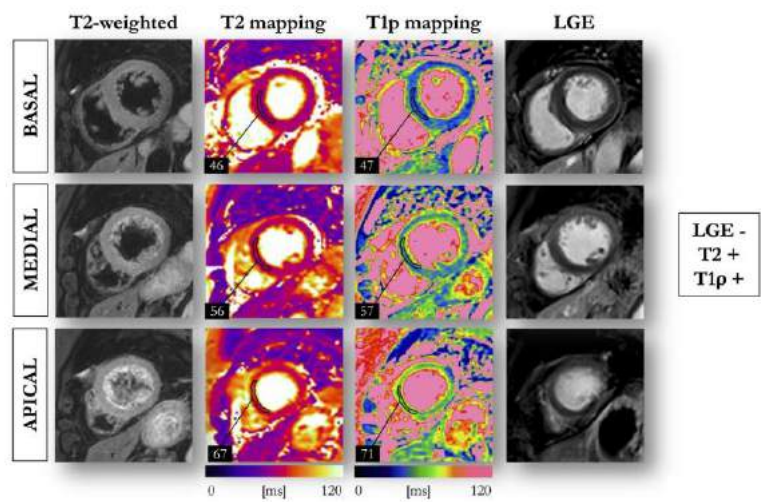
Figure/Table 1



Caption 1

**Figure 1.** Schematic of the proposed 2D myocardial T1 $\rho$  mapping sequence (**left**) with joint T1 $\rho$  fitting and model-based non-rigid motion correction (**right**) (2). T1 $\rho$  mapping is performed using a single-shot ECG-triggered balanced steady-state free precession acquisition where five images with different spin lock times (TSL) are acquired over 13 heartbeats within a single breath-hold.

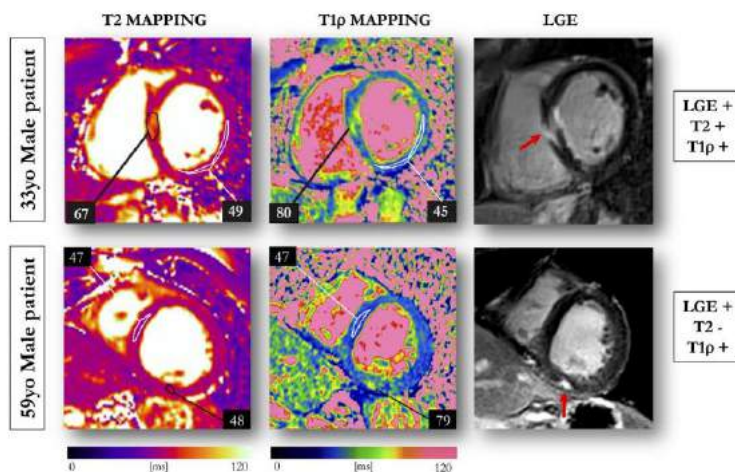
Figure/Table 2



## Caption 2

**Figure 2.** 57-year-old female patient with CMR findings consistent with Takotsubo cardiomyopathy. T2-weighted images and T2 maps exhibit myocardial edema at the medial and apical short-axis levels (T2=67ms) with a clear T1ρ elevation at these locations (T1ρ=71ms) whereas LGE images show a lack of ischemia and delayed hyperenhancement.

## Figure 3



## Caption 3

**Figure 3.** Top: 33-year-old male patient with ischemic cardiomyopathy reflected by basal anteroseptal hyperenhancements on LGE with T2 (67ms) and T1ρ (80ms) elevations. Bottom: 59-year-old male patient with non-ischemic dilated cardiomyopathy with subepicardial inferobasal hyperenhancement on LGE with a clear T1ρ elevation in the same segment (T1ρ=79ms) and normal T2 on T2 mapping (T2=48ms).

## Bibliographic References

1. Witschey WE, et al. In vivo chronic myocardial infarction characterization by spin locked cardiovascular magnetic resonance. J. Cardiovasc. Magn. Reson. 2012;14:1-9., 2. Bustin A, et al. Endogenous assessment of myocardial injury with single-shot model-based non-rigid motion-corrected T1 rho mapping, J. Cardiovasc. Magn. Reson. 2021 (In Press)., 3. Van Oorschot JWM, et al. Single breath-hold T1r -mapping of the heart for endogenous assessment of myocardial fibrosis. Invest. Radiol. 2016;51:505-512.

Speaker: A. Bustin

Category: Parametric Mapping, Contrast, Mapping Techniques

000443

## CMR-derived left ventricular intraventricular pressure gradient analysis to predict response of cardiac resynchronization therapy

J. Vos \* (1); C. Wegen, Van Der (1); G. Pedrizzetti (2); C. P. Allaart (3); A. Zweerink (3); R. Nijveldt (3)

(1) Cardiology, Radboud University Medical Center, Nijmegen, Netherlands; (2) Dipartimento di ingegneria e architettura, University of Trieste, Trieste, Italy; (3) Cardiology, Amsterdam UMC, locatie VUmc, Amsterdam, Netherlands

### Abstract

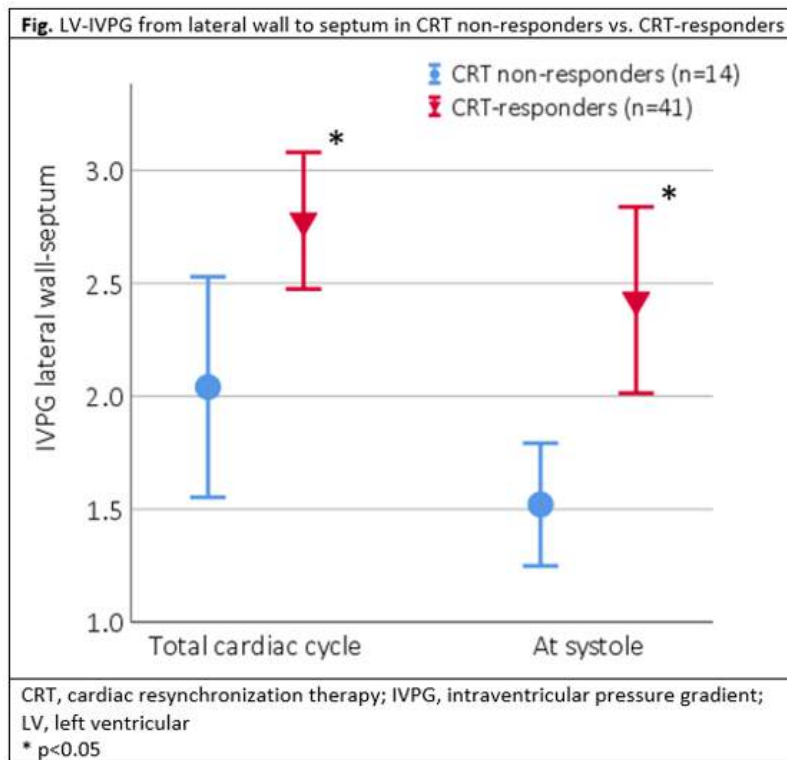
**Background:** Cardiac resynchronization therapy (CRT) is a treatment for heart failure patients with reduced left ventricular (LV) ejection fraction (EF) and ventricular conduction delay. However, in around one third of patients this therapy fails. A new post-processing technique on CMR can estimate LV intraventricular pressure gradients (IVPG) using standard cine images. LV-IVPGs, driving cardiac blood flow, is normally directed from apex to base. In these patients, however, the IVPGs are likely to be altered by the mechanical dyssynchrony, causing a lateral-septal deviation. LV-IVPGs could therefore potentially help predicting which patients can benefit from CRT.

**Methods:** In this multicenter study, patients with heart failure and ventricular conduction delay underwent CMR imaging before CRT-implantation. LV-IVPGs (from apex to base, and from lateral wall to septum) were calculated using the myocardial movement and velocity of the 3D-LV, which is reconstructed by using feature tracking strain on the long-axis cines. CRT-response is defined as a reduction in LV end-systolic volume (ESV) of  $\geq 15\%$  on echocardiography between baseline and 12 months after CRT implantation.

**Results:** Of the 55 patients ( $64 \pm 10$  years, 44% male) included in this study, 41 (75%) were defined as CRT-responders. Compared to CRT non-responders, CRT-responders had higher lateral wall-septum LV-IVPG (during the total cardiac cycle, and at systole; see **Figure**). Both lateral wall-septum LV-IVPG parameters were associated with CRT-response (at systole: OR 3.66 [95% CI 1.12-11.85],  $p=0.03$ , and during total cardiac cycle: OR 3.83 [95% CI 1.19-12.36],  $p=0.03$ , respectively, see **Table**).

**Conclusions:** Higher lateral wall to septal deviation of LV-IVPGs, depicting a higher degree of mechanical dyssynchrony, are associated with CRT-response. This potential parameter for predicting CRT response, measured on standard cine images, might help identifying heart failure patients who can benefit from this therapy.

### Figure/Table 1



**Figure/Table 2**

Table. Univariable association with CRT response (defined as $\geq 15\%$ LV ESV reduction)		
	Heart failure patients (n=55)	
	Odds ratio (95% CI)	p-value
<i>LV Intraventricular pressure gradient analysis</i>		
Apex-base (during the whole cardiac cycle)	1.19 (0.98-1.44)	0.079
Lateral wall-septum (during the whole cardiac cycle)	3.827 (1.19-12.358)	<b>0.025</b>
Apex-base (at systole)	1.06 (0.99-1.13)	0.094
Lateral wall-septum (at systole)	3.66 (1.13-11.85)	<b>0.032</b>
CRT, cardiac resynchronization therapy; ESV, end-systolic volume; LV, left ventricular.		

Speaker: J. Vos

Category: Cardiac Resynchronization , Heart Failure, Cardiac Function

000444

## **Deteriorating coronary microvascular function despite normal coronary angiography in a patient with co-morbid hypertrophic cardiomyopathy and type two diabetes mellitus**

N. Jex \* (1); A. Chowdhary (1); S. Thirunavukarasu (1); D. Broadbent (2); E. Levelt (1)

(1) Leeds institute of cardiovascular and metabolic medicine, University of Leeds, Leeds, United Kingdom; (2) Medical physics, Leeds General Infirmary, Leeds, United Kingdom

### **Abstract**

#### **Description of the clinical presentation**

A 59 year old patient with concomitant type two diabetes (T2D) and hypertrophic cardiomyopathy (HCM) with apical phenotype with no left ventricular outflow tract obstruction at rest or during hemodynamic stress was seen over a 16 year period in our regional inherited cardiac conditions (ICC) clinic. The patient suffered with a significant burden of anginal symptoms which were refractory to standard anti-anginal therapy including calcium channel blockers, beta blockers, nitrates or ranolazine. His past medical history included hypertension and previous lacunar stroke, there was no family history of HCM and he was a lifelong non-smoker. The standard gene panel screening for 21 HCM genes did not reveal any causative sarcomeric mutation and his European Society of Cardiology (ESC) risk score remained below 2%. He was obese and his T2D control was persistently suboptimal with a mean HbA1c of 54mmol/mol. Over the course of 16 years the patient required a total of four hospital admissions to acute cardiology services due to episodes of refractory chest pain at rest with elevated but non-dynamic troponin elevations.

#### **Diagnostic techniques and their most important clinical findings**

Despite repeated invasive X ray-coronary angiography assessments in 2004, 2010 and 2014 showing no significant obstructive atheroma, serial cardiac magnetic resonance (CMR) scans displayed worsening microvascular function as assessed by quantitative perfusion analysis. Changes in clinical characteristics and CMR findings between 2010 and 2019 can be seen in table 1. Global stress Myocardial Blood flow (MBF) reduced over time with a similar stepwise decline in rest MBF and myocardial perfusion reserve index (MPRI). There was associated decline in cardiac contractile function with reduction in left ventricular ejection fraction (LVEF) and global longitudinal strain (GLS). There was a similar decline in CMR markers of diastolic function with a fall in diastolic strain rates. There was a modest increase in maximal LV apical wall thickness and myocardial mass. There was also a decline in left atrial (LA) function with a reduction in LAEF. Finally, there was an increase in myocardial fibrosis burden as assessed by late gadolinium enhancement.

#### **Learning points from this case**

The prevalence of T2D comorbidity is higher in patients with apical HCM phenotype compared to non-apical HCM phenotypes (15% vs 7% respectively), the reasons for this are not well understood(1). Although distinct entities, both T2D and HCM have been independently shown to be associated with coronary microvascular dysfunction(2-4).

This case offers a unique insight into the natural history of these co-morbid conditions with serial CMR imaging and perfusion quantification over a nine-year period. This case demonstrates a synergistic effect between HCM and T2D on coronary microvascular function and LV systolic function with a high symptom burden, despite no significant change in traditional risk stratification scores and without the development of epicardial coronary artery obstruction.

**Figure/Table 1**

<b>Variable</b>	<b>2010</b>	<b>2017</b>	<b>2019</b>
<b>BMI, kg/m<sup>2</sup></b>	34	36	38
<b>Heart rate, bpm</b>	72	64	70
<b>Systolic BP, mmHg</b>	129	130	128
<b>Diastolic BP, mmHg</b>	79	74	84
<b>eGFR, ml/min/1.73m<sup>2</sup></b>	70	64	61
<b>HbA1c, mmol/mol</b>	-	50	58
<b>Medications</b>			
<b>ACEi</b>	-	-	-
<b>Beta blocker</b>	+	+	+
<b>CCB</b>	+	+	+
<b>MRA</b>	+	+	+
<b>ASA</b>	+	+	+
<b>DOAC</b>	-	-	-
<b>Metformin</b>	-	+	+
<b>Statin</b>	-	-	+
<b>DPP4i</b>	-	-	-
<b>GLP-1RA</b>	-	-	-
<b>SGLT2i</b>	-	-	-
<b>Clinical features</b>			
<b>NSVT</b>	-	-	-
<b>NYHA Class</b>	III	III	III
<b>ESC risk score (%)</b>	1.76	1.67	1.69
<b>Angina Class</b>	II	III	III
<b>CMR parameters</b>			
<b>LV end-diastolic volume indexed to BSA, mL/m<sup>2</sup></b>	69	68	69
<b>LV end-systolic volume indexed to BSA, mL/m<sup>2</sup></b>	17	18	24
<b>LV mass, g</b>	243	250	252
<b>LV mass index, g/m<sup>2</sup></b>	103	106	107
<b>LV mass to LV end-diastolic volume, g/mL</b>	1.5	1.6	1.6
<b>LV stroke volume, mL</b>	120	113	96
<b>LV ejection fraction, %</b>	74	72	63



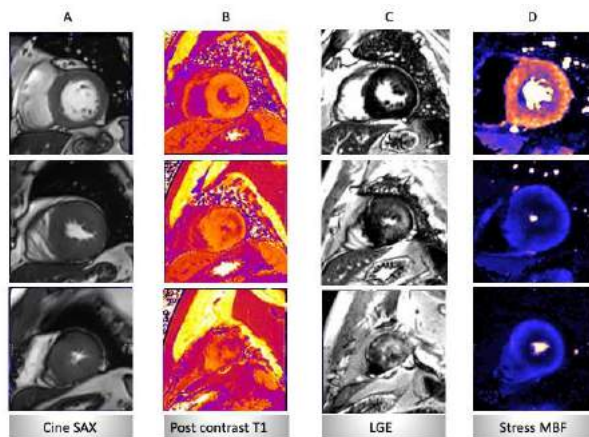
<b>LV maximal wall thickness, mm</b>	21	23	24
<b>RV end-diastolic volume indexed to BSA, mL/m<sup>2</sup></b>	71	61	51
<b>RV end-systolic volume indexed to BSA, mL/m<sup>2</sup></b>	28	23	21
<b>RV stroke volume, ml</b>	102	86	70
<b>RV ejection fraction, %</b>	61	60	58
<b>LA biplane end-systolic volumes, mL</b>	-	66	68
<b>Biplane LA EF, %</b>	-	58	51
<b>Global longitudinal strain, negative (-), %</b>	15	12	8
<b>Peak circumferential diastolic strain rate, s<sup>-1</sup></b>	0.88	-	0.61
<b>Mean native T1, (ms)</b>	-	1351	1395
<b>Extra cellular volume, (%)</b>	-	31	38
<b>Stress MBF, ml/min/g</b>	2.63	1.1	0.75
<b>Rest MBF, ml/min/g</b>	0.9	0.5	0.6
<b>MPR</b>	2.9	2.2	1.3

BMI indicates Body mass index; bpm, beats per minute; BSA, body surface area; LV, Left ventricle; RV, right ventricle; T2D, type 2 diabetes mellitus; HCM, hypertrophic cardiomyopathy; LV, left ventricular; LA, left atrial; LA EF, left atrial ejection fraction; LGE, late gadolinium enhancement; MBF, myocardial blood flow; MPR, myocardial perfusion reserve; eGFR, estimated glomerular filtration rate; HDL, high density lipoprotein; LDL, low density lipoprotein; TG, triglycerides; ACEI, angiotensin converting enzyme inhibitor; ARB, angiotensin receptor blocker; CCB, calcium channel blocker; ASA, aspirin; DOAC, direct oral anticoagulant; DPP4i, dipeptidyl peptidase – 4 inhibitor; GLP-1RA, glucagon-like peptide-1 receptor agonist; MRA, mineralocorticoid receptor antagonist; SGLT2i, sodium glucose co-transporter 2 inhibitor; NSVT, non-sustained ventricular tachycardia; NYHA, New York Heart Association; ESC, European Society of Cardiology.

### Caption 1

Changes in clinical characteristics and CMR parameters between 2010 and 2019

### Figure/Table 2



## Caption 2

Representative examples of basal, mid and apical left ventricular short axis showing cine images (A), post contrast T1 maps (B), late gadolinium enhanced images (C) and stress myocardial blood flow (D).

## Bibliographic References

Petersen SE, Jerosch-Herold M, Hudsmith LE, Robson MD, Francis JM, Doll HA, Selvanayagam JB, Neubauer S and Watkins H. Evidence for Microvascular Dysfunction in Hypertrophic Cardiomyopathy. *Circulation*. 2007;115:2418-2425., Shivu GN, Phan TT, Abozguia K, Ahmed I, Wagenmakers A, Henning A, Narendran P, Stevens M and Frenneaux M. Relationship between coronary microvascular dysfunction and cardiac energetics impairment in type 1 diabetes mellitus. *Circulation*. 2010;121:1209-15., Levelt E, Gulsin G, Neubauer S and McCann GP. MECHANISMS IN ENDOCRINOLOGY: Diabetic cardiomyopathy: pathophysiology and potential metabolic interventions state of the art review. *Eur J Endocrinol*. 2018;178:R127-r139., Wasserstrum Y, Barriales-Villa R, Fernández-Fernández X, Adler Y, Lotan D, Peled Y, Klempfner R, Kuperstein R, Shlomo N, Sabbag A, Freimark D, Monserrat L and Arad M. The impact of diabetes mellitus on the clinical phenotype of hypertrophic cardiomyopathy. *European Heart Journal*. 2018;40:1671-1677.

Speaker: N. Jex

Category: Hypertrophic Cardiomyopathy, Diabetes, Perfusion

000445

## Improving CMR access in Low-Middle Income Countries for Cardiomyopathy Assessment and Improved Cardiac Care: Rapid CMR

K. Menacho \* (1); R. Sara (2); A. Perez Barreda (3); L. Dragonetti (4); D. Perez De Arenaza (5); R. Bertha (6); B. Rajiv (7); A. Seraphim (8); K. Knott (9); A. Peix Gonzalez (3); S. Sharma (10); R. Jacob (11); T. Treibel (9); S. Mohiddin (12); C. Manisty (9); M. Westwood (13); H. Litt (14); N. Ntusi (15); Y. Han (16); A. Herrey (17); M. Walker (18); J. Moon (19)

(1) , University College London, Gower Street, London, United Kingdom; (2) Cardiology department, Peruvian Air Force Hospital, Miraflores, Peru; (3) Cardiac imaging department, Cardiology and Cardiovascular Surgery National Institute, La Havana, Cuba., Havana, Cuba; (4) Radiology department, Instituto Medico De Alta Tecnologia, Buenos Aires, Argentina; (5) Cardiology department, Hospital Italiano de Buenos Aires, Buenos Aires, Argentina; (6) Mri and ct department, Hospital Nacional Edgardo Rebagliati Martins, Jesús María, Peru; (7) Cum medical research institute, Santokba Durlabhji Memorial Hospital (SDMH), Jaipur, India; (8) Cardiac imaging, St Bartholomew's Hospital, London, United Kingdom; (9) Institute of cardiovascular science, University College London, London, United Kingdom; (10) Radiology department, All India Institute Of Medical Sciences, New Delhi, New Delhi, India; (11) Cardiac imaging department, LG Health Physicians Hospitalists, Lancaster, United States of America; (12) Barts heart centre, St Bartholomew's Hospital, London, United Kingdom; (13) Barts heart centre, Barts Health NHS Trust, London, United Kingdom; (14) Department of radiology, School of Medicine - University of Dundee, Philadelphia, United States of America; (15) Department of medicine, University of Cape Town, Cape Town, South Africa; (16) Medicine/cardiology, University of Pennsylvania, Philadelphia, United States of America; (17) Barts heart centre, St Bartholomew's Hospital, West Smithfield London, United Kingdom; (18) The hatter cardiovascular institute, University College Hospital, London, United Kingdom; (19) Cardiac mri, Barts Health, London, United Kingdom

### Abstract

**Background:** To evaluate the impact of a simplified, rapid cardiovascular magnetic resonance (CMR) protocol embedded in clinical care and supported by an international partnership education program on the management of cardiomyopathies in low-and middle income countries (LMICs).

**Methods:** CMR using an abbreviated protocol was focused on the evaluation of cardiomyopathies. Figure 1. The rapid CMR protocol was implemented in eleven centres, seven cities, five countries in three continents. The CMR exams were coupled with no-fee conferences for local professionals and CMR scanning and reporting training for the staff of the participant centres. Patients were followed up for 24 months to assess impact. The rate of subsequent adoption was tracked.

**Results:** Figure 2. Five CMR conferences were delivered to 920 attendees and 18 professionals were newly trained in CMR scanning and reporting in five participant centres. Six-hundred one patients were scanned in eleven hospitals with MRI units, using fourteen different scanners (six models from three manufacturers at two field strengths). Table 1. 98% of the studies were of diagnostic quality.

Indications for CMR included non-contrast T2\* scans for myocardial iron overload (MIO) in 24% of participants, and for the assessment of suspected/ known cardiomyopathies in 72%.

Average scanning time was 22±6 minutes (contrast studies) and 12±4 minutes (non-contrast MIO). Still when adding specific sequences (e.g. myocarditis, for ARVC) the average time of scanning was <30 minutes. A potential cost/throughput reduction of between 30-60%- See table 1. CMR findings impacted management in 62% of patients, including a new diagnosis in 22% and MIO detected in 30% of non-contrast scans. 82% of centres continued using rapid CMR two years later, (typically one to two days per week, 30-minute slots). Table 1.

**Conclusions:** Diagnostic quality CMR can be undertaken more quickly and at lower cost when enabled with a partnership supporting program for education. When implemented in LMICs, rapid CMR utilising available technology has an important impact on patient care.

#### Figure/Table 1

#### Caption 1

Figure 1: Rapid CMR Protocol - A) Contrast-CMR protocol for the assessment of cardiomyopathies, with the option of T1 mapping; B) T2\* protocol to assess iron overload. C) STIR T2w or T2 mapping + T1 mapping for myocarditis, D) T1 or T2w FSE + real-time cine for pericarditis and E) Fat suppression and saturation + RV cine acquisition for ARVC.

#### Figure/Table 2

Country	Argentina	Cuba	Peru		South Africa	India (Non-Contrast T2* CMR)	
City	Buenos Aires N = 69	La Havan a N = 114	Lima N = 248	Arequipa N = 13	Cape Town N = 34	Delhi N = 53	Jaipur N = 70

Centre	Centre 1	Centre 2	Centre 3	Centre 4	Centre 5**	Centre 6	Centre 7**	Centre 8	Centre 9	Centre 10	Centre 11
MRI Brand	Siemens Philips	Siemens	Siemens	Siemens	Philips	Philips	GE	Philips	Siemens x 2	GE	Siemens
MRI Field	1.5T	1.5T	1.5T	1.5T	1.5T	3T	1.5T	1.5T	1.5T - 3T	1.5T	1.5T
MRI Model	Aera and Ingenia	Avanto	Aera	Avanto	Ingenia	Achieva	Signa HDxt	Ingenia	Aera and Skyra	Signa HDxt	Avanto
Before Rapid CMR scan											
Number of days per week	1	2	3	0	1	0	0	0	2	1	0
Number of hours x day	5	5	5	0	5	0	0	0	5	2	0
CMR scans per day	4	5	3-4	0	4	0	0	0	5	2	0
Cost	\$400-500		\$600	\$400-\$600					\$350-\$500	\$70-\$100	
After Rapid CMR scan											
Number of days per week	1	2	3	1	1	1	1	1	2	1	1
Number of hours x day	5	5	5	4	5	4	4	4	5	2	2
CMR scans per day	5-7	6-7	7-9	6	6-8	6	6	6	6-7	4-6	4-6+
RapidCMR Scans											
(30min x contrast)	5-6	3-4	6-8	4	4-6	4	4	4	5	4-6	4-6+
(20min x T2* scan)											
Cost Rapid	\$280-\$380		\$360	\$160-300					\$200-\$400	\$42-\$60	

<b>CMR Scan</b>					
<b>% Saving</b>	30%	40%	50%-60%	25-30%	40%

## Caption 2

Table 1: MRI scanner information and Cardiac Magnetic Resonance practice in the centers before and after the implementation of the Rapid CMR protocol.

*\*\* Faulty scanners stopped CMR service.*

*+Ten scans done after Rapid CMR. Starting CMR scans this year.*

## Figure 3

## Caption 3

Figure 2: Summary of findings of the Rapid CMR project in Low-Middle Income Countrie

Speaker: K. Menacho

Category: Rapid Imaging, Cardiomyopathy, Cardiac Function

000451

## Prognostic Value of Cardiac Magnetic Resonance Imaging Parameters in Left Ventricular Noncompaction with Left Ventricular Dysfunction

W. bai \* (1); R. Xu (2)

(1) Radiology, West China Second University Hospital, Sichuan University, Sichuan, China;  
(2) Radiology, West China Second University Hospital, /, China

### Abstract

**BACKGROUND:** Cardiac magnetic resonance (CMR) has been used to diagnose and risk-stratify patients with left ventricular noncompaction (LVNC). The prognostic value of CMR parameters for LVNC, especially feature tracking (FT), is not well known in LVNC patients with left ventricular dysfunction. The present study aimed to investigate whether the combination of CMR-FT with traditional CMR parameters can increase the prognostic value of CMR for LVNC patients with reduced left ventricular ejection fraction (LVEF).

**METHODS:** A total of 123 candidates were retrospectively included in this multi-center study and 55 LVNC patients (mean age,  $45.7 \pm 16.2$  years; 61.8% men) remained after applying the exclusion criteria. Clinical features, left ventricular (LV) function parameters, global and segment myocardial strain, and late gadolinium enhancement (LGE) were evaluated. The outcomes include the composite events of cardiovascular death, heart transplantation, hospitalization for heart failure, thromboembolic events, and ventricular arrhythmias.

**RESULTS:** After a median follow-up of 5.17 years (interquartile range: 0.17 to 10.58 years), 24 (36.8%) patients experienced at least one major adverse cardiovascular event (MACE). The myocardial strain parameters of patients with events were lower than those of patients without events. For the univariable Cox analysis, LVEF, the presence of LGE, global longitudinal strain (GLS) and the segmental strains including the longitudinal strain at the apical level and radial and circumferential strain at the basal level were significantly associated with MACEs. In the multivariate analysis, LGE (HR 3.452, 95% CI 1.133 to 10.518,  $p=0.029$ ) was a strong predictor of MACEs and significantly improved predictive value (chi-square of the model after adding LGE: 7.51 vs. 13.47,  $p=0.009$ ). However, myocardial strain parameters were no statistically significant for prediction of MACEs after adjusted for age, body mass index (BMI), LVEF and the presence of LGE and cannot increase prognostic value (chi-square of the model after adding GLS: 13.47 vs. 14.14,  $p=0.411$ ) in the multivariate model.

**CONCLUSIONS:** LV strain parameters from CMR-FT have no significant incremental prognostic value in LVNC patients with reduced LVEF while the presence of LGE was a strong independent predictor of MACEs.

### Figure/Table 1

Clinical characters	HR (95% CI)	<i>p</i> value	CMR parameters	HR (95% CI)	<i>p</i> value	CMR parameters	HR (95% CI)	<i>p</i> value

Age	1.024 (0.998-1.050)	0.072	EDV	1.003 (0.998-1.008)	0.253	ARS	0.989 (0.938-1.044)	0.696
Sex	0.484 (0.192-1.222)	0.125	ESV	1.003 (0.999-1.008)	0.165	ACS	1.032 (0.961-1.108)	0.388
BMI	0.883 (0.788-0.988)	0.031*	SV	0.989 (0.971-1.008)	0.259	ALS	1.177 (1.024-1.353)	0.022*
Hypertension	0.440 (0.149-1.300)	0.137	LVEF	0.964 (0.929-0.999)	0.046*	MRS	0.947 (0.886-1.013)	0.113
Smoking	0.581 (0.238-1.419)	0.234	LGE extent	11.385 (0.441-293.9)	0.143	MCS	1.093 (0.981-1.219)	0.108
Diabetes	1.365 (0.504-3.696)	0.541	Patients with LGE	2.768 (1.033-7.419)	0.043*	MLS	1.083 (0.978-1.200)	0.125
Hypercholesterolemia	1.008 (0.385-2.637)	0.987	GRS	0.945 (0.881-1.014)	0.116	BRS	0.950 (0.901-1.002)	0.061
Severe arrhythmia	1.651 (0.723-3.771)	0.234	GCS	1.086 (0.976-1.210)	0.130	BCS	1.178 (1.014-1.369)	0.032*
NYHA Class III/IV	1.194 (0.507-2.816)	0.685	GLS	1.238 (1.018-1.506)	0.033*	BLS	1.000 (0.898-1.114)	0.997

**Caption 1**

\* means significant difference. The univariable HR and 95% CI are shown for the association with MACE. MACE, major adverse cardiovascular event; CI, confidence interval; HR, hazard ratio; BMI, body mass index; NYHA, New York Heart Association; EDV, left ventricular end-diastolic volume; ESV, left ventricular end-systolic volume; SV, stroke volume; LVEF, left ventricular ejection fraction; LGE, late gadolinium enhancement; GRS, global radial strain; GCS, global circumferential strain; GLS, global longitudinal strain; ARS, ACS, ALS, radial, circumferential and longitudinal peak strain at apical level; MRS, MCS, MLS, radial, circumferential and longitudinal peak strain at midlevel; BRS, BCS, BLS, radial, circumferential and longitudinal peak strain at basal level;

**Figure/Table 2**



	<b>Model 1</b>		<b>Model 2</b>	
	<b>Fit</b>	<b>P value</b>	<b>Fit</b>	<b>P value</b>
-2Loglikelihood	120.698		120.604	
Likelihood ratio test	7.42	0.02	7.51	0.06
C-index	0.667 (0.532 to 0.802)		0.663 (0.524 to 0.802)	
Continuous NRI			0.082 (-0.363 to 0.441)	# vs. model 1: p=0.878
<b>Covariates</b>				
Age	1.021 (0.993 to 1.049)	0.145	1.021 (0.993 to 1.049)	0.144
BMI	0.893 (0.796 to 1.003)	0.056	0.889 (0.787 to 1.003)	0.057
LVEF			1.006 (0.967 to 1.047)	0.757
Presence of LGE				
GLS				
	<b>Model 3</b>		<b>Model 4</b>	
	<b>Fit</b>	<b>P value</b>	<b>Fit</b>	<b>P value</b>
-2Loglikelihood	114.785		114.043	
Likelihood ratio test	13.47	0.009	14.14	0.01
C-index	0.712 (0.583 to 0.841)		0.707 (0.570 to 0.844)	
Continuous NRI	0.235 (0.000 to 0.568)	#vs. model 2: p=0.049	-0.226 (-0.527 to 0.306)	# vs. model 3: p=0.585
<b>Covariates</b>				
Age	1.023 (0.993 to 1.053)	0.137	1.022 (0.993 to 1.053)	0.135
BMI	0.872 (0.776 to 0.978)	0.02	0.863 (0.767 to 0.970)	0.014
LVEF	1.017 (0.976 to 1.060)	0.425	1.006 (0.959 to 1.055)	0.816
Presence of LGE	3.452 (1.133 to 10.518)	0.029	3.241 (1.060 to 9.904)	0.039
GLS			0.882 (0.666 to 1.168)	0.381

**Caption 2**

The -2Loglikelihood and c-index (95%IC) of each model for the prediction of MACE were reported. The continuous NRI estimates (95% CI) for comparison of models were compared to evaluate the incremental prognostic value of these nested regression models. For the covariates, HR and 95% CIs were reported instead of fit statistics. NRI, net reclassification improvement. other abbreviations as in Tables 1.

### **Bibliographic References**

5.Arunamata A, Stringer J, Balasubramanian S, Tacy TA, Silverman NH, Pun R. Cardiac Segmental Strain Analysis in Pediatric Left Ventricular Noncompaction Cardiomyopathy. J Am Soc Echocardiogr. 2019;32(6):763-773.e1. doi: 10.1016/j.echo., 4.Fischer K, Obrist SJ, Erne SA, Stark AW, Marggraf M, Kaneko K, Guensch DP, Huber AT, Greulich S, Aghayev A, et al. Feature Tracking Myocardial Strain Incrementally Improves Prognostication in Myocarditis Beyond Traditional CMR Imaging Features. JACC Cardiovasc Imaging. 2020;13(9):1891-1901. doi: 10.1016/j.jcmg.2020.04.025., 3.Towbin JA, Lorts A, Jefferies JL. Left ventricular non-compaction cardiomyopathy. Lancet. 2015;386:813-825. doi: 10.1016/S0140-6736(14)61282-4., 2.Andreini D, Pontone G, Bogaert J, Roghi A, Barison A, Schwitter J, Mushtaq S, Vovas G, Sormani P, Aquaro GD, et al. Long-Term Prognostic Value of Cardiac Magnetic Resonance in Left Ventricle Noncompaction: A Prospective Multicenter Study. J Am Coll Cardiol. 2016;68:2166-2181. doi: 10.1016/j.jacc.2016.08.053. , 1.Aras D, Tufekcioglu O, Ergun K, Ozeke O, Yildiz A, Topaloglu S, Deveci B, Sahin O, Kisacik HL, Korkmaz S. Clinical features of isolated ventricular noncompaction in adults long-term clinical course, echocardiographic properties, and predictors of left ventricular failure. J Card Fail. 2006;12:726-733. doi: 10.1016/j.cardfail.2006.08.002.

Speaker: W. bai

Category: Feature Tracking, Late Gadolinium Enhancement, Congenital Heart Disease

**000452**

**New insights on hyperacute tissue damage dynamics along ischemia-reperfusion in myocardial infarction swine model: T1, T2, and cDTI quantification**

K. Moulin \* (1); L. Petrusca (1); C. Kang (2); M. Bonneau (2); S. Gerelli (3); M. Viallon (1); P. Croisille (1)

(1) Rhône, CREATIS Laboratory, Univ. Lyon, UJM-Saint-Etienne, INSA, CNRS UMR 5520, INSERM, Lyon; (2) G life, G life, Thoiry; (3) Service de chirurgie cardiaque, centre hospitalier annecy-genevois, site annecy, 1 avenue de l'h, G LIFE , Thoiry

**Abstract**

**Background:**

Reperfusion therapy is the most effective strategy against myocardial ischemic damage to limit infarct size while decreasing mortality after acute myocardial infarction (AMI) (1). However, abrupt reperfusion has deleterious effects on so-called reperfusion injury (2), and still justifies the development of cardioprotective strategies to limit final infarct size. With quantitative CMR, there is a crucial need to revisit the dynamics of ischemia-reperfusion to provide advanced imaging protocol to validate such strategies. In this work, CMR imaging with T1, T2 mapping, and cardiac diffusion tensor imaging (cDTI) were performed prior to, during ischemia, and after reperfusion to better understand the respective advantages of these imaging biomarkers.

**Methods:**

Under propofol-fentanyl anesthesia, ten swine (N=10) were imaged at baseline on a 3T scanner (Prisma, Siemens) at baseline (H-2). A medial sternotomy allowed positioning of a LAD occluder at the 2nd-diagonal level. Without moving the subject from the scanner, they were scanned after surgery prior to ischemia (H-1), after occlusion during the 1hour induced ischemia (H=0), and after reperfusion repeatedly during the three hours post-reperfusion (H+1,2,3).

At each time point, T1 mapping (bSSFP MOLLI, 1x1x8mm), T2 (bSSFP T2-prep, 1x1x8mm), and cDTI (free-breathing (3) motion-compensated (4) single-shot EPI, 1.6x1.6x8mm, b-values 0 – 350 s/mm<sup>2</sup>, 12 directions, 10 averages) were acquired. T1, T2, Mean Diffusion (MD), and Fraction of anisotropy (FA) were analyzed in an infarct and remote ROI. A statistical mixed-effects model was used to evaluate the significance of temporal changes.

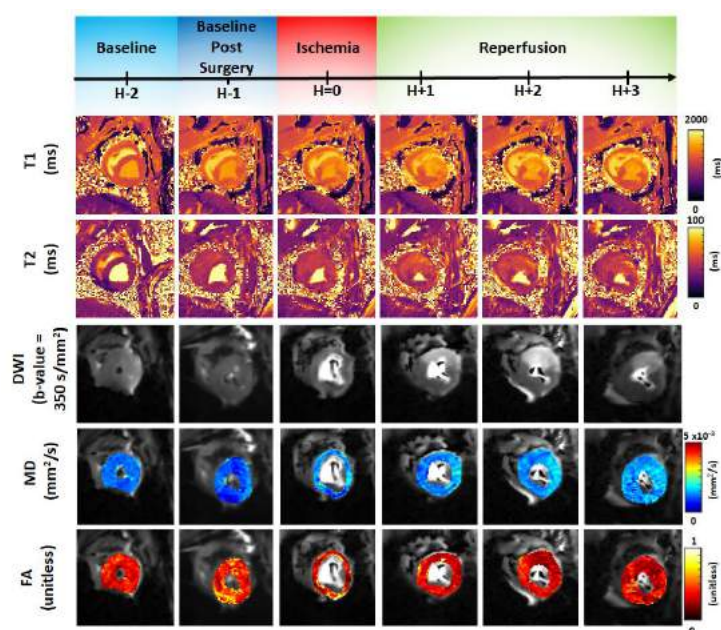
**Results:**

All 10 were successfully imaged pre-ischemia, 9 during ischemia, and a total of 6 underwent the whole procedure with success (1 fatal arrhythmia during ischemia and 3 during post-reperfusion). Figure 1 shows representative maps from the same case at all time points. As shown in Figure 2 for all cases, T1 increased significantly in the infarct region immediately after ischemia, while T2 and MD exhibit a very moderate increase. Two hours post-reperfusion (H+3), MD (+36%), and FA (+21%) show the most significant increase compared to T1 (+16%) and T2 (+18%) (Figure 3).

## Conclusions:

In this study, T1 appears to be the earliest marker of ischemic damage while T2 stands as a marker of the inflammation triggered by the reperfusion. Diffusion markers with current parameters are mainly sensitive to extra-cellular water mobility which could be key to witness long-term reperfusion injury and cellular remodeling.

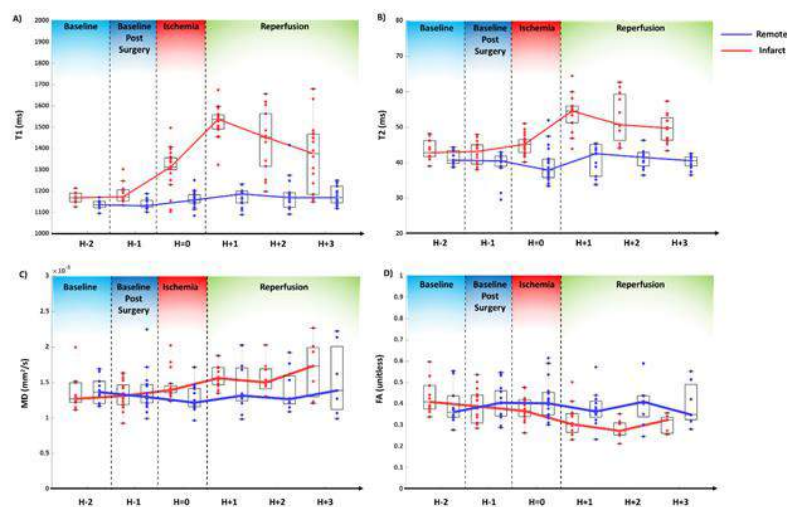
**Figure/Table 1**



**Caption 1**

Figure 1: Illustrative example from the same case with all measured time-points with T1, T2, Diffusion-weighted imaging (DWI) without and with diffusion sensitivity (b-value=350 s/mm²), Mean diffusivity (MD), and fraction anisotropy (FA).

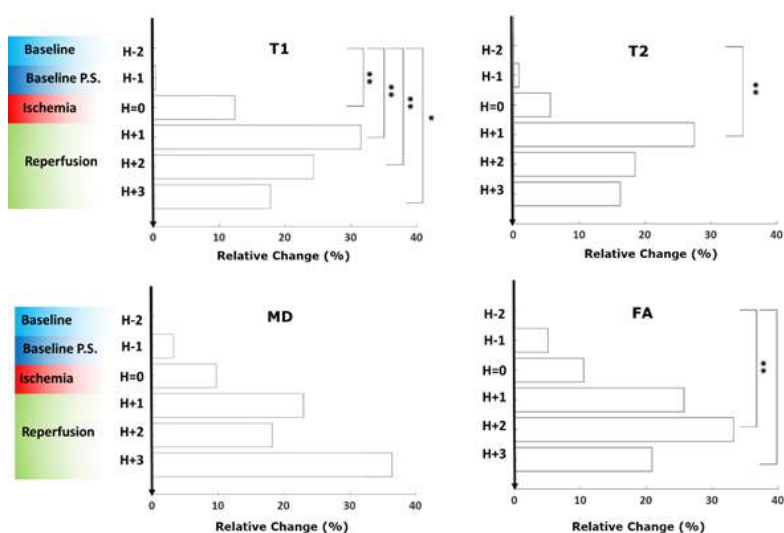
**Figure/Table 2**



**Caption 2**

Figure 2: Mean values across subjects in infarct and remote region for A) T1 maps, B) T2 maps, C) Mean diffusivity (MD) and D) Fraction of Anisotropy (FA) at baseline (H-2), post-surgery (H-1), after occlusion during ischemia (H=0), three hours post-reperfusion (H+1,2,3).

**Figure 3**



**Caption 3**

Figure 3: Relative changes to reference baseline values (in %) and for all time-points in the infarct regions of T1, T2, Mean Diffusivity (MD), and Fraction of Anisotropy (FA) measures. P-values of  $p < 0.05$  (\*) and  $p < 0.01$  (\*\*) are reported.

### **Bibliographic References**

(1) Kristensen SD, Laut KG, Fajadet J, et al. Reperfusion therapy for ST elevation acute myocardial infarction 2010/2011: current status in 37 ESC countries. *Eur Heart J*. 2014;35(29):1957–1970. , (2) Yellon DM, Hausenloy DJ. Myocardial Reperfusion Injury. *N Engl J Med*. 2007;15., (3) Moulin K, Croisille P, Feiweier T, et al. In vivo free-breathing DTI and IVIM of the whole human heart using a real-time slice-followed SE-EPI navigator-based sequence: A reproducibility study in healthy volunteers. *Magn Reson Med*. 2016;76(1):70–82., (4) Stoeck CT. Second order motion compensated spin-echo diffusion tensor imaging of the human heart. 2015;3.

Speaker: K. Moulin

Category: Acute Myocardial Infarction, Animal Experimentation, Quantification

000454

## Cardiac MRI Predictors of Early Right Ventricular Dysfunction After the Cone Operation for Ebstein Anomaly

T. Alsaied \* (1); F. D. S. L. De (2); S. J. Da (3); C. C. Diaz (3); T. Seery, (4); R. Torok, (4); J. Jennifer (4); A. Christopher (4); S. Tadros, (5)

(1) , Children's Hospital of Pittsburgh of UPMC, Pittsburgh, United States of America; (2) Cardiothoracic surgery, Children's Hospital of Pittsburgh of UPMC, Pittsburgh; (3) Cardiothoracic surgery, Children's Hospital of Pittsburgh of UPMC Department of Anesthesiology, Pittsburgh, United States of America; (4) Cardiology, UPMC Children's Hospital of Pittsburgh, Pittsburgh, United States of America; (5) Radiology, UPMC Children's Hospital of Pittsburgh, Pittsburgh, United States of America

### Abstract

**Introduction:** Despite the significant improvement in outcomes after the cone operation, right ventricular dysfunction is frequently seen on early follow up echocardiograms. Preoperative CMR offers a comprehensive evaluation of cardiac size and function and tricuspid valve anatomy before the cone procedure. In this study we sought to evaluate the predictors of right ventricular dysfunction after the cone operation using preoperative CMR.

**Methods:** This was a retrospective review of the last 20 consecutive patients who had a CMR prior to the cone operation. Leaflet distal attachment of the inferior and anterior leaflets to the right ventricular free wall was categorized as focal attachment and linear attachments. Focal attachments are normal attachments and allows free communications between the atrialized and functional right ventricle. Linear attachments occur when there is complete or partial attachment of the leaflet to a muscular shelf at the connection between the atrialized and functional ventricle<sup>1</sup> (Figure1). The Celermajer index is calculated as the right atrium plus the atrialized portion of the right ventricle/(functional right ventricle+ left atrium+ left ventricle) from the 4-chamber view in diastole<sup>2</sup> (Figure 2). The right ventricular outflow tract rotation angle was calculated from the right ventricular 3 chamber view as previously described<sup>2, 3</sup> (Figure 2). The cardiothoracic ratio was calculated from the 4 chamber stack view in diastole (Figure 2). The most recent follow up echocardiogram was evaluated for right ventricular dysfunction, tricuspid valve disease severity and left ventricular function. Right ventricular dysfunction was evaluated by conventional echocardiographic criteria. T-test and chi square tests were used to compare the groups with and without ventricular dysfunction.

**Results:** The median age at the cone operation was 17.9 years (interquartile range 7.2-30.8 years). The median follow up time to most recent echocardiogram was 7.4 months with a range from 1-53 months. There was no mortality. Eleven patients 55% had right ventricular dysfunction by echocardiography. Of them 3 had mild, 6 had moderate and 2 had severe dysfunction. Linear attachments of the anterior leaflet was seen by CMR in 36% and of the inferior leaflet in 57%. Patients with ventricular dysfunction were more likely to have linear attachments of the inferior leaflet, lower ejection fraction and higher cardiothoracic ratio by preoperative cardiac CMR (table). Of note all patients with post operative right ventricular dysfunction had preoperative ejection fraction <48%. Preoperative right ventricular dysfunction (ejection fraction of <48%) had a sensitivity of 100% and specificity of 67% for

post operative dysfunction. Linear attachments of the inferior leaflet had a sensitivity of 86% and specificity of 71% for right ventricular dysfunction.

**Conclusion:**Right ventricular dysfunction is common early after the cone operation and is associated with preoperative right ventricular dysfunction. Additionally, linear attachments of the inferior leaflet of the tricuspid valve is associated with dysfunction.

**Figure/Table 1**

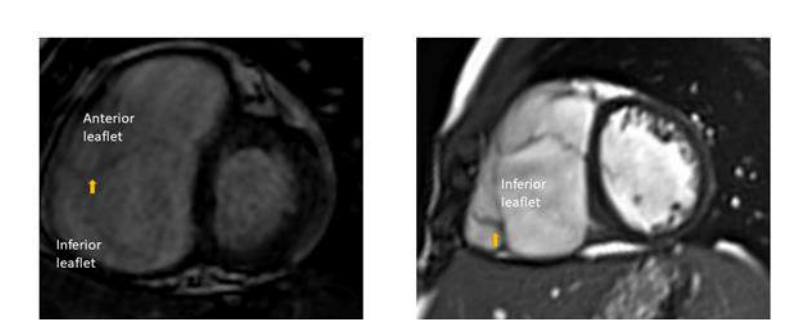
	Right ventricular dysfunction (n=11)	Normal right ventricle function (n=9)	P value
Age at repair	12.4 ± 11.0	24.6 ± 16.8	0.08
<b>Preoperative CMR</b>			
Pre operative RV ejection fraction (%)	35 ± 11	49 ± 17	<b>0.03</b>
RV indexed end diastolic volume (ml/m <sup>2</sup> )	140 ± 84	142 ± 76	0.95
RV indexed end systolic volume (ml/m <sup>2</sup> )	97 ± 70	67 ± 32	0.30
LV indexed end diastolic volume (ml/m <sup>2</sup> )	77 ± 41	63 ± 17	0.36
LV indexed end systolic volume (ml/m <sup>2</sup> )	32 ± 15	38 ± 36	0.66
Preoperative LV ejection fraction (%)	53 ± 11	63 ± 8	0.06
Linear attachments of the anterior leaflet (%)	57%	15%	0.09
Linear attachments of the inferior leaflet (%)	29%	86%	<b>0.03</b>
Celemaier index	0.55 ± 0.26	0.59 ± 0.45	0.82
Cardiothoracic index	44 ± 8	37 ± 6	<b>0.03</b>
Tricuspid valve rotational angle	53 ± 35	27 ± 14	0.49
Tricuspid regurgitant fraction (%)	44 ± 19	48 ± 21	0.77
<b>Most recent follow up echocardiogram</b>			
Tricuspid regurgitation severity moderate or more (%)	9%	11%	0.88
Tricuspid stenosis moderate or more (%)	0%	0%	1.0



Caption 1

**Table 1:** Differences between the groups with and without post operative right ventricular dysfunction.

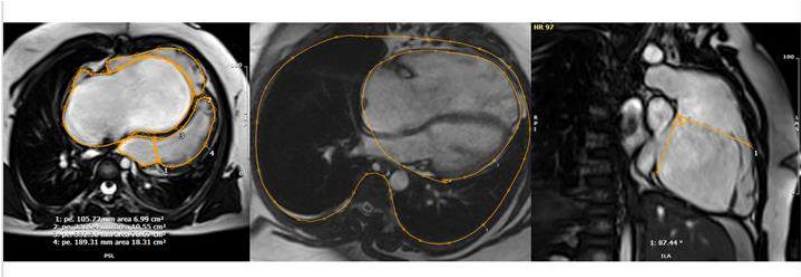
Figure/Table 2



Caption 2

Figure 1: The left panel represents focal attachment of the tricuspid valve to the left ventricular free wall (arrow). The left panel represents linear attachment of the inferior leaflet to the right ventricular free wall (arrow).

Figure 3



Caption 3

Figure 2: The left image: the Celemajer index =the area of the right atrium and atrialized right ventricle /(the area of the functional right ventricle+ left ventricle and left atrium). The middle

panel: cardiothoracic ratio= the cardiac area/ the chest area. The right panel is a right ventricular 3 chamber view to calculate the tricuspid valve rotational angle.

### **Bibliographic References**

3. Celermajer DS, Cullen S, Sullivan ID, Spiegelhalter DJ, Wyse RK and Deanfield JE. Outcome in neonates with Ebstein's anomaly. J Am Coll Cardiol. 1992;19:1041-6., 2.

Hughes ML, Bonello B, Choudhary P, Marek J and Tsang V. A simple measure of the extent of Ebstein valve rotation with cardiovascular magnetic resonance gives a practical guide to feasibility of surgical cone reconstruction. J Cardiovasc Magn Reson. 2019;21:34., 1.

1. Leung MP, Baker EJ, Anderson RH and Zuberbuhler JR. Cineangiographic spectrum of Ebstein's malformation: its relevance to clinical presentation and outcome. J Am Coll Cardiol. 1988;11:154-61.

Speaker: T. Alsaied

Category: Ebstein's Anomaly, Congenital Heart Disease, Tricuspid Valve

000455

## Sex differences in aortic compliance in masters athletes

R. Hughes \* (1); N. Ojzyńska (2); J. Augusto (1); A. Bhuva (2); G. Parry-Williams (3); S. Papatheodorou (3); A. D'silva (3); C. Torlasco (4); C. Manisty (1); A. Hughes (1); S. Sharma (3); J. Moon (1)

(1) Institute of cardiovascular sciences, University College London, London, United Kingdom; (2) Barts heart centre, St Bartholomew's Hospital, London, United Kingdom; (3) Cardiovascular sciences research centre, St George's Hospital, London, United Kingdom; (4) Istituto auxologico italiano, San Luca Hospital, Lucca, Italy

### Abstract

#### Background

Aortic stiffening increases with sedentary age and is associated with cardiovascular disease. Lifelong exercise counteracts this – at least in male masters athletes, but the impact in females is unknown.

#### Methods

We measured aortic compliance in male and female masters athletes [JA1] (n=305, mean age 53.9) and healthy controls (n=50), measuring Pulse Wave Velocity (PWV), aortic distensibility and beta-stiffness ( $\beta$ , a blood pressure independent measure of aortic stiffening). Masters athletes were defined as age  $\geq 40$ , exercised systematically for  $>10$  years and competed in  $>10$  endurance events. Male and female athletes were recruited from the same sporting bodies. CMR was performed at 1.5T, measuring arterial stiffness at ascending, proximal descending and distal descending aorta (Ao-A, Ao-P, Ao-D. Biological vascular age was derived from correlating distensibility with chronological age.

#### Results

All central blood pressure parameters were lower in athletes. Athletes demonstrated expected cardiac adaptation (higher indexed end diastolic, end systolic and stroke volumes, all  $P < 0.005$ ; increased LV mass,  $P = 0.022$ ). Aortic distensibility was equivalent to controls at every aortic level.  $\beta$  was also equivalent, except at Ao-D, where athletes were stiffer (median (IQ range)  $3.06 \times 10^{-3} \text{ mmHg}^{-1}$  (2.54–3.81) vs  $2.63 \times 10^{-3} \text{ mmHg}^{-1}$  (2.18–3.21),  $P < 0.005$ ). PWV was lower in athletes in the descending aorta (6.67m/s (5.86-7.89) vs 8.51m/s (7.00-10.85),  $P < 0.005$ ), but higher across the whole aorta (8.03m/s (6.6-10.1) vs 6.84 (6.10-8.42),  $P < 0.005$ ) and equivalent in the Ao-A ( $P = 0.348$ ). These results showed a similar trend when considering female and males separately. Female athletes have increased distensibility at Ao-P and Ao-D compared with male athletes ( $P = 0.007$ ,  $P < 0.005$  respectively), and lower  $\beta$  ( $P = 0.009$ ,  $P < 0.005$ ). Male masters athletes were biologically older than their chronological age at each aortic level (4.6 years at Ao-A, 9.1 years at Ao-P and 1.5 years at Ao-D). Female masters athletes were biologically older at the levels of Ao-A and Ao-P but by a significantly smaller magnitude than males (0.3 years at Ao-A,  $P < 0.005$  between genders, 2.9 years at Ao-P,  $P < 0.005$ ). Female masters athletes were biologically younger at the Ao-D level (-5.8 years,  $P < 0.005$ ).

## **Conclusion**

Regular exercise to masters athlete level in older age is associated with a sex specific effect on aortic compliance compared with matched non-athletes, with males demonstrating a significant increase in vascular age at each aortic level compared with females. Female masters athletes exhibit age-reversal in the distal descending aorta (-5.8 years).

Speaker: R. Hughes

Category: Aortic Distensibility, Athlete, Pulse Wave Velocity

000456

## Automated compensation of bulk patient movement in free-running whole-heart 4D CMR

C. Roy \* (1); J. Yerly (2); M. Prša (3); E. Tenisch (1); T. Rutz (4); D. Piccini (5); M. Stuber (2)

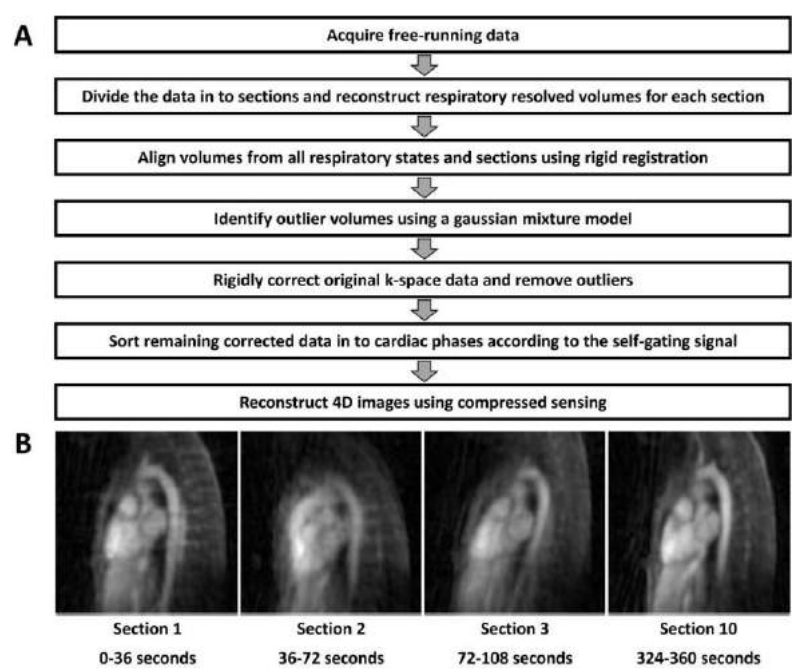
(1) Department of radiology, Lausanne University Hospital (CHUV) and University of Lausanne (UNIL), Lausanne, Switzerland; (2) Department of radiology, Lausanne University Hospital (CHUV), CIBM, and University of Lausanne (UNIL), Lausanne, Switzerland; (3) Department of woman-mother-child, Lausanne University Hospital (CHUV), and University of Lausanne (UNIL), Lausanne, Switzerland; (4) Department of cardiology, Lausanne University Hospital (CHUV) and University of Lausanne (UNIL), Lausanne, Switzerland; (5) Advanced clinical imaging technology, Siemens Healthineers, Lausanne, Switzerland

### Abstract

**Background:** High resolution three-dimensional CINE (4D) whole-heart MRI typically requires ECG gating and respiratory navigation, each of which contribute to unpredictable scan times and add complexity to patient setup. The free-running framework (FRF) provides a simplified workflow by acquiring 3D data continuously for a fixed scan time and then retrospectively extracting self-gating signals to bin the data and reconstruct cardiac and respiratory motion resolved (5D) images (1). Despite the advantages of this approach, FRF acquisition times are typically several minutes long and therefore bulk patient movement remains a limiting factor that can degrade image quality or require patient sedation, especially in children. In this work we present a novel approach that identifies and compensates for patient movement in FRF data sets. We demonstrate the initial feasibility of this framework for reconstructing high-quality 4D images despite the presence of bulk patient movement and compare these to the previously established 5D reconstructions of FRF data. **Methods:** Ten patients with congenital heart disease, (age: 6-23 years, 4 males), with a clinical indication for cardiac MRI, were included in this IRB approved study. These subjects are part of a larger research study and were included in this work based on visually identified bulk motion using the first steps of the framework described in Fig. 1. Examinations were performed without sedation, during free breathing, on a 1.5T clinical MRI system (MAGNETOM Sola, Siemens Healthcare, Erlangen, Germany) after administration of 2 mg/kg of ferumoxytol. A slab-selective spoiled gradient echo prototype free-running 3D radial sequence was used and resulted in uninterrupted acquisitions of six minutes duration (1,2). Main sequence parameters were RF excitation angle: 15°, resolution: (1.15 mm)<sup>3</sup>, FOV (220 mm)<sup>3</sup>, TE/TR: 1.53/2.84 ms, readout bandwidth: 1002 Hz/pixel. All datasets were reconstructed using the previously described approach for cardiac and respiratory resolved 5D imaging (1) and with the proposed method for motion compensated 4D imaging described in Fig. 1. Subsequent comparisons were made between the end-expiratory phase of the 5D images and the proposed 4D images reconstructed from the same data sets. Comparison of image quality was performed using an artificial-intelligence based algorithm trained to grade 3D radial images of the heart. This algorithm was applied to both image reconstruction methods and statistical significance was measured using a paired t-test. **Results:** Fig. 2 and Fig. 3 show 5D image reconstructions and the proposed motion compensated 4D reconstructions of representative patients who displayed severe and moderate bulk motion during the scan, respectively. Despite the varying levels of motion, the proposed algorithm provides excellent delineation of the dynamic cardiac anatomy and shows great improvement in image quality relative to the 5D images for

both examples. When comparing all reconstructed data sets, the AI-based scoring of image quality yielded significantly ( $p<0.01$ ) higher grades for the proposed 4D images ( $3.2\pm0.5$ ) compared to 5D ( $2.5\pm1.0$ ). **Discussion and Conclusions:** We present a novel framework that produces high quality 4D images of the whole heart despite the presence of bulk patient movement. These encouraging preliminary results motivate further validation of our approach in numerical and physical moving phantoms to assess its accuracy and optimize the algorithm in a larger cohort. Overall, the proposed framework presents a new way to significantly improve image quality in un-cooperative patients potentially decreasing the need for sedation, especially in pediatric patients.

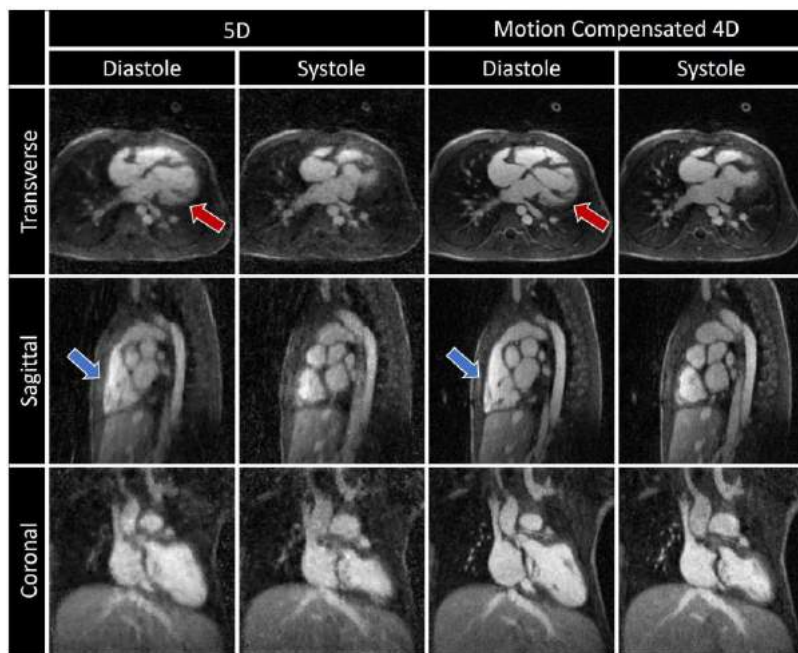
Figure/Table 1



Caption 1

**Fig. 1 A)** Schematic overview of the proposed algorithm for motion compensated 4D imaging. **B)** Example images from individual sections illustrating bulk patient movement occurring throughout the scan.

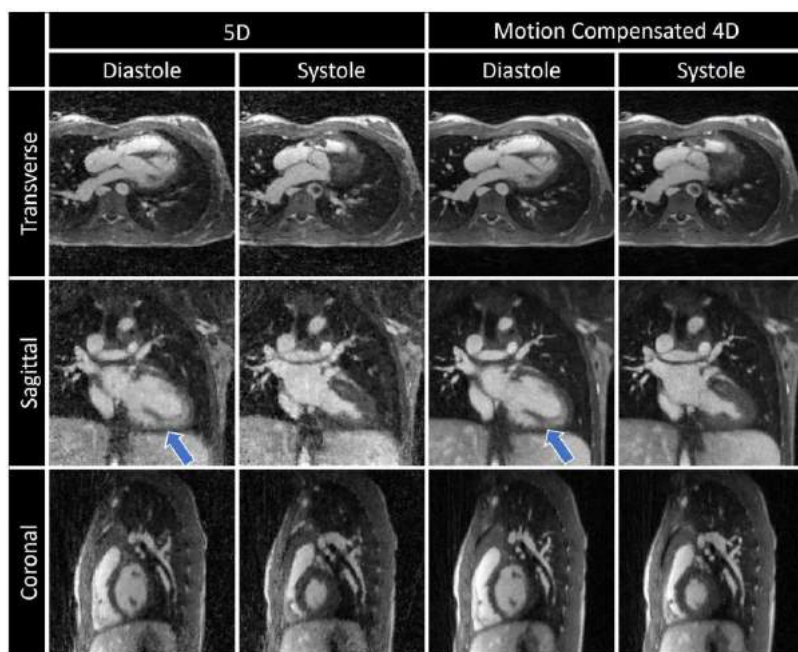
Figure/Table 2



## Caption 2

**Fig. 2** Patient undergoing severe motion. 5D images (left) and the proposed 4D images (right) in diastole and systole in transverse, sagittal, and coronal reformats. The proposed 4D images are able to recover fine details that are otherwise obscured in the 5D images, including papillary muscles (red arrows) and right ventricular trabeculations (blue arrows).

## Figure 3



### Caption 3

**Fig. 3** Patient undergoing moderate movement during the scan. 5D images (left) and the proposed 4D images (right) in diastole and systole in transverse, sagittal, and coronal reformats. 4D images demonstrate an overall high image quality with lower level of artifact relative to 5D with improved delineation of the papillary muscles (blue arrows).

### Bibliographic References

1. Di Sopra L PD, Coppo S, Stuber M YJ. An automated approach to fully self-gated free-running cardiac and respiratory motion-resolved 5D whole-heart MRI. *Magn Reson Med*. 2019;00:1:15., 2. Heerfordt J, Whitehead KK, Bastiaansen JAM, et al. Free-running SIMilarity-Based Angiography (SIMBA) for simplified anatomical MR imaging of the heart. *Magn Reson Med* . 2020., 3. Piccini D, Demesmaeker R, Heerfordt J, et al. Deep Learning to Automate Reference-Free Image Quality Assessment of Whole-Heart MR Images. *Radiol. Artif. Intell*. 2020;2:e190123 doi: 10.1148/ryai.2020190123.

Speaker: C. Roy

Category: Motion Correction, 3D, Cine Imaging



**000457**

**A giant left coronary cusp aneurysm in an asymptomatic patient with multiple vascular aneurysms**

M. Boutsikou \* (1); E. Vernardos (1); C. C. Radulescu (1); D. Apostolou (1); D. Tsilidis (1); G. Kanoupakis (1)

(1) MRI Unit, Mediterraneo Hospital, Athens, Greece

**Abstract**

**Description of Clinical Presentation**

A 67 year old female with no previous medical history, was admitted to the A&E due to four pre-syncope episodes with fall and head injury. The patient had a three hour flight prior to the episodes. There was no familial history of cardiomyopathy, coronary artery disease or sudden cardiac death. She mentioned that she had a known cardiac murmur which was no further investigated.

**Diagnostic Techniques and Their Most Important Findings**

There were no signs of heart failure on clinical examination. A 4/6 systolic cardiac murmur was audible at the left sternal edge, while the rest of the examination was unremarkable. ECG showed atrial fibrillation with high ventricular rate. The echocardiogram showed normal biventricular sizes with preserved ejection fraction and mixed pulmonary valve disease. The patient underwent a CT pulmonary angiography which showed no evidence of pulmonary embolism; however it revealed significant dilatation of the pulmonary arteries and abnormal aortic root. The patient was referred for a cardiac MRI study to assess the vascular abnormalities as well as the pulmonary valve function further. Cardiac MRI study showed a large left coronary cusp aneurysm (31x36x38mm) with no signs of rupture, followed by mild aortic regurgitation. The origins and proximal part of the coronary arteries were also aneurysmatic. The presence of mild pulmonary stenosis with significant dilatation of the main pulmonary arteries was also confirmed (MPA 48x49mm). No late myocardial enhancement was evident at the left or right ventricular myocardium. An invasive coronary angiography followed which showed no compression of the left main coronary artery from the dilated MPA and confirmed that the coronary branches were ectatic with no significant stenoses.

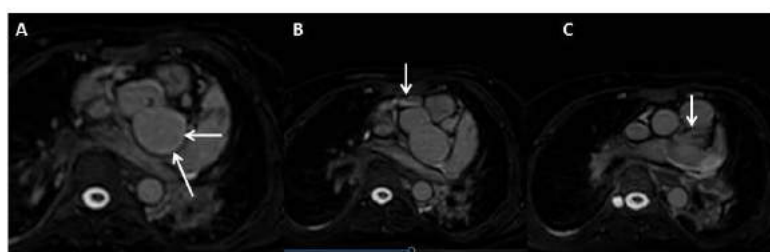
The patient was admitted to the hospital and was initiated on b-blockers and oral anticoagulation. An extended screen for connective tissue abnormalities and vasculitis was suggested to the patient who refused any further investigations. A consultation from a congenital heart disease expert team was asked who suggested close follow up of the patient with no further investigations.

**Learning Points from this case**

Valsalva sinus aneurysms are rare but more frequent in males (3-4times as common in males than females). Congenital aneurysms may be associated with Marfan and Ehlers-Danlos syndromes but frequently are associated with ventricular septal defects (30%–60% of pts), aortic regurgitation (AR) (20%–30%) and bicuspid aortic valve (10%). Acquired Valsalva sinus aneurysms are associated infectious diseases such as bacterial endocarditis. The

mainstay of treatment for a ruptured aneurysm is cardiopulmonary bypass surgery. Perioperative complications include low cardiac output, recurrent ventricular arrhythmia, and anticoagulation treatment–related bleeding while late complications include recurrent AR, endocarditis, and para-aortic, peripatch leakage. In asymptomatic patients, large aneurysms should be repaired to avoid complications, whereas smaller aneurysms may be monitored. Kawasaki disease usually affects medium-sized arteries. Coronary artery disease occurs in about 25% of cases if therapy is omitted or delayed (7–10 days of illness). Rarely, aneurysms of other medium-sized arteries have also been reported to occur.

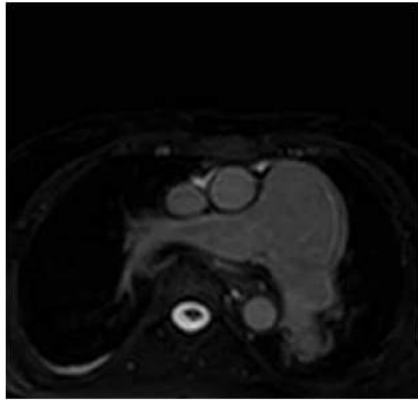
### Figure/Table 1



### Caption 1

Figure 1. Cardiac MRI, 3DSSFP angiography images, axial plane: (A) LCC aneurysm, (B) RCA (C )LM coronary artery. White arrows show the mentioned anatomical structures.

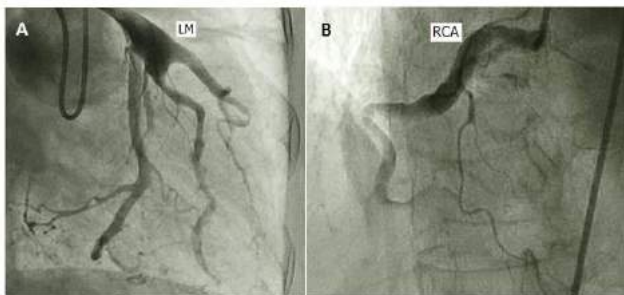
### Figure/Table 2



### Caption 2

Figure 2. Cardiac MRI, 3DSSFP angiography images, axial plane: Significant dilatation of MPA and LPA.

### Figure 3



### Caption 3

Figure 3. Coronary angiography. Ectatic coronary arteries (A) LM (B) RCA

### **Bibliographic References**

3. Jiang LC, Cao JY, Chen M. Coronary artery aneurysm combined with other multiple aneurysms at multiple locations. *Medicine* (2017) 96:50(e9230), 2. Briceno-Medina M, Perez M, Waller BR, Sathanandam S. Systemic pulmonary artery aneurysms in incomplete Kawasaki disease. *J Cardiol cases* 2016; 13:185-188., 1. Aliye Ozsoyoglu Bricker et al . <https://doi.org/10.1148/rg.301095719>

Speaker: M. Boutsikou

Category: Aneurysm, Pulmonary Artery, Aortic Valve

000459

## **Erdheim-Chester Disease: A Rare Cause of Right Atrial Mass**

J. Sutter \* (1); V. Ananthanarayanan (2); F. Leya, (1); M. Kinno, (1)

(1) Cardiology, Loyola University Medical Center, Maywood, United States of America; (2) Pathology, Loyola University Medical Center, Maywood, United States of America

### **Abstract**

#### Description of Clinical Presentation

A 77 year old man with a history of coronary artery disease, hypertension, hyperlipidemia, and monoclonal gammopathy of unknown significance presented to the emergency department with progressive dyspnea on exertion, lightheadedness, and lower extremity swelling. He was found to have a large pericardial effusion and underwent pericardiocentesis. Pericardial fluid analysis was unremarkable. His transthoracic echocardiogram also demonstrated increased LV wall thickness and echogenicity, with an apical-sparing strain pattern, concerning for cardiac amyloidosis. He underwent a cardiac MRI which was not diagnostic of amyloid, but did reveal a mass in the right atrium and right AV groove (Figure 1). PET/CT showed uptake in the right atrial mass (Figure 2), as well as in the right adrenal gland. This led to a CT adrenal with contrast, which was most notable for an extensive infiltrating process encasing the aorta, renal hila, and bilateral adrenal glands (Figure 3). A right adrenal biopsy was inconclusive, so a biopsy of the right atrial mass was performed. It demonstrated histiocytic proliferation, with immunophenotyping consistent with Erdheim-Chester disease.

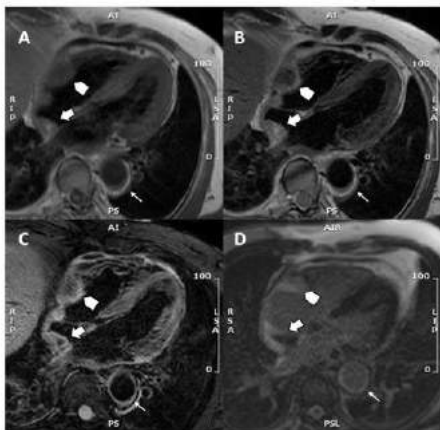
#### Diagnostic Techniques and Their Most Important Findings

The cardiac masses were identified and characterized on cardiac magnetic resonance imaging. The posterior right atrial mass was hyperintense on T1 and T2 imaging, while the right atrioventricular sulcus mass was hypointense on T1 and T2 imaging (Figure 1A-B). Both masses did not saturate on fat saturation images (Figure 1C), and both demonstrated heterogeneous enhancement on delayed gadolinium images (Figure 1D). Perfusion imaging demonstrated enhancement of both masses, suggesting vascularity.

#### Learning Points from This Case

Erdheim-Chester disease is a rare disorder of histiocyte proliferation, with less than 1000 cases published in the literature. It most commonly affects older men in the 6th and 7th decades of life. It is characterized by a clonal proliferation of myeloid progenitor cells via a BRAF V600E mutation, which was noted in our patient on the right atrial mass biopsy. Though it most commonly presents as lytic lesions affecting long bones, it has a propensity for creating extra-osseous lesions as well, most notably as a pseudotumor of the posterior right atrium, as well as infiltration of the right atrioventricular sulcus with encasement of the right coronary artery. On cardiac MRI, these masses are typically hypointense on b-SSFP images, enhance with contrast, and demonstrate patchy late gadolinium enhancement. Patients with cardiac manifestations also often have periaortic fibrosis and pericardial effusion, as was seen in our patient. While the diagnosis was ultimately confirmed by pathology from the right atrial mass biopsy, this case demonstrates the superior ability of magnetic resonance imaging to identify and characterize cardiac masses.

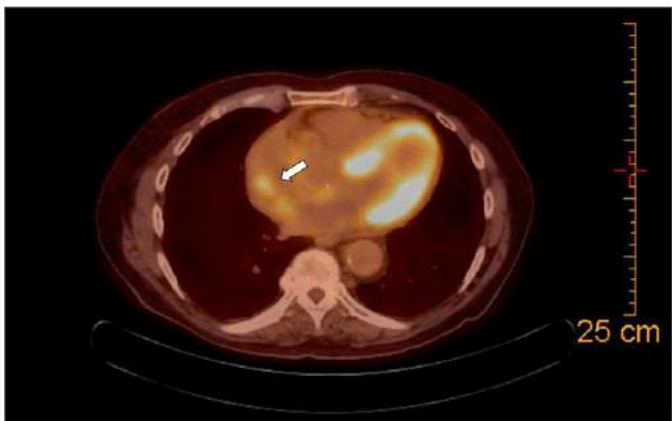
**Figure/Table 1**



**Caption 1**

Figure 1. Cardiac MRI of the posterior RA mass (block arrow), right AV groove mass (pentagon), and thoracic aorta (narrow arrow) on T1 weighted, dark blood imaging (1A), T2 weighted, dark blood imaging (1B), T2 weighted, fat saturation imaging (1C), and late gadolinium enhancement imaging (1D).

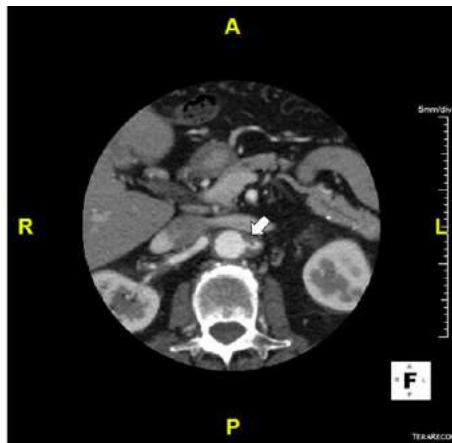
**Figure/Table 2**



**Caption 2**

Figure 2. PET/CT. FDG uptake in the posterior right atrial wall (block arrow).

**Figure 3**



### Caption 3

Figure 3. CT adrenal without IV contrast. Extensive infiltrative process encasing the aorta at the level of the left renal artery origin (block arrow).

Speaker: J. Sutter

Category: Cardiac Mass, Tissue Characterization, Right Atrium

000460

## Validating Contrast-Enhanced Infarct Characterization of a Novel Manganese-based Positive Contrast Agent in a Porcine Model of Myocardial Ischemia Reperfusion

B. Bonner \* (1); S. Yurista (1); J. Coll-Font, (1); A. Foster (1); S. Chen, (1); R. Eder, (1); P. Caravan, (2); E. Gale, (2); C. Nguyen (1)

(1) Cardiology, Massachusetts General Hospital, Cardiovascular Research Center, Charlestown, MA, United States of America; (2) Radiology, Massachusetts General Hospital, Athinoula A. Martinos Center for Biomedical Imaging, Charlestown, MA, United States of America

### Abstract

**Background:** Contrast enhanced cardiac MRI (CE-CMR) is the clinical gold standard technique to non-invasively characterize myocardial infarction post myocardial ischemia reperfusion [1]. Conventionally, Gadolinium based contrast agents (Gd-BCAs) have been used for CE-CMR but are contraindicated in patients with renal impairment defined as a glomerular filtration rate less than 30mL/min/1.73m<sup>2</sup> [2]. This is notably problematic in the workup of cardiac patients, where the coincidence of renal impairment is estimated to be 30-40% [3] thus representing an unmet clinical need for a non-toxic contrast-agent. In the present work, we evaluate a novel Manganese-based contrast agent, Mn-RVP001 ([Mn(PyC3A)(H<sub>2</sub>O)]<sup>-</sup> in the literature), in characterizing myocardial infarct in a porcine ischemia-reperfusion model comparing it to a conventional Gd-BCA (Gd-DOTA). Mn-RVP001 is optimized to exhibit similar pharmacokinetics to conventional Gd-BCAs, but with partial hepatobiliary clearance for effective elimination in patients with renal impairment [4].

**Methods:** We compare the performance of Mn-RVP001 to Gadoteric acid (Gd-DOTA) in a porcine model of myocardial ischemia-reperfusion (MIR). All experiments were performed under approval of the Institutional Animal Care and Use Committee of the Massachusetts General Hospital. MIR was induced for 80 minutes via trans-carotid catheterization and occlusion of the left anterior descending artery distal to the second diagonal branch. evaluation of scar size was performed three days post-MI with both Mn-RVP001 and Gd-DOTA in a 3T MAGNETOM Prisma and a 3T Biograph nMR (Siemens, Erlangen, Germany). The imaging sequence consisted in delayed enhanced T1 weighted images captured at 5, 10, and 15 minutes after contrast injection. These images were acquired with a stack of 2D bSSFP images to cover the entire LV (TR/TE=739/1.1ms, BW=1184Hz/pixel, resolution 1.8x1.8x8mm<sup>3</sup>, 12-15 slices). The second contrast agent was injected 180 +/- 30 min after the first injection to allow for washout of the first contrast agent. The order of the contrast agents was randomized across pigs to avoid bias introduced by contrast remaining in the tissue. Quantification of scar volume was performed semi-automatically using Segment. Statistical analyses were performed using MATLAB and Prism. Statistical significance was assessed with Wilcoxon signed-rank test (significance level p=0.05). Triphenyl tetrazolium chloride (TTC) staining will be performed to histologically validate CA performance.

**Results:** Figure 2 depicts representative images from two different cases. Did ventricle, short axis delayed enhancement sequence images are displayed. In the case encompassing panels A – D, Gd-DOTA was injected first, with Mn-RVP001 following washout. Contrast agent order was reversed in the case spanning panels E – H. Both sequences were captured 15 minutes



after contrast infusion. Figure 3 quantitatively demonstrates the equivalence of the two agents. Panel A shows paired box and whisker plots at 5-, 10- and 15-minutes post-injection. Wilcoxon signed-rank tests revealed no significant differences between contrast agents. Panel B depicts the Bland-Altman plot comparing the two agents. Panel C illustrates the scar volume correlation of the two agents.

**Conclusion:** Our results demonstrate that Mn-RVP001 performs equivalently to Gd-DOTA in the assessment of myocardial ischemic scars in a porcine ischemia reperfusion model. This work indicates the feasibility of Mn-RVP001 as a safe and effective alternative to Gd-BCAs in patients with renal dysfunction.

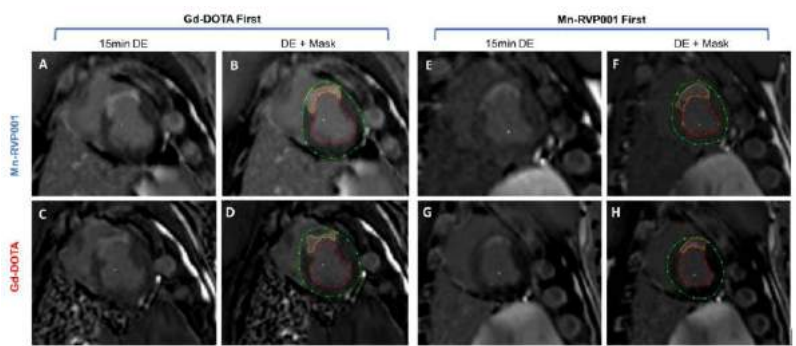
Figure/Table 1



Caption 1

Figure 1: Schematic of experimental pipeline.

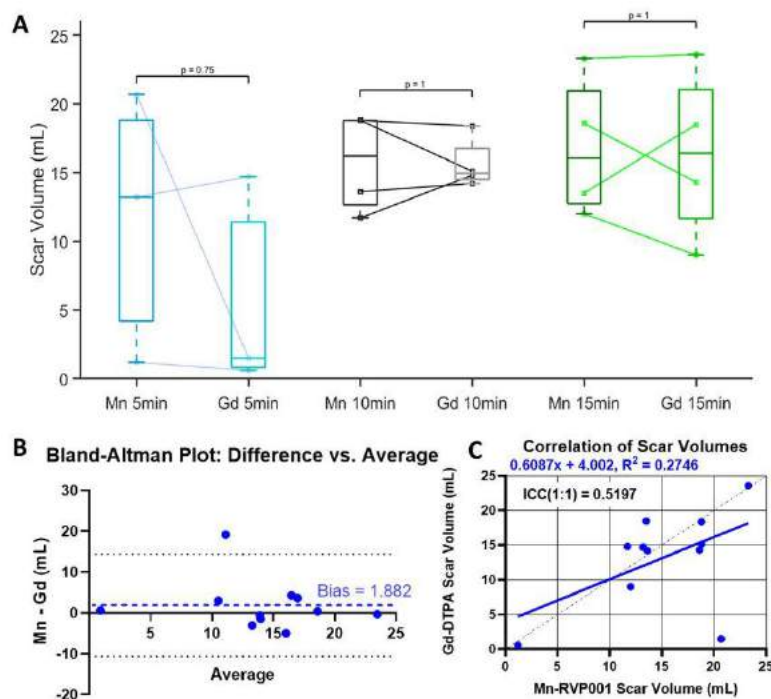
Figure/Table 2



Caption 2

Figure 2: Representative images of native and masked CE-CMR delayed enhancement sequences. Gd-DOTA first in A - D. Mn-RVP001 in E - H. In the masked images, the red and green lines delineate the endo- and epicardium respectively. The area inscribed in yellow denotes the total fibrotic scar. The area inside the pink trace illustrates the weighted affected area.

Figure 3



### Caption 3

Figure 3: A) Paired box and whisker plots comparing RVP-001 and Gd-DTPA. B) Bland-Altman analysis of the two agents. Dotted black lines depict 95% confidence intervals. Bias = 1.882 C) Correlation of contrast agent scar volumes. Dotted black line: identity line. Solid blue line: linear regression. Intraclass correlation coefficient  $ICC(1:1) = 0.5197$ .

### Bibliographic References

- 4) Gale, E. M., Atanasova, I. P., Blasi, F., Ay, I., & Caravan, P. (2015). A Manganese Alternative to Gadolinium for MRI Contrast. *Journal of the American Chemical Society*, 137(49), 15548–15557. <https://doi.org/10.1021/jacs.5b10748>, 3) Foley, R. N., Murray, A. M., Li, S., Herzog, C. A., McBean, A. M., Eggers, P. W., & Collins, A. J. (2005). Chronic kidney disease and the risk for cardiovascular disease, renal replacement, and death in the United States medicare population, 1998 to 1999. *Journal of the American Society of Nephrology*, 16(2), 489–495. <https://doi.org/10.1681/ASN.2004030203>, 2) Weinreb, J. C., Rodby, R. A., Yee, J., Wang, C. L., Fine, D., McDonald, R. J., Perazella, M. A., Dillman, J. R., & Davenport, M. S. (2021). Use of intravenous gadolinium-based contrast media in patients with kidney disease: Consensus statements from the American college of radiology and the national kidney foundation. In *Radiology* (Vol. 298, Issue 1, pp. 28–35). Radiological Society of North America Inc. <https://doi.org/10.1148/RADIOL.2020202903>, 1) Nagel, E., Greenwood, J. P., McCann, G. P., Bettencourt, N., Shah, A. M., Hussain, S. T., Perera, D., Plein, S., Bucciarelli-Ducci, C., Paul, M., Westwood, M. A., Marber, M., Richter, W.-S., Puntmann, V. O., Schwenke, C., Schulz-Menger, J., Das, R., Wong, J., Hausenloy, D. J., ... Berry, C. (2019). Magnetic Resonance Perfusion or Fractional Flow Reserve in Coronary

Disease. New England Journal of Medicine, 380(25), 2418–2428.  
<https://doi.org/10.1056/nejmoa1716734>

Speaker: B. Bonner

Category: Acute Myocardial Infarction, Contrast, Infarct Size

000461

## **CMR Quantification of Aortic Regurgitation Severity to Predict Reverse Remodeling After Aortic Valve Surgery: A Multicenter Study**

M. Malahfji \* (1); D. Kwon (2); A. Senapati (3); G. T. Liu (4); J. J. Ignacio (5); D. J. Shah (1); S. Uretsky (5)

(1) Cardiology, Houston Methodist Hospital, Houston, United States of America; (2) Cardiology, Cleveland Clinic Main Campus, Cleveland, United States of America; (3) Cardiology, Intermountain Medical Center, Salt Lake City, United States of America; (4) Internal medicine, Cleveland Clinic Main Campus, Cleveland, United States of America; (5) Cardiology, Morristown Medical Center, Atlantic Health System, Morristown, NJ, USA, United States of America

### **Abstract**

#### **Background**

We aimed to validate CMR quantification of aortic regurgitation (AR) severity using post-surgical left ventricular (LV) remodeling as the reference standard.

#### **Methods**

In a multicenter study with prospectively enrolled registries, we identified AR patients who underwent aortic valve surgery after baseline CMR. Patients underwent a follow up CMR (31% of scans for research indication and the remainder for clinical indications). Quantification of LV volumes, mass, ejection fraction, and AR severity were done at each site for baseline and follow up scans. Aortic regurgitant volume (Rvol) was determined from phase contrast imaging at the level of sinotubular junction in 80% of patients and mid ascending aorta in 20% of patients. Severity of AR was categorized as follows: mild <30ml, moderate 30-59ml, and severe  $\geq 60$ ml. Regurgitant fraction (RF) was calculated as Rvol/aortic forward stroke volume.

#### **Results**

We enrolled 74 patients (mean age  $55.8 \pm 14.8$  years, 83% male). There were 15 (20.3%) with mild AR, 24 (32.4%) with moderate AR, and 35 (47.3%) with severe AR. Median Rvol was 63 [44-83] ml and median RF was 42 [37-52] %, with 12/54 patients having LVEF < 50%. Fifty-four patients underwent surgery at a median 45 days [25-111] after CMR. Follow up CMR was performed at a median 2.24 years [1.01-3.53] after surgery. There was a significant decrease in LVEDV, LVESV, and LV mass; as well as an increase LVEF post operatively (all  $P \leq 0.001$ ) (table 1). Patients with more severe AR at baseline had a greater reduction in LVEDV after surgery (p for trend 0.02, figure 1). On multivariable linear regression, the reduction in Rvol was independently associated with a post-surgical decrease in LVEDV independent of age, LVEF, hypertension, and coronary artery disease ( $\beta = 0.25$ ,  $P < 0.001$ ). On

follow up CMR, all patients had no or mild AR except for four who had  $\geq$ moderate AR due to prosthetic dysfunction or post valve repair AR. Patients who had  $<20$  ml reduction in Rvol after surgery had a significantly reduced extent of remodeling (figure 2).

## Conclusions

AR quantified by CMR predicts the hemodynamic response of the LV post-surgery. Quantification of AR severity using CMR was an independent predictor of post-surgical LV remodeling. In patients with residual AR post-surgery, there was a significantly lower decrease in LVEDV compared to patients with no residual AR. This finding demonstrates accuracy of CMR in AR assessment.

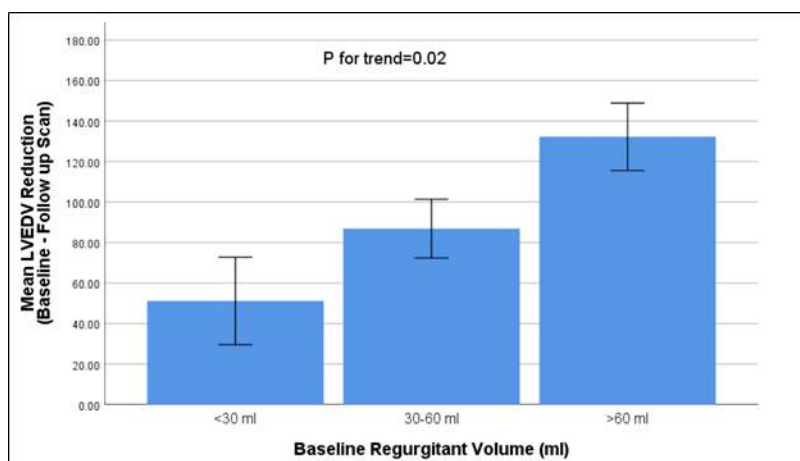
**Figure/Table 1**

Characteristic	Baseline CMR	Follow up CMR	P value
LVEDV (ml)	301.5 (91.3)	199.7 (57.4)	$<0.001$
LVESV (ml)	142.1 (59.3)	88.8 (43.3)	$<0.001$
LV stroke volume (ml)	160.1 (48.1)	110.9 (24.4)	$<0.001$
LVEF (%)	53.2 (9.6)	57.9 (8.6)	0.001
LV mass (gram)	207.1 (62.1)	158.9 (39.1)	$<0.001$
Regurgitant volume (ml)	63 [44-83]	2 [0, 10]	$<0.001$
Regurgitant fraction (%)	42 [37-52]	2 [0, 8]	$<0.001$

## Caption 1

Comparison of pre and post operative CMR findings

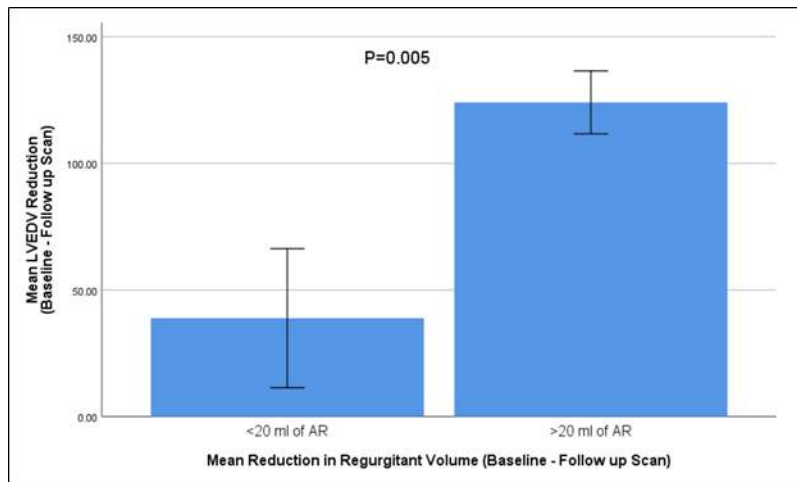
**Figure/Table 2**



## Caption 2

Relationship of baseline regurgitant volume and extent of reduction in LVEDV after surgery

Figure 3



## Caption 3

Comparison of the extent of remodeling (reduction of LVEDV) between patients with >20 ml reduction of AR vs those with <20 ml reduction of RVol (due to relatively low baseline RVol or residual AR (prosthetic dysfunction or post valve repair AR))

Speaker: M. Malahfji

Category: Aortic Regurgitation, Valvular Heart Disease, Ventricular Remodeling

000466

## **IgG4-Related Disease: The Role of Cardiac MRI in Revealing IgG-Related Aortitis After Being Missed For Two Decades**

J. Sutter \* (1); A. Turin, (1); S. Kyung, (1); M. Kinno, (1)

(1) Cardiology, Loyola University Medical Center, Maywood, United States of America

### **Abstract**

#### Description of Clinical Presentation

A 62-year-old man with a history of hypertension and dyslipidemia presented to an outside institution with chest pain for which he underwent cardiac catheterization with intervention after a positive stress test. His post-intervention echocardiogram showed a dilated ascending aorta, and subsequent chest CT and MRI showed findings suggestive of hematoma of the ascending aorta and aortic arch (Figure 1). The aortic thickening was stable in size on repeat CT imaging (Figure 2), and the decision was made to monitor with serial imaging. He was later evaluated in our cardiology clinic for atypical chest pain. He underwent cardiac MRI with stress perfusion, which demonstrated a small subendocardial scar without evidence of ischemia. Importantly, it also showed diffuse LGE of the previously described aortic hematoma. Accordingly, there was a high suspicion for large vessel vasculitis, which was confirmed by significant uptake of FDG on PET/CT (Figure 3). In addition, there was increased mural thickening of the abdominal aorta, just above the superior margin of the renal arteries, extending down along the common iliac arteries, but without FDG uptake. As part of the work up of vasculitis, IgG subclasses were obtained which demonstrated elevated IgG4 subclass. Ultimately, the patient was diagnosed with IgG4-related vasculitis. On further questioning, the patient endorsed a remote history, 20 years prior, of traumatic injury to his back while cycling, and a subsequent diagnosis of retroperitoneal fibrosis, which was confirmed via exploratory biopsy. It was originally attributed to non-specific chronic inflammation from a presumed resolved retroperitoneal hematoma from his traumatic injury.

#### Diagnostic Techniques and Their Most Important Findings

The initial outside CT scan with contrast showed circumferential thickening without enhancement of the ascending aorta and aortic arch encasing the ostia of the arch vessels (Figure 1A). MRI chest with T1-weighted imaging with fat saturation pre- and immediately post-contrast demonstrated that the mural thickening was T1-hyperintense on pre-contrast sequences but not on post-contrast (Figure 1B-C). Accordingly, the mural thickening was thought to be due to hematoma. Follow up CT demonstrated slightly increased signal on pre-contrast but not post-contrast imaging (Figure 2A-B) with stable size of the aorta. The abdominal aorta also demonstrated a somewhat similar process without increased pre-contrast signal (Figure 2C). Cardiac MRI demonstrated hypointense signal on b-SSFP imaging (Figure 3A) with diffuse LGE (Figure 3B), which raised the suspicion for an inflammatory process that was further confirmed by FDG PET imaging (Figure 3C).

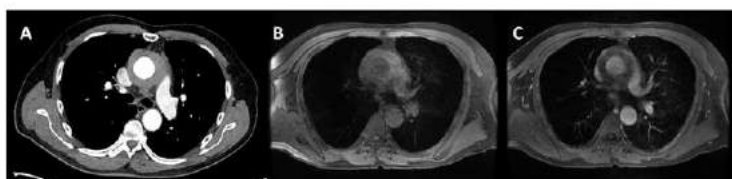
#### Learning Points from this Case

IgG4-related disease is an immune-mediated disease characterized by lymphoplasmacytic infiltration (predominantly IgG4-positive plasma cells) and storiform fibrosis of the affected organs. It is usually associated with elevated serum levels of IgG4. IgG4-related disease is a

relatively new entity first recognized in 2001. It can affect multiple organs with pancreatitis and cholangitis being the most common presentation. Retroperitoneal infiltration and aortitis are uncommon subcategories of this disease with ascending aortitis being the rarest.

This case demonstrates the essential role of cardiac MRI in providing the first clue for IgG4-related disease after being missed for almost 20 years. It also shows the importance of multi-modality imaging (including FDG PET/CT) in confirming the presence of inflammation.

#### Figure/Table 1



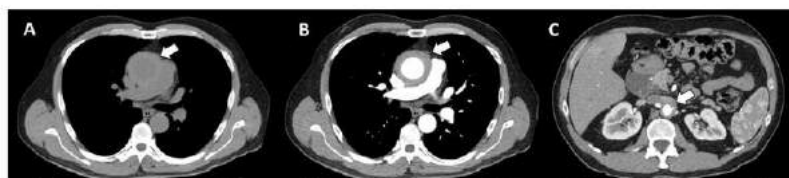
#### Caption 1

Figure 1A. Initial CT chest with contrast.

Figure 1B. Initial MRI of the chest with T1-weighted fat saturation imaging.

Figure 1C. Initial MRI of the chest with post-contrast T1-weighted fat saturation imaging.

#### Figure/Table 2

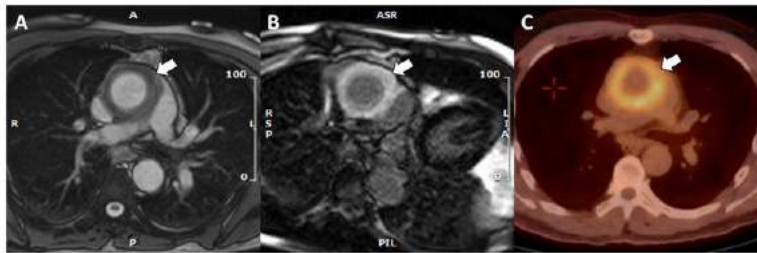




## Caption 2

Figure 2. 6-month follow up CT chest. A. Pre-contrast with increased signal of the mural thickening (arrow). B. Post-contrast without evidence of extravasation or enhancement of the mural thickening (arrow). C. Retroperitoneal fibrosis and circumferential thickening of the abdominal aorta extending into the renal arteries (arrow).

## Figure 3



## Caption 3

Figure 3A. Cardiac MRI SSFP sequence demonstrating the ascending aorta mural thickening (arrow). 3B. Cardiac MRI delayed post-contrast imaging demonstrating diffuse LGE of the mural thickening (arrow). 3C. FDG PET/CT showing significant FDG uptake of the mural thickening (arrow).

Speaker: J. Sutter

Category: Aorta, Abdominal Aorta, Multi-Modality

000467

## Impaired Left Ventricular and Right Ventricular Global Longitudinal Strain by Feature-tracking Cardiac Magnetic Resonance Predicts Survival in Patients with Systemic Sclerosis

A. Feher \* (1); E. J. Miller, (1); D. Peters, (2); H. R. Mojabian, (2); M. Hinchcliff, (3); L. Baldassarre (1)

(1) Department of internal medicine, section of cardiovascular medicine, Yale University School of Medicine, New Haven, United States of America; (2) Radiology, Yale School of Medicine, New Haven, United States of America; (3) Department of internal medicine, section of rheumatology, Yale University School of Medicine, New Haven, United States of America

### Abstract

**Background:** Cardiac involvement is a major determinant of prognosis in patients with systemic sclerosis. Patients with systemic sclerosis have been demonstrated to have impaired left ventricular (1-3) and right ventricular strain (1, 2) by feature-tracking cardiac magnetic resonance. However, it is unknown whether left ventricular or right ventricular strain is predictive of survival in this population.

**Methods:** Patients with systemic sclerosis who underwent cardiac magnetic resonance evaluation for clinical indications between 11/2010 and 07/2020 were retrospectively studied. Images were analyzed using cvi42 software (Circle Cardiovascular Imaging, Inc., Version 5.11.1). Left ventricular and right ventricular strain was evaluated by feature tracking on steady state free precession cine short axis stack, four chamber, three chamber, and two-chamber views. The association between left ventricular or right ventricular global longitudinal strain (GLS) and survival was evaluated with time to event and Cox-regression analyses (SPSS, IBM, Version 27).

**Results:** During the study period, 42 patients with systemic sclerosis (83% female, 57% limited cutaneous systemic sclerosis, age:  $57 \pm 14$  years) underwent cardiac magnetic resonance evaluation. The average left ventricular global radial, circumferential and longitudinal strain values were  $31.6 \pm 8.3\%$ ,  $-18.3 \pm 3.4\%$  and  $-14.8 \pm 3.4\%$ , respectively, whereas average right ventricular global radial, circumferential and longitudinal strain values were  $15.9 \pm 12.1\%$ ,  $-8.6 \pm 7.5\%$  and  $-18.1 \pm 7.2\%$ , respectively. During the median follow-up time of 2.2 years 9 patients died (21%). The cause of death was related to cardiovascular cause in 7 patients, whereas the cause of death was related to pulmonary artery hypertension and was unknown for the remaining two patients. In comparison to patients who survived, patients who did not survive had significantly more positive left ventricular GLS (Table 1,  $-12.4 \pm 4.9\%$  versus  $-15.4 \pm 2.6\%$ ,  $p=0.02$ ) and more positive right ventricular GLS ( $-13.5 \pm 9.6\%$  versus  $-19.3 \pm 9.6\%$ ,  $p=0.03$ ). When stratifying patients into quartiles based on left ventricular GLS, patients within the most positive left ventricular GLS quartile ( $\geq -12.8\%$ ,  $n=10$ ) had worse survival when compared to patients with more negative left ventricular GLS ( $< -12.8\%$ ,  $n=32$ , log rank  $p=0.019$ ). Patients with higher left ventricular GLS ( $\geq -12.8\%$ ) had worse survival even after controlling for age, gender, body mass index, pulmonary hypertension, interstitial lung disease and hypertension (Figure 1, hazard ratio: 10.41 [interquartile range: 1.54 – 70.63],  $p = 0.016$ ). Similarly, when stratifying patients into

quartiles based on right ventricular GLS, patients within the most positive right ventricular GLS quartile ( $\geq -12.4\%$ ,  $n=10$ ) had worse survival when compared to patients with more negative right ventricular GLS ( $< -12.4\%$ ,  $n=32$ , log rank  $p=0.006$ ). Similarly, patients with higher right ventricular GLS ( $\geq -12.4\%$ ) had worse survival even after controlling for age, gender, body mass index, pulmonary hypertension, interstitial lung disease and hypertension (Figure 2, hazard ratio: 10.75 [interquartile range: 1.72 – 67.02],  $p = 0.011$ ).

**Conclusions:** In our retrospective cohort of patients with systemic sclerosis undergoing cardiac magnetic resonance imaging for clinical indications, left ventricular GLS and right ventricular GLS were found to be predictive of overall survival.

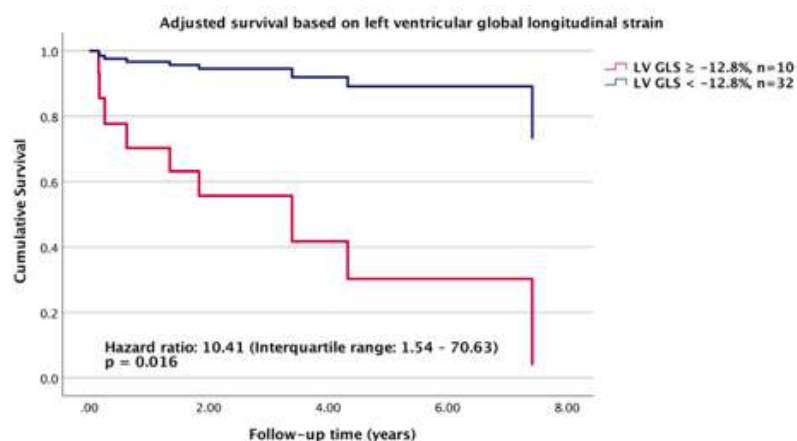
**Figure/Table 1**

		<b>Patient with survival N=33</b>	<b>Patient without survival N=9</b>	<b>P value</b>
<b>Baseline characteristics</b>	Age (years)	58 $\pm$ 13	53 $\pm$ 20	0.51
	Female gender, n (%)	27 (82%)	8 (89%)	0.53
	Body mass index (kg/m <sup>2</sup> )	26 $\pm$ 6	24 $\pm$ 8	0.18
	Limited systemic sclerosis, n (%)	20 (61%)	4 (44%)	0.31
	Pulmonary artery hypertension, n (%)	9 (27%)	3 (33%)	0.51
	Interstitial lung disease, n (%)	9 (27%)	3 (33%)	0.51
	Hypertension, n (%)	10 (30%)	2 (22%)	0.49
	Hyperlipidemia, n (%)	7 (21%)	0	0.16
	Diabetes, n (%)	1 (3%)	0	0.79
	Heart failure, n (%)	3 (9%)	2 (22%)	0.29
<b>LV assessment</b>	LV end diastolic volume (mL)	138 $\pm$ 42	134 $\pm$ 39	0.88
	LV ejection fraction (%)	61 $\pm$ 7	49 $\pm$ 17	0.07
	LV mass indexed to body surface area (g/m <sup>2</sup> )	48 $\pm$ 11	47 $\pm$ 11	0.90
	LV Global radial strain (%)	33.0 $\pm$ 7.2	26.5 $\pm$ 10.4	0.12
	LV Global circumferential strain (%)	-18.9 $\pm$ 2.6	-16.1 $\pm$ 5.1	0.14
	LV global longitudinal strain (%)	-15.4 $\pm$ 2.6	-12.4 $\pm$ 4.9	<b>0.02</b>
	Late gadolinium enhancement, n (%)	11/29 (38%)	5/7 (71%)	0.12
<b>RV assessment</b>	RV end diastolic volume (mL)	153 $\pm$ 54	163 $\pm$ 56	0.70
	RV ejection fraction (%)	50 $\pm$ 13	41 $\pm$ 14	0.08
	RV mass indexed to body surface area (g/m <sup>2</sup> )	12 $\pm$ 6	13 $\pm$ 6	0.89
	RV global radial strain (%)	16.0 $\pm$ 12.6	15.8 $\pm$ 10.4	0.96
	RV global circumferential strain (%)	-8.4 $\pm$ 8.1	-9.2 $\pm$ 5.0	0.89
	RV global longitudinal strain (%)	-19.3 $\pm$ 6	-13.5 $\pm$ 9.6	<b>0.03</b>

**Caption 1**

Baseline and imaging characteristics. LV: left ventricle, RV: right ventricle

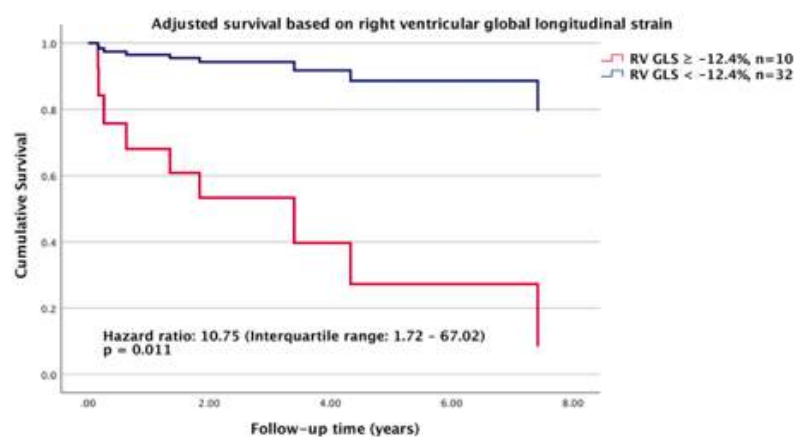
**Figure/Table 2**



**Caption 2**

Figure 1. Adjusted survival based on left ventricular global longitudinal strain (LV GLS)

**Figure 3**



**Caption 3**

Figure 2. Adjusted survival based on right ventricular global longitudinal strain (RV GLS)

### **Bibliographic References**

3. Kobayashi Y, Kobayashi H, J TG, Yokoe I, Hirano M, Nakajima Y and Takei M. Detection of Left Ventricular Regional Dysfunction and Myocardial Abnormalities Using Complementary Cardiac Magnetic Resonance Imaging in Patients with Systemic Sclerosis without Cardiac Symptoms: A Pilot Study. Intern Med. 2016;55:237-43., 2. Lindholm A, Hesselstrand R, Radegran G, Arheden H and Ostenfeld E. Decreased biventricular longitudinal strain in patients with systemic sclerosis is mainly caused by pulmonary hypertension and not by systemic sclerosis per se. Clin Physiol Funct Imaging. 2019;39:215-225., 1. Bratis K, Lindholm A, Hesselstrand R, Arheden H, Karabela G, Stavropoulos E, Katsifis G, Kolovou G, Kitas GD, Sfrikakis PP, et al. CMR feature tracking in cardiac asymptomatic systemic sclerosis: Clinical implications. PLoS One. 2019;14:e0221021.

Speaker: A. Feher

Category: Systemic Sclerosis , Strain, Outcomes

000469

## **The Prognostic Value of Follow-up CMR Assessment in Patients with Non-ischemic Dilated Cardiomyopathy**

Y. Xu \* (1); Y. Li (2); T. Siqi (3); Z. Xiaoyue (4); C. Yucheng (5)

(1) Cardiology, West China Hospital clinics, Chengdu Shi, China; (2) Department of cardiology, West China Hospital of Sichuan University, Chengdu, China; (3) Cardiology, Westchina Hospital, Chengdu, China; (4) Mr collaboration, Siemens Healthineers Ltd., Shanghai, China; (5) Department of cardiology, West China Hospital, Chengdu, China

### **Abstract**

#### **Background**

The evaluation of heart failure progression during follow-up in non-ischemic dilated cardiomyopathy (DCM) patients is mainly based on symptom and biomarkers. Whether follow-up cardiac magnetic resonance (CMR) imaging assessment could better evaluate the treatment efficacy and provide better longer-term prognostic value is relatively understudied.

#### **Methods**

One hundred and ninety-three DCM patients who underwent baseline and follow-up CMR were included in the study. After guideline-directed medical therapy (GDMT) for 12-24 months (median interval of 14.4 months, interquartile range: 12.4-19.2 months), patients underwent simultaneously clinical and imaging evaluations. Clinical assessment including New York Heart Association (NYHA) functional class, blood pressure, electrolytes, and N-terminal prohormone of brain natriuretic peptide (NT-proBNP) level, while CMR assessment including bi-ventricular volume and ejection fraction. During longer-term follow-up, major adverse cardiac events (MACE) were independently assessed by masked cardiologists and defined as cardiovascular death, heart transplantation, and heart failure readmission. Univariable and multivariable Cox regression analyses were performed to determine the best prognostic model. The study is registered with ClinicalTrials.gov (ChiCTR1800017058).

#### **Results**

During the median follow-up of 35.9 months (interquartile range: 22.2–49.5 months) 47 patients (24.4%) had MACE. Both clinical evaluation with NYHA and NT-pro BNP, and imaging evaluation with RVEF and RVEDVi significantly improved even in non-event-free survivors. In multivariable Cox regression, imaging model including age, sex, LVEDVi, and LVEF (Akaike information criterion [AIC], 418; chi-square value, 58.7) showed significantly superior predictive value than clinical model including age, sex, NYHA class and NT-proBNP level (AIC, 341; chi-square value, 39.4) in predicting MACE. Meanwhile, we found that the effectiveness of the CMR model at follow-up was significantly higher compared with baseline CMR model (AIC, 232; chi-square value, 19.0) and the changes of CMR parameters (AIC, 218; chi-square value, 17.5).

#### **Conclusion**

During the follow-up, cardiac functional and volumetric assessments of CMR would provide superior predictive value than clinical status in predicting MACE. The study suggests that imaging examination during follow-up may have important longer-term prognosis in DCM patients.

**Figure/Table 1**

	Patients with Event-free survival (n = 146)			Patients with MACE (n = 47)		
	Baseline	Follow-up	P Value	Baseline	Follow-up	P Value
<b>Clinical parameters</b>						
Age, y	44.8±13.5	46.7±13.9	<0.001	50.0±17.2*	51.5±17.1	<0.001
Males, n (%)	91(62.3)			35 (74.5)		0.128
BMI, kg/m <sup>2</sup>	25.0±4.4	25.5±4.3	0.013	22.9±3.6*	23.3±3.7	0.007
SBP, mmHg	118.2±17.3	122.1±16.0	0.014	110.3±13.7	115.8±18.5	0.167
DBP, mmHg	77.6±13.0	79.4±12.2	0.124	74.4±9.9	72.4±12.4	0.434
HR, beat/min	83.1±18.0	76.8±14.9	<0.001	84.3±25.2	81.1±15.2	0.526
HF duration (mo)	6.0 (2.0 - 24.0)			5.0 (2.0- 24.0)		0.860
New onset HF, n (%)	76 (52.1)			28 (59.6)		0.368
NYHA functional class			<0.001			<0.001
I, n (%)	19(13.0)	88(60.3)		2(4.3)	17(36.1)	
II, n (%)	65(44.5)	51(34.9)		11(23.4)	23(48.9)	
III, n (%)	46(31.5)	7(4.8)		25(53.2)	6(12.8)	
IV, n (%)	16(11.0) (13.0)	0(0)		9(19.1)	1(0.2)	
<b>Comorbidity</b>						
Hypertension, n (%)	26(22.9)	11(22.9)		14(12.8)	14(12.8)	
Diabetes, n (%)	8(19.0)	8(19.0)		9(9.8) *	9(9.8)	
<b>Laboratory examination</b>						
Hct	0.45±0.05	0.44±0.05	0.184	0.46±0.05	0.44±0.04	<b>0.019</b>
NT-proBNP, pg/ml	813 (306-2246)*	145 (37-402)	<0.001	1621(825-4026)	845 (232-1776)#	0.011
Troponin T, ng/L	13 (9 - 21)*	9 (6 -12)	0.017	17 (13 - 30)	22 (11-47)	0.465
<b>CMR parameters</b>						
LVEDVi, ml/m <sup>2</sup>	159.4±46.7	136.8±44.3	<0.001	197.0±54.5	184.7±44.3	0.087
LVESVi, ml/m <sup>2</sup>	118.7±47.8	56.7±19.5	<0.001	157.4±52.8	143.7±60.2	0.074

LV massi, g/m2	74.8±24.5	54.9±16.9	<0.001	75.2±26.9	71.6±21.8	0.285
LVEF, %	27.6±11.5	37.8±11.1	<0.001	21.6±8.9	24.5±11.5	0.148
RVEDVi, ml/m2	98.0±33.4	85.0±20.9	<0.001	110.0±36.2	92.8±28.0	0.003
RVESVi, ml/m2	63.1±34.0	43.6±18.3	<0.001	77.2±38.0	56.9±29.6	0.001
RVEF, %	38.4±13.3	49.6±9.2	<0.001	33.6±15.5	41.5±16.3	0.003
LGE presence	56 (38.4)			32 (68.1)		0.001
LGE location						0.307
Free wall, n (%)#	8 (14.3)			4 (12.5)		
Septal, n (%)#	24 (42.9)			9 (28.1)		
Both, n (%)#	24 (42.9)			19 (59.4)		
LGE pattern						0.429
Midwall, n (%)#	43 (76.8)			21 (65.6)		
Subepicardial, n (%)#	17 (30.4)			12 (37.5)		
Focal, n (%)#	1 (1.8)			2 (6.3)		
Diffuse, n (%)#	7 (12.5)			7 (21.9)		
LGE extent, (%)#	17.2 (9.7-38.8)			18.3 (13.1-32.1)		0.735

### Caption 1

Table 1. Clinical and imaging characteristics at baseline and follow-up.

\*P value indicate significant difference between patients with DCM with and without MACE

Abbreviations: BMI = body mass index; HR = heart rate; SBP = systolic blood pressure; DBP = diastolic blood pressure; NYHA = New York Heart Association functional classification; AF = atrial fibrillation; LBBB = complete left bundle branch block; NT-proBNP = N-Terminal prohormone of brain natriuretic peptide; CMR = cardiovascular magnetic resonance; LVmassi = left ventricular mass index; LVEDVi = left ventricular end-diastolic volume index; LVESVi = left ventricular end-systolic volume index; LVEF = left ventricular ejection fraction; RVEDVi = right ventricular end-diastolic volume index; RVESVi = right ventricular end-systolic volume index; RVEF = right ventricular ejection fraction; LGE = late gadolinium enhancement.

### Figure/Table 2

Parameters	Hazard Ratio	95% CI	p Value
<b>Clinical parameters</b>			
Age, y	1.02	1.00-1.04	0.042
Sex, males	1.49	0.77-2.88	0.234



BMI, kg/m2	0.88	0.88-0.95	0.002
SBP, mmHg	0.97	0.95-0.99	0.028
DBP, mmHg	0.95	0.92-0.99	0.004
NYHA functional class	2.30	1.47-3.59	< 0.001
Log(NT-proBNP)	4.11	2.53-6.69	< 0.001
<b>Imaging parameters</b>			
LVEDVi, ml/m2	1.01	1.01-1.02	< 0.001
LVEF, %	0.92	0.90-0.95	< 0.001
LGE presence, n(%)	3.39	1.80-6.39	< 0.001
LGE extent, %	1.03	1.01-1.04	0.001

## Caption 2

**Table 2. Univariate Cox regression analyses of clinical and imaging parameters at follow-up.**

## Figure 3

Parameters	Hazard Ratio	95% CI	p Value	AIC	Chi-square
<b>During follow-up</b>					
<b>Clinical model</b>				341	39.4
Age, y	0.99	0.96-1.01	0.358		
Sex, males	1.18	0.81-4.15	0.155		
NYHA functional class	1.35	0.77-2.36	0.301		
log (NT-proBNP)	3.50	1.94-6.29	< 0.001		
<b>Imaging model</b>				418	58.7
Age, y	1.00	0.97-1.02	0.633		
Sex, males	1.27	0.65-2.49	0.481		
LVEDVi, ml/m2	1.01	1.00-1.01	0.075		
LVEF, %	0.94	0.91-0.98	0.001		
<b>At baseline</b>					
<b>Imaging model</b>				232	19.0
Age, y	1.02	1.00-1.04	0.038		

Sex, males	1.10	0.54-2.22	0.793		
LVEDVi, ml/m2	1.01	1.00-1.02	0.018		
LVEF, %	0.98	0.94-1.02	0.345		
<b>Dynamic changes</b>					
<b>Imaging model</b>				218	17.5
Age, y	1.02	0.99-1.04	0.154		
Sex, males	1.56	0.78-3.11	0.209		
LVEDVi, ml/m2	1.01	1.00-1.02	0.096		
LVEF, %	0.98	0.95-0.10	0.108		

### Caption 3

**Table 3. Multivariate Cox regression analyses of clinical and imaging Parameters: comparison between clinical and imaging models**

Speaker: Y. Xu

Category: Dilated Cardiomyopathy, Cardiac Function, Prognosis

000472

## **Second trimester fetal cardiac MRI: retrospective anatomical assessment of 153 healthy fetuses between 20 and 28 weeks' gestation**

M. van Poppel \* (1); A. Uus (1); I. Grigorescu (1); J. Matthew (1); J. K. Steinweg (1); J. M. Simpson (2); R. Razavi (1); D. Lloyd (1); M. Deprez (1); K. Pushparajah (1)

(1) School of biomedical engineering & imaging sciences, King's College London, London, United Kingdom; (2) Department of congenital heart disease, Evelina London Children's Hospital, London, United Kingdom

### **Abstract**

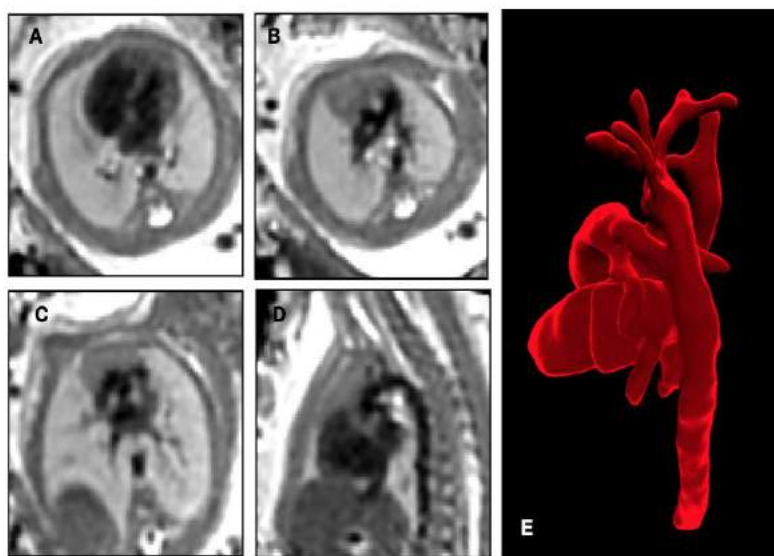
**Background:** Motion-corrected fetal cardiac magnetic resonance imaging (CMR) provides detailed three-dimensional (3D) visualisation of suspected vascular anomalies [1]. However, fetal CMR is largely restricted to the third trimester due to fetal movement and vessel size while initial assessment of the fetal heart is typically conducted during the second trimester. A new reconstruction pipeline [2] has been developed using deformable slice-to-volume registration [3], 3D convolutional neural network and landmark guided pose estimation. This method allows correction of large fetal rotations, creating potential for successful 3D fetal CMR earlier in gestational age (GA). The aim of this study was to investigate the performance of this new fetal CMR pipeline in a large retrospective cohort of healthy fetuses in second trimester.

**Methods:** Fetal CMR datasets of healthy volunteers (GA 20-28 weeks) between July 2015 and August 2018 consisting of  $\geq 6$  two-dimensional T2-weighted single-shot fast spin echo stacks were reconstructed to 3D volumes (0.7mm isotropic) using the new reconstruction pipeline [2]. Twins and fetuses with incidental cardiac findings on echocardiography were excluded, postnatal outcomes were checked for undetected cardiac anomalies. All 3D volumes were reviewed by one observer for image quality and content. Image quality was scored from 0 (inadequate) to 3 (high quality), content was assessed using a structured segmental approach: systemic venous return, pulmonary arterial supply, pulmonary venous return, and aortic and ductal arch anatomy. Additionally, nineteen structures were assessed: unable to visualise, lack of detail or good delineation.

**Results:** Datasets of 153 fetuses were included (median GA 25 weeks, IQR 23-26). Reconstruction time ranged from 30-60min depending on number of input stacks (range 6-11). Image quality was adequate or high in 130/153 datasets (85%) [Figure 1], poor in 22/153 (14%) due to motion or low SNR, and inadequate in one case which was excluded from further assessment. Completion of segmental assessment was high across all areas: systemic venous return (98%), pulmonary venous return (84%), pulmonary arterial supply (88%), and arch anatomy (89%). In total, 50/2888 individual cardiac structures were not visualised (1.7%), predominantly the left or right upper pulmonary vein (27/50) and individual aortic branches (18/50). Two minor incidental cardiovascular anomalies were detected during this study. Overall vessel visualisation is shown in Figure 2.

Conclusion: This is the first study demonstrating feasibility of detailed assessment of the fetal cardiovascular system in late second trimester using 3D fetal cardiac MRI. Overall image quality and vessel visualisation was high, creating new potential for both research directions and antenatal diagnosis of major vascular anomalies. Future work will require review of diagnostic confidence and accuracy for fetuses with suspected congenital heart disease.

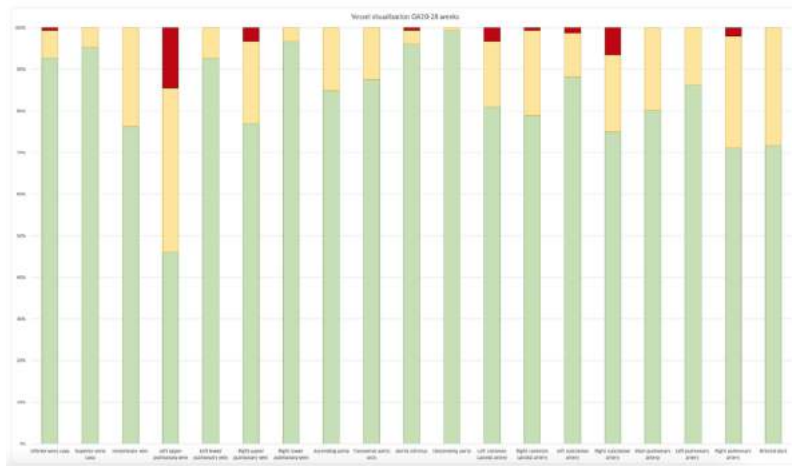
**Figure/Table 1**



**Caption 1**

3D fetal CMR volume of fetus (GA 23+3 weeks) with estimated fetal weight of 0.71kg (using two-dimensional MRI), showing A) equivalent to four chamber view, B) branch pulmonary arteries, C) pulmonary venous return, D) sagittal aortic arch, E) 3D heart model generated using semi-automatic segmentation.

**Figure/Table 2**



## Caption 2

Vessel visualisation per vascular structure assessed; red: unable to visualise, yellow: lack of detail, green: good delineation.

## Bibliographic References

3. Uus A, Zhang T, Jackson LH, Roberts TA, Rutherford MA, Hajnal JV, Deprez M. Deformable Slice-to-Volume Registration for Motion Correction of Fetal Body and Placenta MRI. *IEEE Trans Med Imaging*. 2020 Sep;39(9):2750-2759.
2. Uus A, Grigorescu I, van Poppel MPM, Steinweg JK, Roberts TA, Rutherford MA, Hajnal JV, Lloyd DFA, Pushparajah K, Deprez M. Automated 3D reconstruction of the fetal thorax in the standard atlas space from motion-corrupted MRI stacks for 21-36 weeks GA range. 2021, *BioRxiv preprint* doi.org/10.1101/2021.09.22.461335
1. Lloyd DFA, Pushparajah K, Simpson JM, van Amerom JFP, van Poppel MPM, Schulz A, Kainz B, Deprez M, Lohezic M, Allsop J, Mathur S, Bellsham-Revell H, Vigneswaran T, Charakida M, Miller O, Zidere V, Sharland G, Rutherford M, Hajnal JV, Razavi R. Three-dimensional visualisation of the fetal heart using prenatal MRI with motion-corrected slice-volume registration: a prospective, single-centre cohort study. *Lancet*. 2019 Apr 20;393(10181):1619-1627

Speaker: M. van Poppel

Category: Fetal, 3D, Congenital Heart Disease

000473

## Mitochondrial cardiomyopathy mimicking hypertensive heart disease

E. Watanabe \* (1); N. Michinobu (2); H. Nobuhisa (3)

(1) Cardiology, Tokyo Women's Medical University, Shinjuku City, Japan; (2) Radiology, Tokyo Women's Medical University, Shinjuku City, Japan; (3) Cardiology, Tokyo Women's Medical University, Shinjuku City, Japan

### Abstract

**Description of Clinical Presentation:** A 46-year-old man presented with left chest pain, palpitation and short of breath on exertion to our hospital. He had a past history of hypertension, hyperlipidemia, renal transplantation, and sensorineural hearing loss. He had no family history of diabetes or hearing loss. Chest X-ray showed cardiomegaly. Electrocardiogram (ECG) showed sinus rhythm, left ventricular hypertrophy (LVH) and left axis deviation. Echocardiography showed moderately impaired LV function (LV ejection fraction (EF) =37%) and moderate concentric LVH (septum 14mm). A myocardial SPECT scan showed perfusion defects in the posteroinferior segments. Coronary arteries were normal at coronary angiography. Endomyocardial biopsy (EMB) was inconclusive. He was diagnosed as hypertensive heart disease and treated with beta-blocker and angiotensin converting enzyme inhibitor. However, his LV function was gradually decreased and LVH was increased. After 6 years, his hearing loss was progressive and he visited otorhinolaryngologist. He had genetic test and mitochondrial mutation (m3243) was found. He was diagnosed with mitochondrial myopathy, encephalopathy, lactic acidosis, and stroke-like episodes (MELAS) after genetic test with blood examination and symptoms. At this time, his ECG showed intraventricular conduction delay and complete left bundle branch block.

**Diagnostic Techniques and Their Most Important Findings:** Cardiac MRI (CMR) was performed for further cardiac assessment. CMR demonstrated mild dilated LV and severe LV septal hypertrophy (maximum 24mm) with LVEF of 27%. T2-weighted imaging demonstrated high signal intensity globally in the mid-wall and subepicardial wall except lateral wall from base to apex. On late gadolinium enhancement imaging performed by respiratory gating with free-breathing, extensive hyperenhancement was seen in the corresponding areas of high signal intensity on T2-weighted imaging. Native T1 value was highly elevated in the LV septum. Right ventricular (RV) function and size were normal. These findings were very unique and suggested extensive edema and fibrosis of nonischemic etiology which caused LVH and LV systolic dysfunction.

### Learning Points from this Case:

There are a lot of etiologies in patients with LVH and reduced LV function. As this patient had hearing loss and no family history of MELAS, CMR was not performed or he was not evaluated for MELAS previously. If CMR could be performed previously, unusual findings of CMR might be helpful for early diagnosis of MELAS. This case also demonstrated that the past history was very important to distinguish the etiology of patients with LVH.

Speaker: E. Watanabe

Category: Cardiomyopathy, Heart Failure, Nonischemic Cardiomyopathy

000475

## A diagnostic pathway for cardiac AL amyloidosis

A. Del Torto \* (1); T. Damy (2); M. Kharoubi (2); M. Bezard (2); C. Rapezzi (3); J. Moon (4); R. Patel (5); H. Lachmann (5); S. Dorbala (6); C. Whelan (5); A. Martinez-Naharro (5); G. Pontone (1); C. Bucciarelli-Ducci (7); D. Hutt (5); V. Sanchorawala (8); F. Ruberg (8); L. Escobar-Lopez (9); J. G. Mirelis (9); E. Gonzalez-Lopez (9); P. Garcia-Pavia (9); J. M. Griffin (10); M. S. Maurer (10); A. Wechalekar (5); P. Hawkins (5); D. Davies (11); O. Abouezzeddine (11); A. Dispenzieri (12); M. Grogan (11); J. Gillmore (5); M. Fontana (5)

(1) Cardiovascular imaging, Centro Cardiologico Monzino IRCCS, Milano, Italy; (2) Department of cardiology, Henri-Mondor University Hospital, Créteil; (3) Department of cardiology, Università Degli Studi Di Ferrara Dipartimenti Medicina Clinica, Malborghetto di Boara, Italy; (4) Cardiac mri, Barts heart Center, London, United Kingdom; (5) National amyloidosis centre, Royal Free London NHS Foundation Trust, London, United Kingdom; (6) Department of cardiology and department of radiology, Brigham and Women's Hospital, Boston, United States of America; (7) Department of cardiology, Royal Brompton & Harefield Nhs Foundation Trust, London, United Kingdom; (8) Amyloidosis center, Boston University, Boston, United States of America; (9) Department of cardiology, Puerta de Hierro Majadahonda University Hospital, Majadahonda, Spain; (10) Cardiac amyloidosis program, Columbia University Medical Center, New York, United States of America; (11) Cardiovascular Diseases, Mayo Clinic, Rochester, United States of America; (12) Hematology, Mayo Clinic, Rochester, United States of America

## Abstract

**Background.** Light chain cardiac amyloidosis (AL CA) is a life-threatening cardiomyopathy; a prompt diagnosis is vital, but still challenging, as it relies on an integrated multi-modality approach, including invasive procedures to obtain tissue biopsies, usually performed in specialist referral centers.

**Methods.** In this multicentre study, results of radionuclide scintigraphy, contrast CMR, histology, biochemical investigations, and genetic sequencing were analysed in patients with suspected AL CA who had been referred to specialist amyloidosis centres. All participants underwent a CMR scan with gadolinium-based contrast, both in specialist and non-specialist centers. CMR scans were scored on the basis of the local report as 'Characteristic' - when they reported all of the following: increased wall thickness, increased LV mass, altered gadolinium kinetics, and diffuse subendocardial or transmural LGE; 'Negative' - normal scans or CMR indicating non-amyloid diagnosis; 'Suggestive' - not fulfilling the criteria for 'Negative' or 'Characteristic' such that CA could not confidently be excluded or confirmed

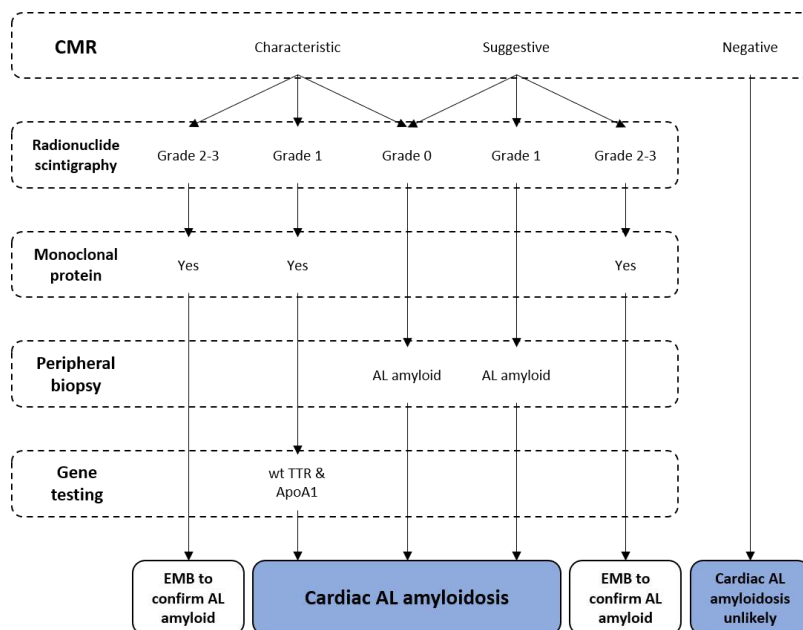
**Results.** Of 1053 patients (296 with endomyocardial biopsy (EMB), EMB-cohort, and 757 with no EMB, non-EMB-cohort), 320 were confirmed to have AL CA, among whom 2.8% had no evidence of a monoclonal protein. The sensitivity of characteristic or suggestive CMR scan for detecting AL CA was 98% in both the EMB and non-EMB-cohorts. The low specificity of a suggestive or characteristic CMR scan was related to cardiac transthyretin amyloidosis, cardiac ApoAIV or ApoAI amyloidosis and non-amyloid cardiomyopathies with overlapping imaging phenotype. The combined finding of a suggestive or characteristic



CMR, grade 0 or 1 radionuclide scan, and presence of AL amyloid in a non-cardiac biopsy was 100% specific for AL CA. The combined finding of a characteristic amyloid CMR, grade 1 radionuclide scan, presence of a monoclonal protein, and absence of a *TTR* or *APOA1* gene variant was also 100% specific for AL CA.

**Conclusions.** CMR is very sensitive for AL CA and should be considered in patients in whom the diagnosis is suspected. When CMR indicates the possibility of CA, it can be used in combination with radionuclide scintigraphy, non-cardiac histology, monoclonal protein studies and targeted genetic sequencing to confirm a diagnosis of AL CA without a requirement for EMB in most patients. EMB remains essential in patients with a grade 2 or 3 radionuclide scan and a monoclonal protein in order to determine the amyloid type.

**Figure/Table 1**



**Caption 1**

**CMR-based Diagnostic Pathway for patients with suspected amyloid cardiomyopathy.** Features characteristic CMR include increased wall thickness and LV mass, altered gadolinium kinetics and diffuse subendocardial or transmural LGE.

Speaker: A. Del Torto

Category: Amyloidosis , Cardiomyopathy, Restrictive Cardiomyopathy

**000478**

**Feasibility of wideband late-gadolinium enhanced imaging of patients with cardiac-implanted electronic devices on 3T: initial clinical experiences**

X. Cai \* (1); J. Cirillo (2); N. Kei (2); E. Sai (2); N. Whitehead (2); P. Pierce (2); B. Goddu (2); X. Bi, (3); R. Nezafat (2)

(1) Mr r&d collaborations, Siemens Medical Solutions USA, Inc., New York, United States of America; (2) Cardiology, Beth Israel Deaconess Medical Center (BIDMC), Boston, United States of America; (3) Mr r&d collaborations, Siemens Medical Solutions USA, Inc, Los Angeles, United States of America

**Abstract**

**Introduction**

The population of patients with a cardiac-implanted electronic device (CIED) is increasing [1] and CMR can play a vital role in the management of device patients. Advances in device and imaging technologies have made it more feasible to image this population. Particularly, wideband late gadolinium enhancement (LGE) has been demonstrated effective in reducing metal-induced artifacts to allow scar evaluation in numerous studies [2,3]. However, these studies have primarily focused on imaging on 1.5T systems and rarely on 3T systems. While there is risk of stronger susceptibility artifacts and additional consideration for SAR, wide-band LGE on 3T can be valuable particularly for clinical settings that are limited to 3T access and has been is demonstrated feasible in an animal study [4].

In this study, we sought to evaluate the performance of wideband LGE on a 3T system in a small cohort of patients with CIED.

**Methods**

Seventeen patients with MR conditional CIED underwent CMR exams on a 3T system (MAGNETOM Vida, Siemens Healthcare, Erlangen, Germany) in accordance with safety guidelines of the institution.

Short-axis stack of 2D LGE images were acquired approximately 10-15 minutes after administration of gadobutrol (Gadavist, Bayer Healthcare Pharmaceuticals, Berlin, Germany) at 0.1 mmol/kg using a wideband free-breathing prototype sequence with GRE readout [3,5]. Protocol parameters included: pixel size = 1.8 x 1.8 mm<sup>2</sup>, slice thickness = 5-8 mm, TE = 1.44 ms, TR = 3.41 ms, bandwidth = 1096 Hz/pixel, flip angle = 10 degrees, GRAPPA acceleration rate = 2, average = 8. Combined magnitude images after motion correction were utilized for further assessment.

Two experienced readers evaluated the image quality in terms of metal-induced artifacts level using a 3-point (1: Severe; 2: Moderate; 3: None) and diagnostic viability (0: Non-diagnostic; 1: Diagnostic).

**Result**

Table.1. Summarizes characteristics of the subjects. Of the 17 subjects, 11 had ICDs, 1 had CRT-D and 5 had pacemakers.

Fig.1. shows examples of wideband LGE images of slices without scar (A,B) and with scars (C,D). For the case in panel (C), transmural scar was present in the inferolateral and inferoseptal segments. For the case in panel (D), mid-layer enhancement can be clearly delineated in the septum. Presence of scar from LGE images in all subjects and slices are shown in Panel (E). Overall, 9 subjects were LGE positive and 8 were LGE negative.

Fig.2. Summarized the image quality evaluation. Both readers scored the majority (13 and 12 out of 17) of the cases to be free of metal-induced artifacts, the rest of the cases (4 and 5 out of 17) with moderate artifacts. None of the cases were scored with severe metal-induced artifacts. For diagnostic viability, reader 1 scored all cases diagnostic, and reader 2 scored all except 1 case non-diagnostic.

## Discussion

Wideband LGE imaging in patients with MR conditional devices at 3T is feasible and produces images of diagnostic quality.

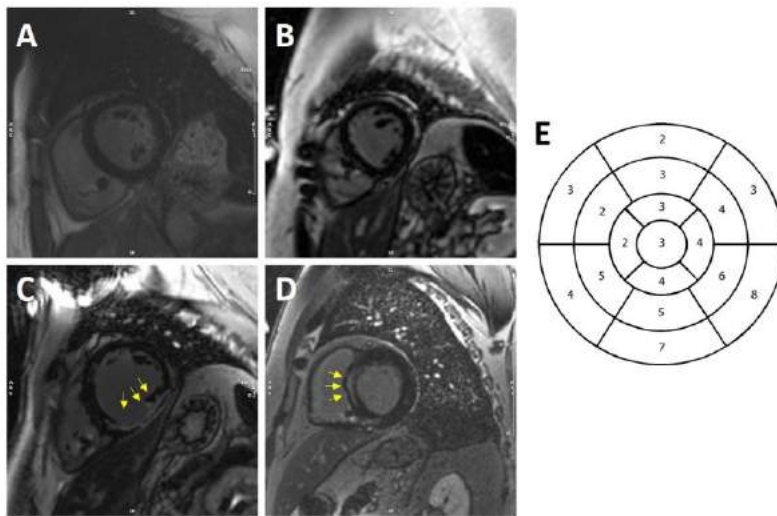
**Figure/Table 1**

Patient characteristics	
N	17
Age/years	61.8 ± 10.8
Sex	
Male	12
Female	5
CIED	
ICD	11
CRT-D	1
Permanent Pacemaker	5
Manufacturer	
Medtronic	10
Boston Scientific	7
Cardiac history	
Past myocardial infarction	3
Ischemic cardiomyopathy	1
Nonischemic cardiomyopathy	5
Infiltrative cardiomyopathy	2
HFrEF	2
Other (Chagas, Congenital WPW)	2
Unclear Diagnosis	2

**Caption 1**

Table.1. Summary of patient characteristic in this study.

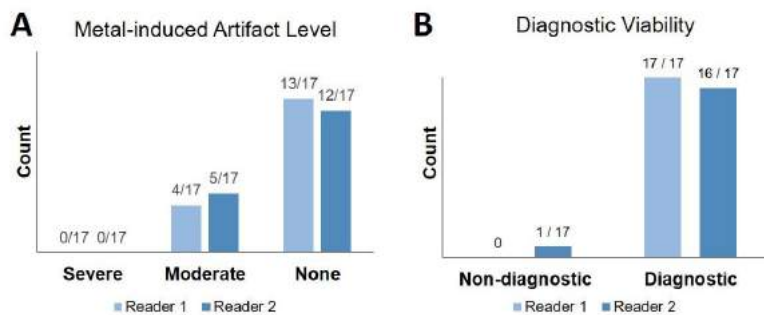
**Figure/Table 2**



**Caption 2**

Fig.1. Exemplary WB LGE images in patients with (A,B) no scars, (C) transmurular scar and (D) mid-wall enhancement (arrows). (E) Prevalence of scar in different AHA segments in all subjects.

**Figure 3**



**Caption 3**

Fig.2. Image quality assessment by 2 readers. (A) Both readers scored the majority (13 and 12 out of 17) of the cases to be free of metal-induced artifacts, the rest of the cases (4 and 5 out of 17) with moderate artifacts, and none of the cases with severe metallic-induced artifacts. (B) Almost all cases are scored as Diagnostic.

## **Bibliographic References**

1. Greenspon, Arnold J., et al. "Trends in permanent pacemaker implantation in the United States from 1993 to 2009: increasing complexity of patients and procedures." *Journal of the American College of Cardiology* 60.16 (2012): 1540-1545. , 2. Rashid S, Rapacchi S, Vaseghi M, Tung R, Shivkumar K, Finn JP, Hu P. Improved late gadolinium enhancement MR imaging for patients with implanted cardiac devices. *Radiology* 2014; 270: 269– 274., 3. Bhuva, Anish N., et al. "Clinical impact of cardiovascular magnetic resonance with optimized myocardial scar detection in patients with cardiac implantable devices." *International journal of cardiology* 279 (2019): 72-78., 4. Ranjan, Ravi, et al. "Wideband late gadolinium enhanced magnetic resonance imaging for imaging myocardial scar without image artefacts induced by implantable cardioverter-defibrillator: a feasibility study at 3 T." *Ep Europace* 17.3 (2014): 483-488., 5. Bhuva A, Ramlall M, Boubertakh R, Knott K, Feuchter P, Sekhri N, Schilling R, Kellman P, Moon J, Manisty CH. Wideband free breathing moco LGE changes patient care in patients with implantable cardiac defibrillators. *Heart* 2017;103(Suppl 1):A1–A25.

Speaker: X. Cai

Category: Late Gadolinium Enhancement, Cardiac Implantable Electronic Devices, Tissue Characterization

000479

**One of a kind, in a class of its own; a very rare case of multiple cardiac localization of hydatid cysts, a unique case of pulmonary valve direct involvement**

F. Mangini \* (1); E. Muscogiuri (1); R. W. Biederman (2)

(1) Radiology, Presidio of Brindisi Di Summa - Perrino, Brindisi, Italy; (2) Center for cardiac mri - allegheny general hospital, Allegheny Health Network, Pittsburgh, United States of America

**Abstract**

Echinococcosis is a parasitosis caused in Human by Echinococcus granulosus at its larval stage; more frequently, the localization of cysts is represented by liver and lungs; however, ideally, no part of the body can be considered spared from hydatid cysts [1]. Cardiac involvement is a much rarer but potentially fatal condition [2][3][4][5].

A 68-year-old patient, with known active lung neoplasm and previous history of hydatids, was admitted to ER for chest pain aggravated in the last period; due to the detection of high values of D-Dimer, the patient was evaluated with Computed Tomography (CT); the exam confirmed several metastases in the lung parenchyma, mediastinum and chest wall; besides, CT angiography revealed a mass at the level of the pulmonary, the mass was labeled as thrombus; thus the patient was hospitalized and put on Fondaparinux 7.5 mg; Electrocardiogram and Chest X Rx showed normal findings.

A transthoracic echocardiography (TTE) was performed showing normal left ventricle and right ventricle cavity size and function, non-significant mitral regurgitation and tricuspid regurgitation, mild pulmonary hypertension, a small circumferential pericardial effusion; the TTE evaluation revealed a cystic-like morphology of the mass attached on pulmonary valve, initially labeled as thrombus on CT scan; the cyst appeared to be attached on the ventricular side of the anterior pulmonary leaflet and showed a mobility consistent with the anterior leaflet excursion (Fig.1, Video.1); the presence of this mass resulted in mild valve obstruction; investigation by transesophageal echocardiography (TEE) confirmed the localization and likely cystic nature of the mass and the related mild valve obstruction (Fig.2, Video.2); an in-depth analysis was therefore carried out by Cardiac Magnetic Resonance Imaging (CMRi); the exam confirmed normal LV and RV size and function and the remaining TTE finding; the mass on pulmonary valve appeared hollow with hyperintense content in the SSFp sequences (Fig.3a) and in the TIR / T2 sequences (Fig.3b), hypointense in the DIR / T1 sequences (Fig.3c) and markedly hypointense (dark) in the LGE sequences (Fig.3d), thus confirming the cystic nature of the mass; besides, in SSFp sequences, the cyst appeared to contain another small cyst structure (daughter cyst) (Video.3); other two masses of a cystic nature were detected intramyocardially at the interventricular septum and at the level of the lower wall of the left ventricle (Fig.4); investigating more deeply into the patient's clinical history, the patient confirmed an Echinococcal infection that occurred about 20 years earlier, with the development of hepatic cysts which were confirmed as still present today with a targeted examination; the patient has been put on Albendazole therapy.

**DISCUSSION**

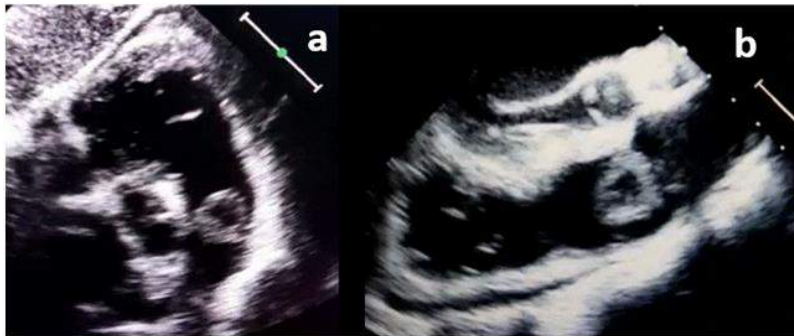
Cardiac involvement of Hydatid disease is a much rarer but fatal condition. Echocardiography generally represents the first approach method for the diagnosis of hydatidosis; Additional

diagnostic steps include CT scan and CMRI, the latter represents the most accurate examination for confirming the cystic nature of the masses.

## CONCLUSION

This represents a rare case of multiple cardiac localization of HC; besides, as far as we know, this represents the first documented case of cystic localization at the level of a pulmonary valve leaflet.

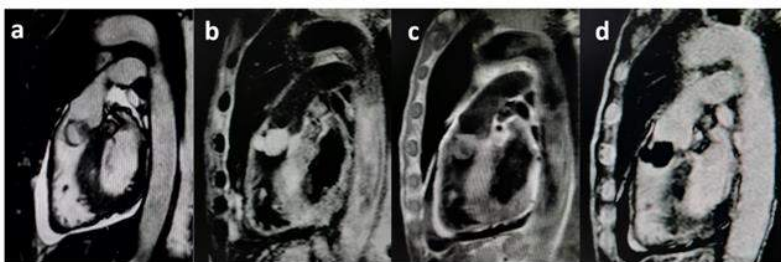
**Figure/Table 1**



**Caption 1**

Fig.1 a and b. The TTE evaluation revealed a cystic-like morphology of the mass attached on pulmonary valve, initially labeled as thrombus on CT scan (a); transesophageal echocardiography confirmed the localization and likely cystic nature of the mass (b)

**Figure/Table 2**



**Caption 2**

Fig.2 a,b,c and d. CMRI: the mass appeared hollow with hyperintense content in the SSFp sequences (a) and in the TIR / T2 sequences (b), hypointense in the DIR / T1 sequences (c) and dark on LGE (d), thus confirming the cystic nature of the mass; besides, in SSFp sequences, the cyst appeared to contain another small cyst structure (daughter cyst)

**Figure 3**



**Caption 3**

Cardiac Magnetic Resonance Imaging, TIR/T2 sequences: another mass of a cystic nature was detected intramyocardially at the interventricular septum and at the level of the lower wall of the left ventricle

### **Bibliographic References**

4. Tandon S, Darbari A. Hydatid cyst of the right atrium: a rare presentation. *Asian Cardiovasc Thorac Ann.* 2006;14:e43–4. doi: 10.1177/021849230601400324. , 5.  
Karadede A, Alyan O, Sucu M, Karahan Z. Coronary narrowing secondary to compression by pericardial hydatid cyst. *Int J Cardiol.* 2008;123(2):204–7. doi: 10.1016/j.ijcard.2006.11.174, 3. Beshlyaga VM, Demyanchuk VB, Glagola MD, Lazorishinets VV. Echinococcus cyst of left ventricle in 10-year-old patient. *Eur J Cardiothorac Surg.* 2002;21:87, 2. Kabbani SS, Jokhadar M, Sundouk A, Nabhani F, Baba B, Shafik AI. Surgical management of cardiac eshinococcosis, report of four cases, 1.  
Yekiler Edral, Karaarslan Kerem, Yazicioglu AkIm, Kaia Sadi, Karaoglanglu Nurettin. Lobectomy for pulmonary hydatid cyst. *Turk. J. Med. Sci.* 2013;43:1024–1029

Speaker: F. Mangini

Category: Cardiac Mass, Echocardiography, Cardiac Magnetic Resonance Elastography



**000480**

**Multiparametric CMR imaging value for patients post Heart Transplantation- when little things really matter**

E. NYKTARI \* (1); M. Efraimidis (2); K. Vlachos (2); P. Rozos (1); S. Zarkadoulas (1); S. Adamopoulos (3); A. Gkouziouta (3)

(1) CMR Unit, Βιοιατρική Αμπελόκηποι, Athina, Greece; (2) Electrophysiology dept, Onassis Cardiac Surgery Center, Kallithea, Greece; (3) Advanced heart failure dept, Onassis Cardiac Surgery Center, Kallithea, Greece

**Abstract**

***Description of Clinical Presentation***

A 45-year-old man with a past medical history significant for advanced heart failure on the grounds of end-stage DCM, status post orthotopic heart transplant, presented with syncope at exertion. At admission, he had recurrent syncope and pulseless cardiac arrest with an escape wide QRS rhythm of 20bpm. Patient was resuscitated successfully and admitted in ICU.

***Diagnostic Techniques and Their Most Important Findings***

A transthoracic echocardiography revealed a normal left ventricular ejection fraction (LVEF) of 60% and no diastolic dysfunction. Endomyocardial biopsy was negative for Acute Cardiac Allograft Rejection (ACAR) and coronary angiography showed diffuse atheromatosis of both LAD and RCA with a single longitudinal stenosis at the most distal RCA.

CMR confirmed normal volumes and EF of both ventricles, absence of hypertrophy or oedema/inflammation of the myocardium as documented by both STIR imaging and T2 mapping covering the entire heart. T1 mapping showed diffuse interstitial fibrosis with high values in all segments (>1100ms, normal values 950-1050ms, 1.5T Siemens Essenza) and increased Extracellular volume fraction (ECV) of 30% (normal 24±3%). Late images after gadolinium injection revealed focal intramyocardial replacement fibrosis in basal and mid-cavity inferior wall with involvement of the adjacent posteromedial papillary muscle. The presence of PM fibrosis (single blood supply from RCA) on LGE along with the documented distal RCA disease raised the question of repetitive RCA spasm/ischaemia induced bradycardia/syncope and a dobutamine stress echo study (DSE) was performed. DSE revealed ischaemia in the distal RCA territory and a PCI was performed.

Five days post PCI patient suffered a new cardiac arrest. Telemetry recorded diffuse ST segment elevation degenerated abruptly in advanced atrioventricular block and asystole. Patient was resuscitated successfully. Coronary angiography excluded occlusion of the stent and diffuse vasospasm. An ICD was implanted as primary prevention measure.

Diffuse increase of T1 values raised the question of accelerated cardiac allograft vasculopathy (CAV) and patients was started on Everolimus. Further course was uneventful until today.

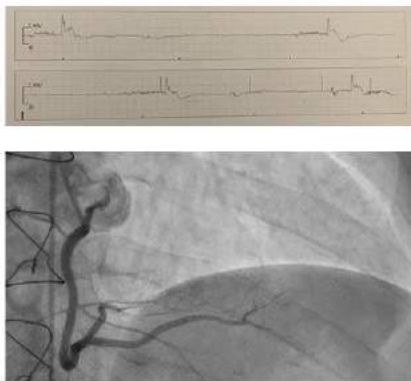
***Learning Points from this case***

The underlying pathogenic mechanism of posttransplant SCD is likely multifactorial and is poorly understood. Alba *et al.* (1) performed a retrospective analysis of the International Society of Heart and Lung Transplantation Registry showing that treated rejection (HR = 1.76; 95% CI, 1.36–2.31) and CAV (HR = 3.32; 95% CI, 2.73–4.03) were important prognostic factors for SCD.

Multi-parametric CMR imaging can provide a non-invasive surveillance method to assess both rejection and CAV in this high-risk population. T1/T2 mapping, ECV calculation and LGE techniques have been studied as both diagnostic markers and prognosticators (2).

In our case, T2 mapping covering the entire heart excluded acute oedema/inflammation whereas diffuse increase of T1 values and LGE pattern raised the issue of accelerated CAV with repetitive RCA spasm/ischaemia inducing bradycardic syncope and cardiac arrest.

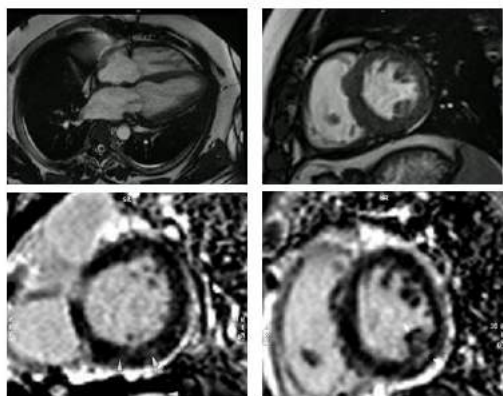
#### Figure/Table 1



#### Caption 1

Figure 1 ECG recording during arrest on top and Coronary angiogram of RCA at the bottom

#### Figure/Table 2



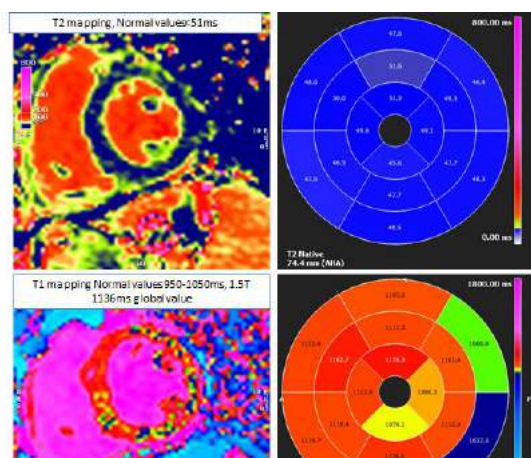
## Caption 2

Figure 2

**Top panel :** b-SSFP cines HLA (A) and mid-cavity SAX (B) showing normal size and ejection fraction

**Bottom panel:** LGE PSIR images basal and mid-cavity level showing intramyocardial foci of fibrosis in inferior wall and the adjacent PM papillary muscle (arrow heads)

## Figure 3



## Caption 3

Figure 3. Myomaps analysis by CMR-42 Circle Imaging

Top panel: T2 mapping covering the entire heart-normal values

Bottom panel: T1 mapping covering the entire heart- diffuse increase of T1 values

### **Bibliographic References**

2. Chaikriangkrai K, Abbasi MA, Sarnari R, et al. Prognostic value of myocardial extracellular volume fraction and T2-mapping in heart transplant patients. *J Am Coll Cardiol Img* 2020;13:1521–30., 1. Alba AC, Fan CS, Manlhiot C, et al. The evolving risk of sudden cardiac death after heart transplant. An analysis of the ISHLT Thoracic Transplant Registry. *Clin Transplant* 2019; 33:e13490

Speaker: E. NYKTARI

Category: Cardiac Allograft Vasculopathy, Mapping Techniques, Transplantation

000486

## Variability of CMR Volumetric and Mass Measurements: Impact of Imaging Planes, Ventricular Hypertrophy and Structured Quality Improvement Intervention

S. Buddhé \* (1); M. Ferguson (2); R. Otto, (3); B. Soriano (4); E. Romberg, (3); E. Caris, (1); S. Bhutta (5); L. Stanescu (3)

(1) Cardiology, Seattle Children's Hospital, Seattle, United States of America; (2) Pediatric radiology, Seattle Children's Hospital, Seattle, United States of America; (3) Radiology, Seattle Children's Hospital, Seattle, United States of America; (4) Pediatrics, Seattle Children's Hospital, Seattle, United States of America; (5) Radiology, University of Washington, Seattle, United States of America

### Abstract

**Background:** Consistency and reproducibility of ventricular measurements on CMR is insured by low inter- and intra-observer variability. There are however limited data on degree of interreader variance for right and left ventricular volumes and mass measurements in pediatric patients, particularly in those with congenital heart disease and varying levels of right ventricular hypertrophy (RVH). Our study aims to assess interobserver variability in ventricular contouring, and the effect of RVH while also describing a structured QI intervention in a large volume pediatric center. **Methods:** In a pediatric center, a total of 4 cardiac MR exams, with variable levels of RVH, were post-processed at baseline by a group of experienced radiologists and cardiologists. Standard protocols were used for imaging and post-processing both right and left ventricular volumes/mass. RV volume, ejection fraction (EF) and mass were analyzed in RHLA (right horizontal long axis) and SAX (short axis) planes while LV in SAX. Of note, clinical standards at our institution are different, with RV evaluated in RHLA and LV in SAX. LV mass is obtained in SAX while RV mass is not typically calculated. Interreader variability was determined at baseline. Following this, all studies were reviewed in extensive detail to identify sources of measurement variability. A group consensus was then developed to address them. Following this, post intervention analysis was performed on 4 new cases with similar extent of RV hypertrophy. Measurement variability was assessed by Levene's test Subjective level of comfort with different measurement techniques was measured using Likert scale after each cycle of post-processing.

**Results:** Eight physicians (3 cardiologists and 5 radiologists) participated in this study. At baseline, interreader variability for RV mass was higher in SAX compared to conventional RHLA plane. Similarly, it was higher compared to LV and for hypertrophied RV compared to nonhypertrophied RV. On review, the sources of variability identified were systole/diastole phase selection, outflow Inclusion, atria/atrial appendage definition/inclusion, RV inferior slice in RHLA, endocardial definition/trabeculations/mass, inclusion of apical slice epicardium without endocardium, and tricuspid valve plane. Post- intervention, RVEF (RV ejection fraction) variance significantly improved in both RHLA and SAX axis in RVH group ( $p < 0.05$ ). In SAX, there was also significant improvement in LV EF, RV mass and LV mass variance. Interestingly even in non-hypertrophied RV- RVEF, LVEF and LV mass variance significantly improved in SAX ( $p < 0.05$ ). While there was significant improvement post-intervention in subjective level of confidence for tracing RV endocardial borders in cases with varying levels of RVH ( $p < 0.05$ ), there was no significant improvement for RV mass.

Conclusion: Interobserver agreement for CMR measurements is overall better for LV compared to RV, especially in cases with hypertrophied RV. Developing a post-processing consensus and structured QI intervention helped improve the variance and also subjective level of comfort in tracing RV endocardial borders. However comfort with RV mass tracing likely needs more interventions.

Speaker: S. Buddhé

Category: Congenital Heart Disease, Post-Processing, Right Ventricle

## Intra-myocardial Fat Quantification in Boys with Duchenne Muscular Dystrophy and Healthy Controls at 3T

N. Maforo \* (1); S. A. Dual, (2); A. Prosper (1); P. Renella (1); N. Halnon (3); H. Wu (4); D. Ennis (5)

(1) Department of radiological sciences, University of California, Los Angeles, Los Angeles, United States of America; (2) Department of radiology, Stanford University, Stanford, United States of America; (3) Department of pediatrics, University of California, Los Angeles, Los Angeles, United States of America; (4) Department of bioengineering, University of California, Los Angeles, Los Angeles, United States of America; (5) Radiological sciences laboratory, Stanford University, Serra Mall, Stanford, CA, USA, Stanford, United States of America

### Abstract

**Background:** Sensitive cardiac MRI biomarkers, including myocardial fibro-fatty infiltration, may help to identify the on-set of microstructural remodeling in DMD) – a fatal X-linked genetic disorder characterized by progressive muscle weakness and pediatric onset cardiomyopathy[1-3]. Conventional late gadolinium enhancement (LGE) imaging is the current gold standard for detecting myocardial replacement fibrosis, but fatty infiltration[1,2,4] is also known to occur. The use of chemical-shift based fat-water separation MRI techniques[5] may help to further distinguish fat-infiltrated tissue from replacement fibrotic tissue detected by LGE. This 3T MRI study aims: 1) to report and compare the left-ventricular (LV) intra-myocardial fat content in boys with DMD and healthy controls; and 2) to determine whether fatty infiltration precedes the appearance of LGE in boys with DMD.

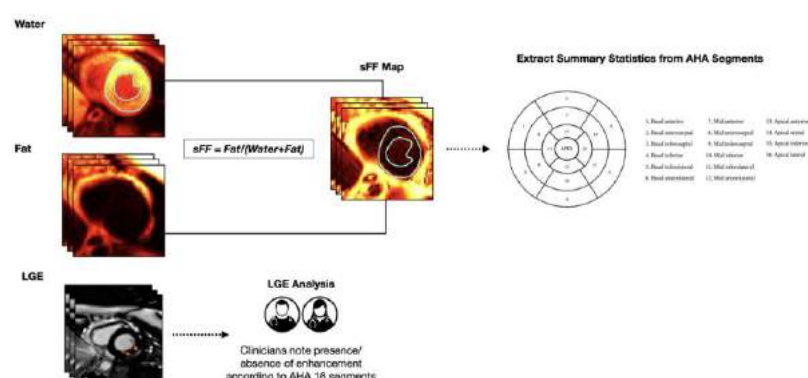
**Methods:** Boys with DMD (N=20, 13±2.9 yo) and healthy age- and sex-matched controls (N=11, 13.2±2.1 yo) were prospectively enrolled (IRB-approved, informed consent) and underwent a 3T (Skyra, Siemens) cardiac MRI (CMR) exam. The CMR exam included standard functional imaging, and a multi-echo (Dixon-type) GRE sequence for fat-water-separated imaging[5] after LGE imaging. Multi-slice, short-axis (SA) datasets spanning from base to apex were acquired. Two expert clinicians performed the functional image analysis and noted the presence or absence of segmental LGE according to the AHA 17-segment model[6]. Water- and fat-separated images for all SA slices were used to calculate signal fat fraction (sFF) maps (**Fig.1**). In each slice, a region of interest (ROI) encompassing the LV myocardium was segmented, extracted, and analyzed for its corresponding global and segmental sFF values. Group-wise comparisons were performed using a Wilcoxon-rank sum test. Data is reported as median and inter-quartile range (IQR).

**Results:** 7 (35%) of the boys with DMD were LGE+. All LGE+ boys with DMD had at least one lateral LGE+ segment (**Fig.2**). Affected segments occurred more frequently in the anterolateral (33%) and inferolateral (33%) LV wall, whereas the septum (6.3%) was less frequently affected. Increased sFF values are observed in LGE+ segments which occurred predominantly in the lateral myocardial wall (**Fig.3**). Compared to controls, LGE- boys with DMD showed significantly increased lateral sFF at the base [10.6(10.2)% v. 6.5(4.4)%;  $p=0.04$ ], mid-ventricle [7.3(3.6)% v. 4.6(1.7)%;  $p=0.003$ ], and apex [11.1(9.5)% v. 5.1(0.8)%;  $p<0.01$ ]. At the apical level only, anterior [6.2(4.1)% v. 3.9(1.2)%;  $p=0.01$ ], septal [5.4(2.9)%

v. 3.2(0.6)%;  $p=0.002$ ], and inferior [6.5(3.9)% v. 4.0(0.9)%;  $p=0.02$ ] sFF values were significantly increased in LGE- boys with DMD compared to healthy controls. LGE+ boys also show increased lateral sFF [7.6(4.2)% v. 4.6(1.7)%;  $p=0.03$ ] compared to controls at the midventricular level.

**Conclusion:** We report increased regional sFF values in LGE+ and LGE- boys with DMD compared to healthy, age- and sex-matched controls. Additionally, we report increased sFF values predominantly in the lateral LV wall – a region most frequently exhibiting LGE+ findings at later stages of cardiovascular disease in DMD. Importantly, this data suggests a progressive increase in LGE and sFF, thus warranting a longitudinal investigation.

**Figure/Table 1**

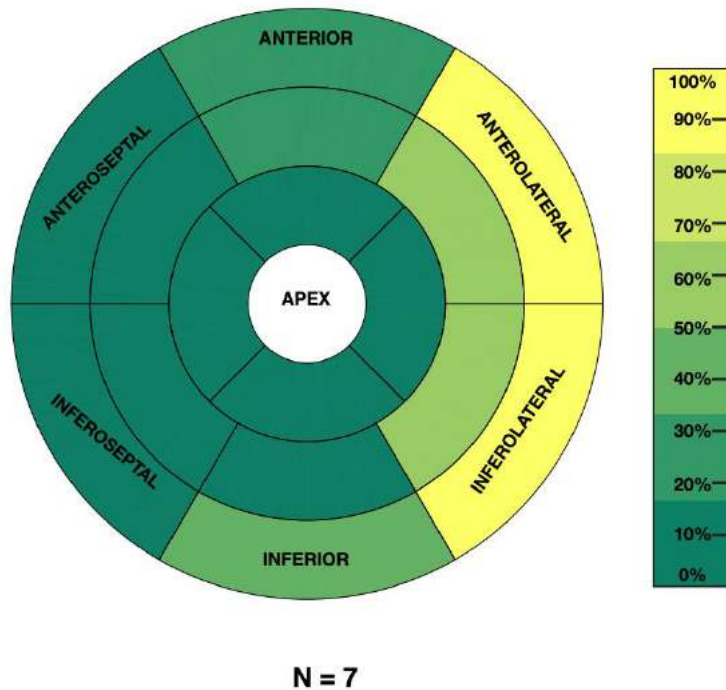


**Caption 1**

Post-processing pipeline for multi-slice short-axis fat-water-separated MR images with example images from an LGE+ DMD patient. Myocardial ROIs were manually drawn on water-separated images. Signal fat fraction (sFF) maps were generated from the fat- and water-separated images. Myocardial sFF values were extracted and analyzed for their corresponding AHA segments. LGE exams were analyzed by expert clinicians.

**Figure/Table 2**

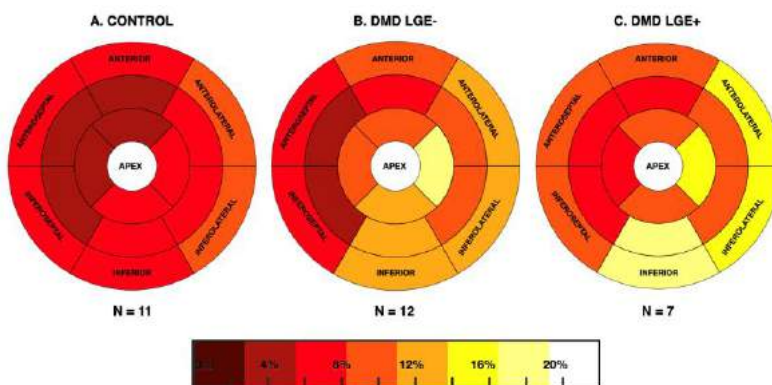




**Caption 2**

Left-ventricular distribution of Late Gadolinium Enhancement (LGE) (left) in 7 LGE+ boys with DMD. Affected segments occur more frequently in the basal and mid-ventricular anterolateral (33%) and inferolateral (33%) LV wall, whereas the basal and mid-ventricular septal segments (6.3%) are less frequently affected. The apical segments (3.3%) are the least affected across the cohort.

**Figure 3**



**Caption 3**

Left-ventricular distribution of signal fat fraction (sFF) in (A) healthy controls; (B) LGE- and (C) LGE+ boys with DMD. Increased sFF values are observed in LGE+ segments, but there is more variability across the segments. Compared to healthy controls, increased sFF values are also observed in LGE- boys with DMD.

### **Bibliographic References**

[3] Florian A et al., Myocardial fibrosis imaging based on T1-mapping and extracellular volume fraction (ECV) measurement in muscular dystrophy patients: diagnostic value compared with conventional late gadolinium enhancement (LGE) imaging. *Eur Heart J Cardiovasc Imaging*. 2014;15(0):1004-12., [1] Ryder S et al., The burden, epidemiology, costs and treatment for Duchenne muscular dystrophy: an evidence review. *Orphanet J Rare Dis*. 2017;12:79. [2] D'Amario D et al., A current approach to heart failure in Duchenne muscular dystrophy. *Heart*. 2017;103(22):1770., [4] Frankel KA et al., The pathology of the heart in progressive muscular dystrophy: epimyocardial fibrosis. *Hum Pathol*. 1976;7(4):375-86. , [5] Kellman et al., Multiecho dixon fat and water separation method for detecting fibrofatty infiltration in the myocardium. *Magn Reson Med*. 2009;61(1):215-21., [6] Cerqueira MD et al., Standardized myocardial segmentation and nomenclature for tomographic imaging of the heart. *Circulation*. 2002;105(4):539-42.

Speaker: N. Maforo

Category: Duchenne Muscular Dystrophy, Fat, Late Gadolinium Enhancement

000495

## Novel Finding of Dynamic Descending Thoracic Aorta Compression Due to Severe Mitral Valve Prolapse in Connective Tissue Disease: A Case-Control Study

S. Hashemi \* (1); T. Slesnick (1); D. Sallee, (1)

(1) Pediatric cardiology, Children's Healthcare of Atlanta - Egleston Hospital, Atlanta, United States of America

### Abstract

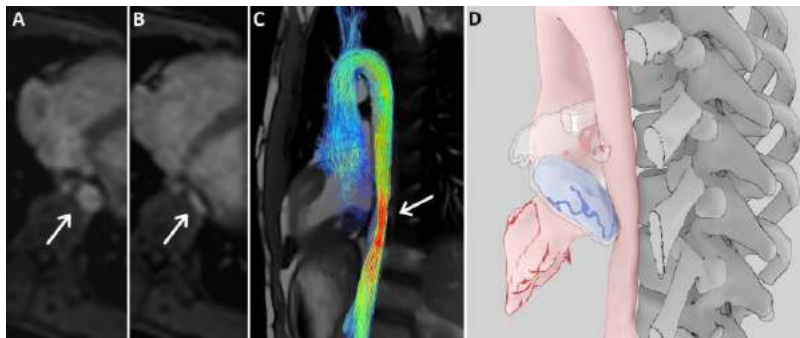
**Background:** Marfan (MS) and Loeys-Dietz (LDS) syndromes have diverse cardiovascular and extracardiac features. Mitral valve prolapse (MVP) has a high prevalence in these populations [1]. We describe a novel finding of dynamic descending thoracic aorta compression (DAC) in patients with significant MVP. In rare cases of MS and LDS, the descending aorta (DA) is compressed between the protrusion of MVP “pouch” and the spine during systole (Figure 1). We designed a case-control study to investigate why this finding manifests only in a small subset of MS and LDS patients.

**Methods:** A retrospective review of CMR studies of all MS and LDS patients in our institution was performed. Patients with significant MVP and DAC were included, and compared to a group of age-matched MS and LDS patient with significant MVP and no DAC. Demographic data, cardiovascular measurements and thoracic geometric indices were recorded (Figure 2).

**Results:** A total of 16 patients (8 cases, 8 controls) were included. There was no significant difference in indexed MVP height, indexed left ventricle (LV) size, aortic root diameter and Z-score, and incidence of aortic root replacement surgery on follow-up between cases and controls. Cases had significantly lower Haller index, less dextroscoliosis, lower axial aorta-LV axis and higher sagittal aorta-LV axis (Figure 3A). In the case group, DAC severity had a strong negative association with Haller index ( $P=0.005$ ,  $R^2=0.76$ ) (Figure 3B), and increase in DA velocity was associated with DAC severity ( $P=0.03$ ,  $R^2=0.57$ ) (Figure 3C).

**Conclusion:** Dynamic DAC in connective tissue disorder has not been previously described. We demonstrate that severe MVP does not independently cause DAC. A combination of severe MVP, lower Haller index, less dextroscoliosis and a more medially and vertically oriented LV is needed to result in approximation of the DA to MVP pouch and therefore to LV pressure during isovolumetric contraction and early systole. In fact, one case developed DAC after surgical correction of their severe dextroscoliosis. We showed significant association between the degree of DAC and velocity increase across the narrowing. This increased afterload may be particularly detrimental in MS and LDS patients who suffer from various forms of aortopathy and valve disease [2], though long term significance of this finding on patient outcomes needs more investigation. In our lab, application of cine and phase contrast imaging of the entire thoracic aorta allows easy identification of DAC. We recommend a cine acquisition in sagittal oblique plane through the LV, MVP and DA in all MS and LDS patients with significant MVP to screen for DAC.

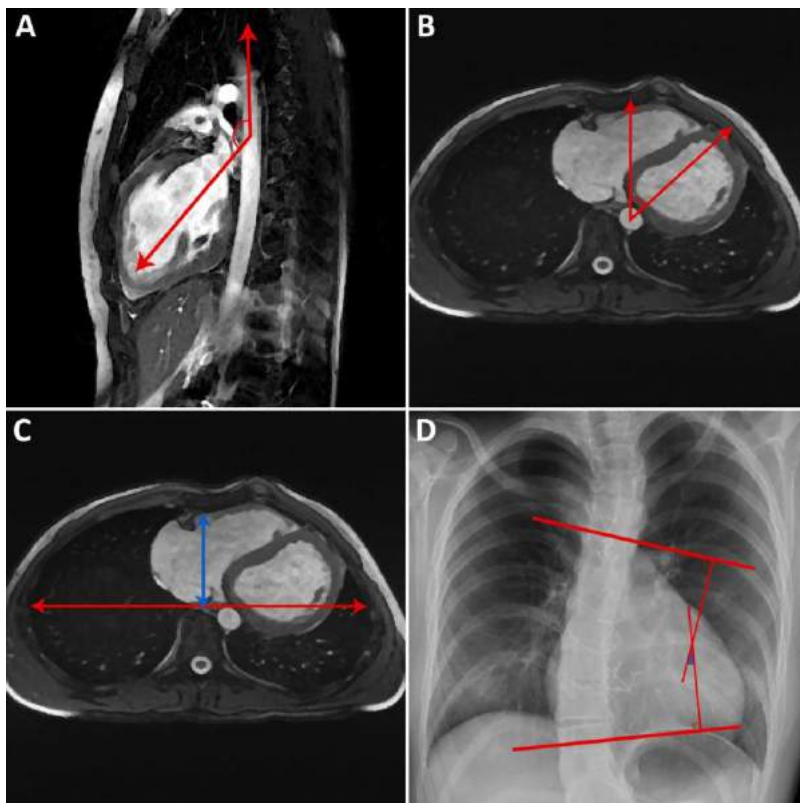
### Figure/Table 1



**Caption 1**

Figure 1. Axial spoiled gradient echo image of DA at the level of lower aspect of left atrium in diastole (A), and systole showing severe DAC (B). Snapshot of modified 2-chamber cine with superimposed 4D flow showing increased velocity distal to DAC (C). Schematic view of DAC (red) between MVP pouch (blue) and spine (Gray) (D).

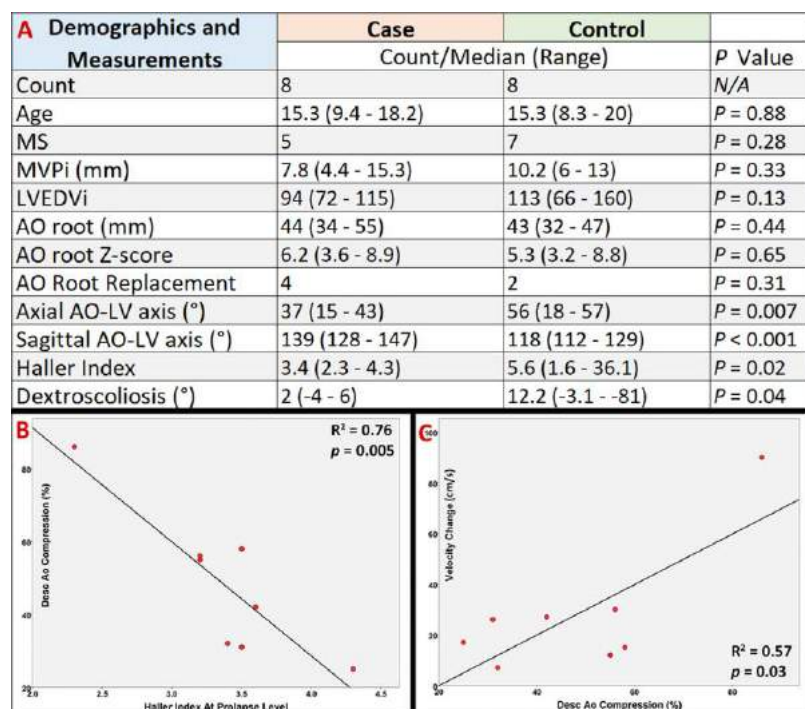
**Figure/Table 2**



**Caption 2**

Figure 2. Thoracic geometric indices used. Sagittal aorta-LV axis: angle between LV apex, center of mitral annulus and DA (A), axial aorta-LV axis: angle between LV apex, DA and sagittal plane (B), Haller index (C), Thoracic Cobb angle for scoliosis (D)

**Figure 3**



**Caption 3**

Figure 3. Summary of the results. MVPi: Height of mitral valve prolapse indexed to BSA, Dextroscoliosis: (-) indicates dextroscoliosis, (+) indicates levoscoliosis. Non-parametric tests were used due to small sample size.

### Bibliographic References

1. Morningstar, J.E., et al., Mitral Valve Prolapse and Its Motley Crew-Syndromic Prevalence, Pathophysiology, and Progression of a Common Heart Condition. J Am Heart Assoc, 2021. 10(13): p. e020919., 2. Isekame, Y., et al., Cardiovascular Management of Adults with Marfan Syndrome. Eur Cardiol, 2016. 11(2): p. 102-110.

Speaker: S. Hashemi

Category: Aorta, Mitral Valve, Marfan

000501

## Quantitative assessment of contrast agent arrival times in pulmonary hypertension

J. Moore \* (1); A. Pathrose, (1); J. Cerne, (1); M. Veer, (1); D. Gordon, (2); M. Markl (1); J. Carr (1)

(1) Radiology, Northwestern University, Chicago, United States of America; (2) Medicine, Feinberg School of Medicine, Chicago, United States of America

### Abstract

#### Background

Pulmonary hypertension (PH) contributes to restricted flow through the pulmonary circulation, with a progressive increase in pulmonary vascular resistance leading to right ventricular failure and death [1]. PH is typically diagnosed with invasive right heart catheterization (RHC). Non-invasive methods such as time-resolved 3D contrast enhanced (CE) MRA have been used to diagnose PH, but prior work has been limited to semi-quantitative assessment of contrast agent (CA) dynamics [2]. Pulmonary transit time has been shown to correlate with heart failure and identify PH [3,4]. This study aimed to develop a method for quantification of regional CA arrival time (CA-AT) maps to test our hypothesis that PH patients will have increased CA-ATs when compared to controls.

#### Methods

This prospective study consisted of 43 PH patients ( $60 \pm 14$  years, 25 female) and 24 healthy age-matched controls ( $52 \pm 14$  years, 8 female) who were enrolled for cardiothoracic MRI within 28 days of PH confirmation using RHC (mean main pulmonary artery (MPA) pressure at rest  $>20$  mmHg [5]). All time-resolved 3D CE-MRA data were acquired at 1.5T (Aera, Siemens) using a Time-resolved angiography With Interleaved Stochastic Trajectories (TWIST) sequence following CA administration (Gadavist, Bayer) with the following parameters: TR=2.08 ms, TE=0.83 ms, flip angle=16°, voxel size=0.8x0.8x2.0 mm, GRAPPA acceleration factor= 4, temporal resolution=1.26 s, 3D MRA volumes=30.

A threshold value was applied to eliminate background signal for all volumes. For each voxel, a signal intensity (SI) time series was used to find the time of peak SI (TT<sub>peak</sub>) corresponding to peak CA concentration (Fig 1A). The CE-MRA time frame showing maximum CA SI in the MPA was used to define the reference time point (t<sub>0</sub>) for CA arrival. TT<sub>peak</sub> = max(SI(t)), t > t<sub>0</sub>.

Voxelwise TT<sub>peak</sub> data were displayed as a maximum intensity projection (MIP) CA-AT map of the cardiopulmonary vasculature. A regional analysis quantified TT<sub>peak</sub> values in 11 regions of interest (ROI): the MPA for t<sub>0</sub>, L/R pulmonary arteries, secondary arterial branches, and L/R superior and inferior pulmonary veins.

#### Results

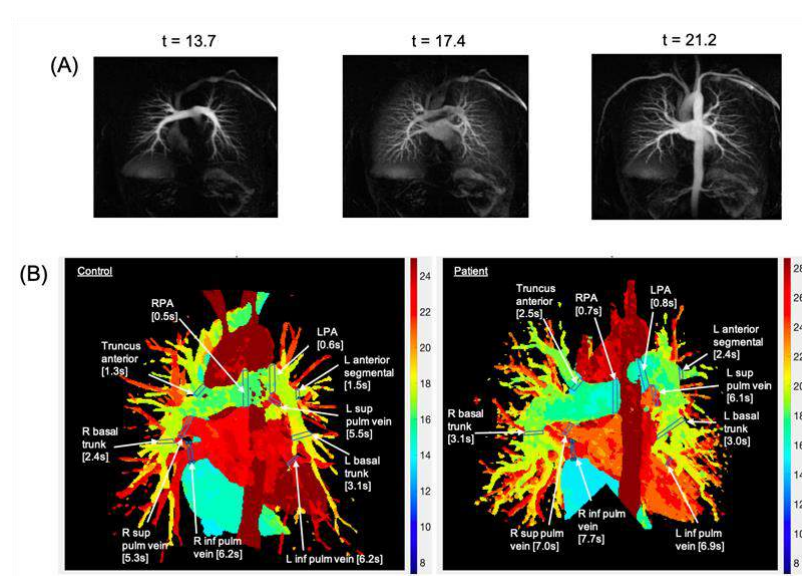
Figure 1B shows example CA-AT maps and raw data of a PH patient and healthy control and illustrates method robustness to slight variations in anatomy. Figure 2 shows raw CA-AT data

relative to t0 with a progressive increase in transit time as CA moves from proximal to distal pulmonary vasculature. CA-ATs were increased in 8/10 regions. Average differences between patients and controls in significant regions range from 0.71s to 1.3s. The arterial secondary branches in patients had an average CA-AT increase of  $0.85 \pm 0.15s$  (47.7%), and the veins had an average CA-AT increase of  $1.0 \pm 0.18s$  (16.9%) compared to controls.

## Conclusions

Our findings indicate that non-invasive assessment of cardiopulmonary CA-AT maps using CE-MRA can detect increased CA-AT in patients with PH of varying phenotypes compared to controls. The L/R pulmonary artery ROIs were not significant- likely due to MPA proximity and low temporal resolution. Future work to determine diagnostic utility of CA-AT maps will include a PH subtype statistical analysis relating reference standard invasive RHC measures.

**Figure/Table 1**

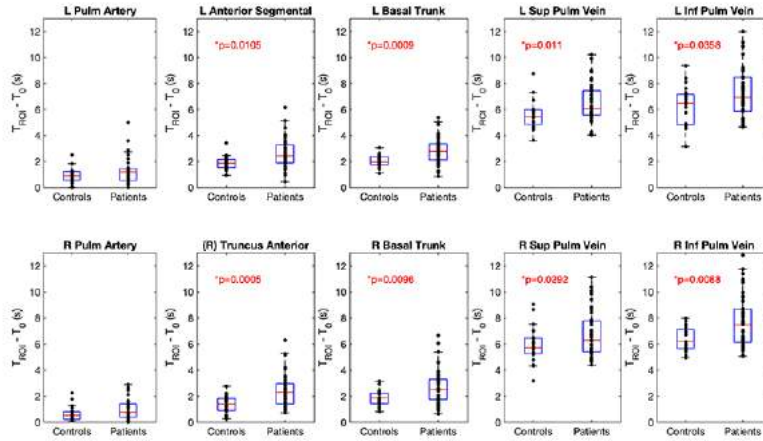


**Caption 1**

Figure 1: CA-AT map generation. (A) Original time resolved 3D MRA MIP time series. Images shown are generated from 3 example volumes in 30-volume dataset. (B) Example CA-AT maps. All 10 analysis regions are shown with CA-ATs relative to t0 from MPA. Example time data shows average increase in CA-AT between patient and control.

**Figure/Table 2**





**Caption 2**

Figure 2: Cumulative CA-AT results over all subjects for each ROI. Times are relative to contrast arrival time  $t_0$  at the Main Pulmonary Artery (MPA). The regional analysis shows a progressive increase in CA-AT as CA moves from proximal to distal pulmonary vasculature, ATs were significantly increased in PH patients compared to controls in 8/10 regions.

**Figure 3**

Characteristic	Controls	Patients
	(n = 24)	(n = 43)
Age (years)	51.5 ± 13.6	59.7 ± 14.3
Percent Female (%)	33.3% [8]	58.1% [25]
Mean Pulmonary Artery Pressure (mmHg)	--	36.7 ± 10.2
Pulmonary Vascular Resistance(Wood units)	--	4.7 ± 3.43
Pulmonary Capillary Wedge Pressure (mmHg)	--	16.4 ± 6.34

**Caption 3**

Table 1: The ROI analysis process was completed for n=67 subjects, where cohort details are summarized in the following table. All patients had a pulmonary arterial (PA) mean pressure of 23 mmHg or greater. The CA-AT analysis was completed for the entire cohort.



## Bibliographic References

1. Writing Committee Members, McLaughlin, V. V., Archer, S. L., Badesch, D. B., Barst, R. J., Farber, H. W., ... & Rosenson, R. S. (2009). ACCF/AHA 2009 expert consensus document on pulmonary hypertension: a report of the American College of Cardiology Foundation task force on expert consensus documents and the American Heart Association: developed in collaboration with the American College of Chest Physicians, American Thoracic Society, Inc., and the Pulmonary Hypertension Association. *Circulation*, 119(16), 2250-2294.
2. Jeong, H. J., Vakil, P., Sheehan, J. J., Shah, S. J., Cuttica, M., Carr, J. C., ... & Davarpanah, A. (2011). Time-resolved magnetic resonance angiography: Evaluation of intrapulmonary circulation parameters in pulmonary arterial hypertension. *Journal of Magnetic Resonance Imaging*, 33(1), 225-231.
3. Houard, L., Amzulescu, M. S., Colin, G., Langet, H., Militaru, S., Rousseau, M. F., ... Gerber, B. L. (2021). Prognostic Value of Pulmonary Transit Time by Cardiac Magnetic Resonance on Mortality and Heart Failure Hospitalization in Patients with Advanced Heart Failure and Reduced Ejection Fraction. *Circulation: Cardiovascular Imaging*, (January), 42–54. <https://doi.org/10.1161/CIRCIMAGING.120.011680>
4. Colin, G. C., Pouleur, A. C., Gerber, B. L., Poncelet, P. A., De Meester, C., D'Hondt, A. M., ... Ghaye, B. (2020). Pulmonary hypertension detection by computed tomography pulmonary transit time in heart failure with reduced ejection fraction. *European Heart Journal Cardiovascular Imaging*, 21(11), 1291–1298. <https://doi.org/10.1093/ehjci/jez290>
5. Simonneau, G., Montani, D., Celermajer, D. S., Denton, C. P., Gatzoulis, M. A., Krowka, M., ... Souza, R. (2019). Haemodynamic definitions and updated clinical classification of pulmonary hypertension. *European Respiratory Journal*, 53(1). <https://doi.org/10.1183/13993003.01913-2018>

Speaker: J. Moore

Category: Pulmonary Hypertension, Magnetic Resonance Angiography, vascular Physiology

**000504**

## **Fibrosing Mediastinitis: A Rare Case Associated with Immune Checkpoint Inhibitor Pembrolizumab**

C. J. Park \* (1); Y. Pokharel (1)

(1) Section on Cardiology, Wake Forest School of Medicine, Winston-Salem, United States of America

### **Abstract**

#### **Description of Clinical Presentation:**

A 58-year-old man with known invasive rectal melanoma presented with six months of progressive dyspnea and peripheral edema consistent with clinical heart failure and found to have a circumferential pericardial mass measuring up to 6.3 cm on transthoracic echocardiography. Previously, the patient underwent cancer immunotherapy with pembrolizumab for two years, which was suspended a year ago due to worsening renal function. He was noted to have bilateral ureteral obstruction and underwent ureteral stenting, and PET and CT scans at that time showed extensive soft tissue thickening throughout the abdomen and pelvis that was contiguous with the newly noted mediastinal mass. Subsequent retroperitoneal fine needle aspiration biopsy revealed fibrotic tissue with chronic lymphocytic inflammation consistent with retroperitoneal fibrosis, which was thought to be related to pembrolizumab use. There was no evidence of interstitial pulmonary fibrosis. In the past year, he also had two non-ST elevation myocardial infarctions, requiring multiple coronary stents. During this presentation, cardiac MRI (CMR) and repeat PET imaging were suggestive of fibrosing mediastinitis. Steroid therapy was initiated.

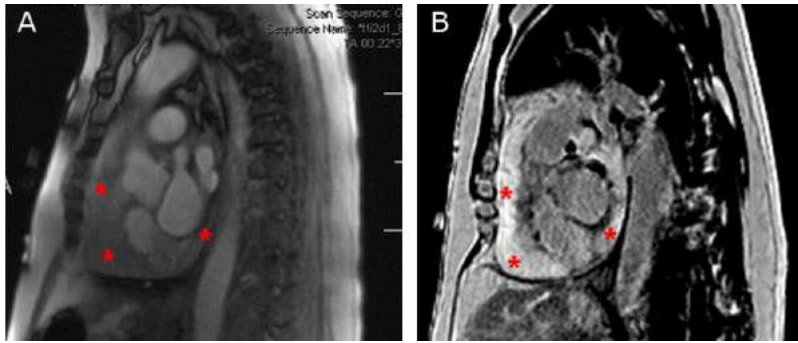
#### **Diagnostic Techniques and Their Most Important Findings:**

CMR demonstrated a diffuse, nearly well-circumscribed mediastinal mass encasing the heart from base to apex, including the great vessels (Figure 1A). Compared with the normal myocardium, the mass was isointense on T1, hyperintense on T2-weighted sequences, and showed enhancement on first pass perfusion sequences. Early (3 minutes post gadolinium infusion) and late gadolinium enhancement (LGE) were present (Figure 1B; Figure 2A and 2B). Subsequent FDG-18 PET scan showed low level FDG uptake in the mediastinum and abdomen, which was interpreted as likely ongoing fibrosis and less likely active malignancy.

#### **Learning Points from this Case:**

- Pembrolizumab exposure has been implicated in idiopathic retroperitoneal and interstitial pulmonary fibrosis [1,2].
- Based on our current literature review, this may be the first documented case of fibrosing mediastinitis putatively from pembrolizumab exposure.
- Pembrolizumab associated fibrosing mediastinitis may manifest on CMR with a mediastinal mass that is isointense on T1, hyperintense on T2 weighted sequences, enhance on first pass perfusion with early and late gadolinium enhancement, and low metabolic activity on PET.

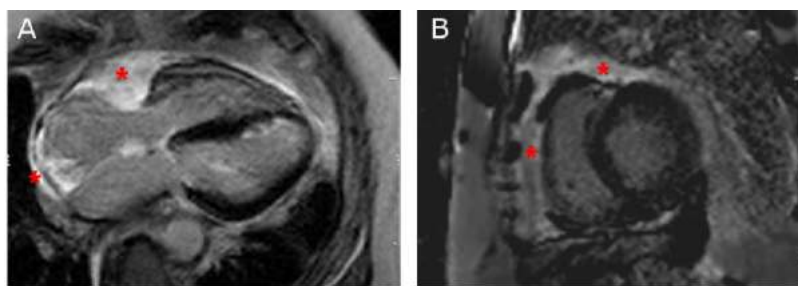
### **Figure/Table 1**



### Caption 1

Figure 1A: Sagittal T1-weighted localizer showing large structure encasing the base of the heart and great vessels (red asterisks). Figure 1B: Phase sensitive inversion recovery image demonstrates late gadolinium enhancement in the same structure (red asterisks).

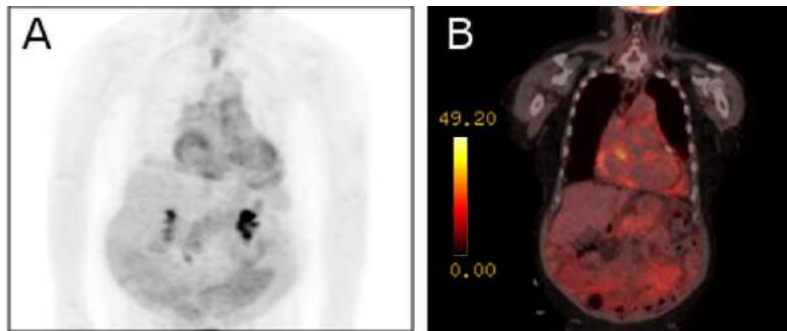
### Figure/Table 2



### Caption 2

Figure 2A: Four chamber phase sensitive inversion recovery image shows structure with late gadolinium enhancement circumscribing the heart (red asterisks). Figure 2B: Short-axis mid left ventricular view shows late gadolinium enhancement (red asterisks).

### Figure 3



### Caption 3

Figure 3A: FDG-18 PET/CT coronal view showing low metabolic activity in the ill-defined structure in the mediastinum and throughout the abdomen. Figure 3B: Fused FDG-18 PET/CT coronal view redemonstrates low FDG avidity surrounding the heart.

### Bibliographic References

Daoussis D, Kraniotis P, Kalofonos F, Kalofonos H. Anti-PD-1 associated retroperitoneal fibrosis. *Rheumatology* 2021;60:e329-e330., Nguyen M, Islam MR, Lim SW, Sahu A, Tamjid B. Pembrolizumab induced ocular hypotony with near complete vision loss, interstitial pulmonary fibrosis and arthritis. *Frontiers in oncology* 2019;9:944.

Speaker: C. J. Park

Category: Cardiac Mass, Late Gadolinium Enhancement, Cardiotoxicity

000505

## Prognostic Role of Late Gadolinium Enhancement in Left Ventricular Noncompaction

K. Rezaei Bookani \* (1); N. Nso, (2); A. Pursnani (1)

(1) Cardiology, UChicago Medicine at NorthShore University HealthSystem - Evanston, Evanston, United States of America; (2) Medicine, Icahn School of Medicine at Mount Sinai, New York, United States of America

### Abstract

#### Background

LGE (Late Gadolinium Enhancement) is based on different regional distribution patterns of gadolinium-based contrast agents within the extracellular space. It also depends on varying uptake and washout patterns within the myocardium. LGE is seen in myocardial injuries including fibrosis, necrosis, inflammation, and edema. LVNC (Left Ventricular Noncompaction) patients are at higher risk for developing heart failure, arrhythmias, thromboembolic events, and sudden cardiac death. This study aimed to determine the potential of LGE to prognosticate or stratify the risk of adverse events in the setting of LVNC.

#### Methods

This systematic review and meta-analysis followed the PRISMA (Systematic Reviews and Meta-Analysis) framework to include nine (prospective/retrospective) studies that used the LGE to investigate MACE (major adverse cardiac events: composite of thromboembolic episodes, heart failure hospitalization, appropriate defibrillator firing, assist device implantation, cardiac transplantation, and/or cardiac death) in LVNC patients. PubMed, EMBASE, JSTOR, and Cochrane library were explored to include the relevant studies published between January 2015 and September 2020.

#### Results

The pooled (random and fixed Mantel-Haenszel) results of five studies revealed 26% incidence of MACE in LGE positive LVNC patients and 10% incidence in LGE negative LVNC patients (Random M-H OR: 8.14 [95% CI 2.01, 32.91],  $p=0.003$ ) (fixed M-H OR: 6.46 [95% CI 4.18, 9.98],  $p<0.001$ ). The findings exhibited high heterogeneity for outcome measures ( $I^2=82\%$ ,  $p<0.001$ ) ( $I^2=79\%$ ,  $p<0.001$ ).

#### Conclusions

Positive LGE is associated with higher likelihood of MACE in the setting of LVNC. Future RCTs should identify and validate comprehensive LGE-based algorithms to improve the risk stratification in LVNC patients.

#### Figure/Table 1

## Caption 1

Table1: Mantel-Haenszel Random Effect Model for LGE in LVNC

## Figure/Table 2

## Caption 2

Table2: Mantel-Haenszel Fixed Effect Model for LGE in LVNC

## Bibliographic References

5. Mazurkiewicz Ł, Petryka J, Śpiewak M, Miłosz-Wieczorek B, Małek ŁA, et al. Clinical and prognostic relevancy of left ventricular trabeculation assessed by cardiac magnetic resonance in patients with dilated cardiomyopathy. *Kardiol Pol.* 2017;75(8):794-803. doi: 10.5603/KP.a2017.0097. Epub 2017 May 25. PMID: 28541593., 4. Ivanov A, Dabiesingh DS, Bhumireddy GP, Mohamed A, Asfour A, et al. Prevalence and Prognostic Significance of Left Ventricular Noncompaction in Patients Referred for Cardiac Magnetic Resonance Imaging. *Circ Cardiovasc Imaging.* 2017 Sep;10(9):e006174. doi: 10.1161/CIRCIMAGING.117.006174. PMID: 28899950., 3. Casas G, Limeres J, Oristrell G, Gutierrez-Garcia L, Andreini D, et al. Clinical Risk Prediction in Patients With Left Ventricular Myocardial Noncompaction. *J Am Coll Cardiol.* 2021 Aug 17;78(7):643-662. doi: 10.1016/j.jacc.2021.06.016. PMID: 34384546., 2. Andreini D, Pontone G, Bogaert J, Roghi A, Barison A, et al. Long-Term Prognostic Value of Cardiac Magnetic Resonance in Left Ventricle Noncompaction: A Prospective Multicenter Study. *J Am Coll Cardiol.* 2016 Nov 15;68(20):2166-2181. doi: 10.1016/j.jacc.2016.08.053. PMID: 27855806., 1. Amzulescu MS, Rousseau MF, Ahn SA, Boileau L, de Meester de Ravenstein C, Vancraeynest D, et al. Prognostic Impact of Hypertrabeculation and Noncompaction Phenotype in Dilated Cardiomyopathy: A CMR Study. *JACC Cardiovasc Imaging.* 2015 Aug;8(8):934-46. doi: 10.1016/j.jcmg.2015.04.015. Epub 2015 Jul 15. PMID: 26189121.

Speaker: K. Rezaei Bookani

Category: Fibrosis, Late Gadolinium Enhancement, Cardiac Events

000509

## Cardiac MRI Used to Identify the Culprit Lesion

R. Iyengar-Kapuganti (1); K. Rabii, (2); P. Mohajer, (2); L. Danso, (3); J. Aguilar-Gallardo, (3); N. Barman, (2); J. Tamis-Holland, (2); S. Talebi \* (2)

(1) Cardiovascular institutie, Mount Sinai Morningside, New York, United States of America;  
(2) Cardiovascular institute, Mount Sinai Morningside, New York, United States of America;  
(3) Medicine, Mount Sinai Morningside, New York, United States of America

### Abstract

**Description of Clinical Presentation:** A 66 year old with past medical history of hypertension hyperlipidemia, and diabetes presented with shortness of breath. On arrival patient became hypoxic and required intubation. Bedside echocardiogram showed severe reduced left ventricle systolic dysfunction (EF:10%). The patient was admitted to the CCU due to concerns of cardiogenic shock. After three days, he was extubated and weaned off the pressors. Left heart catheterization revealed heavily calcified three vessel disease with subsequent intervention of the left circumflex artery (LCX). Patient had multiple episodes of ventricular tachycardia (VT) and ventricular fibrillation(VF) requiring defibrillation. Because of recurrent arrhythmia without response to anti arrhythmia patient was transferred to our hospital for electrophysiology study and possible intra-cardiac defibrillator. A decision was taken to revascularize the right coronary artery (RCA) due to the possibility of ischemic-induced arrhythmia. The intervention of the left anterior descending artery (LAD) was deferred due to the complexity of the lesion. Despite RCA revascularization, the patient continued to have polymorphic VT.

**Techniques and Most Important Findings:** Given the recurrent arrhythmia, it was decided to determine myocardial viability and scar burden before any more intervention. Cardiac MRI showed significant reduced left ventricle systolic dysfunction and wall motion abnormalities at LAD territory. Post-contrast imaging demonstrates delayed myocardial enhancement indicative of a moderate-sized sub endocardial myocardial infarct involving predominantly the midventricular and apical segments of the septum (anteroseptal & inferoseptal) and anterior wall and the base and midventricular of inferolateral wall (Figure 1 and Figure 2). On T2-Mapping images, there was evidence of myocardial edema in the apical segments, anterior and septum, suggestive of acute myocardial injury at LAD territory (Figure 3). On return from CMR, patient had another episode polymorphic VT requiring defibrillation. Given significant viable tissue and acute myocardial injury at LAD territory medical team decided to intervene complex intervention of LAD. Subsequently patient hemodynamically remains stable without any further VT/VF. For seconday prevention patient got discharged with intracardiac defibrillator

### Learning Points from this Case:

Identification of the culprit lesion in patients with acute coronary syndrome allows appropriate coronary revascularization . The culprit lesion can be unclear by coronary angiography in patients with non ST-elevation myocardial infarction and multi vessel disease.



Cardiac MRI could complement conventional angiography and unveil the culprit lesion by offering a high-resolution spatial maps of infarcted and viable myocardium. Delayed-enhancement cardiac magnetic resonance and tissue mapping are considered to be the in vivo reference standard for imaging myocardial injury and infarction. This unique information from T2 mapping, allowing to differentiate acute from chronic infarct.

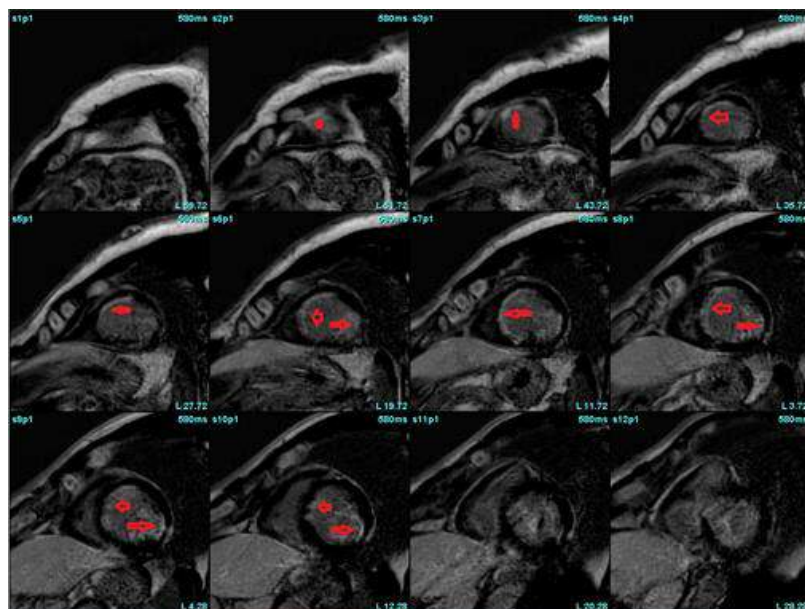
**Figure/Table 1**



**Caption 1**

Post contrast images show only subendocardial myocardial scar with significant viable tissue

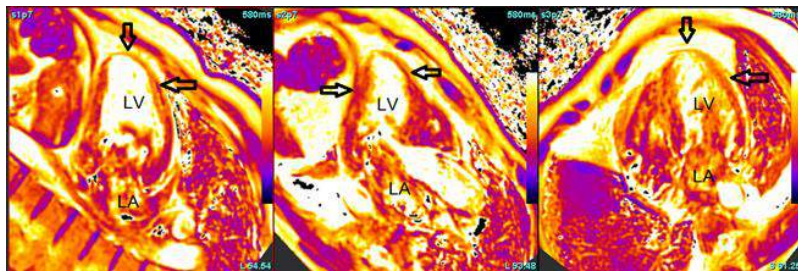
**Figure/Table 2**



**Caption 2**

Post contrast images show only subendocardial myocardial scar with significant viable tissue

**Figure 3**



**Caption 3**

T2 mapping images show significant myocardial edema at left anterior descending artery territory

### **Bibliographic References**

Culprit lesion detection in patients presenting with non-ST elevation acute coronary syndrome and multivessel disease. Matthew Mercieca Balbi et al. Cardiovasc Revasc Med. 2021., Identifying the Infarct-Related Artery in Patients With Non-ST-Segment-Elevation Myocardial Infarction, Heitner JF, et al. Circ Cardiovasc Interv. 2019. PMID: 31035776

Speaker: S. Talebi

Category: Acute Myocardial Infarction, T2, Tissue Characterization

000510

## **Decision Tree Modeling of Cardiac Magnetic Resonance Parametric Mapping Data in Pediatric Heart Transplant Recipients: A Screening Tool for Acute Rejection**

J. Soslow \* (1); K. Yan, (2); J. Godown, (1); D. Bearl, (1); K. Crum, (1); K. George-Durrett, (1); M. Chrisant, (3); K.-C. Chan, (3); D. Dodd, (1); B. Damon, (4); M. Samyn, (5); L. Hernandez, (3)

(1) Department of pediatrics, division of pediatric cardiology, Vanderbilt University Medical Center, Nashville, United States of America; (2) Biostatistics, Medical College of Wisconsin, Milwaukee, United States of America; (3) Pediatric cardiology, Joe DiMaggio Children's Hospital at Memorial Healthcare System, Hollywood, United States of America; (4) Stephens family clinical research institute, Carle Foundation Hospital, Urbana, United States of America; (5) Herma heart institute at children's wisconsin, Medical College of Wisconsin, Milwaukee, United States of America

### **Abstract**

#### **Background:**

Despite advances in pediatric heart transplant (PHTx) care, acute rejection (AR) remains a significant cause of morbidity and mortality. Endomyocardial biopsy (EMB) is the current gold standard for AR detection. Many centers perform routine surveillance EMB to screen for asymptomatic AR. EMB is also used for symptomatic PHTx patients. However, EMB is expensive and associated with potential morbidity. We hypothesized that cardiac magnetic resonance (CMR) could be used to screen for AR.

#### **Methods:**

Thirty PHTx recipients were prospectively enrolled at two sites either within 5 days of AR diagnosis or at surveillance EMB. There were 10 unique episodes of EMB positive AR; 1 subject with EMB negative AR was removed from analysis. CMR included native T1, T2, and extracellular volume (ECV) mapping in 4 slices in the short axis and in the 4-chamber. Global longitudinal and circumferential strain (GLS, GCS) were calculated using feature tracking. Late gadolinium enhancement (LGE) was quantified using the 5 standard deviation method. Native T1 and T2 were normalized as Z-scores based on magnet-specific normal values. A Mann-Whitney U-test was used to assess for a difference between groups. Decision tree analysis to predict AR was performed using the Gini Method and the following variables: GLS, GCS, ECV base, ECV mid, ECV average, T1 base z-score, T1 mid z-score, T1 average z-score, T2 base z-score, T2 mid z-score, T2 average z-score, gender, ethnicity, prior rejection, LGE presence/ absence, LGE quantification, and age at transplant.

#### **Results:**

Median age was 16 years with interquartile range (IQR) of 13-18. 15 (52%) subjects were male. The median left ventricular ejection fraction (LVEF) was 59% with IQR 55%-64%. Approximately 59% of subjects had LGE and there was no difference in LGE presence or quantification between groups. Base ECV, mid ECV, base T2 Z-score, mid T2 Z-score, base T1 Z-score, mid T1 Z-score, GLS, and GCS were increased in AR vs non-rejection (Table 1), while LVEF was decreased. The model chose GLS as the first split with a cut off value of -16% and T2 Z-score at the mid-LV with a cut off of Z=3.7 (Figure 1). The area under the curve for the model was 0.98. Applying this decision tree to the cohort leads to 100% negative predictive value and 100% sensitivity for AR, with a positive predictive value of 83% and a specificity of 89%.

## Conclusions:

Decision tree analysis using GLS and T2 mapping distinguishes between PHTx subjects with and without AR with a high negative predictive value (100%) and adequate positive predictive value (83%). In the future, this algorithm could be used to predict who should undergo invasive catheterization with EMB. Thus, CMR has potential for AR screening, though values must be validated in a larger prospective cohort.

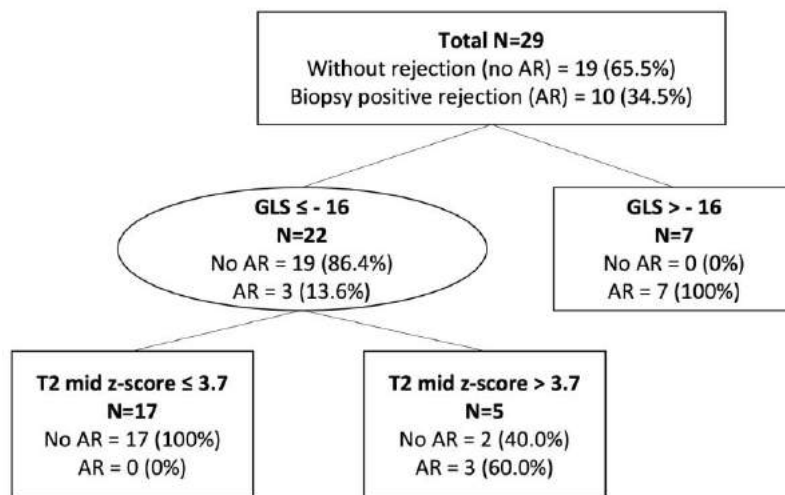
**Figure/Table 1**

	Acute Rejection (n = 10)	Non-rejection (n = 19)	p-value
LVEF %	51 (42,56)	61 (59,64)	<0.001
LGE quantification %	12.6 (10, 22.4)	13.7 (8.3, 16.8)	0.781
Base ECV %	32.8 (31.4, 37.2)	26.3 (23.7, 31.8)	0.013
Mid ECV %	35.7 (31.1, 41.8)	30.0 (26.9, 34.5)	0.025
Average ECV %	34.8 (31.3, 39.4)	27.4 (25.7, 33.4)	0.014
Base T <sub>2</sub> Z-score	4.2 (1.1, 5.8)	0.20(-0.46, 3.1)	0.013
Mid T <sub>2</sub> Z-score	3.0 (0.9, 5.2)	1.1 (-0.3, 2.2)	0.028
Average T <sub>2</sub> Z-score	3.7 (1.0, 5.5)	0.82 (-0.3, 2.9)	0.022
Base T <sub>1</sub> Z-score	4.7 (2.0, 6.8)	2.6 (1.3, 3.9)	0.054
Mid T <sub>1</sub> Z-score	3.6 (2.7, 5.0)	2.0 (0.90, 3.1)	0.039
Average T <sub>1</sub> Z-score	4.5 (2.6, 6.1)	2.6 (1.1, 3.8)	0.028
GLS %	-13.1 (-21.9, -11.4)	-22.7 (-24.5, -19.8)	0.018
GCS %	-25.3 (-28.0, -21.5)	-31.1 (-34.4, -28.8)	0.002

## Caption 1

**Table 1:** Difference [median (IQR)] between groups

**Figure/Table 2**



## Caption 2

**Figure 1:** Decision Tree Analysis to Predict Acute Rejection

Speaker: J. Soslow

Category: Pediatric , Heart Transplant, Parametric Mapping

000513

## Hydroxychloroquine-Induced Cardiomyopathy in SLE: Cardiac MRI and Histopathology Correlation in a Patient with New Onset HFrEF

M. Krishnam \* (1); K. Williams (2); R. Whitteles (3)

(1) Cardiovascular radiology, Stanford University, Palo Alto, United States of America; (2) Cardiothoracic surgery, Stanford University, Palo Alto, United States of America; (3) Cardiovascular medicine, Stanford University, Palo Alto, United States of America

### Abstract

This is a rare case of biopsy-proven antimalarial-induced cardiomyopathy (AMIC) in a patient with systemic lupus erythematosus who presented with new onset heart failure and initially misdiagnosed as lupus myocarditis on cardiac magnetic resonance (CMR). Patient improved symptomatically following discontinuation of hydroxychloroquine.

Electrocardiogram(Fig.1) on arrival showed heart rate of 55, sinus rhythm, new right bundle branch block and new LVH with intraventricular conduction delay. Echocardiogram revealed estimated LVEF of 37% and moderate mitral regurgitation, biventricular dysfunction. Cardiac MRI showed myocardial thickening, global hypokinesis, minimal subtle mesocardial curvilinear increased signal on T2 DIRFSE(Fig.2) in the apical septum, and corresponding late gadolinium enhancement (LGE) in a non-ischemic pattern (Fig 3). She was treated for presumed SLE myocarditis with solumedrol, prednisone, increased mycophenolate, and continued hydroxychloroquine. The patient was stable until approximately six weeks later, when her dyspnea and orthopnea worsened was readmitted after two weeks of worsening symptoms, repeat echo showed LVEF 39%, and marked biventricular hypertrophy. She had chronic troponin leak, elevated lactate, and elevated beta natriuretic peptide out of proportion to her exam or symptoms. These findings suggested hydroxychloroquine toxicity or amyloid cardiomyopathy secondary to smoldering multiple myeloma. Endomyocardial biopsy was pursued, which revealed prominent vacuolization consistent with hydroxychloroquine toxicity. The findings seen in the thick sections correspond to lamellar/myelinoid bodies and curvilinear bodies. The latter are not reported in Fabry's disease. Overall the clinical and morphologic findings support chloroquine cardiotoxicity. The patient underwent diuresis and hydroxychloroquine was stopped. She was discharged after two days and she gradually improved her biventricular functions with recent echocardiogram showed LVEF at 44% has been recovering with physical therapy and no longer requires daily furosemide. Coronary CTA showed no atherosclerotic disease.

### Learning Points:

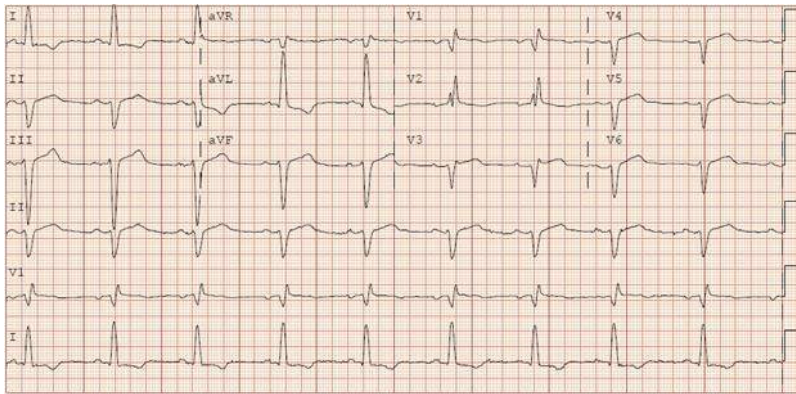
Non-Ischemic cardiomyopathy from hydroxychloroquine is a rare but known life-threatening complication.

Cardiac MRI may be normal but can demonstrate mid wall edema in the region of LGE which can be misdiagnosed as myocarditis.

Cardiac imagers should have a high index of suspicion for AMIC in the right clinical setting, especially if imaging findings on MRI show myocardial thickening, linear mid wall septal edema and corresponding LGE. T2 and T1 myomaps may be helpful.

Vacuolization and lamellar/myelinoid and curvilinear bodies on histopathology from myocardial biopsy are pathognomonic of hydroxychloroquine toxicity of myocardium.

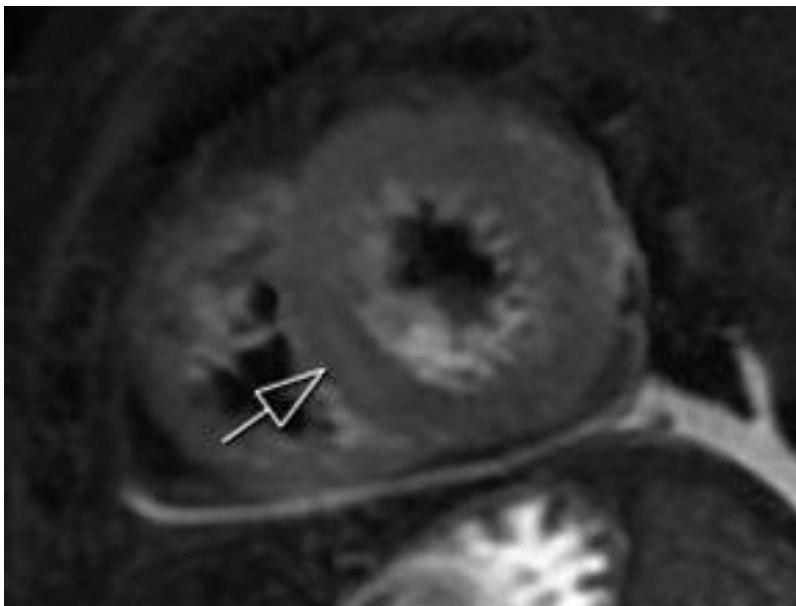
### Figure/Table 1



**Caption 1**

ECG on initial admission. Heart rate of 55, sinus rhythm, new right bundle branch block and new left ventricular hypertrophy with intraventricular conduction delay (IVCD) and ST elevation secondary to IVCD

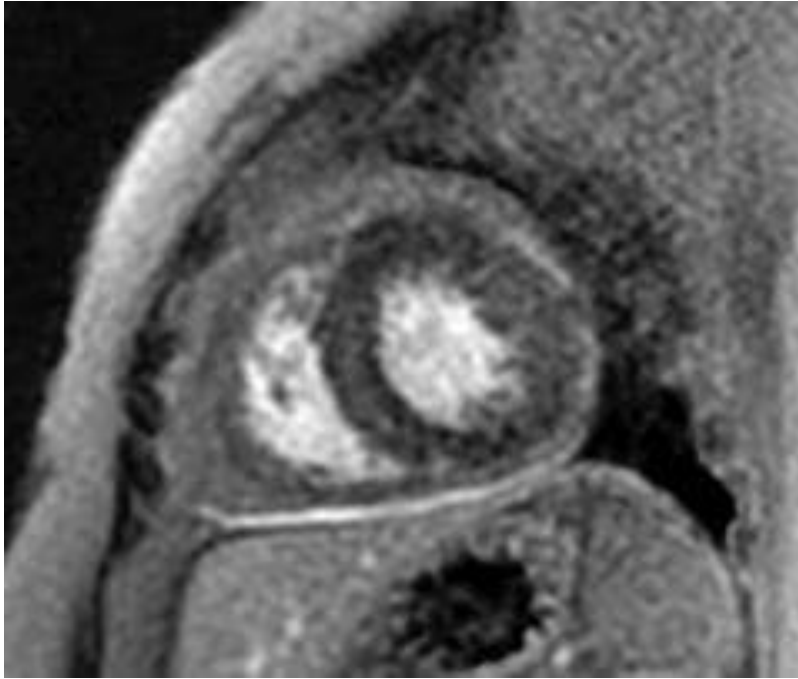
**Figure/Table 2**



**Caption 2**

T2 DIRFSE of apical short axis image shows linear subtle midwall septal high signal, suggestive of edema. No convincing epicardial or transmural hyperintensity/edema.

**Figure 3**



### **Caption 3**

- Single Shot Phase Sensitive Inversion Recovery image of apical short axis shows abnormal mid wall LGE in the septum. No evidence of epicardial, subendocardial or transmural LGE.

### **Bibliographic References**

Abbasi S, Tarter L, Farzaneh-Far R, et al. Hydroxychloroquine: a treatable cause of cardiomyopathy. *J Am Coll Cardiol*. 2012;60:786., selios K, Deeb M, Gladman DD, Harvey P, Urowitz MB. Antimalarial-induced cardiomyopathy: a systematic review of the literature. *Lupus*. 2018;27:591-599, Chatre C, Roubille F, Vernhet H, et al. Cardiac complications attributed to chloroquine and hydroxychloroquine: a systematic review of the literature. *Drug Saf*. 2018;41:919-931

Speaker: M. Krishnam

Category: Cardiotoxicity, Cardiomyopathy, Ejection Fraction



000515

## Noninvasive MRI- and CFD-based left ventricular pressure-volume loops: Initial feasibility and Scan-Rescan reproducibility study

P. Roos \* (1); M. De Vlieger (2); S. Kenjereš (2); J. Westenberg (1); H. Lamb (1)

(1) Radiology, Leiden University Medical Center (LUMC), Leiden, Netherlands; (2) Chemical engineering, Delft University of Technology (TU Delft), Delft, Netherlands

### Abstract

**Background.** Left ventricular (LV) pressure volume loops describe the cardiac mechanics of the left ventricle throughout the cardiac cycle and are therefore a valuable tool in cardiology. Measurement of pressure volume loops is performed invasively, using catheters with pressure measurement and volume estimation. We developed a method to generate pressure-volume loops from noninvasive magnetic resonance imaging, using a patient-specific one-dimensional computational fluid dynamics (CFD) based arterial model. In this study, we tested repeatability of our pressure-volume loops model from scan-rescan MRI data of healthy volunteers.

**Methods.** Cardiovascular MRI was performed twice on 3T MRI (Philips Healthcare) for ten (N=10) healthy volunteers (age  $27 \pm 3$  years). This included multi-slice cine SSFP short axis scan for LV endocardial contour segmentation to assess the LV volume and two-dimensional cine phase-contrast scan through the ascending aorta to assess aortic flow. Image analysis was performed with inhouse software MASS (Leiden University Medical Center, Leiden). Aortic cross-sectional area and aortic flow for each timepoint were calculated for each time-point of the scans.

Aortic flow and ascending aortic cross-sectional area were used as input in a one-dimensional CFD arterial model (based on solving conservation of mass and momentum of blood through arteries with elastic walls), which models 111 arteries and scales patient-specifically.[1]

The model was run until the pressure difference per cycle start was less than 1 mmHg and the ascending aortic pressure was extracted and used in an elasticity model using the relation found by [2] to calculate the LV pressure, where  $V_0$  was taken equal to 0.

Using the left ventricular volume calculated from the short-axis scan, the pressure-volume loops were generated and several characteristics (maximum pressure, minimum pressure, end diastolic pressure, end systolic pressure) were extracted. The slope of the End-systolic pressure volume relationship, Ees, was calculated (with  $V_0 = 0$  ml). The area of the PV-loop is equal to the stroke work. Reproducibility was tested by Pearson correlation.

**Results.** We found a very strong positive correlation ( $r > 0.8$ ) between maximum pressure ( $r = 0.81$ ,  $p = 0.004$ ), minimum pressure ( $r = 0.82$ ,  $p = 0.004$ ), end systolic volume ( $r = 0.82$ ,  $p = 0.004$ ), end-diastolic volume ( $r = 0.98$ ,  $p < 0.001$ ) and stroke work ( $r = 0.81$ ,  $p = 0.004$ ) of the scan and rescan. There was a strong positive correlation ( $0.60 < r < 0.79$ ) for the end systolic pressure ( $r = 0.67$ ,  $p = 0.04$ ), but there was no significant correlation for the end-diastolic pressure ( $r = 0.60$ ,  $p = 0.07$ ) and the Ees ( $r = 0.49$ ,  $p = 0.15$ ).

Conclusion. We have developed an innovative method CFD for noninvasive left ventricular pressure-volume loop generation from magnetic resonance imaging data.

This method show overall good reproducibility, but improvements have to be made to ensure reproducibility of all aspects of the pressure-volume loop.

Future studies are needed to evaluate the clinical value of this noninvasive method.

### Figure/Table 1

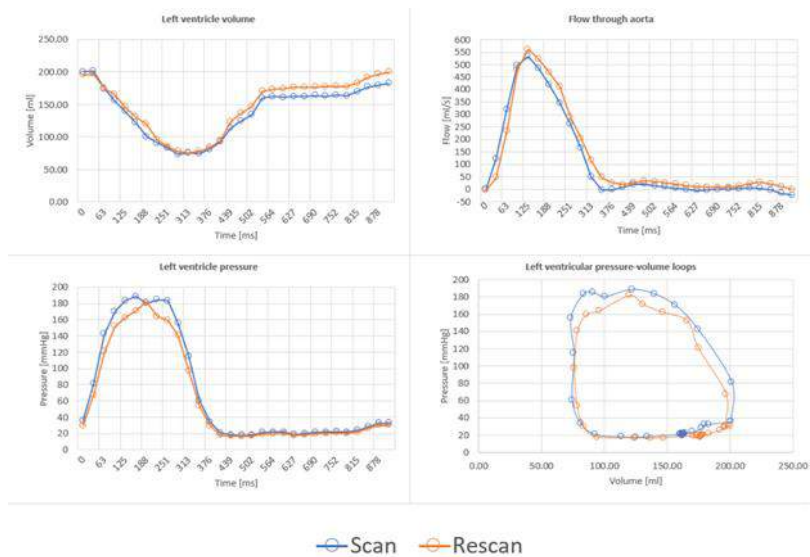
Outcome measure	Mean scan ( $\pm$ CI)	Mean rescan ( $\pm$ CI)	Pearson r	p-value
Maximum pressure [mmHg]	166.95 ( $\pm$ 28.59)	174.27 ( $\pm$ 24.94)	0.816	0.004
Minimum pressure [mmHg]	14.35 ( $\pm$ 3.15)	14.03 ( $\pm$ 2.59)	0.816	0.004
End systolic pressure [mmHg]	131.53 ( $\pm$ 21.39)	128.07 ( $\pm$ 14.65)	0.665	0.036
End diastolic pressure [mmHg]	29.15 ( $\pm$ 6.10)	30.14 ( $\pm$ 5.75)	0.597	0.068
End systolic volume [ml]	55.02 ( $\pm$ 8.56)	52.44 ( $\pm$ 7.15)	0.820	0.004
End diastolic volume [ml]	149.67 ( $\pm$ 20.41)	150.93 ( $\pm$ 17.41)	0.977	0.000
Slope of ESPVR (Ees) [mmHg/ml]	3.23 ( $\pm$ 0.96)	3.20 ( $\pm$ 0.63)	0.495	0.146
Stroke work [mmHg*ml]	11480.74 ( $\pm$ 2759.89)	12437.42 ( $\pm$ 3145.20)	0.812	0.004

*CI = Confidence level; ESPVR = End-systolic pressure volume relationship*

### Caption 1

Table 1: Pearson correlation tests.

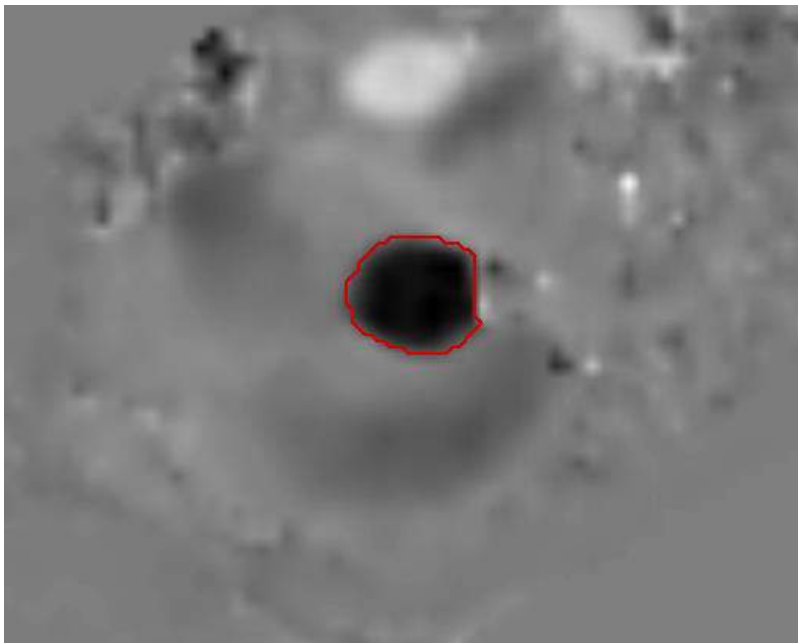
### Figure/Table 2



**Caption 2**

Figure 1: Graphs showing left ventricle volume, aortic flow and left ventricle pressure throughout the cardiac cycle and the pressure-volume loop of one healthy volunteer. Blue graphs represent first scan, orange graphs represent the second scan (rescan).

**Figure 3**



**Caption 3**

Figure 2: Velocity image of a two-dimensional cine phase-contrast scan through the ascending aorta to assess aortic flow. Red contour is drawn around the ascending aorta.

### **Bibliographic References**

2. Senzaki, H., C.H. Chen, and D.A. Kass, Single-beat estimation of end-systolic pressure-volume relation in humans. A new method with the potential for noninvasive application. *Circulation*, 1996. 94(10): p. 2497-506., 1. Hamel, D., Combining MRI blood flow data with one-dimensional blood flow models to perform patient-specific noninvasive pressure prediction, in TU Delft Applied Sciences; TU Delft Electrical Engineering, Mathematics and Computer Science; TU Delft ChemE/Transport Phenomena. 2020, Delft University of Technology: TU Delft Repository.

Speaker: P. Roos

Category: Aorta, Cardiac Function, Blood Flow

000516

## **Role of cardiac MRI in identifying dual pathology with acute myopericarditis and disseminated cysticercosis**

S. Zaman \* (1); K. Leong, (2); G. Cole, (1); D. Gopalan, (2); B. Ariff, (2)

(1) Cardiology, Imperial College Healthcare NHS Trust, London, United Kingdom; (2) Radiology, Imperial College Healthcare NHS Trust, London, United Kingdom

### **Abstract**

#### **Description of clinical presentation**

A previously well male in his 30s of Indian origin with recent travel to Afghanistan presented with chest pain and non-specific ST changes on ECG. Emergency coronary angiography revealed unobstructed coronary arteries. His high sensitivity troponin level peaked at 17,000 ng/L (normal range <34ng/L) and he therefore underwent cardiac MRI (CMR).

#### **Diagnostic techniques and their most important findings**

T2-weighted (STIR) imaging showed extensive areas of high signal in the inferior and anterolateral walls (Figure 1 panels a to c) consistent with myocardial oedema. There was congruent subepicardial and pericardial late gadolinium enhancement in keeping with an acute myopericarditis (figure 1, panels d to f). Furthermore, a small well-defined cystic lesion was found in the basal septum of the myocardium which had isointense T1 signal, high T2 signal and did not enhance on late gadolinium imaging (figure 1 panel f and figure 2). Similar lesions were identified in the chest wall and lungs (figure 3, panels a to c).

CT thorax confirmed multiple non-calcific non-cavitating soft tissue nodules in the lungs (figure 3, panel g), pectoral muscles and myocardium. CT brain showed multiple intra-axial, supra- and infratentorial lesions (cystic with a central focus of high attenuation) in the cerebellum, frontal and temporal lobes in keeping with neurocysticercosis (figure 3, panels d to f). Cysticercosis serology was subsequently positive.

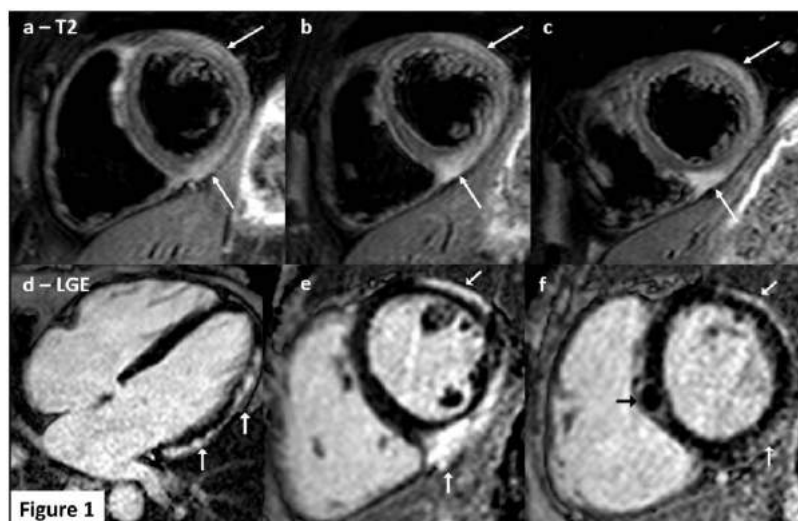
The acute myopericarditis was treated with a course of non-steroidal anti-inflammatory therapy. A multi-disciplinary approach including cardiology, radiology, neurology and infectious diseases opinions recommended a conservative approach given the minimal symptoms (occasional headaches only) and the risk of rebound inflammation after cysticidal therapy in disseminated disease (1).

#### **Learning points from this case**

Cysticercosis is a parasitic infection due to ingestion of the pork tapeworm ova (*Taenia solium*) which disseminate haematogenously via the intestinal tract. Cardiac involvement occurs in up to 25% of cases (2), usually asymptomatic, but can present with arrhythmia and heart failure (3). Diffuse myocardial calcification from degenerating cysticerci can cause restrictive cardiomyopathy (4). On MRI, cysticercosis lesions are well defined, with a

hypointense eccentric nodule within (scolex). This case emphasises the importance of reviewing extracardiac images in CMR, particularly where an expected cardiac finding has been identified. With increasing human movement, cysticercosis is an important differential diagnosis of a cardiac mass even in the developed world.

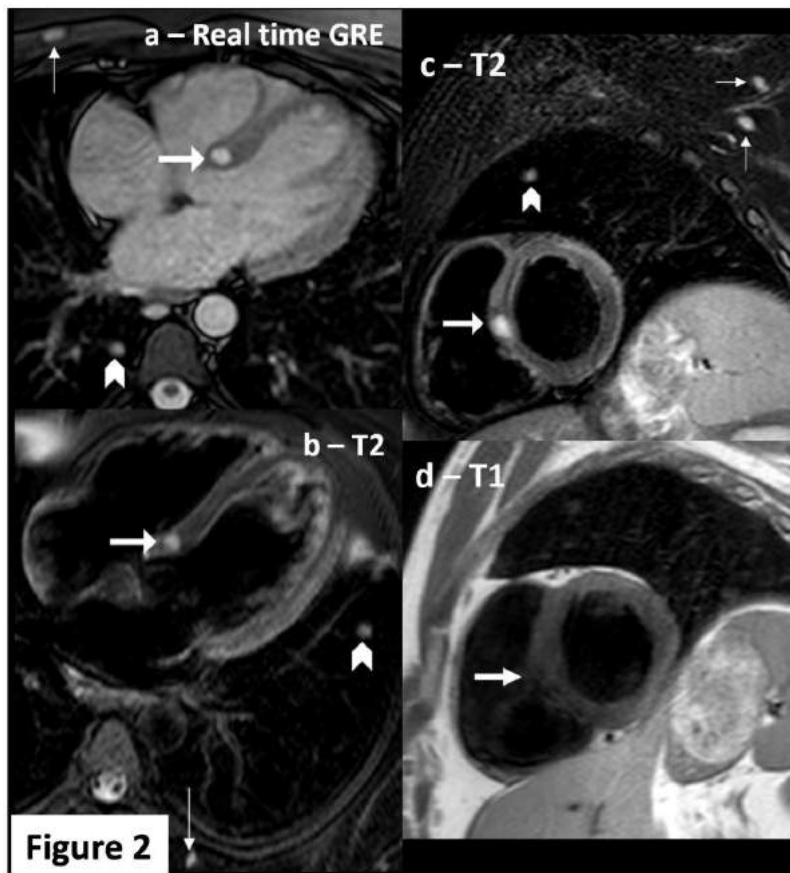
**Figure/Table 1**



**Caption 1**

**Figure 1** - Panels a to c; myocardial oedema indicated by high signal on T2-weighted STIR images in the inferior and lateral walls (white arrows). Panels d to f; corresponding subepicardial delayed enhancement (white arrows). Peripheral rim enhancement of septal cyst demonstrated (panel f, black arrow). No central early or late enhancement.

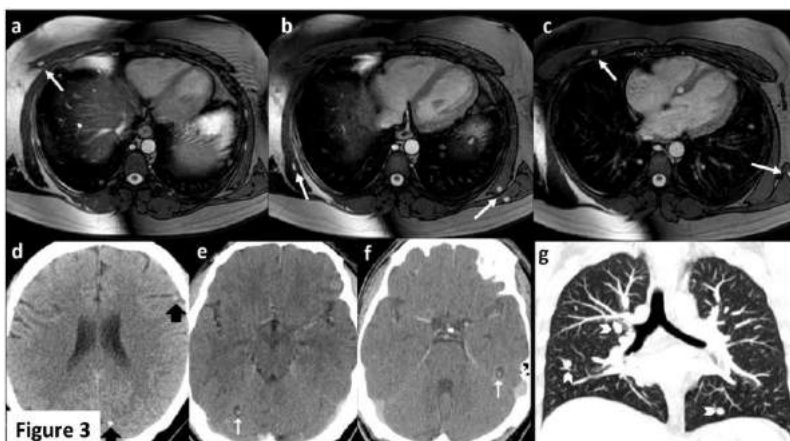
**Figure/Table 2**



**Caption 2**

**Figure 2** - Intramyocardial cystic lesion in the basal septum. T2 hyperintense (panels b and c) and T1 isointense lesion signal characteristics (panel d). Additional cystic lesions demonstrated in skeletal muscle (panels a to c, thin white arrows) and left lung (panels b and c, broad arrowhead).

**Figure 3**



### Caption 3

**Figure 3-** Panels a to c and g; cystic lesions in skeletal muscles (white arrows) and lung parenchyma (white arrowheads). Panels d to f; multiple intra-axial supra and infratentorial cystic lesions. Some with central high attenuation (in cerebellum and left temporal lobe; panels e and f, white arrows). Left parietal and occipital lesions (panel d, black arrows).

### Bibliographic References

1. Garcia HH, Nash TE, Del Brutto OH. Clinical symptoms, diagnosis, and treatment of neurocysticercosis. *Lancet Neurol.* 2014 Dec;13(12):1202–15., 2. Groom ZC, Protopapas AD, Zochios V. Tropical diseases of the myocardium: a review. *Int J Gen Med.* 2017 Apr 7;10:101–11., 3. Jain BK, Sankhe SS, Agrawal MD, Naphade PS. Disseminated cysticercosis with pulmonary and cardiac involvement. *Indian J Radiol Imaging.* 2010 Nov;20(4):310–3., 4. Melo RMV de, Melo Neto AV de, Corrêa LCL, Melo Filho AV de. [Restrictive cardiomyopathy due to myocardial cysticercosis]. *Arq Bras Cardiol.* 2005 Dec;85(6):425–7.

Speaker: S. Zaman

Category: Cardiac Mass, Myocarditis, Incidental Findings



**000518**

## **Nailed it! Diagnosing sarcoidosis amidst list of differentials**

N. Butt \* (1); D. Ali, (1); K. Mikrut (2); N. Asado (3); S. Hussain (1)

(1) Cardiology, Advocate Lutheran, Park Ridge, United States of America; (2) Cardiology, The Ohio State University Wexner Medical Center, Columbus, United States of America; (3) Pathology, Advocate Lutheran, Park Ridge, United States of America

### **Abstract**

#### **Description of Clinical Presentation**

36-year-old male presented with recurrent syncopal episodes. He had a family history of Brugada syndrome in his brother who had an ICD. The patient underwent an extensive cardiac workup at the time of his brother's diagnosis 10 years ago which included a cardiac MRI. At that time no pathology was identified. On current presentation patient's EKG demonstrated a first degree AV block, RBBB-like QRS morphology with inverted T wave in V1, V2 and a possible Epsilon wave. Chest x-ray showed faint opacities in the right upper lobe. He was having episodes of non-sustained ventricular tachycardia (NSVT) and high degree AV block on the telemetry monitor therefore was admitted for further workup.

#### **Diagnostic Techniques and Their Most Important Findings**

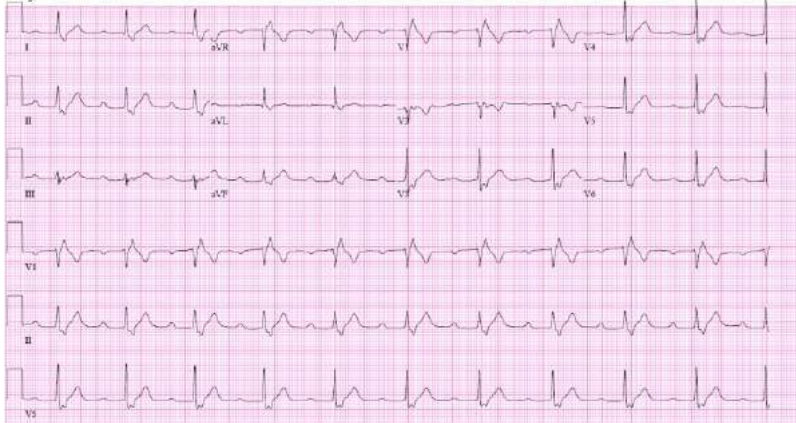
2D echocardiogram showed increased left ventricular (LV) wall thickness, normal ejection fraction (EF). A cardiac MRI revealed LV EF of 40%, mild global hypokinesis, severe hypertrophy of the basal to mid septal wall. Right ventricle was globally hypokinetic with EF of 37% and RV end diastolic volume index (RVEDVI) of 116 mL/m<sup>2</sup> but no areas of akinesis or dyskinesis. Multiple prominent areas of subendocardial and subepicardial late gadolinium enhancement (LGE) were noted most prominent in mid anteroseptal and inferoseptal wall and in the RV free wall (figure 2). Patient underwent endomyocardial biopsy (EMB) which showed granulomatous myocarditis consistent with sarcoidosis (figure 3). Lastly, PET scan showed increased myocardial activity in the distribution of the mid and basal segments of the left ventricular anteroseptal wall and mildly FDG avid upper lobe predominant bilateral pulmonary nodular opacities favoring cardiac and pulmonary sarcoidosis. Patient received a bi-ventricular ICD.

#### **Learning Points from this Case**

Our patient is a young male who presented with recurrent syncopal episodes associated with conduction abnormalities. The initial presentation involves an extensive differential diagnosis. A 2D echo was essentially unrevealing. We had a strong suspicion for ARVD given presence of epsilon waves on EKG. Cardiac MRI was obtained which did demonstrate RV dysfunction and increased RVEDVI but no regional wall motion abnormalities. The striking LGE pattern together with intermittent high degree AV block and runs of NSVT was suspicious for cardiac sarcoidosis which was proven with EMB. The diagnostic sensitivity of EMB to detect sarcoidosis remains low-yield due to patchy nature of the disease. The use of imaging such as cardiac MRI or PET can aid in identifying optimal sites for biopsy. Furthermore, cardiac MRI is a sensitive imaging modality to detect sarcoidosis, which is seen as LGE, but active inflammation and scarring can both cause delayed enhancement. This can be mitigated with T2-weighted MRI sequence as it can differentiate inflammation from scarring, however, the

T2-weighted image quality is often suboptimal, as was in our case. This limitation can be rectified by utilizing PET scan as it can differentiate inflammation from scarring and also identify the extent of the disease. Lastly, our case exemplifies that advances in imaging techniques and utilization of multi-modality imaging can lead to timely diagnosis and treatment of cardiac sarcoidosis.

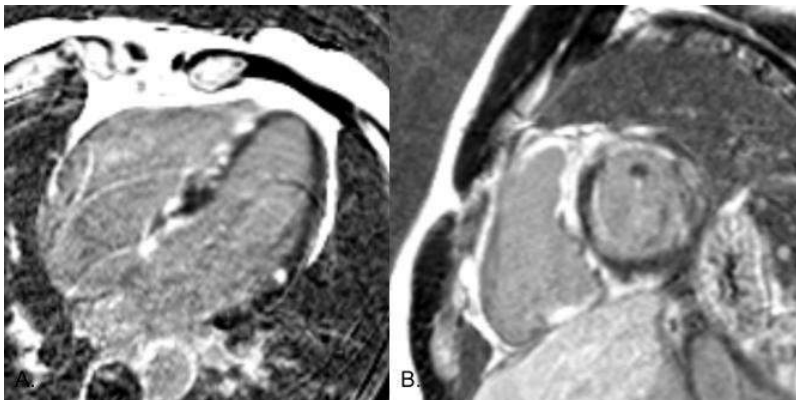
**Figure/Table 1**



**Caption 1**

Presenting EKG with first degree AV block, RBBB-like QRS morphology with inverted T wave in V1, V2 and a possible Epsilon wave.

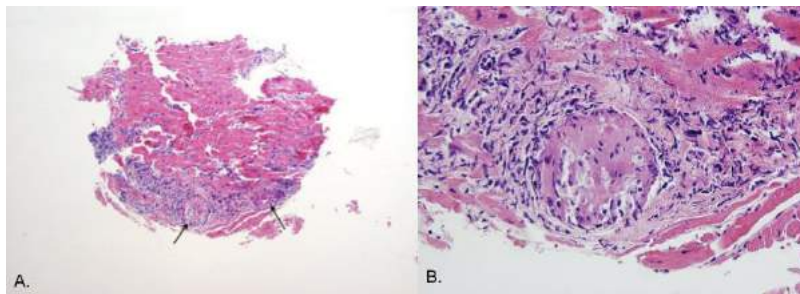
**Figure/Table 2**



**Caption 2**

Dense diffuse areas of late gadolinium enhancement as demonstrated on the 4 chamber (A) and basal short axis slice (B).

**Figure 3**



**Caption 3**

A. H&E stain (100x) demonstrating focal non necrotizing granulomas in the myocardium (black arrows)

B. H&E stain (400x) demonstrating compact collection of epithelioid histiocytes

### **Bibliographic References**

Ordovas KG, Higgins CB. Delayed contrast enhancement on MR images of myocardium: past, present, future. *Radiology* 2011;261(2):358–374 , PET/CT in the Diagnosis and Workup of Sarcoidosis: Focus on Atypical Manifestations Gensuke Akaike, Malak Itani, Hardik Shah, Jitesh Ahuja, Burcak Yilmaz Gunes, Richard Assaker, and Fatemeh Behni *RadioGraphics* 2018 38:5, 1536-1549 Ordovas KG, Higgins CB. Delayed contrast enhancement on MR images of myocardium: past, present, future. *Radiology* 2011;261(2):358–374

Speaker: N. Butt

Category: Sarcoidosis, Late Gadolinium Enhancement, Arrhythmia

000520

## Association of cardiac MR Fingerprinting derived T1 and T2 values with global left ventricular strain in patients with cardiac amyloidosis

J. Cohen \* (1); B. Eck (2); J. Hamilton (3); N. Seiberlich (3); A. Houston (4); D. Tew (4); M. Hanna (5); W. Tang (5); S. Flamm (4); D. Kwon (4)

(1) Cardiovascular Medicine, Miller Family Heart and Vascular Institute at the Cleveland Clinic, Cleveland, United States of America; (2) Imaging institute, Cleveland Clinic Lerner College of Medicine, Cleveland, United States of America; (3) Radiology, University of Michigan, Ann Arbor, United States of America; (4) Section of cardiovascular imaging, Miller Family Heart and Vascular Institute at the Cleveland Clinic, Cleveland, United States of America; (5) Section of advanced heart failure and transplant, Miller Family Heart and Vascular Institute at the Cleveland Clinic, Cleveland, United States of America

### Abstract

**Background:** Cardiac amyloidosis (CA) is an infiltrative cardiomyopathy wherein misfolded amyloid proteins deposit in the myocardium and impair cardiac function. Patients with CA have abnormal T1 and T2 values as well as myocardial strain predominantly thought to be due to amyloid deposition. Cardiac MR Fingerprinting (cMRF) enables simultaneous, rapid mapping of T1 and T2 in a single scan. It is unclear whether these methods of tissue characterization correlate with myocardial contractility. We hypothesize that cMRF T1 and T2 values correlate with global left ventricular strain in patients with cardiac amyloidosis.

**Methods:** Seven patients with confirmed cardiac amyloidosis and five healthy controls were prospectively recruited under an IRB approved protocol. Data were collected in a prospective fashion and subjects were scanned on a Siemens Prisma 3T scanner using cMRF, conventional T1 and T2 mapping (MOLLI, T2-prepared FLASH), and short axis cine sequences. The cMRF acquisition used a prospectively ECG-gated (or peripheral pulse-gated), breath-held scan at end-diastole with a voxel size of 1.6x1.6x8 mm<sup>3</sup>, spiral readout, 254 ms temporal duration, and acquired over 15 heartbeats for three cardiac short axis slices. T1 and T2 maps from the conventional mapping techniques were generated using the vendor's inline reconstruction. The cMRF data were reconstructed using voxelwise inner product matching to scan-specific dictionaries that included slice profile and preparation pulse efficiency corrections. Conventional and cMRF tissue property maps were contoured and segmental T1 and T2 values were obtained. These segmental values were averaged to obtain global cMRF and conventional T1 and T2 measurements. Cine images were processed using CVI42 software with tissue tracking of SSFP images to obtain global longitudinal, radial, and circumferential strain. T1 and T2 values from cMRF and conventional methods were correlated with strain measurements using Spearman's correlation analysis.

**Results:** Baseline demographics, mean T1, T2, and global strain values are shown in table 1. T2 values by cMRF and conventional methods were most closely correlative with all measurements of global strain as compared with T1 values (table 2). CMRF T2 values showed statistically significant correlations with all measures of strain, however, higher rho (r) values as compared to Flash acquired T2 values were only observed for short axis global circumferential strain (r=0.61 vs r=0.51), and short axis global radial strain (r=-0.59 vs r=-

0.49). T1 and T2 values independent of acquisition method similarly correlated with global radial and longitudinal strain acquired in the long axis.

**Conclusions:** T1 and T2 values determined by cMRF correlate with strain measurements in a cohort of patients with CA and healthy controls. T2 values acquired by cMRF seem to have a robust correlation with all measures of global left ventricular strain. In comparison to traditional acquisition of T2 values, cMRF outperforms Flash when correlated with global circumferential and radial strain in the short axis. Correlation of global longitudinal and radial strain in the long axis was similar when T1 and T2 mapping was acquired by cMRF or MOLLI. Our findings suggest that MRF derived T2 values could be a more sensitive correlate between myocardial edema and contractility, a finding which has not previously been clearly demonstrated in patients with cardiac amyloidosis.

**Figure/Table 1**

Measurement	Amyloid (N=7)	Control (N=5)	P value
Age (yr)	63.7 ± 12.4	37.2 ± 10.9	<0.01
Gender (% male)	71.4	20	
SAX Global Circumferential Strain (%)	-15.3 ± 3.7	-18.8 ± 1.9	0.06
SAX Global Radial Strain (%)	23.9 ± 8.3	31.8 ± 4.9	0.07
LAX Global Longitudinal Strain (%)	-12.2 ± 4.6	-19.7 ± 1.8	<0.01
LAX Global Radial Strain (%)	19.2 ± 8.3	36.3 ± 5.9	<0.01
cMRF T1 (ms)	1415 ± 99	1312 ± 46	0.04
cMRF T2 (ms)	38.5 ± 4.4	34.1 ± 2.5	0.05
MOLLI T1 (ms)	1383 ± 111	1245 ± 13	0.02
FLASH T2 (ms)	45.8 ± 2.8	41.2 ± 1.1	<0.01

**Caption 1**

Table 1 shows mean +/- standard deviation for demographics, global strain, T1 and T2 values acquired by cMRF and traditional methods.

**Figure/Table 2**

Peak strain (%)	cMRF T1	cMRF T2	MOLLI T1	FLASH T2
Circumferential (short axis)	0.37	0.61*	0.42	0.51
Radial (short axis)	-0.38	-0.59*	-0.42	-0.49
Radial (long axis)	-0.57	-0.62*	-0.62*	-0.62*
Longitudinal (long axis)	0.66*	0.64*	0.70*	0.73*

## Caption 2

Table 2 shows Spearmans correlation coefficients ( $\rho$ ) for T1 and T2 mapping and global strain. Values with \* are statistically significant at  $p < 0.05$ .

Speaker: J. Cohen

Category: Amyloidosis , Tissue Characterization, Tissue Tracking

000522

## Association of high left ventricular ejection fraction with incident heart failure and cardiovascular mortality: the Framingham Heart Study

M. Chuang \* (1); P. Gona, (2); S. Qazi, (3); C. Salton, (4); G. Chi, (5); G. Mokwatsi, (6); C. Tsao, (7); C. O'donnell, (8); W. Manning (4)

(1) Cardiovascular imaging core laboratory, Beth Israel Deaconess Medical Center, Boston, United States of America; (2) Exercise and health sciences, University of Massachusetts Boston, Boston, United States of America; (3) Cardiovascular medicine, Brigham and Women's Hospital, Boston, United States of America; (4) Cardiovascular medicine, Beth Israel Deaconess Medical Center, Boston, United States of America; (5) Perfuse core laboratory, Beth Israel Deaconess Medical Center, Boston, United States of America; (6) Physiology, nutrition and consumer sciences, North West University - Potchefstroom Campus, Potchefstroom, South Africa; (7) Cardiology, Beth Israel Deaconess Medical Center (BIDMC), Boston, United States of America; (8) Cardiovascular medicine, West Roxbury VA Medical Center, Boston, United States of America

### Abstract

**Background:** Low left ventricular ejection fraction (LVEF) is associated with increased risk of adverse outcomes. High EF is less well studied, but two prior studies have shown greater risk of adverse outcomes among only women with high EF and known or suspected coronary heart disease. We aimed to identify prevalence and determinants of high EF in a longitudinally followed community-dwelling cohort and assess the impact of high EF on event-free survival.

**Methods:** 1794 (53% women) participants of the Framingham Offspring cohort aged 65±9y underwent SSFP CMR at 1.5T during 2002-2006. LV volumes, mass (LVM), EF and concentricity (CONC=LVM/end-diastolic volume) were determined after manual delineation of LV borders. Clinical characteristics and interim history were collected at the adjacent Cycle 7 clinic visit (1998-2001) and followed to the present. A healthy referent subset (no hypertension, diabetes, smoking, or history of cardiovascular disease, CVD) was used to determine sex-specific upper 90th percentile cutpoints (P90) for high EF and for CONC. Multivariable-adjusted (MV) logistic regression analysis was used to determine factors associated with high EF. Cox proportional hazards regression models were used to assess event-free survival for the composite of heart failure (HF) and CVD death.

**Results:** P90 cutpoints for high EF were 72.5% (men) and 75.1% (women). Prevalence of high EF was 16.0% (men) and 14.7% (women). High EF was associated with increasing age (Odds Ratio, OR=1.44/10y, 95% CI 1.23 – 1.68), hypertension (OR=1.91, CI 1.43 – 2.56) and P90 CONC (OR=3.92, CI 2.82 – 5.46). Over median 13.2 years of follow up there were 85 incident HF and CVD death events. In MV-adjusted Cox models accounting for age, sex, hypertension, smoking, diabetes, and LVM indexed to body-surface area (BSA), occurrence of the composite outcome was associated with greater age (hazard ratio, HR=2.80/10y, CI 2.13 – 3.67), LVM/BSA (HR=1.21 per 5g/m<sup>2</sup>, CI 1.10 – 1.32) and high EF (HR=1.81, CI 1.12 – 2.92).

**Conclusions:** High LVEF (>90th percentile) was associated with greater hazard of incident heart failure and death, after adjustment for traditional CVD risk factors and LVM, in a community-dwelling cohort of adults. Factors associated with high EF were greater age, hypertension, and concentric LV geometry. This work extends previous findings in women with excess burden of coronary disease to a cohort of both sexes including participants initially free of CVD.

Speaker: M. Chuang

Category: Ejection Fraction, Outcomes, Population Study



000523

## Abnormalities in Myocardial Contractility, Left Ventricular Strain and Myocardial Tissue Characteristics in Patients with Type 2 Diabetes and no known heart failure

A. Naumova \* (1); N. Balu, (1); B. Chu, (1); X.-Q. Zhao, (2); K. Ordovas (2)

(1) Radiology, University of Washington, Seattle, United States of America; (2) Medicine/cardiology, University of Washington, Seattle, United States of America

### Abstract

**Background.** Individuals with type-2 diabetes have increased risks of heart failure and mortality [1]. Those complications may affect the treatment outcome. Therefore, close monitoring of cardiac symptoms and early detection of cardiac disease by noninvasive imaging methods is desired. Cardiac magnetic resonance (CMR) imaging is a non-invasive technique that can evaluate cardiac morphology, regional contractile function, and myocardial tissue characteristics. The current study aims to describe the ranges of left ventricular volumetric and functional parameters, including strain imaging, and myocardial tissue characteristics in type-2 diabetic patients without known heart disease using quantitative CMR.

**Methods.** 57 patients with type-2 diabetes at least 5 years after diagnosis without clinical heart failure had a cardiac magnetic resonance (CMR) imaging examination at a 3T scanner (Ingenia, Phillips®). CMR protocol included steady state free precession (SSFP) cine imaging to assess left ventricular (LV) morphology and function, T1 mapping (native and post-contrast), T2-mapping, and T2\*-mapping. Volumetric LV analysis and analysis of quantitative maps (T1, T2, T2\*) were performed using Philips IntelliSpace Portal (ISP) software. Extracellular Volume (ECV) maps were generated offline using MATLAB software. Feature tracking was performed using Circle Cardiovascular Software (cvi-42) to measure myocardial strain and strain rate from the SSFP short axis and long axis images. Volumetric parameters are reported as indexes, after adjustment for body surface area. Variables are compared to normal age specific ranges reported in the literature. Association between CMR volumetric and parametric parameters were investigated using correlation coefficient.

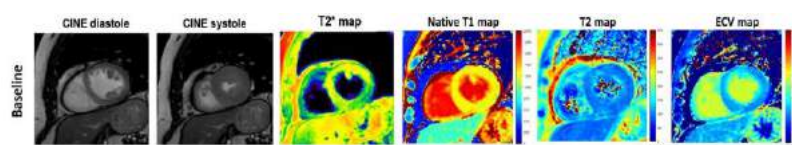
**Results.** Mean age of the patients was  $64 \pm 9$  years; mean BMI  $30 \pm 5$  (88% overweight,  $\text{BMI} \geq 25$ ); 61% males. Global parameters of cardiac function are shown in the Table 1. Type 2 diabetic patients showed lower stroke volume, lower ejection fraction, and lower end-diastolic volume index (EDVi) when compared normal ranges. However, volumetric parameters and ejection fraction were still within normal ranges. Evaluation of regional LV contractility using feature tracking tools revealed decreased left ventricular myocardial strain in the hearts of diabetic patients compared to age and gender specific normal ranges (Table 2). Most notably, radial strain at the mid-ventricular level was  $25.0 \pm 7.6$  %, while literature reports for  $39 \pm 8$  % [1]. Circumferential strain in the mid-ventricular level in diabetic patients was  $-16.0 \pm 2.9$  %, which is also lower than normal ranges ( $-21.44 \pm 2.74$ %).

Quantitative CMR techniques revealed changes in myocardial tissue composition of the left ventricle; specifically, increased T1 and ECV values were seen in comparison with normal scanner specific local data, which can indicate early interstitial fibrosis. Representative

examples of CMR images and parametric mappings are shown in Figure 1. Finally, analysis of association between cardiac functional parameters and biomarkers of tissue characteristics showed that ECV was inversely correlated with cardiac index ( $\rho = -0.7$ ,  $p = 0.024$ ).

**Conclusion.** The current study revealed abnormalities of regional strain and interstitial fibrosis parameters in type 2 diabetes patients without known heart failure and with left ventricular ejection fraction within the lower range of normal. Continuous monitoring of the cardiac changes using CMR techniques may be helpful for early detection of cardiac dysfunction in these patients.

**Figure/Table 1**



**Caption 1**

**Figure 1.** Representative CMR and quantitative maps of type 2 diabetic patient. In the shown example, myocardial T2\* was 26.9 ms; native T1 1241 ms, T2 47.68 ms; ECV 29.22%.

**Figure/Table 2**

CMR measurement	Type 2 diabetic patients	Healthy patients *
ESVi, ml/m <sup>2</sup>	25.8 ± 6.9	26 ± 6
EDVi, ml/m <sup>2</sup>	57.4 ± 12.3	81 ± 12
SV, ml	65.3 ± 12.9	78.1 ± 12.0
EF, %	55.0 ± 5.0	64 ± 6
Cardiac index, L/(min×m <sup>2</sup> )	2.2 ± 0.5	3.3 ± 0.6
LVmassi, g/m <sup>2</sup>	41.8 ± 11.5	67 ± 9
T1, ms	1247 ± 46	1122 ± 57
T2, ms	49.9 ± 3.9	52 ± 6
T2*, ms	25.9 ± 4.6	24 ± 5
ECV, %	28.0 ± 2.6	26.6 ± 3.2

CMR measurement	Type 2 diabetic patients	Healthy patients *
ESVi, ml/m <sup>2</sup>	25.8 ± 6.9	26 ± 6
EDVi, ml/m <sup>2</sup>	57.4 ± 12.3	81 ± 12
SV, ml	65.3 ± 12.9	78.1 ± 12.0
EF, %	55.0 ± 5.0	64 ± 6
Cardiac index, L/(min×m <sup>2</sup> )	2.2 ± 0.5	3.3 ± 0.6
LVmassi, g/m <sup>2</sup>	41.8 ± 11.5	67 ± 9
T1, ms	1247 ± 46	1122 ± 57
T2, ms	49.9 ± 3.9	52 ± 6
T2*, ms	25.9 ± 4.6	24 ± 5
ECV, %	28.0 ± 2.6	26.6 ± 3.2

**Caption 2**

**Table 1.** Heart contractility and tissue relaxation properties in type 2 diabetic patients (n=57). Data is shown as mean  $\pm$  standard deviation. \*CMR normal ranges data from the literature [1, 2, 3].

**Figure 3**

Radial	Strain, %	Strain rate, 1/s
Basal	42.5 $\pm$ 15.4	2.1 $\pm$ 0.7
Mid	25.0 $\pm$ 7.6	1.5 $\pm$ 0.5
Apical	26.1 $\pm$ 10.0	1.7 $\pm$ 1.2
Circumferential		
Basal	-15.2 $\pm$ 3.5	-0.9 $\pm$ 0.3
Mid	-16.0 $\pm$ 2.9	-0.9 $\pm$ 0.4
Apical	-19.1 $\pm$ 3.9	-0.8 $\pm$ 0.9
Longitudinal		
Basal	-8.4 $\pm$ 7.5	-0.5 $\pm$ 0.6
Mid	-9.2 $\pm$ 6.1	-0.5 $\pm$ 0.6
Apical	-14.3 $\pm$ 3.3	-0.8 $\pm$ 0.3

**Caption 3**

**Table 2.** CMR feature tracking results reflecting myocardial strain and strain rate in the basal, mid-ventricular and apical levels of the left ventricle in type 2 diabetic patients (n=57). Data is shown as mean  $\pm$  standard deviation.

### Bibliographic References

[3] Kawel-Boehm et al. Normal values for cardiovascular magnetic resonance in adults and children. JCMR, 2015, 17, article number 29., [2] Roy et al. Age and sex corrected normal reference values of T1, T2 T2\* and ECV in healthy subjects at 3T CMR. JCMR 2017, 19:72., [1] Li et al. The additive effects of type 2 diabetes mellitus on left ventricular deformation and myocardial perfusion in essential hypertension: a 3.0 T cardiac magnetic resonance study. Cardiovasc Diabetol, 2020, 19:161.

Speaker: A. Naumova

Category: Cardiac Function, Parametric Mapping, Strain

000524

## High-resolution Spiral First-pass Myocardial Perfusion Imaging using DEep learning-based rapid Spiral Image REconstruction (DESIRE) at 1.5 T

J. Wang \* (1); P. Rodriguez Lozano (2); M. Salerno (3)

(1) Biomedical Engineering, University of Virginia, Charlottesville, United States of America;  
(2) Medicine, University of Virginia, Charlottesville, United States of America; (3)  
Cardiology, radiology, and medical imaging, University of Virginia, Charlottesville, United States of America

### Abstract

**Background** First-pass contrast-enhanced myocardial perfusion imaging is valuable for evaluating coronary artery disease (CAD)[1]. Recently, we have developed spiral single-slice (SS) and motion-compensated L1-SPiRiT reconstruction capable of whole-heart high-resolution perfusion imaging[2]. However, this compressed-sensing (CS) based reconstruction is time-consuming and takes ~25 minutes per slice location. Hence, it can't provide immediate feedback to doctors and impedes clinical translation. 1.5 T has been the dominant field strength for CMR imaging with better  $B_0$  and  $B_1$  homogeneity than at 3T. Here, we sought to develop high-resolution spiral perfusion imaging at 1.5 T with a DEep learning-based Spiral Image REconstruction technique (DESIRE), to provide fast and high-quality image reconstruction (Figure 1-A).

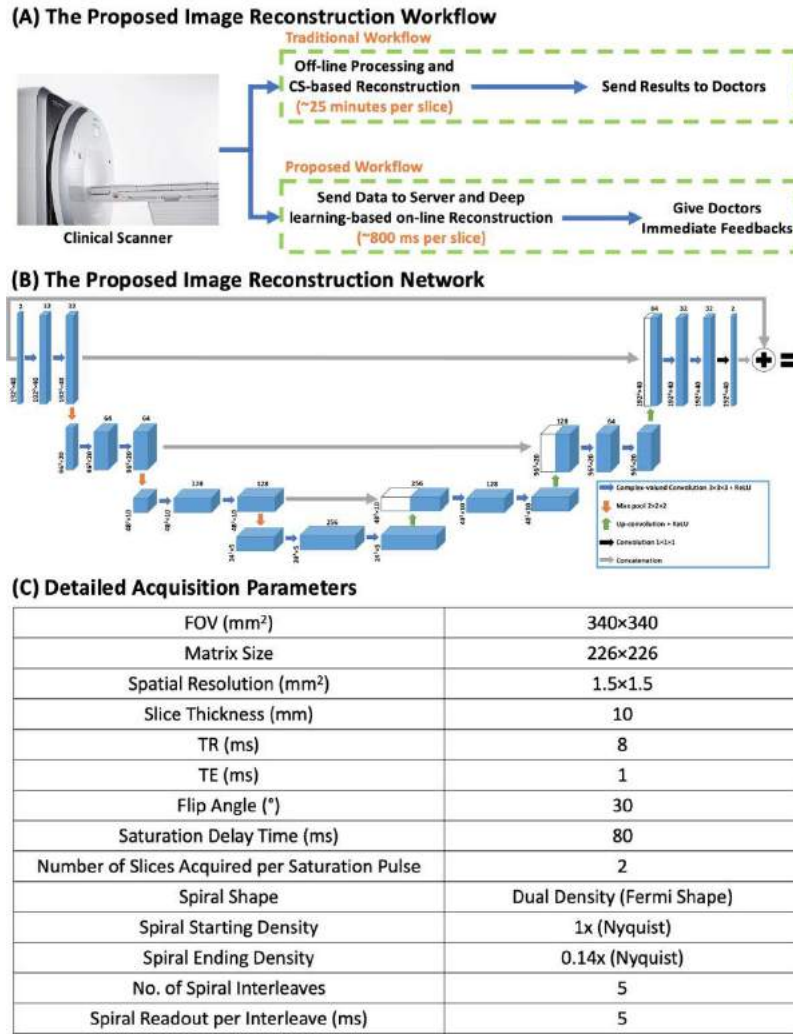
**Methods** Figure 1-B illustrates the proposed 3D U-Net[3] based reconstruction network. The inputs to the network are concatenated complex-valued image series from a single slice location with coil-selection[4], motion-correction[4], and adaptive phase combination[5] of the NUFFT-gridded multi-coil image sets. The outputs are concatenated perfusion image series. The training and validation data were SS golden-angle spiral perfusion data with whole-heart coverage acquired from 18 healthy volunteers and 4 patients undergoing clinical studies at 3T SIEMENS Skyra/Prisma scanners[2]. The reference images were L1-SPiRiT. 156 slices from 20 subjects were used for training, and another 14 slices from 2 subjects were used for validation. The training was conducted using PyTorch on four NVIDIA Tesla P100 GPUs with 150 epochs using an L1 loss.

Prospective SS high-resolution perfusion images with whole-heart coverage at 1.5 T were acquired from 5 patients undergoing clinically ordered CMR studies with gadolinium at 1.5 T SIEMENS Aera scanner. The perfusion image series were reconstructed using both CS-based method (L1-SENSE) and the proposed DESIRE technique. The image quality for both reconstructions were graded on a 5-point scale (5 excellent, 1 poor) by an experienced cardiologist.

**Results** Good image quality was demonstrated with the proposed DESIRE technique. Image quality scores were  $4.6 \pm 0.5$  and  $4.4 \pm 0.5$  for L1-SENSE and DESIRE, respectively. Figure 2 and 3 show example cases from patients. Excellent image quality was demonstrated with a score of 5 and 5 for L1-SENSE and DESIRE, respectively. The reconstruction time was ~800 ms per slice on a NVIDIA Tesla P100 GPU, while the reconstruction time of L1-SENSE was ~25 minutes on an Intel Xeon CPU (2.40 GHz).

**Conclusion** The proposed image reconstruction network (DESIRE) enabled rapid and high-quality image reconstruction for whole-heart high-resolution first-pass spiral perfusion imaging at 1.5 T.

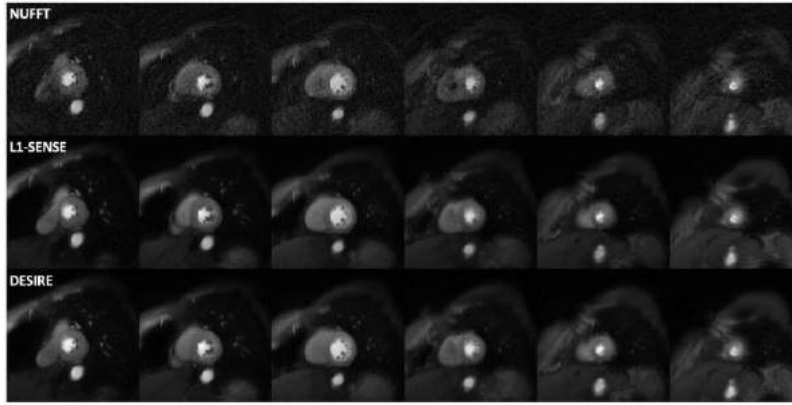
### Figure/Table 1



### Caption 1

Figure 1. The proposed deep learning-based image reconstruction workflow and the proposed 3D U-Net based image reconstruction network for spiral first-pass perfusion imaging. In (B), the numbers above each layer denote the number of kernels at each layer, and the corresponding image shape at each layer is also labelled. (C) shows the detailed acquisition parameters for high-resolution spiral perfusion imaging at 1.5 T.

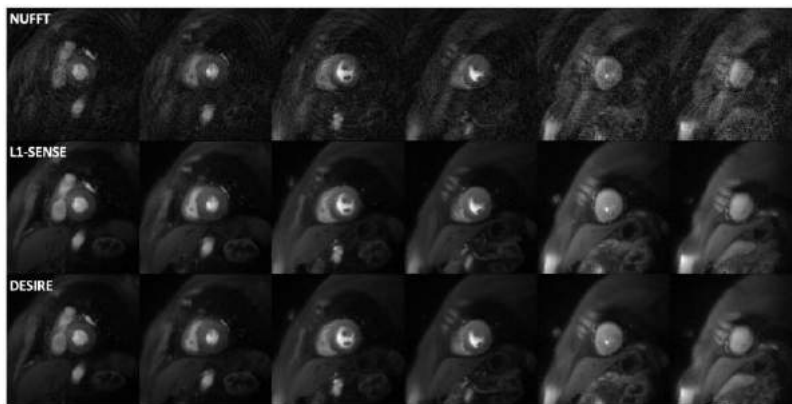
### Figure/Table 2



**Caption 2**

Figure 2. Prospective spiral perfusion images from a patient with 6 slices reconstructed using L1-SENSE and the proposed DESIRE image reconstruction network. Excellent image quality was demonstrated using the proposed image reconstruction network. This case reconstructed using L1-SENSE and DESIRE had a score of 5 and 5 (5 excellent, 1 poor), respectively.

**Figure 3**



**Caption 3**

Figure 3. Prospective spiral perfusion images from a healthy volunteer with 6 slices reconstructed with L1-SENSE and the proposed DESIRE technique. Excellent image quality was demonstrated using the proposed image reconstruction network with a score of 5 and 5 for L1-SENSE and DESIRE (5 excellent, 1 poor), respectively.

## **Bibliographic References**

1. Salerno M, Beller GA. Noninvasive Assessment of Myocardial Perfusion. *Circ Cardiovasc Imaging* 2009;2:412–424.
2. Wang J, Yang Y, Weller DS, et al. High spatial resolution spiral first-pass myocardial perfusion imaging with whole-heart coverage at 3 T. *Magnetic Resonance in Medicine* 2021;86:648–662.
3. Ronneberger O, Fischer P, Brox T. U-Net: Convolutional Networks for Biomedical Image Segmentation. *arXiv:1505.04597 [cs]* 2015.
4. Zhou R, Yang Y, Mathew RC, et al. Free-breathing cine imaging with motion-corrected reconstruction at 3T using SPiral Acquisition with Respiratory correction and Cardiac Self-gating (SPARCS). *Magnetic Resonance in Medicine* 2019;82:706–720.
5. Walsh DO, Gmitro AF, Marcellin MW. Adaptive reconstruction of phased array MR imagery. *Magnetic Resonance in Medicine* 2000;43:682–690.

Speaker: J. Wang

Category: Perfusion, Spiral, Rapid Imaging

000526

## Sex Differences in Cardiac Remodeling in Patients with Ischemic Cardiomyopathy- Impact on Survival

D. Kocyigit \* (1); N. Ho, (1); N. A. Obuchowski, (2); R. Vajapey, (3); Z. Popovic, (1); B. Griffin, (1); S. Flamm (1); W. H. W. Tang, (3); D. Kwon, (1)

(1) Section of cardiovascular imaging, Cleveland Clinic Main Campus, Cleveland, United States of America; (2) Department of quantitative health sciences, Lerner Research Institute, Cleveland Clinic, Cleveland, United States of America; (3) Cardiovascular medicine, Cleveland Clinic Main Campus, Cleveland, United States of America

### Abstract

**BACKGROUND:** There is scarce evidence regarding sex differences in the prognosis of patients with ischemic mitral regurgitation (IMR). Due to emerging diagnostic and prognostic utility of cardiac magnetic resonance imaging (CMR) in IMR, and known limitations of echocardiography (ECHO) in the assessment of secondary MR, we aimed to test the interactions of sex with cardiac remodeling and degree of IMR assessed using CMR as predictors of all-cause mortality, after adjusting for other risk factors.

**METHODS:** Consecutive ischemic cardiomyopathy (ICM) patients who were referred to CMR between 2002-2017 were reviewed. Cardiac structural remodeling and functions, mitral valve geometry and IMR severity (mitral regurgitant fraction [RF]), were assessed on CMR. Primary clinical endpoint was defined as all-cause mortality. Cox proportional hazards regression models were constructed to test to determine independent predictors all-cause mortality. The 2-way interactions of female sex with RF, indexed left ventricular and right ventricular end-diastolic volume (LVEDVi and RVEDVi), late gadolinium enhancement (LGE), mitral valve (MV) coaptation depth, and implantable cardioverter-defibrillator (ICD) were then tested to determine whether the effect of female sex on patient outcome was mediated by these other variables.

**RESULTS:** A total of 790 patients were evaluated ( $62.0 \pm 11.2$  years, 24.7% females). Prevalence of coronary artery disease risk factors, received medications, and previous coronary revascularization were similar when compared between females and males (all  $p > 0.05$ ). Over a mean follow-up of 4.6 years ( $\pm 4.8$ ), 373 deaths occurred. 387 patients underwent coronary artery bypass grafting (CABG), and 154 underwent surgical MV repair/replacement. Although female sex was associated with lower risk of all-cause mortality after adjusting for medical risk factors and treatment (HR: 0.35, 95% CI: 0.17-0.70,  $p = 0.001$ ), females with larger CMR derived LVEDVi had increased risk of all-cause mortality ( $p$  interaction=0.023) (**Table 1**). Risk of mortality was higher in females compared to males when LVEDVi was  $> 250$  mL/m<sup>2</sup> (**Figure 1**). Marginally significant interactions between RF and female sex ( $p = 0.055$ ) and ICD and female sex ( $p = 0.057$ ) also existed. Females experienced a higher mortality rate compared to males when RF increased  $> 40\%$  in the setting of normal LV size (LVEDVi 100 mL/m<sup>2</sup>) (**Figure 1**).



**CONCLUSIONS:** Our large single-center study of patients with ICM with comprehensive CMR assessment has shown that discerning sex differences in survival is complex and depends on the degree of cardiac remodeling and severity of IMR. Our findings, therefore, suggest the importance of deriving sex specific CMR selection criteria for optimal therapeutic management.

**Figure/Table 1**

<b>Independent Variables</b>	<b>Estimated HR [95% Confidence Interval]</b>	<b>p value</b>
<b>Medical risk score <math>\alpha</math></b>	2.35 [1.93, 2.85]	<0.001*
<b>LGE%</b>	1.01 [1.01, 1.02]	<0.001*
<b>Implantable cardioverter-defibrillator</b>	0.75 [0.56, 1.00]	0.054
<b>Cardiac resynchronization therapy</b>	1.20 [0.83, 1.74]	0.340
<b>Pre-CMR coronary artery bypass grafting / percutaneous coronary intervention</b>	1.08 [0.87, 1.34]	0.482
<b>Female sex</b>	0.35 [0.17, 0.70]	0.001*
<b>LVEDVi, mL/m<sup>2</sup></b>	0.99 [0.99, 1.00]	0.530
<b>Mitral RF, %</b>	1.00 [0.99, 1.01]	0.297
<b>Mitral valve coaptation depth</b>	0.30 [0.10, 0.91]	0.033*
<b>Treatment: Revascularization</b>	1.19 [0.94, 1.50]	0.144
<b>Incomplete revascularization</b>	1.59 [1.26, 2.00]	<0.001*
<b>ICD x Female sex</b>	0.58 [0.33, 1.02]	0.057
<b>Mitral RF x Female sex</b>	1.01 [1.00, 1.03]	0.055
<b>LVEDVi x Female sex</b>	1.01 [1.00, 1.01]	0.023*

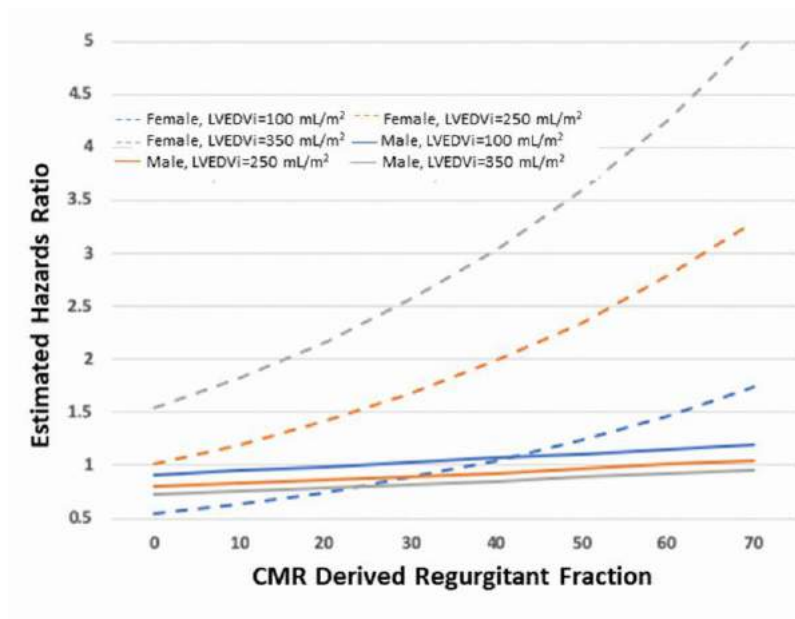
**Caption 1**

**Table 1. Final Multivariable Model for Predicting All-Cause Mortality.**

\* a p value < 0.05 demonstrates statistical significance.

$\alpha$  The variables in the medical risk score model were age, sex, body mass index, diabetes, glomerular filtration rate, hypertension, dyslipidemia, medications (beta-blocker, angiotensin converting enzyme inhibitor/receptor blocker), and an interaction term for sex and diabetes.

**Figure/Table 2**



**Caption 2**

**Figure 1. Model-based estimated hazard ratios for all-cause mortality in females vs. males.** As a function of LVEDVi and severity of mitral regurgitation measured by CMR derived mitral regurgitant fraction.

Speaker: D. Kocyigit

Category: Ischemic Cardiomyopathy, Mitral Regurgitation, Prognosis

000527

## Quality control-driven artificial intelligence for reliable automatic segmentation of LGE images in clinical practice

R. A. Gonzales \* (1); Q. Zhang (1); E. Hann (1); V. Ferreira (1); S. Piechnik (1)

(1) Radcliffe department of medicine, University of Oxford, Oxford, United Kingdom

### Abstract

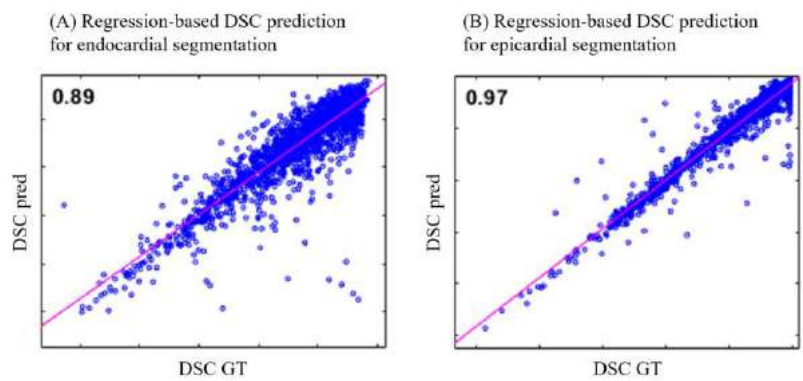
**Background:** Late gadolinium enhancement (LGE) cardiovascular magnetic resonance (CMR) imaging is well-validated for detecting focal myocardial lesions and fibrosis in a variety of cardiovascular diseases. Its analysis requires segmentation of the left ventricular (LV) myocardium, which involves manual contouring or usage of recent automated segmentation methods [1]. However, any unflagged segmentation deficiencies may result in inaccurate scar quantification or misdiagnoses. It is desirable to develop automated LGE segmentation that includes a quality control framework to ensure accuracy, in the absence of a ground truth reference, for reliable automation in clinical practice.

**Methods:** We implemented a quality control-driven (QCD) framework [2] to segment the LV myocardium on LGE images, which provides an inherent mechanism for predicting segmentation accuracy measured by Dice Similarity Coefficient (DSC). Imaging data of 326 hypertrophic cardiomyopathy patients from the multicentre Hypertrophic Cardiomyopathy Registry [3], with manual contours as the ground truth, were used for training with 15% of the data preserved for testing. LGE data was augmented three-fold by generating virtual native enhancement (VNE) images [4] for each subject using ShMOLLI T1-maps and short-axis cines. In short, the deep neural network ensemble comprises of 12 candidate segmentation models including 6 different U-Nets [5] independently trained and 6 combinational models obtained via a label voting scheme. The quality control component involves a multiple linear regression model for each of the 12 candidate segmentation models. The segmentation with the highest predicted DSC is chosen on-the-fly for each LGE image. The accuracy of each selected segmentation was compared against the manual contours measured by DSC and the quality prediction accuracy by the mean absolute error (MAE).

**Results:** The QCD framework successfully and rapidly (<1 second per T1-map) segmented the LV myocardium on LGE images with excellent contouring agreement with human analysts on both endocardium (DSC = 0.94, MAE = 0.04) and epicardium (DSC = 0.96, MAE = 0.03). The scatter plots (Figure 1) reflect the parity between the ground-truth DSC and the predicted DSC. With the resultant endocardial and epicardial contours, the LV myocardium masks can be derived by subtracting the endocardial masks from the epicardial masks (Figure 2).

**Conclusion:** The presented quality control-driven framework is an effective and robust deep neural network ensemble for LV myocardial segmentation on LGE images. It can improve the reliability of automated methods for immediate clinical interpretation.

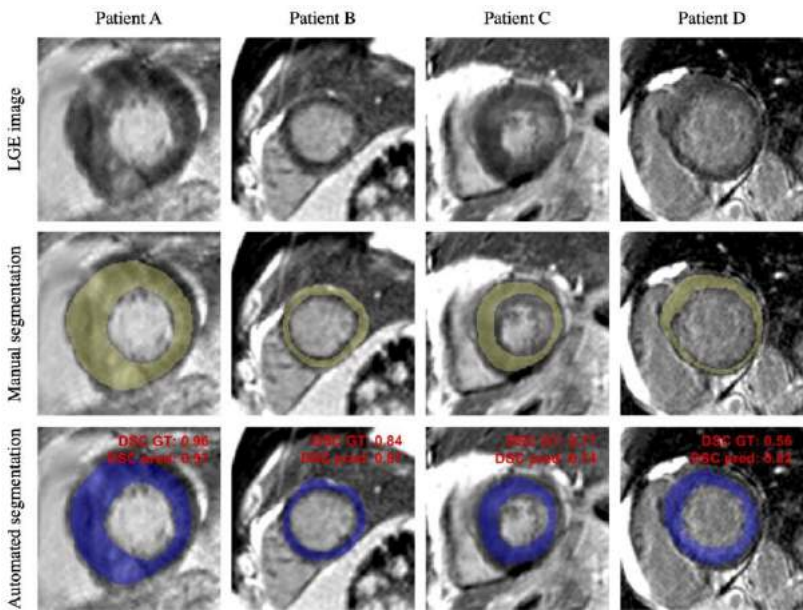
**Figure/Table 1**



**Caption 1**

Scatter plots of the observed ground-truth (GT) Dice similarity coefficient (DSC) (x-axis) versus the regression-based predicted DSC (y-axis) for (A) the endocardium and (B) the epicardium on late gadolinium enhanced images, with shown correlation values.

**Figure/Table 2**



**Caption 2**

4 examples of manual left ventricular myocardial segmentations (in yellow) and derived automated segmentations (in blue), with the corresponding observed ground-truth (GT) Dice similarity coefficient (DSC) and regression-based predicted DSC.

### **Bibliographic References**

[1] Zhuang, X., et al., Cardiac segmentation on late gadolinium enhancement MRI: a benchmark study from multi-sequence cardiac MR segmentation challenge. arXiv preprint arXiv:2006.12434, 2020., [2] Hann, E., et al., Deep neural network ensemble for on-the-fly quality control-driven segmentation of cardiac MRI T1 mapping. Medical Image Analysis, 2021. 71: p. 102029., [3] Kramer, C.M., et al., Hypertrophic Cardiomyopathy Registry: The rationale and design of an international, observational study of hypertrophic cardiomyopathy. American Heart Journal, 2015. 170(2): p. 223-230., [5] Ronneberger, O., P. Fischer, and T. Brox, U-Net: Convolutional Networks for Biomedical Image Segmentation. 2015, Springer International Publishing. p. 234-241., [4] Zhang, Q., et al., Toward Replacing Late Gadolinium Enhancement With Artificial Intelligence Virtual Native Enhancement for Gadolinium-Free Cardiovascular Magnetic Resonance Tissue Characterization in Hypertrophic Cardiomyopathy. Circulation, 2021. 144(8): p. 589-599.

Speaker: R. A. Gonzales

Category: Segmentation, Late Gadolinium Enhancement, Image Analysis

000528

## Myocardial Strain Decline is Associated with Extent of Late Gadolinium Enhancement in Duchenne Muscular Dystrophy by Cardiac Magnetic Resonance Imaging

S. Lee \* (1); M. Lee, (1); J. Williams, (1); K. Hor, (1)

(1) Pediatric cardiology, Nationwide Children's Hospital, Columbus, United States of America

### Abstract

**Background:** Duchenne muscular dystrophy (DMD) is characterized by progressive cardiac dysfunction and early global circumferential strain (GCS) abnormalities. LGE precedes left ventricular dysfunction (LVD) and is associated with lower left ventricular ejection fraction (LVEF)<sup>1,2,3</sup>. However, within the LGE group there continues to be heterogeneity in LVEF, which ranges from normal to severely depressed suggesting better understanding of the extent of LGE will help inform LV function. Therefore, we sought to determine the relationship of LGE, LVEF and myocardial strain to generate a MyoHealth Score based on the technique reported by Korosoglou et al<sup>4</sup>.

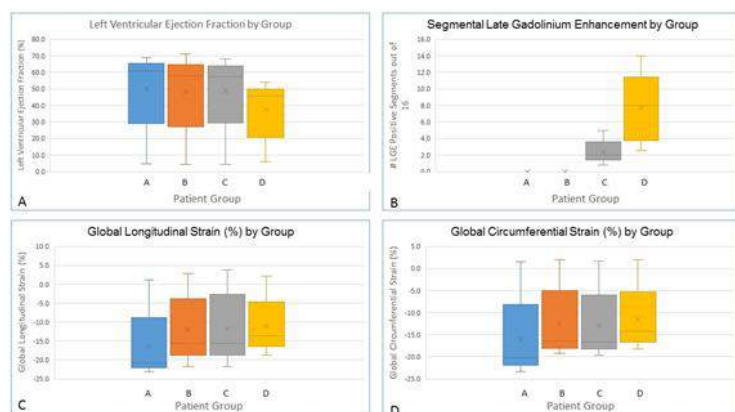
**Methods:** Retrospective review of DMD patients who underwent CMR evaluation from 9/2019 to 3/2021. All studies performed on 3.0T Siemens Skyra (Siemens Healthineers, Germany). We utilized SENC imaging to assess global longitudinal (GLS) and circumferential strain (GCS) using MyoStrain (Myocardial Solutions, Morrisville, NC) generating 37 total segments from 3 short and long axis images. LGE was assessed in segments according to the AHA modified 16 segment model as positive or negative. A healthy control group (Group A) was used to compare LVEF and strain by SENC. DMD patients were categorized into Group B = LGE negative, Group C = LGE positive with LVEF  $\geq 55\%$  and Group D = LGE positive with LVEF  $< 55\%$ . Reduced strain was defined as absolute magnitude  $< 17\%$ , and  $< 10\%$  was considered dysfunctional, statistical significance set at  $p < 0.05$  between groups.

**Results:** 49 DMD patients met inclusion criteria (Group B = 19, Group C = 13 and Group D = 17) along with 18 control subjects. Demographic data and CMR data including LGE, LVEF, GLS, GCS and regional strain are provided in Table 1. All DMD groups had abnormal GLS and GCS compared to control (Table 1). DMD Group B had no LGE, with significantly more positive segments in Group D ( $8.9 \pm 5.9$ , range 8-14) than in Group C ( $2.2 \pm 0.5$ , range 2-5). DMD Groups B and C had no difference in LVEF, GLS or GCS magnitude. Group C, however, had significantly lower LVEF, GLS, and GCS magnitude than either group (Table 1 and Figure 1A-D). Segmentally all DMD groups had more segments with reduced strain (magnitude  $< 17\%$  and  $10\%$ ) than Group A and consequently lower MyoHealth Score. Within the DMD groups there was no difference between Group B and C for segmental strain using magnitude of less than 17 or 10 with similar MyoHealth Score. On the other hand, Group D subjects had more segments with strain below magnitude of 17 or 10 and had a lower MyoHealth Score than either group (Figure 2A-C and Table 1).

**Conclusion:** LGE positive subjects have evidence of more advanced disease. However, the mere presence of LGE does not predict worse function by LVEF or strain. Our data shows that more segmental strain abnormalities ( $> 8$  segments) is associated with lower LVEF.

Together, LGE and strain are precursors to LVD and we show for the first time an association with lower MyoHealth Score in this group. Given the small number of subjects in our study we were not able to perform multi-variate analysis. Future large, longitudinal studies are needed to further understand the extent of injury by LGE and Strain needed to result in overt LVD.

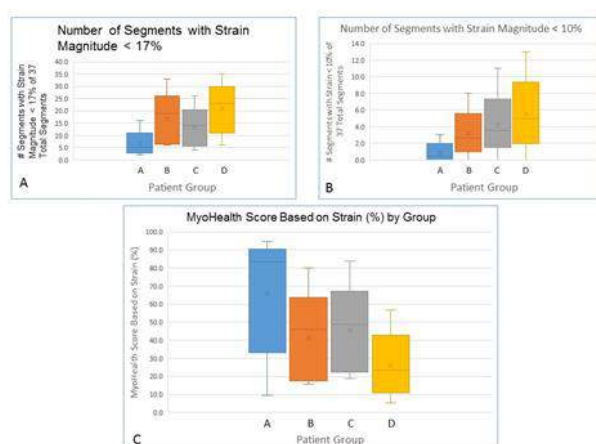
**Figure/Table 1**



**Caption 1**

Figure 1A-D: Left Ventricular Ejection Fraction, Late Gadolinium Enhancement and Global Longitudinal Strain. (A) LVEF normal in all except for Group D. (B) Increasing number of positive LGE segments. (C and D) GLS and GCS worse in all DMD groups vs. controls with incremental decline in Group D with higher number of positive LGE segments.

**Figure/Table 2**



**Caption 2**

Figure 2A-C: Segmental Strain and MyoHealth Score. (A) More abnormal strain segments with magnitude <17% common in DMD groups, particularly Group D. (B) Similar findings in segmental strain magnitude < 10, worst in Group D. (C) MyoHealth Score lower in all DMD Groups with no difference in Groups B or C but incremental decrease in Group D.

**Figure 3**

Demographic/Groups	Control (A)	Group B	Group C	Group D
Number of Subjects	N = 18	N = 19	N = 13	N = 17
Age, years (mean ± SD)	19.3±1.1	13.5±3.6 *p < 0.0001	14.2±5.8 *p < 0.001 **p = ns	16.6±4.2 *p<0.01 **p = 0.01 *** p=ns
LVEF (%)	61.5±4.7	58.1±4.4 *p < 0.02	59.8±4.4 *p = ns	45.5±5.9 *p<0.0001 ** p<0.0001 *** p<0.0001
Number of Positive LGE Segments (mean ± SD, Range)	0	0	2.2±0.8 (2-5)	8.9±2.6 (5-14)
Left Ventricular GLS (%)	-21.0±1.1	-15.6±2.8	-16.0±3.8	-14.1±2.1 *p<0.0001 ** p=0.02 *** p = 0.4
Left Ventricular GCS (%)	-20.2±1.5	-16.4±2	-16.6±1.7	-15.0±1.9 *p<0.0001 ** p < 0.01 *** p = 0.01
# Strain Segments > -17 out of 35	6.1±3.5	19.3±6.6	14.9±7.1	24.9±6
# Strain Segments > -10 out of 35	0.4±0.9	3.1±2.6	3.6±3.6	5.7±3.9
MyoHealth Score (%)	83.6±9.6	46.0±15.8	50.4±18.8	29.0±16.3



				*p<0.0001
				** p < 0.01
				*** p < 0.01

### Caption 3

Table 1: CMR Findings in DMD Patients by Groups Based on LGE Status

\*Significance Compared to control (Group A), \*\*Significance compared to DMD Group B, \*\*\*Significance compared to DMD Group C.

### Bibliographic References

Korosoglou G, Giusca S, Montenbruck M, Patel AR, Lapinskas T, Gotze C, Zieschang V, Al-Tabatabaee S, Pieske B, Florian A, Erley J, Katus HA, Kelle S and Steen H. Fast Strain-Encoded Cardiac Magnetic Resonance for Diagnostic Classification and Risk Stratification of Heart Failure Patients. JACC Cardiovasc Imaging. 2021;14:1177-1188., Tandon A, Villa CR, Hor KN, Jefferies JL, Gao Z, Towbin JA, Wong BL, Mazur W, Fleck RJ, Sticka JJ, Benson DW and Taylor MD. Myocardial fibrosis burden predicts left ventricular ejection fraction and is associated with age and steroid treatment duration in duchenne muscular dystrophy. J Am Heart Assoc. 2015;4., Hor KN, Taylor MD, Al-Khalidi HR, Cripe LH, Raman SV, Jefferies JL, O'Donnell R, Benson DW and Mazur W. Prevalence and distribution of late gadolinium enhancement in a large population of patients with Duchenne muscular dystrophy: effect of age and left ventricular systolic function. J Cardiovasc Magn Reson. 2013;15:107., Hor KN, Wansapura J, Markham LW, Mazur W, Cripe LH, Fleck R, Benson DW and Gottliebson WM. Circumferential strain analysis identifies strata of cardiomyopathy in Duchenne muscular dystrophy: a cardiac magnetic resonance tagging study. J Am Coll Cardiol. 2009;53:1204-10. 2. Hor KN, Taylor MD, Al-Khalidi HR, Cripe LH, Raman SV, Jefferies JL, O'Donnell R, Benson DW and Mazur W. Prevalence and distribution of late gadolinium enhancement in a large population of patients with Duchenne muscular dystrophy: effect of age and left ventricular systolic function. J Cardiovasc Magn Reson. 2013;15:107. 3. Tandon A, Villa CR, Hor KN, Jefferies JL, Gao Z, Towbin JA, Wong BL, Mazur W, Fleck RJ, Sticka JJ, Benson DW and Taylor MD. Myocardial fibrosis burden predicts left ventricular ejection fraction and is associated with age and steroid treatment duration in duchenne muscular dystrophy. J Am Heart Assoc. 2015;4. 4. Korosoglou G, Giusca S, Montenbruck M, Patel AR, Lapinskas T, Gotze C, Zieschang V, Al-Tabatabaee S, Pieske B, Florian A, Erley J, Katus HA, Kelle S and Steen H. Fast Strain-Encoded Cardiac Magnetic Resonance for Diagnostic Classification and Risk Stratification of Heart Failure Patients. JACC Cardiovasc Imaging. 2021;14:1177-1188.

Speaker: S. Lee

Category: Cardiac Strain, Nonischemic Cardiomyopathy, Late Gadolinium Enhancement

000529

## Noninvasive pressure-volume loops from CMR: sensitivity to interobserver and intraobserver variability

P. Arvidsson \* (1); J. Edlund (1); A. Nelsson (1); G. J. Smith (2); M. Magnusson (3); E. Heiberg (1); K. Steding-Ehrenborg (1); H. Arheden (1)

(1) Clinical physiology, department of clinical sciences lund, Lund University, Skåne University Hospital, Lund, Sweden; (2) Cardiology, institution for clinical sciences, Lund University, Skåne University Hospital Lund, Lund, Sweden; (3) Cardiology, institution for clinical sciences malmö, Lund University, Skåne University Hospital Malmö, Malmö, Sweden

### Abstract

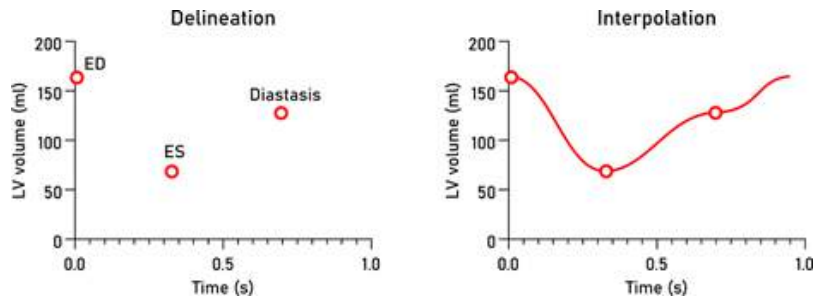
**Background.** Pressure-volume (PV) loop analysis enables detailed study of cardiac pumping, but requires invasive blood pressure measurements and is therefore rarely employed (3). To mitigate this, we have recently developed and validated a noninvasive method for computation of PV loops from short-axis cine images and a brachial blood pressure, enabling safe and detailed evaluation of hemodynamic parameters (1, 2). The established workflow assumes high-fidelity manual segmentation of the left ventricle, preventing clinical implementation and hampering research applications. Here we aimed to evaluate the sensitivity of noninvasive PV loops to intraobserver variability and manual vs. semiautomatic segmentation strategies, testing the hypothesis that PV loops can be rapidly and accurately computed using a simplified workflow.

**Methods.** We studied 12 subjects from a CMR image database of healthy volunteers and heart failure patients. In each dataset, the left ventricular endocardial border was segmented manually over the entire cardiac cycle by two observers with 10 and 2 years of experience in CMR research, respectively. Based on end-systolic and end-diastolic timeframes segmented by the more experienced observer, we also evaluated a spline interpolation approach (Fig. 1) with only minor manual corrections in the most basal slices. PV loops and derived metrics (stroke work, potential energy, ventricular efficiency, external power, and contractility) were computed using Segment 3.2 R9074 (Medviso, Lund, Sweden). Results were evaluated using Bland-Altman plots and Pearson correlation coefficients.

**Results.** Interpolated volume curves differed visually from manual delineations in diastole (Fig. 2). End-diastolic and end-systolic volumes differed on average 4.6 and 3.0 ml between observers. Interobserver analysis revealed very strong correlations ( $r > .96$ ,  $p < 0.0001$  for all measures) and low bias between manual delineations (Fig. 3). Interestingly, despite being visually dissimilar, the interpolation method produced lower bias and narrower limits of agreement compared to the interobserver study.

**Conclusions.** Noninvasive pressure-volume loops can be computed with acceptable accuracy and precision using only manually segmented end-diastolic and end-systolic timeframes as input, being more sensitive to absolute volumes than to specific myocardial motion patterns. This approach enables an approximate 15-fold increase in postprocessing speed, facilitating clinical and research implementation.

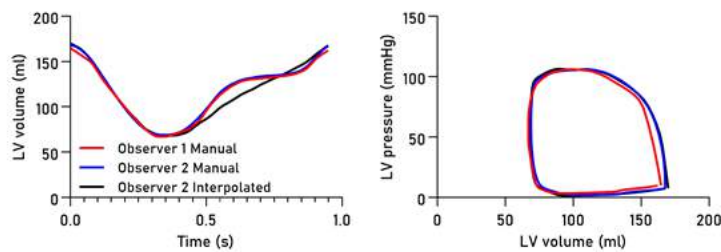
Figure/Table 1



**Caption 1**

**Figure 1.** Overview of interpolation method. **Left:** First, the left ventricle was manually segmented in two or three timeframes (end-diastole, end-systole, and diastasis in cases where present). **Right:** Spline interpolation was used to fill in the missing timeframes and construct a volume-time curve for the entire cardiac cycle.

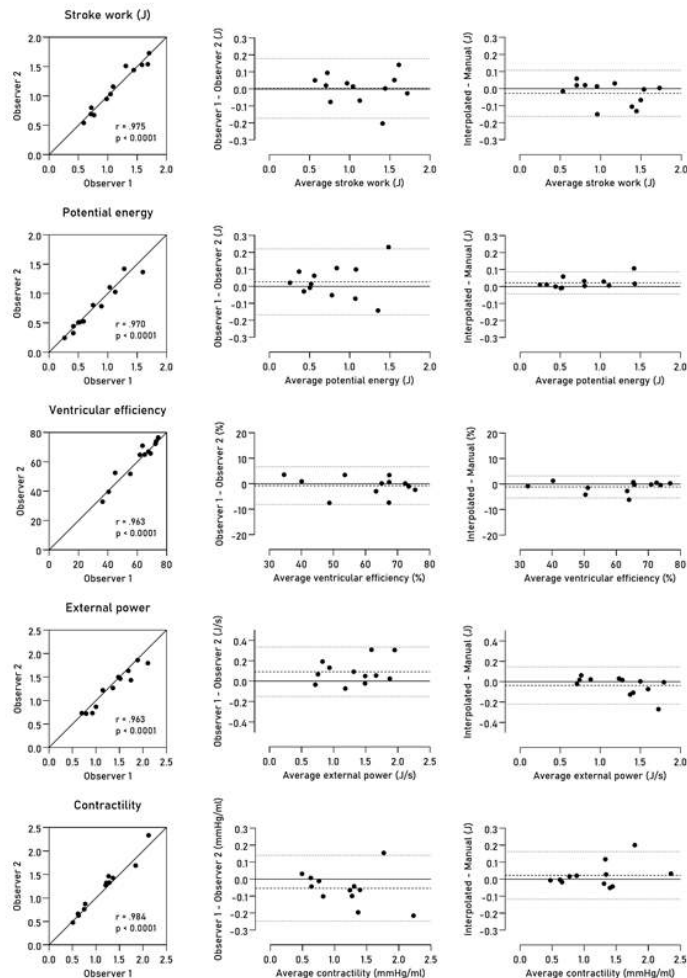
**Figure/Table 2**



**Caption 2**

**Figure 2.** Example of manual and interpolated delineations. **Left:** manual delineations were visually similar but with a small bias in end-diastolic volumes; the interpolated volume curve was less defined in diastole. **Right:** pressure-volume loops in the same individual. Here the end-diastolic volume differences between observers become apparent. Note the visual similarities between observer 2 manual (blue) and interpolated (black).

**Figure 3**



**Caption 3**

**Figure 3.** Pearson correlation and Bland-Altman plots for the evaluated measures. Bias was lower and limits of agreement narrower in manual vs. interpolated (right column) compared to the interobserver evaluation (center column).

### Bibliographic References

Suga H. Ventricular Energetics. *Physiol Rev* 70: 247–277, 1990., Sjöberg P, Seemann F, Arheden H, Heiberg E. Non-invasive quantification of pressure-volume loops from cardiovascular magnetic resonance at rest and during dobutamine stress. *Clin Physiol Funct Imaging* 41: 467–470, 2021. doi: 10.1111/cpf.12718., Seemann F, Arvidsson P, Nordlund D, Kopic S, Carlsson M, Arheden H, Heiberg E. Noninvasive Quantification of Pressure-Volume Loops From Brachial Pressure and Cardiovascular Magnetic Resonance. *Circ Cardiovasc Imaging* 12: e008493, 2019. doi: 10.1161/CIRCIMAGING.118.008493.

Speaker: P. Arvidsson

Category: Heart Failure, Image Analysis, Clinical Utility

000531

## On the reproducibility in cardiac ASL: T1 corrected reconstruction for mitigating physiological and acquisition related variability

M. Bozic-Iven \* (1); S. RAPACCHI (2); I. Pierce (3); G. Thornton (3); Q. Tao, (4); L. Schad (5); T. Treibel (6); S. Weingartner (4)

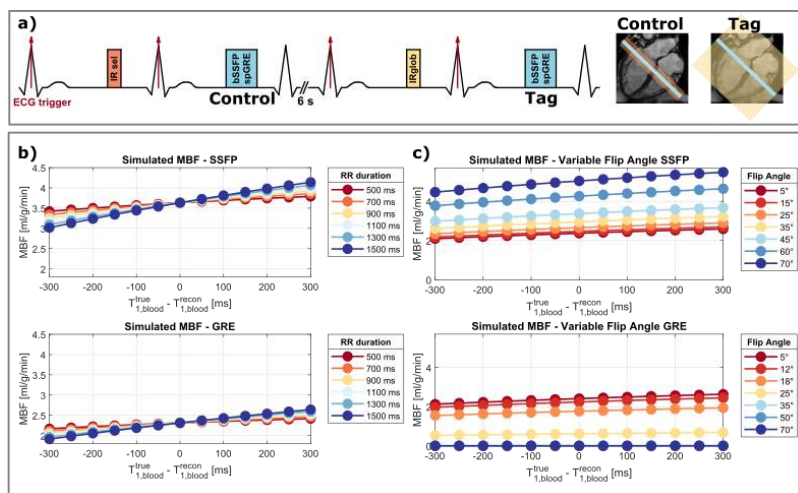
(1) Medical faculty mannheim, Heidelberg University, Mannheim, Germany; (2) Faculté de médecine, Aix-Marseille University, Marseille; (3) Barts heart centre, Barts Health NHS Trust, London, United Kingdom; (4) Department of imaging physics, Delft University of Technology (TU Delft), Delft, Netherlands; (5) Medical faculty mannheim, Heidelberg University, Heidelberg, Germany; (6) Barts heart centre, University College London, Gower Street, LONDON, United Kingdom

### Abstract

**Background:** Myocardial perfusion imaging is the clinical gold standard for detection of myocardial ischemia [1]. Current first pass perfusion based techniques require the use of contrast agents. Arterial spin labelling (ASL) relies on endogenous contrast via magnetically labelled blood and is well established in brain imaging. While good agreement between myocardial ASL (myoASL) and positron emission tomography myocardial blood flow (MBF) has been established [2], a lack of reproducibility and robustness has hampered widespread clinical translation. In this work, we investigate the influence of physiological and sequence parameters on the reproducibility of Flow-Alternating Inversion Recovery (FAIR) myoASL. To further increase robustness of myoASL, we developed a correction method based on separately acquired T1 maps. **Methods:** myoASL sequences were simulated with bSSFP and GRE readout using Bloch-equations. Flip angles (FA) were varied and varying RR intervals, i.e. different effective inversion times (TI), were emulated, with blood volume fraction of 0.14 and in-flow rate of 0.29 Hz. For all measurements, a double ECG-gated FAIR-ASL sequence based on [3] was implemented (Fig.1a). In total, one pair of baseline images (no inversion) and 5/6 (phantom/in vivo) control-tag pairs were acquired in 8mm thick slices, with 2x2mm/1.7x1.7mm base resolution (phantom/in vivo). MOLLI was used for T1 mapping in phantom and in vivo. The experiments were performed across two 3T scanners in a NiCl<sub>2</sub>-doped agarose phantom, as well as in 3 healthy subjects (3 male, 38±5.5 years) with 12-18s long breath-holds per image pair. Group-wise image registration [4] was performed and mistriggered control-tag pairs were excluded. Perfusion values were reconstructed based on Buxton's model [5], in which control and tag signal are corrected with respective TI and blood T1 time (T1B). In previous in vivo studies, T1B was set to a fixed literature based value (~1700ms). Here, a second reconstruction method was employed, using individual MOLLI-T1B times to obtain perfusion maps and septal MBF. In simulations T1B was varied, while in phantom the model T1 was varied. Mean MBF values were obtained by averaging MBF over all ASL pairs and subjects. **Results:** When identical T1B was used in simulation and model, MBF values were constant for varying RR. For non-identical T1B, however, simulated MBF values for a given RR were under-/overestimated (for T1B<0/>0). This effect was stronger for longer RR and is observed in both SSFP and GRE (Fig.1b). Moreover, for higher acquisition FA, SSFP-MBF continuously increased while GRE-MBF decreased (Fig.1c). In phantom the MBF difference due to T1B mismatch is stronger for longer RR, although no zero-crossing is observed (Fig.2a). With increasing FA, MBF values in SSFP increased over the entire FA range, while in GRE the values decreased until 35° (Fig.2b). The obtained MBF maps from

SSFP and GRE (Fig.3a) match previously reported perfusion values [2,3]. With fixed T1B, septal MBF was  $1.46 \pm 1.13 \text{ ml/min/g}$  (SSFP) /  $2.16 \pm 1.73 \text{ ml/min/g}$  (GRE), whereas with adaptive T1B MBF was  $1.39 \pm 1.05 \text{ ml/min/g}$  (SSFP) /  $2.03 \pm 1.60 \text{ ml/min/g}$  (GRE). **Conclusions:** Simulation and phantom results were in good agreement, showing a dependence on acquisition FA, and RR variability in MBF when true and model T1B differ, indicating that physiological and imaging related effects need to be accounted for to improve reproducibility of myoASL. MyoASL based perfusion was more robust when reconstructed with adaptive instead of fixed blood T1, while mean MBF from SSFP and GRE were comparable.

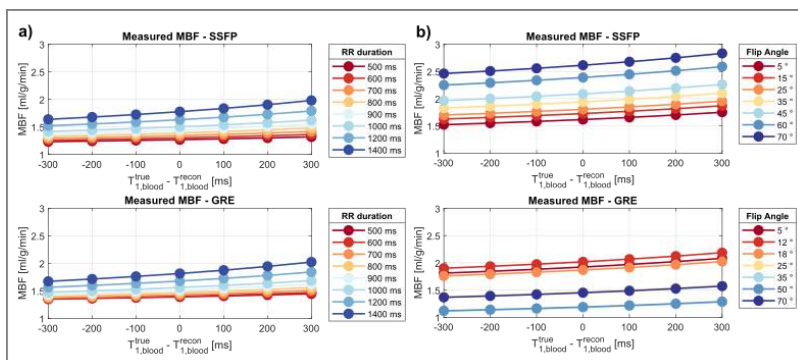
**Figure/Table 1**



**Caption 1**

(a) Control and tag image acquisition in double-gated FAIR myocardial ASL (myoASL). (b) Simulated myoASL-MBF (SSFP/GRE readout) for varying simulation and fixed model blood T1. Larger T1 inaccuracy renders the sequence more susceptible to RR variations. Varying sequence parameters, such as the flip angle (c), lead to further differences in MBF.

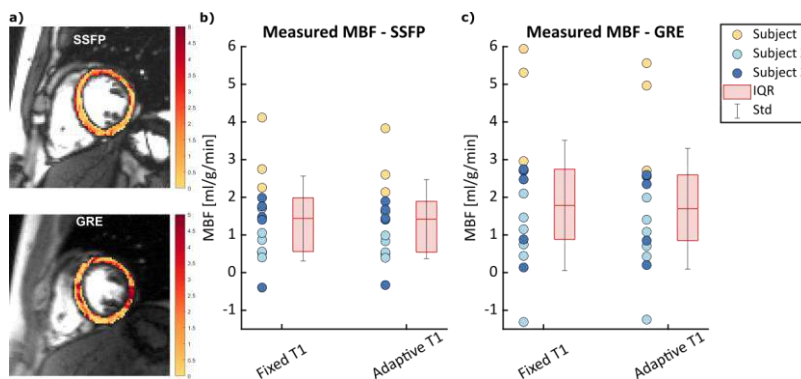
**Figure/Table 2**



## Caption 2

(a) MyoASL-MBF obtained in phantom (T1b: 2100ms) with SSFP and GRE readout vs. difference in vial and reconstruction T1 time of blood for varying RR (500-1500ms) and (b) acquisition flip angle ( $5^{\circ}$ - $70^{\circ}$ ). MBF values exhibit stronger variation in RR duration with increasing difference in T1, and show a flip-angle dependence.

## Figure 3



## Caption 3

(a) Pixelwise myoASL-MBF maps for SSFP and GRE readout. (b) Mean septal MBF values reconstructed with fixed and adaptive blood T1 for SSFP and (c) GRE readout for all subjects (red: interquartile range). The standard deviation (black) was similar in SSFP and GRE, but smaller for adaptive T1 times.

## Bibliographic References

Qayyum, A. A., & Kastrup, J. (2015). Measuring myocardial perfusion: the role of PET, MRI and CT. *Clinical radiology*, 70(6), 576-584., Zun, Z., Wong, E.C. and Nayak, K.S. (2009), Assessment of myocardial blood flow (MBF) in humans using arterial spin labeling (ASL): Feasibility and noise analysis. *Magn. Reson. Med.*, 62: 975-983., Do, H.P., Yoon, A.J., Fong, M.W., Saremi, F., Barr, M.L. and Nayak, K.S. (2017), Double-gated myocardial ASL perfusion imaging is robust to heart rate variation. *Magn. Reson. Med.*, 77: 1975-1980. , Tao, Q., van der Tol, P., Berendsen, F.F., Paiman, E.H., Lamb, H.J. and van der Geest, R.J. (2018), Robust motion correction for myocardial T1 and extracellular volume mapping by principle component analysis-based groupwise image registration. *J. Magn. Reson. Imaging*, 47: 1397-1405., Buxton, R.B., Frank, L.R., Wong, E.C., Siewert, B., Warach, S. and Edelman, R.R. (1998), A general kinetic model for quantitative perfusion imaging with arterial spin labeling. *Magn. Reson. Med.*, 40: 383-396.

Speaker: M. Bozic-Iven

Category: Arterial Spin Labeling, Perfusion, Myocardium



000533

**Low birthweight is associated with unhealthy cardiovascular magnetic resonance phenotypes and higher risk of cardiovascular death: A UK Biobank study**

Z. Raisi-Estabragh \* (1); J. Cooper (2); M. Bethell (3); P. Munroe (2); N. Harvey (4); S. Petersen (5)

(1) William harvey research institute, nihr barts biomedical research centre, Queen Mary University of London, Mile End Road, London, UK, London, UK, United Kingdom; (2) William harvey research institute, Queen Mary University of London, Mile End Road, London, UK, London, UK, United Kingdom; (3) Cardiology, Charing Cross Hospital, Fulham Palace Road, London, UK, London, United Kingdom; (4) Medical research council (mrc) lifecourse epidemiology unit, University of Southampton, Southampton, UK, United Kingdom; (5) William harvey research institute, Queen Mary University of London, Mile End Road, London, United Kingdom

**Abstract**

**Background:** Epidemiological studies have highlighted association of low birthweight with poorer cardiovascular health throughout the life course. However, the full spectrum of the relationship has not been explored and underlying mechanisms are incompletely understood. We studied the association of birthweight with incident cardiovascular events and cardiovascular magnetic resonance (CMR) measures of cardiac structure and function. Additionally, we examined a wide range of potential clinical and biochemical mediating pathways.

**Methods:** We studied 258787 UK Biobank participants. We used competing risk regression models to estimate the association of birthweight with incident myocardial infarction (MI), all-cause mortality, cardiovascular disease (CVD) mortality, and ischaemic heart disease (IHD) mortality, whilst adjusting for age, sex, deprivation, maternal diabetes, maternal hypertension, maternal smoking, and paternal diabetes. We examined potential non-linearity of these relationships using cubic spline models. In 19314 participants with CMR data available, we used linear regression to estimate the association of birthweight with CMR metrics: left ventricular end-diastolic volume (LVEDV), left ventricular stroke volume (LVSV), right ventricular end-diastolic volume (RVEDV), right ventricular stroke volume (RVSV), and aortic distensibility (AD). For the birthweight-MI relationship, we evaluated the mediating effect of childhood height and weight, body mass index, diabetes, hypertension, high cholesterol, serum glucose, glycosylated haemoglobin, serum lipids, and C reactive protein.

**Results:** Higher birthweight was associated with significantly lower risk of incident MI [SHR: 0.90 (0.85-0.95);  $P=7.0 \times 10^{-5}$ ], CVD death [SHR: 0.91 (0.84-0.99);  $P=0.028$ ], and IHD death [0.88 (0.79-0.98);  $P=0.020$ ]. We demonstrated a reverse-J shaped relationship between birthweight-MI, which was significant in individuals with “normal” birthweight

(2.06-4.51Kg) and augmented in those with “low” birthweight (2.05Kg). Higher birthweight was linked to healthier CMR phenotypes across all measures considered; e.g. higher LVSVi (Beta=1.16 (0.96-3.04);  $p=2.65 \times 10^{-29}$ ) and higher RVSVi (Beta=1.31 (1.10 - 3.46);  $p=1.78 \times 10^{-33}$ ). Multiple mediation analysis suggested mediation through adverse alteration of the cardiometabolic profile, in particular, poorer glycaemic control (diabetes, serum glucose), greater inflammation (C reactive protein), worse lipid profile (lipoprotein a, triglyceride level), and higher risk of hypertension.

**Conclusions:** Low birthweight is associated with poorer cardiovascular phenotypes, and greater risk of MI and cardiovascular mortality outcomes. The relationship is partly mediated through adverse lipid profile, poorer glycaemic control, greater inflammation, and hypertension. Prenatal care should be an important focus for public health strategies to improve cardiovascular health in later life.

Speaker: Z. Raisi-Estabragh

Category: Outcomes, Mortality, Susceptibility

000536

## **Active Lupus Myocarditis diagnosed with CMR despite advanced immunotherapy necessitating Rituximab**

U. Gul \* (1); S. Hothi (1); E. Mcalindon (1)

(1) Cardiology, The Royal Wolverhampton NHS Trust, Wolverhampton, United Kingdom

### **Abstract**

#### **Description of Clinical Presentation:**

A 52-year male with known systemic lupus erythematosus (SLE) diagnosed thirteen years ago was referred due to breathlessness, fatigue, and a progressive decline in exercise tolerance to less than one mile. He recently developed hypertension & nephrotic-range proteinuria on dipstick. He felt mild improvement few weeks after commencing an angiotensin converting enzyme inhibitor (ACEi) by his nephrologist but remained breathless. His medical history comprised chronic discoid lupus, arthritis and Raynaud with digital ulcers treated with high dose Mycophenolate, Iloprost, corticosteroids and hydroxychloroquine. There was no family history of coronary artery disease or cardiomyopathy. He was undergoing smoking cessation. A SLEDAI score of 8 indicated active disease and investigations suggested advanced stage lupus nephritis and lupus myocarditis despite being on high dose mycophenolate. This together with no interval improvement in systolic function led to initiation of intensive immunosuppression by Rituximab and he remains under surveillance.

#### **Diagnostic Techniques and Their Most Important Findings:**

The biochemical profile showed negative ANA, negative anti-dsDNA, ESR of 18 mm/h, and normal CRP & complement levels. There was, raised IgA, low serum protein, nephrotic range proteinuria with eGFR >90 mL/min/1.73m<sup>2</sup>. Chest radiography, electrocardiography & a viral screen were unremarkable. The renal biopsy was consistent with Class V renal lupus (or less likely primary membranous nephropathy). Transthoracic echocardiogram in April 2021 revealed low-normal left ventricular systolic function with LVEF 50-54%, and basal to mid lateral wall hypokinesis (figure 1). Stress-perfusion cardiac MRI in August 2021 showed mild left ventricular systolic dysfunction, LVEF 47% with basal to mid lateral wall hypokinesia. T2 STIR imaging demonstrated oedema in the basal to mid inferior & inferolateral segments. T1 mapping showed regional increased T1 values in the same segments (1100ms (c.f. local reference range 1000+/-40ms using a MOLLI sequence, Philips Ingenia 1.5T scanner analysed with Circle CVI42 software). There was epicardial and mid-wall late gadolinium enhancement in the basal to mid inferior and lateral walls (figure 3). There was no stress-induced perfusion defect.

#### **Learning Points from this Case:**

1. Cardiac MRI with parametric and late gadolinium imaging may help differentiating non-ischemic from ischemic & healed versus active myocarditis. Studies are needed to evaluate the MRI response to immunosuppressant therapy.

2. Lupus myocarditis can occur despite patients being on high dose immunosuppressants and markers of disease activity may be suppressed.
3. Lupus nephritis & myocarditis may co-exist suggesting similar immune-mediated pathogenesis for which further studies are needed.

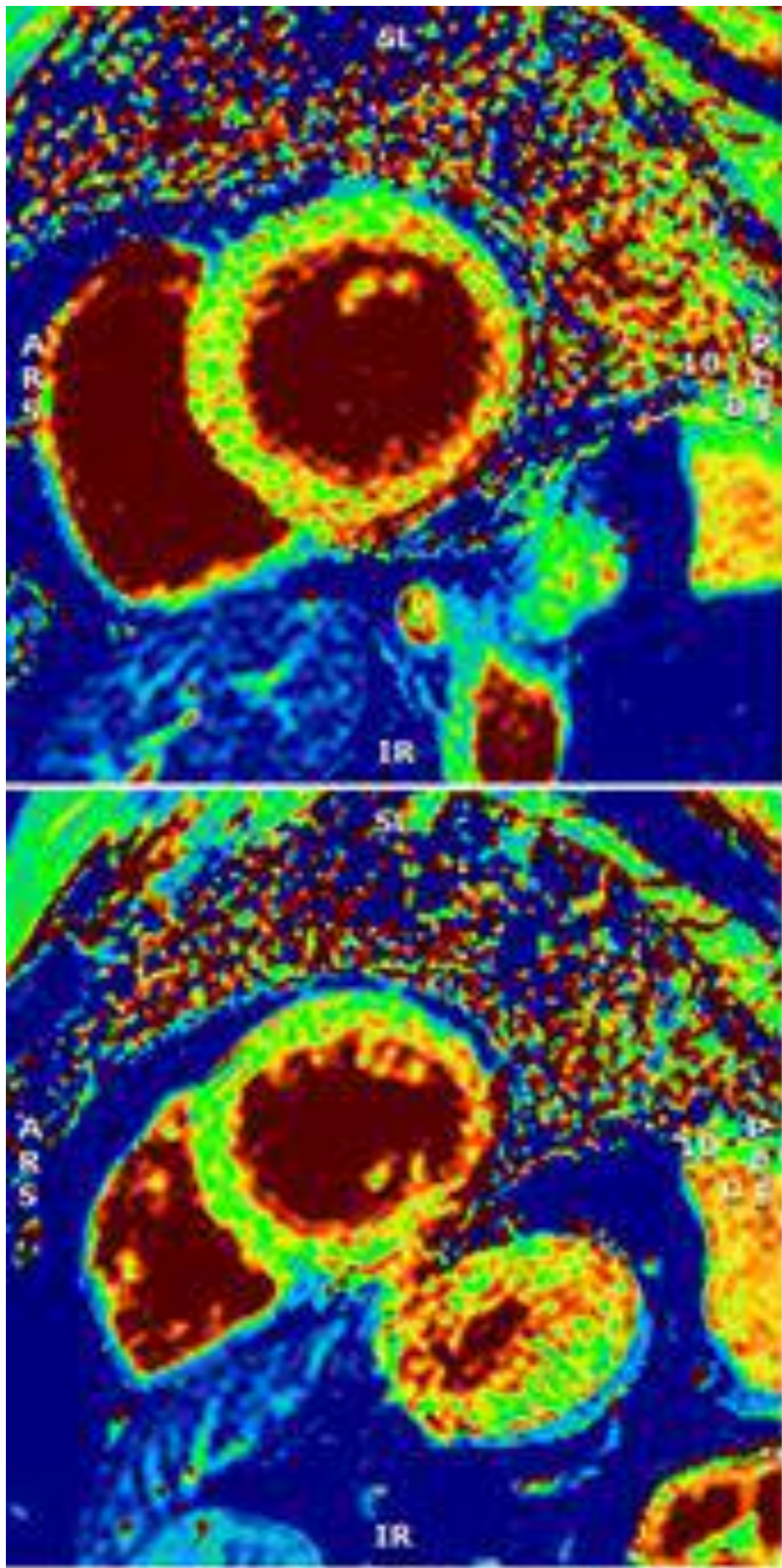
#### Figure/Table 1



#### Caption 1

Figure 1. Transthoracic echocardiogram, end systolic frame from four chamber view; hypokinetic anterolateral wall.

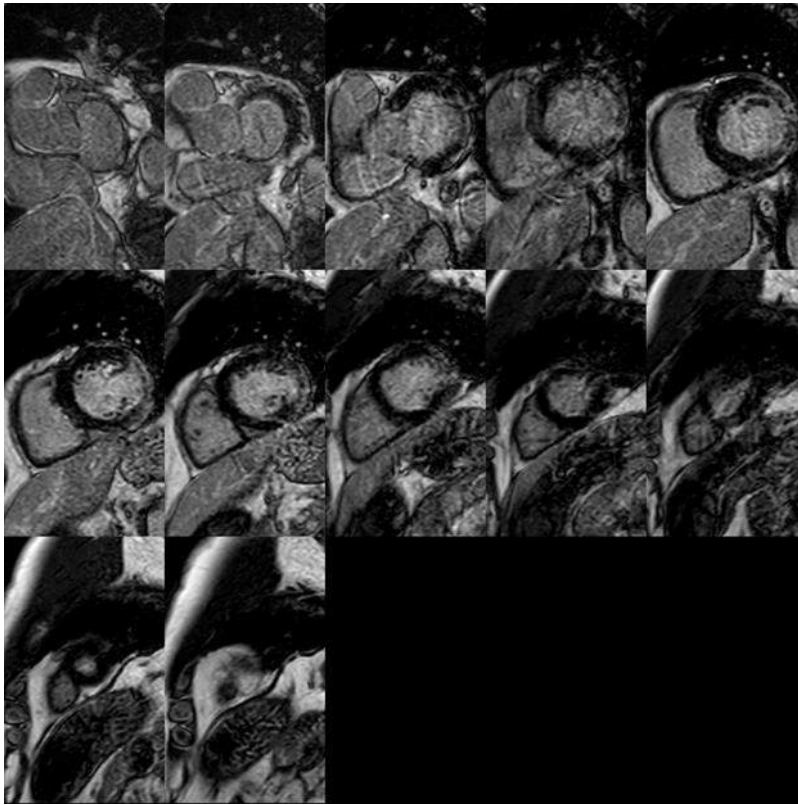
#### Figure/Table 2



**Caption 2**

Figure 2. T1 native map (basal slice uppermost, mid cavity slice lower-most). There are increased T1 values in the basal & mid inferolateral & inferior segments.

**Figure 3**



**Caption 3**

Figure 3. Inversion recovery late gadolinium enhancement (LGE) short axis image stack. There is epicardial & mid-wall LGE in the inferior & inferolateral segments.

### **Bibliographic References**

4. Guillemette Thomas, Fleur Cohen Aubart, Laurent Chiche, et al. Lupus Myocarditis: Initial Presentation and Longterm Outcomes in a Multicentric Series of 29 Patients. *The Journal of Rheumatology*. 2017, 44 (1) 24-32; DOI: 10.3899/jrheum.160493, 3.  
Cheungpasitporn W, Kopecky SL, Specks U, Bharucha K, Fervenza FC. Non-ischemic cardiomyopathy after rituximab treatment for membranous nephropathy. *J Renal Inj Prev*. 2016;6(1):18-25. doi:10.15171/jrip.2017.04, 2. Aimo A, Tavoni A, Buda G, Emdin M. Rituximab as a novel treatment for heart failure: evidence from a case series. *Eur Heart J Case Rep*. 2019;3(4):1-2. doi:10.1093/ehjcr/ytz227, 1. Chrong-Reen Wang, Yi-Shan Tsai, Hung-Wen Tsai. Acute Myocarditis in Patients with Antineutrophil Cytoplasmic Antibody–positive Microscopic Polyangiitis and Receiving Rituximab Therapy. *The Journal of Rheumatology*. 2019, 46 (12) 1645-1646; DOI: 10.3899/jrheum.190569

Speaker: U. Gul

Category: Myocarditis, Lupus, Parametric Mapping

000539

## **Donor-recipient mismatch in pediatric heart transplantation results in long term changes in myocardial structure and function**

N. Husain \* (1); K. Watanabe, (2); J. Arzu, (3); C. Rigsby, (4); M. Markl (5); J. Robinson (6)

(1) , Ann & Robert H. Lurie Children's Hospital of Chicago, Chicago, United States of America; (2) Pediatric cardiology, Ann & Robert H. Lurie Children's Hospital of Chicago, Chicago, United States of America; (3) Preventive medicine, Ann & Robert H. Lurie Children's Hospital of Chicago, Chicago, United States of America; (4) Pediatric radiology, Ann & Robert H. Lurie Children's Hospital of Chicago, Chicago, United States of America; (5) Radiology, Northwestern University, Chicago, United States of America; (6) Cardiology, Ann & Robert H. Lurie Children's Hospital of Chicago, Chicago, United States of America

### **Abstract**

**Background:** Donor-recipient mismatching by age, size and gender is common in pediatric heart transplantation (PHT) due to relative scarcity of donor grafts. Long term effects of mismatching on the graft are largely unknown. The aim of this study was to evaluate the impact of mismatch at the time of PHT on myocardial structure and function by cardiac magnetic resonance imaging (CMR) at long term follow up of the allograft.

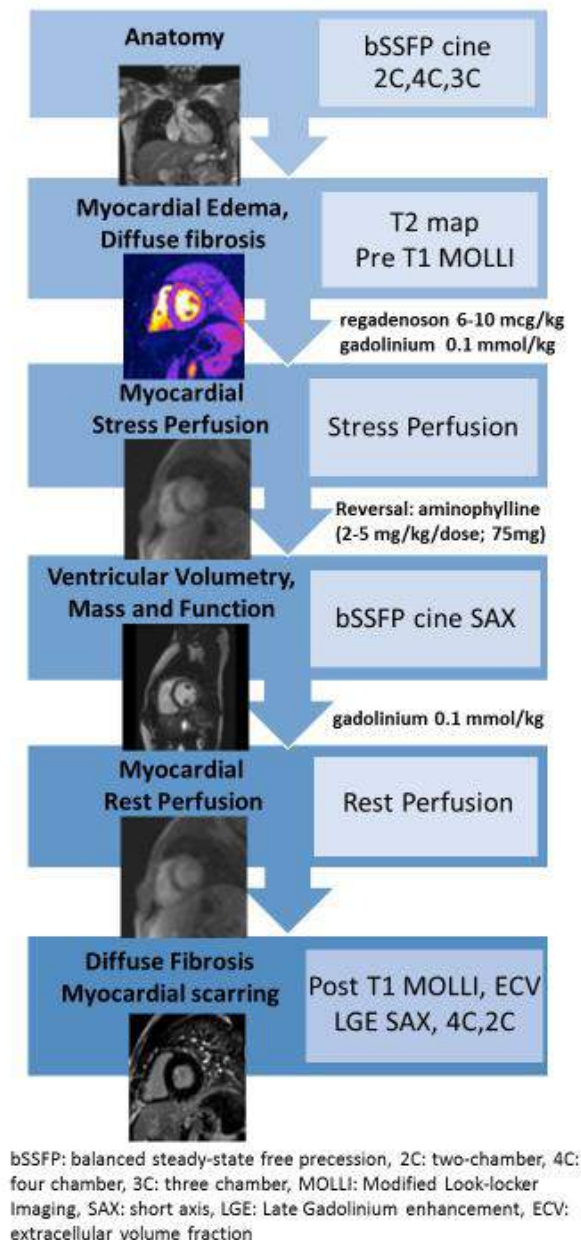
**Methods:** Forty-seven PHT with history of congenital heart disease (n=23), cardiomyopathy (n=21) or prior transplant (n=3) underwent comprehensive CMR (Figure 1) including short-axis 2D cine SSFP for assessing left and right ventricular indexed end-diastolic volumes (LVEDV, RVEDV), ejection fraction (LVEF, RVEF), and LV mass. In addition, global and segmental T2-mapping as well as pre- and post-Gadolinium administration T1-mapping was performed to quantify myocardial T2 (measure of tissue edema) and extracellular volume fraction (ECV, measure of tissue fibrosis). Patient demographics, clinical history and donor characteristics were obtained for all study participants. In the absence of consensus on describing mismatch, we assessed donor and recipient characteristics (height, weight, and age) for mismatch in different ways. We calculated relative differences (donor minus recipient characteristic) divided by donor characteristic\*100; as referenced in the International Society of Heart and Lung Transplantation (ISHLT) registry. In addition, absolute differences (donor minus recipient characteristic) and donor-recipient characteristic ratios were also calculated. Spearman rank correlations coefficients( $\rho$ ) and unadjusted p-values are reported in this exploratory study.

**Results:** Cohort characteristics are described in Figure 2. CMR was performed 6.4 (4.2-13) years post-heart transplant. No PHT recipients had active rejection at time of CMR and only 2/47(4.2%) had moderate to severe CAV on angiography. Gender mismatch was present in 49%(male donor-female recipient 17/47(36%), female donor-male recipient 6/47(13%)) and was associated with modestly lower LVEF (61.5% no mismatch, 59% female donor-male recipient, 56.7% male donor-female recipient;  $p=0.012$ ). Wide ranges of age and size mismatch were noted (Figure 3a). Greater height mismatch was moderately but significantly associated with higher global myocardial T1 and global T2. Greater weight mismatch was associated with higher LVEDV and increased global T1 (Figure 3b).



Conclusion: Donor and recipient gender, age and size mismatching were highly prevalent in our PHT population. In a cohort with low prevalence of comorbidities (like rejection or high-grade CAV), gender mismatch and greater degree of size mismatch at the time of PHT were associated with myocardial structure and function alterations at long term CMR follow up. This preliminary data suggests the potential role of CMR in monitoring long-term effects of mismatching and larger studies may provide further insights into optimal donor selection for PHT.

**Figure/Table 1**



**Caption 1**

Comprehensive CMR protocol in PHT recipients



## Figure/Table 2

DEMOGRAPHICS		N = 47*
<b>Gender</b>		
Female		30 (63.8%)
Male		17 (36.2%)
<b>Age at PHT (years)</b>		8.0 (2.5, 12.5)
<b>Age at MRI (years)</b>		14.0 (11.3, 18.3)
<b>Time since PHT (years)</b>		6.4 (4.2, 13.0)
CLINICAL HISTORY		
<b>Ischemic Time (hours)</b>		3.5 (2.7, 4.1)
<b>CAV History</b>		
No		37 (78.7%)
ISHLT CAV grade 1		5 (10.6%)
ISHLT CAV grade 2		2 (4.2%)
Missing data		3 (6.4%)
<b>Rejection History (within 3 years)</b>		
No		33 (70.2%)
Yes		12 (25.5%)
Missing data		2 (4.3%)

\*n (%); Median (IQR)

## Caption 2

Demographic and clinical characteristics of PHT cohort

## Figure 3

a)

CHARACTERISTIC	DONOR*	RECIPIENT*	MISMATCH	DEGREE OF MISMATCH*
Height (cm)	145 (88-157)	116 (85-146)		

Weight (kg)	34 (12.7-56.7)	23.5 (11.3-40.7)	Relative difference (%)	8.4 % (2.0, 15.9)
			Absolute difference	7.6 cm (2.1, 21.5)
			Donor-recipient ratio	1.1 (1.0, 1.2)
Age (yr)	11 (3.5-16)	8 (2.5-12.5)	Relative difference (%)	19.9 % (0.5, 38.2)
			Absolute difference	3.8 kg (0.1, 11.8)
			Donor-recipient ratio	1.3 (1.0, 1.7)
			Relative difference (%)	20.7 % (-5.0, 41.1)
			Absolute difference	1.0 yr (-0.8, 6.0)
			Donor-recipient ratio	1.2 (0.8, 1.7)

\* Median (IQR)

b)

	LVEDV	LVEF	Global T1	Global ECV	Global T2	Peak T2
Relative height difference			0.27 (0.06)	0.27 (0.07)	0.27 (0.06)	
Absolute height difference			0.33 (0.02)		0.34 (0.02)	
Height donor-recipient ratio				0.28 (0.05)	0.27 (0.06)	
Relative weight difference	0.33 (0.02)	-0.25 (0.08)				
Absolute weight difference			0.31 (0.03)			
Weight donor-recipient ratio	0.27 (0.06)		0.27 (0.06)			

Relative age difference	0.29 (0.05)	-0.28 (0.07)				0.27 (0.08)
Absolute age difference						0.27 (0.06)
Age donor-recipient ratio						0.27 (0.07)

### Caption 3

a) Donor recipient characteristics (height, weight and age) and mismatching noted in our PHT cohort

b) Correlations between mismatching and CMR variables on long term follow up: reported as correlation coefficient, rho (p-value)

Speaker: N. Husain

Category: Heart Transplant, Pediatric , Parametric Mapping

000540

## **Differences in cardiac magnetic resonance findings of myocardial inflammation after Coronavirus Disease 2019 infection and vaccination**

A. Kumar \* (1); D. Clark (1); C. Charnogursky, (2); D. Li, (1); E. Stein, (3); N. Phillips, (3); L. Tran, (3); C. B. Creech, (2); K. George-Durrett, (4); J. Dendy (1); J. Soslow (4); S. Hughes (1)

(1) Division of cardiovascular medicine, Vanderbilt University Medical Center, Nashville, United States of America; (2) Division of pediatric infectious diseases, Vanderbilt University Medical Center, Nashville, United States of America; (3) Department of internal medicine, Vanderbilt University Medical Center, Nashville, United States of America; (4) Division of pediatric cardiology, Vanderbilt University Medical Center, Nashville, United States of America

### **Abstract**

#### ***Background:***

Acute myocarditis after vaccination against Coronavirus Disease 2019 (COVID-19) has received considerable attention during the ongoing pandemic. However, there is a limited understanding of the pathophysiology of post-vaccination myocarditis and how it compares to myocardial inflammation resulting from SARS-CoV-2 itself. Additionally, it is unclear how the presence and extent of parametric mapping and LGE abnormalities differ between post-vaccination and post-infection COVID-19 myocarditis. In this study, we utilized cardiac magnetic resonance (CMR) to evaluate the extent of inflammation in a group of patients after symptomatic myocarditis resulting from COVID-19 infection and vaccination.

#### ***Methods:***

We retrospectively analyzed data from 31 patients with symptomatic myocarditis who underwent contrasted CMR, 22 with myocarditis after COVID-19 infection (post-infection) and 9 with myocarditis after COVID-19 vaccination (post-vaccination). CMR analysis included standard volumetrics and function, as well as presence, location, and quantification of LGE (using full width half-maximum technique). Native T1, T2, and extracellular volume (ECV) maps were obtained in the base and mid short axis and analyzed with global values as well as segmentation using the 17-segment model (excluding the 4 apical segments). Categorical variables were analyzed with a Chi Square and continuous variables were analyzed with a Wilcoxon Rank Sum. Multivariable linear regression was used to correct for age, sex, and time from infection/vaccination to CMR.

#### ***Results:***

There was no difference in age between groups, but there were more males in the post-vaccination group (64% vs 100%,  $p = 0.04$ ). The post-vaccination group underwent CMR significantly earlier (123.9 days vs 11.4 days,  $p = 0.001$ ). LGE quantification was increased in

the post-vaccination cohort, but native T1 and T2 were not (Table). After multivariable adjustment, there was no difference in LGE extent, T1, or T2 time. A higher proportion of vaccinated patients had LGE in the inferolateral wall compared to post-infection patients, who had a higher proportion of LGE in the inferoseptum, though this did not reach significance ( $p = 0.10$ ).

### **Conclusions:**

There is no significant difference in LGE burden in patients with symptomatic myocarditis after COVID-19 infection and vaccination. Our data suggest a proclivity for inflammation of distinct myocardial segments, possibly signifying a divergent pathophysiology. Further studies of larger numbers of patients will be needed to better characterize myocarditis in these two processes and provide more information about the effect of myocardial inflammation on patient outcomes.

**Figure/Table 1**

<b>Characteristics</b>	<b>Post-COVID myocarditis</b>  <b>Mean <math>\pm</math> SE or n (%)</b>	<b>Post-Vaccine Myocarditis</b>  <b>Mean <math>\pm</math> SE or n (%)</b>	<b>P Value</b>
Age	33.9 $\pm$ 4.0	26.9 $\pm$ 4.3	0.21
Male sex	14 (64)	9 (100)	0.04
BSA (kg/m <sup>2</sup> )	2.04 $\pm$ 0.06	2.05 $\pm$ 0.10	0.89
Time since diagnosis (days)	123.9 $\pm$ 18.7	11.4 $\pm$ 3.7	0.001
<b>MRI measures</b>	<b>Post-COVID myocarditis</b>  <b>Mean <math>\pm</math> SE</b>	<b>Post-Vaccine Myocarditis</b>  <b>Mean <math>\pm</math> SE</b>	<b>P Value</b>
LGE quantification (%)	6.6 $\pm$ 0.9	10.9 $\pm$ 1.9	0.045
LVEF (%)	58.2 $\pm$ 2.0	55.9 $\pm$ 2.3	0.14
LVEDVi (ml/m <sup>2</sup> )	90.9 $\pm$ 5.1	82.6 $\pm$ 3.5	0.14
LVESDVi (ml/m <sup>2</sup> )	38.3 $\pm$ 4.5	37.1 $\pm$ 2.4	0.51
LVMi (g/m <sup>2</sup> )	64.1 $\pm$ 3.4	57.1 $\pm$ 3.9	0.28
RVEF (%)	50.6 $\pm$ 1.6	50.9 $\pm$ 1.6	0.91
Mid LV T1 (ms)	971.5 $\pm$ 24.6	929.8 $\pm$ 118.4	0.62
Mid LV T2 (ms)	48.4 $\pm$ 0.7	48.7 $\pm$ 1.3	0.96
Mid LV ECV (%)	26.6 $\pm$ 0.7	24.5 $\pm$ 1.1	0.22

Speaker: A. Kumar

Category: Myocarditis, Inflammation, Late Gadolinium Enhancement

000542

## **Myocardial viability and ischemia assessment in chronic coronary total occlusion according to collaterals distribution: a retrospective analysis**

G. Pinto (1); M. Chiarito (1); G. Liccardo (1); S. Baggio (1); E. Bacci (1); M. Francone (2); B. Reimers (1); G. Gasparini (1); L. Monti \* (2)

(1) Cardiology, Humanitas Research Hospital, Rozzano, Italy; (2) Radiology, Humanitas Research Hospital, Rozzano, Italy

### **Abstract**

#### **Background.**

Whether CTO-PCI (chronic total occlusions – percutaneous coronary intervention) offers clinical benefit over optimal medical therapy is still a matter of debate. Viability and ischemia assessment could improve selection of candidates to PCI. Traditionally, well-developed collaterals are considered a marker of myocardial viability in CTO territory. Current literature offers few data concerning the relationship between viability/ischemia and collaterals distribution.

#### **Methods.**

We retrospectively analyzed the Cardiovascular Magnetic Resonance (CMR) studies with LGE assessment and coronary angiographies of 131 consecutive patients with at least one CTO hospitalized between June 2009 and September 2020. 111 pts (85%) underwent stress-CMR with adenosine. AHA segments (16 segment/patient for a total of 2096 segment assessed) were assessed on 3 short axis projections and scored for WMSI on cine images, for the presence of ischemia with adenosine stress perfusion and for viability on LGE images. Viability was defined as LGE transmural  $\leq 50\%$  and WMSI (wall motion score index)  $> 1$ .

Patients were divided in three groups according to collaterals distribution at coronary angiography: 1) totally developed collaterals (TD) if they had both Rentrop 3 grade and Werner 2 grade collaterals (21 patients); 2) well developed collaterals (WD) if they had Rentrop 3 or Werner 2 grade collaterals (29 patients); 3) poorly developed collaterals (PD) if they had neither Rentrop 3 or Werner 2 grade collaterals (81 patients).

#### **Results.**

Patients with TD collaterals were more likely to have viable segments in the CTO-territory (90% of the segments in TD, 76% in WD and 71% in PD, coeff. 0.107,  $p < 0.001$ ). No statistically significant differences were found between groups as regard the amount of ischemic segments (61% of the segments in TD, 65% in WD and 60% in PD,  $p = 0.189$ ).

#### **Conclusion.**

The presence of myocardial viability is slightly associated with the degree of coronary collateralization at coronary angiography while the amount of ischemia is not. Stress CMR should be considered in CTO patients before a reopening attempt.

Speaker: L. Monti

Category: Stress CMR, Chronic Total Occlusion, Coronary Angiography



000543

## Both non-infarct and infarct myocardial T1 post-STEMI are independent and incremental predictors of long-term outcomes beyond conventional CMR biomarkers

M. Shanmuganathan \* (1); A. Masi, (2); M. Burrage, (2); R. Kotronias, (1); A. Borlotti (1); A. Banerjee (3); R. Scarsini (4); D. Terentes-Printzios (4); E. Tunnicliffe (2); Q. Zhang (3); E. Hann (3); G. De Maria (4); A. Lucking (4); J. Langrish (4); R. Kharbanda (4); A. Banning (4); R. Choudhury (1); K. Channon (1); S. Piechnik (2); V. Ferreira (2)

(1) Division of cardiovascular medicine, University of Oxford, Oxford, United Kingdom; (2) Division of cardiovascular medicine, Oxford Centre for Magnetic Resonance (OCMR), Headington, United Kingdom; (3) Radcliffe department of medicine, University of Oxford, Oxford, United Kingdom; (4) Oxford heart centre, John Radcliffe Hospital, Oxford, United Kingdom

### Abstract

**BACKGROUND:** The degree of acute injury to the infarcted myocardium, such as infarct size (IS), microvascular obstruction (MVO) and intramyocardial haemorrhage (IMH) on CMR immediately after ST-segment elevation myocardial infarction (STEMI) are known independent predictors of both short- and long-term clinical outcomes (1). Although reports of acute alterations in the remote zone of the non-infarcted myocardium have been reported using T1-mapping (2,3), the long-term prognostic value of changes in the entire non-infarcted myocardium is unknown.

Therefore, we aimed to evaluate the acute changes in both the non-infarcted and infarcted myocardium post-STEMI and their long-term predictive value of major adverse cardiac events (MACE) using conventional CMR and T1-mapping indices.

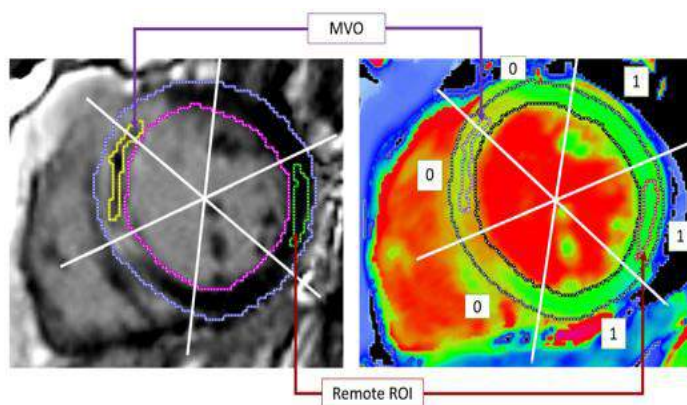
**METHODS:** 219 patients undergoing primary percutaneous coronary intervention post-STEMI prospectively underwent CMR (3T) at 2 days and 6 months, with long-term follow-up for MACE – a composite of cardiac death, sustained ventricular arrhythmia and new-onset heart failure. Blood serum blood levels of NT-pro BNP was measured at the time of the 6-month CMR scan. CMR assessed LVEF, IMH, area-at-risk (AAR), IS and MVO using cine, T2-weighted, T2\*, T1-mapping and late gadolinium enhancement (LGE) imaging. Area without LGE was defined as non-infarcted myocardium (Figure 1). Infarct and non-infarct T1 were derived from T1-maps using anatomically matching LGE images. “High non-infarct T1” was defined as  $T1 > 1250\text{ms}$  ( $>2\text{SD}$  above normal range  $1184 \pm 30\text{ms}$ ). Within the infarction, presence of MVO/IMH can lower infarct T1; this was dichotomised into “Higher infarct T1” ( $\geq 1300\text{ms}$ ) and “Lower infarct T1” ( $< 1300\text{ms}$ ). Good LV coverage with T1 maps was achieved for each patient ( $7 \pm 2$  slices per patient), resulting in 1487 slices overall. Each slice was divided into 6 segments; of these 10.3% (918/8922) were excluded due to artefacts. Conventional CMR markers (LVEF, AAR, IS, MVO, IMH) and novel T1-mapping biomarkers were assessed for their ability to predict MACE using Kaplan-Meier and Cox-regression survival analysis.

**RESULTS:** Mean age of the recruited patients (87% male) was  $61 \pm 11$  years. They underwent an acute CMR scan at a median of 2 (IQR 1-2) days after hospitalization. The median IS was 22% (IQR 13-33) and the mean left ventricular ejection fraction (LVEF) was  $47 \pm 9\%$ . 22/219

patients experienced a MACE at a median of 4 years (IQR 2.5-6yrs). Acute IS, MVO and LVEF were associated with MACE on univariate Cox-regression analysis but AAR and IMH were not. High non-infarct T1 was associated with lower LVEF (51vs55%,  $p=0.002$ ) and higher NT-pro-BNP levels (290vs170 pg/ml,  $p=0.008$ ) at 6 months, and a 2.5-fold increased risk of long-term MACE (Figure 2;  $p=0.035$ ). Lower infarct T1, implying MVO/IMH, was associated with a 3-fold risk of MACE ( $p=0.020$ ). Both non-infarct T1 ( $p<0.001$ ) and infarct T1 ( $p=0.003$ ) remained independent predictors of MACE after adjusting for age, history of MI, ischaemic time, and peak troponin; both significantly improved risk-prediction beyond  $LVEF<40\%$ , IS and MVO (Figure 3; C-statistic  $0.69\pm0.06$  vs  $0.77\pm0.06$ , net reclassification index 42%;  $p=0.027$ ).

**CONCLUSIONS:** A significant acute response in the non-infarcted myocardium, defined as high T1 values on CMR, was associated with significantly lower LVEF and higher levels of natriuretic peptides at 6 months and long-term MACE. Non-infarct and infarct T1 are significant independent predictors of long-term MACE, offer better reclassification and significantly improved predictive performance beyond conventional CMR markers (LVEF, IS and MVO).

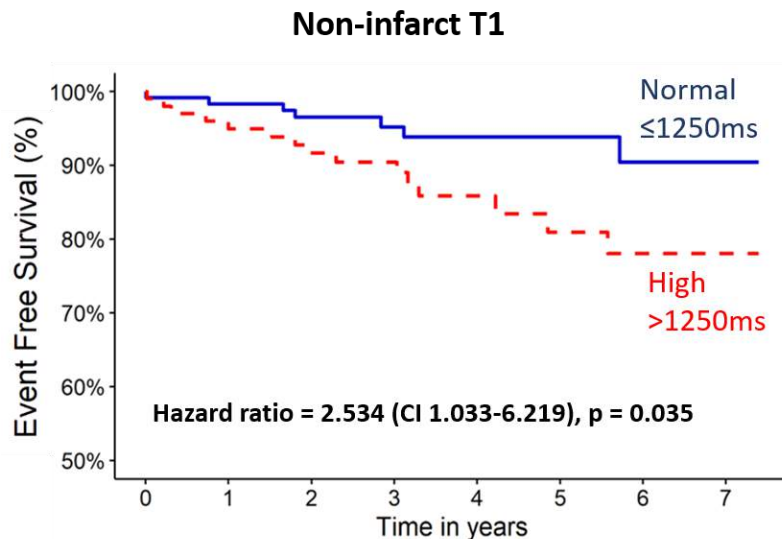
**Figure/Table 1**



**Caption 1**

The LV slice was split into 6 sections. Regions of interest (ROIs) were placed in remote myocardium and in areas corresponding to MVO. Segments on ShMOLLI T1-maps corresponding to delayed enhancement (DE) on LGE imaging were scored as '0'; i.e. infarct. Segments without DE were scored as '1', i.e. non-infarct.

**Figure/Table 2**



**Caption 2**

Kaplan-Meier survival analysis showing high non-infarct T1 carries a significantly higher risk than normal non-infarct T1. Normal T1 was defined as  $\leq 1250$ ms, in line with previous work in our 3T scanner involving healthy volunteers and patients with acute STEMI.

**Figure 3**

Model	CMR indices	C-statistic	Integrated Brier score	Comparison of models		Net Reclassification Index (NRI)		Integrated discrimination improvement Index (IDI)	
				$\chi^2$ difference	p	Index	p	Index	p
Conventional CMR indices	Acute LVEF <60%	0.69 ± 0.06	0.075	N/A					
	MVO presence								
	Infarct size (per 1%)								
	Acute LVEF <60%								
T1 indices added	MVO presence	0.77 ± 0.06	0.064	Conventional CMR model vs model with T1 indices added					
	Infarct size (per 1%)								
	Infarct T1 (per 1ms)								
	Non-infarct T1 (per 1ms)								
				13.21	0.001	42.3% (CI 3.4-66.2%)	0.027	16.1% (CI 4.7-30.1%)	<0.001

**Caption 3**

When infarct T1 and non-infarct T1 are added to the conventional CMR indices, the model prediction of long-term MACE after STEMI is significantly improved as shown by higher C-statistic and lower Brier score and statistically significant and positive NRI and IDI.

## Bibliographic References

2. Carrick D, Haig C, Rauhalammi S, et al. Pathophysiology of LV Remodeling in Survivors of STEMI: Inflammation, Remote Myocardium, and Prognosis. JACC: Cardiovascular Imaging. 2015 Jul 1;8(7):779–89. 3. Reinstadler SJ, Stiermaier T, Liebetrau J, et al. Prognostic Significance of Remote Myocardium Alterations Assessed by Quantitative Noncontrast T1

Mapping in ST-Segment Elevation Myocardial Infarction. JACC: Cardiovascular Imaging. 2018 Mar 1;11(3):411–9, 1. Ibanez B, Aletras AH, Arai AE, et al. Cardiac MRI Endpoints in Myocardial Infarction Experimental and Clinical Trials: JACC Scientific Expert Panel. Journal of the American College of Cardiology. 2019 Jul 16;74(2):238–5

Speaker: M. Shanmuganathan

Category: Acute Myocardial Infarction, Native T1, Prognosis

000546

## **The Utility of a Fully Automated Cardiac Magnetic Resonance Post-Processing Tool and Radiomics Algorithm to Non-Invasively Classify Patients With or Without Significant Coronary Artery Stenosis**

E. Hillier \* (1); M. Benovoy (2); M. Friedrich (3)

(1) Medicine, McGill University Health Centre Glen Site (MUHC), Montréal, Canada; (2) Cardiac imaging, Circle Cardiovascular Imaging, Calgary, Canada; (3) Departments of Medicine and Diagnostic Radiology, Division of Experimental Medicine, Centre Universitaire de Santé McGill Site Glen, Montréal, Canada

### **Abstract**

#### **Background:**

Oxygenation-Sensitive Cardiac Magnetic Resonance (OS-CMR) has emerged as a powerful tool to investigate the underlying physiology of a number of disease states through the assessment of tissue oxygenation status with myocardial oxygenation reserve and functional kinetics of the myocardium with strain. Recently, the analysis of CMR scans with radiomics algorithms has demonstrated to have superior diagnostic accuracy over standard analysis and reporting methods. As up to half of patients undergoing coronary angiography are found to have ischemia with no significant coronary artery obstruction, a non-invasive diagnostic test that can help to more accurately stratify patients presenting with symptoms of ischemia as having significant or no significant coronary artery disease (CAD) would be of great clinical use.

#### **Methods:**

We analyzed 49 patients (38 with significant and 15 without significant obstructive CAD) with a positive stress test and coronary angiography. All participants underwent a non-contrast CMR exam on a clinical 3T MRI system (Magnetom Skyra™, Siemens Healthineers, Erlangen, Germany) within one week of the coronary angiography. Long axis cine CMR for ventricular morphology, volumes, function including strain, and short-axis OS-CMR images were acquired (total image acquisition time less than 15min). The images were imported and analyzed with a fully automated analysis package including an advanced machine learning algorithm (cvi42™ *Cardiom* prototype (Circle Cardiovascular Imaging, Alberta, Canada). Per participant, 602 discrete data points per participant are extracted. A 75% or higher degree of coronary artery stenosis on Quantitative Coronary Angiography (QCA) was used as the ground truth and classified as either 1 vessel disease (VD), 2VD, 3VD, or no significant coronary artery obstruction.

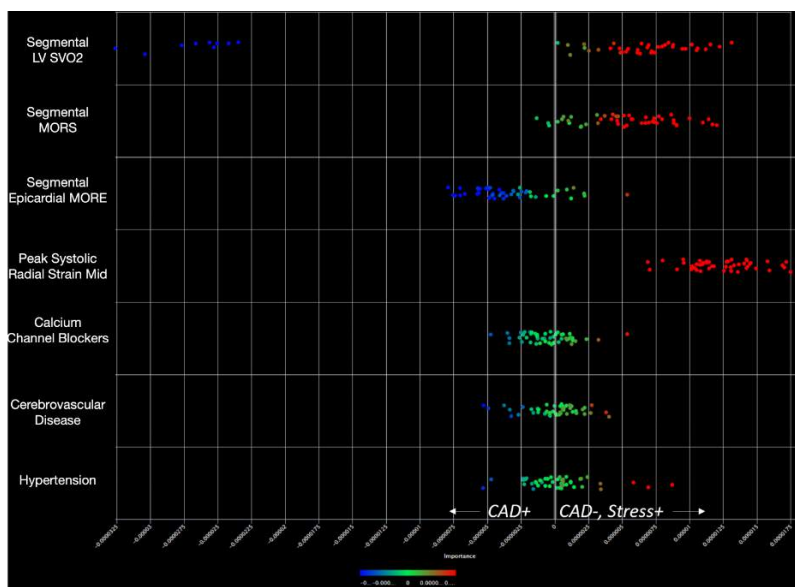
#### **Results:**

Fig. 1 shows the top discriminative features as identified by the algorithm: OS-CMR derived marker: 1) myocardial oxygen saturation (LV SVO2), 2) myocardial oxygenation in response to hyperventilation stress (MORS), and 3) epicardial myocardial oxygenation reserve (MORE). Other predictive markers were: Peak Systolic Radial Strain, treatment with calcium channel blockers, presence of cerebrovascular disease, and hypertension. The algorithm showed a 73% classification accuracy of identifying patients with or without obstructive coronary artery stenosis.

## Conclusion:

In this proof-of-concept analysis, a fully automated post-processing tool and radiomics algorithm has demonstrated the potential to accurately predict clinical classification in healthy volunteers and patients with and without significant CAD with a non-invasive, contrast-free CMR protocol. Further training and refinement of analysis algorithms are likely to further enhance the predictive value.

**Figure/Table 1**



**Caption 1**

Discriminatory value of selected features from a fully automated post-processing analysis and radiomics algorithm for identifying significant vs non-significant coronary artery stenosis from a needle-free cardiac magnetic resonance (CMR) imaging protocol including oxygenation-sensitive CMR. The position of the data points indicates their value to predict coronary artery stenosis.

### **Bibliographic References**

Herscovici R, Sedlak T, Wei J, Pepine CJ, Handberg E, Bairey Merz CN. Ischemia and No Obstructive Coronary Artery Disease (INOCA): What Is the Risk? J Am Heart Assoc. 2018 Sep 4;7(17):e008868. , Raisi-Estabragh Z, Izquierdo C, Campello VM, Martin-Isla C, Jaggi A, Harvey NC, et al. Cardiac magnetic resonance radiomics: basic principles and clinical perspectives. Eur Heart J - Cardiovasc Imaging. 2020 Apr 1;21(4):349–56. , Hillier E, Friedrich MG. The Potential of Oxygenation-Sensitive CMR in Heart Failure. Curr Heart Fail Rep [Internet]. 2021 Aug 1 [cited 2021 Sep 26]; Available from: <https://doi.org/10.1007/s11897-021-00525-y>.

Speaker: E. Hillier

Category: BOLD , coronary Artery Disease, Cardiac Syndrome X

000549

**Baseline 4D flow-derived in vivo hemodynamic parameters characterize and stratify descending aorta dissection patients with enlarging aortas**

C. Stanley \* (1); O. Kilinc (1); E. Weiss (1); J. Baraboo (2); M. Pradella (3); K. Jarvis (3); C. Mehta (4); C. Malaisrie (5); H. Andrew (6); J. Carr (7); M. Markl (8); B. Allen (3)

(1) Department of radiology, Northwestern University Feinberg School of Medicine, Chicago, United States of America; (2) Department of radiology, Northwestern University Feinberg School of Medicine, East Superior Street, Chicago, IL, USA, Chicago, United States of America; (3) Radiology, Northwestern University Feinberg School of Medicine, Chicago, United States of America; (4) Division of cardiac surgery, Northwestern University Feinberg School of Medicine, Chicago, United States of America; (5) Cardiac surgery, Northwestern University Feinberg School of Medicine, Chicago, United States of America; (6) Division of vascular surgery, Northwestern University Feinberg School of Medicine, Chicago, United States of America; (7) Radiology, Feinberg School of Medicine, Chicago, United States of America; (8) Department of radiology, feinberg school of medicine, Northwestern University, Evanston, United States of America

**Abstract**

**Background:** Increasing aorta diameter is associated with increasing morbidity, mortality, and need for surgical or endovascular intervention in patients with descending aortic dissection (DAD). Imaging-based risk-stratification has been limited to evaluation of baseline aortic diameter and diameter increase in follow-up. However, there is emerging evidence that quantitative assessment of true and false lumen (TL and FL) aorta hemodynamics in vivo may better capture the physiologic drivers of adverse outcomes in DAD (1,2). Our study used 4D flow (4DF) MRI to quantify the in vivo volumetric TL and FL kinetic energy (KE), maximum velocity (MV), as well as forward and reverse flow (FF and RF) to determine their relationship with DAD acuity, aortic growth, adverse outcomes, and subtype.

**Methods:** We retrospectively identified DAD patients who underwent standard-of care thoracic aorta MRA including 4DF MRI. Patients with prior DAD intervention were excluded. As described in figure 1, the FL and TL were manually segmented and voxel-wise mean/median KE, MV, FF, and RF were calculated. Total KE, FF and RF were calculated by summing over the cardiac cycle and then over the entire TL or FL volume. KE ratio was defined as total FL-KE/TL-KE. Maximal DAD diameters of the baseline and follow-up MRA were measured by an experienced cardiovascular radiologist. As summarized in table 1, groups were divided into 4 subcategories based on: 1) acuity:baseline acute/subacute vs. chronic dissection, 2) growth rate: < vs.  $\geq$  3 mm/year, 3) adverse outcomes: yes vs. no, and 4) subtype: true DAD vs residual DAD with prior type A dissection repair. Growth rate and adverse outcomes were only evaluated in subjects with follow-up aortic imaging (MRA or CTA) with at least 6 months of follow-up. Parameters were compared between groups, and Pearson correlation test was used to assess relationships with aortic growth rate.

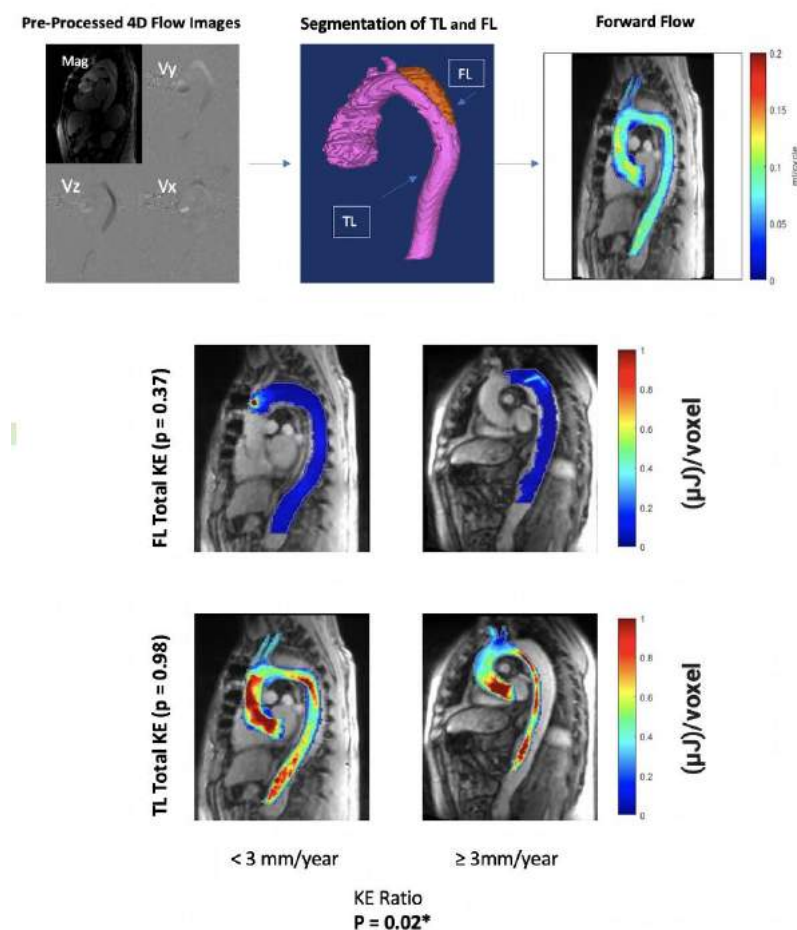
**Results:** A total of n = 39 patients met inclusion criteria (age: 60 (28-94) years, M/F: 24/15, n = 12 with connective tissue disease) and 22 patients had at least 6 months of follow-up. KE ratio was significantly higher in the growth group (p = 0.02). As summarized in table 1, total



FL-KE ( $p = 0.02$ ) and FL-FF (0.04) were significantly lower in acute/subacute patients, while total FL-RF was higher in the growth group ( $p = 0.03$ ). In the TL, median KE was higher in both the growth group ( $p = 0.04$ ) and the adverse outcomes group ( $p = 0.02$ ). TL-mean MV was higher in acute/subacute patients ( $p = 0.01$ ), the growth group ( $p = < 0.001$ ) and the adverse outcomes group ( $p = 0.02$ ). There were no differences in baseline diameter between groups. In figure 2, baseline diameter was also not correlated with aortic growth rate on Pearson correlation test ( $p = 0.72$ ). However, FL-mean FF was negatively correlated ( $r = -0.44$ ,  $p = 0.04$ ).

**Conclusion:** Our study demonstrates that FL-RF, TL-KE, TL-MV, and KE ratio could be predictors of higher aortic growth rate and/or adverse outcomes in DAD patients. In addition, FL-FF could also be used to correlate with growth rate. It is reasonable that more slow-moving RF remaining in the FL would drive growth, while our observed results in KE may reflect the impact of increased luminal dynamic pressure on aortic expansion. Our study is limited by relatively small numbers of patients with adverse outcomes which may reduce our power to detect hemodynamic differences in these groups. Our results suggest that baseline in vivo TL and FL hemodynamics may provide additional risk-stratification tools relative to standard-of-care aortic diameter measurements.

**Figure/Table 1**



**Caption 1**

4DF eddy current and velocity aliasing correction followed by segmentation of the TL/FL and hemodynamics calculation. Voxel-wise parametric maps of parameters included total KE, (shown for one patient in the growth group, one not). Total TL/FL KE did not differ between groups, but KE ratio was higher for the growth group ( $p = 0.02$ ).

**Figure/Table 2**

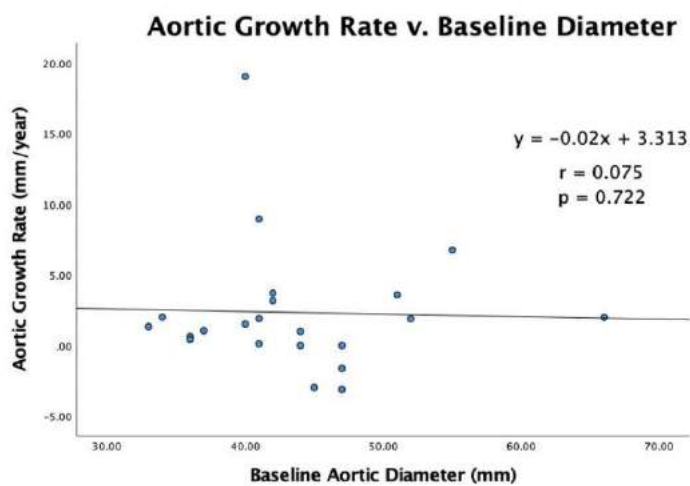
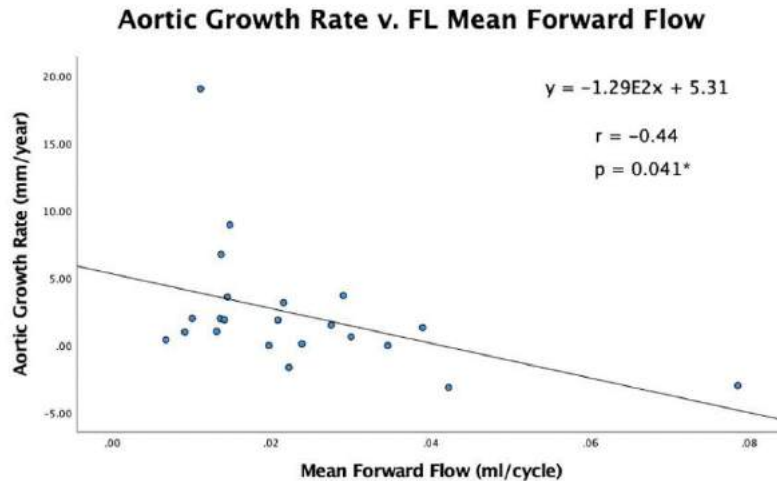
		False Lumen Parameters							
		Acuity		Growth		Adverse Outcomes		Subtype	
		Acute + Subacute (n = 9)	Chronic (n = 28)	<3mm/year (n = 16)	≥3mm/year (n = 6)	No (n = 82)	Yes (n = 10)	Red/Blue DAD (n = 28)	True DAD (n = 88)
Tot. Kinetic Energy (J)	Mean	0.01 ± 0.01	0.08 ± 0.02	0.00 ± 0.00	0.08 ± 0.02	0.02 ± 0.01	0.02 ± 0.01	0.02 ± 0.01	0.02 ± 0.01
	p-value	0.62*		0.27		0.10		0.83	
Tot. Forward Flow (ml/cycle)	Mean	2133.05 ± 1099.04	4001.12 ± 2578.43	5610.54 ± 2153.71	3592.30 ± 1335.09	3305.02 ± 1706.73	4122.23 ± 2709.00	3886.39 ± 2143.55	3110.37 ± 1469.42
	p-value	0.64*		0.44		0.10		0.39	
Tot. Reverse Flow (ml/cycle)	Mean	683.80 ± 280.50	1327.24 ± 1345.00	648.00 ± 445.01	1836.22 ± 1300.17	160.04 ± 208.54	1210.09 ± 1121.05	890.76 ± 857.45	1092.83 ± 1292.43
	p-value	0.00		0.83*		0.88		0.88	
True Lumen Parameters									
Kinetic Energy Median (J)	Mean	0.12 ± 0.07	0.17 ± 0.11	0.10 ± 0.14	0.10 ± 0.06	0.20 ± 0.07	0.20 ± 0.15	0.15 ± 0.12	0.17 ± 0.09
	p-value	0.55		0.94*		0.02*		0.40	
Peak Velocity Mean (m/s)	Mean	1.17 ± 0.27	1.39 ± 0.48	1.17 ± 0.32	1.46 ± 0.38	1.34 ± 0.34	1.51 ± 0.33	1.31 ± 0.48	1.43 ± 0.36
	p-value	0.61*		<0.001*		0.02*		0.06	
Forward Flow (ml/cycle)	Mean	2107.05 ± 1208.82	3800.90 ± 2487.47	5619.10 ± 8882.83	3191.40 ± 1101.01	4079.00 ± 3017.30	4121.40 ± 1101.01	1925.00 ± 6701.02	1183.51 ± 4711.02
	p-value	0.71		0.28		0.61		0.89	
True Lumen Specific Parameters									
KE Ratio	Mean	0.11 ± 0.12	0.10 ± 0.12	0.10 ± 0.13	0.25 ± 0.11	0.33 ± 0.11	0.20 ± 0.12	0.15 ± 0.11	0.10 ± 0.14
	p-value	0.17		0.02*		0.00		0.83	
Reverse/Forward (mm)	Mean	55.86 ± 7.97	65.97 ± 8.28	63.10 ± 8.21	45.17 ± 6.28	62.08 ± 8.28	61.00 ± 8.06	61.08 ± 7.28	48.88 ± 8.80
	p-value	0.00		0.29		0.02		0.79	

\* p < 0.05

**Caption 2**

Comparisons for: 1) DAD acuity (scan <90 vs. ≥90 d. from 1st presentation), 2) growth rate, 3) adverse outcome(s) (death, surgery, growth ≥ 3 mm/year), 4) Subtype. KE ratio, FL-tot. RF, and TL-median KE/mean MV were higher in growth group ( $p = 0.02, 0.03, 0.04, 0.01$ ). These 2 TL parameters also higher in adverse outcomes group ( $p = 0.02, <0.001$ ).

**Figure 3**



### Caption 3

Scatterplots demonstrating relationships between aortic growth rate versus FL mean forward flow (FF) and baseline diameter. Correlations are reported as Pearson's correlation coefficient. Baseline diameter was not correlated with aortic growth rate ( $p = 0.72$ ), but FL mean FF was ( $r = -0.44$ ,  $p = 0.04$ ).

### Bibliographic References

1. Jarvis K, Pruijssen JT, Son AY, Allen BD, Soulat G, Vali A, Barker AJ, Hoel AW, Eskandar MK, Malaisrie SC, Carr JC, Collins JD, Markl M. Parametric Hemodynamic 4D Flow MRI Maps for the Characterization of Chronic Thoracic Descending Aortic Dissection. *J Magn Reson Imaging*. 2020 May;51(5):1357-1368. doi: 10.1002/jmri.26986. Epub 2019 Nov 12. PMID: 31714648; PMCID: PMC7166194., 2.

Allen BD, Aouad PJ, Burris NS, Rahsepar AA, Jarvis KB, Francois CJ, Barker AJ, Malaisrie SC, Carr JC, Collins JD, Markl M. Detection and Hemodynamic Evaluation of Flap Fenestrations in Type B Aortic Dissection with 4D Flow MRI: Comparison with Conventional MRI and CTA. *Radiol Cardiothorac Imaging*. 2019 Apr;1(1):e180009. doi: 10.1148/ryct.2019180009. Epub 2019 Apr 25. PMID: 31598608; PMCID: PMC6784318.

Speaker: C. Stanley

Category: 4D Flow, Aorta, Aortic Dissection

**000550**

## **It is not all regurgitation - left ventricular dilation after pulmonary valve replacement**

N. Misra \* (1); S. Jhaveri, (2); H. Rajagopal, (2)

(1) , Cohen Children's Medical Center, 76th Avenue, New Hyde Park, United States of America; (2) Pediatric cardiology, Cohen Children's Medical Center, New Hyde Park, United States of America

### **Abstract**

#### **Description of Clinical Presentation**

26 y/o female with D-transposition of great arteries, ventricular septal defect and pulmonary stenosis underwent Rastelli Procedure with 14-mm Hancock conduit and patch closure of VSD as a neonate with conduit revision after 6 years. 19 years later, she underwent transcatheter pulmonary valve placement (TPVP) with a 26 mm Edwards-Sapien valve for severe pulmonary regurgitation and right ventricular dilatation. 2 weeks later, she presented with a wet cough and shortness of breath. She had a harsh, high pitch systolic murmur and a holo-diastolic murmur. Transthoracic echocardiogram showed trivial pulmonary regurgitation, left ventricular outflow acceleration (peak gradients of 27 mm Hg), no significant aortic regurgitation, dilated right and left ventricle with qualitative normal systolic function and bilateral pleural effusions that was confirmed on chest X-ray. She was started on diuretics with resolution of symptoms by 2 weeks.

#### **Diagnostic Techniques and Their Most Important Findings**

Cardiac MRI, 3 months post pulmonary valve replacement as per protocol showed the following:

There were significant artefacts related to Edward valve The conduit was anterior and rightward of the aorta with mild pulmonary regurgitation (RF: 13% by PC flows as compared to 48% in pre-valve replacement study).

Severely dilated right ventricle (RVEDVi: 165.4 mL/m<sup>2</sup>; z: +6.5 as compared to prior RVEDVi: 154-mL /m<sup>2</sup>; z: +5.71). Moderately decreased RV systolic function (RVEF: 35.5%; z: -4.8 compared to prior EF of 54%).

By PC flows, there was an aortic regurgitation fraction of 64% with holodiastolic flow reversal seen in the descending aorta. There was an appearance of lack of coaptation of the non-coronary cusp from distortion. There was a loss of phase artefact across the left ventricular outflow indicative of some stenosis.

Severely dilated left ventricle (LVEDVi of 241.8mL/m<sup>2</sup>; z: +7.6 - increased as compared to prior LVEDVi: of 136 mL/m<sup>2</sup>; z: 0.94). Low normal systolic function (LVEF: 56.5% - decreased as compared to prior LV EF of 69%).

Cine images showed a small continuous jet along the right wall of the ascending aorta (close to the sino-tubular junction) opposite to the valved conduit that had not been seen on comparable views in the postprocedural transthoracic echocardiogram.

Presence of aortic regurgitant fraction and left ventricular dilation, raised the concern for a fistulous connection between aorta and conduit likely from the newly placed Sapien valve.

Repeat echocardiogram confirmed the findings of a fistula between the right side of the aorta, and the RV-PA conduit that appeared to involve the site of the stent.

### **Diagnostic Techniques and Their Most Important Findings**

She underwent repair of the aorta-conduit fistulous connection, pulmonary valve replacement (25mm valve) and right ventricular outflow tract augmentation. She has done well subsequently with follow-up CMR showing improvement in biventricular values and ejection fractions. Aorta to conduit fistula after TPVP is a rare complication; the likely cause being trauma from angioplasty or stenting of the RV outflow with subsequent dissection into the closely adjacent vessel through the devitalized tissue. A high level of suspicion is required to diagnose this unusual complication early. This case highlights the importance of CMR analysis of volumes and flows after TPVP, thus assisting in proper surgical and clinical management of the patient.

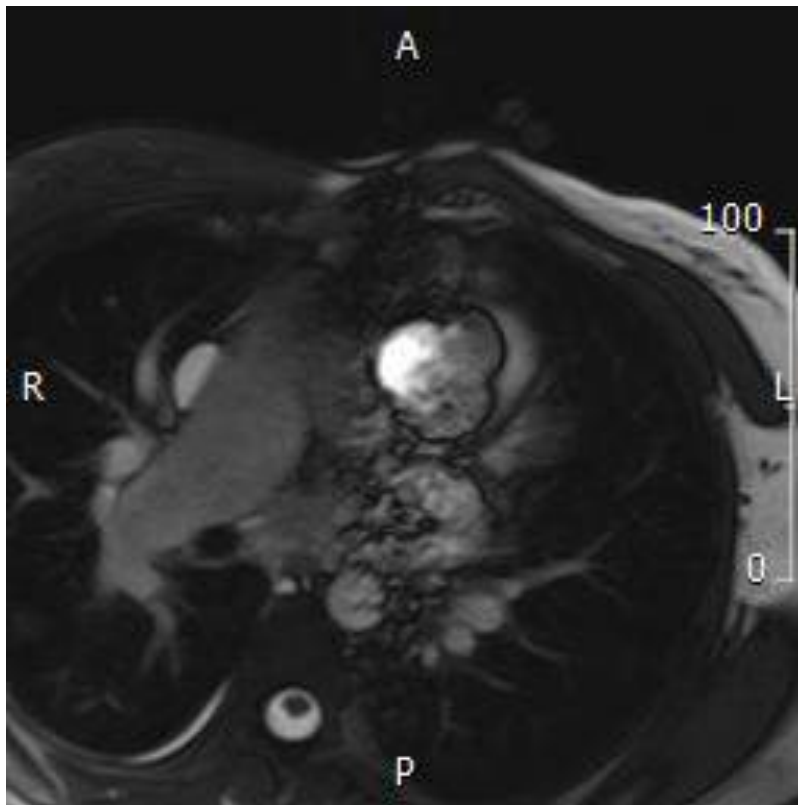
**Figure/Table 1**



**Caption 1**

LV outflow view showing the jet in the pulmonary artery to the right of the aorta.

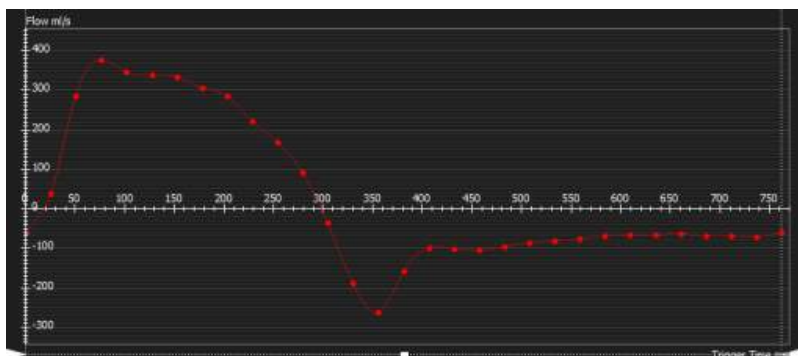
**Figure/Table 2**



**Caption 2**

Cine SSFP showing valved conduit anterior to aorta just below sternum and distortion of the non coronary cusp of aorta

**Figure 3**



**Caption 3**

Holodiastolic flow reversal seen in the descending aorta (PC flow imaging)

### **Bibliographic References**

1. Petra Loureiro, José F. Martins, Alain Fraisse, Rui Rodrigues, José Fragata, Fátima F. Pinto, Iatrogenic fistula between the aorta and the right ventricular outflow tract after Melody valve implantation: Case report and literature review, *Revista Portuguesa de Cardiologia*, 10.1016/j.repc.2018.09.016, (2020)., Kenny D, Holoshitz N, Turner D, Hijazi ZM. Aortopulmonary fistula after transcatheter pulmonary valve replacement. *Circ Cardiovasc Interv*. 2013 Dec;6(6):e67-8. doi: 10.1161/CIRCINTERVENTIONS.113.000654. PMID: 24347658.

Speaker: N. Misra

Category: Pulmonary Valve Replacement, Aortic Regurgitation, Ventricular Dysfunction



000552

## Apical ischaemia – a hallmark feature in apical hypertrophic cardiomyopathy

R. Hughes \* (1); J. Augusto (1); K. Knott (1); A. Seraphim (1); G. Joy (2); S. Mohiddin (3); G. Captur (1); L. R. Lopes (1); P. Kellman (4); J. Moon (1)

(1) Institute of cardiovascular sciences, University College London, London, United Kingdom; (2) Institute of cardiovascular sciences, University College London, Gower Street, London, United Kingdom; (3) Barts heart centre, St Bartholomew's Hospital, London, United Kingdom; (4) National institutes for health, NHLBI, Bethesda, United States of America

### Abstract

#### Background

Perfusion defects have been described in up to 79% of cases of hypertrophic cardiomyopathy (HCM) and are attributable to small vessel disease and associated microvascular ischaemia. Apical HCM (ApHCM) appears distinct from other HCM phenotypes in terms of its genotyping, risk and natural course. Furthermore, the ECG features (giant negative T-waves) point towards ischaemia playing a central role. Clinically, apical hypoperfusion is frequently observed in ApHCM. We hypothesised that quantitative perfusion would be different and distinct in apical HCM.

#### Methods

100 subjects with ApHCM, 50 with septal HCM and 28 healthy volunteer controls underwent perfusion mapping CMR at 1.5T using adenosine vasodilator stress. A visual read plus global and regional map segmentation was performed, with results expressed as myocardial blood flow (MBF, ml/g/min) and myocardial perfusion reserve (MPR). 33 of the ApHCM had 'relative ApHCM' – MWT<15mm but other key features of the disease – typical ECG, apex thicker than septum with loss of apical tapering and apical systolic cavity obliteration.

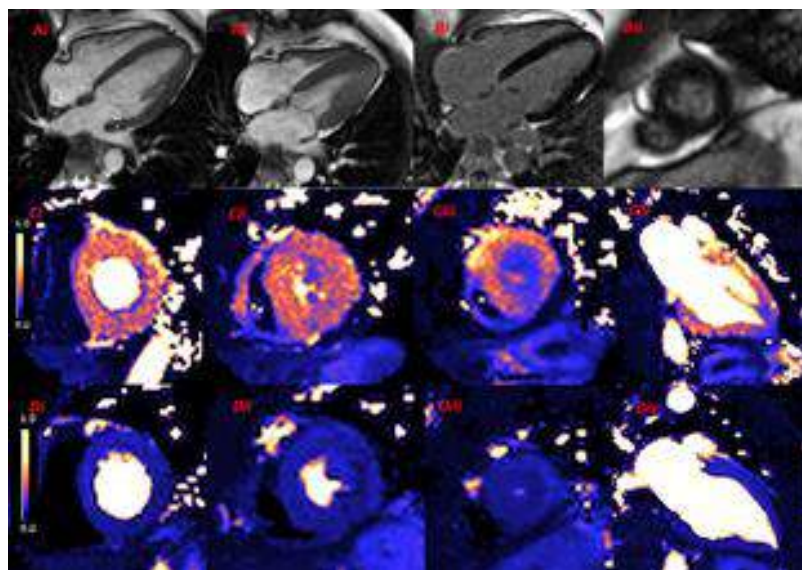
#### Results

All ApHCM subjects (100/100) had apical perfusion defects. Perfusion defects in septal HCM was higher than previously reported (45/50, 90%,  $p=0.012$ ); typically in hypertrophied areas. There were no defects in controls ( $P<0.005$ ). Global stress MBF in ApHCM was equivalent to HCM (mean (IQ range) 1.71ml/g/min (1.5-2.1) vs 1.61ml/g/min (1.3-2.1),  $P=0.44$ ) and lower than controls (2.59ml/g/min (2.3-3.0),  $P<0.005$ ). The reduction in MBF was most pronounced in the apical segments in ApHCM vs HCM (1.27ml/g/min (1.0-1.6) vs 1.59ml/g/min (1.3-2.1ml/g/min),  $P<0.005$ ) and controls (2.54ml/g/min (2.3-3.4),  $P<0.005$ ). The defects were profound, with stress flow *lower* than rest in the apical subendocardium in 27% cases. Flow reductions were less for relative ApHCM than overt ApHCM (apical stress MBF 1.55ml/g/min (1.4-2.0) vs 1.20ml/g/min (0.95-1.5),  $P<0.005$ ), but lower than controls ( $P<0.005$ ). Apical stress MBF correlated negatively with amount/% of LGE (FWHM;  $R=-0.312$ ,  $P<0.005$ /  $R=-0.251$ ,  $P=0.016$  respectively) and with the presence of apical aneurysm ( $R=-0.233$ ,  $P=0.022$ , identified in 31/100 subjects).

#### Conclusions

Apical microvascular ischaemia is a defining feature of ApHCM, even occurring before overt hypertrophy.

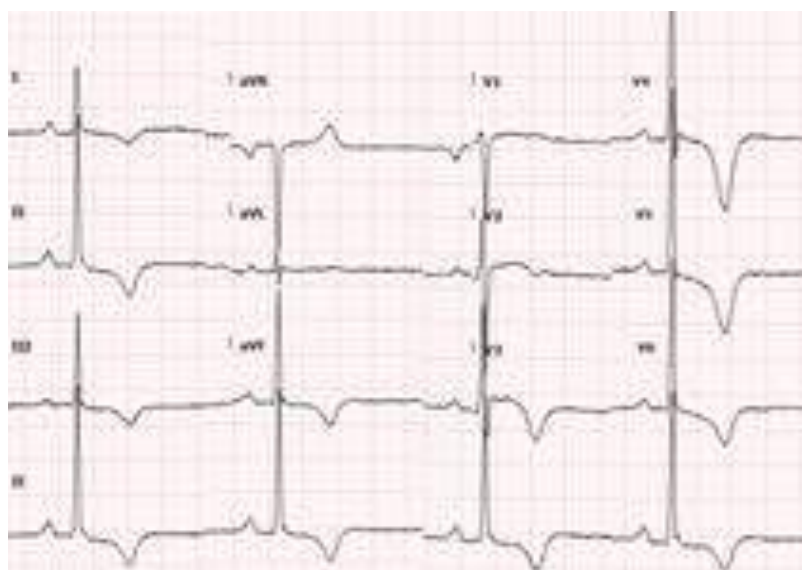
**Figure/Table 1**



**Caption 1**

Perfusion in subtle relative ApHCM. 4-chamber cine in diastole (Ai) showing loss of apical tapering and in end-systole (Aii), apical cavity obliteration. Limited apical LGE shown in the 4-chamber (Bi) and short axis (Bii). Adenosine stress perfusion mapping (Ci-iv) showing a dense perfusion defect apically compared to rest, (Di-iv).

**Figure/Table 2**



## **Caption 2**

Corresponding ECG in patient with subtle relative apical hypertrophic cardiomyopathy demonstrating characteristic giant negative T-waves.

Speaker: R. Hughes

Category: Apical Hypertrophic Cardiomyopathy, Perfusion, Phenotype

**000553**

## **Coronary embolism a rare cause of myocardial infarction**

I. Minga \* (1); K. Hussain (2); S. Gaznabi (2); A. Pursnani (3); J. Rosenberg (2)

(1) Cardiology, UChicago Medicine, Chicago, United States of America; (2) Cardiology, NorthShore Evanston Hospital, Evanston, United States of America; (3) Cardiology, UChicago Medicine at NorthShore University HealthSystem - Evanston, Evanston, United States of America

### **Abstract**

#### **Description of Clinical Presentation:**

A 28-year-old female with no significant past medical history presents with crushing chest pain with exertion. Her medications include an oral contraceptive pill (norgestimate ethinyl estradiol). Her initial EKG showed normal sinus rhythm without any other abnormalities. Her troponin was elevated to 66 ng/L and peaked at 967 ng/L. She denies any symptoms with activity prior. She does not have any risk factors for coronary artery disease and denies any family history of heart disease

#### **Diagnostic Techniques and Their Most Important Findings:**

Echocardiogram showed a normal left ventricular ejection fraction of 60% with no wall motion abnormalities. A cardiac computed tomography with fractional flow reserve analysis was normal and did not demonstrate any obstructive lesions. Cardiac magnetic resonance imaging demonstrated a transmural late gadolinium enhancement in the mid-basal anterior wall consistent with recent myocardial infarction. Cardiac catheterization did not demonstrate any obstructive lesions in the main coronary arteries or small branches. Lower extremity Doppler's and ultrasound did not reveal any evidence of deep vein thrombosis. Echocardiogram was repeated with bubble studies and bubbles were seen crossing over from the right atrium to the left atrial after 3 heart beats consistent with a patent foramen ovale (PFO) This was confirmed with a transesophageal echocardiogram that demonstrated right to left flow of agitated saline bubbles and color Doppler get with left to right flow. . Her coronary embolism was thought to a clot crossing from her PFO and occluding a small branch that was unable to be visualized with angiography. . PFO closure was achieved with a 25 mm Gore Cardioform occluder. Her hypercoagulability testing was negative. She was managed with Plavix and apixaban for antiplatelet and anticoagulation therapy.

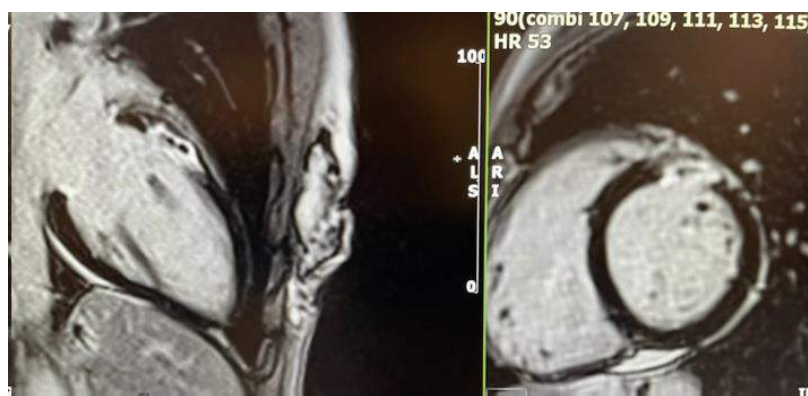
#### **Learning Points from this Case:**

Coronary embolism is a rare cause of myocardial infarction. The most common sources of coronary embolism include atrial fibrillation, valvular abnormalities, deep vein thrombosis and PFO. It represents an important cause of nonatherosclerotic myocardial infarction.

Prevalence of ST segment elevations myocardial infarction from coronary embolism ranges between 4-13%. It is important to keep coronary embolism as part of the differential diagnosis in myocardial infarctions especially in the absence of obstructive coronary atherosclerosis. Identifications of coronary embolism as a source of myocardial infarction has treatment implications. Percutaneous interventions can be very challenging due to risk of distal migrations. Medication treatments and follow up also can be altered based on the source of coronary embolism and extent of myocardium involved.

While this remain a rare cause of myocardial infarction, clinical acumen and multimodality imaging are necessary to reach the accurate diagnosis. Identification of coronary embolism as a source of myocardial infarction has long term treatment and management implications.

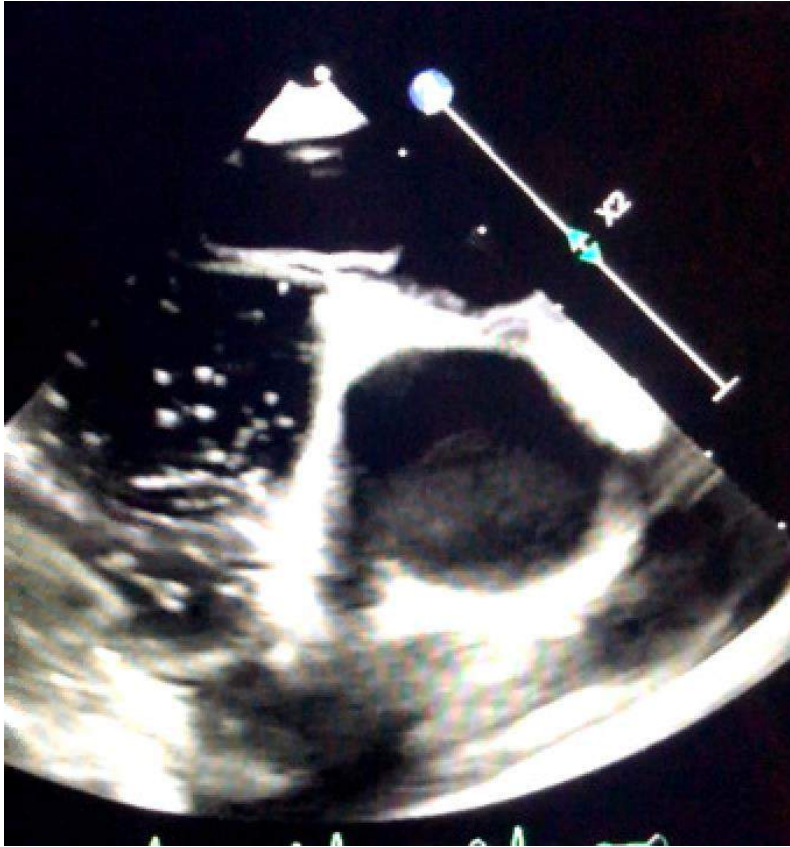
**Figure/Table 1**



**Caption 1**

Cardiac MRI demonstrating subendocardial/nearly transmural late gadolinium enhancement in the mid-basal anterior wall. There is also evidence of microvascular obstruction in this territory. These findings are consistent with myocardial infarction

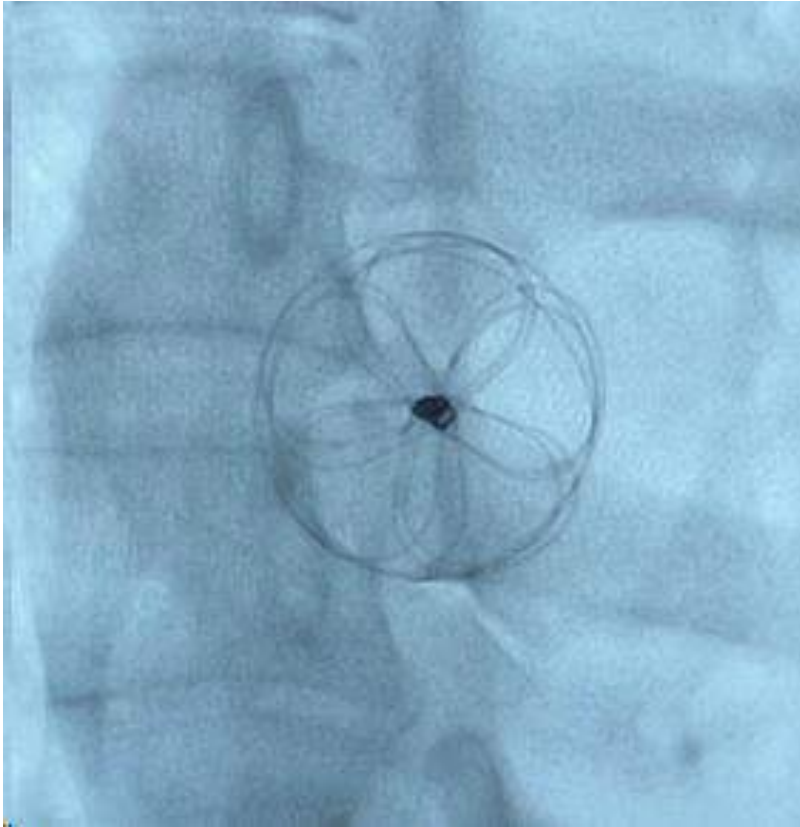
**Figure/Table 2**



### **Caption 2**

Transesophageal echocardiogram demonstrating presence of patent foramen ovale with crossing over of bubbles in the 3rd heart beat

### **Figure 3**



5

### **Caption 3**

X ray image of PFO device closure

Speaker: I. Minga

Category: Acute Myocardial Infarction, Patent Foramen Ovale, Coronary Arteries

000556

## Rare CAT: Calcified amorphous tumour (CAT) of the heart

A. Kini \* (1); C. Dennie (2)

(1) Radiology, The Ottawa Hospital General Campus, Ottawa, Canada; (2) Radiology, Université d'Ottawa, Ottawa, Canada

### Abstract

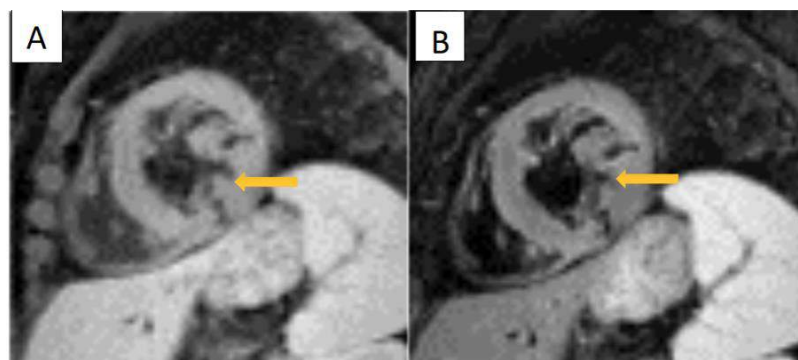
Description of Clinical Presentation: 64 year female presenting with multiple transient ischemic attack (TIAs) like episodes.

Diagnostic Techniques and Their Most Important Findings: ECG shows sinus rhythm. Transoesophageal echocardiography demonstrates a large, echogenic mass at the level of and involving the left ventricular (LV) papillary muscles, protruding into and decreasing the LV cavity size. Cardiac MRI (CMRI) demonstrates hypointense masses around the papillary muscles on T1 and T2 fat-suppressed images with no enhancement on the late gadolinium enhancement (LGE) images. Hypointense areas are seen protruding into the LV cavity. On CT coronary angiography, there is dense calcification around the papillary muscles and in the LV cavity.

Learning Points from this Case: Cardiac calcified amorphous tumour (CAT) is a rare benign, intracavitary tumour of the heart and is a rare cause of cardioembolic stroke. Less than 100 cases have been described in the literature. It can occur in any cardiac chamber, but is most common in the left ventricle and mitral valve. These are often associated with valvular heart disease, mitral annular calcification, diabetes, coronary artery disease and end-stage renal disease. They tend to be highly mobile and more likely to embolize. Treatment usually involves surgical resection. Anticoagulation therapy and long-term follow-up is an alternative to surgical resection. Histologically it is composed of nodular calcium deposits within fibrinous material.

The history of recurrent TIAs and left ventricular intracavitary calcified mass, favours the diagnosis of CAT. The patient was treated with Coumadin and low dose aspirin therapy.

### Figure/Table 1

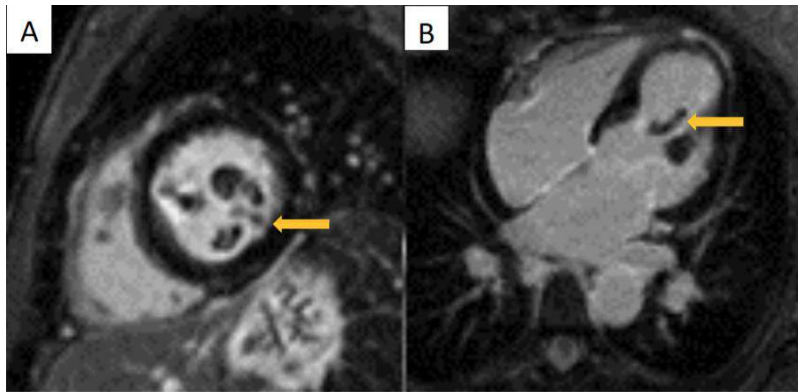


Caption 1



Figure 1 – A. Short-axis T1-weighted and B. T2-weighted fat suppressed images at the level of the mid cavity demonstrates hypointense areas to the myocardium around the anterolateral and posteromedial papillary muscles and within the LV cavity (orange arrows)

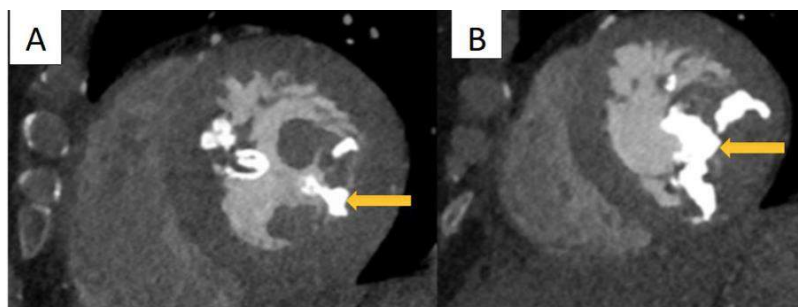
**Figure/Table 2**



**Caption 2**

Figure 2 – A. Short-axis at the level of the mid cavity and B. 4-chamber LGE images demonstrate non-enhancing masses around the anterolateral and posteromedial papillary muscles and within the LV cavity (orange arrows)

**Figure 3**



**Caption 3**

Figure 3 – A & B. Short-axis at the level of the mid cavity CT demonstrates dense calcification around the anterolateral and posteromedial papillary muscles and within the LV cavity (orange arrows)

## **Bibliographic References**

5. Choi EK, Ro JY, Ayala AG. Calcified Amorphous Tumour of the Heart: Case Report and Review of the Literature. *Methodist DeBakey Cardiovascular Journal*. 2014 Jan 1; 10(1):38., 4. De Hemptinne Q, de Cannière D, Vandenbossche J-L, Unger P. Cardiac calcified amorphous tumour: A systematic review of the literature. *IJC Heart & Vasculature*. 2015 Jun; 7:1–5., 3. Kyaw K, Latt H, Aung SSM, Roongsritong C. A Case of Cardiac Calcified Amorphous Tumour Presenting with Concomitant ST-Elevation Myocardial Infarction and Occipital Stroke and a Brief Review of the Literature. *Case Reports in Cardiology*. 2017; 2017:1–4., 2. Shah AC, Marcoff L, Talati S, Donahue J, Uretsky S, Magovern C, et al. A Rare Beast: Cardiac Calcified Amorphous Tumour. *CASE*. 2018 Aug; 2(4):139–41., 1. Formelli B, Farina A, Pescini F, Palumbo V, Grazia D'Alfonso M, Oddo A, et al. Cardiac Calcified Amorphous Tumour as a Rare Cause of Ischemic Stroke: Clinical Case. *Circ: Cardiovascular Imaging* [Internet]. 2020 Jan [cited 2021 Sep 26]; 13(1). Available from: <https://www.ahajournals.org/doi/10.1161/CIRCIMAGING.119.009623>

Speaker: A. Kini

Category: Calcification, Cardiac Mass, Papillary Muscle

000557

## Reduced Feature-Tracking Myocardial Strain and late gadolinium enhancement are Independent Predictors of Long-Term Outcome in Patients with Normal Left Ventricular Systolic Function

K. Fujikura \* (1); J. Weber, (2); N. Fouladi Nashta (2); N. Ngai, (2); J. Craft (1); K. Quijano (2); S. Rao (2); J. Scheiner (2); M. Passick (2); J. J. Cao (1)

(1) Cardiac imaging, St. Francis Hospital & Heart Center, Roslyn, United States of America;  
(2) Cardiac imaging, De Matteis Center-Cardiac Research, Greenvale, United States of America

### Abstract

**Background:** Reduced global longitudinal strain (GLS) has been found in patients with heart failure with preserved ejection fraction (HFpEF) (1). However, such risk has not been fully examined in patient population with normal left ventricular ejection fraction (LVEF). In addition, the relationship of reduced strain and myocardial scar are unknown in this population. In this study we aimed to investigate the relationship of reduced strain with myocardial scar and its associated adverse outcome in patients with normal LVEF using CMR.

**Methods:** Consecutive patients with LVEF  $\geq 50\%$  who underwent echocardiography and CMR within 1 month at our institution between 2010 and 2019 were analyzed in this study. Outcome of the patients were assessed by chart review for HF admission and by National Death Index for all-cause death. Composite adverse outcome was also assessed defined as either HF admission or all-cause death. Volumetric assessment was performed on steady-state free precession (SSFP) cine imaging. Myocardial scar was assessed using late gadolinium enhancement (LGE) which was visually evaluated. Feature-tracking analysis was performed on SSFP cine images to evaluate global longitudinal (GLS), circumferential (GCS), and radial strain (GRS). Normal strain values were derived using healthy controls in our institution (2,3). Strain values below 2 standard deviations of normal were defined as abnormal. Cox proportional hazards models were created to estimate hazards of composite outcome in unadjusted and adjusted models. Kaplan-Meier curve was used to estimate event-free survival.

**Results:** Total 550 patients (59 % male, age  $55 \pm 16$  years, BMI  $26.3 \pm 7.9$  kg/m<sup>2</sup>) were included in the analysis. The average LVEF was  $58 \pm 6$  % and RVEF was  $57 \pm 7$  %. LGE was present in 184 patients (33 %) with a non-ischemic pattern in 149 patients and an ischemic pattern in 35 patients. During a mean follow-up duration of 4 years, 83 patients (15 %) developed adverse outcome: 46 HF admission and 53 all-cause death. Reduced strains were present in 86 patients (36 %) in GLS, 58 patients (26 %) in GCS, and 35 patients (16 %) in GRS. All of the global strain values were significantly reduced in patients with LGE (GLS,  $-13.7 \pm 3.3$  vs.  $-12.0 \pm 3.7$ ; GCS,  $-16.7 \pm 3.5$  vs.  $-15.0 \pm 3.8$ ; GRS,  $27.8 \pm 8.5$  vs.  $24.0 \pm 8.6$  (all  $p < 0.001$ )). Using adjusted and unadjusted Cox proportional hazards models, reduced GLS, GCS and GRS showed significant associations with increased hazards of adverse outcome (Table). Patients with LGE also showed significantly increased hazards for outcome. The Kaplan-Meier curves using GLS as an example showed that the event-free survival was significantly decreased in patients with reduced GLS with or without LGE (Figure). However,

among patients with preserved strain those with LGE were associated with a reduced event-free survival. There were no significant multiplicative interactions between GLS and LGE in adverse outcomes.

**Conclusions:** Among patients with normal LVEF reduced longitudinal, circumferential and radial strain as well as the presence of LGE are all associated with increased risk of adverse clinical outcome. Those with LGE are more likely to have reduced strain. Our findings suggest that the assessment of myocardial strain and LGE is important in risk stratification for patients with normal LVEF.

**Figure/Table 1**

Variables	Unadjusted		Adjusted**		Adjusted***	
	<i>HR</i>	<i>(LL, UL)</i>	<i>HR</i>	<i>(LL, UL)</i>	<i>HR</i>	<i>(LL, UL)</i>
GLS per %	1.11*	(1.10, 1.15)	1.24*	(1.17, 1.31)	1.15*	(1.11,1.20)
GCS per %	1.07*	(1.03, 1.12)	1.20*	(1.13, 1.28)	1.30*	(1.10, 1.17)
GRS per %	0.97*	(0.95, 0.99)	0.93*	(0.90, 0.96)	0.93*	(0.90, 0.96)
LGE(+)	2.47*	(1.61, 3.81)	2.26*	(1.43, 3.58)	2.28*	(1.41, 3.69)

\*Significant at p<0.05 level

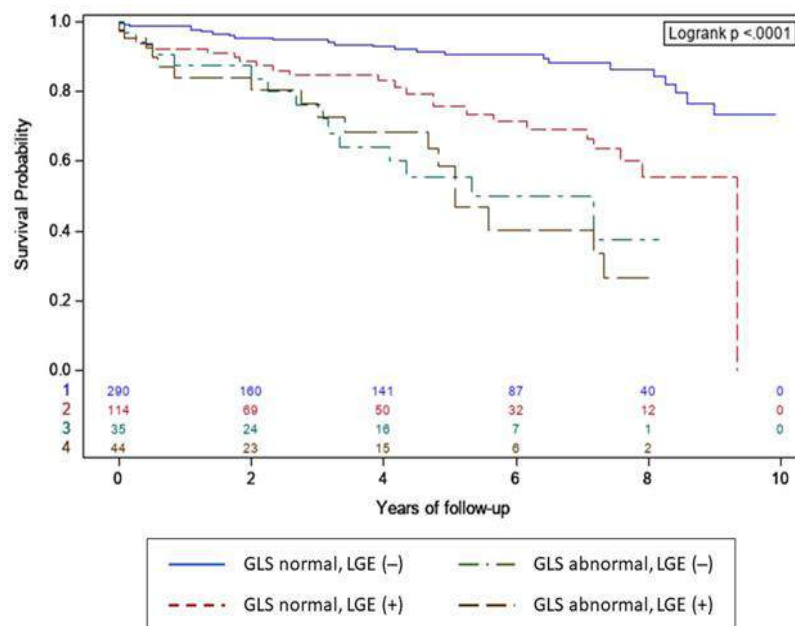
\*\*Adjusted for age and gender

\*\*\*Adjusted for age, gender, diabetes, hypertension

**Caption 1**

**Table.** Cox proportional hazard model for composite outcome.

**Figure/Table 2**



## Caption 2

**Figure.** Kaplan-Meier survival curves stratified by GLS and LGE.

## Bibliographic References

Cao JJ, Ngai N, Duncanson L, Cheng J, Gliganic K, Chen Q. A comparison of both DENSE and feature tracking techniques with tagging for the cardiovascular magnetic resonance assessment of myocardial strain. *J Cardiovasc Magn Reson*. 2018;20:26. doi: 10.1186/s12968-018-0448-9., Jin C, Weber J, Singh H, Gliganic K, Cao JJ. The association of reduced left ventricular strains with increased extracellular volume and their collective impact on clinical outcomes. *J Cardiovasc Magn Reson*. 2021;23:93. doi: 10.1186/s12968-021-00776-7., Halliday BP, Senior R, Pennell DJ. Assessing left ventricular systolic function: from ejection fraction to strain analysis. *Eur Heart J*. 2021;42:789-797. doi: 10.1093/eurheartj/ehaa587.

Speaker: K. Fujikura

Category: Feature Tracking, Late Gadolinium Enhancement, Prognosis

000558

## A bSSFP sequence and image analysis package for automated inline myocardial perfusion quantification

X. Milidonis \* (1); S. McElroy (1); K. Kunze (2); R. Crawley (1); S. Roujol (1); R. Neji (2); A. Chiribiri (1)

(1) School of Biomedical Engineering & Imaging Sciences, King's College London, London, United Kingdom; (2) MR Research Collaborations, Siemens Healthcare Limited, Frimley, United Kingdom

### Abstract

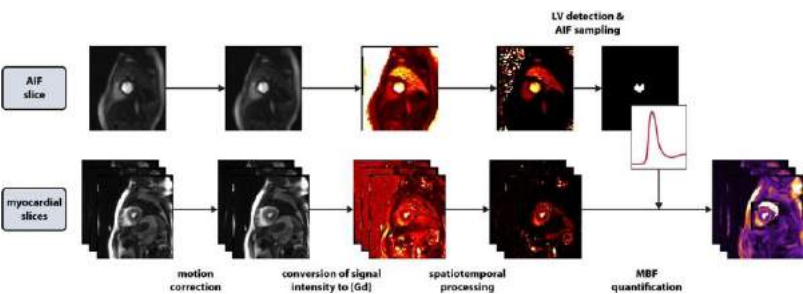
**Background:** Myocardial first-pass perfusion quantification has been established as an invaluable technique for the assessment of coronary artery disease (CAD) and has the potential for becoming a first-line tool for clinical diagnosis and treatment guidance [1]. However, the clinical translation of perfusion quantification is still hampered by its reliance on complicated pipelines and external hardware or software that may prolong processing time and image interpretation. In this study, we present a fully automated pipeline for fast inline myocardial perfusion quantification implemented on a 1.5T system in the vendor's reconstruction environment. The package was tested on patients referred to our cardiac MR service for myocardial stress perfusion assessment.

**Methods:** An ECG-triggered dual-sequence perfusion acquisition was developed and implemented on a Siemens Aera 1.5T system (software version VE11C; Siemens Healthcare, Erlangen, Germany). The sequence acquires a low resolution arterial input slice (FLASH readout, linear k-space ordering, TR 1.12 ms, TE 0.65 ms, saturation recovery time 47 ms, flip angle 8°, resolution 5.6×5.6 mm<sup>2</sup>, slice thickness 10 mm) and three high resolution myocardial slices through the basal, mid and apical LV cavity (bSSFP readout, linear k-space ordering, TR 2.42 ms, TE 1.02 ms, saturation recovery time 89 ms, flip angle 50°, resolution 2×2 mm<sup>2</sup>, slice thickness 10 mm, parallel imaging acceleration: GRAPPA 3) during free breathing. A single contrast bolus at 0.05 mmol/kg is intravenously injected. Acquired images are passed through a C++ data analysis package implemented fully in the scanner's reconstruction environment (Siemens ICE). It performs automated motion correction, conversion of signal intensity to gadolinium concentration using a signal dictionary created using Bloch simulations of the sequence, detection of the left ventricle and extraction of an arterial input function, spatiotemporal processing to prepare data for fitting, and pixelwise quantification of absolute myocardial blood flow (MBF) using Fermi function-constrained deconvolution [2] (Figure 1). For validation, 23 patients with previous coronary imaging via either computed tomography or invasive coronary angiography were assessed. Global MBF was measured based on manual segmentation of the endocardial and epicardial boundaries.

**Results:** Global stress and rest MBF (rest perfusion performed in 18/23 patients, 78%) was 2.72±0.71 mL/g/min and 1.30±0.25 mL/g/min respectively, in agreement with previously published values [3,4]. Pixelwise MBF maps for all three myocardial slices were generated in approximately 20 seconds after the end of image acquisition. Figure 2 shows stress MBF maps for an example case.

**Conclusions:** A prototype package for automated inline myocardial perfusion quantification without user interaction was developed and tested, generating pixelwise MBF maps in a few seconds. The package shows promise for the assessment of CAD and could assist clinical diagnosis and treatment guidance. We are currently testing the package on additional scanners and software versions and in other patient cohorts in order to establish its feasibility for widespread deployment.

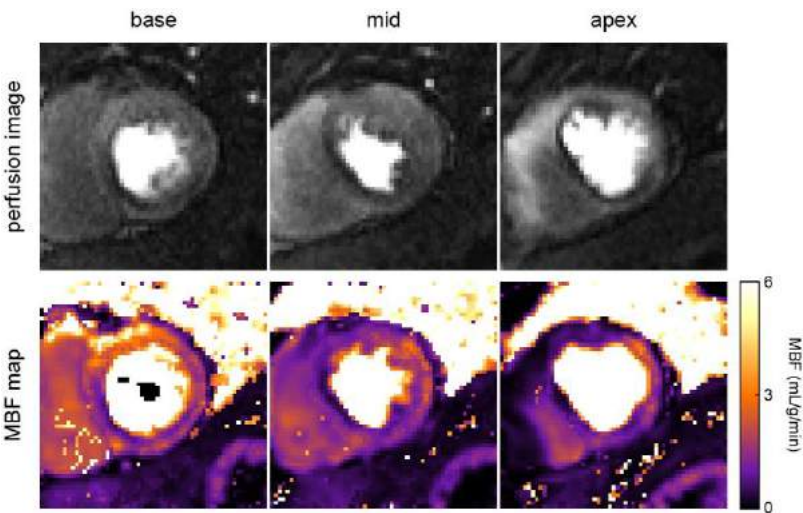
Figure/Table 1



Caption 1

Schematic diagram of the automated inline perfusion quantification pipeline implemented in the Siemens reconstruction environment ICE. Motion corrected images, gadolinium concentration images and pixelwise MBF maps are produced in DICOM format and can be viewed directly on the scanner console.

Figure/Table 2



Caption 2

Quantitative perfusion in a 60 year old male patient. ICA indicated previous mid LAD occlusion, recent RCA infarct and a critical lesion within the proximal first OM branch of LCx. LGE imaging showed scar in the inferior wall. The MBF map (mean 1.42 mL/g/min) is suggestive of basal lateral wall ischemia which was not identified on visual assessment.

### **Bibliographic References**

1. Villa ADM, Corsinovi L, Ntalas I, Milidonis X, Scannell C, Di Giovine G et al. Importance of operator training and rest perfusion on the diagnostic accuracy of stress perfusion cardiovascular magnetic resonance. J Cardiovasc Magn Reson. 2018;20:74., 2. Milidonis X, Franks R, Schneider T, Sanchez-Gonzalez J, Sammut EC, Plein S et al. Influence of the arterial input sampling location on the diagnostic accuracy of cardiovascular magnetic resonance stress myocardial perfusion quantification. J Cardiovasc Magn Reson. 2021;23:35., 3. Biglands JD, Magee DR, Sourbron SP, Plein S, Greenwood JP, Radjenovic A. Comparison of the Diagnostic Performance of Four Quantitative Myocardial Perfusion Estimation Methods Used in Cardiac MR Imaging: CE-MARC Substudy. Radiology. 2015;275:393-402., 4. Rahman H, Scannell CM, Demir OM, Ryan M, McConkey H, Ellis H et al. High-Resolution Cardiac Magnetic Resonance Imaging Techniques for the Identification of Coronary Microvascular Dysfunction. JACC Cardiovasc Imaging. 2020.

Speaker: X. Milidonis

Category: Automated Processing, coronary Artery Disease, First-Pass Perfusion



000560

## **Four-dimensional phase contrast MRI with accelerated dual velocity encoding in patients with complex congenital heart disease**

L. Kalifa, \* (1); A. Fels, (1); G. Chatelier, (1); E. Gouverneur, (2); Y.-W. Kim, (1); F. Bouhajja, (1); M. Zins, (1); A. Azarine (1)

(1) Radiology, Hospital Paris Saint-Joseph, PARIS; (2) 75, Arterys , paris

### **Abstract**

#### **Background :**

Increase use of four-dimensional (4-D) flow MRI has been recently noted to assess congenital heart disease (CHD). In patients with complex CHD we may have to assess flows of different level of velocities, but classical 4D Flow MRI sequence enable only one velocity encoding (Venc) choice: if set too low we may have aliasing artifact, if set too high the dataset may be hampered by a high level of noise. The aim of our study was to test the feasibility of a dual-velocity encoding (Dual-Venc) 4D Flow MR prototype sequence to assess various vascular flows in CHD patients.

#### **Methods:**

Routine cardiac MRI was performed in 17 young adults mostly followed for complex congenital heart disease on a 3T Magnet MRI (Discovery MR 750, GEMS). The usual 4D flow sequence has been replaced by a Kt-ARC accelerated prototype sequence, using two different velocity encoding (venc) with High-Venc / Low-Venc set to 300/100 cm/s; temporal / spatial resolution = 40-45msec /  $2 \times 2 \times 2.2 \text{ mm}^3$ , after a triphasic gadolinium-based contrast agent injection (Gadovist, Bayer, Germany). MRI data was anonymized and sent to a cloud-based software (Arterys). After automatic phase offsets and background correction, a simultaneous analysis of the two separate 4D flow volumes, at high and low Venc, was performed. Velocity-to-noise ratio (VNR), peak velocity and Forward flow were compared between high and low Venc measurements for different vessels: superior and inferior vena cava, pulmonary veins, aorta, portal and hepatic veins. All patients were informed and signed a consent to test the prototype sequence.

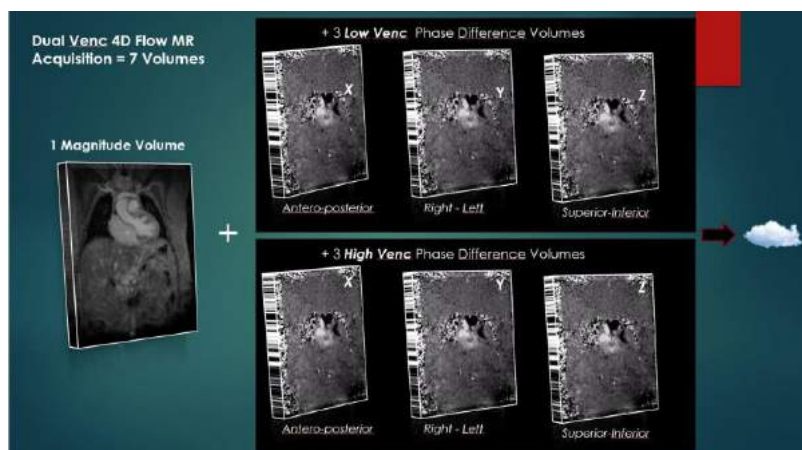
#### **Results:**

All MRIs were successfully acquired in a mean scan time of  $15 \pm 4$  minutes, reducing total scan time by 33% compared to two separate acquisitions. Cloud-based data post-processing enabled simultaneous real-time analysis of the two heavy 4D-flow datasets at low and high Venc. Aliasing artifact occurred more often for arterial measurements performed at low Venc. VNR at low Venc was always significantly better compared to high Venc (average factor of 1,6). The variability of instantaneous Net flow measurements was significantly higher at High Venc than at Low Venc ( $p < 0,05$ , test F) for veins, especially for low velocity and medium caliber veins.

#### **Conclusion :**

Kt-Arc accelerated Dual-Venc 4D Flow MR sequence is particularly well suited for the follow-up of patients with complex congenital heart disease with challenging flows to measure, as it enables optimal assessment of a wide dynamic velocity range of flows, avoiding the risk of aliasing for high-velocity flows while ensuring a good velocity-to-noise ratio for low velocity flows.

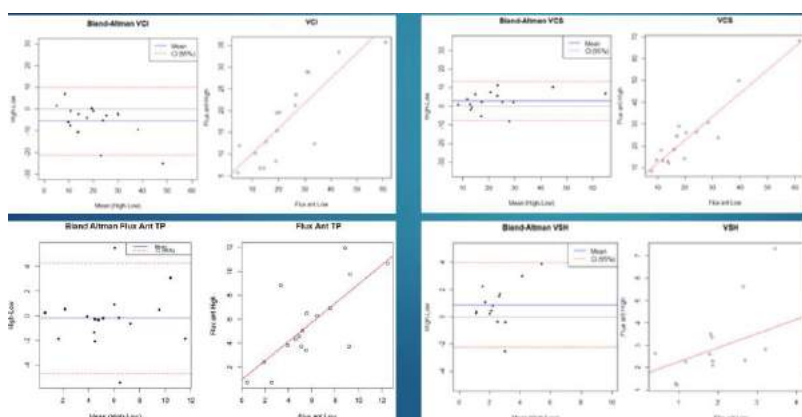
**Figure/Table 1**



**Caption 1**

Dual Venc Datasets are made of 7 volumes: 1 common magnitude volume and 3 phase contrast volumes encoded in the 3 different directions of space at High and at low Venc.

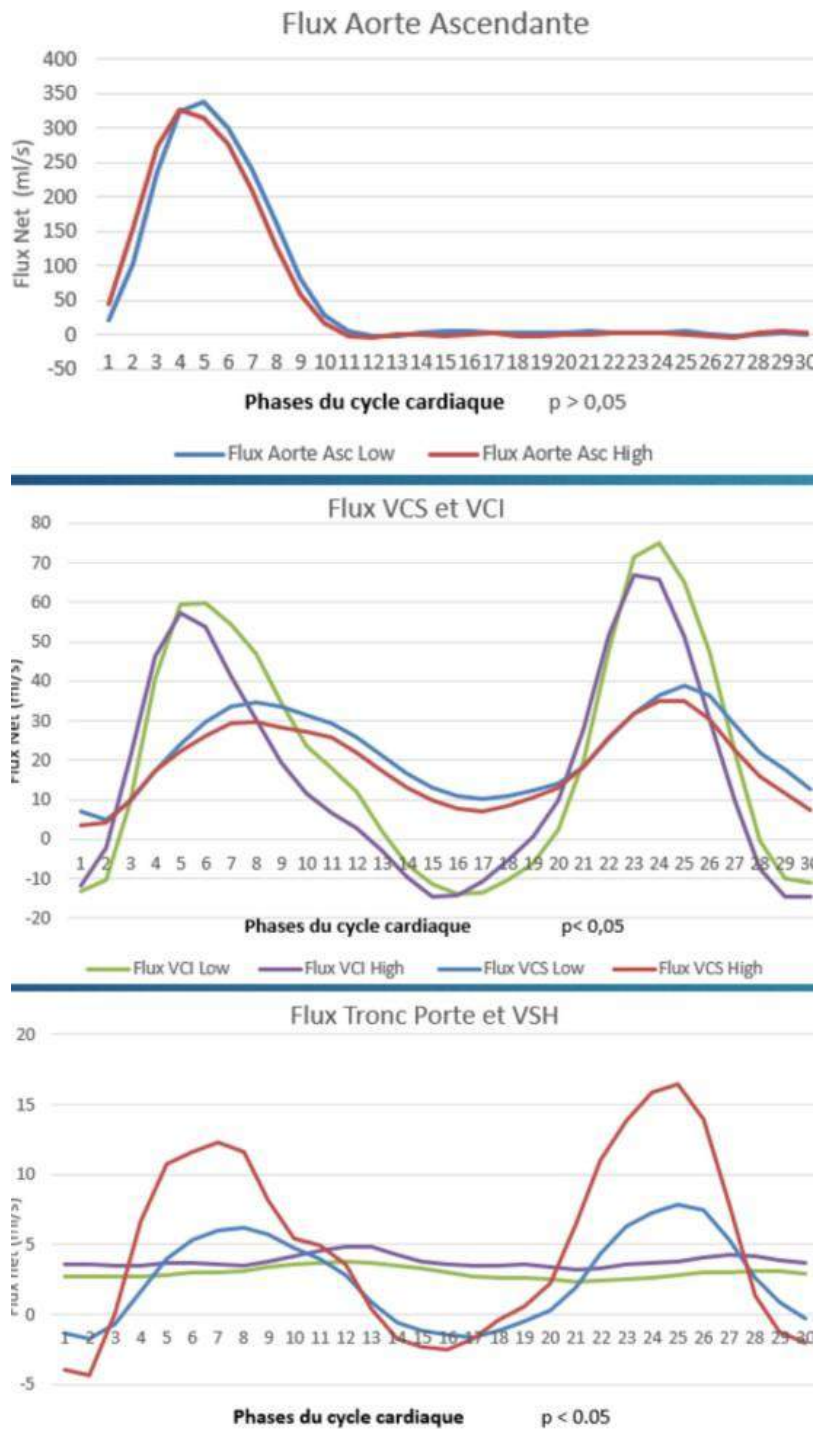
**Figure/Table 2**



**Caption 2**

Good correlation between High and low Venc measurements was noted for high velocity great vessels but not for middle size vessels (hepatic and portal veins).

**Figure 3**



**Caption 3**

Net flow measurement variability is not significant between at High and low Venc for high velocity great vessels but is significant with higher variability at high Venc for venous blood flow and particularly for middle size veins (hepatic and portal veins).

### **Bibliographic References**

Aristova M, Vali A, Ansari SA, Shaibani A, Alden TD, Hurley MC, et al. Standardized Evaluation of Cerebral Arteriovenous Malformations Using Flow Distribution Network Graphs and Dual-venic 4D Flow MRI. *J Magn Reson Imaging* 2019 Dec 9;50(6):1718–30. <https://onlinelibrary.wiley.com/doi/abs/10.1002/jmri.26784>, Schnell S, Ansari SA, Wu C, Garcia J, Murphy IG, Rahman OA, et al. Accelerated dual- venic 4D flow MRI for neurovascular applications. *J Magn Reson Imaging* 2017 Jul;46(1):102–14. <http://doi.wiley.com/10.1002/jmri.25595>, Azarine A, Garçon P, Stansal A, Canepa N, Angelopoulos G, Silvera S, et al. Four-dimensional Flow MRI: Principles and Cardiovascular Applications. *Radiographics*. 2019;39(3):632–48., Dyverfeldt P, Bissell M, Barker AJ, Bolger AF, Carlhäll CJ, Ebbers T, et al. 4D flow cardiovascular magnetic resonance consensus statement. *J Cardiovasc Magn Reson*. 2015;17(1):1–19.<http://dx.doi.org/10.1186/s12968-015-0174-5>

Speaker: L. Kalifa,

Category: Congenital Heart Disease, 4D Flow, Velocity

000562

## **Convergent cavopulmonary connection (CCPC): A novel, efficient design to accommodate mechanical TCPC support**

L. Olivieri \* (1); K. Byeol (2); K. Wang (2); X. Liu, (2); N. Mouzakis, (1); V. Cleveland (3); P. Mass, (1); Y.-H. Loke (3); A. Krieger, (2); P. Sinha, (4)

(1) Cardiology, Children's National - Main Hospital, Washington, United States of America; (2) Biomedical engineering, Whiting School of Engineering, Baltimore, United States of America; (3) Cardiology, Children's National Hospital, Washington, United States of America; (4) Cardiovascular surgery, Children's National - Main Hospital, Washington, United States of America

### **Abstract**

#### **Background:**

Improved total cavopulmonary connection (TCPC) survivorship requires novel treatments for late complications. Competition due to orientation of the two inflows (superior and inferior vena cavae (SVC/IVC)) and outflows adds inefficiencies to the native TCPC and creates unique challenges in providing mechanical circulatory support (MCS) if needed. Computational fluid dynamics (CFD) and virtual surgery have been successfully employed in understanding and improving TCPC failure through use of parameters such as power loss (iPL), hepatic flow distribution (HFD), and assessment of thrombus risk with sub-physiologic wall shear stress (%WSS). Cardiac magnetic resonance (CMR) imaging can provide both anatomic and physiologic data to support surgical design processes. We propose a new configuration for achieving TCPC by converging SVC and IVC flow into a convergent cavopulmonary connection (CCPC). We hypothesize that CCPC conduits that eliminate competitive venous flow and provide easy access for MCS are feasible, with comparable design results using CFD and computer-aided design methods.

#### **Methods:**

Four patient CMR datasets (BSA 0.7 – 2.0 m<sup>2</sup>) including angiography and phase contrast imaging were used to create 3D segmentations of the airway, thoracic vasculature, and Fontan. Inlet/outlet boundary conditions were derived from phase contrast imaging. Nine CCPC design options were created for each patient dataset, with high/mid/low connection and acute/right/obtuse angles of convergence of the superior (SVC) limb onto the IVC using iterative CFD partnered with surgeon input. Designs were evaluated by CFD calculations of iPL, % WSS, and HFD.

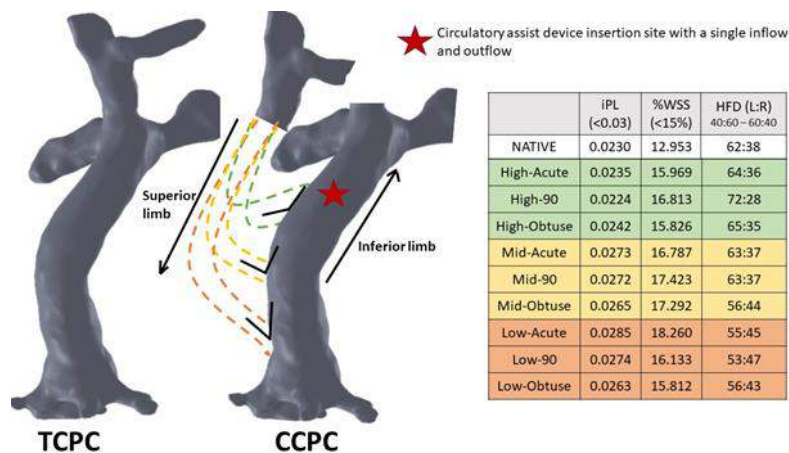
#### **Results:**

All four patients had successful, feasible CCPC designs with 14 mm superior and 18 mm inferior limbs resulting in converged venous flow entering into the pulmonary arteries (Figure 1). Compared to the original TCPC results, the 9 CCPC redesigns either met or were within 50% of native iPL, HFD and %WSS target values. Designs with low SVC entry were associated with best HFD, but elevated %WSS[AK1] .

Conclusions:

The CCPC is both physiologically and surgically feasible using computer-aided design and validated CFD models to calculate important hemodynamic parameters. Further studies to test designs in vivo with patient specific optimization and understand capacity for MCS, are needed.

**Figure/Table 1**



**Caption 1**

Figure 1. Traditional TCPC at left, and convergent cavopulmonary anastomosis (CCPC) in the right with 3 levels (high, medium and low) and 3 angles of entry (acute, 90 degrees, obtuse) of the superior vena cava flow into the inferior vena cava, converging venous flow.

Speaker: L. Olivieri

Category: Fontan, 3D, Computational Fluid Dynamics

000563

## **Clinical Evaluation of High Resolution Stress Myocardial Perfusion Imaging with Whole Heart Coverage at 3T**

P. Rodriguez Lozano \* (1); J. Pan (1); J. Wang (2); A. Robinson (3); C. Kramer (4); M. Salerno (5)

(1) Division of cardiovascular medicine, University of Virginia, Charlottesville, United States of America; (2) Biomedical engineering, University of Virginia, Virginia, United States of America; (3) Cardiology, Scripps Clinic, La Jolla, United States of America; (4) Cardiology, University of Virginia, Charlottesville, United States of America; (5) Cardiology, radiology, and medical imaging, University of Virginia, Charlottesville, United States of America

### **Abstract**

#### **Background**

Novel CMR techniques have enabled whole-heart high-resolution myocardial perfusion imaging. Whole heart coverage may provide the most accurate assessment of myocardial ischemic burden, while high spatial resolution is expected to improve assessment of subendocardial ischemia.

We have previously described the development of spiral-based pulse sequences capable of 1.25 mm spatial resolution and whole heart coverage at 3T. The goal of the present study is to assess performance of high resolution stress myocardial perfusion imaging with whole heart coverage 3T in patients with known or suspected CAD.

#### **Methods**

Subjects with known or suspected CAD undergoing invasive coronary angiography or CT angiography were enrolled for rest and stress first-pass perfusion imaging. First-pass stress perfusion images were acquired on a 3T Siemens scanner (Skyra or Prisma) during adenosine infusion at 140mcg/kg/min with 0.075 mmol/kg Gd (Dotarem or Clariscan). A variable density spiral pulse sequence with 1.25 mm in-plane resolution was used. The spiral trajectory was designed as 4 interleaves with 4ms per interleave, 20% of trajectory fully sampled with ending density of 0.05x Nyquist. Sequence parameters included: FOV=340 mm, TE=1.0 ms, TR=8 ms, saturation time=120 ms, FA=26°, 6 slices with 10 mm slice thickness. The images were reconstructed by L1-SPIRiT using finite temporal difference as the sparsity transform.

#### **Results**

A total of 41 subjects were recruited with a median age of 63, 83% males, 17% females, prior known CAD in 63%. 38 subjects underwent invasive coronary angiography, and 3 subjects underwent CT angiogram. Stress and rest myocardial perfusion images from a representative subject demonstrated stress-induced reductions in myocardial perfusion in the anterior, anteroseptal segments (Figure 1).

Per-patient visual analysis demonstrated a sensitivity of 84% (95% confidence interval [CI], 0.60-0.96), specificity of 81.8 % [95% CI, 0.59-0.94] and accuracy 82% [0.67-0.92]

## Conclusions

Stress myocardial perfusion imaging with whole heart coverage, at 1.25 mm spatial resolution at 3T is technically feasible with spiral pulse sequences. We demonstrated good diagnostic accuracy for this technique.

## Figure/Table 1

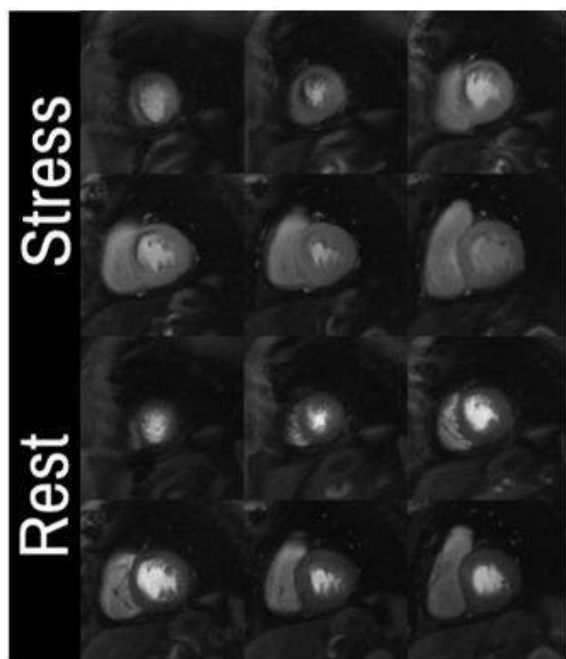


Figure 1: Stress and rest myocardial perfusion images with first-pass gadolinium



Figure 2: Invasive angiography demonstrating total occlusion (arrow) of the proximal left anterior descending artery.

## Bibliographic References

Wang, J, Yang, Y, Weller, DS, et al. High spatial resolution spiral first-pass myocardial perfusion imaging with whole-heart coverage at 3 T. Magn Reson Med. 2021; 86: 648– 662.

Speaker: P. Rodriguez Lozano

Category: coronary Artery Disease, Perfusion, Stress CMR



000564

## Differential sex associated cardiac remodelling in stage B heart failure with Type 2 diabetes

J. L. Yeo \* (1); G. S. Gulsin, (1); E. M. Brady, (1); A. Dattani, (1); J. M. Bilak, (1); K. S. Parke, (1); J. R. Arnold, (1); A. Singh, (1); H. Xue (2); P. Kellman (2); G. P. Mccann, (1)

(1) Cardiovascular sciences, University of Leicester, Leicester, United Kingdom; (2) National heart, lung and blood institute, National Institutes of Health, Bethesda, United States of America

### Abstract

**Background:** Type 2 diabetes (T2D) is associated with pathological myocardial alterations before clinical symptoms manifest, termed stage B heart failure. However, sex differences in prognostic measures such as extracellular volume (ECV) and myocardial blood flow have been poorly characterised in asymptomatic people with T2D at risk of developing heart failure.

**Methods:** Case-control study. Asymptomatic individuals with T2D underwent phenotyping with echocardiography and comprehensive adenosine stress/rest cardiac magnetic resonance imaging. A dual sequence perfusion with fully automated myocardial blood flow maps were generated with injection of gadoterate contrast (Dotarem) 0.05mmol/kg for stress and rest perfusion. Participants with regional perfusion defect indicating obstructive coronary disease or silent myocardial infarction were excluded from perfusion analysis. Native and post-contrast T1 was performed using Modified Look-Locker sequence. Groups were compared with independent-sample T-tests or Mann-Whitney test. ECV was adjusted for haematocrit using analysis of covariance.

**Results:** Individuals with T2D (n=181, 39% female) were compared with age- and ethnicity-matched controls (n=39, 38% female) (see Table 1). Women with T2D had a greater ambulatory systolic blood pressure than controls ( $129\pm13$  vs  $118\pm15$ mmHg,  $p=0.003$ ). Compared to controls, both women and men with T2D had increased LV concentricity (greater LV mass/volume ratio) and impaired systolic (lower global longitudinal strain) and diastolic (higher E/e' ratio) function, with no difference in LV ejection fraction. Women with T2D had lower stress myocardial blood flow ( $1.84\pm0.63$  vs  $2.40\pm0.71$  mL/min/g,  $p=0.008$ ) and myocardial perfusion reserve ( $2.58\pm0.88$  vs  $3.16\pm0.89$ ,  $p=0.043$ ), but not in men. ECV was significantly increased in men with T2D ( $26.3\pm2.5$  vs  $24.8\pm1.3\%$ ,  $p=0.008$ ), but not in women.

**Conclusions:** In a cohort of individuals with T2D at risk of heart failure and without obstructive coronary disease, women had evidence of microvascular dysfunction, driven by reduced stress blood flow, while men had increased diffuse myocardial fibrosis. These data provide novel mechanistic insight into the sex-differences in the development of diabetic cardiomyopathy which may require different strategies to prevent heart failure in men and women.

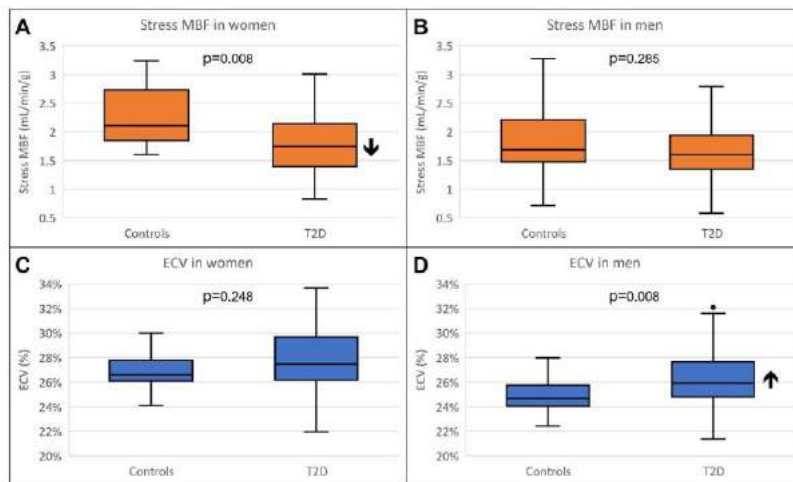
### Figure/Table 1

	Women		Men	
	T2D (n=71)	Control (n=15)	T2D (n=110)	Control (n=24)
Age, years	62.7 ± 7.0	60.5 ± 8.0	64.0 ± 7.4	61.0 ± 7.7
BMI, kg/m <sup>2</sup>	32.3 ± 7.4*	24.7 ± 3.3	30.1 ± 5.1*	27.6 ± 4.3
24hr SBP, mmHg	129 ± 13*	118 ± 15	129 ± 12	126 ± 11
Never smoked	49 (69)	10 (67)	51 (46)	12 (50)
HbA1c, mmol/mol	57.1 ± 11.4*	35.5 ± 3.9	57.4 ± 14.4*	36.7 ± 4.0
Haematocrit, %	39.5 ± 3.5	40.4 ± 2.2	42.1 ± 3.6*	43.7 ± 2.2
<b>Echocardiography measure</b>				
E/e' ratio	10.7 ± 2.9*	8.8 ± 1.7	8.8 ± 2.1	8.3 ± 1.4
<b>MRI measures</b>				
LVM, g	98.0 ± 21.1	96.9 ± 22.5	128.4 ± 25.2	136.0 ± 26.7
LVM index, g/m <sup>2</sup>	52.0 ± 7.9	56.0 ± 9.9	61.0 ± 8.8*	65.7 ± 10.3
LVEDV, mL	111.4 ± 26.1	123.7 ± 20.1	142.6 ± 33.1*	164.4 ± 30.7
LVEDV index, mL/m <sup>2</sup>	59.1 ± 9.5*	71.6 ± 8.0	142.6 ± 33.1*	164.4 ± 30.7
LV mass/volume, g/mL	0.89 ± 0.14*	0.78 ± 0.10	0.92 ± 0.16*	0.83 ± 0.10
LVEF, %	70.0 ± 6.8	67.8 ± 3.9	65.4 ± 7.3	64.5 ± 7.5
GCS, %	20.2 ± 2.5	20.5 ± 2.0	18.6 ± 2.4	18.3 ± 2.1
GLS, %	16.6 ± 2.5*	18.3 ± 2.2	15.5 ± 2.1*	16.5 ± 1.8
Myocardial perfusion reserve	2.58 ± 0.88*	3.16 ± 0.89	2.94 ± 0.79	3.21 ± 0.86
Native T1, ms	1246 ± 38*	1223 ± 28	1214 ± 36	1199 ± 32
ECV, %	27.9 ± 3.0	26.9 ± 1.5	26.3 ± 2.5*	24.8 ± 1.3
Haematocrit adjusted ECV, %	27.3 ± 0.7	28.8 ± 0.3	26.2 ± 0.2*	25.2 ± 0.4

### Caption 1

\*p<0.05 T2D vs controls. Values presented as mean±standard deviation or n(%). Values for haematocrit adjusted ECV are presented as mean±standard error. E/e'= transmitral peak early flow velocity/mitral annular early diastolic velocity, GCS=global circumferential strain, GLS=global longitudinal strain, HbA1c=glycated haemoglobin, LVM=left ventricular mass.

### Figure/Table 2



## Caption 2

Comparison between controls and T2D in women and men for stress myocardial blood flow (panels A and B) and extra-cellular volume (panels C and D).

Speaker: J. L. Yeo

Category: Diabetes, Perfusion, Extracellular Volume Fraction

000566

## **Hemodynamic Evaluation by Cardiac MRI in Adolescent Patient with Shunted Double Inlet Left Ventricle**

M. Marshall \* (1); R. Kharouf (2)

(1) Pediatric cardiology, University of Texas Health Science Center at Houston, Fannin Street, Houston, United States of America; (2) Pediatric cardiology, University of Texas health science center at Houston, Houston, United States of America

### **Abstract**

#### **Clinical Presentation**

Our patient is a 16 year old female with (S,L,L) double inlet left ventricle (LV) with unrestrictive bulboventricular foramen, L-malposed great vessels (aorta arising from the hypoplastic right ventricle (RV)), moderate to severe subvalvar and valvar pulmonary stenosis, and severe aortic root dilation. She underwent left-sided modified Blalock Taussig (mBT) shunt placement at 10 months of age. She presented in January 2020 after a period lost to Cardiology care with chest pain and palpitations. Cardiac magnetic resonance imaging (CMR) revealed Qp:Qs of 2.4:1. In August 2021, she re-presented with chest pain and pulmonary edema concerning for pulmonary overcirculation. CMR showed elevated Qp:Qs 2.3:1 with the mBT shunt and patent ductus arteriosus (PDA) contributing to increased pulmonary blood flow. Decision was made for interventional closure of mBT shunt. She underwent cardiac catheterization (baseline Qp:Qs of 3.1:1) with coil-occlusion of mBT shunt (post-intervention Qp:Qs of 0.81:1.). O<sub>2</sub> saturation decreased from 96 to 85% after intervention.

#### **Diagnostic Techniques**

Visceroatrial situs solitus with normal systemic and pulmonary venous connections. There is levocardia with double-inlet LV, L-looped ventricles, and L-malposed great arteries with aorta arising from outlet chamber (RV). The dominant right-sided LV gives rise to the pulmonary artery. There is subvalvar and valvar obstruction to the pulmonary outflow with dilation of the main and branch pulmonary arteries. There is a large bulboventricular foramen that gives rise to left-sided RV. There is unobstructed aortic outflow. There is moderate to severe dilation of the aortic root, ascending aorta and left-sided transverse arch. There is a small PDA and patent left-sided mBT shunt contributing to increased pulmonary blood flow. The total systemic effective flow was 3.0 L/min and the total effective pulmonary flow (venous) was 6.9 L/min with a Qp:Qs of 2.3:1. Pulmonary flow distribution of 71% flow to right pulmonary artery and 29% to the left with left lung hypoplasia. The physiology is of single ventricle with pulmonary overcirculation. The LV is mildly dilated with an end-diastolic volume (EDV) of 121 ml/m<sup>2</sup>. Normal ventricular systolic function.

#### **Learning Points**

CMR evaluation of complex congenital heart lesions with multiple sources of pulmonary blood flow helps determine sources of excess flow and hemodynamics. Our case is unique with complex sub-pulmonic obstruction and presence of PDA and mBT shunt in an adolescent patient. Evaluation of this complex anatomy with traditional 2D echocardiographic or catheterization exams was inadequate, as there were multiple sources of flow contributing

to Qp:Qs calculations. CMR allowed us to make decisions about hemodynamics and the possibility of shunt occlusion prior to percutaneous intervention. The patient is clinically doing well.

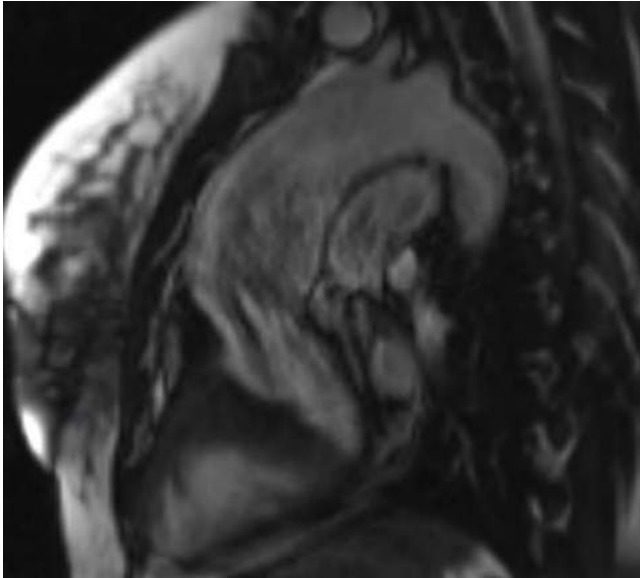
**Figure/Table 1**



**Caption 1**

Volume rendered images demonstrate left-sided Blalock Taussig shunt connected to left pulmonary artery.

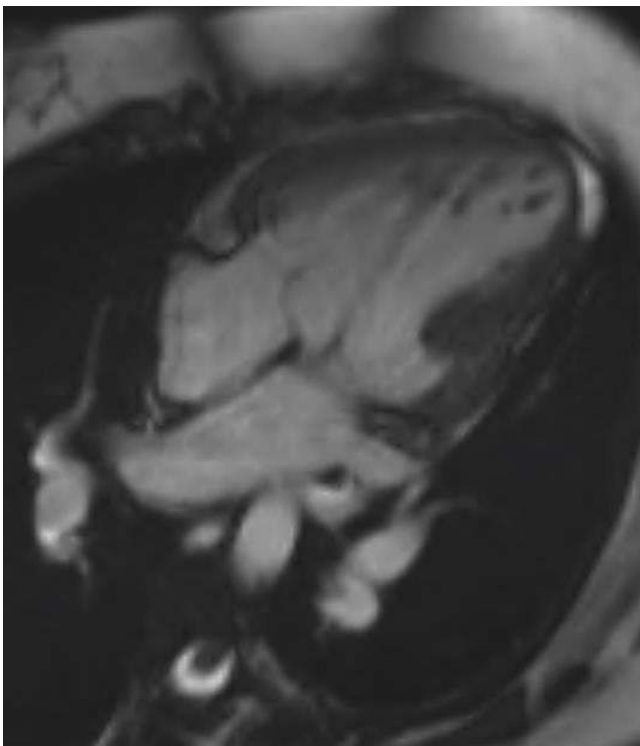
**Figure/Table 2**



**Caption 2**

Aortic outflow SSFP demonstrates patent ductus arteriosus and dilated aortic root and ascending aorta.

**Figure 3**



### **Caption 3**

Four-chamber SSFP demonstrates double inlet left ventricle with complex sub-pulmonic outflow tract obstruction.

Speaker: M. Marshall

Category: Congenital Heart Disease, Shunt, Flow

**000568**

## **An unusual matter of the heart**

S. Kuruvilla Thomas \* (1); E. Nguyen (1)

(1) Joint department of medical imaging, University Health Network, Toronto, Canada

### **Abstract**

#### **Clinical Presentation:**

A 20-year-old male presented with a 1-month history of chest tightness and shortness of breath.

#### **Diagnostic techniques and important findings:**

A chest radiograph showed the presence of cardiomegaly. A subsequent contrast-enhanced CT scan demonstrated a large mass contained within the pericardial sac surrounding the aortic root, narrowing the RVOT (right ventricular outflow tract) and invading the anterior septum and anterior wall of the left ventricle, encasing the left main and LAD. A cardiac MRI, performed a week later, showed right ventricular wall thickening, systolic flattening of the interventricular septum and tricuspid regurgitation suggestive of increased pressure load in the right ventricular due to RVOT obstruction. The pericardial effusion showed significant interval worsening. A decision was subsequently made to perform a CT-guided biopsy of the cardiac mass followed by insertion of a pigtail catheter for pericardial fluid drainage.

Histological features revealed a poorly differentiated synovial sarcoma. Molecular analysis using the Trusight RNA Fusion Panel revealed an SS18-SSX1 gene fusion, diagnostic of synovial sarcoma. The patient was subsequently started on chemotherapy.

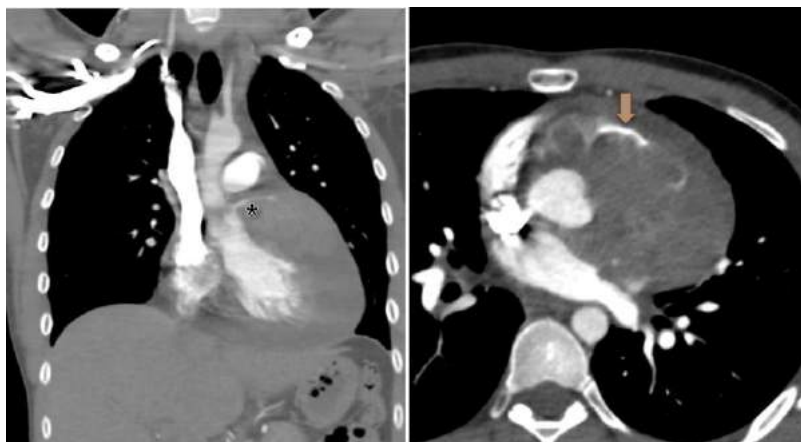
#### **Learning points from this case:**

Primary cardiac synovial sarcomas are extremely rare accounting for <5% of primary cardiac sarcomas. Synovial sarcoma is generally a biphasic tumor, composed of spindle cell and epithelial cells, characterized by X;18 chromosomal translocations. The term synovial sarcoma is a misnomer since the tumor does not arise from the synovium; it only resembles synovial tissue on light microscopy. More than 80% arise in the deep soft tissue of extremities, especially around the knee, and the tumor frequently arises adjacent to joints or tendon sheaths. Primary cardiac synovial sarcomas have a striking male predominance (male to female ratio is approximately 3-20:1) and usually affect 30 to 39-year-olds (mean age of 37.1 years). The most common location is the pericardium followed by the right atrium. Histologically, these may be monophasic, characterized by spindle cell components, or biphasic, composed of both epithelial and spindle cell components. A characteristic t(X; 18) (p11.2; q11.2) translocation is the cytogenetic hallmark of synovial sarcomas. The SYT (SS18)-SSX (SSX1 or SSX2, or both) gene fusion is confirmed by reverse transcription-polymerase chain reaction, and the SYT break-apart signal is confirmed using fluorescence in situ hybridization. Treatment includes surgical resection and chemotherapy, the mainstay



drugs being doxorubicin and ifosfamide. The survival rate is approximately 59.9% at the end of 1 year and 29.9% at the end of five years.

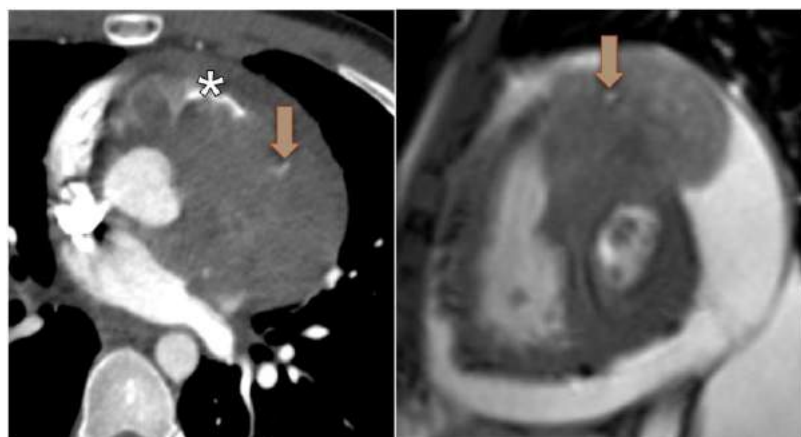
**Figure/Table 1**



**Caption 1**

Figure 1 – Coronal and axial CT sections showing a large cardiac mass causing narrowing of the left main coronary (\*) and right ventricular outflow tract (arrow)

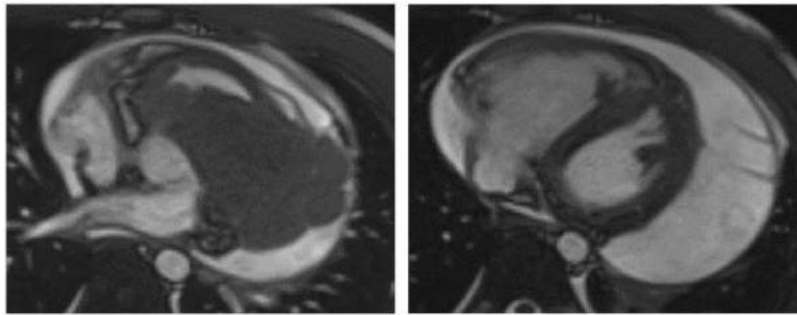
**Figure/Table 2**



**Caption 2**

Figure 2 - CT and MRI demonstrating a lobulated, enhancing mass encasing the left main and LAD (arrow), invading the anterior septum and anterior wall of the left ventricle. The RVOT (\*) is narrowed by the mass.

**Figure 3**



**Caption 3**

Figure 3 – MRI images showing thickening of the right ventricular wall due to chronic RVOT obstruction and a large pericardial effusion with thin septations within.

### **Bibliographic References**

Primary Cardiac Synovial Sarcoma Ji-Gang Wang, MS, and Ning-Ning Li, MD Ann Thorac Surg 2013;95:2202–9, Diagnostic approach to a cardiac mass: a case report of misdiagnosed cardiac synovial sarcoma Safia Ouarrak, Zakaria El Ouali, Asmaa Elkebir, Kawthar Moumna, Mehdi Karkouri, Leila Azzouzi, and Rachida Habbal, Treatment of cardiac synovial sarcoma: experience of two cases. Antonella Coli , Giovanni Alfonso Chiariello, Mariangela Novello, Christian Colizzi and Massimo Massetti, Primary cardiac synovial sarcoma: a clinicopathological, immunohistochemical, and molecular genetics study of five clinical cases. Fei Teng, Dong Chen, Yanwei Li, Wei Fang, Shaomin Yang, Jianfeng Shang, Gonghan Liu, Yayan Cui, Yanli Zhao, Guoliang Lian

Speaker: S. Kuruvilla Thomas

Category: Cardiac Mass, Tumor, Pericardial Disease

000570

## Comparison of DeepStrain Measures of Myocardial Strain to CMR feature tracking

M. morales \* (1); J. Cirillo (1); J. Rodriguez (1); D. Izquierdo-Garcia (2); C. Catana (2); R. Nezafat (1)

(1) Department of medicine (cardiovascular division), Beth Israel Deaconess Medical Center (BIDMC), Boston, United States of America; (2) Radiology, Athinoula A. Martinos Center for Biomedical Imaging, Boston, United States of America

### Abstract

**INTRODUCTION:** Myocardial strain analysis by CMR cine feature tracking provides a detailed characterization of LV deformation that is incremental to ejection fraction. However, feature tracking is a challenging and time-consuming task in practice. Alternatively, we have shown that myocardial motion can be automatically quantified from cine short-axis data using convolutional neural networks (CNN)[1]. Further, we have proposed a deep learning method for automated strain analysis (DeepStrain), and we have compared measures in healthy subjects to tagging CMR [2]. However, comparisons in patient populations between DeepStrain and existing vendor CMR feature tracking have not been reported. Thus, we sought to compare DeepStrain and CMR feature tracking.

**METHOD:** We retrospectively acquired CMR cine data from a total of 201 subjects, including 35 healthy controls, 34 ischemic cardiomyopathy (ICM) patients, 128 non-ischemic cardiomyopathy (NICM) patients, and 4 mixed cardiomyopathy cases. CMR cine data was acquired on either a 1.5T (Phillips) or 3T (Siemens) scanner. Vendor Strain: analyses were performed using CVI42 Tissue Tracking (v. 5.11.1, Circle Cardiovascular Imaging Inc. Calgary, Canada). Endo- and epicardial contours were manually traced for LV strain analyses using cine short-axis stacks and 2 chamber, 4 chamber, excluding the papillary muscles. DeepStrain: global radial (GRS) and circumferential (GCS) strain measures were obtained with our open-source DeepStrain model (<https://github.com/moralesq/DeepStrain>). The model was trained using cine data from 150 subjects evenly divided into five groups: healthy and four cardiovascular disease groups. The data were obtained over a 6 year period on either a 1.5 or 3T (Siemens). DeepStrain uses a 3D U-Net whose input are channel-concatenated cine short-axis stacks from two different time frames (size  $128 \times 128 \times 16 \times 2$ ), and whose output is the cardiac motion between the two frames (size  $128 \times 128 \times 16 \times 3$ ). The U-Net was trained using a loss function with unsupervised image registration and motion smoothness constrain terms, and a supervised anatomical constrain. The Lagrangian strain tensor was evaluated from the generated motion estimates. A second U-Net was used to derive the LV contours, and global strain was calculated by averaging strain values within endo- and epi-epicardial contours.

**RESULTS:** Demographics and strain measures from both techniques are show in Fig 1. Mean differences between CVI and DeepStrain for all subjects were:  $-0.8 \pm 1.6\%$  for GCS, and  $-2.0 \pm 4.8\%$  for GRS. GCS measures displayed higher correlation between techniques ( $R^2=0.9$ , slope=0.9) compared to GRS measures ( $R^2=0.7$ , slope=0.9), although measures from both techniques were remarkably similar (Fig. 2). Strain measures stratified by group showed that the proposed method generates values comparable to CVI. (Fig. 3).

**CONCLUSION:** We reported the first comparison between learning-based strain analyses and vendor CMR feature tracking. Our results showed DeepStrain is a promising technique for automated strain analysis, as shown in healthy controls and patients with non-ischemic and ischemic cardiomyopathies

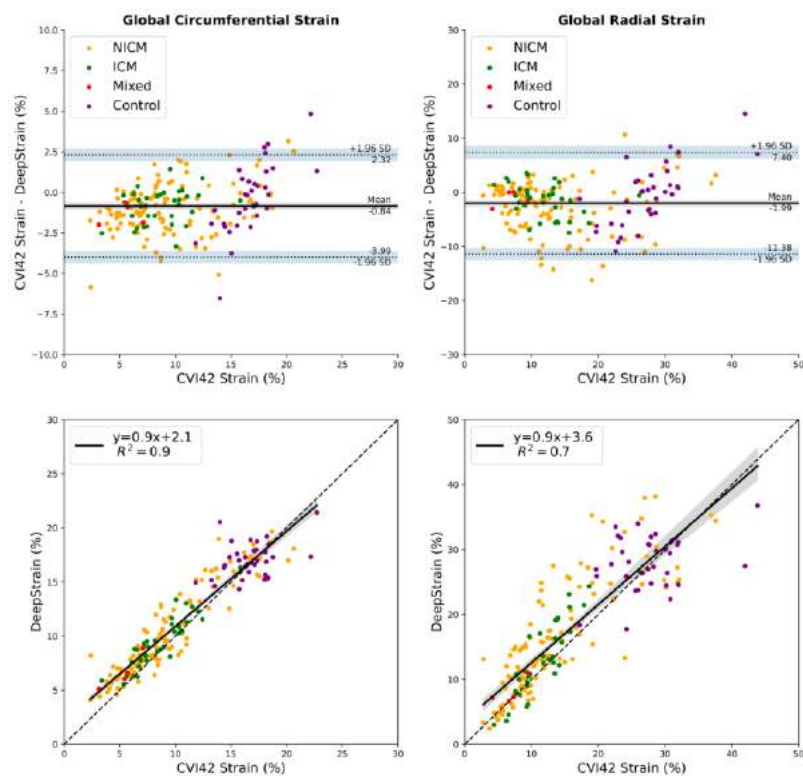
**Figure/Table 1**

	Control	NICM	ICM	Mixed
Age (years)	53.8	54.5	65.9	63.0
Gender (% male)	74	70	79	75
BMI (kg/m <sup>2</sup> )	27.8	28.7	29.1	27.4
<b>Global Circumferential Strain</b>				
CVI42 (%)	16.7	9.4	8.7	5.3
DeepStrain (%)	17.0	10.4	9.5	6.7
<b>Global Radial Strain</b>				
CVI42 (%)	27.5	13.6	11.9	6.9
DeepStrain (%)	28.0	16.2	13.4	8.0

**Caption 1**

Demographics and strain evaluations across groups using vendor CMR feature tracking product (CVI42) and proposed automated learning based approach (DeepStrain).

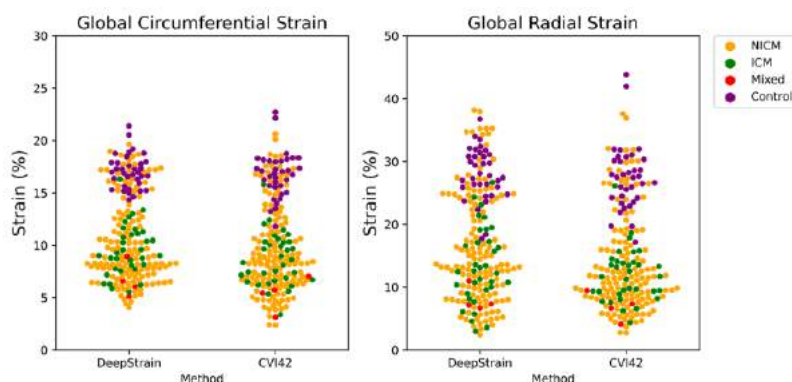
**Figure/Table 2**



**Caption 2**

Comparisons of global circumferential strain (left column) and global radial strain (right column) evaluated with DeepStrain (proposed) and feature tracking (CVI). DeepStrain and CVI generate comparable strain measures based on Bland-Altman analyses and linear regression. NICM = non-ischemic cardiomyopathy; ICM = ischemic cardiomyopathy.

**Figure 3**



**Caption 3**

Evaluation of global circumferential (left) and radial (right) strain in healthy controls, patients with non-ischemic (NICM), ischemic (ICM), and mixed cardiomyopathy. Strain measures were based on DeepStrain (proposed) and feature tracking (CVI). The proposed method generates strain measures comparable to CVI.

### **Bibliographic References**

2. 1 Morales, M. A. et al. Implementation and validation of a three-dimensional cardiac motion estimation network. *Radiology: Artificial Intelligence* 1, e180080 (2019). 2

Morales, M. A. et al. DeepStrain: A Deep Learning Workflow for the Automated Characterization of Cardiac Mechanics. *Frontiers in Cardiovascular Medicine* 8, doi:10.3389/fcvm.2021.730316 (2021), 1. Morales, M. A. et al. Implementation and validation of a three-dimensional cardiac motion estimation network. *Radiology: Artificial Intelligence* 1, e180080 (2019)

Speaker: M. morales

Category: Strain, Cine Imaging, Post-Processing

**000574**

## **Pentalogy of Cantrell**

A. Majeed \* (1); A. Prakash (1); S. Emani, (2); D. Schidlow (1)

(1) Cardiology, Boston Children's Hospital, Boston, United States of America; (2) Cardiac surgery, Boston Children's Hospital, Boston, United States of America

### **Abstract**

#### **Description of Clinical Presentation**

An 8-month-old infant was referred to our institution with a diagnosis of pentalogy of Cantrell with ectopia cordis and tetralogy of Fallot (TOF). She had a history of failure to thrive and cyanotic spells. Due to the ectopia cordis, she had poor echocardiographic windows, precluding a complete evaluation. A CMR was therefore obtained to assess the intracardiac anatomy as well as the relationship of the displaced heart to surrounding thoracic and abdominal structures.

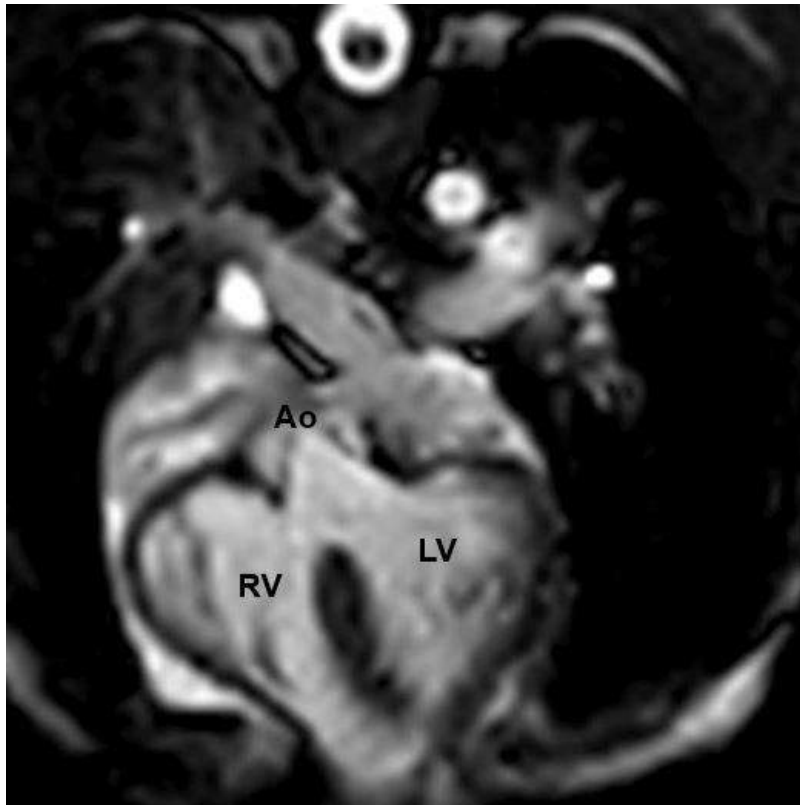
#### **Diagnostic Techniques and Their Most Important Findings**

The examination included conventional steady-state free precession cine imaging, phase-contrast velocity mapping, and 3-dimensional cine gradient echo magnetic resonance angiography using intravenous ferumoxytol as contrast agent. The images confirmed partial ectopia cordis primarily affecting the mid-cavity and apex through a midline sternal and abdominal wall defect with associated rightward and inferior torsion of the cardiac axis. The intracardiac anatomy was consistent with TOF with pulmonary stenosis (Figure 1) with a large conoventricular septal defect, over-riding aorta, and pulmonary stenosis. There were right and left ventricular diverticula protruding through the diaphragmatic defect into the abdominal cavity (Figure 2a). Due to the unusual cardiac position, the right ventricle and its outflow tract were markedly compressed as they protruded through the defect (Figure 2b, 3). Incidentally, a left anterior descending coronary artery myocardial bridge and residual patent ductus arteriosus were also detected.

#### **Learning Points from this Case**

Pentalogy of Cantrell is characterized by five congenital anomalies: cardiac defect, sternal defect, pericardial defect, diaphragmatic defect, and midline abdominal wall defect. 1 In this instance, the CMR was useful in characterizing the unusual extracardiac and intracardiac geometry, particularly with regard to the protrusion of the heart through the midline defect as well as the very elongated right ventricular outflow tract. Ferumoxytol enhanced cine 3-D magnetic resonance angiography facilitated high quality 3-dimensional visualization of the beating heart and its relationship to nearby thoraco-abdominal structures, as well as cine imaging of the intracardiac anatomy. Although similar imaging is possible using CT angiography, our approach avoided the use of ionizing radiation. Following imaging, staged surgical repair of the defects has been planned. The first stage consisting of a valve-sparing tetralogy of Fallot repair has been completed with no significant residual lesions. Future procedures will include repair of the abdominal defect and reconstruction of the chest wall.

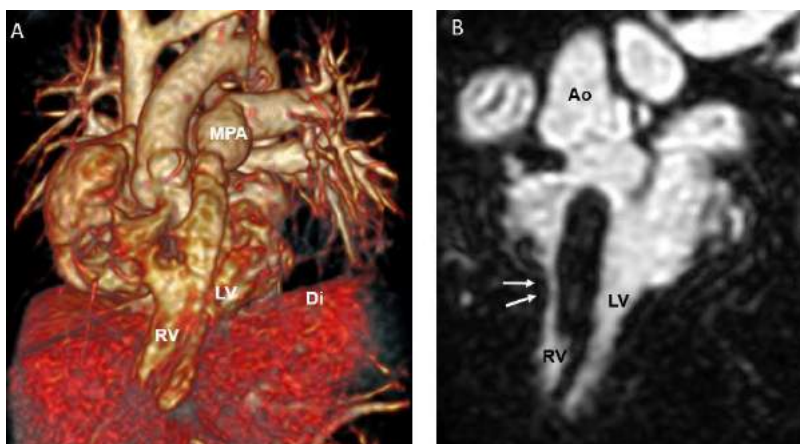
#### **Figure/Table 1**



**Caption 1**

Figure 1. Cine steady-state free precession imaging showing mesocardia, Tetralogy of Fallot with large conoventricular septal defect and overriding aorta. LV, left ventricle; RV, right ventricle; Ao, Aorta; arrows, conoventricular septal defect.

**Figure/Table 2**

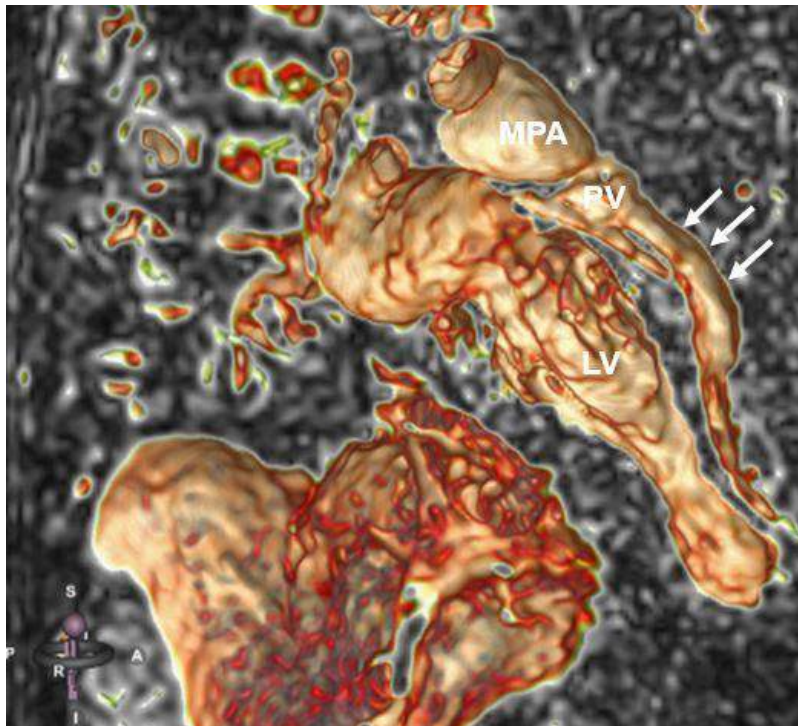


**Caption 2**



Figure 2. A) Three-dimensional reconstruction using three-dimensional Ferumoxytol gradient echo imaging demonstrating both right and left ventricular diverticula protruding through the diaphragm into the abdominal cavity B) Three-dimensional Ferumoxytol gradient echo imaging showing marked compression and near obliteration of the right ventricle (arrows). Ao, aorta; Di, diaphragm; LV, left ventricle; MPA, Main pulmonary artery; RV, right ventricle.

**Figure 3**



**Caption 3**

Figure 3. Three-dimensional reconstruction (endoluminal view) using three-dimensional Ferumoxytol gradient echo imaging demonstrating showing markedly elongated and narrowed right ventricular outflow tract (arrows), hypoplastic pulmonary valve and post-stenotic dilation of the main pulmonary artery. LV, left ventricle; MPA, Main pulmonary artery; PV, pulmonary valve.

Speaker: A. Majeed

Category: 3D, Ferumoxytol, TOF

000576

## An Unusual Location for Heart Transplant Rejection

J. Slivnick \* (1); K. Addetia (1)

(1) Cardiovascular Medicine, UChicago Medicine, Chicago, United States of America

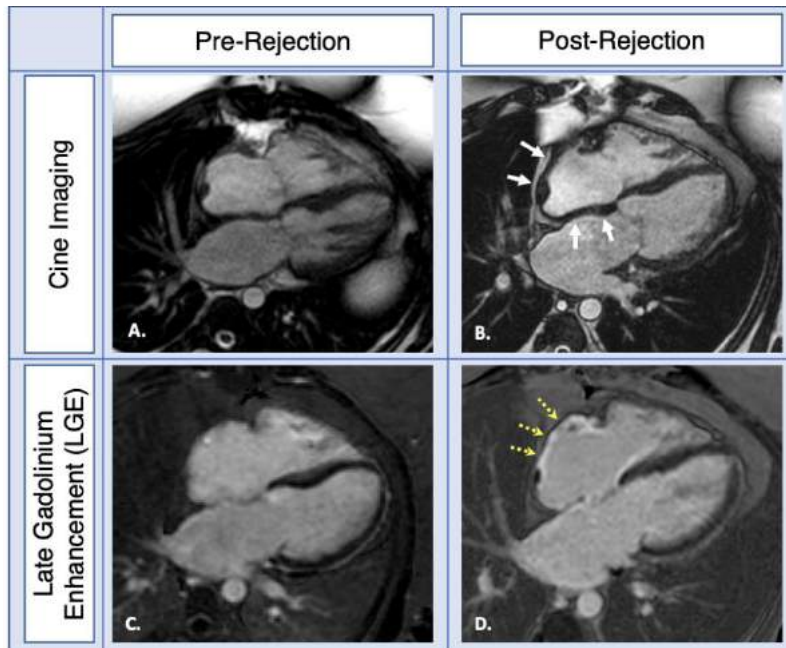
### Abstract

**Clinical Presentation:** A 26 year-old man with a history of hypertrophic cardiomyopathy and orthotopic heart transplantation nine years ago was referred for cardiovascular magnetic resonance imaging (CMR). His post-transplant course had been complicated by an episode of antibody mediated rejection six years prior with associated acute left ventricular (LV) dysfunction which was treated with plasmapheresis and intravenous immunoglobulin. Following treatment, his LV ejection fraction normalized with no evidence for rejection on subsequent echocardiography and right ventricular (RV) heart biopsies. Donor-specific antibodies (DSA), however, were noted to be elevated. In light of this finding, the patient was referred for CMR to evaluate for evidence of rejection.

**Diagnostic Techniques and Their Most Important Findings:** Contrast-enhanced CMR was performed on a Phillips 1.5T scanner. Cine imaging demonstrated normal biventricular size and function with an LV ejection fraction (LVEF) of 66%. T2-weighted imaging did not show evidence of myocardial inflammation, and there was no evidence of LV fibrosis on late gadolinium enhancement (LGE) imaging. Cine imaging, however, revealed diffuse, bi-atrial thickening most prominently involving the right atrium (white arrows, C). Additionally, there was striking, patchy LGE involving both atria (yellow arrows, D). These findings were new when compared to the previous CMR obtained one year ago—prior to the elevation in the patient's DSA (A-B).

**Learning Points from this Case:** Given the patient's new CMR findings, we suspected that the likely mechanism of the patient's elevation in DSA's was a subclinical episode of rejection predominantly involving the right atrium. As the patient's allograft function was preserved with no evidence ventricular involvement, the patient was managed conservatively. A subsequent CMR performed one year later showed stable findings without progression of LGE. To our knowledge, this is the first report of CMR findings concerning for transplant rejection isolated to the atrium. While atrial rejection is not well described, atrial arrhythmias—including atrial fibrillation and atrial flutter—are common in the setting of rejection<sup>1</sup>. Additionally, increasing rejection severity and histologic fibrosis on right ventricular biopsy correlate with risk of atrial arrhythmias<sup>2</sup>. Further studies may help to elucidate whether atrial LGE correlates with histologic rejection and/or the incidence of atrial arrhythmias following heart transplantation. One limitation in our case was the absence of an atrial biopsy to confirm rejection in this chamber; however, this procedure is seldom performed due to the risk of chamber perforation and would not have changed clinical management and therefore was not performed.

### Figure/Table 1



### Caption 1

Figure 1: demonstrating cine imaging (top panel) and late gadolinium enhancement (LGE) findings in our patient both prior to (left) and following (right) the episode of rejection. Cine images demonstrate diffuse thickening of the right atrium with striking, patchy, delayed enhancement of the right atrium seen on LGE imaging.

### Bibliographic References

1. Cui G, Tung T, Kobashigawa J, Laks H, Sen L. Increased incidence of atrial flutter associated with the rejection of heart transplantation. *Am J Cardiol.* Aug 01 2001;88(3):280-4.
2. Ahmari SA, Bunch TJ, Chandra A, et al. Prevalence, pathophysiology, and clinical significance of post-heart transplant atrial fibrillation and atrial flutter. *J Heart Lung Transplant.* Jan 2006;25(1):53-60.

Speaker: J. Slivnick

Category: cardiac Transplant, Heart Transplant, Late Gadolinium Enhancement

000578

## Global Peak Left Atrial Strain is Load-Dependent in Coronary Artery Disease

O. Sharifov \* (1); T. Denney (2); H. Gupta (3); S. Lloyd (1)

(1) Medicine, University of Alabama at Birmingham, Birmingham, United States of America;  
(2) Department of electrical and computer engineering, Auburn University, Auburn, United States of America; (3) Cardiac imaging, Valley Health System, Ridgewood, United States of America

### Abstract

**Background:** Left atrial (LA) functional parameters, including strain are impaired in left ventricular (LV) diastolic dysfunction (LVDD), and expected to reflect LVDD severity. Severe LVDD with increased LV filling pressure (LVFP) is thought to exhibit decreased LA strain.<sup>1,2</sup> Coronary artery disease (CAD) is known to impair both LA and LV function and is associated with LVDD. However, the impact of CAD on the relation of LA functional parameters with the LVFP is not well studied. We examined the relation between the LVFP and LA functional parameters in CAD subjects using cardiac magnetic resonance imaging (CMR).

**Methods:** We studied 19 subjects (age  $61 \pm 6$  years) with NYHA class I-II symptoms who underwent coronary angiography due to chest pain and/or dyspnea. By coronary angiography, all subjects had  $>70\%$  obstruction of major coronary arteries and/or prior history of coronary revascularization. LV catheterization with high-fidelity pressure measurements (Millar Instruments, TX, USA or St Jude, MN, USA) was performed, followed by cine CMR (1.5T, Signa, GE Healthcare, Milwaukee, WI) performed either on the same day or within 3 days. LA and LV volumetric measurements were performed from short-axis views, and LA strain estimates were assessed from 2-chamber and 4-chamber views from long-axis scans. Peak global LA strain (PGLAS) was calculated using the formula:  $(\text{LAEBL}[\text{ES}] - \text{LAEBL}[\text{ED}]) / \text{LAEBL}[\text{ED}] * 100\%$ , where LAEBL is left atrium endocardial border length manually delineated at end of LV diastole [ED] and systole [ES]. PGLAS was measured in 2 to 6 different images and then averaged. Also, Global LA strain (GLAS-Segment) as well as passive (GLASpassive) and active (GLASactive) strain components were measured using automatic feature-tracking Strain Module of Segment Research software (<http://segment.heiberg.se>, Medviso AB, Lund, Sweden)<sup>3</sup> from 2- and 4-chamber views and then averaged. Additionally, peak LA longitudinal shortening (SHORT) was calculated using 2- and 4-chamber views.

**Results:** Subjects had normal LV mass and size with average LV mass index of  $54 \pm 11$  g/m<sup>2</sup>, LV end diastolic volume index of  $64 \pm 15$  ml/m<sup>2</sup>, and LA volume index of  $27 \pm 8$  ml/m<sup>2</sup> (without appendage). Average LV ejection fraction was  $63 \pm 9\%$ , LV fractional shortening (LVFS) was  $25 \pm 10\%$ , LV end diastolic pressure (LVEDP) was  $15.0 \pm 5.2$  mmHg and LV mean diastolic pressure (LVMDP) was  $10.8 \pm 4.2$  mmHg. Average PGLAS was  $23.5 \pm 5.7\%$  and GLAS-Segment was  $22.6 \pm 6.4\%$ , which are lower than normal range.<sup>4</sup> CAD subjects were divided into 2 groups with LVEDP  $<$  or  $>$  16 mmHg ( $n=10$  and  $n=9$ , respectively). Groups have similar clinical characteristics and LV volumetric and functional measurements. However, PGLAS and GLASactive were significantly larger in the group with increased LVFP (table). LVEDP strongly correlated with PGLAS (Pearson  $r=0.75$ ,  $P<0.001$ ) and

GLASactive (Pearson  $r=0.63$ ,  $P<0.01$ ) (figure). Other strain measurements (except GLASpassive), also positively correlated with LVEDP (Pearson  $r=0.59$ ,  $P<0.01$  for GLAS and  $r=0.47$ ,  $P<0.05$  for SHORT). Overall, similar correlation was found between LVMDP and LA strain estimates.

**Conclusions:** In CAD patients, global LA strain and its active component demonstrate a significant load-dependent relationship. This effect should be considered when evaluating LA function. A larger patient cohort study is warranted for validation of our findings.

**Figure/Table 1**

Variables	All Subjects (n=19)	LV EDP<16mmHg (n=10)	LV EDP>16mmHg (n=9)	P value
<i>Clinical Characteristics</i>				
Age	63 ± 6	64±6	61±6	>0.1
Male, %	84	80	89	>0.1
Weight, kg	92 ± 22	94±25	89±19	>0.1
Body Mass Index, kg/m <sup>2</sup>	29.5 ± 6.3	29.9±6.9	29.1±6.1	>0.1
Systolic Blood Pressure, mmHg	134 ± 18	130±18	139±18	>0.1
Diastolic Blood Pressure, mmHg	76 ± 10	75±13	77±7	>0.1
NYHA class I/II, (%)	47/53	50/50	44/56	>0.1
Hypertension, %	100	100	100	>0.1
<i>LV invasive hemodynamic measurements</i>				
LV Minimum Diastolic Pressure, mmHg	8.6 ± 4.1	11.0±3.3	19.4±2.5	<0.001
LV EDP, mmHg	15 ± 5.2	5.4±1.5	12.2±2.7	<0.001
LV MDP, mmHg	10.8 ± 4.2	7.4±1.6	14.6±2.4	<0.001
<i>LV function</i>				
Heart Rate, bpm	69 ± 12	68±14	69±8	>0.1
LV Mass Index, g/m <sup>2</sup>	54 ± 11	50±7	57±13	>0.1
LV ED Volume Index, ml/m <sup>2</sup>	64 ± 15	62.5±19	66±9	>0.1
LV ES Volume Index, ml/m <sup>2</sup>	24 ± 9	24±11	24±7	>0.1
LV Stroke Volume Index, ml/m <sup>2</sup>	40 ± 9	38.5±11	42±5.5	>0.1
LV Ejection fraction, %	63 ± 9	62.5±10	64±8	>0.1
LV Fractional Shortening	25 ± 10	24±10	27±11	>0.1
Cardiac Index, L/min/m <sup>2</sup>	2.7 ± 0.5	2.5±0.5	2.9 ± 0.5	0.085
<i>LA function</i>				
LA Volume Index, ml/m <sup>2</sup>	27±8	25.5±9.1	29.0±7.2	>0.1
Peak Global LA Strain, %	23.5±5.7	19.8±4.7	27.7±3.4	<0.001
Global LA Strain (Segment), %	22.6±6.4	20.2±6.6	25.2±5.4	0.09
Global LA Strainpassive (Segment), %	7.2±4.4	7.2±4.7	7.2±4.2	>0.1

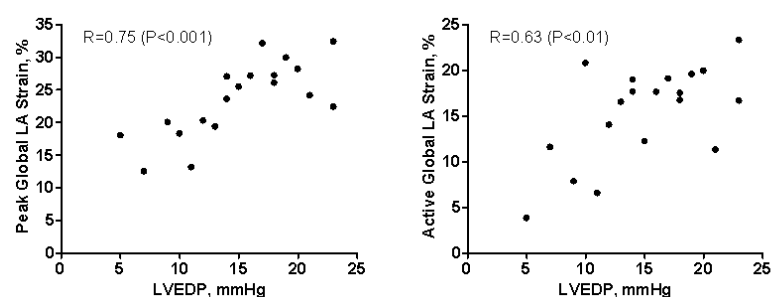
Global LA Strainactive (Segment), %	15.4±5.2	13.0±5.6	18.0±3.2	<0.05
Peak LA Longitudinal Shortening, %	21.7±6.1	19.4±5.6	24.2±5.9	0.09

### Caption 1

**Table.** Comparisons of CAD subjects with normal and increased left ventricular end diastolic pressure.

Values are mean±SD; NYHA= New York Heart Association; LV=left ventricular; EDP=end diastolic pressure; MDP=mean diastolic pressure; LA=left atrial.

### Figure/Table 2



### Caption 2

**Figure.** Representative examples of correlation between left ventricular end diastolic pressure (LVEDP) and estimates of left atrial (LA) strain.

### Bibliographic References

1. Cameli M, et al. Left atrial longitudinal strain by speckle tracking echocardiography correlates well with left ventricular filling pressures in patients with heart failure. Cardiovasc Ultrasound. 8:14 (2010), 2. Posina K, et al. Relationship of phasic left atrial volume and emptying function to left ventricular filling pressure: a cardiovascular magnetic resonance

study. J Cardiovasc Magn Reson. 15:9 (2013) , 3. Heiberg E, et al. Design and validation of segment–freely available software for cardiovascular image analysis. BMC Med Imaging. 10:1. (2010), 4. Truong VT, et al. Normal left atrial strain and strain rate using cardiac magnetic resonance feature tracking in healthy volunteers. Eur Heart J Cardiovasc Imaging. 21(4):446-453 (2020)

Speaker: O. Sharifov

Category: Left Atrium, Strain, coronary Artery Disease

000579

## Relationships between atrial fibrillation and cardiac magnetic resonance quantification of heart chambers and valves in non-ischemic cardiomyopathy

T. K. M. Wang \* (1); D. Kocyigit (2); N. Chan, (1); W. H. W. Tang, (3); B. Griffin, (1); S. Flamm (1); D. Kwon, (1)

(1) Section of cardiovascular imaging, Cleveland Clinic Main Campus, Cleveland, United States of America; (2) Department of cardiovascular medicine, Sydell and Arnold Miller Family Heart, Vascular, and Thoracic Institute, Cleveland Clinic, Cleveland, United States of America; (3) Cardiovascular medicine, Cleveland Clinic Main Campus, Cleveland, United States of America

### Abstract

**Background:** Atrial fibrillation (AF) is a known etiology and complication of cardiomyopathies, however associations between AF and magnetic resonance imaging (MRI) quantification of cardiac chambers and valves have rarely been studied in this setting. We compared the MRI parameters and outcomes between AF and non-AF patients in non-ischemic cardiomyopathy (NICM) patients.

**Methods:** Adult NICM patients (n=633) undergoing MRI in 2002-2017 were divided by baseline AF status to compare clinical characteristics, MRI parameters, and the primary composite endpoint of all-cause death, heart transplant, LVAD and ventricular arrhythmias during follow-up.

**Results:** AF history was present in 141/633 (22.3%) NICM patients, associated with older age and male sex. AF patients had significantly higher biatrial size, left ventricular relative wall thickness, mitral regurgitation, right ventricle size and lower right ventricular ejection fraction by MRI than non-AF patients, while left ventricle size and function were similar (Table). The primary endpoint occurred in 129 (20.4%) patients during follow-up, and AF was associated with the primary endpoint in univariable (HR 1.56, 95%CI 1.08-2.26), but not multivariable Cox proportional hazards regression analyses (P=0.223).

**Conclusion:** AF was associated with greater degree of atrial and ventricular remodeling, functional mitral regurgitation and right ventricular dysfunction in NICM. These findings may explain why AF was associated with adverse outcomes in NICM, although not if clinical and MRI covariates were adjusted for.

### Figure/Table 1



MRI parameter	Non-AF (n=492)	AF (n=141)	P-value
Left atrial volume indexed (mL/m <sup>2</sup> )	43±19	59±25	<0.001
Right atrial volume indexed (mL/m <sup>2</sup> )	43±18	57±24	<0.001
Left ventricular end-diastolic volume indexed (mL/m <sup>2</sup> )	123±39	124±50	0.879
Left ventricular end-systolic volume indexed (mL/m <sup>2</sup> )	85±38	86±48	0.773
Left ventricular ejection fraction (%)	33±11%	33±11%	0.767
Left ventricular mass indexed (g/m <sup>2</sup> )	71±26	71±23	0.911
Relative wall thickness (%)	39±16%	43±20	0.017
Sphericity ratio	1.8±0.3	1.8±0.3	0.653
Late gadolinium enhancement-SSD score (%)	2.7±7.0%	3.2±7.3%	0.445
Right ventricular end-diastolic volume indexed (mL/m <sup>2</sup> )	84±26	90±34	0.040
Right ventricular end-systolic volume indexed (mL/m <sup>2</sup> )	49±23	56±30	0.005
Right ventricular ejection fraction (%)	44±12	40±13	0.005
Mitral regurgitant volume (mL)	10±10	15±15	<0.001
Mitral regurgitant fraction (%)	13±13%	18±15%	<0.001

## Caption 1

Table: Chamber and valve quantification comparisons by cardiac magnetic resonance imaging in non-ischemic cardiomyopathy patients with and without atrial fibrillation (AF).

Speaker: T. K. M. Wang

Category: Nonischemic Cardiomyopathy, Atrial Fibrillation , Mitral Regurgitation

000580

## **An Atlas-Based Method to Improve Differentiation Between Adolescent Athletes and Adolescent Patients with Hypertrophic Cardiomyopathy**

S. Sihra \* (1); S. Govil (2); J. Perry (3); S. Hegde, (3); A. Mcculloch (2); J. Omens (2)

(1) Bioengineering, University of California San Diego, La Jolla; (2) Bioengineering, University of California San Diego, La Jolla, United States of America; (3) Cardiology, Rady Children's Hospital - San Diego, San Diego, United States of America

### **Abstract**

#### **Background**

Similarities between cardiac remodeling in athletes and hypertrophy in hypertrophic cardiomyopathy (HCM) patients complicate differential diagnosis. Athlete's heart (AH) and HCM have been studied in adult populations, but information on adolescents is lacking. The objective of this research was to use a statistical atlas-based approach to quantify differences in ventricular shape between HCM and AH in adolescents. We tested the hypothesis that atlas-derived biventricular shape models are more effective than conventional left ventricular (LV) MRI parameters in discriminating between AH and HCM.

#### **Methods**

Patient ventricular shapes were resolved against a reference atlas derived from asymptomatic adults to identify statistically independent modes of normal biventricular shape variations. Biventricular computational models were generated from cardiac MR imaging of 14 patients with confirmed AH, 20 patients with confirmed HCM and 8 patients with unclear diagnosis.

#### **Results**

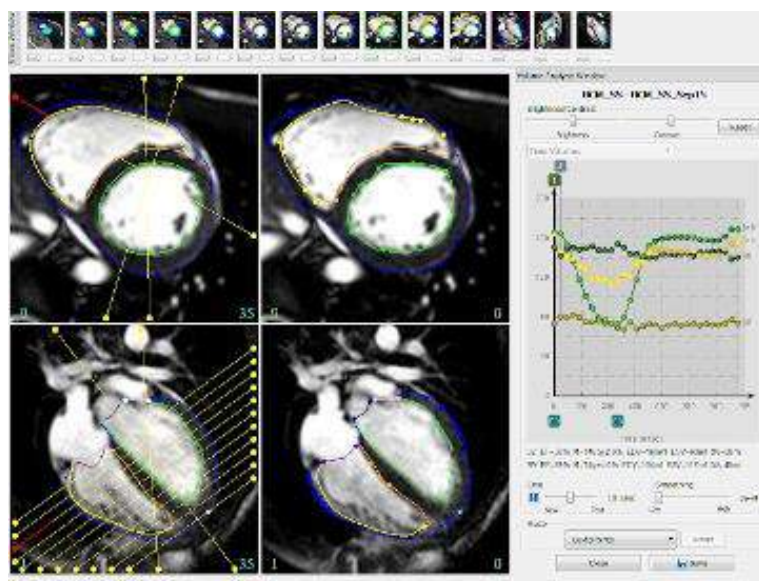
Conventional MR parameters (LV end diastolic volume [EDV; AH mean = 97.9, HCM mean = 78.9], LV end systolic volume [ESV; AH mean = 40.1, HCM mean = 26.7], right ventricular [RV] EDV [AH mean = 91.2, HCM mean = 67.0], RV ESV [AH mean = 44.6, HCM mean = 27.2]) and Z-scores of reference atlas shape modes 1 (AH mean = -1.55, HCM mean = 0.295), 11 (AH mean = 0.227, HCM mean = 1.36), 14 (AH mean = 2.55, HCM mean = 4.63), and 22 (AH mean = 1.64, HCM mean = -0.395) were significantly different between confirmed HCM and AH patients. All volumes were measured in mL and indexed to body surface area. Shape modes that were significantly different between the two groups included notable differences in RV geometry, which is an important finding because RV parameters are not currently considered in the differential diagnosis. Using logistic regression models, we found that a model including shape modes outperformed a model using conventional LV MRI parameters alone (ROC AUC = 0.87, sensitivity = 86.4%; vs. AUC = 0.79, sensitivity = 84.2%). The three best-performing models (AUC = 0.90, sensitivity = 90.5%) included a

combination of conventional MRI parameters and shape modes, indicating that the addition of shape modes improves the predictive ability and the HCM sensitivity of all the models.

## Conclusion

This study showed that atlas-based shape modes may be able to improve differential diagnosis between AH and HCM in adolescents and that the RV may provide important information for diagnosis that is currently overlooked.

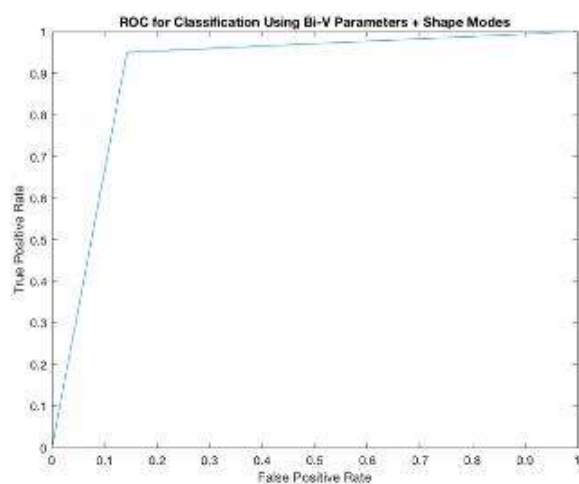
**Figure/Table 1**



**Caption 1**

A screen capture showing the creation of a patient model in CIM including a mid-basal short axis view and a 4-chamber long axis view, both with user-placed guide points, and image slice intersections

**Figure/Table 2**



## Caption 2

ROC for classification using the Bi-V parameters + shape modes logistic regression model

## Figure 3

Table 2. Comparison of Size and Shape Between Athlete and HCM Cohorts

	Athletes (N = 14) <sup>a</sup>	HCM (N = 20) <sup>a</sup>	p <sup>b</sup>
<b>Conventional Parameters</b>			
Indexed LVEDV	97.9 (9.5)	78.9 (14.5)	0.01*
Indexed LVESV	40.1 (11.7)	26.7 (6.4)	< 0.01*
Indexed LV Mass	82.1 (8.3)	85.4 (31.5)	0.89*
LVEF	59.2 (9.6)	66.0 (5.8)	0.05*
Indexed RVEDV	91.2 (13.2)	67.0 (10.6)	< 0.01
Indexed RVESV	44.6 (9.3)	27.2 (7.2)	< 0.01
Indexed RV Mass	39.8 (6.4)	39.9 (9.6)	0.83
RVEF	51.3 (5.2)	59.6 (7.5)	0.04
<b>Atlas-Derived Parameters</b>			
Shape Mode 1	-1.55 (0.9)	0.295 (1.5)	< 0.01
Shape Mode 2	-2.33 (0.5)	-1.66 (1.2)	0.32*
Shape Mode 8	0.703 (1.2)	2.45 (2.0)	0.35*
Shape Mode 10	-0.134 (1.2)	-1.55 (1.7)	0.27*
Shape Mode 11	0.227 (1.2)	1.36 (1.4)	0.02*
Shape Mode 12	1.04 (1.0)	2.09 (1.4)	0.11*
Shape Mode 14	2.55 (1.1)	4.63 (1.7)	< 0.01
Shape Mode 16	1.41 (2.2)	-0.797 (2.0)	0.14*
Shape Mode 17	-0.564 (1.0)	-1.39 (1.2)	0.39*
Shape Mode 18	0.564 (2.1)	-2.00 (2.3)	0.07*
Shape Mode 22	1.64 (1.0)	-0.395 (1.5)	< 0.01*
Shape Mode 31	0.272 (1.6)	-1.30 (2.0)	0.21*
Shape Mode 37	0.891 (2.2)	2.42 (1.5)	0.12*

<sup>a</sup>The table displays mean (standard deviation) for all parameters

<sup>b</sup>All p-values were calculating using independent sample Student's t-tests for unequal variances unless stated otherwise

\*p-value from linear regression

## Caption 3

Comparison of Size and Shape Between Athlete and HCM Cohorts

Speaker: S. Sihra

Category: Hypertrophic Cardiomyopathy, Athlete, 3D

000581

## Can we use CMR in diagnosis of infective endocarditis?

A. Elagha \* (1)

(1) cardiology, Cairo University, cairo, Egypt

### Abstract

#### *Abstract*

**Background:** Echocardiography is a reliable imaging tool in diagnosing infective endocarditis (IE) according to "modified Dukes criteria"; however, it lacks tissue characterization of cardiac masses, and transthoracic echocardiography (TTE) has low sensitivity in detection of vegetations. Moreover, transesophageal echo (TEE) is considered semi-invasive and intolerable in some situations. On the other hand, cardiac magnetic resonance (CMR) is a powerful true 3D imaging tool with wide field of view, and superior capability of tissue characterization of cardiac masses; however, modest information is available about utility of CMR in diagnosing IE. Our aim is to assess the feasibility of CMR to identify vegetations and complications of IE, and compare obtained findings with those obtained from echocardiography regarding: presence, number, size of vegetations, and detection of cardiac complications (e.g. aortic root abscess, periannular abscess, and shunts).

**Methods:** Eighty consecutive patients with suspected IE were enrolled in the study. All patients underwent TTE; only those with left-sided lesions underwent TEE. When clinical situation allowed, CMR examination using 1.5 Tesla magnet were performed using the following sequences: Steady-state free precession (SSFP), T1W ( $\pm$  fat suppression) and T2W, first-pass perfusion, and delayed hyperenhancement. Moreover, chest and abdominal survey was done.

**Results:** Sixty-one patients (45 males and 16 females) were able to undergo and complete CMR study. Affection of tricuspid valve was seen in 39.3%, mitral 31.1%, aortic 24.6%, and pulmonary 4.9% of cases. All vegetations visualized by echocardiography were also clearly detected and confirmed by CMR. The sensitivity, specificity, accuracy and Kappa agreement of CMR with echocardiography in depicting  $>0.5$ cm vegetations were all 100%. By tissue characterization, vegetations resemble features of thrombi (with variation in signal intensity according to age of vegetation). However, in some cases, masses have a unique pattern that is different from vegetations of IE, and subsequently other diagnoses were suggested (e.g. fibroelastoma, Libman-Saks endocarditis). In 22 patients, CMR provided more information than echocardiography, and in 6 patients, CMR made a paradigm shift of diagnosis.

**Conclusion:** Cardiac MRI is a powerful imaging tool in diagnosis of IE and its complications. In comparison with echocardiography, CMR can identify the presence, numbers, and size of vegetations accurately. Moreover, with its unique ability of tissue characterization, CMR helps distinguish vegetations from other masses; therefore changes the diagnosis of IE and subsequent management in some patients.

## **Bibliographic References**

NA

Speaker: A. Elagha

Category: Valvular Heart Disease, Cine Imaging, Heart Failure

000582

## **Stress Perfusion CMR in Children and Young Adults after Heart Transplantation. A Cardiac Catheterization and CMR Pilot Study**

L. Hernandez, \* (1); J. Godown, (2); D. Dodd, (3); D. Bearl, (2); M. Chrisant, (1); K.-C. Chan, (1); J. Soslow, (4)

(1) Pediatric cardiology, Joe DiMaggio Children's Hospital at Memorial Healthcare System, Hollywood, United States of America; (2) Department of pediatric cardiology, Vanderbilt University Medical Center, Nashville, United States of America; (3) Department of pediatrics, division of pediatric cardiology, Vanderbilt University Medical Center, Nashville, United States of America; (4) Pediatrics, Vanderbilt University Medical Center, Nashville, United States of America

### **Abstract**

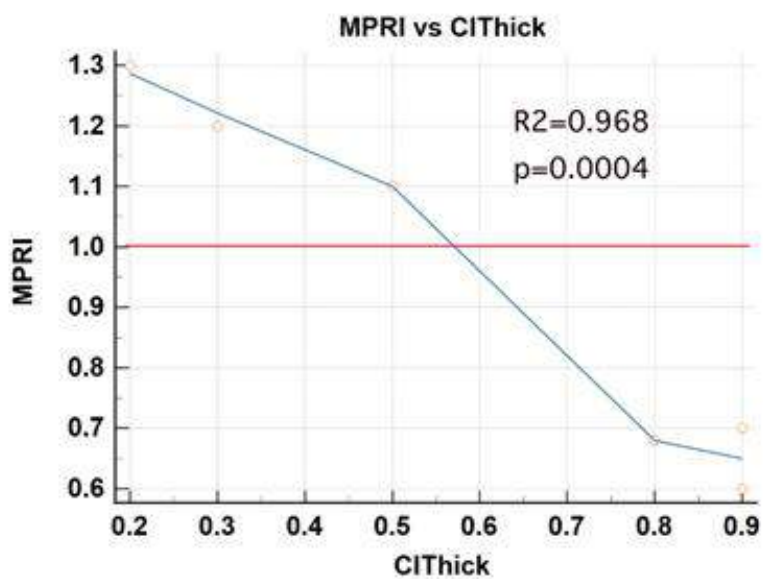
**Background:** Cardiac allograft vasculopathy (CAV) is a form of coronary vascular disease affecting heart transplant recipients, contributing to medium-long term post-transplant morbidity and mortality. Coronary angiography (CA) and intravascular ultrasound (IVUS) are the gold standard invasive diagnostic approach. The purpose of this study was to compare stress perfusion CMR results with invasive data for the detection of CAV in children.

**Methods:** Twelve HTx recipients who underwent routine annual evaluation were retrospectively enrolled in the study from two institutions. Patients with suspected allograft rejection were not included in the study. Time between cardiac catheterization and CMR was  $14.7 \pm 13.9$  days (Range 0-37 days). Time post transplantation  $5 \pm 3$  years (range 1-11). IVUS and coronary flow reserve (CFR) were performed in 6/12, coronary angiography in 12/12. CMR data included first pass perfusion at baseline and during hyperemia (Regadenoson) using a single bolus dual sequence turbo flash technique in 7/12 and dual bolus sequence in 5/12. Subjective assessment of perfusion was performed and myocardial perfusion reserve index (MPRI) was calculated. Late gadolinium enhancement (LGE) was qualitatively evaluated (presence/absence). A regression analysis was used to assess relations of MPRI with coronary intimal thickening (CIThick) and CFR.

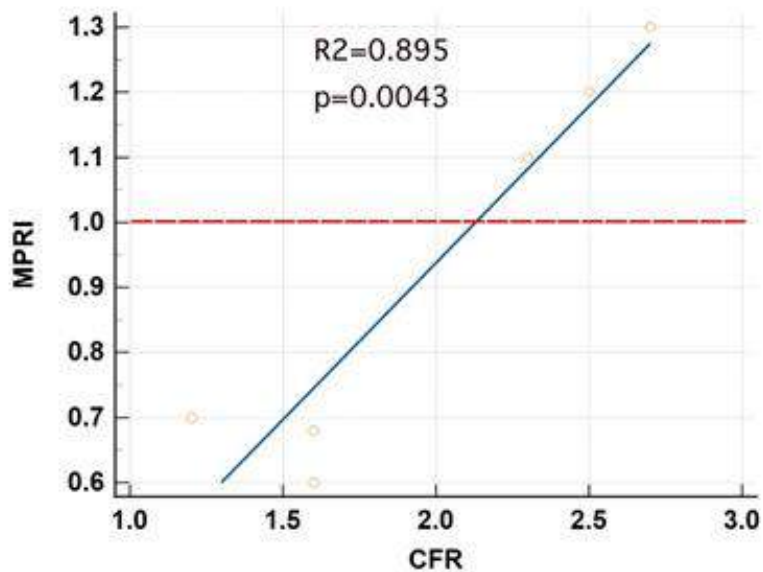
**Results:** Median age was 19 years with interquartile range of 14-23. 8/12 were male. Stress perfusion CMR was completed in 12/12 with no significant side-effects (palpitations 12/12). The mean HR at baseline was  $98.1 \pm 7.9$  bpm and  $121 \pm 7.9$  bpm during hyperemia. 12/12 had normal perfusion at baseline. 3/12 had abnormal myocardial perfusion during hyperemia. Although coronary angiogram was considered to be normal in all cases (CV0), those with abnormal perfusion (n=3) had increased CIThick on IVUS ( $>0.5$  mm) and a diminished CFR. MPRI correlated with CIThick ( $R^2=0.968$ ;  $p=0.0004$ ) and CFR ( $R^2=0.895$ ;  $p=0.0043$ ). LGE was present in those with abnormal myocardial perfusion.

**Conclusions:** Stress perfusion CMR appears to be a safe non-invasive imaging modality to assess myocardial perfusion in children and young adults after heart transplantation. MPRI correlated well with CIThick and CFR in our cohort, though this analysis included only 6 of the 12 subjects. Stress CMR has potential for non-invasive assessment of CAV in pediatric heart transplant recipients but must be validated in a larger cohort before considering clinical use.

Figure/Table 1



Figure/Table 2



Speaker: L. Hernandez,

Category: Heart Transplant, Stress CMR, Coronary Angiography



000583

## **Subtraction angiography for improved visualization of selective contrast injections during invasive cardiac magnetic resonance (iCMR) procedures**

R. Vamsee, \* (1); M. Fares (1); M. Ganigara, (2); M. Nagiub, (1); J. Hernandez (3); S. R. Reddy (1); T. Hussain (1); J. Greer (4)

(1) Pediatric cardiology, UT Southwestern Medical Center, Dallas, United States of America; (2) Pediatric cardiology, UT Southwestern Medical Center, University Park, United States of America; (3) Pediatric anesthesiology, UT Southwestern Medical Center, Dallas, United States of America; (4) Pediatrics, UT Southwestern Medical Center, Dallas, United States of America

### **Abstract**

**Background:** Fluoroscopic catheterisation is used for diagnosis and intervention on arterial and venous collaterals between the systemic and pulmonary circuits and pulmonary arterio-venous malformations (AVMs) in patients with Glenn and Fontan physiology. A growing number of centers are transitioning to perform diagnostic catheterization under MR guidance. Despite improvements made in imaging collaterals and AVMs, we continue to rely on fluoroscopy to identify real-time flow patterns through complex Glenn and Fontan pathways. A prior study at our institute demonstrated the feasibility of selective angiography during MR-guided catheterization [1]. In this study, we aim to further improve the visualization of injected Gd contrast using a subtraction angiography approach.

**Methods:** 7 pediatric patients with Glenn/Fontan physiology underwent MR-guided catheterization under general anesthesia on a 1.5T Philips Ingenia and the iSuite platform (Philips Research, Hamburg, Germany). Dilute gadolinium (Gd) (1/100 Gd/saline) was selectively injected in the SVC to evaluate pulmonary transit times and detect collateral vessels and pulmonary AVMs. Real-time images were acquired using a T1-weighted spoiled GRE to provide distinct signal from the balloon and injected contrast at 4-5fps, TE/TR = 1.2/2.4 ms, flip angle=45°, 2.5 mm voxel size, with a pre-saturation pulse to suppress tissue signal. A 60mm slice thickness was used to maintain visualization of contrast with complex through-plane motion.

These T1W images were previously overlaid on a 3D bSSFP dataset for visualization [1], but suffer from bright fat and background signal contamination (Figure 1). To suppress this unwanted signal, a reference image can be acquired before injecting contrast (Fig 2A). All following dynamic scans are subtracted from the reference image in real-time, and the resulting images (Fig2B) are overlaid within iSuite (Fig2C). Improvements in contrast and background tissue suppression were evaluated by the contrast ratio (CR = enhanced blood signal/background signal) for the original T1W sequence and the proposed subtraction angiography approach (7 patients per group).

**Results:** Subtraction selective angiography provided a marked reduction in background noise and fat in all 7 patients (Fig 1B vs Fig 2C). Figure 3 shows selective subtraction angiography in the RPA (A) and LPA (B) of the same subject for the evaluation of

pulmonary transit times. CR was significantly improved using selective angiography (16.4) over the original T1W approach (5.9),  $p < 0.05$ .

**Discussion:** The utilization of interventional cardiac MRI in patients with congenital heart disease is evolving rapidly, however still continues to depend on fluoroscopy for imaging of collaterals and AVMs. ICMR subtraction angiography may improve visualization of flow patterns within the vasculature and better delineate collaterals and pulmonary AVMs while reducing the need for ionizing radiation.

**Figure/Table 1**



**Caption 1**

(A) Contrast injected into the Glenn anastomosis, shown with T1W GRE and 60mm slab (B) Overlay of bright contrast within iSuite. The poorly suppressed fat and background tissue can also be seen across the imaging slice.

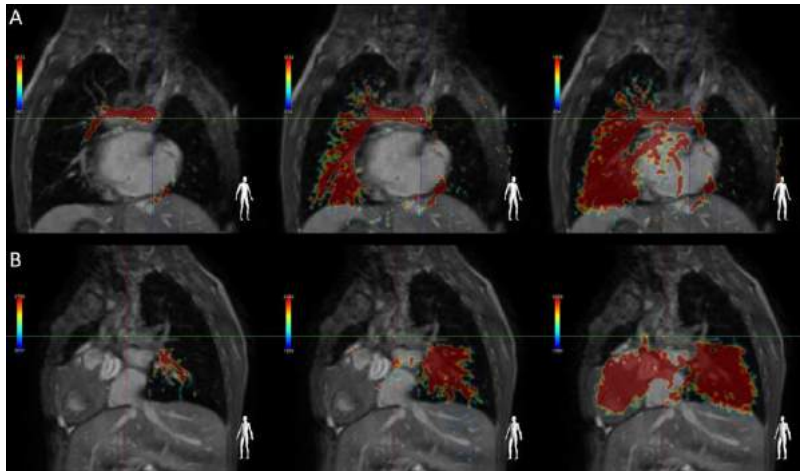
**Figure/Table 2**



**Caption 2**

(A) shows the reference image acquired before contrast injection in the Fontan conduit of another patient. Subtracting all following real-time images from the reference results in excellent suppression of unwanted signal (B), which is more clearly visualized when overlaid within iSuite (C).

**Figure 3**



### Caption 3

Time series of an injection in the RPA (A) and LPA (B) of the same patient, showing the flow of contrast from the Glenn circulation across the pulmonary vasculature. Background tissue and fat are very well suppressed compared to Figure 1B. Selective injection demonstrated a lack of perfusion to the upper left lobe of the lung in this patient (B).

### Bibliographic References

[1] Greer JS, Arar YA, Gooty VD, Castellanos DA, Weiss S, Krueger S, Greil G, Reddy SR, Hussain T, et al. iCMR selective angiography in congenital heart disease. In: SCMR 23rd annual scientific sessions. Orlando, FL: SCMR; 2020.

Speaker: R. Vamsee,

Category: 3D, Congenital Heart Disease, Angiography

000584

## **T2 Elevation Resolves with Time while Late Gadolinium Enhancement Persists in College Athletes Diagnosed with Myocarditis Following SARS-CoV-2 Infection**

J. Heyniger \* (1); P. Chandrasekaran (1); O. Simonetti (2); S. Rajpal (1)

(1) Cardiovascular medicine, The Ohio State University, Columbus, United States of America; (2) Davis heart and lung research institute, Ohio State University, Columbus, United States of America

### **Abstract**

**Background:** The ongoing COVID-19 pandemic has raised concerns over its association with myocarditis, an inflammatory disease of the heart muscle most often caused by viral infection (1). Myocarditis is a significant cause of sudden cardiac death (SCD) in competitive athletes (2) and continued exercise can lead to arrhythmic events, including SCD (3). Our group developed a cardiac screening protocol that includes a comprehensive cardiovascular magnetic resonance (CMR) scan to identify high risk athletes following a SARS-CoV-2 infection before returning to competitive play. Athletes were diagnosed with acute myocarditis defined by the presence of both T1-based criteria (T1 mapping or late gadolinium enhancement (LGE)) and T2 based criteria (T2 mapping). Supportive criteria included pericardial effusion, pericardial enhancement, and left ventricular systolic dysfunction. In addition, we collected data on global longitudinal (GLS) and circumferential (GCS) strain by strain encoding (SENC). Using data from initial and follow-up timepoints, we sought to investigate how these CMR markers suggestive of inflammation and fibrosis, as well as myocardial strain, change with time during recovery from SARS-CoV-2 infection.

**Methods:** We quantified the number segments with elevated T2 (>52 ms), the presence of pericardial effusion or enhancement, and the number of segments with LGE for each visit for all athletes diagnosed with myocarditis. GLS and GCS were measured for those with available data across timepoints.

**Results:** 15 athletes were diagnosed with acute myocarditis; 6 had one follow-up CMR scan and 9 athletes had an additional third scan. The mean time from SARS-CoV-2 positive test date and CMR scan visits 1, 2, and 3 was 29, 75, and 204 days respectively. For all athletes, the number of elevated T2 segments decreased or completely resolved by the second scan, and no athletes had elevated T2 segments by the third scan (Table 1, Figure 1). The number of segments with LGE showed no change for 9 athletes, increased in 1 athlete and decreased in 4 athletes between the initial and first follow-up scan. No changes in the number of segments with LGE were observed between scans 2 and 3. LGE did not completely resolve in any of the 15 athletes (Table 1, Figure 2). Pericardial Effusion resolved in 1 of 4 athletes, and pericardial enhancement resolved in 1 of 5 athletes initially presenting with the finding (Table 1). Myocardial strain varied inconsistently between timepoints.

**Conclusions:** Inflammation, characterized by elevated T2, in collegiate athletes with acute myocarditis following SARS-CoV-2 infection shows rapid and complete resolution with time. Late gadolinium enhancement shows no or limited resolution and persists for as long as 6 months following myocarditis diagnosis. Future work is needed to track the clinical significance of residual LGE in this patient population.

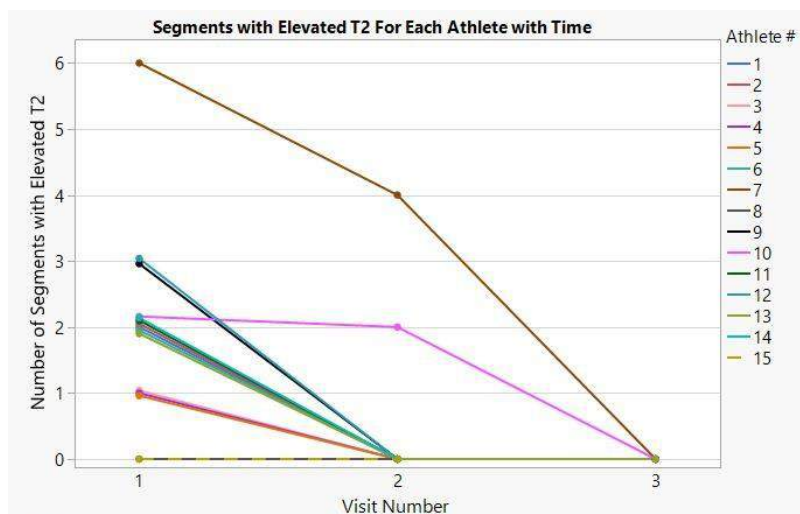
**Figure/Table 1**

	Timeframe	
	Visit 1 to Visit 2 (# of Athletes)	Visit 2 to Visit 3 (# of Athletes)
N	15	9
<b>Change in Number of Segments with Elevated T2</b>		
No Change	3	7
Increase	0	0
Decrease	1	0
Complete Resolution	11	2
<b>Change in Number of Segments with LGE</b>		
No Change	9	9
Increase	1	0
Decrease	5	0
Complete Resolution	0	0
<b>Change in Pericardial Effusion (Present initially in N=4)</b>		
Resolved	1	0
Still Present	3	1
<b>Change in Pericardial Enhancement (Present initially in N=5)</b>		
Resolved	1	0
Still Present	4	3

**Caption 1**

**Table 1.** Changes in number of segments with elevated T2, LGE, pericardial enhancement, and pericardial effusion between visits.

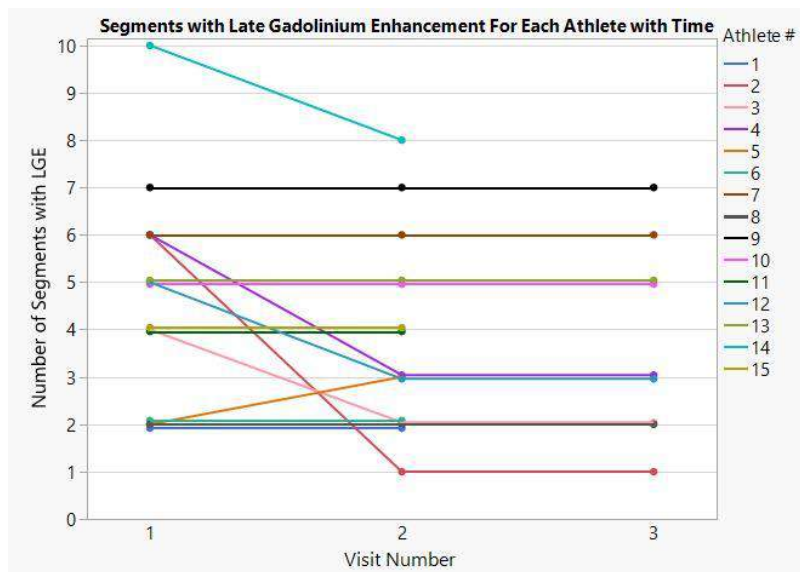
**Figure/Table 2**



**Caption 2**

**Figure 1.** The number of segments with elevated T2 for each athlete, categorized by visit number. Elevated T2 was completely resolved for all by the third visit.

**Figure 3**



### Caption 3

**Figure 2.** The number of segments with LGE for each athlete, categorized by visit number. LGE did not change for the majority of athletes.

### Bibliographic References

1. Fung G, Luo H, Qiu Y, Yang D, McManus B. Circ Res. 2016;118(3):496-514. , 2. Maron BJ, Udelson JE, Bonow RO, et al. Circulation. 2015;132(22):e273-e280. , 3. Tilles JG, Elson SH, Shaka JA, Abelmann WH, Lerner AM, Finland M. Proc Soc Exp Biol Med. 1964;117(3):777-782.

Speaker: J. Heyniger

Category: Myocarditis, T2, Late Gadolinium Enhancement

000585

## Non-invasive assessment of cardioprotective effect of LCZ696 (Sacubitril/valsartan) in a rat model of cardiorenal syndrome by using cardiovascular magnetic resonance

H. Chen \* (1); F. Gao (1)

(1) Department of radiology, West China Hospital, Sichuan University, Chengdu, China

### Abstract

**Background:** Kidney and heart are two major organs that they can affect each other when disfunction occurs, which is known as cardiorenal syndrome (CRS). CRS type 4 is a kind of syndrome that chronic kidney disease (CKD) leading to a reduction in cardiac function. Thus, early diagnosis of cardiac function in CKD patient plays a vital role in the management of whether in cardiovascular disease (CVD) or CKD patient. LCZ696 (Sacubitril/valsartan), a combination of the angiotension II type 1 receptor blocker valsartan and the neprilysin inhibitor sacubitril, can improve cardiac function and delay the progression of kidney disease. The myocardial effects of LCZ696 in CRS have been little studied. Therefore, we aim to investigate the cardioprotective effect of LCZ696 (Sacubitril/valsartan) on CRS type 4 model, and, to assess the early myocardial remodeling by using cardiovascular magnetic resonance tissue tracking (CMR-TT).

**Methods:** Sixty male Sprague Dawley rats were randomly divided into control group (n = 20) and surgical group (n = 40). The surgical group then accepted a standard operation of 5/6 nephrectomy and 6 weeks later the alive CKD rats were randomly divided into no treatment (n = 16) or LCZ696 (n = 16, 60 mg/kg, once-daily by gavage) for two weeks. Serum, urine, heart tissue was collected and CMR-TT was performed at 0W, 6W and 8W time points. CMR acquisition was performed using a 7.0 T preclinical system (Bruker BioSpec 70/30; Ettlingen). CMR analyses including cardiac function and tissue tracking were performed using a commercially available software (CVI42 version 5; Circle Cardiovascular Imaging). The main parameters of CMR-TT are 2D global circumferential strain (2D-GCS), 2D global longitudinal strain (2D-GLS), 2D global radial strain (2D-GRS) and 3D-GCS, 3D-GLS, 3D-GRS.

**Results:** Six weeks after the surgery, CKD versus Control group demonstrated higher Serum Creatinine ( $52.67 \pm 2.81$  vs  $23.67 \pm 1.70$ ,  $P < 0.0001$ ), higher Serum BUN ( $10.71 \pm 1.17$  vs  $4.60 \pm 0.45$ ,  $P < 0.0001$ ), higher 24 h Urine Protein ( $20.53 \pm 2.21$  vs  $5.15 \pm 0.89$ ,  $P < 0.0001$ ) and lower LV ejection fraction ( $63.10 \pm 0.76$  vs  $67.78 \pm 2.06$ ,  $P < 0.001$ ). Two weeks after the LCZ administration, both cardiac function and structure in LCZ group has improved. For CMR-TT analysis, all six strain parameters decreased in 8W compared with the Control group (2D-GRS:  $40.72 \pm 4.25$  vs  $45.46 \pm 6.07$ , 2D-GCS:  $-21.41 \pm 1.21$  vs  $-22.71 \pm 1.73$ , 2D-GLS:  $-20.47 \pm 1.87$  vs  $-22.67 \pm 0.20$ , 3D-GRS:  $41.60 \pm 4.10$  vs  $44.72 \pm 0.39$ , 3D-GCS:  $-22.30 \pm 1.96$  vs  $-25.46 \pm 0.73$  and 3D GLS:  $-16.88 \pm 2.24$  vs  $-20.76 \pm 0.73$   $P < 0.05$ ). While the LCZ group showed a different pattern that there is a slight increase in the value, though with no statistic difference.

**Conclusion:** LCZ696 showed an excellent performance of cardioprotective effect in CRS type 4 model. In addition, CMR has the potential to evaluate the change of myocardial

function and structure in the early stage. Future study is still needed to assess the effect of LCZ in CRS type 4 by extending the time of administration.

**Figure/Table 1**

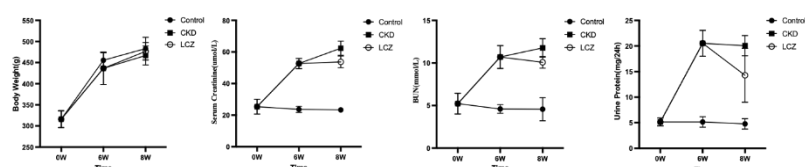
**Table1.** Comparison of some CMR parameters in the Control, CKD and LCZ groups at different time points

Time point	Group	EF(%)	2D Strain (%)			3D Strain (%)		
			GRS	GCS	GLS	GRS	GCS	GLS
0W	Control	68.51±0.25	49.24±4.62	-23.90±1.16	-22.31±1.72	45.18±4.60	-24.46±1.38	-19.89±2.62
6W	Control	67.78±2.06	45.53±3.47	-23.05±0.96	-21.81±0.62	48.81±6.17	-23.25±1.30	-20.27±0.65
	CKD	63.10±0.76	43.09±3.48	-22.30±1.19	-20.91±1.44	49.36±8.32	-22.25±1.61	-17.51±2.94
8W	Control	68.22±0.50	45.46±6.07	-22.71±1.73	-22.67±0.20	44.72±0.39	-25.46±0.73	-20.76±0.73
	CKD	61.07±2.77	40.72±4.25	-21.41±1.21	-20.47±1.87	41.60±4.10	-22.30±1.96	-16.88±2.24
	LCZ	66.38±2.45	43.27±4.40	-22.06±1.22	-21.08±1.89	49.54±4.33	-22.57±2.41	-18.10±2.01

**Caption 1**

Results are presented as mean ± standard deviation. GRS: global radial strain, GCS: global circumferential strain, GLS: global longitudinal strain, EF: ejection fraction.

**Figure/Table 2**

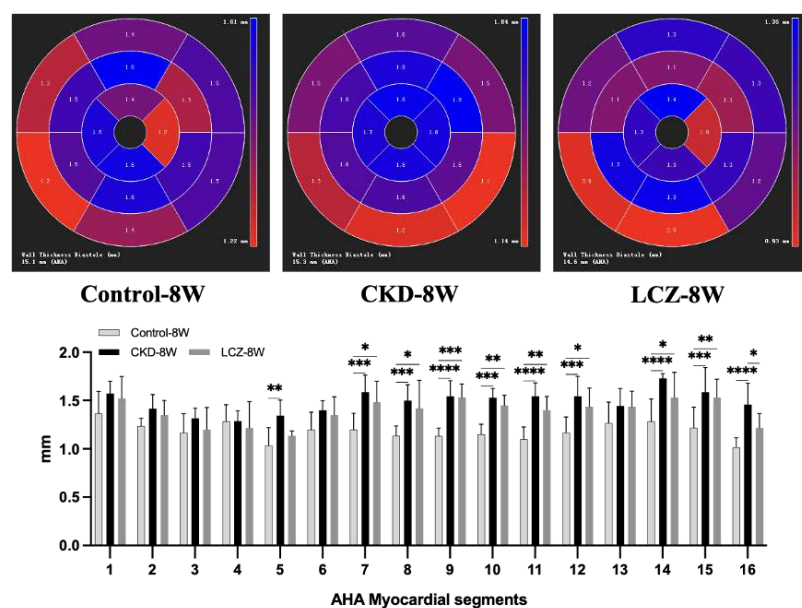




## Caption 2

**Figure1.** Change of body weight, serum creatinine, BUN and 24 urine protein in Control, CKD and LCZ group.

## Figure 3



## Caption 3

**Figure2.** LV wall thickness of 1-16 myocardial segments in Control, CKD and LCZ group detected by CMR at 8W. CKD model showed increased diastolic wall thickness in all 16 segments. While the LCZ reversed such myocardial remodeling. \* $P < 0.05$ , \*\* $P < 0.01$ , \*\*\* $P < 0.001$ , \*\*\*\* $P < 0.0001$ .

Speaker: H. Chen

Category: Cardiorenal, Cardiac Function, Tissue Tracking

000587

## Left Ventricular Fibrosis Pattern in Patients with Severe Tricuspid Regurgitation

M. Umair, \* (1); R. Avery (1); J. Puthumana, (2); J. Thomas, (2); A. Narang (2)

(1) Radiology, Northwestern Memorial Hospital, Chicago, United States of America; (2) Cardiology, Northwestern Memorial Hospital, Chicago, United States of America

### Abstract

**Introduction:** Severe tricuspid regurgitation (TR) is increasingly recognized as an independent risk factor for adverse cardiac outcomes, mostly due to worsening right ventricle (RV) function and pulmonary hypertension. Less is known about the impact of severe TR on left ventricle (LV) myocardial scar as detected by cardiovascular magnetic resonance (CMR) imaging. The purpose of this study was to characterize the patterns of late gadolinium enhancement (LGE) in patients with severe TR who were referred for a CMR.

**Methods:** A retrospective analysis of patients with severe TR noted on transthoracic echocardiogram who were referred for CMR was performed. Patients with other valve lesions assessed to be more than mild in severity were excluded. Each patient underwent a standard CMR protocol with administration of gadolinium-based contrast. LGE was performed with phase-sensitive inversion recovery (PSIR) sequences and without PSIR (magnitude only). The short-axis cine was utilized to determine RV and LV volumes and ejection fraction (EF) and LV LGE was assessed qualitatively.

**Results:** 23 patients were included in the analysis (mean age  $59 \pm 16$  years, 57% female). The LVEF and indexed LV end-diastolic volume (EDV) was  $51.6 \pm 19.6\%$  and  $85.0 \pm 23.1$  ml/m<sup>2</sup> while the RVEF and indexed RV EDV was  $44.6 \pm 15.0\%$  and  $132.5 \pm 30.5$  ml/m<sup>2</sup>. 34.7% of patients (8/23) had focal fibrosis (LGE) noted at the basal inferior septum (RV insertion point). Three of these patients also had an additional LV LGE pattern (two with sub-endocardial pattern and one sub-epicardial pattern). Patients with RV insertion point LGE vs those without tended to have more a dilated RV and lower RVEF ( $143.6 \pm 34.5$  vs  $126.9 \pm 23.9$  ml/m<sup>2</sup>;  $35.0 \pm 11.5\%$  vs  $50.7 \pm 13.5\%$ ).

**Conclusions:** In patients with severe TR, the presence of inferior RV insertion point LGE may reflect more adverse RV remodeling as noted by dilated RV and lower RVEF. This finding may become an important imaging biomarker that is associated

Speaker: M. Umair,

Category: Tricuspid Regurgitation, Valvular Heart Disease, Fibrosis

000588

## **Elevated fractional myocardial blood volume as a marker of myocardial ischemia using ferumoxytol-enhanced MRI**

C. Colbert \* (1); D. Nguyen (2); P. Hu (3); K.-L. Nguyen, (1)

(1) Division of cardiology, VA Greater Los Angeles Healthcare System, Los Angeles, United States of America; (2) Department of computer science, University of California, Berkeley, Berkeley, United States of America; (3) Department of radiology, University of California, Los Angeles, Los Angeles, United States of America

### **Abstract**

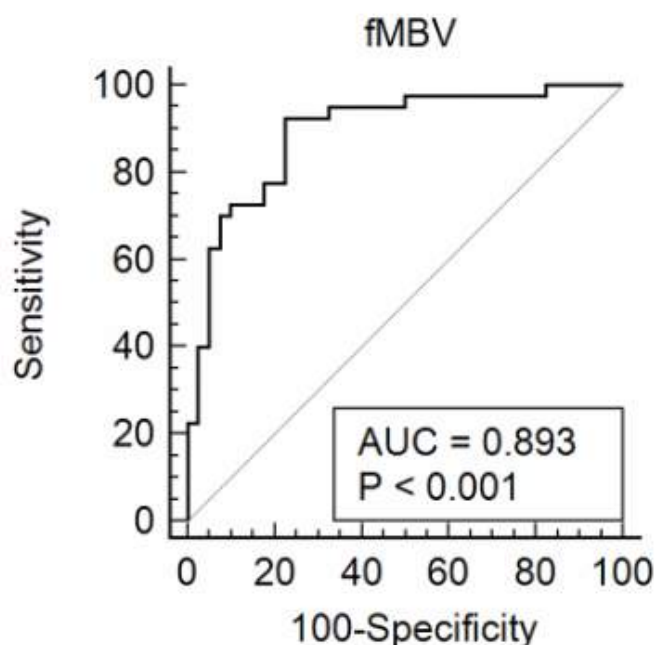
**Background:** Elevated fractional myocardial blood volume (fMBV) has been proposed as a quantitative imaging biomarker for myocardial hypoperfusion and ischemia at rest. We investigated model-fitted fMBV derived from ferumoxytol-enhanced magnetic resonance imaging (MRI) as a measure of myocardial tissue hypoperfusion in a cohort of swine models with moderate to severe coronary stenosis.

**Methods:** We induced an artificial coronary stenosis in the left anterior descending (LAD) artery in 19 swine. [1] We acquired MOLLI T1 maps at multiple ferumoxytol doses (range = 0.0 – 4.0 mg/kg) during contrast steady state. [2] We used the Instantaneous Signal Loss simulation (InSiL) algorithm for T1 fitting of MOLLI images. [3] Following T1 fitting, we co-registered each set of multi-dose InSiL T1 maps. [4] Taking care to exclude trabeculations and papillary muscles, we contoured a central region of the mid-LV blood pool to extract blood R1 at each ferumoxytol dose. We used a two-compartment water exchange model with three-parameter fitting to fit for pixelwise fMBV and water exchange rate in all slices. [2] We segmented fMBV maps according to the AHA model. We performed fMBV group comparisons using paired Student's t-test and sex differences in fMBV between remote and ischemic segments were evaluated.

**Results:** Across 19 swine models of acute myocardial hypoperfusion, mean ischemic fMBV was greater than mean remote fMBV by a factor of 1.42. Ischemic segments showed a mean fMBV of  $11.72 \pm 3.00\%$ , compared to a mean fMBV of  $8.23 \pm 2.12\%$  in remote segments. We found a significant difference in fMBV between ischemic segments and their contralateral, remote segment ( $p < 0.0001$ ,  $N = 40$  ischemic ROIs). Two-way Analysis of Variance (ANOVA) showed no systematic difference between male and female swine ( $p=0.86$ ), while a borderline significant interaction between swine subject sex and ischemia was observed ( $p=0.031$ ). In female swine ( $N=7$ ), the mean fMBV was  $11.20 \pm 2.74\%$  and  $8.57 \pm 1.89\%$  in ischemic ( $N=18$ ) and remote segments ( $N=97$ ), respectively. In male swine ( $N=12$ ), the mean fMBV was  $12.15 \pm 3.20\%$  and  $7.76 \pm 2.35\%$  in ischemic ( $N=22$ ) and remote ( $N=71$ ) segments, respectively. ROC analysis of fMBV as a predictor of wall motion abnormality showed an area under the curve (AUC) of 0.89 (95% CI 0.80, 0.95, Figure 1).

Conclusions: Pixel-wise fMBV maps derived from multi-dose ferumoxytol-enhanced MRI can be used to distinguish ischemic from remote myocardial tissues in large animal models of acute myocardial hypoperfusion.

**Figure/Table 1**



**Caption 1**

Figure 1. ROC curve of segmental fMBV for prediction of tissue hypoperfusion. We found an area under the ROC curve for pixelwise fMBV of 0.89 (95% CI 0.80, 0.95). The fMBV criterion of 9.60% is associated with a specificity of 90.0% (76.3 – 97.2) and a sensitivity of 72.5% (56.1 – 83.4).

### Bibliographic References

1. Colbert CM, Shao J, Hollowed JJ, Currier JW, Ajjola OA, Fishbein GA, Duarte-Vogel SM, Dharmakumar R, Hu P, Nguyen KL. 3D-Printed Coronary Implants Are Effective for Percutaneous Creation of Swine Models with Focal Coronary Stenosis. *J Cardiovasc Transl Res*. Published online May 11, 2020:1-11. doi:10.1007/s12265-020-10018-3, 2. Colbert CM,

Thomas MA, Yan R, Radjenovic A, Finn JP, Hu P, Nguyen KL. Estimation of fractional myocardial blood volume and water exchange using ferumoxytol-enhanced magnetic resonance imaging. *J Magn Reson Imaging*. Published online 2020:1-11. doi:10.1002/jmri.27494, 3. Shao J, Nguyen K-L, Natsuaki Y, Spottiswoode B, Hu P. Instantaneous signal loss simulation (InSiL): An improved algorithm for myocardial T1 mapping using the MOLLI sequence. *J Magn Reson Imaging*. 2015;41(3):721-729. doi:10.1002/jmri.24599, 4. Huizinga W, Poot DHJ, Guyader JM, Klaassen R, Coolen BF, Van Kranenburg M, Van Geuns RJM, Uitterdijk A, Polfliet M, Vandemeulebroucke J, Leemans A, Niessen WJ, Klein S. PCA-based groupwise image registration for quantitative MRI. *Med Image Anal*. 2016;29:65-78. doi:10.1016/j.media.2015.12.004

Speaker: C. Colbert

Category: Ischemic Heart Disease, Perfusion, Microvascular disease

000590

## **Let's do an MRI: Incidental large bronchial cast during cardiac MRI examination in a patient with a Glenn circulation**

M. Nagiub, \* (1); M. Ganigara, (2); M. Fares (1); S. R. Reddy (1); T. Hussain (1); J. Greer (1); L. Zabala (3); J. Hernandez (4)

(1) Pediatric cardiology, UT Southwestern Medical Center, Dallas, United States of America; (2) Pediatric cardiology, UT Southwestern Medical Center, University Park, United States of America; (3) Pediatric cardiac anathesia, UT Southwestern Medical Center, Dallas, United States of America; (4) Pediatric anathesia, UT Southwestern Medical Center, Dallas, United States of America

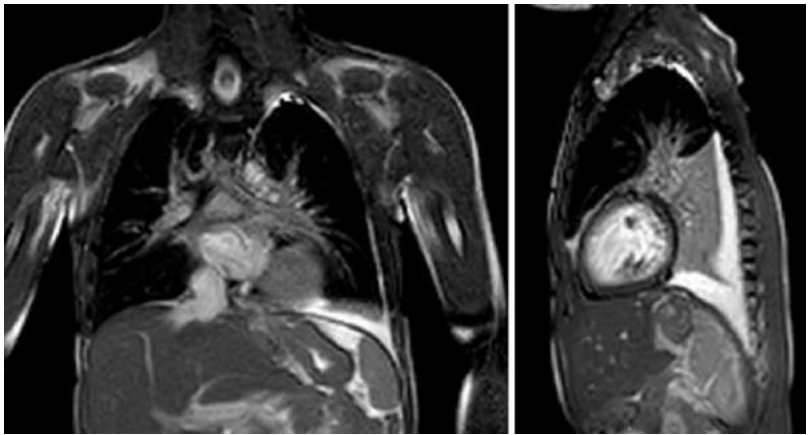
### **Abstract**

Description of Clinical Presentation: Five-year-old female with severe tricuspid and pulmonary hypoplasia and hypoplastic right ventricle was palliated with a right Blalock Taussig Thomas (BTT) shunt during the neonatal period, followed by bidirectional Glenn anastomosis with right pulmonary arterioplasty around 6 months of life. The patient was referred for evaluation for Fontan procedure at 4-years of age due to cyanosis on exertion and reduced effort tolerance. Systemic enquiry revealed intermittent cough not alleviated by bronchodilators. Transthoracic echocardiography evaluation and chest X-ray were unremarkable. As per institutional standard of care, she was referred for diagnostic iCMR to evaluate for Fontan completion.

Diagnostic techniques: After general anesthesia induction, the anesthesiologist noted unequal air entry on auscultation and reviewed the triplanar survey noting left sided atelectasis(Figure1). Per our cardiac MRI protocol, 3D Black-Blood VISTA (Volume Isotropic Turbo Spin Echo Acquisition) sequence is performed. This technique uses slice-selective excitation and non-selective refocusing pulses with variable flip angles to achieve constant echo signal for tissue with T1 (880 ms) and T2 (40 ms)). It focuses on vessel wall imaging and also gives excellent airway delineation (Figure 2). This revealed a large left bronchial cast. In order to confirm lymphatic abnormality, a 3D heavily T2-weighted Turbo Spin Echo (TSE) was performed (TE/TR=600/2500 ms, resolution=1x1x1.8 mm, with respiratory triggering). This confirmed the most severe form of lymphatic abnormality (Dori grade 4) with suprclavicular mediastinal and pulmonary intraparenchymal leak with accompanying pleural effusion(Figure3). Further iCMR evaluation was aborted and instead an emergent bronchoscopy was performed in the cardiac catheterization lab (which is always available for iCMR cases). Histology confirmed the diagnosis of bronchial lymphatic cast and biochemistry confirmed that the 100 ml of pleural fluid drained was chylous. The patient underwent interval selective lymphatic duct embolization with resolution of symptoms and has not undergone Fontan procedure.

Learning Points: iCMR evaluation of the Glenn patient should include airway and lymphatic review as abnormalities are common. The cardiac anesthesiologist is a leading member of any congenital iCMR team and this case clearly highlights the role in directing the correct investigations and treatment. VISTA and T2-weighted sequences are important for the complete assessment of such patient

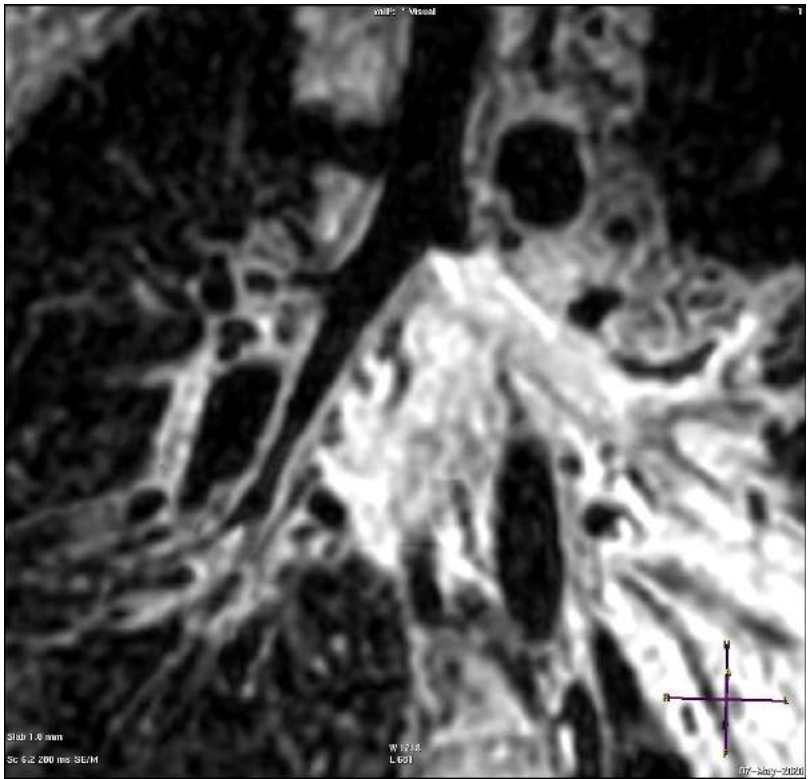
### **Figure/Table 1**



**Caption 1**

Coronal and sagittal survey images revealing left bronchial hyaline cast, left pleural effusion and left lower lobe atelectasis

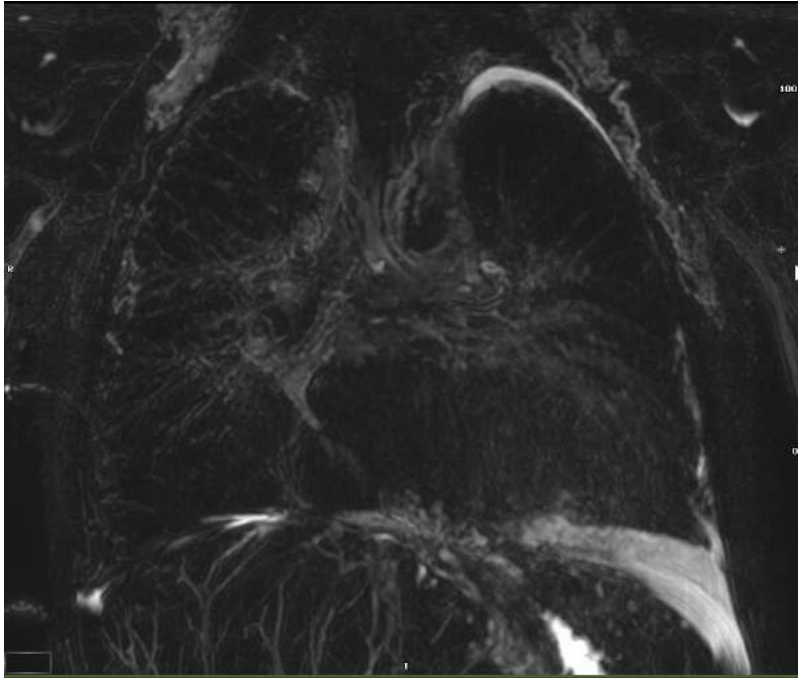
**Figure/Table 2**



**Caption 2**

Figure 2: The bronchial tree was imaged using a 3D fast spin echo (3D FSE) sequence (3D VISTA)

**Figure 3**



**Caption 3**

Figure 3: Heavy T2 weighted imaging confirmed suspicion for hyaline bronchial case and chylous effusion and showed a Dori grade 4 thoracic lymphatic abnormalities.

### **Bibliographic References**

1. Henningson, M., Zahr, R.A., Dyer, A. et al. Feasibility of 3D black-blood variable refocusing angle fast spin echo cardiovascular magnetic resonance for visualization of the whole heart and great vessels in congenital heart disease. *J Cardiovasc Magn Reson* 20, 76 (2018). <https://doi.org/10.1186/s12968-018-0508-1>
2. Dori Y, Keller MS, Rome JJ, Gillespie MJ, Glatz AC, Dodds K, Goldberg DJ, Goldfarb S, Rychik J, Itkin M. Percutaneous Lymphatic Embolization of Abnormal Pulmonary Lymphatic Flow as Treatment of Plastic Bronchitis in Patients With Congenital Heart Disease. *Circulation*. 2016 Mar 22;133(12):1160-70. doi: 10.1161/CIRCULATIONAHA.115.019710. Epub 2016 Feb 10. PMID: 26864093.

Speaker: M. Naguib,

Category: Single Ventricle, T2, 3D



000591

## Left Ventricular Myocardial Remodeling and Prognostic Marker Derived from Feature Tracking in Hypertrophic Obstructive Cardiomyopathy after Surgical Myectomy

S. Yang \* (1); S. Zhao (2)

(1) Mr center, Fuwai Hospital&State Key Laboratory of Cardiovascular Disease, Beijing, China; (2) Mr center, Fuwai Hospital&State Key Laboratory of Cardiovascular Disease, Beijing, China

### Abstract

**Background:** Cardiovascular magnetic resonance (CMR)-feature tracking enables quantify myocardial deformation noninvasively. Surgical myectomy can substantially reduce LVOT obstruction and relieve symptoms in hypertrophic obstructive cardiomyopathy(HOCM), but the prognostic role of postoperative strains remains unknown. This study aimed to validate global and regional myocardial remodeling after septal myectomy using CMR-feature tracking and further investigate the prognostic value of postoperative strains in HOCM after myectomy.

**Materials:** Patients with HOCM after myectomy who underwent preoperative and postoperative CMR between May 2011 to October 2020 were retrospectively reviewed. Exclusion criteria were patients who underwent septal ablation before septal myectomy and redid septal myectomy, the interval of preoperative CMR before surgery>6 months, the interval of postoperative CMR after surgery<3 months, uninterpretable image quality for strain analysis, age<18, right ventricular outflow obstruction, and the presence of comorbidities including congenital heart disease, valvular disease, infiltrative cardiomyopathies, hypertension, and coronary artery disease. Parameters of preoperative and postoperative CMR were compared, including circumferential strain(CS), longitudinal strain(LS), and radial strain(RS) of global left ventricle, septum, and lateral wall accessed by feature tracking. 59 healthy participants with similar age and sex distribution were included for comparison. The composite endpoint consisted of cardiac death(fatal or aborted), heart transplantation, appropriate implantable cardioverter-defibrillator firing, and hospitalization for heart failure.

**Results:** A total of 73 patients(mean age, 43.6±14.3 years; 45 men) were evaluated. Compared with preoperative strains, global CS was impaired, but global LS was improved(all  $P < .05$ ); no significant changes in global RS. Septal CS and septal RS worsened, while septal LS and lateral strains in three directions were improved(all  $P < .05$ ). During a median follow-up of 39.1 months, 16 of 73 patients(21.9%) experienced composite events. Multivariable Cox analysis was performed with significant univariable predictors (family history, postoperative global strains) after forcing preoperative LGE into the final model. Postoperative global CS emerged as the only significant predictor(hazard ratio:1.177, 95% confidence interval:1.023-1.355; $P=.023$ ), which performed best for outcome prediction(area under the curve:0.73) with a cutoff of -16.7%(sensitivity 87.5%;specificity 63.2%).

**Conclusions:** Myectomy results in longitudinal and lateral restorations; however, a negative impact may occur on global and septal CS in HOCM. Postoperative global CS is associated with adverse outcomes in HOCM patients.

**Figure/Table 1**

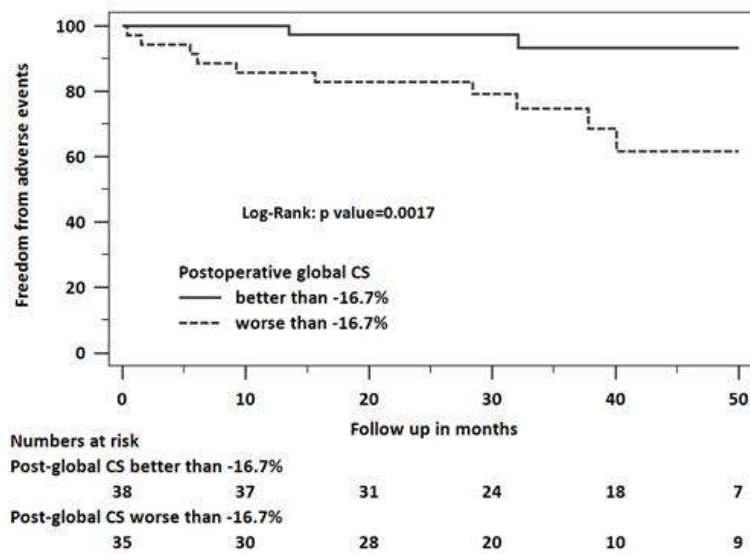
	Pre-myectomy (n=73)	Post-myectomy (n=73)	Healthy controls (n=59)
Maximal LV wall thickness (mm)	29.3±6.8*†	24.3±7.0*	9.9±1.7
LV ejection fraction (%)	64.4±9.0*†	59.7±7.5	61.9±4.7
LV end-diastolic volume index (ml/m <sup>2</sup> )	83.8±24.5*†	78.1±20.4	72.8±12.0
LV end-systolic volume index (ml/m <sup>2</sup> )	32.1±18.3	32.7±15.1	27.8±5.8
LV mass index (g/m <sup>2</sup> )	97.3±51.9*†	80.7±41.6*	41.1±9.6
Cardiac output (l/min)	6.3±1.7*†	5.4±1.2*	5.5±1.3
Global radial strain (%)	27.4±13.5*	27.0±11.5*	36.8±8.3
Global circumferential strain (%)	-17.6±4.4*†	-16.7±3.9*	-21.7±2.7
Global longitudinal strain (%)	-9.3±2.8*†	-10.8±3.3*	-14.1±1.8
Septal radial strain (%)	16.4±10.6*†	13.7±9.5*	28.6±6.0
Septal circumferential strain (%)	-14.2±4.0*†	-11.0±4.4*	-17.5±2.5
Septal longitudinal strain (%)	-8.1±3.5*†	-10.2±3.4*	-13.2±2.6
Lateral radial strain (%)	40.1±16.6*†	54.4±2.6	51.0±10.6
Lateral circumferential strain (%)	-20.2±4.1*†	-23.1±4.8	-23.4±3.3
Lateral longitudinal strain (%)	-5.6±5.6*†	-8.4±5.2*	-11.7±3.3

**Caption 1**

Table 1: CMR Parameters in the Control Group, Pre- and Post-myectomy Group with Hypertrophic Obstructive Cardiomyopathy.

Values are presented as mean ± standard deviation.\*  $P < .05$  compared with healthy controls.  
† $P < .05$  compared with post-myectomy group. LV=left ventricular.

**Figure/Table 2**

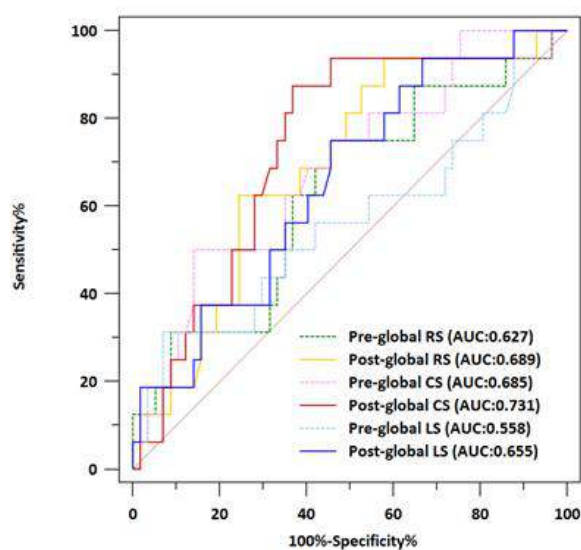


**Caption 2**

Figure 1: Kaplan–Meier event-free survival curve to evaluate the survival free of composite endpoint.

Strain better than 16.7% indicates value  $\leq -16.7\%$ ; strain worse than 16.7% indicates value  $> -16.7\%$ .

**Figure 3**



### **Caption 3**

Figure 2: Receiver operating characteristic curves for composite endpoint in hypertrophic obstructive cardiomyopathy patients using pre- and post-myectomy LV global strains on feature tracking.

CS, circumferential strain; LS, longitudinal strain; RS, radial strain.

Speaker: S. Yang

Category: Hypertrophic Cardiomyopathy, Cardiac Surgery, Cardiac Strain

000593

**Preliminary Assessment of a prototype highly accelerated free-breathing cine sequence with compressed sensing and in-line respiratory motion correction compared to segmented cine imaging**

A. Negm \* (1); J. Pang (2); K. McGee (1); H. Iverson, (1); M. Halverson, (1); R. Davids (3); P. Rajiah (4); A. Bratt (5); E. Williamson, (1); P. Young (4); T. A. Foley (4); C. Francois (1); X. Bi (3); J. Collins (4)

(1) Radiology, Mayo Clinic, Rochester, United States of America; (2) Research collaborations group, Siemens Healthineers, Chicago, IL, USA, United States of America; (3) Cardiovascular imaging, Siemens Medical Solutions USA, Inc., Chicago, United States of America; (4) Radiology, Mayo Clinic, 1st Street Southwest, Rochester, MN, USA, Rochester, United States of America; (5) Radiology, Mayo Clinic, Rochester

**Abstract**

**Background:** Cardiac cine MRI is the accepted gold standard in assessing biventricular size and systolic function. Balanced steady-state free precession (bSSFP) segmented cine imaging (Seg Cine) is the standard of reference technique in clinical practice. Even utilizing accelerated approaches, Seg Cine requires multiple breath-holds to cover the heart in the short axis (SAX) orientation. Real-time imaging methods have been introduced into clinical practice to improve efficiency; early implementations were limited by poor temporal and spatial resolution. Recently, a prototype free-breathing cardiac cine technique with compressed sensing and in-line respiratory motion correction, RTCSCineMoCo, has shown promising results in image quality and quantitative cardiac function measurements when compared to Seg Cine. The purpose of this study is to compare the quantitative performance of RTCSCineMoCo with Seg Cine as the standard of reference in a larger patient cohort.

**Methods:** We retrospectively analyzed data from 57 consecutive adult patients referred for cardiac MRI who underwent both imaging techniques at a single center. Imaging was performed on a 1.5 T clinical scanner (MAGNETOM Aera, Siemens Healthcare, Erlangen, Germany). RTCSCineMoCo images were obtained pre-contrast. Seg Cine images were obtained following bolus infusion of double dose gadobutrol. Our institutional quality review board approved the use of RTCSCineMoCo as an adjunct to seg cine imaging in the clinical routine. Seg Cine Imaging Parameters: (TR/TE 2.87/1.5 ms, FOV 280, temp res 37.3 ms, matrix 224 x 224, slice thickness 6 mm, GRAPPA factor 2, acquisition time / slice 8.5 s / 10 sec pause – 14 HB per slice, end-inspiration). RTCSCineMoCo parameters: (TR/TE 3.07/1.33 ms, FOV 320 mm, temp res 46.05 ms, matrix 192 x 192, slice thickness 8 mm, acquisition time / slice (12 HB / 10.8 sec), acceleration factor 12.8, free-breathing). Both techniques were obtained in the SAX orientation. Quantitative analysis of biventricular size and systolic function was performed on Cvi42 (Circle Cardiovascular Imaging Inc., Calgary, Canada) following the method detailed in the 2020 SCMR white paper, leaving the papillary muscles in the blood pool. We then used Student's paired t-test (two-sided alpha,  $p = 0.05$ ) to assess agreement between paired measures. Bland-Altman plots were generated for statistically significant values. Ten random datasets were re-analyzed by the same observer using Bland-Altman plots for intraobserver variability.

**Results:** Data from 7 patients with arrhythmia and breathing artifacts rendering Seg Cine imaging non-diagnostic was excluded. The study sample comprised 50 subjects (27 men, avg age 61 yrs). RTCSCineMoCo images were analyzable in all subjects. LVEF, LV end diastolic mass, and RV stroke volume (RVSV) were similar between techniques (Table 1). LVEDV, LVESV, RVEF, RVEDV, and RVSV were significantly different between techniques, with a positive bias on Bland-Altman analysis, although limits of agreement included no difference. Test-retest analysis demonstrated excellent intra-observer agreement for LVEDV, LVESV, LVEF, LV end diastolic mass, RVESV, and RVEF and modest agreement between RVEDV and RVSV for both methods. The bias for intra-observer measures of RVEDV and RVESV was similar between methods.

**Conclusions:** Compared to Seg Cine, our study shows that RTCSCineMoCo yields a similar quantitative assessment of LVEF, LV end diastolic mass, and RVESV. LVEDV and LVESV were different between methods, which may relate to end-inspiratory vs free-breathing acquisition. Differences in RVEDV, RVESV, and RVSV between methods were similar in magnitude to intra-observer variability. Work is ongoing in a larger cohort is ongoing to confirm our findings.

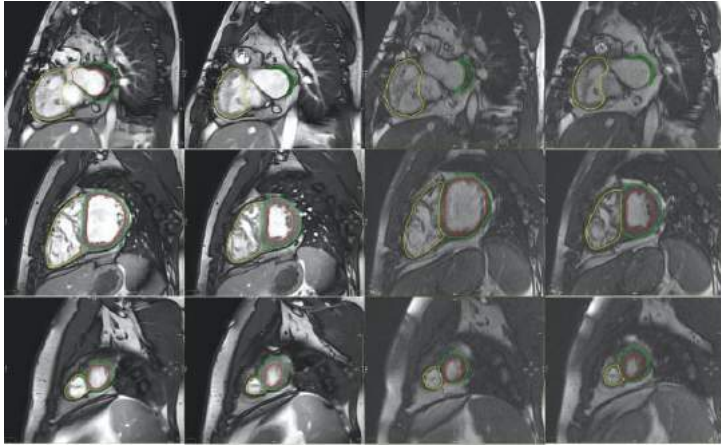
**Figure/Table 1**

Parameter	Student's t-test p-value	Bias	Upper LoA	Lower LoA
<b>RTCSCineMoCo vs Seg Cine</b>				
<i>Left Ventricle</i>				
LVEDV (ml)	$2.81 \times 10^{-8}$	21.2 ml	65.8 ml	-23.4 ml
LVESV (ml)	$1.95 \times 10^{-6}$	10.7 ml	38.2 ml	-16.8 ml
LVEF (%)	> 0.05	-	-	-
Diastolic LV Myo Mass (g)	> 0.05	-	-	-
<i>Right Ventricle</i>				
RVEDV (ml)	0.0457	7.5 ml	57.9 ml	-43 ml
RVESV (ml)	> 0.05	-	-	-
RVEF (%)	0.0094	3.3%	20.1%	-13.5%
<b>Test-Retest RTCSCineMoCo</b>				
<i>Left Ventricle</i>				
LVEDV (ml)		1.1 ml	17.6 ml	-15.4 ml
LVESV (ml)		-2.1 ml	21.3 ml	-25.5 ml
LVEF (%)		-1.5%	18.9%	-21.9%
Diastolic LV Myo Mass (g)		-0.1 g	24.2 g	-24.4 g
<i>Right Ventricle</i>				
RVEDV (ml)		9.7 ml	58.7 ml	-39.3 ml
RVESV (ml)		-2.7 ml	34.2 ml	-39.6 ml
RVEF (%)		5.3%	19.4%	-8.8%
<b>Test-Retest Seg Cine</b>				
<i>Left Ventricle</i>				
LVEDV (ml)		1.6 ml	16.2 ml	-19.4 ml
LVESV (ml)		1.2 ml	26.7 ml	-24.3 ml
LVEF (%)		-1.9%	6.3%	-10.1%
Diastolic LV Myo Mass (g)		-7.3 g	32.6 g	-47.2 g
<i>Right Ventricle</i>				
RVEDV (ml)		7.5 ml	57.9 ml	-43 ml
RVESV (ml)		10.6 ml	42.9 ml	-21.7 ml
RVEF (%)		4.2%	25.1%	-16.7%

**Caption 1**

Table 1: Comparison of quantitative measures of biventricular size and systolic function between RTCSCineMoCo and Seg Cine. Intra-observer variability in n=10 data sets was assessed with Bland-Altman plots; these are provided for both techniques.

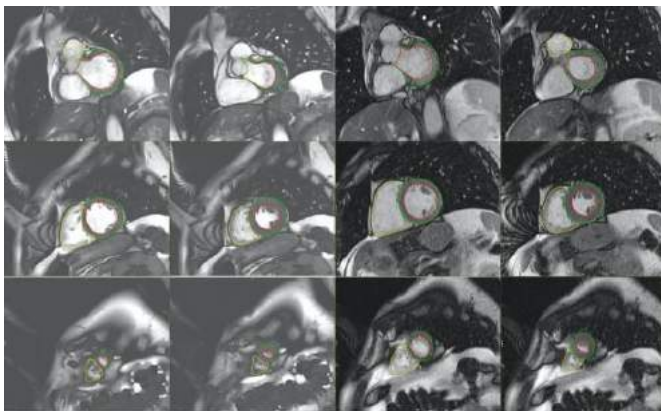
**Figure/Table 2**



**Caption 2**

Figure 1: Cardiac MRI of a 26-year-old male patient. Left 2 columns: FB MOCO cine images in both diastole and systole (base, middle, and apex). Right 2 columns: Seg cine images in both diastole and systole (base, middle, and apex). Seg cine images were obtained post-contrast.

**Figure 3**



**Caption 3**

Figure 2: Cardiac MRI of a 64-year-old male patient. Left 2 columns: FB MOCO cine images in both diastole and systole (base, middle, and apex). Right 2 columns: Seg cine images in both diastole and systole (base, middle, and apex). Seg cine images were obtained post-contrast.

Speaker: A. Negm

Category: Cine Imaging, Accelerated Imaging, Compressed Sensing

000594

## **Challenges in Imaging neonatal late gadolinium enhancement**

S. Philip \* (1); M. Ganigara, (2); B. Sharma, (2); R. Vamsee, (2); J. Greer (2); T. Hussain (3)

(1) Cardiology, Children's Medical Center Dallas, Dallas, United States of America; (2) Pediatrics, UT Southwestern Medical Center, Dallas, United States of America; (3) Pediatric cardiology, UT Southwestern Medical Center, Dallas, United States of America

### **Abstract**

#### **Description of Clinical Presentation:**

A near term newborn with maternal history of chorioamnionitis was admitted to the neonatal ICU for respiratory distress after birth. He was managed as neonatal sepsis. He was soon noted to have persistent atrial tachycardia requiring betablocker therapy. Transthoracic echocardiogram revealed normal cardiac anatomy with initially normal myocardial systolic function. Neonatal myocarditis was suspected due to positive enterovirus PCR and a mild troponin leak. Cardiac MRI at two weeks of age revealed depressed left ventricular function (ejection fraction 41%), with septal dyskinesia but LGE was inconclusive due to motion. Patient clinically improved with supportive therapy; serial echocardiograms revealed improving LV systolic function with new findings of patchy echo-brightness in the basal- and mid-septal walls. A repeat cardiac MRI was requested at four weeks of age.

#### **Diagnostic Techniques and Their Most Important Findings:**

Repeat cardiac MRI with Gadolinium contrast was performed with the feed-and-wrap technique with no sedation, which revealed normal sized left ventricle with normal ventricular mass and systolic function (measured ejection fraction 71%). There was diminished systolic thickening of the basal anteroseptal and basal inferoseptal LV segments (AHA segments 2,3).

PSIR LGE imaging was performed two minutes after administration of Gadolinium contrast to account for the rapid washout of contrast in the setting of high neonatal heart rates. A gradient echo phase-sensitive inversion recovery sequence was used during free-breathing, with the inversion time selected from a four-beat Look-Locker sequence to null the myocardium. Eight thin short-axis slices were acquired through the ventricle (6mm slice thickness), with 1.6 x 1.9mm resolution, a SENSE factor of 1.8 and NSA=2. Because of the high heart rate (120BPM), mid-diastolic imaging with shortened acquisition window (50ms) was performed every 4th RR interval.

This revealed sub-endocardial partial thickness delayed myocardial enhancement of the AHA segments 2 and 3 (Figure 1, arrows). These findings are more consistent with neonatal thromboembolic myocardial infarction. The patient continued to show clinical improvement and was discharged on betablocker therapy. He is now four months old with normal growth and no further symptoms. On the last clinic visit he had no arrhythmia and normal ventricular function (with persisting findings of sub endocardial echo-brightness in the basal septum).

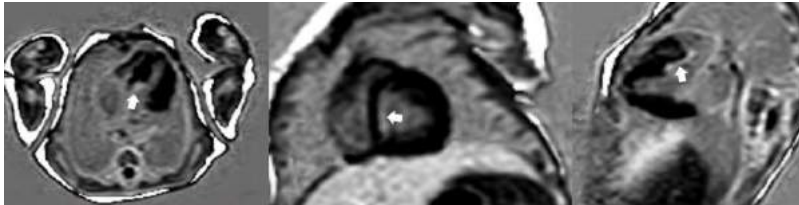
#### **Learning Points from this Case:**

Imaging LGE in neonates is challenging due to the high heart rates and respiratory rates, challenges of balancing spatial resolution with voxel volume and thus signal intensity and the



rapid washout of Gadolinium contrast from the blood pool. However, use of technical modifications such as avoiding delay after contrast administration, selecting appropriately thin slices, appropriate RR interval, short acquisition window and motion compensation makes this clinically feasible. This case demonstrates the crucial role played by cardiac MRI in the diagnosis of neonatal myocardial abnormalities.

#### **Figure/Table 1**



#### **Caption 1**

**Figure 1:** Late Gadolinium enhancement imaging in the 4-chamber, short axis and 3-chamber views (from left to right respectively), showing sub-endocardial partial thickness delayed myocardial enhancement involving the AHA segments 2 and 3 (arrow)

Speaker: S. Philip

Category: Late Gadolinium Enhancement, Ventricular Function, Myocardium

000595

## **Comparison of myocardial T1 mapping from Cardiac Magnetic Resonance Fingerprinting to MOLLI for translation into clinical protocols**

B. Eck \* (1); G. Cruz, (2); C. Prieto (2); H. Friel, (3); K. Kohut, (1); C. Loy, (1); W. W. Tang, (4); D. H. Kwon, (4); S. Flamm (1)

(1) Imaging institute, Cleveland Clinic Main Campus, Cleveland, United States of America; (2) Department of biomedical engineering, King's College London, London, United Kingdom; (3) Mr clinical science, Philips Healthcare, Highland Heights, United States of America; (4) Heart, vascular, and thoracic institute, Cleveland Clinic Main Campus, Cleveland, United States of America

### **Abstract**

#### **Background**

Myocardial T1 mapping provides an objective, quantitative metric for tissue characterization that can support diagnosis and monitoring of cardiovascular disease<sup>1</sup>, for example in detection of cardiac amyloidosis<sup>2</sup>. Cardiac magnetic resonance fingerprinting (cMRF) enables myocardial T1 mapping as well as the potential to acquire additional, co-registered tissue properties in a single breath-held scan<sup>3</sup>. In this work, the use of cMRF in a real-world clinical protocol is evaluated with comparison to conventional myocardial T1 mapping as a step toward clinical translation.

#### **Methods**

Patients (N=23) were scanned under an institutional review board approved protocol on a 1.5T Philips Achieva scanner using a tissue characterization protocol that included native T1 and post-contrast T1 mapping. T1 mapping was performed by breath-held, ECG-gated (end diastole) modified Look-Locker inversion (MOLLI) acquisitions at three cardiac short axis slices (basal, mid-ventricular, apical) and voxel size of 2x2x10 mm<sup>3</sup>. T1 maps were computed using the vendor's inline processing, which included motion compensation. Pre- and post-contrast cMRF scans were performed at the mid-ventricular slice position using a breath-held, ECG-gated (end diastole), 2D radial trajectory with data acquired across 18 heartbeats at 260 ms temporal resolution and voxel size 2x2x10 mm<sup>3</sup>. Constant flip angle (15 deg), constant TR (5.2 ms), and constant TE (2.6 ms) were used. Preparation pulses were used to induce T1 and T2 sensitivity: inversion pulses at heartbeats 1 (TI=15 ms), 5 (TI=75 ms), and 9 (TI=150 ms) and T2-preparation pulses at heartbeats 11, 12, 13, 14 (T2-prep TE=30 ms), and 15, 16, 17, 18 (TE=50 ms). Scan-specific dictionaries for cMRF reconstruction were generated. T1 and T2 maps were computed using an iterative, spatially localized low rank reconstruction. Mid-ventricular T1 maps from MOLLI and cMRF were manually contoured. Segmental and average slice T1 values were analyzed. Extracellular Volume fraction (ECV) values were computed. T1 and ECV values were compared between MOLLI and cMRF by Pearson's correlation and Bland-Altman analyses.

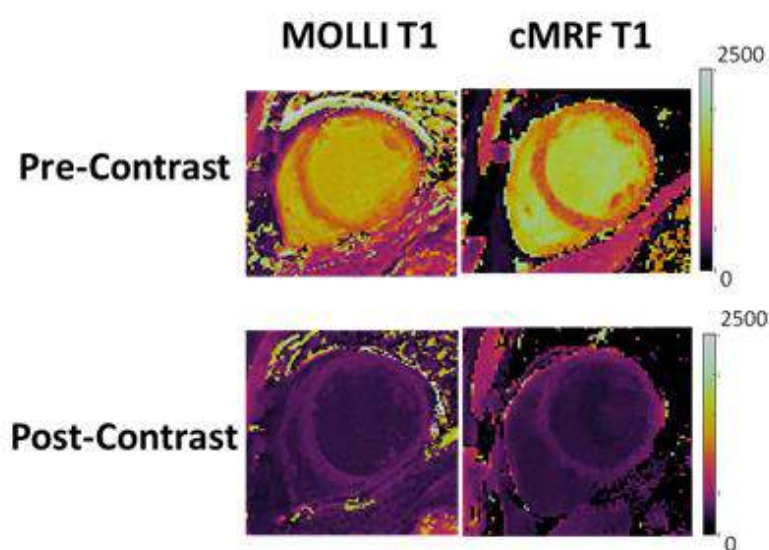
#### **Results**

Representative MOLLI and cMRF tissue property maps are shown in Figure 1. Five patients were excluded due to artifact, giving N=18 patients for subsequent analyses. Among the excluded cases, respiratory motion during cMRF acquisition was observed and suspected to be the cause of artifact and degraded image quality. Correlation and Bland-Altman analyses of remaining cases are shown in Figure 2. Segmental and slice-averaged T1 values had good agreement both pre-contrast and post-contrast, with R ranging from 0.93 to 0.99 (Table 1). ECV values computed from MOLLI and cMRF had generally moderate agreement, R between 0.51 to 0.80.

## Conclusions

Myocardial T1 values from cMRF exhibited good agreement with MOLLI in a real-world setting, although with lesser agreement for pre-contrast blood T1 and ECV values. Disagreement at long T1 values may be partially due to under-estimation of T1 by MOLLI as previously described<sup>4</sup>, although comparison of both techniques to a reference such as endomyocardial biopsy is needed. Motion compensation or cMRF protocol modifications may be needed to mitigate observed artifacts. T2 maps were simultaneously acquired by cMRF and similar real-world comparisons to clinical standard techniques, such as T2 GraSE<sup>5</sup>, are needed. Continued investigation into cMRF is needed to ensure successful translation into clinical practice.

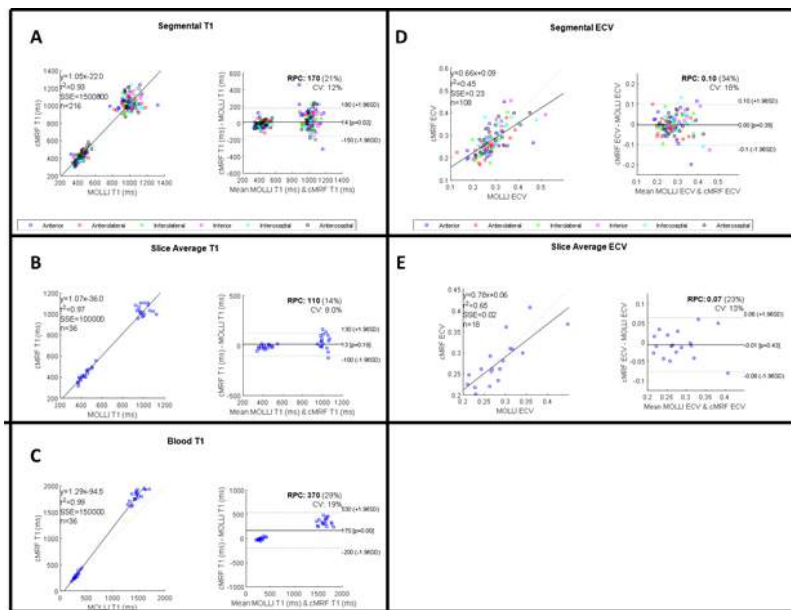
**Figure/Table 1**



**Caption 1**

Figure 1. Example MOLLI and cMRF T1 maps acquired before and after administration of gadolinium contrast material. Data were acquired at a mid-ventricular cardiac short axis orientation.

**Figure/Table 2**



**Caption 2**

Figure 2. Correlation and Bland-Altman Plots of T1 and ECV values from MOLLI and cMRF derived T1 maps. Pre-contrast and post-contrast T1 values for (A) myocardial segments, (B) slice average of myocardial voxels, and (C) left ventricle blood region of interest. ECV values for (D) myocardial segments and (E) slice average of myocardial voxels.

**Figure 3**

	Anterior	Anterolateral	Inferolateral	Inferior	Inferoseptal	Anteroseptal	Slice Average	Blood
T1	0.93	0.97	0.98	0.98	0.97	0.96	0.99	1.00
ECV	0.51	0.70	0.74	0.73	0.64	0.76	0.80	-

**Caption 3**

Table 1. Pearson correlation coefficients for MOLLI and cMRF derived values

## Bibliographic References

1. Puntmann Valentina O., Peker Elif, Chandrashekhar Y., Nagel Eike. T1 Mapping in Characterizing Myocardial Disease. *Circ Res.* 2016;119:277–299. , 2. Karamitsos TD, Piechnik SK, Bannypersad SM, Fontana M, Ntusi NB, Ferreira VM, Whelan CJ, Myerson SG, Robson MD, Hawkins PN, Neubauer S, Moon JC. Noncontrast T1 Mapping for the Diagnosis of Cardiac Amyloidosis. *JACC Cardiovasc Imaging.* 2013;6:488–497. , 3. Jaubert O, Cruz G, Bustin A, Hajhosseiny R, Nazir S, Schneider T, Koken P, Doneva M, Rueckert D, Masci P-G, Botnar RM, Prieto C. T1, T2, and Fat Fraction Cardiac MR Fingerprinting: Preliminary Clinical Evaluation. *J Magn Reson Imaging.* 2021;53:1253–1265. , 5. Sprinkart AM, Luetkens JA, Träber F, Doerner J, Gieseke J, Schnackenburg B, Schmitz G, Thomas D, Homsy R, Block W, Schild H, Naehle CP. Gradient Spin Echo (GraSE) imaging for fast myocardial T2 mapping. *J Cardiovasc Magn Reson.* 2015;17:12. , 4. Kellman P, Hansen MS. T1-mapping in the heart: accuracy and precision. *J Cardiovasc Magn Reson.* 2014;16:1–20.

Speaker: B. Eck

Category: T1 , Extracellular Volume Fraction , Accelerated Imaging

000596

## Developmental Cardiac Segmentation Revisited Using High-Resolution 4-Dimensional CMR in Children

S.-J. Yoo \* (1); G. Perens, (2); K.-L. Nguyen, (2); T. Yoshida, (3); A. Prosper, (3); A. Bedayat, (3); A. G. S. Van (4); P. Finn (5)

(1) Diagnostic imaging, Hospital for Sick Children, Toronto, Canada; (2) Medicine, University of California, Los Angeles, Los Angeles, United States of America; (3) Radiology, University of California, Los Angeles, Los Angeles, United States of America; (4) Surgery, University of California, Los Angeles, Los Angeles, United States of America; (5) Radiology, University of California Los Angeles, Los Angeles, United States of America

### Abstract

**Background:** Recent developments in 4-D CMR have enabled visualization of dynamic 3D relationships among cardiovascular structures within a larger field of view without the need for lengthy image acquisition or reconstruction time. To date, there are few reports on how such tools can inform our understanding of clinically relevant, complex functional anatomy, or how quickly expert reviewers can adapt to the new paradigm for visualization and analysis. In this study, high resolution 4-D CMR studies from 122 pediatric patients imaged at a single institution were analyzed and scored by a senior expert reviewer from an independent, external, quaternary institution who was blinded to all clinical data and correlative imaging.

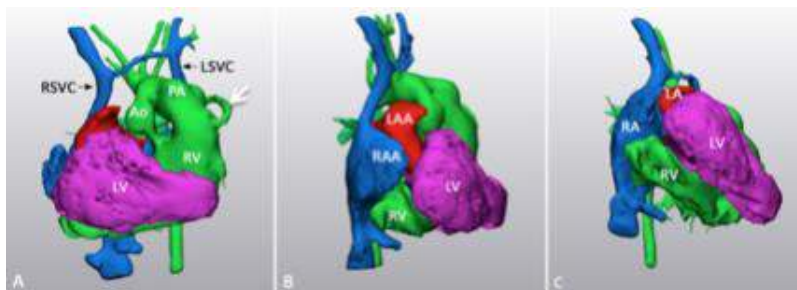
**Methods:** An expert reviewer with >40 years experience in advanced imaging of pediatric congenital heart disease analyzed 4-D MUSIC (1,2) images in 122 patients, acquired at a separate academic medical center. The reviewer had access to the complete, anonymized DICOM sets in all patients and performed an analysis on a Mac-OsiriX workstation. The MUSIC images had spatial resolution between 0.5 mm<sup>3</sup> to 1.0 mm<sup>3</sup>, depending on patient size. The workstation enabled rapid reconstruction of 2D cine images in any plane, as well as MIP and 4D volume rendered reconstruction. The reviewer graded overall image quality on a four-point scale and then used a standard sequential segmental approach for determination of situs, atrioventricular and ventriculoarterial connections, and assessment of associated lesions involving the systemic and pulmonary veins, atria, ventricles, arterial trunks, coronary arteries and systemic and pulmonary arterial branches.

**Results:** Patient age range was 1 day – 3.5 years (1.5 years +/- 2.7 ). There were 62 females and 60 males. The image quality was graded excellent in 98 of 122, good in 19 of 122, acceptable in 4 of 122 and poor in 1 of 122. The diagnoses spanned a wide spectrum of congenital heart diseases including heterotaxy (n=12 cases), tetralogy of Fallot (n=14), transpositions (n=9), various forms of left sided obstructive lesions (n=26), isolated septal defects (n=17) and vascular rings (n=9). A full sequential segmental approach was feasible in all cases. Determination of situs at three hierarchical levels was possible in all except 3 patients including one whose abdominal and bronchopulmonary situs was indeterminate and two patients whose atrial appendage situs was unclear. The atrioventricular connection was defined in all patients. The ventriculoarterial connection was defined in all except one patient. A dynamic 3D volume rendered movie display provided intuitive visualization of complex anatomic anomalies. The resulting contextual overview of the pathology was particularly

helpful in identification of small structures such as severely stenotic right ventricular outflow tract. Display of thin MIP images in cine format allowed anatomic and functional assessment of cardiac valves. Observed limitations of 4-D MUSIC included 1) difficult diagnosis of small secundum atrial septal defect and small perimembranous ventricular septal defect, 2) incomplete visualization of the coronary artery origins in some neonates (n=18), and 3) poor delineation of the tracheobronchial tree.

**Conclusion:** In one high resolution DICOM dataset comprising multiphase, volumetric images, 4D MUSIC provided sufficient detail for an expert reviewer to perform confident segmental cardiac analysis across a full spectrum of congenital heart disease in 122 patients. The reviewer adapted quickly to the 4-D viewing environment for all cardiac sub-structures, and concluded that the technique provided unique insight into global chamber dynamics and time-varying stenoses.

**Figure/Table 1**



**Caption 1**

Diastolic phase, 3D model reconstructed from 4-D CMR in a 6 month old patient with complex CHD. In this rare anomaly, cardiac chamber and vascular anatomy is clearly visualized.

## Bibliographic References

2. Nguyen KL, Rigsby CK, Whitehead KK, et al. 4D Multiphase, Steady-state MRI with Ferumoxytol Enhancement: Early Multicenter Feasibility in Pediatric Congenital Heart Disease. *Radiology* 2021 Apr 20:203696., 1. Han F, Rapacchi S, Khan S, et al. 4-dimensional, Multiphase, Steady-state Imaging with Contrast Enhancement (MUSIC) in the Heart; a Feasibility Study in Children. *Magn Reson Med*. 2015 Oct;74(4):1042-9.

Speaker: S.-J. Yoo

Category: Children, Ferumoxytol, Congenital Heart Disease

000597

## **Use of augmented MR-fluoroscopy overlay guidance for trans-venous pacemaker placement in a congenitally complex heart**

R. Vamsee, \* (1); M. Fares (2); M. Abdulkarim (2); H. H. Nguyen, (2); T. Hussain, (3)

(1) Pediatrics, UT Southwestern Medical Center, Dallas, United States of America; (2) Pediatric cardiology, UT Southwestern Medical Center, Dallas, United States of America; (3) Pediatric cardiology, Children's Medical Center Dallas, Dallas, United States of America

### **Abstract**

#### **Description of Clinical Presentation**

A 14-year-old male teenager was referred to the pediatric electro-physiology clinic for evaluation of bradycardia. Further evaluation by history, examination, electrocardiogram and an echocardiogram suggested a complete heart block in a congenitally anomalous heart with atrial situs inversus, L-looped ventricles and I-looped great arteries ({I;L;I} dextrocardia) (Fig. 1). Based on evidence of LV dilation, and an escape junctional heart rate < 40 bpm, a decision was made to implant a cardiac pacemaker via a trans-venous approach. Due to the complexity of the anatomy, with inverted atria and ventricles, change in venous connections and an alteration of the plane of the ventricular septum, a cardiac MRI was obtained to delineate anatomy; and help guide the electrophysiologist successfully deploy a trans-venous dual-chamber pacemaker using a rather novel technique of MR-fluoroscopy augmented overlay guidance.

#### **Diagnostic Techniques and their most important findings**

Using a 1.5T Philips Ingenia scanner (Philips Healthcare, Best, NL), a respiratory navigated and diastolic ECG gated 3D balanced SSFP sequence with TE/TR = 1.02/2.04 ms, and 1.8 mm voxel size was obtained. The DICOM data thus obtained was used to segment 3D stereolithography models of the heart including the right and left ventricles, along with the venous connections into the atria; and the trachea. The patient was brought to the cardiac catheterization suite, and placed under anesthesia. The 3D stereolithography models were loaded into the Siemens overlay fluoroscopy system [Guide CCI system©, Siemens Healthcare, Erlangen, Germany] (Fig. 2).

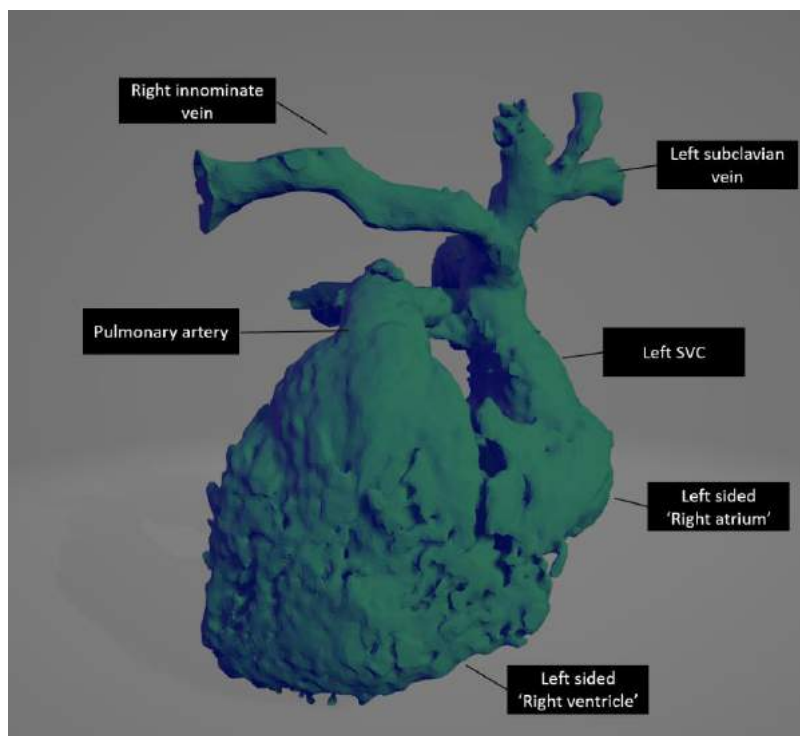
The electrophysiologist obtained access into the left subclavian vein, and using the augmented system displaying a fusion image of the heart and the radiographic image, was able to successfully guide the pacemaker leads into the morphological right atrial appendage and the right ventricular septal surface across the tricuspid valve without any complications (Fig. 3). The system also allowed for attempts to place the ventricular lead at the Bundle of His, but failed due to the difficult anatomic orientation. The patient tolerated the procedure and has since done well clinically over the last 3 months, with normal lead function, no symptoms, and no exercise intolerance.

#### **Learning points from this case**



Placement of trans-venous pacemaker systems is an art that the electrophysiologists have perfected in anatomically normal hearts. However, the radiographic landmarks that they are adept with are often different in children and young adults with congenital heart disease, especially in such cases where the venous connections to the atria and atrio-ventricular connections are variable. While 3D echocardiographic guidance has proved useful in the past [1], the availability and ease of use of advanced cardiac imaging, and overlay provides not just the ability to plan these procedures in advance, but also essentially a ‘real-time’ guidance of anatomic landmarks. This technology has substantial potential for reducing dose of ionizing radiation and improved chance of procedural success.

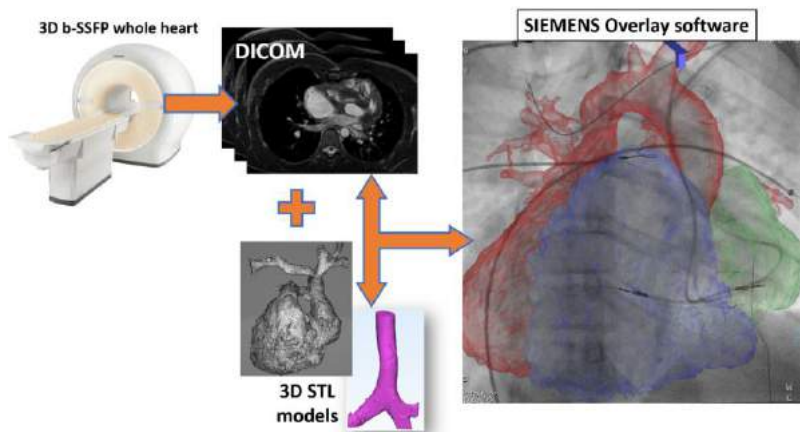
**Figure/Table 1**



**Caption 1**

A 3D stereolithographic model depicting the patient's morphological right heart structures; with the systemic upper body veins emptying into a left sided SVC, which in turn joins the left sided morphologic right atrium, and right ventricle. Note that the plane of the inter-ventricular septum hence faces posterior.

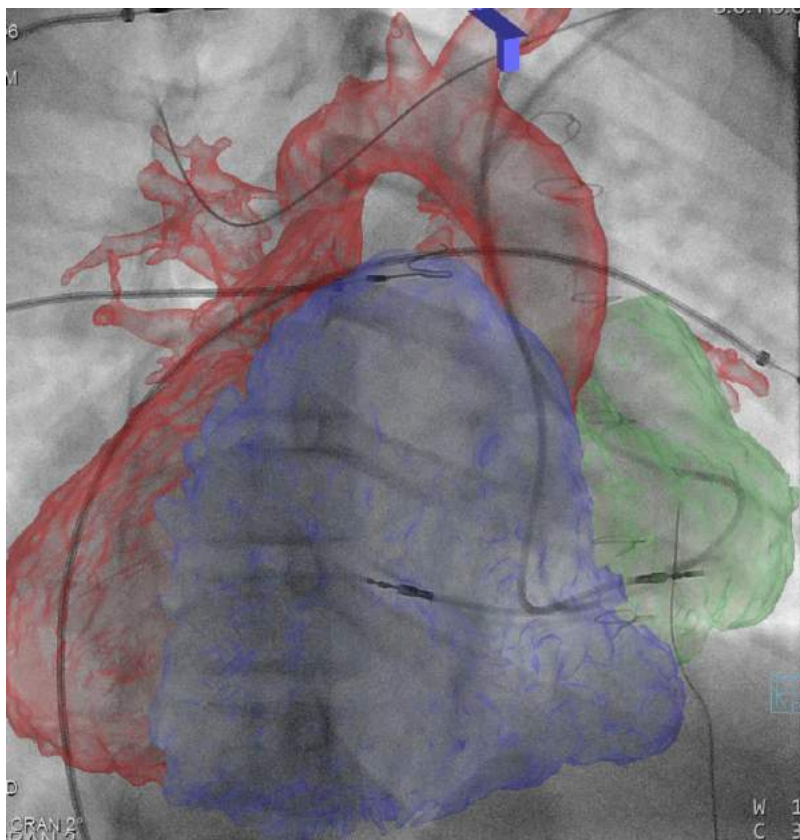
**Figure/Table 2**



## Caption 2

The DICOM images acquired by CMR imaging are used to generate 3D stereolithography (STL) models which are in turn loaded into the Siemens overlay software, with the trachea used for fluoroscopic geographic registration.

## Figure 3



### **Caption 3**

The fusion overlay augmented model generated thus was used for guidance; and shows the final position of the atrial lead in the morphologic right atrial appendage (green) and the right ventricular (blue) lead on the septal surface. The left heart structures are depicted in red to show the plane of the septum.

### **Bibliographic References**

[1] Burkett, Dale A., Pei-Ni Jone, and Kathryn K. Collins. "Transesophageal 3-Dimensional Echocardiographic Guidance for Pacemaker Lead Placement." *JACC: Case Reports* 1.3 (2019): 391-393.

Speaker: R. Vamsee,

Category: Congenital Heart Disease, Interventional CMR, Pacemaker

**000599**

## **The Hidden Ramus Uncovered!**

R. DSouza \* (1); B. Chacko, (1)

(1) Cardiothoracic radiology, University of Toronto, Toronto, Canada

### **Abstract**

#### **Description of Clinical Presentation:**

A 33 year old male with no cardiovascular risk factors or family history of cardiovascular disease presented with sudden onset ,non exertional, non pleuritic chest pressure, sweating, shortness of breath and symptomatic hypotension. He received a second dose of mRNA Covid-19 vaccination 14 days prior to presentation.

ECG showed T wave inversion and mild ST depression in the inferior leads, with high sensitivity troponin T peaking at 1787ng/L (normal<15ng/L). Acute coronary syndrome, despite his young age was the primary clinical diagnosis and viral, idiopathic and vaccine related myocarditis remained possible alternatives.

Echocardiogram showed mildly reduced left ventricular ejection fraction (LVEF), 48% with subtle lateral wall hypokinesis. Catheter angiogram on the following day was essentially normal. MRI was therefore performed in the hope of confirming myocarditis, the presumed diagnosis. Surprisingly however, we found features that were not definitively non-ischemic, with in fact differential considerations favouring an ischemic event.

This led to a more detailed review of the angiogram, which on retrospect delineated a late filling vessel, identified as an occluded ramus intermedius. Although not amenable to angioplasty, this confirmed the diagnosis of a non-ST elevation myocardial infarction.

#### **Diagnostic Techniques and Their Most Important Findings:**

Our institution CMR protocol was performed on day 2 of symptoms. Functional assessment using bSSFP sequence in standard cardiac planes and in the short-axis showed low normal left ventricular function, LVEF 52%, with mild persisting hypokinesia.

Edema imaging using double inversion-recovery turbo-spin-echo confirmed edema in the hypokinetic segments as well as the anterolateral papillary muscle (figure 1).

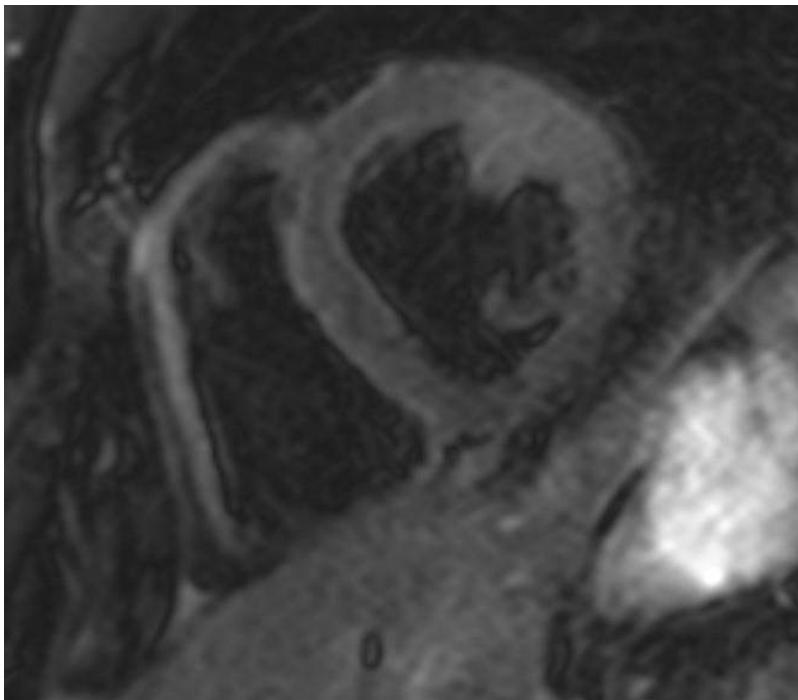
Late gadolinium enhancement acquired 10 minutes post injection of 10ml of Gadovist demonstrated transmural enhancement of the edematous segments (figure 2).

#### **Learning Points from this Case:**

Discerning an angiographically negative, 2-3 segment infarct from myocarditis can be a difficult conundrum. Young age and low cardiovascular risk further eludes the reader. The following are therefore important for an imager to keep in mind.

1. Isolated edema and enhancement in a vascular territory including branch vessels territories (diagonal/obtuse marginal/ramus intermedius territories) must be kept in mind to reaffirm ischemic etiology(1).
2. The involvement of the papillary muscle is more commonly, although not exclusively, ischemic in etiology(2).
3. COVID-19 vaccine related myocarditis is usually reported within 7 days, therefore history and time frame can also provide diagnostic clues(3).
4. A negative angiogram does not exclude an ischemic event. When presented with MRI evidence which could represent an infarct, discussion with the referring physician and considering possibilities of angiographically occult lesions including complete vascular occlusions, spasm or SCAD could help reach a definitive diagnosis.

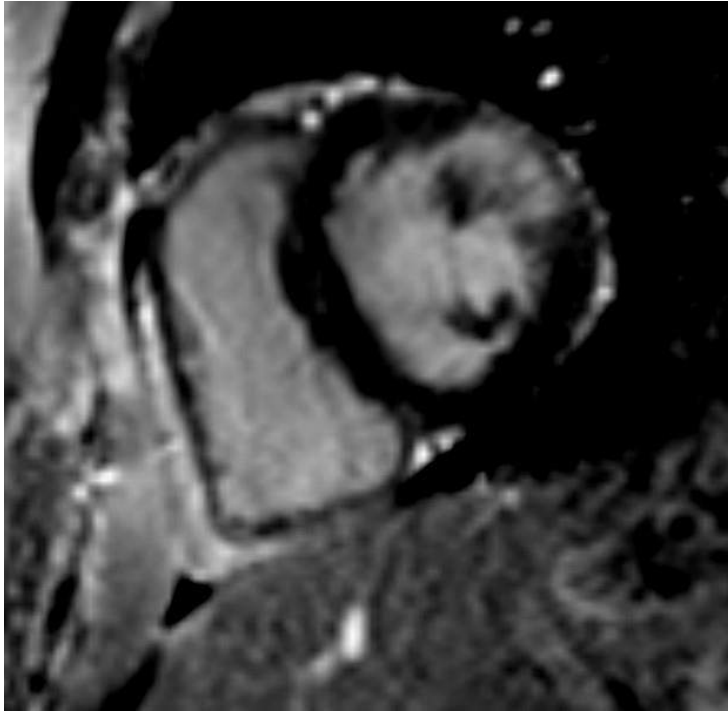
**Figure/Table 1**



**Caption 1**

Figure 1: Double inversion-recovery turbo-spin-echo image in short axis in the mid cavity demonstrating increased signal in the anterolateral wall and papillary muscle.

**Figure/Table 2**



## Caption 2

Figure 2: LGE in short axis in the mid cavity showing transmurial enhancement in the anterolateral segment (proven ramus intermedius territory).

## Bibliographic References

1. Young PM, Gerber TC, Williamson EE, Julsrud PR, Herfkens RJ. Cardiac imaging: Part 2, normal, variant, and anomalous configurations of the coronary vasculature. *AJR Am J Roentgenol.* 2011 Oct;197(4):816-26. doi: 10.2214/AJR.10.7249. PMID: 21940568., 2. Rajiah, P., Fulton, N.L. & Bolen, M. Magnetic resonance imaging of the papillary muscles of the left ventricle: normal anatomy, variants, and abnormalities. *Insights Imaging* 10, 83 (2019). <https://doi.org/10.1186/s13244-019-0761-3>, 3. Public Health Ontario. Adverse Events Following Immunization (AEFIs) for COVID-19 in Ontario: December 13, 2020 to June 12, 2021 [Internet]. [Modified 2021 Jun 17, Cited 2021 Jun 17].

Speaker: R. DSouza

Category: Acute Myocardial Infarction, Myocarditis, Acute Coronary Syndrome

000600

## **A Fully Automated Post-Processing Tool Identifies a Reduced Global Myocardial Oxygenation Reserve in Patients with Ischemia and No Obstructive Coronary Artery Stenosis When Compared to Patients with Significant CAD**

E. Hillier \* (1); K. Lindsay (1); M. Friedrich (2)

(1) Medicine, McGill University Health Centre Glen Site (MUHC), Montréal, Canada; (2) Departments of Medicine and Diagnostic Radiology, Division of Experimental Medicine, Centre Universitaire de Santé McGill Site Glen, Montréal, Canada

### **Abstract**

#### **Background:**

Oxygenation-Sensitive Cardiac Magnetic Resonance (OS-CMR) has been used to assess the myocardial tissue oxygenation status of patients with significant coronary artery disease (CAD) and patients with ischemia and no obstructive coronary artery stenosis (INOCA) independently (1,2). A new post-processing analysis tool has been developed to fully automate the analysis of OS-CMR images. This study utilized the fully automated tissue oxygenation module (TOM) to assess global differences in oxygenation-based biomarkers in patients with and without significant CAD.

#### **Methods:**

38 patients with significant CAD (as defined by quantitative coronary angiography (QCA) > 75%) and 15 patients without significant obstructive CAD (as defined by QCA < 75%) were recruited from the McGill University Health Centre and analyzed. All participants had a positive stress test and underwent a non-contrast CMR exam on a clinical 3T Siemens Skyra MRI system (Siemens Healthineers, Erlangen, Germany) within one week of a coronary angiography. Manual analysis of the myocardial oxygenation reserve (MORE) was performed as previously described (3). Fully automated analysis of OS-CMR images was performed with a TOM prototype build of cvi42 (Circle Cardiovascular Imaging, Alberta, Canada).

#### **Results:**

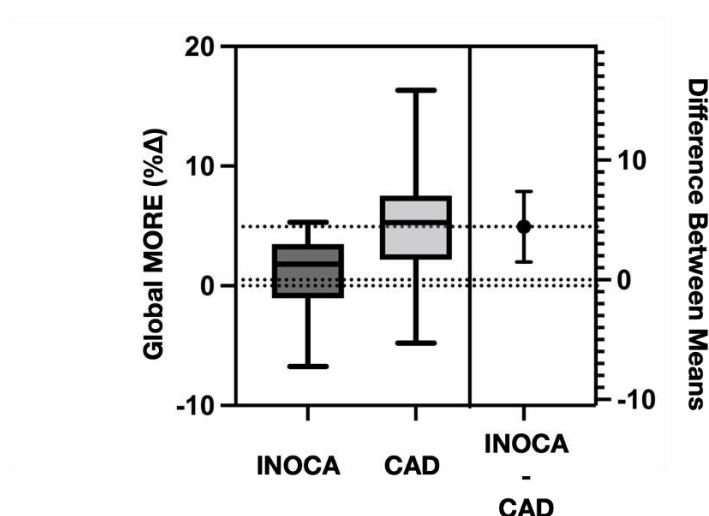
There was no difference in age or BMI between patients with significant CAD (age:  $62.6 \pm 10.1$ , BMI:  $28.0 \pm 4.2$ ) or INOCA (age:  $61.5 \pm 9.8$ , BMI:  $25.8 \pm 2.27$ ). No difference in global MORE was found between a manual and novel fully automated post-processing module for OS-CMR images. Patients with INOCA had a reduced global MORE with both manual (CAD:  $6.0 \pm 4.9$ , INOCA:  $2.9 \pm 2.5$ ,  $p=0.03$ ) and fully automated (CAD:  $4.9 \pm 4.1$ , INOCA:  $0.5 \pm 4.1$ ,  $p=0.004$ ) analysis methods when compared to patients with significant CAD.

## Conclusion:

Patients with INOCA have a global reduction in myocardial oxygenation reserve when compared to patients with significant CAD. This finding may point to the presence of a more global underlying pathophysiologic process in INOCA when compared to the regional oxygenation abnormalities observed in CAD. A fully, automated post-processing tool for the assessment of tissue oxygenation status will decrease analysis time and may allow for the assessment of novel OS-CMR derived biomarkers.

**Figure/Table 1**

### **Estimation Plot of Global Myocardial Oxygenation Reserve in Patients With INOCA and Patients With CAD**



**Caption 1**

The comparison of global myocardial oxygenation reserves in patients with ischemia and no obstructive coronary artery stenosis and patients with significant coronary artery disease assessed with oxygenation-sensitive CMR.

## Bibliographic References

3. Fischer K, Guensch DP, Friedrich MG. Response of myocardial oxygenation to



breathing manoeuvres and adenosine infusion. Eur Heart J Cardiovasc Imaging. 2015 Apr;16(4):395–401. , 2. Elharram Malik, Hillier Elizabeth, Hawkins Selwynne, Mikami Yoko, Heydari Bobak, Merchant Naeem, et al. Regional Heterogeneity in the Coronary Vascular Response in Women With Chest Pain and Nonobstructive Coronary Artery Disease. Circulation. 2021 Feb 16;143(7):764–6. , 1. Fischer K, Yamaji K, Luescher S, Ueki Y, Jung B, von Tengg-Kobligh H, et al. Feasibility of cardiovascular magnetic resonance to detect oxygenation deficits in patients with multi-vessel coronary artery disease triggered by breathing maneuvers. J Cardiovasc Magn Reson. 2018 May 7;20(1):31.

Speaker: E. Hillier

Category: BOLD , Cardiac Syndrome X, coronary Artery Disease

000601

## Clinical and CMR Characteristics of Patients with Tako-Tsubo Cardiomyopathy versus Myocarditis in a Latin-American Center

S. Higuera \* (1); D. Valderrama-Achury (1); C. E. Guerrero-Chalela (1); H. M. Medina (1)

(1) Departamento de cardiología, Fundacion Cardio Infantil Instituto De Cardiologia, Bogotá, Colombia

### Abstract

**Background:** Differentiation between Tako-Tsubo cardiomyopathy (TKSC) and myocarditis remains challenging. Optimal management strategies between these two entities requires high diagnostic yield. We sought to describe clinical and imaging characteristics of patients presenting with acute chest pain of non-ischemic etiology.

**Methods:** Between June 2016 and July 2021, a total of 1308 in-hospital CMR's were performed in our institution. Patients with a final diagnosis of TKSC or myocarditis were included. Data on clinical characteristics was collected from our electronic medical record system and CMR analyses were done blindly by two independent readers.

**Results:** A total of 88 patients had either TKSC (19%) or myocarditis (81%). Mean age was  $48.8 \pm 15.4$  years-old and 51.1% were female (n=45). Mean peak troponin levels were 10.4 ng/dl (ULN 0,014 ng/dl), and 23.8% (n=21) presented on the ECG with ST segment elevation. On CMR, mean LVEF was  $51.4\% \pm 8.5$ . Significant differences were found between groups as described in Table 1. Of note, patients with TKSC tended to be older, with female predominance, had lower TnI, lower LVEF, higher LVESVi and less segments with LGE. Three patients presented with cardiogenic shock, and one of them required ventricular assist device with ECMO (all in the TKSC group). There was no in-hospital mortality in both groups.

**Conclusions:** CMR is an essential tool to differentiate patients presenting with MINOCA, particularly those ultimately diagnosed with TSKC and myocarditis. There are substantial differences in clinical characteristics between these two conditions. However, using CMR as the gold standard for non-invasive imaging assessment, is required for accurate diagnosis and treatment. More efforts are needed in Latin America to implement CMR into clinical practice.

Figure/Table 1

Characteristics	All Patients (n= 88)	TKSC (n= 17)	Myocarditis (n= 71)	P-value
Age $\pm$ SD	48.8 $\pm$ 15.4	65.7 $\pm$ 11.2	44.7 $\pm$ 13.3	<0.000
Female (%)	51.1	94.1	40.8	<0.000
Mean peak TnI $\pm$ SD	10.4 $\pm$ 19.1	2.1 $\pm$ 2.6	12.3 $\pm$ 20.7	0.002
STEMI on admission ECG (%)	23.8	17.6	25.3	0.503
LVEDVi (ml/m <sup>2</sup> )	81.9 $\pm$ 16.1	89.0 $\pm$ 21.1	80.2 $\pm$ 14.3	0.116
LVESVi (ml/m <sup>2</sup> )	39.9 $\pm$ 11.4	47.9 $\pm$ 14.7	38.0 $\pm$ 9.6	0.015
LVEF $\pm$ SD	51.4% $\pm$ 8.5	46.6 $\pm$ 8.5	52.6% $\pm$ 8.2	0.015
Myocardial edema (%)	90.9	82.3	92.9	0.172
LGE (No. segments)	3.1 $\pm$ 2.8	0.5 $\pm$ 1.6	3.7 $\pm$ 2.7	<0.000

## **Caption 1**

Clinical and CMR Characteristics of patients presenting with TKSC and Myocarditis

Speaker: S. Higuera

Category: Myocarditis, Nonischemic Cardiomyopathy, Cardiomyopathy

000603

**Systemic baffle stenosis in d-TGA S/P Mustard patient complicated by extensive venous collaterals**

M. Nagiub, \* (1); R. Vamsee, (1); T. Hussain (1); A. Tandon (1)

(1) Pediatric cardiology, UT Southwestern Medical Center, Dallas, United States of America

**Abstract**

**Description of Clinical Presentation:** This is a 32-year-old male with a past medical history of d-transposition of the great arteries, who underwent an atrial switch (Mustard) surgery at 5 month old. He had a cardiac MRI at an outside institution in 03/2015 for progressive fatigue and lower extremity edema which showed mild superior (11 x 10 mm) and mild-moderate (14 x 8 mm) inferior systemic venous baffle narrowing. RVEF was 26% and the left atrium was small. The abdomen was not interrogated.

In 05/2015 he was admitted for the first time for atrial flutter, and cardioverted. He had an ablation attempt in 07/2015, but the procedure was aborted because the team could not “access his heart due to occluded veins.” This was followed by multiple cardioversions, and he is currently being treated for chronic atrial fibrillation with amiodarone and apixaban. Since 2015 he has had progressive ascites, hepatomegaly, bilateral pitting edema, and secondary varicose veins. At his last clinic visit, his oxygen saturation was 98%. His CXR continued to be unremarkable. His team at the outside hospital was planning another ablation attempt with hepatic access and baffle puncture. To further evaluate the ascites, hepatomegaly, and ventricular function, he was referred for cardiac MRI at our institution.

**Diagnostic techniques:**

EKG: atrial flutter with 2:1 AV conduction at rate of 129 beats/min with right axis deviation, right ventricular hypertrophy, and right bundle branch block.

Cardiac MRI 2015: mild superior and inferior systemic venous baffle obstruction as above.

Cardiac MRI 2021: The patient underwent a comprehensive, ferumoxytol contrast cardiovascular MRI to assess ventricular size and function and systemic and pulmonary venous baffles. Given his atrial fibrillation, we paid special attention to the systemic venous baffles and atrial size. Given his ascites, we evaluated the IVC and abdominal vasculature. To help plan for future interventions, we also assessed the pelvic systemic venous return.

We found that the systemic right ventricle was dilated (RVEDVi 110.2 ml/m<sup>2</sup>), had severely depressed systolic function (EF 16%), and severely hypertrophied. The pulmonary left ventricle was small with moderately depressed systolic function (LVEDVi 46 ml/m<sup>2</sup>, LVEF 30 %). The pulmonary right atrium was dilated.

More interestingly, he had severe narrowing (7.5 mm x 5 mm) of the SVC before joining systemic baffle (8.67 mm x 5 mm)(Figure 1). He had bilateral internal and external jugular venous thrombosis with extensive collateralization in the supraclavicular area. His bilateral femoral veins were not identified. He has impressive collateral veins in groins, subcutaneous abdomen, and in particular, a very large, tortuous venous collateral that courses through the

abdominal cavity and joins renal vein to reconstitute the IVC(Figure 2). Three hepatic veins enter the IVC. This suggests that systemic venous access for a procedure would be impossible from the groin, and hepatic venous access would also be challenging but possible.

**Learning points:** Cardiac MRI can provide multiple types of information for a given clinical scenario. In this single study, we were able to assess ventricular function, systemic venous baffle obstruction, and help plan for future interventions. Especially when a patient with complex anatomy (e.g. atrial switch or Fontan) undergoes a ferumoxytol study, we evaluate venous access to help plan for future interventions (including cardiac catheterization, ablation, and ECMO cannulation).

**Figure/Table 1**



**Caption 1**

Figure 1: severe narrowing (7.5 mm x 5 mm) of the SVC before joining systemic baffle (8.67 mm x 5 mm)

## Figure/Table 2



## Caption 2

Figure 2:collateral veins in groins, subcutaneous abdomen, and in particular, a very large, tortuous venous collateral that courses through the abdominal cavity and joins renal vein to reconstitute the IVC

Speaker: M. Nagiub,

Category: Atrial Switch, Transposition of the Great Arteries, Atrial Fibrillation

**000604**

## **Utility of delayed enhancement in neonatal myocardial dysfunction**

N. Misra \* (1); S. Jhaveri, (2); H. Rajagopal, (2)

(1) , Cohen Children's Medical Center, 76th Avenue, New Hyde Park, United States of America; (2) Pediatric cardiology, Cohen Children's Medical Center, New Hyde Park, United States of America

### **Abstract**

#### **Clinical Presentation**

Full term, large for gestational age female had a prenatal diagnosis of biventricular hypertrophy on fetal echocardiogram done for maternal gestational diabetes. Post-natal echocardiogram showed moderate right ventricular hypertrophy, otherwise normal cardiac anatomy. EKG performed on day of life (DOL) 0 was concerning for prolonged QTc with repeat EKG at DOL 2 showing normalization of QTc but with new ST depression in precordial leads. Repeat echocardiogram showed moderately depressed LV systolic function with no arch or outflow obstruction. The origins of the coronary arteries were thought to be normal. She became increasingly tachypneic. Cardiac biomarkers (troponins and proBNP) were elevated and continued to trend up. Given her worsening clinical course, work up for myocarditis and cardiomyopathy was started. Due to persistently depressed function of unknown etiology, cardiac MRI was performed on DOL 5 to assess for possible myocarditis.

#### **Diagnostic Techniques and their most important findings**

Cardiac MRI showed the following:

LV/ RV end diastolic volume ratio was 1.6. Dilated left ventricle (LVEDVi: 57.8 mL/m<sup>2</sup>) with moderate decrease in the global left ventricular systolic function (LVEF: 31.7%). Normal right ventricular volumes and systolic function. Basal portion of the left ventricle had better contractility than mid and apical portions. There was hypokinesia of lateral and inferior walls of left ventricle from below the papillary muscles to apex and the interventricular septum.

T1w with and without fat saturation sequences: No evidence of fibrofatty infiltration.

T2w with fat saturation sequences: There was increased signal intensity in the sub endocardial region of the left ventricle from below the papillary muscle to the apex.

Resting first pass perfusion sequences: The papillary muscles and the sub endocardial region of the lateral wall in the apex showed perfusion deficits.

Early gadolinium enhancement sequences (Ti: 600 msec): No evidence of hyperemia.

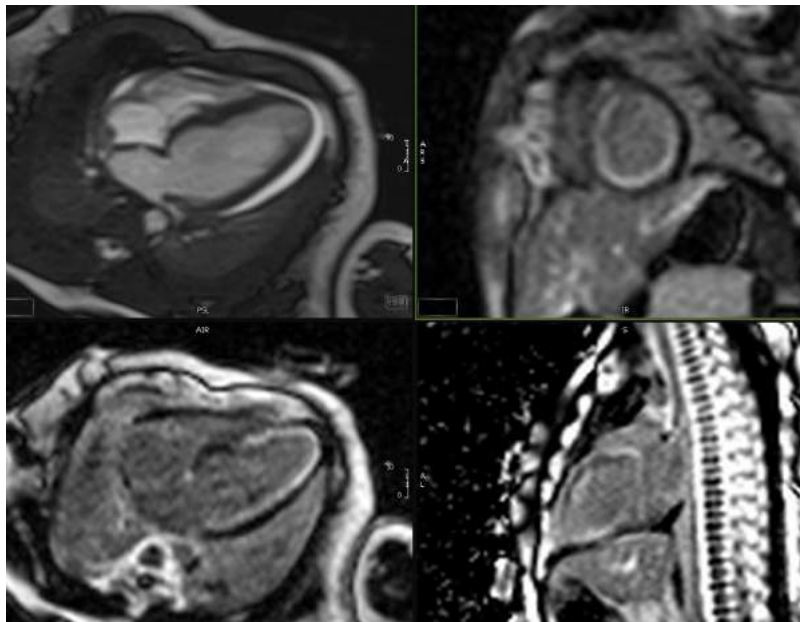
Late gadolinium enhancement sequences: Global subendocardial hyperenhancement (involving all segments) from below the papillary muscle level to the apex with extension into the myocardium (seen in short axis stacks, 4-chamber and 2-chamber views). In the basal and mid ventricular level there was subendocardial/mid myocardial hyperenhancement of the postero-lateral walls with sparing of the interventricular septum and anterior walls.

This was suggestive of ischemia in circumflex and left anterior descending arteries distribution. Cardiac catheterization confirmed anomalous origin of the left coronary artery from pulmonary artery (ALCAPA) with LCA originating from MPA-RPA junction.

### Learning Points

She underwent a successful repair with reimplantation of LCA to the left coronary sinus with normalization of left ventricular systolic function. ALCAPA is a rare congenital coronary anomaly. The infant form usually presents around 6-8 weeks of life when the pulmonary vascular resistance drops with resultant reversal of flow in the left coronary and left ventricular ischemia. This case highlights the additive value of CMR in unusual presentations (timing of presentation in this case) of rare congenital anomalies particularly when echocardiography is not diagnostic.

### Figure/Table 1



### Caption 1

Subendocardial enhancement on Late gadolinium enhancement sequences.

Speaker: N. Misra

Category: Coronary Anomaly, Acute Myocardial Infarction, Late Gadolinium Enhancement



000605

## Diastolic Dysfunction Assessment By CMR Strain Rate Imaging Reveals Differences In Between Hypertrophic Phenotypes Of Fabry's Disease and Hypertensive Heart Disease

M. Halfmann \* (1); E. Wolf (1); C. Kampmann (2); S. Altmann (1); K.-F. Kreitner (1); C. Dueber (1); T. Emrich (3)

(1) Radiology, University Medical Center Mainz, Mainz, Germany; (2) Pediatric cardiology, University Medical Center Mainz, Mainz, Germany; (3) Department of radiology and radiological science, Medical University of South Carolina, Charleston, United States of America

### Abstract

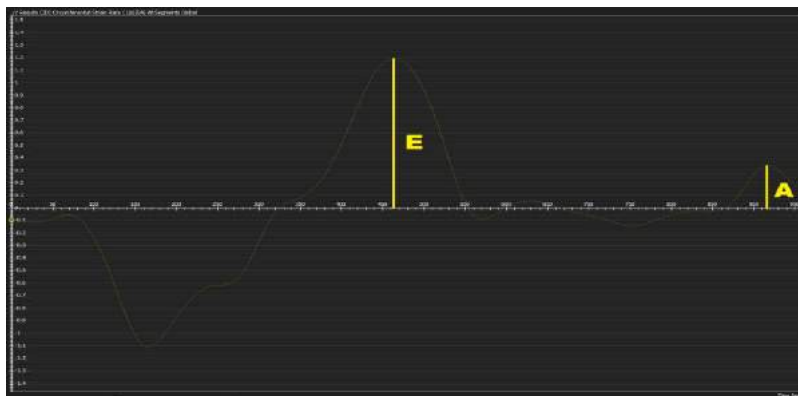
**Background:** Several diseases such as Fabry's disease (FD) and hypertensive heart disease (HHD) lead to myocardial hypertrophy in later stages of disease. However, both diseases differ significantly in their underlying pathomechanism: While FD is characterized by a systemic deposition of sphingolipids that accumulate in the myocardium over the time (1), HHD causes adverse remodeling of the myocardium as a result of chronic pressure overload (2). Ultimately, both disease lead to the development of myocardial stiffening due to fibrosis, diastolic dysfunction and subsequently adverse events. In this study, we aim to evaluate differences in diastolic function assessment between both diseases using feature tracking strain rate imaging.

**Methods:** 20 FD patients with a proven disease causing mutation and signs of severe myocardial involvement ( $56.3 \pm 13.2$  years, 9 (45%) female), and 44 patients with HHD ( $60.2 \pm 13.4$  years, 11 (25%) female) were retrospectively identified from our institutional database. 62 prospectively recruited individuals ( $54.3 \pm 14.7$  years, 34 (55%) female) served as healthy control (HC) group. In addition to clinical standard CMR evaluation including left ventricular and atrial volumetry, T1 mapping, and LGE assessment, feature tracking strain analysis was performed using a commercial available software solution (Circle cvi, Version 5.11). Strain rate curves were utilized to assess diastolic function by assessing passive and active ventricular filling (E- and A-Wave) and calculating of E/A strain rate ratios (Fig. 1).

**Results:** FD and HHD had similar indexed LV myocardial mass ( $92.5 \pm 31.5$  g/m<sup>2</sup> vs  $87.5 \pm 21.1$  g/m<sup>2</sup>,  $p > 0.05$ ), which was significantly higher compared to the HC group ( $58.7 \pm 8.9$  g/m<sup>2</sup>,  $p < 0.001$  for both). FD patients showed similar E/A strain rate ratios compared to HC (FD vs HC:  $4.2 \pm 3.6$  vs  $2.4 \pm 1.6$   $p = 0.09$ ), but HHD showed reduced E/A strain rate ratios compared to both other groups (HHD vs HC vs HD:  $1.4 \pm 1.3$  vs  $4.2 \pm 3.6$  vs  $2.4 \pm 1.6$ ;  $p < 0.01$  for both) (Fig 2a). This relation was mainly driven by a significant reduction of the A wave in FD compared to HC and HHD (FD vs HC vs HHD:  $0.4 \pm 0.2$  vs  $0.6 \pm 0.2$  vs  $0.5 \pm 0.3$ ;  $p < 0.05$  for both) (Fig 2b), and a reduction of the E wave in HHD compared to FD and HC (FD vs HC vs HHD:  $0.9 \pm 0.4$  vs  $1.1 \pm 0.3$  vs  $0.6 \pm 0.3$ ;  $p < 0.01$  for both) (Fig 2c).

**Conclusions:** Despite FD and HHD both lead to left ventricular hypertrophy and stiffening caused by myocardial fibrosis, assessment of diastolic dysfunction using strain rate ratios identified significant differences in between both diseases and healthy controls: FD is characterized by a pseudo-normalization of the E/A strain rate ratio, caused by a reduction of the A-wave, suggesting an co-existing impairment of atrial function in FD. In contrast, HHD caused a reduction in passive ventricular filling (reduction of E-wave) as a sign of disturbed myocardial relaxation, while preserving active ventricular filling by active atrial contraction. Therefore, E/A ratio should be used carefully to assess diastolic dysfunction in FD.

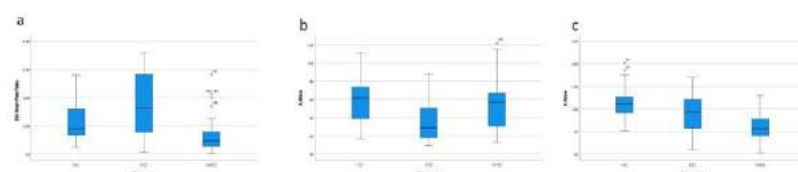
**Figure/Table 1**



**Caption 1**

Strain Rate Curve in a healthy volunteer demonstrating assessment of passive (E-Wave) and active (A-Wave) ventricular filling

**Figure/Table 2**



**Caption 2**

Comparison of E/A strain rate ratio, A- and E-Wave in between HC, FD and HHD

### **Bibliographic References**

2) Tadic M, Cuspidi C, Plein S, Milivojevic IG, Wang DW, Grassi G, Mancia G. Comprehensive assessment of hypertensive heart disease: cardiac magnetic resonance in focus. *Heart Fail Rev.* 2020 Mar 13. doi: 10.1007/s10741-020-09943-x. Epub ahead of print. PMID: 32170529., 1) Perry R, Shah R, Saiedi M, Patil S, Ganesan A, Linhart A, Selvanayagam JB. The Role of Cardiac Imaging in the Diagnosis and Management of Anderson-Fabry Disease. *JACC Cardiovasc Imaging.* 2019 Jul;12(7 Pt 1):1230-1242. doi: 10.1016/j.jcmg.2018.11.039. Erratum in: *JACC Cardiovasc Imaging.* 2019 Sep;12(9):1903. PMID: 31272606.

Speaker: M. Halfmann

Category: Fabry Disease, Hypertensive Heart Disease, Diastole